JOURNAL OF THE ELECTROCHEMICAL SOCIETY

VOL. 129, NO. 7 JULY 1982

JESOAN 129 (7) 1393-1650, 249C-270C

FUTURE MEETINGS

DETROIT, MICHIGAN—OCTOBER 17-22, 1982—HEADQUARTERS AT THE DETROIT PLAZA

The detailed Call for Papers published in the December 1981-May 1982 issues of **This Journal.** Final program published in the August 1982 issue of **This Journal.**

Planned symposia for the Detroit Meeting include the following Divisions, Group, Subcommittee, and subjects: **Battery:** Economic Trade Off Consideration on Batteries for Electric Vehicles, Advanced Batteries for Mobile Applications, Batteries for Electric Vehicles: Near Term, Thin Film, and Novel Structural Batteries, General Session; **Battery/Energy Technology/New Technology Subcommittee**—Reliability and Failure Analysis of Battery Storage Arrays; **Corrosion**—Automotive Corrosion, Crevice Corrosion, General Session; **Corrosion/Energy Technology**—Corrosion in Fossil Fuel Systems; **Dielectrics and Insulation/Electronics**—Automotive Microelectronics and Reliability; **Electrodeposition**—Electrodeposition in Automotive Applications, General Session; **Electronics/Dielectrics and Insulation**—First International Symposium on Very Large Scale Integration Science and Technology, Joint General Session, Joint Recent News Papers Session; **Electrothermics and Metallurgy**—The Metallurgy and Chemistry of Silica Reduction, Thermal Management of Batteries and Electronic Devices; **Electrothermics and Metallurgy/Corrosion**—Materials Aspects of Turbine Technologies; **Energy Technology**—General Session; **Energy Technology/Battery**—Porous Electrodes: Theory and Practice, Progress in Advanced Electric Vehicle Technology; **Energy Technology/Battery/Corrosion/Physical Electrochemistry**—Advanced Electrolytes for Energy Systems; **Energy Technology/Battery/Physical Electrochemistry**—Ion Insertion Electrodes; **Industrial Electrolytic**—Optimization of Industrial Electrochemical Processes, General Session; **Physical Electrochemistry**—General Session; and **Physical Electrochemistry/Battery/Corrosion**—Reactions in High Temperature Batteries and Fuel Cells.

SAN FRANCISCO, CALIFORNIA—MAY 8-13, 1983—HEADQUARTERS AT THE ST. FRANCIS HOTEL

The detailed Call for Papers published in the July-November 1982 issues of **This Journal.** Final program published in the March 1983 issue of **This Journal.**

Planned symposia for the San Francisco Meeting include the following Divisions, Group, Subcommittee, and subjects: **Battery**—Cell Design and Optimization, Cell Testing and Reliability; **Corrosion**—General Session; **Dielectrics and Insulation/Electronics**—Dielectric Isolation, Plasma Processing, Silicon Nitride Thin Films in the Electronics Industry; **Dielectrics and Insulation/Electronics/Corrosion/Electrothermics and Metallurgy/Energy Technology**—Materials and Processing for Photovoltaics; **Dielectrics and Insulation/Electrothermics and Metallurgy**—High Temperature Adhesives; **Electronics**—Automated IC Manufacture, Defects in Semiconductors, Growth and Processing of III-V Compound Semiconductors; **Electronics/Dielectrics and Insulation**—Joint General Session, Joint Recent News Papers Session; **Electrothermics and Metallurgy**—Materials Processing in Space, The Science and Technology of Nucleation and Growth of Particles from the Gas Phase; **Electrothermics and Metallurgy/Corrosion/Dielectrics and Insulation**—Protective Coatings; **Electrothermics and Metallurgy/Physical Electrochemistry/Battery/Energy Technology**—New Solid Electrolytes for Energy Conversion; **Energy Technology**—Extraction of Minerals from the Ocean, Novel Photoelectrochemical Synthetic Routes, General Session; **Energy Technology/Battery/Dielectrics and Insulation**—Conducting Organic Polymers in Energy Conversion and Storage; **Industrial Electrolytic**—Anode and Cathode Materials, Science and Engineering of Membranes and Separation; **Organic and Biological Electrochemistry**—Mechanism and Modeling of Electrochemical Membrane Processes, Structure and Reactivity in Organic Chemistry and Electrochemistry, General Session; **Physical Electrochemistry**—Electrode Process IV, Fourth International Symposium on Molten Salts, General Session; and **Physical Electrochemistry/Corrosion**—In Situ Nonelectrochemical Techniques for the Study of Electrode Reactions.

WASHINGTON, DC—OCTOBER 9-14, 1983—HEADQUARTERS AT THE SHERATON-WASHINGTON HOTEL

The detailed Call for Papers published in the December 1982-May 1983 issues of **This Journal.** Final program published in the August 1983 issue of **This Journal.**

Planned symposia for the Washington Meeting include the following Divisions, Group, Subcommittee, and subjects: **Battery**—Advances in Battery Materials and Processes, New Solid Electrolytes for Energy Conversion, Nonaqueous Systems for Energy Conversion, Reactive Metal-Air Batteries, Redox Batteries, General Session; **Corrosion/Physical Electrochemistry**—Hydrodynamic Aspects of Corrosion, General Session; **Corrosion/Electrodeposition**—New Materials for Electrical Contacts and Convectors; **Corrosion/European Federation of Corrosion**—Fundamental Aspects of Corrosion Protection; **Dielectrics and Insulation/Corrosion/Electronics**—Device Packaging and Corrosion; **Dielectrics and Insulation/Electronics**—Resist and Patterning Technology, Thin Film Interfaces and Interactions; **Electrodeposition**—Nonaqueous Processes, General Session; **Electronics**—Business Aspects of Semiconductors, Low Temperature and Transient Processing; **Electronics/Dielectrics and Insulation**—Interconnects and Contacts, Joint General Session, Joint Recent News Papers Session; **Electrothermics and Metallurgy**—Electrodeposition of Refractory Metals, New Advances in Aluminum Refining; **Electrothermics and Metallurgy/Corrosion**—High Temperature Erosion and Corrosion; **Electrothermics and Metallurgy/Dielectrics and Insulation/Electronics**—Ninth International Conference on Chemical Vapor Deposition; **Energy Technology**—Current Voltage Characteristics of Diodes Including Solar Cells, Requirements for New Applications for Emerging Energy Storage Systems and Conversion, General Session; **Energy Technology/Battery**—Energy Storage for Photovoltaic Systems; **Energy Technology/Battery/Industrial Electrolytic/Physical Electrochemistry**—Oxygen Cathodes in Aqueous Systems; **Energy Technology/Dielectrics and Insulation**—Surface Charge Measurement, Control, and Modification of Industrial Processes; **Industrial Electrolytic**—Fuel Salts in Industrial Processes, General Session; **Physical Electrochemistry**—The Use of Computers in Experimental Electrochemistry, General Session; **New Technology Subcommittee**—Reindustrialization of America, Crisis in Graduate Education; and **New Technology Subcommittee/Battery/Corrosion**—Reliability of Implantable Devices.

THE ELECTROCHEMICAL SOCIETY
BOOKS IN PRINT

Society Proceedings Series

The following softbound proceedings volumes are sponsored and published by The Electrochemical Society, Inc., 10 South Main Street, Pennington, N.J. 08534-2896. Orders filled at the list price given, subject to availability. Enclose payment with order.

Fundamentals of Electrochemical Machining. C. L. Faust, Editor. A 1970 symposium. 365 pages, **$4.50.**

Electron and Ion Beam Science and Technology, Fifth International Conference. R. Bakish, Editor. A 1972 symposium. 420 pages, **$5.50.**

Electrochemical Contributions to Environmental Protection. T. R. Beck, O. B. Cecil, C. G. Enke, J. McCallum, and S. T. Wlodek, Editors. A 1972 symposium. 173 pages, **$4.00.**

Oxide-Electrolyte Interfaces. R. S. Alwitt, Editor. A 1972 symposium. 312 pages, **$9.00.**

Electrochemical Bioscience and Bioengineering. H. T. Silverman, I. F. Miller, and A. J. Salkind, Editors. A 1973 symposium. 268 pages, **$8.00.**

Chlorine Bicentennial Symposium. T. C. Jeffery, P. A. Danna, and H. S. Holden, Editors. A 1974 symposium. 404 pages, **$11.00.**

Metal-Slag-Gas Reactions and Processes. Z. A. Foroulis and W. W. Smeltzer, Editors. A 1975 symposium. 1032 pages, **$20.00.**

Chemistry and Physics of Aqueous Gas Solutions. W. A. Adams, G. Greer, J. E. Desnoyers, G. Atkinson, G. S. Kell, K. B. Oldham, and J. Walkley, Editors. A 1975 symposium. 522 pages, **$11.00.**

Thermal and Photostimulated Currents in Insulators. D. M. Smyth, Editor. A 1975 symposium. 215 pages, **$7.00.**

Electron and Ion Beam Science and Technology, Seventh International Conference. R. Bakish, Editor. A 1976 symposium. 632 pages, **$18.00.**

International Symposium on Molten Salts. J. P. Pemsler, J. Braunstein, K. Nobe, D. R. Morris, and N. E. Richards, Editors. A 1976 symposium. 632 pages. **$16.00.**

Properties of High Temperature Alloys. Z. A. Foroulis and F. S. Pettit, Editors. A 1976 symposium. 851 pages, **$12.00.**

Semiconductor Silicon 1977. H. R. Huff and E. Sirtl, Editors. A 1977 symposium. 1100 pages, **$15.00.**

A History of The Electrochemical Society. The first 75 years. R. M. Burns with E. G. Enck. 160 pages. **$5.00.**

Semiconductor-Liquid Junction Solar Cells. A. Heller, Editor. A 1977 symposium. 340 pages, **$10.00.**

Load-Leveling. N. P. Yao and J. R. Selman, Editors. A 1977 symposium. 412 pages, **$13.00.**

High Temperature Metal Halide Chemistry. D. L. Hildenbrand and D. D. Cubicciotti, Editors. A 1977 symposium. 678 pages, **$17.00.**

Thin Film Phenomena—Interfaces and Interactions. J. E. E. Baglin and J. M. Poate, Editors. A 1977 symposium. 525 pages, **$14.00.**

Semiconductor Characterization Techniques. P. A. Barnes and G. A. Rozgonyi, Editors. A 1978 symposium. 532 pages, **$16.00.**

Industrial Water Electrolysis. S. Srinivasan, F. J. Salzano, and A. R. Landgrebe, Editors. A 1978 symposium. 297 pages, **$12.00.**

Selected Topics in the History of Electrochemistry. George Dubpernell and J. H. Westbrook, Editors. A 1977 symposium. 523 pages, **$11.00.**

Chemical Vapor Deposition, Seventh International Conference. T. O. Sedgwick and H. Lydtin, Editors. A 1979 symposium. 658 pages, **$16.00.**

Laser and Electron Beam Processing of Electronic Materials. C. L. Anderson, G. K. Celler, and G. A. Rozgonyi, Editors. A 1979 symposium. 560 pages, **$13.00.**

Thin Film Interfaces and Interactions, J. E. E. Baglin and J. M. Poate, Editors. A 1979 symposium. 536 pages, **$16.00.**

Electrode Processes, S. Bruckenstein, J. D. E. McIntyre, B. Miller, and E. Yeager, Editors. A 1979 symposium. 500 pages, **$21.00.**

Power Sources for Biomedical Implantable Applications and Ambient Temperature Lithium Batteries. B. B. Owens and N. Margalit, Editors. A 1979 symposium. 652 pages, **$18.00.**

Electronic and Optical Properties of Polycrystalline or Impure Semiconductors and Novel Silicon Growth Methods. K. V. Ravi and B. O'Mara, Editors. A 1980 symposium. 280 pages, **$15.00.**

Electron and Ion Beam Science and Technology, Ninth International Conference, R. Bakish, Editor. A 1980 symposium. 672 pages, **$28.00.**

Lithium Nonaqueous Battery Electrochemistry. E. B. Yeager, B. Schumm, Jr., G. Blomgren, D. R. Blankenship, V. Leger, and J. Akridge, Editors. A 1980 workshop. 328 pages, **$18.00.**

Ion Exchange: Transport and Interfacial Properties. R. S. Yeo and R. P. Buck, Editors. A 1980 symposium. 396 pages, **$15.00.**

Materials and New Processing Technologies for Photovoltaics. J. A. Amick, E. Sirtl, P. Rai-Choudhury, and J. P. Dismukes, Editors. A 1980 symposium. 368 pages, **$14.00.**

Lithium Batteries. H. V. Venkatasetty, Editor. A 1980 symposium, 516 pages, **$26.00.**

Semiconductor Silicon 1981. H. R. Huff, R. J. Kriegler, and Y. Takeishi, Editors. A 1981 symposium. 1064 pages, **$25.00.**

Electrocrystallization. R. Weil and R. G. Barradas, Editors. A 1981 symposium. 352 pages, **$13.00.**

Chemical Vapor Deposition, Eighth International Conference. J. M. Blocher, Jr., G. E. Vuillard, and G. Wahl, Editors. A 1981 symposium. 836 pages, **$30.00.**

Corrosion and Corrosion Protection. R. P. Frankenthal and F. Mansfeld, Editors. A 1981 symposium. 304 pages, **$10.00.**

Third International Symposium on Molten Salts. G. Mamantov, M. Blander, and G. P. Smith, Editors. A 1981 symposium. 600 pages, **$23.00.**

Second International Symposium on Molten Salts. J. Braunstein and J. R. Selman, Editors. A 1978 symposium. 420 pages, **$16.00.**

High Temperature Materials Chemistry. D. D. Cubicciotti and D. L. Hildenbrand, Editors. A 1981 symposium. 498 pages, **$21.00.**

Electrocatalysis. W. E. O'Grady, P. N. Ross, Jr, and F. G. Will, Editors, A 1981 symposium. 428 pages, **$18.00.**

Photoelectrochemistry: Fundamental Processes and Measurement Techniques. W. L. Wallace, A. J. Nozik, S. K. Deb, and R. H. Wilson, Editors. A 1981 symposium. 736 pages, **$35.00.**

The Nickel Electrode. R. G. Gunther and S. Gross, Editors. A 1981 symposium. 324 pages, **$15.00.**

Semiconductor Technology. D. A. Doane, D. B. Fraser, and D. W. Hess, Editors. A 1982 symposium. 264 pages, **$18.00.**

7/82

EDITOR
Norman Hackerman
Jackie Bourne, **Assistant to the Editor**

DIVISIONAL AND GROUP EDITORS

BATTERY
R. J. Brodd
Elton J. Cairns
Eugene G. Gagnon
G. F. Nordblom
Darrel Untereker
C. Joseph Venuto

CORROSION
J. R. Ambrose
J. W. Faust, Jr.
R. P. Frankenthal
Jerome Kruger
D. D. MacDonald
Florian Mansfeld
E. McCafferty
Ken Nobe
W. H. Smyrl

DIELECTRICS AND INSULATION
Robert S. Alwitt
Edmund B. Davidson
Rudolf G. Frieser
Dennis Hess
T. W. Hickmott
George L. Schnable
Alan W. Swanson

ELECTRODEPOSITION
Ugo Bertocci
Huk Y. Cheh
Y. Okinaka
Mordechay Schlesinger

ELECTRONICS
Ephraim Banks
D. M. Brown
Ted F. Ciszek
George R. Cronin
John A. DeLuca
Murray Gershenzon
James S. Harris
Simon Larach
Subhash Mahajan
David L. Nelson
Ernest Paskell
Bertram Schwartz
Frederic N. Schwettmann
Thomas O. Sedgwick
Don W. Shaw
Melvin Tecotzky
C. C. Wang
P. Wang
J. M. Woodall

HIGH TEMPERATURE MATERIALS
William A. Adams
Joan B. Berkowitz
Leo Brewer
E. D. Cater
Daniel Cubicciotti
Lee P. Hunt
V. K. Kapur
Peter J. Meschter
R. A. Rapp
David A. Shores
Gene F. Wakefield
Jack H. Westbrook

ENERGY TECHNOLOGY GROUP
Lee F. Donaghey
A. R. Landgrebe
M. Tomkiewicz
S. Srinivasan

INDUSTRIAL ELECTROLYTIC
Richard C. Alkire
Scott Lynn

ORGANIC AND BIOLOGICAL ELECTROCHEMISTRY
Martin Blank
M. Dale Hawley
Stanley Wawzonek

PHYSICAL ELECTROCHEMISTRY
Gregory C. Farrington
David S. Ginley
Adam Heller
Gleb Mamantov
Barry Miller
William E. O'Grady
Robert A. Osteryoung
David K. Roe
C. W. Tobias
F. G. Will
Ronald H. Wilson
M. S. Wrighton

News Editor—Jack H. Westbrook

JOURNAL OF THE
ELECTROCHEMICAL SOCIETY
(USPS 284-140)
ISSN 0013-4651

The JOURNAL OF THE ELECTROCHEMICAL SOCIETY (USPS 284-140) is published monthly by The Electrochemical Society, Inc. at 215 Canal St., Manchester, N.H. 03108. The address for the Executive Offices, Editorial and Advertising Office, and Circulation Department of The Electrochemical Society, Inc., is 10 South Main St., Pennington, N.J. 08534-2896. Subscription to members as part of membership service; subscription to nonmembers $120.00 plus $15.00 for postage outside U.S. and Canada. Single copies $7.00 to members, $11.00 to nonmembers.
© Copyright 1982 by The Electrochemical Society, Inc. Second Class Postage paid at Pennington, New Jersey and at additional mailing offices.
POSTMASTER: Send address changes to THE ELECTROCHEMICAL SOCIETY, INC., 10 South Main St., Pennington, N.J. 08534-2896.

July 1982

ELECTROCHEMICAL SCIENCE AND TECHNOLOGY

TECHNICAL PAPERS

ELECTROCHEMICAL SOCIETY

Vol. 129 • No. 7

TECHNICAL NOTES

SOLID-STATE SCIENCE AND TECHNOLOGY

TECHNICAL PAPERS

DIVISION AND GROUP OFFICERS

Battery Division
John Pierson, Chairman
Theodore Katan, Vice-Chairman
Gene Gagnon, Secretary-Treasurer
General Motors Corp.
Research Laboratories, Dept. 37
12 Mile and Mounds Rds.
Warren, Mich. 48090

Corrosion Division
Robert P. Frankenthal, Chairman
Florian Mansfeld, Vice-Chairman
Robert A. Rapp, Secretary-Treasurer
Dept. of Metallurgical Engineering
Ohio State University
116 West 19th Ave.
Columbus, Oh. 43210

Dielectrics and Insulation Division
Werner Kern, Chairman
John L. Mauer IV, Vice-Chairman
Laura Rothman, Treasurer
Norman Goldsmith, Secretary
RCA Laboratories
Princeton, NJ 08540

Electrodeposition Division
Lubomyr Romankiw, Chairman
Thomas Franklin, Vice-Chairman
Mordechay Schlesinger, Secretary-Treasurer
Dept. of Physics
University of Windsor
Windsor, Ont., Canada N9B 3P4

Electronics Division
Ronald E. Enstrom, Chairman
Edward H. Nicollian, Vice-Chairman (Semiconductors)
Martin R. Royce, Vice-Chairman (Luminescence)
F. N. Schwettmann, Vice-Chairman (New Electronic Technologies)
Patricia L. Castro, Treasurer
Carlton M. Osburn, Secretary
IBM T. J. Watson Research Center
P.O. Box 218
Yorktown Heights, N.Y. 10598

High Temperature Materials Division
William A. Adams, Jr., Chairman
Lee P. Hunt, Senior Vice-Chairman
Wayne Worrell, Junior Vice-Chairman
Frederick S. Pettit, Secretary-treasurer
University of Pittsburgh
848 Benedum Hall
Pittsburgh, Pa. 15261

Energy Technology Group
James McBreen, Chairman
Arthur J. Nozik, Vice-Chairman
Vijay K. Kapur, Treasurer
A. J. Appleby, Secretary
Electric Power Research Institute
P.O. Box 10412
Palo Alto, Calif. 94303

Industrial Electrolytic Division
Morris Grotheer, Chairman
Robert S. Karpiuk, Vice-Chairman
W. Bruce Darlington, Secretary-Treasurer
PPG Industries
P. O. Box 4026
Corpus Christi, TX 78403

Luminescence and Display Materials Group
Martin Royce, Chairman
Charles Struck, Vice-Chairman
William McAllister, Secretary-Treasurer
Westinghouse Electric Corp.
Bloomfield, NJ 07003

Organic and Biological Electrochemistry Division
John H. Wagenknecht, Chairman
Martin Blank, Vice-Chairman
Petr Zuman, Secretary-Treasurer
Dept. of Chemistry
Clarkson College of Technology
Potsdam, N.Y. 13676

Physical Electrochemistry Division
Elton J. Cairns, Chairman
Robert A. Osteryoung, Vice-Chairman
Larry R. Faulkner, Secretary-Treasurer
Dept. of Chemistry
University of Illinois
Urbana, Ill. 61801

SOCIETY OFFICERS AND STAFF

Frederick J. Strieter, President
Honeywell Inc.
7814 Fallmeadow Lane
Dallas, Texas 75240

J. Bruce Wagner, Vice-President
Center for Solid State Science
Arizona State University
Tempe, Ariz. 85281

Paul C. Milner, Vice-President
Bell Laboratories
Room 1D-259
Murray Hill, N.J. 07974

Richard C. Alkire, *Vice-President*
Dept. of Chemical Engineering
University of Illinois
Urbana, Ill. 61801

Forrest A. Trumbore, Secretary
Bell Laboratories
Room 1E-208
Murray Hill, N.J. 07974

Jerome Kruger, Treasurer
National Bureau of Standards
B254 Materials Building
Washington, D.C. 20234

V. H. Branneky, Executive Secretary
The Electrochemical Society, Inc.
10 South Main Street
Pennington, N.J. 08534-2896

Donna Kimberlin, Administrative Assistant
The Electrochemical Society, Inc.
10 South Main Street
Pennington, N.J. 08534-2896

PUBLICATION STAFF

Sarah A. Kilfoyle, **Publication Editor**
Annette R. Van Deusen, ***Assistant Publication Editor***

PUBLICATION COMMITTEE

Robert P. Frankenthal, **Chairman**
Forrest A. Trumbore
Norman Hackerman
Newton Schwartz
Glenn W. Cullen
Rudolf Keller
Rudolf T. Frieser
Isaac Trachtenberg
Gary McGuire

Manuscripts submitted to the JOURNAL should be sent in triplicate to the Editorial Office at 10 South Main Street, Pennington, N.J. 08534-2896. They should conform to the revised "Instructions to Authors" available from Society Headquarters. Manuscripts so submitted, as well as papers presented before a Society technical meeting, become the property of the Society and may not be published elsewhere in whole or in part without written permission of the Society. Address such requests to the Editor.

The Electrochemical Society does not maintain a supply of reprints of papers appearing in its JOURNAL. A photoprint copy of any particular paper may be obtained from University Microfilms, Inc., 300 N. Zeeb St., Ann Arbor. Mich. 48106.

Inquiries regarding positive microfilm copies of issues *should be addressed to University Microfilms, Inc.*, 300 N. Zeeb St., Ann Arbor, Mich. 48106.

Walter J. Johnson, Inc., 355 Chestnut St., Norwood, N.J. 07648, have reprint rights to out-of-print volumes of the JOURNAL, and also have available for sale back volumes and single issues with the exception of the last two calendar years.

The JOURNAL OF THE ELECTROCHEMICAL SOCIETY combines the JOURNAL and TRANSACTIONS OF THE ELECTROCHEMICAL SOCIETY. Statements and opinions given in articles and papers in the JOURNAL OF THE ELECTROCHEMICAL SOCIETY are those of the contributors, and The Electrochemical Society, Inc. assumes no responsibility for them.

Claims for a missing issue should be reported within 60 days of normal delivery date to the Circulation Dept., The Electrochemical Society, Inc., 10 South Main Street, Pennington, N.J. 08534-2896.

Notice of a change in address should be sent to the Circulation Dept., The Electrochemical Society, Inc., 10 South Main Street, Pennington, N.J. 08534-2896. Include the mailing label or the number from the mailing label from your previous issue of the JOURNAL to ensure proper identification.

SOLID-STATE SCIENCE (Cont.)

TECHNICAL NOTES

ACCELERATED BRIEF COMMUNICATIONS

REVIEWS AND NEWS

JOURNAL OF THE ELECTROCHEMICAL SOCIETY

ELECTROCHEMICAL SCIENCE AND TECHNOLOGY

JULY 1982

Self-Discharge in Acid-Starved Lead-Acid Batteries

Kathryn R. Bullock* and Edwin C. Laird*

Johnson Controls, Incorporated, Corporate Applied Research Group, Milwaukee, Wisconsin 53201

ABSTRACT

A lead-acid battery stored in an acid-starved condition, rather than in a totally flooded state, shows a well-behaved and predictable decline in open-circuit voltage with time. The voltage-time curves of such batteries can be used to determine the rates of the predominant self-discharge reactions and to study the reaction mechanisms. An abrupt change in the slope of the curve indicates a change in the dominant self-discharge process. Acid-starved automotive (SLI) batteries with antimonial-lead grids show a slope change at 1.85 V/cell. This apparently corresponds to a change in the grid corrosion mechanism. Measurements of gas evolution from these SLI batteries show that the rate of hydrogen evolution is dependent on the acid concentration whereas the rate of evolution of carbon dioxide is independent of acid concentration. Oxygen reacts rapidly at the negative plate.

The self-discharge of lead-acid battery plates was first reported in 1882 by Gladstone and Tribe (1), who asked, "Why should a lead plate covered with peroxide and immersed in dilute sulfuric acid, run down so slowly that it requires many hours or even days before its energy is so seriously reduced as to impair its value for practical purposes?" Since then the reactions which limit the shelf life in lead-acid batteries have been well defined (2-4).

At the positive electrode, they are

Oxygen evolution:

$$PbO_2 + H_2SO_4 \Rightarrow PbSO_4 + H_2O + \tfrac{1}{2} O_2 \quad [1]$$

Hydrogen recombination:

$$PbO_2 + H_2 + H_2SO_4 \Rightarrow PbSO_4 + 2H_2O \quad [2]$$

Oxidation of organic contaminants:

$$PbO_2 + \text{organics} + H_2SO_4 \Rightarrow PbSO_4 + H_2O + CO_2 + \text{oxidized organic products} \quad [3]$$

Grid corrosion:

$$PbO_2 + Pb + 2H_2SO_4 \Rightarrow 2PbSO_4 + 2H_2O \quad [4]$$

[A variety of other corrosion reactions can occur as well (5).]

Oxidation of grid alloying metals, such as antimony:

$$5PbO_2 + 2Sb + 6H_2SO_4 \Rightarrow (SbO_2)_2SO_4 + 5PbSO_4 + 6H_2O \quad [5]$$

(Similar reactions can be written for other metals.)

Sulfation of "apparent PbO":

$$PbO + H_2SO_4 \rightleftharpoons PbSO_4 + H_2O \quad [6]$$

At the negative electrode, two more reactions can occur

Hydrogen evolution:

$$Pb + H_2SO_4 \Rightarrow PbSO_4 + H_2 \quad [7]$$

Oxygen recombination:

$$Pb + H_2SO_4 + \tfrac{1}{2} O_2 \Rightarrow PbSO_4 + H_2O \quad [8]$$

Which of these many reactions will dominate the self-discharge process is a complex question. The answer will depend on the design of the battery and the materials used. Studies have been published on the effects of grid alloys (6-10), impurities (11), formation conditions (12), expander composition, and phosphoric acid concentration (13). Various experimental methods have been devised to measure self-discharge rates both for the battery as a whole and for the individual reactions (2, 3, 13-15).

Self-discharge in batteries stored in a damp, rather than a wet, condition is of particular interest for several reasons. First, the ratio of acid to active material is smaller than in a wet battery, so that a smaller percentage of the active material reacts during storage. Secondly, the acid concentration is diluted during storage, since all the self-discharge reactions use acid and generate water. Dilution reduces the rates of self-discharge of the active material (reactions [1] and [7]), a result which is particularly beneficial to the negative plate. It also alters the products which are formed by grid corrosion (reaction [4]). Finally, the damp storage increases the rates of oxygen and hydrogen recombination (reactions [2] and [8]) by permitting gas transport between plates through the vapor phase (13). In wet batteries, the rates of these reactions are severely reduced because of the low solubility of oxygen and hydrogen in battery acid.

Since the acid is diluted by self-discharge and since the open-circuit voltage is a function of the acid concentration, measuring the change in battery voltage with time is a simple method of determining the rate of self-discharge in acid-starved lead-acid batteries. Voltage measurements are nondestructive and thus allow continuous monitoring of the battery's condition without sacrificing information on its performance after storage. This technique has been used previously to study self-discharge in sealed, acid-starved lead-acid cells (13).

In the present work, voltage measurements were used to study the self-discharge process in automotive (SLI) lead-acid batteries stored in an acid-starved

* Electrochemical Society Active Member.
Key words: batteries, voltage-time curves, gas evolution.

condition. Additional information about the self-discharge process in these batteries was obtained by (*i*) using gas chromatography to analyze the gases evolved during storage and (*ii*) using microprobe laser Raman spectroscopy to analyze the corrosion products formed on the positive grid.

Experimental Method

Voltage measurements were made to ±1 mV using a Keithley Model 178 voltmeter with 10 mΩ input impedance. A Hewlett Packard 4328A milliohmmeter was used to measure internal cell impedance by a four-probe a-c method. The acid activities were calculated from open-circuit voltages using on-line BASIC programs written for a Honeywell 66/40 computer.

Gas analysis was done with a dual column Varian 3760 gas chromatograph equipped with dual thermal conductivity detectors and a Valco CV-6-HPa six-port valve. Samples were injected with a Precision Sampling A-2, 100 μl syringe with built-in valve for sealing in gas samples.

Chromatograms were integrated and recorded with a Varian CDS 111C data system and A-25 recorder.

Gas volume measurements were made with a 500 ml burette and leveling bulb. A three-way stopcock directed flow either from the battery head space to the burette or from the burette to exhaust.

Gas analysis samples were taken by syringe through latex tubing. Fifty ml were injected at room temperature and pressure into the chromosorb 104 column of the GC. After the H_2 peak eluted, the valve was manually switched and the CO_2, O_2, and N_2 eluted. The valve changed the relative position of the two columns without changing flow direction. Column reversal was necessary to prevent irreversible adsorption of the CO_2 on the sieve 5A column. A sample chromatogram is shown in Fig. 1.

Matheson Gas Incorporated certified standard gas mixtures were used for calibration of the gas analyses. Linear regression of the peak areas was used for CO_2, O_2, and N_2. Because the peak area of H_2 was not linear with concentration, these results were taken from a graph.

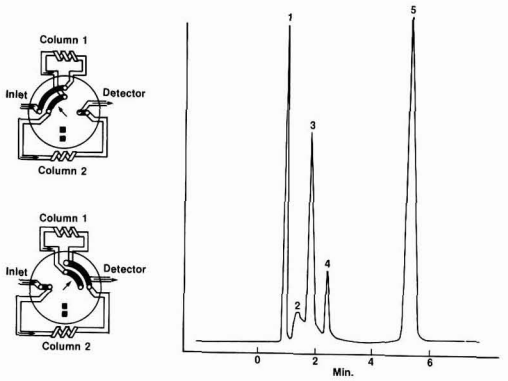

Fig. 1. Gas analysis with column sequence reversal. Column 1: 4 ft. × 1/8 in. SS 80/100 mesh chromosorb 104. Column 2: 6 ft. × 1/8 in. SS 60/80 mesh molecular sieve 5A. Column temperature: 30°C. Flow rate: 20 ml/min He. Range: 0.05 mV. Detector: thermal conductivity, 155 mA, 120°C. Sample: 50 ml.

	v/o	Attenuation
1. Hydrogen	50.0	×4
2. Valve change	—	×4
3. Carbon dioxide	1.0	×4
4. Oxygen	0.3	×4
5. Nitrogen	10.0	×8
Helium	Balance	

Laser Raman microprobe observations were conducted using an Instruments SA, Incorporated MOLE[1] at Walter C. McCrone Associates, Incorporated. For general observations a 1 μm diam beam of radiation (514.5 nm) from an argon ion laser operated at 100 mW power output was employed. A magnification of 100× was used during these examinations.

Although observations of α-PbO_2 Raman spectra from pasted plate sections were made using the general observation conditions, confirmatory Raman spectra from an authenticated sample of α-PbO_2 required the use of minimum laser power (~5 mW) and a 10 μm radiation beam diameter. The pasted plate configuration apparently provides sufficient heat dissipation to prevent decomposition at the observation point.

Results and Discussions

The open-circuit voltage of a lead-acid cell is related to the activity of the electrolyte by the Nernst equation for the double sulfate reaction

$$Pb + PbO_2 + 2H_2SO_4 \rightleftharpoons 2PbSO_4 + 2H_2O$$

$$E = E^\circ + \frac{RT}{F} \ln \frac{a_a}{a_w}$$

where a_a is the activity of H_2SO_4 and a_w is the activity of H_2O.

If complete dissociation of the bisulfate ion is assumed, then $a_a = 4\,\gamma^{\pm 3} m^3$ where $\gamma^\pm$ is the mean ionic activity coefficient of sulfuric acid and m is the molality of the electrolyte. The values of a_a and a_w used in these calculations were calculated from the data of Harned and Hamer (16-18) at 25°, 45°, and 55°C. Thermodynamic equilibrium was assumed because of the slowness of the self-discharge process.

In all the self-discharge reactions listed above, the reactants are sulfuric acid, gases such as H_2 and O_2, and solids such as PbO_2, Pb, and Sb. The only exception is the soluble organic material in reaction [3]. Since the activities of all solids and of gases at atmospheric pressure are 1, the rate of self-discharge should be pseudo-first-order with respect to sulfuric acid, if we assume that reaction [3], the oxidation of organic contaminants, is insignificant.

The kinetic equation for such a first-order reaction may be written as

$$\ln a_a - \ln (a_a)_o = -kT$$

where t is the time, k is the rate constant, a_a is the acid activity at time t, and $(a_a)_o$ is the initial acid activity. Activities are used in this calculation instead of concentrations because of the high initial acid concentration and the wide concentration range covered during the shelf life of the battery. According to this equation a plot of ln a_a as a function of time should be linear with a slope of $-k$.

Typical plots of ln a_a as a function of time are shown in Fig. 2 for commercial acid-starved automotive (SLI) batteries. The curve is approximately linear between ln a_a values of 0 and −7. Deviations from linearity can occur early in the shelf life (ln $a_a > 0$) for several reasons. First, the battery is equilibrating from the formation charge with respect to both temperature and acid concentration. Second, residual atmospheric oxygen, which entered the battery during manufacture, may be discharging the negative plate. Finally, a newly formed cell contains "apparent PbO" and α-PbO_2 in the positive plate (12, 19), both of which self-discharge at a higher rate than β-PbO_2

[1] Molecular Optics Laser Examiner®, Instruments, SA, Incorporated.

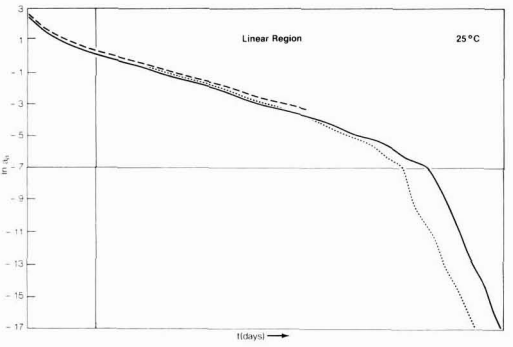

Fig. 2. Typical self-discharge curves for commercial acid-starved lead-acid SLI batteries stored at room temperature.

(20, 21). These initial reactions typically last several weeks.

Once the slope in the linear region is established, the rate constant of the self-discharge reactions can be determined. At higher temperatures, the linearity is excellent, with a least-squares fit of the data giving correlation coefficients of 0.999 or better. At room temperature the plot shows a slight curvature, but the linearity is sufficient to allow calculation of the self-discharge rate.

The precision of the measurement is also encouraging. In Fig. 2, the curves shown for three batteries with the highest, lowest, and mean self-discharge rates represent the total spread in the data for the 19 batteries tested. All the batteries were of the same type and from the same production lot. Since the ln a_a is calculated from the battery voltage divided by 6, each curve represents an average of the six cells in the battery. The individual cell voltages also show a small distribution.

The slope of the curves increases suddenly at a ln a_a of -7, which corresponds to a battery voltage of 11.1 (1.85 V/cell). An abrupt slope change of this type indicates a change in the predominant self-discharge mechanism. This change appears to be common in acid-starved SLI batteries. We have observed similar slope changes at about the same voltage in each of the several types and brands of commercial SLI batteries we have tested.

One possible explanation for this sudden slope change is that a new corrosion reaction is occurring. Thermodynamic and kinetic studies of lead corrosion in sulfuric acid have established that lead corrosion mechanisms change with changing voltage and acid concentration (5, 22, 23). According to Harned and Hamer (18), 1.85V corresponds to a positive plate potential of approximately 900 mV (*vs.* $Hg/Hg_2SO_4/H_2SO_4$). Constant potential corrosion studies by Pavlov *et al.* (24) have shown that α-PbO_2 is the principal corrosion product from 900 to 1200 mV in 1*N* H_2SO_4. Below 900 mV, tetragonal PbO and $PbSO_4$ are the principal products, along with minor amounts of $PbO \cdot PbSO_4$, $3PbO \cdot PbSO_4 \cdot H_2O$, orthorhombic PbO, and α-PbO_2. Formation of tetragonal PbO is also favored by reduced hydrogen and sulfate ion activities (22, 25).

This hypothesis is supported by our observations of the corrosion layers formed on the positive plates of acid-starved SLI batteries during storage. Figures 3a and b show cross sections of lead grids removed from batteries stored at 45°C for 50 days and 9 months, respectively, after the critical 11.1V level was reached. The grid in Fig. 3b has a thick corrosion layer at the lead interface which has only just begun to form in the sample in Fig. 3a. Under cross-polarized light, this layer looks red, suggesting that it is tetragonal PbO. The dense corrosion layer in the center of each picture is black under cross-polarized light, which suggests that it is α-PbO_2. Analyses of the two samples by laser Raman spectroscopy confirmed these conclusions. Tetragonal PbO was identified at the Pb interface in Fig. 3a and in the inner corrosion layer in Fig. 3b. In the center of the adjacent black corrosion layers in both samples, weak signals were observed which matched the signal from a prepared sample of α-PbO_2. β-PbO_2 may also be present. However, it appears to be Raman inactive and is therefore not observed (26).

An increase in the internal cell impedance accompanies the growth of the tetragonal PbO film. This increased impedance is evident on high-rate discharge. We tested many batteries by discharging them at 75% of the cold cranking rate and monitoring the half-cell potentials during discharge. Batteries stored below the 11.1V level show a substantially larger *IR* drop in the positive electrode potential under load.

All of the SLI batteries we tested had antimonial-lead grids. Batteries containing other lead alloys or pure lead may show somewhat different behavior. Ln acid activity-time curves for sealed, acid-starved lead-acid cells made with pure lead grids (13) show a sudden slope change at ln $a_a = -12$ rather than -7. Furthermore, thick tetragonal PbO layers do not form at low voltages. Figure 4 show a photomicrograph of a positive grid taken from a sealed, acid-starved lead-

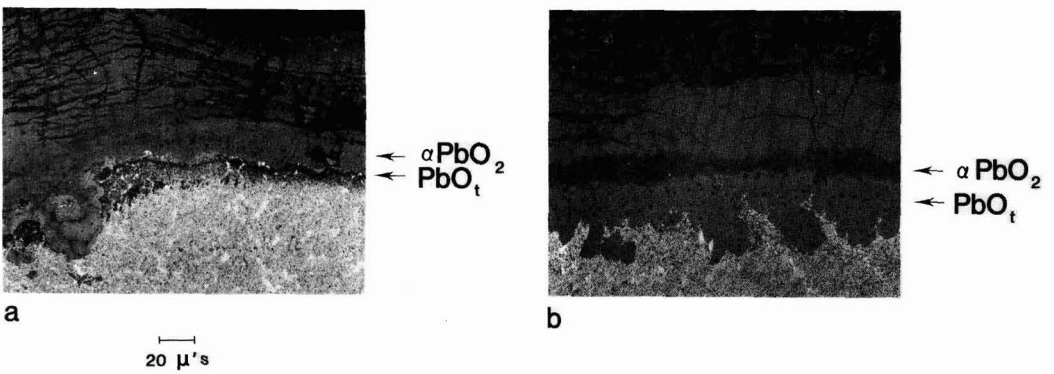

Fig. 3. Photomicrographs of positive grids taken from an SLI battery stored at 45°C. (a) 50 days after the critical voltage was reached; (b) 9 months after the critical voltage was reached.

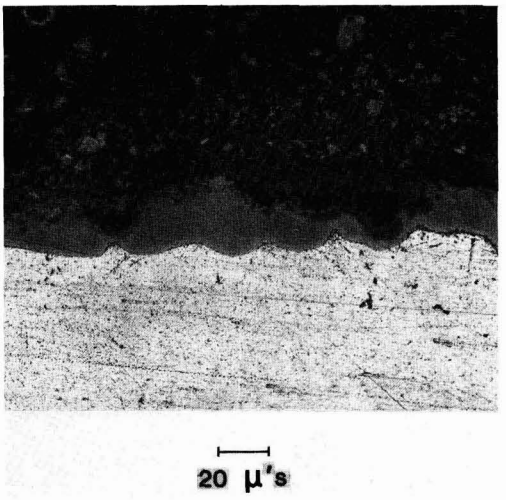

Fig. 4. Photomicrograph of positive grid taken from a sealed, acid-starved cell stored at 45°C to 1.158V.

acid cell stored at 45°C to 1.158V. The black PbO_2 layer is present, but only thin regions of tetragonal PbO are found at the interface. Whether this difference is due to the use of pure lead grids or to the oxygen deficient environment in a sealed cell or to some other factor is an interesting question.

Near the point where the slope change occurs in the SLI batteries (see Fig. 2), the distribution of battery voltages gets broader because the individual cells reach the critical voltage at different times. Open-circuit voltages below this point often become unstable and difficult to measure, presumably because the reaction rate becomes too fast to maintain cell equilibrium. Thus the fundamental assumption that the open-circuit voltage is related to the acid concentration by the Nernst equation breaks down and reaction rates cannot be accurately measured below 11.1V.

The effect of storage temperature on self-discharge is shown in Fig. 5. As would be expected from kinetic theory and previous studies of self-discharge in lead-acid batteries (9-13), the rate of self-discharge increases as the temperature increases. The Arrhenius equation may be applied to these results to obtain the activation energy of the dominating self-discharge reaction

$$\ln k = \ln A - \frac{E_a}{RT}$$

where k is the rate constant, A is the Arrhenius constant, E_a is the activation energy, and T is the storage temperature in degrees Kelvin.

According to this theory, a plot of ln k *vs.* $1/T$ should be linear with a slope of $-E_a/R$. Such a plot is shown in Fig. 6. Although the plot is linear up to 45°C, the point at 55°C is higher than expected, probably because the same mechanisms that lead to higher initial self-discharge rates at room temperature are operating throughout the short shelf life at 55°C. An activation energy of about 11 kcal/mol is calculated from a least-squares fit of the data taken at 25°-45°C. The slope change shown in Fig. 2 for room temperature also occurs at 40° and 45°C at the same acid activity. However, at 55°C, the initial slope is so steep that the slope change is not well defined.

In addition to storage temperature, many other factors affect the slope of the self-discharge curve. Some of these factors are common to all lead-acid batteries. For example, organic impurities in the cell can increase the self-discharge rate by oxidizing at the positive plate (reaction [3]). Formation conditions can affect the amounts of α-PbO_2 and residual PbO in the positive plate. Both these compounds self-discharge at faster rates than β-PbO_2 (reaction [1]). Since a well-formed battery has less residual PbO, it will have a better shelf life than a poorly formed battery. The grid alloy is also an important variable, since metallic impurities can oxidize at the positive electrode (reaction [5]), plate out at the negative electrode, and increase the rate of hydrogen evolution (reaction [7]). Thus the self-discharge rates of batteries with antimonial lead grids are controlled primarily by hydrogen evolution at the negative plate, whereas the self-discharge rates of batteries with non-antimonial lead grids are controlled primarily by oxygen evolution at the positive plate (13). Metallic impurities in the paste, separator, and electrolyte can also increase the rate of hydrogen evolution (11).

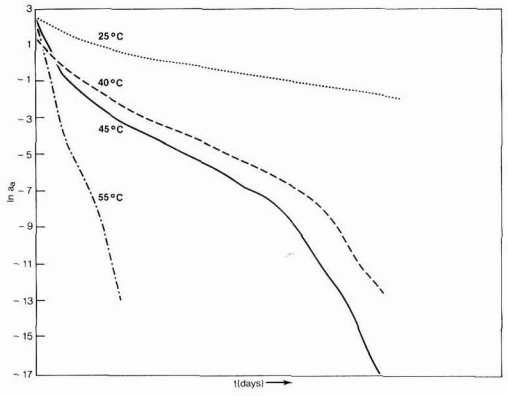

Fig. 5. Effect of temperature on self-discharge curves of commercial, acid-starved lead-acid SLI batteries.

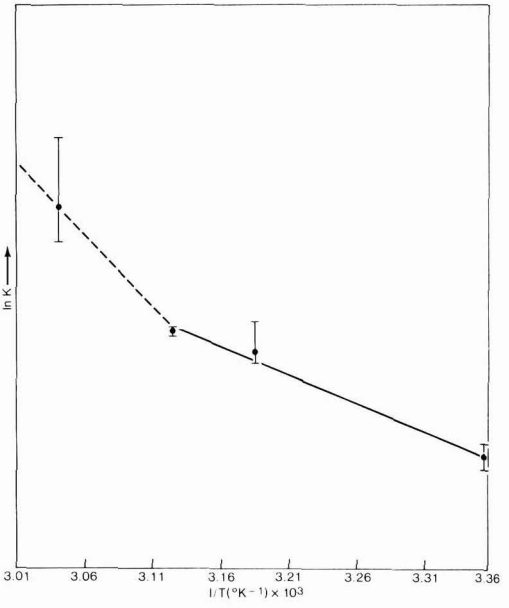

Fig. 6. Arrhenius plot for self-discharge rates in acid-starved lead-acid batteries. Rate constants were calculated from the slopes of the curves in Fig. 5.

In acid-starved lead-acid batteries, several additional variables influence the slope of the self-discharge curve. One important variable is the acid volume relative to the amount of active material in the cell. A large volume of acid will be diluted more slowly by the self-discharge reactions than a small volume. This will in turn decrease the rate constant and increase the shelf life. The beneficial effect of a large acid volume must, however, be balanced against two adverse consequences. First, more of the active material will self-discharge so that more capacity will be lost and more sulfation will occur over the shelf life. Second, since the potential and acid concentration will remain high longer, the initial rate of self-discharge will be greater. This will produce more rapid sulfation, a condition that appears to be especially harmful to the negative plate.

The second variable that specifically influences self-discharge in acid-starved lead-acid batteries is the amount of oxygen available to the negative plate. Some self-discharge occurs when oxygen evolved from the positive plate discharges the negative plate (reaction [8]). However, rapid self-discharge will occur if atmospheric oxygen is available. We confirmed this by removing the vent caps from a freshly made acid-starved SLI battery. The voltage plunged from over 12 to below 10V in 7 days. Further testing and analysis confirmed that the negative plate was severely sulfated.

Additional evidence that oxygen can react at the negative plate was obtained by measuring the volume of the gases evolved from an acid-starved SLI battery with antimonial-lead grids during storage at 45°C and analyzing samples of this gas for O_2, N_2, H_2, and CO_2. The total gas volume and the percentage of each of the four component gases is shown in Fig. 7. The total gas volume decreases rapidly with time until, when the battery reaches an open-circuit voltage of 11.8, gas evolution stops. The percentage of nitrogen in the gas samples also decreases rapidly as the air present in the battery after manufacture is used up. The limiting value for N_2 is an indication of the amount of leakage in our gas collection line. The amount of oxygen found is less than 1% throughout the test, with the ratio of N_2 to O_2 varying from 94/1 at the beginning of storage to about 15/1 at the point where gassing stops. Since the ratio of N_2 to O_2 in air is 4/1, and since O_2 is evolved at the positive plate during storage (reaction [1]), these results indicate that oxygen is reacting at the negative plate (reaction [8]).

As the amount of air evolved from the battery decreases, the percentages of CO_2 and H_2, which are produced by reactions [3] and [6], respectively, increase. By multiplying the percentages of each of these gases by the total volume of gas evolved over a 9 hr period, the volume of each gas evolved in this time period was obtained. The number of mols of each gas was calculated using the general gas law

$$n = \frac{PV}{RT}$$

where P is the measured atmospheric pressure, V is the gas volume, R is the gas constant, 82.054 cm³ atm/deg mol, and T is the absolute temperature.

Since the battery voltage was also monitored during the experiment, the self-discharge rate could be calculated and compared to the rates of gas evolution. Figure 8 shows the results. The number of mols of hydrogen evolved decays exponentially with time, indicating a first-order reaction. A plot of the ln of the number of mols of H_2 *vs.* time is a straight line with the same slope as the linear region of the ln acid activity-time curve. The amount of CO_2 evolved, on the other hand, is relatively constant and is independent of the acid concentration, at least early in the shelf life. The volume of gases evolved eventually becomes so small that the uncertainty in the volume measurements increases. This leads to the widely scattered points shown on the graph.

At room temperature, the amount of gas evolved is so low that the volume measurement is difficult and uncertain even early in the shelf life. However, the percentages of each gas can be determined accurately. As shown in Fig. 9, the results are quite similar to

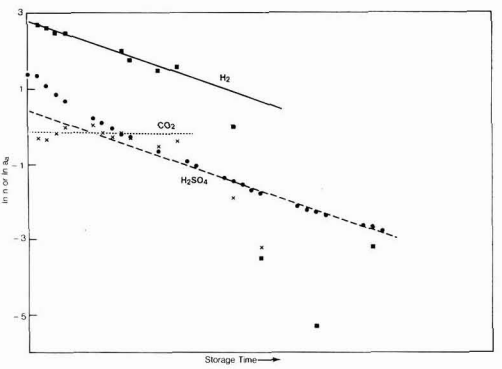

Fig. 8. Rates of hydrogen and carbon dioxide evolution compared to the rate of change of acid concentration. ■, H_2; ×, CO_2; ●, H_2SO_4.

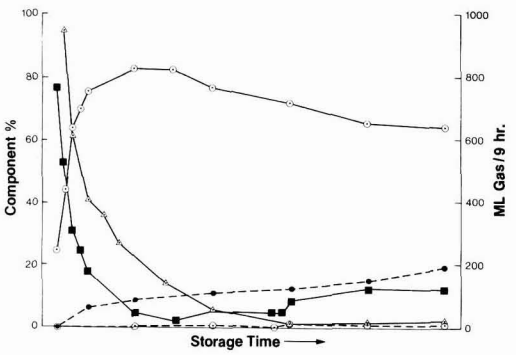

Fig. 7. Gases evolved from an acid-starved SLI battery stored at 45°C. △—△ ml displaced/9 hr day; ○—○, % H_2; ■—■, % N_2; ●---●, % CO_2; ○---○, % O_2.

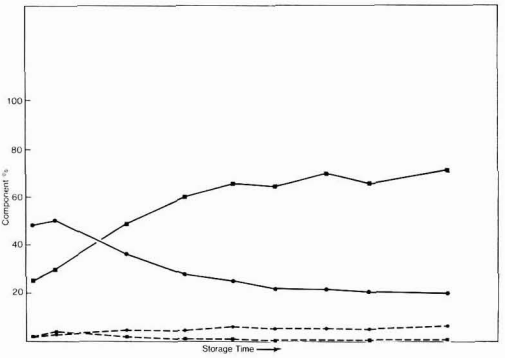

Fig. 9. Gases evolved from an acid-starved SLI battery stored at 25°C. ■—■, % H_2; ●—●, % N_2; ●---●, % CO_2; ■---■, % O_2.

those obtained at 45°C, except that the percentage of CO_2 is only about 3-6%, compared to 10-20% at 45°C. Leakage problems are also more significant. Gas evolution stops at about 12.3V. These results are consistent with similar measurements of gas evolution from sealed, acid-starved lead-acid cells (26).

Conclusions

1. The self-discharge reaction in an acid-starved lead-acid battery is first order with respect to the sulfuric acid concentration. The rate of reaction can be determined by calculating the change in the acid activity as a function of time from open-circuit voltage measurements.

2. An abrupt change in the slope of the ln acid activity *vs.* time curve indicates a change in the predominant self-discharge reaction. Such a slope change is consistently observed in commercial, acid-starved lead-acid automotive batteries and may be due to the formation of tetragonal PbO on the positive grid.

3. Oxygen can react rapidly at the negative plate. Hydrogen evolves early in the shelf life at a rate that decreases with decreasing acid concentration. Carbon dioxide evolves at a rate independent of acid concentration.

Acknowledgments

The authors are grateful to R. Johnson, who supplied the batteries used in these studies and provided much helpful advice and information, to M. Mueller, who did much of the experimental work, to G. Trischan, who did the laser Raman spectroscopy, and to W. Tiedemann, D. Marshall, and C. K. Morehouse for helpful discussions.

Manuscript submitted Oct. 23, 1981; revised manuscript received Dec 14, 1981. This was Paper 56 presented at the Denver, Colorado, Meeting of the Society, Oct. 11-16, 1981.

Any discussion of this paper will appear in a Discussion Section to be published in the June 1983 JOURNAL. All discussions for the June 1983 Discussion Section should be submitted by Feb. 1, 1983.

Publication costs of this article were assisted by Johnson Controls, Incorporated.

REFERENCES

1. J. H. Gladstone and A. Tribe, *Nature*, **25**, 221 (1882).
2. J. J. Lander, *This Journal*, **99**, 339 (1952).
3. P. Ruetschi and R. T. Angstadt, *ibid.*, **105**, 555 (1958).
4. G. Dalibard, J. Atkins, J. Pothet, and N. Viaud, *Rev. Générale L'Electricité*, **84**, 463 (1975).
5. J. Burbank, A. C. Simon, and E. Willihnganz, in "Adv. in Electrochemistry and Electrochemical Engineering," Vol. 8, C. W. Tobias, Editor, p. 157, Wiley-Interscience, New York (1971).
6. J. T. Crennell and A. G. Milligan, *Trans. Faraday Soc.*, **27**, 103 (1931).
7. H. E. Haring and U. B. Thomas, *Trans. Electrochem. Soc.*, **68**, 293 (1935).
8. J. W. R. Byfield, *ibid.*, **79**, 259 (1947).
9. A. C. Zachlin, *ibid.*, **92**, 259 (1947).
10. G. Gabrielson, *J. Appl. Chem.*, **8**, 748 (1958).
11. H. C. Gillette, *Trans. Electrochem. Soc.*, **41**, 217 (1922).
12. R. H. Greenburg and B. P. Caldwell, *Trans. Electrochem. Soc.*, **80**, 71 (1941).
13. K. R. Bullock and D. H. McClelland, *This Journal*, **123**, 327 (1976).
14. A. C. Zachlin, *Trans. Electrochem. Soc.*, **82**, 365 (1942).
15. G. W. Vinal, "Storage Batteries," 4th ed., John Wiley, New York (1955).
16. W. J. Hamer, *J. Am. Chem. Soc.*, **57**, 9 (1935).
17. H. S. Harned and W. J. Hamer, *ibid.*, **57**, 27 (1935).
18. H. S. Harned and W. J. Hamer, *ibid.*, **57**, 33 (1935).
19. V. H. Dodson, *This Journal*, **108**, 401 (1961).
20. V. H. Dodson, *This Journal*, **108**, 406 (1961).
21. P. Ruetschi, J. Sklarchuk, and R. T. Angstadt, *Electrochim. Acta*, **8**, 333 (1963).
22. K. R. Bullock, *This Journal*, **127**, 662 (1980).
23. J. L. Dawson, in "The Electrochemistry of Lead," A. T. Kuhn, Editor, p. 309, Academic Press, London (1979).
24. D. Pavlov, C. N. Poulieff, E. Klaja, and N. Iordanov, *This Journal*, **116**, 316 (1969).
25. P. Ruetschi and R. T. Angstadt, *ibid.*, **111**, 1323 (1964).
26. K. R. Bullock, G. M. Trischan, and R. G. Burrows, Paper to be presented at The Electrochemical Society Meeting, Detroit, Michigan, Oct. 17-22, 1982.

Corrosion Rates and Electrochemical Studies of a Depleted Uranium Alloy Tungsten Fiber Metal Matrix Composite

Patricia P. Trzaskoma*

Naval Research Laboratory, Code 6314, Washington, DC 20375

ABSTRACT

The corrosion rates of a tungsten reinforced depleted uranium alloy metal matrix composite have been measured, by immersion tests, in three environments (laboratory air, distilled water, and 3.5% NaCl) and compared to the rates of the matrix alloy (DU-0.75 Ti) alone. The corrosion rates of both specimens are negligible in laboratory air, increase in distilled water, and are greatest in NaCl for a 30 day period. In all environments the matrix alloy is preferentially attacked. In distilled water the corrosion rate of the matrix alloy is 3 times greater than the composite whereas in NaCl the corrosion rate of the composite is 1.3 times greater than the matrix. In electrochemical tests the composite was simulated by coupling separate samples of the fiber and matrix and the short-circuit (galvanic) currents were measured. A comparison of the corrosion rates calculated from the galvanic currents and from immersion tests shows the principal reaction of the composite in NaCl is galvanic coupling of the matrix and fiber.

The requirements for materials with improved mechanical properties, *i.e.*, strength, hardness, fracture toughness, for various engineering applications, have motivated the development of fiber reinforced metal matrix composites. While much work has focused on the fabrication and mechanical testing of metal matrix composites, more attention is now directed toward the measurement and evaluation of their corrosion behavior.

The corrosion rate of a metal system consisting of two dissimilar phases could reasonably be expected to be different from that of either phase alone. Local inhomogeneities in composition, structure, and stress

* Electrochemical Society Active Member.
Key words: corrosion, metal matrix composite, depleted uranium-0.75Ti, galvanic corrosion.

could result in increased environmental attack of either phase and bring about the deterioration of the composite bond. In addition, when the reinforcement phase is a conducting material, galvanic coupling with the matrix would result in a greater dissolution rate of the more active phase. Since galvanic corrosion is generally observed at metal-metal contact points (1), this phenomena would also affect the composite bond. Naturally, these problems would produce a serious degradation of the desired mechanical properties.

Depleted uranium (DU) is a surplus product obtained during the enrichment of natural uranium for nuclear applications. Because of the high strength and density of DU and its alloys, several non-nuclear applications have evolved in recent years.

While the corrosion rates of depleted uranium (DU) alloys in various environments have been measured (2-5), the corrosion rates of DU composites have not been extensively studied. The purpose of this paper is to report recent results on the corrosion behavior of a composite consisting of tungsten fibers in a matrix of a depleted uranium alloy. The effect of the tungsten fibers on the corrosion behavior of the composite was determined from immersion studies and electrochemical measurement. In the case of immersion studies, weight losses were measured for the composite material and for the host uranium alloy (without the tungsten fiber) in three environments: air, distilled water, and 3.5% NaCl. Galvanic currents were measured in NaCl for simulated composites consisting of tungsten metal coupled to depleted uranium for various surface area ratios of the tungsten. By a comparison of corrosion rates from environmental tests and from electrochemical studies, it was possible to determine the principal mode of corrosion attack for this system.

Experimental Procedures

Sample Preparation

The composite specimens were cylindrical samples of depleted uranium-0.75 weight percent (w/o) titanium (DU-0.75 Ti) containing about 50 volume percent (v/o) tungsten fiber. The diameter of the tungsten fiber was 508 μm (0.020 in.). The composite was prepared by liquid metal infiltration of the fiber and is designated DU/50W. The DU alloy specimens, also cylindrical, were the same composition as the alloy used in the composite. The nominal composition of this alloy is 0.75% Ti, 60 ppm C, 14 ppm N, 14 ppm H, 30 ppm O, and the remainder depleted uranium. The thickness of the samples was about 0.65 cm, and the diameter was about 2.3 cm and 2.1 cm for the composite and alloy, respectively. For the immersion studies a hole with a diameter of 0.48 cm was drilled in each specimen so that it could hang freely in solution. The exposed surface area was approximately 13.1 cm^2 and 11.1 cm^2 for the composite and alloy, respectively. Both specimens were obtained from Battelle Laboratories in Columbus, Ohio.

For immersion studies the samples were degreased in acetone for 2 hr, rinsed with distilled water, and cleaned in 1:1 HNO_3 for 15 min in order to remove the oxide coating. Finally they were again rinsed in distilled water, then acetone, allowed to dry 5 min, weighed, and hung in air or solution.

For the electrochemical measurements the alloy and composite specimens were mounted in epoxy, polished through 3/0 SiC paper, rinsed in water, then 95% ethanol, and placed in an electrochemical cell. Tungsten wire, 760 μm (0.030 in.) in diameter, was encased in shrinkable polytetrafluoroethylene (PTFE) tubing except for a portion to be exposed to solution. The exposed wire was abraded with 300 grade SiC paper, and rinsed in distilled water prior to immersion in the cell. The tungsten wire, type NS-55, was obtained from GTE Sylvania. The sodium chloride solution was prepared from Fisher certified reagent dissolved in distilled water from a Barnstead still. The pH of the solution was about 6.

Immersion Tests and Electrochemical Measurements

Immersion tests.—The cleaned samples were weighed and hung from PTFE thread into beakers containing the test environment (air, distilled water, or 3.5% NaCl). At all times the beakers were open to the atmosphere at temperatures of 22°-25°C. For each sample 175 ml of solution were used.

The weight loss with respect to time was found by taking samples from solution at various times, removing the loose products by gentle rubbing with a rubber scraper, rinsing with distilled water, acetone, drying, and weighing. The samples were then reimmersed in their respective solutions and the procedure was repeated. The weight loss was the difference between the weight at a given time and the original weight of the sample.

At the end of 30 days the samples were weighed and then cleaned in 1:1 HNO_3 to remove adherent corrosion products, rinsed, dried, and reweighed to obtain the total weight loss. The total weight loss was corrected for the weight change attributable to the dissolution of the samples by the nitric acid solution for the period of cleaning. (The weight loss due to the dissolution of the base material in 1:1 HNO_3 was found by measuring the weight loss of clean samples after immersion in this solution for 10 min. The results, 0.0194 mg/cm^2/min for the alloy and 0.5082 mg/cm^2/min for the composite, are an average of triplicate tests.) Thus weight losses, in the various environments, up to and including 30 days, are due to loose corrosion products while the total weight losses are due to both loose and adherent products for a 30 day period of immersion. In most cases the tests were run in triplicate.

Electrochemical measurements.—Open-circuit potentials were measured with respect to a saturated calomel electrode, in 3.5% NaCl solution. The potentials were continuously monitored, up to 3 days, using a strip chart recorder.

For the galvanic current measurements an epoxy mounted depleted uranium alloy sample and tungsten wire (760 μm diam) was immersed in solution in the corrosion cell and coupled through the potentiostat. The exposed surface area of the depleted uranium alloy was 3.26 cm^2. Using the potentiostat as a zero resistance ammeter the short-circuit current between the alloy and tungsten wire was recorded. The current output was monitored continuously until a constant value was maintained for 1 hr. This steady current was interpreted as the galvanic short-circuit current. This technique for measuring short-circuit currents has been described in the literature (6). The experiment was repeated using various lengths of tungsten wire in order to simulate composite samples of various surface area ratios of fiber. About 500 ml of solution were used for each test.

Results and Discussion

Immersion Tests

In laboratory air the alloy initially developed a copper-colored coating, which turned black in a few days. This coating was also observed on the composite at the exposed matrix metal areas. For both specimens the weight change was less than a milligram in 30 days.

In water and 3.5% NaCl, a black adherent film, a fine loose black product, and a powdery voluminous yellow product formed on both specimens. These products are believed to be UO_2 and various other hydrated uranium oxides. The attack was localized beginning

with a few scattered pits, which enlarged with time and covered the entire surface of the alloy in the NaCl solution. Within 12-13 days the attack in NaCl was sufficient to separate some fibers in the composite specimens. At the conclusion of the tests fibers along the edge had actually fallen free.

Figure 1 is a plot of the observed weight loss with respect to time of specimens in distilled water and NaCl solution. These points represent the weight losses due to loose product. The weight loss of the composite is greater than the alloy in both solutions (3 times greater in water and 1.5 times greater in NaCl in 30 days). For both materials the weight loss is significantly greater in NaCl solution.

Table I shows the total weight losses of samples in 30 days (adherent and loose products) and the ratio of adherent to total products in both solutions. The total weight loss of the composite in water is less than that of the depleted uranium alloy, whereas in NaCl the total weight loss of the composite is significantly greater than that of the alloy. Examination of the ratio of adherent products to total corrosion products shows that significantly more adherent product is formed on the alloy than on the composite in water. This could be due to the fact that the composite has a lower surface area of uranium, but also suggests a different corrosion mechanism. In NaCl the product ratios are comparable for the alloy and composite. Thus while the overall corrosion rate of the depleted uranium alloy is greater in water, the loss of material (loose products) is less than that of the composite. In NaCl solution the product ratio of the alloy decreases significantly and the corrosion rate increases sharply. This suggests that the adherent product provides some protection to the metal in solution. The corrosion rate of the composite (total weight loss) is 1.3 times that of the alloy in NaCl solution.

Table I. Weight losses of specimens immersed in distilled water and 3.5% NaCl for 30 days

Sample	Environment	All products (mg/cm²)	Adherent products (mg/cm²)	Loose products (mg/cm²)	Ratio (adherent: total)
DU-0.75Ti	Distilled H_2O	6.16	5.53	0.63	0.90
DU/5oW		2.38	0.42	1.96	0.18
DU-0.75Ti	3.5% NaCl	34.14	11.14	23.00	0.33
DU/50W		43.56	8 59	34.97	0.20

Electrochemical Tests

Open-circuit potential-time measurements.—The open-circuit potentials of the depleted uranium alloy, tungsten fiber, and composite were measured in 3.5% NaCl for times up to 90 hr. Figure 2 is a plot of this data. The potential of the alloy changes slightly from the initial value of −0.805 to −0.800V and remains constant after 4 hr immersion. A black product formed on the samples; some fell into solution while the rest adhered to the surface. This product was discontinuous and fluctuations in the potential after 5 hr were associated with loose product falling into solution. Some gas evolution was observed on the metal. The initial potential of the tungsten fiber is −0.380V and reaches a steady value of −0.250V in about 15 min. The points on the tungsten curve in Fig. 2 are the results of triplicate runs. No visual changes were observed on the tungsten surface in these tests. The potential of the composite stabilizes in about 2 hr at a value of −0.775V. Patches of a black product appeared on the surface and the fluctuations in potential after 10 hr were once again associated with the product falling into solution.

The close agreement between the open-circuit potentials of the alloy and composite (−0.800 and −0.775V, respectively) indicates the anodic reaction on the composite in NaCl is the dissolution of uranium. This is borne out by observations from immersion studies. However, the slightly more anodic open-circuit potential of the composite suggests the combination of metals affects the kinetics of the anodic reaction. This effect could be due to an increase of reaction sites on the alloy surface in the composite or a shift of the cathodic reaction to the tungsten surface. The large open-circuit potential differences between the alloy and fiber indicate that significant galvanic effects should take place on the composite.

Galvanic current measurements.—Galvanic currents were observed upon coupling the alloy and tungsten wire in NaCl solution. In Fig. 3 the short-circuit galvanic current between the alloy and fiber is plotted for various surface area ratios of fiber. In every case the current decreases with time and stabilizes in from 1 to 3 hr. The stabilized current is taken to be the galvanic current of the couple. As the surface area ratio of the fiber increases, the galvanic current increases. The potential of the couple, also measured during the tests, is shown in Fig. 3. These potentials are comparable to that of the composite in NaCl solution. Therefore, it is concluded that the experimental arrangement simulates the situation of a composite sample in solution. The potential of the couple

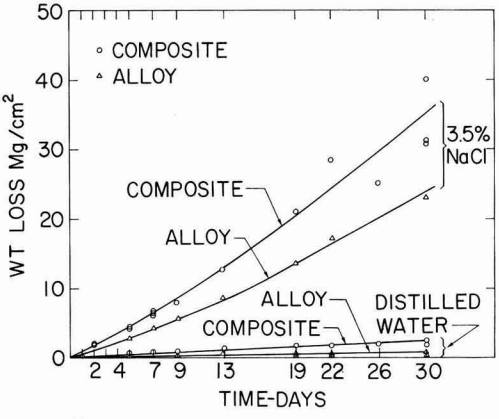

Fig. 1. Weight loss of DU-0.75Ti and DU/50W due to loose corrosion products in distilled water and 3.5% NaCl solution.

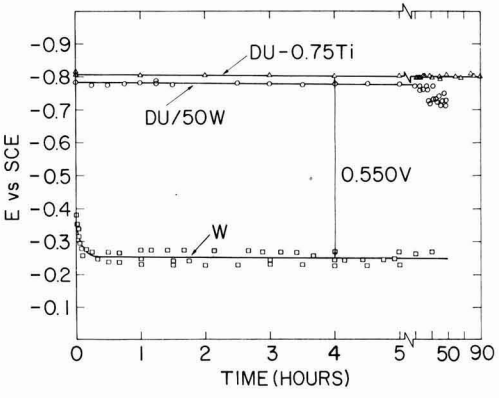

Fig. 2. Open-circuit potentials of DU-0.75Ti, tungsten fiber, and DU/50W in 3.5% NaCl solution.

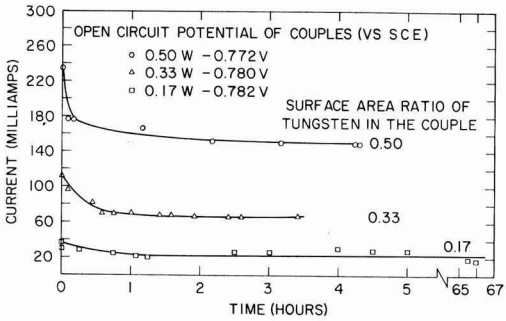

Fig. 3. Galvanic current between DU-0.75Ti and tungsten fiber in 3.5% NaCl for various surface area ratios of fiber.

becomes slightly more anodic as the surface area ratio of fiber increases.

Figure 4 shows a plot of galvanic current *vs.* the surface area ratio of fiber. The galvanic current is observed to increase linearly with increasing surface area ratio of fiber. A current of 0.100 mA is associated with the actual surface area ratio of tungsten in the composite (0.38). (The actual surface area ratio of fiber in the composite was determined by counting the fibers and multiplying by the surface area of each then dividing by the total surface area.) Assuming that alloying with small amounts of titanium does not influence the thermodynamics of the uranium equilibrium in aqueous solution, reference to the Pourbaix diagram (7) shows that uranium dissolves in the +4 state at the potential and pH of these experiments. Using this information and Faraday's law, the weight loss of uranium due to galvanic currents for the composite was calculated to be 5.33 mg/day. Dividing by the total surface area of the simulated composite, the weight loss is 1.01 mg/cm²-day. The actual weight loss of the composite in NaCl solution, from the immersion tests, was 1.72 mg/cm² in two days (see Fig. 1) or 0.86 mg/cm²-day. This value, it should be recalled, represents the weight loss due to loose products. If it is assumed that the ratio of adherent/loose products is constant, the total weight loss of the composite in NaCl solution can be calculated per day; this value is 1.08 mg/cm²-day. These data are summarized in Table II. Since the corrosion rates from immersion studies and galvanic current measurements are in such close agreement, it can be concluded that the composite corrodes by the dissolution of the matrix through galvanic coupling with the fiber. The cathodic reaction takes place predominantly on the fiber surface.

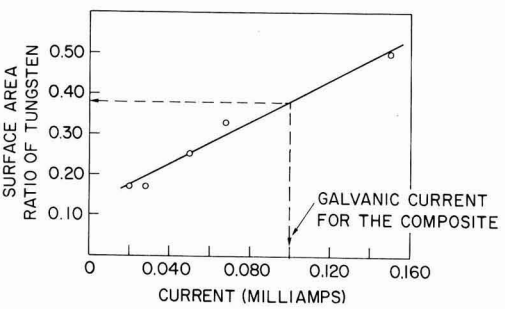

Fig. 4. Galvanic current of DU-0.75Ti, tungsten couples in 3.5% NaCl as a function of the ratio of surface area of tungsten to total surface area.

Table II. Corrosion rate of DU/50W in 3.5% NaCl

Total weight loss from immersion tests	Total weight loss from galvanic current measurements
1.08 mg/cm²-day	1.01 mg/cm²-day

Summary

The corrosion rates of the composite (DU/50W) have been measured and compared to the rates of the matrix alloy alone in air, distilled water, and 3.5% NaCl solution. In air the rates of the alloy and composite are negligible in a 30 day period. In distilled water the corrosion rate of the matrix alloy (total weight loss) is 3 times greater than the composite; however, in NaCl solution the corrosion rate of the composite is 1.3 times greater than the matrix alloy. In all cases the depleted uranium is preferentially attacked by the environment.

The reaction of uranium with water is probably the principal reaction in the distilled water environment; thus the corrosion rate of the composite is less than the metal matrix alone due to a lower exposed surface area of uranium. There is evidence that the presence of the fiber influences this reaction somewhat for there is not a direct correlation between surface area of metal matrix and corrosion rate (*i.e.*, surface area of uranium to fiber is 1.5:1 in the composite while the corrosion rate of the alloy to the composite is 3:1).

Comparison of the corrosion rate from immersion and electrochemical measurements has shown the principal reaction of the composite material in 3.5% NaCl is the galvanic coupling of the matrix and fiber. In this system it is therefore possible to lower the corrosion rate by decreasing the quantity of fiber in the composite.

Finally, this investigation has shown it is possible to measure the galvanic current between the metal matrix and fiber in a composite system through appropriate electrochemical modeling. This information, in conjunction with environmental tests, can be used to determine the extent to which galvanic effects direct the corrosion behavior in metal matrix/metal fiber composite systems.

Acknowledgments

The author wishes to acknowledge the discussions with Dr. R. J. Weimer and helpful suggestions of Dr. E. McCafferty, both of the Naval Research Laboratory, during the course of this work. This work was sponsored by DARPA under order No. 3388.

Manuscript submitted May 4, 1981; revised manuscript received Dec. 10, 1981.

Any discussion of this paper will appear in a Discussion Section to be published in the June 1983 JOURNAL. All discussions for the June 1983 Discussion Section should be submitted by Feb. 1, 1983.

Publication costs of this article were assisted by the Naval Research Laboratory.

REFERENCES

1. A. Brasunas and N. E. Hamner, "NACE Basic Corrosion Course," National Association of Corrosion Engineers, Houston, TX, March 11, 1970.
2. D. J. Sandstrom, "A Review of the Early A P Penetrator Work at LASL Which Led to the Selection of U-3/4Ti Alloy," Report No. LA-UR-76-1614 (1978).
3. L. J. Weirick, H. R. Johnson, and J. W. Dini, "Corrosion and Protection of Uranium Alloy Penetrators," Report No. SAND 75-8243 (1975).
4. A. Gallaccio and J. Joworski, "Performance and Properties of GAU-8 Production Uranium Penetrators," II, "Corrosion of Depleted U-3/4Ti and U-3/4 Quad Alloys in Salt Fog and Cyclic Tem-

perature-Humidity Conditions," Report No. F.A.-TR-75084 (1975).
5. L. J. Weirick and D. L. Douglass, *Corrosion*, **32**, 209 (1976).
6. D. A. Jones, *Electrochem. Technol.*, **6**, 241 (1968).
7. M. Pourbaix, "Atlas of Electrochemical Equilibria in Aqueous Solutions," p. 209, Pergamon Press, New York (1966).

Corrosion Resistance of Microcrystalline Stainless Steels

T. Tsuru and R. M. Latanision*

Corrosion Laboratory, Massachusetts Institute of Technology, Cambridge, Massachusetts 02139

ABSTRACT

The corrosion behavior of microcrystalline stainless steels, rapidly solidified and then hot extruded to form rods having 2-5 μm grains, was studied in aqueous solutions with and without chloride additions. In a chloride-free solution, the microcrystalline alloys showed electrochemical behavior virtually identical to that of conventionally processed alloys of the same composition. Resistance to pitting corrosion of the microcrystalline alloys in 0.5*N* NaCl at 60°C was found to be greater than that of the conventional counterparts. It is concluded that the high degree of homogeneity characteristic of the microcrystalline alloys, which resulted from rapid solidification, is the principal reason for their resistance to pitting corrosion.

In recent years considerable interest has developed in the corrosion resistance of metallic alloys produced by rapid solidification processing. For the most part, this interest has focused on metallic glasses that are typically produced by rapid quenching of some rather specific alloy composition from the liquid at rates of the order of 10^{6}°C/sec. Many of the metallic glasses are found to be remarkably resistant to general and localized corrosion (1-5).

On the other hand, because of the required quenching rates, such glassy alloys are necessarily produced in the form of filaments, wires, or thin sheet. Moreover, if such materials are heated after solidification, they may crystallize and in consequence lose their corrosion resistance (6, 7) as well as other useful properties.

There is, however, a second family of alloys produced by rapid solidification processing. In this category are alloys of virtually any composition that are, for example, quenched into the form of thin strips, subsequently compacted together, and finally hot extruded into the form of sections of rather larger sizes. The alloys processed in this way are not amorphous, but have grain size on the order of a micron. Likewise, because of the rapid solidification, they are chemically more homogeneous than conventionally wrought alloys of the same composition. Such materials may be produced in large sections and are often remarkably stable with regard to grain growth (8). To this point, however, little attention has been directed toward the corrosion behavior of microcrystalline alloys.

In this paper we report the results of studies of the uniform and localized corrosion behavior of microcrystalline stainless steels and their wrought counterparts. In a subsequent publication (9) the stress corrosion cracking resistance of these alloys will be described.

Experimental

Materials.—The composition of the iron-based alloys produced in microcrystalline form are shown in Table I. Alloy A is fully austenitic and alloys B and C are duplex, ferrite-austenite microstructures. Conventionally processed and microcrystalline specimens of each alloy were examined.

The conventional or wrought specimens of alloys A and B were annealed for 2 hr in air at 1000°C, then water quenched. The average grain sizes were approximately 70-100 μm. Samples, 3 × 1 × 0.5 cm, were cut from the plate. In the case of alloy C, samples were cut from the alloy in the as-cast condition. For comparison, commercial stainless steels, AISI 304 and 316, and an amorphous alloy (METGLAS[1] 2826A, $Fe_{32}Ni_{36}Cr_{14}P_{12}B_{6}$) were examined also.

The microcrystalline alloys were produced by Professor N. J. Grant, of the Department of Materials Science and Engineering at MIT, in the following manner: Rapidly solidified foils, 0.05-0.07 mm thick, were produced by a two roller quench method in which the alloy, melted by induction heating to 1600°C, is dropped from a ceramic crucible into the gap between two rollers spinning at 1800 rpm. The operation was carried out in a positive pressure of helium gas. To form a rod, cut and mixed foils were cold compacted at 200 Torr to approximately 85% of the density of the final alloy. The compacted foils were heated to 593°C in vacuum for 48-72 hr, then extruded through a circular die of 1.4 cm diam at 1065°C. This process produces a uniform microcrystalline (2-5 μm) structure. Samples approximately 5 mm thick were cut from the extruded rod. Figure 1 shows typical microstructures of the conventional alloy A and microcrystalline alloys. It is readily seen that the latter have very fine grains.

All specimens were mounted in an epoxy resin and wet polished to 600 grit on silicon carbide paper. The polished samples were cleaned with methanol in an ultrasonic washer.

The edge of the samples, used in a chloride-free solution, were coated several times with an acid resistant copolymer, and prior to each experiment the exposed surface was abraded with 500 grit paper.

[1] METGLAS is the trademark of Allied Corporation.

Table I. Chemical composition of alloys (balance iron)

	Element (w/o)						
	C	Si	Mn	Ni	Cr	Mo	Cu
Alloy A (Avesta* 254 SMO)	0.10	0.46	0.48	18.02	19.91	6.11	
Alloy B (Avesta* 3RE60)	0.02	1.54	1.52	5.0	18.6	2.83	
Alloy C (NAS** 45M)	0.035	0.62	0.53	5.02	23.42	1.49	1.03

* Avesta is the trademark of Avesta Jernverks Aktiebolag.
** NAS is the trademark of Nippon Yakin Kogyo.

* Electrochemical Society Active Member.
Key words: solidification, polarization, pitting potentials, dissolution potentials.

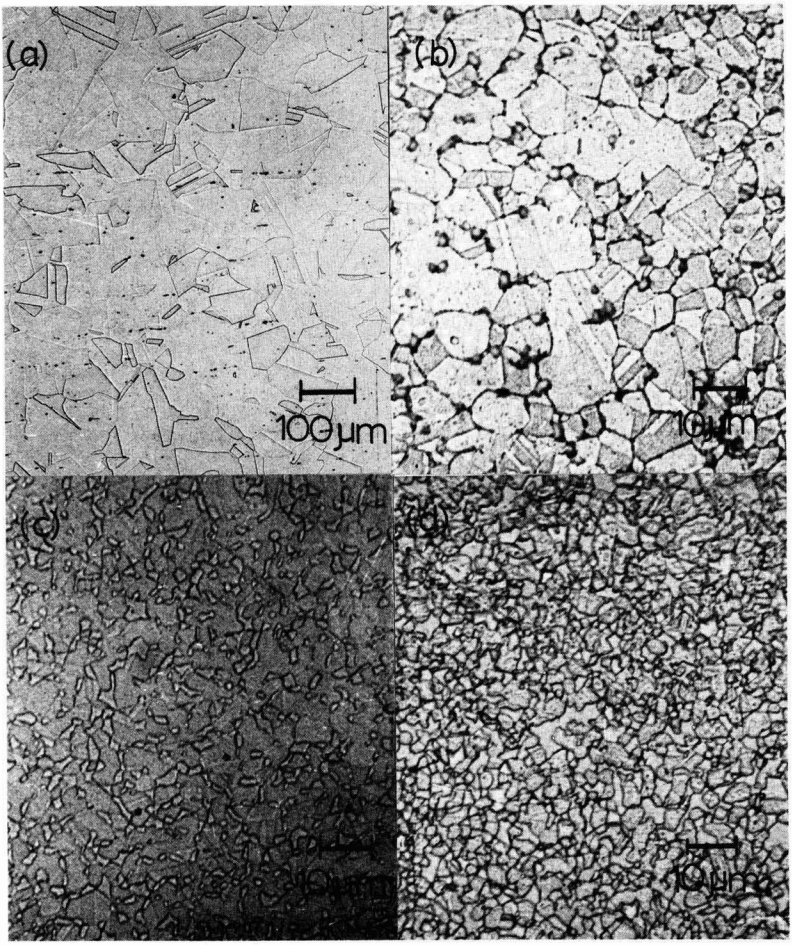

Fig. 1. Microstructure of conventionally processed alloy A (a), rapidly solidified alloys A (b), B (c), and C (d).

The samples used in the measurement of pitting potential were passivated in 20% HNO_3 for more than 1 hr and masked by tape to provide a window of 6.2 mm diam. To remove a passive film, the exposed area was abraded with 400 grit emery paper before an experiment. This preparation avoids crevice corrosion under the coating materials.

Electrolyte and cell.—A mixture of 0.5*N* Na_2SO_4 and H_2SO_4 of various concentrations was used as a chloride-free solution. For experiments in acid chloride solutions, 5*N* NaCl solutions with sulfuric acid were used. These solutions were deaerated by high purity nitrogen gas for more than 24 hr and, throughout the experiments, the solution in the cell was bubbled with gas.

For pitting studies, an aerated solution of 0.5*N* NaCl at 60° ± 1°C was used.

The electrolytic cell was a 300 ml multi-neck flask in which the specimen, a counterelectrode, and the Luggin-Haber probe for the calomel reference electrode were suspended in the electrolyte from ports in the flask. All the potentials were referred to a saturated calomel electrode.

Polarization measurements.—In a chloride-free solution, specimens were immersed in the solution for 10-20 min, then polarized in the active direction to the potential at which the cathodic current exceeded 1 mA/cm². After holding this potential for 5 min, the potential was scanned in the noble direction up to 1.0V or 1 mA/cm² of anodic current.

In acid chloride solutions, the specimens, which were activated just before the polarization by an immersion in 20% H_2SO_4 for 5 sec at 60°C, were then polarized in the noble direction from a potential 30 mV less noble than the immersion potential.

The potential scanning rate was 1 mV/sec in these experiments.

Measurement of pitting potential.—The specimen, first chemically passivated and then abraded, was polarized to −0.1V for 5 min, then anodically polarized at a scan rate of 0.4 mV/sec until the total current exceeded 1 mA whereupon the scanning direction was reversed. After the experiment, inspection was made under the tape for crevice corrosion and the data were omitted if crevice attack was observed.

Results and Discussion

Polarization curves in chloride-free solutions.—The polarization curves for conventional 316 stainless steel in a solution of 0.5*N* Na_2SO_4 with various concentrations of H_2SO_4 and that of the microcrystalline alloy A are shown for comparison in Fig. 2 and 3, respectively. Figure 4 shows the polarization curves of the microcrystalline and the conventional alloys of three stainless steels.

All the polarization curves measured were similar to these figures. Each curve exhibits four distinct po-

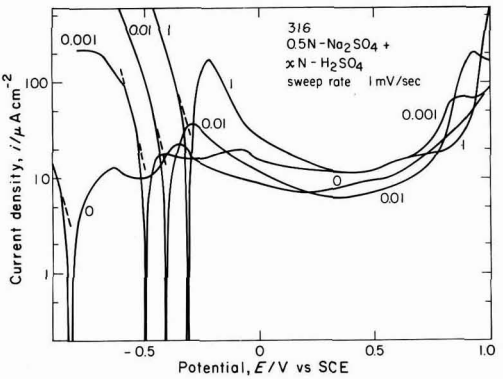

Fig. 2. Polarization curves of 316 stainless steel in 0.5*N* Na_2SO_4 + H_2SO_4. Numbers in the figure indicate the concentration of H_2SO_4 expressed in terms of normality.

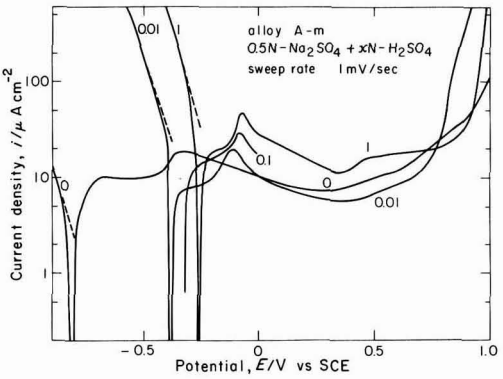

Fig. 3. Polarization curves of the microcrystalline alloy A in 0.5*N* Na_2SO_4 + H_2SO_4. Numbers in the figure indicate normal concentrations of H_2SO_4.

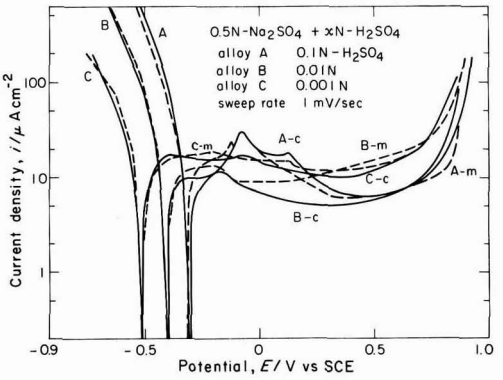

Fig. 4. Comparison of polarization curves between microcrystalline (m, dashed curve) and conventionally prepared (c, solid curve) alloys in 0.5*N* Na_2SO_4.

tential regions; namely, cathodic hydrogen evolution, anodic dissolution, passivity and transpassive dissolution, and/or oxygen evolution.

In the cathodic region, a Tafel relation is observed in all the cases and the slope is in the range of 90-140 mV/dec, most often 100-120 mV/dec. Decreasing the acidity of the solution shifted the cathodic polarization curves in the active direction. The *p*H dependence of the potential at which the cathodic current reached 100 $\mu A/cm^2$ was approximately 60 mV/*p*H, regardless of the specimen. On this basis, the hydrogen evolution reaction on the alloys is not affected significantly by the alloy composition or the crystalline grain size.

In the region of the anodic dissolution and the active-passive transition, the anodic curve shifted in the active direction with increasing *p*H of the solution. This means that the anodic dissolution rate of the alloy decreases with increasing *p*H. This kind of response is well known and has been reported by many investigators in relation to the study of anodic dissolution kinetics on iron and iron-base alloys (10).

As the *p*H of the solution increases, the anodic peak at the active-passive transition decreases and converts into two small peaks or a flat plateau.

In the passive region, the minimum current did not depend on the *p*H of the solution or the alloy and was typically 5-15 $\mu A/cm^2$ for all the experiments.

It might be expected that the anodic dissolution rate of the microcrystalline alloy should be larger than that of the conventional materials, because the former includes a much higher grain boundary area per unit volume and, hence, more dissolution sites. On the other hand, from studies of the oxidation behavior of microcrystalline stainless steel at elevated temperature (11) it was concluded that the oxide film on this alloy is thinner and more adherent than that on the conventionally processed alloy. Likewise, similar behavior and correspondingly lower passive current densities might be expected for the microcrystalline alloys.

The effect of the grain size (25-150 μm) and cold-work on anodic dissolution kinetics was reported by Zamin and Ives (12). They found no differences on the anodic dissolution kinetics and the peak current for pure nickel in a chloride-containing acid solution. Similarly, the polarization curves measured in the present work did not exhibit any significant differences between conventional crystalline and microcrystalline structures in chloride-free environments.

These facts suggest that the grain size may not be a significant factor in determining the anodic dissolution kinetics of polycrystalline alloys. With regard to passivity, more detailed investigations are required to establish the role of grain size.

Corrosion potential and corrosion current.—The *p*H dependence of the corrosion potential, E_{cor}, is shown in Fig. 5. The dependency is approximately −60 mV/*p*H for a *p*H lower than 4 and slightly higher at more alkaline *p*H.

The corrosion current density, i_{cor}, estimated by Tafel extrapolation from the cathodic part to the corrosion potential, decreased with increasing *p*H as shown in Fig. 6.

That the *p*H dependence of the corrosion current is −0.2 to −0.3 dec/*p*H and the corrosion potential −60 mV/*p*H can be understood by the fact that both the anodic and cathodic polarization curves shifted in the less noble direction with increasing *p*H of the solution. On the basis of typical mechanisms proposed for the anodic dissolution of iron, one expects these parameters to be in the range of −0.3 to −0.6 dec/*p*H and −50 to −90 mV/*p*H, respectively (10).

The corrosion current of the amorphous alloy, 2826A, is shown for comparison and is one order of magnitude smaller than that of the crystalline alloys which were all of nearly the same order of magnitude, Fig. 6.

The estimation of the corrosion current by the Tafel method was checked by the polarization resistance, R_{cor}, which was calculated from the slope of the po-

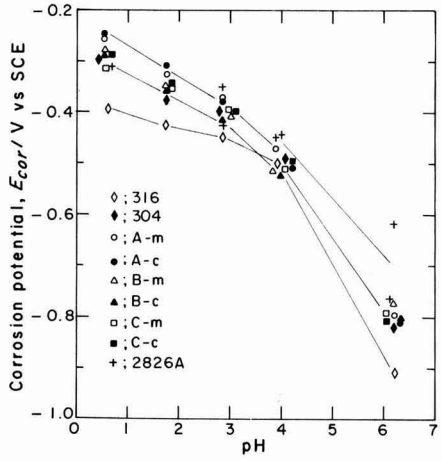

Fig. 5. pH dependence of the corrosion potential in chloride-free sulfate solutions.

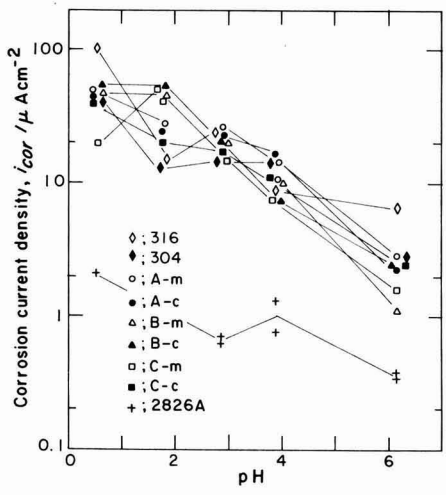

Fig. 6. pH dependence of the corrosion current density in chloride-free sulfate solutions.

larization curve within ± 5 mV of the corrosion potential. Figure 7 shows the plot of i_{cor} against R_{cor}. There is a good relationship, $i_{cor} = K/R_{cor}$, between these two values with a few exceptional points. This means that the polarization resistance measurements and the Tafel extrapolation were compatible.

Summarizing our finds in the chloride-free solutions, the corrosion behavior and electrochemical properties of the microcrystalline and the conventional alloys were very similar.

Pitting potentials.—Initially the pitting potential of the alloys was measured by the potential scanning method at 0.4 mV/sec in a 0.5*N* NaCl solution at ambient temperature. Since the pitting potential of the alloys A, B, and C fell into the transpassive potential region at this temperature, a reproducible pitting potential and pitting without coincident crevice corrosion under the masking tape were difficult to obtain. Hence, the experiments were conducted at 60°C and results on alloys B and C are reported. In the following discussion, current is described by total

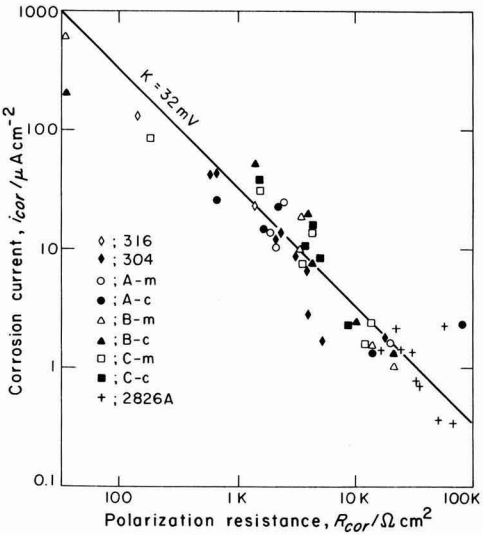

Fig. 7. Relationship between polarization resistance at corrosion potential and corrosion current estimated from Tafel extrapolation.

current and the surface area exposed was fixed as 0.30 cm².

Typical potential-current curves are shown in Fig. 8. During potential scan in the noble direction, current oscillations preceded a continuous increase at which point pits grew continuously. For the microcrystalline alloys the current usually increased more sharply and at more noble potentials, but this was preceded by more frequent current oscillations.

Three potentials were used to characterize the pitting susceptibility (13). The first is the pit initiation potential, E_{cri}, defined as the potential at which the current exceeded 10 μA. Pits nucleated above this

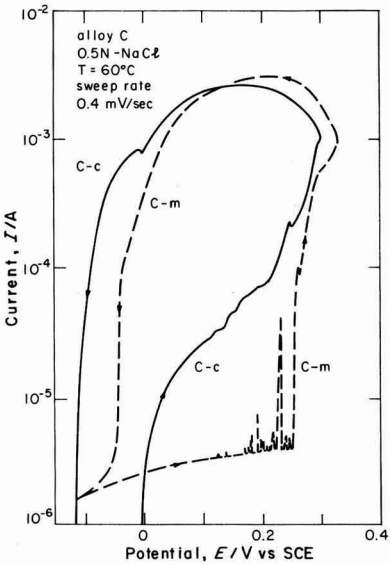

Fig. 8. Anodic polarization curve of alloy C in 0.5*N* NaCl at 60°C. Direction of potential sweep was reversed at 10^{-3} A. The m and c denote the microcrystalline and conventional alloy.

potential will grow continuously as pitting corrosion proceeds. The second is the pit propagation potential, E_{pro}, at which pits propagate at a certain rate, defined by current in excess of 1 mA in the forward scan. The third is the pit repassivation potential, E_{pas}, at which all the pits were passivated and below which pit propagation ceases. The latter was determined as the point at which the current was reduced to less than 10 μA in the reverse scan. Although these definitions and interpretations are still a matter of dispute (14), they may be used as an index of the susceptibility to pitting corrosion, provided that these parameters were measured under the same condition.

Results are summarized in Table II. It should be noted that all the characteristic potentials for the microcrystalline alloys were more noble than those for the conventional materials, and the conventional alloy C showed the most active potential for pit initiation.

On this basis, it can be concluded that the microcrystalline alloys are more resistant to pit initiation and propagation and are more easily repassivated than the conventional alloys.

One may consider that the pits initiate at sites where impurity elements in the alloy, for example, sulfur or phosphorus, segregate. These elements may be incorporated into the passive films, thereby leading to locally more defective films. When an aggressive anion, such as Cl^-, attacks such points in the film, pit nucleation occurs. A growing or propagating pit needs a critical volume and a certain nucleus shape, because the dissolution reaction depends intimately on the chemistry of the electrolyte in the pit.

Whether the nucleus will grow or not may depend on the concentration of impurities accumulated at the site. Local attack on less defective films (perhaps characterized by a lower segregate concentration or a more uniform partitioning of impurities) may also nucleate, however, self-repair or repassivation may be extremely rapid. Hence, the probability of pit initiation should be a function of the development of weakened films, which depends on the segregation of impurities, and the frequency of attack which may depend on the distribution of defects, the concentration of the aggressive anions, and the electrode potential.

According to Zamin and Ives (12), a small grained pure nickel specimen exhibited a greater susceptibility to pitting than a larger grained specimen, and all the pits were found at grain boundaries which were considered by them as a structurely disturbed region. On the other hand, grain boundaries are also considered as the sites where the segregation is most likely to occur. Similar behavior may not be typical of microcrystalline alloys, however, because the most important factor should not be the grain size but the concentration and distribution of impurities at segregated sites. In microcrystalline alloys, because of rapid solidification processing, impurities are dispersed uniformly in the alloy.

Microscopic examination of the specimen surface that was anodically polarized for a short time around the critical potential, E_{cri}, revealed that most of the pits initiated at grain boundaries on both the microcrystalline and conventional alloys, as shown in Fig. 9. In the case of microcrystalline alloys, however, some small pits, which may have stopped growing at an early stage, are also found in the matrix [Fig. 9(b)]. By a spot electron microprobe analysis at these points, they were confirmed as pits. This fact suggests that the microcrystalline alloys have many sites for pit initiation even in the matrix, but at most of these sites solute or impurity accumulation is insufficient to propagate pits because of the rapid solidification pro-

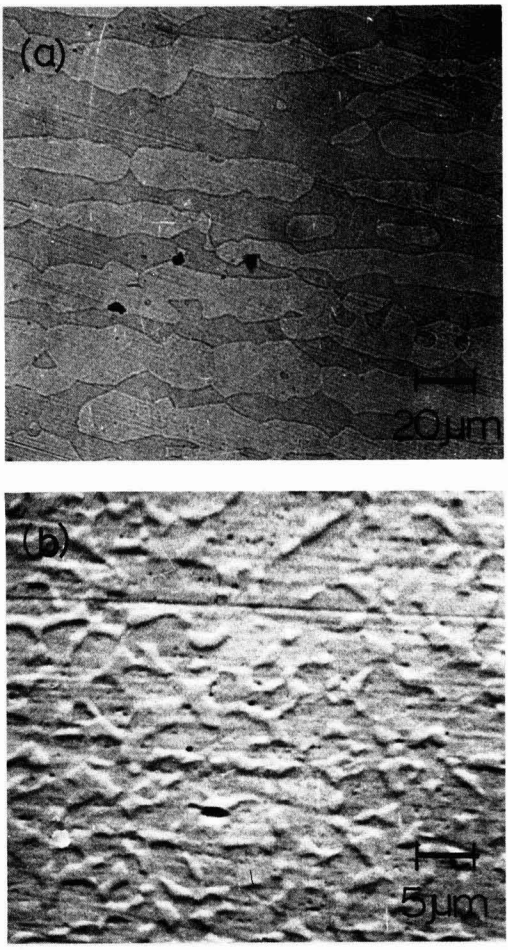

Fig. 9. Pit nuclei on the conventional and the microcrystalline alloy B formed in 0.5*N* NaCl at 60°C. (a) The conventional alloy was polarized at 250 mV for 25 sec, (b) the microcrystalline alloy was polarized at 280 mV for 1 min (SEM). Both were slightly etched in HNO_3 + HCl + glycerol for 5 sec after the polarizations.

Table II. The characteristic potentials E_{cri}, E_{pro}, and E_{pas} for pitting corrosion (0.5*N* NaCl, 60° ± 1°C, deaerated)

	E_{cri}/mV	S.D.* σ	N.R.	E_{pro}/mV	S.D. σ	N.R.	E_{pas}/mV	S.D. σ	N.R.
316	195	14.3	4	237	15.3	4	25		3
Alloy B-c	216	39.5	7	270	26.7	7	−14	13.8	7
B-m	240	34.9	5	313	32.5	5	11	7.8	4
Alloy C-c	49	80.1	8	282	48.5	8	−109	12.1	7
C-m	247	18.7	6	314	14.2	6	−49	9.0	5

* S.D., standard deviation; N.R., number of runs; c, conventional; m, microcrystalline alloy.

cessing. By this processing, impurities are dispersed uniformly in the alloy so that impurity segregation or accumulation is expected to be minimal. This situation is even more likely in amorphous alloys, which exhibit great resistance to pitting corrosion (5, 15).

In some cases, more frequent oscillations were observed on microcrystalline alloys just before the critical potential. This may perhaps be accounted for by considering that the alloy has many sites for pit nucleation, but the amount of segregated impurities at such sites may be less than some critical concentration required for growth. The same argument can be applied to pit initiation in the conventional alloy C which was used in the as-cast condition. Since the degree of segregation in the cast structure should be larger than that in a wrought or a microcrystalline alloy, pits can initiate and grow more easily resulting in pit initiation at a less noble potential.

Nowak (16) has reported the susceptibility to pitting corrosion of a microcrystalline 304 stainless steel which was prepared by sputtering with very small grains of 15-30 nm in diameter. Diffraction patterns of the grain indicated both bcc and fcc phases. He found that the pitting potentials of these microcrystalline alloys, especially with addition of about 1% of Al and/or Si, in 1M NaCl were markedly higher than those of the conventionally prepared 304 steel, and that a heat-treatment at 450°C for 1 hr in vacuum lowered the pitting potential of the sputtered alloy. He considered that the high resistance to pitting corrosion of the microcrystalline alloys should be attributed to structural differences, but it was not clear whether this arose from the bcc structure or the microcrystalline nature of the sputtered alloys. His results suggest that the as-sputtered alloy may be more homogeneous than the conventional alloy and that the degree of segregation is increased by the heat-treatment of the sputtered alloys which has the consequence of making E_{cri} more active.

Polarization curves in acid chloride solutions.—In the case of localized corrosion, such as pitting, crevice corrosion, and stress corrosion cracking, the chemistry of the electrolyte in the pit, the crevice, and the crack tip is likely to be quite different than that in bulk solution. In these occluded cells, one expects to find an increase in the concentration of metal ions, chloride ions, and protons, the latter produced by metal ion hydrolysis. For example, a solution characteristic of what might be observed in an occluded cell (which contained 3.5 mol/liter chloride ion with 0.5, 2.1, and 0.9 mol/liter of Na^+, Fe^{2+}, and Cr^{3+}, respectively) exhibited a pH of 1.3-1.5. Hence, it was considered useful to measure polarization behavior in an acid chloride solution in order to understand localized corrosion, especially pitting and crevice corrosion (17).

The solutions used were 5*N* NaCl with 0.1 and 0.01*N* H_2SO_4 and 4.5*N* NaCl with 0.9*N* H_2SO_4 at 25°C.

The polarization curves, shown in Fig. 10 and 11, shifted upward with increasing acidity. It should be noticed that the peak currents at active dissolution for the microcrystalline and the conventional alloys were almost the same and the conventional alloy showed a large secondary dissolution peak near 0.0V.

The potential in the growing pit should be in the range of +0.1 to −0.2V, because the repassivation potential falls in this range. At the repassivation potential the ohmic drop between the pit and the free surface is likely to become very small and the potential in the pit is considered nearly equal to that on the free surface. Comparing the current in this range, therefore, we can roughly judge the susceptibility to pitting corrosion. Furthermore, this can be applied also to crevice corrosion.

In the case of 316, the active dissolution peak rose higher and shifted in the noble direction with increasing acidity. As localized corrosion proceeds, corresponding to an increase in the acidity of the solution, the dissolution mechanisms should change from the secondary dissolution rate process to active dissolution.

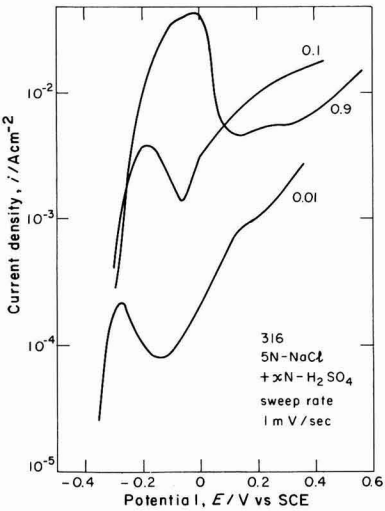

Fig. 10. Anodic polarization curves of 316 stainless steel in acid chloride solution.

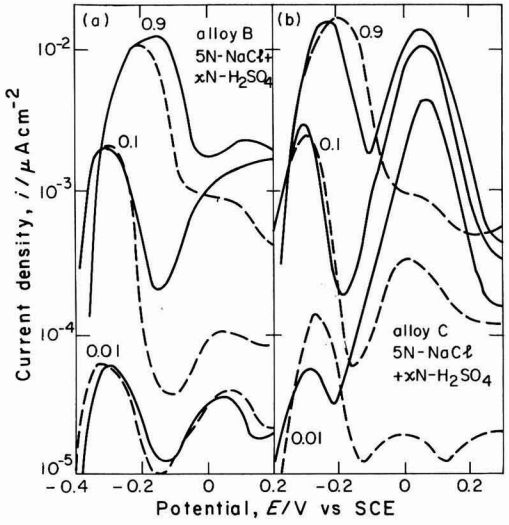

Fig. 11. Anodic polarization curves of alloy B (a) and C (b) in acid chloride solution. Solid and broken lines denote conventional and microcrystalline alloy, respectively. Potential sweep rate 1 mV/sec.

For alloy B, the polarization curves in 0.01*N* H_2SO_4 + 5*N* NaCl were just the same for both microcrystalline and conventional alloys. With increasing acidity the currents observed on the microcrystalline alloy in the potential range +0.1 to −0.2V were several times smaller than that of the conventional one. This may be interpreted to suggest that to initiate localized corrosion is not so different for both materials, but when pits propagate and increase the acidity in the occluded cell the propagation rate of the conventional alloy should be several times larger than that of the microcrystalline alloy. In a practical sense, once the

corrosion rate has increased, more rapid accumulation of metal cations occurs with subsequent rapid decrease of *p*H. Hence, the difference in the propagation rate may be much larger than that estimated from the polarization curves.

The differences in the polarization curves are clearer for alloy C. The secondary peak for the conventional alloy was very large in a solution of low acidity. A very active value of the pit initiation potential for conventional alloy C may be attributed to this secondary peak, because the nuclei of the pit can grow easily without a large acidification.

The heights of the secondary peak are in the order of as-cast alloy C, wrought alloy B, and both microcrystalline alloys. Since this order corresponds to the degree of segregation expected in the alloys, the secondary peak may be a characteristic of the preferential dissolution of the segregated sites in a concentrated chloride solution. In other words, the degree of the segregation influences the susceptibility to localized corrosion, not only with regard to pitting but also crevice corrosion and, therefore, the microcrystalline alloys have a larger resistance to the localized corrosion.

Summary

1. In chloride-free solution, the corrosion behavior and electrochemical properties of the microcrystalline and the conventional stainless steels were very similar.

2. Measurement of pitting potential in 0.5*N* NaCl solution at 60°C revealed that the microcrystalline alloys were more resistant to pit initiation and propagation and that pits were more easily passivated than in the case of the conventional alloys. Higher homogeneity or lower segregation in the microcrystalline alloys, due to rapid solidification processing, might account for the higher resistance to pitting corrosion.

3. The degree of segregation in the alloys affects polarization behavior in acid chloride solutions. The susceptibility to pitting corrosion may be examined by such polarization experiments.

4. The microcrystalline alloys, produced by rapid solidification followed by hot extrusion, may be expected to exhibit a high resistance to localized corrosion.

Acknowledgments

The authors thank Professor N. J. Grant of the Department of Materials Science and Engineering at Massachusetts Institute of Technology for providing the microcrystalline alloys and valuable comments. The support of this research by the Center for Materials Science and Engineering at Massachusetts Institute of Technology, under NSF-MRL Core fund DMR 78-24185, is also gratefully acknowledged.

Manuscript received July 27, 1981.

Any discussion of this paper will appear in a Discussion Section to be published in the June 1983 JOURNAL. All discussions for the June 1983 Discussion Section should be submitted by Feb. 1, 1983.

Publication costs of this article were assisted by Massachusetts Institute of Technology.

REFERENCES

1. R. M. Latanision, J. C. Turn, Jr., and C. R. Compeau, in "Mechanical Behavior of Materials," K. J. Miller and R. F. Smith, Editors, p. 475, Pergamon, Oxford (1979).
2. J. C. Turn, Jr., Ph.D. Thesis, M.I.T. (1979).
3. T. Masumoto and K. Hashimoto, *Ann. Rev. Mater. Sci.*, **8**, 215 (1978).
4. K. Hashimoto, *Suppl. Sci. Rep. RITU, Series A*, 201 (1980).
5. R. B. Diegle, N. R. Sorensen, T. Tsuru, and R. M. Latanision, in "Corrosion: Treatise on Material Science and Technology," J. C. Scully, Editor, Academic Press, In press.
6. R. B. Diegle and J. E. Slater, *Corrosion*, **32**, 155 (1976).
7. M. Naka, K. Hashimoto, and T. Masumoto, *ibid.*, **36**, 679 (1980).
8. M. Suga, J. L. Goss, G. B. Olson, and J. B. Vander Sande, in "Proceedings of 2nd International Conference on Rapid Solidification Processing Principles and Technologies," (Virginia, 1980), In press.
9. S. X. Zhang and R. M. Latanision, Unpublished research.
10. J. O'M. Bockris and A. K. N. Reddy, "Modern Electrochemistry," Vol. 2, p. 1080, Plenum, New York (1976).
11. M. D. Merz, *Met. Trans.*, **10A**, 71 (1979).
12. M. Zamin and M. B. Ives, in "Localized Corrosion," R. W. Staehle, *et al.*, Editors, p. 337, NACE, Houston (1971).
13. S. Smialowska and M. Czachor, in "Localized Corrosion," R. W. Staehle *et al.*, Editors, p. 353, NACE, Houston (1971).
14. P. E. Manning, *Corrosion*, **36**, 468 (1980).
15. T. M. Devine, *This Journal*, **124**, 38 (1977).
16. W. B. Nowak, *Mater. Sci. Eng.*, **23**, 301 (1976).
17. I. Matsushima and J. Sakai, *Tetsu to Hagana*, **63**, 598 (1977).

EPR Investigation of Fe, Mixed Fe-Mo, and Mo Naphthalocyanines

Application to the Electrocatalysis of Oxygen Reaction

M. Savy*

Laboratoire d'Electrochimie Interfaciale du C.N.R.S., 92190 Meudon, France

and J. E. Guerchais and J. Sala-Pala

U.E.R. des Sciences, Faculté de Bretagne Occidentale, 29283 Brest, France

ABSTRACT

Fe, mixed Fe-Mo, and Mo naphthalocyanine samples electrochemically investigated in previous work have been prepared and studied by the EPR technique. In the case of the Fe compounds, kinetically slow changes have been shown to occur from axial to octahedral symmetry. The resulting Fe^{III} configuration is close to the multispin criterion for electrochemical activity. With Mo samples two kinds of sites are visible on which Mo oxidation proceeds much faster than Fe^{III} formation. The most stable Mo sites in the presence of conducting solutions are also the most reactive ones for oxygen adsorption.

The importance of iron naphthalocyanine compounds as electrocatalytic materials has been shown recently (1). Improvement of their stability and electrocatalytic activity for the oxygen reaction may be expected by the addition of aromatic rings to the ligands (2). Molybdenum naphthalocyanine compounds have also been investigated for oxygen electrocatalysis and have proved to be equivalent or better than iron compounds (3). Changes in spin multiplicity during reaction have been well documented (4), and in the case of oxygen reactions it has been shown that the easy crossover from high to low spin can favor several reaction paths with activation of adsorption and desorption steps of the oxygen molecule (5). This effect cannot take place in the case of molybdenum naphthalocyanine samples, however it should be pointed out that EPR data can yield information on the spin configuration of the central ion in the Fe^{III} (6a) or $Mo^{(V)}$ (6b) states.

The aim of the present work was, firstly, to use the EPR technique to investigate the electronic configuration of iron (I), mixed iron molybdenum (II), and molybdenum naphthalocyanine compounds (III). Secondly, in presence of solutions to detect some effects associated with the presence of radical species by the addition of a scavenger such as glutathione (7). As shown in Ref. (7), this compound gives rise simultaneously to depletion of oxygen radicals and to specific adsorption on the central ion.

Experimental

Synthesis of materials.—The synthesis of iron naphthalocyanines was conducted by the reaction of 1-2 dicyanonaphthalene with an iron bis β-diketonate in a sealed tube.

Preparation of 1-2 dicyanonaphthalene.—This derivative was synthesized from naphthylamine sulfonic acid following the reaction procedure described in Ref. (8), *i.e.*, diazotization followed by fixation of the first nitrile function through the use of the potassium cyanide/copper sulfate couple and the introduction of the second nitrile function by action of potassium ferrocyanide. However, the experimental equipment was modified during the last step. The mixture $C_{10}H_6(SO_3K)CN\text{-}K_4Fe(CN)_6$ was placed in the center of a Pyrex tube of about 80 cm length inside a tubular furnace of 30 cm length. The tube was connected at one end to a nitrogen inlet, with the other end to the inlet of a vacuum pump.

The pressure was fixed at 10^{-1} Torr and the temperature between 300°-350°C. Dicyanonaphthalene crystals were sublimed on the cooler part of the tube. During this procedure nitrogen was bled into the tube in order to aid the migration of the compound that was finally recrystallized in absolute methanol.

Preparation of 1,2 iron (Fe-NP_c) and iron molybdenum and Mo naphthalocyanines.—An intimate mixture of 1-2 dicyanonaphthalene (2×10^{-3} mols) and of iron bis (2,2,6,6-tetramethyl-3.5 heptane dionato) iron ($Fe(Me_3\text{-}C\text{-}CO\text{-}CH\text{-}CO\text{-}C\text{-}Me_3)_2$) ($0.5 \times 10^{-3}$ mols) was sealed under vacuum in a glass tube and heated to 300°C for 24 hr. After opening the tube, the mixture was washed successively with dilute HCl followed by water up to neutral *p*H, then by benzene, ethanol, and ether. It was dried at 100°C under vacuum for several hours.

Elementary analysis.—With samples I($FeNP_c$) the elementary analysis is given as follows. Found: C, 75.5%; H, 3.1%; N, 13.3%; Fe, 5.3%; and expected: C, 75.0%; H, 3.1%; N, 14.6%; Fe, 7.3%.

The 1,2 iron molybdenum naphthalocyanine was obtained by a similar procedure, by adding ammonium paramolybdate $(NH_4)_6Mo_7O_{24}4H_2O$) totaling 50 mg ($0.04\ 10^{-3}$ mols) to the same starting mixture of 1,2 dicyanonaphthalene and iron bis (β-diketonate) iron derivative. The elementary analysis of this material (II) is given as follows. Found: C, 75.0%; H, 3.4%; N, 13.2%; Fe, 4.7% ± 0.2%; Mo, 5.5 ± 0.2%; and expected: C, 75.0%; H, 3.1%; N, 14.6%; Fe, 2.69%; Mo, 4.61%.

As a systematic deficiency in nitrogen was found, Fe and Mo contents have also been determined by x-ray fluorescence induced by proton bombardment[1] to avoid an error due to the above method of analysis. Protons of 2.3 MeV were passed through a 1 μm thick aluminum foil containing evaporated silver. The sample was bombarded by the resulting 1.8 MeV beam and the x-ray fluorescence was detected with an SiLi detector. Quantitative analysis was carried out by comparison with the Kα-ray of silver. From the results obtained it must be concluded that a nonnegligible amount of Mo must be transformed into an oxide form in addition to the naphthalocyanine ligand.

In order to discriminate between the effects of molybdenum and those of iron, a synthesis of molybdenum naphthalocyanine was also undertaken, in this case using only ammonium paramolybdate with di-

* Electrochemical Society Active Member.
Key words: Mo^{V} and Fe^{III} EPR catalysis, chelates, adsorption.

[1] The authors acknowledge Professor Decomminck, Faculté N.D. de la Paix, Namur, Belgique, for the achievement of this experiment.

cyanonaphthalene (DCN) in the initial ratio of 4 DCN per 1 mol of molybdenum. The product samples were thoroughly washed in a glove box with benzene, ethanol, HCl, 10% distilled water, and ethanol [samples (III)].

EPR measurements.—The EPR spectra were recorded on a Bruker BER 420 spectrometer operating in the X-band (modulation frequency 100 kHz at 24°C), a 5 mm diam tube was used for the dry powder and the experiments with solutions were carried out in a 1 mm diam EPR tube. All the samples were of high purity and used without further purification. Glutathione (Merck for biochemical uses) was checked for impurities by EPR.

Results

EPR spectra of samples (I, II, and III).—The EPR spectra of samples (I) freshly prepared (A) and after prolonged exposure to air (B) are given in Fig. 1. The (A) form shows a signal in an axial configuration with g // = 1.9894 and g ⊥ = 2.0152. These spectra remain stable after a few days of exposure to air. However, after more than a month of air exposure they change to form (B).

In presence of pure water signals (A) or (B) are not modified even after treatment of the samples by a wetting agent such as ethanol. A slow drift of g iso (isotrope) with form (B) can be observed up to g iso = 2.00245 close to the free electron value. This limit is reached more rapidly with the powder than with crystalline samples, the drift being speeded up by grinding under air atmosphere.

The EPR spectra of iron-molybdenum naphthalocyanine samples (II) and molybdenum naphthalocyanine samples (III) are both shown in Fig. 2. They show similar characteristics. Three g values characterize the Mo^V ion (9) that in the present case is located in at least two different environments. Two values are smaller than 2 ($g_x = 1.9760$ and $g_y = 1.9814$) and two are higher $g_z = 2.0023$ (this value being less accurate due to the overlapping signal at $g = 2.0018$). A hyperfine constant (60G) between the electron and the 95 and 97 isotopes of Mo is in good agreement with the values of Ref. (9). The other species has an isotrope g value $g_i = 2.0018$.

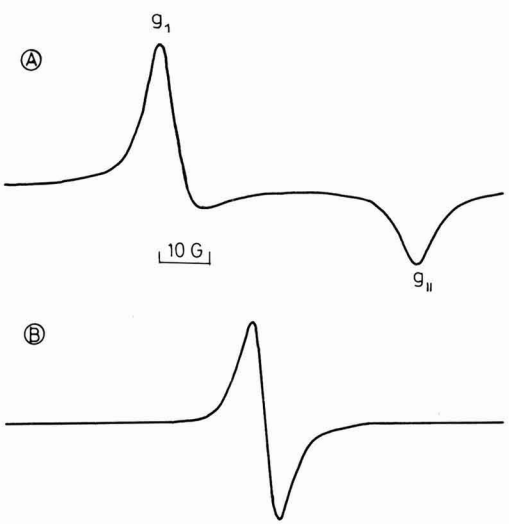

Fig. 1. EPR spectra of iron naphthalocyanines: (a) under nitrogen or short exposure at air or in presence of water and (b) after more than one month exposure at air or in presence of water.

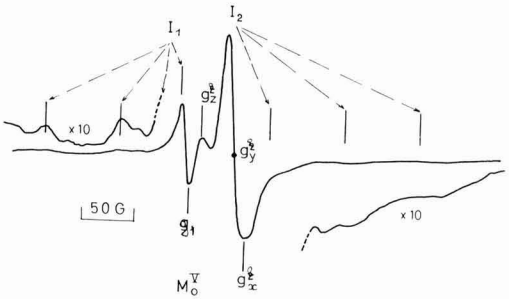

Fig. 2. EPR spectra of iron-molybdenum and Mo naphthalocyanines [samples (II) and (III)].

In contrast to samples (I) the EPR signal of samples (II) and (III) remains unchanged after a long exposure at air. The results concerning samples (II) or (III) prepared in a glove box with an oxygen pressure maintained below 1000 ppm are represented in Table I. They show the differences in affinity *vs.* oxygen pressure of the two main molybdenum environments. The lowering of the oxygen pressure induces a lowering in the same ratios of both Mo^V signal intensities I_1 and I_2. After introduction of oxygen, I_2 increases only slightly while I_1 almost doubles. On prompt return to a $4 \cdot 10^{-6}$ Torr vacuum, I_1 drops only slightly while I_2 still increases. After a new exposure to air both signals pass through a maximum then stabilize.

In the presence of conducting electrolytes, reduced oxygen adducts can arise simultaneously with protonation (10), which can perturb the voltage distribution at the applied electric field at the interface both in the double layer region or through nucleation (11) and diffusion processes inside the catalyst material. In all cases a 0.7M NaCl solution was used as a supporting electrolyte to maintain a constant double layer structure. To vary the oxygenated radical concentrations at the surface of the materials, a scavenger (glutathione) (7, 12) was added in various concentrations. A 0.7 HCl solution has been used to show any effect associated with protonation. This effect has been proven to occur simultaneously with specific adsorption on the central ion (7, 11). On samples kept under vacuum (Table II) the solutions have been thoroughly deaerated through argon. On those left in air the experiments have been conducted with oxygen-saturated solutions (Table III). The modifications of I_1 and I_2 are given in these tables, respectively.

In all the cases investigated the ratio I_2/I_1 was shown to grow continuously as a function of time. This effect is inhibited by the presence of glutathione, but enhanced in presence of HCl. For the same solution, it was more intense with deaerated samples.

Table I. Variation of I_1 and I_2 Mo^V signal intensities in the iron-molybdenum (II) and (III) naphthalocyanines samples *vs.* successive treatments under oxygen

No. treatment	I_1	I_2	I_1/I_2
1. Under N_2 (p_N = 1 atm; < 1000 ppm O_2)* (several days)	4.2	23.9	5.62
2. Under vacuum (5×10^{-5} Torr) (30 min)	3.1	17.8	5.72
3. Under oxygen (p_{O_2} = 1 atm) (20 hr)	6.1	18.8	3.08
4. Under vacuum (4×10^{-6} Torr) (10 min)	5.8	20.8	3.58
5. In air† (30 min)	9.6	27.3	2.84
6. In air† (several days)	8.0	25.5	3.18

* Reproduced values.
† The "absolute" intensities are not comparable with previous measurements.

Table II. The effect of wetting on Fe^{III}-Mo^{V}-NPC in presence of glutathione (GSH) (samples under vacuum 10^{-5} Torr). I_{10} and I_{20} corresponding intensities in air.

Solutions	I_1/I_{10}	I_2/I_{20}	I_2/I_1	t
NaCl (0.7M)	1	1	3.20	0
	0.78	0.80	3.30	10 min
	0.61	0.83	4.33	22 hr
	0.58	0.86	4.76	6 days
NaCl (0.7M) + GSH (10^{-5}M)	1	1	3.14	0
	0.69	0.69	3.15	10 min
	0.63	0.75	3.78	10 min
	0.57	0.78	4.23	6 days

Discussion

Identification of the signals.—The O_2-EPR signal has been reported at room temperature (13). It always presents 3 g values and never an axial symmetry. While Fe^{III} porphyrin signals can only be obtained at liquid nitrogen temperature (14), EPR spectra of Fe^{III} phthalocyanine compounds have been reported at ambient temperature (6a). The slow variation of the signal symmetry under oxygen is compatible with the low values of the diffusion coefficients for electrons and holes measured in the phthalocyanine structures (7). It is characteristic of a slow oxygen penetration into the structure with the metal site symmetry being initially square pyramidal then octahedral. The stability of the signal in the presence of water under wetting conditions precludes the existence of a cation radical (15) especially if the active Fe^{III} sites are located on the first layers in contact with the electrolyte as seen by ESCA (3, 7).

Spin configuration of Fe^{III}.—Classical analysis (16) of the g values of form (A) with samples (I) leads to a low spin ferric ion. A rapid check of the crystal field parameters (17) yields $\Delta E^{x2y2} = 228{,}000$ cm^{-1} and $\Delta E^{xy} = 319{,}000$ cm^{-1}, which are completely unrealistic values. The spin orbit coupling constant ξ was taken equal to the free ion value ($\xi = 400$ cm^{-1}) (6a, 16). In contrast, the calculations of Caro *et al.* (6a) which involve the 252 wave vector basis set. yield completely different conclusions. The experiments at g values around 2 correspond either to a low spin domain close to the border for C_{2v} distortion of the C_{4v} symmetry to high or intermediate spin domains. In the border line situation the g values are very sensitive to variations in the crystal field parameters because of the rapid variation of composition of the wave vectors in crossover situations. In the iron naphthalocyanines (I) the following crystal field parameters are obtained: $B_4^0 = 37{,}500$ cm^{-1} and $B_4^4 = 23{,}000$-25.000 cm^{-1}. These are in the experimental range of electronic excitation energies. The samples are in the low spin domain but not too far away (less than 2000 cm^{-1}) from the high spin-low spin border as given by Fig. 9 of Ref. (6a).

Table III. The effect of wetting on Fe^{III}-Mo^{V}-NPC in presence of GSH (sample kept in air N) I_{10} and I_{20} as in Table II

Solutions	I_1/I_{10}	I_2/I_{20}	I_2/I_1	t
NaCl (0.7M)	1	1	3.29	0
	0.89	0.89	3.30	10 min
	0.73	0.93	4.22	3 days
	0.73	0.95	4.29	6 days to 10 days
NaCl (0.7M) + GSH (10^{-6}M)	1	1	3.18	0
	0.80	0.83	3.29	10 min
	0.70	0.91	4.16	3 days
	0.70	0.91	4.14	6 days to 12 days
NaCl (0.7M + GSH (10^{-3}M dimerized)	1	1	3.32	0
	0.95	0.94	3.29	10 min
	0.82	0.98	3.95	4 days
	0.80	0.98	4.08	6 days
HCl (0.7M)	1	1	3.31	0
	0.80	0.82	3.41	10 min
	0.70	0.95	4.50	3 days
	0.69	0.95	4.60	6 days to 10 days

Mo^{V} structures and electrochemical interest.—In (Fe-Mo) samples (II), only Mo^{V} ions are apparent. From Table I the two main sites are both sensitive to oxygen pressure variations. This effect involves either a segregation of both sites at the surface or a much faster oxygen penetration into the Mo structure than into the pure iron samples (I). Due to the relative stability of I_2, in contrast to I_1, *vs.* the oxygen pressure, the reversibility for O_2 uptake appears greater for I_1 than for I_2. Their relative variation suggests with one phase compound a surface segregation of I_1 sites compared to I_2 or with a mixture of two phases a better oxygen penetration into I_1 sites.

In presence of aqueous solutions the absolute variations of I_1 and I_2 are difficult to interpret (18) due to the modification of the solution dielectric constant in association with double layer effects. Mo^{V} ions present within the structure may act as "probes" (19) and give information on the transitions Mo^{IV}/Mo^{V} or Mo^{V}/Mo^{VI} in the presence or absence of the solution.

In this respect, it may be pointed out that the relative growth of I_2 depends on the oxygen concentration at the compound surface and is inhibited by glutathione (decrease of surface oxygenated radical concentration) as shown in Table II. The unexpected differences in NaCl solutions in Tables II and III may involve wetting processes that are more rapid in the absence of oxygen radicals on the surface.

Oxygen reduction takes place simultaneously with Mo^{IV}/Mo^{V} oxidation on I_2 sites. In the presence of HCl the oxidation is enhanced, which may be due to easier HO_2 radical formation (10) in the presence of protons.

On the basis of EPR data alone, it is not possible to identify unambiguously the nature of I_1 and I_2 sites. I_2 sites can be due either to molybdenum oxide (9) or molybdenum naphthalocyanine. In some references I_1 sites have been identified as deposited carbon (20, 21). In the present experiments however, this interpretation can be ruled out as the corresponding peak I_1 is oxygen sensitive in dry atmosphere (see Table I). The intensity of peak I_1 can therefore be related to electrochemical activity or oxygen reduction.

The difference in behavior of Fe-MoNPc samples (II) and (III) under vacuum (Table I) or under air (Table III) may be presumed to be due to the difference in wetting which in presence of glutathione (GSH) stabilizes the lower valencies of molybdenum as shown for iron (7). The adsorbed oxygen impedes the process of wetting and the further development of the Mo^{VI} form that is shown to be associated with it. At high concentration, on the air exposed samples the glutathione is dimerized under the influence of adsorbed oxygen and has only a minor effect in the I_2/I_1 ratios.

Conclusion

EPR studies on iron, mixed iron-molybdenum, and molybdenum naphthalocyanine compounds electrochemically investigated in previous work (1, 3) have provided information concerning the effects of structural factors on the electrochemical activity of these compounds.

As in other phthalocyanine or porphyrin compounds a border-line situation has been found to exist for the spin configuration of iron (III). This finding is an illustration of the theories developed on the influence of the Fe-O_2 bonding on the kinetic constants of the electroreduction of dioxygen. It is of special interest in support of theories relating the mixed spin con-

figuration of Fe^{III} to the lowering of the overall activation energy for this process.

In the case of iron naphthalocyanines the diffusion of dioxygen molecules into the lattice and the fixation of two molecules to the iron appear to be very slow processes. Under electrochemical conditions, the bulk of the material is not involved in the reaction, since ohmic limitations are observed for finite thickness deposits. The most effective electrode structures would consist of one or no more than two layers spread out uniformly on the carbon black supports.

With Mo naphthalocyanine compounds the oxygen intake into the lattice is much faster and gives rise to higher valencies of molybdenum ions compared with iron. At least two different Mo sites have been shown in our preparations, each possessing a different activity *vs.* oxygen adsorption and a different stability in conducting solutions, the most active for oxygen adsorption being also the most stable.

From the view point of electrochemical activity in the case of molybdenum naphthalocyanine, in contrast to iron, many layers can participate in the reaction at least from the view point of the conduction process in the solid phase.

Acknowledgments

The authors acknowledge Professor E. Derouane and J. B. Nagy for obtaining the EPR spectra, Dr. R. Parsons for his interest to this work and a critical reading of the manuscript, and the Direction d'Etudes et de Realisations Techniques and the Franco Belgium Cultural Exchanges for their financial support.

Manuscript submitted Oct. 15, 1980; revised manuscript received Nov. 18, 1981.

Any discussion of this paper will appear in a Discussion Section to be published in the June 1983 JOURNAL. All discussions for the June 1983 Discussion Section should be submitted by Feb. 1, 1983.

Publication costs of this article were assisted by Laboratoire d'Electrochimie Interfaciale du C.N.R.S.

REFERENCES

1. G. Magner, M. Savy, and G. Scarbeck, *This Journal*, **127**, 1076 (1980).
2. L. Salem, "M.O. Theory of Conjugated Ring Systems," p. 287, W. Benjamin, New York (1966).
3. G. Magner, M. Savy, and G. Scarbeck, *This Journal*, **128**, 1674 (1981).
4. E. V. Dose, M. A. Hosetton, N. Sutin, M. F. Tweedle, and L. J. Witson, *J. Am. Chem. Soc.*, **100**, 1141 (1978).
5. A. J. Appleby, P. Caro, and M. Savy, *J. Electroanal. Chem. Interfacial Electrochem.*, **111**, 91 (1980).
6. (a) P. Caro, M. Faucher, M. Savy, and H. Pankowska, *J. Chem. Phys.*, **68**, 1045 (1978); (b) A. Nason, K. Y. Lee, S. S. Pan, and R. Erickson, *J. Less-Common Met.*, **36**, 449 (1974).
7. O. Contamin, E. Levart, and M. Savy, *J. Electroanal. Chem. Interfacial Electrochem.*, **115**, 267 (1980).
8. E. F. Bradbrook and R. P. Lindstead, *J. Chem. Soc.*, 1744 (1936).
9. R. C. Bray and J. C. Swanes, *Struct. Bonding*, **11**, 107 (1972).
10. A. J. Appleby, J. Fleisch, and M. Savy, *J. Catal.*, **44**, 281 (1976).
11. J. H. Fuhrop, in "Porphyrins and Metalloporphyrins," K. M. Smith, Editor, p. 593, Elsevier, New York (1975).
12. M. Kosower, W. Correa, J. Kinon, and S. Kosower, *Biochem. Biophs. Acta*, **264**, 39 (1972).
13. H. M. Swarts, J. R. Bolton, and D. C. Borg, Editors, "Biological Application of Electron Spin Resonance," p. 281, Wiley-Interscience, New York (1972).
14. J. Subramanian, "Porphyrins and Metalloporphyrins," K. M. Smith, Editor, p. 575, Elsevier, New York (1975).
15. J. Swart and J. H. Van Wolpert, *J. Mol. Catal.*, **5**, 51 (1979).
16. G. M. Harris Loew, *Biophs. J.*, **10**, 196 (1970).
17. N. M. Atherton, "Electron Spin Resonance," p. 197, Ellis Horwood, New York (1973).
18. S. S. Eaton and G. R. Eaton, *Bull. Magnetic Resonance*, **1**, 130 (1980).
19. C. Tenret and J. J. Verbist, *J. Microscop. Spectrosc. Electron*, **1**, 255 (1976).
20. J. M. Peacock, M. J. Sharp, A. J. Parker, P. G. Ashmoore, and J. A. Hockey, *J. Catal.*, **15**, 379 (1969).
21. N. Sotani, *Rev. Phys. Chem. Jpn.*, **46**, 9 (1976).

A Model of Crack Electrochemistry for Steels in the Active State Based on Mass Transport by Diffusion and Ion Migration

A. Turnbull and J. G. N. Thomas*

National Physical Laboratory, Teddington, Middlesex TW11 0LW, England

ABSTRACT

A model of the electrochemical conditions in a static crack has been developed for steel in the active state based on the steady-state mass transport of species by diffusion and ion migration. The main reactions considered were anodic dissolution, hydrolysis of ferrous ions, and cathodic reduction of hydrogen ions and water with the assumption that the electrode reactions were taking place both at the tip and on the walls of the crack. The reduction of oxygen in the crack was not included since it was demonstrated in a separate analysis that this reaction is insignificant in a static crack at steady state. The pH and potential drop in the crack have been evaluated as a function of external potential, crack dimensions, and other parameters assuming a bulk solution of 3.5% NaCl. The effect of dissolution and hydrolysis of alloying elements and also the buffer reactions of seawater on the pH within a crack were also assessed, but mass transport by ion migration was neglected in these cases. The theoretical predictions of the potential drop and pH were in reasonable agreement with values determined experimentally in an artificial crevice of the structural steel BS 4360 50D in 3.5% NaCl and in artificial seawater.

The electrochemical conditions within cracks are important in governing the rate of crack propagation in stress corrosion cracking and in corrosion fatigue since this will depend on the rate of metal dissolution and/or the rate of production of hydrogen atoms at the crack tip. A problem in characterizing the rates of electrode reactions within a crack is the lack of knowledge of the local solution composition and the electrode potential, which because of the restricted geom-

* Electrochemical Society Active Member.

Key words: crack electrochemistry, model, structural steels, sodium chloride, seawater.

etry, can vary from the values associated with the bulk solution and external metal surface. In addition, there are difficulties in measuring the electrochemical conditions in cracks because access with measuring probes is not easy although a variety of techniques has been developed to overcome this problem (1-4).

Thus experimental measurement has been supplemented by various mass transport models that have been developed to describe the solution composition and electrode potential in cracks (5-9), mainly stress corrosion cracks. These models have in general related to metal/environment systems in which a passive film is formed with only the crack tip active and are not applicable to structural steels in seawater in which both the tip and walls of the crack would be expected to be active. A model to describe the electrochemical conditions in a static (parallel-sided) crack in structural steel in 3.5% NaCl and also in seawater was developed by Turnbull and Thomas (10) based on mass transport by diffusion only. The current paper describes an extension of this model to include mass transport by ion migration. In addition, improved data for the input parameters, *viz.*, rates of metal dissolution, hydrogen-ion reduction, and water reduction for the steel BS 4360 50D in chloride solutions for a range of potential, pH, and chloride-ion concentration, have been obtained (11) and these have led to further modifications and improvements in the original model.

Electrochemical Reactions in the Crack

The model assumes that the steel section containing the crack is immersed in 3.5% NaCl solution, except in the case of the buffering reactions described later, and that the electrode reactions, anodic dissolution and cathodic reduction, occur on the walls and tip of the crack. The following basic reactions are considered to occur within the crack

$$Fe \rightarrow Fe^{2+} + 2e^- \quad [1]$$

$$Fe^{2+} + H_2O \rightleftharpoons FeOH^+ + H^+ \quad [2]$$

$$H_2O \rightleftharpoons H^+ + OH^- \quad [3]$$

$$H_2O + e^- \rightarrow H + OH^- \quad [4]$$

$$H^+ + e^- \rightarrow H \quad [5]$$

For the purpose of this analysis: $[Fe^{2+}] = C_1$, $[H_2O] = C_2$, $[FeOH^+] = C_3$, $[H^+] = C_4$, $[OH^-] = C_5$, $[Na^+] = C_6$, and $[Cl^-] = C_7$.

The sodium and chloride ions do not take part in the reactions but contribute to the transfer of current and hence influence the magnitude of the potential drop, $\phi(x)$, which is defined as $E^{ext} - E(x)$, *i.e.*, the difference in the electrode potential at the external surface and a point along the crack. The reduction of oxygen in the crack is not included since it has been previously demonstrated that this reaction is insignificant in a static crack at steady state (10, 12).

The dissolution of alloying elements and also the buffering reactions of seawater were considered, but because of the additional reactions and equations involved, mass transport by ion migration was neglected in these cases (see later). The appropriate reactions for dissolution and hydrolysis of the alloying elements are represented by

$$M \rightarrow M^{n+} + ne^- \quad [6]$$

$$M^{n+} + H_2O \rightleftharpoons M(OH)^{(n-1)+} + H^+ \quad [7]$$

The buffering reactions of seawater are associated with the dissolved carbon dioxide equilibria (10, 13), the significant relationships for this analysis being

$$H_2CO_3^* \rightleftharpoons H^+ + HCO_3^- \quad [8]$$

$$HCO_3^- \rightleftharpoons H^+ + CO_3^{2-} \quad [9]$$

where $H_2CO_3^* = [H_2CO_3] + [CO_2(aq]$ and $[CO_2(aq)] >> [H_2CO_3]$ (13).

For values of pH less than 8, Eq. [8] is the dominant reaction; but for higher pH values, the dominant reaction is Eq. [9].

In previous work the rates of anodic dissolution and cathodic reduction of hydrogen ions and water on the structural steel BS 4360 50D in 3.5% NaCl were shown to have a complex dependence on pH and potential (11). The rate of anodic dissolution was observed to decrease with decreasing pH for pH values < 3, but to decrease with increasing pH for pH values > 8.5. In the intermediate region the anodic current was little affected by pH and could be represented by

$$i_a = k_\gamma \exp\left(\frac{\beta \mathbf{F} E}{RT}\right) \quad [10]$$

This is the expression used in this analysis with $\beta = 1$ and $k_\gamma = 2.7 \cdot 10^7$ A cm^{-2}, where E is the electrode potential with respect to the saturated calomel electrode, $\mathbf{F}$ the Faraday constant, R the gas constant, and T the temperature ($\simeq 293$ K).

The rate of reduction of hydrogen ions had a first-order dependence on hydrogen-ion concentration and could be represented by

$$i_{H^+} = k_\alpha C_4 \exp\left(-\frac{\beta' \mathbf{F} E}{RT}\right) \quad [11]$$

with $\beta' = 0.5$, $k_\alpha = 2 \cdot 10^{-5}$ A mol^{-1} cm, where C_4 is in mols cm^{-3}.

The reduction of water was observed to be independent of pH for pH values less than or equal to 10, but decreased with increasing pH above this value. The following expression was derived for pH ≤ 10, *viz.*

$$i_{H_2O} = k_\beta^* \exp\left(-\frac{\beta^* \mathbf{F} E}{RT}\right) \quad [12]$$

with $\beta^* = 0.5$ and $k_\beta^* = 8 \cdot 10^{-14}$ A cm^{-2}.

The dependence of the current density for water reduction on pH above pH 10 is complex, but for pH values between 10 and 12 a least squares analysis of the data indicates that $\beta^* = -(0.167 \ln C_4 + 4.49)$ and $k_\beta^* = \exp(7.56 \ln C_4 + 196.57)$.

Since the variation of the concentration of water in the crack is treated in this model, albeit in a very approximate manner, the pre-exponential factor k_β^* is replaced by $k_\beta C_2$ where k_β is calculated assuming C_2 was about $55.5 \cdot 10^{-3}$ mols cm^{-3} in the above investigation.

Mass Conservation Equations

The general formulation, based on dilute solution theory, for the conservation of species in a crack can be written as (14)

$$\frac{\partial C_i}{\partial t} + v\nabla C_i = D_i \nabla^2 C_i + \frac{z_i}{RT} \mathbf{F} D_i \nabla (C \nabla \phi) + R_i \quad [13]$$

convection diffusion migration reaction

This equation shows the dependence of the rate of change of concentration ($\partial C_i/\partial t$) on (*i*) convection where v is the fluid velocity, (*ii*) diffusion where D_i is the diffusion coefficient, (*iii*) ion migration where z is the charge, (*iv*) homogeneous reactions in solution where R_i represents the rate of production or depletion of species by chemical reaction. The heterogeneous reactions such as dissolution and reduction normally appear in the boundary conditions. In constructing the material balance equations for this system only the steady-state form was considered ($\partial C_i/\partial t = 0$) and in addition the following assumptions and approximations have been made.

1. The crack is parallel-sided of length l, width w, and through-thickness B (Fig. 1) and the area of metal

external to the crack is very much greater than the crack area such that changes in the conditions in the crack do not affect the potential of the specimen as a whole.

2. The crack is static or propagating at such a slow rate that induced convective motion can be neglected. In addition the gravitational field is assumed to be in a direction parallel to the x-axis and directed toward the tip, and hence natural convection resulting from density changes can be neglected.

3. Mass transport in the through-thickness, z-direction, is neglected. This is a reasonable approximation if the thickness dimension is much greater than the crack length and will also apply if the sides of the crack are sealed, *e.g.*, by a coating.

4. The mass conservation equations can be reduced to a one-dimensional form by neglecting concentration and potential gradients between the walls of the crack. It was demonstrated in a previous two-dimensional analysis (12) that this was a good approximation for the former and it is likely also to be valid with respect to the potential gradient. A consequence of this approximation is that the electrode reactions on the walls of the crack now appear in the material balance equation and essentially can be considered as additional source or sink terms.

It should be emphasized that the model applies strictly to dilute solutions and the applicability of this assumption is discussed later.

Mass conservation equations based on Eq. [13] but using the above approximations were derived for each of the solute species. These were then rearranged, with the assumption that the hydrolysis reactions were at equilibrium to give the following set of equations [see Ref. (10) which is available on request] based on reactions [1]-[5]

$$D_1\frac{d}{dx}\left[\frac{dC_1}{dx}+\frac{2\mathbf{F}}{RT}C_1\frac{d\phi}{dx}\right]+D_3\frac{d}{dx}\left[\frac{dC_3}{dx}+\frac{\mathbf{F}}{RT}C_3\frac{d\phi}{dx}\right]=-\frac{2}{w}\frac{k_\gamma}{2\mathbf{F}}\exp\left\{\frac{\beta\mathbf{F}(E^{ext}-\phi)}{RT}\right\} \quad [14]$$

$$D_3\frac{d}{dx}\left[\frac{dC_3}{dx}+\frac{\mathbf{F}}{RT}C_3\frac{d\phi}{dx}\right]-D_4\frac{d}{dx}\left[\frac{dC_4}{dx}+\frac{\mathbf{F}}{RT}C_4\frac{d\phi}{dx}\right]+D_5\frac{d}{dx}\left[\frac{dC_5}{dx}-\frac{\mathbf{F}}{RT}C_5\frac{d\phi}{dx}\right]=-\frac{2}{w}\frac{k_\alpha}{\mathbf{F}}C_4\exp\left\{-\frac{\beta'\mathbf{F}(E^{ext}-\phi)}{RT}\right\}-\frac{2}{w}\frac{k_\beta}{\mathbf{F}}C_2\exp\left\{-\frac{\beta^*\mathbf{F}(E^{ext}-\phi)}{RT}\right\} \quad [15]$$

and for $0 < x < 1$

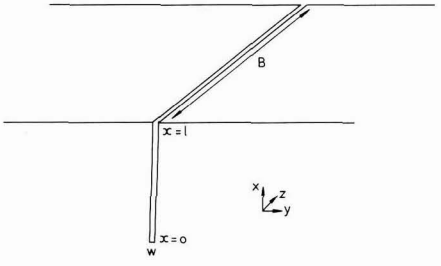

Fig. 1. Slot-like crack

$$\frac{C_4C_5}{C_2}=\frac{K_w}{55.5\cdot10^{-3}} \quad [16]$$

$$\frac{C_4C_3}{C_1C_2}=\frac{K_H}{55.5\cdot10^{-3}} \quad [17]$$

$$C_2=C_2^{\infty}\,[1-\bar{\nu}C_1] \quad [18]$$

$$C_6=C_6^{\infty}\exp\left(-\frac{\mathbf{F}\phi}{RT}\right) \quad [19]$$

$$C_7=C_7^{\infty}\exp\frac{\mathbf{F}\phi}{RT} \quad [20]$$

In addition the electroneutrality equation states that

$$\Sigma z_iC_i=0 \quad [21]$$

The boundary conditions are

$$x=1\;\; C_1=0,\; C_3=0,\; C_4=C_4^{\infty},\; C_5=C_5^{\infty},\; \phi=0 \quad [22]$$

$$x=0\quad D_1\left[\frac{dC_1}{dx}+\frac{2\mathbf{F}}{RT}C_1\frac{d\phi}{dx}\right]+D_3\left[\frac{dC_3}{dx}+\frac{\mathbf{F}}{RT}C_3\frac{d\phi}{dx}\right]=-m\frac{k_\gamma}{2\mathbf{F}}\exp\left\{\frac{\beta\mathbf{F}(E^{ext}-\phi)}{RT}\right\} \quad [23]$$

$$D_3\left[\frac{dC_3}{dx}+\frac{\mathbf{F}}{RT}C_3\frac{d\phi}{dx}\right]-D_4\left[\frac{dC_4}{dx}+\frac{\mathbf{F}}{RT}C_4\frac{d\phi}{dx}\right]+D_5\left[\frac{dC_5}{dx}-\frac{\mathbf{F}}{RT}C_5\frac{d\phi}{dx}\right]=-\frac{k_\alpha}{\mathbf{F}}C_4\exp\left\{-\frac{\beta'\mathbf{F}(E^{ext}-\phi)}{RT}\right\}-\frac{k_\beta}{\mathbf{F}}C_2\exp\left\{-\frac{\beta^*\mathbf{F}(E^{ext}-\phi)}{RT}\right\} \quad [24]$$

The appearance of a factor m in Eq. [23] is to allow for the influence of crack tip straining on the dissolution rate. D_1 to D_5 are the diffusion coefficients of the relevant species. The concentration of water will only deviate from the bulk value C_2^{∞} when the concentration of ferrous chloride becomes significant and in this case it is assumed to be determined by the partial molar volume, $\bar{\nu}_1$, of ferrous chloride (10) (Eq. [18]). This is an approximate expression and does not take into account the mass transport of water out of the crack in the form of a hydration sphere attached to the ferrous ion. In any case, the model is not expected to be particularly accurate in describing concentrated solutions. K_w is the ionic product of water and K_H is the equilibrium constant for the hydrolysis of ferrous ions. The factor $55.5\cdot10^{-3}$ (mols cm^{-3}) represents the bulk concentration of water. Note that the boundary condition of $\phi = 0$ at $x = 1$ is in fact determined also by the electroneutrality equation, Eq. [21].

Although mathematical solution of these equations was obtained for a wide range of parameters, considerable numerical difficulties arose at negative potentials when the dissolution rate tended to a very small value and the sign of ϕ changed. Nevertheless, it was possible to obtain a solution under these conditions by neglecting dissolution and considering only the reduction of hydrogen ions and water within the crack. It was further assumed, for ease of mathematical analysis, that the flux at the crack tip could be neglected. This derives from the fact that the area of the walls is very much greater than the area of the crack tip and hence the flux at the crack tip will have only

a very small effect on the solution composition or potential in the crack unless the reaction rates are significantly affected by straining at the tip, and this is discussed later.

In order to solve the equations involving the dissolution and hydrolysis of alloying elements or the buffering reactions of seawater, mass transport equations were established assuming transport by diffusion only. The transport equations were based on Eq. [14]-[24], but with the inclusion of additional equilibrium relationships in the form of Eq. [17]. In addition, an equation of the form of [14] was used for the dissolution of the alloying element (15). The dissolution rate of the alloying element was assumed to be in proportion to its concentration in the steel, based on the experimental results of Sandoz *et al.* (16). The reactions at the crack tip were neglected in this analysis for reasons described previously, and this assumption is validated later. Deviation of the concentration of water from its bulk value was also neglected.

Mathematical Treatment

The mathematical equations were initially converted to a nondimensional form suitable for numerical analysis (15). The detailed method of solving the equation is described by Ferriss and Miller (17) and only a brief summary is given here. Early attempts to obtain a numerical solution of the equations involving diffusion only made use of a computer algorithm in which the dependent variables were represented by finite Chebyshev series. However, only limited success was achieved with this method because the dependent variables were poorly represented by polynomials. In order to obtain a reasonable accuracy, polynomials of very high degree were needed, but computer storage was limited. An improved technique was developed for solving the "diffusion-only" problem and also the equations involving diffusion and migration. In this method the ordinary differential equations were converted to nonlinear integral equations and then solved numerically using a variant of the Newton-Raphson iterative technique

The values of the parameters used in this analysis were as follows: $D_1 = D_2 = D_3 = D_8 = D_9 = 10^{-5}$ cm^2 sec^{-1}, $D_4 = 9.3 \cdot 10^{-5}$ cm^2 sec^{-1}, and $D_5 = 5.3 \cdot 10^{-5}$ cm^2 sec^{-1}, where D_8 and D_9 represent diffusion coefficients of the M^{n+} and $M(OH)^{(n-1)+}$ species where M refers to the alloying element: $K_w = 10^{-20}$ (mols cm^{-3})^2, $K_H = 10^{-12.5}$ mols cm^{-3} (18), $K = 1 \cdot 10^{-9}$ mols cm^{-3} (seawater) (13) for $H_2CO_3^* = H^+ + HCO_3^-$, $K = 1 \cdot 10^{-12}$ mols cm^{-3} (seawater) (13) for $HCO_3^- = H^+ + CO_3^{2-}$, and in seawater at pH 8 $[H_2CO_3^*]^\infty = 2 \cdot 10^{-8}$ mols cm^{-3} and $[HCO_3^-]^\infty = 2 \cdot 10^{-6}$ mols cm^{-3}.

Results and Discussion

The steady-state distribution of the species Fe^{2+} and $FeOH^+$, along a crack of length 2 mm and width 10 μm is shown in Fig. 2. The external electrode potential is −700 mV (SCE) which approximates to the free corrosion potential of the steel BS 4360 50D in 3.5% NaCl. The initial predictions of the model indicated values of the ferrous ion concentration slightly in excess of the equilibrium value at the appropriate potential in the crack as shown in Fig. 2. For longer or narrower cracks this is even more significant. The equilibrium concentrations were calculated assuming (10)

$$Fe \rightleftharpoons Fe^{2+} + 2e^-$$

with $E = -0.684 + 0.0295 \log [Fe^{2+}]$ (V SCE).

The equilibrium value shown in Fig. 2 depends on the distance from the crack tip as a consequence of the variation of the potential drop along the crack. The model was modified to take into account metal-ion deposition explicitly, but it was not possible to obtain

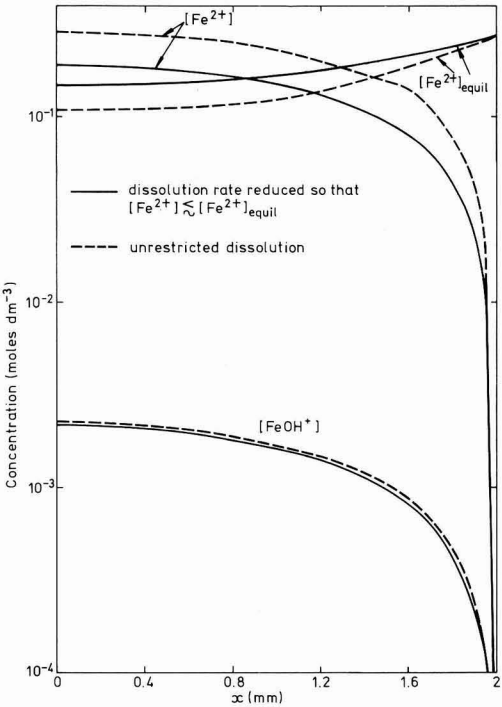

Fig. 2. Variation of the concentration of ferrous and ferrous hydroxyl ions with distance from the crack tip ($x = 0$) at $E = -700$ mV (SCE), crack length 2 mm, crack width 10 μm.

a solution to the differential equations for the parameters of relevance. As an approximation it was assumed that the ferrous-ion concentration was limited to values $\lesssim [Fe^{2+}]_{equil.}$ at the appropriate potential and this was achieved by reducing the dissolution rate accordingly. The resultant rate of dissolution is effectively related to the mass tranport of ferrous ions out of the crack. It was necessary in practice to reduce the dissolution rate by a constant amount along the crack in satisfying the above conditions because of mathematical difficulties. However the error introduced is unlikely to be very significant since, as a result of dissolution from the walls, the ferrous-ion concentration is a slowly changing function of x except close to the mouth of the crack (Fig. 2).

The conditions under which the equilibrium concentration is exceeded depend on the crack dimensions and potential. For example, at the crack length 2 mm and width 10 μm the equilibrium value is exceeded for external potentials $\lesssim$ −700 mV (SCE). The above treatment was applied in such cases, but the influence of the formation of magnetite or ferrous hydroxide on the ferrous-ion concentration was not considered, and this is discussed later.

The variation of the hydrogen-ion concentration with distance from the crack tip for the same crack dimensions is shown in Fig. 3 at the free corrosion potential, −700 mV (SCE), and at −940 mV (SCE) where anodic dissolution is negligible. A feature of the data at −700 mV (SCE) is that the hydrogen ion concentration shows little variation with x except at the mouth of the crack where the concentration must satisfy the boundary condition. Indeed the small variation that is observed is a consequence of the potential drop and in the absence of this factor the profile is flat except at the mouth of the crack (10). This indicates that

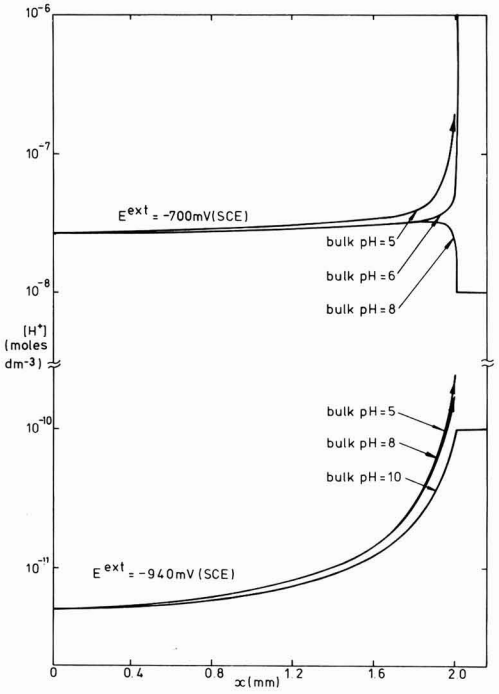

Fig. 3. Variation of hydrogen ion concentration with distance from the crack tip ($x = 0$) for different values of the potential and bulk pH. The crack length is 2 mm and width 10 μm and the bulk solution is 3.5% NaCl.

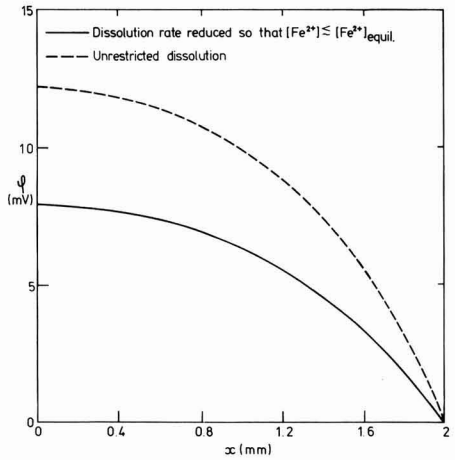

Fig. 4. Variation of the potential drop (ϕ) with distance from the crack tip ($x = 0$) at $E = -700$ mV (SCE), crack length 2 mm and crack width 10 μm.

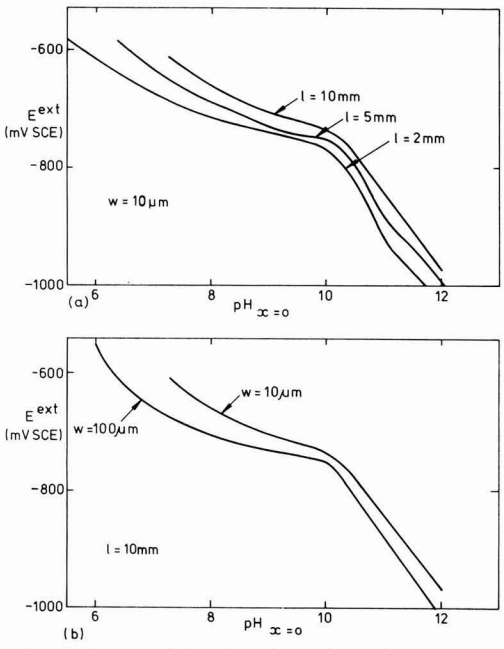

Fig. 5. Variation of the pH at the crack tip with external potential for (a) constant crack width, varying crack length and (b) constant crack length, varying crack width.

the hydrogen-ion concentration is determined mainly by the balance between the rate of production of hydrogen ions by dissolution and hydrolysis and the rate of removal by reduction of hydrogen ions and indirectly by reduction of water. Thus mass transport of hydrogen ions by diffusion has a much less significant effect except at the mouth of the crack. At the potential of −940 mV (SCE)the rate of change of the hydrogen-ion concentration with distance from the crack tip is slightly greater but, as before, is most significant close to the mouth. The variation of the potential drop with distance from the crack tip at an external potential of −700 mV (SCE) is shown in Fig. 4. It can be observed that the potential drop changes slowly with distance from the crack tip, but close to the mouth of the crack the rate of change increases and can be very marked when the potential drop in the crack is large (see Fig. 9). This is a feature of the predictions of the model when the net current from the walls of the crack dominates that from the tip, but when the reverse is true, *e.g.*, when the walls are passive, the potential drop falls off very rapidly with distance from the tip.

Effect of Variation in External Potential

The influence of external electrode potential on the pH and potential drop at the crack tip is shown in Fig. 5 and 6 for different values of the crack length and crack width. It is evident from Fig. 5(a) and (b) that the pH at the crack tip depends on potential in a complex fashion. At potentials more positive than ~ −700 mV (SCE) the potential drop in the crack becomes significant (Fig. 6). Since the change in potential at the tip is less than the change in external potential, the rate of change of pH at the tip with external potential decreases as the potential is made more positive. At potentials more negative than −760 mV (SCE) (Fig. 5) a transition in the rate of change of pH with external potential is observed and the pH increases more slowly as the potential is made more negative. This cannot be attributed to potential drop effects as is evident from Fig. 6, and two factors are suggested in explanation, *viz.*, (*i*) the transition to a pH determined predominantly by water reduction and (*ii*) the decrease in the rate of reduction of water for pH values $\gtrsim$10 (11, 19).

A detailed explanation for the form of the variation of the potential drop with external potential E^{ext} has

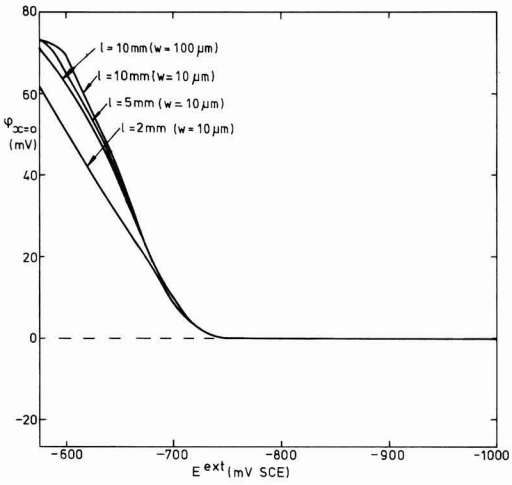

Fig. 6. Variation of potential drop at crack tip with external potential for various crack lengths and crack widths.

been given elsewhere (15, 32). The potential drop is zero when $E^{ext} = -760$ mV, which is the free corrosion potential of steel in the deaerated solution in the crack. At more positive or negative values of E^{ext} the potential drop reflects the increasing anodic or cathodic current flowing into the crack. Under cathodic polarization, the potential drop remains very small because the increasing pH in the crack retards the rate of water reduction.

At positive potentials the predicted concentration of ferrous ions in long narrow cracks was found to exceed the solubility limit of ferrous chloride, *viz.*, ~4.5M. To account for this a reduced dissolution rate was assumed with the condition $[Fe^{2+}] \lesssim 4.5M$. This was only necessary at quite positive potentials (> -600 mV SCE) for the crack dimensions examined and is indicated by a marked decrease in the rate of change of the potential drop with external potential (Fig. 6). It should not be expected that this theoretical model would accurately predict the pH or potential drop in concentrated solutions since it is well established that the activity coefficient of the various dissolved species, in particular the hydrogen ion, can increase significantly with increasing salt concentration (20-22). In addition, deposition of a salt film on the metal surface could lead to a significant potential drop across the film (23).

Effect of Crack Length and Crack Width

The influence of the reactions at the crack tip is an important factor in analyzing the effect of crack length and crack width on the pH and potential drop. When the flux at the crack tip was set to zero it was observed that for a range of parameters this had a negligible effect on the solution composition or potential. For example with $l = 2$ mm and $w = 10$ μm the difference in potential drop and concentration of the various species in these conditions was less than 0.4% for a range of potentials. It can be shown (15) that when the mass transport equations are expressed in nondimensional form the length and width always appear as the combined parameter l^2/w except in the boundary conditions at the crack tip, but since these have only a minor effect on the solution composition and electrode potential in the crack, they can be neglected. Hence the effects of crack length and width on the normalized concentration and potential profiles can be expressed in terms of the combined parameter l^2/w, certainly for $l^2/w > 400$ mm which probably includes most practical crack dimensions. This is a useful parameter because it implies that similar values of the pH etc. at the crack tip ($x = 0$) should be obtained for different values of l and w provided l^2/w is unchanged. However this is only relevant to a slot-like crack and for a wedge-shaped crack the important parameter is $l/\tan\theta$ where θ is the crack angle.

It is evident from Fig. 5(a) and (b) that the pH at the crack tip increases as l^2/w increases at all potentials (although it should be noted that while the pH is a function of this parameter it is not directly proportional to it). At potentials $\lesssim -800$ mV (SCE) where the pH depends only on reduction of water it would be expected (15) that the pH would increase with increasing l^2/w as is indeed observed. At more positive potentials the situation is more complex because the potential drop is more significant and also the limitation on the ferrous ion concentration is an important factor. In the absence of these factors the hydrogen-ion concentration would be predicted to be invariant with crack length or width (10) since the parameter l^2/w appears in the equations involving dissolution and also cathodic reduction (15). However the potential drop increases with l^2/w (Fig. 6) and the potential in the crack is consequently more negative than that associated with the external surface with the result that the pH tends to be higher. In addition since the rate of dissolution is limited to maintain $[Fe^{2+}] \lesssim [Fe,^{2+}]_{equil.}$, but no such restriction is imposed on the rate of hydrogen evolution, the pH will tend to increase with l^2/w.

The effect of crack dimensions on the potential drop is shown in Fig. 6 and can be explained as follows. At potentials $\gtrsim -800$ mV (SCE) it would be expected that the potential drop would increase when l^2/w increased, but the extent was very much less than expected despite a large change in l^2/w and was too small to be distinguished on the scale used in Fig. 6. The reason is that the pH tends to increase with l^2/w and for pH $\gtrsim$ 10 this has the effect of decreasing the water reduction current. Hence, despite a more restricted geometry the lower current means that the potential drop is not too significant and much smaller than would be anticipated if the rate of water reduction was independent of pH. This will obviously have an important influence on the cathodic protection of static cracks and narrow crevices.

At more positive potentials the potential drop at the crack tip generally tends to increase for higher values of l^2/w, but becomes limited because of the reduction in dissolution current necessary to maintain $[Fe^{2+}] \lesssim [Fe^{2+}]_{equil.}$. However, this latter effect may be less significant if magnetite or ferrous hydroxide is formed to any great extent.

Effect of Straining

Plastic strain at the crack tip will enhance the rate of metal dissolution and also the rate of hydrogen evolution (24-30). The effect on the metal dissolution rate depends on whether the metal surface is filmed or not. When the metal is in the active region any film present is only partially protective, but the relative dissolution current can increase by four orders of magnitude for some systems (27). In the absence of a film the average increase in dissolution current is comparatively small (less than a factor of 10) (24, 26), but calculations of local dissolution currents as specific sites, slip step edges, or high index planes suggest much greater local increases possibly as high as 10^4 depending on slip step spacing etc. (28, 29). The cathodic reduction current is also increased by plastic straining but experiment shows that this effect is relatively small for

structural steels in the active state (30). Consequently only the enhancement of the metal dissolution rate will be considered. This can be assessed simply by varying the value of m in Eq. [23], but this would be expected to lead to an increase in the concentration of ferrous ions relative to the equilibrium value. In order to ascertain the maximum effect on the solution composition and potential this aspect was neglected. Calculations were made for $E = -700$ mV (SCE), $l = 2$ mm, $w = 10$ μm, and values of m equal to 10^3 and 10^4. With $m = 10^3$ the pH at the crack tip decreased from 7.4 to 7.0 and the potential drop increased from 12 to 27 mV. It should be noted that the calculated value of the potential drop in Fig. 4 is influenced by the limitation on the ferrous ion concentration. With $m = 10^4$ the pH decreased to 6.6 and the potential drop increased to 50 mV. The magnitude of the effect is exaggerated by virtue of the fact that a relatively wide crack was studied and hence it is reasonable to conclude that for straining factors $\lesssim 10^4$, the effect on the pH within real cracks will be small for this system. This conclusion is based, however, on a steady-state analysis and may not adequately represent the time-dependent phenomenon associated with localized straining at the crack tip.

Effect of Bulk pH

The effect of variation in pH of the bulk solution, at constant potential, on the hydrogen-ion concentration in the crack was examined in the pH range 5-10 and the results are shown in Fig. 3 for $E = -700$ and -940 mV (SCE), $l = 2$ mm, $w = 10$ μm. Numerical difficulties arose in obtaining a solution at lower pH values probably because of the range of the scale of the data, and for bulk pH values greater than 8 the same difficulties occurred at $E = -700$ mV (SCE). It is evident from these data that the external pH has only a marginal effect on the pH at the crack tip at both potentials despite the fact that the crack width is relatively large compared to more common practical values for this crack length. It was noted previously in this discussion that at -700 mV (SCE) mass transport by diffusion had only a minor effect on the hydrogen-ion concentration in the crack and hence it would not be expected that a change in the bulk concentration would significantly alter the concentration in the crack. At -940 mV (SCE) where the only significant reaction is reduction of water the explanation is less apparent, but is clearly associated with the fact that, at any value of the bulk pH, most of the pH change occurs over a region close to the mouth of the crack. The lack of influence of bulk solution pH on the pH within the crack is consistent with the experimental measurements of the pH in stress corrosion cracks carried out by Smith *et al.* (2) in which the pH near the tip was found to be independent of the bulk value.

Effect of Buffer Reactions of Seawater

As a substitute for seawater, 3.5% NaCl has often been used in laboratory studies, but in the former there are significant buffering reactions, Eq. [8] and [9], that will tend to act against a change in the pH of the solution. The important reaction for pH values below 8 is represented by Eq. [8] and for pH values above 8, by Eq. [9]. The effect of the buffering reactions is shown in Fig. 7 for two potentials -700 and -640 mV (SCE) corresponding to pH values in the crack below the bulk value of 8, and for comparison data obtained in 3.5% NaCl at pH 8 are also shown. Note that the potential drop is assumed zero in this analysis. It is evident that the buffering reaction of seawater has a definite but only slight effect on the pH within the crack despite the short crack length considered. The main factor determining the influence of

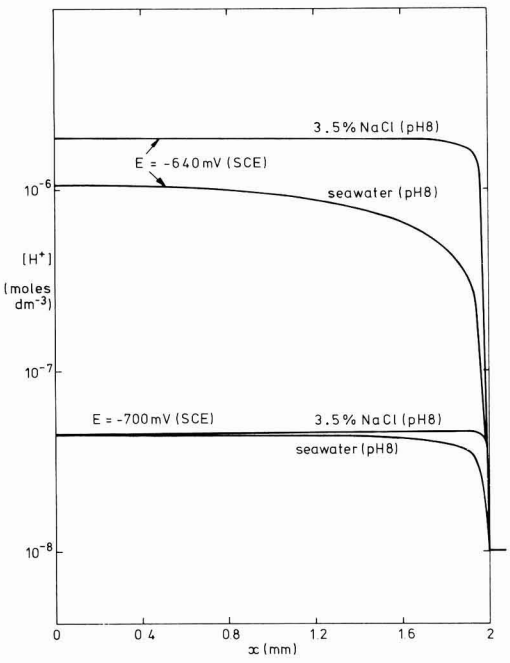

Fig. 7. Effect of the buffer action of seawater on the pH within the crack at a crack length of 2 mm and width 10 μm.

the buffering reaction appears to be the rate of replenishment of the buffer species, *e.g.*, dissolved carbon dioxide, from the bulk solution, and this is in general slow compared to the rates of production and removal of hydrogen ions. The analysis was not applied to more negative potentials because of lack of information about calcareous deposition (31) at the high pH values expected at these potentials.

Effect of Alloying Elements

The hydrolysis constants of various alloying elements of relevance are shown in Table I and it is evident from this that only the dissolution and hydrolysis of chromium is likely to have any effect on the pH within the crack. In assessing the effect of chromium in the steel the electrochemical polarization data for the steel BS 4360 50D was used, but it should be recognized that the detailed electrode reaction rates may change for a chromium-containing steel. It was assumed further that the alloying elements dissolve at a rate, in relation to the metal dissolution rate, in proportion to its concentration in the steel. However, no restriction on the dissolution of chromium was imposed when the ferrous ion concentration was limited to its equilibrium value. The effect of chromium on the pH in the crack is shown in Fig. 8 for a potential of -700 mV (SCE) and $l = 2$ mm, $w = 10$ μm. It is evident that the presence of chromium in the steel even at the 1% level, which would correspond approximately to AISI 4340 steel, has a very significant effect on the pH in the crack.

Table I. Hydrolysis constants (18) (mols dm^{-3})

$Fe^{2+} + H_2O = FeOH^+ + H^+ \log K = -9.5$
$Mn^{2+} + H_2O = MnOH^+ + H^+ \log K = -10.59$
$Ni^{2+} + H_2O = NiOH^+ + H^+ \log K = -9.86$
$Cr^{3+} + H_2O = Cr(OH)^{2+} + H^+ \log K = -4.0$

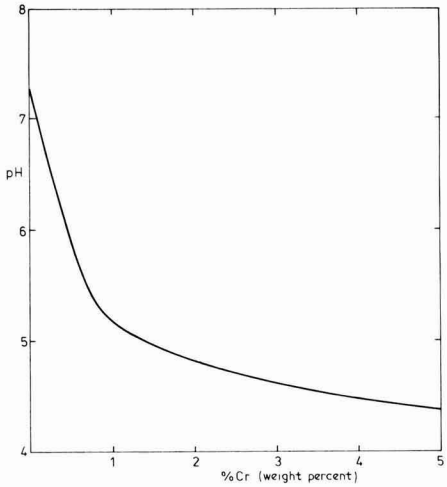

Fig. 8. Effect of chromium content of the steel on the pH at the crack tip for a crack of length 2 mm and width 10 μm at E = −700 mV (SCE).

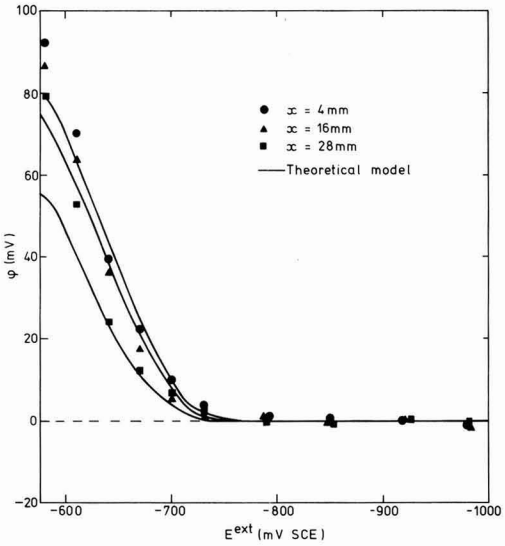

Fig. 9. Variation in potential drop in artificial crevice with external potential at distance x from crevice tip (length = 33 mm, width = 150 μm).

Comparison of Theoretical Predictions and Experimental Measurements

In order to test the predictions of the model under well-defined and relevant conditions an artificial crevice was developed to allow the measurement of the distribution of potential and pH in the crevice (32). The steel BS 4360 50D was used and the bulk solutions employed were 3.5% NaCl (pH 6) and artificial seawater (pH 8.2). The measured potential drop at three points along the crevice for steel in 3.5% NaCl is compared with the theoretical predictions in Fig. 9. The fact that one side of the crevice was inert was taken into account in these comparisons. It is evident that the agreement is qualitatively and quantitatively very reasonable except at potentials more positive than $\simeq$ −600 mV (SCE). Disagreement at these potentials is not unexpected since the solution in the crevice is predicted to be highly concentrated in ferrous chloride, close to the limit of solubility, and the model is based on dilute solution theory.

A comparison of the experimentally measured pH values with the theoretical predictions is shown in Fig. 10. The data for both 3.5% NaCl and seawater are included. The theoretical predictions show the same qualitative form as the experimental results, but quantitatively the agreement is less satisfactory particularly in the potential region −700 to −800 mV (SCE) where the most rapid variation of pH with potential occurs. The most likely explanation for the discrepancy is that the formation of magnetite, or possibly ferrous hydroxide, contributes to the lowering of the pH in the experimental crevice. Although these reactions are likely thermodynamically they were not considered because insufficient data are available to describe the kinetics of the formation and dissolution of these compounds in a form suitable for inclusion in the model. It is pertinent to note that the ferrous-ion concentration predicted by the model in this potential region significantly exceeds the equilibrium value associated with magnetite formation and hence magnetite formation would be expected. This would result in a lower-

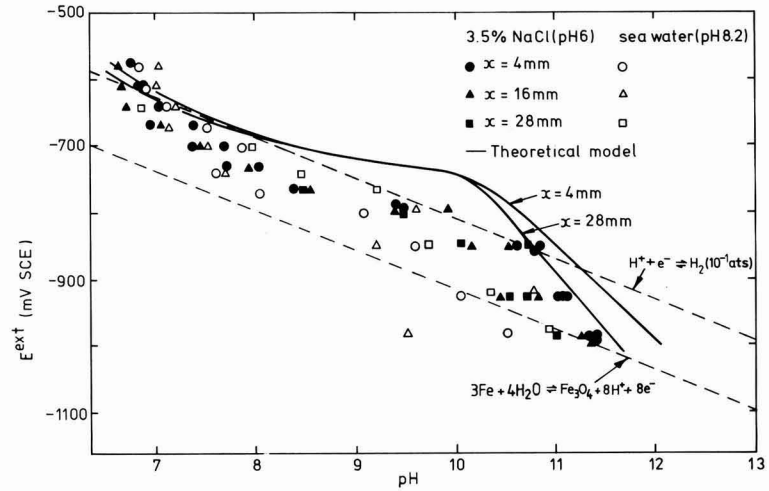

Fig. 10. Variation of pH in artificial crevice with external potential at distance x from the tip of the crevice; length = 33 mm, width = 150 μm (data points from a number of tests are shown).

ing of the pH and a decrease in the ferrous-ion concentration. The extent of metal deposition must therefore be reconsidered in this context.

In addition to the effect of magnetite formation the pH could be limited in principle because of the reversibility of the hydrogen electrode. Calculation of the partial pressure of hydrogen in the crevice is not straightforward, but for these dimensions and the range of potential and pH considered it is unlikely to be less than 10^{-1} atm. The dependence of the reversible hydrogen electrode, at this partial pressure, on the pH and potential is shown in Fig. 12, but it should be noted that in comparing this with the experimental and theoretical pH values allowance must be made for the potential drop in the crevice that is significant at potentials $\gtrsim -700$ mV (SCE). At potentials between -700 and -800 mV (SCE) the pH values predicted by the model are in excess of those associated with the reversible hydrogen electrode. This suggests that the reverse reaction of hydrogen-ion formation would limit the increase in pH but, in view of the uncertainties involved in this analysis based on equilibrium partial pressures in a crack, the formation of magnetite is considered to provide the more likely explanation for the discrepancy between the predictions of the theoretical model and the experimental results.

Relation Between Crack Electrochemistry and Crack Growth Rates

The essential objective in studying the electrochemical conditions in cracks is to predict the rates of metal dissolution and production of hydrogen atoms at the crack tip since these will influence the rate of crack growth. The uncertainty in the extent of magnetite formation and metal deposition makes predictions of the dissolution rate at the crack tip subject to considerable error. Although prediction of the rate of production of hydrogen atoms due to hydrogen-ion reduction and water reduction is subject to the same limitations there is, nevertheless, considerable value in examining this on a qualitative basis. A schematic plot of the variation of the total cathodic reduction current (hydrogen ions and water) at the crack tip as a function of potential and for various values of l^2/w is shown in Fig. 11. The total current is observed to be a minimum at a potential E_1 and to peak at a potential E_2 for each crack dimension. A further minimum, plateau, or change of slope may be observed at more negative potentials depending on the magnitude of the parameter l^2/w. The appearance of the minimum at E_1 is associated with the fact that as the potential is made more negative the pH of the solution in the crack increases, mainly because of reduced dissolution and hydrolysis, and this has a greater effect on the current density for hydrogen-ion reduction than the variation in potential (because of the high Tafel slope). The rate of reduction of water increases as the potential is made more negative and is independent of pH except at high pH values ($\gtrsim 10$). A potential is reached, *viz.*, E_1, at which the current density for water reduction is equal to that for reduction of hydrogen ions. The pH at which this equivalence is obtained will depend on the polarization characteristics of the individual steel, but for the steel BS 4360 50D in 3.5% NaCl it is about 5.4. However, these polarization measurements in 4360 50D steel were made using a stationary electrode and Turnbull and Gardner (11) pointed out that because activation control of the current density occurred only over a narrow range of potential, uncertainty in the hydrogen-ion concentration at the surface could mean that this value is somewhat low. Nevertheless, the potential at which this pH value in the crack is obtained will depend on the crack dimensions and tend to more positive values as l^2/w increases.

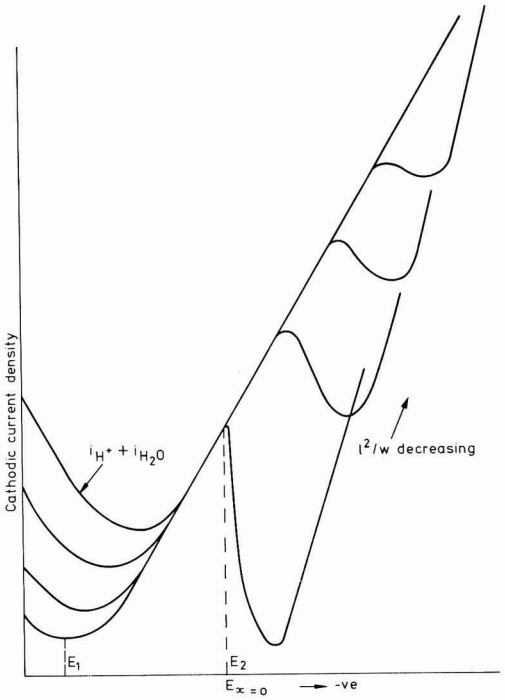

Fig. 11. Schematic illustration of the total current density for production of hydrogen atoms at the crack tip as a function of potential at the tip, for different values of l^2/w.

The peak in the rate of production of hydrogen atoms at potential E_2 is associated with the onset of a decrease in the rate of reduction of water when the pH exceeds 10. The current density decreases initially for potentials $<E_2$, but then subsequently increases as the potential is made still more negative. This is because the extent of the influence of pH on the rate of reduction of water decreases as the potential is polarized to more negative values. As l^2/w decreases the potential E_2 corresponding to pH $\simeq$ 10 will tend to more negative values [Fig. 5(a) and (b)], and the subsequent decrease in current density will be less significant because the influence of pH is diminishing for the reason described above.

The above ideas can be demonstrated in practice using the potential and pH data obtained experimentally in an artificial crevice (32) and the data obtained by Smith *et al.* (2) for a stress corrosion crack in AISI 4340 steel. The calculated current densities are shown in Fig. 12 as a function of the potential close to the tip of the crevice or crack. Note that polarization data for BS 4360 50D steel were used in performing these calculations. The lower pH values obtained by Smith *et al.* for the 0.88% chromium steel result in a minimum at -700 mV (SCE), but for the BS 4360 50D steel the calculations suggest the minimum occurs at potentials more positive than -660 mV (SCE) (the limit in polarization due to potential drop effects). At more negative potentials a peak in the current density is observed for BS 4360 50D steel, but this is less well-defined for the AISI 4340 steel. The value of l^2/w for the artificial crevice was 7260 mm, but calculation of this parameter for the stress corrosion crack is not readily possible in the absence of the relevant data. However, it seems reasonable to assume that the crack length was short since the thickness of the specimen was only 3 mm and this

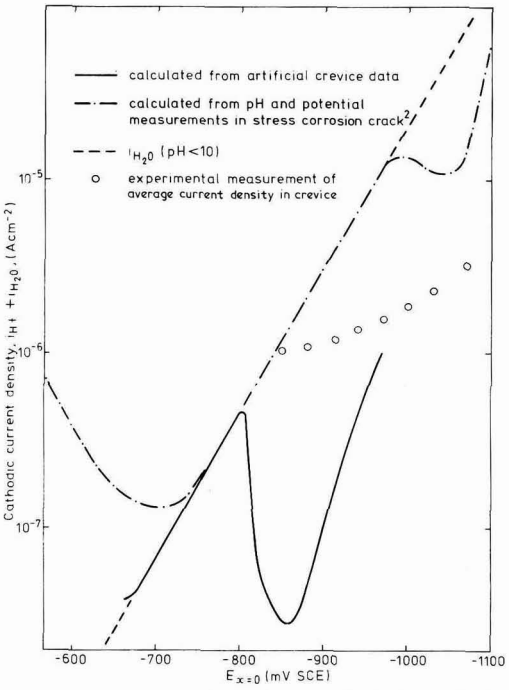

Fig. 12. Calculation of the total current density for production of hydrogen atoms at the crack tip as a function of potential at the tip, based on experimental *p*H and potential measurements.

would tend to suggest a lower value of l^2/w. Actual measurement of the current entering the artificial crevice has been made (Fig. 12) (32), but the absence of a minimum in the current density at about −850 mV may be attributed to the oxygen reduction current at the mouth of the crevice that may have obscured the features described above. It is intended to repeat these measurements in deaerated solution at a future date. If the mechanism of stress corrosion cracking in the AISI 4340 steel is associated with hydrogen interaction with the steel at all potentials as suggested by Brown (33) then the crack growth rate should be related to the rate of production of hydrogen atoms depicted in Fig. 12. The actual crack growth rate data (33) do indicate a minimum, but at a potential of −800 mV (SCE). This is 100 mV more negative than the value calculated above, but this calculation was based on polarization data for BS 4360 50D steel, and in addition the *p*H of 5.4, corresponding to equivalence of the rates of hydrogen-ion reduction and water reduction, was considered to be possibly somewhat low.

The small plateau region in Fig. 12 at potentials $\simeq$ −1025 mV (SCE) was not observed in the crack growth data, but this is not unexpected in view of the errors in monitoring and evaluating crack growth rates. It would clearly be useful to conduct polarization tests on AISI 4340 steel using a rotating disk electrode to obtain more reliable data.

An important point to note about the calculations associated with Fig. 12 is that they are based solely on experimental data and do not involve theoretical modeling.

Conclusions

1. The potential drop in a static crack in the steel BS 4360 50D in 3.5% NaCl is predicted to be significant at potentials positive to the free corrosion potential [$\simeq$ −700 mV (SCE)], but at more negative potentials it is small and can be neglected for potentials more positive than −1V. The important implication is that cathodic protection of narrow cracks or crevices in structural steels in 3.5% NaCl should not be limited significantly by potential drop.

2. The *p*H in the crack, in the same system, is predicted to be greater than or about 6 (the bulk *p*H) for potentials in the crack more negative than −660 mV (SCE).

3. Increasing the crack length and decreasing the crack width lead in general to an increase in the potential drop and an increase in the *p*H.

4. The *p*H at the crack tip is predicted to be almost invariant with change in the *p*H of the bulk solution. It is influenced by the buffering action of seawater, but the effect is relatively small in the absence of calcareous deposition.

5. Comparison of the theoretical predictions of the model with experimental measurements of the potential drop and *p*H in an artificial crevice using the steel BS 4360 50D in 3.5% NaCl and in seawater has shown good agreement with regard to the variation of the potential drop with external potential, but the prediction of the *p*H was less satisfactory particularly at potentials in the range −700 to −800 mV (SCE). The formation of magnetite, which was not included in the model, is suggested to explain the discrepancies observed.

6. The presence of chromium in the steel is predicted to have a very significant effect on the *p*H of the solution in the crack even at the 1% level.

Acknowledgments

L. N. McCartney and D. H. Ferriss provided valuable assistance with the mathematical construction of the model.

Manuscript submitted March 3, 1981; revised manuscript received Dec. 2, 1981.

Any discussion of this paper will appear in a Discussion Section to be published in the June 1983 JOURNAL. All discussions for the June 1983 Discussion Section should be submitted by Feb. 1, 1983.

REFERENCES

1. B. F. Brown, C. T. Fujii, and E. P. Dahlberg, *This Journal*, **116**, 218 (1969).
2. J. A. Smith, M. H. Peterson, and B. F. Brown, *Corrosion*, **26** (12), 539 (1970).
3. J. A. Davis, in "Localized Corrosion," p. 168, NACE, Houston (1974).
4. O. V. Kurov and R. H. Mekekhov, *Zasch. Metal.*, **15** (3), 314 (1979).
5. J. G. Hines, *Corros. Sci.*, **1**, 21 (1961).
6. T. R. Beck and E. A. Grens, *This Journal*, **116**, 177 (1969).
7. G. Faita, F. Mazza, and G. Bianchi, in "Localized Corrosion," p. 34, NACE, Houston (1974).
8. R. R. Shuck and J. L. Swedlow, in "Localized Corrosion," p. 190, 208, NACE, Houston (1974).
9. P. Doig and P. E. J. Flewitt, *Met. Trans., A*, **9**, 357 (1978).
10. A. Turnbull and J. G. N. Thomas, NPL Report DMA (A) 11 (1979).
11. A. Turnbull and M. K. Gardner, *Paper submitted to Corrosion Science.*
12. A. Turnbull, *Br. Corros. J.*, **15** (4), 162 (1980).
13. W. Stumm and J. J. Morgan, "Aquatic Chemistry," John Wiley & Sons, Inc., New York (1970).
14. J. Newman, "Electrochemical Systems," Prentice-Hall, Englewood Cliffs, NJ (1973).
15. A. Turnbull and J. G. N. Thomas, NPL Report DMA (A) 23 (1980).
16. G. Sandoz, C. T. Fujii, and B. F. Brown, *Corros. Sci.*, **10**, 839 (1970).
17. D. H. Ferriss and G. F. Miller, NPL Report, NAC 22/79 (1979).
18. C. F. Baes and R. E. Mesmer, "Hydrolysis of Cations," John Wiley & Sons, Inc., New York (1976).
19. F. A. Posey, A. A. Palko, and A. L. Bacarella, Oak Ridge National Laboratory Report No. ORNL/

TM-5688 (1976), ORNL/TM-5863 (1977), ORNL/TM-6159 (1977), ORNL/TM-6308 (1978).
20. K. Schwabe, *Electrochim. Acta*, **12**, 67 (1967).
21. M. Takahashi, *Boshoku Gijutsu*, **23** (12), 615 (1974).
22. J. Mankowski and Z. Szklarska-Smialowska, *Corros. Sci.*, **15**, 493 (1975).
23. H. S. Isaacs, *This Journal*, **120**, 1456 (1973).
24. R. A. Despic, R. G. Raicheff, and J. O'M. Bockris, *J. Chem. Phys.*, **47**, 2198 (1967).
25. A. Windfeldt, *Electrochim. Acta*, **9**, 1139, 1295 (1964).
26. C. Patel, T. Pyle, and V. Rollins, *Met. Sci.*, 185 (June 1979).
27. R. W. Staehle, G. Turlver, and D. McWright, EPRI Progress Rept., Jan-June, 1975 Project Rep. 311-1 (reported by R. B. Diegle and W. K. Boyd in ASTM STP 665, 26, 1979).
28. D. Howard and T. Pyle, *Philos. Mag.*, **14**, 132, 1179 (1966).
29. D. Howard and T. Pyle, *Br. Corros. J.*, **3**, 301 (1968).
30. C. Patel, V. Rollins, and T. Pyle, 2nd International Congress on Hydrogen in Metals, Paris (1977).
31. W. H. Hartt and S. L. Wolfson, in Corrosion/80, Paper 152, NACE, Houston (1980).
32. A. Turnbull and M. K. Gardner, *Br. Corros. J.*, **16** (3), 140 (1981).
33. B. F. Brown "Theory of Stress Corrosion Cracking in Alloys," p. 186, NATO (1971).

Electrochemical Studies of the Film Formation on Lithium in Propylene Carbonate Solutions under Open-Circuit Conditions

Y. Geronov,[1] F. Schwager, and R. H. Muller*

Materials and Molecular Research Division, Lawrence Berkeley Laboratory, University of California, Berkeley, California 94720

ABSTRACT

The nature of protective surface layers formed on lithium in propylene carbonate solutions of $LiClO_4$ and $LiAsF_6$ at open circuit has been investigated by electrochemical pulse measurements. The results are consistent with the fast formation of a compact thin layer resulting from the reaction with residual water. This layer acts as a solid ionic conductor. Slow corrosion or decomposition processes produce a thicker porous overlayer.

Lithium is thermodynamically unstable in contact with most nonaqueous battery electrolytes and can be used only because of the formation of protective films on the metal (1). It is now generally assumed (2-5) that in most cases the rate-determining step (rds) of the dissolution-deposition process of alkali metals in nonaqueous solutions is not the electron charge transfer but the migration of cation lattice defects through the surface layer. Properties of films on Li in propylene carbonate (PC) solutions have been shown to affect the cycling efficiency of secondary Li electrodes (6, 7). Alloying with an aluminum substrate has been found to be beneficial (8). On the basis of SEM observations, Dey (1) has derived the formation of an "extremely thin" Li_2CO_3 layer on Li on PC. The same author, as well as Peled (3), has used the previous data of Scarr (9) dealing with the dual Tafel behavior of Li in PC solutions in order to support his assumption of the existence of a surface layer and its influence on the electrode kinetics. Scarr had analyzed his experimental results by means of the Butler-Volmer equation.

The aim of this study is to investigate the kinetics of film formation on lithium in propylene carbonate solutions with different solutes and to determine some film characteristics such as resistance conductivity, and thickness.

Two principal ways of investigating these problems were chosen: electrochemical (galvanostatic pulse techniques) and optical (ellipsometry). This paper is dealing mainly with electrochemical measurements, while the results from ellipsometry will be presented separately. The basic assumption of this study is that lithium in PC is covered by a dense surface layer. It acts as an Li-conducting solid electrolyte (6) with no electronic conductivity and has been called solid electrolyte interphase (SEI) (3). The capacitance across this film is assumed to be electrically connected in series with that of the electrolytic double layer.

The electrochemical behavior of SEI electrodes will be governed by the properties of the SEI. When the SEI is thick enough, the migration of ions through it may be the rate-determining step. In this case it is possible to use the basic equation of the classical theory of ionic conduction in solids developed by Frenkel, Varwey, Cabrera, Mott, and Young (10)

$$i = 4q\nu Fan_+ \exp(-W/RT) \sinh(aqFE/RT) \quad [1]$$

where i is the current density, q the charge of the mobile ion, ν the vibration frequency, W the barrier energy, a the half-jump distance, and E the electric field strength. At high electric fields, Eq. [1] can be simplified to

$$i = i_o \exp(BE) = i_o \exp(B\eta/Y) \quad [2]$$

where i_o is the zero-field ionic current density, B is the field coefficient, η is the potential difference across the film, and Y is the film thickness. Equation [2] represents a Tafel-like polarization dependence.

From this equation a Tafel slope, b, which increases with the film thickness, is obtained

$$b = 2.3Y/B \quad [3]$$

For low electric fields Eq. [1] reduces to Ohm's law

$$i = \kappa\eta/Y \quad [4]$$

where κ is the specific conductivity of the SEI. The reaction resistance R_p of an electrode is defined as

$$R_p = (\eta/i)_{\eta\to 0} \quad [5]$$

Thus

$$R_p = 1/\kappa \times Y \quad [6]$$

When the field strength approaches zero, one obtains from Eq. [1]

$$(i)_{E=0} = i_o BE \quad [7]$$

Ohm's law is then applicable and Eq. [4] and [7] result in

* Electrochemical Society Active Member.
[1] Permanent address: Central Laboratory of Electrochemical Power Sources, Bulgarian Academy of Sciences, Sofia, Bulgaria.
Key words: interfaces, batteries, corrosion, films.

$$\kappa = (\partial i/\partial E)_{E=0} = i_o B \quad [8]$$

where i_o is the extrapolated zero-field ionic current density.

Experimental

An electrochemical cell was built to make simultaneous electrochemical and ellipsometric measurements *in situ*. Clean, optically smooth lithium electrodes were prepared and inserted into the cell in inert atmosphere by pressing 3 mm thick, 5 cm^2 round lithium disks (Foote Mineral, high purity, scraped with a blade) on a polycarbonate foil [cleaned with hexane, alcohol, boiling water (1 hr), steam (2-3 hr), and dried in vacuum at 90°-100°C] in a special jig. The cross section of a 3.2 mm diam freshly extruded Li wire, positioned 1 mm from the periphery of the test electrode, served as reference electrode. Two types of solutions were used

(a) propylene carbonate—$LiClO_4$

(b) propylene carbonate—$LiAsF_6$

Propylene carbonate (Burdick and Jackson, Muskegon, MI 49442; distilled in glass) was distilled in a low-pressure distillation column under He atmosphere. The reflux ratio was between 60 and 100, and the head temperature was 145°C. Gas chromatographic analysis showed the water content to be always below 50 ppm. $LiClO_4$ (Alfa p.a.) was dried under vacuum (4-5 mm Hg) at 220°C for 48-73 hr. $LiAsF_6$ (Alfa p.a.) was dried under vacuum at ambient temperature for 7-8 days.

The solutions with 0.05 and 0.1% H_2O were prepared by adding water to PC. The solutes were dissolved in the above solutions. In order to avoid any possible reaction of PC vapor with the lithium surface before contact with the liquid, different glove boxes were used for the preparation of electrodes and solutions.

The delay in electrochemical measurements from the moment of electrode scraping was up to 30-45 min; the delay after electrolyte filling was 15-30 sec. Film formation under open-circuit conditions was followed by periodic determinations of electrode capacitance and polarization resistance $R_p = (\partial\eta/\partial i)_{\eta=0}$ by means of the galvanostatic pulse polarization technique. For the capacitance measurements, pulses were typically of 0.1 mA/cm^2 amplitude and 5 μsec duration; for polarization measurements, amplitudes typically were 1-20 mA/cm^2 and duration 10 msec. Ohmic potential drop in the electrolyte was derived from the initial fast potential rise of the short pulses. The transients were recorded with a Tektronix 5111 storage oscilloscope, equipped with a Tektronix C-50 camera. A 214B Hewlett Packard pulse generator was used either through a high resistance or through a potentiostat with 2 μsec risetime (PAR-371).

The capacitance was derived from the initial slope of short $\eta - t$ transients (5-10 μsec). Anodic and cathodic pulses produced the same results. The steady-state *IR*-free overpotential values for the determination of R_p were obtained from oscilloscopic traces with a duration of up to 20 msec. To avoid damage to the film, pulses with the smallest possible electric charge were applied.

Results and Discussion

Film thickness.—The thickness Y of the film formed during contact of the lithium electrode with propylene carbonate solutions has been derived from the capacitance measurements by use of the formula for two capacitors connected in series (3, 4)

$$Y = \sigma\epsilon/0.113C - Y'\epsilon/\epsilon' [\text{Å}] \quad [9]$$

where ϵ is the dielectric constant of the lithium film, $\epsilon' = 65$ that of PC, C is the capacitance of the electrode in μF/cm^2, and σ is the roughness factor, which is assumed to be unity. The thickness Y' of the Helmholtz layer in concentrated electrolytes can be approximated by the length of the dipole (*ca.* 5Å for PC); the second right-hand term in Eq. [9] can therefore be neglected. In order for Eq. [9] to be used, the film dielectric constant and the film morphology should be known.

Dielectric constant of film material.—According to Dey (1) and Dousek *et al.* (11), PC reacts with Li to form Li_2CO_3. On the other hand, Butler *et al.* (12) have demonstrated the predominant role of small amounts of water in the kinetics of fresh Li surfaces. Dousek *et al.* have pointed out the lack of any decomposition reaction in the bulk Li surface, and even a drastically decreasing rate of PC decomposition on Li amalgam at only 45 ppm H_2O in the PC-$LiClO_4$ solution. Recently, Epelboin *et al.* (13) have claimed, by ESCA analysis, that PC leads to the chemical formation of a polymeric membrane on the Li substrate.

Investigation of the composition of the films formed on Li in different PC solutions by Auger spectroscopy has so far been inconclusive [see surface film observations—Auger electron spectroscopy (AES)]. For the calculation of film thickness from pulse measurements a dielectric constant of 5 was used. This value is close to that of Li_2CO_3 (14), and results in a lower limit of film thickness. One should keep in mind that, for example, with $\epsilon = 10$ [which is close to the value of 8.9 for Li_2O (15)] the film thickness would be twice that shown here. This difference does, however, not affect the present conclusions.

Morphology of film.—The primary passive film formed on Li in $SOCl_2$-$LiAlCl_4$ solutions has recently been shown to be dense and pore-free (4). The porosity of films formed in pure propylene carbonate over periods up to 120 hr was investigated by immersion in solutions of different conductivity (0.15M and 1.0M $LiClO_4$/PC). The electrode capacitance and polarization resistance were found to be the same for both solutions and did not change during two days ($C = 0.14 \pm 0.02$ μF/cm^2 and $R_p = 380 \pm 20$ Ω cm^2). This result is evidence for the absence of electrolyte-filled pores in the film which controls the pulse measurements.

As will be shown further, higher water amounts in the PC solutions increase secondary porous film formation. The porous film does not possess protective properties and presumably would influence the passive behavior of lithium in PC solutions to a negligible extent, since the passivity of Li is governed by the primary nonporous film.

High-field experiments.—The steady-state *IR*-free overpotential values were calculated from the transients in the range of current densities between 0.050 and 20 mA/cm^2. At the higher current densities (*i.e.*, higher electric fields, above about 10^6 V/cm), a Tafel-like polarization dependence is expected (Eq. [2]). Figure 1 presents a series of Tafel plots obtained by the pulse technique after immersion for 0-6 days, resulting in different film thicknesses. As required for a field-assisted ion current across an insulating film, the Tafel slope, b, increases with film thickness. The extrapolated lines intersect at zero overpotential at the zero-field current density, $i_o = 3$ mA/cm^2.

Curve 1 of Fig. 1 was obtained a few minutes after electrolyte filling. The value of the zero-field current density i_o of 5.5 mA/cm^2 obtained by this plot can be compared to exchange currents reported by other authors in terms of the electron transfer reaction mechanism. For example, Butler *et al.* (12) have reported an extrapolated value of the exchange current in 0.001M H_2O/PC/$LiClO_4$ on freshly cut Li surface of 12 mA/cm^2. An exchange current of 3.3 mA/cm^2 was reported by Epelboin *et al.* (13) by using anodic polarization techniques for surface cleaning. The value

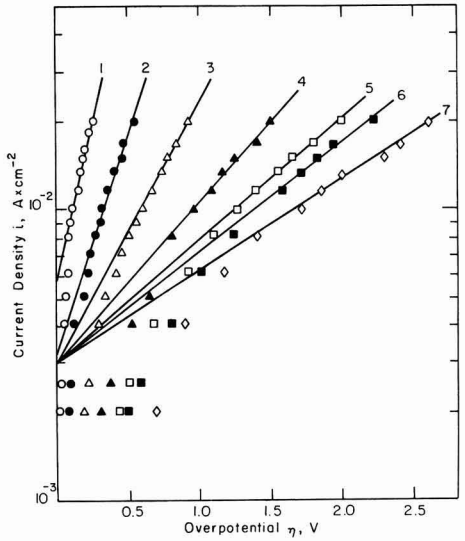

Fig. 1. Tafel plots at constant film thickness (derived for $\epsilon = 5$, anodic polarization), curve 1, 25Å; curve 2, 37Å; curve 3, 65Å; curve 4, 103Å; curve 5, 130Å; curve 6, 138Å; curve 7, 162Å.

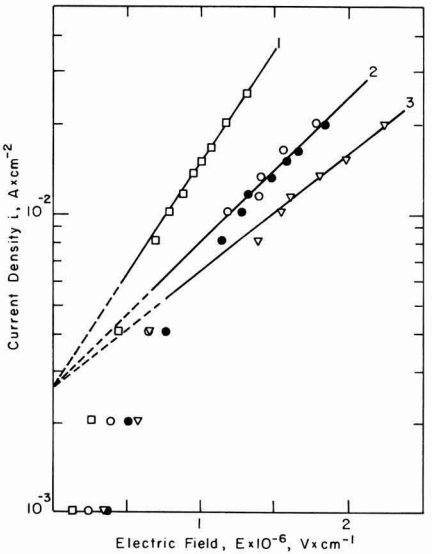

Fig. 3. Tafel plots, log i vs. E, in different propylene carbonate solutions, 30-200Å films: curve 1, 0.5M $LiAsF_6$; curve 2, 0.5M $LiClO_4$; curve 3, 0.5M $LiClO_4$ + 0.1% H_2O.

of 5.5 mA/cm² obtained in this study for the specularly reflecting Li surface agrees well with the value of 12 mA/cm² (12) for a roughness factor of 2-3 given by the previous authors (13). This is evidence for comparable cleanliness of the Li surfaces used in both studies.

This higher value of i_o obtained just after immersing the electrode, as compared to the zero-field current (2.7-3.0 mA/cm²), suggests that immediately after electrode immersion into the solution the electron charge-transfer step is rate determining.

The electrode capacitance of 1.3-1.6 μF/cm² is lower than that of the double layer which supports the presence of a film of 15-30Å (ϵ = 5-10) at the time of immersion.

The value of the field coefficient B (Eq. [3]) may be obtained from the slope of the b-Y plot presented in Fig. 2. This value, $B = 1.2 \pm 0.1 \times 10^{-6}$ cm/V, is very close to that of typical barrier films (10).

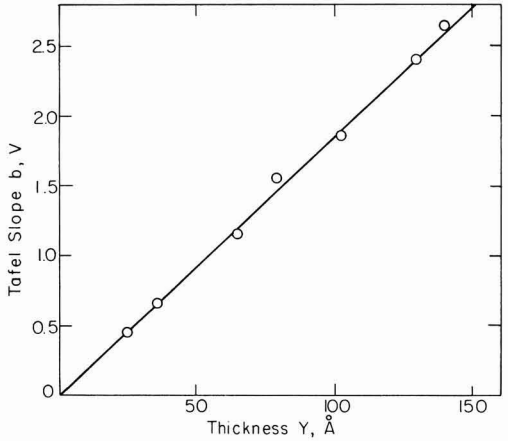

Fig. 2. Relationship between film thickness Y and Tafel slope b

Plots of log i vs. field strength E in different solutions are given in Fig. 3. It is found that the current density does not depend on the film thickness. This finding supports the assumption of the rate-determining step being the ion migration through the film. From the plot log i – E, using Eq. [2] the value of B can also be determined. It can be seen that adding water to $LiClO_4$ solutions decreases the field coefficient, B (slope, Eq. [2]). For $LiAsF_6$ solutions, the field coefficient is larger ($1.8 \pm 0.1 \times 10^{-6}$ cm/V). The zero-field current density is the same for the three solutions ($2.9 \pm 0.2 \times 10^{-3}$ A/cm²), indicating similar film properties in different media. These values of B and i_o were used to calculate the specific conductivity of the film by the low-field approximation, Eq. [8], resulting in $(3.1 \pm 0.25) \times 10^{-9}$ Ω^{-1} cm^{-1} for $LiClO_4$ solutions and $(5.1 \pm 0.2) \times 10^{-9}$ Ω^{-1} cm^{-1} for $LiAsF_6$ solutions.

Experimentally determined values of the Tafel slope, b, at different film thicknesses can be derived from Fig. 1. As has been seen from Eq. [1]-[3], the Tafel slope is equal to

$$b = 2.3RT\,Y/aq\mathbf{F} \qquad [10]$$

For $q = 1$ and $a = 3$Å, this formula is simplified to

$$b(\text{mV}) = 20\,Y \qquad [11]$$

A comparison between the experimental and theoretical values of b is given in Table I. If one considers that other combinations of dielectric constant ϵ and half-jump distance a of the film could be used, the

Table I. Comparison between experimental and theoretical Tafel slopes

Y (Å)	b_{exp} (mV)	$b_{theor.} = 20Y$ (mV)
25	460	500
37	670	740
65	1150	1300
103	1840	2060
130	2400	2600
138	2650	2760
162	3255	3240

agreement of measured and computed Tafel slopes (for $\epsilon = 5$ and $a = 3$Å) is satisfactory.

Low-field experiments.—Figures 4 and 5 present typical sets of experimental plots reflecting the increase of the electrode resistance R_p and the reciprocal capacitance $1/C$ with time for Li electrodes immersed in PC/$LiClO_4$ and PC/$LiAsF_6$ solutions, respectively. It was found in more than 30 experiments that all $1/C$ — R plots intersect at the same point with the coordinates: $1/C = 0.70 \pm 0.10$ cm$^2/\mu$F and $R = 8 \pm 2\ \Omega$ cm^2. This observation supports the existence of a capacitance connected in series with the capacitance across the passive film. This capacitance is low compared to that of the Helmholtz double layer (10-20 μF/cm^2) (8, 12, 13), and probably it is a capacitance of a surface layer formed in the glove box (16).

Hence the thickness of the film formed during the contact of lithium with the solution can be calculated from Eq. [12] instead of Eq. [9]

$$Y = 8.85 \times 10^{-8} \epsilon\sigma (1/C - 1/C_d)\ (\text{cm}) \qquad [12]$$

where C is the film capacitance and C_d is the intersection of the plot ($1/C - R_p$) with the $1/C$ ordinate (actually this involves an error of a few Å if, instead of $R_p = 5\text{-}8\ \Omega$ cm^2, $R_p = 20$ is taken).

From the slope of $1/C - R_p$, using Eq. [6] and [12], the values of specific conductivity of the primary passive film in different PC solutions can be derived. This value for PC/$LiClO_4$ solutions is $2.7 \pm 0.2 \times 10^{-9}\ \Omega^{-1}$ cm^{-1} (Fig. 4) and for PC/$LiAsF_6$ — $5.1 \pm 0.25 \times 10^{-9}\ \Omega^{-1}$ cm^{-1} (Fig. 5). Both are very close to the value of κ, estimated from the low-field approximation (Eq. [8]).

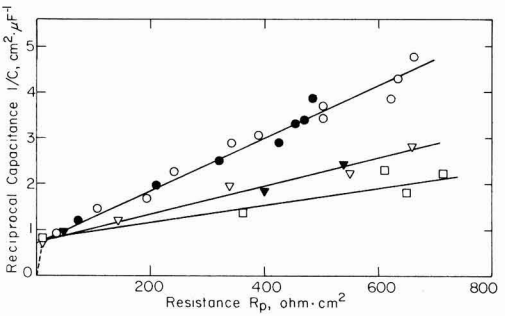

Fig. 4. Reciprocal capacitance, 1/C vs. polarization resistance, R_p, in the following propylene carbonate solutions: ○, ●, 1M $LiClO_4$; ▽, 1M $LiClO_4$ + 0.05% H_2O; ▼, 1M $LiClO_4$ + 0.1% H_2O; □, 0.5M $LiClO_4$ + 0.1% H_2O.

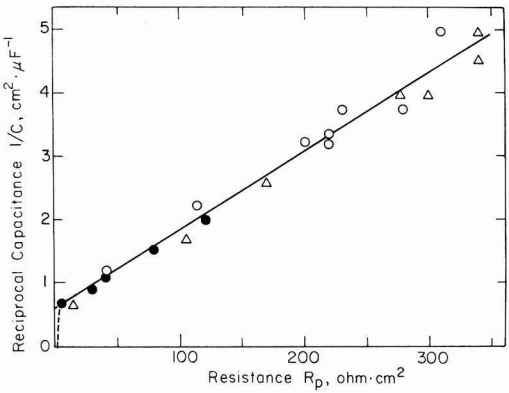

Fig. 5. Reciprocal capacitance, 1/C vs. polarization resistance R_p, in hexafluoroarsenate solutions. ●, ○, 0.5M $LiAsF_6$; △, 0.5M $LiAsF_6$ + 0.1% H_2O.

Effect of water.—Figure 6 presents the change of the electrode resistance during the time of immersion. In the same figure, curves 1 and 2 are for 0.5M $LiAsF_6$ solutions with 20 and 1000 ppm H_2O, respectively, and curves 3, 4, and 5 are for 0.5M $LiClO_4$ solutions with 20, 500, and 1000 ppm H_2O, respectively. The curves show that the rate of film formation increases with water concentration. This trend is much stronger in PC/$LiClO_4$ solutions than in $LiAsF_6$.

From Fig. 5 it can also be seen that there is no difference between the conductivity of films formed in PC/0.5M $LiAsF_6$ with 20 ppm H_2O and those with 1000 ppm H_2O. On the other hand, the film conductivity in $LiAsF_6$ solutions is always higher than in $LiClO_4$ solutions independent of the water concentration. For example, from the lower two curves in Fig. 4, one calculates values of 0.8 to $1.5 \times 10^{-9}\ \Omega^{-1}$ cm^{-1} for κ for $LiClO_4$ solutions with 500-1000 ppm H_2O. The corresponding value for $LiAsF_6$ solutions (Fig. 5) is 3-4 times higher. The former values are 2-3 times lower than the conductivity of passive films formed in $LiClO_4$ solutions with 20 ppm H_2O ($2.5\text{-}3.5 \times 10^{-9}\ \Omega^{-1}$ cm^{-1}).

The same tendency of thin film conductivity change is also demonstrated from the high-field experiments (see Fig. 3), but to a lesser extent. For example, the expected field coefficient, B, for PC/0.5M $LiClO_4$ solutions with 1000 ppm of water should be approximately two times lower in order to fit the calculated value of specific conductivity according to Eq. [8] ($\kappa = i_o B$) to that obtained from low-field experiments (Fig. 4). This disagreement, found only in PC/$LiClO_4$ solutions of high water content, is probably due to some influence of the secondary porous film. On the other hand, it is noteworthy that the Tafel plots $\log i - E$ taken from the passivated lithium electrode in pure PC, PC with 0.5M $LiAsF_6$, and PC/$LiAsF_6$ with 1000 ppm H_2O show the same slope, the same field coefficient $B = 1.8 \times 10^{-6}$ V^{-1} cm, and zero field current density $i_o = 2.7 \times 10^{-3}$ A/cm^2 (Fig. 7). The specific conductivity calculated using these values of B and i_o

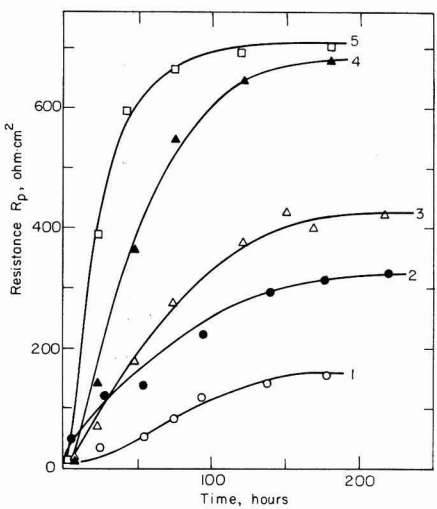

Fig. 6. Time dependence of Li electrode resistance in different propylene carbonate solutions: curve 1, 0.5M $LiAsF_6$; curve 2, 0.5M $LiAsF_6$ + 0.1% H_2O; curve 3, 0.5M $LiClO_4$; curve 4, 0.5M $LiClO_4$ + 0.05% H_2O; curve 5, 0.5M $LiClO_4$ + 0.1% H_2O.

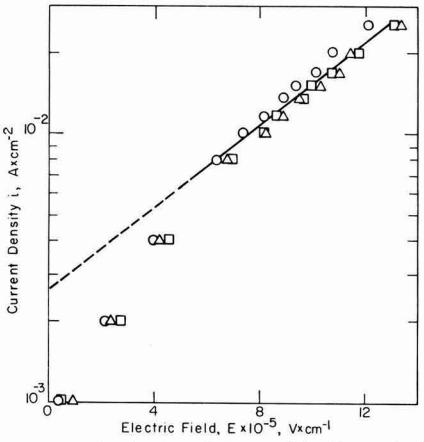

Fig. 7. Tafel plots, log i vs. E, for: △, PC without salt, Y = 307Å; □, PC/0.5M $LiAsF_6$, Y = 215Å; ○, PC/0.5M $LiAsF_6$ + 0.1% H_2O, Y = 205Å.

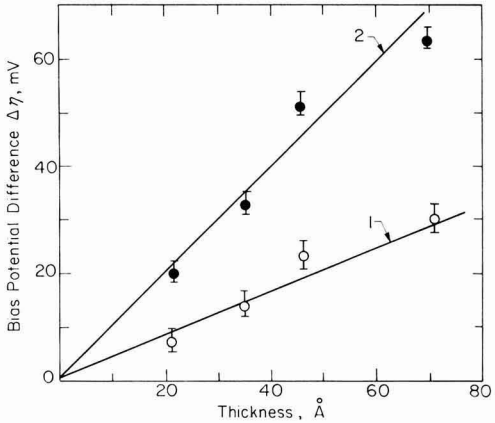

Fig. 8. Dependence of the excess voltage, $\Delta\eta$, on the film thickness in 1M $LiClO_4$ at: curve 1, 0.5 mA/cm²; curve 2, 1 mA/cm².

is very close to the one found for $LiAsF_6$ solutions from low-field experiments (see Fig. 5), 4.9×10^{-9} Ω^{-1} cm^{-1}.

This observation supports the following ideas: (*i*) passive layers are formed the same way in PC without any salt and with $LiAsF_6$ as solute, (*ii*) $LiAsF_6$ does not take part in the film formation, and (*iii*) film is formed as a result of reaction of Li with water impurity. The last suggestion is reinforced by the increase of the rate of formation with increasing water concentration.

A surprising result from this set of experiments was that lithium corroded faster in PC (without salt) containing 0.1% H_2O than in solutions of $LiClO_4$ and $LiAsF_6$ with the same amount of water (Fig. 11-12). After seven days of immersion in PC with water, a mirror-like bright lithium surface turns dark gray. This has never happened in the solutions with $LiClO_4$ or $LiAsF_6$ with the same water concentrations. The water activity appears to be reduced by the presence of salts.

So far, there is no reasonable explanation for the decrease in film conductivity with increasing water content of $LiClO_4$ solutions. However, the fact that even in $LiClO_4$ solutions with low H_2O concentration the film conductivity is always lower than in $LiAsF_6$ solutions and pure PC suggests the important role of $LiClO_4$ in the film formation.

Effect of cathodic pulse polarizations.—The overpotential behavior of the Li electrode in PC/$LiClO_4$ was found to be different for anodic and cathodic polarization. In Fig. 8, the difference between cathodic and anodic overpotentials, $\Delta\eta$, is related to the film thickness for 0.5 and 1 mA/cm² current pulses of 10 msec duration.

The higher overpotential (or higher resistance) of the process of the Li deposition in $LiClO_4$ can be attributed to the difficulty of the Li^+ transport across the solution/film or the film/metal interfaces. In PC/$LiAsF_6$ solutions completely symmetric behavior was observed up to 15 mA/cm². A similar effect of asymmetric overpotential behavior of magnesium electrodes in $SOCl_2$ solutions was reported by Peled and Strase (17). They explained the effect as being due to the rather difficult process of solvated molecules shedding their solvent before entering the passivating layer. The dependence of the excess cathodic voltage $\Delta\eta$ on film thickness (Fig. 8) is, however, not consistent with solvent molecule shedding at the solution/passive layer interface.

Film growth.—As it was recently demonstrated (18), a good agreement with experimental results of the passive film growth in $SOCl_2$-$LiAlCl_4$ solutions can be obtained if an additional slow film corrosion is taken into account. The corrosion rate is assumed to rule the growth of the secondary porous film in the postulated dual-film model.

The same approach is used in this study, especially for solutions containing 0.05 and 0.1% H_2O where the corrosion rate is higher. The equations used are

$$v = (\partial Y/\partial t) = v_g - v_c \quad [13]$$

$$v = \Delta\phi V_m \kappa / Y\mathbf{F} - v_c \quad [14]$$

$$v = A/Y - v_c \text{ (cm/sec)} \quad [15]$$

Here v is the instantaneous net rate of film growth calculated by graphical differentiation of the Y-t curves, v_g is the rate of the primary passive film growth by field-assisted ionic migration in the solid phase, v_c is the rate of corrosion assumed to be independent of film thickness and time, $\Delta\phi$ is the potential difference in the film, V_m is the molar volume of the passive film in cm^3/mol, and κ is the specific conductivity of the film.

In Fig. 9, v is plotted *vs.* the reciprocal film thickness $1/Y$. The slopes of the plot v *vs.* $1/Y$ yield the kinetic constant, A, the intercept with the abscissa gives a steady-state thickness Y_∞ for $v = 0$. Under this condition, Eq. [15] yields the corrosion rate of the film

$$v_c = A/Y_\infty \text{ (cm/sec)} \quad [16]$$

Table II presents the kinetic data obtained from the plots in Fig. 9. For comparison, data on Li in $SOCl_2$/$LiAlCl_4$ are also included (18).

Film growth rates derived from simultaneous ellipsometric measurement in the same solutions (19) are of the same order of magnitude as those presented in Table II. For example, ellipsometry gives for v_c in PC/1M $LiClO_4$ solution with 0.1% H_2O a value of 0.15-

Table II. Kinetic data of film growth in different media

Electrolyte	Y (Å)	$\kappa \times 10^9$ (Ω^{-1} cm^{-1})	A (cm²/sec)	v_c (cm/sec)
PC/0.5M $LiClO_4$, 0.1% H_2O	114	0.81	1.3×10^{-18}	1.15×10^{-12}
PC/1.0M $LiClO_4$, 0.1% H_2O	167	1.34	1.8×10^{-18}	1.08×10^{-12}
PC/0.5M $LiAsF_6$, 0.1% H_2O	167	5.3	4×10^{-18}	2.4×10^{-12}
$SOCl_2$/1M $LiAlCl_4$	200	0.64	2×10^{-16}	1×10^{-10}

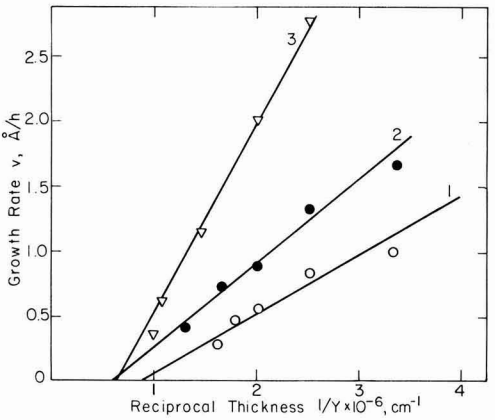

Fig. 9. Dependence of the net rate of film growth, v, on the reciprocal film thickness, 1/Y. Propylene carbonate solutions with 0.1% H_2O: curve 1, 0.5M $LiClO_4$; curve 2, 1.0M $LiClO_4$; curve 3, 0.5M $LiAsF_6$.

0.3×10^{-12} cm/sec, assuming a constant growth of the porous film during 10 days of storage.

Corrosion rates of Li in PC solutions can be seen to be two orders of magnitude lower than in $SOCl_2$-$LiAlCl_4$ solutions.

Temperature dependence.—With a dielectric constant of 5, assuming that ϵ does not depend on the solute and the film density, a field constant B, typical for barrier films, was derived. This value is for PC/$LiAsF_6$ $1.8 \pm 0.2 \times 10^{-6}$ V^{-1} cm, and for PC/$LiClO_4$ solutions 0.8 to 1.3×10^{-6} V^{-1} cm, depending on the water content. This agreement of the experimental results with the basic equation of the ionic transport, and especially the accuracy of the experimentally found thickness used for calculating the kinetic constants, could be determined once more.

Following Young (10), the Eq. [2] $i = i_0 \exp(BE)$ is valid when the backward current is negligible compared to the forward current. Hence, the ratio P will indicate this validity

$$P = \exp -(W - qaE)/\exp -(W + qaE) \quad [15]$$

where W is the activation (barrier) energy, q is the ion charge of the mobile ion, a is the half-jump distance, and E is the field strength.

The apparent activation energy of the ionic conductivity was assessed by the temperature dependence of κ of the passive film, formed in PC/0.5M $LiClO_4$ in the temperature range $-20°$ to $+20°$C. The Arrhenius plot (Fig. 10) yields 0.61V. This value with $a = 3$Å and $q = e$ for a field $E = 10^6$ V/cm gives $P \simeq 10$. This means that at electric fields of 10^6 V/cm a Tafel-like behavior is expected. The experimental results summarized in Fig. 3 and 7 have confirmed this theoretical expectation.

Surface-film observations.—Scanning electron microscopy (SEM).—Electrode surfaces resulting from exposure to pure PC and solutions of $LiClO_4$ and $LiAsF_6$ of different water content have been examined by SEM. The lithium specimens were transferred from the glove box to the SEM in a transfer device under 10-20 mTorr of helium. Transfer time was about 1 hr. The film morphology was found to depend on the electrolyte composition as well as on storage time. With higher water concentration and longer storage time, a coarser crystalline film with higher porosity was observed. At low water concentration the film formed in $LiClO_4$ appears less porous than that formed in $LiAsF_6$.

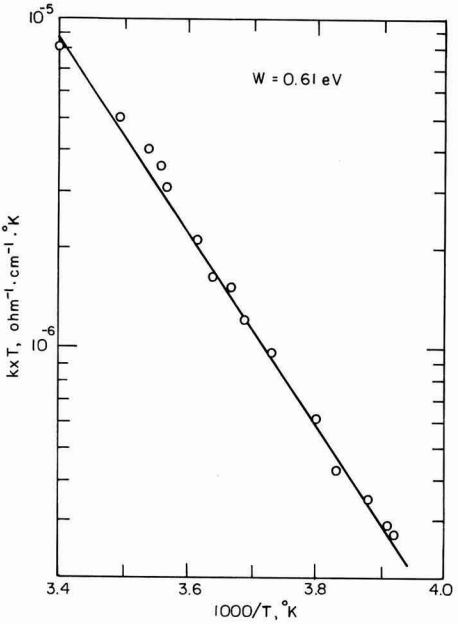

Fig. 10. Temperature dependence of the ionic conductivity through the film on lithium formed in 0.5M $LiClO_4$ solution.

However, nearly the same rough and porous structure was observed in both solutions when the water level was increased to 0.1%.

Microstructures seen in scanning electron micrographs agree with the findings about the importance of electrolyte salts for film growth and corrosion. A pore-free dense structure was observed after exposure to pure PC. This structure is consistent with electrochemical experiments mentioned before. The porous overlayer formed in less than six days was assumed to possess low protective properties, and not to influence the investigated Li passivity. This assumption may not be valid for the longest exposure times.

Auger electron spectroscopy (AES).—Auger spectra and depth profiles on Li electrodes stored in different PC solutions have been determined. The most reproducible results were obtained with lithium stored in PC without salt. A 5 min depth profile of Li, C, O on electrodes exposed to pure PC for two weeks shows that the bare Li surface is reached after 3 min of sputtering, indicating an approximate film thickness of 400-500Å based on a calibrated sputter rate of 150 Å/min for Ta_2O_5 under the same conditions. This value is of the same order as 300-350Å obtained by capacitance measurements (0.12-0.14 μF/cm^2; $\epsilon = 5$). No firm conclusions about the chemical composition of the film could be drawn from the Auger spectra. An initial carbon content of 33 atomic percent (a/o), which decreased to below 5% after 1.5 min, could have been caused by residual CO in the UHV-chamber, and is not necessarily indicative of the presence of Li_2CO_3. Oxygen content increased from 37 a/o to 50% after 0.5 min and decreased to less than 10% after 3 min. Chlorine content decreased from 2% to less than 1% after 0.5 min.

General Discussion and Conclusions

The present study supports the idea that the stability of Li in PC solutions at open circuit and ambient temperature can be attributed to the formation of a non-

Fig. 11. SEM picture of Li surface after five days of storage in PC with 0.1% H_2O, 1000×.

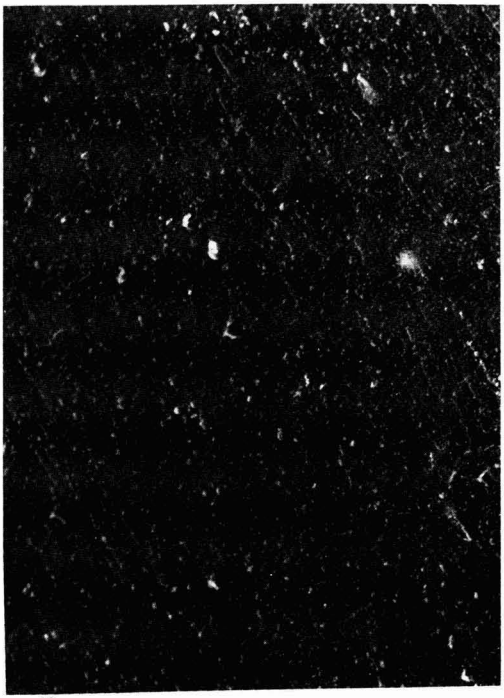

Fig. 12. SEM picture of Li surface after five days of storage in PC + 0.1% H_2O + 1.2M $LiClO_4$, 2000×.

porous ionically conducting and electronically insulating film.

The increase of film formation rate at higher water concentration and the independence of the specific conductivity of the films on the water level in PC-$LiAsF_6$ solutions demonstrate the importance of the reaction of Li with water in propylene carbonate solutions, which is also supported by SEM observations. Li_2O is the thermodynamically favored reaction product. The importance of water has also been pointed out by Butler *et al.* (12) and Besenhard and Eichinger (20).

Recently, Froning *et al.* (16) and Keil *et al.* (21) have shown that even at extremely low oxygen exposures (66 Langmuirs) the freshly cut Li surface is immediately covered by an Li_2O film. Oxygen exposure of the lithium electrode during preparation in the dry box has been larger, and an initially present film of 15-30Å thickness is indicated by the capacitance measurements.

In this study it has been shown that the specific conductivity of the passive film formed in PC/$LiAsF_6$ is two to three times higher than that in PC/$LiClO_4$. Anodic and cathodic overpotentials were found to be symmetric in $LiAsF_6$-solutions, whereas the cathodic overpotential was higher than the anodic in $LiClO_4$-solutions. This finding is in agreement with that by Brummer *et al.* (22) that AsF_6^- improves the Li cycling efficiency in PC solution, probably as a result of the higher conductivity of the film formed in AsF_6^- solutions as compared to films from ClO_4^- solutions.

In addition to the nonporous layer responsible for inhibiting the spontaneous reaction of lithium, a nonprotective outer porous film region seems to be formed by a corrosion (or decomposition) process. This part of the film does not affect electrochemical measurements but is visible in scanning electron micrographs and is found in ellipsometer measurements.

Acknowledgment

This work was supported by the Assistant Secretary for Conservation and Renewable Energy, Office of Advanced Conservation Technologies, Electrochemical Research Division of the U.S. Department of Energy under Contract No. W-7405-ENG-48.

Manuscript submitted June 29, 1981; revised manuscript received Dec. 4, 1981. This was Paper 706 RNP presented at the Hollywood, Florida, Meeting of the Society, Oct. 5-10, 1980.

Any discussion of this paper will appear in a Discussion Section to be published in the June 1983 JOURNAL. All discussions for the June 1983 Discussion Section should be submitted by Feb. 1, 1983.

Publication costs of this article were assisted by the University of California.

REFERENCES

1. A. N. Dey, *Thin Solid Films*, **43**, 131 (1977).
2. E. Peled and H. Yamin, 18th Power Sources Symposium, Atlantic City, NJ p. 273 (1978).
3. E. Peled, *This Journal*, **126**, 2047 (1979).
4. R. V. Moshtev, Y. Geronov, B. Puresheva, and A. Nasalevska, 28th ISE Meeting, Varna, Extend. Abstract 153 (1977).
5. A. Leef and A. Gilmour, *J. Appl. Electrochem.*, **9**, 663 (1979).
6. R. D. Rauh and S. B. Brummer, *Electrochim. Acta*, **22**, 75 (1977).
7. M. Garreau, J. Thevenin, and D. Warin, "Progress in Batteries," Vol. 2, p. 54, JEC Press, Cleveland, OH (1979).
8. I. Epelboin, M. Froment, M. Garreau, J. Thevenin, and D. Warin, in "Power Sources for Biomedical Implantable Applications and Ambient Temperature Lithium Batteries," B. B. Owens and N. Margalit, Editors, p. 417, The Electrochemical Society Softbound Proceedings Series, Princeton, NJ (1980).
9. R. F. Scarr, *This Journal*, **117**, 295 (1970).

10. L. Young, "Anodic Oxide Films," Academic Press, New York (1961).
11. F. P. Dousek, J. Jausta, and L. Riha, *J. Electroanal. Chem. Interfacial Electrochem.*, **46**, 281 (1973).
12. J. N. Butler, D. R. Cogley, and J. C. Synott, *J. Phys. Chem.*, **73**, 4026 (1969).
13. I. Epelboin, M. Froment, M. Garreau, L. Thevenin, and D. Warin, *This Journal*, **127**, 2100 (1980).
14. "American Institute of Physics Handbook," McGraw-Hill, New York (1963).
15. Landolt-Bornstein, "Zahlenwerte und Funktionen aus Naturwissenschaften und Technik," Vol. II, Part 6, p. 455, Springer, New York (1959).
16. M. H. Froning, T. N. Wittberg, and W. E. Modeman, Paper 14 presented at The Electrochemical Society Meeting, Los Angeles, California, Oct. 14-19, 1979.
17. E. Peled and H. Straze, *This Journal*, **124**, 1030 (1977).
18. R. V. Moshtev, Y. Geronov, and B. Puresheva, *ibid.*, **128**, 1851 (1981).
19. F. Schwager, Y. Geronov, and R. Muller, Paper 37 presented at The Electrochemical Society Meeting, Hollywood, Florida, Oct. 5-10, 1980.
20. J. O. Besenhard and G. Eichinger, *J. Electroanal. Chem. Interfacial Electrochem.*, **68**, 1 (1976).
21. R. Keil, J. Hoenigman, W. Modeman, T. Wittberg, and J. Peters, Interim Techn. Report, October 1979. AFWAL-TR-80-2018, Univ. of Dayton Research Inst., Dayton, OH.
22. S. B. Brummer, in "Lithium Nonaqueous Battery Electrochemistry," E. B. Yeager *et al.*, Editors, p. 13, The Electrochemical Society, Princeton, NJ (1980).

Lithium-Aluminum Electrodes at Ambient Temperatures

T. R. Jow* and C. C. Liang*

Electrochem Industries Incorporated, Clarence, New York 14031

ABSTRACT

Investigations were conducted to study the effect of composition on the electrode potential of the lithium-aluminum alloy system and the diffusivity of lithium in β-LiAl at ambient temperatures. The electrode potentials of pyrometallurgically formed and electrochemically formed Li-Al alloys were determined in the $LiClO_4$ in 1,3-dioxolane electrolyte. The various single phase and multiphase regions in terms of the alloy composition were delineated from the electrode potential characteristics and the results agree well with those obtained at elevated temperatures. The behavior of the potential change on electrodeposition of lithium on aluminum or lithium-aluminum suggests slow diffusion rates of lithium in the lithium-aluminum alloy system at ambient temperatures. Both potentiostatic and galvanostatic techniques were used to determine the diffusivity of lithium in β-LiAl. A value of $(7 \pm 3) \times 10^{-9}$ cm^2/sec was found to be the chemical diffusivity of Li in β-LiAl at 24° ± 2°C.

For the development of ambient temperature secondary lithium batteries, efforts have been made by various investigators to find organic electrolytes that are stable with respect to lithium (1-5) and metal substrates that form alloys with lithium to facilitate the rechargeability of the anode (6-12). It appears that aluminum is the most promising alloying metal with lithium (9). Thermodynamic properties of the lithium-aluminum alloys have been studied by Rao *et al.* (8) and Garreau *et al.* (12) using electroformed lithium-aluminum on thin aluminum foils. Garreau *et al.* (12) also studied their kinetic properties. In addition, lithium diffusion in the lithium-aluminum alloy system has been studied by several workers (14-17) at elevated temperatures, and by Schone *et al.* (18) and Willhite *et al.* (19) at ambient and low temperatures.

For the practical application of Li-Al alloys in ambient temperature lithium secondary cells, it is important to understand the thermodynamic properties and diffusion characteristics of the alloys in a practical environment. Accordingly, investigations were conducted in this laboratory using such a practical organic electrolyte as $LiClO_4$ in 1,3-dioxolane. The electrode potential was determined as a function of composition for both electroformed and pyrometallurgically formed Li-Al alloys. Furthermore, the diffusion process of lithium in the pyrometallurgically formed Li-Al alloys was studied at ambient temperatures.

Experimental

Materials preparation.—Lithium-aluminum alloys with various compositions were prepared by the following procedure. Proper amounts of Li (Foote Mineral, high purity) and Al lumps (Alfa, 99.999%) were sealed in stainless steel cans and heated at a temperature between 720° and 800°C for 2-3 hr, followed by an annealing treatment. The annealing temperature and duration depend on the composition. Alloys containing higher than 60 atomic percent (a/o) of lithium were annealed at 160° ± 5°C for at least 72 hr, while alloys containing lower concentrations of lithium were annealed at 550° ± 20°C for about 24 hr. After annealing, the alloys were ground to −200 mesh for use.

Lithium-aluminum alloy electrodes were formed by pressing the Li-Al powder in a stainless steel die of 1.3 cm diam at a pressure of 6300 kg/cm^2. Disks of nickel Exmet with welded nickel ribbons were used as the electrical leads. A 25 μm thick aluminum foil (Alfa, 99.997%) was used as a starting material for the electroformed Li-Al.

The 1,3-dioxolane solvent was distilled over sodium benzophenone ketyl in the dry box according to the procedure used by Koch (20). Lithium perchlorate (Cerac) was dried under vacuum at 200°C. A solution of 2M $LiClO_4$ in 1,3-dioxolane was used as the electrolyte in all experiments.

Cell assembly.—A three-electrode cell was used for potentiostatic and galvanostatic measurements. The schematic arrangement of the electrodes is shown in Fig. 1. The circumference and one side of the working electrode with an Ni lead were covered by heat-shrunk polyethylene tubing. Only one side of the electrode was exposed to the electrolyte. Lithium was used as the reference and counterelectrodes. For the electroformation of Li-Al a 25 μm thick aluminum foil was used as the starting electrode. A nickel foil of similar diameter with a welded nickel tab was used as the current collector. The contact between the aluminum and the nickel foil was ensured by stacking the Ni foil, the Al foil, two layers of Celgard 2402 microporous separator material, and a lithium counterelectrode together under pressure between a threaded Teflon plunger and a Teflon plate. The reference Li

* Electrochemical Society Active Member.

Key words: alloy, diffusion, electrodeposition, organic electrolyte.

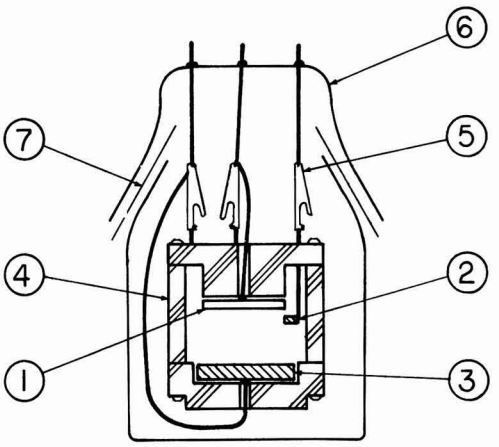

Fig. 1. Cell assembly for potentiostatic and galvanostatic measurements: 1) working electrode, 2) reference electrode, 3) counter-electrode, 4) Teflon cell holder, 5) alligator clip, 6) 55/50 ground glass joint, 7) Teflon sleeve.

electrode was positioned adjacent to the aluminum electrode.

Electrical measurement.—The electrode potential of the electroformed or pyrometallurgically formed Li-Al alloy was measured using a Keithley 616 electrometer (input impedance $10^{14}\Omega$). The open-circuit potential was recorded after the rate of change in potential ($\Delta E/\Delta t$) had reached 0.5 mV/hr. The potentiostatic and the galvanostatic measurements were made using a Princeton Applied Research Model 173 potentiostat/galvanostat and Model 376 logarithmic current converter. The current or voltage was measured by a Keithley 177 multimeter and recorded on a Soltec Model KA series strip chart recorder. All experiments were performed in a Vacuum Atmospheres dry box under an argon atmosphere at 24° ± 2°C (ambient). The electrical leads of the cell were connected to the PAR 173 potentiostat/galvanostat outside the dry box through proper feedthroughs.

Results

Electrode potentials of the lithium-aluminum alloys.—The electrode potentials of pyrometallurgically formed lithium-aluminum are shown in Fig. 2 as a function of lithium concentration between 20 and 70 a/o. It is noted that in the concentration range between 48 and 57 a/o Li, the Li-Al potential varies with concentration indicating a single phase that corresponds to the β-phase LiAl in the phase diagram published by Myles *et al.* (21). Indeed, the experimental results of the present investigation agree well with the phase diagram (21) in regard to the single-phase regions (potential varies with concentration) and multiphase regions (potential remains constant). Accordingly, the various phases in the Li-Al system are assigned in Fig. 2 in accordance with the results obtained by Myles *et al.* (21).

Electrochemical method was also used to form the lithium-aluminum alloys. On a 25 μm thick aluminum foil, lithium was deposited at a cathodic current of 75 $\mu A/cm^2$. The potential of the electrode was monitored during and after the Li deposition. Figure 3 shows that at the onset of current the potential decreases rapidly toward a value of 330 mV, indicating the formation of β-LiAl at the surface. On open-circuit after a predetermined deposition period corresponding to a lithium concentration less than 44.5 a/o, the potential increases slowly toward an equilibrium value indicating the formation of the α-phase by the diffusion of Li toward the interior of the Al foil. Figure 4 shows the potential of the electrochemically formed Li-Al alloys having an Li concentration less than 44.5 a/o is about 380 mV, which approximates the result of the pyrometallurgically formed Li-Al alloys. However, at lithium concentrations higher than 44.5 a/o the open-circuit potentials of the electroformed Li-Al electrodes are very much lower than those of the pyrometallurgically formed Li-Al alloys having corresponding lithium concentrations (see Fig. 2 for comparison). Indeed, the open-circuit potential *vs.* lithium concentration characteristics found in this study are quite different from those reported by Rao *et al.* (8) and by Garreau *et al.* (12). The results obtained by these authors (8, 12) are also presented in Fig. 4 for comparison.

Diffusion studies.—The diffusion of lithium in the pyrometallurgically formed β-LiAl was determined using the potentiostatic and the galvanostatic tech-

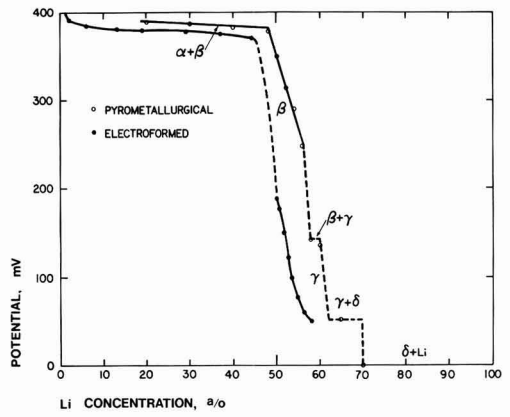

Fig. 2. Electrode potential of pyrometallurgically and electrochemically formed Li-Al as a function of lithium concentration.

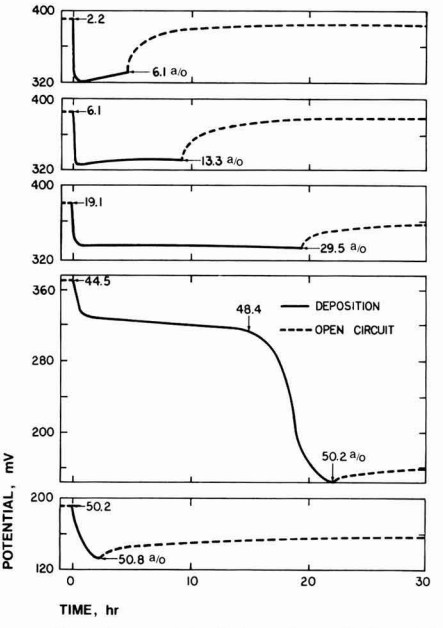

Fig. 3. Electrode potential of electrochemically formed Li-Al during and after lithium deposition.

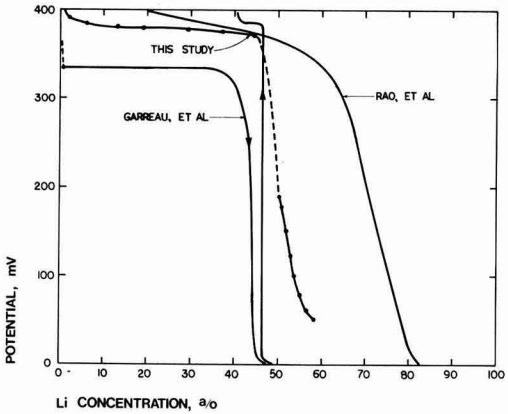

Fig. 4. Electrode potential of electrochemically formed Li-Al as a function of lithium concentration.

niques. The techniques have been discussed in detail in the literature (17, 22-24). A brief review will be presented along with the experimental results.

Potentiostatic measurements.—The initial potential $E°$ corresponding to the initial concentration $C°$ of the working electrode, Li-Al, is suddenly changed to a new potential E which corresponds to a new concentration C at the electrode/electrolyte interface. The current flow within Li-Al for maintaining the surface concentration C can be obtained from the solution of Fick's second law, assuming one-dimensional transport

$$\frac{\partial C_{Li}}{\partial t} = D\frac{\partial^2 C_{Li}}{\partial X^2} \quad [1]$$

where X is the distance of a given point in the solid to the electrode/electrolyte interface, C_{Li} is the Li concentration, and D is the chemical diffusion coefficient. D is assumed to be independent of the Li concentration in Li-Al in the concentration range studied. The solution of Eq. [1], $C_{Li}(X, t)$, can be obtained using the following initial and boundary conditions for an Li-Al electrode having a thickness L

$$C_{Li} = C° \quad 0 \leq X \leq L, t = 0 \quad [2]$$

$$C_{Li} = C \quad X = 0, t > 0 \quad [3]$$

$$\frac{\partial C_{Li}}{\partial X} = 0 \quad X = L, t \geq 0 \quad [4]$$

Substituting C_{Li} (X, t) into the following relation

$$I(t) = -\mathbf{F}AD\left(\frac{\partial C_{Li}}{\partial X}\right)_{X=0} \quad [5]$$

the current as a function of time, $I(t)$, can be expressed explicity as

$$I(t) = \mathbf{F}A(C - C°)\left(\frac{D}{\pi t}\right)^{1/2} \quad \text{if } t << L^2/D \quad [6]$$

where $\mathbf{F}$ is Faraday constant, and A is the cross-sectional area of the electrode in contact with the electrolyte. Therefore, in accordance with Eq. [6] the chemical diffusion coefficient D can be obtained from the slope of the linear plot of I *vs.* $t^{-1/2}$ and the value of $(C - C°)$ which can be obtained from Fig. 2.

Figure 5 shows the I *vs.* $t^{-1/2}$ plots for the potential steps of ±5, ±10, and ±20 mV starting from about 350 mV. It should be noted that in plotting the I *vs.* $t^{-1/2}$ relations, only the magnitude of the current was considered. The direction of the current is not shown in Fig. 5. Thus the anodic (positive) and cathodic (negative) currents are shown as ● and ×, respectively in Fig. 5. Straight lines passing through the origin are noted in the time intervals between 500 and 1000 sec for all potential steps. The slopes of these straight lines and the chemical diffusivities calculated based on Eq. [6] are shown in Table I.

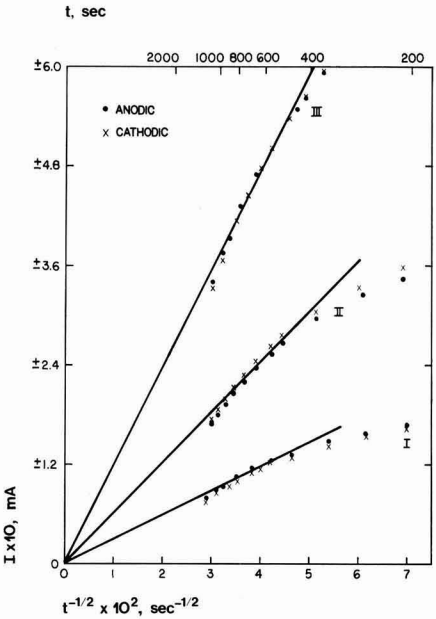

Fig. 5. Current and time relations (I *vs.* $t^{-1/2}$) from potentiostatic measurements. Starting potential: 350 mV; potential steps: I, ±5 mV, II, ±10 mV, III, ±20 mV.

Galvanostatic measurements.—Instead of imposing a new potential to the Li-Al electrode, one imposes a constant current, I, through the cell and measures the potential of Li-Al (relative to the Li reference electrode), E, as a function of time during the current flow. The solution of Eq. [1], C_{Li} (X,t) is obtained using the following initial and boundary conditions

$$C_{Li} = C° \quad 0 \leq X \leq L, t = 0 \quad [7]$$

$$-D\frac{\partial C_{Li}}{\partial X} = \frac{I}{\mathbf{F}A} \quad X = 0, t > 0 \quad [8]$$

$$\frac{\partial C_{Li}}{\partial X} = 0 \quad X = L, t > 0 \quad [9]$$

The concentration at the electrode/electrolyte interface is expressed as

$$C_{Li}(0,t) - C° = 2I\,t^{1/2}/\mathbf{F}A\,(D\pi)^{1/2} \quad \text{if } t << \frac{L^2}{D} \quad [10]$$

Table I. Results of potentiostatic measurements. Slope of the I *vs.* $t^{-1/2}$ plot for each ΔE step ($E°$ = 350 mV) and chemical diffusivity of Li in β-LiAl at 24° ± 2°C

	Anodic (positive) step		Cathodic (negative) step	
ΔE (mV)	Slope (A · sec$^{1/2}$)	D (cm^2/sec)	Slope (A · sec$^{1/2}$)	D (cm^2/sec)
5	2.93×10^{-3}	4.85×10^{-9}	2.84×10^{-3}	4.41×10^{-9}
10	6.04×10^{-3}	5.15×10^{-9}	6.18×10^{-3}	5.14×10^{-9}
20	11.92×10^{-3}	5.19×10^{-9}	11.92×10^{-3}	4.70×10^{-9}
Average D (cm^2/sec)		5.06×10^{-9}		4.75×10^{-9}

Equation [10] may be expressed as

$$\frac{dE}{dt^{1/2}} = \frac{2IV_m}{FA(D\pi)^{1/2}} \frac{dE}{d\delta}, \quad t << \frac{L^2}{D} \qquad [11]$$

or

$$D = \frac{4}{\pi}\left(\frac{IV_m}{FA}\right)^2 \left[\left(\frac{dE}{d\delta}\right) \Big/ \left(\frac{dE}{dt^{1/2}}\right)\right]^2, \quad t << \frac{L^2}{D} \qquad [12]$$

by differentiating Eq. [10] with respect to the square root of time and then expanding it by dE. The surface concentration, C_{Li} $(0,t)$, is expressed in terms of the parameters using the relationship $C_{Li} = (y + \delta)/V_m$ for $Li_{y+\delta}Al$, where V_m is the molar volume of Li-Al. Therefore, D can be determined from the slope of E *vs.* $t^{1/2}$ plot and $dE/d\delta$, which can be obtained from the potential-composition curve of Li-Al (Fig. 6).

Figure 7 shows the E *vs.* $t^{1/2}$ relations under cathodic currents ranging between 0.1 and 3.2 mA. Similar relations under anodic currents are shown in Fig. 8. Linear relationships between E and $t^{1/2}$ are noted in Fig. 7 and 8. Accordingly, the values of $dE/dt^{1/2}$ were obtained and the corresponding values of the chemical diffusivity, D, were determined and shown in Table II.

Discussion

Potential vs. alloy composition.—The potential measurements of the pyrometallurgically formed lithium-aluminum alloys were conducted at ambient temperatures (24° ± 2°C). It was found that the lithium concentration range for the single phase, presumably β-LiAl was between 48 and 57 a/o (Fig. 2). These results agree well with those reported at high temperatures (17, 25). Moreover, the potential difference of the two-phase mixtures $\beta + \gamma$ and $\alpha + \beta$ shown in Fig. 2 is about 240 mV approximating the value of 233 mV observed by Wen *et al.* at 423°C (17).

The electroformation of lithium-aluminum alloys appeared to be a slow process at ambient temperatures. Figure 3 shows that the alloy electrodes approach their equilibrium potentials after standing at open circuit for a long period of time. The slowness in approaching the equilibrium potential indicates a low diffusion rate of lithium in the lithium-aluminum alloys at ambient temperatures (24° ± 2°C). Indeed, the discrepancies noted in the potential profiles between the pyrometallurgical alloys and the electroformed alloys may be attributable to the slow diffusion at ambient temperatures.

It is noted in Fig. 4 that for electrodes containing less than 44.5 a/o lithium, the potential remains relatively constant at 382 ± 7 mV. Thus, at a lithium concentration less than 44.5 a/o the electroformed lithium-aluminum alloy exhibits the characteristics of a multiphase mixture similar to those of the pyrometallurgical alloy having a lithium concentration less than 48 a/o. It is noted that the slope of the potential profile at low lithium concentration (20-44 a/o) is much less than that observed by Rao *et al.* (8), although the potential values are similar in magnitude. Garreau *et al.* (12) reported that at a lithium concentration less than 40 a/o, the Li-Al alloy which was formed by cathodically depositing lithium on aluminum exhibited an open-circuit potential of 335 mV. These authors also noted that when lithium was anodically stripped off the Li-Al alloy having a higher lithium concentration, the open-circuit potential approached 380 mV or higher at 40-45 a/o of lithium. The causes for the discrepancy between the potential profile obtained from this study and that obtained by Garreau *et al.* are not understood. Nonetheless, we have observed that the electrode potential during the lithium deposition at less than 44.5

Table II. Results of galvanostatic measurements. Slope of the transient voltage, $E - E\ (t = 0)$, *vs.* $t^{1/2}$ plot and chemical diffusivity of Li in β-LiAl at 24° ± 2°C

Current (mA)	Anodic		Cathodic	
	Slope ($V \cdot sec^{-1/2}$)	D (cm^2/sec)	Slope ($V \cdot sec^{-1/2}$)	D (cm^2/sec)
0.1	7.60×10^{-5}	8.57×10^{-9}	-8.71×10^{-5}	6.52×10^{-9}
0.2	1.64×10^{-4}	7.36×10^{-9}	-1.73×10^{-4}	6.61×10^{-9}
0.4	3.25×10^{-4}	7.49×10^{-9}	-3.42×10^{-4}	6.77×10^{-9}
0.8	6.24×10^{-4}	8.13×10^{-9}	-6.92×10^{-4}	6.61×10^{-9}
1.6	1.17×10^{-3}	9.25×10^{-9}	-1.40×10^{-3}	6.46×10^{-9}
3.2	2.24×10^{-3}	10.1×10^{-9}	-2.92×10^{-3}	5.94×10^{-9}
	Average D	8.48×10^{-9}		6.44×10^{-9}

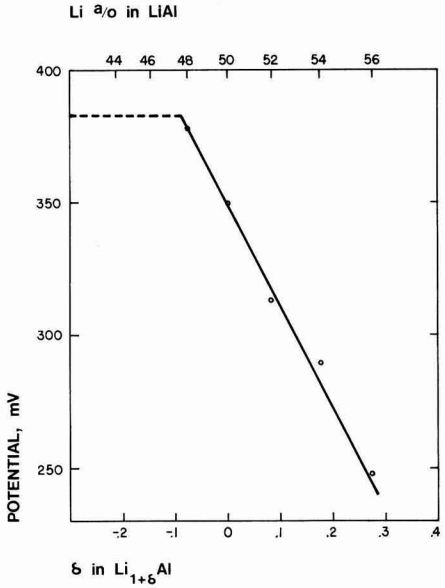

Fig. 6. Electrode potential of pyrometallurgically formed Li-Al as a function of composition.

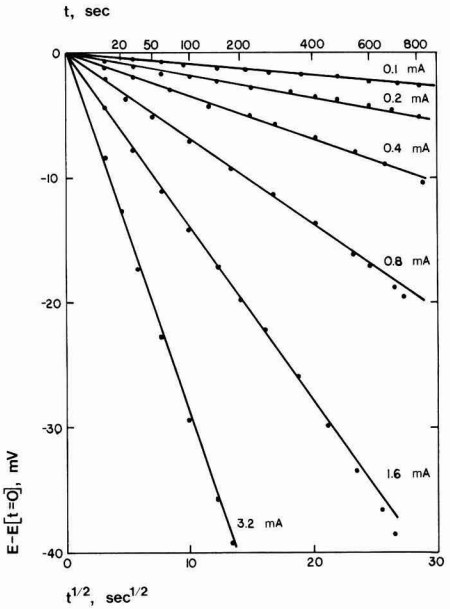

Fig. 7. Potential and time relations ($E - E\ [t = 0]$ *vs.* $t^{1/2}$) from galvanostatic measurements (cathodic).

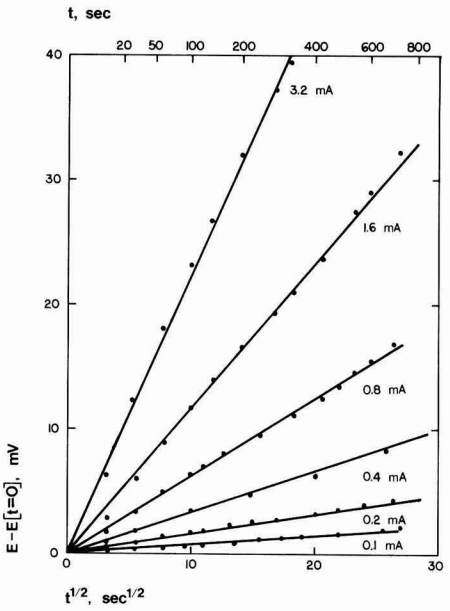

Fig. 8. Potential and time relations ($E - E\ [t = 0]$ vs. $t^{1/2}$) from galvanostatic measurements (anodic).

a/o of lithium remains at about 320-330 mV, approximating the open-circuit potential observed by Garreau *et al.*

At a lithium concentration between 44.5 and 58 a/o the potential profile of the electroformed Li-Al alloy is different from that of the pyrometallurgical Li-Al alloy. It is noted in Fig. 4 that the open-circuit potential begins a sharp drop at a lithium concentration greater than 44.5 a/o. Based on the results of the pyrometallurgical Li-Al, the potential should begin to decrease at 48 a/o of Li at the onset of the single-phase β-LiAl. However, the fact that electroformed Li-Al alloy shows a potential decrease beginning at 44.5 a/o of Li and the fact that the potential is generally lower than that of the corresponding pyrometallurgical Li-Al alloy may be attributed to the slow diffusion rate of lithium at ambient temperatures. Inasmuch as the diffusion rate of lithium into the Li-Al alloy is slow, an excess of Li and/or Li-rich phases (γ, δ, etc.) remain on the electrode surface resulting in a lower electrode potential. Indeed, one notes that deposition potential of lithium on Li (44.5 a/o)-Al alloy (Fig. 3) shows a rather sharp decrease after the lithium concentration has reached 48 a/o.

Rao *et al.* (8) noted a substantially higher open-circuit potential at lithium concentration greater than 50% than we did. Inasmuch as the aluminum foil used by Rao *et al.* was relatively thick (130 μm), the deposition current density was rather high (3.8 mA/cm^2) and the open-circuit duration after deposition was short (15 min), it is reasonable to speculate that the lithium distribution may not be homogenous in the electrode. Nonetheless, in view of the slow diffusion rate of lithium in the Li-Al alloy, these experimental conditions may result in a lower rather than higher electrode potential. Thus it is difficult to reconcile the differences between the results obtained by Rao *et al.* (8) and those obtained in this study.

Diffusion Studies.—Potentiostatic measurements.—According to Eq. [6], the I vs. $t^{-1/2}$ plots are expected to be straight lines passing through the origin when $t << L^2/D$. Indeed, Fig. 5 shows that the transient currents deviate from the straight lines when t is greater than 1000 sec for all voltage steps. On the other hand, deviations from straight lines are also noted when t is shorter than 500 sec. The deviation at shorter times is presumably due to the inaccuracy of the potential control of the working electrode, which is attributable to the uncompensated IR between the working and the reference electrodes.

The chemical diffusivity, D, of Li in LiAl obtained from this study is about one order of magnitude lower than the self-diffusivity of Li in LiAl obtained by Willhite *et al.* using NMR technique (19) which is 8.1×10^{-8} cm^2/sec at 23°C. It should be noted that similar to the behavior of Li in an electrolyte solution, Li-Al may react with the organic solvent forming a layer of surface film (12, 13). It is reasonable to assume that the surface film on Li-Al may have some effect on the apparent diffusivity of Li in the Li-Al electrode.

Galvanostatic measurements.—The E vs. $t^{1/2}$ plot is expected to be a straight line when $t << L^2/D$ (see Eq. [11]). Indeed, Fig. 7 and 8 show that straight lines were obtained at $t \leq 600$ sec. The fact that no deviation from the linear relationship was noted at short time periods may be attributed to the fact that in the galvanostatic measurement the uncompensated IR between the working and the reference electrodes remains constant at a given applied current. Consequently, the measurement of the transient potential is not affected.

Table II shows that the values of diffusivity obtained from measurements in the anodic direction are higher than those obtained from measurements in the cathodic direction. It is reasonable to speculate that the onset of an anodic current may disrupt the film on the Li-Al electrode resulting in a reduction of the film effect on the apparent diffusivity.

Manuscript submitted Aug. 27, 1981; revised manuscript received Dec. 11, 1981.

Any discussion of this paper will appear in a Discussion Section to be published in the June 1983 JOURNAL. All discussions for the June 1983 Discussion Section should be submitted by Feb. 1, 1983.

Publication costs of this article were assisted by Electrochem Industries Incorporated.

REFERENCES

1. R. D. Rauh and S. B. Brummer, *Electrochim. Acta*, **22**, 75 (1977).
2. V. R. Koch and S. B. Brummer, *ibid.*, **23**, 55 (1978).
3. V. R. Koch and J. H. Young, *Science*, **204**, 499 (1979).
4. L. P. Klemann, G. H. Newman, and E. L. Stogryn, *Proc. Power Sources Conf.*, **29**, 211 (1980).
5. L. P. Klemann, G. H. Newman, T. A. Whitney, E. L. Stogryn, and D. Farcasiu, in "Lithium Batteries," H. V. Venkatasetty, Editor, p. 179, The Electrochemical Society Softbound Proceedings Series, Pennington, NJ (1981).
6. A. N. Dey, *This Journal*, **118**, 1547 (1971).
7. M. M. Nicholson, *ibid.*, **121**, 736 (1974).
8. B. M. L. Rao, R. W. Francis, and M. A. Christopher, *ibid.*, **124**, 1490 (1977).
9. J. R. Van Beek and P. J. Rommers, *Power Sources*, **7**, 595 (1979).
10. J. O. Besenhard, *J. Electroanal. Chem. Interfacial Electrochem.*, **94**, 77 (1978).
11. I. Epelboin, M. Froment, M. Garreau, J. Thevenin, and D. Warin, *This Journal*, **127**, 2100 (1980).
12. M. Garreau, J. Thevenin, D. Warin, and Ph. Campion, in "Lithium Nonaqueous Battery Electrochemistry," E. B. Yeager *et al.*, Editors, p. 158, The Electrochemical Society Softbound Proceedings Series, Pennington, NJ (1980).
13. J. O. Besenhard, *Prog. Batt. Solar Cells*, **3**, 87 (1980).
14. S. D. James, *Electrochim. Acta*, **21**, 157 (1976).
15. A. L. L'vov and A. A. Gnilomedov, *Elektrokhimiya*, **11**, 1322 (1975).
16. C. A. Melendres, *This Journal*, **124**, 650 (1977).
17. C. J. Wen, W. Weppner, B. A. Boukamp, and R. A. Huggins, *ibid.*, **126**, 2258 (1979).

18. H. E. Schone and W. D. Knight, *Acta Met.*, **11**, 179 (1963).
19. J. R. Willhite, N. Karnezos, P. Cristea, and J. O. Brittain, *J. Phys. Chem. Solids*, **37**, 1073 (1976).
20. V. R. Koch, *This Journal*, **126**, 181 (1979).
21. K. M. Myles, F. C. Mrazek, J. A. Smaga, and J. L. Settle, in "Proc. of the Symp. and Workshop on Advanced Battery Research and Design," Argonne National Laboratory, p. B-69, March 22-24, 1976.
22. D. O. Raleigh and H. R. Crowe, *This Journal*, **116**, 40 (1969).
23. J. Goldman and J. B. Wagner, *ibid.*, **121**, 1318 (1974).
24. W. Weppner and R. A. Huggins, *ibid.*, **124**, 1569 (1977).
25. N. Y. Yao, L. A. Heredy, and R. C. Saunders, *ibid.*, **118**, 1039 (1971).

Vibrational Spectroscopic Determination of Structure and Ion Pairing in Complexes of Poly(ethylene oxide) with Lithium Salts

B. L. Papke, M. A. Ratner, and D. F. Shriver*

Department of Chemistry and Materials Research Center, Northwestern University, Evanston, Illinois 60201

ABSTRACT

A structural model for crystalline complexes of poly(ethylene oxide) (PEO) with various lithium salts is presented, based on vibrational spectroscopic studies; these complexes are known to exhibit ionic conductivities of $> 10^{-5}$ $(\Omega\text{-cm})^{-1}$ at 100°C. Cation-dependent vibrational bands observed in the Raman indicate that significant cation-oxygen atom interactions occur and suggest that the polyether chain may wrap around the lithium cations. Spectroscopic studies indicate extensive contact ion pairing occurs in the PEO · $LiNO_3$ complex, and this may contribute to the somewhat lower ionic conductivity of this complex as compared to other lithium salt complexes with similar structures but weaker cation-anion interactions.

Solvent-free complexes of poly(ethylene oxide), PEO, $(CH_2CH_2O)_n$, with alkali metal salts have been prepared (1-7), and are potentially useful as electrolytes in high energy density battery applications (3-5, 8-13). Recently we have reported infrared and Raman spectroscopic studies of crystalline sodium salt complexes with PEO, and amorphous rubidium and cesium thiocyanate complexes (7). Based on these studies and other considerations a structural model was proposed for these complexes (7). We report here the results of spectroscopic and conformational studies on anhydrous PEO · LiX complexes.

Experimental

Inorganic salts and SiO_2 were removed from poly(ethylene oxide), average molecular weight 600,000 (Aldrich), by ion exchange and filtration, as described elsewhere (7). Reagent grade alkali metal salts were dried at 110°C under vacuum and subsequently were weighed in an N_2-filled dry box to ensure accurate stoichiometries. The complexes were prepared in air using reagent grade acetonitrile (Mallinckrodt) (3, 4). Thin films (50-100 μm) were cast on Teflon plates, and water or traces of solvent were removed under vacuum (10^{-3} Torr) at 25°C for 24 hr. Films prepared in this manner are anhydrous, as determined by the absence of O—H stretching and H—O—H deformation bands in the infrared near 3350 and 1610 cm^{-1}, respectively.

The PEO · $LiNO_3$ complex was prepared by dissolving the polymer and salt in separate portions of acetonitrile, followed by mixing the solutions. Once the solvent was removed from this mixture a solid complex formed, which appears to be insoluble in acetonitrile. All of the PEO · LiX complexes in the present study were prepared at 4.5:1 ratio of ether oxygens to lithium cation. The maximum complex stoichiometry is not precisely defined, however, it generally appears to be around 4:1 (1, 6, 7).

Infrared measurements were performed on Perkin-Elmer 399 or 283 grating infrared spectrophotometers. Films were mounted in an evacuated cell containing KCl windows, or sealed between polyethylene sheets (500-250 cm^{-1} range) to exclude atmospheric moisture. Water bands at ~1610 cm^{-1} began to appear in the polyethylene sealed films after 10-15 min. Raman studies using 514.5 nm exciting line with backscattering illumination were made on thin (3 mm) pressed pellets mounted in an evacuated cell. The bandpass was 2 cm^{-1} except for the 1000-1100 cm^{-1} region of the PEO · $LiNO_3$ complex where a 0.5 cm^{-1} bandpass was used.

Results and Discussion

Polymer conformation studies.—Extensive spectroscopic studies have been made on PEO in the crystalline state, the molten state, and in solution. Based on these studies the conformation was determined to be trans (CC—OC), trans (CO—CC), gauche (OC—CO), or T_2G; these results were later confirmed by an x-ray structure determination. [See Ref. (7) and references cited therein for a complete description of these studies.] The crystalline PEO · LiX complexes have infrared and Raman spectra similar to those observed for pure PEO, and nearly identical to spectra for crystalline PEO · NaX complexes (see Fig. 1, Tables I and II). Therefore, the arguments and evidence used to deduce a reasonable conformational model for the crystalline PEO· NaX complexes may also be used here (7).

In particular, the mid-infrared data indicate a gauche (G) or gauche minus ($\overline{G}$) conformation exists about the O—$(CH_2)_2$—O linkage. This assignment is supported by studies of Davidson, who used ethylene dichloride to model the O—$(CH_2)_2$—O portion of the PEO chain (15). Two strong infrared bands at about 880 and 944 cm^{-1} are expected for CH_2 rocking modes in a gauche conformation, in agreement with the infrared bands recorded in Table I. In contrast, the CH_2 rocking absorption bands for a trans conformation are expected around 773 and 992 cm^{-1}. A strong Raman active band at 870 cm^{-1} for the PEO · $LiCF_3SO_3$ and PEO · $LiBF_4$ complexes is similar to a band found at 865 cm^{-1}, which is characteristic of all the PEO · NaX complexes (7). Sato and Kusumoto have obtained Raman spectra for a number of crown ether alkali metal salt complexes, and in all cases an intense polar-

* Electrochemical Society Active Member.
Key words: solid electrolytes, polymer electrolytes, infrared spectra, Raman spectra, ionic conductivity.

Table I. Mid-infrared bands and assignments for crystalline PEO · LiX complexes (2500-250 cm^{-1})

PEO 600,000	PEO · $LiNO_3$	PEO · $LiCF_3SO_3$	PEO · $LiCF_3CO_2$	PEO · $LiBF_4$	Assignments
~1960 vw		~1960 w	~1960 w		Overtone (PEO)
			~1810 w		
	1763 vw				
			1705 sh*		
			1690 vs*		
1473 sh	1474 m	1477 m	1473 s*	1477 s	$\delta(CH_2)_a$
1466 m	1457 m	1460 mw	1460 mw	1467 sh	$\delta(CH_2)_a$
1461 m					$\delta(CH_2)_a$
1453 m		1455 mw	1440 m	1453 mw	$\delta(CH_2)_a$
	~1416 s*				$\nu_3(NO_3^-)$
	1363 m		1365 m	1372 w	
1358 m		1352 s	1352 w	1358 w	$w(CH_2)_s$, $\nu(CC)$
		1345 m			
1342 s		1340 m	1343 s	1343 s	$w(CH_2)_a$
	~1324 vs*				$\nu_3(NO_3^-)$
		1290 sh*	1290 m	1293 sh	
1283 m	1285 sh	1270 vs*	1282 m	1282 m	$t(CH_2)_a$, $t(CH_2)_s$
			1270 vw	1268 vw	
1244 m	1248 w	1231 m*	1245 m	1247 s	$t(CH_2)_a$
			1205 vs*		
		1161 vs*	1175 vs*	1180 s	
1147 s	1143 s				$\nu(CC)$, $\nu(COC)_a$
~1103 vs	1105 vs	1095 vs	~1110 vs	~1090 ws*	$\nu(COC)_a$
	1089 vs	1040 s*		~1000 vs*	
958 s	957 m	968 ms	951 s	970 sh	$r(CH_2)_s$
948 s		951 m	946 sh	950 sh	$r(CH_2)_s$, $\nu(COC)_a$
		928 vw		928 sh	$r(CH_2)_s$, $\nu(COC)_a$
	872 mw	859 w	863 w*	858 m	
844 s	839 m	842 m	839 s	842 s	$r(CH_2)_a$
		832 w	832 sh	836 sh	
	827 m*				$\nu_2(NO_3^-)$?
			798 s*		
		760 m*		778 m*	
			721 s*		
	729 vw*				$\nu_4(NO_3^-)$
	719 vvw*				$\nu_4(NO_3^-)$
		640 vs*			
		580 w*	601 w*		
	553 w			543 w*	
530 w	530 vw			527 vvw	$\delta(OCC)_a$
	518 w	519 m*	518 w*	519 w*	
			~490 w*		
	~432 m	425 m	428 w		
				~400 m*	
			375 m		
330 w		335 w		334 vw	$\delta(COC)$, $\delta(OCC)$
	321 m			313 vw	
	270 w				
		250 w*			

* Indicates bands due at least in part to anion internal modes. mw (medium-weak); m (medium); s (strong); vs (very strong); sh (shoulder). Assignments are based on those made by Yoshihara *et al.* (15) for pure PEO. Mode assignments: r (rocking); t (twisting); ν (stretching); w (wagging); τ (torsion); δ (bending). The subscripts a and s denote the asymmetric and symmetric motions with respect to the two-fold axis perpendicular to the helix axis and passing through the O atom or through the center of the C—C bond.

Table II. Raman bands for PEO · alkali metal salt complexes (1500-100 cm^{-1}) (medium and strong intensity bands)[a]

Pure PEO 600,000	PEO · $LiCF_3SO_3$[c]	PEO · $LiBF_4$[d]	PEO · $LiNO_3$	Assignments[b]
1487 s				$\delta(CH_2)_s$
1480 s	1473 m	1477 s	1475 s	$\delta(CH_2)_a$
1470 ms		1469 sh	1452 w	$\delta(CH_2)_a$
2181 s	1280 m	1280 s	1284 m	$t(CH_2)_a$, $t(CH_2)_a$
	1263 m	1264 m	1267 m	
	1242 w	1243 mw	1240 mw	
1233 m	1232 m			$t(CH_2)_s$
1144 m	1143 m	1142 m	1152 w	$\nu(CC)$, $\nu(COC)_a$
			1140 m	
1125 mw				$\nu(CC)$, $w(CH_2)_s$
1065 m	1056 m	~1065 mw	1062 sh	$\nu(COC)_s$, $\tau(CH_2)_s$
	1045		1047 vvs	$\nu(SO_3)_s$, $\nu_1(NO_3^-)$
	870 s	870 s	873 w	M-O_n sym. str.
861 mw	859 m	858 m	857 s	$r(CH_2)_s$, $\nu(COC)_s$
846 s	836 m	830 m	841 m	$r(CH_2)_a$
		775 m		$\nu_1(BF_4^-)$
			730 vw	$\nu_4(NO_3^-)$
			718 w	$\nu_4(NO_3^-)$
583 mw			581 w	$\delta(OCC)_a$, $\delta(COC)$, $\nu(COC)_a$
537 mw			550 w	$\delta(COC)$, $\delta(OCC)_s$
364 mw				$\delta(OCC)_s$, $\delta(COC)$
279 mw			297 m	$\tau(CC)$

[a] Band intensities: mw (medium-weak); m (medium); ms (medium-strong); s (strong).
[b] Assignments are those made by Yoshihara *et al.* (15) for pure PEO. Mode assignments: see footnote on Table I.
[c] Data collected 1500-800 cm^{-1} only.
[d] Data collected 1500-750 cm^{-1} only.

ized band at 865-870 cm^{-1} was observed after complexation occurred (16). This band was tentatively assigned to a totally symmetric A_{1g} mode involving a metal-oxygen breathing motion. By analogy, the 870 cm^{-1} band in the PEO · LiX complexes may be assigned to a M-O_n breathing mode. The high frequency of this mode is attributed to the participation of CH_2 rocking motion in this breathing mode. In other words, the primary restoring force for this symmetric M-O stretching mode may originate from force constants within the polymer backbone. This result indicates that the PEO chain wraps around the lithium cation. A strong Raman band at 857 cm^{-1} for the PEO · $LiNO_3$ complex may also be assigned to this mode, although

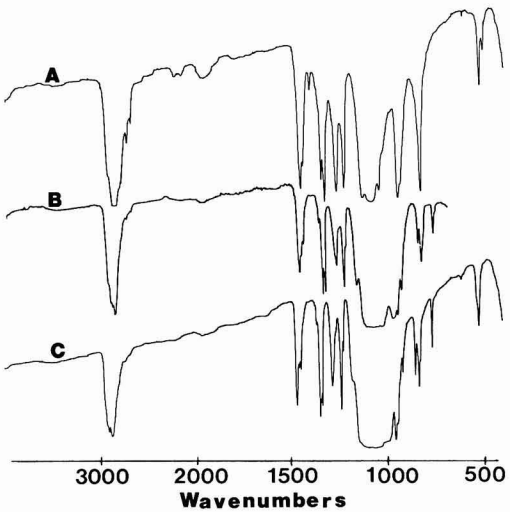

Fig. 1. Comparison of infrared spectra for (A) pure PEO 600,000, (B) PEO · $LiBF_4$, and (C) PEO · $NaBF_4$, representative of a typical PEO · NaX complex.

it is slightly lower in frequency than normally observed for the PEO complexes (7).

Cation-dependent far infrared bands were observed for the PEO complexes with Na^+, K^+, Rb^+, or Cs^+ salts (7), and similar bands at about 400 cm^{-1} are present in the PEO · LiX complexes. These bands are not Raman active, and are similar to solvent-cage type vibrations observed for alkali metal salt solutions and crown ether complexes (17-19). Ion-cage vibrations are more difficult to clearly identify and study for PEO · LiX complexes than for the remaining alkali metal anions, owing to various anion modes that are present in the same spectral region. For the PEO · $LiCF_3SO_3$ complex a somewhat broad band at ~425 cm^{-1} appears to be an ion-cage mode; a band at ~375 cm^{-1} in the PEO · $LiCF_3CO_2$ complex is tentatively given the same assignment. A band at 432 cm^{-1} is found for the PEO · $LiNO_3$ complex, as well as a band of medium intensity at 321 cm^{-1} and a weak band at 270 cm^{-1}; these bands may arise from a variety of Li^+ modes relative to the polymer cage and anions. A broad band centered around 400 cm^{-1} is also observed for the PEO · $LiBF_4$ complex; however, this band may be a superposition of the ion-cage mode and a mode derived from the BF_4^- ν_2 mode. Formally, the ν_2 mode is infrared inactive for the tetrahedral BF_4^- anion, however, the BF_4^- symmetry is slightly perturbed in PEO · $LiBF_4$. For example, the ν_1 mode is also formally infrared inactive but is seen at 778 cm^{-1} in the $LiBF_4$ complex, and several bands are present around 530 cm^{-1}, which may arise from a lifting of degeneracy for the $\nu_4(F_2)$ mode of BF_4^- in a tetrahedral symmetry.

The PEO · LiX complexes listed in Tables I and II are all highly crystalline when anhydrous; the PEO · $LiCF_3CO_2$ and PEO · $LiCF_3SO_3$ complexes are even crystalline when hydrated. Melting ranges for complexes prepared at room temperature are indicated below, obtained using a hot-stage polarizing microscope and a 10°/min heating rate: PEO · $LiNO_3$, 100°-108°C; PEO · $LiCF_3CO_2$, 121°-126°C; PEO · $LiBF_4$, 138°-146°C; PEO · $LiCF_3SO_3$, 176°-184°C. A PEO · LiSCN complex at 4.5:1 stoichiometry was also prepared, however, this complex remained amorphous; Chabagno has suggested that Li^+-SCN^- ion pairs may prevent crystallization here (20).

Similarities in spectroscopic data and physical characteristics between the PEO · NaX and PEO · LiX complexes strongly suggest that these complexes have closely related structures. The trans (CC—OC), trans (CO—CC), gauche (OC—CO), trans (CC—OC), trans (CO—CC), and gauche-minus (OC—CO) conformation ($T_2GT_2\bar{G}$) proposed for the PEO · NaX complexes (7) is also consistent with data for PEO · LiX complexes. Polar oxygen atoms are directed inward in a $T_2GT_2\bar{G}$ conformation, lining the tunnel cavity while the CH_2 groups all face outward. This preferential orientation helps to explain why such a large mol ratio of salt may be complexed by the polyether. Space filling molecular models (see Fig. 2) indicate this conformation has a tunnel radius of 1.3-1.5Å, large enough to readily accommodate Na^+ cations (radius 0.99Å) or Li^+ cations (radius 0.58Å) (20). Undoubtedly some bond conformation distortions from an exact $T_2GT_2\bar{G}$ conformation are present, and the polyether helix may wrap somewhat more tightly to coordinate the small Li^+ cation more effectively.

Evidence for ion pair interactions in PEO · $LiNO_3$.— Strong cation-anion interactions are expected to reduce cation mobility in polyether · salt solid electrolytes. Evidence for ion pair interactions has been presented for the PEO · $NaBH_4$ and PEO · $NaBD_4$ complexes (22), and weak ion pairing may occur in the PEO · NaSCN complex. The nitrate ion has proven extremely useful as a spectroscopic "probe" to investigate structure and cation-anion interactions in solution (23). Therefore, the PEO · $LiNO_3$ complex was chosen to study ion pairing in the lithium complexes.

The unperturbed nitrate anion has a D_{3h} symmetry with four normal modes: $\nu_1(A_1')$ ~ 1050 cm^{-1}, $\nu_2(A_2'')$ ~830 cm^{-1}, $\nu_3(E')$ ~ 1380 cm^{-1}, and $\nu_4(E')$ ~ 716 cm^{-1}. The ν_3 and ν_4 modes are Raman and infrared active, ν_1 is Raman active only, and ν_2 is infrared active. These internal modes are readily perturbed by the local environment, and Irish has summarized approximate Raman band positions for the nitrate anion in various environments, as shown in Table III (23). Even in dilute aqueous solutions the $\nu_3(E')$ band of NO_3^- is split. This doublet structure is thought to arise from an asymmetric solvent environment rather than ion pairing, because the splitting is insensitive to cation identity and to solution concentration below 1 mol liter^{-1} (23). Typically, components of ν_3 in aqueous solutions are separated by about 60 cm^{-1}. In concentrated aqueous $LiNO_3$ solutions or molten $LiNO_3$ the splitting increases to over 110 cm^{-1}, which is attributed to the influence of ion pairing. This interpretation is supported by a shift of the ν_4 band to *ca.* 740 cm^{-1}, which is a diagnostic feature of ion pair formation (23-25).

Close examination of the spectrum of PEO · $LiNO_3$ shows that two bands are present in the ν_4 region, at about 730 and 718 cm^{-1} in both the Raman and infrared (see Table I and II). The ν_2 band is probably present at 829 cm^{-1} in the infrared, although several CH_2 rocking modes from the polymer tend to obscure this region; the ν_2 band is not seen in Raman spectra.

Table III. Approximate Raman band positions/cm^{-1} for $Li^+\cdots NO_3^-$ in various environments [from data in Ref. (24)]

"Free" NO_3^-	NO_3^- aqueous solvate	$M^+(H_2O)NO_3^-$ solvent-separated ion-pair	$Li^+NO_3^-$ ion-pair
716 (ν_4)	717 dp	717 dp	740 dp 815[a]
830[a] (ν_2)	830[a]	830[a]	
1050 (ν_1)	1049 p	1049 p	1056 p
	1350 dp	1350 dp	1350 dp
1380 (ν_3)	1410 dp		
		1420 dp	
			1465 dp

[a] Infrared values, p (polarized), dp (depolarized).

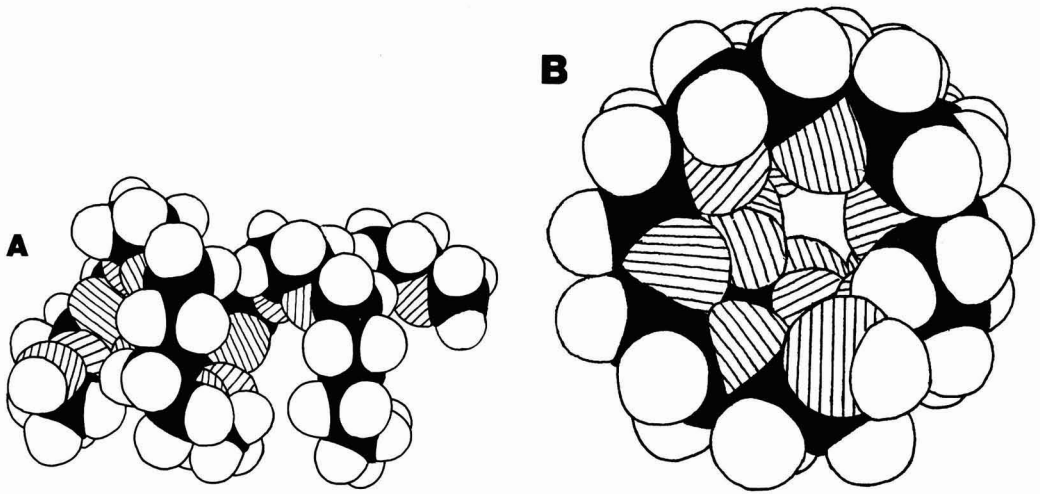

Fig. 2. Molecular models of poly(ethylene oxide) in a $T_2GT_2\bar{G}$ conformation as proposed for complexation to sodium and lithium cations, (A) side view, (B) end view. Hydrogen atoms are not shaded, carbon atoms are black, and oxygen atoms are cross-hatched.

A single intense ν_1 band is present at 1047 cm^{-1} in the Raman; if this band has any infrared intensity it is probably buried under strong polymer bands in this region. Components derived from ν_3 are observed at 1324 and 1416 cm^{-1} in the infrared, the bands are quite strong and a CH_2 wagging mode expected around 1350 cm^{-1} is apparently obscured by the 1324 cm^{-1} band. The ν_3 modes in PEO · $LiNO_3$ are very weak in the Raman, and are easily confused with weak polymer bands present in the same region.

Comparison of the spectroscopic data for NO_3^- in the PEO · $LiNO_3$ complex with data in Table III indicates that at least some of the NO_3^- anions form contact ion pairs, the main features diagnostic of ion pairing being the presence of an ν_4 band at 730 cm^{-1}, as well as the large separation of bands derived from ν_3 of the isolated ion (92 cm^{-1}). Evidence to data indicates that complex formation in aqueous media does not remove the degeneracy of the $\nu_4(E')$ mode (23). Therefore, the presence of an additional band derived from $\nu_4(E')$ at 718 cm^{-1} in PEO · $LiNO_3$ suggests that two sites might exist for the nitrate anion with the 718 cm^{-1} band arising from uncoordinated nitrate ions. The possibility that the 730 cm^{-1} band may arise from uncomplexed crystalline $LiNO_3$ may be rejected as the intense ν_1 band for $LiNO_3$ at 1071 cm^{-1} is not observed in the PEO · $LiNO_3$ 4.5:1 complex (24). The presence of a single ν_1 band argues against the existence of two anion sites; however, this band could result from two closely spaced unresolved bands. This band is slightly asymmetric on the high frequency side in the Raman. Additional ν_3 bands are also expected for two NO_3^- environments, but these bands may be weak and easily obscured by polymer bands.

Spectroscopic studies of molten nitrates (26, 27) and of concentrated $LiNO_3$ aqueous solutions (25) support the hypothesis of two distinct NO_3^- sites in the PEO · $LiNO_3$ complex. Two bands are observed in the ν_4 (NO_3^-) region for both systems, similar to the PEO complex, and these bands are thought to arise from nitrate anions in two environments. The ν_1 band for molten $LiNO_3$ is slightly asymmetric on the low frequency side in the Raman, supporting a two-site model. Only a single ν_1 band is observed for concentrated $LiNO_3$ aqueous solutions; however, this band is suggested to be a composite of two closely spaced lines (25). The nonspecific nature of the $M^+ \cdots NO_3^-$ interaction prevents definite anion symmetry assignments from being made (23).

Contact cation-anion interactions are expected to result in significantly lower ionic conductivity values than those measured for structurally and physically similar nonion paired complexes (22). Conductivity measurements were obtained on the PEO · $LiNO_3$ 4.5:1 complex using complex admittance techniques and Pt ion-blocking electrodes. (The electrodes were warm pressed onto the pellet at 70°C and 50,000 psi.) The variable temperature conductivity values exhibit a two-slope behavior, with a knee observed in ln σT *vs.* $1/T$ plots at about 65°C; the extrapolated conductivity at 20°C is about 8×10^{-10} $(\Omega\text{-cm})^{-1}$ increasing to about 6×10^{-6} $(\Omega\text{-cm})^{-1}$ at 80°C. These conductivity values are comparable to those reported by Chabagno for the PEO · LiI complex, and are lower than those for any of the remaining crystalline PEO · LiX complexes at a 4.5:1 stoichiometry. More detailed conductivity measurements on well-characterized PEO · LiX complexes are necessary before a correlation between conductivity values and the extent of ion pairing can be made. However, it is clear from spectroscopic data that extensive ion-pair interactions do occur in the PEO · $LiNO_3$ complex.

Acknowledgments

We thank Ryan Dupon who performed the conductivity measurements. This research was supported under the NSF-MRL program through the Materials Research Center of Northwestern University (Grant No. DMR79-23573).

Manuscript submitted Sept. 3, 1981; revised manuscript received Dec. 24, 1981.

Any discussion of this paper will appear in a Discussion Section to be published in the June 1983 JOURNAL. All discussions for the June 1983 Discussion Section should be submitted by Feb. 1, 1983.

Publication costs of this article were assisted by Northwestern University.

REFERENCES

1. D. E. Fenton, J. M. Parker, and P. V. Wright, *Polymer*, **14**, 589 (1973).
2. P. V. Wright, *Br. Polymer J.*, **7**, 319 (1976).
3. M. B. Armand, J. M. Chabagno, and M. J. Duclot, Abstract 6.5, Extended Abstracts, 2nd International Conf. on Solid Electrolytes, St. Andrews, Scotland, Sept. 20-22, 1978.
4. M. B. Armand, J. M. Chabagno, and M. J. Duclot, in "Fast Ion Transport in Solids," P. Vashishta,

J. N. Mundy, and G. K. Shenoy, Editors, pp. 131-136, North-Holland, New York (1979).
5. M. B. Armand, M. J. Duclot, and Ph. Rigaud, Abstract C116, 3rd International Meeting on Solid Electrolytes—Solid State Ionics and Galvanic Cells, Tokyo, Japan, Sept. 15-19, 1980.
6. D. B. James, R. S. Stein, and W. J. Macknight, *Bull. Am. Phys. Soc.*, **24**, 479 (1979).
7. B. L. Papke, M. A. Ratner, and D. F. Shriver, *J. Phys. Chem. Solids*, **42**, 493 (1981).
8. W. I. Archer and R. D. Armstrong, *Electrochim. Acta*, **25**, 1689 (1980).
9. W. I. Archer and R. D. Armstrong, *ibid.*, 26, 167 (1981).
10. F. L. Tanzella, W. Bailey, D. Frydrych, G. C. Farrington, and H. S. Story, *Solid State Ionics*, **5**, 367 (1981).
11. J. R. Owen, S. C. Lloyd-Williams, G. Lagos, P. C. Spurdens, and B. C. H. Steele, in "Lithium Nonaqueous Battery Electrochemistry," E. B. Yeager *et al.*, Editors, p. 293, The Electrochemical Society Softbound Proceedings Series, Pennington, NJ (1980).
12. W. B. Johnson and W. L. Worrell, *Solid State Ionics*, **5**, 367 (1981).
13. J. R. Owen, J. Drennan, G. E. Lagos, P. C. Spurdens, and B. C. H. Steele, *Solid State Ionics*, **5**, 343 (1981).
14. T. Yoshihara, H. Tadokoro, and S. Murahashi, *J. Chem. Phys.*, **41**, 2902 (1964).
15. W. H. T. Davidson, *J. Chem. Soc.*, 3270 (1955).
16. H. Sato and Y. Kusumoto, *Chem. Lett.*, 635 (1978).
17. W. F. Edgell, in "Ions and Ion Pairs in Organic Reactions," M. Szwarc, Editor, Vol. 1, Chap. 4, Wiley Interscience, New York (1972).
18. A. I. Popov, *Pure Appl. Chem.*, **41**, 275 (1975).
19. A. T. Tsatsas, R. W. Stearns, and W. M. Risen, Jr., *J. Am. Chem. Soc.*, **94**, 5247 (1972).
20. J. M. Chabagno, Thesis, Grenoble, France (1980).
21. Cation radii obtained from R. D. Shannon, *Acta Crystallogr. Sect. A*, **32**, 751 (1976), for cations with a fourfold coordination number.
22. B. L. Papke, R. Dupon, M. A. Ratner, and D. F. Shriver, *Solid State Ionics*, **5**, 685 (1981).
23. D. E. Irish and M. H. Brooker, in "Advances in Infrared and Raman Spectroscopy," Vol. 2, R. J. H. Clark and R. E. Hester, Editors, pp. 212-311, Heyden, London (1976), and references therein.
24. M. H. Brooker and D. E. Irish, *Can. J. Chem.*, **48**, 1183 (1970).
25. D. E. Irish, D. L. Nelson, and M. H. Brooker, *J. Chem. Phys.*, **54**, 654 (1971).
26. M. H. Brooker, A. S. Quist, and G. E. Boyd, *Chem. Phys. Lett.*, **9**, 242 (1971).
27. M. Peleg, *J. Phys. Chem.*, **77**, 2252 (1973).

An Estimate of the Heat of Adsorption of the Hydroperoxyl Radical on Platinum

James P. Hoare*

General Motors Research Laboratories, Electrochemistry Department, Warren, Michigan 48090

ABSTRACT

In the two-electron reduction of O_2 in acid solution, an adsorbed hydroperoxyl radical, HO_2, must be discharged. The standard potential of the homogeneous discharge reaction is 1.5V, which is ~0.7V higher than the potential (0.8V) at which O_2 is reduced at a Pt cathode. It is possible that the heat of adsorption lowers this high potential to the reaction potential of 0.8V. Assuming that the standard potential of the heterogeneous reaction occurs at 0.8V, subtraction of the heterogeneous from the homogeneous equations gives −16.5 kcal/mol for the ΔG_{ads} of HO_2 radicals. From statistical thermodynamic calculations, the ΔS_{ads} is −28.2 eu for an immobile layer with $\theta = 0.01$. Then a value of −24.9 kcal/mol is found for ΔH_{ads} for HO_2 radicals, which is an acceptable value. A discussion of this result is given.

At most cathode surfaces where peroxide is detected during the reduction of oxygen, it is implied that O_2^- or HO_2 may be formed as an intermediate. It is generally accepted (1-3) that these intermediates are adsorbed on the cathode surface as shown in Fig. 1, and although it has been reported in the literature (4) that O_2 may be reduced to peroxide without the O_2^-(ads) intermediate, such a one-electron mechanism has been severely criticized (5). Even though a number of paths to HO_2(ads) are shown in Fig. 1, the path through O_2(ads) is preferred in this report (6). In any event, the path is not important since thermodynamics is concerned only with initial and final states. In aqueous solutions the $(O_2^-)_{ads}$ is rapidly converted to an adsorbed hydroperoxyl radical by reaction with H_3O^+ ions in acid or H_2O molecules in alkaline solutions, since the O_2^- ion is unstable in aqueous solutions unless stabilized by the presence of surfactants added to the solution (7).

From a logarithmic plot of the data for the reduction of O_2 at a dropping Hg electrode in 0.1*N* NaOH containing 0.05% triphenylphosphine oxide, Divisek and Kastening (7) found a value of −0.284V for the O_2/O_2^- couple. Although Chevalet and co-workers (8) reported a value of −0.27V from O_2 reduction data at Hg cathodes in 1M NaOH stabilized with 0.017M α-quinoline, the corrected value from this data was shown (9) to be −0.29V. Studies of O_2^- ions generated in alkaline solutions by radiolysis made by Czapski and

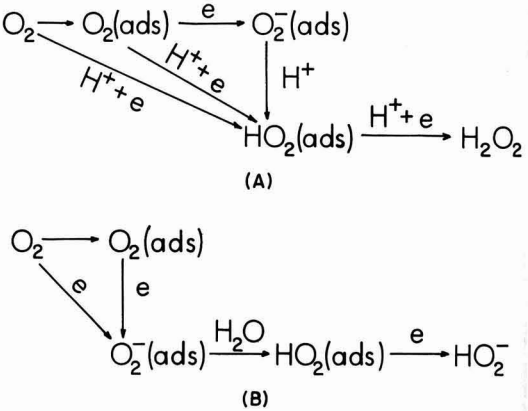

Fig. 1. O_2-reduction paths involving the discharge of adsorbed HO_2 radicals in (A) acid, and (B) alkaline solutions.

* Electrochemical Society Active Member.
Key words: catalysis, oxygen reduction, surfaces, superoxide ion.

co-workers (9, 10) yielded potential values for the O_2/O_2^- couple ranging between −0.33 and −0.325V. In biochemical studies using superoxide dismutase (9), the $E°$-value was recorded as −0.32V. Since the radiolysis studies involved the thermodynamic calculations of equilibrium processes, the $E°$-value of −0.33V is favored for the O_2/O^- couple and is in agreement with that tabulated by Fee and Valentine (11) in a recent review of superoxide chemistry. With

$$O_2 + e \rightarrow O_2^-, \; E° = 0.33V \qquad [1]$$

one obtains a value of 7.61 kcal/mol for the free energy of formation of O_2^- ion.

The perhydroxyl radical acts as a weak acid with a pK of 4.88 (12). From the latest values of $\Delta G°$ for OH^- ion (aq), −37.594; HO_2^- (aq), −16.1; and H_2O (l) −56.687 kcal/mol (13), the $\Delta G°$ value for Eq. [2] is found to be 2.993 kcal/mol

$$O_2 + H_2O + 2e \rightarrow OH^- + HO_2^-, \; E° = 0.0649V \qquad [2]$$

If one adds the $\Delta G°$ of Eq. [1] and [2] along with that obtained from the pK values for HO_2 (4.88) and for H_2O (13.995), one calculates a $\Delta G°$ for the HO_2/HO_2^- reaction of 18.99 kcal/mol

$$HO_2 + e \rightarrow HO_2^-, \; E° = 0.823V \qquad [3]$$

From Eq. [3], the value for the free energy of formation of the HO_2 radical in solution is 2.89 kcal/mol.

From the standard tables of oxidation potentials (13), the potential for the discharge of HO_2 radicals is very high

$$(HO_2)_{aq} + (H^+)_{aq} + e \rightarrow (H_2O_2)_{aq}, \; E° = 1.5V \qquad [4]$$

$$(O_2^-)_{aq} + (H_2O)_{aq} + e \rightarrow (HO_2^-)_{aq} + (OH^-)_{aq}, \quad E°_B = 0.2V \qquad [5]$$

Thus these potentials against a Pt/H_2 electrode in the same solution are well over a volt, a situation that has prompted a number of researchers (14) to believe that the two-electron peroxide path does not involve the discharge of O_2^- or HO_2 species. To account for the two-electron kinetics, a number of complex chemical steps have been invoked.

One must remember that the potentials quoted in Eq. [4] and [5] concern species in solution only and do not pertain to adsorbed species. It is possible that the heats of adsorption, the heats of desolvation, and reorganization of the solution structure during adsorption may lower the potential values into a region where discharge of an $(HO_2)_{ads}$ or $(O_2^-)_{ads}$ may take place with facility. From the literature (15), however, it appears that the reduction of O_2^-(ads) on Au in alkaline solution takes place by the dismutation of the O_2^-(ads) species instead of electron transfer.

It is the purpose of this report to estimate the heat of adsorption of an HO_2 radical on a Pt surface from existing data in the literature and from statistical thermodynamical calculations to see if the result gives a reasonable value to account for the lowering of the discharge potential of the HO_2 radical.

Estimate of ΔH_{ads} for the HO_2 Radical

We will consider the discharge of O_2 at a Pt cathode at 0.8V *vs.* Pt/H_2 in an acid solution of $pH = 0$ (*e.g.*, $2N$ H_2SO_4) at 25°C. Since O_2 is reduced at Pt cathodes in acid solution at relatively high rates at 0.8V (16), we must account for a lowering of only 0.7V from the potential of Eq. [4]. Assume that the standard potential for the discharge of $(HO_2)_{ads}$ radicals (Eq. [4A]) is the experimentally observable value of 0.8V. If Eq. [4A] is reversible, then 0.8V represents an upper limit since a lower value would be observed if Eq. [4A] were irreversible. We now convert these potential values to free energy values

$$(HO_2)_{aq} + (H^+)_{aq} + e \rightarrow (H_2O_2)_{aq}, \quad \Delta G = -34.9 \text{ kcal/mol} \qquad [4]$$

$$(HO_2)_{ads} + (H^+)_{aq} + e \rightarrow (H_2O_2)_{aq}, \quad \Delta G \geq -18.4 \text{ kcal/mol} \qquad [4A]$$

By subtracting these two equations, we arrive at the free energy of adsorption of the HO_2 radical

$$(HO_2)_{aq} \rightarrow (HO_2)_{ads}, \; \Delta G \leq -16.5 \text{ kcal/mol} \qquad [6]$$

To obtain the heat of adsorption from the Gibbs-Helmholtz equation, we must estimate the entropy of adsorption. For a gaseous molecule with three degrees of translational freedom, it can be shown (17) that the entropy of translation, S_{tr}, is given by Eq. [7]

$$S_{tr} = R \ln M^{3/2}T^{5/2} - 2.30 \qquad [7]$$

where M is the molecular weight, 33, and T is 298 K. This gives $S_{tr} = 36.4$ eu.

Since the H_2O_2 molecule has a skew, chain structure (18), the HO_2 radical should be angular (19) with the angle between the O—H and O—O bonds close to 97° found for H_2O_2. Because the HO_2 radical is unsymmetrical and possesses no symmetry elements except the identity operation, it belongs to the group, C_1 (20).

From statistical thermodynamic considerations, the expression for the entropy of rotation is (17)

$$S_{rot} = R\left\{\ln \frac{1}{\pi\sigma}\left[\frac{8\pi^3(I_A{}^aI_B{}^bI_C{}^c)^{1/n}\,kt}{h^n}\right]^{n/2} + \frac{n}{2}\right\} \qquad [8]$$

where $n = a + b + c$ = the number of degrees of freedom (in the case of the adsorbed HO_2 radical, $n = 3$). The rotational symmetry factor, σ, which gives the number of equivalent spatial orientations that a molecule can occupy as a result of simple rotation (21), is unity for the nonlinear, unsymmetrical HO_2 radical. The I's are the three moments of inertia involved in the three rotational modes. If the x-axis is taken as colinear with the O—O bond, then rotation about this axis involves only the O—H bond. We approximate this moment from that given for the OH radical (22) by assuming a value of 1.5×10^{-40} g cm^2. The moments of inertia associated with rotations about the y- and z-axes involve not only the O—H but also the O—O bonds and are equal. We approximate these moments from that given for the O_2 molecule (22) by assuming a value of 20×10^{-40} g cm^2. Using the values in Eq. [8], we calculate a value for S_{rot} of 27.3 eu in the gas phase.

Because the vibrational frequencies of many small molecules are large ($\sim 10^{13}$ sec^{-1}, $\sim$1000 cm^{-1}), the vibrational partition function is close to unity and the entropy of vibration, S_{vib}, determined from Eq. [9] is small if not negligible (17, 23, 24)

$$S_{vib} = R[W(e^W - 1)^{-1} - \ln(1 - e^{-W})] \qquad [9]$$

where $W = h\nu/kT$ and ν is the frequency of vibration. If the temperature is high enough, some vibrational contribution to the entropy will be made.

The entropy of HO_2 radicals in the gas phase at 298 K is

$$S_{HO_2}(g) = S_{tr} + S_{rot} + S_{vib}$$
$$= 36.4 + 27.3 + 0 \quad = 63.7 \text{ eu}$$

To obtain the entropy of HO_2 radicals dissolved in water, we consider the entropy loss incurred when H_2O_2 gas molecules are dissolved in water ($1M$). Using the NBS tables (13), we find $S_{H_2O_2}(g) = 55.6$ eu and $S_{H_2O_2}(aq) = 34.4$ eu giving a loss of entropy of 21.2 eu or a 38.1% decrease from the gaseous value. Assuming that a similar percentage loss in entropy would be suffered by the dissolution of HO_2 radicals in water ($1M$), we obtain an entropy value of 39.4 eu for $S_{HO_2}(aq)$.

Usually, the adsorption of O_2 on various metals produces immobile, adsorbed layers (25). Consequently, we assume that the layer of adsorbed HO_2 radicals is immobile and partial with a coverage, θ, no greater than 0.3. It is reported in the literature (26, 27) that on open circuit the coverage of a Pt surface with adsorbed oxygen lies between $0.23 < \theta < 0.3$. Although an immobile layer means the loss of three degrees of translational and three degrees of rotational entropy, there is a configurational contribution that takes into account the number of ways to distribute N molecules among Nx sites where $1/x = \theta$ (17).

$$S_{conf} = R[x \ln x - (x-1) \ln (x-1)] \quad [10]$$

Letting $1/x = 0.3$, $S_{conf} = 3.8$ eu, which must be subtracted from $S_{HO_2}(aq)$.

The entropy of adsorption ΔS_{ads}, for a layer of HO_2 radicals with a coverage of $\theta = 0.3$ at 25°C on a Pt cathode surface is

$$\Delta S_{ads} = S_{HO_2}(aq) - S_{conf} = -39.4 + 3.8 = -35.6 \text{ eu}$$

From the Gibbs-Helmholtz equation

$$\Delta G_{ads} = \Delta H_{ads} - T\Delta S_{ads}$$

$$\Delta H_{ads} = -16.5 + 298\ (-35.6)/1000 \leq -27.1 \text{ kcal/mol.}$$

Discussion

Since the heat of adsorption, as well as S_{conf}, depend on the surface coverage, θ, and since it has been shown (28) that there is a linear relationship between the coverage of a Pt surface with adsorbed oxygen and the potential of the Pt electrode, the value of θ for HO_2 radicals at 0.8V may be 0.1 or as low as 0.01. If θ is 0.1, S_{conf} is 6.5 eu, ΔS_{ads} is -32.9 eu, and ΔH_{ads} is -26.3 kcal/mol. For $\theta = 0.01$, $S_{conf} = 11.2$ eu, ΔS_{ads} is -28.2 eu, and ΔH_{ads} is -24.9 kcal/mol. A low value of θ agrees with the mechanism for O_2 reduction with the transfer of the first electron as the rate-determining step (28).

It is also possible that with an immobile layer adsorption process, a translational degree of freedom perpendicular to the surface may be transformed to a vibrational degree of freedom. This would cause an increase in entropy of less than 3 eu (23). The resultant change in ΔH_{ads} would then be less than 1 kcal/mol.

It appears that only a value of about -25 kcal/mol for the ΔH_{ads} of HO_2 radical is required to account for the lowering of 0.7V from the 1.5V potential for the homogeneous discharge of HO_2 radical in acid solutions. Such values of ΔH_{ads} are compatible with reported heats of chemisorption. In alkaline solutions, the homogeneous discharge potential of the superoxide ion, O_2^-, is 1.03V *vs.* Pt/H_2 from Eq. [5] and requires a lowering of only 0.23V to the O_2 evolution potential (0.8V). This observation agrees with the fact that O_2 is reduced more easily in alkaline than in acid solutions.

It is concluded from these considerations that there is enough energy available in the heat of adsorption (even without consideration of solvent effects and restructuring of the metal-solution interface) to permit the discharge of adsorbed HO_2 radicals or O_2^- ions in the two-electron peroxide path (1) for O_2 reduction without resorting to artificial, complex paths as diagrammed recently (29). One must use redox potentials quoted in the tables [*e.g.*, (13)] with caution since such values are not determined for the adsorbed species or for heterogeneous reactions. As seen here, a heat of adsorption as low as -25 kcal/mol can produce a difference of 0.7V in the potential of the heterogeneous reaction as compared to the homogeneous one.

Acknowledgments

The author wishes to express his gratitude to Prof. E. Yeager of Case Western Reserve University for our stimulating discussions and to one of the reviewers for his helpful suggestions.

Manuscript submitted Oct. 12, 1980; revised manuscript received Dec. 7, 1981.

Any discussion of this paper will appear in a Discussion Section to be published in the June 1983 JOURNAL. All discussions for the June 1983 Discussion Section should be submitted by Feb. 1, 1983.

Publication costs of this article were assisted by General Motors Research Laboratories.

REFERENCES

1. D. S. Gnanamuthu and J. V. Petrocelli, *This Journal*, **114**, 1067 (1967).
2. J. P. Hoare, "The Electrochemistry of Oxygen," p. 122, Wiley, New York (1968).
3. A. Damjanovic, *Mod. Aspects Electrochem.*, **5**, 369 (1969).
4. D. T. Sawyer and E. T. Seo, *Inorg. Chem.*, **16**, 499 (1977).
5. R. K. Sen, J. Zagal, and E. Yeager, *ibid.*, **16**, 3379 (1977).
6. J. P. Hoare, *Electrochim. Acta*, **20**, 267 (1975).
7. J. Divisek and B. Kastening, *J. Electroanal. Chem. Interfacial Electrochem.*, **65**, 603 (1975).
8. J. Chevalet, F. Rouille, L. Gierst, and J. P. Lambert, *ibid.*, **39**, 201 (1972).
9. Y. A. Ilan, G. Czapski, and D. Meisel, *Biochim. Biophys. Acta*, **430**, 209 (1976).
10. G. Czapski, *Ann. Rev. Phys. Chem.*, **22**, 171 (1971).
11. J. A. Fee and J. S. Valentine, "Superoxide and Superoxide Dismutases," p. 19, Academic Press, New York (1977).
12. D. Behar *et al.*, *J. Phys. Chem.*, **74**, 3209 (1970).
13. D. D. Wagman *et al.*, *NBS Tech. Note 270-3*, U.S. Gov't Printing Office, Washington, D.C., Jan. 1968.
14. Discussions at "Oxygen Workshop" E. B. Yeager, Chairman, Painesville, Ohio, May 1979.
15. R. W. Zurilla, R. K. Sen, and E. Yeager, *This Journal*, **125**, 1103 (1978).
16. J. P. Hoare, "The Electrochemistry of Oxygen," p. 118, Wiley, New York (1968).
17. C. Kemball, *Adv. Catal.*, **2**, 233 (1950).
18. F. A. Cotton and G. Wilkinson, "Advanced Inorganic Chemistry," p. 415, Wiley Interscience, New York (1972).
19. N. V. Sidgwick, "The Chemical Elements and Their Compounds," p. 870, Oxford Press, Oxford, England (1950).
20. F. A. Cotton, "Chemical Applications of Group Theory," p. 46, Wiley, New York (1975).
21. S. Glasstone, "Thermodynamics for Chemists," p. 109, Van Nostrand, New York (1947).
22. S. Glasstone, "Thermodynamics for Chemists," p. 110, Van Nostrand, New York (1947).
23. B. M. W. Trapnell, "Thermodynamics for Chemists," p. 210, Van Nostrand, New York (1947).
24. S. Glasstone, "Thermodynamics for Chemists," p. 193, Van Nostrand, New York (1947).
25. B. M. W. Trapnell, "Chemisorption," p. 215, Butterworths, London (1955).
26. M. L. B. Rao, A. Damjanovic, and J. O'M. Bockris, *J. Phys. Chem.*, **67**, 2508 (1963).
27. R. Thacker and J. P. Hoare, *J. Electroanal. Chem. Interfacial Electrochem.*, **30**, 1 (1971).
28. J. P. Hoare, "Encyclopedia of Electrochemistry of the Elements," Vol. 2, p. 220 (1974).
29. J. D. E. McIntyre and W. F. Peck, in "Electrode Processes," S. Bruckenstein, J. D. E. McIntyre, B. Miller, and E. Yeager, Editors, p. 321, The Electrochemical Society Softbound Proceedings Series, Pennington, NJ (1980).

The Effect of Sulfur on the Anodic H_2 (Ni) Electrode in Fused Li_2CO_3 -K_2CO_3 at 650°C

W. M. Vogel* and S. W. Smith*

United Technologies Corporation, Power Systems Division, South Windsor, Connecticut 06074

ABSTRACT

Steady-state polarization curves for rotating Ni wires in Li_2CO_3-K_2CO_3 (62 m/o Li) at 650°C are reported for H_2-containing gas of different H_2S contents. In the absence of sulfur, the diffusion-limiting currents are only slightly larger than the observed limiting currents. A reduction in the observed limiting currents by the presence of H_2S is interpreted as a decrease of the reaction-limiting current, *i.e.*, as poisoning of the Tafel reaction. The sulfur effect levels off at $P_{H_2S}/P_{H_2} \sim 10^{-4}$ which suggests that the sulfur coverage approaches a saturation value, and that a sulfur-saturated Ni surface retains a finite activity for H_2 oxidation. H_2S is not oxidized at a significant rate at potentials below that of Ni sulfide formation. An approximate rate equation for H_2 oxidation is derived for small sulfur coverages.

Sulfur tends to increase the polarization of Ni anodes in molten carbonate fuel cells (1). Sammells *et al.* (2) found essentially no effect of H_2S on the apparent exchange current for sulfur levels up to 50 ppm in the gas. However, the open-circuit potential (ocp) was increased suggesting mixed potentials. Townley *et al.* (3) attempted to explain this effect of sulfur on fuel cell anodes entirely by conversion of carbonate to sulfide and sulfate.

From these results, it is difficult to explain the observation that the polarization of fuel cell anodes increases immediately on introduction of H_2S in the fuel gas stream. During such short times, too little sulfur enters the cell to cause any significant change in melt composition. The small time constants suggest, rather, that sulfur interferes primarily by adsorption.

If sufficiently extensive, carbonate conversion to sulfate certainly can be expected to affect anode behavior. In addition, and primarily shortly after sulfur introduction, other effects may be important. Sulfur probably poisons the internal shift reaction which is required for satisfactory performance at high fuel utilization (4). Sulfur may also poison the anodic H_2 reaction despite the findings in Ref. (2). It is very difficult to separate the several effects of sulfur on the basis of tests with porous anodes where all phenomena may contribute to the result. Finally, sulfur may change the wetting angle of melt on the anode catalyst. An increase in wetting angle may isolate pockets of melt within the porous structure which, for small θ, were continuously connected by liquid films.

The present study sought to determine in more detail the effect of sulfur on only the H_2 reaction.

Experimental Materials and Procedures

The apparatus used has been described elsewhere (5). The working electrode was an Ni 201 wire, 0.10 cm in diameter and 1.8 cm long. The wire was bent in the shape of an inverted "L" with the vertical portion 1.5 cm long and 0.2 cm off the axis of rotation. Rotational speeds were measured with a General Radio Stroboscope, Model 1531-AB.

All experiments were done at 650°C in 62 mol percent (m/o) Li_2CO_3-38 m/o K_2CO_3, purified as in Ref. (5). The gases were "high-purity grade." mixed with a Matheson Mass Flow Controller, Model 8249. The gas mixture used in all tests comprised at operating temperature 0.534 atm H_2, 0.110 atm CO_2, 0.103 atm CO, and 0.253 atm H_2O. H_2S was added to the gas by splitting the entry line, saturating one leg to the desired dew point, and passing the other one over a Dynacal Tubular type permeation tube.[1] The H_2S level was controlled by varying the tube length and temperature. All H_2S analyses were made using Type B Kitagawa tubes.[2]

Determining the equivalent H_2S pressure in the melt proved to be a problem. Even very long saturation times did not initially produce the expected equilibrium. Thus in one test, inlet gas with 44 ppm H_2S was flowed for 500 hr through the cell. Even after this long time the exit gas still contained only 8-10 ppm H_2S. An electrochemical method, based on the Ni sulfide formation potential and described more fully later on, indicated an equivalent H_2S pressure in the melt of 20-23 ppm. Extending the saturation time resulted in very little change. The amount of sulfur that had entered the cell during 500 hr was at least 280 times larger than had been apparently absorbed by the melt. When gas samples were taken directly above the melt surface by means of a ceramic tube they contained 23 ppm H_2S, in good agreement with the electrochemical result. Apparently, sulfur was being consumed continuously by cell parts that were not in direct contact with the melt and these consisted of SS-316 and/or Incoloy 800. This consumption of H_2S prevented complete equilibrium in the system.

The system was then changed by replacing the SS-316 inlet tube with Ni 201, and extending it to just above the melt surface. With these changes equilibrium between melt and inlet gas was established in a relatively short time even though the upper gas space regions continued to be depleted of H_2S. Thus after only 50 hr saturation time, the analyses of gas samples from inlet stream and from just above the melt surface agreed with each other and with the electrochemically determined value for the melt (43, 42, and 42 ppm, respectivelv). These tests confirmed the validity of determining H_2S pressures in the melt electrochemically, and also demonstrated that serious errors can be committed if equilibrium is assumed even after many hours of saturation. Because of the simplicity of the electrochemical method it was used in most of these experiments.

Results and Discussion

As described in the experimental section, the achievement of equilibrium between the gas and the melt in the apparatus used in this study proved to be difficult and time consuming. For this reason the H_2S equivalent pressure in the melt was determined electrochemically in most tests from the Ni sulfide formation potential. Preliminary tests had shown that this reaction is very fast, at least initially. Nickel sulfide is formed according to

$$3Ni + nH_2S = Ni_3S_n + nH_2, \quad n \geq 1 \qquad [1]$$

* Electrochemical Society Active Member.
Key words: hydrogen, electrodes, molten carbonate, sulfur.

[1] Metronics Associates, Incorporated.

[2] Scientific Gas Products.

with the equilibrium constant for initial sulfide formation at 650°C (6)

$$K = P_{H_2S}/P_{H_2} \sim 1.5 \cdot 10^{-3} \quad [2]$$

The H_2 pressure at the metal surface is not directly available except at open circuit because of the gradient of H_2 pressure through the diffusion layer. The H_2 pressure does not approach zero at the surface at limiting current[3] however, because of the contribution of the reaction-limiting current to the observed limiting current. It is more practical, therefore, to use the following partial reaction of reaction [1]

$$3Ni + nH_2S + nCO_3^{=} = Ni_3S_n + nH_2O + nCO_2 + 2ne^- \quad [3]$$

with the equilibrium potential measured against the 1/3 atm O_2-2/3 atm CO_2 reference electrode

$$E = -1242.1 + 91.58 \log P_{H_2O}P_{CO_2}/P_{H_2S} \text{ (mV)} \quad [4]$$

The standard potential was calculated using the thermodynamic data of Ref. (6).

H_2O and CO_2 concentration gradients for anodes are usually small even at the limiting current (4) except for gases rich in H_2 and low in H_2O and CO_2. This is especially true in the presence of sulfur where I_{lim} is smaller than in the absence of sulfur (see Fig. 3). The H_2S pressure at the metal surface can be estimated, therefore, from the potential of Ni sulfide formation, using Eq. [4] with[4] $P_{H_2O}P_{CO_2} \sim P_{H_2O}{}^\circ P_{CO_2}{}^\circ$, provided H_2S is not oxidized and Ni sulfide formation is little hindered. H_2S oxidation could contribute partial currents as large as, or even larger than H_2 oxidation owing to the large solubility of H_2S. Using data of Ref. (7) for the latter and of Broers *et al.* (8) for the hydrogen solubility one obtains for the equivalent equilibrium concentration (assuming oxidation of H_2S to sulfate)

$$(H_2S)/(H_2) \sim 10^5 P_{H_2S}/P_{H_2}, \text{ equivalent/equivalent} \quad [5]$$

The electrochemical method for determining P_{H_2S} in the melt was tested by comparing results with direct gas analysis results, as described in the experimental section. The agreement was satisfactory (±4%). This result indicates that H_2S is not noticeably oxidized at potentials below that for Ni sulfide formation, and that the product $P_{CO_2} \cdot P_{H_2O}$ is close to that of the bulk pressures. At $P_{H_2S}/P_{H_2O} \leq 5 \cdot 10^{-6}$ the electrochemical method breaks down because NiO formation precedes sulfide formation. For the mixture used in this study, this is equivalent to $P_{H_2S}/P_{H_2} \leq 2.5 \cdot 10^{-6}$. Figure 1 presents polarization curves for sulfur-free gas. The dashed lines represent concentration overvoltage calculated with

$$\eta = -\frac{RT}{2F} \ln (1 - I/I_{lim}) = -91.58 \log (1 - I/I_{lim}) \text{ (mV)} \quad [6]$$

The moderately small deviations of the experimental data presumably reflect the facts that H_2O and CO_2 concentration losses were neglected in Eq. [6], and that Eq. [6] does not apply accurately to a rotating wire electrode. However, no further attempts at achieving better accuracy were made because the differences were small, and because a rotating disk electrode is difficult to use in molten carbonate.

In Fig. 2 the values of $I_{lim}{}^{-1}$ of Fig. 1 are plotted against reciprocal square root of rotational speed ($\omega^{-1/2}$). I_{lim} is mostly diffusion controlled as shown by the small value of the intercept at infinite rotation

[3] The term limiting current shall be used for the observed limiting current. The diffusion and reaction limiting current shall be identified as such or by symbol (I_{lim}, I_d, I_r).

[4] The superscript (°) refers to the partial pressures in the bulk gas phase.

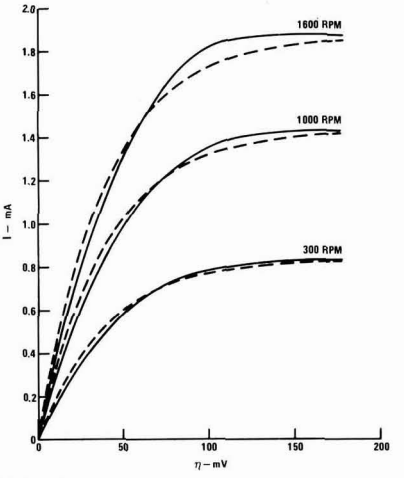

Fig. 1. Steady-state polarization curves for H_2 oxidation in the essential absence of sulfur. Rotating Ni wire electrode of 0.56 cm^2 geometric surface area.

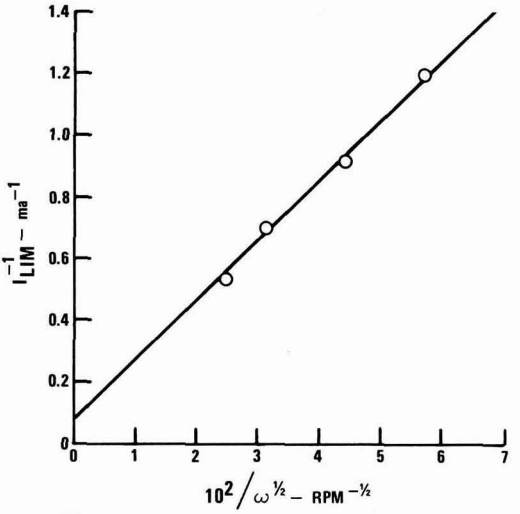

Fig. 2. Limiting currents in the absence of sulfur. $I_R{}^\circ \sim 14$ mA, $I_d = 0.0519 \cdot \omega^{1/2}$, mA.

rate. The reaction-limiting current may reflect poisoning by sulfur traces. The initial Li_2CO_3 used contained up to 2000 ppm sulfur (as sulfate) which is very difficult to remove completely. Long purging times with sulfur-free gas had increased the Ni sulfide formation potential to a value above that for NiO formation at which point P_{H_2S}/P_{H_2} becomes smaller than $2.5 \cdot 10^{-6}$. At such small levels P_{H_2S} in the melt becomes extremely difficult to measure. The actual value of P_{H_2S}/P_{H_2} in these tests with sulfur-free gas was therefore unknown but less than $2.5 \cdot 10^{-6}$. In the following, the data in Fig. 1 and 2 shall be considered to be for the sulfur-free system.

Figure 3 shows the effect of H_2S on the polarization curves at 1600 rpm. The main effect is a decrease in I_{lim}. Since only diffusion and chemical processes lead to limiting currents, this result indicates a decrease in the reaction-limiting current. It seems justified, there-

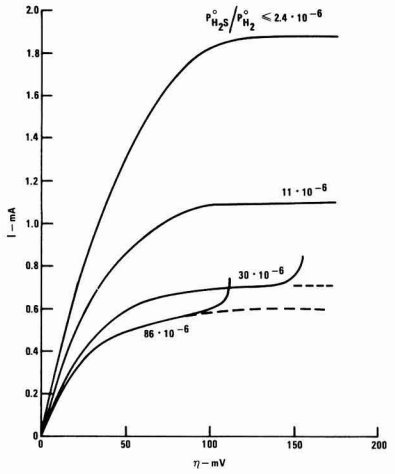

Fig. 3. Steady-state polarization curves of Ni wire anode at 1600 rpm. The sudden increase in I at larger values of η is due to anodic Ni sulfide formation.

fore, to assume a Tafel-Volmer type mechanism, adjusted for molten carbonate, with the Tafel reaction as rate-determining step of the surface reaction

$$H_2 + 2M = 2MH^* \text{ (rds)} \qquad [8]$$

$$2MH^* + CO_3^= = 2M + H_2O + CO_2 + 2e^- \qquad [9]$$

The presence of H_2S decreases the rate (v_T) of reaction [8]. The current is

$$I = 2\mathbf{F} \cdot v_T = 2\mathbf{F}\,[kP_{H_2}\theta_m^2 - k'\theta_H^2] \qquad [10]$$

The quantities θ_M and θ_H are activities of the sites available for hydrogen adsorption and of adsorbed hydrogen, respectively. At higher polarization θ_H becomes zero and the current approaches a limiting value

$$I_{lim} = 2\mathbf{F}k\ (P_{H_2}\theta_M^2)_{lim} \qquad [11]$$

The subscript (lim) indicates the respective values at I_{lim}.

Using Fick's first law

$$(P_{H_2})_{lim} = P_{H_2}^{\circ}(1 - I_{lim}/I_d) \qquad [12]$$

where I_d is the stirring-dependent diffusion-limiting current (Fig. 2) and therefore

$$1/I_{lim} = 1/I_d + 1/I_R,\ I_R \equiv 2\mathbf{F}P_{H_2}^{\circ}\ (k\theta_M^2)_{lim} \qquad [13]$$

With H_2S present Eq. [13] does not, however, provide a complete separation of I_{lim}^{-1} into stirring-dependent and independent terms as in the sulfur-free case where $(\theta_M)_{lim} = 1$, see Fig. 2. With sulfur present, $(\theta_M)_{lim}$ is not unity, but varies with sulfur coverage. In fact, k also may depend on sulfur coverage.

Sulfur presumably is adsorbed according to (9, 10)

$$H_2S + M = MS^* + H_2 \qquad [14]$$

with the equilibrium constant

$$K_S \equiv \theta_S \cdot P_{H_2}/\theta_M' \cdot P_{H_2S} \qquad [15]$$

where θ_S is the activity of adsorbed sulfur and θ_M' is the activity of the sites available for sulfur adsorption. If θ_S is assumed to be proportional to the sulfur coverage, it is proportional to P_{H_2S}/P_{H_2} at small coverages. Since H_2S is not noticeably oxidized at I_{lim}

$$(P_{H_2S}/P_{H_2})_{lim} = P_{H_2S}^{\circ}/P_{H_2}^{\circ}(1 - I_{lim}/I_d) \qquad [16]$$

Thus, sulfur coverage and thereby the reaction-limiting current varies with stirring in contrast to the sulfur-free condition.

Figure 4 was constructed by calculating I_R with Eq. [13] and [16], using the values of I_d of Fig. 2. The curve represents the variation of $2\mathbf{F}(k\theta_M^2)_{lim}$ with the value of P_{H_2S}/P_{H_2} prevailing at the metal surface. If reflects the effect of sulfur coverage on the activity of the sites available for H_2 oxidation at negligible hydrogen coverage. To the extent that θ_H is not negligible at smaller polarizations, θ_M will be smaller at $I < I_{lim}$. The curve in Fig. 4 therefore reflects the variation of the maximum surface area, free to adsorb hydrogen, with sulfur coverage

$$(\theta_M)_{lim} = (\theta_M + \theta_H)_I = f(\theta_S) \qquad [17]$$

Figure 4 shows that the sulfur coverage approaches a saturation value at large values of P_{H_2S}/P_{H_2}, *i.e.*, the product $(k\theta_M^2)_{lim}$, which is a measure of the activity of sites available for H_2 oxidation, levels off at a finite value. This suggests that H_2 is oxidized even at a sulfur-saturated surface, and that the mechanism remains that given by Eq. [8] and [9]. The Tafel reaction [8] may proceed on adsorbed sulfur (formation of S — H*), or on Ni. Adsorption of hydrogen on Ni even at full sulfur coverage seems plausible because of the difference in size of adsorbed sulfur and Ni atoms. Presumably, sulfur is adsorbed most strongly when the Ni-S distance is smallest, *i.e.*, for 1:1 adsorption. However, such strongly adsorbed sulfur cannot cover the entire Ni surface. Rather, some fraction of the surface will always remain free to adsorb hydrogen ("strong adsorption model"). Alternatively, sulfur may cover the entire surface either accompanied by distortion of Ni-S bonds, or because the adsorbed sulfur may carry a charge of less than (−2) and therefore be smaller in size. However, adsorption will progressively weaken at large coverage and hydrogen may displace weakly adsorbed sulfur ("competitive adsorption model").

Although plausible, neither of these models lends itself readily to the derivation of a rate equation for

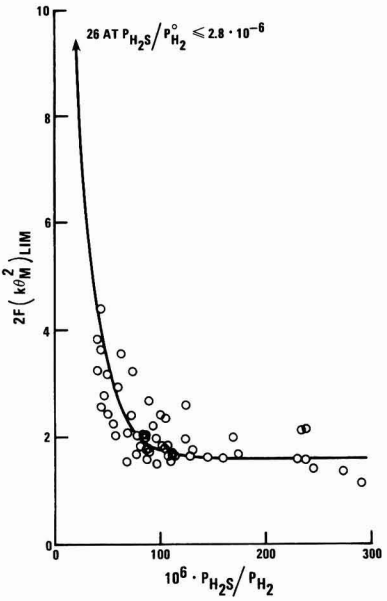

Fig. 4. Anodic reaction limiting currents, normalized to 1 atm H_2 pressure. Empirically, $2\mathbf{F}\ k_I\ \theta_m^2 \sim 1.6 + 24.4 \exp\ [-52{,}000\ P_{H_2S}/P_{H_2}^{\circ}]$.

H_2 oxidation. The difficulty lies primarily in defining rationally the quantities θ_S and θ_M' in Eq. [10], [11], [13], and [15]. Substituting fractional surface areas, the value of θ_M' in Eq. [15] has to approach zero for large values of P_{H_2S}/P_{H_2}. At the same time, however, the corresponding value of θ_M remains finite. Thus θ_M' and θ_M are not generally equal. The problem is not solved by using surface sites instead of fractional surface areas.

An approximate rate equation can be derived for small sulfur coverages. Substituting fractional surface areas for activities, and assuming that sulfur adsorbs essentially only on the free Ni surface, θ_M will be equal to θ_M'. Therefore

$$\theta_M + \theta_S + \theta_H = 1 \quad [18]$$

With reaction [9] near equilibrium

$$\theta_H \sim \theta_M (P_{H2O} \cdot P_{CO_2})^{1/2} \exp [\mathbf{F}(E_v^\circ - \epsilon)/RT] \quad [19]$$

where E_v° is the standard potential of the Volmer reaction. Combining Eq. [18] and [19] with Eq. [15]

$$\theta_M = [1 + K_S \cdot P_{H_2S}/P_{H_2} + (P_{H2O} \cdot P_{CO_2})^{1/2} \exp [\mathbf{F}(E_v^\circ - \epsilon)/RT]^{-1} \quad [20]$$

Assuming that the rate constants k and k' in Eq. [10] do not vary with coverage, the exchange current is

$$I_o = 2\mathbf{F}kP_{H_2}^\circ (\theta_M^\circ)^2 = 2\mathbf{F}k'(\theta_H^\circ)^2 \quad [21]$$

and therefore

$$I = I_o(\theta_M/\theta_M^\circ)^2[P_{H_2}/P_{H_2}^\circ - (\theta_H \cdot \theta_M^\circ/\theta_H^\circ \cdot \theta_M)^2] \quad [22]$$

From Eq. [19]

$$(\theta_H \cdot \theta_M^\circ/\theta_H^\circ \cdot \theta_M)^2 = (P_{H2O} \cdot P_{CO_2}/P_{H2O}^\circ \cdot P_{CO_2}^\circ) \exp [-2\mathbf{F}\eta/RT] \quad [23]$$

and now[5]

$$I = I_o(\theta_M/\theta_M^\circ)^2[P_{H_2}/P_{H_2}^\circ - (P_{H2O} \cdot P_{CO_2}/P_{H2O}^\circ \cdot P_{CO_2}^\circ) \exp (-2\mathbf{F}\eta/RT)] \quad [24]$$

It is easier and more accurate to determine the reaction-limiting current without sulfur (I_R°) than the exchange current in the presence of sulfur (I_o). For a sulfur-free melt θ_M approaches unity for $\eta \to \infty$, and therefore

$$I_{\substack{\omega\to\infty \\ \eta\to\infty}} \equiv I_R^\circ = 2\mathbf{F}kP_{H_2}^\circ = I_o/(\theta_M^\circ)^2 \quad [25]$$

Replacing I_o in Eq. [24] with I_R°

$$I = I_R^\circ \theta_M^2[P_{H_2}/P_{H_2}^\circ - (P_{H2O} \cdot P_{CO_2}/P_{H2O}^\circ \cdot P_{CO_2}^\circ) \exp (-2\mathbf{F}\eta/RT)] \quad [26]$$

Equations [26] and [20] represent the approximate rate equation for small sulfur coverages. The pressure ratios (P/P°) can be obtained from Fick's law.

The limiting current is obtained for $\epsilon, \eta \to \infty$, or directly from Eq. [19] for $\epsilon \to \infty$ and Eq. [13] and [25]

$$1/I_{lim} = 1/I_d + [1 + (K_S P_{H_2S}/P_{H_2}^\circ)/(1 - I_{lim}/I_d)]^2/ \cdot I_R^\circ \quad [27]$$

The curves in Fig. 5 were calculated with Eq. [27] for several values of $K_S \cdot P_{H_2S}/P_H^\circ$. The value for I_R° and I_d were taken from Fig. 2. Corresponding plots of the experimental data are shown in Fig. 6. The correspondence between experimental and theoretical results is poor. Qualitatively, the disagreement is a consequence of the fact that the hydrogen activity does not decrease in correspondence with the increase in sulfur coverage. As can be seen from Fig. 6, the ratio I_{lim}/I_d is smaller than unity at higher values of

[5] Superscripts (°) refer to ocp.

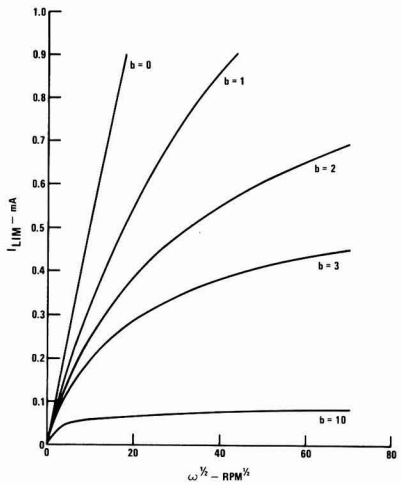

Fig. 5. Theoretical limiting currents (Eq. [27]). Parameter: $K_S P_{H_2S}/P_H^\circ \cdot 10^6$.

ω, but increases toward unity with decreasing rotational speed. This means that P_{H_2S}/P_{H_2} increases in the same direction at any given value of $P_{H_2S}/P_{H_2}^\circ$ (Eq. [16]). Thus the reaction-limiting current, and thereby I_{lim} decrease, but to a lesser degree than is predicted by the simple theory.

The difficulty of defining surface activities for hydrogen and sulfur appears to be fundamental in nature and not restricted to the problem of interpreting electrochemical test results. Thus the adsorption isotherms in Ref. (9) and (10) differ by more than one order of magnitude in P_{H_2S}/P_{H_2}. In these experiments in the gas phase the respective gas pressures at the metal surface are well defined and cannot be the cause of such discrepancies. It has been suggested (11) that the observed differences are due, rather, to sulfur adsorption leading to a saturation coverage at moderately large values of P_{H_2S}/P_{H_2}, but that at still larger values adsorption increases again. The same seems to be true in the present case with the result that activity

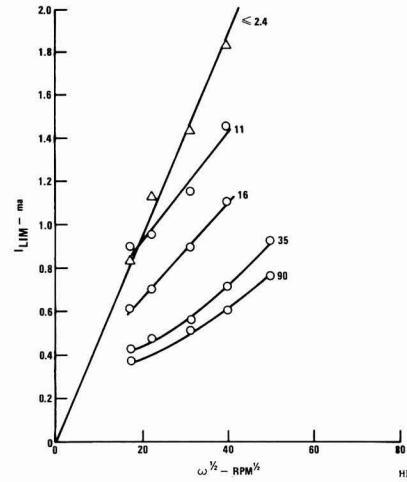

Fig. 6. Experimental limiting currents. Parameter: $K_S P_{H_2S}/P_H^\circ \cdot 10^6$.

for H_2 oxidation is not completely lost even when the sulfur coverage appears complete.

Conclusions

The Tafel-Volmer mechanism, adjusted for molten carbonate, provides a satisfactory explanation for the oxidation of H_2 in the presence of sulfur as well as without sulfur. In the absence of H_2S the reaction-limiting current is so large that the limiting current is essentially diffusion controlled at all but very high stirring rates. A chemical rate constant of the Tafel reaction of approximately $k \sim 4 \cdot 10^{-8}$ mol/atm cm^2 sec follows from the data for the sulfur-free case. The Volmer reaction is not noticeably hindered. H_2S decreases the reaction-limiting current, *i.e.*, the rate of the Tafel reaction. The mechanism appears to remain the same. The stirring dependency of the reaction-limiting current with sulfur is due to the effect of stirring on the H_2 pressure at the metal surface, and thereby on the value of P_{H_2S}/P_{H_2} and the sulfur coverage.

Acknowledgments

Support of this work by the U.S. Department of Energy under the management of Dr. J. Ackerman is gratefully acknowledged.

Manuscript submitted Sept. 8, 1981; revised manuscript received Dec. 10, 1981.

Any discussion of this paper will appear in a Discussion Section to be published in the June 1983 JOURNAL. All discussions for the June 1983 Discussion Section should be submitted by Feb. 1, 1983.

Publication costs of this article were assisted by United Technologies Corporation.

REFERENCES

1. United Technologies, "Advanced Technology Fuel Cell Program," EPRI, Sept. 1978, Molten Carbonate Fuel Cell Seminar, Oak Ridge National Laboratory, Oct. 1978.
2. A. F. Samme.ls, S. B. Nicholson, and P. G. P. Ang, *This Journal*, **127**, 350 (1980).
3. D. Townley, J. Winnick, and H. S. Huang, *ibid.*, **127**, 1104 (1980).
4. W. M. Vogel, L. J. Bregoli, and S. W. Smith, *ibid.*, **127**, 833 (1980).
5. W. M. Vogel, L. J. Bregoli, and S. W. Smith, National Fuel Cell Seminar, June 25, 1981, Norfolk, VA. Submitted to *This Journal*.
6. T. Rosenquist, *J. Iron Steel Inst.*, **176**, 37 (1954).
7. S. W. Smith, Submitted to *This Journal*.
8. G. H. J. Broers, M. Schenke, and H. J. J. van Ballegoy, Extended Abstract II 77, 20th ISE Meeting, Druzhba, Bulgaria, Sept. 1977.
9. J. R. Rostrup-Nielsen, *J. Catal.*, **11**, 220 (1968).
10. M. Perdereau and J. Oudar, *Surf. Sci.*, **20**, 80 (1970).
11. J. Bett, Private communication.

Use of a High Temperature *p*H Sensor as a "Pseudo-Reference Electrode" in the Monitoring of Corrosion and Redox Potentials at 285°C

Leonard W. Niedrach*

General Electric Corporate Research and Development, Schenectady, New York 12345

ABSTRACT

Corrosion and redox potentials measured at 285°C against a zirconium oxide, membrane-type *p*H sensor have been found to be more stable than similar measurements against more conventional reference electrodes. This is attributed to the excellent resistance of zirconium oxide to attack by high temperature water and to the absence of a liquid junction that permits exchange of an internal filling solution with the medium being monitored.

In monitoring corrosion and redox potentials in aqueous systems one ideally determines the *p*H as well, because the two parameters are intimately related. When the *p*H of the system is known to remain within narrow bounds, *e.g.*, as in the cooling water of nuclear reactors, measurement of only the corrosion or redox potential against a conventional reference electrode can be adequate (1-3). Under such conditions, however, it is equally possible to employ a *p*H sensor as a "pseudo-reference electrode." It has been our experience that at 285°C, corrosion and redox potentials measured against a zirconium oxide, membrane-type *p*H sensor (4) have been more stable than any we have achieved against more conventional reference electrodes. This is not surprising in view of the excellent resistance of zirconium oxide to attack by high temperature water. Further, there is no liquid junction to introduce an uncertain junction potential and to permit exchange of an internal filling solution with the medium being monitored and thereby cause drift. Because of the stability of zirconium oxide *p*H sensors we can visualize their being inserted at many critical monitoring sites in power plants, chemical processing plants, or other installations to provide useful corrosion potential measurements over extended periods with a minimum of maintenance. They could also be useful in laboratory tests, particularly with static autoclaves when consumption of oxygen deliberately added to the starting solution can be rapid, and when undetected changes of this type could lead to serious misinterpretation of data.

The use of a *p*H sensor in this proposed fashion is not of itself a new idea. Glass electrodes have been so employed in the past (5). The new, high temperature *p*H sensor merely facilitates extension of the idea to higher temperature systems. It is the purpose of the present paper to review some of the background on the zirconia sensor, indicate how its potential can be related to the standard hydrogen electrode (SHE) scale, and present data relating to corrosion and redox potential monitoring.

Background

Preferred form of the pH sensor.—The concept of the new, high temperature *p*H sensor and many of its properties have been discussed elsewhere (4). A

* Electrochemical Society Active Member.
Key words: cell, *p*H sensor, water, emf.

photograph of the device is shown in Fig. 1 and structural details are given in Fig. 2. The ceramic is a ¼ in. OD tube of yttria [8.0 weight percent (w/o)] stabilized zirconia (obtained from Corning Glass Works, Ceramics Products Division, Solon, Ohio, their composition 1372). It is retained in a Conax Type EG-125 Gland with a seal consisting of Teflon, Vespel, silver, and alumina elements as shown. On the basis of previous work we have selected the dry copper/cuprous oxide mixture as our preferred internal junction over the previously employed aqueous internal junctions. This has been done for several reasons: (*i*) we have found it to be readily prepared by simple mixing of the powders and packing into the tube; (*ii*) when prepared in this fashion it has been found to be extremely stable and reproducible; (*iii*) in contrast to aqueous internals it permits ready designation of the active region of the sensor because it does not wet the wall with a conducting film; and (*iv*) in the absence of an internal aqueous phase, seal fabrication is simplified. It also has the virtue of permitting a straightforward calculation of its standard potential against the SHE, a very desirable feature since it is common practice to normalize experimental data to the SHE scale.

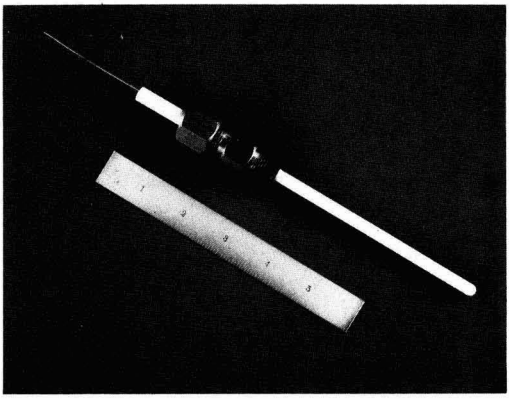

Fig. 1. Photograph of an assembled sensor

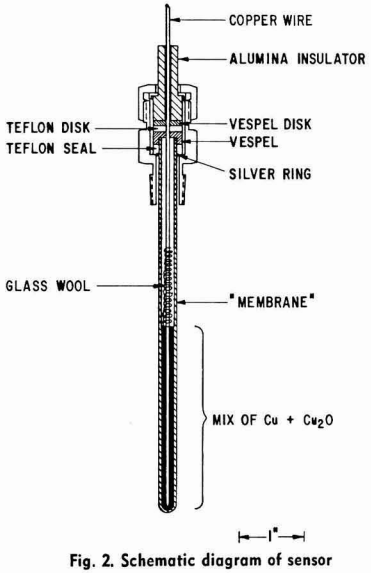

Fig. 2. Schematic diagram of sensor

For the junction we are employing a 1:1 (by weight) mixture of finely divided copper and cuprous oxide (Fisher Copper Metal-Electrolytic Dust, purified; Baker Cuprous Oxide Powder, Analyzed Reagent) to a depth of 2 in. A 30 mil copper wire serves as the contact and lead from the sensor.

Calculation of the standard potential of the sensor vs. the SHE.—For the sensor as shown in Fig. 2, several interphase potentials are involved in series between the external terminal (copper lead wire) and the solution being monitored. These and the thermodynamic balances involved in the potential determining reactions at the various interfaces are summarized in Fig. 3 after the approach of Vetter (6). The balances are derived from the fact that at equilibrium the algebraic sum of the electrochemical potentials, $_i\eta_s$, of the reacting species is zero

$$\Sigma_i \nu_s \cdot {}_i\eta_s = 0 \qquad [1]$$

where

$$_i\eta_s = {}_i\mu_s + {}_iz_s \cdot \mathbf{F} \cdot {}_i\phi \qquad [2]$$

and where $_i\mu_s$ is the chemical potential of reacting species s in phase i, $_iz_s$ is the charge on the species, $_i\phi$ is the Galvani (inner) potential in phase i, $_i\nu_s$ is the stoichiometric factor of the species involved in the potential determining reaction, and **F** is the faraday.

In summing up the interphase potentials between phases 1 and 4 it is seen in Fig. 3 that the net change is equivalent to that for the simple copper/cuprous oxide couple

$$2Cu + H_2O \rightleftarrows Cu_2O + 2H^+ + 2e^- \qquad [3]$$

the thermodynamics for which relative to the SHE are well established.[1]

This is turn means that to relate the standard potential of the sensor to the SHE, the half-reaction for which also involves two hydrogen ions

$$H_2 \rightleftarrows H^+ + 2e^- \qquad [4]$$

we require only the free energy of the reaction

$$2Cu + H_2O \rightleftarrows Cu_2O + H_2 \qquad [5]$$

which does not involve the hydrogen ion concentration. If the zirconia sensor is to be used as a reference in a solution other than one containing the hydrogen

[1] The membrane may therefore be looked upon as a protective sheath that prevents the metal and its oxide from interacting directly with the solution or redox active species in the solution. While a copper/cuprous oxide mix could be exposed to water and dilute acids and bases without significant attack, such would not be the case with strongly acid or basic solutions. Under any conditions use of the unsheathed metal/metal oxide mix would necessitate alternative protection from direct interaction with hydrogen or oxygen. This behavior suggests that the arrangement might be useful in studying the electrochemistry and thermodynamics of other metal/metal oxide or mixed metal oxide systems.

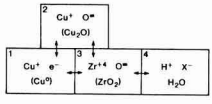

PHASES	THERMODYNAMIC BALANCES	INTERPHASE POTENTIALS
1-2	$_1\mu_{Cu^+} - (_1\mu_{e^-} - F_1\phi) - (_2\mu_{Cu^+} + F_2\phi) = 0$	$\Delta\phi_{1-2} = 1/F(_2\mu_{Cu^+} - {}_1\mu_{e^-} - {}_1\mu_{Cu^+})$
2-3	$(_2\mu_{O^=} - 2F_2\phi) - (_3\mu_{O^=} - 2F_3\phi) = 0$	$\Delta\phi_{2-3} = 1/F(½{}_2\mu_{O^=} - ½{}_3\mu_{O^=})$
1-3		$\Delta\phi_{1-3} = 1/F(_2\mu_{Cu^+} + ½{}_2\mu_{O^=} + {}_1\mu_{e^-} - ½{}_3\mu_{O^=} - {}_1\mu_{Cu^+})$ $1/F(_2\mu_{Cu_2O} + {}_1\mu_{e^-} - ½{}_3\mu_{O^=} - {}_1\mu_{Cu^+})$
3-4	$_4\mu_{H_2O} - (_3\mu_{O^=} - 2F_3\phi) - 2(_4\mu_{H^+} + F_4\phi) = 0$	$\Delta\phi_{3-4} = 1/F(-½{}_4\mu_{H_2O} + ½{}_3\mu_{O^=} + {}_4\mu_{H^+})$
1-4		$\Delta\phi_{1-4} = 1/F(_2\mu_{Cu_2O} + ½{}_2\mu_{H^+} - {}_1\mu_{e^-} - ½{}_4\mu_{H_2O} + {}_1\mu_{e^-})$

Which is equivalent to the potential of the half-reaction:

$$Cu^0 + ½H_2O = ½Cu_2O + H^+ + e^-$$

Fig. 3. Interphase potentials and related thermodynamic data for the sensor.

ion at unit activity, a pH correction must be applied in relating back to the SHE scale.

Relationship between the sensor potential and that of the oxygen electrode.—Also of interest in the monitoring of aqueous systems containing dissolved oxygen is the relationship between the sensor potential and that of the oxygen electrode. In this case the overall reaction is obtained from the sum of reaction [3] and the half-reaction for the oxygen electrode

$$\tfrac{1}{2}\,O_2 + 2H^+ + 2e^- \rightleftarrows H_2O \qquad [6]$$

to give

$$2Cu + \tfrac{1}{2}\,O_2 \rightleftarrows Cu_2O \qquad [7]$$

The potential of this cell can therefore be calculated directly from the free energy of formation of cuprous oxide from the elements.

Experimental

Determination of the standard potential of the sensor at 285°C.—Using equipment and procedures described in Ref. (4), the potential of the sensor has been measured against the hydrogen electrode. A well-passivated titanium autoclave was employed and the water entering the autoclave at a flow rate of approximately 15 ml/min was equilibrated with "forming gas" (10% hydrogen in nitrogen) at 25°C. A platinized platinum flag served as the sensing element of the hydrogen electrode. The results of three separate experiments, each yielding steady potentials for about 36 hr, are summarized in Table I.

In calculating the correction term for the hydrogen concentration in the water it was assumed that the concentration at 285°C was equal to that obtained in the equilibration at 25°C. This is reasonable since the test system was operated about 200 psi above the saturation pressure of water at 285°C and no gas phase was present in the autoclave. From data of Himmelblau (7) the hydrogen concentration in equilibrium with the 10% H_2-N_2 mixture at 25°C was estimated to be 0.152 ppm. At 285°C the concentration of hydrogen in equilibrium with 1 atm of hydrogen is 7.40 ppm. These concentrations coupled with the slope of 110.76/2 mV/decade at 285°C give the correction term of 93 mV. For the standard potential of reaction [5] data of Macdonald (8) were interpolated to 285°C. It is seen in Table I that the agreement between the measured and theoretical is very satisfactory.

Measurement of the potential of the sensor vs. the oxygen electrode.—Data for this combination were obtained over the pH range from 0.0005*m* sulfuric acid to 0.001*m* sodium hydroxide using aerated solutions containing about 8.2 ppm dissolved oxygen. In this case the agreement with theory was less satisfactory than in the case of hydrogen, and the value varied with pH as shown in Fig. 4. The theoretical potential of 635 mV was calculated from literature data for the free energy of formation of cuprous oxide (9) applying a correction term to allow for an oxygen concentration below that in equilibrium at 1 atm. The solubility of oxygen at 285°C at a pressure of 1 atm was taken as 110 ppm (7). The discrepancies are most likely associated with the oxygen electrode which is probably not yet sufficiently reversible even at 285°C.

Table I. Comparison of the measured value of the standard potential of the sensor with the calculated value at 285°C

Run	*E* of sensor *vs.* hydrogen electrode (mV)	Δ*E* for hydrogen activity* (mV)	*E*° (mV)
A	274		
B	272		
C	280		
	Mean 275	93	368
			Calculated value 366**
			Difference 2

* $\Delta E = (2.303\,RT/nF)\log(C_1/C_a) = 55.38 \log(7.40/0.152) = 93$ mV, where C_1 is the solubility of hydrogen at 285°C and 1 atm pressure and C_a is the actual hydrogen concentration in water. [Solubility data from Ref. (7).]

** Based on data from Ref. (8).

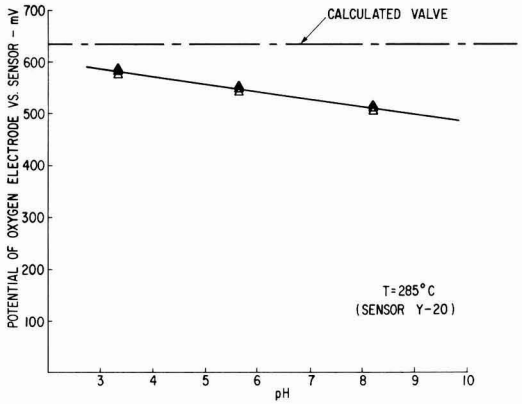

Fig. 4. Comparison of measured and calculated values of the potential of the oxygen electrode *vs.* the pH sensor. (Oxygen concentration in equilibrium with air at 25°C, *i.e.*, 8.2 ppm.)

Monitoring corrosion and redox potentials.—In the course of the development of the zirconia pH sensor two tests of about 40 days duration were performed to demonstrate long-term stability. During most of the period of these tests the system was exposed to aerated water at 285°C, but periodically excursions to 0.0005*m* H_2SO_4 and 0.001*m* NaOH were introduced. Potentials of the sensor (with Cu/Cu_2O internal), a platinum probe, and the 316 S.S. autoclave were monitored throughout using an Ag/AgCl reference electrode (10) initially charged with water and AgCl crystals, *i.e.*, no KCl was added. (This type of filling solution has proved to be more stable than those containing 0.01 or 0.1*m* KCl.) The potential of the zirconia sensor *vs.* the platinum probe was also followed directly throughout the tests. We have now reexamined the data as they bear upon the monitoring of corrosion and redox potentials with the autoclave serving as the corroding electrode.

The relative stabilities of the various electrodes against the reference electrode are shown in Fig. 5, and similar data for the corrosion and redox potentials against the pH sensor are shown in Fig. 6. In connection with the latter figure, it should be noted that, in contrast to the platinum probe, the potential of the autoclave was not monitored directly against the pH sensor during the tests. As a result, all of the corrosion potentials have been derived from independent measurements of the autoclave and the pH sensor against the Ag/AgCl reference. This may account in part for the greater scatter. Nevertheless, both sets of measurements indicate that the potentials measured against the pH sensor are at least as reliable as those measured against the more conventional reference electrode.

While the data in Fig. 5 and 6 pertain to the dilute acid solutions, similar results were obtained with water and the dilute base. This is evident from the clustering of the data points obtained throughout the tests and plotted for Run ZR02-19 in Fig. 7 and 8. Here we see additionally that the influence of pH on the corrosion potential essentially parallels that of the pH sensor. The slope of the redox probe response

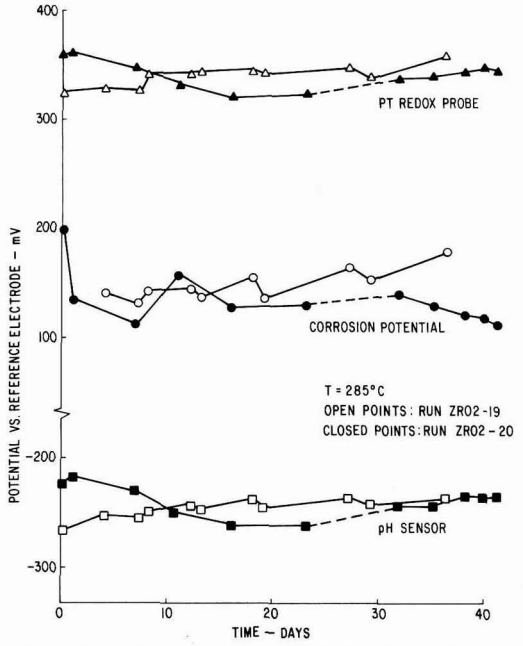

Fig. 5. Potentials measured against an Indig reference electrode. (0.0005*m* H_2SO_4 electrolyte; 8.2 ppm dissolved oxygen.)

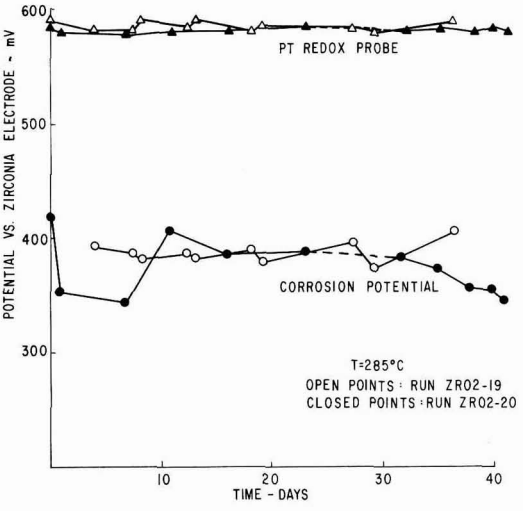

Fig. 6. Corrosion and redox potentials measured against the pH sensor. (0.0005*m* H_2SO_4 electrolyte; 8.2 ppm dissolved oxygen.)

(from the oxygen/water couple) is somewhat greater. As noted in the previous section this probably reflects *remaining* irreversibility in the oxygen reduction reaction at 285°C.

All of these data support the use of the *p*H sensor as an alternative reference electrode for the measurement of corrosion and redox potentials. They also indicate that using the *p*H sensor as a reference electrode automatically eliminates spurious *p*H change effects from the measurement of real interest, *i.e.*, the shift in the relative oxidation level of the system

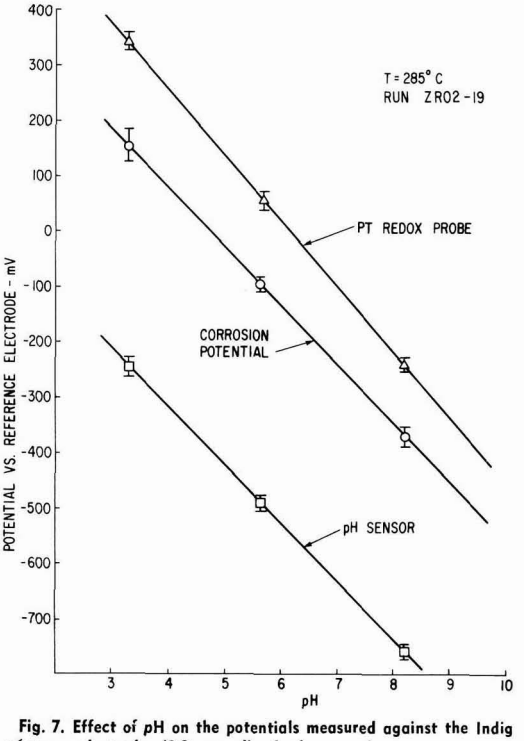

Fig. 7. Effect of *p*H on the potentials measured against the Indig reference electrode. (8.2 ppm dissolved oxygen.)

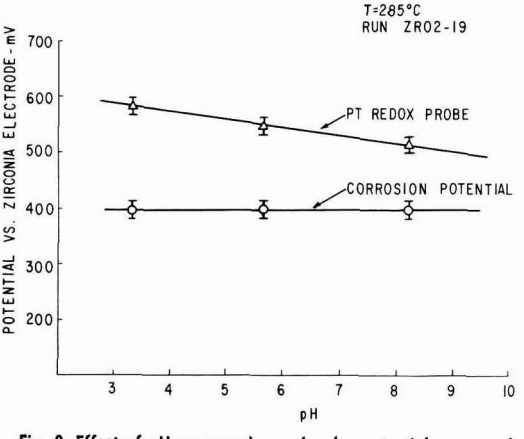

Fig. 8. Effect of *p*H on corrosion and redox potentials measured against the *p*H sensor. (8.2 ppm dissolved oxygen.)

through changes in concentration of redox active species *per se*.

In-Plant Applications

For in-plant applications we would envision the insertion of zirconia electrodes at a variety of locations where monitoring of corrosion and/or redox potential(s) were felt appropriate. In its simplest form the probe would be inserted through the wall of a pipe or flange. Only a female ¼ in. NPT is required for mounting. To monitor corrosion potentials a high impedance meter could be connected directly across the sensor and the pipe as indicated in Fig. 9. Because a small

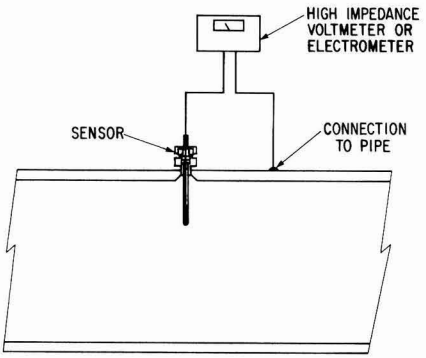

Fig. 9. Mounting of sensor for direct monitoring of the corrosion potential of a pipe.

platinum redox probe will respond more rapidly to changes in water chemistry than will the large area piping, it would generally be desirable to include such a probe in the monitoring system. This too can be inserted through a ¼ in. NPT, and it can be multiplexed to a common high impedance meter.

To allow for possible breakage of a zirconia tube, a slightly more sophisticated arrangement might be desired in which the zirconia sensor is surrounded by a screen or perforated shield that could retain any broken pieces. The screen or shield could be constructed of the same alloy as the piping and connected electrically to the piping. Under such conditions it would assume the corrosion potential of the more massive system and should not interfere with measurements.

It is conceivable that sensors would be desired at several sites around a plant as indicated in Fig. 10 where a boiling water reactor power plant is used as an example. In such a case it would probably be desirable to monitor potentials immediately after the demineralizers, farther along the feedwater train, and in the cooling water recirculation loop.

Acknowledgment

The author wishes to thank W. H. Stoddard for assistance with the fabrication of sensors and many of the measurements.

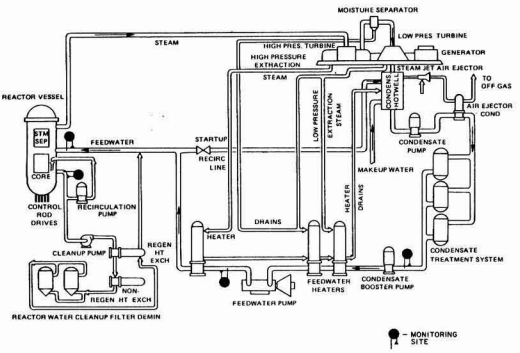

Fig. 10. Potential sites for monitoring corrosion potentials

Manuscript submitted Nov. 16, 1981; revised manuscript received Dec. 10, 1981. This was Paper 427 presented at the Denver, Colorado, Meeting of the Society, Oct. 11-16, 1981.

Any discussion of this paper will appear in a Discussion Section to be published in the June 1983 JOURNAL. All discussions for the June 1983 Discussion Section should be submitted by Feb. 1, 1983.

Publication costs of this article were assisted by General Electric Company.

REFERENCES

1. R. L. Cowan and A. I. Kaznoff, *Corrosion,* **29,** 123 (1973).
2. M. E. Indig, J. E. Weber, and A. D. Miller, *ibid.,* **34,** 3 (1978).
3. D. D. Macdonald, A. C. Scott, and P. Wentrcek, *This Journal,* **128,** 250 (1981).
4. L. W. Niedrach, *ibid.,* **127,** 2122 (1980).
5. D. J. G. Ives and G. J. Janz, Editors, pp. 261-263, "Reference Electrodes," Academic Press, New York (1961).
6. K. J. Vetter, "Electrochemical Kinetics," Translated by S. Bruckenstein and B. Howard, p. 17 ff, Academic Press, New York (1967).
7. D. M. Himmelblau, *J. Chem. Eng. Data,* **5,** 10 (1960).
8. D. D. Macdonald, G. R. Shierman, and P. Butler, AECL-4136, December 1972.
9. JANAF Supplement 54, December 1978.
10. M. E. Indig and A. R. McIlree, *Corrosion,* **35,** 288 (1979).

Reactions of Formation and Stability of Iron (II) and (III) Oxides in LiCl-KCl Eutectic Melt at 470°C

G. Picard, F. Seon[1], and B. Tremillon*

Laboratoire d'Electrochimie Analytique et Appliquée, Laboratoire associé au C.N.R.S., No. 216, Ecole Nationale Supérieure de Chimie de Paris, Université Pierre et Marie Curie, F. 75231 Paris Cedex 05, France

ABSTRACT

The study of the different oxides of iron (II) and iron (III) was carried out potentiometrically in LiCl-KCl eutectic at 470°C by means of an yttria-stabilized zirconia electrode indicator of the oxide ion activity and an iron electrode indicator of the ferrous ion activity. These measurements were complemented by the determination of cyclic voltammograms and by x-ray diffraction and infrared spectrophotometry analysis of certain compounds formed. The main results obtained are the following: strong oxidizing power (oxidation of Cl^- ions into Cl_2) and high oxoacidity (great stability of ferric oxide) of Fe^{3+} ions; possible redissolution of Fe_2O_3 in the oxide ion rich media by the formation of ferrate (III) ion; $FeO_2^- \cdot Fe^{2+}$ ions react with O^{2-} ions to form ferrous oxide, which is probably stabilized in the form of a solid solution FeO-$LiFeO_2$ of composition $Fe_{1-y}Li_yO$. Magnetic oxide, Fe_3O_4, is stable and can be obtained by the action of oxide ions on a mixture of iron (II) and iron (III). The standard potentials of the different electrochemical systems, which involve iron in its different oxidation states, and the expressions of these potentials as a function of the oxide ion activity and different concentrations were given. The solubility products of iron oxides were also determined; the values corresponding to ferrous oxide, magnetic oxide, and ferric oxide are, respectively, $10^{-5.4}$, $10^{-36.3}$, and $10^{-29.6}$ (molality scale). The constant of formation of ferrate (III) ion (from ferric oxide) has the rough value $10^{1.9}$ mol $\cdot$ kg^{-1}. These results were assembled in the form of a potential $-p_{O^{2-}}$ equilibrium diagram which shows, in particular, that in oxobasic media, magnetic oxide disproportionates into ferrate (III) and FeO. In the presence of a high concentration of oxide anion, FeO leads to the formation of metallic iron because of its disproportionation into FeO_2^- and Fe (s).

In fused chlorides, and in particular in LiCl-KCl eutectic, iron exists in the oxidation states O, II, and III (1). Iron (II) and iron (III) are known to form numerous chemical combinations with oxide ion, such as ferrous oxide, magnetic oxide, and ferric oxide. Certain compounds, which are richer in O^{2-} ions than the oxides of iron of the same oxidation state, are also known; ferrates (III) of the type $MFeO_2$ (M = Li, K, for example) or $M'Fe_2O_4$ (M' = Co, Ni, Mn, Zn, Mg). Iron is also included in the composition of many more complex compounds existing in the natural state, such as chromite, FeO $\cdot$ Cr_2O_3; ilmenite, FeO $\cdot$ TiO_2; hercynite, FeO $\cdot$ Al_2O_3, etc.

The large number of chemical combinations involving the O^{2-} ion and iron (II) and iron (III) (alone or in the presence of other metals), underlines the interest of an analytical study of their chemical and electrochemical formations.

As a result of their role in the construction of rechargeable and high performance batteries, the properties of sulfide compounds of iron in LiCl-KCl melt have been the subject of many studies (2), but the oxides, on the other hand, have been studied very little. Delarue has qualitatively established the potential-$p_{O^{2-}}$ diagram of iron and has considered that ferric oxide is not stable in this medium and decomposes to magnetic oxide (3); Iwanec and Welch have showed the formation of hematite by oxidation of ferrous chloride with oxygen (4). Inman *et al.* (5) and Legey (6) have studied iron and chromium in LiCl-KCl eutectic in order to elucidate the chemical behavior of chromite, FeO $\cdot$ Cr_2O_3. However, they have not determined any solubility product corresponding to the oxides of the elements studied; only Molina (7) has given a value for ferrous oxide (*i.e.*, $10^{-5.0}$ mol^2 $\cdot$ kg^{-2}) at 480°C.

Thus there is little experimental data concerning iron oxides in fused chlorides. In addition, the data is sometimes contradictory (as is the case of ferric oxide). The aim of this study was to determine the nature and the stability of the different oxides of iron (II) and iron (III), by defining the conditions of their formation in LiCl-KCl eutectic at 470°C, the temperature of our previous studies (8-11).

This aim was achieved by carrying out potentiometric titrations involving, on the one hand, O^{2-} ions, and, on the other hand, iron (II) and iron (III), while the oxide ion activity was measured by means of an yttria-stabilized zirconia electrode. To facilitate the interpretation of these titration curves, analysis of the compounds formed was carried out by x-ray diffraction and infrared spectrophotometry analysis. Finally, this study was completed by analysis of several voltammograms obtained at a glassy carbon electrode.

Experimental

Technique and procedure. — *Potentiometry.* — The electrochemical cell, the furnace, the programmable regulation, the reference electrode (Ag/Ag$^+$ 0.75 mol $\cdot$ kg^{-1}), and the yttria-stabilized zirconia electrode have been described previously (8). All potentials are *vs.* the standard chlorine electrode whose potential is +1.027V with respect to our reference electrode (9). The iron electrodes used for the coulometric generation of Fe^{2+} ions and for the measurement of their activities consisted of a 1 mm diam iron wire of high purity, supplied by Johnson-Matthey. The electrodes were cleaned before each experiment by means of concentrated hydrochloric acid. The coulometric production of Fe^{2+} ions in the eutectic was carried out automatically by means of a previously described electronic apparatus (9). Measurements of weight loss of the iron electrode as a function of the quantity of electricity have given the number of electrons exchanged during the oxidation reaction, *i.e.*, $n = 2.05 \pm 0.07$. The auxiliary compartment used for the coulometries was analogous to the one designed by Legey (6); it is formed from a Pyrex closed end tube having a sintered Pyrex side arm 2.0 cm from the bottom. The cathode was composed of liquid bismuth that forms an alloy with the lithium produced during the reduction of the eutectic. This device prevents any metallic dendritic growth that could damage the sintered glass. The electric contact was made from a tungsten wire that was covered with Pyrex glass. The iron (II) solutions produced are colorless.

The values of $p_{O^{2-}}$ were deduced from measurements of the potential of an yttria-stabilized zirconia electrode. Standardization of this electrode was carried out by the oxoacidobasic HCl(g)/H_2O(g) couple before

* Electrochemical Society Active Member.
[1] Present address: Rhone-Poulenc Recherches, Centre de Recherches d'Aubervilliers, 93308 Aubervilliers, Cedex, France.
Key words: thermodynamics, fused salts, solubility, voltammetry.

each titration experiment, and by the $CO_3^{2-}/CO_2(g)$ couple or of an excess of oxide ions at the end of the experiment, as was described earlier (8).

The variation of the potential of the iron electrode as a function of the number of coulombs of Fe(II) ions introduced was measured by an Aries 20000 Tacussel millivoltmeter as a function of the logarithm of this concentration and is indeed linear (Fig. 1). Two experiments were carried out, and the observed experimental slope is close to the theoretical value of 0.074V. The standard potential of the Fe(s)/Fe(II) electrochemical system (*vs.* the standard chlorine electrode) is: $E_o°(Fe(s)/Fe(II)) = -1.447 \pm 0.010V$ (1). This value is comparable to that obtained at 450°C by Laitinen *et al.* (12, 13) (−1.478V) and subsequently confirmed by Saboungi *et al.* (2c).

Cyclic voltammetry.—The voltammetric scans were performed with a Tacussel "PRT 30" fast-rise potentiostat coupled with a GSTP-3 function generator. The *i-E* curves were recorded on an XY Sefram TRP 10-100. The indicator electrode used was made from 3 mm diam glassy carbon rod (quality V.25) supplied by Carbone-Lorraine.

X-ray diffraction analysis.—The precipitates formed *in situ* were kept in a desiccator under vacuum. At the time of their analysis, they were reduced to powder, then washed, and dried. The washing operation is indispensable in order to dissolve a large quantity of eutectic (lithium and potassium chlorides) whose presence leads to very pronounced lines that can mask those of the compounds formed; it has the disadvantage, however, of also eliminating all the other soluble compounds. Nevertheless, the x-ray diffraction patterns permit qualitative identification of the products as well as an estimation of their proportions.

Infrared spectrophotometry.—The procedure is that described by Brunet and Labbe (14): 1 mg of recovered product is mixed with 200 mg of cesium bromide, then made into a pellet by means of a hydraulic press under a pressure of 1500 bars. The infrared spectra of the products, determined by means of a Perkin-Elmer 457 double-beam spectrophotometer, were compared with those of the reference compounds (Fe_2O_3, Fe_3O_4) and their mixtures in different proportions (in particular at the wave numbers 350, 400, 450, and 500 cm^{-1}).

Products.—The oxides α-Fe_2O_3 (purity: 99.999%) and $FeCl_3$ (purity: 98%) were supplied by Alpha-Ventron; Fe_3O_4, Na_2CO_3, LiCl, and KCl were PROLABO (quality: R.P.) products. The experimental details for the preparation and purification of the lithium chloride-potassium chloride eutectic have been described earlier (8). Potassium tetrachloroferrate was obtained by melting a mixture of KCl and $FeCl_3$ which was prepared previously in a glove dry box. Sodium carbonate was melted at 1000°C before use. All products were kept in a desiccator under vacuum.

Experimental Results

Behavior of hematite.—Delarue (3) has postulated that ferric oxide was not stable in this medium and that it led to the formation of magnetite, according to the decomposition reaction

$$3Fe_2O_3(s) \rightarrow 2Fe_3O_4(s) + 1/2\,O_2(g) \qquad [1]$$

It was necessary as a preliminary to verify experimentally the stability of ferric oxide. Part of the oxide used gave x-ray diffraction patterns of pure α-Fe_2O_3. Another part (8g) was introduced into 100g of eutectic at 470°C, which corresponded to a total Fe(III) concentration of 1 mol · kg^{-1}. After 3 hr of contact with the molten salt with vigorous stirring, the solid, which still showed a dark red coloration, was isolated and then analyzed with x-rays. The x-ray diffraction pattern obtained still corresponded to that of pure hematite and did not show the characteristic lines (2.967 and 4.85) of magnetite. It can be concluded that hematite remains stable in the molten salt. Furthermore, this conclusion confirms that of Iwanec and Welch (4).

Titrations of ferrous and ferric chloride solutions by sodium carbonate.—Adding potassium tetrachloroferrate into the eutectic, at total concentration C_o, leads to the formation of chlorine and ferrous chloride, whose concentration (which is the initial concentration at the beginning of titrations), $|Fe^{2+}|_i$, is related to that of the remaining ferric chloride, $|Fe^{3+}|_i$, by the relation

$$C_o = |Fe^{3+}|_i + |Fe^{2+}|_i \qquad [2]$$

Each experimental curve of the three titrations carried out (Fig. 2) shows two equivalence points, α_1 and α_T, corresponding to two successive chemical reactions; visual observation during these titrations, as well as the shape of the curves obtained, indicate the formation of precipitates. Table I gives the characteristic values of these titrations, *i.e.*, the values of α (defined as: α = added carbonate/C_o) corresponding to the equivalence points and the values of $p_{O^{2-}}$ referring to the beginning of each of the precipitation reactions. Finally, the results of x-ray diffraction and infrared

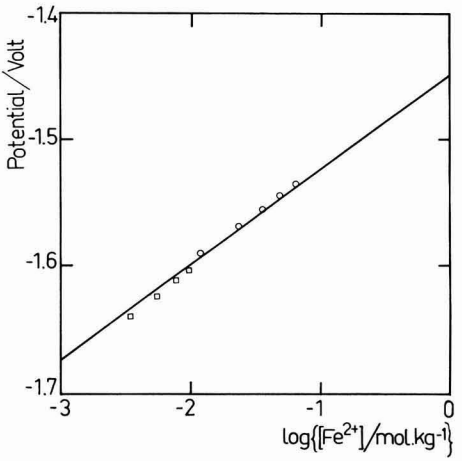

Fig. 1. Potentiometric determination of the standard potential of the Fe(s)/Fe(II) electrochemical system.

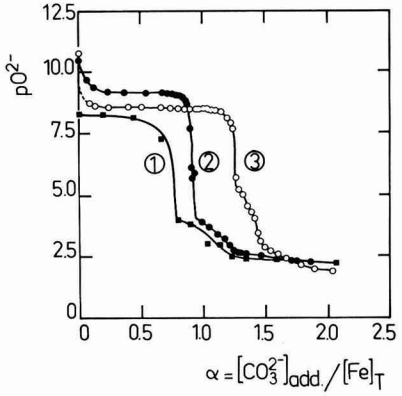

Fig. 2. Potentiometric titrations of iron (II) and (III) solutions of total concentration C_o by sodium carbonate in LiCl-KCl eutectic melt at 470°C. Curve 1: $C_o = 7.60 \cdot 10^{-2}$ mol · kg^{-1} (■); curve 2: $C_o = 0.63$ mol · kg^{-1} (●); curve 3: $C_o = 1.0$ mol · kg^{-1} (○).

Table I. Characteristics of the titration curves of ferrous and ferric chloride solutions by sodium carbonate in LiCl-KCl eutectic. Results of x-ray and infrared analysis of the products obtained. (α_1 = equivalence point corresponding to the end of the first reaction; α_T = cumulative equivalence point.)

Quantities	Experiment 1 C_o = $7.60 \cdot 10^{-2}$ mol · kg^{-1}	Experiment 2 C_o = 0.63 mol · kg^{-1}	Experiment 3 C_o = 1.00 mol · kg^{-1}
α_T	1.20	1.25	1.42
α_1	0.76	0.92	1.25
$p_{O_1}{}^{2-}$	8.4	9.2	8.8
$p_{O_2}{}^{2-}$	4.1	4.0	5.4
%Fe_2O_3 X-ray	—	Not analyzed	67.0
%Fe_2O_3 Infrared	—		60 ± 5
%Fe_3O_4 X-ray	54.5		33.0
%Fe_3O_4 Infrared	—		40 ± 5
%FeO X-ray	45.5		—

analysis of the products obtained, which permit identification of their nature and estimation of their proportions, are also given in the table. Thus, one notes that only the experiment carried out with the highest iron concentration (C_o = 1 mol · kg^{-1}) led to the formation of ferric oxide.

Titrations of oxide ion by potassium tetrachloroferrate.—As a result of the strong oxidizing strength of iron (III) chloride and its instability (5b), it is not possible, as in the case of aluminum (8), to carry out titrations of ferric chloride alone by sodium carbonate. But since the formation of stable oxide decreases the oxidizing strength it was possible to carry out the inverse titration (O^{2-} by the addition of Fe^{3+}).

When oxide ion is introduced by dissolution of sodium carbonate, under bubbling argon and then under vacuum, a solution of only Na^+ and O^{2-} ions is obtained. The curve corresponding to the titration of this solution (0.8 mol · kg^{-1}) by potassium tetrachloroferrate is shown in Fig. 3. We can see a weak increase of $p_{O^{2-}}$ for α_1 = 0.5 and a more pronounced increase for α_T = 0.66.

X-ray diffraction analysis of the recovered precipitate at the end of the experiment indicates clearly the formation of hematite. The product formed at the beginning of the titration was recovered in a second experiment carried out under the same conditions as the first but stopped at the value α = 0.42; x-ray diffraction patterns indicate that it is the ferrate $LiFeO_2$ in the presence of a certain quantity of $LiFe_5O_8$.

Electrochemical behavior of iron (II) and (III) at a glassy carbon electrode.—In a "neutral" medium.—In a "neutral" medium (without an oxoacidobasic system) the LiCl-KCl eutectic is not buffered with regard to oxide ions. The $p_{O^{2-}}$ value, measured by the zirconia electrode, before scanning of the voltammograms is only given as an indication; it indicates the presence of residual oxide ions and O^{2-} donor impurities.

The residual current at a glassy carbon electrode with a geometric area 7.07 mm^2 in LiCl-KCl eutectic (initial $p_{O^{2-}}$: 4.7) is shown as a function of the rate of variation of the potential, by curves 1, 2, and 3 in Fig. 4. A high cathodic intensity is observed toward −2.427V (peak b) followed by a reoxidation peak c.

In the presence of iron (II) (produced by coulometric oxidation of iron), the voltammograms have the general shape represented by curves 4, 5, and 6 in Fig. 4, obtained for an Fe^{2+} concentration of 4.88×10^{-3} mol · kg^{-1} [*i.e.*, 8.0×10^{-6} mol · cm^{-3}, using the density, 1.637 g · cm^{-3} determined by Van Artsdalen and Yaffe (15)] and with the respective voltage sweep rates of 0.121, 0.143, and 0.199 V · sec^{-1}. In addition to the preceding peaks (b and c), a reduction peak a and two reoxidation peaks d and e are observed. The intensity of the reduction peak a varies as a function of the rate of variation of the potential as shown in Table II.

Figure 5 shows the voltammograms corresponding to the oxidation of an Fe^{2+} solution of concentration 5.81×10^{-3} mol · kg^{-1}, where the rate of variation of the potential is between 0.131 and 0.031 V · sec^{-1} and the $p_{O^{2-}}$ initially measured is 5.7. These curves are entirely analogous to those obtained by Uchida *et al.* (16) with a tin oxide electrode. The magnitude of the residual current on the glassy carbon electrode does not permit one to obtain well-defined oxidation peaks of iron (II). The oxidation potential of Fe^{2+} into Fe^{3+} is very close to that of Cl^- into chlorine.

In oxobasic medium.—After a coulometric addition of $4.88 \cdot 10^{-3}$ mol · kg^{-1} of iron (II), the $p_{O^{2-}}$ of LiCl-KCl eutectic was buffered at a value of 0.1 (measured by the zirconia electrode) by adding sodium carbonate, whose decomposition was made complete by the creation of a partial vacuum. The curves obtained (Fig. 6) have the same general shape as that corresponding to

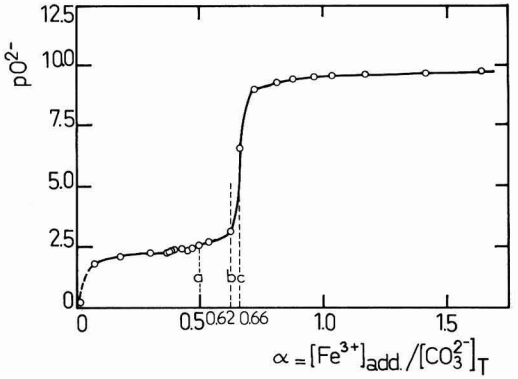

Fig. 3. Potentiometric titration of oxide ion (initial concentration 0.80 mol · kg^{-1}) by potassium tetrachloroferrate (III).

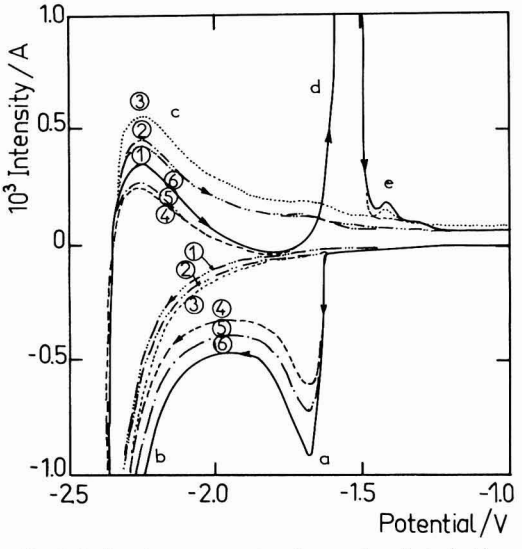

Fig. 4. Cyclic voltammograms at a glassy carbon electrode (A = $7.07 \cdot 10^{-2}$ cm^2) in LiCl-KCl eutectic melt at 470°C. Curves 1, 2, and 3, without Fe^{2+}; curves 4, 5, and 6, with Fe^{2+} $4.88 \cdot 10^{-3}$ mol · kg^{-1}. Voltage sweep rates: curves 1 and 4, 0.121 V · sec^{-1}; curves 2 and 5, 0.143 V · sec^{-1}; curves 3 and 6, 0.199 V · sec^{-1}.

Table II. Electrochemical behavior of iron, at a glassy carbon electrode ($A = 7.07$ mm^2) in LiCl-KCl eutectic melt at 470°C (C_o = concentration of Fe^{2+} initially introduced)

Medium	v/V · sec^{-1}	$-10^5 I_p$/A
"Neutral," $p_{O^{2-}} \sim 4.7$	0.121	58
$C_o = 8.0 \cdot 10^{-6}$ mol · cm^{-3}	0.143	68
	0.199	87
Oxobasic, $p_{O^{2-}} \sim 0.1$	0.115	50
$C_o = 8.0 \cdot 10^{-6}$ mol · cm^{-3}	0.230	73
	0.454	79-80

the neutral medium. Again, a reduction peak (a') is observed, followed by a sharp increase of the cathodic current (b'), and reoxidation makes three peaks (c', d', and e') appear. It should be noted, first of all, that peak e' is correspondingly larger when the potential has previously attained more negative values (compare curve 1 to curves 2, 3, and 4), and secondly, that the difference in potential between the reoxidation peaks d' and e' is virtually equal to that observed for peaks d and e in neutral medium (Fig. 4). The rates of variation of the potential and the corresponding intensities of the reduction peak a' are given in Table II.

Interpretation and Discussion

Formation of Ferric, Magnetic, and Ferrous Oxides and Determination of Their Solubility Products

Principle of interpretation of the titration curves of ferrous and ferric chloride solutions.—The initial concentrations of Fe^{3+} and Fe^{2+} ions are expressed on the basis of their sum (relation [2]) and their ratio x

$$|Fe^{3+}|_i = xC_o(1 + x)^{-1} \quad [3]$$

and

$$|Fe^{2+}|_i = C_o(1 + x)^{-1} \quad [4]$$

where $x = |Fe^{3+}|_i/|Fe^{2+}|_i$. In the formation of ferric, magnetic, and ferrous oxides, two cases were considered: (*i*) the first oxide to precipitate is ferric oxide and (*ii*) the first oxide to precipitate is magnetite. In each case, the relations between the values of α corresponding to the titration equivalence points, the values of $p_{O^{2-}}$ of the precipitation of the oxides, and the proportions of oxides formed, on the one hand, and the values of x and C_o, on the other hand, were established.

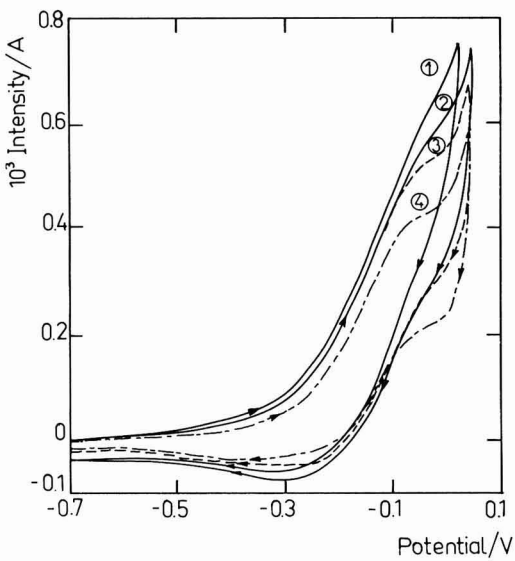

Fig. 5. Cyclic voltammograms at a glassy carbon electrode ($A = 7.07 \cdot 10^{-2}$ cm^2) corresponding to the Fe(II)/Fe(III) system in LiCl-KCl eutectic at 470°C containing Fe^{2+} $5.81 \cdot 10^{-3}$ mol kg^{-1}. Voltage sweep rates: curve 1, 0.131 V · sec^{-1}; curve 2, 0.123 V · sec^{-1}; curve 3, 0.076 V · sec^{-1}; curve 4, 0.031 V · sec^{-1}.

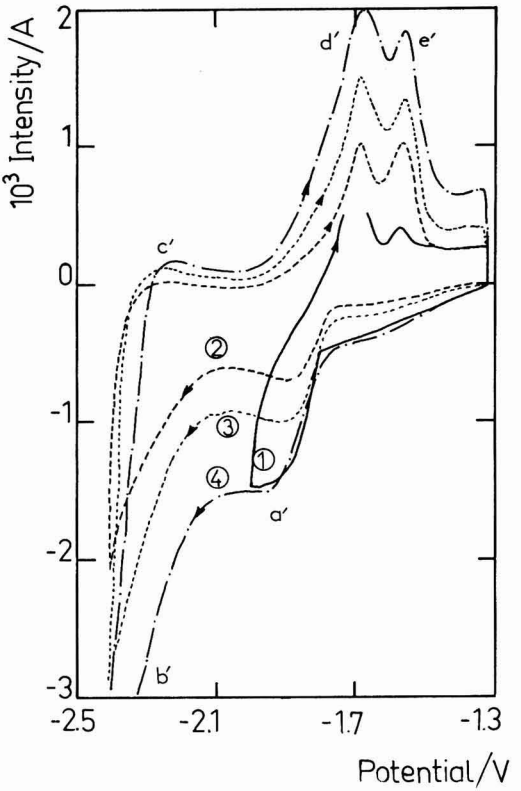

Fig. 6. Cyclic voltammograms at a glassy carbon electrode ($A = 7.07 \cdot 10^{-2}$ cm^2) corresponding to the reduction of iron (III) produced by the disproportionation of Fe(II) $4.88 \cdot 10^{-3}$ mol · kg^{-1}. LiCl-KCl eutectic buffered at $p_{O^{2-}} = 0.1$. Voltage sweep rates: curves 1 and 4, 0.454 V · sec^{-1}; curve 2, 0.115 V · sec^{-1}; curve 3, 0.230 V · sec^{-1}.

Only the calculations corresponding to the first hypothesis are shown here, as an example; only the results are given for the second hypothesis. In addition, the ferrous oxide formed is assumed to be stoichiometric as postulated by Delarue (3), Molina (7), and Legey (6).

Establishment of the relation $\alpha = f(x)$.—The equivalence point corresponding to the end of the precipitation reaction

$$2Fe^{3+} + 3CO_3^{2-} \rightarrow Fe_2O_3(s) + 3CO_2(g) \quad [5]$$

is such that the concentration of carbonate added, $|CO_3^{2-}|_{add.}$, is expressed as a function of the initial iron (III) concentration by the relation

$$|CO_3^{2-}|_{add.} = 1.5\,|Fe^{3+}|_i = 1.5\,xC_o(1 + x)^{-1}$$

The relationship α_1 between the quantity of carbonate added and the quantity of tetrachloroferrate introduced is therefore

$$\alpha_1 = \frac{|CO_3^{2-}|_{add.}}{C_o} = 1.5x(1 + x)^{-1}$$

This first equivalence point thus depends on the value of x and is not necessarily equal to 1.5. As $x \rightarrow \infty$,

i.e., when there is no iron (II), $\alpha_1 \rightarrow 1.5$ (formation exclusively of Fe_2O_3).

When the formation of ferric oxide is finished, the excess carbonate can react with the Fe^{2+} ions to form ferrous oxide. But, thermodynamically, this oxide is likely to reduce ferric oxide to form magnetite. It will thus be postulated that the reaction is, in fact, the following

$$Fe_2O_3(s) + Fe^{2+} + CO_3^{2-} \rightarrow Fe_3O_4(s) + CO_2(g) \quad [6]$$

whose equilibrium constant is deduced from the constant K of the reaction

$$Fe_2O_3(s) + Fe^{2+} + O^{2-} \rightarrow Fe_3O_4(s)$$

and from the dissociation constant, K_D, of the carbonate ions.

Two cases can be distinguished: either limitation of reaction [6] by the quantity of Fe_2O_3 formed (if $x < 2$), or limitation by the concentration of iron (II) (if $x > 2$).

The case of $x > 2$: formation of Fe_3O_4: The concentration of carbonate added during reaction [6] is thus expressed by

$$|CO_3^{2-}|_{add.} = |Fe^{2+}|_i = C_o(1 + x)^{-1}$$

and the second equivalence point α_2 by the relation

$$\alpha_2 = (1 + x)^{-1}$$

The same value of α_2 would be obtained by postulating the formation of FeO. The value of α_T, corresponding to the total quantity of carbonate necessary for the formation of Fe_2O_3 and then Fe_3O_4, is thus

$$\alpha_T = \alpha_1 + \alpha_2 = (1.5x + 1)\ (1 + x)^{-1}$$

Case of $x < 2$: formation of Fe_3O_4 and then FeO: The quantity of ferric oxide produced during reaction [5] limits the quantity of Fe_3O_4 which is obtained. The second equivalence point (reaction [6]) thus corresponds to the relations

$$|CO_3^{2-}|_{add.} = 0.5\ |Fe^{3+}|_i = 0.5x\ C_o(1 + x)^{-1}$$

where $\alpha_2' = 0.5x\ (1 + x)^{-1}$.

It is then possible to form ferrous oxide by means of an excess of sodium carbonate, according to

$$Fe^{2+} + O^{2-} \rightarrow FeO(s)$$

In this case a third equivalence point appears, whose value depends on the quantity of Fe^{2+} remaining, $|Fe^{2+}|_r$, at the end of the second precipitation (reaction [6])

$$|Fe^{2+}|_r = |Fe^{2+}|_i - 0.5|Fe^{3+}|_i = C_o(1 + x)^{-1} - 0.5xC_o(1 + x)^{-1}$$

The equivalence point α_3' is thus given by

$$\alpha_3' = (1 - 0.5x)\ (1 + x)^{-1}$$

and the total quantity of carbonate added is given by

$$\alpha_T = (1.5x + 1)\ (1 + x)^{-1}$$

α_T is thus independent of whether x is greater or less than 2.

Relations between the proportions of oxides formed and the value of the ratio x.—Case of $x > 2$: formation of Fe_2O_3 and then Fe_3O_4: The number of mols $[n(Fe_2O_3)]$ of Fe_2O_3 produced during reaction [5] is given by

$$n(Fe_2O_3) = 0.5n\ (Fe_i^{3+})$$

where $n(Fe_i^{3+})$ represents the number of mols of Fe^{3+} initially contained in an amount m of eutectic (where m is expressed in grams). Its value is

$$n(Fe_2O_3) = 0.5xC_o(1 + x)^{-1} \cdot m \cdot 10^{-3} \quad [7]$$

The number of mols $[n(Fe_3O_4)]$ of Fe_3O_4 formed during reaction [6] is equal to that which corresponds to iron (II)

$$n(Fe_3O_4) = C_o(1 + x)^{-1}\ m \cdot 10^{-3} \quad [8]$$

The number of mols of Fe_2O_3 remaining at the end of the experiment is thus

$$n(Fe_2O_3)_r = (0.5x - 1) \cdot C_o(1 + x)^{-1} \cdot m \cdot 10^{-3} \quad [9]$$

From relations [8] and [9] it is possible to deduce the proportions of oxides formed during the experiment; they are equal to $(x - 2)x^{-1}$ for ferric oxide and to $2x^{-1}$ for magnetite.

Case of $x < 2$: formation of Fe_2O_3 and then Fe_3O_4 and FeO: The number of mols of Fe_2O_3 produced during reaction [5] is given by Eq. [7]. However, reaction [6] leads to the total transformation of ferric oxide into magnetite. The quantity of Fe_3O_4 formed is therefore given by the same relation [7]

$$n(Fe_3O_4) = 0.5xC_o(1 + x)^{-1}\ m \cdot 10^{-3}$$

and

$$n\ (Fe_2O_3) = 0$$

The quantity of ferrous oxide subsequently obtained depends on the number of mols of Fe^{2+} remaining

$$n(FeO) = \alpha_3' \cdot C_o \cdot m \cdot 10^{-3}$$

and thus

$$n(FeO) = (1 - 0.5x)\ (1 + x)^{-1} \cdot C_o \cdot m \cdot 10^{-3}$$

The proportions of oxides are therefore the following: $0.5x$ for magnetite and $1 - 0.5x$ for ferrous oxide.

$p_{O^{2-}}$ at the beginning of precipitation as a function of x, C_o, and the solubility products of the oxides.—Case of $x > 2$: Ferric oxide precipitates from the value of $p_{O^{2-}}$ given by

$$p_{O_1^{2-}} = 1/3\ [pK_s(Fe_2O_3) - 2pFe_i^{3+}] \quad [10]$$

where pFe_i^{3+} is obtained from Eq. [3].

The beginning of the precipitation of Fe_3O_4 takes place at a value of $p_{O^{2-}}$ equal to

$$p_{O_2^{2-}} = pK - pFe_i^{2+} \quad [11]$$

where the value of pFe_i^{2+} is deduced from relation [4]. (The constant K corresponds to reaction [6], where the partial pressure of carbon dioxide is very low.)

Case of $x < 2$: As in the preceding case, ferric oxide, Fe_2O_3 precipitates first at a value of $p_{O^{2-}}$ given by Eq. [10], then magnetic oxide at a value of $p_{O^{2-}}$ given by expression [11], and finally ferrous oxide when the value of $p_{O^{2-}}$ attained is given by

$$p_{O_3^{2-}} = pK_s\ (FeO) - pFe^{2+}$$

where

$$pFe^{2+} = -\log |Fe^{2+}|_r = -\log [(1 - 0.5x)\ C_o(1 + x)^{-1}]$$

Diagnostic criteria.—The same calculations carried out, taking as a hypothesis that Fe_3O_4 precipitates first, give different results, which are presented in Table III, along with those just established above. These results depend on the hypothesis used to obtain them. They can thus be used, by comparison with experimental values, to "choose" the most realistic hypothesis concerning the reactions that really take place. These quantities (Table III) thus serve as "diagnostic criteria" and are used in the following way.

Criterion (n) shows that the quantity α_T depends only on the value of x; its expression is independent of the hypothesis which is postulated, and it remains valid whether the value of x is greater than, less than, or equal to 2. It thus, permits unambiguous determination of the value of x corresponding to a given titration; this value permits determination of the equivalence points corresponding to the different hypotheses

Table III. Interpretation of the titration curves of iron (II) and (III) solutions. Criteria corresponding to hypothesis I and II.

Hypothesis I	Hypothesis II
A—$x > 2$	
1. Precipitation of Fe_2O_3(s)	1. Precipitation of Fe_3O_4(s)
(a) $\alpha_1 = 1.5x\ (1 + x)^{-1}$	(i) $\alpha_1 = 4\ (1 + x)^{-1}$
(b) $p_{O_1}{}^{2-} = \frac{1}{3}\ [pK_s\ (Fe_2O_3) + 2 \log \{xC_o\ (1 + x)^{-1}\}]$	(j) $p_{O_1}{}^{2-} = \frac{1}{4}\ [pK_s\ (Fe_3O_4) + 2 \log \{xC_o\ (1 + x)^{-1}\} + \log \{C_o\ (1 + x)^{-1}\}]$
2. Precipitation of Fe_3O_4(s)	2. Precipitation of Fe_2O_3(s)
(c) $\alpha_2 = (1 + x)^{-1}$	(k) $\alpha_2 = 1.5\ (x - 2)(1 + x)^{-1}$
(d) $p_{O_2}{}^{2-} = pK + \log \{C_o\ (1 + x)^{-1}\}$ and $[pK = pK_s\ (Fe_3O_4) - pK_s\ (Fe_2O_3)]$	(l) $p_{O_2}{}^{2-} = \frac{1}{3}\ [pK_s\ (Fe_2O_3) + 2 \log \{C_o\ (x - 2)(1 + x)^{-1}\}]$
B—$x < 2$	
1. Precipitation of Fe_2O_3(s)	1. Precipitation of Fe_3O_4(s)
(a) $\alpha_1 = 1.5x\ (1 + x)^{-1}$	(m) $\alpha_1' = 2x\ (1 + x)^{-1}$
(b) $p_{O_1}{}^{2-} = \frac{1}{3}\ [pK_s\ (Fe_2O_3) + 2 \log \{xC_o\ (1 + x)^{-1}\}]$	(j) $p_{O_1}{}^{2-} = \frac{1}{4}\ [pK_s\ (Fe_3O_4) + 2 \log \{xC_o\ (1 + x)^{-1}\} + \log \{C_o\ (1 + x)^{-1}\}]$
2. Precipitation of Fe_3O_4(s)	2. Precipitation of FeO(s)
(e) $\alpha_2' = 0.5x\ (1 + x)^{-1}$	(g) $\alpha_2' = (1\text{-}0.5x)(1 + x)^{-1}$
(f) $p_{O_2}{}^{2-\prime} = pK + \log \{C_o\ (1 + x)^{-1}\}$	(h) $p_{O_2}{}^{2-\prime} = pK_s\ (FeO) + \log \{C_o\ (1\text{-}0.5x)(1 + x^{-1}\}$
3. Precipitation of FeO(s)	
(g) $\alpha_3' = (1\text{-}0.5x)(1 + x)^{-1}$	
(h) $p_{O_3}{}^{2-\prime} = pK_s\ (FeO) + \log \{(1\text{-}0.5x)\ C_o\ (1 + x)^{-1}\}$	
C—Value of α_T	
(n) $\forall$ hypothesis and $\forall\ x, \alpha_T = (1.5x + 1)(1 + x)^{-1}$	

D—Percentages of oxides precipitated

$\forall$ Hypothesis, they depend only on x

	$x > 2$	$x < 2$
$\%Fe_2O_3$	(o) $100\ (x - 2)\ x^{-1}$	0
$\%Fe_3O_4$	(p) $100 \times 2\ x^{-1}$	(q) $100 \times 0.5x$
%FeO	0	(r) $100\ (1\text{-}0.5x)$

and, consequently, comparison of them with experimental values. The order of the precipitation of oxides is thus determined and their solubility products are calculated from the values of $p_{O^{2-}}$ at the beginning of precipitation.

Results: The different characteristics of the curves shown in Fig. 2 were interpreted according to the previously defined criteria.—First experiment.—The equivalence point corresponds to $\alpha_T = 1.20$ (Table I), that gives, for the ratio x of the concentrations of iron (III) and iron (II), the value 0.67 (Table IV). The order of precipitation of the oxides is known from comparison of the two criteria (a) and (m). The value 0.80 of α_1' obtained by means of criterion (m) (Table IV) corresponds to the experimental value 0.76 (Table I). It is thus established that magnetic oxide, Fe_3O_4, precipitates first. Its solubility product (38.0) is obtained by applying criterion j. The solubility product of ferrous oxide, which is then formed, is estimated by means of criterion h: its value is equal to 5.6. Finally criteria q and r give the following proportions of these two oxides: 33.5% for Fe_3O_4 and 66.5% for FeO.

Table IV. Interpretation of the titration curves of iron (II) and (III) solutions (obtained by adding $KFeCl_4$ at the concentration C_o (mol · kg^{-1}) into LiCl-KCl eutectic at 470°C). $x = |Fe^{3+}|/|Fe^{2+}|$; see the text for the definition of criteria.

Quantities	Criteria	Experiment 1 $C_o = 7.6 \cdot 10^{-2}$	Experiment 2 $C_o = 0.63$	Experiment 3 $C_o = 1.00$
x	n	0.67	1.00	5.25
α_1	a	0.60	0.75	1.26
	i			0.64
α_1'	m	0.80	1.00	
$pK_s\ (Fe_2O_3)$	b			26.6
pK	d			6.2
$pK_s\ (Fe_3O_4)$	d			32.8
$pK_s\ (Fe_3O_4)$	j	38.0	38.3	
$pK_s\ (FeO)$	h	5.6	4.8	
$\%Fe_2O_3$	o			61.9
$\%Fe_3O_4$	p			38.1
$\%Fe_3O_4$	q	33.5	50.0	
%FeO	r	66.5	50.0	

Second experiment.—The value $\alpha_T = 1.25$ corresponds to $x = 1.0$. Determination of the first equivalence point by criteria a and m indicates, in this case as well, that magnetic oxide precipitates first ($\alpha_1' = 1.0$ and $\alpha_{exp} = 0.92$).

Thus, as previously, the solubility products of the two oxides are obtained: 38.3 for Fe_3O_4 and 4.8 for FeO.

By employing the same criteria as were used for the first experiment, it is shown that equivalent quantities of oxides were formed.

Third experiment.—This titration, carried out with the highest concentration of tetrachloroferrate, corresponds to the value $\alpha_T = 1.42$ or $x = 5.25$ (criterion n).

Application of criteria a and i indicates that ferric oxide precipitates first (α_1 calculated: 1.26; α_1 measured: 1.25). The solubility product of this oxide is given by criterion b: 26.6. The latter value is used to determine the solubility product of magnetic oxide by applying criterion d: 32.8. The percentages of these two oxides (criteria o and p) are: 61.9 for Fe_2O_3 and 38.1 for Fe_3O_4.

Conclusion.—X-ray diffraction analysis of the products formed during titration corroborates the preceding treatment of the titration curves with regard to the identification of the oxides formed and their respective proportions.

The percentages of ferric oxide and magnetite obtained during the third titration were, in fact, identical according to the different means of determining them (see Tables I and IV). In the case of the first titration, the proportion of magnetic oxide determined with x-ray diffraction is higher than that obtained from the titration curve. This seems to be due to partial oxidation of ferrous oxide to magnetic oxide by the carbon dioxide used at the end of the experiment (under a pressure of 1 atm) to realize a supplementary standardization of the zirconia electrode.

The variation of $p_{O^{2-}}$ obtained at the beginning of the second titration might suggest the transitory formation of oxychloride, but this seems improbable. Such a variation was not, in fact, observed during the first experiment, nor does the titration curve O^{2-} by tetrachloroferrate (Fig. 3) suggest this formation. It therefore seems more probable that this variation is due either to the slowness of the precipitation reaction or to the reaction of dissolved chlorine (produced by oxidation of Cl^- by potassium tetrachloroferrate introduced) with CO_3^{2-} ions

$$Cl_2(\text{dissolved}) + CO_3^{2-} \rightarrow \tfrac{1}{2}\,O_2(g) + CO_2(g) + 2Cl^-$$

Solubility Product of Ferric Oxide and Formation of Ferrate (III)

Solubility product of Fe_2O_3.—X-ray diffraction analysis showed that hematite precipitates during titration of oxide ion by potassium tetrachloroferrate (Fig. 3). After the equivalence point corresponding to the formation of this oxide ($\alpha = 0.66$), redissolution equilibrium can be envisaged by the formation of oxychloride

$$Fe_2O_3(s) + Fe^{3+} \leftrightarrows 3FeO^+ \qquad [12]$$

However, it should be noted that no equivalence point is observed for the value $\alpha = 1$ (which corresponds to the formation of 0.8 mol · kg^{-1} of oxychloride). Furthermore, the values given in Table V show that the equation

$$pK_s(Fe_2O_3) = 2pFe^{3+} + 3p_{O^{2-}}$$

corresponding to the sole dissociation equilibrium of Fe_2O_3 into Fe^{3+} and O^{2-} is confirmed. This permits a precise determination of the solubility product of ferric oxide

$$pK_s(Fe_2O_3) = 29.6 \text{ (with the standard deviation of 0.2)}$$

Contrary to the case of alumina (8), it is the most stable form of ferric oxide, according to x-ray diffraction analysis, that precipitates and the solubility product obtained is, thus, that of hematite, α-Fe_2O_3.

Formation of ferrate (III).—In Fig. 3, the equivalence points corresponding to the possible formation of $LiFeO_2$ and $LiFe_5O_8$ and then to the formation of Fe_2O_3, according to the reactions

$$2\,O^{2-} + Fe^{3+} \rightarrow FeO_2^- \qquad [13]$$

$$4FeO_2^- + Fe^{3+} + Li^+ \rightarrow LiFe_5O_8(s) \qquad [14]$$

$$3LiFe_5O_8(s) + Fe^{3+} \rightarrow 8Fe_2O_3(s) + 3Li^+ \qquad [15]$$

have been indicated by letters a, b, and c.

Table V. Determination of the solubility product of Fe_2O_3 by analysis of the end of the titration curve of the oxide ion (concentration C_o) by iron (III) introduced in the form of $KFeCl_4$. The concentration of Fe^{3+} is given by $|Fe^{3+}| = (\alpha - 0.66)C_o$.

α	pFe^{3+} calculated	$p_{O^{2-}}$ measured	$pK_s = 2pFe^{3+} + 3p_{O^{2-}}$
0.8	0.95	9.25	29.6_5
0.9	0.72	9.45	29.7_0
1.0	0.56	9.50	29.6_2
1.2	0.36	9.60	29.5_2
1.4	0.23	9.65	29.4_1
1.6	0.12	9.70	29.3_4

X-ray diffraction analysis of the product obtained for $\alpha = 0.42$ showed the presence of $LiFeO_2$ and $LiFe_5O_8$, which suggests that the three reactions given above take place during titration. Nevertheless, $LiFe_5O_8$ can also be produced, during partial washing of the recovered precipitate, by hydrolysis of $LiFeO_2$ according to

$$5LiFeO_2 + 2H_2O \rightarrow LiFe_5O_8 + 4LiOH$$

In this case, the reactions corresponding to the beginning of titration are reaction [13] and the reaction

$$3FeO_2^- + Fe^{3+} \rightarrow 2Fe_2O_3(s)$$

which seems more probable because of the value of α corresponding to the second equivalence point (0.66). Thus, for $\alpha = 0.50$, the equilibrium to be considered is

$$2FeO_2^- \leftrightarrows Fe_2O_3(s) + O^{2-} \qquad [16]$$

for which the corresponding constant is

$$K(FeO_2^-) = |FeO_2^-|^2/|O^{2-}|$$

Since the concentration of ferrate(III) ion is virtually equal to half the concentration of oxide ions initially added and the measured $p_{O^{2-}}$ is 2.7, it is possible to calculate this constant

$$\log K(FeO_2^-) = 1.9$$

which is comparable to the value previously estimated (1.7) for the formation of aluminate (8).

Solubility Product of Ferrous Oxide

Evaluation of the solubility product by ferrous oxide, assumed stoichiometric, and determination of the standard potentials $E°_1$ and $E°_5$ of the electrochemical systems Fe/FeO and FeO/Fe_3O_4.—The equilibrium constants of the oxide ion exchange reactions permit determination of the solubility products of metallic oxides by taking, as a reference, an oxoacidobasic couple of known constant such as HCl/H_2O (17, 18).

The solubility product of ferrous oxide, for example, can be obtained from the constant of the exchange reaction

$$FeO(s) + 2HCl(g) \leftrightarrows FeCl_2(\text{dissolved}^1) + H_2O(g) \qquad [17]$$

$$K = \frac{P(H_2O) \cdot [FeCl_2(\text{dissolved})]}{P(HCl)^2} = K_s(FeO)/K(H_2O/HCl)$$

This constant K can be determined from the variation of standard free enthalpy ΔG^* of reaction [17], but employing pure $FeCl_2(s)$ instead of $FeCl_2$(dissolved) and of the activity coefficient of ferrous chloride, which is related to the variation of standard free enthalpy, ΔG^{solv} of the dissolution reaction

$$FeCl_2(s) \rightarrow FeCl_2(\text{dissolved})$$

by the equation

$$\Delta G^{solv} = 2.3RT \log f(FeCl_2)$$

which gives

$$pK_s(FeO) = pK(H_2O/HCl) + \frac{\Delta G^*}{2.3RT} + \log f(FeCl_2)$$

The activity coefficient of ferrous chloride is calculated from the electromotive force $\Delta E°$ of the cell $Fe(s)/FeCl_2(\text{dissolved})/Cl_2(g)$ and the variation of standard free enthalpy ΔG_f^* of the formation of solid ferrous chloride, by means of the equation

$$\log f(FeCl_2) = (-2F\Delta E° - \Delta G_f^*)/2.3RT$$

where $\Delta E° = E°(Cl^-/Cl_2) - E°_o(Fe/Fe^{2+}) = 1.447V$, and $\Delta G^*_f = -249.2$ kJ (19).

[1] Which is generally noted as Fe^{2+}.

The experimental value of pK of the H_2O/HCl couple (8), the logarithm of the activity coefficient of ferrous chloride thus determined (−2.1), and ΔG^* obtained from the data in the literature (35.0 kJ) lead to the value $pK_s(FeO) = 5.4$, which is close to the experimental sum $p_{O^{2-}} + pFe^{2+} = 5.3$, which is observed during titration of ferrous ions by oxide ions (20). Furthermore, this value is in good agreement with the value experimentally determined by Molina (7), *viz.*, 5.0 at 480°C.

The variation of the standard free enthalpy, ΔG, of the reaction

$$Fe(s) + Fe_3O_4(s) \rightarrow 4FeO(s)$$

in related to the difference of standard potentials $E°_1$ and $E°_5$ (Table VI) of the electrochemical systems

$$Fe(s) + O^{2-} \rightarrow FeO(s) + 2e^- \qquad [18]$$

and

$$3FeO(s) + O^{2-} \rightarrow Fe_3O_4(s) + 2e^-$$

The standard potential $E°_0$ of the $Fe(s)/Fe^{2+}$ electrochemical system, −1.447V, and the solubility product of FeO(s), 5.3, give the standard potential, $E°_1 = -1.839$V, from which it is possible to obtain $E°_5$ (Table VI), knowing $\Delta G = -22.8$ kJ)

$$E°_5 = E°_1 - \frac{\Delta G}{2F} = -1.721\text{V}$$

The precision of this value depends largely on the value of the chemical potential of FeO, which is known with a lower precision since the variation of standard free enthalpy of formation of FeO from iron and magnetite is small.

The different standard potentials of the electrochemical systems using Fe^{2+} and FeO_2^- ions and the solids Fe, FeO, and Fe_3O_4 are collected in Table VI that also gives the variation of equilibrium potential corresponding to these various systems as a function of $p_{O^{2-}}$ and the different ionic concentrations in solution.

On the basis of these values, one can establish the potential-$p_{O^{2-}}$ equilibrium diagram represented in Fig. 7 that shows in a very oxobasic medium (high O^{2-} ion activity) that magnetite and ferrous oxide necessarily disproportionate according to

$$Fe_3O_4(s) + O^{2-} \rightarrow 2FeO_2^- + FeO(s) \qquad [19]$$

and

$$3FeO(s) + O^{2-} \rightarrow 2FeO_2^- + Fe(s) \qquad [20]$$

For sufficiently low values of $p_{O^{2-}}$, Fe_3O_4 is disproportionated, yielding metallic iron directly, through the formation of ferrate FeO_2^-

$$3Fe_3O_4(s) + 4\,O^{2-} \rightarrow 8FeO_2^- + Fe(s) \qquad [21]$$

The diagram in Fig. 7 is a simplified representation of the phenomena that presuppose a full range of existence of ferrous oxide. Not only is this oxide well known to be unstable at temperatures below 580°C, but the temperature at which our experiments were carried out is in the neighborhood of that (480°C) which corresponds to the maximum rate of disproportionation of pure ferrous oxide into magnetic oxide and metallic iron (21). It can thus be deduced that the presence of LiCl-KCl eutectic has a stabilizing effect on ferrous oxide. It has, indeed, been shown that it is possible to replace, in the ferrous oxide structure, two Fe^{2+} ions by an Fe^{3+} ion and a lithium ion (22), thus leading to solid solutions $Fe_{1-2y}{}^{2+}Fe_y{}^{3+}Li_y{}^+O^{2-}$ whose composition $[(1 - 2y)FeO + yLiFeO_2]$ can vary continuously from the oxide FeO ($y = O$) to lithium ferrate (III) $LiFeO_2$ ($y = 0.5$).

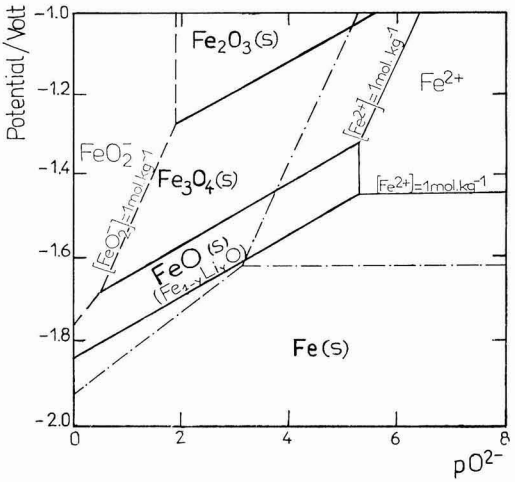

Fig. 7. Potential-$p_{O^{2-}}$ equilibrium diagram of iron in LiCl-KCl eutectic at 470°C: range of the most negative potentials. (The lines shown in this diagram correspond to the following concentrations: ———, — — —: 1 mol · kg^{-1}; — · —: 4.88 · 10^{-3} mol · kg^{-1}.

Taking these considerations into account, it is thus likely that what is precipitated is not pure ferrous oxide, but a stable solid solution according to the reaction (20)

$$(1 - 0.5y)Fe^{2+} + O^{2-} + (yLi^+) \rightarrow [Fe_{1-y}Li_yO](s) + 0.5yFe(s) \qquad [22]$$

Interpretation of Results Obtained by Cyclic Voltammetry

"Neutral" medium.—Part b of curves 1, 2, and 3 in Fig. 4 corresponds to the formation of intercalation compounds of lithium inside the carbon of the electrode.

Table VI. Expressions of the equilibrium potentials of the electrochemical systems of iron in LiCl-KCl eutectic melt at 470°C ($2.3RT/2F = 0.074$V; concentrations are expressed in the molality scale).

Electrochemical systems	Equilibrium potentials	Standard potentials/V (*vs.* Cl^-/Cl_2 (1 atm))
$Fe(s) - 2e^- = Fe^{2+}$	$E = E_0° + 0.074 \log \lvert Fe^{2+}\rvert$	$E_0° = -1.447$
$Fe(s) - 2e^- + O^{2-} = FeO(s)$	$E = E_1° + 0.074p_{O^{2-}}$	$E_1° = E_0° - 0.074pK_s\,(FeO) = -1.839$
$Fe^{2+} - e^- = Fe^{3+}$	$E = E_2° + 0.148 \log \{\lvert Fe^{3+}\rvert/\lvert Fe^{2+}\rvert\}$	$E_2° = -0.212$
$2Fe^{2+} - 2e^- + 3\,O^{2-} = Fe_2O_3(s)$	$E = E_3° + 0.222p_{O^{2-}} - 0.148 \log \lvert Fe^{2+}\rvert$	$E_3° = E_2° - 0.074pK_s\,(Fe_2O_3) = -2.402$
$3Fe^{2+} - 2e^- + 4\,O^{2-} = Fe_3O_4(s)$	$E = E_4° + 0.296p_{O^{2-}} - 0.222 \log \lvert Fe^{2+}\rvert$	$E_4° = E_2° - 0.074pK_s\,(Fe_3O_4) = -2.898$
$3FeO(s) - 2e^- + O^{2-} = Fe_3O_4(s)$	$E = E_5° + 0.074p_{O^{2-}}$	$E_5° = E_2° + 0.074\,[3pK_s\,(FeO) - pK_s\,(Fe_3O_4)] = -1.721$
$2Fe_3O_4(s) - 2e^- + O^{2-} = 3Fe_2O_3(s)$	$E = E_6° + 0.074p_{O^{2-}}$	$E_6° = E_2° + 0.074\,[2pK_s\,(Fe_3O_4) - 3pK_s\,(Fe_2O_3)] = -1.415$
$Fe_3O_4(s) + 2\,O^{2-} = 3FeO_2^- + e^-$	$E = E_7° + 0.296p_{O^{2-}} + 0.444 \log \lvert FeO_2^-\rvert$	$E_7° = E_0° + 0.222pK\,(FeO_2^-) = -1.837$
$FeO(s) + O^{2-} = FeO_2^- + e^-$	$E = E_8° + 0.148p_{O^{2-}} + 0.148 \log \lvert FeO_2^-\rvert$	$E_8° = E_2° + 0.074\,[pK\,(FeO_2^-) - pK_s\,(Fe_2O_3) + 2pK_s\,(FeO)] = -1.759$
$Fe(s) + 2\,O^{2-} = FeO_2^- + 3e^-$	$E = E_9° + 0.990p_{O^{2-}} + 0.049 \log \lvert FeO_2^-\rvert$	$E_9° = (2E_1° + E_8°)/3 = -1.812$
$Fe^{2+} + 2\,O^{2-} = FeO_2^- + e^-$	$E = E_{10}° + 0.296p_{O^{2-}} + 0.148 \log \{\lvert FeO_2^-\rvert/\lvert Fe^{2+}\rvert\}$	$E_{10}° = E_2° + 0.074\,[pK\,(FeO_2^-) - pK_s\,(Fe_2O_3)] = -2.543$

These compounds have been studied by Fondanaiche (23), James (24), and Selman (25). Their formation can be written schematically

$$xC + Li^+ + e^- \rightarrow C_xLi$$

They are reoxidized to give the oxidation peak c.

In the presence of Fe^{2+} ions (curves 4, 5, and 6) the cathodic peak is due to the reduction of these ions into metallic iron. The observed potential of reduction is in good agreement with that given by the previously determined Eq. [1]. The peak potential (−1.671V) is independent of the rate of variation of the potential; the difference between the peak potentials and the half-peak potentials (0.032V) is close to the theoretical value $0.773\ RT/n\mathbf{F} = 0.025$V at 743 K (26-28). Consequently, given the accuracy of reading the voltammograms, the Fe/Fe^{2+} electrochemical system can be considered reversible on the glassy carbon electrode. The intensities corresponding to the peaks on the voltammograms in Fig. 4 are thus expressed theoretically by (26, 27).

$$I_p = 2.33 \cdot 10^5\, n^{3/2} C A D^{1/2} v^{1/2} \qquad [23]$$

where the number of electrons exchanged $n = 2$, the concentration $C = 8.0 \cdot 10^{-6}$ mol · cm^{-3}, and the area of the electrode $A = 7.07 \cdot 10^{-2}$ cm^2. From this relation, the following equation can be deduced

$$AD^{1/2} = 0.19 I_p v^{-1/2}$$

The values of the product $AD^{1/2}$ thus obtained are $3.17 \cdot 10^{-4}$, $3.42 \cdot 10^{-4}$, and $3.71 \cdot 10^{-4}$ cm^3 · sec$^{-1/2}$ for the rates of the variation of the potentials, 0.121, 0.143, and 0.199 V · sec^{-1}, respectively. These values exhibit a significant shift between the value corresponding to the first curve scanned and the third. This difference is explained by the increase of the area of the glassy carbon electrode during successive cycles as a consequence of the formation of intercalation compounds C_xLi [this phenomenon has been used to obtain large-area electrodes (29)].

Using the value corresponding to the first voltammogram and supposing that the real area of the electrode was then close to the geometric area, it is possible to determine the diffusion coefficient of the Fe^{2+} ions. Its value of $2.0 \cdot 10^{-5}$ cm^2 · sec^{-1}, is in good agreement with the value obtained at 500°C by Inman *et al.* (5b) by chronopotentiometry with a tungsten electrode (average value $2.2 \cdot 10^{-5}$ cm^2 · sec^{-1}); this is nevertheless slightly higher than the value at 470°C deduced from the results of Poignet and Barbier (30) obtained as a function of the temperature, by chronopotentiometry with an iron electrode ($1.2 \cdot 10^{-5}$ cm^2 · sec^{-1}).

After reduction of the Fe^{2+} ions, part b of the voltammetric curve (Fig. 4) cannot be due to the formation of lithium-iron alloys. James (24) has shown that lithium deposits on the iron electrode and that the potential then takes the value corresponding to the electrochemical system Li/Li^+. Since this phenomenon was not observed here, it is probable that the iron deposit is not uniform (powdery or dendritic); it permits the lithium to attain the glassy carbon and form the compounds of intercalation previously mentioned. This formation is independent of the activity of oxide ions, as is shown by comparison of Fig. 4 and 6. Peak c thus corresponds to the reoxidation of C_xLi compounds, as in the absence of iron (II) ions, but nevertheless with lower intensity, which may be due to more difficult diffusion of Li^+ ions toward the carbon electrode to form C_xLi compounds. Peak d corresponds to the reoxidation of deposited metallic iron. The small peak (e') is not observed in the absence of previous reduction of Fe^{2+} ions and does not depend on $p_{O^{2-}}$; it is probably due to reoxidation of metallic iron which has diffused into the glassy carbon.

Oxobasic medium.—During the experiment corresponding to Fig. 6, iron (II), which has been introduced, was disproportionated upon addition of carbonate ions, according to the overall reaction

$$3Fe^{2+} + 4\,O^{2-} \rightarrow 2FeO_2^- + Fe(s)$$

Thus a solution is formed of FeO_2^-, whose concentration equals 2/3 of the concentration of Fe^{2+} ions initially introduced, *viz.*, $5.34 \cdot 10^{-6}$ mol · cm^{-3}.

With cathodic sweep, ferrate (III) is directly reduced to metallic iron, as is indicated by the potential-$p_{O^{2-}}$ diagram in Fig. 7, according to the electrochemical reaction

$$FeO_2^- + 3e^- \rightarrow Fe(s) + 2\,O^{2-}$$

The corresponding peak shows a difference between potential E_p and the half-peak potential which is clearly greater than the theoretical value for a reversible system with three electrons, *i.e.*, 0.017V. Effectively, the experimental values obtained are, for curves 2, 3, and 4 in Fig. 6, −0.070, −0.083, and −0.090V, respectively. Since the Fe/FeO_2^- electrochemical system is thus not reversible on the glassy carbon electrode, it was not possible to calculate the diffusion coefficient of ferrate (III) ions from the current of the peak. On the other hand, the limiting value m_1 of the semi-integral of the current, which is independent of whether or not the electrochemical system is reversible (31, 32), permits an estimation of the diffusion coefficient of ferrate (III) ion by means of the equation

$$m_1 = n\mathbf{F}ACD^{1/2}$$

In the case of curve 3 (Fig. 6) the value of m_1 was determined. The residual current was assumed to be identical to that obtained by linear extrapolation of the existing current before reduction of ferrate (III) ion. Since m_1 is $4.7 \cdot 10^{-4}$ As$^{1/2}$, we deduce an approximate value of the diffusion coefficient of FeO_2^- ($1.8 \cdot 10^{-5}$ cm^2 · sec^{-1}), which is slightly weaker than the diffusion coefficient of Fe^{2+} [or, in reality, $FeCl_4^{2-}$ (33)].

The standard potential of the $Fe(s)/FeO_2^-$ electrochemical system can be calculated from the constant of formation of ferrate ion and from the solubility products of ferric and ferrous oxides (Table VI). The equation for the equilibrium potential is thus obtained

$$E/V = -1.812 + 0.099\, p_{O^{2-}} + 0.049 \log |FeO_2^-| \qquad [24]$$

The values $p_{O^{2-}} = 0.1$ and $|FeO_2^-| = 3.25 \cdot 10^{-3}$ mol · kg^{-1} permit calculation of the value −1.924V, which is slightly lower than that determined from the voltammograms, in Fig. 6, but close to the peak potentials (−1.887, −1.895, and −1.947V). This shift and the fact that the electrochemical system is not reversible may be explained by the influence of the reduction of ferrous oxide (in solid solution), which is formed transiently and which might be not fully disproportionated. Therefore, only the value determined by relation [24] was taken into consideration.

Determination of the Solubility Product of Fe_3O_4 and the Standard Potential of Fe^{2+}/Fe^{3+} Electrochemical System

It is possible, as in the case of ferrous oxide, to estimate the solubility product of magnetic oxide by considering the exchange reaction of O^{2-}

$$Fe_3O_4(s) + 8HCl(g) \rightarrow$$

$$4H_2O(g) + FeCl_2(\text{dissolved}) + 2FeCl_3(\text{dissolved})$$

However, the activity coefficient of ferric chloride is not known and would have to be evaluated. Thus, it is preferable to determine both the solubility product $pK_s(Fe_3O_4)$ and the standard potential E°_2 of the Fe^{2+}/Fe^{3+} electrochemical couple, as follows.

Table VI provides the expressions of the equilibrium potentials of the iron electrochemical systems that can be considered on the basis of the existence of different iron oxides and of ferrate (III). One notes that the standard potential E°_5 of the $FeO(s)/Fe_3O_4(s)$ elec-

trochemical system depends on the standard potential $E°_2$ and the solubility products of ferrous oxide and magnetic oxide. In addition, the standard potential $E°_6$ of the $Fe_3O_4(s)/Fe_2O_3(s)$ electrochemical system depends on the standard potential $E°_2$ and the solubility products of magnetic and ferrous oxides.

The standard potentials $E°_5$ and $E°_6$ were obtained from the standard potential $E°_1$ of the Fe(s)/FeO(s) electrochemical couple [which is deduced from the solubility product $pK_s(FeO)$ and the potential $E_o{}^6$ of the $Fe(s)/Fe^{2+}$ couple] and from the values of the variations of standard free enthalpy of the reactions

$$Fe_3O_4(s) + Fe(s) \rightarrow 4FeO(s) \qquad [25]$$

and

$$3Fe_2O_3(s) + Fe(s) \rightarrow 2Fe_3O_4(s) + FeO(s) \qquad [26]$$

which permits calculation of the differences of standard potentials $E°_5 - E°_1$ and $E°_6 - E°_1$.

The solubility product of magnetic oxide and the standard potential $E°_2$ are then obtained by means of the following two equations

$$E°_5 - 0.222pK_s(FeO) = E°_2 - 0.074pK_s(Fe_3O_4)$$

and

$$E°_6 + 0.222pK_s(Fe_2O_3) = E°_2 + 0.148pK_s(Fe_3O_4)$$

The experimental values $E°_o = -1.447V$, $pK_s(FeO) = 5.3$, and $pK_s(Fe_2O_3) = 29.6$, as well as the variations of standard free enthalpies of reaction [25] (−22.79 kJ) and [26] (−81.83 kJ), give

$$E°_2 = -0.212V$$

$$pK_s(Fe_3O_4) = 36.3$$

The solubility product of magnetic oxide is close to the estimation based on titration curves of iron (II) and (III) solutions. Furthermore, the position of the Fe_3O_4/Fe_2O_3 electrochemical system in relation to that of oxygen (20), in the potential-$p_{O^{2-}}$ diagram (Fig. 8), clearly shows that there is no decomposition of ferric oxide into magnetic oxide and oxygen in this molten salt (stability of hematite).

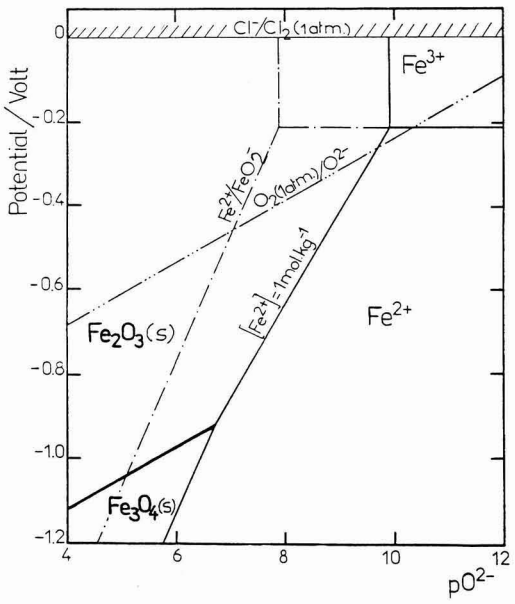

Fig. 8. Potential-$p_{O^{2-}}$ equilibrium diagram of iron in LiCl-KCl eutectic at 470°C: range of the most positive potentials (the lines shown in this diagram correspond to the following concentrations: ——: 1 mol · kg^{-1}; — · —: 4.88 · 10^{-3} mol · kg^{-1}.

The standard potential of the Fe^{2+}/Fe^{3+} electrochemical system is in good agreement with that found in the literature (1), which is −0.236V, with regard to the chlorine electrochemical system at 450°C, while ours was determined at the slightly higher temperature of 470°C. The latter value corresponds to that which can be obtained from voltammetric curves scanned with glassy carbon electrodes (Fig. 5) and explains the strong oxidizing strength of ferric chloride which is expressed by oxidation of LiCl-KCl eutectic according to (5b)

$$2Fe^{3+} + 2Cl^- \leftrightarrows Cl_2(g) + 2Fe^{2+} \qquad [27]$$

The kinetics of this reaction has been studied by Slàma and Mála (34) between 400° and 500°C. The constant K of equilibrium [27], $K = P(Cl_2) \cdot |Fe^{2+}|^2 \cdot |Fe^{3+}|^{-2}$, can be calculated from standard potentials of the two electrochemical systems involved

$$pK = [E°(Cl^-/Cl_2) - E°_2(Fe^{2+}/Fe^{3+})]/0.074 = 2.86$$

The relation which gives the partial pressure of chlorine as a function of the ratio of the concentrations of iron (II) and iron (III) is thus

$$\log P(Cl_2) = -pK + 2\log\{|Fe^{3+}|/|Fe^{2+}|\}$$

If one postulates a residual pressure of 10^{-3} atm of chlorine in LiCl-KCl eutectic, the addition of iron (III) leads to the formation of iron (II), until one obtains a ratio $|Fe^{3+}|/|Fe^{2+}| = 0.85$, which corresponds, at equilibrium to reduction of 54% of the iron (III) added.

Conclusion

The existence of oxidation states (II) and (III) of iron in LiCl-KCl eutectic at 470°C complicates the chemical and electrochemical behavior of this element in this molten salt. The potential-$p_{O^{2-}}$ equilibrium diagram of iron which has been established permits summing up, in an easily comprehensible form, the properties founded.

Without oxide ion, iron (III) is highly oxidizing and can oxidize the LiCl-KCl eutectic into chlorine, with the simultaneous formation of ferrous chloride. This reaction is very favorable for the formation of chlorine since more than 50% of the ferric chloride that is introduced into the eutectic is reduced. Thus the Fe^{3+} ion is stable only at high values of $p_{O^{2-}}$ and in the presence of a large quantity of ferrous ions that are necessary in order to lower the potential of the Fe^{2+}/Fe^{3+} electrochemical system.

It has also been shown that the presence of lithium oxide, even in small quantities, leads to the precipitation of ferric oxide, Fe_2O_3. This oxide is stable and does not decompose into oxygen and magnetic oxide in the fused bath. In addition, the oxide formed *in-situ* is hematite, *i.e.*, the most stable oxide of iron (III). One thus notes the different behavior of iron (III) and aluminum (III) in this eutectic; in the second case, it had been shown that it was possible to obtain a more reactive oxide than the α-alumina (8).

In a sufficiently basic medium (low value of $p_{O^{2-}}$) the oxide Fe_2O_3 redissolves, forming ferrate (III) ions, FeO_2^-. The existence of this ion plays a very large role in the chemical and electrochemical properties of iron in the eutectic.

It has been shown that in basic medium, iron (II) leads to the formation of ferrous oxide which is probably stabilized by the presence of the lithium of the eutectic. The ferrous oxide becomes unstable in highly basic media in which it disproportionates to give metallic iron and ferrate (III) ion in solution. Thus, in these media, metallic iron oxidizes directly to the oxidation state (III) (FeO_2^-).

In addition, it has been shown that the simultaneous presence of iron (II) and iron (III) can lead to the formation of magnetic oxide, Fe_3O_4. This oxide, which is stable when the activity of oxide ions is weak, dispro-

portionates into FeO and FeO_2^- in basic media, and even into metallic iron and FeO_2^- when the basicity is high enough to provoke also the disproportionation of the ferrous oxide.

Finaliy, it should be noted that a ferrate (II) of the type Li_2FeO_2, corresponding to the Li_2FeS_2 phase which has been shown in particular by Saboungi *et al.* (2c) in the case of sulfides, cannot be considered here according to our experimental results. Furthermore, while it was possible to determine unambiguously the solubility products of iron oxides, nevertheless, there exists an uncertainty concerning the value of the constant of formation of ferrate (III) ion.

Acknowledgments

We are grateful to the P.U.K. Company for the financial support of this research, and we would like to express our thanks especially to MM. Bertaud, Cohen, and Crussard of this company, for their interest in this work.

Manuscript submitted Feb. 23, 1981; revised manuscript received Oct. 27, 1981.

Any discussion of this paper will appear in a Discussion Section to be published in the June 1983 JOURNAL. All discussions for the June 1983 Discussion Section should be submitted by Feb. 1, 1983.

Publication costs of this article were assisted by Laboratoire d'Electrochimie Analytique et Appliquée.

REFERENCES

1. J. A. Plambeck, in "Encyclopedia of Electrochemistry of the Elements," Vol. X, A. J. Bard, Editor, Marcel Dekker, New York (1976).
2. See for instance: (a) G. Delarue, *Bull. Soc. Chim. Fr.*, 1654 (1960); *Rec. Trav. Chim. Pays Bas*, **79**, 510 (1960); (b) F. C. Mrazek and J. E. Battles, *This Journal*, **124**, 1556 (1977); (c) M. L. Saboungi, J. J. Marr, and M. Blander, *ibid.*, **125**, 1567 (1978); (d) G. Santarini, *C.R. Acad. Sci., Ser. C*, **288**, 457 and **289**, 421 (1979); (e) D. O. Raleigh, J. T. White, and C. A. Ogden, *This Journal*, **126**, 1087, 1093 (1979); (f) K. W. Kham and K. E. Johnson, *J. Electroanal. Chem. Interfacial Electrochem.*, **115**, 53 (1980).
3. G. Delarue, (a) *J. Electroanal. Chem.*, **1**, 285 (1959/1960); (b) Thesis, Paris, France (1960).
4. J. Iwanec and B. J. Welch, *Aust. J. Chem.*, **22**, 1783 (1969).
5. D. Inman, J. C. Legey, and R. Spencer, (a) *J. Electroanal. Chem. Interfacial Electrochem.*, **61**, 289 (1975); (b) *J. Appl. Electrochem.*, **8**, 269 (1978).
6. J. C. Legey, Ph.D., London, England (1973).
7. R. Molina, *Bull. Soc. Chim. Fr.*, 301, 1184 (1961); Rep. CEA No. 2125 (1962).
8. G. Picard, F. Seon, and B. Tremillon, *J. Electroanal. Chem. Interfacial Electrochem.*, **102**, 65 (1979).
9. G. Picard, F. Seon, B. Tremillon, and Y. Bertaud, *Electrochim. Acta*, **25**, 1453 (1980).
10. G. Picard, F. Seon, and Y. Bertaud, *ibid.*, **27**, 401 (1982).
11. F. Seon, Thesis, Paris, France (1981).
12. H. A. Laitinen and C. H. Liu, *J. Am. Chem. Soc.*, **80**, 1015 (1958).
13. H. A. Laitinen and J. W. Pankey, *ibid.*, **81**, 1053 (1959).
14. G. Brunet and J. P. Labbe, *Verres Refract.*, **33**, 695 (1979).
15. E. R. Van Artsdalen and I. S. Yaffe, *J. Phys. Chem.*, **59**, 118 (1955).
16. I. Uchida, K. Niki, and H. A. Laitinen, *This Journal*, 125, 1759 (1978).
17. G. Picard and J. Vedel, *J. Chim. Phys.*, **6**, 767 (1975).
18. B. Tremillon and G. Picard, *Anal. Chim. Acta*, **82**, 273 (1976).
19. I. Barin and O. Knacke, "Thermochemical Properties of Inorganic Substances," Springer Verlag, Berlin, Heidelberg, New York (1973).
20. F. Seon, G. Picard, and B. Tremillon, *J. Electroanal. Chem. Interfacial Electrochem.*, In press.
21. G. Chaudron, *C.R. Acad. Sci.*, **172**, 152 (1921); *Ann. Chim.*, **9**, 16 (1921).
22. R. Collongues and G. Chaudron, *C.R. Acad. Sci., Ser. C*, **231**, 143 (1950); R. Collongues, Thesis, Paris, France (1954); Publ. Scient. Min. Air. No. 324 (1957).
23. J. C. Fondanaiche and T. Kikindai, *Bull. Soc. Chim. Fr.*, **3**, 875 (1966); J. C. Fondanaiche, *C.R. Acad. Sci., Ser. C*, **264**, 805 (1967).
24. S. D. James, *This Journal*, **122**, 921 (1975).
25. J. R. Selman, "Electrochemistry of Lithium Carbide," ANI-75-43, 33 (1975).
26. P. Delahay, "New Instrumental Methods in Electrochemistry," p. 122, Interscience Publishers, Inc., New York (1954).
27. T. Berzins and P. Delahay, *J. Am. Chem. Soc.*, **75**, 555 (1953).
28. W. K. Behl, *This Journal*, **118**, 889 (1971).
29. H. A. Adams, U.S. Pat. 3,428,493 (1969).
30. J. C. Poignet and M. J. Barbier, *Electrochim. Acta*, **17**, 1227 (1972); J. C. Poignet, Thesis, Grenoble (1971).
31. L. Nadjo, J. M. Saveant, and D. Tessier, *J. Electroanal. Chem. Interfacial Electrochem.*, **52**, 403 (1974).
32. K. B. Oldham, *Anal. Chem.*, **44**, 196 (1972).
33. D. M. Gruen and R. L. McBeth, *Pure Appl. Chem.*, **6**, 23 (1963).
34. I. Slàma and J. Malá, *Coll. Czech. Chem. Com.*, **34**, 2134 (1969).

Characterization of n-Type Semiconducting Tungsten Disulfide Photoanodes in Aqueous and Nonaqueous Electrolyte Solutions

Photo-oxidation of Halides with High Efficiency

Joseph A. Baglio*

GTE Laboratories, Incorporated, Waltham Massachusetts 02154

Gary S. Calabrese†

Department of Chemistry, Massachusetts Institute of Technology, Cambridge, Massachusetts 02139

Emil Kamieniecki*

GTE Laboratories, Incorporated, Waltham, Massachusetts 02154

Robert Kershaw

Department of Chemistry, Brown University, Providence, Rhode Island 02912

Clifford P. Kubiak and Antonio J. Ricco†

Department of Chemistry, Massachusetts Institute of Technology, Cambridge, Massachusetts 02139

Aaron Wold

Department of Chemistry, Brown University, Providence, Rhode Island 02912

Mark S. Wrighton*

Department of Chemistry, Massachusetts Institute of Technology, Cambridge, Massachusetts 02139

and Glenn D. Zoski*

GTE Laboratories, Incorporated, Waltham, Massachusetts 02154

ABSTRACT

Synthetic, single crystal, n-type semiconducting WS_2 (bandgap $\approx$ 1.3 eV) has been characterized as a photoanode in aqueous and nonaqueous electrolyte media. The WS_2 was synthesized from the elements by bromine and chlorine transport to yield plates up to 3 × 3 mm in dimension. Interface characterization includes (*i*) cyclic voltammetry in the presence of a large number of fast, one-electron redox couples in CH_3CN/0.1M [*n*-Bu_4N]ClO_4 solutions; (*ii*) steady-state photocurrent-voltage properties in aqueous and nonaqueous solutions of X^- (X^- = Cl^-, Br^-, I^-); (*iii*) tests of durability; (*iv*) wavelength dependence of photocurrent and photovoltage; and (*v*) high resolution (~5 μm) laser mapping of the surface to reveal surface inhomogeneity with respect to output photovoltage. Highlights of the results are: (*i*) n-type WS_2 is durable in aqueous electrolytes containing high concentrations of X^- to yield efficient visible light-assisted oxidation of X^-; *e.g.*, $Cl^- \rightarrow 1/2\ Cl_2$ has up to 6.9% and $Br^- \rightarrow 1/2\ Br_2$ up to 12% efficiency at a 632.8 nm input power of 16 mW/cm²; (*ii*) in aqueous, but not nonaqueous, solutions I^- adsorbs such that the onset of photocurrent is shifted several hundred millivolts as for other metal dichalcogenide photoanodes; the shift is sufficient that visible light can be used to sustain the conversion of 2HI to H_2 and I_2 with no other energy input; (*iii*) cyclic voltammetry in CH_3CN/0.1*M* [*n*-Bu_4N]ClO_4 for a number of redox couples shows that a photovoltage of up to ~0.7V is possible; photovoltage varies from 0.0 to ~0.7V for redox couples having $E_{1/2}$ from ~0.0V *vs.* SCE to ~+0.8V while the photovoltage is fixed at ~0.7V for $E_{1/2}$'s more positive than ~ +0.8V *vs.* SCE; (*iv*) efficiency for halogen generation in aqueous solutions generally exceeds efficiency in CH_3CN solutions; and (*v*) the diffusion length of holes parallel to the surface is ~200 μm which explains the dramatic influence of the steps on the recombination of carriers on layered compounds.

Metal dichalcogenides have been shown to be relatively durable and efficient photoanode materials for use in photoelectrochemical cells for conversion of visible light to electricity or to chemical energy in the form of oxidation and reduction products (1-7). The materials MoS_2, WSe_2, and $MoSe_2$ have received most attention, but there are a number of other metal dichalcogenide materials that might serve as durable and efficient photoanodes. One of the intriguing findings concerning WSe_2 is that it is an anode material apparently capable of sustaining the photoelectrolysis of HI represented by Eq. [1] with no energy input

$$2HI \xrightarrow{2h\nu} H_2 + I_2 \qquad [1]$$

other than visible light (3). This is important, in part, because H_2 and I_2 can be separated, stored, and used in a fuel cell for the generation of electricity. The $E^\circ(H^+/H_2) - E^\circ(I_2/I^-)$ difference is ~0.5V (8). Very few illuminated photoelectrode materials have been found that are capable of sustaining such photoelectrolyses without additional energy input in the form of electricity (9).

* Electrochemical Society Active Member.
† Electrochemical Society Student Member.
Key words: photoelectrolysis, solar energy, laser mapping, surface photovoltage.

In general, the ability to drive an uphill electrochemical reaction such as that represented by Eq. [2] requires the set of interface energetics

$$A + B^+ \xrightarrow{h\nu} A^+ + B \qquad [2]$$

represented by Scheme I. The key feature is that the bottom of the conduction band at the interface, E_{CB}, is more negative than the E° of the cathode couple, B^+/B, and the top of the valence band at the interface, E_{VB}, is more positive than the E° of the anode couple, A^+/A (9). Under these conditions the electrons available at E_{CB} are sufficiently reducing that the $B^+ \rightarrow B$ reduction is possible, while the holes available at E_{VB} are sufficiently oxidizing that the $A \rightarrow A^+$ oxidation is possible. The differences in potential between E_{CB} and $E^\circ(B^+/B)$ and E_{VB} and $E^\circ(A^+/A)$ can be regarded as the excess driving force needed to have sufficient rate (current density) for the electrode reactions. These differences need to be minimized in order to achieve high energy conversion efficiency, since they represent losses in output. For solar energy conversion applications it is important to seek a bandgap, E_g, that comes close to 1.4 eV to achieve high efficiency in a single photoelectrode cell (10).

Part of the difference between E_{CB} and $E^\circ(B^+/B)$ for an n-type semiconductor [or between E_{VB} and $E^\circ(A^+/A)$ for a p-type semiconductor] must be used to inhibit the recombination of photogenerated electron-hole pairs by appearing as a potential drop across the semiconductor, E_{BB}, to create a region near the surface where the bands are bent. The band bending region near the surface is depleted of majority charge carriers and provides the field that inhibits electron-hole recombination. The field drives the hole to the interface and the electron into the bulk such that a full cell in operation would have the energetics represented by Scheme II where E_f and E_f' are the photoelectrode and counterelectrode potentials, respectively. Note that since the two electrodes are short-circuited they are at the same potential, $E_f = E_f'$, but when current passes to produce A^+ and B optical energy is converted to chemical energy with an efficiency, η, that is proportional both to the quantum yield for electron flow, Φ_e, and to the ratio of the photon energy, $h\nu$, to the difference in $E_{redox}(A^+/A)$ and $E_{redox}(B^+/B)$. Generally, E_{BB} must be ~0.3V in order to achieve Φ_e near 1.0. Further, E_f is generally ~0.1V below the bottom of the conduction band in the bulk. This leaves only (E_g — 0.4V) as the available photovoltage. In order to achieve a good rate for the cathode and anode processes, we can conservatively add another 0.3V to

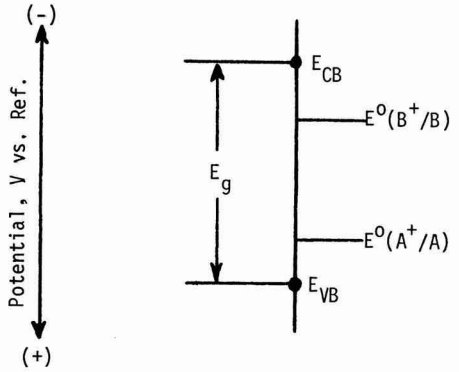

Scheme I. Interface energetics required to drive the reaction $A + B^+ \rightarrow A^+ + B$ with no other energy input other than light of $> E_g$.

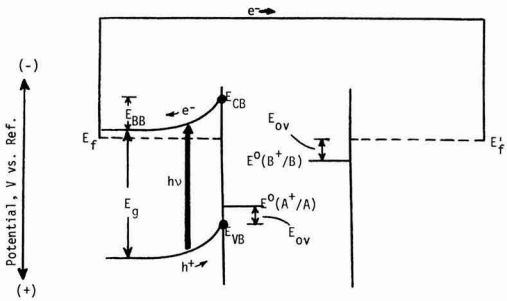

Scheme II. Full cell energetics for an n-type semiconductor-based photoelectrochemical cell in operation for the light driven reaction $A + B^+ \rightarrow B + A^+$.

the loss of photovoltage. This 0.3V is partly the difference in E_{VB} and $E^\circ(A^+/A)$ needed to drive the oxidation and partly the extra voltage needed to drive the $B^+ \rightarrow B$ reduction at the cathode, E_{ov}. This leaves only ~(E_g — 0.7V) as the available photovoltage when good photocurrents (high Φ_e) result. This means that a 1.4 eV bandgap material will, at best, only be able to efficiently drive processes represented by Eq. [2] where $E^\circ(B^+/B)$ and $E^\circ(A^+/A)$ differ by no more than about 0.7V. These considerations illustrate, in part, why it is difficult to find photoelectrochemical processes to store chemical energy that can be efficient. Not only must an appropriate bandgap semiconductor be found, but the half-cell reactions must have E°'s properly disposed relative to the interface energetics of the semiconductor (9).

In addition to the issues already raised, there are two other practical problem areas. First, photoelectrodes, and particularly photoanodes, are thermodynamically unstable when illuminated with $\geq E_g$ light in the presence of the electrolyte solution (11). Thus, even when all energetic problems are solved, the photoanodic decomposition of the photoanode may be kinetically competitive with the desired $A \rightarrow A^+$ process. Second, recent studies, from several groups on a number of small bandgap materials, reveal that the maximum available photovoltage from the photoelectrode is smaller than might be expected (12-14). The low photovoltages have been attributed to surface states situated between E_{CB} and E_{VB} or to carrier inversion. It should now be apparent why we attach special significance to being able to effect the photoelectrolysis of HI, requiring a photovoltage exceeding 0.5V, with visible light as the only energy input.

We now report the full characterization of n-type WS_2, a visible light responsive ($E_g \approx 1.3$ eV) photoanode material. A prior report (15) has described the application of n-type WS_2 in cells for the process represented by Eq. [3] using no energy input other than light

$$2H_2O + SO_2 \xrightarrow[6M\ H_2SO_4]{2h\nu} H_2 + H_2SO_4 \qquad [3]$$

and where $E_{redox}(SO_4^{2-}/SO_2)$ and $E_{redox}(H_2O/H_2)$ differ by ~0.3V. The ability to oxidize SO_2 to H_2SO_4 requires the use of I^- as a mediator, suggesting that photoelectrolysis of HI can also be sustained. Much of the present characterization relates to the study of the WS_2/electrolyte solution interface without regard for the counterelectrode process, except for the HI system. In particular, we set out to (*i*) establish the E_{CB}, E_{VB} positions of WS_2 as a function of the contacting medium to determine whether there is an important role for surface states or carrier inversion, (*ii*) establish the conditions where illuminated WS_2 is durable, (*iii*)

establish factors influencing the efficiency of optical to electrical energy conversion, and (*iv*) identify combinations of half-cell reactions that might be useful in photoelectrochemical energy storage or electricity generation.

Experimental

Preparation of WS_2 crystals.—Tungsten powder (Materials Research Corporation, 99.999%) was reduced in a dry 15% H_2/85% Ar atmosphere for 8 hr at 800°C to remove oxygen impurities. Sulfur (Gaillard-Schlesinger, 99.999%) was resublimed in vacuo at 80°C before use. Large single crystals of WS_2 were prepared by chemical transport using a concentration of 5 mg/cm³ of bromine as the transporting agent. A melting point capillary containing the calculated weight of bromine was sealed at a pressure of 10^{-3} Torr and placed in an H-tube filling apparatus (16).

Stoichiometric quantities of tungsten and sulfur were added, and the apparatus was evacuated to 10^{-5} Torr and sealed off. The bromine capillary was then opened and the bromine distilled onto the charge. The silica transport tube was then sealed off. The dimensions of the completed transport tube were 1.2 cm diam × 28 cm long. This tube was then placed in a transport furnace. The furnace was operated so that the empty portion of the tube, or growth zone, was heated to 1100°C, while the charge end was heated to 700°C. This temperature profile was maintained for 15 hr, allowing the charge powder to react, and for back transport to clean the growth zone of unwanted nucleation sites. The charge zone was then raised to 1100°C over a 5 hr period. The temperature of the growth zone was then programmed to 1050°C at 1°C/hr. Crystal growth was allowed to proceed for 4 days, after which the furnace was turned off. The transport tube was removed when cold, opened, and the crystals washed with CCl_4 to remove the bromine. Crystals in the form of plates up to 3 × 3 mm were grown using this technique. In an analogous manner WS_2 crystals were grown by chlorine vapor transport except that the concentration of chlorine was 0.2 mg/cm³.

Electrode preparation and testing.—Flat, plate-like crystals of n-WS_2 were peeled apart using fine tweezers to give paper-thin crystals, 0.01-0.1 cm² in surface area. Crystal supports were made by hammering the end of heavy gauge copper wire flat and sanding with emery paper to give a smooth, oxide-free surface; the remainder of the wire was passed through ~10 cm of 4 mm Pyrex tubing. One side of the crystal was rubbed with Ga-In eutectic to insure ohmic contact, then attached to the support using conducting silver epoxy and cured in an oven at ~100°C for ~1 hr. Electrodes were completed by sealing in two part epoxy [leaving only the WS_2 (001) face exposed] and curing at ~100°C for ~15 min. Each electrode was tested in the dark and under illumination by observing the cyclic voltammetry for 1 mM TCNQ in CH_3CN/0.1*M* [*n*-Bu_4N]ClO_4, 25°C at 100 mV/sec. Leakage, photovoltage, and peak shapes were considered in selecting electrodes for use in further experiments; Fig. 1 is representative of the voltammetry for a good electrode.

Electrochemical procedures and equipment for cyclic voltammetry and current-voltage data.—Cyclic voltammograms were recorded in Ar- or N_2-purged CH_3CN/0.1*M* [*n*-Bu_4N]ClO_4 solutions with redox reagents present at 1 mM (current-voltage curves under conditions indicated elsewhere) using a PAR Model 173 or ECO Model 551 potentiostat controlled by a PAR Model 175 programmer; scans were recorded with a Houston Instruments Model 2000 X-Y recorder. Except where otherwise stated, a single compartment, three-electrode cell was used with a Pt counterelectrode and saturated calomel reference electrode (SCE). Measurements were made at 25°C.

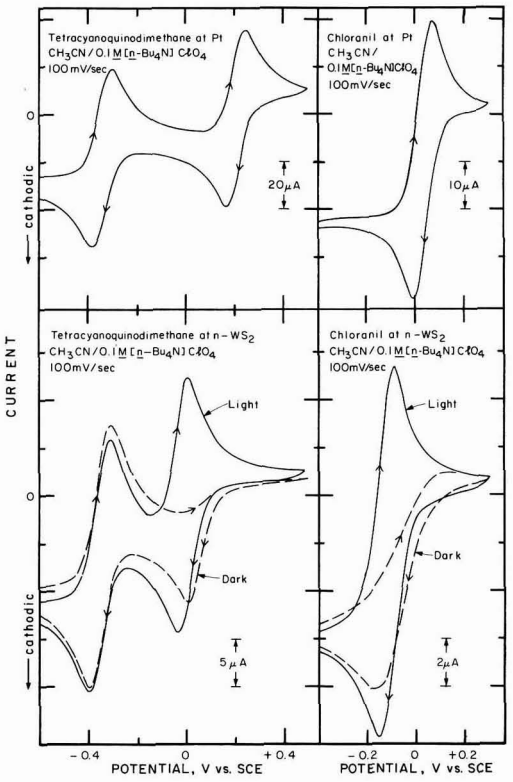

Fig. 1. Comparison of the cyclic voltammetry of ~1 mM tetracyanoquinodimethane and chloranil at Pt and n-WS_2 (dark, - - -; and illuminated, ———) in deoxygenated solution at 25°C. For the illuminated situations the irradiation is at 632.8 nm, ~20 mW/cm².

Light sources included a 5 mW He-Ne laser (632.8 nm, 500:1 polarized; Aerotech Model LS5P) and a 5W Ar ion laser (514.5 nm; Spectra Physics Model 164). Intensities were varied using a beam expander and/or polarizing filter in the case of the He-Ne laser and by adjusting the power control for the Ar ion laser. A Tektronix J16 digital radiometer equipped with J6502 probe was used to measure intensities. For the electrolysis of HI, a 500W tungsten-halogen lamp served as a light source. Efficiency data are uncorrected for reflection losses or losses from electrolyte/redox couple/solution absorption.

Photoelectrolysis of HI with a platinized single crystal of n-WS_2.—A single crystal of n-WS_2 (~3 × 3 × 0.1 mm) was mounted over a hole drilled in a 2 × 2 in. piece of plexiglass. The crystal was sealed to the plexiglass with ordinary epoxy such that the top and bottom faces of the crystal were each exposed on different sides of the plexiglass sheet. Two additional holes were drilled in the plexiglass and these were covered with Nafion film. A cell was constructed by clamping the plexiglass sheet containing the crystal and Nafion between two glass vessels with O-ring connector joints. One side of the cell was filled with a solution of 1*M* NaI in 50% H_3PO_4. The n-WS_2 crystal was platinized on its second side by filling that side of the cell with a solution of ~1 m*M* K_2PtCl_6 in 5% H_3PO_4 and then irradiating the opposite side with a 5 mW He-Ne laser for 45 min. After platinization the

cell and crystal were rinsed four times with distilled water. The cell half containing the naked n-WS_2 crystal face was filled with a fresh solution of 1*M* NaI in 50% H_3PO_4. The cell half containing the platinized face of the crystal was filled with 50% H_3PO_4 and fitted with an inverted pipette for gas collection. The naked face of the crystal was irradiated with a 500W tungsten-halogen source. Gas evolution was monitored during a 100 hr period.

Surface photovoltage measurements.—Surface photovoltage measurements were obtained in both "dry" and "wet" cell configurations using both stationary (wide beam) and scanning (narrow beam) procedures. In the "dry" cell configuration, the crystals were illuminated through a semitransparent metallic oxide film (Corning Pyrex Infrared Reflecting Glass) counterelectrode which was separated from the crystal by a transparent (2.5 μm) "Mylar" polyester film (du Pont 10c). In the "wet" or electrochemical cell configuration, the measurements were made in dry, deoxygenated CH_3CN/0.1*M* [*n*-Bu_4N]BF_4 with Pt as the counterelectrode (no active redox couples).

For spectral measurements, the optical systems consisted of a tungsten light source and a double prism Zeiss monochromator. The mapping arrangement utilized a 5 mW He-Ne laser (632.8 nm) that was focused to give a ~5 μm diameter spot on the crystal. The crystal was moved by means of a motor-driven dual axis translation stage. The intensity of the incident light was reduced with neutral density filters so that the photovoltage signal was directly proportional to the photon flux (ϕ) and reciprocally proportional to the chopping frequency. The photon flux incident on the crystal was chopped at a frequency of 45 Hz and measured with a spectrally flat pyroelectric detector (Oriel 7089). Adjustments in the experiments were made to account for cell absorption and reflections, but no corrections were made for the reflectance at the crystal surface.

The system that was used to measure the photovoltage consisted of a high input impedance source follower, a PAR Model 124A lock-in amplifier, and Hewlett Packard Model 7047A X-Y recorder.

Photoacoustic spectroscopy.—The photoacoustic spectra of n-WS_2 crystals (from the same batch used for preparation of photoanodes) were recorded on a PAR Model 6001 photoacoustic spectrometer employing three gratings and order filters under microprocessor control to cover the 200-2600 nm wavelength range. A beam splitter reflects ~10% of the light to a pyroelectric detector, providing continuous compensation for light intensity fluctuations; nonidealities in the optical system were corrected by dividing the spectra by a carbon black reference spectrum. Using the sample cell supplied with the instrument (air as the coupling gas), 1.0 V/W sensitivity is attained by modulation of the 1 kW xenon arc lamp source at 40 Hz. A 1.0 mm slit width provided 4.0 nm resolution; scan rate was 100 nm/min.

Photoaction spectroscopy.—Photoaction spectra were obtained by interfacing the photoacoustic spectrometer with a potentiostat. The photoacoustic sample cell was replaced by a single compartment, three-electrode electrochemical cell with n-WS_2 photoanode positioned in the light beam. While maintaining the photoanode at a fixed potential on the plateau of the appropriate current-voltage curve (Fig. 6), the wavelength was scanned and the output of the potentiostat, a signal proportional to photocurrent, sent to the microprocessor. Because the photoacoustic spectrometer provided constant intensity illumination, it was possible to obtain relative quantum yield spectra by dividing the photocurrent spectra by a signal (stored in the reference channel) proportional to wavelength. A modulation frequency of 100 Hz and scan rates of 20 and 50 nm/min were used; 1.0 mm slit width gave 4.0 nm resolution. Spectra were recorded under conditions given in Table V for n-WS_2; similar conditions were used for the photoaction spectra of n-MoS_2 and n-$MoSe_2$.

Chemicals.—HPLC grade CH_3CN (Baker) was further purified and dried by distillation from P_2O_5. The H_2O was deionized and distilled. The [*n*-Bu_4N]ClO_4 electrolyte was obtained from Southwestern Analytical Company and dried at 70°C under vacuum for 24 hr prior to use. All other electrolytes were obtained commercially in reagent grade and used without purification after ensuring the absence of electroactive impurities in the potential range of interest. Most redox reagents listed in Table I were commercially available or have been synthesized and used previously in related studies (5, 12); these were used without additional purification, and cyclic voltammetry at Pt confirmed the absence of electroactive impurities.

Results and Discussion

Classification of redox couples in CH_3CN/0.1M [n-Bu_4N]ClO_4.—Cyclic voltammetry of fast, one-electron redox couples at semiconductor electrodes allows establishment of the essential interface energetics without the complication of poor electrode kinetics (5, 17). We adopt the redox couple classification scheme used in the study (5) of $MoSe_2$ where the redox couples are put into one of five classes according to their behavior at the n-type semiconductor electrode:

Class I: E° more negative than E_{CB}; reversible electrochemistry in the dark unaffected by $\geq E_g$ illumination.

Class II: E° near E_{CB} such that dark redox behavior appears sluggish kinetically; $\geq E_g$ illumination moves the anodic current peak more negative and improves kinetics.

Class III: No dark oxidation of reduced form of the couple; $\geq E_g$ illumination gives anodic current peak that is more negative than at a reversible electrode to an extent that depends on E°; more positive E°'s give larger photovoltages.

Class IV: E° sufficiently positive that photovoltage is independent of E°.

Class V: E° so positive that photoelectrode decomposition precludes study of the couple.

In our studies we typically employed Pt as a reversible electrode to compare with n-type WS_2 photoanodes. All couples were studied in dry, deoxygenated CH_3CN/0.1*M* [*n*-Bu_4N]ClO_4 at ~1 m*M* concentration and the E°'s ranged from ~ −0.5 to +1.8V. For redox couples belonging to Classes II-V, illumination at 632.8 nm, 20 mW/cm² or 514.5 nm, 200 mW/cm² and 1 W/cm² was used. Table I and Fig. 1-5 summarize the significant findings from a wide range of redox reagents.

The redox reagent tetracyanoquinodimethane, TCNQ, has proved to be particularly useful, inasmuch as $E_{1/2}(TCNQ^{-/2-})$ falls at a potential where reversible electrochemical behavior is found, Class I, while $E_{1/2}(TCNQ^{0/-})$ is in a region where the oxidation is essentially blocked in the dark, Class III. Thus, these two redox levels straddle the E_{CB} position and allow a rather definitive measure of the value of E_{FB}, the value of E_f where the bands are not bent. As shown in Fig. 1, the onset of photocurrent is close to −0.2V *vs.* SCE as is found for the other redox couples for $E_{1/2}$ no more positive than ~ +0.7V *vs.* SCE. We thus take −0.2V *vs.* SCE as E_{FB} in CH_3CN. The TCNQ svstem has been our routine "test" couple for n-type WS_2 electrodes. Good, nonleaking electrodes show essentially reversible behavior for the $TCNQ^{-/2-}$ couple and no dark oxi-

Table I. Comparison of n-WS_2 with Pt: anodic current peaks, photovoltages, and classification of a range of redox couples*

Redox couple (No.)**	Potential, V *vs.* SCE					
	Pt		n-WS_2			
	$E_{1/2}$***	E_{PA}***	E_{PA} (dark)	E_{PA} (light)†	E_V, V‡	Class§
$[MV]^{+/0}$	−0.85	−0.82	−0.82	−0.82	—	I
$[MV]^{2+/+}$	−0.45	−0.41	−0.40	−0.40	—	I
$[TCNQ]^{-/2-}$	−0.35	−0.32	−0.31	−0.31	—	I
[Decamethylferrocene]$^{+/0}$	−0.10	−0.06	−0.02	−0.02	—	I
[Chloranil]$^{0/-}$ (No. 1)	0.02	0.06	0.11	−0.02	0.08	II
$[TMPD]^{+/0}$ (No. 2)	0.10	0.14	0.25	0.00	0.14	II
[Tetrachloro-o-benzoquinone]$^{0/-}$ (No. 3)	0.11	0.15	—	0.03	0.12	III
[Pentamethylferrocene]$^{+/0}$ (No. 4)	0.12	0.16	—	0.06	0.10	III
$[TCNQ]^{0/-}$ (No. 5)	0.20	0.23	—	0.02	0.21	III
$[TCNE]^{0/-}$ (No. 6)	0.21	0.24	—	0.05	0.19	III
[1,1-Dimethylferrocene]$^{+/0}$ (No. 7)	0.28	0.32	—	0.06	0.26	III
[Biferrocene]$^{+/0}$ (No. 8)	0.30	0.33	—	0.03	0.30	III
[Ferrocene]$^{+/0}$ (No. 9)	0.38	0.42	—	0.06	0.36	III
[1,1′-*Bis*(trimethylsilyl)ferrocene]$^{+/0}$ (No. 10)	0.39	0.42	—	0.06	0.36	III
[Ferrocenecarboxylic acid]$^{+/0}$ (No. 11)	0.62	0.66	—	0.15	0.51	III
[Acetylferrocene]$^{+/0}$ (No. 12)	0.63	0.66	—	0.17	0.49	III
[Biferrocene]$^{2+/+}$ (No. 13)	0.65	0.68	—	0.16	0.52	III
$[TMPD]^{2+/+}$ (No. 14)	0.68	0.72	—	0.10	0.62	III-IV
[1,1′-Diacetylferrocene]$^{+/0}$ (No. 15)	0.85	0.89	—	0.22	0.67	III-IV
$[Ru(2,2'\text{-bipyridine})_3]^{3+/2+}$ (No. 16)	1.26	1.30	—	0.56	0.74	IV
$[ClRe(CO)_3(4\text{-cyanopyridine})_2]^{+/0}$ (No. 17)	1.51	1.55	—	0.86	0.69	IV
$[(CH_3CN)Re(CO)_3(phen)]^{2+/+}$ (No. 18)	1.76	1.81	—	1.08	0.73	IV-V

* All data are for $CH_3CN/0.1M$ $[n\text{-}Bu_4N]ClO_4$ solutions at 25°C, 100 mV/sec.

** Redox couples present at ~1 m*M*. Abbreviations: MV is *N*,*N*′-dimethyl-4,4′-bipyridinium; TCNQ is tetracyanoquinodimethane; TMPD is *N*,*N*,*N*′,*N*′-tetramethyl-*p*-phenylenediamine; TCNE is tetracyanoethylene. Numbers are keyed to Fig. 5.

*** $E_{1/2}$'s were calculated from cyclic voltammetric data according to $E_{1/2} = (E_{PA} + E_{PC})/2$, where E_{PA}, E_{PC} are the anodic and cathodic current peaks, respectively.

† Illumination of n-WS_2 was with 514.5 nm light from an Ar^+ laser, ~200 mW/cm², with the exception of the four most positive redox couples, where 632.8 nm light from an He/Ne laser, ~20 mW/cm², was used.

‡ $E_V = E_{PA,Pt} - E_{PA,illum \cdot WS_2}$.

§ See text for explanation of classes.

dation of $TCNQ^-$. A photoanodic peak at ~0.0V *vs.* SCE for the $TCNQ^- \rightarrow TCNQ^0$ process typifies good electrodes. The lower left portion of Fig. 1 is representative of the characterization of electrodes used in this study. Electrodes showing dark current, poorly developed photoanodic waves or a photoanodic wave significantly positive of 0.0V *vs.* SCE were found to give poor energy conversion efficiency with respect to X_2/X^- systems (*vide infra*) and were not used in these studies.

For redox couples having $E_{1/2}$ in the range ~ +0.1 to +0.8V *vs.* SCE we find Class III behavior. For such couples we find that the photoanodic peak for the oxidation of the reduced form of the couple is in the range 0.0 to +0.2V *vs.* SCE. Taking the photovoltage, E_V, to be the difference in the anodic peak at Pt, $E_{PA,Pt}$, and the photoanodic peak at n-WS_2, $E_{PA,illum.WS_2}$, Eq. [4], we find that E_V depends on $E_{1/2}$ in a linear fashion for the $E_{1/2}$'s in the ~ +0.1 to +0.8V *vs.* SCE range

$$E_V = |E_{PA,Pt} - E_{PA,illum.WS_2}| \qquad [4]$$

Even for the two-electron reductants, TMPD and biferrocene, Fig. 2, we find that nearly ideal semiconductor/liquid interface considerations apply in that the two-electron oxidation TMPD → $TMPD^{2+}$ or biferrocene → biferricenium^{2+} occurs in the 0.0 to +0.2V *vs.* SCE range. For an ideal semiconductor/liquid interface there should be one, two-electron photoanodic wave, not two, one-electron waves as at Pt. The n-type WS_2 comes close to this ideal for Class III redox couples.

For the $E_{1/2}$'s that are more positive than ~ +0.8V *vs.* SCE we find that E_V is nearly constant at ~0.7V. Figure 3 shows behavior of a representative couple in this range. Photoanodic decomposition current does not onset significantly until ~ +1.5V. Thus, couples having $E_{1/2}$ in the range ~ +0.8 to +1.8V *vs.* SCE still give reliable cyclic voltammetry data and are given the Class IV designation, since E_V is fixed. Redox couples more positive than ~ +1.8V *vs.* SCE cannot be studied owing to the significant photoanodic decomposition and such couples would be assigned to Class V.

Figure 4 illustrates that the presence of more than one redox reagent does not affect the cyclic voltammetry response. This tends to rule out significant problems from adsorption of a given redox couple. Figure 5 summarizes all of the E_V measurements for several electrodes and light intensities for a wide range of redox couples. The extrapolation of the plot of E_V *vs.* $E_{1/2}$ is consistent with the value of E_{FB} of −0.2V *vs.* SCE assigned above based on the onset of photocurrent in the cyclic voltammetry. The data show three regions of behavior: (*i*) reversible electrochemistry, $E_V = 0$; (*ii*) E_V depends on $E_{1/2}$; and (*iii*) E_V fixed at ~0.7V, independent of $E_{1/2}$. Photovoltage is observed for a range of $E_{1/2}$ values that exceeds the separation of E_{CB} and E_{VB} which is E_g = 1.3 eV (*vide infra*). These results are very similar to those reported earlier for n-type MoS_2 and $MoSe_2$, except that the values of E_{FB} are somewhat different, and most importantly, the

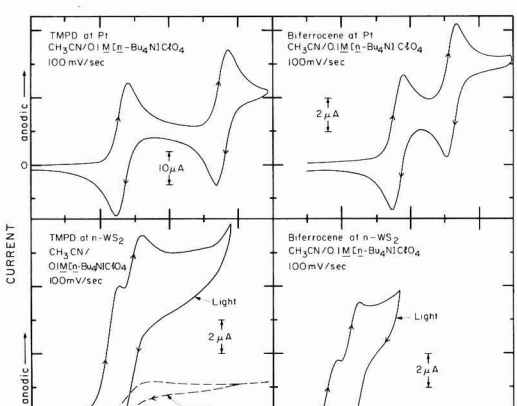

Fig. 2. Cyclic voltammetry at Pt and n-WS_2 as in Fig. 1 except data are for TMPD and biferrocene.

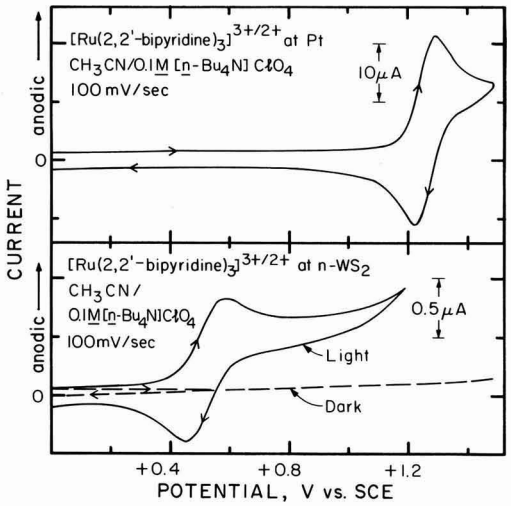

Fig. 3. Cyclic voltammetry at Pt and n-WS_2 as in Fig. 1 and 2 except data are for $Ru(bipy)_3^{2+}$.

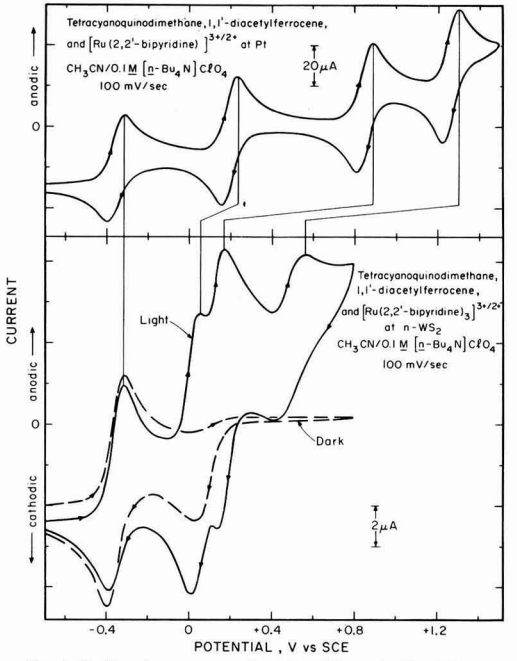

Fig. 4. Cyclic voltammetry at Pt and n-WS_2 as in Fig. 1-3 except data are for a solution containing several redox reagents each at ~1 mM.

E_V for the Class IV couples is ~0.7V for WS_2, somewhat higher than for MoS_2 (5, 14) and $MoSe_2$ (5, 14) or WSe_2 (3, 14). This means that n-type WS_2-based cells could have significantly higher efficiency for the conversion of optical energy than would MoS_2- or $MoSe_2$-based cells when using Class IV redox couples.

The establishment of a wide range of redox couples that belong to Class IV and the finding of significant E_V's for $E_{1/2}$'s spanning a range greater than E_g indicate that there is an important role for surface states and/or carrier inversion. A similar conclusion has been drawn for other n-type metal dichalcogenides (14). Whether the effect is due to surface states or to carrier inversion is not easily determined from the experimental results presented. Phenomenologically, the Class II and III couples give nearly ideal semiconductor/liquid interface behavior, Scheme III, in that E_{BB} changes with variation in $E_{1/2}$ while the E_{CB} and E_{VB} positions remain fixed, while Class IV couples have a fixed value of E_{BB} and variation in $E_{1/2}$ changes the E_{CB} and E_{VB} positions. For Class IV the variations in potential drop across the semiconductor/liquid interface occur across the Helmholtz double layer at the interface, while for the Class II and III couples the variation in potential drop occurs across the semiconductor. Either carrier inversion or a low density of surface states situated below E_{CB} will accommodate the findings. Despite the fact that WS_2 might be expected

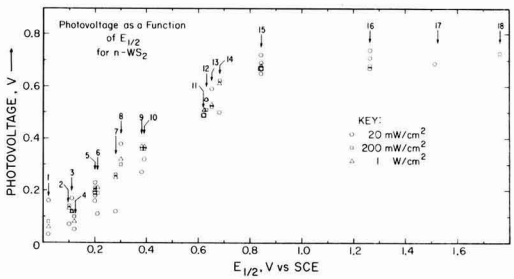

Fig. 5. Plot of photovoltage against the $E_{1/2}$ value of the associated redox couple. Photovoltage is as defined in text. Individual number entries are identified in Table I. Where several data points are included these reflect variation in WS_2 samples and light intensity.

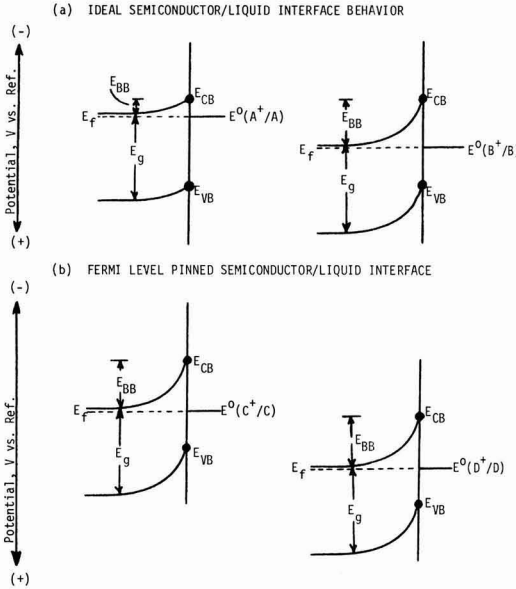

Scheme III. Effect of variation of solution redox couples in Class II and III (a) and Class IV (b) on the potential drop across the semiconductor, E_{BB}. For Class II and III the E_{CB} and E_{VB} positions are fixed and E_{BB} varies, while for Class IV the E_{BB} is fixed and the E_{CB} and E_{VB} positions vary.

to be relatively free of surface states, we prefer to invoke a role for surface states, because we find that it is possible to reduce the oxidized form of Class II and III redox couples at potentials that are significantly positive of E_{FB}. The fact that such reduction can occur more positive than E_{FB} has been previously interpreted as due to surface states below E_{CB} (17). It is especially noteworthy that dark reduction positive of E_{FB} occurs for couples whose $E_{1/2}$ value is such that E_{BB} is less than one-half of the bandgap where effects from carrier inversion would not be important. Thus, we attribute the nonideal interface behavior to surface states, although they may be present only in low density (18). When E_V is independent of $E_{1/2}$ the semiconductor is said to be Fermi level pinned (12a), meaning that the Fermi level of the semiconductor, E_f, is pinned at the surface to a certain value relative to E_{CB} independent of the contacting medium. We have taken E_V at high light intensity to be a good measure of E_{BB} as has previously been done for both solid-state Schottky barrier devices and for liquid junction systems. Generally, we regard a particular E_V determination to have an error of ± 0.05V.

As we have pointed out, the data here for WS_2 are qualitatively similar to those for MoS_2 (5, 14) and $MoSe_2$ (5, 14). Additionally, WSe_2 (3, 14) is similar to WS_2 even in quantitative terms: The maximum value of E_V and the value of E_{FB} in CH_3CN solution are quite similar in the two cases. For the MoS_2, $MoSe_2$, and WSe_2 though, other authors (14) attributed the Class IV region to carrier inversion. While carrier inversion may be important when E_{BB} exceeds one-half the bandgap, it is expected to be unimportant when E_{BB} is small where, at least with WS_2, $MoSe_2$ (5), and MoS_2 (5), we are able to detect reductions positive of E_{FB} in the dark. In any event, WS_2 and WSe_2 appear to yield quite similar output parameters in CH_3CN solutions with respect to E_V and have a very similar value of E_{FB}.

Photoelectrochemical oxidation of halides in aqueous and nonaqueous media.—Figure 6 and Table II summarize the findings concerning the photoelectrochemical conversion of optical energy in CH_3CN or H_2O electrolyte solutions of X_2/X^- (X = Cl, Br, I). In all cases the solution contains sufficient X_2 and X^- to poise the solution and the full cell chemistry consists of oxidizing halide at the WS_2 photoanode and reducing halogen at the counterelectrode. The nature of the species actually present (I_3^-, Br_3^-, Cl_2, etc.) depends on X and the amount of added X_2 and X^-. Since no net chemistry occurs in the cells summarized by the data in Table II and Fig. 6, the output from the cells is electricity. With reference to Scheme II, the full cell is one where the anode and cathode half-cell couple are the same. In such a case the efficiency, η, for the generation of electricity is given by Eq. [5]

$$\eta \text{ in } \% = \frac{(E_V \times i)100\%}{\text{Input Optical Power}} \qquad [5]$$

where $E_V \equiv$ photovoltage in volts, $i \equiv$ photocurrent in amperes, and Input Optical Power is in watts. The maximum efficiency, η_{max}, occurs when $(E_V \times i)$ is maximized and the associated value of E_f of the photoelectrode is the so-called maximum power point. The value of E_V is the extent to which E_f is more negative than E_{redox} of the solution and is expected to depend on light intensity and the $E_{1/2}$ of the particular redox couple used. In general, the E_V in CH_3CN at high light intensity should be predictable from the data in Table I for the fast, one-electron redox couples where the E_V's correspond closely to the high light intensity value. However, the X_2/X^- couples are two-electron systems and are known to interact strongly with electrode surfaces. Adsorption effects from I_3^-/I^- on

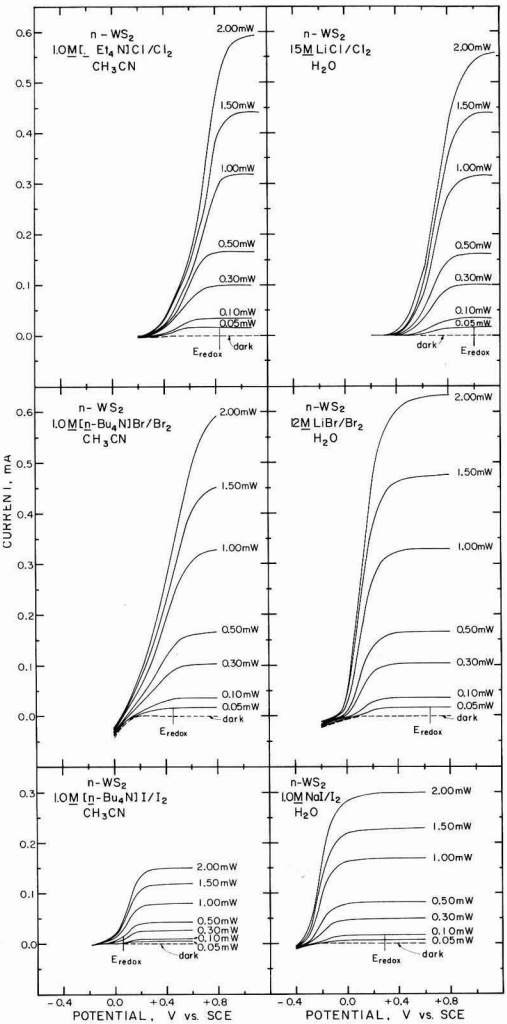

Fig. 6. Steady-state photocurrent-voltage curves for n-WS_2 electrodes in CH_3CN or H_2O containing X_2/X^-. Data in Table II are culled from these and other curves: upper left is run 1, middle left is run 2, lower left is run 3, upper right is run 4; middle right is run 5; lower right is run 6 in Table II.

metal dichalcogenide electrodes are particularly strong (15) in H_2O solutions. Thus, the energetics and kinetics associated with the X_2/X^- couples at WS_2 are not necessarily a straightforward extrapolation of the data for the fast, one-electron, outer-sphere couples used to establish the interface properties in CH_3CN/0.1M [n-Bu_4N]ClO_4.

In CH_3CN solution the X_2/X^- couples do give a value of E_V(max), the open-circuit photovoltage, that accords well with expectation based on $E_{1/2}$ values: The value of E_V(max) varies in the order X = Cl > Br > I. Further, the Cl_2/Cl^- couple apparently yields the highest energy conversion efficiency in CH_3CN solution and I_3^-/I^- the lowest efficiency. The poor efficiency for I_3^-/I^- in CH_3CN is attributable to the low value of E_V(max). The Cl_2/Cl^- couple exhibits the lowest visible absorption of the three couples and represents a potential practical advantage. All of the combinations of $WS_2/X_2/X^-$ are durable in CH_3CN

Table II. Representative output parameters for the n-WS_2-based photoelectrochemical cells in halogen/halide media

Run No*	WS_2 No.**	Solvent/X_2/X^- (E_{redox}, V *vs.* SCE)***	Input power, mW†	Φ_e at E_{redox}††	E_V (max), mV (E_V at η_{max}, mV)†††	η_{max}, %‡	Fill factor‡‡
1	1	CH_3CN/1.0*M* [Et_4N]Cl/Cl_2 (+0.83)	0.05	0.67	470 (230)	6.4	0.39
			0.10	0.67	510 (230)	6.4	0.37
			0.30	0.66	555 (230)	5.9	0.32
			0.50	0.65	570 (180)	4.7	0.25
			1.00	0.52	590 (180)	2.8	0.18
			1.50	0.52	600 (150)	2.3	0.14
			2.00	0.51	610 (150)	2.0	0.13
2	2	CH_3CN/1.0*M* [*n*-Bu_4N]Br/Br_2 (+0.46)	0.05	0.63	290 (140)	3.3	0.36
			0.10	0.62	310 (140)	3.2	0.32
			0.30	0.59	350 (120)	2.5	0.24
			0.50	0.55	370 (120)	2.1	0.21
			1.00	0.46	390 (100)	1.6	0.17
			1.50	0.37	400 (100)	1.3	0.17
			2.00	0.33	410 (100)	1.1	0.16
3	1	CH_3CN/1.0*M* [*n*-Bu_4N]I/I_2 (+0.06)	0.30	0.05	150 (80)	0.07	0.13
			2.00	0.05	220 (80)	0.07	0.11
4	3	H_2O/15*M* LiCl/Cl_2 (+1.00)	0.05	0.67	480 (260)	6.2	0.38
			0.10	0.68	530 (260)	6.5	0.35
			0.30	0.66	600 (260)	6.9	0.35
			0.50	0.63	630 (260)	6.8	0.33
			1.00	0.64	660 (240)	6.0	0.28
			1.50	0.57	680 (240)	5.0	0.25
			2.00	0.54	680 (240)	4.6	0.25
5	4	H_2O/12*M* LiBr/Br_2 (+0.64)	0.05	0.63	560 (440)	9.7	0.54
			0.10	0.67	610 (440)	11.4	0.54
			0.30	0.69	660 (440)	12.5	0.55
			0.50	0.65	680 (440)	12.1	0.54
			1.00	0.65	710 (440)	11.9	0.51
			1.50	0.62	720 (440)	11.0	0.48
			2.00	0.61	720 (440)	10.0	0.45
6	2	H_2O/1.0*M* NaI/I_2 (+0.28)	0.05	0.31	490 (390)	4.0	0.50
			0.50	0.33	580 (390)	5.5	0.56
			2.00	0.28	625 (390)	4.8	0.52
7	1	H_2O/1.0*M* NaI/I_2 (+0.28)	0.05	0.26	520 (430)	2.6	0.41
			0.50	0.26	600 (430)	4.1	0.57
			2.00	0.22	620 (430)	4.1	0.59
8	2	H_2O/12*M* LiBr/Br_2 (+0.64)	0.05	0.67	570 (400)	10.0	0.55
			0.50	0.66	670 (400)	12.4	0.50
			2.00	0.63	710 (340)	8.7	0.38
9	2	H_2O/15*M* LiCl/Cl_2 (+1.00)	0.05	0.63	420 (260)	4.0	0.29
			0.50	0.56	600 (260)	5.1	0.30
			2.00	0.47	700 (260)	4.6	0.26
10	2	CH_3CN/1.0*M* [Et_4N]Cl/Cl_2 (+0.83)	0.05	0.63	290 (210)	3.2	0.34
			0.50	0.58	420 (210)	3.9	0.32
			2.00	0.44	480 (210)	2.5	0.23
11	1	CH_3CN/1.0*M* [*n*-Bu_4N]Br/Br_2 (+0.46)	0.05	0.59	340 (140)	2.0	0.19
			0.50	0.47	420 (140)	1.3	0.13
			2.00	0.26	440 (140)	0.8	0.12
12	2	CH_3CN/1.0*M* [*n*-Bu_4N]I/I_2 (+0.06)	0.30	0.04	120 (60)	0.05	0.10
			2.00	0.04	190 (60)	0.05	0.09

* Run No. 1-6 are given in Fig. 6. Data in all cases are from steady-state (10 mV/sec) photocurrent-voltage curves.
** WS_2 No. refers to the particular electrode sample used.
*** Electrolyte solutions were prepared and X_2 was added to the concentration necessary to bring the solution potential, E_{redox}, to the value indicated.
† Input power is at 632.8 nm. Multiply by 32 cm^{-2} to obtain power density.
†† Quantum yield for electron flow measured at E_{redox}. Data are ±15% and are uncorrected for reflection or solution absorption.
††† Photovoltages. E_V(max) is difference in onset of photocurrent and E_{redox}. E_V at η_{max} is difference between maximum power point and E_{redox}.
‡ η_{max}, % defined as $\dfrac{(E_V \times i)_{max}}{\text{Input power}}$.
‡‡ Fill factor is $\dfrac{(\Phi_e \text{ at } \eta_{max})\,(E_V \text{ at } \eta_{max})}{(\Phi_e \text{ at } E_{redox})\,(E_V(\text{max}))}$.

under the conditions indicated. The low absolute efficiencies appear to be attributable to the fact that $E_{BB} > 0.3V$ is required to achieve good Φ_e values. For example, in run 1, the E_V(max) at the highest intensity is ~610 mV meaning that $E_f \approx E_{FB} \approx +0.22V$ *vs.* SCE, since E_{redox} is at 0.83V *vs.* SCE. At the maximum power point E_V is only ~150 mV meaning that $E_f = +0.68V$ *vs.* SCE where E_{BB} is thus ≥0.36V. The Φ_e at the maximum power point is significantly less than Φ_e at E_{redox}. The poor current-voltage behavior is quantitated by the fill factor that is given in Eq. [6]

$$\text{Fill Factor} = \frac{(\Phi_e \text{ at } \eta_{max})\,(E_V \text{ at } \eta_{max})}{(E_V\ (\text{max}))\,(\Phi_e \text{ at } E_{redox})} \qquad [6]$$

The data in Table II show that the fill factor is ≤0.25 for input power of >16 mW/cm^2. Phenomenologically, poor fill factors mean that recombination of photogenerated e^--h^+ pairs is important even though there may be a significant value of E_{BB} as for the Cl_2/Cl^- couple. When E_{BB} is sufficiently large, as when $E_f = E_{redox}$ for the Cl_2/Cl^- and Br_2/Br^- couples, the value of Φ_e is ~0.6, uncorrected for a significant reflection loss. For I_3^-/I^- the value of E_{BB}, even at $E_f = E_{redox}$, is too small to give good values for Φ_e. In most respects, the output parameters from n-WS_2 in CH_3CN/X_2/X^- solutions are similar to those for n-$MoSe_2$ in the same solutions (5). The WS_2 does give a somewhat larger value of E_V(max), but this is offset by the higher fill factors for the $MoSe_2$.

In H_2O the highest efficiencies significantly exceed the highest efficiencies obtained in CH_3CN. As for other metal dichalogenides, there appears to be adsorption of I_3^- in H_2O, but not in CH_3CN that results in a good value of E_V(max) for the I_3^-/I^- couple in H_2O. However, light absorption of the I_3^-/I^- does attenuate the uncorrected values of Φ_e. Correcting for light absorption would improve the Φ_e's and give efficiencies that are similar to those for the Br_2/Br^- couple. The efficiency for the Br_2/Br^- couple approaches 13% in the best case, significantly exceeding the efficiency previously reported for the n-$MoSe_2$ or n-MoS_2 under similar conditions (19). The lower efficiency for the Cl_2/Cl^- couple in H_2O may be due to

a weaker interaction of the Cl_2/Cl^- couple with the MY_2 surfaces as reflected in the diminished fill factors compared to those obtained with the Br_2/Br^- couple.

The n-WS_2 is durable in the high concentration LiBr or LiCl as we previously reported for MoS_2 and $MoSe_2$ (19). Data in Table III show some representative examples for Cl_2 generation from 15*M* LiCl. In no case do we observe deterioration of properties for the time periods and current densities reported. Similarly, the durability of n-WS_2 in 12*M* LiBr/0.1*M* Br_2 is good: At ~40 mA/cm² the output is constant, ±5%, for a 0.002g n-WS_2 electrode held at +0.2V *vs.* SCE for a period of time long enough to pass 90C. At low concentrations of Br^- or Cl^- the n-WS_2 is photocorroded in H_2O but not in CH_3CN, a result that again parallels earlier findings for MoS_2 and $MoSe_2$ (19). Thus, the main difference between WS_2 and the materials studied earlier is that the efficiency of WS_2 is significantly better.

Photoelectrolysis of HI in aqueous solution.—The data in Table II and Fig. 6 show that the onset of photoanodic current for the $3I^- \rightarrow I_3^-$ reaction occurs at ~ −0.4V *vs.* SCE for high light intensity. This negative onset in aqueous solution indicates that n-WS_2 can be used to effect the photoelectrolysis of HI, Eq. [1], in acid medium, since $E^\circ(H^+/H_2) = -0.24$V *vs.* SCE under standard conditions. With the good fill factors for the I_3^-/I^- couple and the knowledge that platinized Pt requires only a small value of E_{ov} (20), Scheme I, for H_2 evolution, the efficient photoelectrolysis of HI should be possible in a photoelectrochemical device consisting of an n-WS_2 photoanode, a platinized Pt cathode, and an aqueous acid electrolyte.

The photo-oxidation of $3I^-$ to I_3^- and simultaneous reduction of $2H^+$ to H_2 can be effected using an n-WS_2-based photoelectrochemical device with visible light as the only energy input. The cell was configured in a number of different ways as detailed in Table IV. In all cases the initial current efficiency for H_2 generation was unity. After significant photoelectrolysis, though, the cells generally decline in efficiency owing to the diffusion of I_3^- to the cathode compartment where $I_3^- \rightarrow 3I^-$ can compete with H_2 evolution. But more importantly, we typically find that the E_{ov} required at Pt goes up with time to a value that significantly attenuates the photocurrent when the n-WS_2 is merely short-circuited to Pt. We established that the E_{ov} for Pt changes during photoelectrolysis experiments by running the steady-state current potential curve for H_2 evolution before and after photoelectrolysis. By way of contrast, the photocurrent-voltage properties for the n-WS_2 were constant during such experimentation. For example, potentiostating the n-WS_2 at ~ −0.2V *vs.* SCE, the maximum power point, results in no change in photocurrent during a 100 hr period whereas cells where the WS_2 and Pt are just short-circuited show significant photocurrent decline during the same time period.

One final experiment concerning the photoelectrolysis of HI is worth describing. We prepared a two-compartment cell separated by a Nafion membrane and a single crystal of n-WS_2 as described in the Experimental. One side of the WS_2 was platinized by photoelectrochemically reducing $PtCl_6^{2-}$. The cell was then used to effect the simultaneous generation of H_2 and I_3^- using visible light generation from a 500W tungsten halogen lamp to excite the n-WS_2. The solution contacting the naked n-WS_2 was 50% H_3PO_4/1*M* NaI and the platinized side was contacted only by 50% H_3PO_4 initially. During 100 hr of irradiation approximately 5 ml of H_2 gas was collected above the illuminated crystal and the generation of gas was linear in time up to 100 hr. During the 100 hr the generation of I_3^- in the other compartment was obvious from change of the colorless to red-orange solution. After 100 hr the yellow color began to appear in the compartment where H_2 is generated and net H_2 production ceased. This result again shows that WS_2 is capable of sustaining the photoelectrolysis of HI, but separator problems may ultimately be a limiting factor. In H_2O splitting, where the H_2 and O_2 products are not too soluble in H_2O and where O_2 does not poison the H_2 electrode, such separator problems may not be as severe.

Table III. Durability of N-type WS_2 for the generation of Cl_2*

Exp. No.	Initial wt. of WS_2 Xtal (μ mols)	Charge passed, C	Volume Cl_2, ml**	Current efficiency, %†	Turnover No.††	Current density, mA/cm²
1	0.004g (16.1)	68	7.4	86	22	60
2	0.003g (12.1)	87	10.0	91	38	67
3	0.009g (36.3)	360	42.0	92	52	80

* Data are for n-WS_2 photoanodes potentiostated at +0.8V *vs.* SCE in 15*M* LiCl in a two-compartment cell with an ultrafine glass frit separator. Electrodes were illuminated with a 632.8 nm He-Ne laser providing ~1 W/cm², Exp. No. 1 and 2, or with a 514.5 nm Ar ion laser providing ~4 W/cm², Exp. No. 3.
** Chlorine was collected in a graduated cylinder over the photoanode.
† Efficiency for generation of Cl_2 based on number of electrons passed.
†† Mols of chlorine produced per mol of n-WS_2; in all cases electrode is unchanged after the experiment.

Table IV. Experimental data relating to the photoelectrolysis of HI

Experiment*	Q, coulombs	N_e, mol**	V_{H_2}, ml†	N_{H_2}, mol††	j, mA/cm²‡ Max	Min.	Mean	t, hr‡‡	η_I, %§
I	60.77	6.30×10^{-4}	6.79	3.03×10^{-4}	8.4	3.9	6.7	28.7	96
II	117.4	12.2×10^{-4}	12.4	5.54×10^{-4}	9.2	4.6	7.2	51.6	91
III	61.00	6.32×10^{-4}	6.68	2.98×10^{-4}	11.1	1.9	4.0	44.3	94
IV	43.11	4.47×10^{-4}	4.75	2.12×10^{-4}	2.3	1.2	1.9	64.0	95

* I: n-WS_2 #2/Pt separated by Nafion membrane. WS_2 side contains 2M NaI/H_2O. Pt side contains 30% H_2SO_4. II: n-WS_2 #2/Pt separated by Nafion membrane. Both sides contain 1M NaI in 25% H_2SO_4. III: n-WS_2 #47/Pt 0.65M HI in 6.5M HCl. The I_2 product was extracted from cell with cyclohexane which was introduced through a frit at the bottom of the cell and pumped through with a peristaltic pump. IV: n-WS_2 #47/Ru plated Pt 0.65M HI in 6.5M HCl. HI/HCl solution is constantly renewed from a reservoir of fresh solution by pumping.
** Mols of electrons passed through circuit during operation.
† Volume H_2 gas collected in inverted pipette.
†† Mols of H_2 gas collected.
‡ Maximum, minimum, and mean current densities at n-WS_2 electrode during operation.
‡‡ Time of operation
§ Current efficiency for H_2 collected.

The data for the I_3^-/I^- couple in Table II and Fig. 6 likely reflect optimistic values for the photoelectrolysis of HI using WS_2, except for the optical absorption of I_3^-/I^- that could be reduced further by smaller path lengths. Thus, photoelectrolysis efficiencies for HI are probably in the range of ~5% for 632.8 nm light and considerably lower for solar light that is polychromatic.

Optical properties of WS_2 and surface inhomogeneities.—Several different techniques have been used to determine the wavelength response of the n-WS_2 samples used in this study. Photoacoustic spectroscopy, photoaction spectra, and surface photovoltage measurements as a function of wavelength have yielded internally consistent information concerning the onset of the indirect transition of the WS_2 samples.

The photoacoustic spectrum of a typical WS_2 sample is shown in Fig. 7. Consistent with published properties of WS_2 (21), the onset of the photoacoustic signal occurs in the vicinity of 950 nm (1.3 eV). The signal more or less flattens at wavelengths shorter than 700 nm. The photoaction spectra under various conditions also show onsets in the vicinity of 950 nm. Figure 7 includes two different experiments where the effect from absorption of the I_3^-/I^- couple is plainly obvious at the wavelengths shorter than ~600 nm. Even the Cl_2/Cl^- couple absorbs some, but the attenuation of the relative Φ_e is not as severe in this case. The photoaction spectra clearly show that the high values of Φ_e are for wavelengths shorter than ~700 nm despite the onset in the 950 nm.

The onset region of the photoaction spectra and the photoacoustic spectra are consistent with a region of relatively low absorptivity associated with indirect transitions as reported earlier for MoS_2, $MoSe_2$, and WSe_2 by other workers (22). A plot of (relative signal $\times h\nu)^{1/2}$ in the photoaction spectra in the onset region vs. $(h\nu)$ is a straight line with an intercept on the energy axis that should correspond to the indirect gap (23), E_g. Data from photoaction spectra give $E_g = 1.3 \pm 0.05$ eV and these data are summarized in Table V.

For the region of strong absorption, a plot of (relative signal $\times h\nu)^2$ *vs.* $(h\nu)$ should give a straight line with an energy axis intercept corresponding to the onset of the direct transition(s) (23). Such plots give values of 1.78 eV. The assignment of this as the true direct gap is doubtful and we simply use the designation "direct" to refer to the onset of relatively high absorptivity.[1]

Another technique used to evaluate the optical properties of the n-WS_2 samples is the surface photovoltage measurement *vs.* wavelength. These results accord well with the photoacoustic and photoaction spectra. At low intensity wide beam illumination, the absolute magnitude of the photovoltage signal for a crystal (24) under depletion conditions is given by the relation given in [7]

$$|\delta V_s| \propto \phi/\nu \left[1 - \frac{\exp(-\alpha W)}{1 + \alpha L_{||}}\right] W \qquad [7]$$

where W is the width of the space charge depletion region, α is the absorption coefficient, and $L_{||}$ is the parallel component of the diffusion length of the minority carriers (along the c-axis). The sign of δV_s depends on the doping type of the crystal. In all measured crystals (both n-and p-type) the signs of δV_s coincide with the type of the crystal expected from the growth procedure. The signs of δV_s were not observed to change during surface photovoltage mapping, and hence, no domains of opposite type were observed in any of these samples.

Spectral dependencies of the δV_s were used to determine the bandgap of WS_2. Near the onset of the indirect absorption both αW and αL will be much less than unity. In this case, [7] can be simplified to expression [8]

$$|\delta V_s| \propto \phi/\alpha(L_{||} + W)W \qquad [8]$$

Thus, $|\delta V_s|$ can be used to determine spectral dependence of the absorption coefficient. As shown in Fig. 8, photon energy dependence of the absorption coefficient ($\alpha \propto |\delta V_s|/\phi$) can be described by the relation given in [9]

$$(\alpha h\nu)^{1/2} \propto (h\nu - E_G) \qquad [9]$$

which is characteristic of indirect transitions (22, 23, 25). Similar results are reported from photocurrent measurements of other transition metal dichalcogenides (26). The bandgap value derived from photovol-

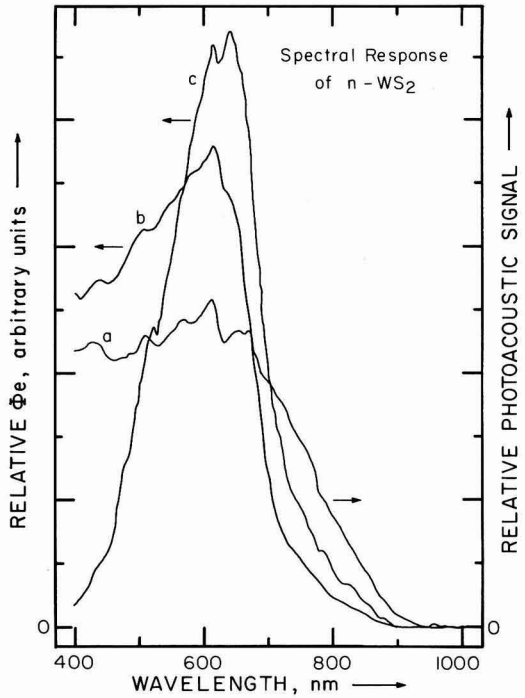

Fig. 7. (a) Photoacoustic spectrum of n-WS_2 (right scale). (b) Relative quantum yield for electron flow, Φ_e, vs. wavelength measured at +1.3V *vs.* SCE in H_2O/15M LiCl/Cl_2 (sat'd.) (left scale). (c) Relative Φ_e measured at +0.2V *vs.* SCE in H_2O/5M NaI/1 mM I_2. Note that the relative loss in Φ_e at shorter wavelengths is due to light absorption by the I_2/I^- redox couple.

[1] Ref. (21) and (23) discuss the nature of the transitions in the low energy region of strong absorption as due to excitons.

Table V. Bandgap of WS_2 electrodes from photoaction spectra*

Electrode No.	Solvent	Electrolyte/redox couple	Potential	Bandgap, eV Direct	Bandgap, eV Indirect
12	H_2O	15*M* LiCl/Cl_2 (satd.)	+1.3	1.78	1.33
9	H_2O	5*M* NaI/1 m*M* I_2	+0.2	1.77	1.34
9	CH_3CN	1*M* [Et_4N]Cl	+1.2	1.78	1.35
5	CH_3CN	0.1*M* [*n*-Bu_4N]I/1 m*M* I_2	+1.0	1.77	—

* Data taken from plots of Φ_e *vs.* λ as in Fig. 7. Data are plotted using equations in text to give the direct and indirect bandgaps. N-type WS_2 photoanode was irradiated in the indicated solvent/electrolyte/redox couple combination at the potential indicated. The potential is V *vs.* SCE.

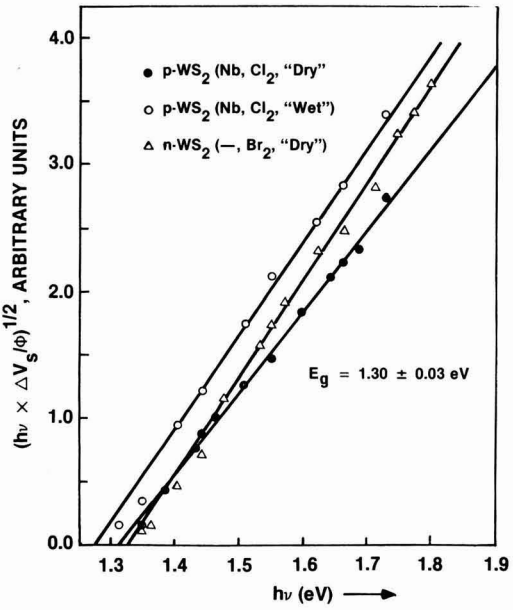

Fig. 8. Surface-photovoltage spectra near the absorption threshold of p-(Nb doped) and n-type WS_2 grown by Cl_2 and Br_2 vapor transport techniques. The intercept with the energy axis is taken as the indirect bandgap (E_g).

tage measurements is independent of the donor type and sample configuration (wet and dry). The value of 1.30 (±0.03 eV) compares favorably with the results from photoaction spectra shown in Table V. Table VI summarizes the results for WS_2 and other MY_2 samples that have been evaluated.

In order to assess the role of surface inhomogeneities, mapping of the crystals was performed at short wavelength illumination, *i.e.*, at high absorption coefficient. Under this condition the dependence of δV_s on αW and $\alpha L_{||}$ (described by [7]) can be neglected. Therefore, the height of the photovoltage signal will be a measure of the width of the space charge depletion region (W). The width of δV_s peak *vs.* distance is determined by either the size of the light spot or the perpendicular component of the diffusion length ($L_{\perp}$), whichever is larger. A typical result for n-WS_2 is shown in Fig. 9. The photovoltage signal increased at the steps. This demonstrates that the width of the space charge is larger at steps. For an n-type crystal

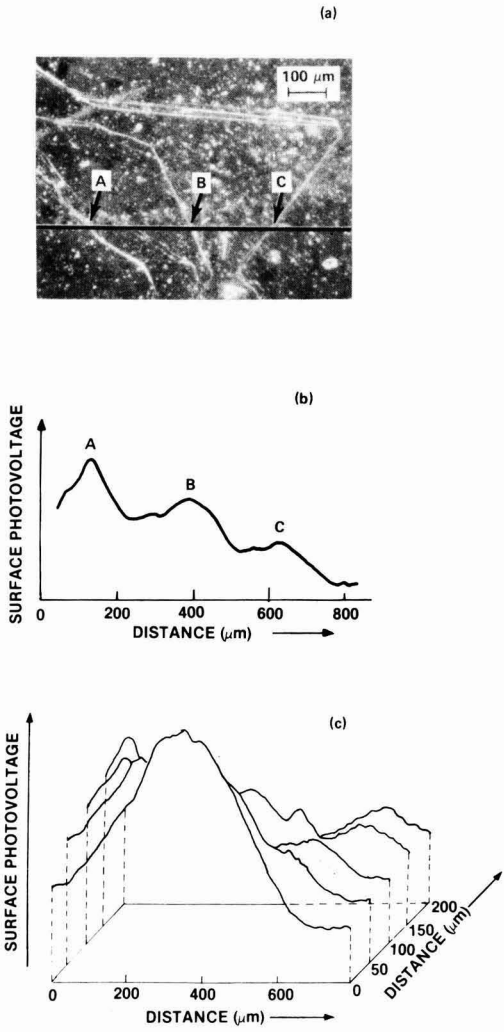

Fig. 9. (a) Optical micrograph of n-WS_2 showing steps on the surface. (b) Single surface-photovoltage scan. Horizontal line in (a) indicates path of this scan. The photovoltage maxima A, B, and C coincide with points A, B, and C in (a). (c) Three dimensional surface photovoltage micrograph over the same portion of crystal shown in (a).

Table VI. Summary of bandgap data for group VI metal dichalcogenides

Semiconductor	Bandgap, eV			
	"Direct"		Indirect	
	This work	Literature	This work	Literature††
MoS_2	1.77 (1)	1.75*	1.22 (4)	1.17 (3)
$MoSe_2$	1.38 (1)	1.4**	1.10 (2)	1.06 (3)
WS_2	1.78 (1)	Not available	1.34 (2)	Not available
WSe_2	Not det'd.	1.57†	Not det'd.	1.16 (3)

* H. Tributsch, *Z. Naturforsch., Teil A*, 32, 972 (1977).
** H. Tributsch, *Ber. Bunsenges. Phys. Chem.*, 82, 169 (1978).
† J. Gobrecht, H. Gerischer, and H. Tributsch, *ibid.*, 82, 1331 (1978).
†† W. Kautek, H. Gerischer, and H. Tributsch, *This Journal*, 127, 2471 (1980).

this increase of W at the steps can be connected with either a high negative charge at the step and/or with lower net doping concentrations ($N_D - N_A$) in this region (24). The width of the peaks at the steps is much larger than the size of the spot (5 μm). Therefore, we attribute this broadening of the peaks to the large values of the perpendicular component of the diffusion length ($L_{\perp}$) at the surface. Measurements of the width of αV_s peaks corresponding to a single edge lead to $L_{\perp} \simeq 200$ μm which is much larger than typical values of $L_{||}$ found for transition metal dichalcogenides (for MoS_2, $L_{||} \simeq 1$ μm) (22). The large ratio of $L_{\perp}/L_{||}$ is partly associated with the anisotropy of the hole mobility perpendicular and parallel to the c-axis of the crystal as well as with the local electric field generated around the step. The latter is due to

the large negative charge (n-type materials) at the steps. Similar effects were also observed for p-type crystals. Thus, as other workers have found (27), the surface quality of the layered semiconductors is an important parameter in determining recombination rates. Surface steps can account for the variation in efficiencies observed from sample to sample.

In terms of efficiency for photoelectrochemical applications the weak response in the 950-700 nm wavelength region seriously undermines the expected efficiency for solar applications. Apparently, holes created by light in this wavelength range simply do not come to the field region near the surface, paralleling the frustrations encountered in attempting to use indirect bandgap semiconductors in any photovoltaic application. The indirect gap limits the photovoltage, and absorptivity and/or hole mobility is not sufficiently great that good Φ_e values are possible until the onset of the "direct" transition that is ~0.5V away from the indirect gap of 1.3 eV.

Acknowledgments

Work done at the Massachusetts Institute of Technology was supported by GTE Laboratories, Incorporated. The use of the M.I.T. Tunable Laser Facility is also gratefully acknowledged. The authors from Brown University would like to thank the Office of Naval Research of Arlington, Virginia, for support. Acknowledgement is also made to Brown University for the use of the Materials Research Laboratory facilities.

Manuscript submitted July 14, 1981; revised manuscript received March 17, 1982.

Any discussion of this paper will appear in a Discussion Section to be published in the June 1983 JOURNAL. All discussions for the June 1983 Discussion Section should be submitted by Feb. 1, 1983.

Publication costs of this article were assisted by Massachusetts Institute of Technology.

REFERENCES

1. (a) H. Tributsch and J. C. A. Bennett, *J. Electroanal. Chem. Interfacial Electrochem.*, **81,** 97 (1977); (b) H. Tributsch, *Z. Naturforsch., Teil A,* **32,** 972 (1977); *Ber. Bunsenges. Phys. Chem.*, **81,** 361 (1977); **82,** 169 (1978); *This Journal,* **128,** 1261 (1981).
2. (a) H. J. Lewerenz, A. Heller, and F. J. DiSalvo, *J. Am. Chem. Soc.*, **102,** 1877 (1980); (b) S. Menezes, F. J. DiSalvo, and B. Miller, *This Journal,* **127,** 1751 (1980).
3. (a) F.-R. F. Fan, H. S. White, B. L. Wheeler, and A. J. Bard, *J. Am. Chem. Soc.*, **102,** 5142 (1980); *This Journal,* **127,** 518 (1980); (b) H. S. White, F.-R. F. Fan, and A. J. Bard, *ibid.*, **128,** 1045 (1981); (c) G. Nagasubramanian and A. J. Bard, *ibid.*, **128,** 1055 (1981).
4. D. Canfield and B. A. Parkinson, *J. Am. Chem. Soc.*, **103,** 1279 (1981).
5. (a) M. S. Wrighton and L. F. Schneemeyer, *ibid.*, **101,** 6496 (1979); **102,** 6964 (1980); (b) L. F. Schneemeyer, M. S. Wrighton, A. Stacy, and M. J. Sienko, *Appl. Phys. Lett.*, **36,** 701 (1980).
6. J. Gobrecht, H. Tributsch, and H. Gerischer, *This Journal,* **125,** 2085 (1978).
7. P. G. P. Ang and A. F. Sammuells, in Third International Conference on Photochemical Conversion and Storage of Solar Energy, Book of Abstracts, Solar Energy Research Institute, Golden, Colorado 80401, p. 473 (1980).
8. W. M. Latimer, "Oxidation Potentials," 2nd ed., Prentice-Hall, New York (1952).
9. M. S. Wrighton, *Acc. Chem. Res.*, **12,** 303 (1979).
10. "American Physical Society Study Group on Photovoltaic Energy Conversion," H. Ehrenreich, Chairman, The American Physical Society, New York (1979).
11. (a) A. J. Bard and M. S. Wrighton, *This Journal,* **124,** 1706 (1977); (b) H. Gerischer, *J. Electroanal. Chem. Interfacial Electrochem.*, **82,** 133 (1977); (c) S.-M. Park and M. E. Barber, *ibid.*, **99,** 67 (1979).
12. A. J. Bard, A. B. Bocarsly, F.-R. F. Fan, E. G. Walton, and M. S. Wrighton, *J. Am. Chem. Soc.*, **102,** 3671 (1980); (b) A. Aruchamy and M. S. Wrighton, *J. Phys. Chem.*, **84,** 2848 (1980); (c) F.-R. F. Fan and A. J. Bard, *J. Am. Chem. Soc.*, **102,** 3677 (1980); (d) A. B. Bocarsly, D. C. Bookbinder, R. N. Dominey, N. S. Lewis, and M. S. Wrighton, *ibid.*, **102,** 3683 (1980); (e) R. N. Dominey, N. S. Lewis, and M. S. Wrighton, *ibid.*, **103,** 1261 (1981).
13. (a) J. A. Turner, J. Manassen, and A. J. Nozik, *Appl. Phys. Lett.*, **37,** 488 (1980); (b) J. A. Turner, J. Manassen. and A. J. Nozik, *ACS Symposium Series*, **146,** 253 (1981).
14. W. Kautek and H. Gerischer, *Ber. Bunsenges. Phys. Chem.*, **84,** 645 (1980).
15. G. S. Calabrese and M. S. Wrighton, *J. Am. Chem. Soc.*, **103,** 6273 (1981).
16. R. Kershaw, M. Vlasse, and A. Wold, *Inorg. Chem.*, **6,** 1599 (1967).
17. (a) S. N. Frank and A. J. Bard, *J. Am. Chem. Soc.*, **97,** 7427 (1975); (b) P. A. Kohl and A. J. Bard, *ibid.*, **99,** 7531 (1977); (c) D. Laser and A. J. Bard, *J. Phys. Chem.*, **80,** 459 (1976).
18. (a) A. Kama and R. Enari, *Conf. Ser.-Inst. Phys.*, No. 43, Chap. 5 (1979); (b) J. C. McMenamin and W. E. Spicer, *Phys. Rev. B*, **16,** 5474 (1977).
19. C. P. Kubiak, L. F. Schneemeyer, and M. S. Wrighton, *J. Am. Chem. Soc.*, **102,** 6898 (1980).
20. D. A. Skoog and D. M. West, "Fundamentals of Analytical Chemistry," p. 523, Holt, Rinehart, and Winston, New York (1963).
21. J. A. Wilson and A. D. Yoffe, *Adv. Phys.*, **18,** 193 (1969).
22. W. Kautek, H. Gerischer, and H. Tributsch, *This Journal,* **127,** 2471 (1980).
23. J. I. Pankove, "Optical Processes in Semiconductors," pp. 35-38, Dover Publications, Inc., New York (1971).
24. E. Kamieniecki, *J. Vac. Sci., Technol.*, **19,** (1982).
25. E. J. Johnson, in "Semiconductors and Semimetals," Vol. 3, R. K. Willardson and A. C. Beer, Editors, p. 153, Academic Press, New York (1967).
26. B. L. Evans, in "Physics and Chemistry of Materials with Layered Structure," Vol. 3, P. A. Lee, Editor, p. 1, D. Reidal Publishing Co., Boston (1976).
27. (a) H. Gerischer, *ACS Symposium Series,* **146,** 1 (1981); (b) H. J. Lewerenz, A. Heller, H. J. Leamy, and S. D. Ferris, *ibid.*, **146,** 17 (1981).

The Galvanostatic Method: Analysis of Error and Computation of Parameters

Hannah Reller and Emilia Kirowa-Eisner

Institute of Chemistry, Tel-Aviv University, Tel-Aviv 69978, Israel

ABSTRACT

Galvanostatic transients arising from multi-step processes of the type: $\nu_o O + ne = \nu_R R$ are treated mathematically for systems subjected to both activation and diffusion control. Analysis of error based on the error matrix is presented. The galvanostatic method is characterized by the information contents [$I(i_o)$ and $I(C_{dl})$] for a single-estimate analysis (*i.e.*, estimate of i_o for known C_{dl} or the reverse) and that for a two-estimate analysis (simultaneous determination of i_o and C_{dl}). The correlation between the estimates of i_o and C_{dl} is given as a function of the dimensionless scale T/τ_c. Information contents for i_o and C_{dl} in single and two-estimate systems are given and this permits the determination of the accuracy and the limits of the method as well as the choice of optimal experimental conditions. The optimal full time scale for estimation of i_o depends on the value of τ_c/τ_d. For τ_c/τ_d between 0.5-500, T_{opt}/τ_c varies from 6 to 18 (single-estimate system) and from 4 to 25 (two-estimate system). The upper limit for i_o in a single-parameter estimation is 3-12 A cm^{-2} (for C_{dl} 10-40 μF cm^{-2}) and the upper limit for $k_s(\alpha_a = \alpha_c = 0.5)$ is 8 cm sec^{-1}. This is three times greater than k_s for the coulostatic method. For a given value of k_s, the accuracy of the galvanostatic method is better than that of the coulostatic for systems when $\tau_c/\tau_d > 0.6$, but is not as good when $\tau_c/\tau_d < 0.6$. The upper limit of k_s and the accuracy of the galvanostatic method for two-estimate analysis (i_o and C_{dl}) are considerably lower than those for single-estimate analysis. An iteration method is developed with which a large improvement is achieved. Estimation of i_o and C_{dl} with a computerized curvilinear regression analysis is proposed.

The galvanostatic method is one of the oldest techniques employed in electrochemistry and is currently used in the study of fast electrochemical reactions. Equations describing the galvanostatic potential-time relationship have been derived by Berzins and Delahay (1) for a simple redox system of the type $O + ne = R$ subjected to both activation and diffusion control (and with double-layer-charging currents taken into account). More complex cases incluing coupled chemical reactions or adsorption of reactants have been also treated (2).

Sluyters *et al.* have done a thorough analysis of the method: nomograms, tables and a complex plane analysis for treatment of experimental data were proposed (3-6); the accuracy of the approximation methods was discussed (3) and optimal experimental conditions were proposed (4).

$$\eta = -\frac{i}{C_{dl}(\gamma-\beta)}\left\{\begin{array}{l}\dfrac{\gamma}{\beta^2}\left[\exp(\beta^2 t)\,\mathrm{erfc}(\beta t^{1/2}) + 2\beta\left(\dfrac{t}{\pi}\right)^{1/2} - 1\right] \\ -\dfrac{\beta}{\gamma^2}\left[\exp(\gamma^2 t)\,\mathrm{erfc}(\gamma t^{1/2}) + 2\gamma\left(\dfrac{t}{\pi}\right)^{1/2} - 1\right]\end{array}\right\} \qquad [1]$$

In this work we treat some of the problems encountered in the study of fast electrode reactions by the galvanostatic method.

1. Mathematical expressions are developed for multi-step reactions $\nu_o O + ne = \nu_R R$, where ν_o and ν_R differ from unity.

2. Simple criteria for optimal experimental conditions are given.

3. The accuracy of the method and its limits are estimated on the basis of error analysis. The analysis is extended to cases in which i_o is a single estimate (known C_{dl}) and to cases in which i_o is estimated simultaneously with C_{dl}.

4. The correlation between the estimates i_o and C_{dl} is given.

5. An iteration method for the simultaneous determination of i_o and C_{dl} based on measurements at different parts of the transient curves is proposed.

6. Estimation of i_o and C_{dl} with a computerized curvilinear regression analysis, based on the method of least squares, is proposed.

The approach applied in this work is similar to that used previously for the coulostatic method (7, 8). The application of statistical methods in this work permitted the extension of that treatment to the case of the simultaneous estimation of i_o and C_{dl}.

Key words: diffusion, galvanostatic method, regression analysis.

Computation of Parameters

Potential-time relationship for the galvanostatic method at small perturbation ($|\eta| \leq RT/\alpha\mathbf{F}$) for a redox system $O + ne = R$ subjected to both activation and diffusion control with accounting for double layer charging has been derived by Berzins and Delahay (1), Eq. [1]. Treatment for multi-step processes of the type $\nu_o O + ne = \nu_R R$ results in identical expressions in terms of τ_c and τ_d. The relaxation constants τ_c and τ_d contain the parameters ν_o, ν_R, and ν of the multi-step process. All discussions about the applicability of those equations are identical to those in previous work on the coulostatic method (7)

where

$$\beta = [\tau_d^{1/2} + (\tau_d - 4\tau_c)^{1/2}]/2\tau_c \qquad [2]$$

$$\gamma = [\tau_d^{1/2} - (\tau_d - 4\tau_c)^{1/2}]/2\tau_c \qquad [3]$$

$$\tau_c = \frac{\nu}{n}\frac{RT}{\mathbf{F}}\frac{C_{dl}}{i_o} \qquad [4]$$

$$\tau_d^{1/2} = \frac{RT\,C_{dl}}{n^2\mathbf{F}^2}\left(\frac{\nu_o^2}{C_O^o D_O^{1/2}} + \frac{\nu_R^2}{C_R^o D_R^{1/2}}\right) \qquad [5]$$

There are two common methods of data handling for the estimation of parameters (*e.g.*, i_o, C_{dl}) from a transient η/t:

(*i*) Selecting a single point along the transient and calculating p from the relation $p = p\ (\eta, t)$. For an implicit p-η relationship (as in the case of the galvanostatic method), p cannot be easily isolated. Kooijman *et al.* have facilitated this problem by the nomogram method (4).

(*ii*) Fitting the experimental points from given sections of the transient to the theoretical function by the least-squares method. This method is well suited for implicit relationships; it is important in cases of

two-parameter estimation (*e.g.*, i_o and C_{dl}) and serves as the basis for all discussions in the present work. Sluyters *et al.* (6) have elaborated a transformation procedure by which transients are converted into impedances and subsequently treated by the complex-plane method.

Our approach for the estimation of the parameters is to use direct parameter fitting of the analytical η-t expression (Eq. [1]) to the experimental data (from a section of the transient) by means of computerized curvilinear regression analysis. By this method, the estimates of i and C_{dl} are those which minimize the sum of squares

$$Q^2 = \sum_{t=0}^{T} \frac{(\eta_t(\text{exp}) - \eta_t(\text{calc})^2}{\sigma(\eta)^2} \qquad [6]$$

for $t = 0, \Delta T \ldots (N - 1)\Delta T, T$. Equally weighted points from the experimental η-t curve are fitted to the analytical expression of η-t (Eq. [3]), by the use of the library program MINUIT (10). The same approach was applied to the coulostatic method (8).

Analysis of Error

Our approach in the analysis of error is based on the use of the concept "information content," I. This has been defined in a previous paper, where it was applied to the analysis of the coulostatic method (8). The quantity I is a dimensionless parameter, which determines quantitatively the amount of information on a calculated parameter, p, contained in a measured quantity, η. It characterizes the power of the method, independently of the precision of the instrumentation or of the accuracy by which measurements are made.

The higher the information content of a parameter the better is its characterization. The power of different methods or of the same method under different conditions can be compared on the basis of information content. It also enables an immediate calculation of the standard deviation of the estimated parameter p, provided the standard deviation of η is given (Eq. [10]). The instantaneous information of the parameter p (all other parameters exactly known) at time t along the transient, is defined as

$$I(p) = \frac{p}{\eta_{max}} \left(\frac{\partial \eta}{\partial p}\right)_t \qquad [7]$$

where η_{max} is the maximum value of the measured quantity, η. In the galvanostatic method, η_{max} is the value of η at the end of a given transient (at $t = T$), because the overpotential rises with time. However, in the coulostatic method, η_{max} is the value of η at $t = 0$, since in the latter method the overpotential decays with time.

As stated above, the computation of parameters is made with data taken from sections of the transient, and thus the integrated information[1] $I(p)$, contained in that section is relevant

$$\bar{I}(p) = \frac{1}{T} \int_0^T I(p)\,dt \qquad [8]$$

The limits for $\bar{I}$ (as for I) are 0-1. A zero value for $\bar{I}(p)$ means that the measured parameter η is independent of p (does not provide information about p). $\bar{I}(p) = 1$, corresponds to a first-power relationship $\eta = \text{const } p^{\pm 1}$, where p is the only parameter that determines η. $\bar{I}(p) = \frac{1}{2}$ corresponds to $\eta = \text{const} \cdot t \cdot p^{\pm 1}$.

A knowledge of I (or $\bar{I}$) allows the estimation of (*i*) the optimal experimental conditions, (*ii*) the limits of the method, and (*iii*) the standard deviation of the estimate of the parameter p under given experimental conditions [with known variance of the overpotential $\sigma(\eta)$]. The relation between the information content $I(p)$ and the population standard deviation σ_p is obtained by replacing $\partial\eta/\partial p$ by $(\sigma(\eta)/N^{1/2})/\sigma(p)$ (see Appendix A)

$$I(p) = \frac{p}{\sigma(p)} \frac{\sigma(\eta)}{\eta_{max}} \frac{1}{N^{1/2}} \qquad [9]$$

The quantity of interest is not the absolute value of $\sigma(p)$, but its coefficient of variation, $\epsilon(p) = \sigma(p)/p$, since for a given ratio τ_c/τ_d,[2] $\epsilon(p)$ [as well as $I(p)$] is a single-valued function of t/τ_c. In most measurements $\sigma(\eta)$ is independent of η, for a given sensitivity of the measuring device. Furthermore, we idenitfy $\sigma(\eta)/(\eta_{max}N^{1/2})$ by $\epsilon(\eta_{max})$, which represents the instrumental precision of the measurement. With the use of this parameter, Eq. [9] becomes

$$\epsilon(p) = \frac{\epsilon(\eta_{max})}{I(p)} \qquad [10]$$

where $\epsilon(p)$ is the relative error in the determination of p at a confidence level of 68.3% (1 standard deviation unit). Given the instrumental precision $\epsilon(\eta_{max})$ it enables us to predict the precision by which p can be measured. Equation [10] correlates the instrumental precision with the power of the method.

Error analysis based on the error matrix.—In the case of the coulostatic method, $\bar{I}(p)$ was calculated according to Eq. [8] for different values of τ_c/τ_d over a wide range of time (8). By this method only $\bar{I}$ values for single-estimate systems can be acquired. Here, we have applied a more general method, based on the error matrix (Eq. [10]). It allows determinatin of $\bar{I}$ in a two-estimate system which is of importance in the simultaneous determination of i_o and C_{dl}.

The error matrix E [called also variance-covariance matrix (Ref. 11, p. 62)] contains the variances of the parameters i_o and C_{dl} as diagonal elements, and the covariance, $\rho[{}_2\sigma(i_o)][{}_2\sigma(C_{dl})]$ as the off-diagonal elements. ρ is the correlation coefficient between the two parameters

$${}_2E = \begin{pmatrix} {}_2\sigma(i_o)^2 & \rho \cdot {}_2\sigma(i_o) \cdot {}_2\sigma(C_{dl}) \\ \rho \cdot {}_2\sigma(i_o) \cdot {}_2\sigma(C_{dl}) & {}_2\sigma(C_{dl})^2 \end{pmatrix} \qquad [11]$$

The prescript stands for the number of estimated parameters. The principle of the method is to calculate the population variances and population covariances of the estimated parameters (i_o and C_{dl}) in the functional relationship $\eta = f(t; i_o, C_{dl})$, where η has a known analytical expression (Eq. [1]); η is a dependent variable with a standard deviation $\sigma(\eta)$; t is an independent variable, bearing no error of measurement, *i.e.*, the errors are practically negligible as compared with the error of η; the respective ${}_2I$ values are

[1] In previous work (8) the expression "average information" was used for this function.

[2] It will be noted that the ratio τ_c/τ_d is a measure of the relative contribution of the activation and of the diffusion control. Systems with identical τ_c/τ_d behave identically when compared on a dimensionless scale t/τ_c (regardless of individual values of i_o and C_{dl}) (4). τ_c/τ_d can be conveniently estimated from $\tau_c/\tau_d \sim n^2C^2/(i_oC_{dl})$ for $C = C_O^o = C_R^o$; $D_O = D_R = 10^{-5}$ cm^2 sec^{-1}, $\nu = \nu_O = \nu_R = 1$, C in mM, i_o in A, C_{dl} in F cm^{-2}). For orientation purposes it will be added that systems with $\tau_c/\tau_d > 1000$ have low diffusion contribution, and systems with $\tau_c/\tau_d < 10$ have a high degree of diffusion control.

calculated according to Eq. [9]. ${}_1\bar{I}$ values are calculated from ${}_2\bar{I}$ and ρ as shown later.[3]

The error matrix E is calculated by inverting the information matrix G. Since the least-squares estimator is used in the estimation of the parameters i_o and C_{dl}, the elements of the information matrix G are [Ref. (11), pp. 126 and 169]

$$G_{ij} = \frac{1}{\sigma(\eta)^2} \sum_{t=0}^{T} \left[\left(\frac{\partial \eta}{\partial p_i} \right)_t \left(\frac{\partial \eta}{\partial p_j} \right)_t \right]$$

$$\text{for } t = 0, \frac{T}{N}, \frac{2T}{N}, \ldots \frac{(N-1)T}{N}, T \text{ and } N \to \infty$$

The limits of the summation are 0 and T, since for calculating the integrated information $\bar{I}(p)$, the population variances $\sigma(p)$ for entire sections of the transient are needed.

The quantities ${}_2\sigma(i_o)$, ${}_2\sigma(C_{dl})$, and ρ appearing in the matrix E thus calculated are the integrated values corresponding to a given time scale T. Calculations were made for various time scales with different values of τ_c/τ_d and these yielded the parameters of interest, summarized in Fig. 1, 2, and 3. The graphs of these three parameters $\bar{I}(i_o)$, $\bar{I}(C_{dl})$, and ρ plotted *vs.* T/τ_c depend on τ_c/τ_d only (as mentioned before).

If one of the parameters is "fixed" at the correct value, the standard deviation of the estimated parameter is always smaller than is the case when the estimation is carried out for the two parameters (Eq. [11]). This is so, since by fixing one of the parameters,

[3] ${}_1\bar{I}(p)$ calculated according to the statistical method may in some cases differ from that calculated according to Eq. [8]. The statistically calculated ${}_1\bar{I}(p)$ is given by ${}_1\bar{I} = (1/T)\left(\int_0^T {}_1I^2 dt\right)^{1/2}$ (Appendix B), while the nonstatistical one is ${}_1\bar{I} = (1/T)\int_0^T {}_1I dt$ (Eq. [8]). The difference beween them stems from differences in estimators: the statistical $\bar{I}$ is calculated with the least-squares estimator, while the latter can be derived by minimizing the square of the sum of the absolute values of the deviations (*not* the sum of squares of the deviations). The difference depends on the type of relation between the parameters p and η. They may not differ at all, as in the case of $\bar{I}$ (i_o) or may differ by several percent as in the case of $\bar{I}(C_{dl})$. While the correct function is the statistically calculated one, the differences between them are negligible in the application to which they are put here.

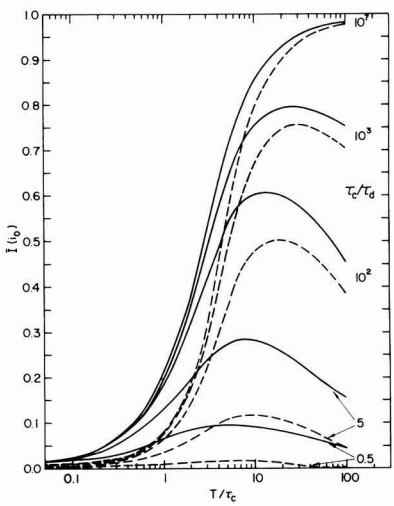

Fig. 1. ${}_1\bar{I}(i_o)$ and ${}_2\bar{I}(i_o)$ as function of T/τ_c at various τ_c/τ_d. ——— ${}_1\bar{I}(i_o)$ [single-estimate system (i_o-estimate, C_{dl}-fixed)]; - - - - ${}_2\bar{I}(i_o)$ [two-estimate system (i_o and C_{dl}-estimates)].

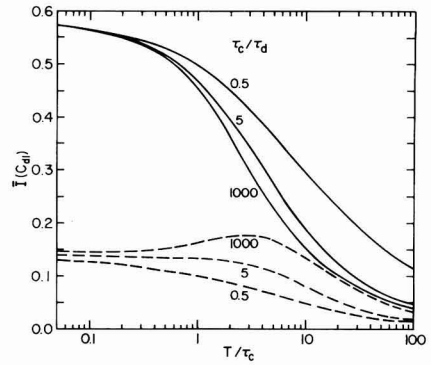

Fig. 2. ${}_1\bar{I}(C_{dl})$ and ${}_2\bar{I}(C_{dl})$ as a function of T/τ_c at various τ_c/τ_d. ——— ${}_1\bar{I}(C_{dl})$ [single-estimate system (C_{dl}-estimate, i_o-fixed)]; - - - - ${}_2\bar{I}(C_{dl})$ [two-estimate system (i_o and C_{dl}-estimates)]

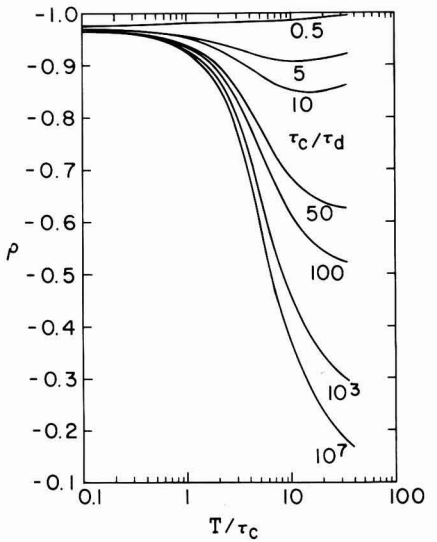

Fig. 3. Correlation coefficient between i_o and C_{dl} as function of T/τ_c.

one is supplying information about the other. This information is transmitted by means of the correlation between i_o and C_{dl} [Ref. (11), p. 198]

$$ {}_1\sigma(p) = {}_2\sigma(p)\,(1-\rho^2)^{1/2} \qquad [14]$$

The relation between the information content for a system with two estimates $[{}_2\bar{I}(p)]$ and that for a system with one estimate $[{}_1\bar{I}(p)]$ (with a frozen parameter) is derived from Eq. [9] and [12]

$$ {}_1\bar{I}(p) = {}_2\bar{I}(p)\,(1-\rho^2)^{-1/2} \qquad [15]$$

Concerning the form of the information curves (Fig. 1 and 2): For $T << \tau_c$, the double layer is charged and the overpotential increases linearly with time ($\eta = it/C_{dl}$). In this region, η is a function of C_{dl} only, but not of i_o and thus $\bar{I}(i_o) = 0$ and $\bar{I}$ (C_{dl}) obtains its maximum value. In an intermediate range of T/τ_c (5-30 depending on τ_c/τ_d), maximum values for $I(i_o)$ are reached. At $T >> \tau_c$, the influence of the diffusion is increased, and thus $\bar{I}(i_o)$ decreases. For the specific

case $\tau_c/\tau_d \to \infty$ (negligible diffusion contribution), the overvoltage reaches a constant value, independent of time and of capacitance [$\eta = (i/i_o)(\nu/n)\ (RT/\mathbf{F})$]. Thus a limiting value for $\bar{I}(i_o)$ is obtained: $I(i_o) = 1$. (This is the maximum information that is obtained in a linear relationship between measured value and calculated parameter.) In the coulostatic method (8) the limiting value for $\bar{I}(i_o)$ (obtained for $\tau_c\tau/_d \to \infty$) is only 0.30.

The time scale, on which the maximum value of $\bar{I}(i_o)$ is reached (see Fig. 1) depends on τ_c/τ_d. The larger τ_c/τ_d, the larger the value of the dimensionless time scale T/τ_c (Fig. 4). The optimal time scale, T/τ_c, varies from 4 to ∞ for τ_c/τ_d varying from 10^{-2} to ∞. The importance of Fig. 4 is that it supplies information on how to choose the optimal scale for measuring the galvanostatic transient.

In fact, optimal results for each τ_c/τ_d can be obtained for quite a wide range of time scales. For example, for $\tau_c/\tau_d = 5$, $T/\tau_c \simeq$ 5-15 (for a single-estimate system) and T/τ_c 5-20 (for a two-estimate system) can be used (Fig. 1). For $\tau_c/\tau_d = 100$, the respective time scales are 5-20 and 9-30. Sluyters *et al.* (4) also estimated the optimal time for single parameter estimation. However, their calculations correspond to single point determinations and not to determinations based on entire sections from the transient, as it is in our case. One can see from Fig. 1, Ref. (4), that the optimal time is shifted to larger values with the increase of τ_c/τ_d. The extent of the shift in the range shown $0.2 < \tau_c/\tau_d < 100$, is small, which is in good agreement with our results (*cf.*, Fig. 4, solid line). According to the case we consider, T/τ_c is 6 for $0.1 < \tau_c/\tau_d < 5$; for $\tau_c/\tau_d > 10$, the optimal full time scale increases rapidly with τ_c/τ_d.

While the optimal time scale for the galvanostatic measurements increases with τ_c/τ_d, that for the coulostatic measurements is independent of τ_c/τ_d and is $T/\tau_c = 2$ (8). The reason for this difference stems from the fact that for a galvanostatic transient, η increases with time (or reaches a constant value for $\tau_c/\tau_d \to \infty$) while for a coulostatic transient, η decays to zero (that is, after a certain time, the information content decreases to zero even for cases without diffusion control).

The values of ${}_1\bar{I}(i_o)$ and ${}_2\bar{I}(i_o)$ at which the information curves (Fig. 1) reach maxima are plotted as functions of τ_c/τ_d in Fig. 5. There is a considerable loss of information in the two-estimate system. As will be shown in a future publication, in the coulostatic method this loss is much smaller.

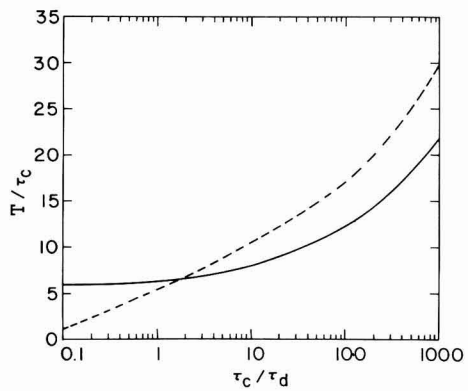

Fig. 4. Optimal time scale for estimation of i_o as function of τ_c/τ_d. ——— Single-estimate system (i_o-estimate, C_{dl}-fixed); - - - - two-estimate system (i_o and C_{dl}-estimates).

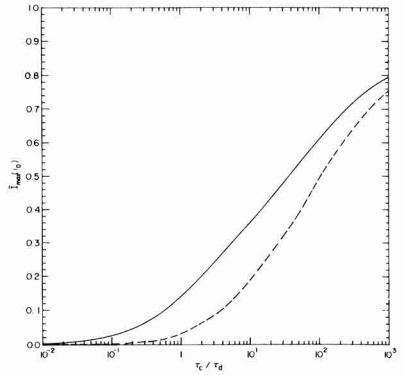

Fig. 5. Maximal values of ${}_1\bar{I}(i_o)$ and ${}_2\bar{I}(i_o)$ as function of τ_c/τ_d. ——— Single-estimate system (i_o-estimate, C_{dl}-fixed); - - - - two-estimate system (i_o and C_{dl}-estimates).

Conditional dependence between parameters.—In the case of single-estimate analysis, an error Δp_2 of the "known" (fixed) parameter brings about an error $\rho(_2\sigma(p_1)/_2\sigma(p_2))\Delta p_2$ in the estimated parameter [Ref. (11), p. 63]. Thus

$$\Delta i_o/\Delta C_{dl} = \rho[_2\sigma(i_o)/_2\sigma(C_{dl})] \qquad [14]$$

The negative sign of the correlation coefficient (Fig. 3) indicates that a positive error in C_{dl} causes a negative error in i_o (and vice versa). General presentation of the conditional dependence is achieved by the use of relative rather than absolute variations in Eq. [14]

$$(\Delta i_o/i_o)/(\Delta C_{dl}/C_{dl}) = \rho[_2\sigma(i_o)/i_o]/[_2\sigma(C_{dl})/C_{dl}] \qquad [15]$$

The rhs of Eq. [15] depends on τ_c/τ_d only when compared on a dimensionless time scale T/τ_c, while the rhs of Eq. [41] depends also on i_o, C_{dl}, and concentrations. Plots of $(\Delta i_o/i_o)/(\Delta C_{dl}/C_{dl})$ *vs.* T/τ_c for different τ_c/τ_d values are given in Fig. 6 and are used to calculate the relative error in i_o as result of an error in C_{dl} and vice versa.

The larger the diffusion contribution (the smaller τ_c/τ_d), the larger the systematic error $\Delta i_o/i_o$ caused by error in C_{dl}. This error increases with decrease of the time scale.

It should be stressed that although the accuracy in the estimation of a parameter is conditionally dependent on the error of the "known" parameter, the precision is independent of it. The precision, and thus the information content are those for single-estimate analysis with a precisely known value of the fixed parameter [Ref. (11), p. 63].

Iteration Method for Simultaneous Determination of i_o and C_{dl}

The precision achieved in the single-estimate determination of i_o is substantially higher than that for the case in which i_o and C_{dl} are both estimated parameters (compare full lines with dotted lines in Fig. 1 and 2). The usual technique in the latter case is the determination of C_{dl} from the initial part of the transient, in which η *vs.* t is linear ($C_{dl} = i(\partial\eta/\partial t)^{-1}$). But when dealing with fast electrode reactions, the linear region is shortened to such an extent that this method is impractical. For example, if it is desired to estimate C_{dl} with an error of 5% in a system with $C_{dl} = 20$ μF/cm^2 and $i_o = 0.5$ A/cm^2, measurements must be carried out at a full time scale $T \sim 0.1$ μsec. Noises at the beginning of the pulse (due to unmatched impedances, stray capacitance, and inductance) may last about 50 nsec) make the use of a full time scale

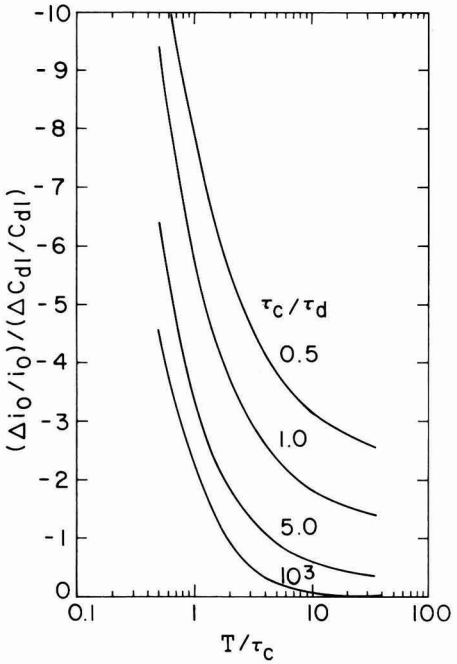

Fig. 6. Conditional dependence of relative error of estimated parameter on relative error of fixed parameter (i_o-estimate, C_{dl}-fixed or C_{dl}-estimate, i_o-fixed) as function of T/τ_c. $\lambda = |(\Delta i_o/i_o)/(\Delta C_{dl}/C_{dl})|$.

shorter than 0.5 μsec impractical. In such a case, i_o and C_{dl} must be determined by the two-parameter fitting procedure proposed here.

The precision in the simultaneous determination of i_o and C_{dl} is greatly enhanced by using an iteration procedure, in which the two parameters are determined for several time scales. Due to the fact that the optimal time scale for the determination of i_o and C_{dl} differs greatly (*cf.*, Fig. 1 and 2), the following iterative method is proposed.

Initial step, $n = 0$: Simultaneous estimation of i_o and C_{dl}. The two parameters are estimated by the curve-fitting procedure from several arbitrarily chosen time scales. The mean value of each parameter is calculated.

nth iteration step, C_{dl} single estimate: i_o is fixed at a value calculated from the $(n-1)$ iteration step. Data from the transient with the shortest full time scale are used.

nth iteration step, i_o single estimate: C_{dl} is fixed at a value calculated from the nth step above. The optimal time scale for this estimation is chosen on the basis of Eq. [20] as will be discussed in the next paragraph. The last two steps are repeated until i_o and C_{dl} remain unchanged, within the expected error as estimated from Eq. [20] and [21].

The enhancement of the accuracy achieved by the iteration procedure will be demonstrated by following the decrease of the relative error of the estimates. The errors are calculated at the 68.3% confidence level, corresponding to one standard deviation.

At the initial step, $n = 0$, i_o and C_{dl} are simultaneously estimated with relative random errors ${}^{o}\epsilon(i_o)$ $(= {}_{2}\sigma(i_o)/i_o)$ and ${}^{o}\epsilon(C_{dl})$ $(= {}_{2}\sigma(C_{dl})/C_{dl})$. According to Eq. [10], ${}^{o}\epsilon(i_o) = \epsilon(\eta_{max})/{}_{2}\bar{I}(i_o)$ and ${}^{o}\epsilon(C_{dl}) = \epsilon(\eta_{max})/{}_{2}\bar{I}(C_{dl})$ where ${}_{2}\bar{I}(i_o)$ and ${}_{2}\bar{I}(C_{dl})$ are the information contents for a two-estimate system (the respective average values over the time scale used).

The relative error in the determination of C_{dl}, ${}^{n}\epsilon(C_{dl})$, at a fixed value of i_o at the nth iteration step, comprises two terms. One is a random error, arising from uncertainty in η, which is incorporated in the single-parameter estimation and is ${}_{1}\sigma(C_{dl})/C_{dl} = \epsilon(\eta_{max})/{}_{1}\bar{I}(C_{dl})$, where ${}_{1}\bar{I}(C_{dl})$ is the information content corresponding to the data from the shortest time scale used in the initial step. The second term is an error conditional on the error of the fixed parameter and is equal to ${}^{n=1}\epsilon(i_o)/\lambda(T_c)$, where $\lambda(T) = |(\Delta i_o/i_o)/(\Delta C_{dl}/C_{dl})|$. The value of $\lambda(T)$ varies with T/τ_c (Fig. 6). $\lambda(T)_c$ is the value of $\lambda(T)$ corresponding to the time scale used for the determination of C_{dl}.

For the total relative error, ${}^{n}\epsilon(C_{dl})$, we have

$$ {}^{n}\epsilon(C_{dl}) = {}^{n-1}\epsilon(i_o)/\lambda(T_c) + \epsilon(\eta_{max})/{}_{1}\bar{I}(C_{dl}) \quad [16] $$

In the case of $n = 1$, the first term on the rhs of Eq. [16] will be ${}^{o}\epsilon(i_o)/\lambda(T_c) = \epsilon(\eta_{max})/({}_{2}\bar{I}(i_o)\lambda(T_c))$.

The total relative error of i_o at the nth step is

$$ {}^{n}\epsilon(i_o) = {}^{n}\epsilon(C_{dl}) \cdot \lambda(T_i) + \epsilon(\eta_{max})/{}_{1}\bar{I}(i_o) \quad [17] $$

where $\lambda(T_i)$ is the value of $\lambda(T)$ at the optimal time scale for the determination of i_o.

Combining Eq. [16] and [17] and substituting $\epsilon(\eta_{max})/{}_{2}\bar{I}(i_o)$ for ${}^{o}\epsilon(i_o)$, one obtains (See Appendix C)

$$ \frac{{}^{n}\epsilon(i_o)}{\epsilon(\eta_{max})} = \left(\frac{\lambda(T_i)}{\lambda(T_c)}\right)^{n} \cdot \frac{1}{{}_{2}\bar{I}(i_o)} + \frac{1-\left(\frac{\lambda(T_i)}{\lambda(T_c)}\right)^{n}}{1-\frac{\lambda(T_i)}{\lambda(T_c)}} \left(\frac{\lambda(T_i)}{{}_{1}\bar{I}(C_{dl})} + \frac{1}{{}_{1}\bar{I}(i_o)}\right) \quad [18] $$

and

$$ \frac{{}^{n}\epsilon(C_{dl})}{\epsilon(\eta_{max})} = \left(\frac{\lambda(T_i)}{\lambda(T_c)}\right)^{n-1} \cdot \frac{1}{\lambda(T_c)} \cdot \frac{1}{{}_{2}\bar{I}(i_o)} + \frac{1-\left(\frac{\lambda(T_i)}{\lambda(T_c)}\right)^{n-1}}{1-\frac{\lambda(T_i)}{\lambda(T_c)}} \left(\frac{\lambda(T_i)}{\lambda(T_c)} \frac{1}{{}_{1}\bar{I}(C_{dl})} + \frac{1}{\lambda(T_c)} \frac{1}{{}_{1}\bar{I}(i_o)}\right) + \frac{1}{{}_{1}\bar{I}(C_{dl})} \quad [19] $$

It is seen from Eq. [18] and [19] that the smaller the ratio $\lambda(T_i)/\lambda(T_c)$, the smaller the errors in i_o and C_{dl} and the sooner the minimal values of the error are reached. At an infinite number of iterations

$$ \frac{{}^{\infty}\epsilon(i_o)}{\epsilon(\eta_{max})} = \frac{1}{1-\frac{\lambda(T_i)}{\lambda(T_c)}} \left(\frac{\lambda(T_i)}{{}_{1}\bar{I}(C_{dl})} + \frac{1}{{}_{1}\bar{I}(i_o)}\right) \quad [20] $$

$$ \frac{{}^{\infty}\epsilon(C_{dl})}{\epsilon(\eta_{max})} = \frac{1}{1-\frac{\lambda(T_i)}{\lambda(T_c)}} \left(\frac{\lambda(T_i)}{\lambda(T_c)} \frac{1}{{}_{1}\bar{I}(C_{dl})} + \frac{1}{\lambda(T_c)} \frac{1}{{}_{1}\bar{I}(i_o)}\right) + \frac{1}{{}_{1}\bar{I}(C_{dl})} \quad [21] $$

Optimal time scale for estimation of i_o with the iteration procedure.—When a single-estimate determination of i_o is made with C_{dl} known from independent measurements, the optimal time scale is the one at which $\bar{I}(i_o)$ reaches its maximum value (Fig. 1). In

cases in which the interation procedure is applied, the precision depends on the values of $\bar{I}(p)$ and $\lambda(T)$ (Eq. [20]), and the choice of time scale for the estimation of i_o is a bit more complicated (there is no doubt that the time scale for estimating C_{dl} is the shortest time scale that the instrumental setup permits). In the case of i_o there are two contradictory requirements: maximum ${}_1\bar{I}(i_o)$ and minimum $\lambda(T_i)$. Since the first requirement has a larger weight than the second, the optimal time scale is largely determined by it. As a rule of thumb, a time scale 10-50% larger than the one at which ${}_1\bar{I}(i_o)$ reaches its maximum value is suitable, and in most cases, any time scale in this range is suitable, since the information curve of i_o (Fig. 1) has a broad peak. Data from Fig. 1, 2, and 6 can be used in Eq. [20] to ensure that for a given system, the best time scale is chosen.

Example of the efficiency of the iteration procedure.—The enhancement of the accuracy is exemplified by a system with $\tau_c/\tau_d = 0.5$ and $\tau_c = 1$ μsec. The experimentalist who has no previous knowledge of the system will record transients, say in three full time scales, 0.5, 5, and 50 μsec. If we choose the following typical values for each transient: $\eta_{max} = 5$ mV, $\sigma_\eta = 0.1$ mV, and $N = 10$, then $\epsilon(\eta_{max}) = 0.6\%$ (according to Eq. [9]).

In order to follow the iteration procedure theoretically, it is necessary that $\bar{I}(i_o)$, $\bar{I}(C_{dl})$, $\lambda(T_i)$, and $\lambda(T_c)$ be known. Data extracted from Fig. 1, 2, and 6 are given in Table I. At the initial step ($n = 0$), i_o and C_{dl} are simultaneously estimated from data of the three time scales. The average information content ${}_2\bar{I}(i_o)$ over the three scales is low (0.01), and corresponds to a relative error ${}^o\epsilon(i_o)$ of 60%. The respective value for C_{dl} is ${}^o\epsilon(C_{dl}) = 10\%$. The errors in i_o and C_{dl} at each iteration step are calculated according to Eq. [16] and [17] and presented graphically in Fig. 7. After the fifth iteration step, $\epsilon(i_o)$ has decreased from 60 to 20% and $\epsilon(C_{dl})$ from 10 to 3%. Better accuracy could be achieved if a shorter time scale for the determination of C_{dl} were chosen. For the sake of comparison, if i_o (or C_{dl}) were determined for an exactly known C_{dl} (or i_o), $\epsilon(i_o) = 7\%$ [or $\epsilon(C_{dl}) = 1\%$ would be obtained].

Limits of the Galvanostatic Method

The upper limit for i_o in a single-parameter estimation is determined as follows. The shortest full time scale to be used is limited by instrumental problems and is $T \sim 0.5$ μsec. Since at the lower range of τ_c/τ_d the optimal dimensionless full time scale T/τ_c is 6 (Fig. 4), the smallest of τ_c is 0.08 μsec, which in terms of i_o is 3-12 A cm^{-2} (for C_{dl} 10-40 μF cm^{-2}). The same limits for τ_c and i_o are reported by Sluyters *et al.* (3) with considerations based on ohmic drop miscompensation. The galvanostatic method enables determination of exchange currents six times larger than those determined by the coulostatic method (8).

The upper limit for k_s in a single-parameter estimation is calculated for the case of a simple electrode reaction for which $k_s = i_o[n\mathbf{F}(C_O{}^o)^{\alpha_c}(C_R{}^o)^{\alpha_a}]^{-1}$. Combining this expression with Eq. [4] and [5] and substituting $C_O{}^o = C_R{}^o$; $\alpha_a + \alpha_c = 1$; $D_O = D_R = 10^5$ cm^2 sec^{-1}, an expression of k_s as function of τ_c and τ_c/τ_d (τ_c in sec) is obtained

$$k_s = 1.6 \times 10^{-3}(\tau_c)^{-1/2}(\tau_c/\tau_d)^{-1/2} \quad [22]$$

The highest value of k_s is obtained for the smallest possible value of τ_c that can be measured (0.08 μsec as estimated above) and the corresponding smallest value of τ_c/τ_d. The estimation of the minimal value of τ_c/τ_d may be carried out in the following manner. τ_c/τ_d depends on the value of $\bar{I}$ (*cf.*, Fig. 5), which in turn is dependent on the required accuracy at which the exchange current is determined and on the experimental error $\epsilon(\eta_{max}) = \sigma(\eta)/(\eta_{max}N^{1/2})$ (*cf.*, Eq. [9]). Assuming a maximum relative error of 10% for i_o [$\sigma(i_o)/i_o = 0.1$ at a confidence level of 68.3%] and an experimental error $\epsilon(\eta_{max}) = 1\%$ ($\sigma(\eta)/\eta_{max} = 0.03$ and $N = 10$), $\bar{I}$ is determined to be 0.1. This value of $\bar{I}$ corresponds to $\tau_c/\tau_d \sim 0.5$ (*cf.*, Fig. 5). Substituting $\tau_c/\tau_d = 0.5$ and $\tau_c = 0.08$ μsec in Eq. [22] one obtains that k_s as high as 8 cm sec^{-1} can be measured. Sluyters *et al.* (3) have estimated under similar conditions that the limiting value of k_s is 5 cm sec^{-1}.

Concentration limits of electroactive species.—Increase in concentration of the electroactive species increases τ_c/τ_d (*cf.*, Eq. [4] and [5]) and thus brings about an increase in accuracy in the determination of i_o (Fig. 5). However, the concentration can be increased only up to a certain limit, determined by the instrumental limitations on i_o. For the simple case of $C_O{}^o = C_R{}^o = C$ and $\alpha_a + \alpha_c = 1$, the upper limit of concentration [C (up. lim)] and of exchange current [i_o (lim)] are related as follows ($i_o = n\mathbf{F}Ck_s$)

$$C(\text{up. lim}) = 10^{-5}\frac{i_o(\text{lim})}{nk_s} \quad (\text{mol cm}^{-3})$$

Thus for a system with $k_s = 1$ cm sec^{-1}, C(up. lim) = $10/n$ mM and for $k_s = 0.1$ cm sec^{-1}, C(up. lim) = $600/n$ mM [i_o (lim) has been assumed to be 6 A cm^{-2}, calculated as shown above for $C_{dl} = 20$ μF cm^{-2}]. In general, for different reasons (keeping constant activity coefficients and avoiding adsorption of electroactive species), the concentration is kept lower than 50 mM.

The lower limit of the concentration is determined from the minimal value of τ_c/τ_d for which reasonable accuracy can be achieved. It was shown above that the smallest acceptable value of τ_c/τ_d is about 0.5.

Table I. Data for a system with $\tau_c/\tau_d = 0.5$

T/τ_c	${}_2\bar{I}(i_o)$ ×10²	${}_1\bar{I}(i_o)$ ×10²	${}_2\bar{I}(C_{dl})$	${}_1\bar{I}(C_{dl})$	λ
0.5	0.9	4.3	0.11	0.53	11.2
5	1.5	9.3	0.06	0.36	3.9
50	0.7	6.0	0.02	0.16	2.5

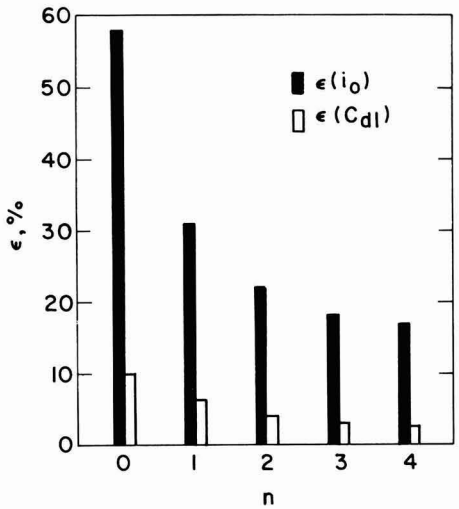

Fig. 7. Variation of $\epsilon(i_o)$ and $\epsilon(C_{dl})$ along iteration procedure for a system with $\tau_c/\tau_d = 0.5$, $\tau_c = 1$ μsec, and $\epsilon(\eta_{max}) = 0.6\%$.

Combining that requirement with Eq. [5] and [22] one obtains

$$C(\text{low. lim}) = 10^{-6}\frac{k_s}{n^2} \quad [\text{mol cm}^{-3}]$$

For $k_s = 1$ cm sec^{-1}, $C(\text{low. lim}) = 1/n^2$ mM and for $k_s = 0.1$ cm sec^{-1}, $C(\text{low. lim}) = 0.1/n^2$ mM.

The higher k_s, the narrower the concentration limits. Sluyters *et al.* (3) point out that for a system characterized by limitingly small values of the parameters τ_c and τ_c/τ_d, the concentration can neither be decreased, nor increased from an "optimal" value of about 10 mM (for $n = 1$), since either of those changes bring about a decrease of one of the parameters below its limiting value.

The accuracy of the galvanostatic method in a single-parameter estimation is superior to that of the coulostatic method for systems with $\tau_c/\tau_d > 0.6$ [compare solid line in Fig. 5 with Fig. 6 in Ref. (8)]. For $\tau_c/\tau_d < 0.6$, a somewhat lower accuracy is obtained.

The limit and the accuracy of the galvanostatic method for the determination of i_o in a two-estimate analysis (i_o and C_{dl}) are considerably lower than those for single-estimate analysis (C_{dl} known) ($_2\bar{I}(i_o) < {}_1\bar{I}(i_o)$). Application of the iteration method for the simultaneous determination of i_o and C_{dl} results in considerable improvement. It is estimated that k_s as high as 2 cm sec^{-1} can be measured (see example in section "Iteration Method"). Comparison with the coulostatic method cannot be made at that stage since $_2\bar{I}(i_o)$ values were not calculated in the earlier coulostatic work (8) (and their presentation here is beyond the scope of this work). It will be only mentioned that in two-parameter analysis, better accuracy is obtained with the coulostatic method. Comprehensive comparison of several transient methods will be the subject of a future paper.

Acknowledgments

This work was supported by The Israel National Academy of Sciences. Thanks are due to Dr. J. Penciner for critical reading of the manuscript.

Manuscript submitted May 29, 1981; revised manuscript received Nov. 8, 1981.

Any discussion of this paper will appear in a Discussion Section to be published in the June 1983 JOURNAL. All discussions for the June 1983 Discussion Section should be submitted by Feb. 1, 1983.

APPENDIX A

The matrix of error E for a single-estimate system contains a single element, the population variance $_1\sigma(p)^2$. The error matrix E is the inverse of the information matrix G. $_1G = \frac{1}{2}\frac{\partial^2 Q^2}{\partial p^2}$. Thus

$$_1\sigma(p)^2 = \left(\frac{1}{2}\frac{\partial^2 Q^2}{\partial p^2}\right)^{-1} \quad [A\text{-}1]$$

for N measurements taken at time t

$$Q^2 = \Sigma\frac{[\eta(\text{exp}) - \eta(\text{calc})]^2}{\sigma(\eta)^2} \quad [A\text{-}2]$$

Combining Eq. [A-1] and [A-2] and for $N \to \infty$

$$\frac{1}{{}_1\sigma(p)} = \frac{1}{\sigma(\eta)^2}\Sigma\left(\frac{\partial\eta}{\partial p}\right)_t^2 = \frac{N}{\sigma(\eta)^2}\left(\frac{\partial\eta}{\partial p}\right)_t^2 \quad [A\text{-}3]$$

Thus

$$\left(\frac{\partial\eta}{\partial p}\right)_t = \frac{1}{N^{1/2}}\frac{\sigma(\eta)}{{}_1\sigma(p)} \quad [A\text{-}4]$$

APPENDIX B

The integrated information $\bar{I}(p)$ for a one-estimate system is given by Eq. [8]. Substituting Q^2 from Eq. [6] into Eq. [A-1] and for an infinite large number of observations along the transient, in the time limits O-T,

$$\frac{1}{{}_1\sigma(p)^2} = \frac{1}{{}_1\sigma(\eta)^2}\sum_{t=0}^{t=T}\left(\frac{\partial\eta}{\partial p}\right)_t^2 = \frac{1}{{}_1\sigma(\eta)^2}\frac{N}{T^2}\int_0^T\left(\frac{\partial\eta}{\partial p}\right)_t^2 dt \quad [B\text{-}1]$$

Substituting $\frac{1}{N^{1/2}}\frac{\sigma(\eta)}{{}_1\sigma(p)}$ by $\bar{I}(p)\cdot\frac{\eta_{max}}{p}$ (analogous to Eq. [11] and $\partial\eta/\partial p$ by I (Eq. [7])

$${}_1\bar{I}(p) = \frac{p}{\eta_{max}}\frac{1}{T}\left[\int_0^T I(p)^2\,dt\right]^{1/2} \quad [B\text{-}2]$$

APPENDIX C

The recursion equations for calculating $^n\epsilon(i_o)$ and $^n\epsilon(C_{dl})$ are

$$\frac{^n\epsilon(i_o)}{\epsilon(\eta_{max})} = \frac{^{n-1}\epsilon(i_o)}{\epsilon(\eta_{max})}\cdot\frac{\lambda(T_1)}{\lambda(T_c)} + \frac{\lambda(T_1)}{{}_1\bar{I}(C_{dl})} + \frac{1}{{}_1\bar{I}(i_o)} \quad [C\text{-}1]$$

$$\frac{^n\epsilon(C_{dl})}{\epsilon(\eta_{max})} = \frac{^{n-1}\epsilon(i_o)}{\epsilon(\eta_{max})}\cdot\frac{1}{\lambda(T_c)} + \frac{1}{{}_1\bar{I}(C_{dl})} \quad [C\text{-}2]$$

Combining Eq. [C-1] and [C-2]

$$\frac{^n\epsilon(i_o)}{\epsilon(\eta_{max})} = \frac{^0\epsilon(i_o)}{\epsilon(\eta_{max})}\left(\frac{\lambda(T_i)}{\lambda(T_c)}\right)^n + \left(\frac{\lambda(T_1)}{{}_1\bar{I}(C_{dl})} + \frac{1}{{}_1\bar{I}(i_o)}\right)\sum_{k=0}^{n-1}\left(\frac{\lambda(T_i)}{\lambda(T_c)}\right)^k \quad [C\text{-}3]$$

Substituting for the sum of the geometric series, Eq. [18] is obtained. Combining Eq. [C-1] and [18] yields Eq. [19].

LIST OF SYMBOLS

C_{dl}	double layer capacity
C_O^o, $[C_R^o]$	bulk concentrations of oxidized [reduced] form
D_O, $[D_R]$	diffusion coefficients of oxidized [reduced] form
E; G	error matrix; information matrix. The presubscript when present stands for the number of estimates
i_o, $[i_F]$; i	exchange [faradaic] current density; applied current density
$I(p)$	instantaneous information in respect to parameter p
$_2\bar{I}(p)$, $[_1\bar{I}(p)]$	integrated information in respect to parameter p for a two-estimate [one estimate] system. The presubstitute stands for the number of the estimates in the system. In case no presubstitute is specified, the number of estimates is either one or two depending on the meaning of the other parameter in the equation
N	number of points along the transient used for the computation of the parameters. The points are equally spaced in a given time scale T and originate from zero
p	parameter (i_o or C_{dl}), estimated or fixed
Δp	difference between estimated and true value of p
t	time elapsed from the start of the potential transient
T	full time scale reading
T_{opt}	optimal value of T for the determination of i_o
Q^2	defined by Eq. [8]
$\epsilon(p)$	relative error in the determination of p at a confidence level of 68.3% (1 standard deviation unit), Eq. [12]
$^n\epsilon(p)$	relative error of parameter p. The prescript n stands for the number of the iteration steps
$\epsilon(\eta_{max})$	$\equiv \sigma(\eta_{max})/(\eta_{max}N^{1/2})$
η, $[\eta_{max}]$	overpotential [overpotential at $t = T$]

$\eta_t(\text{exp})$, $[\eta_t(\text{calc})]$ experimental (calculated) value of η at time t
λ $\equiv |(\Delta i_o/i_o)/(\Delta C_{dl}/C_{dl})|$
$\lambda(T_1)$, $[\lambda(T_c)]$ value of λ at the optimal time scale for measuring $i_o[C_{dl}]$
ν stoichiometric number
ν_O, $[\nu_R]$ stoichiometric coefficients of O [R] in the overall electrode reaction
ρ correlation coefficient between i_o and C_{dl}
$_2\sigma(p)^2$, $[_1\sigma(p)^2]$ population variance of parameter p in a two-estimate (single-estimate) system. The presubscript stands for the number of estimates. In case no subscript is specified, the number of estimates is either one or two depending on the meanings of the other parameters in the equation
$\sigma(\eta)^2$ population variance of η
τ_c, $[\tau_d]$ charge-transfer [diffusional] relaxation constant

REFERENCES

1. T. Berzins and P. Delahay, *J. Am. Chem. Soc.*, **77**, 6448 (1955).
2. E. Yeager and J. Kuta, in "Physical Chemistry, An Advanced Treatise," Vol. IX A, H. Eyring, D. Henderson, and W. Fost, Editors, Academic Press, New York (1970).
3. D. J. Kooijman and J. H. Sluyters, *Electrochim. Acta*, **12**, 693 (1967).
4. D. J. Kooijman and J. H. Sluyters, *ibid.*, **12**, 1579 (1967).
5. D. J. Kooijman, *J. Electroanal. Chem. Interfacial Electrochem.*, **18**, 81 (1968).
6. H. P. Van Leeuwen, D. J. Kooijman, M. Sluyters-Rehbach, and J. H. Sluyters, *ibid.*, **23**, 475 (1969).
7. H. Reller and E. Kirowa-Eisner, *ibid.*, **103**, 335 (1979).
8. H. Reller and E. Kirowa-Eisner, *This Journal*, **127**, 1725 (1980).
9. W. D. Cooper and R. Parsons, *Trans. Faraday Soc.*, **66**, 1698 (1970).
10. F. James and M. Roos, *Comp. Phys. Commun.*, **10**, 343 (1975).
11. W. T. Eadie, D. Drijard, F. E. James, M. Roos, and B. Sadoulet, "Statistical Methods in Experimental Physics," North-Holland Pub. Co., Amsterdam (1971).

Modeling of Porous Insertion Electrodes with Liquid Electrolyte

K. West, T. Jacobsen,* and S. Atlung*

Fysisk-Kemisk Institut, The Technical University of Denmark, DK-2800 Lyngby, Denmark

ABSTRACT

The dynamics of porous insertion electrodes during charge or discharge is described by a simplified mathematical model, accounting for the coupled transport in electrode and electrolyte phases. A numerical method to evaluate the response of this model to either controlled potential or controlled current is outlined, and numerical results for the discharge of a porous TiS_2-electrode in an idealized organic electrolyte are presented. It is demonstrated how electrolyte depletion is the principal limiting factor in the capacity obtained during discharge of this electrode system. This depletion is a consequence of the mobility of the ions not inserted, hence the performance of this type of electrode is optimized by choosing electrolytes with transport number as close to unity as possible for the inserted ion.

One of the consequences of the energy crisis is a renewed interest in secondary batteries for traction purposes. As a partial electrification of the transport sector would make the energy consumption pattern of the community more flexible, and thus less sensitive to changes in the availability of the different fuels, much effort is invested in development of battery systems for this purpose.

Parallel to the continuous development of existing battery systems, much research is devoted to alkali metal batteries because of the high energy density offered by these systems. One of the systems considered to have potential application as a high rate battery is a negative lithium or lithium alloy electrode couple with a positive insertion electrode[1] (1, 2). The insertion materials under investigation for this purpose are primarily layered transition metal dichalcogenides [*e.g.*, TiS_2 (3), VSe_2 (4)] and oxide framework structures like V_2O_5 (5), V_6O_{13} (6), and recently $(Mo, V)_2O_5$ (7), but also amorphous chalcogenides (8) have received some interest.

Until now no entirely satisfactory combination of electrodes and electrolytes has been found, although it has been demonstrated (9) that a lithium/organic electrolyte/titanium disulfide battery could be adapted to electric vehicle propulsion. In any case, the development of new electrode and electrolyte materials is proceeding very fast, and it is of importance to obtain a better understanding of the transport processes in this type of batteries in order to anticipate the combinations of electrode and electrolyte properties that can meet the requirements corresponding to a given set of battery specifications.

In a previous paper (10) thin, nonporous insertion electrodes were treated in detail. In the present paper a mathematical description of porous insertion electrodes is presented to extend these calculations to more realistic electrodes.

Porous electrode theory has been reviewed by deLevie (11) and more recently by Newman and Tiedemann (12). The porous insertion electrode is, however, different from the electrode types treated previously, as it involves transport in both electrolyte and electrode phases. These two transport systems are coupled both through mass balances and through the variation of the electrode potential with the surface composition of the electrode phase. This variation is typically large for intercalation compounds (hundreds of millivolts) and current distribution in the pores due to charge transfer resistance is of minor importance compared to the effect of the varying surface composition. The transient behavior of porous electrodes with low charge transfer resistance has been treated by Pollard and Newman (14) for the case where the equilibrium electrode potential is not a function of the utilization of the electrode material.

Model Formulation

An electrode with irregularly shaped pores and cavities will be difficult if not impossible to describe mathematically. Therefore, we have chosen to model the porous insertion electrode with systems of much

* Electrochemical Society Active Member.

Key words: intercalation, battery capacity, simulation.

[1] The term "insertion electrode" used here covers as well intercalation of a "guest" species in a "host" lattice, as the formation of solid solutions during the electrode process.

simpler geometry, but still possessing the important functional features of the real electrodes. The geometry of these models is shown in Fig. 1 and 2.

Each of these model systems consist of a porous slab of electrode material of high electronic conductivity and of thickness l. On one side ($z = 0$) this slab is contacted by a metallic conductor serving as current collector, and on the other ($z = l$) by an electrolyte also filling the pores of the electrode. This electrolyte is considered to be liquid with mobile anions and cations.

The three model geometries consist of equally sized particles uniformly distributed in the electrode and of one of the following shapes: parallel sheets (Fig. 1); long cylinders (transport across the ends of the cylinders should be negligible) (Fig. 2a); and spheres (Fig. 2b).

The packing of the cylinders or the spheres should ensure that all particles are in electronic contact with the current collector, and they should be evenly distributed so the porosity does not change significantly in any directions within the electrode. There are no restrictions on the orientation of the cylinders, but as the concentration will be taken to be constant around a cross section of the particles, the diameter of the cylinders or the spheres should be small compared to the thickness of the electrode.

In order to keep the transport equations from getting too involved and to keep the computational work at a reasonable level, the model systems are simplified further by the following assumptions:

1. The particle-particle distance (the width of the pores) is so small compared with the thickness of the electrode that the potential and concentrations in the pores can be considered as varying in one dimension only (*i.e.*, along the length of the pore).

2. The ionic conductance of the electrode phase is low compared with the conductance of the electrolyte, so diffusion in the electrode phase parallel to the surface of the electrode particle will not contribute significantly to the overall transport. Solid-state diffusion in the electrode phase thus only removes the inserted species from the electrode/electrolyte interfaces as indicated in Fig. 1.

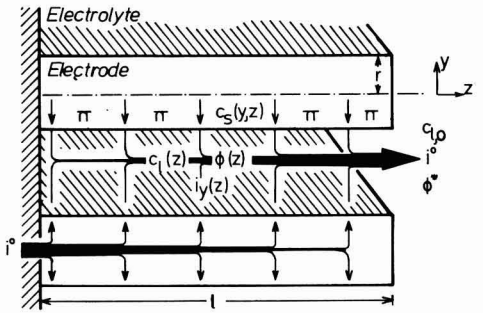

Fig. 1. Schematic diagram of electrode model (plane geometry). Arrows indicate directions of fluxes considered.

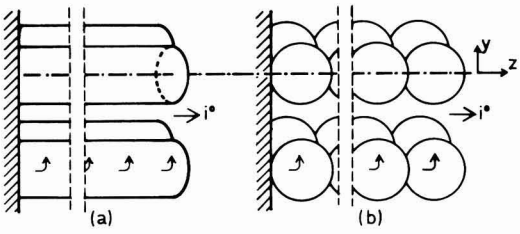

Fig. 2. Schematic diagrams of electrode models: (a) cylindrical geometry; (b) spherical geometry.

3. Space charge accumulation is negligible. This implies that the electroneutrality principle can be applied in the derivation of the transport equations instead of the more involved Poisson-Boltzmann equation.

4. Charge transfer overvoltages are negligible.

5. The electronic conductivity of the electrode phase is so high that the Fermi potential (π) in this phase is constant.

6. The electrolyte salt considered is mono-mono valent.

7. Volume flow due to expansion of the solid matrix and concentration changes in the electrolyte are neglected.

Basic Equations

On the basis of these assumptions the equations governing transport in the model pore system can be formulated. As there is no significant transport parallel to the surface of the electrode particles, the diffusion equation for the solid phase will be one-dimensional in the coordinate system belonging to the symmetry class of the electrode particles (cartesian, cylindrical, or spherical, respectively). The electric field in this phase is small, and the diffusion can be treated according to the Fick laws. With concentration and chemical diffusion coefficient of the inserted species designated by c_s and D_s and the time by t, the diffusion equation is

$$\frac{\partial c_s(y,z)}{\partial t} = \nabla \cdot D_s \nabla_y c_s(y,z) \qquad [1]$$

where ∇_y is the nabla-operator for the direction perpendicular to the particle surface. The boundary conditions in the center ($y = 0$) and at the surface of the electrode particles ($y = r$) are

$$\nabla_y c_s(y,z)\,|_{y=0} = 0 \qquad [2]$$

$$\nabla_y c_s(y,z)\,|_{y=r} = -i_y(z)/\mathbf{F}D_s \qquad [3]$$

where i_y is the current density across the particle/electrolyte interface.

The transport in the electrolyte will be treated as one-dimensional diffusion and migration according to the Nernst-Planck equation. For the cations an additional term must be included in this equation to account for the flux of cations across the particle/electrolyte interface (given by the transfer current density i_y). Due to electroneutrality the anion and cation concentrations are equal (c_l)

$$\frac{\partial c_l(z)}{\partial t} = \frac{\partial}{\partial z} D_- \left[\frac{\partial c_l(z)}{\partial z} - c_l(z) \cdot \frac{\mathbf{F}}{RT} \frac{\partial \phi(z)}{\partial z} \right] \qquad [4]$$

$$\frac{\partial c_l(z)}{\partial t} = \frac{\partial}{\partial z} D_+ \left[\frac{\partial c_l(z)}{\partial z} + c_l(z) \cdot \frac{\mathbf{F}}{RT} \frac{\partial \phi(z)}{\partial z} \right] + i_y(z)\, g/\mathbf{F} \qquad [5]$$

where D_+ and D_- are diffusion coefficients of cations and anions, respectively, and ϕ is the electric potential in the electrolyte. The geometric factor g is the average ratio between the circumference and the cross-sectional area of the pore.

The boundary conditions for these equations at the bottom of the pore ($z = 0$) and at the electrode surface ($z = l$) are

$$\left.\frac{\partial c_l}{\partial z}\right|_{z=0} = \left.\frac{\partial \phi}{\partial z}\right|_{z=0} = 0 \qquad [6]$$

$$c_l(l) = c_{l,0}; \quad \phi(l) = \phi^* \qquad [7]$$

where $c_{l,0}$ and ϕ^* are constants or specified functions of time. Furthermore it is assumed that the electrode initially is in equilibrium

$$t = 0 \Rightarrow c_l = c_{l,0} \text{ and } \phi = \phi^o \text{ (all } z\text{)}$$
$$c_s = c_{s,0} \quad \text{(all } y \text{ and } z\text{)} \qquad [8]$$

where ϕ^o is given by the equilibrium electrode potential ($\pi - \phi^o$) corresponding to the composition $c_{l,0}$, $c_{s,0}$.

The last constraint necessary to couple the electrode and electrolyte systems is the potential relation

$$(\pi - \phi(z)) = h(c_s^*(z), c_l(z)) \qquad [9]$$

where $c_s^*(z)$ is the local surface concentration of the inserted ion. As local electrochemical equilibrium at the electrode/electrolyte interface is assumed (no charge transfer overvoltage), h is a single valued function of c_s^* and c_l only. The exact form of this function h will depend on the electrode material chosen. In many instances, however, a function of the following type will give a reasonable good approximation (13)

$$(\pi - \phi) = (\pi - \phi)^\theta + \frac{RT}{\mathbf{F}} (\ln((c_s^o - c_s^*)/c_s^*) + \ln(c_l) - f(c_s^*/c_s^o) - 0.5) \qquad [10]$$

where c_s^o is the saturation concentration of the inserted species in the electrode phase. $(\pi - \phi)^\theta$ and f are characteristic constants of the electrode material. Applying this expression implies that the insertion process is equivalent to an adsorption process with linear interaction term (Frumkin isotherm).

As π is constant in space, $\partial\phi(z)/\partial z$ in Eq. [4] and [5] can be replaced by $-\partial(\pi - \phi(z))/\partial z$, and the space and time variations of concentrations and potential in the model pore system are thus determined by [1], [4], [5], and [9] together with the appropriate boundary conditions.

Dimensionless Parameters

In the limited universe of a numerical model it is often inconvenient to measure quantities relative to standards (*e.g.*, SI-units) which are not part of the model. Often it is an advantage to measure the quantities relative to some of the characteristic parameters of the system and transform the equations into dimensionless forms. With a proper choice of reference parameters, the dimensionless variables can give a simpler description of the state of the system than the corresponding dimensioned variables.

A dimensionless form of Fick's laws where time is measured relative to a time constant of diffusion and length relative to the dimension of the diffusion region is often used (15). Considering diffusion in the electrode phase, this transformation gives the dimensionless time and length

$$T = tD_s^o/r^2; \quad Y = y/r \qquad [11]$$

where D_s^o is a characteristic value of the diffusion coefficient of the inserted ion.

Measuring the concentration of the inserted ion relative to its saturation concentration $X = c_s/c_s^o$, the transport equation for the electrode phase [1], assumes the following form

$$\frac{\partial}{\partial T} X(Y) = \nabla \cdot U_s \nabla_Y X(Y) \qquad [12]$$

where U_s is a dimensionless mobility

$$U_s = D_s/D_s^o \qquad [13]$$

The dimensionless electrode current density or cation flux density across the electrode/electrolyte interface corresponding to this transformation is defined as

$$I_y = i_y \cdot r \cdot n_g/\mathbf{F} \cdot c_s^o \cdot D_s^o \qquad [14]$$

Noting that the surface to volume ratio of the three types of electrode particles considered is n_g/r, where n_g is 1, 2, or 3 for planar, cylindrical, or spherical geometry, respectively, it can be seen that I_y is the transfer current density measured relative to the specific charge density available in the electrode phase and to the time constant of diffusion.

The transport equations for the electrolyte [4] and [5] must be transformed in a slightly different way, utilizing the dimensionless time T already defined in Eq. [11]. Introducing the dimensionless variables

$$C = c_l/c_{l,0}; \quad E = (\pi - \phi)\mathbf{F}/RT; \quad Z = z/l \qquad [15]$$

and the dimensionless mobilities

$$U_+ = (D_+/D_s^o)(l/r)^2; \quad U_- = (D_-/D_s^o)(l/r)^2 \qquad [16]$$

the equations governing transport in the electrolyte assume the following nondimensional forms

$$\frac{\partial C}{\partial T} = \frac{\partial}{\partial Z} U_- \left(\frac{\partial C}{\partial Z} + C \frac{\partial E}{\partial Z} \right) \qquad [17]$$

and

$$\frac{\partial C}{\partial T} = \frac{\partial}{\partial Z} U_+ \left(\frac{\partial C}{\partial Z} - C \frac{\partial E}{\partial Z} \right) + I_y G \qquad [18]$$

The dimensionless geometric factor $G = g \cdot r \cdot c_s^o/(c_{l,0} \cdot n_g)$ contains information on the "shape" of the pores. For the simple geometries described above, g is equal to $n_g(1 - P)/(r \cdot P)$, and G's dependence on system parameters is given by $G = (1 - P)c_s^o/(P \cdot c_{l,0})$. Parallel to the definition of I_y, the dimensionless overall electrode current I_z is defined as the total electrode current relative to the stoichiometric capacity of the electrode and the time constant of the electrode particles

$$I_z = \int_0^1 I_y(Z)dZ = \frac{i_z}{\mathbf{F} \cdot c_s^o(1 - P) \cdot l} \cdot \frac{r^2}{D_s^o} \qquad [19]$$

[I_z is identical to $1/Q$ as defined in Ref. (10).]

Length is measured in different units for directions parallel and perpendicular to the pore surface in order to obtain length parameters that always vary between 0 and 1, regardless of the physical dimensions of the pore system. Also concentration is measured relative to different standards in the electrode and the electrolyte phases.

The porous insertion electrode is thus described by the local variables $C(Z)$, $E(Z)$, $I_y(Z)$ and $X(Y, Z)$, and transport in this system is governed by Eq. [12], [17], and [18] together with an expression for the dependence of E on C and X^*

$$E = E^o + \ln((1 - X^*)/X^*) + \ln(C) - f(X^* - 0.5) \qquad [20]$$

The transport equations are subject to the following boundary equations:

$$\nabla_Y X|_{Y=0} = 0 \qquad [21]$$

$$\nabla_Y X|_{Y=1} = -I_y/U_s \cdot n_g \qquad [22]$$

$$\left.\frac{\partial C}{\partial Z}\right|_{Z=0} = \left.\frac{\partial E}{\partial Z}\right|_{Z=0} = 0 \qquad [23]$$

$$C(Z = 1) = 1 \qquad [24]$$

$$E(Z = 1) = E^* \qquad [25]$$

where E^* is the (dimensionless) potential difference between the electrode phase and the electrolyte just outside the pore.

Computational Methods

This set of coupled, nonlinear differential equations cannot be solved analytically in the general case. Numerical approximations to the solution can, however, be obtained by finite difference methods (16, 17), where the continuous variables are replaced by a set of approximate values defined at certain mesh points, and where the differential operators are replaced with difference operators.

A linearization of $X^*(Z)$ on T and $I_y(Z)$ is obtained at each time step from the numerical solution of Eq. [12] together with the boundary conditions specified above. The resulting set of coupled, nonlinear equations in C, X^*, E, and I_y is solved simultaneously with no further decoupling or linearizations, following the iterative scheme proposed by Brumleve and Buck (18). Using this technique, very stable numerical solutions are obtained, which are only slightly affected (less than 2%) by changing the number of discretization points between 10 and 100 in any dimension.

The boundary condition [25] used above, represents the potentiostatic case, where the charge or discharge of the electrode proceeds at controlled potential. In practice, however, batteries are operated at conditions more similar to the galvanostatic case, where the electrodes are charged or discharged with a controlled current. To account for this case, an iterative loop is added to the calculations at each time step, in which the potential just outside the pore (E^*) is adjusted until the specified value of the electrode current (I_z) is obtained.

Results

The salient features of the model electrode system under load are illustrated with results from constant current simulations. The material properties used in these simulations are those of a porous titanium disulfide electrode filled with an ideal organic electrolyte.

Lithium transport in TiS_2 crystals is anisotropic as there is virtually no mobility for lithium ions in the direction of the crystallographic c-axis (23). Consequently, transport in the typically disk shaped TiS_2 particles is adequately described by the cylinder model, as they fulfill the requirements of no significant transport across the ends of the cylinders, even though the "cylinders" are very short.

A reasonable approximation to the emf of Li_xTiS_2 *vs.* a lithium reference electrode ($c_l = c_l^o$) as measured at this laboratory is given by

$$\pi_{Li_xTiS_2} - \pi_{Li(c_l=c_l^o)} = 2.17V + \frac{RT}{F}\left[\ln\left(\frac{1-X^*}{X^*}\right) + \ln(C) - 16.2(X^* - 0.5)\right] \quad [26]$$

This expression does not reproduce the fine structure of the emf curve [see (19) and (20)], but the overall approximation is satisfactory for practical purposes.

The values of the transport parameters used in the simulations are listed in Table I. $D_\pm$ and t_+ are experimental values for a 1M solution of $LiClO_4$ in propylene carbonate. All transport parameters are taken to be independent of the composition of the phases although this condition is hardly ever met by practical electrode systems. Detailed experimental determinations of the variation of these parameters with concentration are, however, not available at present, and as this variation is only considered to introduce second-order effects, the idealized case is chosen to illustrate the behavior of the model.

The magnitude of the geometrical parameters also listed in Table I are characteristic values of a battery optimized for traction purposes (9).

On Fig. 3 the equilibrium emf curve is compared with a simulated constant current discharge. The constant current load chosen, 5 mA/cm², is equivalent to a stoichiometric discharge time of 4:21 hr, which is reasonable for traction purposes. The maximal coulombic efficiency predicted for this load is 80%. The reason for this limitation is the evolution of an electrolyte depletion region during discharge, as shown in Fig. 4, where some of the dimensionless parameters of the model are depicted as functions of the length coordinate (Z) at the three different degrees of discharge indicated on Fig. 3. Figure 4a shows how the electrolyte concentration in the center of the electrode approaches zero during discharge, as the transport of lithium ions from the bulk electrolyte cannot keep pace with the lithium ion consumption. This is a consequence of the relatively high anion mobility. Simultaneous with this electrolyte depletion, the surface of the electrode particles in the outer parts of the electrode gradually becomes saturated with lithium (Fig. 4b). When the surface concentration cannot be increased further, the discharge current in this region is limited to a value just large enough to support the equilibration process until all the underlaying electrode material eventually becomes saturated. The electrode current is thus limited both in the depletion region, due to the low lithium ion concentration, and in the saturation region. As these regions approach each other during the discharge, the major part of the electrode reaction is confined to a narrowing zone (Fig. 4c), until it finally becomes impossible to discharge the electrode further with the chosen current.

The charge transfer resistance of a titanium disulfide electrode in $LiClO_4$/PC electrolyte is less than 150 Ω cm² for vaules of X between 0 and 1 (23). From the current distributions of Fig. 4c, it can be seen that

Table I. Simulation parameters

Transport data, electrolyte:		
Transport number: $t_+ = 0.20$		Ref. (21)
Salt diffusion coefficient	$D_\pm = 2.58 \times 10^{-6}$ cm²/sec	Ref. (22)
	$D_+ = 1.61 \times 10^{-6}$ cm²/sec	
	$D_- = 6.45 \times 10^{-6}$ cm²/sec	
Transport data, electrode:		
Chemical diffusion coefficient of Li in Li_xTiS_2	$D_s^o = D_s = 10^{-10}$ cm²/sec	Ref. (23)
Geometrical data:*		
Electrode thickness	= 0.1 cm (l = 0.05 cm)	
Particle diameter	= $1 \cdot 10^{-4}$ cm ($r = 5 \cdot 10^{-5}$ cm)	
Porosity	= 0.35	
Discharge current density	= i_z = 5 mA/cm²	
Electrolyte concentration (start)	= $c_{l,0} = 1 \times 10^{-3}$ mol/cm³	
Saturation concentration of electrode	= $c_s^o = 2.5 \times 10^{-2}$ mol/cm³	

* The geometrical data correspond roughly to those of Ref. (9).

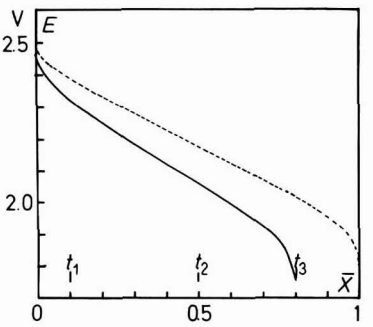

Fig. 3. Equilibrium emf curve (broken line) as given by Eq. [26] compared with a simulated constant current discharge curve. Simulation parameters are given in Table I.

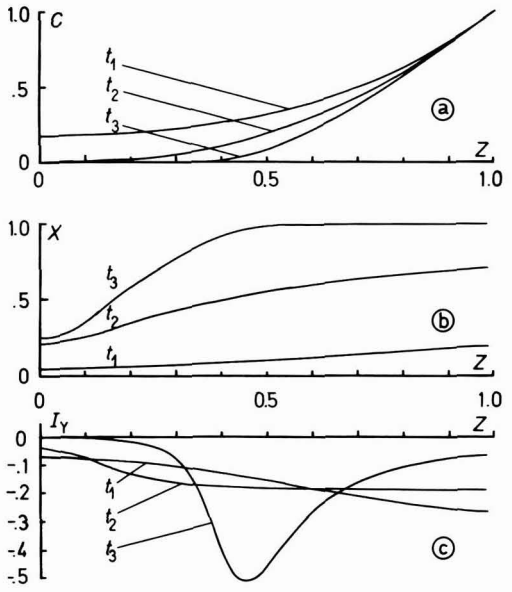

Fig. 4. Spatial variation of: (a) electrolyte concentration (C), (b) surface concentration at electrode/electrolyte interface (X^*), and (c) current density at electrode/electrolyte interface (I_y). The curves correspond to the different degrees of discharge indicated on Fig. 3 ($t_1 \simeq 10\%$, $t_2 \simeq 50\%$, $t_3 \simeq 79\%$).

inclusion of charge transfer resistance in the model would change the electrode polarization less than 20 mV, which is in agreement with the initial assumption of negligible influence of the charge transfer overvoltage on the electrode performance.

For low current loads or thin electrodes this depletion phenomenon will not occur, but still the electrode utilization can be limited due to the loading of the electrode particles as described in Ref. (10). This is illustrated in Fig. 5, where the electrode utilization is shown as function of the electrode thickness (l) and the constant current load (i_z). The loci of 90%, 50%, and 10% maximal coulombic utilization is shown both as they emerge from the porous electrode simulations and as predicted from plane insertion electrode theory (10). For a fixed electrode current density it can be

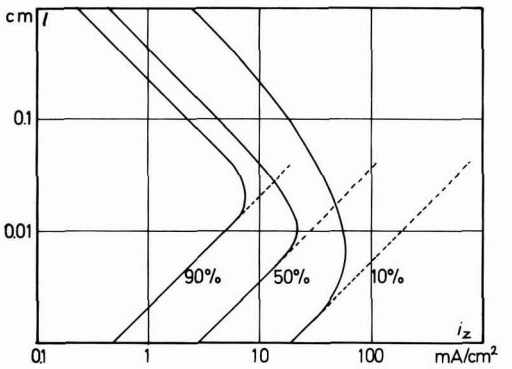

Fig. 5. Maximal electrode utilization as function of electrode thickness (l), and electrode current (i_z). All other parameters are as given in Table I. The dashed lines are utilizations predicted from plane electrode theory (10).

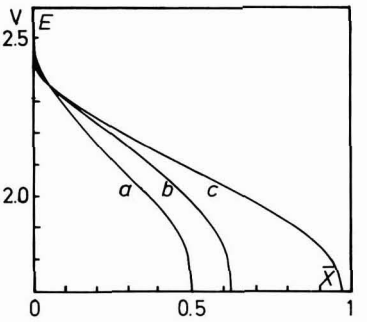

Fig. 6. Simulated discharge curves for varying anion diffusion coefficients [$D_- = 6.45 \times 10^{-6}$ cm²/sec (a); 1.79×10^{-7} cm²/sec (b); 1.63×10^{-8} cm²/sec (c)]. Electrode thickness $l = 0.1$ cm, electrode current $i_z = 4.2$ mA/cm², all other parameters as given in Table I. The cation transport numbers are: $t_+ = 0.2$ (a); 0.9 (b), 0.99 (c).

seen that increasing the electrode thickness first increases the electrode utilization as the average loading of the individual electrode particles decreases. Later, when electrolyte depletion limits the electrode utilization, further increase of the electrode thickness only decreases the average utilization, as the added material is not utilized.

As mentioned above, changes in the cation transport number (t_+) are expected to influence the maximal electrode utilization. This is illustrated in Fig. 6, where three simulated discharge curves are compared. The only parameter varied between the simulations is the anion mobility, whereas the cation mobility, geometrical parameters, and current load are kept constant. It can be seen that even though the overall electrolytic conductivity is decreased, a substantial increase in electrode utilization can be obtained when the cation transport number is raised toward unity. From these examples it is concluded that the porous insertion electrode with conventional organic electrolyte is mainly limited by diffusion either in the pore or in the electrode particles. Optimization of these electrodes therefore requires careful consideration of the coupled transport in both the electrode and the electrolyte phases. Furthermore it can be concluded that better utilization can be obtained using electrolytes with unity transport number of the active cation (*e.g.*, solid electrolytes), if a satisfactory solution to the contact problems between a solid electrode phase and a nonliquid electrolyte can be found.

Acknowledgments

The authors wish to acknowledge the inspiration gained from discussions with colleagues participating in the joint British-Danish Energy Research Programme (Contracts 315, 316-78-1 EE DK, UK) and the financial support to one of us (Keld West) from the Danish Department of Energy.

Manuscript submitted Dec. 29, 1980; revised manuscript received *ca.* Dec. 1, 1981.

Any discussion of this paper will appear in a Discussion Section to be published in the June 1983 JOURNAL. All discussions for the June 1983 Discussion Section should be submitted by Feb. 1, 1983.

LIST OF SYMBOLS

c_l	anion and cation concentration in electrolyte
$c_{l,0}$	anion and cation concentration in electrolyte at time $T = 0$ or at $z = l$
c_s	concentration of inserted species in electrode
$c_{s,0}$	concentration of inserted species in electrode at $T = 0$

c_s^o saturation concentration of inserted species in electrode
c_s^* value of c_s at electrode/electrolyte interface
C dimensionless concentration in electrolyte = $c_l/c_{l,0}$
D_s diffusion coefficient of inserted species in electrode phase
D_s^o reference value of D_s
D_+ diffusion coefficient of cation in electrolyte
D_- diffusion coefficient of anion in electrolyte
E dimensionless potential difference between electrode and electrolyte = $(\pi - \phi) \cdot \mathbf{F}/RT$
E^o constant in Eq. [20]
E^* dimensionless potential difference between electrode phase and electrolyte just outside the pore
f "Interaction" parameter in Eq. [10]
$\mathbf{F}$ Faraday's number
g ratio between circumference and cross-sectional area of pore
G dimensionless geometric factor = $g \cdot r \cdot c_s^o/c_{l,0} \cdot n_g$
i_y current density at particle/electrolyte interface
I_y dimensionless current density at electrode/electrolyte interface = $i_y \cdot r \cdot n_g/\mathbf{F} \cdot c_s^o \cdot D_s^o$
i_z overall electrode current density
I_z dimensionless current density at electrode surface = $i_z \cdot r^2/\mathbf{F} \cdot c_s^o \cdot D_s^o(1 - P) \cdot l$
l distance from center to surface of electrode
n_g geometry type (1, 2, 3)
P porosity
r distance from center to surface of electrode particle
RT product of gas constant and absolute temperature
t time
t_+ cation transport number
T dimensionless time = $t \cdot D_s^o/r^2$
U_+ dimensionless mobility = $(D_+/D_s^o)\,(l/r)^2$
U_- dimensionless mobility = $(D_-/D_s^o)\,(l/r)^2$
U_s dimensionless mobility = D_s/D_s^o
X dimensionless concentration in electrode phase = c_s/c_s^o
X^* value of X at electrode/electrolyte interface
$\overline{X}$ mean value of X
y spatial variable across electrode particle (perpendicular to electrode/electrolyte interface)
Y dimensionless spatial variable = y/r
z spatial variable across electrode (parallel to the pore)
Z dimensionless spatial variable = z/l
ϕ potential in electrolyte
ϕ^* potential in electrolyte just outside the pore
π potential in electrode phase (Fermi potential)
$(\pi - \phi)^\theta$ constant in Eq. [10]

REFERENCES

1. M. S. Whittingham, *Prog. Solid State Chem.*, **12,** 41 (1978).
2. D. W. Murphy and F. A. Trumbore, *J. Cryst. Growth*, **39,** 185 (1977).
3. M. S. Whittingham, *This Journal*, **123,** 315 (1976).
4. M. S. Whittingham, *Mater. Res. Bull.*, **13,** 959 (1978).
5. J. S. Gore and C. R. Walk, U.S. Pat. 3,929,504 (1975).
6. D. W. Murphy, P. A. Christian, F. J. DiSalvo, and J. V. Waszczak, *Inorg. Chem.*, **18,** 2800 (1979).
7. G. Pistoia, M. Pasquali, and P. Fiordiponti, Ext. Abstract, 32nd I.S.E. Meeting (1981).
8. A. J. Jacobson, R. R. Chianelli, and M. S. Whittingham, *This Journal*, **126,** 2272 (1979).
9. L. H. Gaines, R. W. Francis, G. H. Newman, and B. M. L. Rao, 11th Intersociety Energy Conversion Engineering Conference, Stateline, NV (1976).
10. S. Atlung, K. West, and T. Jacobsen, *This Journal*, **126,** 1311 (1979).
11. R. deLevie, *Adv. Electrochem. Electrochem. Eng.*, **6,** 329 (1967).
12. J. Newman and W. Tiedemann, *AIChE J.*, **21,** 25 (1975).
13. M. Armand, Thesis, University of Grenoble (1978).
14. R. Pollard and J. Newman, *Electrochim. Acta*, **25,** 315 (1980).
15. J. Crank, "Mathematics of Diffusion," p. 186, Oxford University Press, (1956).
16. S. W. Feldberg, *Electroanal. Chem.*, **3,** 199 (1969).
17. A. R. Mitchel, "Computational Methods in Partial Differential Equations," John Wiley & Sons, Inc. (1969).
18. T. R. Brumleve and R. P. Buck, *J. Electroanal. Chem. Interfacial Electrochem.*, **49,** 1 (1978).
19. A. H. Thompson, *This Journal*, **126,** 608 (1979).
20. T. Jacobsen, K. West, and S. Atlung, *ibid.*, **126,** 2169 (1979).
21. R. Jasinski, *Adv. Electrochem. Electrochem. Eng.*, **8,** 291 (1972).
22. J. M. Sullivan, D. C. Hanson, and R. Keller, *This Journal*, **117,** 779 (1970).
23. K. West, T. Jacobsen, B. Zachau-Christiansen, and S. Atlung, Ext. Abstract, A 11, 32nd I.S.E. Meeting (1981).

Use of Liquid Chromatography for Studying Interfacial Properties of Inorganic Solutes Relevant to Reverse Osmosis Separations

Yutaka Taketani, Takeshi Matsuura, and S. Sourirajan

National Research Council of Canada, Division of Chemistry, Ottawa, Ontario, Canada K1A OR9

ABSTRACT

High performance liquid chromatography (HPLC) offers a means of investigating the properties of inorganic solutes at polymer (cellulose acetate)-aqueous solution interfaces. Equilibrium constants of solutes distributed between interfacial- and bulk-phases and restricted diffusion of solutes in the interfacial region can be evaluated using retention volume and half-width data from HPLC experiments. These data offer a means of correlating and predicting the differences in free energy parameters governing the reverse osmosis separation of inorganic solutes.

The study of the properties of water at the polymer-solution interfacial region (interfacial water) is fundamental for understanding the transport of solute and solvent water in a reverse osmosis membrane. This is particularly so since the properties of water in the membrane pore are practically the same as those in the interfacial water, as long as the membrane pore size is sufficiently small. It is considered that high performance liquid chromatography (HPLC) in which solvent water flows through a column packed with a polymer material simulates the interfacial phenomena taking place during the reverse osmosis transport involving membranes made of that polymer material. By applying the already well-established theories of chromatography to the analysis of the experimental retention time and related data, quantities characterizing interfacial properties, such as the equilibrium constant for the solute distributed between the bulk and

Key words: reverse osmosis, cellulose acetate, inorganic solutes, interfacial properties, HPLC.

interfacial waters and the mobility of the solute in the interfacial water region, can be easily obtained.

It has already been shown that HPLC data for retention times of selected reference solutes in aqueous solutions can be used for quantitatively characterizing the polar and nonpolar nature of polymeric membrane materials (1). The thickness of the interfacial water layer was also estimated for several cellulosic materials, such as cellulose diacetate (Eastman E-398 and E-383) and cellulose triacetate (2). A parameter, called the β-parameter, was generated as a measure of the relative adsorption capability of a polymeric material to organic and inorganic solutes (3), which was further related to the parameters associated with solute transport through membranes made of various polymer materials (4). Equilibrium constants for organic solutes evaluated by HPLC experiments were also used to determine the form of the interfacial potential function expressed by a Lennard-Jones type equation (5). HPLC retention volume data and/or the ratio of the amount of solute eluted from the column to the total amount of solute injected were used as a measure of pregel or gel formation during the separation of high molecular weight solutes by a membrane (6).

All the works described above indicate that HPLC data are useful for providing information on the property of water at the solution-polymer (membrane material) interfacial region and thus offering a unique method for understanding the reverse osmosis membrane transport, which is strongly governed by the nature of the interfacial water.

This paper is a further extension of the application of the HPLC method to the study of cellulose acetate (Eastman E-398) reverse osmosis membranes, for which chromatographic data were obtained with aqueous solutions of 32 inorganic solutes and the results are discussed in conjunction with reverse osmosis separation data obtained in earlier work (7-9). While retention volume data of HPLC experiments were of primary importance in the analysis of chromatographic data in all of the earlier works, the use of data for the half-width of chromatography peaks was tried in this work for the first time, in order to evaluate the relative mobility of solutes in interfacial water compared to that of sodium chloride, which was chosen as the reference solute. Quantities representing the properties of interfacial water thus generated from HPLC experiments were then used for the prediction of the membrane performance in reverse osmosis with respect to the inorganic solutes studied in this work.

Experimental

HPLC experiments.—The liquid chromatograph model ALC 202 of Waters Associates fitted with a differential refractometer was used in this work. The method of the column preparation and the general experimental technique used were the same as those reported earlier (1). All experiments were carried out at the laboratory temperature (23°-25°C). The solvent (water) flow rate through the column of 0.6m length was fixed at 0.275 cm^3/min. The pressure drop through the column was 2068 kPa (=300 psi). The 32 inorganic solutes including various combinations of alkali metal-, alkaline earth-, and ammonium-cations and halides-, nitrite-, nitrate-, chlorate-, bromate-, iodate-, and sulfate-anions were injected into a column which was packed by the powder (diameter 38-51 μm) of cellulose acetate (Eastman E-398) polymer. The sample solution of 10 μl (solute concentration in the range of 1 ± 0.2%) was injected into the column, and the retention volume as well as the half-width of the chromatography peak for each solute were determined. D_2O was also injected to give the retention time for water, which was used as the solvent. Raffinose whose retention time was the least among all of the solutes studied was used as the unretained component to establish the position of the solvent front. Both the retention volume and the half-width measurements were duplicated and the average values obtained were used for computations; in most cases, the results of duplicated measurements were identical.

Reverse osmosis data.—This work makes further use of the reverse osmosis performance data for aqueous solutions of various inorganic solutes and the data for free energy parameters, $-\Delta\Delta G/RT$, for ions with respect to cellulose acetate (Eastman E-398) membranes obtained in earlier work (7-9).

Theoretical

Analysis of liquid chromatography data.—Chromatography theory in terms of the solute distribution between the interfacial and bulk water phases was developed in an earlier work (2). The analysis stems from the experimental result that the retention volumes of many inorganic solutes and polyfunctional organic solutes such as sugars are less than that of heavy water, which is assumed to be the same as that of solvent water. This phenomenon can be explained by the existence of two water phases, one the interfacial water phase and the other the bulk water phase. While the former phase has less dissolving power for the solutes mentioned above than the latter (10), heavy water may be assumed to be equally soluble in both phases. It is further assumed that the interfacial water phase and the bulk water phase constitute the stationary phase and the mobile phase of liquid chromatography, respectively. This assumption is justified since the interfacial water is necessarily less mobile than the bulk phase water (11).

According to liquid chromatography theory (12), the retention volume is given by

$$V_R = V_m + K_{Ai}'V_s \quad [1]$$

where

$$K_{Ai}' = \frac{\text{concentration of solute A in the stationary phase}}{\text{concentration of solute A in the mobile phase}} \quad [2]$$

Since the experimental data for retention volume, V_R', include an amount of dead space, V_d, (caused by connecting tubes, fittings, refractometer cells, etc.) Eq. [1] can be written as

$$V_R' = V_R + V_d = V_m + K_{Ai}'V_s + V_d \quad [3]$$

The following assumptions were made in order to calculate V_s and K_{Ai}' using Eq. [3].

(*i*) $K_{Ai}' = 1$ for water (which is the same as for D_2O). This value is justified on the basis that the probability of a water molecule existing in the mobile or in the stationary phase is the same. When $K_{Ai}' = 1$, let $V_R' = [V_R']_{water}$.

(*ii*) $K_{Ai}' = 0$ for a reference solute with the lowest retention volume. This value is justified on the basis that such a reference solute is repelled mostly from the polymer surface and hence the concentration of the solute in the interfacial water is close to zero. When $K_{Ai}' = 0$, let $V_R' = [V_R']_{min.}$. From Eq [3]

$$[V_R']_{water} = V_m + V_s + V_d \quad [4]$$

$$[V_R']_{min.} = V_m + V_d \quad [5]$$

Therefore

$$V_s = [V_R']_{water} - [V_R']_{min.} \quad [6]$$

Combining Eq. [3], [4], [5], and [6]

$$K_{Ai}' = \frac{V_R' - [V_R']_{min.}}{[V_R']_{water} - [V_R']_{min.}} \quad [7]$$

Using raffinose as a reference solute (whose retention volume was the least), the values of K_{Ai}' for various solutes were calculated using Eq. [7] and they are listed in Table I.

Some of the K_{Ai}' values in Table I were compared to literature values. Using the cation partition coefficients and the water contents reported in the work of Heyde *et al.* (13), the coefficient of the solute distribution between the water contained in a cellulose acetate (E-398) membrane and in the bulk water can be calculated. The result was 0.1-0.3 for NaCl solute and 0.4-0.7 for $NaNO_3$ solute. Considering the difference in the two experimental methods, one that uses the polymer particle in a chromatography column and the other that uses a polymeric membrane for the partition measurement, and the large errors involved in both experiments ($\sim \pm 25\%$) the agreement of the above distribution coefficients with those in Table I is fair.

According to the theoretical plate height concept, the equivalent height of a theoretical plate is contributed from each of several components involved. For these components, one may consider those from the flow patterns and the eddy diffusion (H_p), the longitudinal molecular diffusion (H_d), the diffusion in the stationary phase (H_s), and the diffusion in the mobile phase (H_m). With respect to a particular solute A, the total plate height (H_A) can be written as the additive sum of all these components (12)

$$H_A = H_p + H_d + H_s + H_m$$

$$= 2\lambda d_p + \frac{2\gamma D_{AB}}{v} + \frac{qR(1-R)d^2v}{D_{Ai}} + \frac{\omega d_p^2 v}{D_{AB}} \qquad [8]$$

(see Appendix A). All of the symbols are defined in the List of Symbols. R is the retention ratio (the fraction of the solute in the mobile phase) and is given by

$$R = \frac{V_m}{V_m + K_{Ai}'V_s} \qquad [9]$$

Since

$$V_m = [V_R']_{min.} - V_d \qquad [10]$$

Eq. [9] becomes

$$R = \frac{[V_R']_{min.} - V_d}{[V_R']_{min.} - V_d + K_{Ai}'V_s} \qquad [11]$$

V_d was determined by the retention volume measurement without an attached column. V_m and V_s were evaluated by using Eq. [10] and [4] from data for the retention volumes of raffinose as the reference solute and D_2O. The results were 0.360, 1.257, and 0.363 cm^3 for V_d, V_m, and V_s, respectively. As pointed out earlier, at the polymer-solution interfacial region under consideration, the interfacial water phase is regarded as the stationary phase in the chromatography system, while ordinary water in the bulk water is regarded as the mobile phase. Therefore, the diffusion coefficients D_{AB} and D_{Ai}, denoting those for mobile and stationary phases, respectively, are in effect quantities in the bulk and the interfacial waters.

Let us calculate the approximate magnitude of each component involved in Eq. [8]. Assuming $\lambda = 8$, $d \approx d_p = 46 \times 10^{-6}$m, $\gamma = 0.6$, $D_{AB} = 10^{-9}$ m^2/sec, $v = 14 \times 10^{-2}$ m/sec, $q = 0.1$, $R = 0.9$, $D_{Ai} = 10^{-11}$ m^2/sec, and $\omega = 1$, H_p, H_d, H_s, and H_m were calculated to be 7×10^{-4}, 8×10^{-9}, 3×10^{-1}, and 3×10^{-1}m, respectively. The object of this model calculation is simply to show that in Eq. [8], the quantities H_p and and H_d can be ignored as compared with H_s and H_m, and the latter two quantities contribute almost equally to H_A.

Among all quantities involved in Eq. [8], only R, D_{Ai}, and D_{AB} depend on the solute; the rest are constants as long as a constant flow rate is maintained during the chromatography experiment. Besides, though D_{AB} changes from solute to solute, the ratio of the largest to the smallest value of D_{AB} can be assumed to be far less than that for D_{Ai}. This assumption will be justified later in the calculation of D_{Ai} from the chromatographic half-width data. Therefore, as a practical approximation D_{AB} is regarded as a constant in Eq. [8]. This is particularly true, since according to the above approximation the last two terms of Eq. [8] (H_s and H_m) involving D_{Ai} and D_{AB} contribute equally to H_A.

Since R and D_{Ai} are dependent on the solute, Eq. [8] can be written as

$$H_A = \frac{\alpha R_A(1-R_A)}{D_{Ai}} + \Omega \qquad [12]$$

where

$$\alpha = qd^2v \qquad [13]$$

and

Table I. Chromatography data and some physicochemical properties of solutes

Solute number	Solute	V_R' (cm^3)	$H \times 10^2$ (m)	K_{Ai}'	$\ln\left[\frac{D_{Ai}}{(D_{Ai})_{NaCl}}\right]$	$\ln\left[\frac{D_{Ai}}{(D_{Ai})_{NaCl}} \cdot \frac{K_{Ai}'}{(K_{Ai}')_{NaCl}}\right]$	$D_{AB} \times 10^9$ (m^2/sec)	$\Delta\left(\frac{-\Delta\Delta G}{RT}\right)_A$
1	LiF	1.727	1.521	0.303	−1.752	−1.847	1.2127	−0.51
2	LiCl	1.738	1.327	0.333	−1.094	−1.094	1.3667	−0.20
3	LiBr	1.727	1.288	0.303	−1.001	−1.095	1.3777	0.15
4	LiI	1.760	1.187	0.394	−0.121	0.047	1.3702	0.42
5	$LiNO_3$	1.782	1.209	0.455	−0.196	0.116	1.3358	0.74
6	NaF	1.727	1.402	0.303	−1.438	−1.532	1.4008	−0.49
7	NaCl	1.738	1.163	0.333	0	0	1.6110	0
8	NaBr	1.760	1.084	0.394			1.6263	0.17
9	NaI	1.793	1.093	0.485			1.6159	0.44
10	$NaNO_2$	1.749	1.202	0.364	−0.316	−0.227	1.4294	0.57
11	$NaNO_3$	1.793	1.195	0.485	−0.032	0.344	1.5683	0.76
12	$NaClO_3$	1.749	1.311	0.364	−0.954	−0.865	1.5028	0.32
13	$NaBrO_3$	1.738	1.271	0.333	−0.837	−0.837	1.4060	−0.47
14	$NaIO_3$	1.683	1.476	0.182	−2.089	−2.693	1.1928	−1.27
16	Na_2SO_4	1.683	1.416	0.182	−1.925	−2.529	1.2307	−2.99
17	NH_4Cl	1.760	1.134	0.394	0.563	0.731	1.9933	0.18
19	KF	1.870	1.246	0.697	−0.141	0.598	1.6828	−0.38
20	KCl	1.738	1.163	0.333	0	0	1.9948	0.11
21	KBr	1.760	1.083	0.394			2.0182	0.28
22	KI	1.782	1.157	0.455	0.321	0.633	2.0018	0.55
23	KNO_3	1.782	1.157	0.455	0.321	0.633	1.9297	0.87
24	$KClO_3$	1.760	1.187	0.394	−0.121	0.047	1.8315	0.43
25	CsCl	1.760	1.083	0.394			2.0453	−0.07
26	CsBr	1.738	1.327	0.333	−1.091	−1.091	2.0700	0.10
27	CsI	1.771	1.172	0.424	0.088	0.330	2.0531	0.37
28	RbCl	1.771	1.172	0.424	0.088	0.330	2.0516	0.06
29	$MgCl_2$	1.727	1.288	0.303	−1.001	−1.095	1.2502	−1.49
30	$MgBr_2$	1.727	1.232	0.303	−0.687	−0.781	1.2625	−1.15
31	$Mg(NO_3)_2$	1.771	1.389	0.424	−1.124	−0.882	1.2160	0.03
32	$CaCl_2$	1.738	1.384	0.333	−1.298	−1.298	1.3355	−1.33
34	$SrCl_2$	1.716	1.480	0.273	−1.743	−1.847	1.3351	−1.45
33	$BaCl_2$	1.738	1.384	0.333	−1.298	−1.298	1.3865	−1.71

$$\Omega = \text{components of } H_A \text{ other than } H_s \quad [14]$$

H_A, R_A, and D_{Ai} are all quantities which correspond to solute A, and α as well as Ω are both constants for a given column at a given flow rate of the solvent water. Rearrangement of Eq. [12] gives

$$D_{Ai} = \frac{\alpha R_A(1 - R_A)}{H_A - \Omega} \quad [15]$$

Further, dividing D_{Ai} by that for sodium chloride (chosen as a reference solute)

$$\frac{D_{Ai}}{(D_{Ai})_{NaCl}} = \frac{R_A(1 - R_A)}{R_{NaCl}(1 - R_{NaCl})} \cdot \frac{H_{NaCl} - \Omega}{H_A - \Omega} \quad [16]$$

where subscript NaCl denotes the quantities that correspond to those for sodium chloride.

R is calculated from Eq. [9], and H is obtained from

$$H = \frac{L}{4}\left(\frac{w}{V_{R'}}\right)^2 \quad [17]$$

(see Appendix B) where L is the column length and w and $V_{R'}$ are the chromatographic data for the half-width and the retention volume (12), respectively, and the ratio $(D_{Ai})/(D_{Ai})_{NaCl}$ can be calculated from Eq. [16], if the value for the constant Ω is known.

The values of H obtained from Eq. [17] for the different solutes are included in Table I, which shows that the value of $H_A = 1.083 \times 10^{-2}$m for both potassium bromide and cesium chloride is the least. Since H_A is more than Ω from Eq. [12], Ω must be less than the value of H_A mentioned above. After a trial and error calculation, we finally adopted the quantity 1.080×10^{-2}m as the constant Ω, which value is used in this paper. It has to be noted, however, that the essential conclusion obtained in the analysis presented in this paper remains valid, even when the numerical value for Ω is changed.

Free energy parameters of inorganic solutes in reverse osmosis systems.—The transport phenomena of reverse osmosis membranes can be described by the following fundamental equations

$$A = (PWP)/M_B \cdot S \cdot 3600 \cdot P \quad [18]$$

$$N_B = A[P - \pi(X_{A2}) + \pi(X_{A3})] \quad [19]$$

$$= kc_1(1 - X_{A3}) \ln\left(\frac{X_{A2} - X_{A3}}{X_{A1} - X_{A3}}\right) \quad [20]$$

$$N_A = \left(\frac{D_{AM}}{K\delta}\right)(c_{A2}X_{A2} - c_{A3}X_{A3}) \quad [21]$$

Equation [19] describes the effect of osmotic pressure on the solvent water flux. Equation [20] is the expression for the boundary concentration increase due to concentration polarization. Equation [21] describes the solute flux by pore diffusion due to the concentration difference on both sides of the membrane, where $(1/K)$ is the equilibrium coefficient of the solute distribution between the membrane pore and the bulk solution, D_{AM} is the diffusion coefficient of solute in the membrane pore, and δ is the effective thickness of the membrane. $D_{AM}/K\delta$ as a single quantity plays the role of the mass transfer coefficient with respect to the solute transport in the membrane (14).

At a specified operating temperature and pressure, a reverse osmosis membrane can be specified in terms of its performance data with respect to a reference solute in an aqueous solution (in this case NaCl is taken as a reference solute). A single set of experimental reverse osmosis data on (PWP), (PR), and f (solute rejection) for a reference NaCl-H_2O feed solution under known operating conditions is enough for use in Eq. [18]-[21] to obtain the required data for the specification of A, $(D_{AM}/K\delta)_{NaCl}$, and k_{NaCl} (14). The membranes used in the experiments were all specified by the parameters stated above and the results are given in Table II.

For dilute solution systems, Eq. [18]-[21] can be reduced to

$$(D_{AM}/K\delta) = v_s \frac{1 - f}{f}[\exp(v_s/k)]^{-1} \quad [22]$$

where v_s equals AP/c and indicates the linear velocity of the product solution through the membrane (15). Applying Eq. [22] to the experimental solute separation and the product rate data for dilute solution systems of various inorganic solutes, $(D_{AM}/K\delta)$ for each solute can be obtained.

For completely ionized solutes, $(D_{AM}/K\delta)$ can be further split into contributions from constituent ions. Thus, $(D_{AM}/K\delta)$ can be written as

$$\ln(D_{AM}/K\delta) = \ln C_{NaCl}^* + \left\{ n_c\left(\frac{-\Delta\Delta G}{RT}\right)_{cation} + n_a\left(\frac{-\Delta\Delta G}{RT}\right)_{anion}\right\} \quad [23]$$

where $\ln C_{NaCl}^*$ is a measure of the average pore size on the surface of the membrane, n_c and n_a are the number of mols of cation and anion, respectively, in one mol of ionized solute, and $-\Delta\Delta G/RT$ represents the contribution of each ion constituting the electrolytic solute to $(D_{AM}/K\delta)$, whose numerical value characterizes the solute transport through the porous membrane.

The quantity $\Delta\Delta G$ was originally defined as the energy required to bring an ion from the bulk water phase to the interfacial water phase and it may be expressed as the difference in the free energy of hydration in the bulk phase (ΔG_B) and in the interfacial phase (ΔG_I) (7).

The numerical values of $-\Delta\Delta G/RT$ were obtained experimentally from reverse osmosis data in previous work (7-9). Though $-\Delta\Delta G/RT$ values so obtained are based on experimental data with the dilute aqueous solutions they are also applicable to the concentrated solution systems (8). It has to be noted that the value of $-\Delta\Delta G/RT$ so obtained is an experimental quantity, set on a relative scale, representing the interfacial transport of ions during reverse osmosis.

Using Eq. [23] and taking the difference of $\ln(D_{AM}/K\delta)_A$ between solute A and that of the reference solute NaCl

$$\ln(D_{AM}/K\delta)_A - \ln(D_{AM}/K\delta)_{NaCl} = (-\Delta\Delta G/RT)_A - (-\Delta\Delta G/RT)_{NaCl} \quad [24]$$

where $(-\Delta\Delta G/RT)_A$ and $(-\Delta\Delta G/RT)_{NaCl}$ denote $\{n_c(-\Delta\Delta G/RT)_{cation} + n_a(-\Delta\Delta G/RT)_{anion}\}$ corresponding to the solute A and NaCl, respectively.

Table II. Film specification

Film No.	6	7
1724 kPa gauge (=250 psig)		
Pure water permeability constant A, $\left[\frac{\text{kg-mol } H_2O}{m^2 \cdot \text{sec} \cdot \text{kPa}}\right] \times 10^7$	2.35	3.78
Solute transport parameter $(D_{AM}/K\delta)_{NaCl}$, (m/sec) $\times 10^7$	6.10	17.70
Solute separation, %	85.00	74.70
Product rate,* (kg/hr) $\times 10^3$	28.64	45.00

* Area of film surface: 13.2 cm². Film pressurized at 2068 kPa gauge = 300 psi. Feed concentration: 3500 ppm NaCl-H_2O = 0.06 molal. Mass transfer coefficient: 16×10^{-6} m/sec.

From Eq. [24]

$$\ln \frac{(D_{AM}/K\delta)_A}{(D_{AM}/K\delta)_{NaCl}} = \Delta\left(\frac{-\Delta\Delta G}{RT}\right)_A \quad [25]$$

where $\Delta(-\Delta\Delta G/RT)_A$ is equal to $(-\Delta\Delta G/RT)_A - (-\Delta\Delta G/RT)_{NaCl}$. Equation [25] can be further rearranged to

$$\ln\left[\frac{D_{AM}}{(D_{AM})_{NaCl}} \cdot \frac{(1/K)_A}{(1/K)_{NaCl}}\right] = \Delta\left(\frac{-\Delta\Delta G}{RT}\right)_A \quad [26]$$

A single quantity $(D_{AM}/K\delta)$ is now split into two physicochemical properties, *i.e.*, D_{AM} and $1/K$. Both quantities refer to the properties in the capillary pore and must be under a strong interaction force from the polymer surface as long as the pore size is small enough. Under such conditions it is known that the quantity $\Delta(-\Delta\Delta G/RT)$ in Eq. [26] is practically independent of the pore size (7-9).

Considering that D_{Ai} and K_{Ai}' indicate the diffusivity and the equilibrium term, respectively, in the chromatography system, while D_{AM} and $1/K$ indicate those in the membrane system, an analogous expression to Eq. [26], such as

$$\ln\left[\frac{D_{Ai}}{(D_{Ai})_{NaCl}} \cdot \frac{K_{Ai}'}{(K_{Ai}')_{NaCl}}\right] = f\left[\Delta\left(\frac{-\Delta\Delta G}{RT}\right)_A\right] \quad [27]$$

can be expected. Equation [27] is used in the following discussion to relate the chromatography data for the diffusion and distribution coefficients to the change in the free energy parameter based on the data for solute transport through the porous membranes.

Results and Discussion

Correlation of K_{Ai}' and free energy parameter.—Since $\Delta\Delta G$ was originally defined as the change of the free energy in the transfer of the solute from the bulk water to the interfacial-water phase, it is reasonable to expect that $\ln [K_{Ai}'/(K_{Ai}')_{NaCl}]$ must be a unique function of $\Delta(-\Delta\Delta G/RT)_A$. Figure 1 shows a plot of $\Delta(-\Delta\Delta G/RT)_A$ *vs.* $\ln [K_{Ai}'/(K_{Ai}')_{NaCl}]$. The correlation exhibits an apparent linear relationship with a slope of 0.20 ± 0.08. The observation that this slope is far from unity is understandable from Eq. [27] that shows $\ln [K_{Ai}'/(K_{Ai}')_{NaCl}]$ is only one of the quantities affecting $\Delta(-\Delta\Delta G/RT)_A$.

Correlation of $\ln [D_{Ai}/(D_{Ai})_{NaCl}]$ to $\Delta(-\Delta\Delta G/RT)_A$.—Figure 2 shows a correlation of $\Delta(-\Delta\Delta G/RT)_A$ *vs.* $\ln [D_{Ai}/(D_{Ai})_{NaCl}]$. Though there is some scatter in the figure, there seems to be a definite trend in the correlation; the quantity $\ln [(D_{Ai})/(D_{Ai})_{NaCl}]$ increases with an increase in $\Delta(-\Delta\Delta G/RT)_A$. By applying regression analysis the slope was found to be 0.60 ± 0.27. This implies that the contribution to $\Delta(-\Delta\Delta G/RT)_A$ from the diffusion term in Eq. [27] is about three times as much as the distribution term.

Correlation of D_{AB} vs. D_{Ai}.—The ratio of the diffusion coefficient in the interfacial water phase of solute A to that of the reference solute sodium chloride, designated as $D_{Ai}/(D_{Ai})_{NaCl}$ was correlated with the corresponding quantity in the bulk water phase, $D_{AB}/(D_{AB})_{NaCl}$ in Fig. 3. The diffusion coefficient data for totally ionized inorganic solutes in the bulk water phase were obtained by using the Nernst equation (16). The straight line correlation illustrated in Fig. 3 is the result of regression analysis, which corresponds to

$$D_{Ai}/(D_{Ai})_{NaCl} \propto (D_{AB}/(D_{AB})_{NaCl})^{3.0} \quad [28]$$

Figure 3 indicates that the effect of the change of the solute species on the diffusion coefficient is significantly enhanced in the interfacial water phase as compared with that in the bulk water phase. Accordingly, the

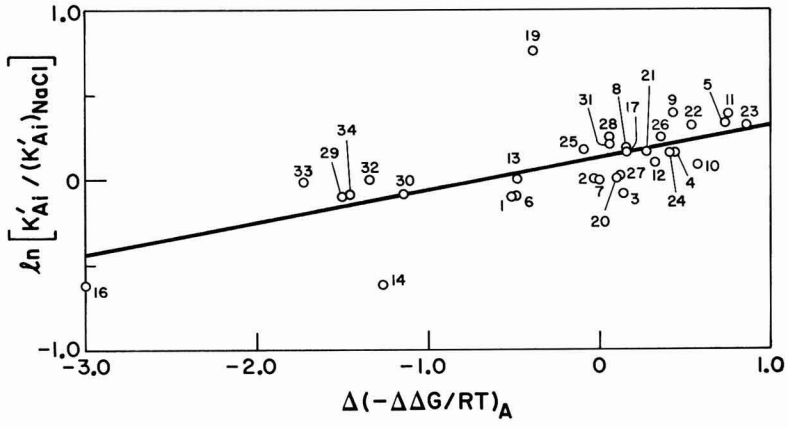

Fig. 1. $\Delta(-\Delta\Delta G/RT)_A$ *vs.* $\ln [K_{Ai}'/(K_{Ai}')_{NaCl}]$. Solute numbers the same as in Table I.

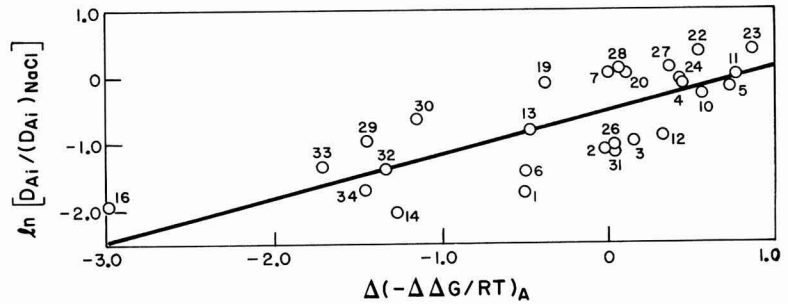

Fig. 2. $\Delta(-\Delta\Delta G/RT)_A$ *vs.* $\ln [D_{Ai}/(D_{Ai})_{NaCl}]$. Solute numbers the same as in Table I.

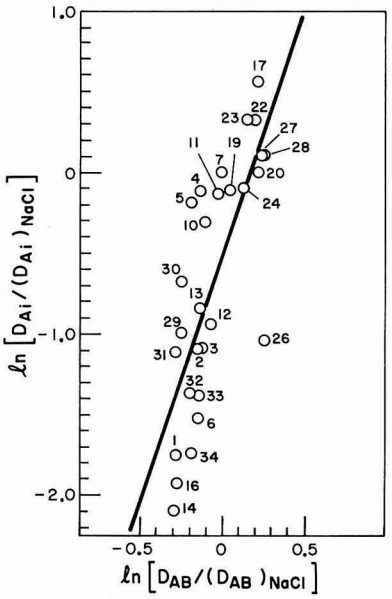

Fig. 3. Ln $[D_{AB}/(D_{AB})_{NaCl}]$ *vs.* ln $[D_{Ai}/(D_{Ai})_{NaCl}]$ at 25°C. Solute numbers the same as in Table I.

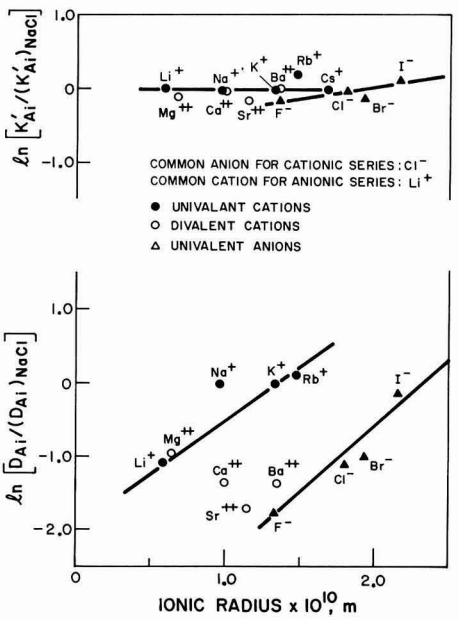

Fig. 4. Ionic radius *vs.* ln $[K_{Ai}'/(K_{Ai}')_{NaCl}]$ and ln $[D_{Ai}/(D_{Ai})_{NaCl}]$

diffusion coefficient of the inorganic solute changes through a far wider range in the interfacial water phase, which leads to the high exponential power indicated in Eq. [28]. This also justifies assuming D_{AB} as practically constant in developing Eq. [12].

Correlation of equilibrium distribution coefficient and diffusion coefficient vs. ionic radius.—Figure 4 illustrates the correlation of ln $[K_{Ai}'/(K_{Ai}')_{NaCl}]$ and ln $[D_{Ai}/(D_{Ai})_{NaCl}]$ *vs.* the ionic radius. While changing the ionic radius of monovalent alkali cations and divalent alkaline earth cations, the anion was fixed as a chloride. Similarly, lithium ion was used consistently as the cation, while the ionic radius of the monovalent halide anions was changed. Though Fig. 4 illustrates the trend shown by the particular series of alkali halide-salts and alkaline earth halide-salts described above, the general tendency summarized in the following is the same in other series.

1. ln $[K_{Ai}'/(K_{Ai}')_{NaCl}]$ remains practically unchanged with the change in the ionic radius of mono- and divalent cations.
2. ln $[K_{Ai}'/(K_{Ai}')_{NaCl}]$ values of divalent cations are slightly lower than those of monovalent cations.
3. ln $[K_{Ai}'/(K_{Ai}')_{NaCl}]$ values of halide anions increase with an increase in the ionic radius.
4. ln $[D_{Ai}/(D_{Ai})_{NaCl}]$ values of monovalent alkali cations increase with an increase in the ionic radius.
5. ln $[D_{Ai}/(D_{Ai})_{NaCl}]$ values of divalent alkaline earth cations are generally less than those of monovalent alkali cations.
6. ln $[D_{Ai}/(D_{Ai})_{NaCl}]$ values of monovalent halide anions increase with an increase in ionic radius.

All of these trends are consistent with the formation of a larger hydration sphere around a monoatomic ion of a smaller ionic radius or an ion of higher valence, which decreases both the equilibrium distribution coefficient K_{Ai}' and the diffusion coefficient D_{Ai}.

Comparison of ionic transport in the polymer particle and in the membrane.—Figure 5 illustrates a correlation between ln $[D_{Ai}/(D_{Ai})_{NaCl} \cdot K_{Ai}'/(K_{Ai}')_{NaCl}]$ and $\Delta(-\Delta\Delta G/RT)_A$. Though the figure exhibits a definite tendency for the former quantity to increase with the increase in the latter, the scatter is even more significant than in both the correlations illustrated in Fig. 1 and 2. When Fig. 5 is investigated in detail, however, it is found that the scatter is very systematic. When the salts which include the lithium cation, the fluoride anion, and monovalent anions containing oxygen atoms such as NO_2^-, NO_3^-, ClO_3^-, BrO_3^-, and IO_3^- are indicated separately (in Fig. 5 as closed circles), they form a separate group located consistently below the rest of the inorganic solutes (in Fig. 5, open circles). For convenience, the latter (open circles) and the former groups are designated as group I and II, respectively. This leads to the conclusion that the scatter in Fig. 5 is not of a random nature caused by experimental errors, but that there are at least two discrete correlations involved in the same graph.

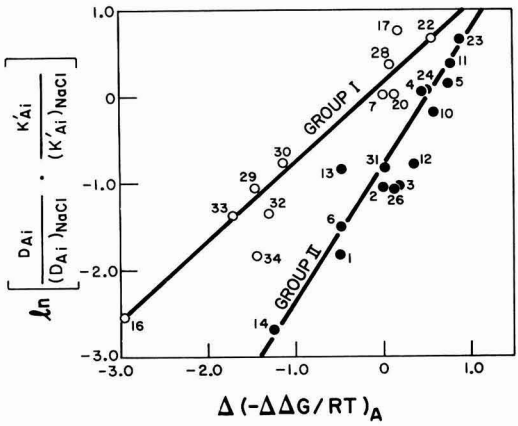

Fig. 5. $\Delta(-\Delta\Delta G/RT)_A$ *vs.* ln $\left[\frac{D_{Ai}}{(D_{Ai})_{NaCl}} \cdot \frac{K_{Ai}'}{(K_{Ai}')_{NaCl}}\right]$. Solute numbers the same as in Table I.

When regression analysis was applied to the above two correlations independently, it resulted in

$$\ln\left[\frac{D_{Ai}}{(D_{Ai})_{NaCl}}\cdot\frac{K_{Ai}'}{(K_{Ai}')_{NaCl}}\right] = 0.96\Delta\left(\frac{-\Delta\Delta G}{RT}\right)_A + 0.136 \quad [29]$$

and

$$\ln\left[\frac{D_{Ai}}{(D_{Ai})_{NaCl}}\cdot\frac{K_{Ai}'}{(K_{Ai}')_{NaCl}}\right] = 1.47\Delta\left(\frac{-\Delta\Delta G}{RT}\right)_A - 0.844 \quad [30]$$

for groups I and II, respectively.

Prediction of the separation of inorganic solutes.— Using the two separate correlations given by Eq. [29] and [30] the separation of the inorganic solutes from the dilute aqueous solutions of a single solute system can be predicted from single sodium chloride experimental data. The prediction procedure is as follows:

1. By applying Eq. [18]-[21] to the reverse osmosis experimental data with respect to the reference sodium chloride aqueous solution, the constants A, $(D_{AM}/K\delta)_{NaCl}$, and k_{NaCl}, are obtained.
2. For a given solute for which prediction is needed the value of $\ln[D_{Ai}/(D_{Ai})_{NaCl}\cdot K_{Ai}'/(K_{Ai}')_{NaCl}]$ is found in Table I.
3. $\Delta(-\Delta\Delta G/RT)_A$ is calculated by either Eq. [29] or [30]. For solutes involving Li^+, F^-, NO_2^-, NO_3^-, ClO_3^-, BrO_3^-, and IO_3^- Eq. [30] is applied and for the rest of the solutes Eq. [29] is used.
4. $(D_{AM}/K\delta)_A$ for the particular solute is calculated by Eq. [25].
5. Using k_{NaCl} obtained in step 1, k_A for the solute under consideration is obtained by using the equation

$$k_A = \left[\frac{D_{AB}}{(D_{AB})_{NaCl}}\right]^{2/3}\cdot k_{NaCl} \quad [31]$$

6. Equation [22] is now rearranged to

$$f = \frac{1}{1+\left(\frac{D_{AM}}{K\delta}\right)_A \Big/ \; v_s \times \exp\left(\frac{v_s}{k_A}\right)} \quad [32]$$

where $v_s = AP/c$ and the numerical value can be obtained by the given A, the operating pressure P, and the molar concentration c, which can be approximated to that of pure water.

This calculation procedure was applied to the reverse osmosis separation of the solutes listed in Table I by the membranes which were characterized in Table II and the results were compared with the experimental data in Fig. 6. The agreement found between calculated and experimental separation data testifies to the validity of the general approach provided in the present work.

Conclusion

1. HPLC offers an effective means of studying the properties of interfacial fluids.
2. Diffusivities of completely ionized inorganic solutes through water at the cellulose acetate polymer-aqueous solution interface are proportional to the third power of the corresponding diffusivities in the bulk water phase.
3. The existence of a unique correlation between the quantities $\ln[D_{Ai}/(D_{Ai})_{NaCl}\cdot K_{Ai}'/(K_{Ai}')_{NaCl}]$ and $\Delta(-\Delta\Delta G/RT)_A$ confirms the physicochemical significance of the data for free energy parameters relevant to reverse osmosis.

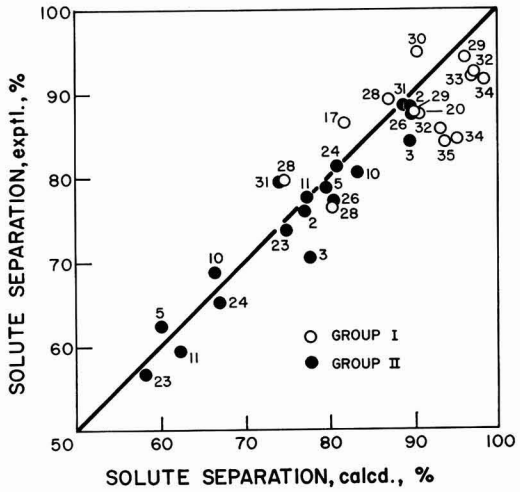

Fig. 6. Comparison of calculated solute separation and experimental solute separation. Solute numbers the same as in Table I. Specification of cellulose acetate membranes used, as shown in Table II; operating pressure. 1724 kPa gauge (= 250 psig); solute concentration in feed, ~300 ppm; feed flow rate, 400 cm³/min.

Manuscript submitted July 23, 1980; revised manuscript received Nov. 15, 1981. This was Paper 615 presented at the Hollywood, Florida, Meeting of the Society, Oct. 5-10, 1980.

Any discussion of this paper will appear in a Discussion Section to be published in the June 1983 JOURNAL. All discussions for the June 1983 Discussion Section should be submitted by Feb. 1, 1983.

APPENDIX A

The theoretical plate height given by Eq. [8] is not universally accepted. In the literature (17) the simple additive sum in the form of Eq. [8] has been replaced by a coupling expression such as

$$H_A = H_p + H_d + H_s + \frac{1}{\frac{1}{H_p}+\frac{1}{H_m}} \quad [A\text{-}1]$$

By using approximated values of each component we can ignore H_d and $1/H_m$. Then H_A becomes

$$H_A \approx 2H_p + H_s \quad [A\text{-}2]$$

Since H_p is a constant for a given column at a given flow rate the validity of form of Eq. [12] and [16] is maintained.

APPENDIX B

The theoretical plate height, H, is defined as

$$H = \frac{L}{N} \quad [B\text{-}1]$$

where L and N are the chromatography column length and the number of theoretical plates. N can be expressed as

$$N = \left(\frac{t_R}{\sigma}\right)^2 \quad [B\text{-}2]$$

where t_R is the retention time of the solute from the injection to the peak maximum and σ is the peak standard deviation. Furthermore

$$V_R' = vt_R \quad [B\text{-}3]$$

and

$$w = 2v\sigma \quad [B\text{-}4]$$

where V_R', w, and v are the retention volume of the solute from the sample injection, the peak half-width

in volume units, and the velocity of the mobile phase in the column. Combining all the above equations, we obtain for the theoretical plate height

$$H = \frac{L}{4}\left(\frac{w}{V_{R'}}\right)^2 \qquad [B\text{-}5]$$

LIST OF SYMBOLS

A	pure water permeability constant, kg-mol $H_2O/m^2 \cdot sec \cdot kPa$
$\ln C_{NaCl}^*$	constant representing the pore structure of the membrane as given by Eq. [23]
c	molar density of aqueous solutions, kg-mol/m^3
c_A	molar density of the solute, kg-mol/m^3
D_{AB}	molecular diffusion coefficient for the mobile phase, same as the diffusion coefficient of the solute in bulk water, m^2/sec
D_{Ai}	molecular diffusion coefficient for the stationary phase, same as the diffusion coefficient of the solute in interfacial water, m^2/sec
D_{AM}	diffusion coefficient of the solute in the membrane pore, m^2/sec
$(D_{AM}/K\delta)$	solute transport parameter (treated as a single quantity), m/sec
d	length of diffusion path for the solute in the stationary phase, m
d_p	mean particle diameter, m
f	fraction solute separation
ΔG_B	free energy of hydration in the bulk water phase, J/g-mol
ΔG_I	free energy of hydration in the interfacial water phase, J/g-mol
$-\Delta\Delta G/RT$	free energy parameter
H	theoretical plate height, m
K_{Ai}'	equilibrium coefficient of the solute distributed between the stationary and mobile phases
$(1/K)_A$	equilibrium coefficient of the solute distributed between the membrane pore and the bulk solution
k	mass transfer coefficient for the solute on the high pressure side of the membrane, m/sec
L	chromatography column length, m
M_B	molecular weight of water
N_A	solute flux through the membrane, kg-mol/m$^2 \cdot$ sec
N_B	solvent flux through the membrane, kg-mol/m$^2 \cdot$ sec
n_a, n_c	number of mols of anion and cation, respectively, in one mol of ionized solute
P	operating pressure, kPa
(PR)	product rate through a given area of membrane surface in the presence of a solute in the feed solution, kg/hr
(PWP)	pure water permeation rate through a given area of membrane surface in the absence of a solute in the feed solution, kg/hr
q	configuration factor
R	retention ratio defined by Eq. [9]
S	effective membrane area, m^2
V_d	volume of dead space, cm^3
V_m	volume of the mobile phase, cm^3
V_R	retention volume of the solute, cm^3
$V_{R'}$	$V_R + V_d$, cm^3
V_s	volume of the stationary phase, cm^3
v	regional velocity of the mobile phase, m/sec
v_s	permeation velocity of the product solutions, m/sec
w	half-width of a chromatography peak in volume units (half-width as time $\times$ solvent flow rate), cm^3
X_A	mol fraction of solute

Greek letters

α	constant defined by Eq. [13]
γ	obstruction factor for the diffusion through granular material
λ	eddy diffusion coefficient
$\pi(X_A)$	osmotic pressure of the solution corresponding to mol fraction X_A of the solute, kPa
Ω	constant defined by Eq. [14]
ω	coefficient of the mobile phase plate height contribution

Subscripts

1	bulk feed solution
2	concentrated boundary solution on the high pressure side of the membrane
3	membrane permeated product solution on the low pressure side of the membrane

REFERENCES

1. T. Matsuura, P. Blais, and S. Sourirajan, *J. Appl. Polym. Sci.*, **20**, 1515 (1976).
2. T. Matsuura and S. Sourirajan, *J. Coll. Int. Sci.*, **66**, 589 (1978).
3. T. Matsuura and S. Sourirajan, in "Proceedings of the Sixth International Symposium on Fresh Water from the Sea," Las Palmas, Gran Canaria, Sept. 17-22, 1978. A. Delyannis and E. Delyannis, Editors, pp. 227-237, Athens (1978).
4. T. Matsuura and S. Sourirajan, *Ind. Eng. Chem. Process Des. Dev.*, **17**, 419 (1978).
5. T. Matsuura, Y. Taketani, and S. Sourirajan, in "Synthetic Membranes," Vol. II, A. F. Turbak, Editor, p. 315, ACS Symposium Series 154 (1981).
6. S. Sourirajan, T. Matsuura, F. Hsieh, and G. R. Gildert, in "Ultrafiltration Membranes and Applications," A. R. Cooper, Editor, p. 21, Plenum Press, New York (1980).
7. T. Matsuura, L. Pageau, and S. Sourirajan, *J. Appl. Polym. Sci.*, **19**, 179 (1975).
8. R. Rangarajan, T. Matsuura, E. C. Goodhue, and S. Sourirajan, *Ind. Eng. Chem. Process Des. Dev.*, **15**, 529 (1976).
9. S. Sourirajan and T. Matsuura, in "Proceedings of EPA Symposium on Textile Industry Technology," Williamsburg, Dec. 5-8, 1978, EPA-6001 2-79-104 (May 1979).
10. G. N. Ling, in "Water Structure at the Water-Polymer Interface," H. H. G. Jellinek, Editor, pp. 4-13, Plenum Press, New York (1972).
11. R. Schultz and S. Asunmaa, in "Recent Progress in Surface Science," Vol. 3, J. F. Danielli, A. C. Riddiford, and M. D. Rosenberg, Editors, pp. 291-332, Academic Press, New York (1970).
12. F. Baumann, in "Basic Liquid Chromatography," N. Hadden, *et al.*, Editors, pp. 3-1–3-19, Varian Aerograph (1971).
13. M. E. Hyde, C. R. Peters, and J. E. Anderson, *J. Coll. Int. Sci.*, **50**, 467 (1975).
14. S. Sourirajan, "Reverse Osmosis," Chap. 3, Academic Press, New York (1970).
15. S. Sourirajan and T. Matsuura, in "Reverse Osmosis and Synthetic Membranes," S. Sourirajan, Editor, Chap. 3, National Research Council Canada, Ottawa (1977).
16. R. C. Reid and T. K. Sherwood, "The Properties of Gases and Liquids," p. 293, McGraw-Hill, New York (1958).
17. J. C. Giddings, "Dynamics of Chromatography, Part I, Principles and Theory," Chap. 2, pp. 13-94, Marcel Dekker, New York (1965).

The Adsorption and the Potentiodynamic Electro-Oxidation of Acetylene on Platinized Platinum

A. B. Delgado, A. M. Castro Luna, W. E. Triaca, and A. J. Arvía*

Instituto de Investigaciones Fisicoquímicas Teóricas y Aplicadas, INIFTA, División Electroquímica, 1900 La Plata, Argentina

ABSTRACT

The adsorption and the potentiodynamic electro-oxidation of acetylene on platinized platinum in 1*N* H_2SO_4 have been studied in the 16°-80°C temperature range. The perturbation conditions were chosen to avoid the influence of acetylene readsorption. The steady-state coverage by the adsorbed species was studied as a function of the potential and the hydrocarbon partial pressure. The estimated values of the average number of electrons per adsorption site and the number of the electrocatalyst sites blocked per adsorbed species are 4.7 and 2.1, respectively. Aging effects of the adsorbed species are also reported. The kinetic parameters obtained under potentiodynamic conditions suggest that the electro-oxidation of the adsorbed acetylene proceeds through a reaction pathway involving a slow initial monoelectronic transfer step.

The electrochemical oxidation of acetylene on platinum electrodes in acid electrolytes yields carbon dioxide and hydrogen ions with a current efficiency near 100% (1, 2). The electrochemical reaction has been investigated by both stationary-state and relaxation techniques (1-7). From earlier works it was concluded that the overall reaction includes an adsorption stage, but there are fundamental aspects related to the number and kind of adsorbed species and to the type of adsorption process involved in the electrochemical reaction that have not yet been completely elucidated. The present paper refers to the characteristics of the acetylene adsorption on platinized platinum in sulfuric acid solution in the 16°-80°C range and to the potentiodynamic electro-oxidation of the adsorbed species.

Experimental

A conventional three-compartment Pyrex glass electrolysis cell was used. The working electrode was a platinized-platinum electrode, 6×10^{-2} cm² apparent area. The preparation and pretreatment of the working electrode are described in previous publications (8, 9). The working electrode real area was determined through the charge of the hydrogen electrodesorption current peaks. The counterelectrode was a platinum sheet, 5 cm², and an RHE in the same electrolyte was used as reference. The base electrolyte was 1*N* H_2SO_4 prepared from the AR chemical (Merck) and triply distilled water. Occasionally, $NaHSO_4$ was added to the electrolyte covering the $0.35M \leq c \leq 2.35M$ concentration range. The electrolyte was saturated with acetylene at partial pressures ranging from 10^{-2} atm to 1 atm. For experiments at $p_{C_2H_2}$ lower than 1 atm, purified nitrogen was used to prepare the saturating gas mixture. Nitrogen was previously passed through liquid air and 98% H_2SO_4 containing traps. Acetylene from a pressure cylinder was passed through multiple washing water containing traps and through a purification column (La Oxigena S.A.) to remove traces of acetone. The purity of the gas entering the cell was controlled by gas chromatography. Experiments were run at 16°, 40°, 60°, and 80°C.

Prior to the acetylene adsorption measurements, the working electrode was subjected to the pretreatment already described in a previous publication (9). After the electrode pretreatment the potential was held at a preset value, E_{ad}, to adsorb acetylene during a certain time, t_{ad}. Immediately afterward a triangular potential sweep was applied either toward the positive, program (a), or the negative going potential direction, program (b), at a constant potential sweep rate, v (Fig. 1). Most of the results are reported at 60°C and at $p_{C_2H_2} = 10^{-2}$ atm where no readsorption of acetylene from the solution was detected at $v \geq 0.4$ V/sec.

* Electrochemical Society Active Member.
Key words: metals, electrode, chemisorption, voltammetry.

Results and Interpretation

The adsorption characteristics of acetylene on platinum.—A typical *I/E* display resulting with a TPS run from 0.25 to 1.65V at 0.4 V/sec immediately after holding the potential at $E_{ad} = 0.25$V during $t_{ad} = 20$ min in the electrolyte under acetylene saturation at 10^{-2} atm pressure (Fig. 2) shows a net broad anodic current peak at *ca.* 1.18V, which is associated with the electro-oxidation of the adsorbed hydrocarbon species. The first positive going potential scan exhibits the complete absence of hydrogen adatoms electro-oxidation current contribution. This indicates that under the above-mentioned conditions the whole surface is fully covered by the acetylene adsorbed species. The same behavior is observed at higher acetylene partial pressures. Furthermore, during the first TPS the potential of the oxygen electrodesorption current peak is more negative than that recorded during the following cycles. Correspondingly, the oxygen electrodesorption charge is slightly lower than that observed in the blank, due to the incomplete electro-oxidation of adsorbed acetylene under the experimental conditions depicted in Fig. 2. After the third TPS, since there is no acetylene readsorption, the *I/E* display practically reproduces that of the blank. The charge corresponding to the electro-oxidation of adsorbed acetylene, Q_{ox}, is calculated from the relationship

$$Q_{ox} = [(Q_T) - (Q_c)_1] + [(Q_c)_b - (Q_c)_1] \quad [1]$$

where (Q_T) is the total anodic charge obtained in the

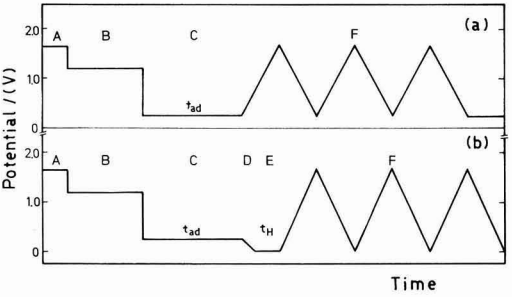

Fig. 1. Potential perturbation programs. Time axis arbitrary scale. Step width: A = 5 sec; B = 120 sec (gas bubbling) or 60 sec (gas bubbling) + 120 sec (quiescent solution); C = t_{ad}; D = initial negative going potential sweep; E = t_H; F = triangular potential sweeps.

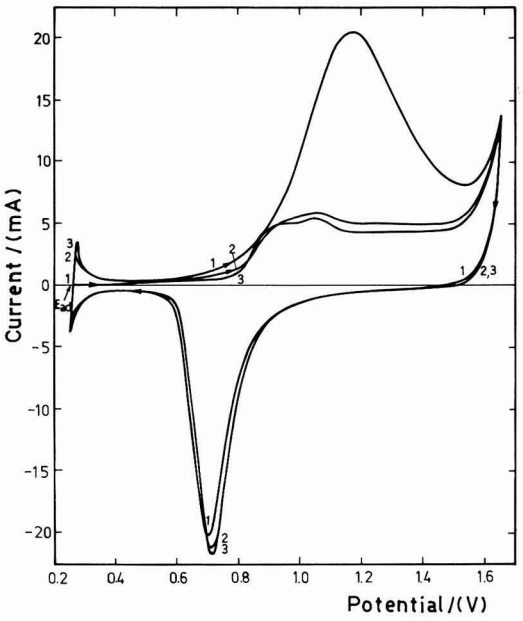

Fig. 2. Potentiodynamic *I/E* profiles run at 0.4 V/sec using the perturbation program (a) shown in Fig. 1. E_{ad} = 0.25V; t_{ad} = 20 min; $p_{C_2H_2}$ = 0.01 atm; 60°C; real electrode area = 19 cm². Numbers (1), (2), and (3) indicate the first, second, and third potential scan, respectively. Profile (3) approaches the blank contour (nitrogen saturated electrolyte).

presence of acetylene and $(Q_c)_1$ and $(Q_c)_b$ are the oxygen electrodesorption charges recorded during the first potential sweep in the presence and in the absence of acetylene, respectively. (Q_T), $(Q_c)_1$, and $(Q_c)_b$ are corrected for the double layer effect.

The dependence of Q_{ox} on t_{ad} at E_{ad} = 0.25V was obtained at v = 0.4 V/sec and $p_{C_2H_2} = 10^{-2}$ atm. For $t_{ad} \geqslant 5$ min a constant Q_{ox} value is reached. Also, the influence of E_{ad} on Q_{ox} was determined after equilibration at $p_{C_2H_2} = 10^{-2}$ atm during the time required to attain the acetylene stationary coverage, $t_{ad,ss}$ (Fig. 3). The maximum charge related to the electro-oxidation of adsorbed acetylene, $(Q_{ox})_M$ is found at E_{ad} = 0.25V, the corresponding charge value being 0.98 mC/cm² of real area. At $E_{ad} < 0.2$V the acetylenic electrosorbed species is electroreduced to ethylene and ethane (10) and at $E_{ad} > 0.35$V it undergoes the electro-oxidation to carbon dioxide and hydrogen ions. In order to correct for the readsorption effect on the evaluation of Q_{ox} at $p_{C_2H_2} > 10^{-2}$ atm the following procedure was used: (*i*) after the acetylene adsorption at E_{ad} during t_{ad}, a 20 min nitrogen washing was made and then the adsorbed species were electro-oxidized at a constant v; (*ii*) the Q_{ox} values were plotted as a function of $1/v$ and Q_{ox} at $V \to \infty$ was obtained. For $p_{C_2H_2}$ = 1 atm, the $(Q_{ox})_M$ value resulting at $v \to \infty$ is 0.95 mC/cm² (Fig. 4). There is no appreciable change of the acetylene surface coverage at the maximum adsorption potential in the 10^{-2}-1 atm pressure range. Taking into account the electrode roughness factor, the $(Q_{ox})_M$ coincides with the maximum charge corresponding to the electro-oxidation of adsorbed ethylene on platinized platinum (8).

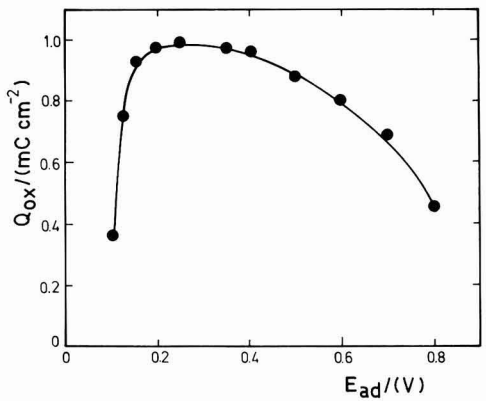

Fig. 3. Dependence of Q_{ox} on E_{ad} at $t_{ad,ss}$. $p_{C_2H_2}$ = 0.01 atm; 60°C.

The acetylene adsorption process.—To decide whether the initial interaction between acetylene and platinum was either an adsorption or an electrosorption process, the electrochemical interface was subjected to a potentiostatic step at E_{ad} = 0.25V just after step B of the electrode pretreatment (Fig. 1), and simultaneously recording the anodic transient current. The latter was practically negligible and the charge involved during the current relaxation was smaller than 1% of the electro-oxidation charge of the residual adsorbed species as determined through the potentiodynamic scan run immediately after the potential holding at E_{ad}. The conclusion from these runs is that the adsorption of acetylene on platinum is a nondissociative process occurring through the partial break of the triple bond in the molecule and its direct interaction with the metal surface.

The dependence of E_p on t_{ad}. Aging of the electrosorbed species.—The runs made at 0.4 V/sec after adsorbing acetylene at E_{ad} = 0.25V during different t_{ad} exceeding $t_{ad,ss}$ show a gradual change of the electro-oxidation *I/E* profile (Fig. 5). Thus the $(Q_{ox})_M$ value remains constant within 3% but the current peak, i_p, slightly increases in height and the corresponding current peak potential, E_p, becomes progressively more positive (Table I). Under these experimental conditions the electrochemical characteristics of the oxygen electrodesorption current peak are independent of t_{ad}. These results indicate that the electro-oxidation of the adsorbed species requires a larger overpotential as t_{ad} increases. The effect can be associated with the aging of the acetylenic species adsorbed on the electrode surface.

To determine whether the aging effect involves the contribution of ionic adsorption, potentiodynamic runs were made in 0.1*N* H_2SO_4 + 0.35M $NaHSO_4$ and in 0.1*N* H_2SO_4 + 2.35M $NaHSO_4$ solutions at $p_{C_2H_2}$ = 1 atm and at E_{ad} = 0.25 and 0.68V and at different t_{ad} exceeding $t_{ad,ss}$. There is practically no influence of the $NaHSO_4$ concentration on the location of the current peak potential. This suggests that ionic adsorption

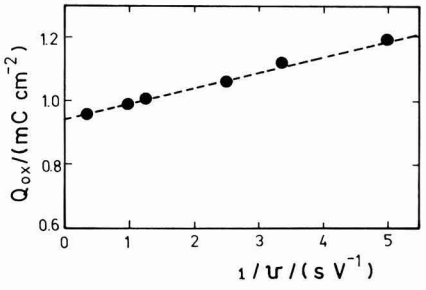

Fig. 4. Dependence of Q_{ox} on $1/v$ at $p_{C_2H_2}$ = 1 atm. E_{ad} = 0.25V; t_{ad} = 10 min (hydrocarbon saturated electrolyte) + 20 min (nitrogen washing); 60°C.

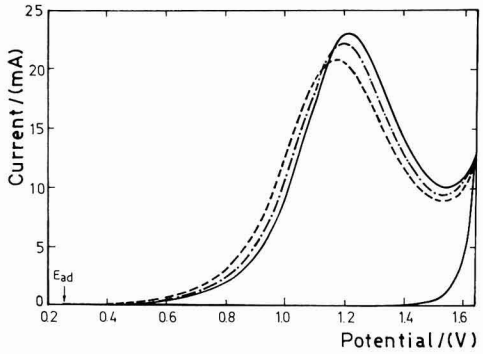

Fig. 5. Potentiodynamic *I/E* profiles run at 0.4 V/sec after the hydrocarbon adsorption at E_{ad} = 0.25V during different t_{ad}. $p_{C_2H_2}$ = 0.01 atm; 60°C; real electrode area = 21 cm². Curve (- - -), t_{ad} = 10 min; curve (– · –), t_{ad} = 25 min; curve (——), t_{ad} = 60 min.

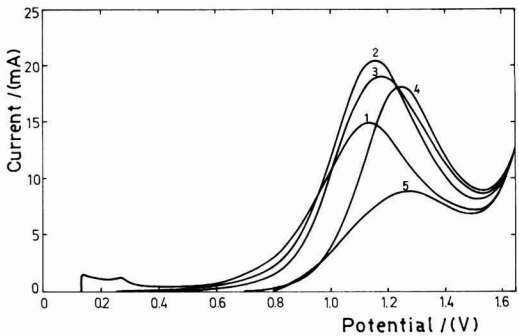

Fig. 6. Potentiodynamic *I/E* profiles run at 0.4 V/sec after the hydrocarbon adsorption during t_{ad} = 20 min at different E_{ad}. $p_{C_2H_2}$ = 0.01 atm; 60°C; real electrode area = 18.5 cm². Curve 1, E_{ad} = 0.13V; curve 2, E_{ad} = 0.25V; curve 3, E_{ad} = 0.4V; curve 4, E_{ad} = 0.7V; curve 5, E_{ad} = 0.8V.

plays no major role in the adsorption and electro-oxidation of the acetylenic adsorbed species.

The dependence of E_p on E_{ad}.—Potentiodynamic runs made at a constant v after acetylene adsorption during a constant t_{ad} at different E_{ad}, in the $0.1V \leq E_{ad} \leq 0.8V$ range (Fig. 6), show a shift of E_p toward more positive potentials when E_{ad} increases. This shift is more remarkable when the adsorption is carried out at $E_{ad} > 0.5V$, and it occurs independently of the Q_{ox} value (Fig. 3). This monotonous trend at any acetylene surface coverage negates the possibility that the surface activity of the adsorbed species could determine the electro-oxidation potential value.

The temperature influence on the acetylene adsorption.—At $p_{C_2H_2} = 10^{-2}$ atm the maximum adsorption potential as well as the $(Q_{ox})_M$ value are practically independent of the temperature in the 16°-80°C range. After the hydrocarbon adsorption at E_{ad} = 0.25V during $t_{ad,ss}$ the hydrogen adatoms formation is inhibited at any temperature. This behavior is similar to that already reported for the electro-oxidation of adsorbed ethylene on platinum in the same electrolyte (8). As the temperature increases, the potential of the anodic current peak moves toward lower values and the current peak becomes thinner and more symmetric in shape as deduced from the peak height to peak width at one-half peak height ratio, r (Table II). The thermal coefficient of the current peak potential, (dE_p/dT), is 5×10^{-3} V/°C.

The possible hydrogenation of the adsorbed species.—The possibility of hydrogenation of the species adsorbed under present conditions (E_{ad} = 0.25V, t_{ad} = 20 min, $p_{C_2H_2} = 10^{-2}$ atm, and 60°C) was studied by running the potentiodynamic scan toward the negative going potential direction immediately after the adsorption process according to program b (Fig. 1). The negative going potential scan was extended to *ca.* 0.01V and then either the potential sweep was reversed or the potential was held at *ca.* 0.01V during a certain time, t_H, before continuing the positive going potential scan. Thus, when $t_H = 0$, practically no hydrogen adatoms electrosorption current is observed and the Q_{ox} value decreases appreciably (Fig. 7), but in the potential range preceding the hydrocarbon electro-oxidation current peak the anodic current is slightly increased as compared to the runs without electrochemical hydrogenation. On the other hand, when the potential is held at 0.01V during t_H = 50 sec, the electro-oxidation current peak corresponding to the acetylenic adsorbed species is practically no longer observed (Fig. 8). Under these circumstances, a small anodic current contribution appears at *ca.* 0.7V, which is the potential range where the COH-type adsorbed species are likely electro-oxidized (11). These species are probably residual products formed through the interaction between adsorbed acetylene, hydrogen adatoms, and water in contact with the electrocatalyst.

The amount of charge assigned to the electro-oxidation of the COH-type adsorbed residue increases when E_{ad} is fixed at potentials more positive than 0.25V. This is clear when E_{ad} = 0.4V (Fig. 9), but at this potential carbon dioxide is already formed during the electro-oxidation of the acetylenic adsorbed species. Therefore, the relative increase of the current peak at *ca.* 0.7V caused by hydrogenation may result from the interaction between carbon dioxide and hydrogen adatoms (12).

Evaluation of the number of electrons per adsorption site.—The average number of electrons per adsorption site and the number of sites blocked by each adsorbed species can be derived from the data obtained at 60°C. The average $(Q_{ox})_M$, equal to 0.98 mC/cm², divided by the charge of the hydrogen adatoms monolayer on polycrystalline platinum, which is taken as 0.21 mC/cm², gives 4.7 electrons per adsorption site and since the electro-oxidation of each C_2H_2 species requires 10 electrons, the number of sites blocked by each ad-

Table I. Dependence of i_p and E_p on t_{ad}. E_{ad} = 0.25V; v = 0.4 V/sec; 60°C

t_{ad} (min)	i_p (mA cm⁻²)	E_p (V)	$(Q_{ox})_M$ (mC cm⁻²)
	$p_{C_2H_2}$ = 0.01 atm		
10	0.99	1.170	0.97
15	1.02	1.180	0.97
25	1.06	1.200	0.99
60	1.09	1.220	0.98
	$p_{C_2H_2}$ = 0.1 atm		
5	1.00	1.190	0.99
10	1.02	1.195	0.97
20	1.06	1.210	0.98
30	1.08	1.220	0.99
60	1.11	1.235	0.99

Table II .Values of E_p, r, and $(Q_{ox})_M$ at different temperatures. E_{ad} = 0.25V; t_{ad} = 20 min; v = 0.4 V/sec; $p_{C_2H_2}$ = 0.01 atm

T (°C)	E_p (V)	$r \cdot 10^3$ (A V⁻¹ cm⁻²)	$(Q_{ox})_M$ (mC cm⁻²)
16	1.408	1.30	0.96
40	1.282	2.00	0.95
60	1.180	2.51	0.98
80	1.080	2.89	0.97

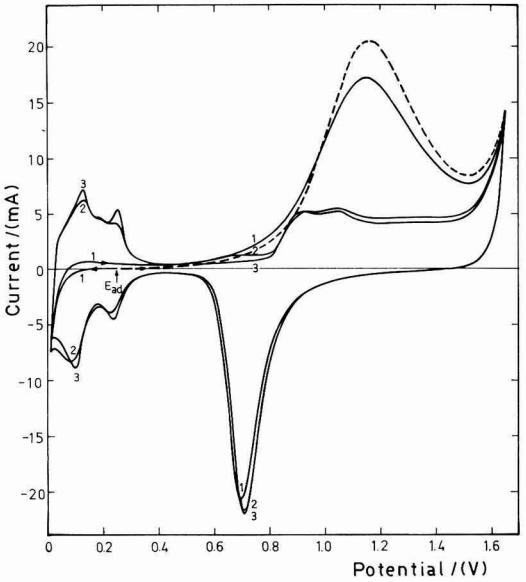

Fig. 7. Potentiodynamic *I/E* profiles run at 0.4 V/sec after the hydrocarbon adsorption at E_{ad} = 0.25V during t_{ad} = 20 min. $p_{C_2H_2}$ = 0.01 atm; 60°C; real electrode area = 18 cm². - - -, first *I/E* profile run with program (a); ——, first (curve 1), second (curve 2), and third (curve 3) *I/E* profiles run with program (b); t_H = 0.

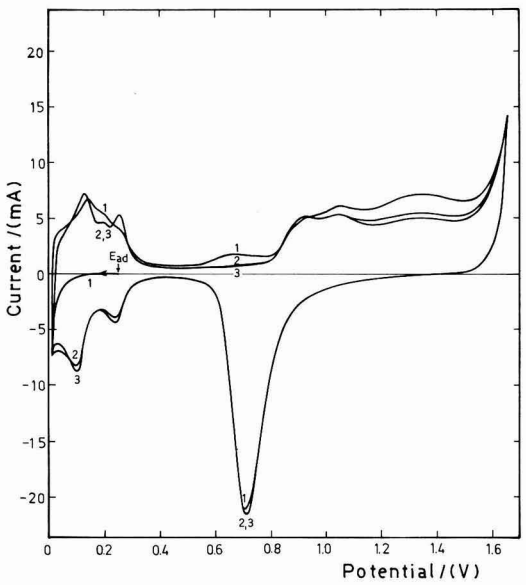

Fig. 8. Potentiodynamic *I/E* profiles run at 0.4 V/sec using the perturbation program (b). E_{ad} = 0.25V; t_{ad} = 20 min; t_H = 50 sec at 0.01V; $p_{C_2H_2}$ = 0.01 atm; 60°C; real electrode area = 18 cm².

sorbed C_2H_2 species, x, is 2.1. This result can be confirmed through the data obtained from the experiments involving the inhibition of the hydrogen adatoms adsorption produced by the organic species, whose charge, Q_b, is given by

$$Q_b = Q_{H,O} - Q_{H,A} \qquad [2]$$

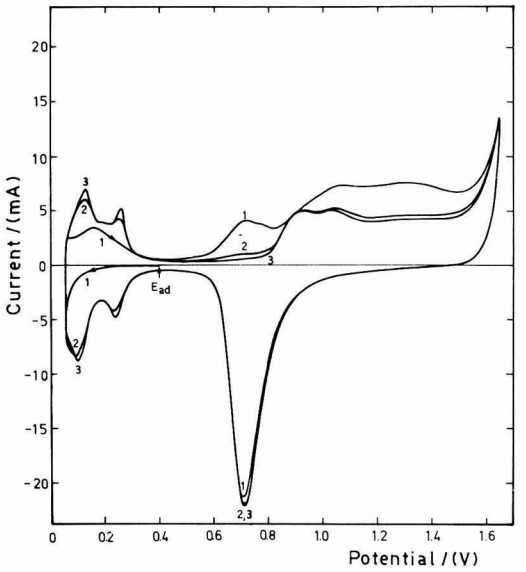

Fig. 9. Potentiodynamic *I/E* profiles run at 0.4 V/sec using the perturbation program (b). E_{ad} = 0.4V; t_{ad} = 10 min; t_H = 1 min at 0.05V; $p_{C_2H_2}$ = 0.01 atm; 60°C; real electrode area = 18 cm².

where $Q_{H,O}$ is the charge of the hydrogen adatoms monolayer in the absence of acetylene and $Q_{H,A}$ is the charge related to the hydrogen adatoms formation in the presence of acetylene. The average Q_b value obtained from the potentiodynamic runs after acetylene adsorption at E_{ad} = 0.25V during $t_{ad,ss}$ is 0.20 mC/cm². This figure includes a correction for the small electroreduction of the acetylenic adsorbed species during the negative going potential scan. Hence, the number of sites blocked by each acetylenic adsorbed species, derived from $x = 10$ (Q_b/Q_{ox}), is 2.04, in good agreement with the previous estimation. Furthermore, the values of the average number of electrons per adsorption site and the number of sites blocked by the acetylenic adsorbed species practically coincide with those found for the ethylene electrosorption on platinized platinum (8).

Kinetic relationships derived from the potentiodynamic runs.—The height of the adsorbed acetylene electro-oxidation current peak increases linearly with v (Fig. 10). The low potential sweep rate data are corrected for the contribution of the acetylene readsorption. The peak height is also corrected for the current corresponding to the oxygen electrosorption process. Under the experimental conditions where the hydrocarbon saturation coverage is reached, no definite dependence of the current peak height on $p_{C_2H_2}$ is found. The potential of the electro-oxidation current peak fits a linear E_p *vs.* log v relationship in the 0.05 V/sec $\leq v \leq$ 1 V/sec range (Fig. 11). The slope of the straight line is practically equal to the 2.3 ($2\,RT/F$) ratio. This can be interpreted as a Tafel slope associated with a constant surface coverage by the acetylenic adsorbed species.

Discussion

The electro-oxidation of acetylene on platinum in acid electrolytes in the temperature range investigated is represented by the overall reaction

$$C_2H_2 + 4H_2O = 2CO_2 + 10H^+ + 10\,e \qquad [3]$$

Reaction [3] takes place at least in part through the participation of an adsorbed species on the electro-

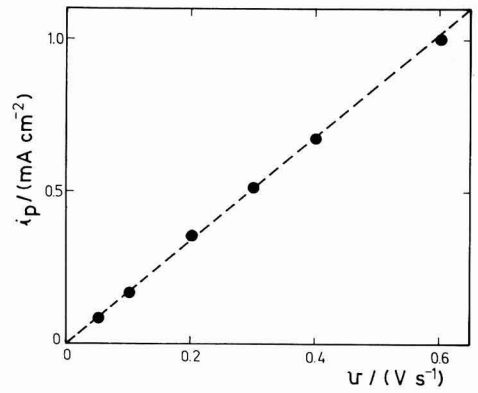

Fig. 10. Dependence of the anodic current peak related to the electro-oxidation of the adsorbed hydrocarbon species on v. E_{ad} = 0.25V; t_{ad} = 5 min; $p_{C_2H_2}$ = 0.01 atm; 60°C.

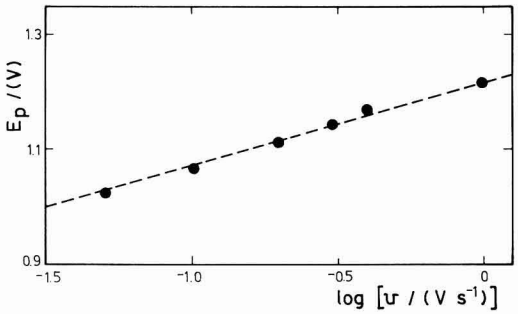

Fig. 11. Dependence of the anodic current peak potential related to the electro-oxidation of the adsorbed hydrocarbon species on v. E_{ad} = 0.25V; t_{ad} = 5 min; $p_{C_2H_2}$ = 0.01 atm; 60°C. The slope of the dashed line is 0.140 V/decade.

catalyst. This conclusion is derived in a straightforward manner from the above described results. However, a possible contribution of a direct electro-oxidation of acetylene under stationary conditions is not precluded.

The maximal interaction between the adsorbed species and the electrocatalyst occurs in the neighborhood of 0.25V, a potential value at which most organic molecules exhibit their largest interaction with platinum. This potential value is close to the potential of zero charge of platinum in the base electrolyte (13).

The $(Q_{ox})_M$ value obtained from acetylene adsorption compares reasonably well with that found after the ethylene electrosorption, but both adsorption processes appear entirely different. Thus, while the former adsorbs in a nondissociative manner, the latter adsorbs in a dissociative manner. However, the stoichiometric composition of the adsorbed species in both cases is apparently the same, namely a C_2H_2 species, as concluded from the same average number of electrons per adsorption site. Therefore, the initial step in reaction [3] corresponds to the adsorption process represented by

$$C_2H_2 + x(H_2O)\ Pt = (C_2H_2)\ Pt_x + x\ H_2O \quad [4]$$

The value of x, the average number of platinum sites occupied by the adsorbed species, is *ca.* 2.1. No evidence of any significant dehydrogenation of acetylene on platinum is detected under the present experimental conditions, in contrast with previously reported data (3).

When the acetylene readsorption is avoided, the electro-oxidation of the adsorbed species is well characterized through the kinetic relationships derived from the potentiodynamic runs. Thus the linear dependence of i_p on v and that of E_p on log v, and the Tafel slope derived from the E_p *vs.* log v plot, equal to 2.3 ($2\ RT/\mathbf{F}$), which corresponds to a constant surface coverage (θ_{peak} = 0.37), are in agreement with the predictions of the theory developed for the adsorption pseudo-capacitance peaks under a linear potential sweep, when the initial monoelectronic transfer reaction associated with either the electrosorption or the electrodesorption of intermediates is highly irreversible (14). Hence, the simplest explanation of the kinetics of the adsorbed acetylene electro-oxidation is through a single electron transfer rate-controlling step. The formalism of this stage can be put forward in terms of deprotonation process of the adsorbed species, which may occur either through the following reaction

$$(C_2H_2)Pt_x = (R)\ Pt_{(x-1)} + H^+ + Pt + e \quad [5a]$$

or through the solvent participation as follows

$$(C_2H_2)Pt_x + H_2O = (RHOH)\ Pt_{(x-1)} + H^+ + Pt + e \quad [5b]$$

R and RHOH denote intermediates produced in the course of the electrochemical reaction. After either reaction [5a] or [5b] the water reacts with the surface organic intermediates yielding finally CO_2 and H^+ ions through a sequence of undetermined fast reactions. These reactions can be expressed by the overall anodic process

$$\text{Surface organic intermediates} + H_2O \rightarrow CO_2 + H^+ + Pt + e \quad [6]$$

If either step [5a] or [5b] is rate determining, on the assumption that the intermediate follows a Langmuir isotherm, the rate equation becomes

$$i = k'\,\theta \exp(\alpha \mathbf{F} E/RT) \quad [7]$$

where k' is the formal rate constant in electrical units, θ refers to the electrode surface coverage by C_2H_2 species, and α is the transfer coefficient assisting the reaction in the anodic direction. An equation similar to [7] also results in terms of Temkin-type isotherms for the adsorbed species, because there is a compensation effect of the influence of coverage by the C_2H_2 species or by the R or RHOH species on the activation energy of reactions [5a] or [5b], respectively. Under constant surface coverage conditions, the Tafel slope deduced from Eq. [7] is equal to the $RT/\alpha\mathbf{F}$ ratio. The experimental Tafel slope derived from the E_p *vs.* log v plot agrees with the latter for α = 0.5.

Although the present results are explained only through the participation of C_2H_2 as the main adsorbed species, the idea must not be discarded that traces of other types of dehydrogenated adsorbed particles, which probably become important at potentials higher than 0.40V (5) or at higher temperatures (15), may contribute to a small extent in the electro-oxidation process.

The aging of the adsorbed species, as detected through the shift of the anodic current peak potential toward more positive values as t_{ad} increases, can be explained considering two types of interactions. On one side, the adsorbed species become more strongly bound to the substrate on increasing t_{ad}. This is also reflected through the shift of E_p on E_{ad} at a constant t_{ad} (Fig. 6). On the other hand, there is an increase of the interaction between the adsorbed particles on increasing t_{ad}, so that a surface polymer-type species may be formed on the electrode surface.

The bonding energy change associated with the aging effect can be reasonably related to a time dependence of the structure of the adsorbed species. This explanation is supported to some extent from the gas phase chemisorption studies of hydrocarbons on platinum

surfaces at lower temperatures (16), where it was suggested that two structures of chemisorbed acetylene may occur, one weakly distorted and another strongly distorted.

Similar aging effects were reported for the electrosorbed species formed on platinum from methanol (17), where both the stoichiometric composition of the electrosorbed species and its amount on the surface remain constant during the aging process.

Acknowledgment

INIFTA is sponsored by the Consejo Nacional de Investigaciones Científicas y Técnicas, the Universidad Nacional de la Plata, and the Comisión de Investigaciones Científicas (Provincia de Buenos Aires). This work was also partially sponsored by the Regional Program for the Scientific and Technological Development of the Organization of the American States.

Manuscript submitted May 8, 1981; revised manuscript received Jan. 5, 1982.

Any discussion of this paper will appear in a Discussion Section to be published in the June 1983 JOURNAL. All discussions for the June 1983 Discussion Section should be submitted by Feb. 1, 1983.

Publication costs of this article were assisted by the Instituto de Investigaciones Fisicoquímicas Teóricas y Aplicadas.

REFERENCES

1. J. W. Johnson, H. Wroblowa, and J. O'M. Bockris, *This Journal*, **111**, 863 (1964).
2. J. O M. Bockris, H. Wroblowa, E. Gileadi, and B. J. Piersma, *Trans. Faraday Soc.*, **61**, 2531 (1965).
3. T. M. Beloslyudova and D. V. Sokolskii, *Elektrokhimiya*, **1**, 1182 (1965).
4. S. Gilman, *Trans. Faraday Soc.*, **62**, 466 (1966).
5. S. Gilman, *ibid.*, **62**, 481 (1966).
6. S. Gilman, *This Journal*, **113**, 1036 (1966).
7. K. G. Bogoslovskii and L. A. Mirkind, *Elektrokhimiya* **13**, 462 (1977).
8. W. E. Triaca, T. Rabockai, and A. J. Arvía, *This Journal*, **126**, 218 (1979).
9. W. E. Triaca, A. M. Castro Luna, and A. J. Arvía, *ibid.*, **127**, 827 (1980).
10. H. J. Davitt and L. F. Albright, *ibid.*, **118**, 236 (1971).
11. M. G. Sustersic, R. Córdova O., W. E. Triaca, and A. J. Arvía, *ibid.*, **127**, 1242 (1980).
12. S. B. Brummer and K. Cahill, *J. Electroanal. Chem. Interfacial Electrochem.*, **21**, 463 (1969).
13. R. S. Perkins and T. N. Andersen, in "Modern Aspects of Electrochemistry," Vol. 5, J. O'M. Bockris and B. E. Conway, Editors, Plenum Press, New York (1969).
14. S. Srinivasan and E. Gileadi, *Electrochim. Acta*, **11**, 321 (1966).
15. G. A. Somorjai, *Surf. Sci.*, **89**, 496 (1979).
16. J. E. Demuth, *ibid.*, **84**, 315 (1979).
17. V. S. Bagotskii, Yu. B. Vassiliev, and O. A. Khazova, *J. Electroanal. Chem. Interfacial Electrochem.*, **81**, 229 (1977).

Electrochemistry of Prussian Blue Modified Electrodes: An Electrochemical Preparation Method

Kingo Itaya*

Research Institute of Electrical Communication, Tohoku University, Sendai 980, Japan

and Haruo Akahoshi* and Shinobu Toshima

Department of Applied Chemistry, Faculty of Engineering, Tohoku University, Sendai 980, Japan

ABSTRACT

A new type of Prussian blue modified electrode is described. The Prussian blue modified electrode is electrochemically prepared in a solution of ferric-ferricyanide. The amount of Prussian blue on electrodes such as platinum, glassy carbon, and SnO_2 is easily controlled by changing the current density, the electrode potential, and the time of the electrolysis. The waves observed at +0.2 and +1.0V *vs.* SCE are due to the reduction and the oxidation of the ferric part and of the ferrous part in the Prussian blue crystal, $KFe^{III}Fe^{II}(CN)_6$ or $Fe_4^{III}[Fe^{II}(CN)_6]_3$, respectively. This electrode exhibits excellent stability in aqueous solution. A spectroelectrochemical property of the modified electrode is also described.

Prussian blue (PB) has been manufactured as an important pigment for paints, lacquers, printing inks, and other color uses (1). As is well known, there are two well-characterized formulas of PB that have been called "water insoluble PB," $Fe_4^{III}[Fe^{II}(CN_6)]_3$, and "water soluble PB," $KFe^{III}Fe^{II}(CN)_6$ (2, 3). This pigment is an iron (III)-hexacyanoferrate (II) that has been definitely shown to be the case by the infrared absorption spectrum (4), the Mössbauer resonance spectrum (5), and the optical absorption spectrum (6). It has been also shown that chemical reduction and oxidation of PB can lead to Prussian white, $K_2Fe^{II}Fe^{II}(CN)_6$ and Prussian green (Berlin green), $Fe^{III}Fe^{III}(CN)_6$, respectively (7). Although PB has long been an important pigment, the electrochemistry of PB has not yet been fully investigated. This might be due to lack of knowledge of techniques for the preparation of the thin film on suitable substrates.

Recently reports by Neff have briefly shown a method of preparation of a thin film of PB on platinum electrodes in which a platinum electrode was simply immersed in a ferric-ferricyanide solution (8, 9). The deposition of PB on platinum and gold electrodes, which was undertaken in a condition of nonelectroplating, seems to be due to auto- or catalytic-reduction of ferric-ferricyanide (7). As is pointed out by Ellis *et al.* (9), the data obtained by a nonelectroplating method had been highly dependent on the chemical procedures and the nature of the substrate surface. We found that organic substrates such as commercial polyester sheets, silicon rubbers, and so on could be very rapidly covered by blue PB, so that they could not be used even as the materials for the electrode mounting. In order to minimize contaminations of organics, we

* Electrochemical Society Active Member.
Key words: metals, carbon, voltammetry, electrolysis.

used a platinum disk sealed in a glass tube. This electrode was polished with alumina slurry (0.05 μm particle size) and then cleaned in concentrated sulfuric acids for 30 min before use. Although well-reproducible results were obtained with this care, a maximum coverage of PB of about 3 mC/cm^2, as a total amount of the charge consumed by the reduction of PB, was obtained for 30 min in a solution of 10 m*M* in $FeCl_3 \cdot 6H_2O$, 10 m*M* in $K_3Fe(CN)_6$, and 0.01*N* in HCl. No more than 3 mC/cm^2 could be obtained on platinum electrodes. This was visually merely slightly blue.

We observed an open-circuit potential, 0.98V *vs.* SCE, for a platinum disk electrode in the above solution. Such an extraordinary positive value could not be obtained either in solutions of ferric chloride or of potassium ferricyanide, indicating that a solution of ferric-ferricyanide is a very strong oxidant. This is probably the reason why organics were covered by blue PB so quickly. Although mechanistic studies of the deposition of PB in the procedure proposed by Neff would be of special interest, we wish to address a new versatile method for the preparation of PB modified electrodes in this paper. This new method is a much more straightforward way for the preparation of the thin film and is based on an electrochemical reduction of the ferric-ferricyanide solution. A fresh solution of reagent grade $FeCl_3 \cdot 6H_2O$ (0.02*M*) and 0.02*M* of $K_3Fe(CN)_6$ was prepared in distilled water. The electrodes such as SnO_2, Pt, and glassy carbon, immersed in the ferric-ferricyanide solution were cathodically polarized for 120 sec under galvanostatic conditions with current density of about 40 μA/cm^2. A large platinum foil electrode was used as a counterelectrode. The blue color due to the formation of Prussian blue on electrodes is observed at the beginning of the electrolysis. The electrochemistry of the electrodes covered by the thin film of PB was examined in an acidic 1*M* KCl solution (*p*H = 4.0). The *p*H of the 1*M* KCl solution was adjusted by hydrochloric acid. Figure 1 shows a cyclic voltammogram of a film of PB on an SnO_2 electrode. Note that PB could not be deposited on a well-cleaned SnO_2 electrode by a dipping method proposed by Neff (8). Only a small amount of PB, less than 0.08 mC/cm^2, could be deposited on SnO_2 electrodes for 30 min immersion. Two surface waves observed at about 0.2 and 1.0V *vs.* SCE are due to the reduction and the oxidation of PB, respectively. As mentioned above, Prussian white, a reduced form of PB, can be formed by the electrochemical reduction and Prussian green, an oxidized form of PB, can be also formed by the oxidation process. The electrochemistry of the electrochemically prepared PB is almost the same as that reported by Neff *et al.* (8, 9). The electrochemical processes of the reduction and of the oxidation are formulated as the following equations using two formulas of PB

(reduction of PB)

$$KFe^{III}Fe^{II}(CN)_6 + e^- + K^+ \rightarrow K_2Fe^{II}Fe^{II}(CN)_6 \quad [1]$$

or

$$Fe_4^{III}[Fe^{II}(CN)_6]_3 + 4e^- + 4K^+ \rightarrow K_4Fe_4^{II}[Fe^{II}(CN_6]_3 \quad [2]$$

(oxidation of PB)

$$KFe^{III}Fe^{II}(CN)_6 - e^- - K^+ \rightarrow Fe^{III}Fe^{III}(CN)_6 \quad [3]$$

or

$$Fe_4^{III}[Fe^{II}(CN)_6]_3 - 3e^- + 3Cl^- \rightarrow Fe^{III}[Fe^{III}(CN)_6 \cdot Cl]_3 \quad [4]$$

It is noteworthy that the oxidation of PB must involve penetrations of anions (Eq. [4]) for maintaining electroneutrality, if the formula of PB is "water insoluble PB," $Fe_4^{III}[Fe^{II}(CN_6]_3$. Specific dependence of the oxidation of PB on the kind of anions of supporting electrolyte would be of interest. The composition of the electrochemically prepared PB would be very important in mechanistic studies. It is very interesting that the chromophores of Fe^{III} are reduced at a more negative potential than that of hydrated Fe^{3+} and that the chromophores of Fe^{II} are oxidized at a much more positive potential than that of ferrocyanide.

Figure 2 shows cyclic voltammograms of the reduction of PB on a platinum electrode. The linear dependence of the peak current, i_{pc} and i_{pa}, on the scan rate

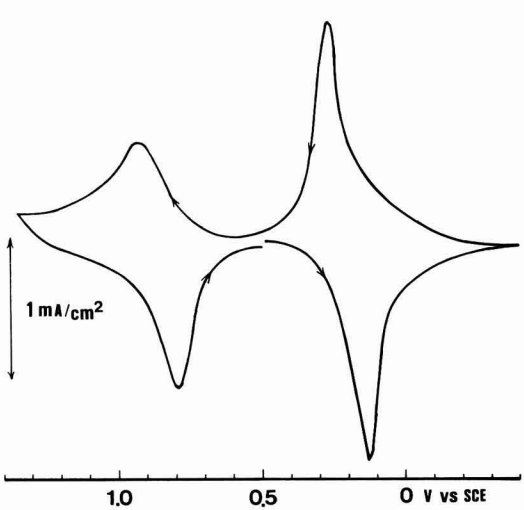

Fig. 1. A cyclic voltammogram of a Prussian blue modified SnO_2 electrode in 1*M* KCl solution (*p*H 4.0). The charge consumed by the reduction of the Prussian blue modified electrode was about 4.8 mC/cm^2. Scan rate of the electrode potential was 50 mV/sec. The electrode; Corning (10 $\Omega/\square$).

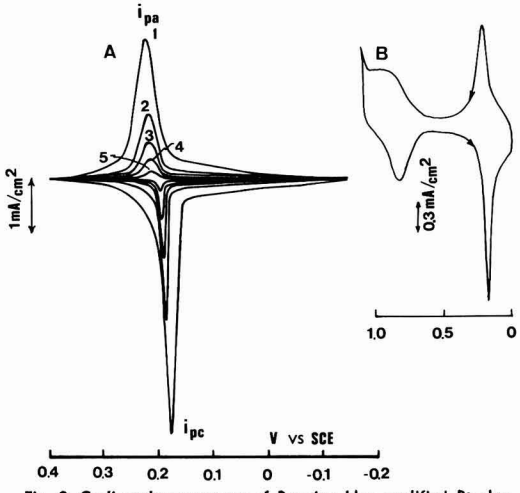

Fig. 2. Cyclic voltammograms of Prussian blue modified Pt electrodes in a 1*M* KCl solution (*p*H 4.0). A, cyclic voltammograms on the reduction side of a Prussian blue modified Pt disk electrode at different scan rates (1, 50 mV/sec; 2, 20 mV/sec; 3, 10 mV/sec; 4, 5 mV/sec; 5, 2 mV/sec). The charge consumed by the reduction of the electrode was about 4.8 mC/cm^2. B, a cyclic voltammogram through the both waves of a Prussian blue modified Pt electrode. Scan rate of the electrode potential was 100 mV/sec. The charge consumed by the reduction of the electrode was about 0.48 mC/cm^2.

of the electrode potential was obtained up to 100 mV/sec indicating that the waves observed here are essentially surface waves like polymer modified electrodes (10-12). Very fast current responses, less than 100 msec, were observed on a platinum electrode by stepping the electrode potential between −0.3 and +0.6V (16). The waves obtained on a platinum electrode are much sharper than those obtained on SnO_2 electrodes. This is probably due to the ohmic resistance in SnO_2 electrodes. The behavior observed on other metallic electrodes such as gold or glassy carbon was the same as obtained on platinum electrodes. SEM of films prepared electrochemically on SnO_2, Au, and Pt electrodes reveal very uniform structures. A preliminary value of density of PB film was about 1.4 determined by a measurement of the thickness of a PB film, which is almost the same as a literature value [d = 1.78 (2)]. The thickness of about 1000Å was obtained for the film of 5 mC/cm². These results show that an electrochemical method is satisfactory for the preparation of PB films with a uniform thickness on substrates.

The separation between the peak potentials of the anodic and cathodic waves depends on the scan rate of the electrode potential and on the amount of PB on the electrode, as shown in Fig. 2A and B. Note that the total amounts of the charge consumed by the reduction of PB in Fig. 1 and Fig. 2A were about 4.8 mC/cm², which was almost the same as the charge passed through a cell for the preparation of PB described above. This strongly suggests that the efficiency of the electrochemical reduction of the ferric-ferricyanide solution to form PB is about unity. The formation of a one-to-one complex, $Fe^{III}...Fe^{III}(CN)_6$, between ferric and ferricyanide ions has been studied (13-15) and this might be important in the electrochemical deposition of PB. The electrochemical investigation of the deposition process of PB would be of special interest.

The stability of PB on the electrodes was excellent. No degradation of the peak height was observed under repeated scanning over the reduction of PB, between −0.3 and +0.6V after 10^5 cycles at a scan rate of 100 mV/sec.

Figure 3 shows the absorption spectrum of a PB modified SnO_2 electrode obtained *in situ* at various electrode potentials. A similar spectrum has been recently reported by Ellis *et al.* (9) using a gold semitransparent electrode. A line labeled A, obtained at 0.5V, is essentially the same as the spectrum of the colloidal form of PB reported by Robin (6). A strong band observed at 690 nm is assigned to an optical transition from an electric configuration of $Fe^{III}Fe^{II}(CN)_6$ to $Fe^{II}Fe^{III}(CN)_6$ (6). The spectrum labeled B was obtained at −0.3V where no distinct absorption band was obtained in the visible region. The spectrum labeled C, obtained at 1.4V, has a band at 430 nm, which may be the origin of the color of Prussian green. The molar extinction coefficient of PB has been measured as 9800 at 14,700 cm^{-1} using aqueous dispersions of PB (6). The absorbance obtained by a film having 5.4 mC/cm² as the total charge consumed in the reduction of PB was about 0.45 at 700 nm. Based on these values, the molar absorption coefficient is calculated as about 7000, assuming one-electron transfer reactions (Eq. [1]). The change of the absorption spectra of PB obtained at different electrode potentials is reversible, which can be considered as a material for an electrooptical signal modulator (16).

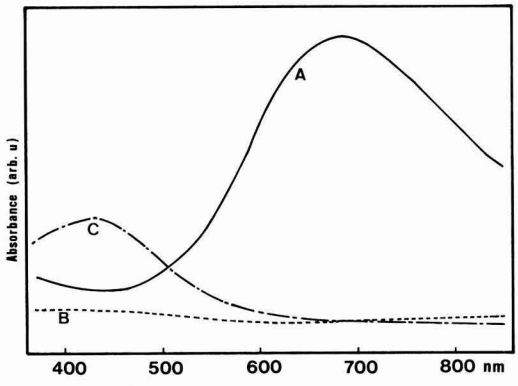

Fig. 3. Absorbance changes of a Prussian blue modified SnO_2 electrode obtained at different electrode potentials. A, B, and C were obtained at +0.5, −0.3, and +1.4V vs. SCE, respectively.

Manuscript submitted July 27, 1981; revised manuscript received Dec. 17, 1981.

Any discussion of this paper will appear in a Discussion Section to be published in the June 1983 JOURNAL. All discussions for the June 1983 Discussion Section should be submitted by Feb. 1, 1983.

Publication costs of this article were assisted by Tohoku University.

REFERENCES

1. H. Holtzman, *Ind. Eng. Chem.*, **37**, 855 (1945).
2. A. Ludi and H. U. Güdel, *Struct. Bonding (Berlin)*, **14**, 1 (1973).
3. M. B. Robin and P. Day, *Adv. Inorg. Chem. Radiochem.*, **10**, 247 (1967).
4. R. E. Wilde, S. N. Ghosh, and B. J. Marshall, *Inorg. Chem.*, **9**, 2512 (1970).
5. A. Ito, M. Suenaga, and K. Ono, *J. Chem. Phys.*, **48**, 3597 (1968).
6. M. B. Robin, *Inorg. Chem.*, **1**, 337 (1962).
7. J. F. De Wet and R. Rolle, *Z. Anorg. Allg. Chem.*, **336**, 96 (1965).
8. V. D. Neff, *This Journal*, **125**, 886 (1978).
9. D. Ellis, M. Eckhoff, and V. D. Neff, *J. Phys. Chem.*, **85**, 1225 (1981).
10. K. Itaya and A. J. Bard, *Anal. Chem.*, **50**, 1487 (1978).
11. H. Akahoshi, S. Toshima, and K. Itaya, *J. Phys. Chem.*, **85**, 818 (1981).
12. M. Umana, P. Denisevich, D. R. Rolison, S. Nakahama, and R. W. Murray, *Anal. Chem.*, **53**, 1170 (1981).
13. J. A. Ibears and N. Davidson, *J. Am. Chem. Soc.*, **73**, 476 (1951).
14. R. G. Walker and K. Q. Watkins, *Inorg. Chem.*, **7**, 885 (1968).
15. D. L. Sengleton and J. H. Swinehart, *Inorg. Chem.*, **6**, 1636 (1967).
16. K. Itaya, K. Shibayama, H. Akahoshi, and S. Toshima, *J. Appl. Phys.*, In press.

Studies on Photoelectrochemical Properties of SnO_2 Films Prepared from Organic Resinate Solution

David E. Stilwell* and Su-Moon Park**

Department of Chemistry, University of New Mexico, Albuquerque, New Mexico 87131

ABSTRACT

Tin oxide (SnO_2) thick films have been prepared on glass surfaces from organometallic tin resinate solutions, and their photoelectrochemical properties have been studied. The antimony-doped tin oxide film showed similar photoelectrochemical properties to those of the n-SnO_2 single crystal electrode. No anodic dark current was observed for the electrolysis of water up to the bias potential of 2.0V *vs.* SCE and saturation currents were observed upon illumination. These and other results indicate that SnO_2 films prepared from the resinate show purer semiconducting properties with less degenerate energy levels than those prepared from aqueous $SnCl_4$. Possible reasons are discussed from experimental observations.

Tin oxide films on glass have been used widely as an electrically conductive glass. Some of the methods used for producing SnO_2 films on glass include oxidation of deposited tin on glass, precipitation of tin hydroxides with ammonium hydroxide followed by washing, drying, and heating, chemical vapor deposition of $SnCl_4$ onto heated substrates, and d-c glow discharge sputtering (1). Recently, a chemical vapor deposition technique using tetramethyl tin also produced the oxide film (2). Various methods of thin and thick oxide film preparations are reviewed in the literature (1). The most common method of preparation of SnO_2 films is by using aqueous $SnCl_4$ solutions (1, 3). In this method, a solution containing stannic chloride, HCl and dopant such as antimony or the halogen itself is sprayed on the substrate surface and decomposed thermally. This method produces highly stable conducting films on glasses. Besides near metallic conductivity, these n-type semiconductors exhibit optical transparency, high oxygen overpotential, low background current, low sorption of organics, chemical durability, and mechanical stability. Commercial conducting glasses made by this method are available. Much work has been carried out to characterize the optical and electrical properties of films produced by this method (2-18).

There are several electrochemical applications of such films. These applications include the use of films on glasses as working electrodes in photoelectrochemical cells (19) and spectroelectrochemical cells (13). They can also serve as a substrate for the deposition of other polycrystalline semiconductors such as n-CdS (20).

In this study, we report a new method of the SnO_2 film preparation on the surface of glasses using organic tin resinate solution. The physical and electrochemical properties of SnO_2 films thus prepared are also characterized and compared with those of films prepared from $SnCl_4$ solutions.

Experimental

Stannic chloride (Baker's Analyzed), antimony trichloride (Allied Chemical), hydrochloric acid (Mallinkrodt), nitric acid (DuPont), and sodium hydroxide (Baker's Analyzed) were used as received. Tin resinate solution (Hanovia Liquid Gold, Engelhard, No. 118-B) had an Sn content of 3.1%. Elemental analysis of this sample gave 74.61% carbon and 8.73% hydrogen with no detectable nitrogen. The infrared absorption spectrum showed a high content of the carbonyl group. The sample also contained no detectable amount of chloride, when it was subjected to the concentrated nitric acid and hydrogen peroxide to decompose organic components, followed by the addition of silver nitrate to the clear aqueous solution. The solute was soluble in acetone and a precipitate was formed when mixing with water. The solution was filtered and used after mixing with about 60% of acetone.

Films were prepared on glass surfaces by the pull method, horizontal coat method, and spray method (1). Soda-lime silica glass microscope slides (Fischer) were used for the baking cycle lower than at 550°C. Above 550°C, vitreous silica (quartz) glass microscope slides (Heraeus-Amersil, Sayreville, New Jersey) were used as the substrate. In a spray method, a Paasche air brush (Model H-3) was used to spray the resin/acetone mixture onto the glass. An all-glass chromatography atomizer was used when the $SnCl_4$ solution was sprayed. The carrier gas used was oxygen with the applied pressure of 13 psi and the distance from substrate to the air brush was 15 cm from the leading edge with a spray angle of 60°. The solution flow rate was 0.05-0.07 ml/sec. The solution was sprayed for 4-12 sec for each coating.

The conductivity of films thus prepared was measured by a two-point probe with a distance of 1.0 cm by applying 4.00V and measuring the current. The thickness of films was measured by weight gain employing the density of SnO_2 of 6.95 g/cm^3 for the nonreflective films (21). For the reflective films, it was measured by the Tolansky method by recording an absorption spectrum of the film (22). For a weakly absorbing thin film, the thickness, t, is given by

$$t = \frac{M \cdot \lambda_1 \cdot \lambda_2}{2(n_{\lambda_1} \cdot \lambda_2 - n_{\lambda_2} \cdot \lambda_1)}$$

where M is the number of oscillations between the two extremes of the reflective pattern, and n_{λ_1} and n_{λ_2} are refractive indexes of the film at two wavelengths, λ_1 and λ_2, respectively. In the case of SnO_2, the refractive index is approximately 2.0 (5) at the two wavelengths used and thus the above equation reduces to

$$t = \frac{M \cdot \lambda_1 \cdot \lambda_2}{4(\lambda_2 - \lambda_1)}$$

The film thickness measured by these two methods was consistent within about 10%.

Electrochemical measurements were made with a Princeton Applied Research (PAR) Model 173 potentiostat-galvanostat with a Model 176 I/E converter and a Model 175 universal programmer. Electrochemical cells had a three-electrode configuration with the SnO_2 film as a working electrode, the platinum foil as a counterelectrode, and the saturated calomel electrode (SCE) as a reference electrode. The electrode was illuminated from the backside or frontside using an Oriel Xenon arc lamp (1000W) with an Oriel 8540 universal power supply. Monochromatic light was ob-

* Electrochemical Society Student Member.
** Electrochemical Society Active Member.
Key words: n-SnO_2 film, organic resinate solution, photoelectrochemistry, semiconductor.

tained using an Oriel 7240 monochromator with a bandpass of approximately 20 nm. The photon flux was measured by using an International Light Model IL-700 radiometer. The electrode area exposed to the solution was approximately 0.38 cm^2.

Results and Discussion

The films prepared by the pull method and the horizontal coat method (1) had very poor mechanical and electrical properties. Films prepared on a soda-lime silica glass microscope slide were heated to 500°C. Three temperature zones were noted. Up to 150°-200°C white fumes were seen and the resin spread out. Between 200° and 350°C the coating turns from amber to black color. Heating at 450° ~ 500°C or higher made the coated surface clear. Generally the films were non-reflecting and spongy yellow-white. Microscopic examination revealed large amounts of entrained particulate foreign matter. This could be somewhat driven off by heating at 580°C for 12-24 hr. This heat-treatment, however, caused the coating to lose most of its conductivity. Films thus prepared had resistances of greater than 10^8 Ω-cm. and a thickness of about 1800-2500Å as determined by the weight gain. Further, reproducible films could not be prepared by these methods.

Since films prepared by the pull method and the horizontal coat method were very poor in their mechanical, optical, and electrical properties, we decided to use the spray method. The spray method gave much more reproducible results than the above methods, as can be seen in Fig. 1-3. Figure 1 shows that the increase in weight of the oxide film can be made reproducible, provided the flow rate, spray duration per coat, and substrate temperature are maintained constant. The amount of tin oxide deposited on glass surfaces can also be controlled by the substrate temperature as is shown in Fig. 2. Films thus prepared had some interference reflecting properties, which were considerably enhanced by filtration of the resin. The film made from the unfiltered resin had many black/amber impurities of 1-40 microns, while those from filtered resin had particles of 1-8 microns with much less frequency.

The undoped films made by this method had resistances of greater than 10^7 Ω-cm, even after as many as 15 coats. The thickness determined by the Tolansky method varied between 5000 ~ 7500Å. Resistances can be made significantly lower to the range of about 5000 Ω-cm by doping with antimony. Doping was accomplished by dissolving 1.5 mol percent $SbCl_3$ with respect to the tin content in the solution sprayed. In order to compare the properties of SnO_2 films, we also prepared the film using a mixture of $3M$ $SnCl_4 \cdot 5H_2O$, and 0.03 ~ $0.05M$ $SbCl_3$ in water (3, 17). Thicknesses of 5000 ~ 10,000Å with resistances of 1-500 Ω-cm were obtained by this method. The mechanical quality of films made from the $SnCl_4$ solution was almost always superior to that of films made from the resinate solutions. Resistances were lower for films made from the $SnCl_4$ solution than for those from the resinate solution. This indicates that impurities (mostly chloride) contributing to conductivities are much higher in films made from the aqueous solution than from the resinate. Also, as mentioned earlier, the fact that further heat-treatment made films lose their conductivity suggests that impurities play a major role for making undoped film conductive. It should be pointed out, however, that this heat-treatment may also remove the oxygen deficiency. Although antimony trichloride was used as a dopant both in the aqueous and the resinate solutions, we believe that very low or practically no

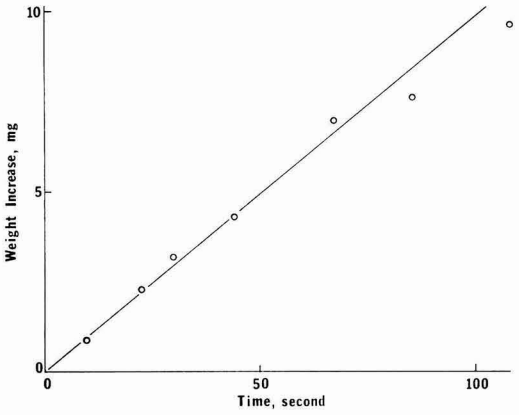

Fig. 1. Increase in the weight of the oxide film as a function of the total resinate spray time. See the text for the experimental details.

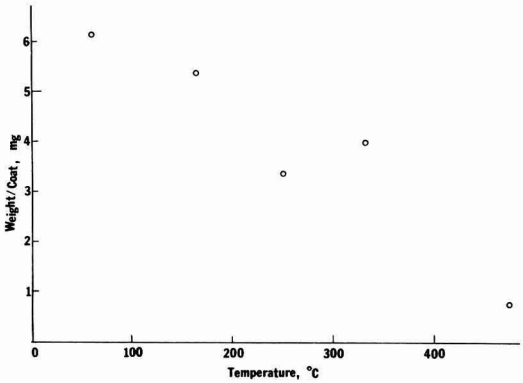

Fig. 2. Weight per coating as a function of the substrate temperature. The spray duration was held constant at 10 sec.

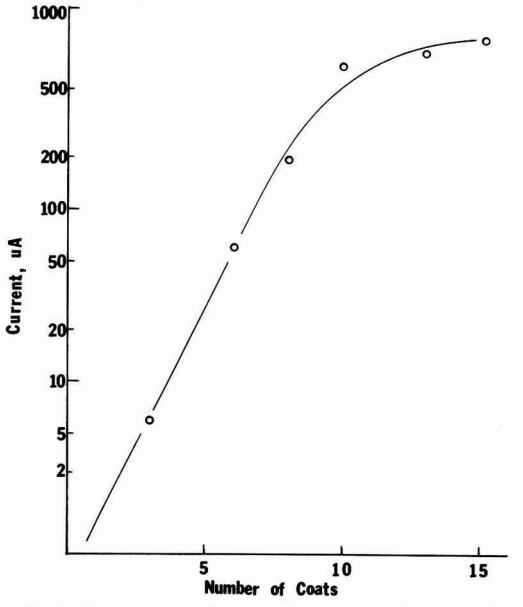

Fig. 3. Currents across the two probes at an applied potential of 4.0V as a function of the number of coatings. The thickness of films after 15 coatings was about 750 nm.

chloride was trapped in the film prepared from the resinate solution, resulting in lower conductivities. The chloride entrapment would be very low due to the small quantity of $SbCl_3$ used and due to the high volatility of $SbCl_3$ in organic solvents as opposed to the aqueous medium.

Since our major interests are their application to the photoelectrochemical work, we carried out electrochemical studies using films thus prepared. Figures 4 and 5 show the results of the photocurrent *vs.* applied potential at the illuminated electrode. The results obtained using films made from aqueous stannic chloride (Fig. 4) are in excellent agreement with the ones reported by Kim and Laitinen (3, 17). No limiting current is observed at the electrode made from aqueous $SnCl_4$ solution. Even in the dark, a significant amount of the current was observed above 1.0V *vs.* SCE. Although photocurrents were observed as shown in Fig. 4, they were completely absent when the doping level was made high. Also, photocurrents were not observed at the commercial tin oxide electrode (NESA glass, Pittsburgh Plate Glasses, Pittsburgh, Pennsylvania), probably due to its high doping level. Thus the tin oxide electrode prepared from the aqueous $SnCl_4$ solution shows its intermediate properties between semiconductor and the metal. As pointed out, this may be because of the high doping level and many degenerate energy levels probably due to chloride. Background current observed at about 1.0V *vs.* SCE in the dark and at about 0.6 ~ 0.8V *vs.* SCE under illumination may be due to the water oxidation as well as chloride oxidation at the surface (4, 17).

At the SnO_2 electrode prepared from the resinate solution the photoelectrochemical behavior was quite different as can be seen in Fig. 5. In the dark, there was practically no current up to about 2.0V *vs.* SCE. Limiting photocurrents were observed at higher potentials than 0.5V *vs.* SCE. This behavior resembles the observation reported by Wrighton *et al.* on the single crystal SnO_2 electrode (23). For long time (~2 days) electrolysis, we were able to collect about 0.5 ml of the gas product, but we did not perform the product analysis.

An interesting difference between these two electrodes can be seen in Fig. 6. The photocurrent rises and decays much faster at the electrode prepared from $SnCl_4$ than the one from the resinate solution. The decay rate does not follow a simple exponential function. Moreover, the decay rate was not significantly potential dependent. A simple *R-C* circuit model would predict an exponential, potential dependent decay. We speculate that this decay could be due to chemical

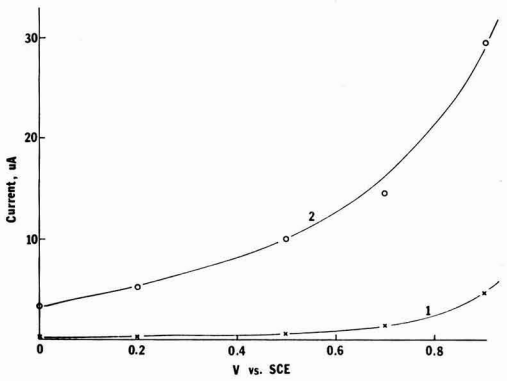

Fig. 4. Photocurrents *vs.* applied potential at the SnO_2 electrode prepared from $SnCl_4$. The solution was 1M in NaOH and the electrode was illuminated from the backside. 1, Current in the dark and 2, current under illumination.

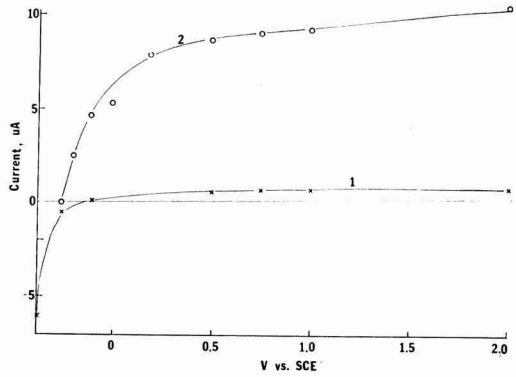

Fig. 5. Photocurrent *vs.* applied potential at the SnO_2 electrode prepared from the resinate solution. The electrode was doped with antimony. Experimental conditions were almost identical to those for Fig. 4.

reactions of adsorbed/entrained organic radicals that are photochemically formed. Note that the decay is

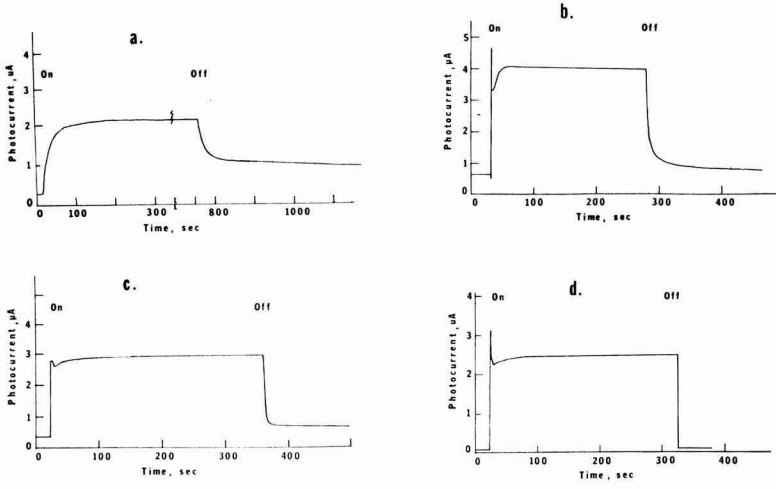

Fig. 6. Time dependency of the photocurrent rises and decays. (a) Film prepared from unfiltered, doped resinate solution baked at 550°C. Time to decay 90% was longer than 300 sec. (b) Film prepared from filtered, doped resinate solution baked at 550°C. Time to decay 90% was about 30 sec. (c) Film prepared from filtered, doped resinate solution baked at 650°C. Time to decay 90% was about 10 sec. (d) Film prepared from $SnCl_4$ methods. Time to decay 90% was less than 1 sec.

fastest when the resin is filtered and the film is baked at 650°C, when the film is purest with respect to organic material. This was not pursued further, since the composition of the resinate was known no more than already described from our analysis.

Wavelength dependence of photocurrents is shown in Fig. 7 and 8 for both films obtained by front and backside illumination. The photocurrent rises sharply near the absorption edge for SnO_2. The photocurrent spectra closely resemble those reported by Wrighton *et al.* (23) and Möller and Memming (25). These two figures will be discussed in more detail later in this section.

The photocurrent for the water oxidation increases as a function of the light intensity illuminated (Fig. 9). The linearity of the photocurrent-light intensity plot indicates that the photoelectrochemical oxidation rate is controlled by the rate of the hole generation. Note in the plot that the photoanodic process for the oxidation of water appears to require a threshold intensity as shown by lines 1 and 2 at lower applied potentials, *i.e.*, 0.0 and 0.20V *vs.* SCE, respectively. When the bias potential becomes high enough, the photocurrent-intensity curves pass through the origin as expected. A possible explanation for this observation could be that the hole diffusion lengths are small enough at the lower bias potential and at a low light intensity that holes generated at the glass-film interface may not reach the electrode-liquid interface, where oxidation of water takes place. Note that in all experiments, the electrode was illuminated from the backside.

In order to examine this postulate we carried out the thickness dependence of the photocurrent. The results

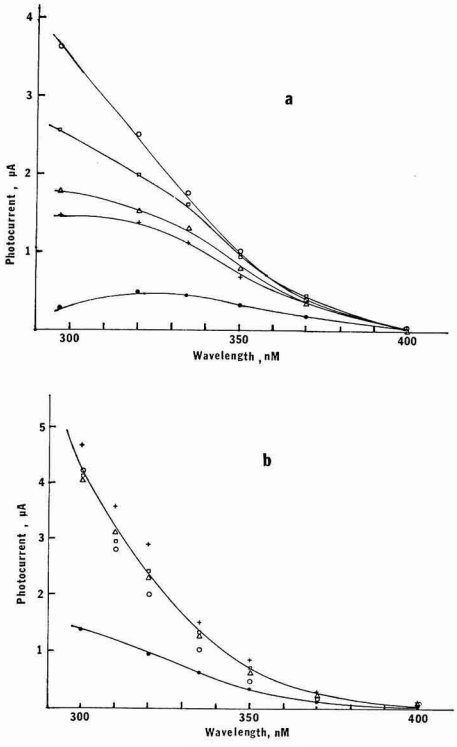

Fig. 7. Photocurrents *vs.* illumination wavelengths for SnO_2 films prepared from $SnCl_4$. (a) Backside illumination. The solution was 1*M* NaOH and the potential applied was +0.50V *vs.* SCE. Film thickness: ○, 160 nm; □, 284 nm; △, 370 nm; +, 470 nm; ●, 1000 nm. (b) Frontside illumination. The same experimental conditions were used as in (a).

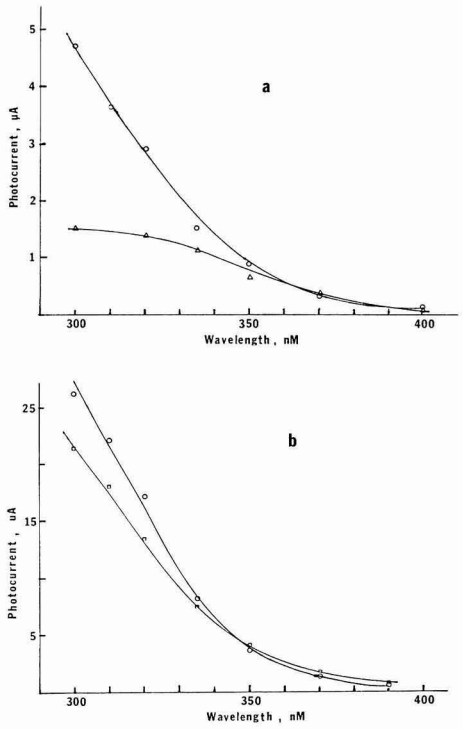

Fig. 8. Photocurrents *vs.* illumination wavelengths. (a) The SnO_2 film prepared by $SnCl_4$ methods. The thickness of the film was 470 nm. All other conditions were the same as those in Fig. 7. ○, frontside illumination; △, backside illumination. (b) The SnO_2 film prepared by resinate methods. The film thickness was 440 nm. All other experimental conditions were the same as in (a). ○, frontside illumination; □, backside illumination.

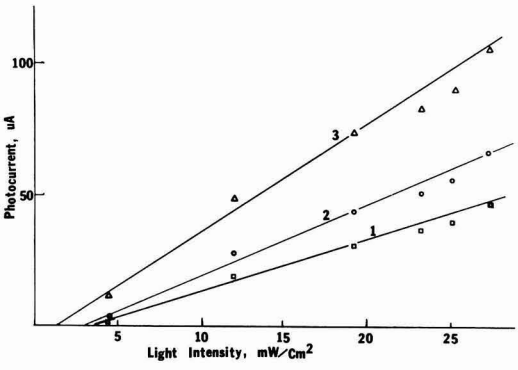

Fig. 9. Photocurrent *vs.* the intensity of light illuminated. Monochromatic light (335 nm) was used for this experiment. The solution was 1*M* in NaOH. The potential applied was curve 1, 0.0V; curve 2, 0.20V; and curve 3, 0.50V *vs.* SCE, respectively.

are shown in Fig. 10. These experiments were performed at the SnO_2 electrode prepared from the aqueous $SnCl_4$ solution due to its superior mechanical properties, *i.e.*, durability in the solution. The photocurrent, highest when the thickness is approximately 100 nm, decreases as the thickness of the film increases. Our observation does not agree with that of Möller *et al.* (25), who reported that the photocurrent at the TiO_2 film electrode increased as the thickness of the film in-

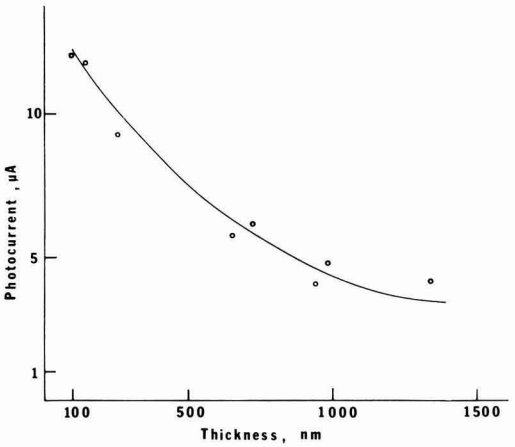

Fig. 10. Photocurrent *vs.* thickness of the film. The film was prepared from $SnCl_4$ for this experiment. Monochromatic illumination (335 nm) was used in 1M NaOH solution. The potential applied was 0.50V *vs.* SCE.

creased, when illuminated at the backside. They, on the other hand, observed the reverse trend when the electrode was illuminated through the electrolyte. These authors attributed their observation due to the electron trapping before electrons reach the contact of the TiO_2 film with the substrate. In our case, the holes generated upon illumination at the glass-SnO_2 interface appear to be trapped before they reach the SnO_2 film-electrolyte interface. This can be substantiated by comparing the photocurrent as a function of wavelengths for backside and frontside illumination. As one varies the excitation wavelength from 335 to 300 nm at a constant illumination intensity, the fraction of photons actually absorbed in the space charge region is expected to decrease with increasing film thickness for backside illumination for films thicker than about 200 nm. This is due to higher absorption coefficients at shorter wavelengths. This argument would hold true only if the donor density is very high as in the films from the $SnCl_4$ methods, resulting in small space charge regions. For frontside illumination this fraction is expected to rise, independent of thickness. Thus the photocurrents for frontside illumination should rise with shorter wavelengths and be independent of thickness, while backside illumination should show attenuation of photocurrent at lower wavelengths as a function of thickness. Further the photocurrent for frontside illumination is predicted to be higher for all thicknesses. This is shown in Fig. 7a and b. When the thickness is large for frontside illumination (Fig. 7b), electrons in the space charge region may be trapped before they reach the contact, as Möller *et al.* (25) pointed out.

When the film has a lower donor density as indicated by high resistivity, the space charge region will be very large; expected photocurrent behavior for the frontside and backside illumination should be different. Figure 8a and b compares the action spectrum of films prepared by $SnCl_4$ and resinate methods. Note that the films prepared from the resinate show much less attenuation for backside and frontside illumination, and that the photocurrent is about an order of magnitude higher. Also, the photocurrent increased with the film thickness of up to about 450 nm for both frontside and backside illumination (not shown in the figure). This indicates that the space charge region is very large; high fractions of the photons are collected as electron-hole pairs up to the film thickness of about 450 nm.

These data suggest that the chloride serves as trapping centers in films prepared from $SnCl_4$, while the films from the resinate contain much fewer trapping centers. Due to lower donor densities, the space charge region for the films from the resinate should be very large, as already pointed out. This should be the reason for the increased photocurrents with larger thickness for frontside and backside illumination.

For these measurements the intensity output of the lamp was adjusted to compensate for absorption through the quartz glass and the apparatus, such that the intensity at all wavelengths were the same within about 10%, as well as identical intensity for frontside *vs.* backside illumination. For these measurements a cell was constructed so that the comparison could be made by merely rotating the cell 180° about the film, *i.e.*, the film remained at the same area in space.

These observations agree well with our previous observation that the threshold photon flux is required at lower bias potentials. When the bias potential is high, however, the length of the space charge region may become comparable with the film thickness, requiring a low photon flux to produce the anodic photocurrent at the film-solution interface.

Conclusion

Our study has shown that the oxide film semiconductors can be produced more purely from organometallic compounds. Films produced from the organotin compound have poorer mechanical and electrical properties. The stability of films were poorer under the photoelectrochemical experimental conditions and the films had generally higher resistances than the SnO_2 films prepared from the aqueous $SnCl_4$ solution. Photoelectrochemical experiments show that films from the organotin compound have similar properties to those of the single crystal SnO_2 electrode. No anodic currents were observed in the dark up to 2.0V *vs.* SCE, whereas the onset potential for the photocurrent for the oxygen evolution was about −0.28V. The saturation current was observed at this electrode, while it was not observed at the film made from $SnCl_4$. Some of these properties are summarized in Table I for comparison.

These observations as well as results obtained from the time dependence of photocurrents indicate that the depletion layer should be larger for the films from the resinate solution. This is probably because the chloride in the polycrystalline SnO_2 film provides many energy levels and trapping centers. Thus our studies indicate that films that more resemble single crystals are obtained by avoiding an aqueous solution as a source of metal oxides. We attempted to determine the chloride content in films prepared by two methods using the energy dispersive spectroscopy (EDS) method but the technique was not sensitive enough to detect any chloride from any films.

Experiments on the film thickness dependence of photocurrents show the importance of hole trapping.

Table I. Comparison of films prepared by two methods

	SnO_2 by resinate method	SnO_2 by $SnCl_4$ method
Time to prepare film 400 nm thick	8-15 hr	0.5-1 hr
Resistance	5 kΩ up[a]	1-500Ω
Stability of film	Film eventually swells and falls	Stable
Stability of photoresponse	Decreases slowly with time	Mostly stable
Initial photoresponse	About an order of magnitude greater than $SnCl_4$ method	—
Batch reproducibility of photoresponse	Poor-fair	Fair

[a] When films were prepared side by side but using regular glass and quartz as substrate, only the film on quartz substrate was conductive.

Holes generated would be trapped before they reach the film-electrolyte interface to oxidize water, if the film thickness is larger than the space charge region.

Acknowledgment

Grateful acknowledgment is made for support of this research by the U.S. Department of Energy, Fossil Fuel Program (DE-AC21-81MC16377). We would also like to thank Mrs. Nancy Dhooge of Sandia Laboratories for her analysis of the chloride in various SnO_2 films.

Manuscript submitted June 23, 1981; revised manuscript received Dec. 2, 1981.

Any discussion of this paper will appear in a Discussion Section to be published in the June 1983 JOURNAL. All discussions for the June 1983 Discussion Section should be submitted by Feb. 1, 1983.

Publication costs of this article were assisted by the University of New Mexico.

REFERENCES

1. See chapters by H. Schroeder, M. H. Fromcombe, and J. E. Johnson, and W. M. Feist, S. R. Steele, and D. W. Readey, in "Physics of Thin Films," Vol. 5, G. Hass and R. E. Thun, Editors, Academic Press, New York (1969).
2. Y.-S. Hsu and S. K. Ghandi, *This Journal*, **126**, 1434 (1979).
3. H. Kim, Ph.D. Dissertation, University of Illinois, Urbana-Champaign, IL (1973).
4. H. A. Laitinen, C. A. Vincent, and T. M. Bednarski, *This Journal*, **115**, 1024 (1968).
5. J. C. Manifacier, M. DeMurcia, F. P. Fillard, and E. Vicario, *Thin Solid Films*, **41**, 127 (1977).
6. I. Uchida, H. Akahoshi, and S. Toshima, *J. Electroanal. Chem. Interfacial Electrochem.*, **88**, 79 (1978).
7. L. D. Loch, *This Journal*, **110**, 1081 (1963).
8. M. Gleria and R. Memming, *J. Electroanal. Chem. Interfacial Electrochem.*, **65**, 163 (1975).
9. J. A. Aboaf, V. C. Marcotte, and M. J. Chou, *This Journal*, **120**, 70 (1973).
10. S. M. Budd, *J. Non-Crystalline Solids*, **19**, 55 (1975).
11. C. A. Vincent, *This Journal*, **119**, 515 (1972).
12. T. Arai, *J. Phys. Soc. Jpn.*, **15**, 916 (1960).
13. J. W. Strojek and T. Kwana, *J. Electroanal. Chem. Interfacial Electrochem.*, **16**, 471 (1968).
14. E. Elliot, D. L. Zellmer, and H. A. Laitinen, *This Journal*, **117**, 1343 (1970).
15. L. M. Wier and R. W. Murray, *ibid.*, **126**, 617 (1969).
16. R. R. Mehta and S. F. Vogel, *ibid.*, **119**, 752 (1972).
17. H. Kim and H. A. Laitinen, *ibid.*, **122**, 53 (1975).
18. K. Ishiguro, T. Sasaki, T. Arai, and I. Imai, *J. Phys. Soc. Jpn.*, **13**, 296 (1958).
19. H. Gerischer, *Photochem. Photobiol.*, **16**, 243 (1972).
20. M. Tsuiki, H. Minoura, T. Nakamura, and Y. Ueno, *J. Appl. Electrochem.*, 523 (1978).
21. P. G. Stecher, Editor, The Merck Index, 8th ed., Merck & Co., Inc., Rahway, NJ (1968).
22. (a) J. C. Manifacier, J. Gasiot, and J. P. Fillard, *J. Phys. E. Sci. Instrum.*, **9**, 1002 (1976); (b) J. C. Manifacier, M. DeMarcia, and J. P. Fillard, *Thin Solid Films*, **41**, 127 (1977).
23. M. S. Wrighton, D. L. Morse, A. B. Ellis, D. S. Ginley, and B. Abrahamson, *J. Am. Chem. Soc.*, **98**, 44 (1976).
24. F. Möller, H. J. Tolle, and R. Memming, *This Journal*, **121**, 1160 (1974).
25. F. Möller and R. Memming, *Ber. Bunsenges. Phys. Chem.*, **76**, 469 (1972).

Ternary Chalcogenide-Based Photoelectrochemical Cells

II. The n-$CdIn_2Se_4$/Aqueous Polysulfide System

Reshef Tenne, Yehudith Mirovsky, Ya'acov Greenstein, and David Cahen

Department of Plastics Research and Structural Chemistry, The Weizmann Institute of Science, Rehovot 76100, Israel

ABSTRACT

$CdIn_2Se_4$ is a cross-substitutional analogue of CdSe with an incomplete cation lattice. We have carried out an investigation of the n-$CdIn_2Se_4$/aqueous polysulfide photoelectrochemical cell. A selective photoelectrochemical etching of the semiconductor surface leads to a dramatic increase in the photocurrent of the cell (up to 15 mA · cm^{-2} at small reverse bias) and greatly improved output stability. The spectral response of the cell reveals a considerable sub-bandgap photocurrent for the etched electrode. This is attributed to excitation via surface states located ~0.27 eV within the bandgap. After photoetching the electrode, most of the sub-bandgap response disappears and the response to supra-bandgap excitation increases by at least an order of magnitude that shows that these surface states serve also as recombination centers or traps for the photogenerated holes. We have analyzed the shape of the spectral response and observed two distinct transition modes: an indirect transition at 1.55 eV and a direct one at 1.72 eV, both of which are within the acceptable range for efficient solar energy conversion. Preliminary results using thin film polycrystalline photoelectrodes of this semiconductor are presented. They show that this material tends to lend itself fairly well to preparation of such electrodes.

II-VI materials, and especially Cd-chalcogenides, are among the most studied photoelectrodes for photoelectrochemical solar cells (PEC's) (1). From this class of materials have come thin film polycrystalline-based PEC with up to 8% solar efficiency (2), and ~1 year day/night output stabilities have been measured so far with CdSe electrodes, all in polysulfide electrolyte. Some progress has also been made toward understanding the possible corrosion processes occurring in these systems on an atomic scale (3). From the point of view of chemical (compositional) flexibility, the II-VI class of materials is somewhat limited, both in terms of possible constituents and their optical and electrical properties (*e.g.*, optical bandgap). Many more possibilities for choosing electrode materials exist if ternary and higher analogues, which can be obtained by cross-substitution of the electropositive constituent, are considered. Up to now only $CuInS_2$ (the true ternary analogue of $Zn_{0.5}Cd_{0.5}S$) has been studied as an electrode in a PEC (4). Its remarkable output stability prompted us to look at a slightly different ternary analogue (of CdSe, in this case), namely $CdIn_2Se_4$.

Figure 1 illustrates the relationships between several adamantine (zinc blende or wurtzite-related) structures, and their parent structure, diamond. In all of these chalcogen is tetrahedrally coordinated by "ca-

Key words: solar cells, special response measurements, bandgap, transition mode, thin film electrodes.

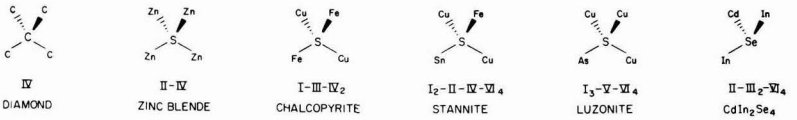

Fig. 1. Illustration of the tetrahedral bonding between the central chalcogen ion and the electropositive ions in adamantine compounds, as compared to the parent structure-diamond.

tions," *i.e.*, the more electropositive species, and bonding is thought to be predominantly by sp^3 hybrids (see however below). In all of them a (nearly) close-packed partial structure of the chalcogens is found. [Similar series exist, derived from III-V materials, *e.g.*, InP, $CdSnP_2$, and other tetrahedrally coordinated ones (6).]

As can be seen from Fig. 1, the remarkable aspect of $CdIn_2Se_4$ and related II-III_2-VI_4 compounds (as well as some II_2-IV-VI_4 and I_2-II-VII_4 ones) is the incomplete lattice of electropositive ions. This is sometimes, incorrectly, referred to as a "defect" lattice (no defects as such are implied by the structure). Their structure can be described as a cubic close-packed one in which only 3/8 of the tetrahedral sites are occupied, as compared to 1/2 occupancy in "normal" adamantine materials. While most of the II-III_2-VI_4 materials adopt this structure, some, like $CdIn_2S_4$ take on a more or less disordered spinel one. $CdIn_2Se_4$ crystallizes in space group $P\bar{4}2m$ (D_{2d}^1) and thus has a pseudocubic) tetragonal structure with lattice dimensions a = 5.817Å and c = 5.817Å (Z = 1). At higher pressures it undergoes transformations to either the spinel structure of $CdIn_2S_4$ (at lower temperatures) or to the rocksalt structure (at higher temperatures) (6, 7).

While in all adamantine-type materials the (valence) electron to atom ratio is 4, it is apparently higher in the II-III_2-VI_4 ones, unless the "vacant" site is counted as well (6), leading to the notation II-□-III_2-VI_4.

The presence of "vacant" sites (pseudovacancies) seems to affect the valence band characteristics of $CdIn_2Se_4$, in that it introduces a high density of states near the top of the valence band, as compared to II-VI compounds (8, 9). This effect has been attributed to the quasi-lone pair electron states of the anions around, and directed toward, the pseudovacancies. These states can be considered somewhat akin to those arising from dangling bonds. Such bonds, on the surface of a II-VI compound, give rise to states within the forbidden gap. In the case of $CdIn_2Se_4$, a slight displacement of the anions around the pseudovacancies apparently increases the binding energies of the quasi-lone pair electrons sufficiently to "pull" these states into the valence bands. This leads to a widening of the upper valence band (8) and to the previously mentioned high density of states near the top of this band. Such a high density of states is found also in I-III-VI_2 chalcopyrites, where it has been attributed to the admixture of d-levels to the upper valence band (10) [up to 45% d-orbital contribution is estimated for $CuInS_2$ (11)]. In $CdIn_2Se_4$ such a contribution is expected to be rather small because of the depth of the Cd 4d levels, with respect to the top of the valence band (8, 9).

While in the case of CdSe (and other II-VI compounds) the upper valence band is composed entirely of states of bonding electrons (from s and p orbitals) the above discussion indicates that this is not necessarily so for the I-III-VI_2 chalcopyrites and for $CdIn_2Se_4$ [or $ZnIn_2Se_4$ (9)], where states of electrons, which are to some extent nonbonding, make up the top of the valence band. This offers the possibility of using these materials as photoelectrodes in a PEC, without weakening the chemical bonds to the same extent as apparently occurs in, *e.g.*, CdSe, where the Cd-Se bond is known to be prone to hole attack (3). In other words, such photoelectrodes might be expected to be more stable than those made up of their binary analogues. [Results for n-$CuInS_2$ do indeed confirm this (4).]

Although $AgInSe_2$ would be the logical choice to study as a true ternary analogue of CdSe, the fact that appreciable ionic conductivity may occur in it (11) will complicate any comparison that can be made in terms of PEC performance. Therefore we turned to $CdIn_2Se_4$ and investigated its behavior as a photoanode in a polysulfide PEC. The width of the forbidden gap of $CdIn_2Se_4$ (1.55 eV, see below) is closer to the optimal value for terrestrial photovoltaics than that of its binary analogue, CdSe (1.7 eV), or that of $AgInSe_2$ (1.2 eV). This value is clearly influenced by the presence of In-atoms (lowering it, compared to CdSe), although the higher charge on Cd than on Ag places it intermediate between its two analogues. While the material has rather poor solar conversion efficiencies at present, initial results on its output stability and photocurrents (under bias) were sufficiently encouraging to warrant a more detailed study.

Methods and Materials

Materials.—$CdIn_2Se_4$ crystals, synthesized from the constituent elements were grown and doped by W. Giriat (Centro de Fisica, Inst. Venez. de Invest. Cient., Caracas, Venezuela). Their resistivity was several ohm · cm. Crystals were polished to 0.05 μm finish with alumina paste (Buehler). They were etched with fresh aqua regia (1:4 HNO_3:HCl mixture) and immersed for a few seconds in polysulfide solution to dissolve any free Se from the surface of the electrode. Immersion in 10% KCN solution for 60 sec was found beneficial and was applied at a later stage of this study when we measured the photoresponse of these cells (see below). Ohmic contact was established by rubbing In-Ga alloy on the back surface of the crystal and soldering pure In on top of that layer. A copper wire was attached to the crystal by means of silver epoxy (Type 50, Transene). Insulating epoxy was used to seal the electrode except for its front surface. Photoetching of the electrode was carried out in 10 times diluted aqua regia by connecting the photoelectrode, a Pt wire reference electrode, and a carbon counterelectrode to a potentiostat and illuminating at intensity of ~ AM1.

Polysulfide solution which was 2M with respect to added KOH, S, and Na_2S, each, was prepared from AR grade reagents (Frutarom and Merck) and deionized water. Light intensities were varied with neutral density filters (Schott), except where noted.

Instrumentation.—This included a standard photoelectrochemical setup with a variable intensity tungsten-halogen light source, Elscint Model CHP-1 potentiostat; Yokogawa Model 3066 X-t recorder; and Tabor DMM 4021 multimeter.

Net photocurrents under monochromatic excitation were measured with a phase-sensitive technique which included a tungsten-halogen light source, Schoeffel monochromator, mechanical chopper, Wenking LB 75 L potentiostat, homemade potential sweep generator, Brookdeal Model 9505-SC two-phase lock-in amplifier, and Houston Instruments X-Y recorder (Model 165).

Results and Discussion

Photoelectrochemical investigation.—Figure 2 shows the *I-V* curves in the dark[1] and under illumination for an electrode after chemical etching and short photo-

[1] Similar to Cd-chalcogenides in polysulfide electrolyte the dark current decays with time under small forward bias, but goes through a minimum *vs.* time under forward bias greater than ~500 mV (12).

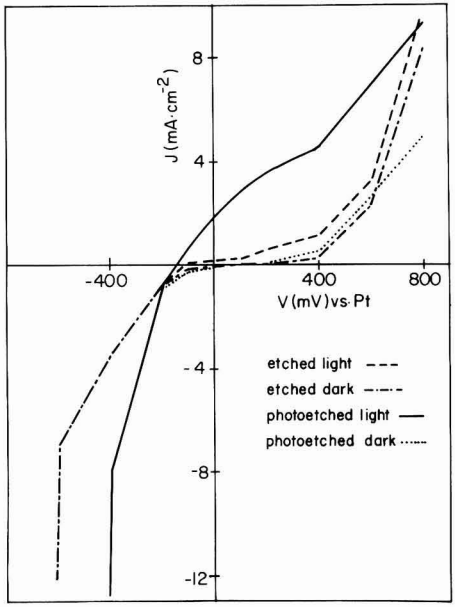

Fig. 2. *I-V* curves for $CdIn_2Se_4$ in (2;2;2) polysulfide electrolyte (2M with respect to each OH^-, $S^=$, and S) in the dark and under illumination of ~80 mW · cm^{-2}. Photoetching at +1V vs. Pt. E_{redox} = −0.78 vs. SCE.

etching. A large difference in the photocurrent is observed between the etched and photoetched electrode. Whereas the photocurrents measured for the etched electrode under reverse bias never exceeded 1 mA · cm^{-2} under AM1 illumination, typical currents of 5-7 mA · cm^{-2} were obtained with the photoetched electrode under reverse bias. Furthermore by dipping the best electrode for a few minutes in 10% KCN solution, an insulating layer that forms after the photoetching was at least partially removed and a short-circuit current as high as 8.1 mA · cm^{-2} (~15 mA · cm^{-2} under reverse bias of 400 mV) was obtained. Etching with other conventional etchants like 2% Br_2/methanol or HNO_3 (aq) did not improve the performance of the cell after the aqua regia etching.

In the case of Cd-chalcogenides (2, 13) photoetching was carried out by short-circuiting a carbon electrode to the photoelectrode in appropriate acidic solutions (usually the diluted etchant of the particular electrode) and illuminating the electrode. In the present case potentiostatic photoetching under large reverse bias was necessary as shown in Fig. 3. Apparently, under short-circuit conditions and up to +750 mV *vs.* Pt the space-charge field in the semiconductor is too small to enable efficient collection of the photogenerated holes into the solid-liquid interface. Biases in excess of +1000 mV during the photoetching led to dramatic increases in the photocurrent of the cell in polysulfide electrolyte. Furthermore after photoetching the large dark currents that were observed under reverse bias decreased considerably. This is shown in Fig. 2 where, after photoetching, the dark current decreases considerably, at least at biases exceeding +600 mV.

The large dark currents under reverse bias may explain the maximum in the photocurrent that was observed (after photoetching at high bias) under +200 to +400 mV reverse bias voltage. This maximum is shown in Fig. 3. Under larger reverse bias the dark current is very large so that surface recombination of the photogenerated holes is considerable and thus a decrease in the photocurrent at anodic potentials exceeding ~400 mV is observed.

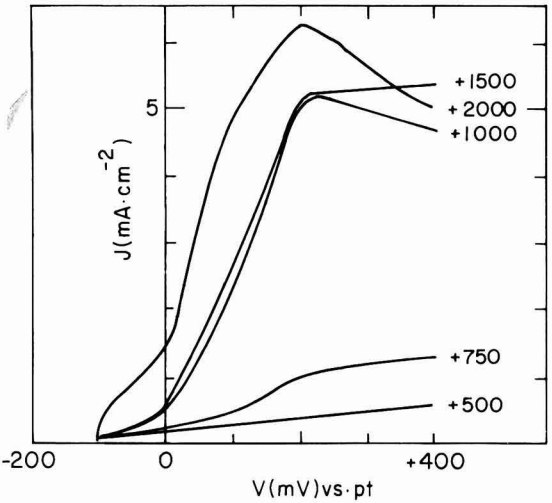

Fig. 3. Net photocurrent *vs.* potential for photoetched $CdIn_2Se_4$ in (2;2;2) polysulfide. The bias voltage (in mV) of the photoetching is indicated for each curve. Light intensity as in Fig. 2.

SEM micrographs of the photoetched $CdIn_2Se_4$ electrodes (which were not dipped in KCN solution) were very unclear as if charging of the electrode surface occurs. However, the black mat color of the photoetched electrode (Fig. 4) suggests that some pitting of the electrode surface occurs during photoetching as in CdSe (13a) and CdTe (13c).

Recently we have worked out a kinetic model that shows the almost obvious correlation between the quantum yield of Cd-chalcogenide/polysulfide cells and their output stability (14).[2] The rationale behind the performance-stability correlation is that any impediment to the flow of holes across the solid-liquid interface results in a longer stay of the photogenerated holes on the electrode surface so that accumulation of holes on the surface occurs, leading to larger recombination and deactivation by photooxidation of the crystal (15). Considering the improved performance of the photoetched electrode compared with the etched one the former electrode is expected to be the more stable one, which is indeed the case, as shown in Fig. 5. Note that the photoetched electrode was illuminated by ~6 AM1 light (by increasing the lamp current),

[2] Surface recombination is assumed to be the dominant loss mechanism in this model.

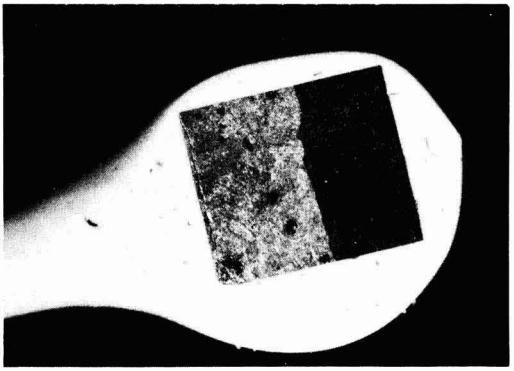

Fig. 4. Magnified photograph of $CdIn_2Se_4$ electrode. Gray part is etched; black mat is photoetched, white part is insulating epoxy.

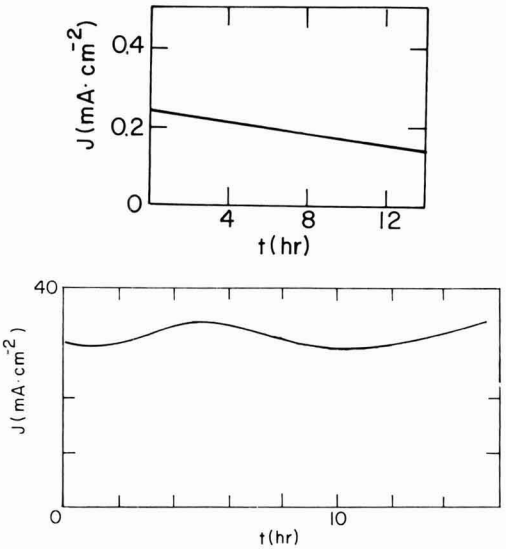

Fig. 5. Output stability of (a, top) etched (b, bottom) photoetched $CdIn_2Se_4$ electrode in (2;2;2) polysulfide under reverse bias of +400 mV vs. Pt electrode.

whereas the etched electrode was illuminated with AM1 light only. The amount of charge that passed through the photoetched electrode was sufficient to consume all of the electrode material if corrosion was extensive, but we did not detect any visible morphological change on the electrode surface. We can conclude, therefore, that the photocurrent through the photoetched electrode was the result of electrolyte oxidation only.

In Fig. 6 we compare the relative quantum yields (photocurrents) of etched and photoetched electrodes *vs.* light intensity, ϕ. The two salient features of this experiment are: (*i*) The quantum yield of the photoetched electrode is much larger than that of the etched electrode (see next section for further details). (*ii*) The quantum yield of the photoetched electrode is constant (photocurrent is linear with light intensity) up to very high light intensities in this solution. This shows that the rate of hole transfer across the interface between the photoetched $CdIn_2Se_4$ and the polysulfide electrolyte is very fast.

In Fig. 7 we show the dependence of the open-circuit voltage on the light intensity. The observed slope of the curve (60 mV/decade; $n \sim 1$) is substantially smaller than that observed for Cd-chalcogenides ($n > 2$). It was claimed (16) and further supported by our own experience (12) that n values larger than one are possible when chemical adsorption of the electrolyte on the surface of the electrode occurs. Capacity measurements are necessary to clarify this point.

Several samples have shown open-circuit voltages between 200 and 300 mV, and one sample gave an open-circuit voltage of up to 350 mV, which however, is still considerably less than that obtained with CdSe electrodes (~700 mV).

Dipping in $ZnCl_2$ solution (17) resulted in smaller dark currents under forward bias and the open-circuit voltage increased by 30 mV typically.

As we will show now photoetching is also responsible for considerable changes in the electronic properties of the interface and especially for a strong decrease in the density of surface states at the interface.

Electronic properties from spectral response measurements.—Figure 8 shows the short-circuit spectral response of n-$CdIn_2Se_4$ that was etched in aqua regia, rinsed with deionized H_2O, immersed in 10% KCN solution for 60 sec, and rinsed again with H_2O. We see that in addition to the response at wavelengths shorter than 800 nm (1.55 eV), which corresponds to an indirect transition (see Fig. 10), the spectrum shows a wide sub-bandgap photoresponse with a peak at 970

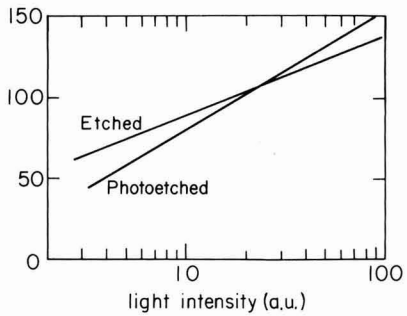

Fig. 7. Dependence of the open-circuit voltage of the cell on the light intensity.

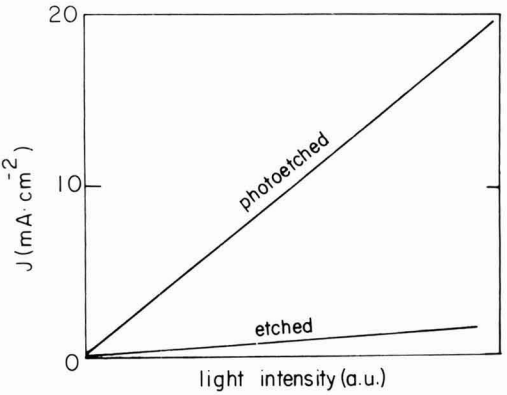

Fig. 6. Net photocurrent *vs.* light intensity of $CdIn_2Se_4$ in (2;2;2) polysulfide at +200 mV reverse bias. Strongest light intensity is ~3 AMI.

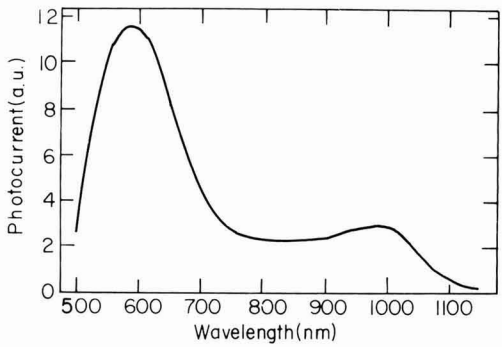

Fig. 8. Normalized spectral response of etched $CdIn_2Se_4$ electrode in (2;2;2) polysulfide electrolyte under short-circuit conditions. Normalization is made for the spectrum of the lamp. The short wavelength decrease in the response is due to absorption by the orange-red polysulfide solution.

nm. The peak corresponds to a light-induced current through a distribution of surface states located some 0.27 eV below the bandgap energy. Figure 9 shows the equivalent spectra after photoetching of the $CdIn_2Se_4$ and immersing it in a separate polysulfide solution for a few seconds to remove any free Se. A large decrease in the photorespnse to sub-bandgap illumination and a large increase of the supra-bandgap photoresponse is obtained. The fact that the sub-bandgap photoresponse did not disappear altogether may indicate that the present procedure used for photoetching is insufficient to provide a "perfect" surface.

The large difference in the spectral response of etched and photoetched $CdIn_2Se_4$ can help to explain the effect of photoetching on the electrode surface. It is well known that surface or near-surface defects lead to sub-bandgap spectral response. At the same time these defects serve as surface recombination centers and carrier traps that cause a considerable decrease in the photocurrent obtained from bandgap excitation. Upon removal of a large part of these defects by photoetching an increase of the photocurrent under short-circuit conditions by a factor of ~40 was observed in this particular experiment, in addition to a small increase in the photovoltage. The fill factor for the photoetched electrode was 0.33 at room temperature. Surface defects which are likely to impede the hole transfer across the semiconductor-electrolyte interface, and therefore to increase the rate of recombination, are also most prone to photocorrosion. Hence by deliberate photocorrosion we are able to remove these defects preferentially and to improve the rate of hole transfer across the interface.

Another remarkable feature of the spectral response is the gradual increase of the photocurrent with decreasing excitation wavelength. This behavior is typical of single crystals that are either highly doped or have a large defect surface. However, in the present case the reason for the gradual increase of the photocurrent with decreasing wavelength is because the lowest energy transition of $CdIn_2Se_4$ is an indirect one.

Determination of the bandgap and the transition mode.—Some of the first physical parameters that have to be determined when a semiconductor is evaluated as a possible candidate for photovoltaic conversion of solar energy are its bandgap energy and the nature of the electronic transition mode. From theoretical considerations one finds that under ~AM1 illumination, the optimal bandgap (E_g) is ~1.4 eV. In addition to the optimal bandgap, it is desirable to use semiconductors with direct electronic transition modes. In this case the absorption coefficients for photons with energies higher than the bandgap energy are large so that most of these photons are absorbed in the space charge layer or close to it and the collection efficiency of the photogenerated holes is high.

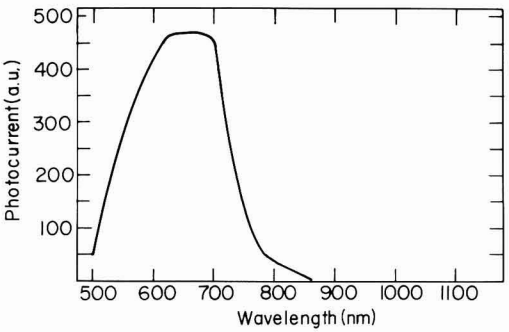

Fig. 9. Normalized spectral response of the same electrode after photoetching.

A variety of experimental techniques has been used for the determination of the modes of optical transitions in $CdIn_2Se_4$ and related semiconductors. These include photoconductivity 18), reflectance (19), spectral response (20), photoemission (21), intrinsic conductivity measurements at high temperatures (22), optical absorption measurements (23), and electroreflectance (24).

Some of these techniques are tedious, others rely on involved theoretical analyses that do not always lead to a decisive interpretation, especially if a number of energy gaps with different types of transition modes exist, as is the case for $CdIn_2Se_4$ (22).

We used photoelectrochemical measurements in which we measured the net photocurrent of the $CdIn_2Se_4$/polysulfide cell. Determination of the absolute quantum yield of the cell was not necessary here which simplifies the experiments and the analysis considerably.

For the analysis of the results we employ the Gärtner model (7) which gives the photocurrent density of the cell i_{ph}

$$i_{ph} = qF_o\left(1 - \frac{e^{-\alpha W}}{1 + \alpha L_p}\right) \quad [1]$$

Here q is the elementary charge, F_o is the photon flux, L_p is the hole diffusion length, and W is the width of the depletion layer

$$W = \left(\frac{2\epsilon\epsilon_o(V - V_{FB})}{qN_d}\right)^{1/2} \quad [2]$$

where $\epsilon\epsilon_o$ is the dielectric constant of the semiconductor, N_d is the donor concentration, and $V - V_{FB}$ is the band bending. With $J\gamma \alpha \cdot L_p << 1$ and $\alpha W << 1$ we can expand the exponent and in this case i_{ph} is proportional to α. Near the absorption edge, α can be described as follows

$$\alpha = A\frac{(h\nu - E_{ind})^2}{h\nu} \quad [3a]$$

for an indirect transition, and

$$\alpha = A\frac{(h\nu - E_d)^{1/2}}{h\nu} \quad [3b]$$

for a direct transition. Therefore the photocurrent dependence on the energy of the exciting light photon $h\nu$ is given by

$$i_{ph} = C\frac{(h\nu - E_{ind})^2}{h\nu} \quad \text{for indirect mode} \quad [4a]$$

and

$$i_{ph} = C\frac{(h\nu - E_d)^{1/2}}{h\nu} \quad \text{for direct mode} \quad [4b]$$

We can now develop $i_{ph}^{1/2}$ of Eq. [4a] in the parameter $h\nu - E_{ind}$ up to the linear term. For small values of the expansion parameter, $i_{ph}^{1/2}$ is linear in $h\nu$ and it vanishes when $h\nu = E_{ind}$. Similarly we can expand i_{ph}^2 of Eq. [4b] in the parameter $h\nu - E_d$ up to the linear term. In this case i_{ph}^2 is linear in $h\nu$ close to E_d and it vanishes at $h\nu = E_d$. So, by plotting the different values of $i_{ph}^{1/2}$ and i_{ph}^2 *vs.* $h\nu$, the values of the energy gaps can be determined. As shown in Fig. 10 and 11 two types of gaps are clearly observed. The lowest gap is at 1.55 eV and the other one is at 1.73 eV.

Knowing the values of the energy gaps, the transition modes can be determined by plotting log $(i_{ph}h\nu)$ log $(h\nu - E_g)$ for wavelengths close enough to the transition energy. If the slope of such a curve equals 2, the transition is an indirect one, whereas for a direct transition the slope is 1/2. Figure 12 reveals that the lowest transition of $CdIn_2Se_4$ (1.55 eV) is an indirect one (slope = 2.03) whereas the higher transition (1.73 eV) is a direct one as confirmed in Fig. 13 (slope = 0.54).

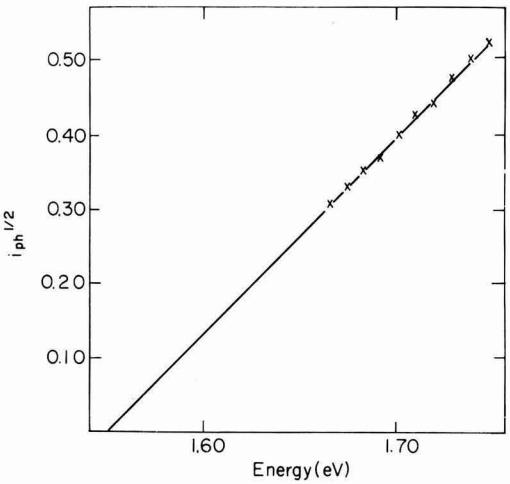

Fig. 10. Determination of the bandgap of the indirect transition mode (1.55 eV). Photocurrent (a.u.) was normalized to the spectrum of the lamp.

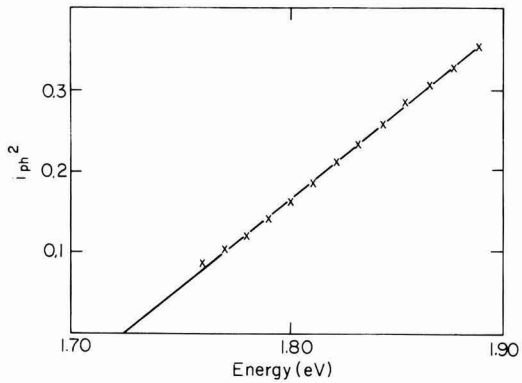

Fig. 11. Determination of the bandgap of the direct transition (1.73 eV).

The occurrence of both an indirect and direct transition is common for the $CdIn_2VI_4$ family of materials. The difference between E_{ind} and E_d decreases from 0.22 eV for $CdIn_2Se_4$ to 0.1 eV for $CdIn_2Te_4$.

Whether the nature of the lowest transition of $CdIn_2S_4$ is an indirect one or due to some impurity transition has been the subject of some controversy. For that material it was concluded that it is an indirect transition (19) and our measurements confirm this as far as $CdIn_2Se_4$ is concerned.

Thin film polycrystalline $CdIn_2Se_4$ electrodes.—Although not the primary goal of this study, it was of interest to apply methods developed by us for the preparation of thin film polycrystalline photoelectrodes by slurry pasting (17) to $CdIn_2Se_4$. From previous experience the crucial role of the quality of the starting material in determining the performance of such films is known (4b). Therefore, in these preliminary experiments small grains and chips, left from the crystals, were used. These were milled together with some polymethylmethacrylate in acetonitrile for ~15 hr and the resulting slurry was pasted onto a Ti substrate as previously described (17). Best results were obtained if no inorganic flux (CdI_2) was added. The layers were

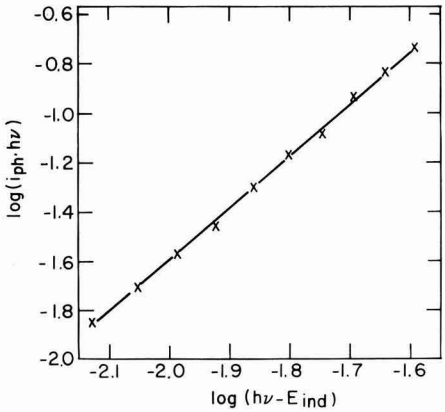

Fig. 12. Determination of the indirect transition mode (n = 4.06) for $CdIn_2Se_4$. E_{ind} energy of indirect transition (1.55 eV).

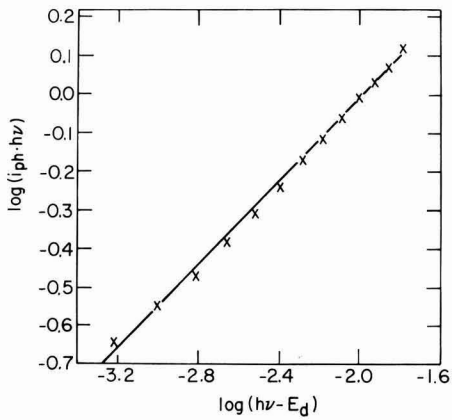

Fig. 13. Determination of the direct transition mode (n = 1.08) for $CdIn_2Se_4$. E_d = 1.73 eV.

fired for 10 min in argon at 490°C or higher temperatures. If the annealed layers were used as such, very high dark currents under short-circuit conditions (*e.g.*, 1.1 mA · cm^{-2} compared to 1.6 mA · cm^{-2} photocurrent) were obtained. Subsequent etching in 3% HNO_3 in HCl somewhat improved the net photocurrent (the dark current decreased) but, as in the case of single crystal electrodes, by far the best performance was obtained after a few seconds photoetching in a 10 times diluted etching solution at +1V bias. Figure 14 shows the dark and light *I-V* plot for a 1 cm^2 thin film electrode and we see that its performance reaches 30% of that of the best single crystal, which is encouraging as undoubtedly the conditions of preparation were not yet optimized [as they were adapted from those found for (17a) CdSe on the one hand, and MoS_2 (17b) on the other hand].

Conclusions

Three main conclusions can be drawn from this study.

1. As has been shown for Cd-chalcogenides, selective photoelectrochemical etching of the photoelectrode is a powerful tool for the removal of surface defects that decrease the quantum efficiency of solar cells.

2. *In situ* measurements of the spectral response are an important tool in the characterization of the present photoelectrochemical cell as well as many others. This

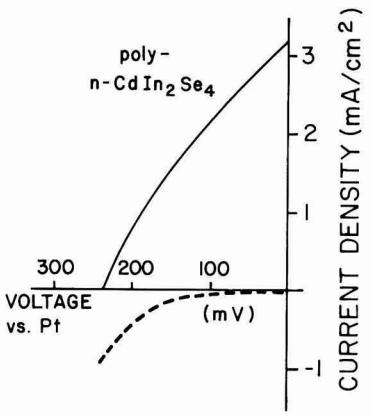

Fig. 14. *I-V* curves in the dark (- - -) and under illumination for polycrystalline CdInSe electrode in polysulfide electrolyte. Light intensity ~80 mW · cm^{-2}.

technique is particularly useful for the characterization of cells based on thin film photoelectrodes where other methods are either cumbersome or fail completely.

3. The $CdIn_2Se_4$/aqueous polysulfide cell showed good quantum yields and output stability. The good stability of the cell shows that the pseudovacancies in the crystal structure, which could cause rapid diffusion and drift of ionic species, leading to fast deactivation of the electrode under illumination, do not have a detrimental effect. Rather it seems plausible that the presence of quasi lone pair states in the upper valence band allows electronic excitation of the semiconductor without breaking the chemical bonds. It is tempting to connect the occurrence of an indirect and direct optical transition within the presence of these electronic states. The fact that they occur in $CdIn_2S_4$, too, shows that other factors must be involved as well.

Acknowledgment

We thank G. Djemal for the data on the polycrystalline electrode. Part of this work was supported by the U.S.-Israel Binational Science Foundation, Jerusalem, Israel.

Manuscript submitted Sept. 14, 1981; revised manuscript received *ca.* Nov. 25, 1981.

Any discussion of this paper will appear in a Discussion Section to be published in the June 1983 JOURNAL. All discussions for the June 1983 Discussion Section should be submitted by Feb. 1, 1983.

REFERENCES

1. For a recent summary see, A. Nozik, Editor, "Photoeffects at Semiconductor-Electrolyte Interfaces," ACS Symposium Series 146, Washington, DC (1981).
2. G. Hodes, *Nature (London)*, **285**, 29 (1980).
3. D. Cahen, G. Hodes, J. Manassen, and R. Tenne, in "Photoeffects at Semiconductor-Electrolyte Interfaces," A. Nozik, Editor, pp. 369-385, ACS Symposium Series 146, Washington, DC (1981).
4. (a) M. Robbins, K. J. Bachmann, V. G. Lambrecht, F. A. Thiel, J. Thomson, Jr., R. G. Vadimsky, S. Menezes, A. Heller, and B. Miller, *This Journal*, **125**, 831 (1978); (b) Y. Mirovsky, D. Cahen, G. Hodes R. Tenne, and W. Giriat, *Solar Energy Mater.*, **4**, 169 (1981).
5. A. F. Wells, "Structural Inorganic Chemistry," 4th ed., Clarendon Press, Oxford (1975).
6. E. Parthé, "Crystal Chemistry of Tetrahedral Structures," Gordon and Breach, New York (1964).
7. O. Muller and R. Roy, "The Major Ternary Structural Families," Springer, Berlin (1974).
8. F. Cerrina, C. Quaresima, I. Abbati, L. Braicovich, P. Picco, and G. Margaritondo, *Solid State Commun.*, **33**, 429 (1980) and references therein.
9. G. Margaritondo, A. D. Katnani, and F. Lévy, *Phys. Status Solidi B*, **103**, 725 (1981).
10. R. A. Pollak, S. Kowalczyk, L. Ley, and D. A. Shirley *Phys. Rev. Lett.*, **29**, 274 (1972).
11. J. L. Shay and J. H. Wernick, "Ternary Chalcopyrite Semiconductors, Growth, Electronic Properties and Applications," Pergamon, Oxford (1975).
12. R. Tenne, *Ber. Bunsenges. Phys. Chem.*, **85**, 413 (1981).
13. (a) R. Tenne and G. Hodes, *Appl. Phys. Lett.*, **37**, 428 (1980); (b) R. Tenne, *Appl. Phys.*, **25**, 13 (1981); (c) N. Müller and R. Tenne, *Appl. Phys. Lett.*, **39**, 283 (1981).
14. R. Tenne, N. Müller, Y. Mirovsky, and D. Lando, Submitted to *This Journal*.
15. D. Cahen, J. Manassen, and G. Hodes, *Solar Energy Mater.*, **1**, 343 (1979).
16. H. Tributsch, *Solar Energy Mater.*, **1**, 257 (1979).
17. (a) G. Hodes, D. Cahen, J. Manassen, and M. David, *This Journal*, **127**, 2252 (1980); (b) G. Djemal, N. Müller, U. Lachish, and D. Cahen, *Solar Energy Mater.*, In press.
18. R. Horiba, H. Nakanishi, S. Endo, and T. Irie, *Surf. Sci.*, **86**, 498 (1979).
19. H. Fujita and Y. Okada, *Jpn. J. Appl. Phys.*, **13**, 1823 (1974).
20. A. M. Redon, J. Vigneron, and J. Chavallier, *This Journal*, **127**, 613 (1980).
21. I. T. McGovern, R. H. Williams, and A. W. Parke, *J. Phys. C*, **12**, 2680 (1979).
22. L. S. Koval, S. I. Radautsan, and V. V. Sobolev, *Inorg. Mater.*, **8**, 1776 (1972) (translated from Russian).
23. A. M. Goldberg, A. R. Beal, F. A. Lévy, and E. A. Davis, *Philos. Mag.*, **32**, 367 (1975).
24. J. L. Shay, B. Tell, H. M. Kasper, and L. M. Schiavone, *Phys. Rev. B*, **5**, 5003 (1972).
25. W. W. Gärtner, *Phys. Rev.*, **116**, 84 (1959).

DSC Study of Two Reactions in the Lithium-Boron Alloy System

Donald Ernst*

Naval Surface Weapons Center, Electrochemistry Branch, Silver Spring, Maryland 20910

In an earlier paper by Dallek, Ernst, and Larrick (1) the differential scanning calorimetry technique (DSC) was used to determine the reactions that occur in the lithium-boron (Li-B) system. This was part of an effort to develop the Li-B alloy for use as an anode material in thermal batteries. A minor objective was to determine the phase diagram. However, the two compounds LiB_3 [25.0 atomic percent (a/o) Li] and Li_7B_6 (53.8 a/o Li) are products of irreversible reactions, and therefore an equilibrium phase diagram for the alloy system could not be determined. The two reactions are

$$x\mathrm{Li} + 6\mathrm{B} \rightarrow 2\mathrm{LiB_3} + (x - 2)\mathrm{Li} \quad [1]$$

$$2\mathrm{LiB_3} + (x - 2)\mathrm{Li} \rightarrow \mathrm{Li_7B_6} + (x - 7)\mathrm{Li} \quad [2]$$

The reactions are complex in nature and there are a number of factors that influence the type of end product (Li_7B_6 and Li) obtained. Examples of these are heating rate, stirring *vs.* convection, and composition (1). It was noted in this earlier work that certain boron samples dissolved more readily than other boron samples and that the start of the first reaction was sometimes detectable as soon as the lithium melted. A possible explanation is that the boron oxide present on the surface of the boron may have some influence on the reaction. The present paper discusses the effect of boron particle size on the rate of the reactions in the lithium-boron system as determined by DSC experiments.

The rate constants for the two exothermic reactions (1, 2) were first calculated using data obtained earlier (1). The method, described in du Pont Applications Brief No. 8 (2), applies to first-order reactions and is used extensively in kinetic studies of the thermal decomposition of polymer materials (3, 4) and explosives (5-7). Currently, there are no reports on kinetic studies of the nature presented here. Two criteria for applying this method are that the reaction be first order, and homogeneous. The first exothermic reaction can be considered to be first order because there is always excess lithium present; however, excess lithium is only present for the second exothermic reaction at lithium concentrations greater than 70 a/o. Because of the liquid solid interfaces between Li and B and Li and LiB_3, the reactions are heterogeneous and not homogeneous. However, the half-lifes as determined by this method were in good agreement with the observations made during actual alloy preparations and indicated that more work in this area was warranted since this information would be helpful when preparing larger amounts of the alloy.

Experimental

Samples were made from three nines lithium foil from Foote Mineral Company and three nines boron lump from Atomergic Chemical Company. The latter was pulverized and sieved to give three different mesh sizes (40-80, 80-100, and 200-270 mesh). Boron powder and lithium foil were mixed by rolling and pressing. The samples, about 10 mg total weight, were then enclosed in Armco iron cups that give a hermetic seal when properly closed. No evidence of lithium seeping out of the cup was observed in any of the eight runs made. The sample preparative work was done in a dry room at a humidity of 2% or less. The compositions for each run are given in Table I. The percentages reported were calculated from the actual weights of the components and the data for one curve are obtained from this one sample. The DSC experiments were carried out in a series of steps using a du Pont 990 thermal analyzer with a standard DSC cell at a 5 K/min heating rate. The first step started at 413 K (140°C) and went to 498 K (225°C). This step provides data on the lithium endotherm and the area under the peak represents the amount of lithium present in the sample. The second step started at 498 K and went to the completion of the first reaction usually between 623 K (350°C) and 648 K (375°C). Because of the heat released in the first reaction it is referred to as the first exotherm. The sample was then allowed to cool below the freezing point of lithium and the first step repeated. This produced another lithium endotherm which, when subtracted from the first endotherm, gives the amount of lithium used in the first exothermic reaction. The fourth step started at 723 K (450°C) and ran at 5 K/min until the second reaction was completed between 873 K (600°C) and 923 K (650°C). This reaction is referred to as the second exotherm. The sample was allowed to cool down and the first step repeated for a third time.

The method (2) used to determine the rate constant assumes first-order reaction conditions where

$$\mathrm{Rate} = k[c] \quad [3]$$

Table I. Summary of data

Run	a/o Li	*E* (kcal/mol)	Frequency factor	Half-life: Min at K	Half-life: Min at K
			First exotherm data		
7	62.9	22.7	6.3 (5)	7.7 at 581	1.5 at 625
5	75.1	25.5	6.9 (6)	8.2 at 581	1.3 at 625
3	57.0	27.4	3.0 (7)	9.9 at 581	1.3 at 625
6	61.2	30.8	2.9 (8)	19.2 at 581	2.4 at 625
8	62.3	30.2	1.6 (8)	22.0 at 581	2.8 at 625
4	72.4	37.4	6.6 (10)	29.6 at 581	2.2 at 625
2	75.2	35.8	1.6 (10)	28.9 at 581	2.5 at 625
1	59.0	36.8	2.6 (10)	33.0 at 581	3.4 at 625
			Second exotherm data		
6	61.2	74.7	4.2 (16)	60.8 at 803	5.5 at 847
8	62.3	92.1	1.6 (21)	115.5 at 800	6.2 at 844
4	72.4	100.5	8.1 (23)	72.2 at 793	6.0 at 826
2	75.2	93.8	1.4 (22)	60.8 at 793	4.6 at 829
7	62.9	104.2	1.6 (24)	105.0 at 810	7.7 at 844
5	75.1	94.1	1.0 (22)	57.8 at 800	8.7 at 826
1	59.0	184.4	2.0 (44)	57.8 at 840	3.7 at 862

Runs 7, 5, 3 used 200-270 mesh boron.
Runs 6, 8, 4, 2 used 80-100 mesh boron.
Run 1 used 40-80 mesh boron.

* Electrochemical Society Active Member.
Key words: Li-B, alloy, battery, DSC.

In DSC work the rate of heat flow (dH/dT) continuously monitors the rate at which a reaction takes place and is the difference in temperature (ΔT) between the sample pan and the reference pan of the DSC cell. The total amount of reactant (A) is represented by the total area under the DSC peak. The amount of material reacted (a) up to time t is the partial area under the peak up to time t. The amount of material remaining (C) is then given by ($A - a$). Putting the two rates equal to each other and solving for k gives

$$k = (dH/dT)/(A - a) = \Delta T/(A - a) \quad [4]$$

The two variables, dH/dT and temperature (T), are plotted as a function of time. The partial and total area under the dH/dT peak are determined with a planimeter and T is determined from the linear T *vs.* time plot. The advantages of the method are that k is independent of the sample mass and DSC cell calibration. Errors can arise from the planimeter measurements and the recorder y-axis sensitivity settings, both of which were minimized by collecting the data with a Vidar data acquisition system and storing it on magnetic tape. Measurements of dH/dT (0.01 mV), T (0.001 mV), and t (0.1 sec) were taken at 1 sec intervals and about 2000 data points were obtained for each exothermic reaction. The data were analyzed on a CDC 6500 computer. Simpson's rule of integration was used to calculate both the partial and total areas (mV-sec) under the DSC peak. Rate constants, when calculated using Eq. [3], have units of reciprocal seconds. The errors associated with the temperature measurement (1%) and area calculations (<1%) when taken with a data acquisition system and reduced on a computer are smaller than the error (which is unknown) made in assuming that the system is homogeneous when it is more likely to be heterogeneous. The method is presented because it is a new technique that can furnish additional information about a chemical system and the results obtained were in agreement with experimental observations.

The k values obtained by this procedure are plotted in Fig. 1 and 2 for the first and second exothermic reactions, respectively. Activation energies (E) and frequency factors obtained from a least-squares fit of the data are listed in Table I. The half-life data were calculated using the relationship

$$t_{1/2} = \ln 2/k \quad [5]$$

Discussion

For the first reaction, the boron particle size appears to have a significant effect on the reaction rate (Fig. 1). The smaller or finer sized boron (top three curves) gives higher rate constants than the coarser boron. The activation energy is also lower for the finer sized boron.

In Fig. 2 it can be seen that for the second reaction there is no apparent dependence of the reaction rate on the particle size of the boron used, but there is a dependence upon the lithium content of the sample. For a given particle size of boron, a higher lithium content gives a higher reaction rate. The top three curves have lithium contents greater than 70 a/o while the middle three are in the 62 a/o region.

Crystalline boron is made up of icosahedral clusters of boron atoms either connected to each other (rhombohedral form) or to single boron atoms (tetragonal form). Lithium, because of its small size, easily penetrates the smaller pieces of boron and attacks the boron lattice, breaking it up into icosahedral boron clusters. These clusters are then further attacked by lithium to form LiB_3. LiB_3 reacts with additional lithium atoms at a specific temperature, forming Li_7B_6. Because of the liquid-solid interfaces, these reactions would be heterogeneous ones, however, if Li atoms first penetrate the solids (B and LiB_3) and saturate them, the reactions may not be heterogeneous. This may explain why the calculated half-life agreed with the experimental times observed when preparing the

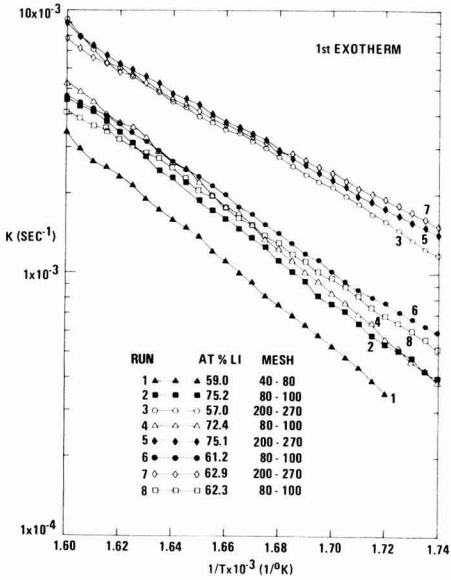

Fig. 1. Arrhenius plot for the reaction $Li + 3B \rightarrow LiB_3$

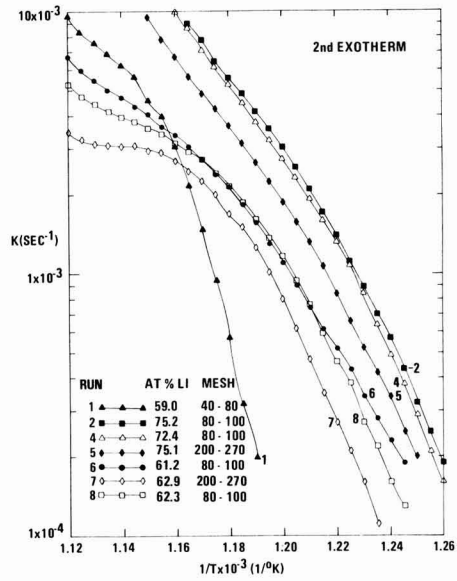

Fig. 2. Arrhenius plot for the reaction $5Li + 2LiB_3 \rightarrow Li_7B_6$

alloy. This would also account for the dependence of the reaction rate for the second exotherm on the percentage of lithium in the sample, since one would expect that saturation of the LiB_3 particles would be more complete when larger amounts of lithium are available.

This type of reaction, where a liquid phase at low temperatures solidifies as the temperature is increased is unusual. In an equilibrium phase diagram, it is called a metatectic reaction (8) and is quite rare. Several examples can be found in In-Li, Ag-Li, Ga-In, Ag-In, and Cu-Sn phase diagrams. Many of these contain lithium or a period III A element. Comparison of these systems with the Li-B system suggests that other

Li-B compounds, such as Li_2B, might exist. The earlier DSC work (1) did not indicate that Li_2B was present, but electrochemical studies (9, 10) indicate that it is. In this work the rounding of the curves in the second exotherm data (Fig. 2) may be a clue that Li_2B only forms at the higher temperatures. Further investigation in this area is needed.

Acknowledgment

This work was supported by the IR board of NSWC. I would like to express my appreciation to Dr. S. D. James and Mr. Glen Smith for their helpful discussions.

Manuscript submitted Dec. 16, 1980; revised manuscript received Dec. 4, 1981. This was Paper 121 presented at the Los Angeles, California, Meeting of the Society, Oct. 14-19, 1979.

Any discussion of this paper will appear in a Discussion Section to be published in the June 1983 JOURNAL. All discussions for the June 1983 Discussion Section should be submitted by Feb. 1, 1983.

Publication costs of this article were assisted by the Naval Surface Weapons Center.

REFERENCES

1. S. Dallek, D. W. Ernst, and B. F. Larrick, *This Journal*, **126**, 866 (1979).
2. DuPont Thermal Analysis Application Brief No. 8, Dec. 1967.
3. A. A. Duswalt, "Analytical Calorimetry," R. S. Porter and J. F. Johnson, Editors, p. 313, Plenum Press, New York (1968).
4. M. Uricheck, *Perkin-Elmer Instrum. News*, **17**, 8 (1966).
5. R. N. Rogers, *Anal. Chem.*, **44**, 1336 (1972).
6. R. N. Rogers and E. D. Morris, *ibid.*, **38**, 412 (1966).
7. R. L. Bohon, *ibid.*, **33**, 1451 (1961).
8. A. Prince, "Alloy Phase Equilibria," p. 116, Elsevier Publ. Co., New York (1966).
9. S. D. James and L. E. DeVries, *This Journal*, **123**, 321 (1976).
10. L. E. DeVries, L. D. Jackson, and S. D. James, *ibid.*, **126**, 993 (1979).

Observations of Flaws on Preconditioned Aluminum Surfaces

G. E. Thompson, P. E. Doherty, and G. C. Wood

Corrosion and Protection Centre, University of Manchester Institute of Science and Technology, Manchester M60 1QD, England

Pitting has been studied extensively, leading to the conception in the literature of at least three stages in the overall process, *i.e.*, initiation, propagation, and termination. The latter stages are relatively well understood in terms of local changes in chloride concentration and *p*H, and the build-up of stifling corrosion product, respectively. Pit initiation is less clear and many of the mechanisms proposed earlier depend to some extent on the techniques employed to study the phenomenon (1-5). The literature relating to the stages prior to and during pit initiation on iron and aluminum has been reviewed recently (6). For aluminum there is growing evidence for the involvement of pre-existing flaws or weak spots, which are always present in the thermal/passive films on aluminum (7-10). To progress further and model the behavior whereby flaws are breached and develop into pits, and gain further insight into the likely roles of salt accumulation, complex formation, *p*H reduction, and crack/heal processes, it is necessary to obtain detailed information about the geometry of flaws and their relationship to the aluminum substrate. Key aspects of a relatively novel investigation to allow direct, high resolution observation of flaws at various stages of development into pits are presented here.

Experimental

Superpure aluminum (0.002 Cu; 0.004 Fe; 0.003 weight percent Si) was electropolished initially in a nitric acid/methanol mixture and subsequently anodized under standard conditions at 50 A m^{-2} in 0.4M phosphoric acid at 298 K for 10 min to produce a steady-state porous anodic film. Removal of this film from the aluminum substrate, in boiling chromic/phosphoric acids, produced a preconditioned substrate with fewer but larger cells than the original electropolished substrate, representing the imprint of the scalloped cell base pattern of the porous anodic film.

Individual preconditioned substrates were anodically polarized, immediately after immersion, in 0.1M potassium chloride solution (*p*H 6) at selected potentials for various times. In order to examine the effects of such polarization on the aluminum substrate, a second film removal treatment and second anodizing procedure were employed. The film removal treatment overcame any problems arising from likely chloride contamination of the specimens during subsequent anodizing. Anodizing was undertaken under the standard conditions for 1 min, a time associated with nonuniform film growth prior to the onset of pore development (11). In this investigation, the nonuniform film growth behavior is used to highlight subtle changes in the substrate topography, resulting from prior polarization studies, which became apparent when the anodic film is detached from the aluminum substrate in mercuric chloride solution and examined in the transmission electron microscope.

Key words: metals, electrode, passivation.

Results and Discussion

Anodizing of the standard preconditioned substrate results in the growth of locally thicker film at the boundaries where the approximately hexagonal cells meet, effectively highlighting the original cellular appearance (Fig. 1a). The stripped anodic film from the specimen which had been polarized at −605 mV (SCE), a potential above the so-called breakdown potential, for 175 min is shown in Fig. 1b. The typical cellular appearance is again observed, together with occasional relatively coarse, rectangular-shaped features of population density about 10^{10} m^{-2} and length of sides in the range 0.8-2.4 μm. These features are true developing pits and are reproduced clearly by the anodizing procedure. In addition, the pit sides and bottoms have been replicated; the darker band surrounding the pits represents the film formed on the pit sides and this can be resolved more clearly by tilting the specimen to the electron beam. The crystallographic nature of the pits is revealed, probably with the {100} faces exposed, and the finely faceted nature of the metal dissolution sites at the pit bottom is also evident. In order to gain further information about the sites at which such pits develop, preconditioned substrates were polarized for shorter times at −605 mV and/or

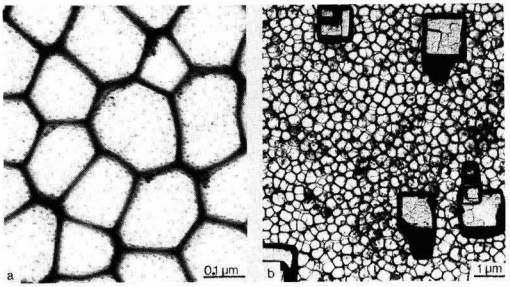

Fig. 1. Transmission electron micrographs of stripped anodic films, formed for 1 min at 50 A m^{-2} in 0.4M phosphoric acid at 298 K on the variously treated aluminum substrates: (a) the preconditioned substrate, formed by anodizing the electropolished specimen for 10 min at 50 A m^{-2} in 0.4M phosphoric acid at 298 K and subsequently removing the film from the surface in boiling chromic/phosphoric acids; (b) the preconditioned substrate after anodic polarization for 175 min at −605 mV (SCE) in 0.1M potassium chloride solution (pH 6) at 298 K.

at more negative potentials. For such treatments, no true developing pits were observed readily in the stripped films. However, interesting local features were revealed at most of the triple point boundaries where impinging cells meet (Fig. 2). The features appear to show generally three narrow intersecting channels (effective diameter <10 nm and lengths up to about 50 nm) that breach the boundary from the neighboring cells. The features vary in effective size from boundary to boundary, but appear relatively regular in shape, with the channels intersecting at angles of about 120° ± 10°. Comparisons with the standard substrate showed that no changes had occurred in that case at the linear cell boundaries, or within the cells themselves. However, similar features were present in the specimen that had been polarized at −605 mV but are not resolved in the low magnification micrograph presented in Fig. 1b.

Clearly from the two-dimensional image of the stripped anodic film presented in the micrograph of Fig. 2, it is not possible to indicate the precise geometry of the original flaws, *e.g.*, the breached region of the pre-existing air-formed film/passive film and the likely penetration into the aluminum substrate beneath the film. However, future examination of ultramicrotomed sections of corresponding substrates and their films will shed more light on the precise geometry of the flaws.

The results of this study give further convincing evidence for the involvement of flaws in the air-formed/passive film on preconditioned aluminum substrates, which are breached upon polarization in chloride solution. Particularly active flaws appear in the vicinity of the triple point boundaries where metal ridges intersect. Highly localized stress development during growth of the air-formed film may be visualized in such regions, which aids local cracking of the film when solution encounters the film at the flaw base. In addition, impurities (such as copper) may deposit preferentially at these sites during specimen preparation. It is interesting that almost all the triple point boundaries appear to be breached (about 10^{13} m^{-2}) yet the population density of developing pits is only about 10^{10} m^{-2}, suggesting that repassivation of the less active flaws occurs at the potentials used. The topography of the preconditioned substrate is not regular on the microscopic scale but is comprised of metal ridges of various sizes giving rise to a spectrum of flaw activities (12). After the initial cracking event, the most active flaws, from mass transport considerations, are likely to be those of critical fissure lengths ≥10 nm (13). This is within the range of channel lengths observed in the stripped anodic films, although in reality the original channels may have extended through the air-formed film and into the metal substrate. The pH reduction in the critical size flaws maintains them active and metal dissolution proceeds, possibly aided by local temperature rises through the large effective current densities channeled into these regions, although such rises may be precluded by transient salt film accumulation (14).

In summary, the anodizing technique effectively highlights flaws developing into pits, allowing their observation at relatively high resolution. Further studies are in progress in order to determine how the flaws, which are influenced by substrate topography, develop by stages into pits that grow in favored crystallographic directions. Examination of ultramicrotomed sections will also throw light upon the transient formation of salt films or otherwise.

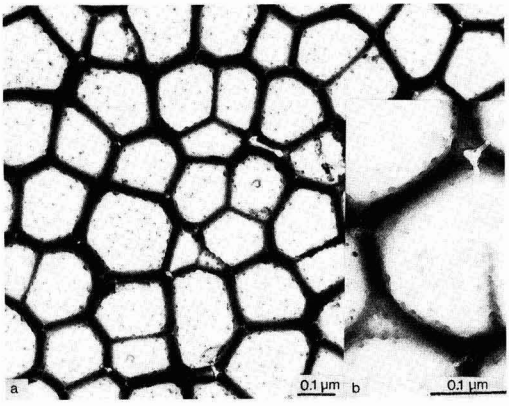

Fig. 2. Transmission electron micrographs of the stripped anodic film, formed for 1 min at 50 A m^{-2} in 0.4M phosphoric acid at 298 K on the preconditioned substrate, which had been anodically polarized for 75 min at −615 mV (SCE) in 0.1M potassium chloride solution at 298 K: (a) showing the flawed regions at the triple point boundaries; (b) higher magnification image of (a).

Manuscript submitted March 12, 1981; revised manuscript received Dec. 14, 1981.

Any discussion of this paper will appear in a Discussion Section to be published in the June 1983 JOURNAL. All discussions for the June 1983 Discussion Section should be submitted by Feb. 1, 1983.

REFERENCES

1. A. F. Beck, M. A. Heine, D. S. Keir, D. J. van Rooyen, and M. J. Phyor, *Corros. Sci.*, **2**, 133 (1962).
2. M. A. Heine, D. S. Keir, and M. J. Pryor, *This Journal*, **112**, 24 (1965).
3. T. P. Hoar and W. R. Jacob, *Nature London*, **216**, 1299 (1967).
4. T. P. Hoar, D. C. Mears, and G. P. Rothwell, *Corros. Sci.*, **5**, 279 (1965).
5. T. P. Hoar, *ibid.*, **1**, 341 (1967).
6. M. Janik-Czachor, G. C. Wood, and G. E. Thompson, *Br. Corros. J.*, **15**, 154 (1980).
7. J. A. Richardson and G. C. Wood, *Corros. Sci.*, **10**, 313 (1970).
8. G. C. Wood, J. A. Richardson, W. H. Sutton, T. N. K. Riley, and A. G. Malherbe, "Localized Corrosion," p. 526, N.A.C.E., Houston, Texas (1974).
9. J. A. Richardson, G. C. Wood, and W. H. Sutton, *Thin Solid Films*, **16**, 99 (1973).
10. G. E. Thompson and G. C. Wood, *Corros. Sci.*, **18**, 721 (1978).

11. G. E. Thompson, R. C. Furneaux, G. C. Wood, J. A. Richardson, and J. S. Goode, *Nature London*, **273**, 433 (1978).
12. G. E. Thompson, R. C. Furneaux, J. S. Goode, and G. C. Wood, *Trans. Inst. Met. Finish.*, **56**, 159 (1978).
13. J. R. Galvele, *This Journal*, **123**, 464 (1976).
14. T. R. Beck and R. C. Alkire, *ibid.*, **126**, 1662 (1979).

Visual Detection of Hydrated Aluminum Oxide by Staining with Fluorescing and Nonfluorescing Dyes

Ned E. Cipollini

Sprague Electric Company, Research, Development, and Engineering, North Adams, Massachusetts 01247

In the cases where the reaction of aluminum or barrier aluminum oxide with water is considered undesirable, the reaction is inhibited with a passivating agent such as phosphate (1, 2), chromate (3), or certain weak organic acids (2). In these cases, the aluminum or aluminum oxide-water reactions occur only at sites where this passivation layer has been destroyed, possibly at widely separated points on the surface of a sample. Since both passivation layer and corrosion product are colorless, no evidence of reaction is apparent in its early stages. Microprobe analysis would be time consuming, if not totally out of the question for large area samples. This report describes a technique to identify and locate the corrosion product, hydrous aluminum oxide (4), on large area samples by staining them with organic dyes producing either color or fluorescence. Once located, these areas can be inspected by microprobe analysis for the cause of depassivation (1). The selectivity of the stain allows distinction between hydrous oxide and: (*i*) bare, untreated aluminum, (*ii*) phosphate-treated aluminum, and (*iii*) barrier oxide produced in neutral aqueous phosphate or borate electrolytes or ammonium pentaborate in ethylene glycol. This technique could be useful for locating corrosion areas on aluminum capacitor foils and aluminum metallization in integrated circuits.

The basic approach here is to selectively stain hydrous aluminum oxide with fluorescent or nonfluorescent dyes. These dyes are applied to the surface of a test specimen only after it contacts pure water or water vapor for a specific reaction time. The specimen is then inspected for a stain in ultraviolet or visible light, but does not contact water again. There are three reasons for this approach. First, many organic compounds, especially weak acids and bases, a class that includes nearly all the dyes mentioned in this report, either retard or accelerate the reaction rate of aluminum and water (1) and more importantly accelerate the depassivation rate of phosphate treated aluminum (2). Second, if a reaction of aluminum and water in a closed system such as an electrolytic capacitor or a molded integrated circuit has occurred, it can be detected after testing. Third, the job of selectively staining hydrous aluminum oxide is quite easy because the reaction product of aluminum and water at temperatures between 90° and 100°C, pseudoboehmite (5), possesses a high surface area, 133-154 m^2/g (6), fibrous structure (7) which will absorb much more dye than the solid aluminum surface. The reaction product of aluminum and water for temperatures between 20° and 90°C consists of a porous duplex structure of a pseudoboehmite inner layer and bayerite outer layer (6, 8). This hydrous oxide can also be stained with comparable intensity to the stain on pseudoboehmite. In this report, the general term hydrous oxide refers to the reaction product of aluminum and water at temperatures between 20° and 100°C.

Key words: adsorption, capacitor, corrosion, electrode.

Our approach differs from that of White *et al.* (9) who place the dye on the sample surface before exposure to a humid ambient atmosphere and bias voltage. The observations of these authors can be explained as resulting from the process of either the anodization or the electrochemical etching of aluminum depending on the impurities in their solutions. We chose not to use this technique because there exists strong evidence that since the dyes themselves are weak acids, they can enter into the reactions mentioned above (10). An interesting aside is the trouble these authors encountered with fluorescein upon solvent evaporation; an explanation is given below.

There are important differences between the technique described in this report and some existing techniques. To inspect for cracks or porosity in, for example, a glass or ceramic material, an intensely colored dye solution may be forced into pores and cracks under pressure. When the sample surface is washed, dye solution will remain in cracks and pores because convective transfer of dye is impossible in these small voids so that dye is removed only by diffusion, a much slower process. In the present case, the dyes are adsorbed. Thus coloration is due to thermodynamic interactions rather than kinetics as for dye intrusion, and the dye will not be removed unless a solvent of more eluting power is used. The interactions involved here are more akin to those used in dyeing anodized aluminum, although the surfaces have different adsorptive properties, the freshly prepared anodic film being much more active than the hydrous oxide. In fact, the dye stain test used for porous anodic coatings (11, 12), is the antithesis of the test described in this report. For anodic coatings, the test dye will not stain if the anodic oxide is hydrated (sealed).

Experimental

Dyes of 95% or better purity were used with no further purification. Test specimens were dipped into a solution of a dye or a mixture of dyes in 2-propanol. Upon removal from the dye bath, before drying, excess solution was washed from the sample surface with acetone. This is chromatography in reverse, *i.e.*, the dye is applied to the stationary phase with the solvent of greater eluting power and rinsed with one of less eluting power. The specimens were then dabbed dry to avoid water condensation on the surface. Water condensation causes a blurring of the image of hydrous oxide formed.

Table I shows the concentration of the various fluorescent dyes examined. For fluorescent stains, a 5 sec dip at room temperature gave about the maximum fluorescence intensity when viewed under ultraviolet light. Nonfluorescing stains were obtained by soaking the test specimen in a saturated solution of the dye for

Table I. Fluorescent stains on pseudoboehmite

Dye	Concentration[a] % (w/v)	Relative fluorescence intensity[b]
Fluorescein	0.08	S
Rhodamine B	0.34	S
Rhodamine 6G	0.30	M
4-Methyl umbelliferone	0.1-1	W
Ammonium salicylate	0.1-1 (H_2O)	M
Coumarin 1	0.1	N
Anthracene	Saturated	N
9,10-dichloroanthracene	Saturated	N
9,10-diphenylanthracene	Saturated	N
Thianthrene	Saturated	N

S = strong, M = moderate, W = weak, N = imperceptible.
[a] Solvent: 2-propanol except where stated otherwise, excess solution rinsed with acetone.
[b] Relative intensities observed on electroetched foil.

Table II. Nonfluorescent stains on pseudoboehmite

Dye	Relative absorption intensity[a] H_2O solvent	Relative absorption intensity[a] 2-propanol solvent
Thionin	M	S
Eosin Y	S	S
Uranine	M	S
Superchrome black TS[b]	S	S
1-(1-hydroxy-2-naphthylazo)-5-nitro-2 naphthol-4 sulfonic acid sodium salt	S	S
Crystal violet	N	N
Aluminion	S	W
Aurin tricarboxilic acid ammonium salt	S	W
Alizarin Red S	M	M
Fuchsin	N	N
Methylene blue	M	S

S = strong, M = moderate, W = weak, N = imperceptible.
[a] Relative intensities observed on electroetched foil rinsed in acetone immediately upon removal from dye bath.
[b] 1-(1-hydroxy-2-naphthylazo)-6-nitro-2 naphthol-4 sulfonic acid sodium salt.

5 min at about 82°C. Satisfactory results were obtained with this dye bath at room temperature, but a darker stain is obtained at the higher temperature due, presumably, to increased dye solubility.

Test specimens were cut from sheets of 4 mil thick 99.99% or 99.97% pure annealed aluminum foil. Surface treatments prior to reaction with water such as electropolishing, sodium hydroxide etching, soaking in ammonium dihydrogen phosphate, chromic-phosphoric acid etching, brightening in a nitric-phosphoric acid mixture, or anodizing in aqueous borate or phosphate solutions at neutral pH's had no effect on the adsorption properties of dyes on the hydrous oxide formed after reaction with water. Experiments were performed on capacitor anode and cathode foils having surface gains ranging from approximately 10 to 70. Using the same experimental procedure resulted in stains of deeper color than on unetched foil. Several samples of evaporated aluminum films were examined. These consisted of approximately 200Å of 99.99% pure aluminum evaporated onto a 10 μm thick sheet of polypropylene. In nearly all cases mentioned in this report, hydrous oxide was obtained on a sample by immersion for various lengths of time in distilled water at 100°C although similar results were obtained at 25° and 75°C. No difference in staining capacity was observed whether foils were placed in actual boiling water, or water heated to just below the boiling point.

All intensity measurements mentioned in this report were qualitative in nature. Fluorescence intensity was inspected while the sample was viewed under a 25W, low pressure mercury lamp fitted with a short wavelength filter. Nonfluorescent stains were judged in a relative sense while viewed under ambient lighting conditions.

Results and Discussion

Tables I and II summarize the results of a limited search for dyes that stain hydrous aluminum oxide with enough material to be seen by the naked eye. Note that the relative intensities were ascribed from experiments with electroetched foil having a surface area gain of about 18. This number was obtained by comparing capacitances measured on anodized etched and anodized electropolished samples. The intensity of the fluorescent or nonfluorescent stain seemed nearly independent of the etch gain of electro-etched foil. This apparent anomaly may be explained by the fact that electro-etching produces both a surface etch structure and a network of pores which extend deep into the foil (14). What is viewed visually is this surface etch structure. The surface area gain, typically about ten (15), depends less on the type of etch than does the internal structure. Water was not used as a solvent in subsequent experiments because: (*i*) some dyes, namely xanthene, decompose by air oxidation in water (13), (*ii*) the dyes are weak acids or bases and can promote corrosion reactions observed in concentrated aqueous dye baths, and (*iii*) the dye affinity is sensitive to pH.

Because of the intermolecular interactions of fluorescent dyes (16), the fluorescence quantum yield decreases as the surface concentration of dye increases due, presumably, to cooperative radiationless transitions. Therefore, as the surface concentration of dye is increased from zero at constant surface area and ultraviolet light intensity, the fluorescence light intensity first will increase, reach a maximum, and then decrease. Experimental parameters that influence the amount of dye adsorbed are temperature, solvent, dye concentration, pH, and time. The solvent 2-propanol with no added acids, bases, or salts was chosen. The parameters of dye concentration, time, and temperature were approximately optimum for a mixture of Rhodamine B and fluorescein dyes at concentrations of 0.34% (w/v) and 0.08%, respectively, at 5 sec at room temperature.

Being much more strongly adsorbed on the hydrous oxide surface, fluorescein is much more sensitive to experimental parameters than is Rhodamine B. When a sample stained with Rhodamine B and fluorescein is washed with methanol, the fluorescence changes from orange to bright yellow, characteristic of fluorescein, indicating that the Rhodamine B was washed off the surface. If the test sample is placed in a mixture of the dyes for several hours, the fluorescence is red, characteristic of Rhodamine B. Since we know the fluorescein is present, it must be adsorbed to such a large extent that its fluorescence quantum yield is nearly zero. This is precisely why White *et al.* (9) observed that fluorescein fluorescence ceased upon solvent evaporation. Rhodamine B, being adsorbed much more weakly than fluorescein, does not build to a high enough surface concentration from a dye bath at room temperature and 0.34% concentration that its fluorescence intensity drops perceptibly. If, however, a concentrated solution of Rhodamine B is allowed to dry on the sample surface, no fluorescence is observed.

Fluorescent staining possesses a few advantages over actual color staining. Staining with fluorescent dyes is more sensitive, i.e., can detect thinner layers of hydrous oxide than coloration. Since fluorescence can be excited by electron bombardment, stained areas can be located in an electron probe (for microanalysis) optically *while the sample is under electron bombardment*. A disadvantage of fluorescent stains is that they must be viewed under ultraviolet light. Therefore, for convenience, colored stains were developed.

For the actual coloration of hydrous aluminum oxide, we try to adsorb the maximum amount of dye possible. Therefore, staining is done from saturated

solutions at elevated temperatures and for longer periods of time than for fluorescent stains. Table II summarizes the results of a limited search for dyes that will deposit enough material to produce a visible coloration of hydrous oxide. Aluminum samples were the same as those described in fluorescent stains. Note that some of the dyes listed under nonfluorescent stains are normally considered fluorescent dyes, notably, Eosin Y and uranine, but they are adsorbed with such high surface concentrations that the fluorescence quantum yield is nearly zero.

Figure 1, a micrograph of an electro-etched foil with a gain of about 70, shows localized corrosion sites. This foil was passivated in aqueous ammonium dihydrogen phosphate before being placed in boiling water. After 1.5 hr the foil was removed from the water bath, dried, and dyed for 10 min in a saturated solution of Eosin Y in 2-propanol at its boiling point. The picture was taken while the sample was illuminated through a green filter. The fine grain structure in the micrograph results from the etch structure of the foil. Dark spots about 0.3 cm in diameter on the left half of the micrograph are localized corrosion areas. As the micrograph is viewed from left to right, one can see that the localized areas grow in size and coalesce to form the larger darkened areas on the right half of the micrograph. Off the picture to the right, the hydrated area has become continuous.

The contrast between the hydrated, dyed, and nonhydrated areas is, actually, more easily viewed at the same magnification in white light than is apparent in the photograph. The contrast is caused by the different morphology of the hydrous oxide and the passivation layer and the difference in dye affinity of the hydrous oxide and passivation layer on aluminum. For example, after reacting for 3 min with boiling water, the hydrous oxide layer was 0.32 μm thick, had a 53% porosity, a density of 2.4 g/cm^3, and a specific surface area of 140 m^2/g (6). These numbers yielded a surface area increase of 58 cm^2 per cm^2 of original surface. In other words, because of the porous nature of the hydrous oxide a gain of 58 was built into the test. The other surfaces such as the passivation layer (1) and barrier anodic oxide (17) are nonporous.

The contrast due to area increase upon hydration depends of course on the degree of hydration. For example, the stain on 300Å of hydrous oxide on electro-etched foil can easily be seen. However, at low levels of hydration, the intrinsic adsorption differences among the hydrous oxide and other types of oxide play a larger role. Owing to the high concentration of surface hydroxyl groups (4), a hydrogen bonding mechanism for dye adsorption is probable, although ion exchange at the surface is also possible. These and other mechanisms of dye adsorption on porous anodic oxide appear in the literature (18, 19).

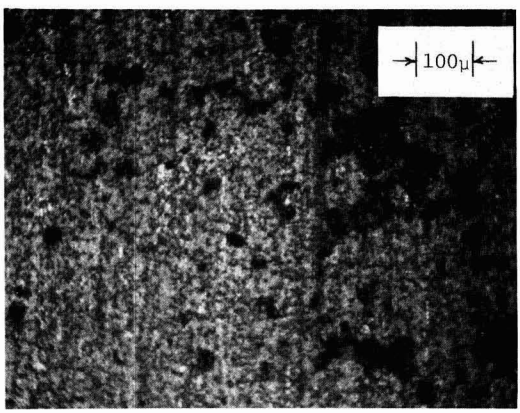

Fig. 1. Micrograph of an aluminum foil electro-etched to a gain of approximately 70 and passivated in phosphate. Foil was placed in flowing water at 100°C for 1.5 hr. Dye is Eosin Y. Sample illuminated through a green filter. See text for further details.

Summary

The techniques described in this report can be useful in locating corrosion centers on etched aluminum capacitor foils after, for example, shelf or life testing. The technique may also be useful for detecting corrosion of evaporated aluminum films used in integrated circuits; however a limited number of experiments have been done in this laboratory with evaporated films. Yet, clearly perceptible fluorescent or nonfluorescent stains can be affected when 200Å of evaporated aluminum on polypropylene is hydrated. The idea of staining hydrous aluminum oxide is an old technique from pigment technology (20), but the application of dyes from nonaqueous solvents to selectively stain the hydrous oxide distinguishing it from anodic barrier oxide and unreacted aluminum or passivated aluminum surfaces is new.

Acknowledgment

The author wishes to thank Dr. S. D. Ross and Dr. G. A. Shirn for many helpful discussions.

Manuscript submitted Aug. 24, 1981; revised manuscript received Jan. 14, 1982.

Any discussion of this paper will appear in a Discussion Section to be published in the June 1983 JOURNAL. All discussions for the June 1983 Discussion Section should be submitted by Feb. 1, 1983.

Publication costs of this article were assisted by Sprague Electric Company.

REFERENCES

1. D. A. Vermilyea and W. Vedder, *Trans. Faraday Soc.*, **66**, 2644 (1970).
2. J. M. Sanz, J. M. Albella, and J. M. Martinez-Duart, *Electrocomp. Sci. Tech.*, **6**, 63 (1980).
3. J. C. Cessna, H. M. Joseph, and R. A. Powers, *Corrosion*, **20**, 1t (1964).
4. W. Vedder and D. A. Vermilyea, *Trans. Faraday Soc.*, **65**, 561 (1969).
5. W. Bernard and J. J. Randall, Jr., *This Journal*, **107**, 483 (1960).
6. R. S. Alwitt, "Oxides and Oxide Films," Vol. 4, J. W. Diggle and A. K. Vijh, Editors, p. 169, Marcel Dekker, Inc., New York (1976).
7. T. Kudo and R. S. Alwitt, *Electrochim. Acta*, **23**, 341 (1978).
8. R. K. Hart, *Trans. Faraday Soc.*, **53**, 1020 (1957); R. S. Alwitt and L. C. Archibald, *Corros. Sci.*, **13**, 687 (1973).
9. L. K. White, R. B. Comizzoli, C. A. Deckert, and G. L. Schnable, *This Journal*, **128**, 953 (1981).
10. T. Valand, *Electrochim. Acta*, **25**, 287 (1980).
11. S. Wernick and R. Pinner, "The Surface Treatment and Finishing of Aluminum and Its Alloys," 4th ed., Vol. 2, p. 791, Robert Draper Ltd. (1972); M. S. Hunter, P. F. Towner, and D. L. Robinson, *Proc. Am. Electroplaters Soc.*, **1959**, 220 (1959).
12. C. J. Amore and J. F. Murphy, *Metal Finishing*, **1965**, 50 (1965).
13. K. H. Drexhage, *J. Res. Nat. Bur. Stand.*, **80A**, 421 (1976).
14. C. G. Dunn, R. B. Bolon, A. S. Alwan, and A. W. Stirling, *This Journal*, **118**, 381 (1971).
15. N. E. Cipollini and G. A. Shirn, Unpublished results.
16. J. Lavorel, *J. Phys. Chem.*, **61**, 1600 (1957).
17. W. J. Bernard, *This Journal*, **124**, 403C (1977).
18. C. H. Giles, in "Proc. Conf. on Anodizing Alumi-

num," p. 174, Nottingham, England (1961).
19. C. H. Giles, H. V. Mehta, C. E. Stewart, and R. V. R. Subramanion, *J. Chem. Soc.*, **1954**, 4360 (1954); C. H. Giles, H. V. Mehta, S. M. K. Rahman, and C. E. Stewart, *J. Appl. Chem.*, **9**, 457 (1959).
20. L. S. Pratt, in "The Chemistry and Physics of Organic Pigments," p. 112, John Wiley and Sons, New York (1947).

Dependence of the Diffusion Current on the Degree of Polymerization of Nitrocellulose in Acetone-Isopropyl Alcohol

Jin Mizuguchi

Sony Corporation Research Center, Yokohama 240, Japan

Nitrocellulose plays an extremely important role in the acetone suspensions used for the electrodeposition of aluminum oxide (1), and even a minute change of its concentration can have a noticeable effect on the process of electrodeposition. Because of this, an attempt was made in a previous investigation to develop a reliable method of analyzing nitrocellulose (2). It was found that nitrocellulose in acetone-isopropyl alcohol (IPA) exhibits a well-defined reduction wave at the dropping mercury electrode and that the diffusion current is directly proportional to a concentration up to 0.6×10^{-3} mols of nitro groups per liter. The addition of IPA to acetone was important, because IPA eliminated the problem due to the adsorption of nitrocellulose and its reduction products at the dropping mercury electrode that caused the polarogram to be ill-defined. The above experiment was performed, however, only for nitrocellulose whose degree of polymerization was about 720. Therefore, the present investigation is intended to examine the relation between the diffusion current and the concentration of nitrocellulose over a wider range of the degree of polymerization and also to examine how the degree of polymerization affects the diffusion current.

This paper describes the dependence of the diffusion current on the degree of polymerization of nitrocellulose in an acetone-IPA mixture with supporting electrolytes of perchloric acid and sodium perchlorate. The observed dependence of (diffusion current) $\propto -\log$ (degree of polymerization) is discussed on the basis of both the Stokes-Einstein relation and the random coil model of nitrocellulose in the mixed solvent.

Experiment

Definition of the concentration of nitrocellulose.—Nitrocellulose has the molecular formula $[C_6H_7O_2(NO_2)_x(OH)_{3-x}]_n$, where x and n denote the average degree of substitution of hydroxyl groups and the degree of polymerization, respectively. In the present report, the concentration of nitrocellulose is defined as the amount of nitro groups per unit volume of solution: If V is the volume of the solution containing the mass, m, of nitrocellulose, the concentration, c, is then given by the following equation

$$c = m/MV \qquad [1]$$

where M is the molar mass of $(1/x)$ $[C_6H_7O_2(NO_2)_x(OH)_{3-x}]$.

Characterization of nitrocellulose.—The degree of nitration that is necessary for calculating the degree of substitution (x) was determined by ASTM D 301-56. The degree of polymerization was calculated from the intrinsic viscosity according to ASTM 1762-62.

The basic relation between the intrinsic viscosity $[\eta]$ and the molecular weight, M', is empirically given as follows (3)

$$[\eta] = KM'^{\alpha} \qquad [2]$$

where K and α are constants that depend on the solvent, the polymer, and the temperature. Measurements of the viscosity of the solvent containing a given amount of nitrocellulose were made at 25° ± 0.1°C by means of a calibrated glass capillary of an Ubbelohde-type viscometer.

Chemicals.—Nitrocellulose of various degrees of polymerization from about 100 to 850 was obtained from Daicel Limited. IPA, sodium perchlorate, perchloric acid (70% aqueous solution), which were guaranteed grade, and acetone of "electronic grade" were obtained from Kanto Chemical Company, Incorporated. All the chemicals were used without further purification.

Experimental setup.—A potentiostat-type d-c polarograph constructed in our laboratory was employed for recording polarograms. The electrical circuit was similar to that described by Smith (4). The construction of the polarographic cell is illustrated in Fig. 1.

A spiral platinum wire and an Ag/AgCl electrode were used as the counter and the reference electrodes, respectively. The Ag/AgCl electrode was prepared by electrolytically oxidizing a spiral wire in 1M hydrochloric acid at a current density of 0.4 mA/cm² for 15 min. All potentials were referred to this electrode. The currents were corrected for the residual current.

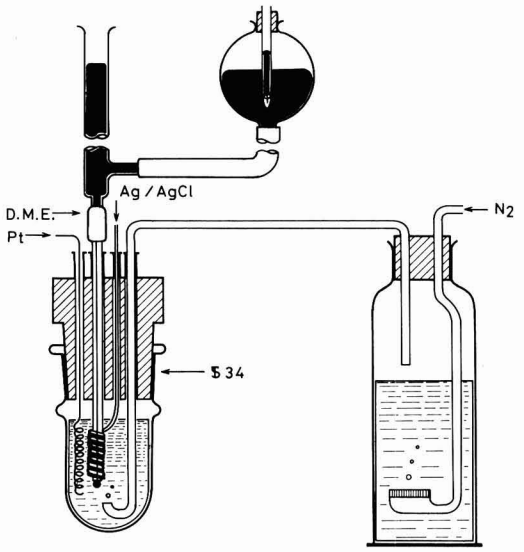

Fig. 1. The assembly of the polarographic cell

Key words: nitrocellulose, diffusion current, dropping mercury electrode.

The characteristics of the dropping mercury electrode were as follows: m = 1.9 mg/sec, t_d = 5.45 sec at a mercury head of 45 cm at −1.0V *vs.* Ag/AgCl in the experimental solution at 25°C.

Experimental procedure.—A stock solution of each 6×10^{-3}M nitrocellulose was prepared by dissolving a weighed amount of the substance in acetone. The mixed solvent of one volume of acetone and five volumes of IPA was freshly prepared before use. The procedure was as follows: Five milliliters of the diluted solution of nitrocellulose was placed in the electrolytic cell, 0.37g of sodium perchlorate anhydrate was dissolved in the solution, and 50 μl of 70% aqueous perchloric acid was added. The solution was diluted with 25 ml of IPA. Nitrogen gas saturated with the mixed solvent was vigorously bubbled through the solution for 45 min. (Deoxygenation is very slow in this solvent.) Then a polarogram was recorded. All measurements were performed at 25° ± 0.1°C. The rate of potential scan was 3.5 mV/sec.

Results

Characterization of nitrocellulose.—Measured values of degree of nitration, intrinsic viscosity, and viscosity of the solvent (1 volume of acetone + 5 volumes of IPA) containing nitrocellulose of 0.5×10^{-3}M are listed in Table I for each nitrocellulose investigated. Table I shows also the degree of substitution of hydroxyl groups and the degree of polymerization calculated from the results of both the degree of nitration and the intrinsic viscosity, respectively. As can be seen from the table, the viscosity of the solvent decreased only slightly as the degree of polymerization decreased, approaching the value of the pure mixed solvent of 0.935 cp. The change in the viscosity was within 1% in the degree of polymerization range of about 100-850.

Diffusion current.—Figure 2 shows a typical polarogram. The limiting current was diffusion controlled as shown by the fact that it was proportional to the square root of the mercury pressure. Figure 3 shows a series of diffusion currents of nitrocellulose of various polymerization degrees plotted against concentration. A good linearity is maintained up to 0.6×10^{-3}M, but the nonlinear dependence caused by nitrocellulose adsorption at the dropping mercury electrode becomes noticeable when the concentration exceeds 1×10^{-3}M (2). It is also apparent from Fig. 3 that the diffusion current gives a straight line, as in Fig. 4, in which the concentration of nitrocellulose is 0.5×10^{-3}M.

Discussion

Linear dependence of diffusion current on the concentration.—As is shown in Fig. 3, diffusion currents are linearly dependent on the concentration of nitrocellulose up to 0.6×10^{-3}M in the range of the degree of polymerization from about 100 to 850, corresponding to a molecular weight from about 2×10^4 to 2×10^5. This result allows us to determine even an extremely small amount of nitrocellulose of any degree of polymerization investigated in acetone-IPA alcohol. This analytical method is further extended to the determination of nitrocellulose of lower and higher degree of polymerization in acetone suspensions used for the

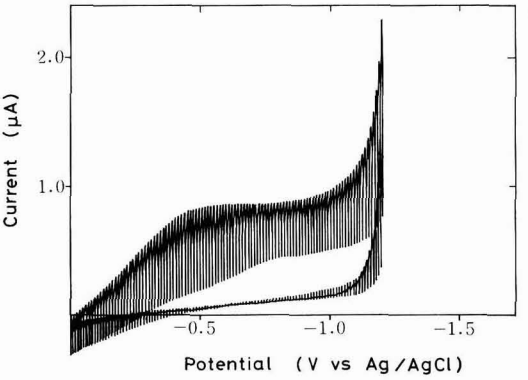

Fig. 2. Polarogram of 0.5 × 10^{-3}M nitrocellulose in acetone-IPA mixed solvent.

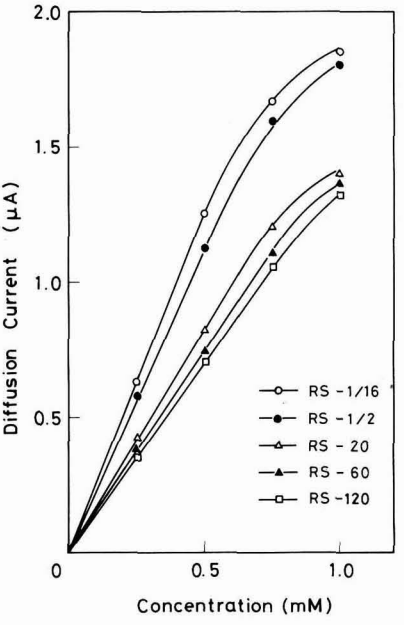

Fig. 3. Diffusion current vs. concentration for the nitrocellulose of various degrees of polymerization.

Table I. Nitrocelluloses* and their characteristics

Type	Degree of nitration** (%)	Degree of substitution (x)	Degree of polymerization†	Intrinsic viscosity, [η]	Viscosity of the solvent‡ (cp)
RS-120	11.55	2.13	832	0.279	0.946
RS-60	11.77	2.19	724	0.242	0.946
RS-20	11.59	2.14	584	0.197	0.946
RS-1/2	11.52	2.12	190	0.063	0.941
RS-1/16	11.53	2.12	114	0.038	0.937

* $[C_6H_7O_2(ONO_2)_x(OH)_{3-x}]_n$, where x and n denote the degree of substitution and the degree of polymerization, respectively.
** After ASTM D 301-56.
† After ASTM 1716-62.
‡ Viscosity of the solvent (1 volume of acetone + 5 volumes of IPA) at a nitrocellulose concentration of 0.5 mM. The viscosity of the pure mixed solvent was 0.935 cp.

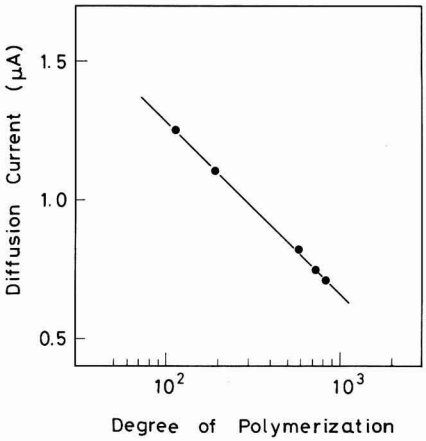

Fig. 4. Diffusion current *vs.* degree of polymerization

electrodeposition of aluminum oxide, which contained nitrocellulose, aluminum oxide, and traces of certain inorganic impurities, if an appropriate amount of IPA is added to the acetone solution. The addition of IPA is essential, and it should be noted that in acetone solution, nitrocellulose and its reduction product are adsorbed strongly at the mercury surface even at very low concentrations. Consequently, the polarographic wave is ill-defined, and its limiting current shows nonlinear dependence on the concentration as described above. The addition of an appropriate amount of IPA eliminates the difficulty due to the adsorption, as shown by the previous report (2). The precision of this analytical method is as follows: The mean diffusion current of eleven separate test solutions (0.5×10^{-3}M of RS-60) is 0.745 μA with an estimated standard deviation of 4.37×10^{-3} μA (degree of freedom = 10).

Dependence of the diffusion current on the degree of polymerization.—As shown in Fig. 4, the experimental relation of (diffusion current) $\propto -\log$ (degree of polymerization) is operative in the mixed solvent containing nitrocellulose. This relation is quite useful for the cases in which only one type of nitrocellulose (*e.g.,* RS-60) is calibrated and other types are not. The calibration curves for the other types are automatically obtained by using the above relation. Our attention is now directed toward an understanding of this mechanism.

At a constant concentration, the diffusion current i_d is directly proportional to $D^{1/2}$, as shown by the Ilkovic equation

$$i_d \propto D^{1/2} \quad [3]$$

where D is the diffusion coefficient. For diffusion particles that are larger than the solvent molecules, the Stokes-Einstein relation predicts that D is inversely proportional to the viscosity of the medium and to the radius r of diffusion particle

$$D = \frac{RT}{6\pi r N \eta} \quad [4]$$

where R and T denote the gas constant and the temperature, respectively, and N is Avogadro's number.

Since the change in the viscosity of the solvent is within 1% in the range of the degree of polymerization from about 100 to 850, as is clearly seen in Table I, the viscosity is not the factor that is responsible for the change in the diffusion coefficient. Another factor may be the shape of the polymer in the solvent, which is inversely proportional to the diffusion coefficient. The random coil model is often employed to evaluate the most probable radius r. This model is valid when the chain of a polymer is not so stretched in the solvent and the excluded volume effect is negligible. In the present experiment, IPA which alone cannot be a solvent for nitrocellulose was added to the good solvent of acetone in an attempt to avoid the nitrocellulose adsorption at the electrode mentioned previously. The addition of IPA makes the good solvent poor so that nitrocellulose chains are not stretched and the random coil model thus provides a good approximation for the present system.

According to the random coil model, the radius r is regarded as the end-to-end distance of a polymer chain and the mean square end-to-end distance $\langle r^2 \rangle$ is given as follows (5)

$$\langle r^2 \rangle = nb^2 \quad [5]$$

where b and n denote the length of a link and the number of links in a chain (*i.e.,* the degree of polymerization), respectively. The most probable value of r is also given on the basis of the Gaussian approximation

$$r = (2\langle r^2 \rangle/3)^{1/2} \quad [6]$$

This equation indicates that r is proportional to the square root of its mean square value, and the radius r is thus proportional to the square root of n through Eq. [5]. So the relation between the diffusion current and the degree of polymerization is derived through the use of Eq. [3] and [4]

$$i_d \propto n^{-1/4} \quad [7]$$

Table II shows the relative values of the observed diffusion current normalized at the current of RS-1/16. Figure 5 is a plot of these relations. As can be seen from this figure, the observed diffusion current obeys the Ilkovic equation up to the polymerization degree of about 600, suggesting that all the nitro groups of nitrocellulose that have been transferred to the dropping mercury electrode can be reduced at the electrode. A slight deviation from the slope of $-1/4$ is, however, observed in Fig. 5 in the higher degree of polymerization, showing that the nitro groups transferred to the electrode are reduced less and less at the electrode as the degree of polymerization increases, which means that some portion of nitro groups remain unreduced. This is probably caused by the steric effect of coiled up nitrocellulose in the mixed solvent, and the nitro groups that are located in the inner part of the macroscopic sphere of nitrocellulose cannot take part in the electrode reaction. The chain coiling is expected to increase as the degree of polymerization increases. Because of this steric effect, the diffusion current observed is smaller than that calculated as shown in Fig. 5, and this explains why the experimental relation $i_d \propto -\log(n)$ is operative in the mixed solvent containing nitrocellulose.

Conclusions

The diffusion current dependence of nitrocellulose on the degree of polymerization has been investigated in acetone-IPA in the polymerization-degree range from

Table II. Observed and calculated diffusion currents*

	Observed diffusion current	Calculated diffusion current†
RS-120	0.568	0.608
RS-60	0.596	0.631
RS-20	0.656	0.663
RS-1/2	0.880	0.879
RS-1/16	1.000	1.000

* Diffusion currents are normalized at the current of RS-1/16.
† Diffusion currents are calculated from the relations $i_d \propto n^{-1/4}$ where n denotes the degree of polymerization listed in Table I.

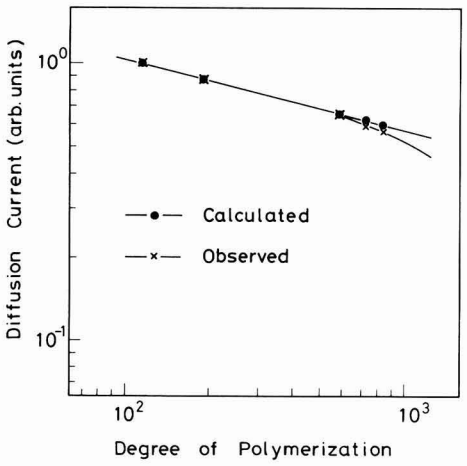

Fig. 5. Log-log plot of diffusion current *vs.* degree of polymerization of nitrocellulose.

about 100 to 850. Conclusions drawn from the present study can be summarized as follows:

1. Diffusion currents are linearly dependent on the concentration up to 0.6×10^{-3}M in any range of polymerization degrees investigated. The result can be applied to the determination of nitrocellulose of various degrees of polymerization contained in acetone suspensions used for the electrodeposition of aluminum oxide.

2. The experimental relation of (diffusion current, i_d) $\propto$ — log (degree of polymerization, n) is largely explained by considering the most probable radius r of nitrocellulose on the basis of the random coil model, which gives the relation: $i_d \propto n^{-1/4}$. A slight deviation from the slope of $-1/4$ in the high degree of polymerization is attributed to the steric effect of coiled up nitrocellulose, reducing the effective numbers of nitro groups that can participate in the electrode reaction. These considerations explain the above experimental relation.

Acknowledgments

The author wishes to express his sincere thanks to Professor G. P. Satô of Sophia University and Dr. J. Seto for valuable discussions and to Dr. N. Watanabe for his critical reading of the manuscript.

Manuscript submitted June 18, 1981; revised manuscript received *ca.* Dec. 4, 1981.

Any discussion of this paper will appear in a Discussion Section to be published in the June 1983 JOURNAL. All discussions for the June 1983 Discussion Section should be submitted by Feb. 1, 1983.

Publication costs of this article were assisted by Sony Corporation Research Center.

REFERENCES

1. Y. Tomita, *Hitachi Hyôron,* **50,** 39 (1967) (in Japanese).
2. J. Mizuguchi and K. Ueno, *Rev. Polarog. (Jpn.),* **18,** 51 (1972).
3. W. J. Moor, "Physical Chemistry," Prentice-Hall, Inc., Englewood Cliffs, NJ (1962).
4. D. E. Smith, in "Electroanalytical Chemistry," Vol. 1, A. J. Bard, Editor, Edward Arnold Ltd., London (1966).
5. K. J. Smith, in "Polymer Science," Vol. 1, A. D. Jenkins, Editor, North-Holland Publishing Co., Amsterdam, London (1972).

JOURNAL OF THE ELECTROCHEMICAL SOCIETY

SOLID-STATE SCIENCE AND TECHNOLOGY

JULY 1982

Use of HBr-CH_3COOH-$K_2Cr_2O_7$ Etchant to Etched-Mirror Laser Fabrication

Sadao Adachi, Yoshio Noguchi, and Hitoshi Kawaguchi

Nippon Telegraph and Telephone Public Corporation, Musashino Electrical Communication Laboratory, Musashino-shi, Tokyo 180, Japan

ABSTRACT

InGaAsP/InP planar-stripe lasers are fabricated monolithically in which cavity mirrors are formed by wet chemical etching using a new solution of HBr-CH_3COOH-$K_2Cr_2O_7$. The lowest threshold current density of these lasers is almost the same as that of conventionally fabricated cleaved-mirror lasers.

Fabrication of etched-mirror lasers makes possible the realization of monolithic integrated optical circuits that consist of lasers and other optical and/or electronic components, such as waveguides, light modulators, detectors, and laser driving circuits (FET's). There have been many reports on the monolithic fabrication of etched-mirror lasers in the GaAlAs/GaAs system by using various etching solutions, such as superoxol (1), NaOH-H_2O_2-NH_4OH (2), H_2SO_4-H_2O_2-H_2O (3, 4), and CH_3OH-H_3PO_4-H_2O_2 (5). The HCl-CH_3COOH-H_2O_2 (6-8) and Br_2-CH_3OH systems (9-11) have recently been used to fabricate etched-mirror lasers in the InGaAsP/InP system.

Recently, we reported a new chemical solution composed of HBr, CH_3COOH (or H_3PO_4), and a $K_2Cr_2O_7$ aqueous solution for use in etching InP and InGaAsP (12). The etching-characteristic data that one can find in the literature (12) involve studies only of the temperature and composition-proportion dependences of the etching rates, the dissolution mechanism, the etched-surface quality and degree of undercutting, the shape of etch-revealed channels, the quality of mesa-shaped structures, and the chemical aggressiveness of the solution toward photoresist mask. It was found that this etchant system provides high-quality etched surfaces without any undesirable roughness or etch pits. The etching rate for (001)InP varies from 0.1 to 10 μm/min, depending on the component proportion of the solutions and/or on the normality of the $K_2Cr_2O_7$ aqueous solution. This solution does not erode photoresists, such as AZ-1350, and provides a desirable mesa-shaped structure on the InGaAsP/InP double-heterostructure (DH) wafer with good photoresist-pattern definition. The solution is thereby attractive for a variety of device applications, particularly for mesa-shaped photodetectors.

The purpose of this paper is twofold: (*i*) to provide additional information about the HBr-CH_3COOH-$K_2Cr_2O_7$ system; in particular, to demonstrate the effect of varying the $K_2Cr_2O_7$ composition on etching profiles, and (*ii*) to report the results of the fabrication of InGaAsP/InP DH lasers with chemically etched mirrors using this etchant system, comparing the results with those obtained using Br_2-CH_3OH solution.

Key words: chemical etching, etching profile, InGaAsP/InP laser.

Experimental and Results

Etching profile.—The etching solution was prepared by freshly mixing an HBr (9*N*), CH_3COOH (17*N*), and 1*N* $K_2Cr_2O_7$ aqueous solution (purity $\geq$ 99.8%). The 1*N* $K_2Cr_2O_7$ solution was prepared by dissolving 14.7g $K_2Cr_2O_7$ in deionized water (100 cm^3). The etching profiles of the InGaAsP/InP DH wafer in the solutions of the HBr-CH_3COOH-$K_2Cr_2O_7$ system are shown in Fig. 1: (a) HBr:CH_3COOH:$K_2Cr_2O_7$ = 2:2:1 (hereafter referred to as BCK-221) (nonstirring, 4 min), (b) HBr:CH_3COOH:$K_2Cr_2O_7$ = 1:1:3 (BCK-113) (nonstirring, 4 min), and (c) HBr:CH_3COOH:$K_2Cr_2O_7$ = 1:1:5 (BCK-115) (nonstirring, 8 min). The InGaAsP/

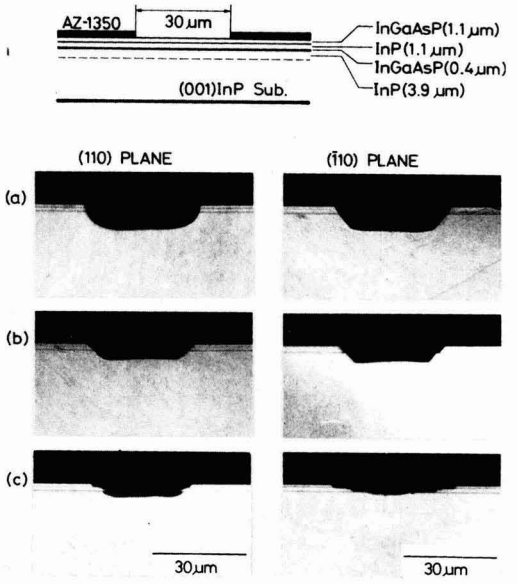

Fig. 1. Etching profiles of InGaAsP/InP DH wafer in various solutions of the BCK system: (a) BCK-221 (nonstirring, 4 min), (b) BCK-113 (nonstirring, 4 min), and (c) BCK-115 (nonstirring, 8 min). (Composition of these solutions is given in the text.)

InP DH wafer used was grown by liquid-phase epitaxy. The wafer consists of four epitaxial layers grown on a (001) n-InP substrate: n-InP (Sn-doped, 3.9 μm thick, InGaAsP (undoped, 0.4 μm thick), p-InP (Zn-doped, 1.1 μm thick), and p-InGaAsP (Zn-doped, 1.1 μm thick). The cross-sectional view of the DH wafer used is drawn schematically in the top of the figure. The etching profiles are examined by cleaving the wafer in orthogonal directions along the (110) and ($\bar{1}$10) planes. The etch-channel width is defined to be 30 μm (see Fig. 1).

It is clear from Fig. 1 that the etching profiles change in shape with a change of the 1N $K_2Cr_2O_7$ solution proportion. The BCK-221 etchant [Fig. 1(a)] has almost equal etching rates for both InP and InGaAsP and thus provides very smooth etch-revealed walls on the etching profiles. The system gives a mesa-shaped profile for the (110) cleavage plane, exhibiting no clear crystal habit. The system also gives mesa-shaped profile for the ($\bar{1}$10) cleavage plane, where the profile exhibits clear crystal habit in contrast with that for the (110) cleavage plane. The etch-revealed walls can be identified to be the {$\bar{1}$10} and {$\bar{1}\bar{1}$1}A planes for the (110) and ($\bar{1}$10) cleavage planes, respectively. The BCK-221 etchant has an etching rate of $\sim$2.5 μm/min for (001)InP (12). The etching rate of the BCK-221 etchant estimated from the etched depth of Fig. 1(a) is about 2.1 μm/min, which coincides with that for the (001)InP within experimental error. The BCK-113 etchant [Fig. 1(b)] has slightly different etching rates for the InP and InGaAsP layers, whereas the BCK-115 etchant [Fig. 1(c)] has quite different etching rates for the InP and InGaAsP layers. These etch rate differences produce complex etching profiles on the InGaAsP/InP DH wafer, as clearly seen in Fig. 1(c). The BCK-221 and BCK-113 etchants have no clear dependence of undercutting on the crystallographic direction. The degree of the undercutting for the InGaAsP top layer (1.1 μm thick layer) is about 3 μm for the BCK-221 [see Fig. 1(a)] and 2 μm for the BCK-113 etchant [see Fig. 1(b)]. The BCK-115 etchant, on the other hand, has strong dependence of the undercutting on the crystallographic direction [1.5 μm for the (110) cleavage plane and 5 μm for the (110) cleavage plane].

To fabricate good-quality etched-mirror lasers on a DH wafer, it is necessary to employ an etching solution that provides an etching profile with vertical-mirror walls and gives almost the same etching rates for the individual DH layers (*i.e.*, in the present case, for InP and InGaAsP). The BCK-221 etchant provides nearly vertical-mirror walls for the (110) cleavage plane. In fact, vertical and smooth mirror walls, similar to Fig. 1(a), can be produced by the BCK-11m etchant with a range of value of m (volume ratio) from 0.2 to 2.

Etched-mirror laser.—The fabrication steps of the etched-mirror laser are shown schematically in Fig. 2. The InGaAsP/InP DH wafer used was grown on a (001)InP by liquid-phase epitaxy. The $In_{1-x}Ga_xAs_yP_{1-y}$ quaternaries can be epitaxially grown on InP for $0 \leq y \leq 1.0$, provided $x \simeq 0.46y$ (13). The wavelength of laser emission varies from $\lambda = 0.93$ to 1.67 μm over this compositional range. The wafer used consists of four epitaxial layers: n-InP confining layer (Sn-doped, 2.9 μm thick), undoped InGaAsP active layer ($\lambda \simeq 1.5$ μm, 0.3 μm thick), p-InP confining layer (Zn-doped, 1.0 μm thick), and p-InGaAsP contact cap layer (Zn-doped, 0.3 μm thick). To prepare the contact-stripe laser, an SiO_2 film was sputtered onto the p-InGaAsP top layer and 10 μm wide stripe windows were opened by standard photolithographic techniques. In order to investigate some effects of the mirror-facet

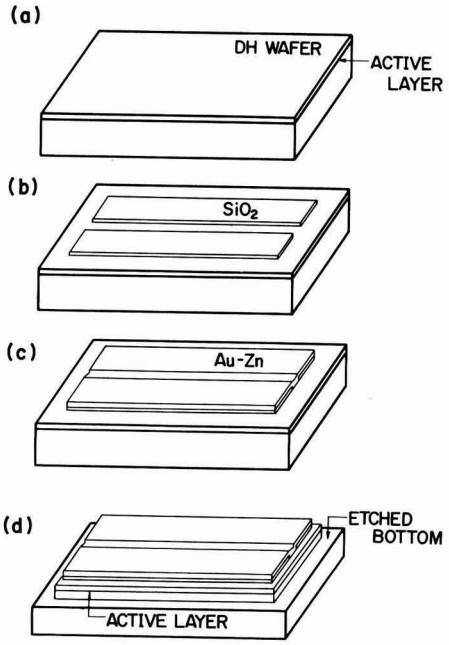

Fig. 2. Fabrication steps of etched-mirror contact-stripe InGaAsP/InP DH laser.

directions on lasing characteristics, the stripes were aligned either in the [110] or [$\bar{1}$10] directions. The wafer was then thinned to about 150 μm, and Au-Zn and Au-Ge-Ni ohmic contacts were applied to the p-side and substrate area, respectively. Rectangular Au-Zn contacts were then defined by photolithographic processing using a KI-I_2-H_2O solution as an etchant of the Au-Zn metal. After definition of the Au-Zn contacts, photolithography was employed once more to define an AZ-1350 mask (Shipley) 275 μm long and 200 μm wide directly over the Au-Zn contact for making the etched-mirror facets, where the defined SiO_2 and Au-Zn contact were slightly smaller than the AZ-1350 mask to prevent contact by the subsequent etched-mirror fabrication procedure. The wafer was then etched with the HBr:CH_3COOH:$K_2Cr_2O_7$ = 1:1:1 (BCK-111) solution for 2 min at 20°C without stirring. After the fabrication of the mirrors by etching, the lasers were separated into individual units by cleaving.

Figure 3 shows a scanning electron microscope photograph of the chemically etched-mirror laser. It can be seen that the etched-mirror wall and etched bottom tend to be very smooth. The etching rates, however, are slightly different for the InGaAsP active layer than for the surrounding InP confining layers. This may be due to a pn-junction field-induced enhancement of the etching rate in the InGaAsP active layer (*i.e.*, staining effect) (12). Optical microscope photographs of the ($\bar{1}$10)-mirror (stripe aligned along the [$\bar{1}$10] direction) and (110)-mirror profile (stripe aligned along the [110] direction) are also shown in the lower part of Fig. 3. The profiles are very similar to those of Fig. 1(a) (BCK-221). As discussed before, the ($\bar{1}$10) mirror is defined by the {$\bar{1}$10} plane that in principle forms an angle of 90° with respect to the (001) surface plane, while the (110) mirror is defined predominantly by the {$\bar{1}\bar{1}$1}A slow-etching-rate plane that forms an angle of 54.7° with respect to the (001) surface plane.

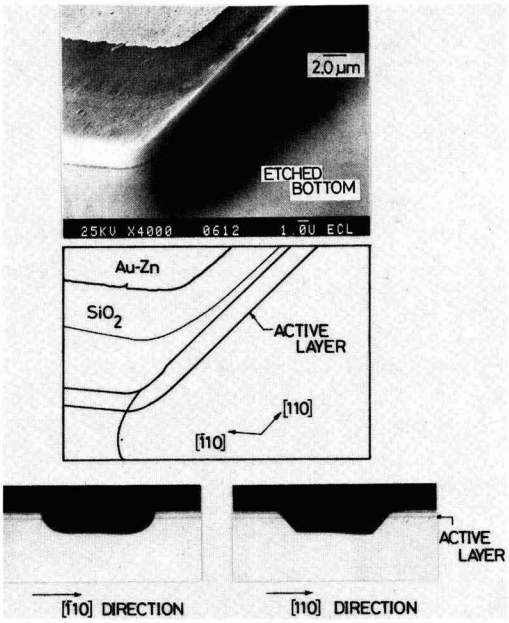

Fig. 3. SEM and cross-sectional views of etched-mirror facet

In order to evaluate the performance of the etched-mirror lasers, contact-stripe lasers were also fabricated from the same wafer using conventional cleaving. Figure 4 shows typical light-output *vs.* injection current characteristics for InGaAsP/InP cleaved- (left-hand side) and etched-mirror lasers (right-hand side). The cleaved-mirror laser has a cavity length (L) of 170 μm. The ($\bar{1}10$)-etched-mirror lasers have L = 250 μm [one etched and one cleaved mirrors (solid line)] and 270 μm [two etched mirrors (dashed line)]. The (110)-etched-mirror laser has L = 270 μm [two etched mirrors (dotted line)]. The lasers were driven with 1 μsec long pulses at 1 kHz at 18°C. The typical threshold current (I_{th}) of the cleaved-mirror laser is 320 mA which corresponds to a threshold current density (J_{th}) of 18.8 kA/cm^2. The ($\bar{1}10$)-etched-mirror lasers have

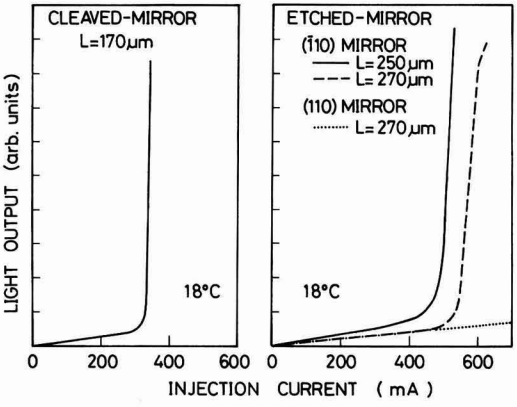

Fig. 4. Typical light-ouput *vs.* injection current characteristics for InGaAsP/InP cleaved- (left-hand side) and etched-mirror lasers (right-hand side). The etched-mirror lasers have one etched- and one cleaved-mirror (solid line) and two etched-mirrors (dashed and dotted lines).

I_{th} of 485 mA (solid line) and 540 mA (dashed line) which correspond to J_{th} = 19.4 and 20.0 kA/cm^2, respectively. The ($\bar{1}10$)-etched-mirror lasers, thus, have nearly the same threshold current density as the standard cleaved-mirror lasers. The (110)-etched-mirror lasers, on the other hand, exhibited no lasing characteristics at a current level of up to ~1000 mA (see dotted line). This is probably due to the tapered profile of the (110)-mirror walls, since the mirror reflectivity is considerably smaller for the tapered (110) mirror than for the nearly vertical ($\bar{1}10$) mirror. In previous work (11), we fabricated stripe-geometry InGaAsP/InP DH lasers with etched mirrors using a Br_2-CH_3OH solution as an etchant. In that work, the nearly vertical (100)-mirror lasers exhibited clear lasing behavior, while the tapered (110)-mirror lasers did not, just as in the present case. From these experimental facts, it can be concluded that the vertical, smooth mirror profile provides high reflectivity and low scattering-loss mirrors and, as a result, improves the characteristics of laser diodes (threshold current, quantum efficiency, etc.).

In conclusion, contact-stripe InGaAsP/InP DH lasers with chemically etched mirrors have been fabricated successfully using an HBr-CH_3COOH-$K_2Cr_2O_7$ solution as an etchant for mirror definition. This solution does not erode photoresists and gives high-quality etched surfaces with a good resist-pattern definition. The solution, moreover, provides very smooth and nearly vertical-mirror walls for stripe, alignment along the [$\bar{1}10$] direction, with good reproducibility. A Br_2-CH_3OH solution also provides smooth and nearly vertical-mirror walls, but it erodes photoresists and restricts the stripe direction along only the [100] axis (45° off from the [$\bar{1}10$] cleavage axis). The threshold current density of the etched-mirror lasers obtained here is nearly the same as that of conventionally fabricated cleaved-mirror lasers. It seems that this fabrication procedure allows for much variety of device design and fabrication compared with the conventional cleaving technique.

Acknowledgment

The authors wish to thank M. Watanabe, T. Suzuki, T. Ikegami, and G. Iwane for their encouragement throughout this work. The authors also wish to thank H. Nagai and K. Takahei for helpful advice.

Manuscript submitted July 17, 1981; revised manuscript received Nov. 30, 1981.

Any discussion of this paper will appear in a Discussion Section to be published in the June 1983 JOURNAL. All discussions for the June 1983 Discussion Section should be submitted by Feb. 1, 1983.

Publication costs of this article were assisted by Nippon Telegraph and Telephone Public Corporation.

REFERENCES

1. J. L. Merz, R. A. Logan, and A. M. Sergent, *IEEE J. Quantum Electron.*, **qe-15,** 72 (1979).
2. K. Itoh, K. Asahi, M. Inoue, and I. Teramoto, *ibid.*, **qe-13,** 628 (1977).
3. C. E. Hurwitz, J. A. Rossi, J. J. Hsieh, and C. M. Wolfe, *Appl. Phys. Lett.*, **27,** 241 (1975).
4. Y. Tarui, Y. Komiya, T. Sakamoto, H. Iida, and A. Shoji, *Jpn. J. Appl. Phys. (Suppl.),* **15,** 293 (1976).
5. J. L. Merz and R. A. Logan, *J. Appl. Phys.*, **47,** 3503 (1976).
6. B. I. Miller and K. Iga, *Appl. Phys. Lett.*, **37,** 339 (1980).
7. K. Iga, M. A. Pollack, B. I. Miller, and R. J. Martin, *IEEE J. Quantum Electron.*, **qe-16,** 1044 (1980).
8. K. Iga and B. I. Miller, *Electron. Lett.*, **16,** 830 (1980).
9. P. D. Wright, R. J. Nelson, and T. Cella, *Appl. Phys.*

Lett., **36**, 518 (1980).
10. P. D. Wright and R. J. Nelson, *IEEE Electron Device Lett.*, **edl-1**, 242 (1980).
11. S. Adachi and H. Kawaguchi, *J. Appl. Phys.*, **52**, 3176 (1981).
12. S. Adachi, *This Journal*, **129**, 609 (1982).
13. R. E. Nahory, M. A. Pollack, W. D. Johnston, Jr., and R. L. Barns, *Appl. Phys. Lett.*, **33**, 659 (1978).

Crystalline Structure Changes of Molybdenum Silicide Films Deposited by Sputtering and by Coevaporation after Isochronal Annealing

Kenji Shibata, Shohei Shima, and Masahiro Kashiwagi*

Toshiba Corporation, Toshiba Research and Development Center, 1, Komukai Toshiba-cho, Saiwai-ku, Kawasaki-city Kanagawa 210 Japan

ABSTRACT

Crystalline structure changes of molybdenum silicide films after isochronal annealing are studied by x-ray and transmission electron microscopy. Two types of films deposited by sputtering from a hot pressed $MoSi_2$ source and coevaporation of molybdenum and silicon, with controlled stoichiometry of $MoSi_2$, are prepared. For both types of depositions, the films that are as-deposited and annealed at temperatures below 350°C are amorphous, but those annealed between 400° and 600°C show hexagonal $MoSi_2$. Transformation from hexagonal to tetragonal $MoSi_2$ occurs above 700°C for the coevaporated film, whereas it proceeds gradually above 800°C for the sputtered film. A carbon stabilized phase Si_3Mo_5 is observed above 750°C for the sputtered film, which suggests that the sputtered film is contaminated by carbon during the deposition. Formation of the Mo-rich silicides Mo_3Si_2 and Si_3Mo_5 above 700°C is evidence that the deposited films become Mo-rich during the annealing due to slight oxidation of the film surface.

Increase in packing density and switching speed demands low resistivity materials for gate electrode and interconnections of MOS devices. Refractory metal silicides, such as molybdenum silicide ($MoSi_2$) and tungsten silicide (WSi_2), are alternative materials to conventional polycrystalline silicon (polysilicon) because of their high conductivity and process compatibility with silicon technology.

Although many publications have been reported on device fabrication with these silicides (1-7), and on their physical properties (8-22), the silicide technology is still in its formative stage. Some of the principal problems with these silicides at present are physical properties such as crystalline structure and internal stress, and electrical properties under the subsequent high temperature heat-treatments. Another key problem appears to be impurity contamination in the silicide films, which may originate in deposition sources and systems. These problems with the silicide films suggest that the deposition method should be the subject of further investigation.

In this paper, we study the crystalline structure change of the deposited $MoSi_2$ films in isochronal annealing by means of x-ray diffraction and transmission electron microscopy (TEM). Comparison of the metallurgical properties is emphasized for the films prepared by the different methods, *i.e.*, coevaporation of molybdenum metal and silicon, and sputtering of a composite target by the d-c magnetron technique.

Experimental Procedures

Single crystalline silicon wafers with (100) orientation were thermally oxidized at 1000°C for 5 hr in a pyrogenic-steam ambient, resulting in a 1 μm thick SiO_2 layer. The wafers were divided into two groups. In one group, molybdenum silicide films about 3000Å thick were deposited by d-c magnetron sputtering from a hot-pressed target made of tetragonal $MoSi_2$ (Fig. 1). Before deposition, base pressure of the deposition chamber is about 10^{-6} Torr. The sputtering ambient was argon at a pressure of 2×10^{-3} Torr, and the deposition rate was about 2 Å/sec. The substrate temperature was kept below 80°C. On another group of wafers, the silicide films were deposited by coevaporation from two individually rate-controlled E-beam sources of molybdenum and silicon. The stoichiometry of the film is measured by Mo-blue spectrophotometry and inductivity coupled plasma emitter spectrophotometry techniques, and controlled at $MoSi_2$. The vacuum during deposition at a rate of 10 Å/sec was maintained at about 10^{-6} Torr. The films were then isochronally annealed at temperatures ranging from 200° to 1000°C for 30 min in dry nitrogen.

The structures of the as-deposited and annealed molybdenum silicide films were analyzed by x-ray diffraction with CuK_α ($\lambda = 1.542$Å). Besides x-ray analysis, the films were investigated by transmission electron microscopy (TEM) operating at 200 kV. Bright- and dark-field images of the films were taken to observe the film crystallization and determine the phase of crystallized grains. Since the reflected x-ray intensities were very weak, transmission electron diffraction patterns (TEDP) were also taken. For film structure analysis with TEDP, x-ray data were used as reflection standards. Samples for TEM were made by etching the SiO_2 layer underlying the silicide films in a buffered hydrofluoric acid (HF) solution. During the SiO_2 layer etching, the silicide films were not attacked by the buffered HF solution.

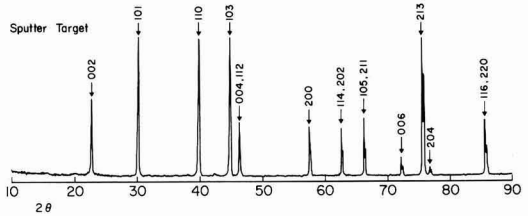

Fig. 1. X-ray reflection peaks of a hot-pressed $MoSi_2$ target for sputtering.

* Electrochemical Society Active Member.
Key words: crystal structure, molybdenum silicide, sputtering, coevaporation, isochronal annealing.

Experimental Results

X-ray diffraction.—For the as-deposited films made both by sputtering and by coevaporation, x-ray diffraction analysis data did not show any specific peaks, indicating that their structure was amorphous. After annealing at temperatures below 300°C, both films still did not have any x-ray diffraction peaks, which shows that the deposited films do not crystallize when annealed below 300°C for 30 min. At 400°C, however, both films showed reflection peaks corresponding to (100), (101), and (111) hexagonal $MoSi_2$. Figure 2 shows the x-ray data for a sputtered film after annealing at 400°C. As the annealing temperature increased from 400° to 600°C, the peak height increased slightly, but the width did not change significantly, indicative of incomplete crystallization.

In the annealing temperature range between 700° and 900°C, the structures of the two types of films were different.

Figures 3(A) and (B) show the x-ray diffraction data of the sputtered and coevaporated films after annealing at 700°C, respectively. It is notable that tetragonal $MoSi_2$ phase grains are present in the coevaporated film, whereas hexagonal $MoSi_2$ grains, which are the low temperature phase, still remain in the sputtered film. The difference in structure between the two types of films suggests that the film properties and/or quality are different in the two cases. For the sputtered film, weak tetragonal $MoSi_2$ peaks as well as hexagonal $MoSi_2$ peaks were observed at an annealing temperature of 800°C. The tetragonal $MoSi_2$ peaks became stronger, and the intensities of the two different phase $MoSi_2$ reflection peaks were comparable at 900°C, as shown in Fig. 4(A). On the other hand, the coevaporated film shows only tetragonal $MoSi_2$ peaks at temperatures between 700° and 900°C, though the intensity of the reflection peaks became stronger, as the annealing temperature increased.

It was confirmed from the x-ray data that when the annealing was performed at 1000°C, simultaneous formation of tetragonal $MoSi_2$ and another covalent silicide of tetragonal Mo_3Si_2 (23) occurred for both sputtered and coevaporated films. Figure 4(B) shows the typical x-ray diffraction data of the sputtered film after annealing at 1000°C. The Mo_3Si_2 peaks are not as strong and sharp as the $MoSi_2$ peaks, which indicates that poorly crystallized Mo_3Si_2 phase grains coexist with $MoSi_2$ grains in the annealed silicide films. In the case of annealing at 1000°C, hexagonal $MoSi_2$ was not observed even after annealing for shorter time. Figure 5 shows x-ray data for the sputtered film annealed at 1000°C for 10 min, which shows weak tetragonal $MoSi_2$ peaks and very weak Mo_3Si_2 peaks.

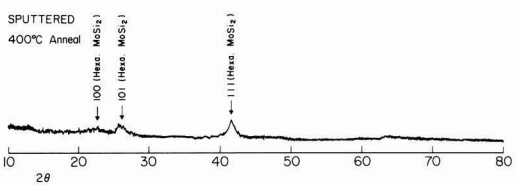

Fig. 2. X-ray reflection peaks for a sputtered film after annealing at 400°C for 30 min.

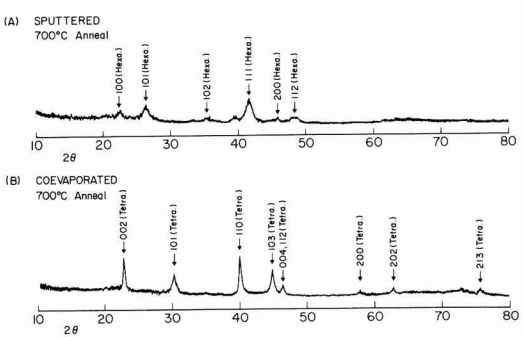

Fig. 3. X-ray reflection data for (A) sputtered, and (B) coevaporated films after annealing at 700°C for 30 min.

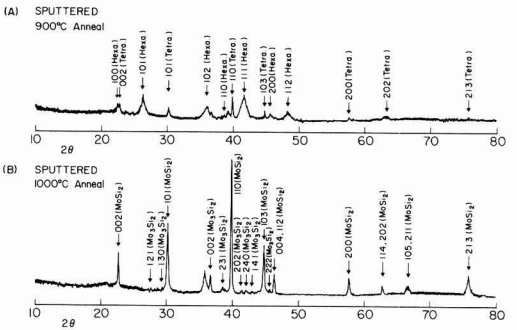

Fig. 4. X-ray reflection data for sputtered films after annealing at (A) 900°C, and (B) 1000°C for 30 min.

In Table I, the structures of as-deposited and isochronally annealed films deposited by sputtering and coevaporation are summarized. A large difference between the structures of the two types of films is observed in the annealing temperature range between 700° and 900°C. Tetragonal $MoSi_2$ formed above 700°C for the coevaporated film, whereas it formed above 800°C coexisting with hexagonal $MoSi_2$ for the sputtered film.

TEM study.—Because of high level background from silicon wafers and the 1 μm thick SiO_2 layer, the sensitivity in x-ray analysis is limited. Thus in order to confirm the formation of other low concentration silicides with different crystalline structure, deposited films were also studied by TEM after removing the SiO_2 layer and silicon substrate. Figures 6(a) and (b) show a TEM bright-field image micrograph and a TEDP of the as-deposited film by sputtering, respectively. In Fig. 6(a), the film appears to be very smooth and no specific grain structure is observed. The TEDP [in Fig. 6(b)] shows a halo pattern without specific reflection lines. These TEM results strongly support the conclusion that the as-deposited films are amorphous. After annealing below 350°C, covalent silicides did not form in the sputtered film, consistent with x-ray analysis data shown earlier. Very similar TEM results were obtained for the coevaporated film.

After annealing at temperatures between 400° and 600°C, a definite grain structure was observed for all annealed films, although the grain size increased as the temperature increased. Identification of the reflection lines of TEDP's was done with ASTM cards utilizing the above x-ray results as a standard. For two types of films, it revealed the formation of hexagonal $MoSi_2$

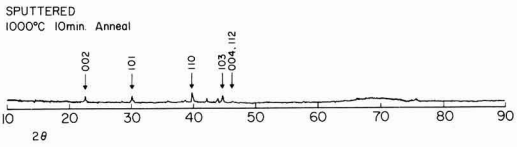

Fig. 5. X-ray reflection peaks for a sputtered film annealed at 1000°C for 10 min.

Table I. Crystalline structure for the sputtered and coevaporated films as-deposited and after 30 min isochronal annealing at temperatures ranging between 200° and 1000°C

Annealing temperature (°C)	Sputtered			Coevaporated		
	$MoSi_2$			$MoSi_2$		
	Hexagonal	Tetragonal	Mo_3Si_2	Hexagonal	Tetragonal	Mo_3Si_2
as depo.	No	No	No	No	No	No
200	No	No	No	No	No	No
300	No	No	No	No	No	No
400	Strong	No	No	Strong	No	No
500	Strong	No	No	Strong	No	No
600	Strong	No	No	Strong	No	No
700	Strong	No	No	No	Strong	No
800	Strong	Weak	No	No	Strong	No
900	Strong	Strong	No	Nc	Strong	No
1000	No	Strong	Weak	No	Strong	Weak

after annealing at temperatures between 400° and 600°C. Figures 7(a) and (b) show a typical bright-field image and the TEDP of the sputtered film after annealing at 600°C, respectively. In Fig. 7(a), there are rodlike grains surrounded by an uncrystallized region. These grains were identified as hexagonal $MoSi_2$ by the dark-field imaging technique. The average grain size is less than 500Å, with the maximum length of the rodlike grains being about 1000Å. In Fig. 7(b), the reflection lines of hexagonal $MoSi_2$ are observed.

In the case of the annealing at 700°C, it was found that tetragonal $MoSi_2$ and tetragonal Mo_3Si_2 simultaneously exist in the coevaporated film, whereas the hexagonal $MoSi_2$ remained in the sputtered film. This TEDP result for the coevaporated film is different from that obtained by x-ray, where no formation of Mo_3Si_2 for the annealed film has been detected. The intensity of the tetragonal Mo_3Si_2 reflection rings in the TEDP are weak in the temperature range between 700° and 800°C; however, they are as strong as that of the tetragonal $MoSi_2$ at 900°C.

On the other hand, a carbon stabilized structure of hexagonal Si_3Mo_5 (24) as well as hexagonal $MoSi_2$ is observed in the sputtered film after annealing at 750° and 800°C. The identified TEDP of the annealed film at 800°C is shown in Fig. 8. After annealing at 900°C, reflection rings of tetragonal $MoSi_2$ as well as the above two phases are observed in the TEDP of the sputtered film, which is contrary to the case of the coevaporated film mentioned above.

After annealing at 1000°C, both sputtered and coevaporated films show large increases in grain size. Figure 9 shows a typical bright-field image of the grain structure with average grain size less than 1000Å for the coevaporated film. The annealed film contains many twin structures, which is very similar to that of thermally annealed polysilicon films. Figure 10 shows a TEDP of the coevaporated film annealed at 1000°C. This was identified by measuring lattice spacings. Two phases of tetragonal $MoSi_2$ and Mo_3Si_2 are simultaneously present, which is consistent with the x-ray analysis. For the sputtered film, however, the presence of hexagonal Si_3Mo_5 phase grains as well as the above two phases is confirmed by the TEDP analysis, which is contrary to the x-ray analysis.

Discussion

Combined x-ray and electron diffractions determined that both sputtered and coevaporated molybdenum silicide films (Si/Mo ratio ~2) are amorphous as-deposited and annealed at temperatures below 350°C, and hexagonal $MoSi_2$ in films annealed between 400° and 600°C. At temperatures higher than 700°C, the coevaporated film gives different results from those obtained for the sputtered film. One of the major differences is the transformation temperature from hexagonal $MoSi_2$ to tetragonal $MoSi_2$, and another is the formation of

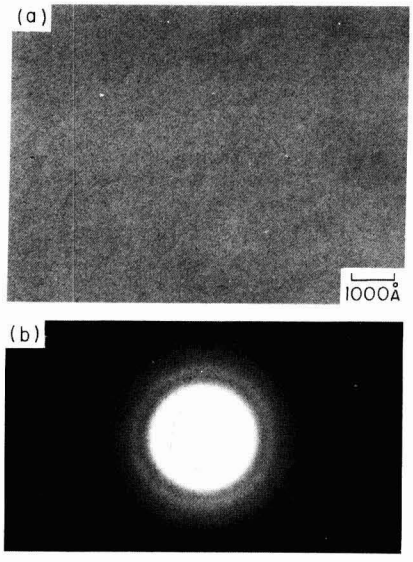

Fig. 6. (a) TEM bright-field image, and (b) TEDP for as-deposited film by sputtering.

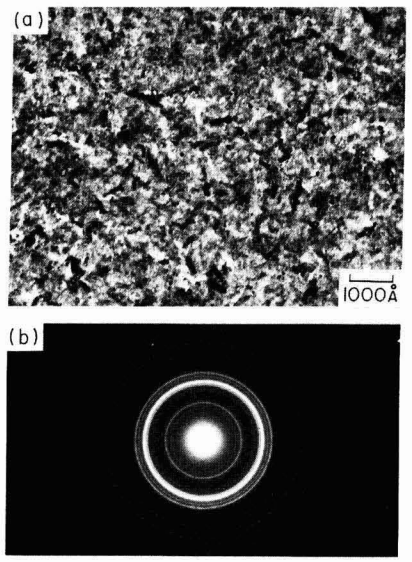

Fig. 7. (a) TEM bright-field image, and (b) TEDP for the sputtered film after annealing at 600°C for 30 min.

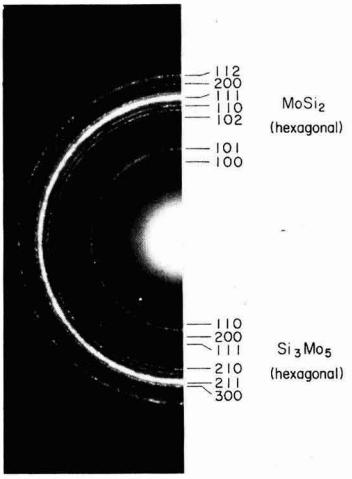

Fig. 8. Identified TEDP for a sputtered film after annealing at 800°C for 30 min, which shows a carbon stabilized structure of hexagonal Si_3Mo_5 simultaneously formed with hexagonal $MoSi_2$.

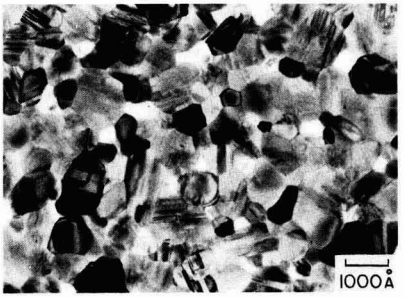

Fig. 9. TEM bright-field image of grain structure for a coevaporated film after annealing at 1000°C for 30 min, which is very similar to that of thermally annealed polysilicon films.

the carbon stabilized phase of hexagonal Si_3Mo_5 for the sputtered film.

For the coevaporated film, tetragonal $MoSi_2$ was identified by two different diffraction methods, indicating that a complete transformation of hexagonal to tetragonal $MoSi_2$ is attained at a temperature at 700°C. On the other hand, for the sputtered film, we could not detect tetragonal $MoSi_2$ below 750°C, but have detected the two silicide phases, hexagonal and tetragonal $MoSi_2$, simultaneously after annealing at temperatures ranging from 800° to 900°C. This is evidence that the transformation temperature is higher than 800°C for the sputtered film. Yanagisawa and Fukuyama (25), who worked on reactions between molybdenum films and silicon, have also found the coexistence of these two phases. Since these two phases cannot coexist in a thermal equilibrium state, it is thought that the transformation is incomplete during annealing at 800° and 900°C for 30 min, which means that the decomposition process of hexagonal $MoSi_2$ and formation of tetragonal $MoSi_2$ needs more than 30 min of annealing at these temperatures.

We have observed the hexagonal Si_3Mo_5 phase for the sputtered film after annealing above 750°C. This phase is not seen in the x-ray diffraction analysis but detected in TEDP. The discrepancy between the two methods is due to the analytical sensitivity limits. The samples for x-ray analysis were not discrete thin films, but a thin film structure on SiO_2 over silicon. Therefore, the sensitivity in x-ray analysis is limited by the background reflection intensity from the silicon wafer and the thickness of the amorphous SiO_2 layer. Although the correlation between these samples and those analyzed by TEDP is not clear, electron diffraction analysis has higher sensitivity, and can provide more information on the low concentration of silicides than that obtained by x-ray analysis.

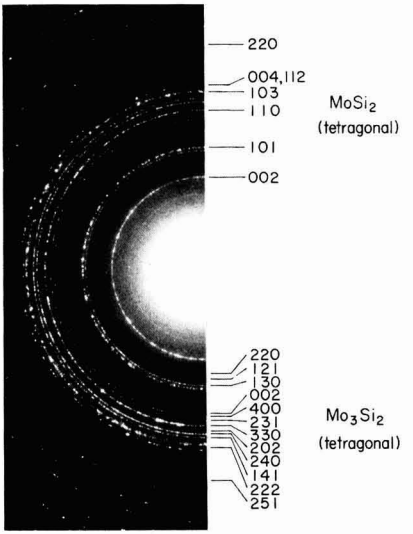

Fig. 10. Identified TEDP for a coevaporated film after annealing at 1000°C for 30 min. Two phases of tetragonal $MoSi_2$ and Mo_3Si_2 are simultaneously present.

The presence of the Si_3Mo_5 phase in the annealed film indicates that a small amount of carbon is introduced from the hot-pressed sputtering source into the deposited film. Carbon content of the sputter target is measured 0.14%, and carbon contamination in the deposited films is confirmed by Auger analysis. From above results, we suggest that the transformation temperature of hexagonal to tetragonal $MoSi_2$ is increased and its rate is drastically decreased by the carbon contaminant.

Besides the Si_3Mo_5 phase for the sputtered film, the simultaneous formation of the Mo-rich silicide phase Mo_3Si_2 and $MoSi_2$ is observed for the coevaporated and sputtered films after annealing at 700° and 1000°C, respectively. The presence of these Mo-rich phases Si_3Mo_5 and Mo_3Si_2 in annealed films at high temperature is evidence that the films are Mo-rich. Guivarc'h *et al.* (26) reported that during heat-treatment at 1000°C in argon ambient, an SiO_2 layer formed at the $MoSi_2$ surface. When the oxidation of the $MoSi_2$ silicide film on SiO_2 proceeds, an SiO_2 layer grows at the film surface, and the silicide film becomes Mo-rich (27). Therefore, we suggest that the Mo-rich phases are generated at the interface between the thin SiO_2 layer and $MoSi_2$ during annealing above 700°C in nitrogen as a result of the surface oxidation of deposited silicide films.

Summary

Crystalline structural changes of molybdenum silicide films in 30 min isochronal annealing were investigated by x-ray and TEM. Two types of films, deposited by sputtering and coevaporation, are used, and their properties are compared. As deposited films for both type are amorphous. They do not crystallize with annealing below 350°C, but show hexagonal $MoSi_2$ between 400° and 600°C. The tetragonal $MoSi_2$ phase appears above 700°C for the coevaporated film, and it

coexists with hexagonal $MoSi_2$ above 800°C for the sputtered film. A carbon stabilized phase, Si_3Mo_5, is observed above 750°C for the sputtered film, indicating carbon contamination during the deposition. Besides Si_3Mo_5, the Mo-rich phase Mo_3Si_2 is detected at above 700°C, which suggests slight oxidation during the annealing, resulting in the Mo-rich film.

Acknowledgments

The authors would like to thank S. Shikanai for x-ray diffraction, and T. Mochizuki for continual encouragement and discussion during this investigation. They also thank Dr. Y. Ohmura for critical readings of this manuscript.

Manuscript submitted Oct. 5, 1981; revised manuscript received Jan. 4, 1982.

Any discussion of this paper will appear in a Discussion Section to be published in the June 1983 JOURNAL. All discussions for the June 1983 Discussion Section should be submitted by Feb. 1, 1983.

Publication costs of this article were assisted by Toshiba Corporation.

REFERENCES

1. T. Mochizuki, K. Shibata, T. Inoue, and K. Ohuchi, *Jpn. J. Appl. Phys.*, **17-1**, 37 (1977).
2. P. L. Shah, *IEEE Trans. Electron Devices*, **ed-26**, 631 (1979).
3. T. P. Chow, A. J. Steckl, M. E. Motamedi, and D. M. Brown, Tech. Digest of 1979 IEDM Meeting, p. 458.
4. K. C. Saraswat, F. Mohammadi, and J. D. Meindl, Tech. Digest of 1979 IEDM Meeting, p. 462.
5. H. J. Geipel, Jr., N. Hsieh, M. H. Ishaq, C. W. Koburger, and F. R. White, *IEEE Trans. Electron Devices*, **ed-27**, 1417 (1980).
6. T. Mochizuki, T. Tsujimaru, M. Kashiwagi, and Y. Nishi, *ibid.*, **ed-27**, 1431 (1980).
7. Y. Mizutani, K. Maeguchi, T. Mochizuki, M. Kimura, M. Isobe, and Y. Uchida, *Jpn. J. Appl. Phys.*, **20-1**, 117 (1981).
8. S. Zirinsky, W. Hammer, F. d'Heurle, and J. Baglin, *Appl. Phys. Lett.*, **33**, 76 (1978).
9. T. Inoue and K. Koike, *ibid.*, **33**, 826 (1978).
10. F. Mohammadi, K. C. Saraswat, and J. D. Meindl, *ibid.*, **35**, 529 (1979).
11. B. L. Crowder and S. Zirinsky, *IEEE Trans. Electron Devices*, **ed-26**, 369 (1979).
12. S. P. Murarka, Tech. Digest of 1979 IEDM Meeting, p. 454.
13. F. Mohammadi and K. C. Saraswat, *This Journal*, **127**, 450 (1980).
14. S. Yanagisawa and T. Fukuyama, *ibid.*, **127**, 1120 (1980).
15. S. P. Murarka, *J. Vac. Sci. Technol.*, **17**, 775 (1980).
16. S. P. Murarka, D. B. Fraser, A. K. Sinha, and H. J. Levinstein, *IEEE Trans. Electron Devices*, **ed-27**, 1409 (1980).
17. S. P. Murarka, D. B. Fraser, T. F. Retajczyk, Jr., and T. T. Sheng, *J. Appl. Phys.*, **51**, 5380 (1980).
18. T. F. Retajczyk, Jr. and A. K. Sinha, *Thin Solid Films*, **70**, 241 (1980).
19. T. P. Chow and A. J. Steckl, Tech. Digest of 1980 IEDM Meeting, p. 149.
20. S. Inoue, N. Toyokura, T. Nakamura, and H. Ishikawa, Tech. Digest of 1980 IEDM Meeting, p. 152.
21. R. S. Nowicki and J. F. Moulder, *This Journal*, **128**, 562 (1981).
22. R. F. Pinizzotto, K. L. Wang, and S. Matteson, in "Semiconductor Silicon 1981," H. R. Huff, R. J. Kriegler, and Y. Takeishi, Editors, p. 562, The Electrochemical Society Softbound Proceedings Series, Pennington, NJ (1981).
23. M. Someno and H. Nagasaki, *Nihon Kinzoku Gakkaishi*, **22**, 528 (1958).
24. H. Schachner, E. Cerwenka, and H. Nowotny, *Monatsu. Chem.*, **85**, 245 (1954), ASTM Card No. 8-429.
25. S. Yanagisawa and T. Fukuyama, *This Journal*, **127**, 1150 (1980).
26. A. Guivarc'h, P. Auvray, L. Berthou, M. LeCun, J. P. Boulet, P. Henoc, G. Pelous, and A. Martinez, *J. Appl. Phys.*, **49**, 233 (1978).
27. T. Mochizuki and M. Kashiwagi, *This Journal*, **127**, 1128 (1980).

Heterogeneous Decomposition of Silane in a Fixed Bed Reactor

S. K. Iya, R. N. Flagella, and F. S. DiPaolo

Union Carbide Corporation, Tonawanda, New York 14150

ABSTRACT

Heterogeneous decomposition of silane in a fluidized bed offers an attractive route for the low-cost production of silicon for photovoltaic application. To obtain design data for a fluid bed silane pyrolysis reactor, deposition experiments were conducted in a small-scale fixed bed apparatus. Data on the decomposition mode, plating rate, and deposition morphology were obtained in the temperature range 600°-900°C. Conditions favorable for heterogeneous decomposition with good deposition morphology were identified. The kinetic rate data showed the reaction to be first order with an activation energy of 38.8 kcal/mol, which agrees well with work done by others. The results are promising for the development of an economically attractive fluid bed process.

Fluid bed pyrolysis of silane involves the heterogeneous decomposition of silane gas on hot silicon seeds to produce free-flowing particles of silicon. The method offers the potential for converting high purity silane into pure, low cost silicon that is directly processable using Czochralski or ribbon growth technology for photovoltaic application.

Under the sponsorship of the Jet Propulsion Laboratory, Union Carbide is currently engaged in the design of a first-generation fluid bed silane pyrolysis development unit. This development effort was initiated after a preliminary assessment of the technology indicated that the process has an economically attractive potential for the production of low cost silicon. However, a sustained development effort is required to demonstrate the technical feasibility of the fluid bed process. In order to assemble a suitable design of the process development unit, it was determined that important data were required on permissible silane feed concentrations, deposition rates, and silicon product morphology. A review of pertinent literature revealed that data on critical silane concentration, above which unfavorable homogeneous decomposition occurs, were available only at high temperatures in the range 800°-1100°C. For economical operation of the fluid bed reactor, temperatures in the 600°-700°C range are pre-

Key words: production of silicon, silane decomposition, heterogeneous decomposition, fluid bed reactor.

ferred since silane feed concentration can be higher at lower temperatures. Thus the cost of recycling hydrogen for diluting the feed is less at lower temperatures. Also, literature data on plating rates were available only for epitaxial deposition, and no information was available on growth of irregularly shaped particles. Furthermore, there was some question as to whether a dense and coherent deposition morphology could be obtained in the temperature range of interest.

In order to obtain the above design information with a modest expenditure of time and effort, it was decided to conduct silicon deposition experiments in a small-scale fixed bed reactor. The specific objectives of the fixed-bed experiments were to: (*i*) identify bed temperatures and silane feed concentrations which favor heterogeneous decomposition and suppress the homogeneous mode; (*ii*) determine the heterogeneous decomposition rate of silane, and (*iii*) obtain a qualitative description of the deposition morphology.

Experimental Procedure

Apparatus.—The experimental apparatus, shown in Fig. 1, consisted of a quartz reactor with an internal diameter of 1 in. The bed of silicon particles was contained in a 0.78 in. ID quartz liner inserted into the reactor. The liner was used to protect the reactor in the event the silicon bed became plugged during a run. Packed bed height ranged from 4 to 6 in. for decomposition mode experiments, and was held fixed at 2.5 in. for kinetic rate experiments. Three thermocouples, one each in the top, middle, and bottom portions of the bed, were used to measure the temperature. Bed heating was accomplished by inductive coupling on a metal sleeve surrounding the quartz reactor. The sleeve extended ¼ in. above and below the silicon bed. End effects were countered by concentrating heat input at the ends by adjusting the coil pitch. It was, therefore, possible to obtain a nearly uniform temperature distribution through the length of the packed bed. Temperature variation from top to bottom of the bed during kinetic experiments was typically of the order of 10°C. A 5 kW, 455 kHz generator was used for the induction power source. The gas exiting the silicon bed was cooled by a cooling coil wrapped around the bottom part of the reactor. Such cooling ensured that undecomposed silane leaving the bed during kinetic rate experiments did not react on the reactor wall.

A mixture of hydrogen and 20% silane, together with hydogen used for further diluting the feed gas, and helium used for purging was stored in cylinders in a secure, well-ventilated shed located outside the experimental area. All cylinders were properly valved and pressures were regulated to suitable levels before the gases were brought to the reactor vicinity. Pressure relief valves were provided in all the gas lines. The gases were passed through 0.6 micron filters and check valves were provided in the lines to prevent reverse flow. The gas flow rates were controlled by hand needle valves and monitored by rotameters. A gas mixing chamber filled with glass beads was provided to ensure proper mixing of the feed gases to the reactor. The pressure drop across the reactor and reactor filter was measured, and the reactor exit stream was cooled and directed to a burner for safe disposal. A sample from the exit gas was sent to a Gow-Mac thermal conductivity cell to monitor silane concentration in the stream.

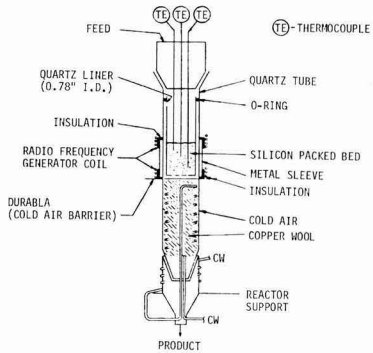

Fig. 1. Fixed bed reactor

Silicon preparation.—The silicon used to make up the bed particles was obtained by crushing 3 in. diam rods produced by chemical vapor deposition. The ground particles were screened to a size in the range of 1190-2000 microns, giving an average particle size of 1595 microns. Initial experiments on the mode of silane decomposition were conducted using the above particles. Later in the experimental program, in an attempt to control fibrous growth, the crushed silicon particles were washed first with hot hydrochloric acid for 30 min to remove metallic impurities introduced by crushing. The particles were then etched with a mixture of acetic acid, nitric acid, and hydrofluoric acid in the ratio 1:1.5:1, respectively. To prevent excessive reaction, the etch duration was limited to about 2 min, which resulted in a 10-12% weight loss in the silicon sample. The particles were then washed with deionized water followed by a wash with methanol. Since the use of silicon particles prepared in the above manner resulted in a reduction of surface fiber growth, all further experiments, including the kinetic rate experiments, used etched particles.

The etching procedure reduced the total metallic impurities in the silicon from 48 to 5 ppm, as determined by induction coupled plasma emission spectroscopy. The etching step also resulted in a reduction in particle size to a surface-average diameter of 1509 microns.

The poured and tapped bulk densities of the etched silicon were determined to be 1.14 and 1.27 g/cm^3, respectively. The void fraction was calculated to be 0.51 (poured) and 0.46 (tapped). The surface area of the etched particles was measured by BET method using krypton at −196°C, and found to be 0.20 m^2/g.

Test procedure.—The silicon bed was heated to the desired temperature and the desired flow rates of feed gases were established through the reactor. Concentration of silane in the feed and effluent streams was measured. The pressure drop across the bed was monitored continuously throughout the run. The desired run duration was typically 30 min for decomposition mode experiments, unless the bed started to plug up with fine powder, in which case the run was terminated immediately. After the completion of the run, the bed of particles was poured from the quartz liner and visually examined. A sample from the bed was also examined with a scanning electron microscope. The microscope pictures showed powder if the reaction was homogeneous, and no powder if the reaction was heterogeneous. By mounting and polishing the particles into cross sections, the microscope also revealed the deposition morphology. The above experiments covered a temperature range of 600°-900°C.

For decomposition rate experiments, a typical run duration was 10 min. The rates were measured by noting the reduction in silane concentration as the gas stream passed through the packed bed held at a specified temperature. At each bed temperature, runs were conducted at several flow velocities. The rate data were obtained at 576°, 627°, and 676°C.

Discussion of Results

Mode of decomposition and deposition morphology.— A number of experimental runs was conducted on the mode of decomposition. These experiments covered silane feed concentrations in the range 0.5-20 mol percent (m/o) and bed temperatures in the range 600°-900°C. Each run was made at a predetermined temperature and silane concentration, and the result of that run was then interpreted as either homogeneous or heterogeneous decomposition, depending on the presence or absence of fine powder in the bed. Because of this procedure, the distinction between homogeneous and heterogeneous decomposition appears as a band instead of a line in Fig. 2, which presents the data as a relation between silane feed concentration and bed temperature. The two lines connecting the solid and open circles in the figure constitute the boundary of a band that separates the homogeneous and heterogeneous decomposition regions. The critical silane concentration curve above which gas phase, homogeneous decomposition predominates, lies within this band. For instance, the critical silane concentration is between 1.5 and 5% at 800°C and between 10 and 16% at 700°C.

Data obtained by Eversteijn (1) and by Murthy *et al.* (2) in horizontal epitaxial reactors at higher temperatures are also shown in Fig. 2 for comparison. Critical concentration curves in these two cases were determined by gradually increasing the silane concentration in a constant temperature reactor until powder was visually observed. It may be seen that at any temperature, the critical silane concentration determined by the above investigators differs from each other by an order of magnitude even though both of them used analogous reactor systems.

Most of the initial experiments in the current work were conducted using a packed bed of high purity, unetched silicon particles. Data on the mode of decomposition for these particles appear to agree well with the extrapolation of data points obtained by Murthy *et al.* Scanning electron micrographs of these particles after deposition showed fibrous growth to be dominant. Figure 3A shows fine powder, whereas Fig. 3B is a typical illustration of fibers. Some nodular growth, which is the preferred morphology, was also

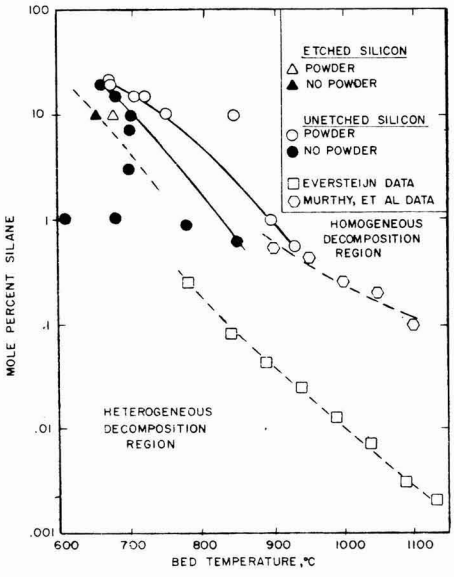

Fig. 2. Temperature dependence of critical silane concentration

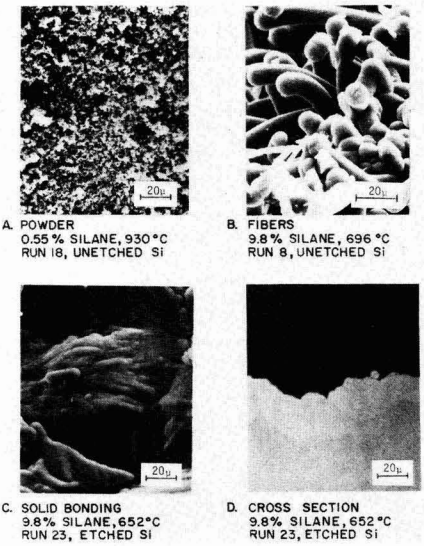

Fig. 3. Scanning electron microscope and photomicrograph pictures of silicon particles.

observed, but fibers were predominant. In the experiments it was observed that at a fixed silane feed concentration, the fibers became smaller in diameter as the decomposition temperature was increased. If the temperature was well into the homogeneous region, the fibers eventually disappeared and fine powder was formed.

Pressure drop across the silicon bed was usually a good indication of the type of decomposition and the deposition morphology. Figure 4 shows pressure drop across the bed during typical experimental runs. In run 22, the rapid increase in the pressure drop indicated immediate generation of large quantities of fine powder. When the deposition on particle surface was fibrous, as in run 8, the rise in bed pressure drop was more gradual. This is verified by the scanning electron micrograph in Fig. 3B, which shows fibrous growth.

After many tests with unetched silicon particles which showed predominantly fibrous growth, it was suspected that metallic impurities on the particle surfaces were providing nucleation points for fiber growth and, if the surfaces were clean, fibers could be eliminated. Recent work by Osada *et al.* (3) tended to confirm the thought that fibers were caused by metallic impurities on the particle surface. To test this hypothesis, a sample of high purity silicon was acid-

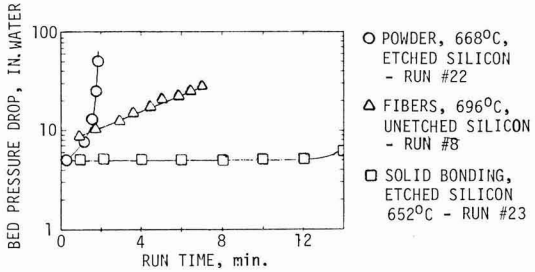

Fig. 4. Packed bed pressure drop curves with etched and unetched silicon for 9.8% silane, different decomposition modes.

washed and etched as described earlier. Tests with etched silicon did, indeed, result in particles with a dramatic reduction in fiber growth. This is illustrated in the scanning electron microscope picture 3C. Figure 3D shows the polished cross section of a silicon particle from the above experiment. The deposition was dense, firmly attached to the particle surface, and averaged about 25 microns in thickness. This is the type of silicon plating that is most desirable in a fluid bed pyrolysis reactor. As shown in Fig. 4, the pressure drop across the bed was constant in time when there was dense growth on etched silicon particles (run 23).

In the decomposition experiment using etched silicon particles, a feed silane concentration of 9.8 m/o was used. Powder formation was observed at 701° and 668°C; however, at 652°C no powder was formed, as illustrated in Fig. 2. Previous tests at the same silane feed concentration using unetched silicon particles had indicated no powder formation at 696°C. Thus the operating temperature for heterogeneous decomposition using high purity, acid-washed and etched silicon particles was lowered by 44°C compared to the case with unetched particles. No further experiments were conducted on the decomposition mode; the lower boundary of the band separating homogeneous and heterogeneous regions was estimated by drawing a line parallel to the one obtained for unetched particles.

In the above experiments, it was possible for a small portion of the incoming silane to have deposited on the reactor wall approximately ¼ in. above the top of the packed bed. However, since the surface area of the wall was substantially smaller than that of the particles, depletion of the feed silane before reaching the bed was considered to be negligible.

Heterogeneous decomposition rate.—The decomposition of silane into silicon and hydrogen is an irreversible reaction whose rate becomes significant at temperatures above 400°C. In the present work, kinetic rate measurements were conducted at 576°, 627°, and 676°C. The data were correlated by a first-order rate equation.

The integrated form of the rate equation for a first-order irreversible reaction in a plug flow reactor for a system of changing density is given by Levenspiel (4), as follows

$$kT = -(1 + \epsilon_A) \ln (1 - X_A) - \epsilon_A X_A \qquad [1]$$

where k = reaction rate constant, sec^{-1}; T = space time, sec; ϵ_A = fractional change in system volume between no silane conversion and complete silane conversion; X_A = fractional conversion of silane = $(C_{A_0} - C_A)/C_{A_0}$; C_{A_0} = mol percent silane in feed; and C_A = mol percent silane in effluent. A plot of the right-hand side of Eq. [1] *vs.* T will result in a straight line of slope k for data points at constant temperature. As shown in Fig. 5, the current data fit well with the first-order rate Eq. [1].

Equation [1] assumes that true plug flow existed in the reactor. This implies that while lateral mixing is permissible, there can be no mixing or diffusion along the flow path. In Fig. 6, the normalized reactor effluent concentration (5) is plotted against kT. If there is no deviation from plug flow, the slope of the least-squares regression line will be −1 and the intercept will be 1. From the current data plotted as shown in Fig. 6, the slope is equal to −1.0033 and the intercept is equal to 1.0047. This is a good fit and verifies that for the range of conditions of the current tests, there is no diffusional effect and plug flow is a valid assumption.

The rate measurements showed no dependency on either feed composition or flow velocity, within the range of current experiments that covered silane concentrations from 5 to 10% and feed superficial velocities from 0.4 to 1.3 ft/sec. The reaction rate constants at

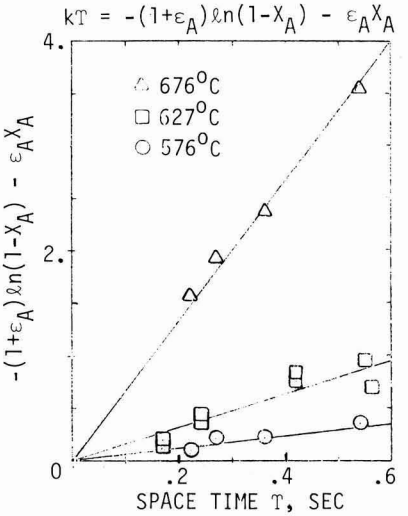

Fig. 5. Plot of first-order rate data for silane decomposition in a packed bed of silicon particles.

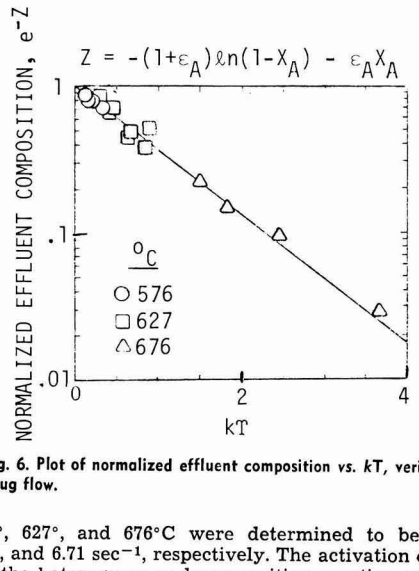

Fig. 6. Plot of normalized effluent composition *vs.* kT, verification of plug flow.

576°, 627°, and 676°C were determined to be 0.585, 1.55, and 6.71 sec^{-1}, respectively. The activation energy for the heterogeneous decomposition reaction was determined by plotting ln k vs. $1/T$ as shown in Fig. 7. The calculated activation energy is 38.8 kcal/mol, which is close to the value of 37 kcal/mol reported by Eversteijn and Put (6). Based on the current experiments, the rate constant for the decomposition reaction may be written in the Arrhenius form

$$k = 5.14 \times 10^9 \exp(-38{,}800/RT) \qquad [2]$$

Figure 8 shows a plot of silicon growth rate in microns per minute per percent silane plotted as a function of temperature. Data points from the current work compare well with the results obtained by Eversteijn and Put (6) from epitaxial deposition.

Conclusions

The current work has identified feed silane concentrations and bed temperatures favorable for heterogeneous decomposition of silane in a packed bed reac-

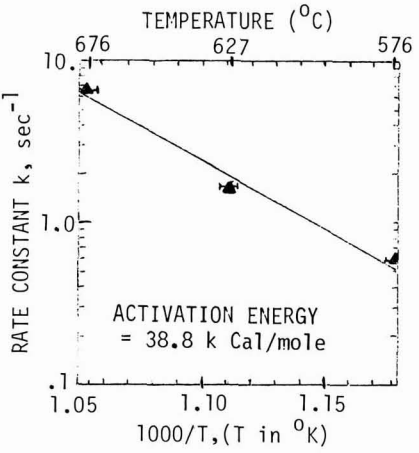

Fig. 7. Arrhenius plot of first-order reaction rate constants

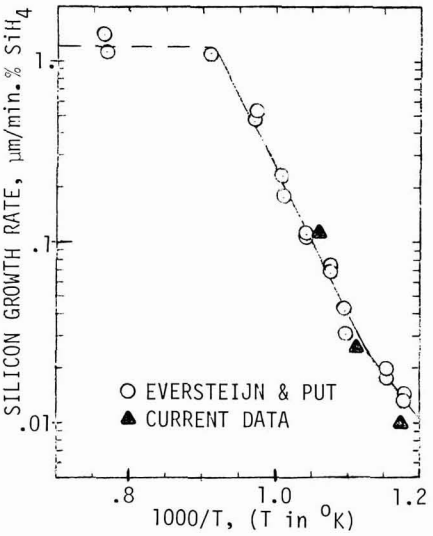

Fig. 8. Silicon growth rate as a function of temperature

tor. It has also shown that deposition morphology is significantly influenced by the purity of the silicon particle surface. Acid-washed and etched high purity silicon particles yield dense growth. The decomposition rate measurements have shown the reaction to be first order, with an activation energy of 38.8 kcal/mol, within the range of current experimental conditions.

Based on the above conclusions, it is recommended that fluid bed silane pyrolysis work should utilize a starter bed of acid-washed and etched high purity silicon. A good operating point for the pyrolysis reactor is 10% silane feed concentration and a bed temperature in the vicinity of 640°C. Under these conditions, the decomposition should be primarily heterogeneous, the reaction rates should be sufficiently high so that complete silane conversion can be expected in a small fluid bed, and the deposition morphology should be dense and coherent.

Acknowledgment

The authors gratefully acknowledge support for this work by the Jet Propulsion Laboratory, California Institute of Technology, Pasadena, California, under Contract No. 954334.

Manuscript submitted Aug. 14, 1981; revised manuscript received Dec. 3, 1981.

Any discussion of this paper will appear in a Discussion Section to be published in the June 1983 JOURNAL. All discussions for the June 1983 Discussion Section should be submitted by Feb. 1, 1983.

Publication costs of this article were assisted by the Union Carbide Corporation.

REFERENCES

1. F. C. Eversteijn, *Philips Res. Rep.*, **26**, 134 (1971).
2. T. V. M. S. Murthy, N. Miyamoto, M. Shimbo, and J. Nishizava, *J. Cryst. Growth*, **33**, 1 (1976).
3. Y. Osada, H. Nakayama, M. Shindo, T. Odaka, and Y. Ogata, *This Journal*, **126**, 31 (1979).
4. O. Levenspiel, "Chemical Reaction Engineering," 2nd ed., John Wiley & Sons, Inc., New York (1972).
5. G. E. Raines and T. E. Corrigan, *Chem. Eng. Prog. Symp. Series*. No. 72, **63**, 90 (1967).
6. F. C. Eversteijn and D. M. Put, *This Journal*, **120**, 103 (1973).

An Experimental Study of Motion of Electrons and Holes in Y_2O_2S Crystal as Revealed by Cathodoluminescence

Lyuji Ozawa*,[1]

Zenith Radio Corporation, Glenview, Illinois 60025

ABSTRACT

The average migration distance (L) of radiation-induced carriers in Y_2O_2S insulator, under no externally applied field, has been studied by measuring the inflection points of the concentration dependence curve of activator luminescence and crystal sizes. A quasi-one-directional migration of free carriers, for which the relationship $L = dC^{-1}$, is inferred from the experimental results.

Electron beam irradiation of crystals creates plasma electrons (1) (*i.e.*, incident electrons plus internally generated secondary electrons) and pairs of electrons and holes (EH's) (2) (*i.e.*, radiation-induced carriers) in the volume in which the incident electrons have penetrated. The EH's can move out from the place in which they are created. Under irradiation by an electron beam of phosphor crystals, therefore, the ac-

* Electrochemical Society Active Member.
[1] Present address: Central Research Laboratories, Chicago, Matsushita Electric Industrial Company, Limited, Franklin Park, Illinois 60131.
Key words: luminescence, phosphor, photoconductor.

tivator ions in crystals are excited directly by the plasma electrons, resulting in a weak cathodoluminescence (CL), and/or indirectly through mobile EH's, giving rise to an efficient CL. If the activator ions are excited by mobile EH's, the number of the directly excited activator ions (in the penetration volume) by the plasma electrons is negligibly small (less than 1%) and activator ions are predominantly excited by mobile EH's. Hence, the radiative recombination of EH's at activator ions in the phosphors is a major concern in the discussion of the efficient CL. However, the mechanism of the efficient CL in phosphors is not clearly understood because of the vagueness of the motion of EH's in phosphor crystals under no externally applied field. One experimental difficulty in determining the motion of EH's in the crystals, which are placed under no externally applied field, is the lack of any internal detector of the motion of the mobile EH's in the highly insulated phosphor crystals. Then, three-dimensional spreading of EH's has been assumed under the conditions of no applied field. Several attempts to explain the CL mechanism, based on three-dimensional spreading of EH's, have been made in the last several decades (3). They are not able to explain satisfactorily all of the experimental results (*e.g.*, linear, sublinear, and superlinear dependence of CL on the exciting intensities and on activator concentrations). Thus a clarification of the motion of EH's in phosphor crystals is an essential necessity to discuss cathodoluminescence.

Recently, it has been shown that the activator luminescence can be used as a good internal detector of EH's (4, 5). The activator ions are uniformly distributed in the crystal and never move out of their positions under ordinary conditions to generate EH's in crystals. For the excitation of activator ions, the activator ions must be visited (or sampled) by EH's that are traveling in the crystal. Hence, the activator ions which are distributed randomly on cation sites and emit a characteristic luminescence when excited are good internal detectors of the motion of EH's, and the various aspects of the motion of the mobile EH's can be revealed by studying the activator luminescence as a function of concentration of the activator ions [*i.e.*, the concentration dependence (CD) curve of the activator luminescence]. In this report, we shall try to figure out, as a first-order approximation, a motion of EH's in Y_2O_2S by measuring the inflection points of the CD curves of the particular activator CL as a function of the median crystal sizes (ϕ_M).

In CL study, we usually measure the time-averaged activator luminescence intensity, $\langle I \rangle$, which is given by a result of the volume integral of the action of EH's to activator ions in the finite crystal volume and unit time (4). In order to obtain a mathematical solution of the volume integral, we must know the physical properties such as the capture cross section of activator ions, mobility of the carriers, charge density, charge distribution in the crystal, and so on. We do not determine the physical properties because of the difficulty of obtaining the single crystals of the phosphors, and within a limitation of our knowledge, there are no available data regarding the physical properties of the carriers in the rare earth phosphors. We measured $\langle I \rangle$ as the total results of the action of the EH's to activator ions in the crystal and in unit time under the given excitation conditions, regardless of the details of physical properties. In the analysis of the results of $\langle I \rangle$, therefore, one may be allowed to draw a macroscopic (instead of a microscopic) picture of the motion of EH's. Although it is the macroscopic picture, a quasi-one-directional migration of EH's in the crystal, under no externally applied field, can be inferred from the experimental results of $\langle I \rangle$.

Experimental Results

The average migration distance (L) of EH's in the tiny crystals of Y_2O_2S, which were distributed in log-normal distribution (6), has been studied by measuring the CD curves of $\langle I \rangle$ of CL from the screens. The preparation of the samples of Y_2O_2S (6) and the measurements of $\langle I \rangle$ of CL (7) have been reported in the previous publications. The measurements of $\langle I \rangle$ were made on the phosphor screens. In the screen, $\langle I \rangle$ is proportional to the number of quanta emitted from the excited activator ions in the crystals on the screen in unit time. The screen is usually large (*e.g.*, 1 cm^2) compared with the crystal size (*e.g.*, about 10 μm). In such a screen, the excitation of activator ions only occurs in the crystals in the first layer of the irradiation side because the penetration depth of the incident electrons (10 kV) is about 0.4 μm (8), and EH's are never transferred to other crystals [the crystal is covered with surface recombination centers of EH's (9)]. When the size of the electron beam on the screen is kept constant for all measurements (it is usually so), $\langle I \rangle$ is proportional to the number of the excited activator ions in one crystal on the screen in unit time. Thus, we can take account of $\langle I \rangle$ as the results of the action of EH's to activator ions in one crystal (in the median size) laying on the screen.

We assume that EH's in the crystal can be moved out from the volume in which they are created, and that the migration of an EH terminates on the first visit to an unexcited activator ion; the average migration distance of EH's increases as activator concentration (C) decreases. Thus the CD curve should be inflected (*i.e.*, have a discontinuity in the curve) at the activator concentration C^* corresponding to the average migration distance which is of the order of the crystal size (*i.e.*, $L = \phi_M$). Therefore, when the activator ions are distributed randomly on cation sites, and there is no energy transfer between activator ions, the relationship between the L of the first-trapped carriers (electrons or holes) and activator concentration can be studied by using the crystal size and activator concentration C^* of the CD curve; L is equal to the crystal size ($L = \phi_M$) at C^*. (It should be noted that the experimental value L is only average migration distance because L is determined from the crystal size; in the present case, there is a log-normal distribution of crystal size of Y_2O_2S phosphor, *i.e.*, the crystals are not all the same size and ϕ_M is the median size of the crystals.)

The inflection of the CD curves plotted on a logarithmic basis can be observed when the measurements are carried out in the wide C range, including the area in which the concentration quenching mechanisms are involved (*e.g.*, 10^{-6} to 5×10^{-1} mol fraction). However, many reported CD curves are not studied in the entire C range mentioned above; the CD curves studying for the analytical purpose (10) were made in the wide C region but below C^* where $\langle I \rangle$ was proportional to C, and for the determination of the optimum activator concentration which was of practical interest, the measurements were carried out in the C region above C^*. In both cases, one could not observe the inflection of the CD curves.

Y_2O_2S offers us a favorable case to study because the motion of both electrons and holes in the crystal can be detected separately by their Eu^{+3} and Tb^{+3} luminescence and because microcrystals of different sizes can be prepared (6). The study, however, is complicated by the fact that the value of C^* of the given crystal size of Y_2O_2S:Eu differs greatly with the excitation mode [*e.g.*, d-c and pulse excitation (4)]. For instance, the value of C_p^*, for 1 μsec pulse excitation, of Y_2O_2S:Eu (3 μm) is 1×10^{-4}, whereas the value of C_D^*, for d-c excitation, is 2×10^{-3} (20 times greater). A set of CD curves showing a pulse width effect on the value of C^* is given in Fig. 1; the CD curves covering short pulse excitation to d-c excitation were obtained with a constant peak intensity at repetition of 16.7 msec in the C region from 2×10^{-5} to 1×10^{-2}. It may be seen that for pulse widths shorter than 2 μsec, the

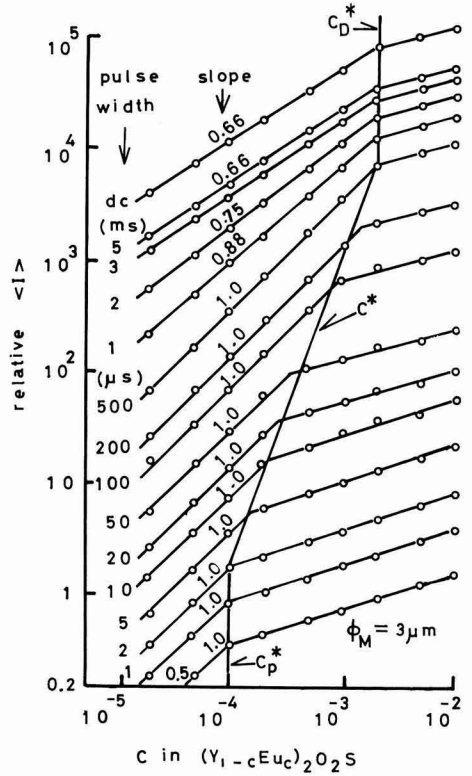

Fig. 1. Concentration dependence curves of time-averaged Eu^{+3} ($^5D_0 \rightarrow {}^7F_2$) luminescence intensities of Y_2O_2S:Eu ($\phi_M = 3\ \mu m$) under irradiation of various pulse widths of electron beam.

value of C_p^* is independent of activator concentration and remains at $C = 1 \times 10^{-4}$; the value of C_p^* is not influenced by the excitation intensity. For pulse widths longer than 500 μsec, the value of C_D^* also stays constant, but $C = 2 \times 10^{-3}$ and is influenced by the excitation intensity; the value of C_D^* increases as the excitation intensity increases. The transition from C_p^* to C_D^* (*i.e.*, C^*) occurs in the pulse width range between 2 and 500 μsec.

The above results allow us to use the value of C_p^* for the study of the relationship between L of the EH's and C. Tb is used to detect hole migration and Eu is used for electron migration (4). Figure 2 shows the

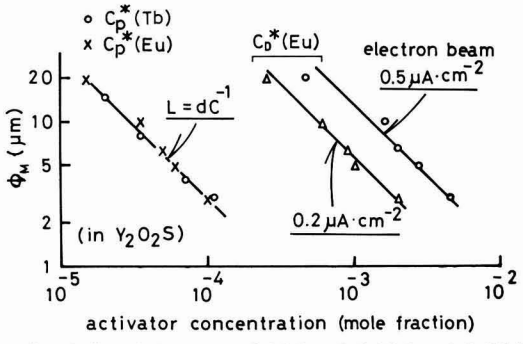

Fig. 2. Crystal size ϕ_M *vs.* C_p^*(Tb) and C_p^*(Eu), and C_D^*(Eu) obtained under two different beam densities: 0.2 and 0.5 μA/cm².

experimental curves of ϕ_M ($= L$) *vs.* C_p^*(Tb) and C_p^*(Eu), together with C_D^*(Eu) for two different intensities of the excitation (0.2 and 0.5 μA/cm²). ϕ_M is the median crystal size, which is determined from the sedimentation weight method ($\phi_M \pm 0.5\ \mu m$). It can be seen that the values of C_p^*(Tb) and C_p^*(Eu) fit a straight line, which is expressed as

$$L = dC^{-1} \qquad [1]$$

where d is the distance between the nearest cations (Y-Y); $d = 3.5$Å for Y_2O_2S. Because the migration distance of electrons and holes is expressed by Eq. [1] and the activator luminescence substantially arises from the recombination of EH's at activator ions, and for general reasons, we use the term EH instead of the term "first-trapped electron" (or hole) in the following discussion, even though the recombination process is determined by the first-trapped carriers at activator ions.

Discussion

The experimental results in Fig. 1 and 2 show that the values of C^* and slopes of the CD curves of Y_2O_2S:Eu in the same crystal size are changed with the conditions of the excitations. There is an explanation for the different values of C^* by the change in the ratio of the surface area to the volume of the crystals in the different sizes (11), but this is not the present case. The values of C^* are changed with the pulse widths (instead of the crystal sizes) even though the ratio of the surface area to the volume maintain constant (with the same crystal size). In order to explain the experimental results, we shall discuss the following: (*i*) the quasi-one-directional migration of EH's; (*ii*) the pulse width effect on C^*; and (*iii*) the nature of the carriers. It should be noted that as already mentioned. the discussion made from the results of $\langle I \rangle$ only allow giving a first (or zero) order approximation of the motion of the EH's. For a microscopic picture, we must study further the physical properties of the carriers and activator ions in the single crystal, but we only study the time-averaged-luminescence intensities on phosphor crystals in a log-normal distribution.

Quasi-one-directional migration of EH's.—Using activator luminescence as the internal detector, we have experimentally studied the migration distance of EH's in highly insulated crystals (the resistivity being greater than 10^{10} Ω-cm) under no externally applied field, which is difficult to study with other techniques. We have found experimentally the relationship $L = dC^{-1}$ for the migration of the carriers in Y_2O_2S. An explanation of this result is given below.

We assume that the migration of an EH is terminated on the first visit to an unexcited activator ion. Because C^{-1} is the average number of cations per activator ion, dC^{-1} is in accordance with the average length $\bar{l}$ "walked" by the EH before the EH is trapped at the unexcited activator ion. The relation of $L = \phi_M = \bar{l} = dC^{-1}$ can be interpreted as the average distance of the migration of the EH's is equal to the average length walked by one EH, giving rise to the relationship $L = \bar{l}$. Therefore, the migration of each EH terminates at the activator ion arranged on one-directional line of cations. Thus, a quasi-one-directional migration of EH's is deduced from the experimental results of $\langle I \rangle$.

This is a significantly different viewpoint from the three-dimensional migration. In the three-dimensional case, the average displacement $\bar{l}_{3D}$ of the EH is given by the edge of the volume containing one activator ion (the number of cations in the volume is given by dC^{-1}), and $\bar{l}_{3D} = dC^{-1/3}$, even as the average walked-length of the EH is given by dC^{-1}. Thus the three-dimensional migration distance L_{3D} ($= \phi_M$) is not equal to $\bar{l}_{3D}$ and should be proportional to $dC^{-1/3}$, *i.e.*, $L_{3D} = k_1 dC^{-1/3}$, but this is not observed.

The results of the quasi-one-directional migration of EH's in the crystal, under no externally applied field, indicate that the migration of EH's is not by the random walk (5); for one-directional migration, EH's must be under a driving force that is generated internally in the crystal. The internal driving force may be related to the electric field created by one or combination of (*i*) the static field produced by the impurities or by the electric charges trapped at the chemical impurities (including activator ions) and at the crystal defects; (*ii*) the gradient field produced by the charges and/or thermal distribution induced by irradiation of electron beam (12); and (*iii*) the charges created in the surface volume of the crystal as a consequence of the ejection of the true secondary electrons from the crystal (13). However, these are not yet clearly understood. Further study may prove an interesting subject.

Pulse width effect on C.*—The values of C^* of Y_2O_2S:Eu in the same crystal size are changed with the pulse widths of the electron beam (Fig. 1). For the explanation of these experimental results, the kinetic model (11) is incompetent because of the same crystal size. The dependence of C^* on the pulse widths is probably related to (*i*) the lifetime of the excited activator ions; (*ii*) the number of activator ions in the domain (as defined afterward); (*iii*) the random sampling of the domains by EH's; and (*iv*) the correlated migration of EH's. We shall discuss these below.

Lifetime of the excited activator ions.—A statistical description of the lifetime of the excited activator ions is as follows. Each excited activator ion emits a photon after remaining (holding) for sometime in its excited state (*i.e.*, lifetime) and returns to the ground state. The holding time of many excited activator ions in the crystal is not constant and it likely follows the general rule of holding time, *i.e.*, a Bernoulli distribution in which the probability density $G(t)$ is given by

$$G(t) = \lambda e^{-\lambda t} \qquad [2]$$

Therefore, the distribution function $g(t)$ is given by

$$g(t) = e^{-\lambda t} \qquad [3]$$

where λ is a constant and, for luminescence, is given by $1/\tau$ where τ is average lifetime as computed from

$$\tau = \int_0^\infty e^{-t/\tau}\, dt \qquad [4]$$

τ is related to $1/A$ where A is Einstein coefficient.

The decay curve of the $^5D_0(Eu^{+3})$ luminescence from Y_2O_2S:Eu under pulsed cathode ray excitation holds Eq. [3] and $\tau = 500$ μsec (τ is determined at $1/e$ of the maximum intensity). Since 99.999% of the Eu^{+3*} in the excited state returns to the ground state (Eu^{+3}) in 5 msec, it can be said that at the repetition rate of 16.5 msec, almost all of the Eu^{+3*} excited by the EH's created by one pulsed electron beam of 10 msec pulse width return to the ground state before (the migration of the EH's created by) the next electron pulse starts. This leads to the experimental results of Fig. 1, obtained with pulse width shorter than 10 msec: $\langle I \rangle$ is proportional to the number of the excited activator ions by the EH's (*i.e.*, the outcome of the trials of the EH's) created by a single pulse of the electron beam. For this reason, the discussion on $\langle I \rangle$ of Fig. 1 will deal with the statistical outcome of the trials of the EH's created by a single electron beam pulse shorter than 10 msec in the crystal.

Number of activator ions in domains.—To compute this, we take account of a crystal cube equal to the crystal size ϕ_M. In this cube, $\phi_M = L = d/C_p^*$ and the number of cations on the cube edge is given by

$$\frac{L}{d} = \frac{1}{C_p^*} \qquad [5]$$

We assume that the direction of the forward migration of EH's coincides with that of the incident radiation (because the total area of the one side of the crystal is uniformly irradiated with electron beam), and the first cation on the incident plane begins the one-directional line of cations. The length of the line is limited by the crystal size. We shall hereafter call this crystal-size-limited line of cations the "domain." Hence, $(1/C_p^*)$ domains can be arranged in any plane parallel to the migration direction, and $(1/C_p^*)^2$ available domains can be arranged in the cube crystal.

The value of $(1/C_p^*)^2$ is also in accordance with the number of activator ions in the crystal cube and each domain, of the length $\phi_M = d/C_p^*$, statistically contains one activator ion. It follows that each domain always contains more than one activator ion when $C > C_p^*$. In contrast, when $C < C_p^*$, the number of activator ions in the crystal is less than the number, $(1/C_p^*)^2$, of available domains; some domains contain no activator ion and others contain only one activator ion each. Thus there are two entirely different situations of the domains containing activator ions, depending on whether $C > C_p^*$. This calculation shows that the inflection point of the CD curve may not be simply related to the saturation of the excited activator ions (5).

Random sampling of domains by EH's.—The probability that the number of the EH's migrating in a specified domain during the lifetime of the excited activator ions, under the ordinary CL excitation conditions, can be computed as follows. The migration process of carriers on the lattice sites is a Markov process; the lattice site that has released the carrier to the next lattice site is ready to receive other migrating carriers because the lattice site has no previous history (*i.e.*, statistical independence). This suggests that each EH has a statistically independent migration in the domains. This means that the EH's can migrate in the same domain, although not at the same time. Thus the possible number of simultaneously coexisting EH's in the crystal may be greater than the number of the domains calculated as $(1/C_p^*)^2$ ($= 10^9$ EH's for 10 μm crystal). As an extreme case, the maximum number of the coexisting EH's in the crystal is equal to the number of cations in the crystal and is computed to be $(1/C_p^*)^3$, or about 10^{13} for 10 μm crystal. This large number is for EH "droplets" but it is far from the actual number of CL conditions; the number of EH's created by the ordinary CL conditions (10 kV, 1 μA/cm^2 beam in 500 μsec for 10 μm crystal) is about 10^7 EH's indicating that EH's in the crystal are better described as EH "gas." (It can be said that the excitation conditions of ordinary CL are far from the saturation for EH's creation.) The calculated results suggest that the EH's should migrate randomly in the domain, *i.e.*, a random sampling of the domains by EH's. The probability that an EH randomly migrates in a specified domain during τ is computed as $10^7/10^9 = 10^{-2}$; therefore, the probability that two EH's randomly migrate in the same domain during τ is given by $(10^{-2})^2 = 10^{-4}$ which is negligibly small for consideration. Accordingly, it can be said that each domain may have one EH during τ if the domains are randomly sampled by the EH's. In this case, L of EH's is equal to $\bar{l}$ walked by one EH, and the relationship $\phi_M = L = \bar{l}$ retains for all the pulse widths. Consequently, $C_p^* = C^* = C_D^* = d/L =$ constant for a given crystal, and the value of C^* exhibits no pulse width effect. This has been observed Y_2O_2S:Tb (the hole migration in Y_2O_2S).

Correlated migration of EH's.—In the case of Y_2O_2S:Eu (detecting the electron migration), however, $C_D^* \neq C^* \neq C_p^*$. The values of C^* are changed with the pulse width (Fig. 1), and the curve of C_D^* *vs.* ϕ_M are simply shifted, in parallel with the curve of $L = dC^{-1}$, to high activator concentration as the excitation intensity increases (Fig. 2). These results indicate that the ran-

dom sampling of the domains by EH's is not applicable to the electron migration in Y_2O_2S.

The results in Fig. 2 show that the linear relationship between the average migration distance and the values of C_D^* is held for the d-c excitation at the various excitation intensities, indicating that the quasi-one-directional migration of EH's is thoroughly retained for the d-c excitation. Therefore, the shift of the values of C_D^* (and C^*) with the excitation intensities is possibly due to the increase in the number of EH's, which have the quasi-one-directional migration, in the same domain during the lifetime of the excited activator ions. In other words, the domains may have EH's more than one during the lifetime of the excited activator ions. If this is true, the EH generated recently in the pulse duration selectively (rather than randomly) migrates in the domain in which the previous EH's have been migrated (*i.e.*, a correlated migration).

To estimate the number of the correlated EH's migrating in the same domain during the pulse duration, we assume one activator ion is excited only once in its lifetime (*i.e.*, activator ion in an excited state is no longer acting as the recombination center of EH). We also assume that when the n EH's migrate in the same domain at different times during the single pulse duration, the walked length of the first migrating EH is calculated as $\bar{l} = d/C^*$, and the walked length of the nth EH is n times of the $\bar{l}$ ($= n\bar{l}$). Accordingly, at C^* the crystal size ϕ_M is no longer equal to $\bar{l}$ but is equal to the migration length walked by the last EH (*i.e.*, $\phi_M = n\bar{l} = nd/C^* = d/C_p^*$). Under the above assumptions, we estimated the experimental number of the EH's, which migrate in the same domain using the equations of

$$C^* = nC_p^* \quad \text{or} \quad n = \frac{C^*}{C_p^*} \qquad [6]$$

C_p^* is constant for a given crystal, so that C^* increases as n increases.

Figure 3 shows the experimental curve of n ($= C^*/C_p^*$) as a function of the pulse widths of the electron beam. The data are replotted from Fig. 1. It can be seen that for the pulse widths shorter than 2 μsec, only one EH migrates in the same domain (*e.g.*, $n = 1$), giving rise to C_p^*. The value of n increases with increasing pulse widths longer than 2 μsec, and gives rise to the observed value of C^*.

In reality, the length of the recently migrating EH during the pulse duration longer than the lifetime of the excited activator ions might be slightly complicated. For pulse widths longer than the lifetime of the excited activator ions (*e.g.*, longer than 10 μsec), some excited activator ions are de-excited and they have a chance of the re-excitation by the recently migrating EH's. In this case, ϕ_M should be equal to the longest length walked by the EH in the domain under the equilibrium conditions between excited and de-excited activator ions. The longest time interval for the equilibrium is likely the average lifetime τ ($= 500$ μsec), where τ is of course a constant for the given phosphors. Therefore, the value of C^* is no longer dependent on the pulse widths longer than τ and remains a constant, equal to C_D^*. The values of C_D^* and C^* shift to higher C as the excitation intensity increases (Fig. 2) because of the increase in the n value.

Thus we gave an explanation of the pulse width effect on C^* (and C_D^*) with the correlated EH's migration. The reason why the highly correlated electron migration occurs in Y_2O_2S is not understood.

Nature of carriers.—In the above discussion, we have not specified the nature of the carriers (excitons or free carriers). It is, however, found that the study made on the CD curves provides for a clue of the nature of the carriers in Y_2O_2S. There is a difference between the values of C_D^* with Tb and Eu; as already described, the values of C_D^*(Eu), detecting the electrons, depend on the excitation intensity and shift parallel to itself to higher values as the excitation intensity increases. In contrast, no difference was observed with C_D^*(Tb), detecting the holes. Because the lifetime of Eu^{+3*} is almost the same as that of Tb^{+3*} (about 500 μsec) and the measurements of C_D^*(Tb) and C_D^*(Eu) were made with the same excitation conditions, one allows us to draw a conclusion from above results that electrons and holes in Y_2O_2S are not associated with each other, *i.e.*, each is a free carrier.

A Proposed Model of Cathodoluminescence

The results of the quasi-one-directional migration of EH's and the radiative recombination mechanisms of EH's at activator ions (4) may allow one to propose the following atomistic model of generation of EH's, migration, and recombination at activator ions in the highly insulated phosphor crystals. Using Y_2O_2S:Eu as an example, we shall try to explain the proposed model as follows. We assume that EH's are generated by electron transfer from O^{-2} (and/or S^{-2}) to Y^{+3}, and since no bandgap luminescence is observed, the inverse electron transfer, from Y^{+2} to O^{-1} (or S^{-1}), is forbidden. We also assume that the lattice ions (*i.e.*, yttrium, oxygen, and sulfur) are not acting as recombination centers for EH's. For the case of Y_2O_2S, Y^{+3} (which has received an electron) is converted to Y^{+2}, which then releases the electron to the next nearest Y^{+3}. The electron migrates on Y^{+3} sites arranged on a line by repetition of the above mechanism. The hole migrates on O^{-2} (or S^{-2}) sites arranged on a line by similar migration mechanisms. The migration terminates by electron trapping at an Eu^{+3} site; this gives rise to the relationship $L = dC^{-1}$. The Eu^{+3} is converted to Eu^{+2}, producing a negatively charged local field. A hole is attracted to this region and is captured by the Eu^{+2} to form the excited state (Eu^{+3*}). The Eu^{+3*} emits a

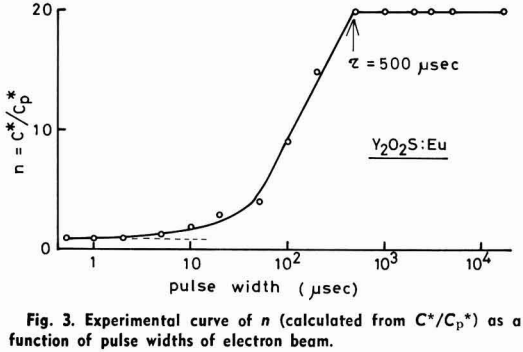

Fig. 3. Experimental curve of n (calculated from C^*/C_p^*) as a function of pulse widths of electron beam.

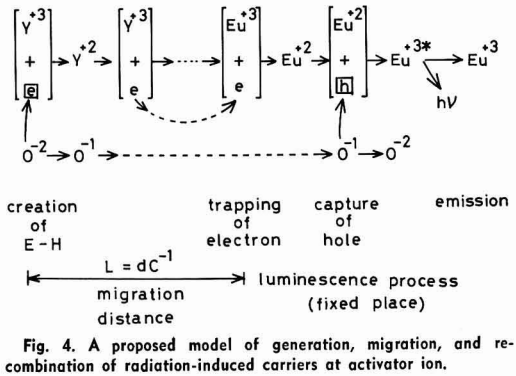

Fig. 4. A proposed model of generation, migration, and recombination of radiation-induced carriers at activator ion.

photon and returns to the ground state (Eu^{+3}) to repeat the excitation process with another EH. Figure 4 illustrates the proposed model. The reduction process ($Y^{+3} \rightarrow Y^{+2}$) and ($Eu^{+3} \rightarrow Eu^{+2}$) are observed in polarographic studies (14).

As a concluding remark, it has been shown that the activator luminescence is a new tool in studying the motion of mobile (radiation-induced) carriers in insulator crystals. Even though it is only allowed to draw the macroscopic (first-order approximation of) picture from the present work, a quasi-one-directional migration of free carriers and the correlated migration of the electrons in Y_2O_2S crystal are inferred from the experimental results. Further experiments by using a single crystal or a thin film and the theoretical consideration are, we feel, necessary to illustrate a complete picture of the motion of the carriers in highly insulated phosphor crystals.

Manuscript submitted Sept. 2, 1981; revised manuscript received Dec. 7, 1981.

Any discussion of this paper will appear in a Discussion Section to be published in the June 1983 JOURNAL. All discussions for the June 1983 Discussion Section should be submitted by Feb. 1, 1983.

Publication costs of this article were assisted by Matsushita Electric Industrial Company, Limited.

REFERENCES

1. D. Bohn and D. Pine, *Phys. Rev.*, **92,** 609 (1953).
2. C. A. Klein, *J. Appl. Phys.*, **39,** 2029 (1968).
3. M. Balkanski and F. Gans, "Luminescence of Organic and Inorganic Materials," H. P. Kallman, Editor, John Wiley and Sons, Inc., New York (1962); G. F. F. Garliek, "Luminescence of Inorganic Solids," P. Goldberg, Editor, Academic Press, New York (1966); J. D. Kingsley and G. W. Ludwig, *This Journal*, **117,** 353 (1970); A. Rothwarf, *J. Appl. Phys.*, **44,** 752 (1973); H. Yamamoto and A. Tonomura, *J. Lumin.*, **12,** 947 (1976); R. C. Alig and S. Bloom, *This Journal*, **124,** 1136 (1977).
4. L. Ozawa, *This Journal*, **128,** 140 (1981).
5. L. Ozawa and H. N. Hersh, *Phys. Rev. Lett.*, **36,** 683 (1976).
6. L. Ozawa, *This Journal*, **124,** 413 (1977).
7. L. Ozawa, *ibid.*, **122,** 1222 (1975).
8. J. S. Prener, *ibid.*, **122,** 1516 (1975).
9. U. Fano, *Phys. Rev.*, **58,** 544 (1940); G. Gergely, *J. Phys. Chem. Solids*, **17,** 112 (1960); "Surface Physics of Phosphors and Semiconductors," C. C. Scott and C. E. Reed, Editors, Academic Press, New York (1975).
10. S. Larach, *Anal. Chim. Acta*, **42,** 407 (1968); R. N. Kinseley, F. C. Laabs, and V. A. Fassel, *Anal. Chem.*, **41,** 50 (1969).
11. F. Morehead, *Phys. Rev. B*, **17,** 3433 (1978).
12. D. J. Gibbons, *J. Phys. D*, **7,** 433 (1974).
13. G. F. Amelio, *J. Vac. Sci. Technol.*, **7,** 593 (1970); A. J. Dekker, *Solid State Phys.*, **6,** 251 (1958); R. Kollath, *Handbook Phys.*, **21,** 232 (1956); Bruining "Physics and Application of Secondary Electron Emission," Pergamon Press, London (1954).
14. C. P. Sinha, "Complexes of the Rare Earths," Pergamon Press, New York (1966).

Preparation, Optimization, and Cathodoluminescent Properties of a Line Emission Penetration Phosphor

Thomas E. Clark* and Charles T. Burilla

Sperry Research Center, Sudbury, Massachusetts 01776

ABSTRACT

A multicolor line emission penetration phosphor, suitable for use in high brightness CRT's, has been developed. The system consists of multilayered powder particles containing a green-emitting La_2O_2S:Tb core, a nonluminescent $La_2O_2SO_4$:Tb middle layer, and a cover coating of small (~1 μm) red-emitting YVO_4:Eu particles. Preparation of the phosphor involves two basic steps: (*i*) the controlled oxidation of La_2O_2S:Tb particles to produce an onionskin surface layer of $La_2O_2SO_4$:Tb and (*ii*) coating of the core particles with the small YVO_4:Eu particles using a gelatin adsorption technique. Optimization with respect to brightness and color range yielded a system that was significantly brighter than previously developed line emission penetration phosphors while providing a comparable color range. Further, large size core particles were found to improve the phosphor system performance due to a saturation of the red component brightness at high working voltages. The paper discusses details of the preparation, optimization, and cathodoluminescent properties of this system.

Multicolor penetration cathode-ray tubes enjoy a range of applications in modern display systems (1-2). In the case of avionic displays, the system must be designed to operate under the extreme condition of sunlight falling perpendicular to the faceplate (~10,000 fcd), as well as the more typical lighting levels of daytime flight (~100 fcd) (2-3). Display readability under high lighting levels is normally maintained by increasing the display brightness and employing a contrast enhancement device. However, for a given penetration phosphor screen, increased brightness, which is obtained by increasing the beam current density, leads to a decrease in the screen lifetime (4). This fact, coupled with limitations in the coulomb ratings, luminous efficiencies, or designed operating voltages for state-of-the-art multicolor penetration phosphors has led to the employment of directional filters in order to simultaneously meet display readability requirements and obtain satisfactory screen lifetimes. The attendant disadvantage of directional filters caused by the need for the viewer to carefully position his head with respect to the display is accepted in order to take advantage of the improved light transmission and hence improved screen lifetimes obtainable with these filters. Although selective filters (*e.g.*, narrow passband filters) do not suffer the mentioned disadvantage of the directional filter, their use has been limited by the lack of a penetration phosphor with acceptable cathodoluminescent properties. An improved penetration phosphor, designed for such an application, has been developed. Its preparation, performance, optimization, and cathodoluminescent properties form the subjects of this paper.

* Electrochemical Society Active Member.

Key words: cathodoluminescence, penetration phosphors, color, rare earth.

Approach.—The ability to control the depth of electron penetration into the phosphor screens of CRT's by

adjusting the electron beam voltage (5) is exploited in multicolor penetration tubes by employing a multilayered phosphor system. Thus at low voltages only the phosphor "closest" to the electron source is excited yielding an output color corresponding to its emission, while at the highest voltage inner phosphor layers are also excited yielding an output color that is determined by the relative emission intensities from the contributing phosphors. Intermediate voltages then give rise to different relative emission intensities and hence different colors.

Of the various possible approaches for constructing the requisite multilayered phosphor system, those utilizing multilayered powder particles (6-12) have received considerable attention for reasons of enhanced luminous efficiencies (7) or ease of subsequent tube manufacture (10). An early version (7) of a mixed two-component system using red- and green-emitting phosphors involved the formation of a nonluminescent "onionskin" on the surface of ZnS:Cu (green-emitting) powder particles. This dead-layer green (DLG) component was then mixed with a commercially available red-emitting phosphor allowing the preparation of a multicolor phosphor screen using the same procedure employed in monochrome tube preparation. ZnS:Cu, however is not ideally suited for use in high brightness displays because of its reduced luminous efficiency under the high current density conditions found in these displays (11). Furthermore, it is not ideally suited for use with selective filters because of the broad-band nature of its emission.

In another approach, Galves (10) developed an efficient penetration phosphor consisting of a Zn_2SiO_4:Mn core particle covered with a nonluminescent layer on top of which was a coating of small red-emitting YVO_4:Eu particles. He also demonstrated the enhanced efficiency of this single-particle system as compared to a dual-particle system in which the DLG containing a Zn_2SiO_4:Mn core was simply mixed with standard size YVO_4:Eu particles. These penetration phosphors, however, also use a broad-band green-emitting phosphor which reduces their suitability for use with selective filters.

An early version of a single-particle penetration phosphor system containing only line-emitting phosphor components was developed by Tecotzky and Mattis (12). Its preparation involved a controlled sulfidization of R_2O_3:Pr (R = Y or Gd) particles to yield a core of red-emitting R_2O_3:Pr and a contiguous surface layer of green-emitting R_2O_2S:Pr. Although, the narrow-band aspect of the component phosphor emissions makes this system well suited for use with selective filters (13), the presence of alternative red- and green-emitting phosphor components with superior cathodoluminescent efficiencies and color saturation (11, 12, 14, 15) provide opportunities for improvement in the system performance.

The penetration phosphors that have been under development in this laboratory employ only line-emitting phosphor components. The earliest version (8) included standard size YVO_4:Eu particles mixed with a DLG consisting of La_2O_2S:Tb particles covered with an onionskin layer of nonluminescent $La_2O_2SO_4$:Tb. A subsequent improvement in color coordinates was obtained by using a red-emitting phosphor particle containing a nonluminescent core (9). In an attempt to improve upon the luminous efficiencies of these previous efforts, development of a performance optimized single-particle penetration phosphor was undertaken. It consists of the previously described La_2O_2S:Tb DLG core particle coated with small red-emitting YVO_4:Eu particles. The specific objectives of the performance optimization were to prepare and characterize the penetration phosphor that: (*i*) yielded a "red to green" color range, (*ii*) required a voltage change less than 15 kV, and (*iii*) had the maximum red brightness. The optimization sequence included four basic steps. First, the efficiency of the coating process (*i.e.*, surface coverage per coating application) was optimized. This was followed by the selection of a preferred particle size for the DLG core material. The red component brightness was then maximized and finally the working voltage for the red mode was maximized.

Experimental

Synthesis.—Preparation of the single-particle penetration phosphor involved the initial formation of a DLG component with the appropriate barrier-layer thickness, followed by a coating step in which small YVO_4:Eu particles were adhered to the surface of the DLG particles. The DLG synthesis followed the procedure of Ignasiak and Veron (8) which consisted of a controlled oxidation of La_2O_2S:Tb particles to yield a contiguous surface layer of $La_2O_2SO_4$:Tb. The relative inefficiency of $La_2O_2SO_4$ as a host for Tb-activated cathodoluminescence allows this oxidation product to act as a nonluminescent barrier layer on the green-emitting core material. Coating of the DLG with small red particles was accomplished using the gelatin adsorption process described by Kell (16). This process involved three basic steps: (*i*) coating the DLG powder particles with an adsorbent film of gelatin, (*ii*) exposing the filmed DLG particles to a liquid dispersion of the small red-emitting particles, and (*iii*) removal of the excess small particles via the differential sedimentation rates that result from the particle size differences. The resulting coated core particles contained essentially a monoparticle thick layer of small phosphor particles. In the following synthetic procedure, the conditions given correspond to the penetration phosphor found to yield the optimum performance.

Synthesis of La_2O_2S:Tb-$La_2O_2SO_4$:Tb particles.—10g of La_2O_2S:Tb (commercial phosphor, P-44) that had been previously size classified to remove particles smaller than 16 μm in diameter were oxidized in a rotating quartz chamber for 60 min at 749°C. [See Ref. (8) for details of the reaction chamber.] A moist oxygen flow of 20 cm^3/min was maintained during reaction and, although thermogravimetric, low voltage electronic and surface analysis data (17) indicate a negligible oxidation rate below 500°C, a blanket of argon was kept over the material during the complete preheat and cool-down periods.

Coating procedure.—50 ml of a 1% stock solution of gelatin, prepared as described by Kell (16), were diluted with water to 500 ml, clarified by warming to 30°C, and acidified with glacial acetic acid to a *p*H of 4.0. Then 50 ml of the acidified gelatin solution were placed in a 75 ml polyethylene bottle containing 5.0g of the core phosphor particles, agitated for 25 min, settled, and the supernatant removed by aspiration. This was followed by 5-6 water washes to remove any excess gelatin. A liquid dispersion of the small red phosphor particles, prepared by ultrasonically agitating 1.65g of YVO_4:Eu (Levy West Type 1505q) in 50 ml of water and acidifying to a *p*H of 3.9, was then added to the filmed core particles, agitated 25 min, settled, and the supernatant removed by aspiration. Following two water washes a second coating of gelatin was applied to the particle-coated particles and the excess gelatin was again removed with water washes. Following a wash with a 37% formaldehyde solution to harden the gelatin, the excess nonadhering small phosphor particles were removed by washing with ethanol as many times as necessary. Finally, the material was air dried, lightly crumbled, and sifted through a 30 μm sieve.

Measurements.—Cathodoluminescent properties, except where noted, were measured via transmission

through samples held in a demountable CRT designed to handle up to 16 samples at a time. [See Ref. (8) for details of the apparatus.] A pulsed electron beam of 50 μsec duration and a 1 kHz refresh rate, operated at 0.5 μA, was focused to a spot of 3.0 mm diam for each accelerating voltage level. Brightness measurements were made using a Spectra Brightness Spot Meter (Model UB ½, Photo Research Corporation) and emission spectra were obtained with a Jarrel-Ash ½ meter Ebert scanning monochromator. Using a scanning rate of 25 nm/min, digitized spectra were recorded at 1 nm intervals. Corrections in the spectra for photomultiplier response, grating losses, and baseline variations were made prior to calculating the color coordinates using the 1931 C.I.E. colorimetric system. Phosphor screen samples were prepared on Nesatron glass using standard settling techniques and were not aluminized, except where otherwise noted. Optimized screen loading densities (mass per screen area) were obtained for the three types of phosphors evaluated: green-emitting core particles, small-particle-coated penetration phosphors, and the standard size red-emitting YVO_4:Eu. These screen coating densities yielded the maximum brightness for the respective phosphor types and were used in subsequent screen preparations.

Discussion and Results

The first step in the performance optimization of the single-particle penetron was to optimize the coating efficiency. Beginning with preparative parameters used by Kell (16), a trial-and-error adjustment of several parameters was then conducted in order to find a set of conditions that yielded a satisfactory coating efficiency for this system. Factors considered in the optimum search included the quantity and *p*H of the small particle dispersion and the length of time that the small particle dispersion was exposed to the filmed DLG core particles. On the basis of scanning electron microscopic analysis, a practical optimum coating efficiency of about 75% was obtained. Scanning electron photomicrographs of a coated particle, shown in Fig. 1, illustrate the level of surface coverage obtained as well as the size distribution of the small coating particles. As can be seen, the coating particle diameters range from considerably less than 1 μm to greater than 2 μm.

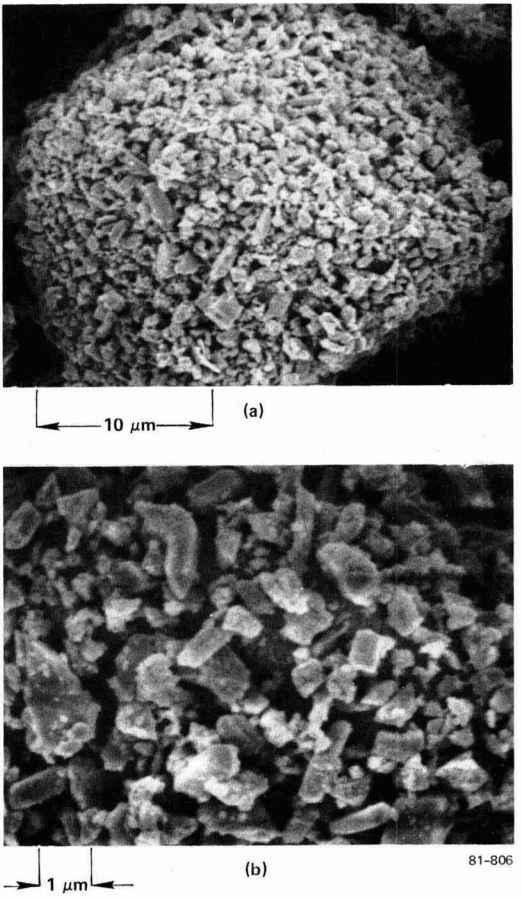

Fig. 1. Scanning electron micrographs of a core particle containing a single coating of small YVO_4:Eu particles.

The influence of the core particle size on the brightness *vs.* voltage curves was determined experimentally by coating undoped La_2O_2S particles of various size. A batch of La_2O_2S, reported to be 1.6% greater than 32 μm and 1.8% less than 5 μm in diameter, was size classified into four categories: <6, 6-10, 10-16, and >16 μm. Coated samples for the three larger diameter categories were prepared in a manner so as to minimize differences in the nature of the coatings. Several phosphor screens, differing in screen loading density, were prepared for each of the size categories. Red brightness *vs.* voltage curves for these samples are shown in Fig. 2. In Fig. 2a, we see that the screen loading density range used encompasses the optimum value for the particle size range considered. This is seen by the fact that the relative brightness diminishes as the screen loading density is increased or decreased from 6.8 mg/cm². A comparable range of screen loading densities was used for the 6-10 and 10-16 μm core material, but in neither case was an optimum screen loading density established. However, in both cases, the brightness increased as the screen loading density decreased, for the entire density range covered. Thus, the optimum screen loading densities for these smaller sized particles apparently occur at lower values than that for the >16 μm core material.

A comparison of brightness *vs.* voltage curves for the three groups of core material is shown in Fig. 2d. The curves shown are for the screen loading density that yielded the maximum brightness in each of Fig. 2a, b, and c. As can be seen, the >16 μm diam core material resulted in a sublinear red brightness curve while the other two core materials yielded essentially linear curves. Since the diminished red emission of the >16 μm diam core material at high voltage would lead to a greener output color in the completed system, this size core material was selected for use in the subsequent optimization steps. The fact that the screen loading densities for the two groups with the smaller core diameter were not completely optimized simply means that they would be as bright or brighter at the optimum screen loading density. Thus, the reason for preferring the >16 μm core material remains valid.

The reason that the coated >16 μm diam core material exhibits a greater degree of sublinearity than the other two groups of material derives from differences in the amount of beam energy absorbed in the red-emitting coating *vs.* the nonluminescent core for these different size core particles. The three curves in Fig. 2d should have a common region at the lower accelerating voltages corresponding to electron penetration that is essentially limited to the coating layer of luminescent particles. As the accelerating voltage, and therefore electron penetration, is increased, the ratio of beam energy absorbed in luminescent *vs.* nonluminescent material becomes dependent on the core particle size. For the limit of a very small diameter core particle the phosphor screen would appear to the elec-

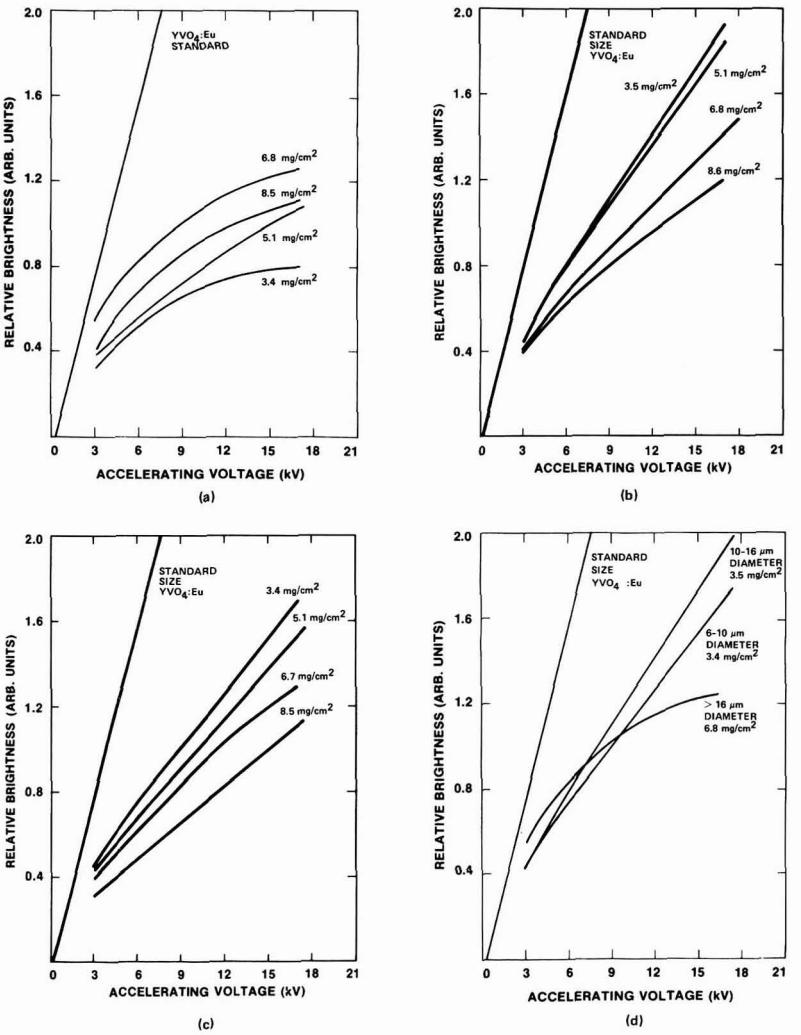

Fig. 2. Red brightness vs. voltage curves for several screen loading densities of: (a) >16 μm, (b) 10-16 μm, and (c) 6-10 μm diam core particles coated with one layer of small YVO_4:Eu particles. Figure 2d compares the maximum red brightness vs. voltage curves obtained for each group of material represented in Fig. 2a-c.

tron beam to consist essentially of a multiparticle thick layer of small luminescent coating particles. The brightness in this case would show a linear dependence on voltage similar to that found for the standard size YVO_4:Eu in Fig. 2d. At the other extreme of a very large diameter core particle, the phosphor screen would appear to the electron beam to consist of a monoparticle thick layer of the small YVO:Eu coating particles. The shape of the brightness *vs.* voltage curve in this case would be similar to the sublinear curves found for thin luminescent films (10, 18).

The luminous efficiency of the red-emitting component in the penetration phosphor was next maximized by coating successive layers of the YVO_4:Eu onto La_2O_2S:Tb particles and evaluating the influence on the output color coordinates. The only constraint limiting the number of coating layers was the requirement of being able to produce a "green" color output at an acceptable working voltage. Untreated La_2O_2S:Tb was used here as the core particle material because it would provide the greatest green emission intensity at any operating voltage (compare the relative brightness of the untreated La_2O_2S:Tb *vs.* DLG samples in Fig. 4) and thus would yield the greenest color output at any red phosphor coating level.

Data in Table I indicate that with more than one coating layer the desired green output at the high working voltage is shifted to yellow. As Fig. 3 illustrates, this is due, in part, to the increased red emission from the thicker luminescent coating layer. However, it is also due to the diminished green emission from the core particle that results from the reduced beam energy reaching the core in the double layered material.

The final step in the performance optimization was to obtain the highest possible red mode working volt-

Table I. Colorimetric properties at 17 kV of La_2O_2S:Tb particles coated with successive layers of small YVO_4:Eu particles

No. of red phosphor layers	Color coordinates		Equivalent wavelength (nm)
	x	y	
1	0.378	0.571	562
2	0.445	0.508	573

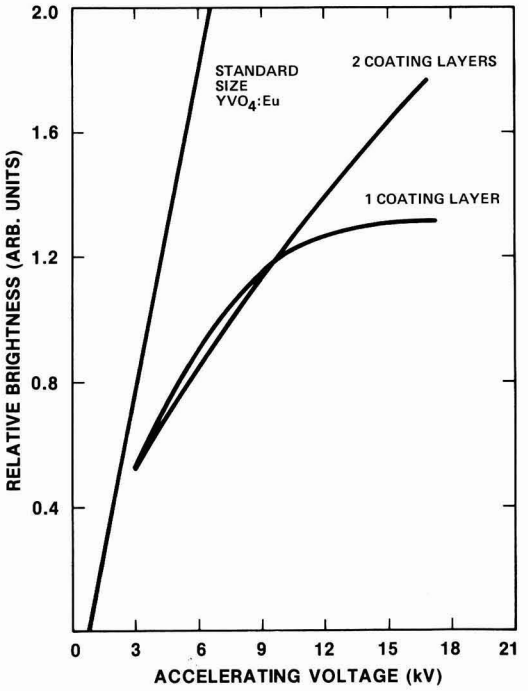

Fig. 3. Red brightness *vs.* accelerating voltage curves for >16 μm diam core particles coated with 1 and 2 layers of small YVO_4:Eu particles.

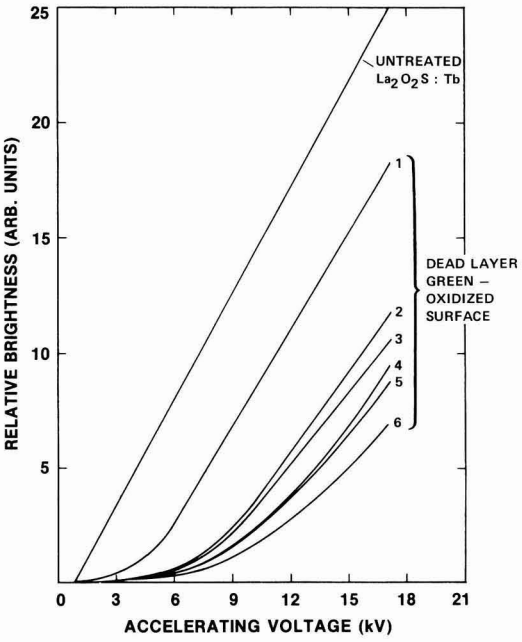

Fig. 4. Green brightness *vs.* accelerating voltage curves for commercial La_2O_2S:Tb and several dead-layer green samples consisting of a nonluminescent $La_2O_2SO_4$:Tb surface and a green-emitting La_2O_2S:Tb core. The curve numbers refer to the sample identification of Table II where the respective oxidation treatments are listed.

age so as to yield the maximum red brightness at a given beam current density. To accomplish this, the core particle with the thickest barrier layer that would still yield an acceptable green output within 15 kV of the red working voltage was determined by trial-and-error. Table II contains the preparative conditions, while Fig. 4 illustrates the relative green brightness *vs.* voltage for the DLG's investigated in this step. Cathodoluminescent data for the red phosphor coated DLG's are presented in Tables III-V and Fig. 5.

Figure 5 contains plots of the equivalent wavelength and relative brightness of the samples at two beam voltages *vs.* the core particle oxidation time. Curves are shown for beam voltages of 9 and 17 kV. The equivalent wavelength curves show a steady shift to longer wavelengths as the oxidation time is increased. This red shift is due to the reduction in green emission from the core particle as the barrier layer thickness is increased. Indeed, if the oxidation time was increased sufficiently, the two curves would eventually converge at the equivalent wavelength corresponding to the

Table II. Oxidation conditions for the dead-layer green sample preparations*

Sample	Reaction time (min)	Reaction temp (±2°C)	Mass (g)
1†	60	751	8.0
2	60	749	10.0
3	75	750	8.0
4	90	752	8.0
5	105	750	8.0
6	120	750	8.0

* Maintained a moist oxygen flow rate of ~20 cm³/min during all oxidation runs.
† Maintained an argon flow rate of ~40 cm³/min during this oxidation run.

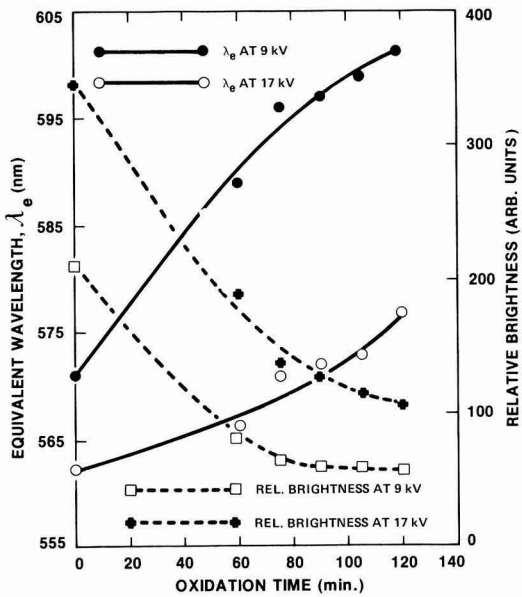

Fig. 5. Plot of equivalent wavelength and relative brightness, at 9 and 17 kV, as a function of the core particle oxidation time.

red emission of the coating particles. Examination of the brightness curves shows that the brightness at both voltages decreases with an increase in oxidation time. This is also due to the reduction in green emission as the barrier layer thickness is increased. Here, the two

Table III. Cathodoluminescent data for dead-layer green particles (La_2O_2S:Tb-$La_2O_2SO_4$:Tb) coated with small YVO_4:Eu particles*

Core particle type**	Number of coating layers	9 kV accelerating voltage				17 kV accelerating voltage			
		Color coordinates		Relative brightness (%)†	λ_e (nm)‡	Color coordinates		Relative brightness (%)†	λ_e (nm)‡
		x	y			x	y		
Untreated La_2O_2S:Tb	1	0.438 (0.417)	0.520 (0.538)	210 —	571 (568)	0.378 (0.346)	0.571 (0.598)	345 —	562 (557)
Untreated La_2O_2S:Tb	2	0.544	0.434	110	588	0.445	0.508	219	573
1	1	0.454	0.508	153	574	0.381	0.570	271	563
2	1	0.554	0.425	82	589	0.399	0.549	190	566
3	1	0.596 (0.607)	0.392 (0.381)	66 —	596 (598)	0.438 (0.422)	0.520 (0.532)	138 —	571 (569)
4	1	0.604 (0.619)	0.387 (0.371)	61 —	597 (600)	0.441 (0.425)	0.518 (0.529)	129 —	572 (570)
5	1	0.615	0.376	61	599	0.445	0.513	116	573
6	1	0.622	0.370	58	601	0.475	0.486	107	577

* The values in parenthesis correspond to measurements made through 2 mm of BG20, a selective filter.
** The numbers refer to the sample preparation in Table II.
† The brightness measurements are relative to that obtained for standard size commercial YVO_4:Eu.
‡ The equivalent wavelength was calculated *vs.* the CIE source C.

Table IV. Comparison of the voltage dependent output color for two coated samples differing in the dead-layer thickness of the core particles

Sample*	Voltage (kV)	Color coordinates		Equivalent wavelength (λ_e)†
		x	y	
2	6	0.642	0.355	604
	7	0.613	0.378	599
	9	0.554	0.425	589
	10.5	0.516	0.459	583
	17	0.399	0.549	566
	19	0.388	0.564	564
4	7	0.636	0.359	603
	9	0.604	0.387	597
	10	0.584	0.401	594
	13	0.517	0.455	584
	17	0.441	0.518	572
	20	0.434	0.512	572

* The numbers refer to the sample preparation in Table II.
† The equivalent wavelength was calculated *vs.* the CIE source C.

Table V. Cathodoluminescent properties of two line emission penetration phosphors. See the text for details of the phosphor systems*

Phosphor system	Voltage (kV)	Luminous eff. (lumen/W)	Color coordinates†	
			x	y
Single-particle	9	3.1	0.622	0.351
	20	8.3	0.394	0.550
Dual-particle	8	1.9	0.634	0.353
	18	6.3	0.398	0.547

* Properties measured in sealed aluminized CRT's using a raster scan. Breakthrough voltages were ~3 kV.
† Color coordinates were measured through 2 mm of BG20 filter.

curves would converge to the brightness value due to the coating particles if the oxidation time were increased sufficiently.

Since a red shift in color output at 9 kV corresponds to an effective increase in the red mode working voltage, we see that this increase occurs at the cost of reduced brightness and a degraded green output color at 17 kV. Both of these deficiencies, however, can be overcome by using a sufficiently high green mode working voltage. From this point of view, the increased red mode working voltage leads to an increased green mode working voltage. However, Table IV indicates that an increase in the red mode working voltage also leads to an increase in the minimum voltage change required to produce both desired output colors. Thus, whereas sample 2 requires an 11 kV voltage change (6-17 kV) to produce a given color change (λ_e from 604 to 566 nm), sample 4 requires considerably more than 13 kV (from less than 7 kV to more than 20 kV), to produce the same color change.

Based on the previously stated objectives and the above discussion, entry 4 in Table III was selected as the optimum single-particle penetration phosphor. The color range of the phosphor, as a function of voltage, is shown in Fig. 6. As can be seen, four distinct colors are obtainable within an 11 kV voltage change. Table V gives data obtained for the optimum single-particle phosphor presented here and the dual-particle system previously developed by this laboratory (9). The latter system employed the same type of DLG particles; however, they were mixed with normal sized red-emitting particles containing a luminescent La_2O_2S:Eu onionskin surface and a nonluminescent core. As can be seen, the single-particle system results in luminous efficiency increases in the red and green modes of 63% and 32%, respectively, without a loss in color range. Furthermore, the higher red mode operating voltage for the single-particle system implies an 84% improvement in brightness under conditions of equal current density. These results are consistent with those of Galves (10), to the extent that the two approaches are comparable.

Conclusions

A four color line emission penetration phosphor, suitable for use in high brightness displays, has been developed. The system consists of multilayered powder

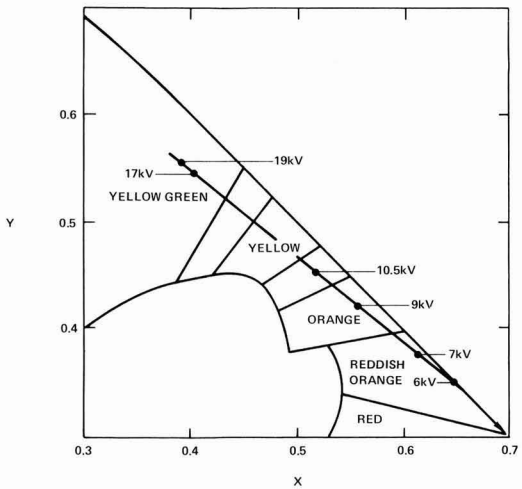

Fig. 6. Color coordinates at the indicated voltages (kV) for entry 4 in Table III.

particles containing a green-emitting La_2O_2S:Tb core, a nonluminescent $La_2O_2SO_4$:Tb middle layer, and a cover coating of small red-emitting YVO_4:Eu particles. Optimization with respect to brightness and color range yielded a system that was significantly brighter than previously developed line emission penetration phosphors while providing a comparable color range. Further, large size core particles were found to improve the phosphor system performance due to a saturation of the red component brightness at high working voltages. Finally, the line emission nature of the phosphors used in this system makes it ideally suited for use with selective filters.

Acknowledgment

The authors wish to acknowledge the assistance of G. Knutsen and J. R. Trimmier for making the cathodoluminescent measurements contained in Table V.

Manuscript submitted Aug. 17, 1981; revised manuscript received *ca.* Nov. 24, 1981. This was Paper 157 presented at the Minneapolis, Minnesota, Meeting of the Society, May 10-15, 1981.

Any discussion of this paper will appear in a Discussion Section to be published in the June 1983 JOURNAL. All discussions for the June 1983 Discussion Section should be submitted by Feb. 1, 1983.

Publication costs of this article were assisted by the Sperry Research Center.

REFERENCES

1. A. F. Martin and J. P. Galves, "New Trends in Professional Colour Multilayered CRTs," Thomson-CSF, St. Egreve, France.
2. J. P. Galves, "New Possibilities Offered by Cathode-Ray Tubes with Multifunction Penetration Screens," Presented at the Electronic Displays Meeting, London (1978).
3. J. P. Galves and J. Brun, "Colour and Brightness Requirements for Cockpit Displays: Proposals to Evaluate Their Characteristics," Presented at the 29th AGARD Avionics Panel Technical Meeting on Electronic Displays, Edinburgh (1975).
4. J. P. Galves and J. Brun, "Reliability of High Brightness CRTs for Airborne Displays," Thomson-CSF, Paris, France.
5. C. Feldman, *Phys. Rev.*, **117**, 455 (1960).
6. P. J. Messineo, Skillman, and S. M. Thomsen, U.S. Pat. 3,294,569 (1966).
7. J. S. Prener and J. D. Kingsley, *This Journal*, **119**, 1254 (1972).
8. S. Ignasiak and H. Veron, *ibid.*, **123**, 1493 (1976).
9. C. T. Burilla, M. J. Rafuse, and M. Kestigian, *SID 79 Digest*, 70 (1979).
10. J. P. Galves, Abstract 196, p. 519, The Electrochemical Society Extended Abstracts, Las Vegas, Nevada, Oct. 17-22, 1976.
11. A. F. Martin, Electro-Optical Systems Design, June (1977).
12. (a) M. Tecotzky and J. J. Mattis, Abstract 159, p. 405, The Electrochemical Society Extended Abstracts, Cleveland, Ohio, Oct. 3-8, 1971; (b) M. Tecotzky and J. J. Mattis, U.S. Pat. 3,791,844 (1974).
13. C. D. Lustig and B. J. Thaxter, U.S. Pat. 3,946,267 (1976).
14. R. A. Buchanan, K. W. Wichersheim, J. L. Weaver, and E. E. Anderson, *J. Appl. Phys.*, **39**, 4342 (1969).
15. (a) P. N. Yocom and R. E. Shader, Abstract 50, p. 146, The Electrochemical Society Extended Abstracts, Los Angeles, California, May 10-15, 1970; (b) P. N. Yocom and R. E. Shrader, Proceedings of the Seventh Rare Earth Research Conference, Vol. 2, p. 601, October 1968.
16. R. D. Kell, U.S. Pat. 3,275,466 (1966).
17. (a) J. W. Haynes and J. J. Brown, Jr., *This Journal*, **115**, 1060 (1968); (b) D. Gutzler, *ibid.*, **126**, 571 (1979).
18. J. D. Kingsley and J. S. Prener, *J. Appl. Phys.*, **43**, 3073 (1972).

Saturation of (Zn, Cd)S:Cu, Al Cathodoluminescent Phosphors at High Current Densities

I. Experimental Phenomena

James R. McColl

GTE Laboratories, Incorporated, Waltham, Massachusetts 02254

ABSTRACT

Efficiency loss due to high electron beam current density in green-emitting (Zn, Cd)S:Cu, Al phosphors has been measured for Cu and Al concentrations ranging from 27 to 1500 ppm. The severe loss of efficiency exhibited by commercial phosphors with activator concentrations in the 20-75 ppm range is somewhat alleviated at higher concentration. However, the improvement is far less than expected from a simple activator-depletion model, and saturation effects are nearly constant from 100 to 500 ppm, showing that a second mechanism for saturation is important in this material. It is also found that saturation is independent of repetition rate, but depends rather on the net dose of electron beam charge delivered in a single pulse or scan. Laser photoexcitation experiments in the blue and u.v. show that analogous saturation occurs for all modes of excitation. Thus the second saturation mechanism is neither a thermal effect nor electric field quenching. The second paper in this series will show that the second saturation mechanism in ZnS-type phosphors is excited-state absorption.

It has long been known that phosphors of the ZnS family, like ZnS or (Zn, Cd)S activated with Cu, Ag, or Au and coactivated with Al, Ga, In, or halide ions, exhibit sublinear response, *i.e.*, their efficiency drops at high current density (1). Most cathodoluminescent phosphors exhibit this saturation behavior to some degree, but the effect is much more pronounced for ZnS-type phosphors than for other types (2-5). The effect is important for color television picture tubes because ZnS:Ag,Al or ZnS:Ag,Cl is used as the blue primary, and (Zn,Cd)S:Cu,Al, as the green. For example, in a 19 in. picture tube operated at 2 mA beam current, typical for a highlight scene, the efficiency of the green-emitting primary is typically 20-35% lower

Key words: cathodoluminescence, phosphors, CRT phosphors, saturation.

than at 0.1 mA. In addition to this loss of potential picture tube brightness, a color shift toward pink can be detected in highlight scenes because the europium-activated red-emitting primaries used in most color picture tubes do not exhibit saturation. The effect is significant but tolerable in conventional picture tubes, but would be accentuated in picture tube designs with higher beam current density, such as postdeflection acceleration tubes, projection TV tubes, or conventional tubes with improved gun design.

In the research reported in this paper, I have experimentally investigated saturation in (Zn,Cd)S:Cu,Al phosphors induced by high electron beam current density. There have been previous reports on measurements of phosphor efficiency *vs.* current density. Generally, these reports have compared (Zn,Cd)S:Cu,Al of a single composition with other, less easily saturated phosphors. One of the goals here is to characterize the effect of varying activator concentration on saturation behavior. It has been a recurring theme in the literature of this subject that one of the saturation mechanisms in ZnS-type phosphors is activator depletion (1). This term refers to the loss of efficiency caused by using up the available activator centers with an excitation density comparable to or exceeding the activator concentration. This mechanism can be tested by varying activator concentration, since activator depletion should be less pronounced for a given level of excitation when the activator concentration is raised, and vice versa. The effect of electron beam dwell time and repetition rate on saturation are also characterized in this paper, both to provide information necessary for standardizing phosphor measurements and to yield insight into saturation mechanisms.

The content of this paper follows its original presentation (6). That is, it is a report of an experimental survey of phenomena relevant both for design of cathode ray tubes and for gaining insight into mechanisms causing nonlinear response. The research presented here shows that activator depletion is indeed an important mechanism for saturation in ZnS-type phosphors, but that another mechanism is also important, particularly at the higher activator concentrations where activator depletion becomes less pronounced. The results of a second, more theoretical investigation (7), will be presented in another publication. The latter investigation shows that the second mechanism for saturation in ZnS-type phosphors is excited state absorption.

Experimental

The phosphors used in this study were prepared at the GTE Chemical and Metallurgical Division, Towanda, Pennsylvania, by standard production techniques. The samples of (Zn,Cd)S:Cu,Al contained 8% CdS by weight before firing. Cu and Al concentrations ranged from 27 to 1485 ppm. expressed as weight metal per weight of phosphor. The phosphors were settled onto tin oxide coated glass plaques using potassium silicate-barium acetate as binder. The plaques were not aluminized. Saturation measurements were carried out at screen weights optimized for maximum brightness, determined individually for each sample.

The dependence of phosphor efficiency on beam current density was measured by an adaptation of the method of Gibbons *et al.* (4). Figure 1 presents a schematic illustration of the apparatus. An electron gun produced a beam of 4 kV electrons, which was then accelerated to typically 20 kV by a postacceleration cage, in which was mounted a rotatable sample holder with eight plaques. The whole apparatus was mounted in a stainless steel vacuum chamber, with fused quartz windows, that was capable of maintaining a pressure of 2×10^{-7} mm Hg.

Light emitted by the phosphors was measured through the glass plaques by means of a microspot

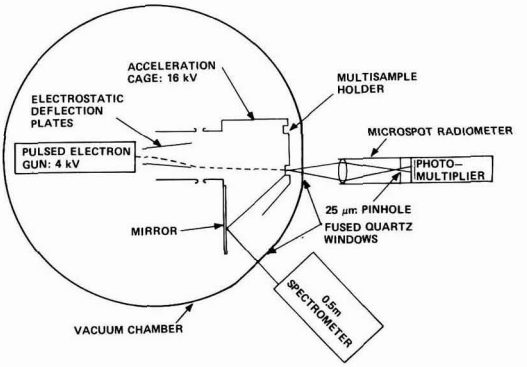

Fig. 1. Schematic illustrations of apparatus used for pulsed stationary spot phosphor saturation measurements.

radiometer. This device consists of an achromatic lens, a 25 μm diam pinhole set at twice the focal length of the lens, and an RCA C31034 photomultiplier, which has essentially flat spectral response in the visible spectrum. When properly focused, the microspot radiometer views a spot of 25 μm diam; this is sufficiently smaller than the typically 1 mm electron beam spot diameter that one may consider the area viewed as being excited by essentially constant current density.

Relative efficiency of phosphors was measured by alternately moving test samples and reference phosphors into the path of the electron beam, keeping the beam and radiometer fixed. This departure from the method of Gibbons *et al.* (4), avoids possible changes in beam spot profile that might be caused by deflecting the beam (in our case, electrostatically). In each series of measurements, five test phosphors and three standards were mounted in the apparatus. One of the standards, red-emitting $Y_2O_3:Eu^{3+}$, was used to determine beam current density, as described in detail below. Test phosphor efficiency was measured relative to a second standard, green-emitting $La_2O_2S:Tb^{3+}$. Although $La_2O_2S:Tb^{3+}$ displays slightly sublinear response, its use as a reference was advantageous since its color and brightness are comparable to the test phosphors. A third standard, a reference sample of (Zn,Cd)S:Cu,Al, was included to check reproducibility.

The measurements were made with a pulsed, stationary beam. Pulses of from 0.25 to 2 μsec duration from a Hewlett Packard Model 214A Pulse Generator were applied to the grid of the electron gun. Repetition rate was varied from 7 to 60 pps. In contrast to Gibbons *et al.* (4), intensity measurements were always made at the brightest part of the electron beam spot, and current density was varied by varying total beam current. In a typical run, each plaque was measured at four different places at each current density to average out small nonuniformities. Most samples were resettled and measured in three separate runs.

As mentioned above, the intensity of light emitted from $Y_2O_3:Eu^{3+}$ was used to obtain beam current density. It was first ascertained that this phosphor does not saturate under the conditions of this experiment. This was done by modifying the microspot radiometer to view the whole spot, rather than a small portion, by replacing the pinhole with a neutral density filter. The electron beam was then set to a relatively high current and the focus was varied; this changed the current density but not the total power delivered to the plaque. Thus a change in total light output was expected only for those phosphors that saturate. No change was noted with $Y_2O_3:Eu^{3+}$. A decrease in light output amounting to a few percent was noted with $La_2O_2S:Tb^{3+}$ when the beam was focused; as expected,

there was a sharp drop with the (Zn,Cd)S:Cu,Al phosphors.

Electron beam current density calibration was carried out as follows. To be determined was the calibration constant K between current density J and microspot radiometer photomultiplier current I with the $Y_2O_3:Eu^{+3}$ plaque as target, related by $J = KI$. Since the total beam current i is equal to the integral of current density over the area of the plaque, the following equalities can be stated

$$i = \int\int J dx dy = K \int\int I dx dy \qquad [1]$$

The total beam current i on the left-hand side of Eq. [1] was measured with a Pearson Electronics Model 2100 current transformer, through which was passed the high voltage lead to the postacceleration cage; the latter acts as a Faraday cage. The integral for the right-hand side of Eq. [1] was determined by slowly scanning the beam in a 2 × 2 mm raster pattern of 20 lines with 22 measured points per line. The resulting two-dimensional intensity profile was measured and stored in a Nicolet Model 1073 Signal Averager. The needed integral was computed numerically. An example of an intensity profile and its integral are presented in Fig. 2.

The linearity of response of the microspot radiometer system was assured by operating the photomultiplier at average and peak currents low enough to prevent saturation. Linearity of response was also tested with neutral density filters.

Experimental Results and Discussion

The first goal of this investigation was to ascertain the role of activator concentration on nonlinearity. Activator concentrations in phosphors for color TV tubes are usually chosen to yield maximum brightness at relatively low current density, corresponding to about 50 μA beam current in a conventional tube. The resulting optimum concentration for (Zn,Cd)S:Cu,Al is typically 20-75 ppm for Cu, depending on the particular measurement conditions of a given manufacturer. Somewhat higher concentrations can be used, however, with little loss in low-current-density brightness. Since the activator-depletion model predicts that saturation should be alleviated by higher activator concentration, raising the activator concentration seems to be a reasonable approach.

Figure 3 presents data on phosphor efficiency relative to $La_2O_2S:Tb^{3+}$ for five sets of Cu and Al concentrations. The measurements were carried out with a pulsed stationary spot of 0.5 μsec duration, 60 pps repetition rate, and peak current density up to 0.12 A/cm^2. The ratio of Cu to Al concentration is constant for this set of phosphors.

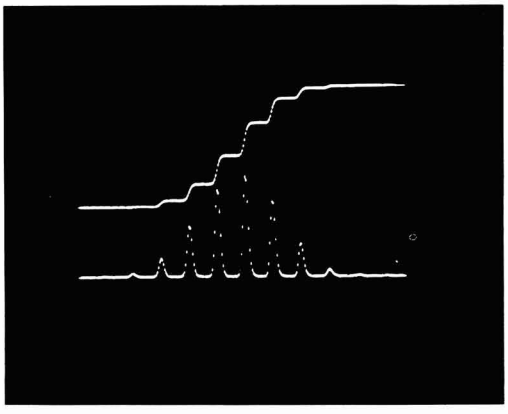

Fig. 2. Oscillogram of photomultiplier response from spot radiometer during slow raster scan of $Y_2O_3:Eu^{3+}$ phosphor. Lower trace: photomultiplier response. Each "hump" represents one horizontal scan. Upper trace: integral of lower trace.

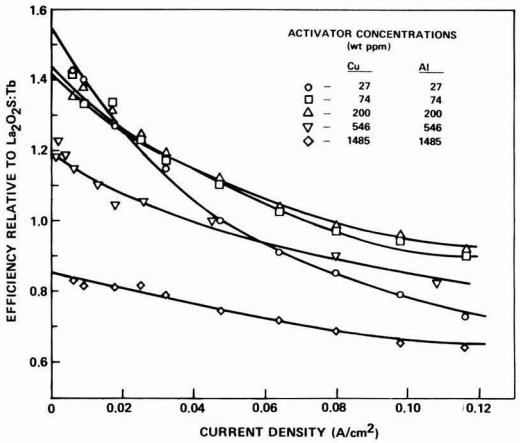

Fig. 3. Efficiency of (Zn,Cd)S:Cu,Al phosphors relative to $La_2O_2S:Tb^{3+}$ *vs.* peak current density in pulsed stationary spot experiment with repetition rate = 60 pps and pulse duration = 0.5 μsec.

It is evident from Fig. 3 that there is significant saturation in this range of current densities and that activator concentration strongly affects both low-current-density efficiency and saturation behavior. The efficiency extrapolated to zero current density is highest for the lowest activator concentration, and vice versa. Conversely, saturation is reduced with higher activator levels.

It can be concluded that saturation behavior is at least in part an activator depletion effect, especially at very low activator concentration; increasing the Cu concentration from 27 to 74 ppm reduces the magnitude of saturation substantially. However, further increases in Cu concentration yield much less improvement, showing that either another phenomenon is contributing or that some of the increased activator concentration is inactive. Above 500 ppm, concentration quenching becomes severe.

A second goal of this investigation was to characterize how the peak current density J_p, dwell time τ, and repetition frequency f contribute to saturation behavior. These factors contribute to the average current density J_{av} according to

$$J_{av} = J_p \tau f \qquad [2]$$

Saturation effects are often reported as a function of J_{av}, but it seems obvious that phosphor efficiency might well depend separately on the factors that determine J_{av}.

Figure 4 presents phosphor emission intensity *vs.* repetition frequency for (Zn,Cd)S:Cu,Al, $La_2O_2S:Tb^{3+}$, and $Y_2O_3:Eu^{3+}$. For all three phosphors, intensity is proportional to repetition frequency, even though the sulfide was being excited so strongly during the experiment that its efficiency was only 45% as great as its low-current-density value. That is, the efficiency is independent of repetition rate even when there is strong saturation. This was true over the whole available range of current densities and dwell times.

The pattern of the excitation could also be varied with little effect on efficiency. For example, nearly constant emission intensity from the sulfides was obtained with 60 single pulses/sec, 30 sets/sec of two

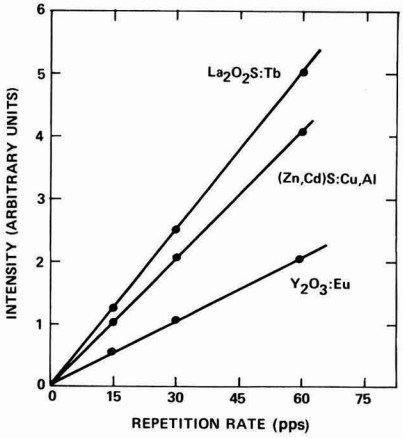

Fig. 4. Photomultiplier response *vs.* repetition rate in pulsed stationary spot experiment.

pulses 63.5 μsec apart (the NTSC horizontal scan period), and 15 sets/sec of four pulses 63.5 μsec apart. This implies that the phenomena responsible for saturation in the sulfides recover in a TV horizontal scan period. One conclusion that can be drawn from this is that sample heating does not contribute to phosphor saturation under these conditions. The instantaneous temperature rise resulting from a pulse is

$$\Delta T = \frac{J_p V \tau}{\mu C d} \qquad [3]$$

where V is beam voltage, μ is beam penetration depth, and C and d are phosphor heat capacity and density, respectively. For $J_p = 0.12$ A/cm^2, $V = 20$ kV, $\tau = 0.5$ μsec, and $\mu = 3$ μm, the temperature rise per pulse is $\Delta T \simeq 1°$C, far too small to change phosphor efficiency. The lack of a repetition frequency effect implies that the time-averaged temperature rise is also insufficient to change phosphor efficiency.

Figure 5 presents relative phosphor efficiency *vs.* pulse duration and peak current density in an experiment in which the product $J_p\tau$ was held constant. It is apparent from Fig. 5 that the phosphor efficiency is constant under these conditions, even though the efficiencies are significantly reduced by saturation. These experiments were repeated for a variety of other activator concentrations and other values of the product $J_p\tau$, with similar results. It is reasonable to conclude that the loss of efficiency due to saturation depends on the dose ρ of beam charge per unit area per pulse: $\rho = J_p\tau$. Furthermore, since the maximum dwell time used in this experiment was 2 μsec, it can also be concluded that the phenomena responsible for saturation do not recover significantly in times less than 2 μsec.

From the above results on pulsed stationary beam experiments, it is reasonable to suggest that when a phosphor is excited by a scanned electron beam (with dwell time ≤ 2 μsec), the efficiency loss depends on the integrated dose of beam charge per unit area per scan

$$\rho = \int J(t)\,dt \qquad [4]$$

Since the center of the beam may not pass over a given phosphor particle, a further average over the transverse dimensions of the beam spot is also necessary.

These results can now be applied to a raster-scanned cathode ray tube. Let i be the beam current, D be the average beam diameter, t be the time for a horizontal scan, and H and V be the horizontal and vertical dimensions of the raster, respectively. Then the average dose of beam charge per unit area per scan is

$$\rho = \frac{it}{DH} \qquad [5]$$

For an elongated beam spot shape, the correct value of D to use in Eq. [5] is the spot dimension transverse to the beam scan direction. Thus beam current, spot size, and scan velocity affect phosphor saturation directly, not average current density. Let us choose typical values for a representative calculation: $i = 1.2$ mA, $D = 1$ mm, $H = 40$ cm, $V = 30$ cm, and $t = 53.5$ μsec. These values yield $J_{av} = i/HV = 1$ μA/cm^2 for the time- and screen-averaged current density, and $\rho = 16$ nC/cm^2. This corresponds to $J_p = 32$ mA/cm^2 in our 0.5 μsec pulsed stationary spot experiment. Figure 6 presents efficiencies of (Zn,Cd)S:Cu,Al phosphors relative to $La_2O_2S:Tb^{3+}$ measured both at $J_p = 32$ mA/cm^2 and extrapolated to $J_p = 0$. It is evident that in con-

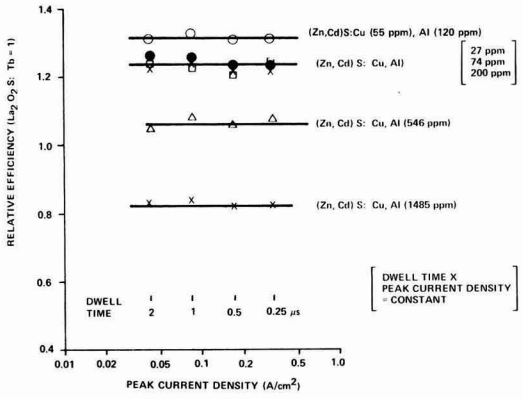

Fig. 5. Efficiency of (Zn,Cd)S:Cu,Al phosphors relative to $La_2O_2S:Tb^{3+}$ *vs.* peak current density in 60 pps pulsed stationary spot experiment. Product of peak current and pulse duration was kept constant by adjustment of pulse duration with a value corresponding to $J_{av} = 5$ μA/cm^2.

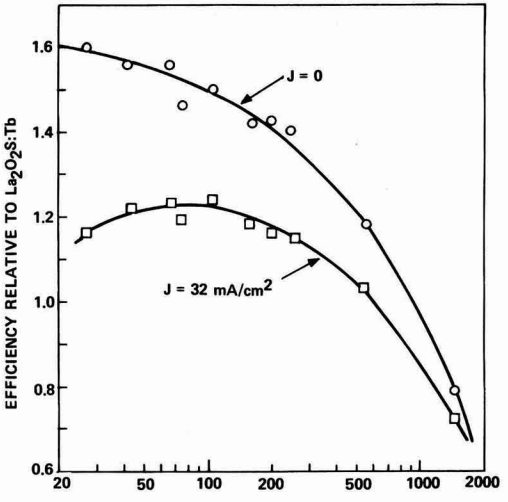

Fig. 6. Efficiency of (Zn,Cd)S:Cu,Al phosphors relative to $La_2O_2S:Tb^{3+}$ *vs.* Cu concentration, with [Al]/[Cu] = 1.

trast to the case at $J_p = 0$, the response curve at $J_p = 32$ mA/cm² displays a maximum efficiency *vs.* Cu concentration occurring in the range 50-120 ppm. Measurements at lower current density would shift the peak to lower concentration, and vice versa. Within the range of optimum concentrations for $J_p = 32$ mA/cm², the average loss of efficiency due to saturation is 20%. This is in satisfactory agreement with experience in raster scanned color TV tubes, in which a typical saturation loss at an average current density of 1 μA/cm² is 15%.

Another variable affecting saturation behavior in CRT displays is anode potential. It is sometimes observed that color TV tubes exhibit greater phosphor saturation for a given beam current at higher anode potentials. The experiments about to be described were aimed at determining whether this is due to phosphor-intrinsic properties or extraneous effects. It was first determined that the light output from $Y_2O_3:Eu^{3+}$ is proportional to anode potential in the range from 20 to 30 kV. This made it possible to determine current density in the usual way with adjustment of the conversion factor K for anode potential. Measurements of relative efficiency *vs.* current density for anode potentials of 20, 25, and 30 kV for one sample are presented in Fig. 7. It is evident that, for this sample, saturation behavior depends solely on current density and not on anode potential. Similar measurements were made on three other samples whose Cu concentrations ranged from 67 to 257 ppm, with similar results and conclusions. It can therefore be concluded that the greater phosphor saturation observed in tubes operated at higher anode potentials is not phosphor-intrinsic, but is probably due to the smaller beam size at higher anode potential, which results in larger beam current density for the same beam current.

The lack of dependence of phosphor saturation on anode potential is unexpected, and probably results from a compensation between two competing effects of increasing anode potential: increased incident energy/unit area, but decreased energy/unit volume within the phosphor. The latter results from the superlinear dependence of electron penetration depth on beam energy.

The efficiency data can be usefully summarized in an empirical formula

$$\epsilon(\rho,c) = \frac{\epsilon_0(c)}{[1 + \rho/\rho_0(c)]^{1/2}} \qquad [6]$$

where $\epsilon(\rho,c)$ is the relative efficiency as a function of ρ (dose of beam charge/cm²), c is activator concentration, $\epsilon_0(c)$ is the relative efficiency extrapolated to $\rho = 0$, and $\rho_0(c)$ is a parameter expressing the beam charge/cm² required to reduce the efficiency by a factor of $\sqrt{2}$.

For any of the samples investigated, Eq. [6] represents the dependence of efficiency on beam current density within 2%. The dependence of ϵ_0 on Cu concentration is presented in Fig. 6; the variation of ρ_0 with c is given in Fig. 8. While Eq. [6] has no theoretical basis, it is a useful formula in conjunction with Fig. 6 and 8 for determining the saturation performance of a given phosphor, or for obtaining the optimum activator concentration for a given level of excitation.

Note that, with one exception to be discussed below, the data on ρ_0 *vs.* Cu concentration are independent of Al concentration, provided that the [Al]/[Cu] ratio is greater than unity, *i.e.*, as long as the Al content is great enough to guarantee that the dominant emission center is the Cu-green center. The single exception in Fig. 8 occurs for [Cu] = 27 ppm and [Al] = 200 ppm. This sample exhibited a significant shift from Cu-green emission to "self-activated" blue emission as current density was increased, so it is hardly surprising that its saturation behavior differs from samples that did not exhibit self-activated blue emission.

Saturation under Photoexcitation

Several measurements of relative efficiency *vs.* excitation density were performed under photoexcitation, to yield insight into the mechanism of phosphor saturation. Excitation at 337 nm from a pulsed nitrogen laser lies at the peak of the u.v. excitation spectrum for (Zn,Cd)S:Cu,Al, and creates free electrons and holes by band-to-band excitation. A pulsed dye laser operating at 420 nm was also used. Light at this wavelength is absorbed by promotion of electrons from Cu^+ centers to the conduction band yielding Cu^{2+} centers and free electrons. Thus there are three distinct modes of excitation (including electron beam) to compare. Excitation density in the photoexcitation experiments was varied by insertion of neutral density filters in the light path; these filters were checked by also measuring the response of a lamp phosphor which was known to respond linearly.

The comparison of saturation behavior induced by the three modes of excitation is presented in Fig. 9. The data shown here are for one sample, but are representative of samples with Cu concentration ranging from 27 to 1485 ppm. The obviously common saturation behavior for the three modes of excitation points toward a common mechanism.

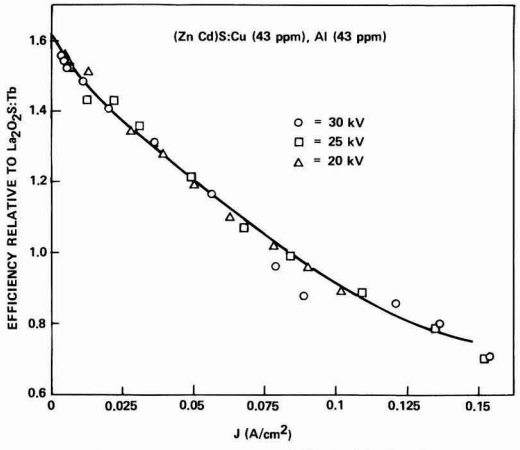

Fig. 7. Relative efficiency of (Zn,Cd)S:Cu,Al phosphor *vs.* current density for three electron beam energies.

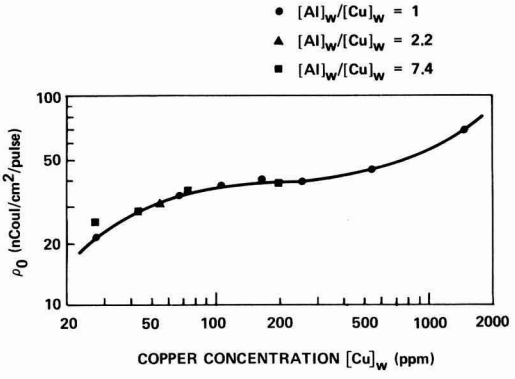

Fig. 8. Dose of electron beam charge per pulse at 20 kV required to reduce phosphor efficiency by a factor of $\sqrt{2}$ *vs.* Cu concentration.

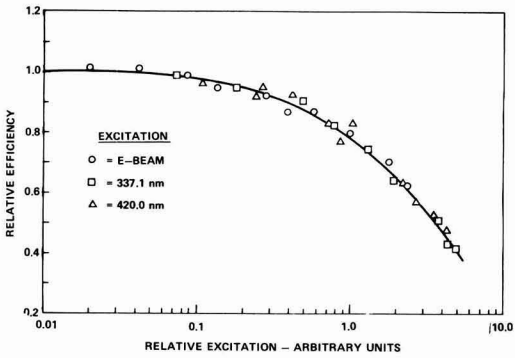

Fig. 9. Relative efficiency *vs.* relative excitation intensity in (Zn,Cd)S:Cu, Al for electron beam excitation and photoexcitation at 337 and 420 nm. Both ordinate and abscissa have been scaled for the three modes of excitation to facilitate illustrating the similarity of the shapes of the three curves.

One mechanism for phosphor saturation that may be operative in $Y_2O_3:Eu^{3+}$ is a quenching effect due to electric fields resulting from electron beam charging (8). The fact that apparently equivalent saturation is induced in (Zn,Cd)S:Cu,Al by u.v. and blue light and by electron beam excitation, reduces the possible importance of this effect for this material.

Conclusion

Loss of efficiency of (Zn,Cd)S:Cu,Al phosphors has been measured as electron beam current density is increased, and this saturation behavior has been characterized with respect to dependence on activator concentration, repetition rate, pulse duration, and anode potential. Saturation is more severe at low Cu concentration (25-100 ppm) than at medium concentration (100-500 ppm). This indicates that activator depletion is a mechanism for the sublinear response in these phosphors. A simple calculation illustrates that this is reasonable: at a dose of beam charge of 20 nC/cm^2, the efficiency of a sample containing 27 ppm Cu is reduced by 30%. Assuming that an electron-hole pair is created for each 10 eV of beam energy and that the beam penetration depth is 3 μm at 20 kV, the carrier density created by 20 nC/cm^2 within a penetration depth i $\simeq 10^{18}$ cm^{-3}. The Cu concentration of 27 ppm corresponds to a number density also of 10^{18} cm^{-3}, so it is indeed reasonable that activator depletion would be appreciable under these conditions.

However, the near absence of concentration dependence in the 100-500 ppm range and the fact that samples in this range are only about twice as resistant to saturation as a 27 ppm sample indicates either that a second saturation mechanism is involved or that not all of the added Cu is effective in the luminescence process. There appears to be no corroborating evidence for the latter; for example, concentration quenching is not particularly severe in the 100-200 ppm range. Thus there is evidence that another mechanism is responsible for the sublinear response of these phosphors at other than very low activator concentrations. Other experiments reported here indicate that the other mechanism is not thermal or electric field quenching.

These results show that saturation in (Zn,Cd)S:Cu,Al phosphors can be improved somewhat by moderate increases in activator concentration. A clear understanding of the second mechanism is necessary to judge if further improvements are possible. The second paper in this series, based on an earlier presentation (7), will show that this second mechanism is excited-state absorption: a combination of (*i*) reabsorption of emitted radiation by excited Cu centers (Cu^+ centers that have captured holes to become Cu^{2+}) and (*ii*) the analogous Forster-Dexter (9) process.

Acknowledgments

I wish to thank R. Dodds for preparing the phosphors, W. Persun for determining optimum screen weights, and B. Hawkins for expert technical assistance.

Manuscript submitted Aug. 20, 1981; revised manuscript received Dec. 7, 1981.

Any discussion of this paper will appear in a Discussion Section to be published in the June 1983 JOURNAL. All discussions for the June 1983 Discussion Section should be submitted by Feb. 1, 1983.

Publication costs of this article were assisted by GTE Laboratories, Incorporated.

REFERENCES

1. See, for example, H. W. Leverenz, "An Introduction to Luminescence in Solids," pp. 349 ff., Wiley, New York (1950).
2. D. C. Stupegia and H. Forest, Paper 324 presented at The Electrochemical Society Meeting, Seattle, Washington, May 21-26, 1978.
3. V. D. Meyer and F. C. Pallila, *This Journal*, **116,** 535 (1969).
4. E. F. Gibbons, R. G. DeLosh, T. Y. Tien, and H. L. Stadler, *ibid.*, **120,** 1730 (1973).
5. M. Stevens, L. Ozawa, G. Ban, and H. N. Hersh, *IEEE Trans. Consumer Electron.*, **ce-21,** 1 (1975).
6. J. R. McColl and R. E. Dodds, Paper 325 presented at The Electrochemical Society Meeting, Seattle, Washington, May 21-26, 1978.
7. J. R. McColl, Paper 216 presented at The Electrochemical Society Meeting, Boston, Massachusetts, May 6-11, 1979.
8. D. J. Robbins, *This Journal*, **123,** 1219 (1976).
9. D. L. Dexter, *J. Chem. Phys.*, **21,** 836 (1953).

Luminescence of Rare Earth Activated Lutetium Oxyhalide Phosphors

Jacob G. Rabatin*

General Electric Company, Quartz and Chemicals Department, Cleveland, Ohio 44110

ABSTRACT

Lutetium oxychloride and oxybromide phosphors have been prepared using Tb^{3+}, Tm^{3+}, Ce^{3+}, Sm^{3+}, and Dy^{3+} activators. In general, luminescent characteristics are similar to those found for corresponding lanthanum oxyhalide phosphors. The stability of lutetium oxyhalides is markedly decreased apparently due to the effect of the lanthanide contraction phenomenon. Apparently for the same reason, emissions from the Tm^{3+} $^3P_0$ excited states occur about 10 nm lower than those for corresponding lanthanum oxyhalide phosphor emissions. Tb^{3+}, Tm^{3+}, and Ce^{3+} activated phosphors are efficient under x-ray excitation and may have use in image intensifiers for high kilovolt peak applications in medical radiography. Emissions from the Tm^{3+} $^3P_0$ have a broad-band character similiar to that found in LaOBr:Tm phosphors.

The luminescent properties of rare earth activated yttrium, lanthanum, and gadolinium oxyhalide phosphors have been reported (1-6). LaOBr:Tb phosphors are efficient under ultraviolet (2), cathode-ray, and x-ray excitations (3). LaOBr:Tm phosphors are efficient under cathode-ray and x-ray excitations and show broad-band type emissions at 300 and 370 nm (4). LaOBr phosphors activated with Ce^{3+} (5) and Dy^{3+} (6) are also relatively efficient under cathode-ray and x-ray emissions. In the process of filling the 4f electronic shell in the lanthanide series, a large contraction of ionic radius occurs from La^{3+} at 1.06Å to Lu^{3+} at 0.85Å. This so called lanthanide contraction affects the basicity and other chemical properties of the rare earth ions. It is the primary reason for reduced stability of lutetium oxyhalides as will be shown in this paper. A major purpose of this paper is to compare the luminescent properties of the new lutetium oxyhalide phosphors with corresponding lanthanum oxyhalides. Because of the cost of Lu_2O_3 at over six dollars per gram, a limited number of phosphor compositions were studied.

Experimental

Sample preparation.—The desired amounts of the activator and lutetium oxide were first dissolved in nitric acid and then coprecipitated as oxalates. The mixed oxalates were fired back to appropriate mixed oxides at about 1000°C to obtain a highly dispersed activator. About 10g samples of each lutetium oxyhalide phosphor were prepared using a gaseous hydrogen halide method previously described (9). Since lutetium oxyhalides are relatively unstable at higher humidities, the phosphors were washed in methanol that contained stearic acid to impart hydrophobic moisture resistant phosphor surfaces. The phosphors were kept in air tight glass containers between measurements.

Thermogravimetry (TGA).—TGA analyses were made using a du Pont 950-1090 Thermal Analyzer. Sample sizes were 20 mg. Heating rates were 20°C per minute using a dry air atmosphere. The data in Fig. 1 are reported as weight percent changes *vs.* sample temperatures.

Reflectance and emission spectra.—Reflectance spectra were obtained on powder plaques using a Cary 14 spectrophotometer. CaF_2 powder was used as a reference sample. The results in Fig. 2 are reported as percent reflectance as a function of wavelength. The emission spectra were also obtained using a Cary 14 apparatus that was coupled to a demountable cathode-ray apparatus or to a 254 mm excitation source as required. The cathode-ray excitation energies were 10 kV and 10A. For these measurements the samples were settled onto quartz disks placed in methanol. The disks were dried at 100°C before being placed in the demountable CR generator. The emission spectra shown in Fig. 3-9 were corrected for differences in photomultiplier sensitivities over the spectral range.

Other measurements.—X-ray diffraction analyses were performed using a Diano apparatus. The diffraction patterns were compared to LaOBr and LaOCl patterns and to results reported in the literature (10, 11). Absolute densities were measured using the well-known pycnometer method.

Output under x-ray excitations were measured on powder plaques using a special apparatus which contains a GE dental unit x-ray generator coupled to a

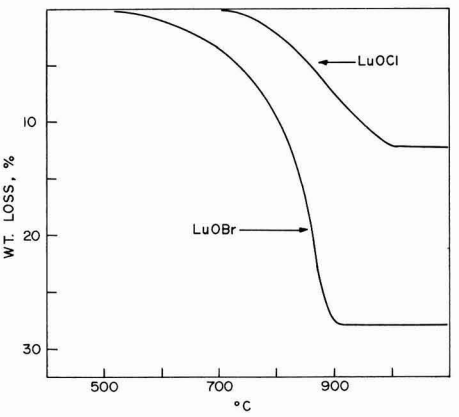

Fig. 1. TGA curves for LuOCl and LuOBr between 400° and 1100°C run in dry air at 20°C per minute heating rates.

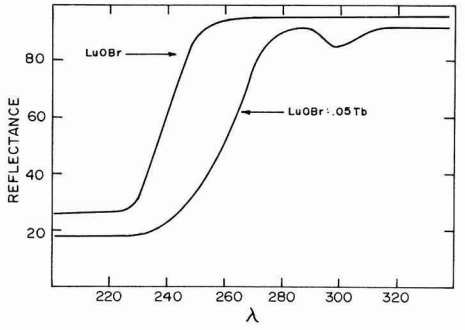

Fig. 2. Reflectance curves for LuOBr and LuOBr:0.05 Tb from 200 to 330 nm.

* Electrochemical Society Active Member.

Key words: lutetium oxyhalides, luminescence, preparation, characterization.

photomultiplier and suitable readout devices. Relative readings were compared to LaOBr:0.002 Tb commercial phosphor whose output was set equal to 100.

Results and Discussion

During the preparation of lutetium oxyhalides, it was found that these compounds are much less stable compared to lanthanum oxyhalides. The relative instabilities of LuOCl and LuOBr are evident from the TGA results shown in Fig. 1. In dry air, the decomposition of LuOBr begins at about 500°C and is complete by about 900°C with a weight loss of 27.5% that is nearly theoretical for the reaction

$$2LuOBr + 1/2\ O_2 \rightarrow Lu_2O_3 + Br_2$$

In sharp contrast, under these conditions, LaOBr is stable to over 1000°C. The decomposition of LuOCl begins at about 700°C and is complete at 1000°C. At room temperatures and relative humidity above 60%, lutetium oxyhalides slowly decompose due to a reaction with condensed moisture according to the reaction

$$3LuOBr + 3H\ OH \rightarrow 2Lu(OH)_3 + LuBr_3$$

The hydroscopic nature of $LuBr_3$ accelerates this reaction. Apparently because of the decreased basicity of Lu compared to La due to the lanthanide contraction, the lutetium oxyhalides are much less stable.

LuOCl and LuOBr were characterized by x-ray diffraction techniques that show similar patterns to LaOCl and LaOBr, respectively. According to Templeton *et al.* (10), LuOCl does not crystallize into the PbFCl-type tetragonal structure found for LaOCl. Mayer *et al.* (11) found that LuOBr does crystallize into the PbFCl-type structure, with space group D_{4h}^7 P4/nmm and with two molecules in the unit cell. These structural differences between LuOCl and LuOBr may explain some of the differences in emission characteristics. The measured absolute density of LuOBr is 7.1 in good agreement with the value calculated from lattice constants (11). The crystal habit of both compounds is plate-like and the refractive indexes are greater than 2.1.

To some extent optimum LaOBr phosphor compositions were used as guides to choose activator concentrations for the lutetium oxyhalide systems. Some qualitative results on color and emission intensities are listed in Table I. In general, the LuOBr phosphor have more intense emissions than the corresponding LuOCl phosphors. Also, the emission colors and intensities are similar to the corresponding lanthanum oxyhalide phosphors. Figure 2 shows the diffuse reflectance spectra for LuOBr and LuOBr:0.05Tb. The absorption edge is at about 240 nm for LuOBr and at about 265 nm for LuOBr:0.05Tb. Under 254 nm excitation, the absorption process involves the strong broad-band transition 4f-5d of Tb^{3+} (1).

Spectral emission curves were obtained for several phosphors using CR and 254 nm excitations. These results are presented in Fig. 3-9. Only selected regions of the emission spectra are shown for each phosphor so that more detailed aspects of these emissions can be observed. The complete spectra between 300 and 700 nm showed no other unusual emission characteristics and are similar to emission spectra reported for the corresponding LaOCl phosphors. Assignments of transitions are not indicated in most cases since these correspond closely to those reported previously for LaOBr phosphors (1-6). The emission spectra, under CR excitation, for LuOBr:0.002 Tb are shown in Fig. 3. $^5D_3$-^7F_j emissions predominate in the ultraviolet-blue spectral region similar to those for LaOBr:0.002Tb (2). However, the $^5D_4$-$^7F_5$ emissions at about 542 nm are more intense by a factor of 3 compared to LaOBr:0.002Tb. It appears that the quenching of the $^5D_3$-^7F_j emission occurs at lower Tb concentrations compared to LaOBr:Tb phosphor. Possibly the quenching of the $^5D_3$ emissions due to the cross-relaxation process (12) is favored in LuOBr phosphors because Tb-Tb near neighbors are more likely to occur since the ionic radii of Lu^{3+} and Tb^{3+} are more alike and Tb-Tb near neighbors should cause less crystal distortions. This quenching phenomenon is more clearly observed in LuOBr:0.05Tb (Fig. 4) where only $^5D_4$-^7F_j emissions are detected while in the case of LaOBr:0.05Tb significant $^5D_3$-^7F_j emissions are observed (3). The emission spectra of LuOCl:0.05Tb are shown in Fig. 5. The $^5D_4$-$^7F_5$ emissions at about 540-550 nm are more intense

Table I. Colors and emission intensities of various lutetium oxyhalide phosphors

Phosphor	Excitations and emissions*		
	254 nm	CR	X-ray
LuOBr:0.05Tb	Green, S	Green, S	Green, S
LuOBr:0.002Tb	Blue, W	Blue, S	Blue, S
LuOBr:0.003Tb	0	Blue, M	Blue, M
LuOBr:0.005Sm	Orange, M	Orange, S	Orange, M
LuOBr:0.005Dy	0	Yellow, M	Yellow, W
LuOBr:0.005Ce	Blue, S	Blue, S	Blue, S
LuOCl:0.05Tb	Green, S	Green, S	Green, S
LuOCl:0.005Ce	Blue, W	Blue, M	Blue, W
LuOCl:0.003Tm	Blue, W	Blue, M	Blue, M

* S = strong, M = medium, W = weak emission.

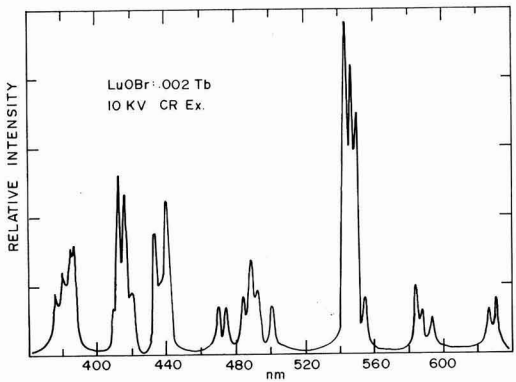

Fig. 3. Emission spectra for LuOBr:0.002 Tb under CR excitation

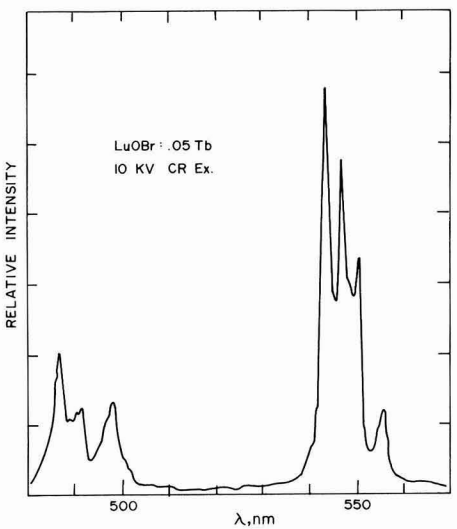

Fig. 4. Emission spectra for LuOBr:0.05 Tb under CR excitation

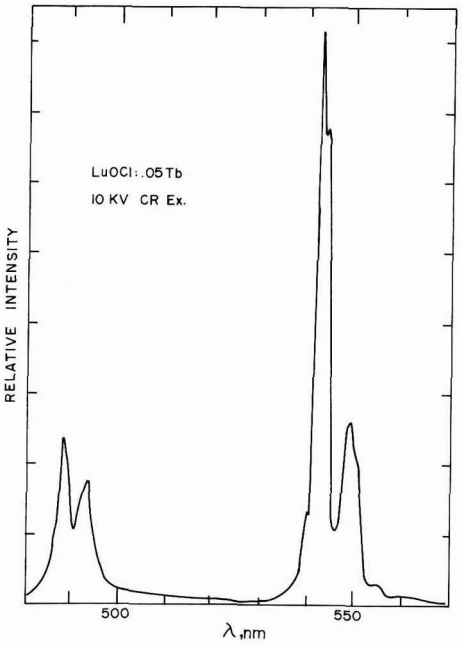

Fig. 5. Emission spectra for LuOCl:0.05 Tb under CR excitation

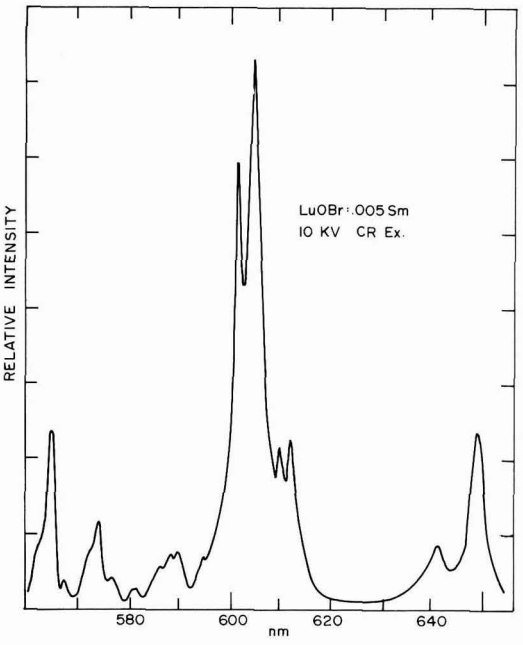

Fig. 7. Emission spectra for LuOBr:0.005 Sm under CR excitation

and show different crystal field splitting characteristics compared to LuOBr:0.05Tb emissions as might be expected if LuOCl has a different crystal structure (10).

The emission spectra for LuOBr:0.005Ce are shown in Fig. 6 using CR and 254 nm excitations. Two distinct broad-band emissions occur at 403 and 432 nm corresponding to emissions to the doublet ground states, $^2F_{5/2}$ and $^2F_{7/2}$, respectively. The 403 nm emissions are more intense under 254 nm excitation. By contrast, LaOBr:0.005Ce has a single emission peaking at 430 nm with a half-intensity width of 70 nm (5). Figure 7 shows the emission spectra for LuOBr:0.005Sm using CR excitation. The dominant emissions occur at about 605 nm and correspond to $^4F_{5/2}$-$^6H_{7/2}$ transitions. Significant differences are observed when compared to the emissions of LaOBr:0.005Sm. The emission spectra for

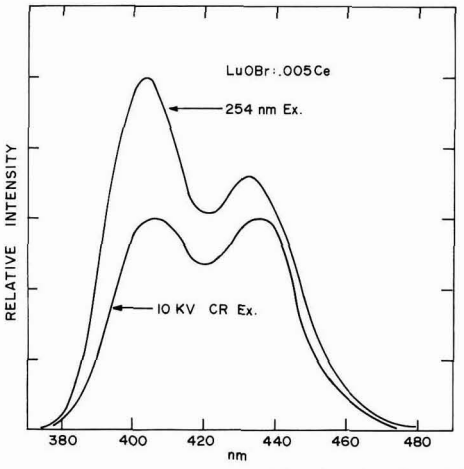

Fig. 6. Emission spectra for LuOBr:0.005 Ce under CR and 254 nm excitations.

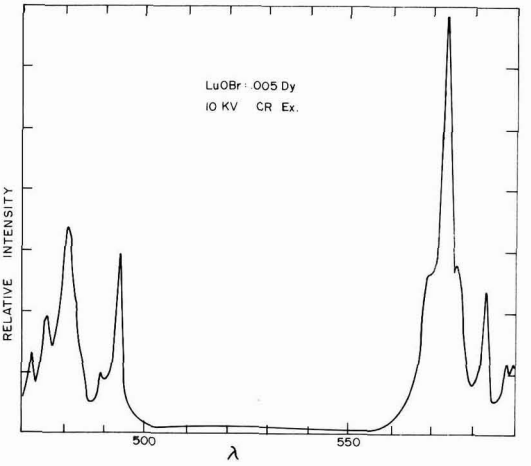

Fig. 8. Emission spectra for LuOBr:0.005 Dy under CR excitation

LuOBr:0.005Dy under CR excitation are shown in Fig. 8. The principal emissions occur at about 572 nm and are almost identical to those found for LaOBr:0.005Dy (6).

Figure 9 shows the emission spectra for LuOBr:0.005Tm under CR excitation. Of particular interest is the fact that the emissions at 357, 368, 388 nm from the highest excited states of Tm^{3+} (^3P levels) have significant broad-band character as compared to the $^1G_4$-$^3H_6$ narrow-band emission at 460 nm typical of rare earth activators. Previous studies (4) on LaOBr:0.005 Tm show this striking broad-band character even more clearly using high resolution spectrophotometry. Significantly these emissions from the ^3P_j levels are about 10 nm lower compared to those found in LaOBr:0.005Tm. Studies are in progress to better define these interesting differences in emission spectra and the

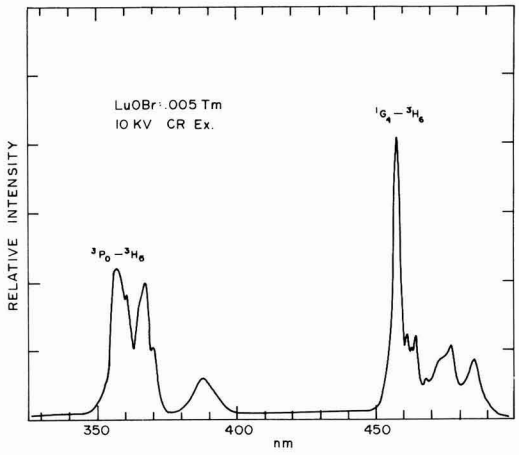

Fig. 9. Emission spectra for LuOBr:0.005 Tm under CR excitation

causes for broadening of the emissions from the highest excited states of Tm^{3+}.

Since LuOBr:Tb phosphors are efficient under 254 excitation, emission colors and relative quantum efficiencies were measured for several phosphors. These results are presented in Table II and are compared to LaOBr:0.05Tb. In general the emission colors are similar to LaOBr:0.05Tb. LuOBr:0.05Tb has a greener emission color as would be expected from the spectra shown in Fig. 5. The relative quantum efficiencies are quite high.

The relative outputs and emission colors were measured for several phosphors using 90 kV peak x-ray excitation. These results are listed in Table III. The emission intensities were compared to those for LaOBr:0.002 Tb set equal to 100. Based on a conversion efficiency of LaOBr:Tb of about 18-20% (13), the relative energy efficiencies of LuOBr:Tm, LuOBr:Tb, and LuOBr:Ce phosphors exceed 10%. These phosphors may have application in image intensifiers for use in medical radiography where high kV peak x-rays are required and where high phosphor costs are not important. A comparison of color points for LuOBr:0.05Tb under 254 nm (Table II) and x-ray (Table III) excitations indicates a significant difference in X-coordinates. Possibly the $^5D_4$-$^7F_4$ and $^5D_4$-$^7F_3$ emissions have higher intensities under x-ray excitations thus contributing to a color shift.

Table II. Emission colors and relative quantum efficiencies of terbium-activated lutetium oxyhalides under 254 nm excitation

Phosphor	Rel. QE	Color	
		x	y
LaOBr:0.05Tb	85%	0.316	0.503
LuOBr:0.05Tb	92%	0.313	0.543
$Lu_{0.5}La_{0.5}OBr$:0.05Tb	89%	0.327	0.524
LuOCl:0.05Tb	84%	0.246	0.662

Table III. Relative brightness and emission colors of various lutetium oxyhalide phosphors under 90 kV peak x-ray excitation (LaOBr:0.002Tb = 100)

Phosphor	Rel x-ray output	Color	
		x	y
LaOBr:0.05Tb	87	0.365	0.529
LuOBr:0.002Tb	60	0.276	0.190
LuOBr:0.005Cl	63	0.180	0.022
LuOBr:0.005Sm	—	0.668	0.298
LuOBr:0.003Tm	47	—	—
LuOCl:0.05Tb	49	—	—
LuOCl:0.005Ce	10	—	—
LuOCl:0.003Tm	25	—	—

Summary

The lanthanide contraction occurring between La and Lu affects both chemical stability and luminescent properties of lutetium oxyhalide phosphors. Lutetium oxyhalides are less stable at higher temperatures and are more readily hydrolyzed by water compared to lanthanum oxyhalides. In general LuOBr phosphors have more intense emissions compared to LuOCl phosphors. Quenching of the $^5D_3$-$^7F_4$ emissions occurs at lower Tb^{3+} concentrations in lutetium oxyhalide phosphors apparently due to a greater tendency for formation of Tb-Tb near neighbor associated pairs increasing the probability for a cross-relaxation process to occur. As in the case of LaOBr:Tm phosphors, emissions from the ^3P_j levels of LuOBr:Tm have significant broad-band character even under high resolution spectrophotometry. Further, these emissions have unexpectedly shifted to lower wavelengths by about 10 nm. In general, other luminescent properties are similar to those found for lanthanum oxyhalide phosphors.

Terbium-activated lutetium oxybromides and oxychloride phosphors are efficient under 254 nm excitations. Under x-ray excitations LuOBr:Tb, LuOBr:Tm, and LuOBr:Ce phosphors have energy efficiencies in excess of 10%. Potential applications for these phosphor are in image intensifiers for use in medical radiography where high kilovolt x-rays are required.

Acknowledgment

The author gratefully acknowledges the important assistance of Robert Evans in making many measurements and preparing numerous samples.

Manuscript submitted Sept. 21, 1981; revised manuscript received *ca.* Nov. 29, 1981. This was Paper 346 presented at the Seattle, Washington, Meeting of the Society, May 21-26, 1978.

Any discussion of this paper will appear in a Discussion Section to be published in the June 1983 JOURNAL. All discussions for the June 1983 Discussion Section should be submitted by Feb. 1, 1983.

Publication costs of this article were assisted by the General Electric Company.

REFERENCES

1. G. Blasse and A. Bril, *Philips Res. Rep.*, **22**, 481 (1967).
2. J. Rabatin, Abstract 78, p. 189, The Electrochemical Society Extended Abstracts, New York, New York, May 4-9, 1969.
3. J. Rabatin, Abstract 102, p. 250, The Electrochemical Society Extended Abstracts, San Francisco, California, May 12-17, 1974.
4. J. Rabatin, Abstract 198, p. 467, The Electrochemical Society Extended Abstracts, Toronto, Ontario, Canada, May 11-16, 1975.
5. J. Rabatin, Abstract 218, p. 563, The Electrochemical Society Extended Abstracts, Boston, Massachusetts, May 6-11, 1979.
6. J. Rabatin, Abstract 306, p. 788, The Electrochemical Society Extended Abstracts, Los Angeles, California, Oct. 14-19, 1979.
7. J. Rabatin, U.S. Pat. 3,617,743 (1971).
8. J. Rabatin, U.S. Pat. 3,795,814 (1974).
9. J. Rabatin, U.S. Pat. 3,607,770 (1971).
10. D. H. Templeton and C. H. Dauben, *J. Am. Chem. Soc.*, **75**, 6069 (1953).
11. I. Mayer, S. Zolotov, and F. Kassierer, *Inorg. Chem.*, **4**, 1637 (1965).
12. A. D. Pearson, G. E. Peterson, and W. R. Northover, *J. Appl. Phys.*, **37**, 729 (1966).
13. G. W. Ludwig, Private communication.

The Influence of Intermittent Growth Procedures on Dislocation Densities in InP Epi-Layers

S. Mahajan,* V. G. Keramidas,* and W. A. Bonner

Bell Laboratories, Murray Hill, New Jersey 07974

ABSTRACT

The influence of intermittent growth procedures on dislocation densities in iso-epitaxial layers, grown on highly dislocated (001) InP substrates by LPE, has been assessed using etch pitting. It is observed that the incorporation of an isothermal hold in the growth sequence reduces the density of dislocations in the epi-layer. The major reduction occurs during growth following the isothermal arrest. However, the interrupted growth schemes involving partial melt-back of an epi-layer as well as melt-back followed by an isothermal hold are not effective in reducing the dislocation density.

It is generally agreed that the performance, reliability, and degradation behavior of opto-electronic devices are affected by the presence of dislocations (1-7). Olsen (2) has investigated the influence of interfacial lattice mismatch on III-V compounds on device performance. It is found that the increased mismatch has deleterious effects on the electro-optical properties of transmission photocathode and transmission secondary electron multipliers. Furthermore, that dislocations play an important role in the degradation behavior of (Ga,Al)As/GaAs DH lasers is well documented (3-5). A consensus has emerged that dark line defects (DLD's) observed in degraded regions originate from existing dislocations. DLD's oriented along the <110> directions may evolve by the glide of threading dislocations, whereas the growth of <100> DLD's could occur by glide and climb. In addition, the recent work on optically degraded InGaAsP epi-layers indicates that non-luminescent regions, as revealed by spatially resolved photoluminescence, contain dislocation networks (6). These clusters also appear to form by the glide of threading and inclusion-generated dislocations. More recently, Dutt *et al.* (7) have shown that dislocations and stacking faults have a marked effect on the performance of (Ga,Al)As/GaAs DH LED's.

It is apparent from above that to enhance the performance and device reliability, it is desirable to reduce the density of threading dislocations in epi-layers. Several attempts have been made to achieve this objective in the past (8-13). They can be broadly grouped into two categories: growth schemes involving either the imposition of a stress (8-12) or intermittent growth procedures (13). Using the latter approach, Saul (13) has achieved a drastic reduction in dislocation density in GaP epi-layers. In the present study, we have evaluated, using etch pitting, the influence of different growth procedures on the dislocation density of homo-epitaxial layers grown on InP substrates by LPE. These results constitute the present paper.

Experimental Details

These studies were carried out on highly dislocated ($\rho > 10^5$ cm^{-2}), {100} oriented InP substrates doped with S($n \cong 1 \times 10^{19}$ cm^{-3}). Prior to the epitaxial growth by LPE, substrates were polished with 0.5% Br-methanol solution to an optically smooth finish. Source-piece protection and a shallow In melt-back were incorporated in the growth sequence to eliminate the deleterious effects of thermal decomposition of the substrate (14). Three different growth cycles, schematically illustrated in Fig. 1, were employed in the present experiments. In cycle A, epi-growth was initiated at 700°C and the resulting homoepitaxial layer was isothermally aged for 2 hr at 660°C in contact with the melt from which it was grown. To assess whether or not the growth of an epi-layer after the isothermal hold is essential to discern the effects of aging on dislocation density, one wafer was aged for 2 hr at 640°C in contact with the melt and was then withdrawn from the furnace without subsequent cooling. In cycle B, an epi-layer was partially back-melted by raising the temperature from 660° to 670°C and then an additional thickness was grown on the back-melted surface. In cycle C, A and B were combined with B preceding A.

The Huber etch (15) has been shown to reliably delineate all of the macrostructural features in InP (16). Consequently, the spatial distribution of dislocations in epi-layers was assessed using this etchant and Nomarski interference contrast microscopy. To evaluate the variation in dislocation density with depth, material was removed in a controlled manner in a 1.5% Br-methanol solution in which the removal rate has been measured to be ~6.75 μm/min. After a dip in Br-methanol solution for a specified period, samples were Huber

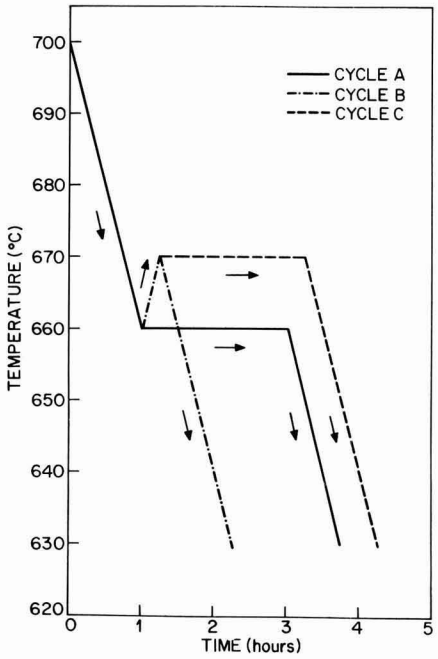

Fig. 1. Schematic representation of intermittent growth procedures used for growth of LPE layers. Heating and cooling rates were 0.7°C/min.

* Electrochemical Society Active Member.
Key words: etch pitting, growth, dislocation.

etched. This procedure was repeated several times depending upon the intermittent growth procedure used.

Results

Shown in Fig. 2 is a typical example of etch pit distribution observed on the (001) surface of the as-grown crystal at low magnification. A distinctive feature of this micrograph is the clustering of pits into bands that lie along the <110> directions. It is inferred that these bands are due to slip and must be caused by thermal gradient-induced stresses that exist during crystal growth. Furthermore, the dislocation density in these substrates averages between $\sim 2\text{-}7 \times 10^5$ cm^2.

Figures 3(a) and (b) show schematically the spatial distribution of dislocations in samples that have undergone cycle A and "modified" cycle A, respectively. The latter refers to the isothermal aging experiment in which a layer was not grown after the hold. It is clear from Fig. 3(a) that a slight reduction in dislocation density, i.e., ~15%, occurs during the epi-growth that precedes the isothermal hold. A similar decrease in dislocation density is observed in Fig. 3(b). However, if an epi-layer is grown after the pause, dislocation density is further reduced, leading to an overall reduction of ~42% with respect to the underlying substrate.

Figure 4(a) shows a weakly developed slip band in an epi-layer which has been subjected to cycle A. The layer that was grown after the isothermal hold was removed prior to etching. Figure 4(b) depicts a well-delineated slip band in the adjoining region of the substrate on which an epi-layer was not grown. In comparing Fig. 4(a) and (b) it is apparent that the distributions of dislocations within the slip bands are markedly different in the two cases. It appears from these observations that dislocations may undergo rearrangement, annihilate each other, and form closed loops during the epi-growth.

The variations in dislocation density with depth observed in samples subjected to cycles B and C are schematically illustrated in Fig. 5(a) and (b), respectively. Again, a progressive reduction in dislocation density during the epi-growth is seen. However, the dislocation density appears to increase when layers are

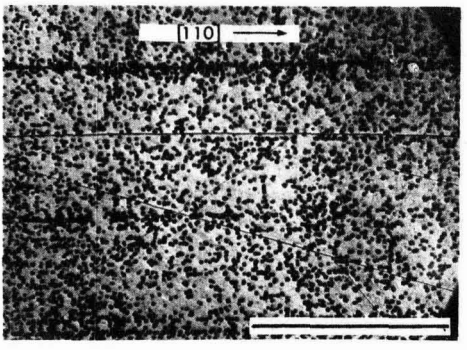

Fig. 2. Typical dislocation etch pit distribution observed on a (001) InP:S substrate. The marker represents 0.1 mm.

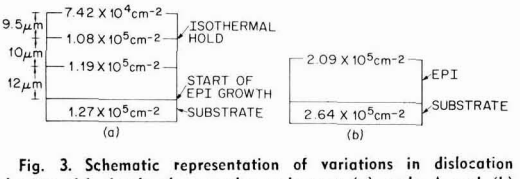

Fig. 3. Schematic representation of variations in dislocation density with depth: the samples underwent (a) cycle A and (b) isothermal hold but no growth after the hold.

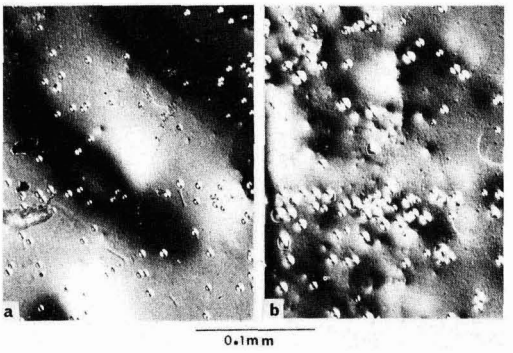

Fig. 4. Micrographs comparing the arrangement of dislocations within slip bands in (a) epi-layer and (b) the adjoining region of the substrate.

grown either after the melt-back or after the melt-back and isothermal hold.

Queisser (17) has suggested that the migration of surface ledges across the substrate dislocations could reorient them in epi-layers. He envisages that in some situations imperfections could be oriented parallel to the epi-substrate interface, and this could lead to reduced dislocation density in epi-layers. To assess whether or not this occurs during the epi-growth, thin homoepitaxial layers, 2 μm thick, were grown on back-melted InP:Sn substrates, and the distribution of dislocations in the epi-layer was correlated with that of the underlying substrate by etch pitting. Illustrated in Fig. 6(a) is an etch pit pattern observed on an epitaxial layer. Figure 6(b) shows the same area as in Fig. 6(a) except that the layer has been removed using a Br-methanol solution. Comparing the patterns observed in Fig. 6(a) and (b) (see the area marked A), it is clear that in the majority of cases there is one-to-one replication of imperfections during the epitaxial growth of thin layers. Furthermore, even though the etch pit patterns in Fig. 6(a) and (b) are essentially identical, the separation between the corresponding pits in these two micrographs is not the same. This effect must be due to the fact that dislocations in the substrate are not oriented normal to the (001) plane.

Discussion

Several interesting observations emerge from the preceding study. First, if the dislocation density in substrates is moderately high ($\sim 2\text{-}7 \times 10^5$ cm^{-2}) and some of the dislocations are clustered into slip bands, a progressive reduction in dislocation density is observed during the epi-growth. Second, it is clear from Fig. 3(a) and (b) that an epi-layer must be grown after an isothermal hold to effect a further reduction in dislocation density. Third, cycles B and C are not effective in reducing the number of dislocations in iso-epitaxial layers. Fourth, there is essentially one-to-one replication of imperfections during iso-epitaxy and dislocations in epi-layers do not appear to be oriented parallel to the epi-substrate interface.

The moderate decrease in dislocation density observed during the epi-growth as well as the effectiveness of cycle A in reducing dislocations can be comprehended as follows. Consider a possibility where two edge dislocations having opposite Burgers vectors are close to each other in the substrate, Fig. 7(a). This situation is likely to exist within slip bands that consist of positive and negative dislocations. When an epi-layer is grown, the two dislocations could come together to form a closed loop as schematically shown in Fig. 7(b). The formation of closed loops would be facilitated by glide and climb. Both of these processes could be af-

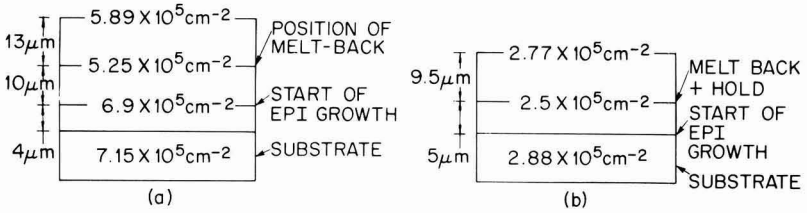

Fig. 5. Schematic representation of variations in dislocation density with depth: the samples underwent (a) cycle B and (b) cycle C.

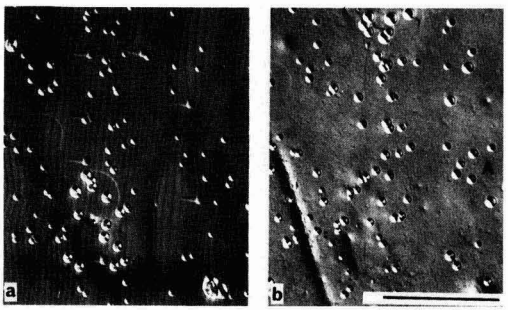

Fig. 6. Etch pit pattern observed on (a) a 2 μm thick, epitaxial layer and (b) the underlying InP:Sn substrate. Compare etch pit patterns around areas marked A in both micrographs.

fected by the attractive elastic interactions that occur between dislocations of opposite signs. Furthermore, it is implicit in the preceding discussion that the rearrangement of dislocations occurs within the slip band only during the epi-growth. This suggestion is consistent with the observations of Fig. 4.

It is visualized that the incorporation of an isothermal hold during growth would allow more time for glide and climb to occur. In addition, as suggested by Saul (13), the climb kinetics should be enhanced because of the influx of point defects from the melt into the epi-layer. This suggestion is borne out by the recent work of Small *et al.* (18) on the diffusion of Al into GaAs. They have observed that when GaAs epi-layers are in contact with a Ga-Al-As melt, Al diffuses considerably faster into GaAs epi-layers. It is therefore envisaged that two fairly well separated dislocations having opposite Burgers vectors could come close to each other by glide and climb. During the subsequent epi-growth, dislocations could come together to form a closed loop as envisaged in Fig. 7(b).

Figure 6(a) shows the typical terrace morphology observed in the present investigation. Pak *et al.* (19) have seen similar morphologies in LPE grown InP. Furthermore, the layer growth probably occurs by the lateral movement of these terraces. Since the substrate dislocations do not appear to undergo terrace-induced reorientation in the epi-layer as envisaged by Queisser (17), it is unlikely that this mechanism is responsible for the reduction in dislocation density observed during cycle A.

It is tempting to speculate on the lower limit of dislocation density for cycle A to be effective. It can be seen from Fig. 3 that an isothermal hold is effective in reducing the dislocation density from $\sim 10^5$ cm^{-2} to 7.4×10^4 cm^{-2}. It is envisaged that a dislocation density of $\sim 10^5$ cm^{-2} may represent the lower limit. Assuming that these dislocations are homogeneously distributed, the interdislocation spacing would be ~ 30 μm. Since both climb and glide are assumed to be involved in the formation of closed loops and since the attractive force between dislocations of opposite Burgers vectors varies inversely as a function of the separation, a distance of greater than ~ 30 μm would be difficult to bridge in a reasonable amount of time.

It has been demonstrated in Fig. 6 that when a thin epi-layer is grown on the back-melted, polished substrate, dislocation densities in the epi-layer and the substrate are comparable. On the other hand, a slight increase in dislocation density is observed in epi-layers grown on samples that have undergone cycles B and C. To trace the origin of these differences, surface-morphologies of back-melted InP substrates and epi-layers were examined, and these results are reproduced as Fig. 8. It appears that the back-melting of polished substrates produces roughness on a very fine scale [Fig. 8(a)], whereas the characteristic terrace morphology of epi-layers is retained after the melt-back [Fig. 8(b)].

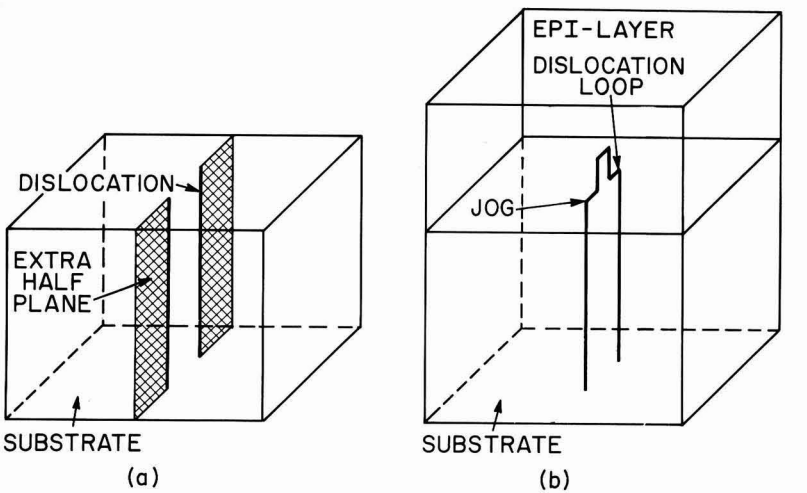

Fig. 7. Schematic illustrating the formation of a closed loop from two edge dislocations of different Burgers vectors: (a) two edge dislocations within the substrate and (b) after they have come together within the epi-layer to form a closed loop. This process is facilitated by glide and climb.

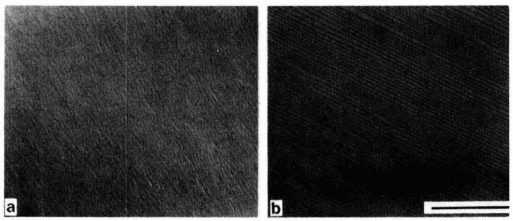

Fig. 8. Typical surface morphologies observed on (a) a back-melted InP substrate, and (b) a back-melted epi-layer. The marker represents 1.0 mm.

Acknowledgments

The authors gratefully acknowledge the help of D. Brasen and J. A. Lourenco in different phases of the experiment and appreciate the comments of G. Y. Chin, J. V. DiLorenzo, and J. H. Wernick on the manuscript.

Manuscript received Oct. 9, 1981.

Any discussion of this paper will appear in a Discussion Section to be published in the June 1983 JOURNAL. All discussions for the June 1983 Discussion Section should be submitted by Feb. 1, 1983.

Publication costs of this article were assisted by Bell Laboratories.

REFERENCES

1. G. S. Stringfellow, *J. Appl. Phys.*, **43**, 3455 (1972).
2. G. H. Olsen, *J. Cryst. Growth*, **31**, 223 (1975).
3. P. M. Petroff and R. L. Hartman, *Appl. Phys. Lett.*, **23**, 469 (1973).
4. P. W. Hutchinson and P. S. Dobson, *Philos. Mag.*, **32**, 745 (1975).
5. K. Ishida, T. Kamejima, and J. Matsui, *Appl. Phys. Lett.*, **31**, 397 (1977).
6. S. Mahajan, W. D. Johnston, Jr., M. A. Pollack, and R. E. Nahory, *ibid.*, **34**, 717 (1979).
7. B. V. Dutt, S. Mahajan, R. J. Roedel, G. P. Schwartz, D. C. Miller, and L. Derick, *This Journal*, **128**, 1573 (1981).
8. M. Ettenberg, S. H. McFarlane, and S. L. Gilbert, Proc. of the 4th International Symposium on GaAs and Related Compounds, p. 23, Boulder, CO (1973).
9. G. A. Rozgonyi, P. M. Petroff, and M. B. Panish, *Appl. Phys. Lett.*, **24**, 251 (1974).
10. G. H. Olsen, M. S. Abrahams, C. J. Buiocchi, and T. J. Zamerowski, *J. Appl. Phys.*, **46**, 1243 (1974).
11. M. Ettenberg, C. J. Nuese, J. R. Appert, J. J. Gannon, and R. E. Enstrom, *J. Electron. Mater.*, **4**, 37 (1975).
12. S. N. G. Chu, S. Mahajan, K. E. Strege, W. D. Johnston, Jr., and A. A. Ballman, *Appl. Phys. Lett.*, **38**, 766 (1981).
13. R. H. Saul, *This Journal*, **118**, 793 (1971).
14. H. Temkin, V. G. Keramidas, and S. Mahajan, *This Journal*, **128**, 1088 (1981).
15. A. Huber and N. T. Linn, *J. Cryst. Growth*, **28**, 80 (1975).
16. S. Mahajan and A. K. Chin, *ibid.*, **54**, 138 (1981).
17. H. Queisser, *ibid.*, **17**, 169 (1972).
18. M. B. Small, R. Ghez, R. Potemski, and W. Reuter, *This Journal*, **127**, 1177 (1980).
19. K. Pak, T. Nishinaga, and S. Uchiyama, *Jpn. J. Appl. Phys.*, **16**, 949 (1977).

Growth Kinetics of Silicon Thermal Nitridation

Ching-Yuan Wu and Chwan-Wen King

Institute of Electronics, National Chiao-Tung University, Hsin-Chu, Taiwan, China

and Ming-Kwang Lee* and Chin-Tang Chen

IC Development Center, Electronics Research and Service Organization, Industrial Technology Research Institute, Hsin-Chu, Taiwan, China

ABSTRACT

An analytic model for the growth kinetics of silicon thermal nitridation has been developed, in which the nitrogen radicals diffused across the as-grown thermal silicon nitride layer have been characterized by a characteristic diffusion length. It has been shown that the direct thermal nitridation of silicon in ammonia gas or nitrogen gas is similar to the silicon oxidation in oxygen or steam when the characteristic diffusion length of the nitrogen radicals is much larger than the as-grown silicon nitride layer. However, when the thickness of the as-grown silicon nitride film is larger than the characteristic diffusion length of the nitrogen radicals, the thickness of the as-grown silicon nitride film tends to saturate. The self-limiting growth has been verified to be the "logarithmic" relation of the developed model, and the activation energy of the quasi-saturation thickness has been shown to be the activation energy of the characteristic diffusion length. Based on comparisons between the experimental data and the developed model, the characteristic diffusion length has been shown to be very short and has been estimated to be smaller than 10Å for nitridation temperature below 1200°C, and its activation energy has been estimated to be of 0.181 eV. Moreover, the linear growth rate constant and the parabolic growth rate constant of the as-grown thermal nitride films have been estimated to be of 1.286 and 1.546 eV, respectively, which are smaller than those of the silicon oxidation in dry oxygen or steam ambient. In addition, it has been shown that the linear growth rate constant of the thermal nitridation using ammonia gas is larger than that of the thermal oxidation using dry oxygen or steam ambient, which predicts that the surface-limited reaction of the silicon surface in ammonia gas is faster than that in dry oxygen or steam ambient.

Silicon nitride films, which exhibit high structure density, high dielectric constant, good electrical properties, and strong inertness toward chemicals, have been widely used in semiconductor devices and integrated circuit fabrications. However, high quality silicon nitride films have been prepared by expensive methods such as chemical vapor deposition (CVD) or plasma deposition. In modern silicon technologies, thicker silicon diode films (>1000Å) with satisfactory quality and precise thickness can be easily obtained by the direct thermal oxidation of the silicon surface. However, thin silicon dioxide films (<500Å) with high quality and reproducible properties have become a challenge for the present technique. Before 1976, much effort was made to prepare the silicon nitride films by using the reaction of the silicon surface in nitrogen ambient; however, no continuous nitride films had been obtained (1-5). Until 1978, Fujitsu Laboratories

* Electrochemical Society Active Member.
Key words: diffusion, oxidation, silicon nitride.

Limited (6) had reported that continuous and uniform silicon nitride films could be obtained by the direct nitridation of the silicon surface in nitrogen or ammonia ambient. Later, thermally grown silicon nitride films for the gate insulator of the IGFET devices had been successfully fabricated (7), and the dielectric constant of the as-grown films was shown to be about 30% larger that that of the silicon dioxide films. Moreover, it had been shown that low surface state density and high electron mobility could be obtained for an n-channel MOSFET. It is believed that thermally grown silicon nitride films will be the important materials for device applications, especially for the gate insulator of future submicron MOS devices. However, no detailed reports on the growth kinetics of the as-grown thermal nitride films have been given. It has been shown (5, 6, 8) that the thermal nitridation of the silicon surface was quite different from the thermal oxidation of the silicon surface. In the case of thermal oxidation the growth kinetics can always be described by the expression, $X_o^2 + AX_o = B(t + \tau)$, where X_o is the oxide thickness, t is the oxidation time, τ is the initial oxide thickness, and A and B are the growth rate constants. The major difference between the thermal nitridation and the thermal oxidation is that the as-grown thermal nitride films have higher structure density, so "self-limiting" growth can easily occur for the thermal nitridation of the silicon surface in nitrogen or ammonia ambient. Although the growth kinetics of the as-grown thermal nitride films are not yet clear, this self-limiting growth property does become a unique advantage for some semiconductor devices in which thin insulator films with high quality and precise thickness are needed.

In this paper an analytical model for the thermal nitridation of the silicon surface has been developed to interpret the growth kinetics of the as-grown thermal nitride films at different nitridation temperature. Experimental results of the as-grown thermal nitride films using ammonia gas for nitridation temperature from 700° to 1200°C are given and compared with the developed model. Based on comparisons between the experimental results and the developed model, the growth rate constants and characteristic parameters of the thermal nitridation in ammonia gas have been first deduced. Moreover, discussions and conclusions are given.

Growth Kinetics Model

There are three basic steps for the thermal nitridation of the silicon surface. These steps can be easily understood from Fig. 1. First, the nitridant species must be transported from the bulk of the ammonia gas to the thermal nitride-gas interface. Second, the nitridant species diffuse across the thermal nitride film. Third, the nitridant species react with the silicon surface. According to Fig. 1, the three fluxes corresponding to each step must be equal at each boundary. In region (I), the nitridant flux F_1 can be expressed by (7)

$$F_1 = h_G(C_G - C_S) \quad [1]$$

where C_G is the concentration of the nitridant species in the ammonia ambient, C_S is the concentration of the nitridant species at the thermal nitride-gas interface, and h_G is the mass-transfer coefficient.

If we assume that Henry's law is valid, then the concentration at the outer surface of the thermal nitride C_O is proportional to the partial pressure of the nitridant species next to the thermal nitride surface P_S, *i.e.*, $C_O = HP_S$, where H is the Henry law constant. In addition, if we assume the equilibrium concentration of the nitridant species in the bulk of the ammonia gas to be C^*, then C^* can be related to the partial pressure of the nitridant species P_G by $C^* = HP_G$. According to the ideal gas law, $C_G = P_G/k_BT$ and $C_S = P_S/k_BT$, we may then rewrite Eq. [1] as

$$F_1 = h(C^* - C_O) \quad [2]$$

where h is the gas phase mass-transfer coefficient in terms of concentrations in the solid, which is given by $h = h_G/Hk_BT$.

In region III, the reaction rate at the nitride-silicon interface, which is proportional to the concentration of the nitridant species at the interface C_i, can be expressed by

$$F_3 = k_3 C_i \quad [3]$$

where k_s is the chemical surface-reaction rate constant for thermal nitridation.

In region II, the flux of the nitridant species can be assumed to be a diffusive flux, and is expressed as

$$F_2(x) = -D_N \frac{dC(x)}{dx} \quad [4]$$

where D_N is the diffusivity of the nitridant species in the thermal nitride film.

According to the continuity equation, we define a characteristic time constant τ_N for the nitridant species across the thermal nitride. We may then write the continuity equation as

$$\frac{\partial C(x,t)}{\partial t} = \nabla \cdot \vec{F}_2(x) + \frac{C(x,t)}{\tau_N} \quad [5]$$

For steady state, the diffusion equation for the nitridant species across the thermal nitride film can be written as

$$\frac{d^2C(x)}{dx^2} - \frac{C(x)}{L_N{}^2} = 0 \quad [6]$$

where $L_N = (D_N\tau_N)^{1/2}$ is the characteristic diffusion length for the nitridant species across the thermal nitride film.

Using the boundary conditions at $x = 0$ and X_o, *i.e.*, $C(0) = C_O$ and $C(X_o) = C_i$, Eq. [6] can be easily solved. The result is

$$C(X) = \frac{C_i \sinh\left(\frac{X}{L_N}\right) + C_O \sinh\left(\frac{X_o - X}{L_N}\right)}{\sinh\left(\frac{X_o}{L_N}\right)} \quad [7]$$

Since the flux must be continuous at each boundary, *i.e.*, $F_1 = F_2(x = 0)$, $F_3 = F_2(X = X_o) = -D_N \left.\frac{dC(x)}{dx}\right|_{x=x_o}$, the concentration of the nitridant species at the thermal nitride-silicon interface can be expressed in terms of C^*. The result is

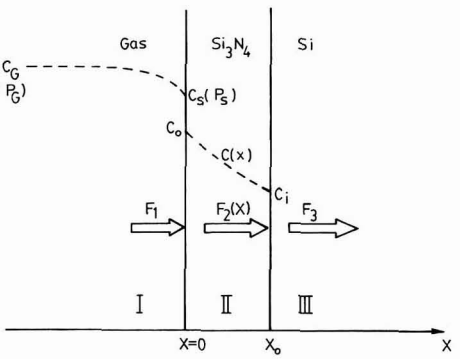

Fig. 1. Growth kinetics diagram of the thermal nitridation

$$C_1 = \frac{C^*}{\left(\frac{k_s L_N}{D_N} + \frac{D_N}{L_N h}\right)\sinh\left(\frac{X_o}{L_N}\right) + \left(1 + \frac{k_s}{h}\right)\cosh\left(\frac{X_o}{L_N}\right)} \quad [8]$$

The flux of the nitridant species reaching the thermal nitride-silicon interface is given by

$$N_1 \frac{dX_o}{dt} = F_3 = F_2(X = X_o) = k_s C_1 = \frac{k_s C^*}{\left(\frac{k_s L_N}{D_N} + \frac{D_N}{L_N h}\right)\sinh\left(\frac{X_o}{L_N}\right) + \left(1 + \frac{k_s}{h}\right)\cosh\left(\frac{X_o}{L_N}\right)} \quad [9]$$

where N_1 is the number of the nitridant species incorporated into a unit volume of the thermal nitride.

Solving Eq. [9] and assuming $X_o = 0$ for $t = 0$ we obtain

$$L_N A \sinh\left(\frac{X_o}{L_N}\right) + 2L_N^2\left[\cosh\left(\frac{X_o}{L_N}\right) - 1\right] = Bt \quad [10]$$

where A and B are separately defined as

$$A = \frac{2L_N\left(1 + \frac{k_s}{h}\right)}{\left(\frac{k_s L_N}{D_N} + \frac{D_N}{L_N h}\right)} \quad [11]$$

$$B = \frac{2L_N k_s C^*}{N_1\left(\frac{k_s L_N}{D_N} + \frac{D_N}{L_N h}\right)} \quad [12]$$

Note that Eq. [10] can be used to calculate X_o in terms of t, and the result is

$$X_o = L_N \ln\left\{\frac{(2L_N^2 + Bt) + [(Bt)^2 + L_N^2A^2 + 4L_N^2Bt]^{1/2}}{2L_N^2 + AL_N}\right\} \quad [13]$$

The growth rate of the thermal nitride is then written as

$$\frac{dX_o}{dt} = L_N \left\{\frac{B + \frac{1}{2}[(Bt)^2 + L_N^2A^2 + 4L_N^2Bt]^{1/2}(2B^2t + 4L_N^2B)}{(2L_N^2 + Bt) + [(Bt)^2 + L_N^2A^2 + 4L_N^2Bt]^{1/2}}\right\} \quad [14]$$

There are two extreme cases that deserve further discussion. In the case of $X_o << L_N$, Eq. [10] can be simplified to

$$X_o^2 + AX_o = Bt \quad [15]$$

where $\sinh(X_o/L_N) \cong X_o/L_N$ and $\cosh(X_o/L_N) \cong 1 - \frac{1}{2}(X_o/L_N)^2$ are used in Eq. [10] to obtain Eq. [15].

From Eq. [15] it is clearly seen that when X_o is very small and $X_o << L_N$, the surface reaction growth will be dominant, which is the same as the conventional oxidation of the silicon surface. In this case, the constants A and B can be reduced to the conventional expressions, *i.e.*,

$$A = 2D_N\left(\frac{1}{h} + \frac{1}{k_s}\right) \quad [16]$$

$$B = \frac{2D_N C^*}{N_1} \quad [17]$$

Similarly, two distinguished regions can also be classified. From Eq. [15], when $X_o << A$, we may obtain $X_o = \frac{B}{A}t$ where $\frac{B}{A}$ is referred to be the linear rate constant; when $X_o >> A$, we obtain $X_o = (Bt)^{1/2}$ where B is the parabolic rate constant. Note that Eq. [15] is valid when the condition $X_o << L_N$ is satisfied, so the parabolic relationship may not exist if the diffusion length is very short.

In the case of $X_o >> L_N$, Eq. [10] or Eq. [13] can be simplified to

$$X_o = L_N \ln\left[\frac{Bt}{L_N^2 + \frac{A}{2}L_N}\right] \quad [18]$$

The growth rate in this case can be written as

$$\frac{dX_o}{dt} = \frac{L_N}{t} \quad [19]$$

It is clearly seen that the growth rate in this region is very small when the nitridation time is long and the diffusion length of the nitridant species across the thermal nitride layer is short. This region is called the "logarithmic region." Due to higher structure density of the as-grown thermal nitride films, the characteristic diffusion length is very small, so the logarithmic relationship can be easily accomplished for shorter nitridation time. That is why thermal nitridation has the property of "self-limiting" growth. Moreover, based on Eq. [19], the characteristic diffusion length of the nitridant species across the thermal nitride film can be deduced.

A typical plot of Eq. [13] is shown in Fig. 2 for reference. It is clear that A, B, and L_N can be deduced by matching Eq. [13] and the experimental data if three regions can be clearly classified.

Experimental Results and Discussion

Silicon p-type <100> oriented wafers were used as the starting materials. After degreasing in an organic solvent such as ACE and TCE, the wafers were boiled in sulfuric and nitric acids. Before loading into the quartz tube, the cleaned wafers were dipped into buffered hydrofluoric acid for 1 min in order to remove the native oxide on the silicon surface, and then were rinsed in deionized water. The wafers were kept dry using a nitrogen gun, and immediately loaded into the prepurged quartz tube for nitridation. During the nitridation, the flow rate of ammonia gas was kept at

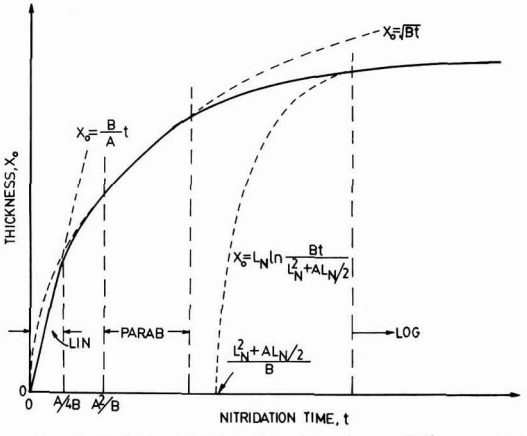

Fig. 2. Typical nitridation time dependence of the as-grown thermal nitride film thickness.

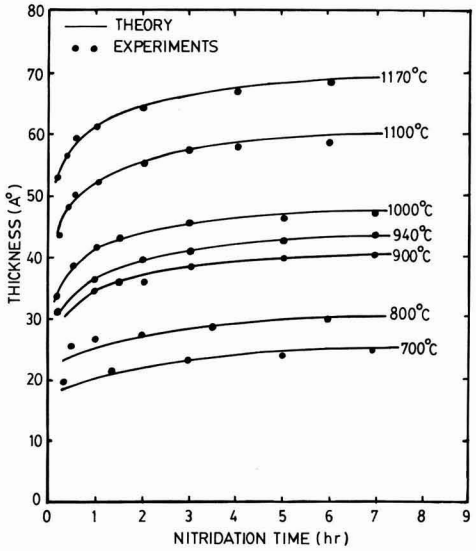

Fig. 3. Comparisons between the growth rate data of the as-grown thermal nitride films and the theoretical model.

about 400 cm³/min. The thickness of the fabricated thermal nitride films were measured by an ellipsometer. Figure 3 shows the thickness of the as-grown thermal nitride films as a function of nitridation time in ammonia gas for nitridation temperature from 700° to 1200°C, which indicates an initial rapid growth followed by an inhibited growth. Comparisons between the experimental data and the developed model are also shown in Fig. 3 and the parameters used are listed in Table I. It is clearly seen that good agreement between the experimental results and the theoretical calculations is obtained. Moreover, the characteristic diffusion length of the nitridant species across the thermal nitride film is shown to be smaller than 10Å for the nitridation temperature below 1200°C. Figure 4 shows the linear rate constant B/A as a function of the inverse temperature, which gives the activation energy of about 1.286 eV. Note that the activation energy of the linear rate constant for the thermal nitridation is much smaller than that of the thermal oxidation ($E_a = 2.0$ eV for dry O_2 oxidation). The main reason for smaller activation energy during the initial nitridation is mainly due to slow surface reaction between the nitridant species and the silicon surface. Similarly, the parabolic rate constant B as a function of the inverse temperature is shown in Fig. 5, in which the activation energy is estimated to be about 1.546 eV. Figure 6 shows the characteristic diffusion length as a function of the inverse temperature which gives the activation energy of about 0.181 eV. It is clearly visualized that the logarithmic region of the thermal nitride growth is mainly due to the limited diffusion of the nitridant species across the thermal nitride film rather than due to the surface reaction between the nitridant species and the silicon surface. From the

Table I. The characteristic parameters used to calculate the theoretical curves shown in Fig. 3

PARAMETERS / TEMPERATURE	DIFFUSION LENGTH L_N (Å)	PARABOLIC RATE CONSTANT B (μ^2/hr)	LINEAR RATE CONSTANT B/A (μ/hr)
1170°C	5.049	4.717×10^{-2}	168.5
1100°C	4.671	1.864×10^{-2}	69.94
1000°C	4.152	8.141×10^{-3}	35.4
940°C	3.699	3.531×10^{-3}	16.81
900°C	3.607	2.046×10^{-3}	11.16
800°C	3.071	4.832×10^{-4}	3.35
700°C	2.454	2.169×10^{-4}	2.01

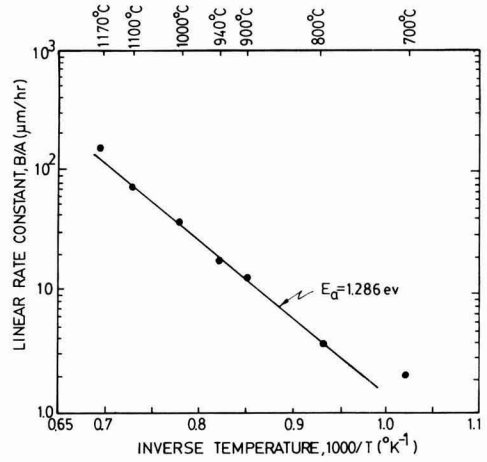

Fig. 4. The measured linear growth rate constant of the as-grown thermal nitride films as a function of the inverse temperature.

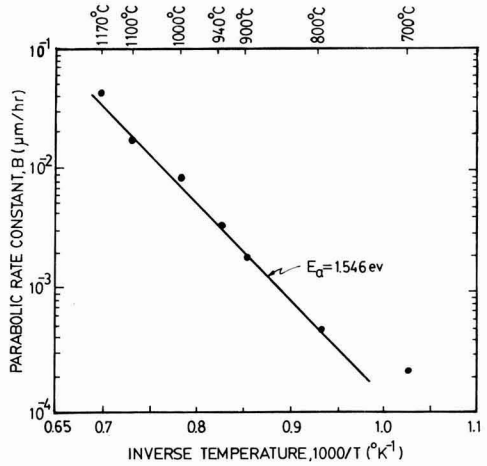

Fig. 5. The measured parabolic growth rate constant of the as-grown thermal nitride films as a function of the inverse temperature.

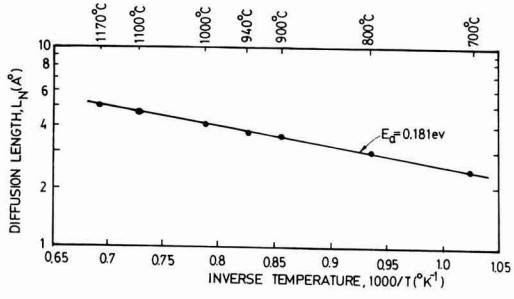

Fig. 6. The measured characteristic diffusion length of the nitridant species across the as-grown thermal nitride films as a function of the inverse temperature.

estimated activation energy, we may conclude that the reaction between the silicon wafer and the ammonia gas is slow and the as-grown thermal nitride films do have higher structure density than that of the thermally grown silicon dioxide.

Conclusions

An analytical model for the growth kinetics of silicon thermal nitridation has been developed and compared to the experimental data. The characteristic parameters of silicon nitridation in ammonia gas, such as the linear rate constant, the parabolic rate constant, and the diffusion length of the nitridant species across the thermal nitride film, have been deduced and characterized. It has been shown that the diffusion length of the nitridant species across the thermal nitride film is smaller than 10Å when the nitridation temperature is below 1200°C. In addition, the self-limiting growth property of the silicon thermal nitridation in nitrogen or ammonia is shown mainly due to the shorter characteristic diffusion length of the nitridant species across the as-grown thermal nitride films which have higher structure density.

Acknowledgment

The authors would like to express their sincere thanks to Dr. D. H. Hu and Dr. C. T. Shih of the Electronics Research and Service Organization, Industrial Technology Research Institute (ITRI) for their grant support and stimulating discussions. Special thanks to all the technical staff of Semiconductor Research Center, National Chiao-Tung University for their assistance during the experimental studies.

Manuscript received Sept. 9, 1981.

Any discussion of this paper will appear in a Discussion Section to be published in the June 1983 JOURNAL. All discussions for the June 1983 Discussion Section should be submitted by Feb. 1, 1983.

Publication costs of this article were assisted by the National Chiao-Tung University.

REFERENCES

1. F. K. Heumann, D. M. Brown, and E. Mets, *This Journal*, **115**, 331 (1968).
2. S. M. Hu, *ibid.*, **113**, 693 (1966).
3. R. G. Frieser, *ibid.*, **115**, 1092 (1968).
4. S. I. Raider, R. A. Gdula, and J. R. Petrak, *ibid.*, **27**, 150 (1975).
5. E. Kooi, J. G. Van Lierop, and J. A. Appels, *ibid.*, **123**, 1117 (1976).
6. T. Ito, S. Hijiya, T. Nozaki, H. Arakawa, M. Shinoda, and Y. Fukukawa, *ibid.*, **125**, 448 (1978).
7. T. Ito, T. Nozaki, H. Arakawa, and M. Shinoda, *Appl. Phys. Lett.*, **32**, 330 (1978).
8. S. P. Murarka, C. C. Chang, and A. C. Adams, *This Journal*, **126**, 996 (1979).

Doping of $Ga_{1-x}Al_xAs$ Grown by LPE with Si and Ge

V. Swaminathan,* M. D. Sturge, J. L. Zilko, N. E. Schumaker,* and W. R. Wagner

Bell Laboratories, Murray Hill, New Jersey 07974

and C. A. Gaw

Bell Laboratories, Reading, Pennsylvania 19604

ABSTRACT

The electrical and optical properties of p-type Ge and Si-doped $Ga_{1-x}Al_xAs$ ($x \sim 0.39$-0.42) layers grown by liquid phase epitaxy in an He ambient have been investigated as a function of the atom fraction of Si in the melt, X_{Si}. For X_{Si} in the range 1.5×10^{-5} to 1.5×10^{-2} the hole concentration at room temperature is relatively unaffected while the hole mobility decreases monotonically with addition of Si, suggesting close compensation of Si species. As a result, in the low temperature photoluminescent spectra, the pair transition via the shallow Si acceptors is quenched relative to that via the deep Ge_{As} centers. For $X_{Si} < 5 \times 10^{-5}$, adding 0.9 ppm O_2 to the growth ambient decreases the compensation due to the removal of the background S donor, and thereby increases the hole concentration by a factor of 2-3 and enhances the pair transition via the Si acceptors as well. The addition of O_2 during LPE growth is not, however, always practical as it has been found to affect the uniformity of thin epitaxial layers.

Germanium (1) is frequently used as a p-type dopant in the $Ga_{1-x}Al_xAs$ ($x \sim 0.40$) cladding layer of the GaAs-(GaAl)As double heterostructure (DH) grown by liquid phase epitaxy (LPE) for the fabrication of injection lasers, and is preferred over other acceptor dopants like Be, Zn, or Cd which have either hazardous properties (Be), high diffusivity (Zn) (2), or low solubility (Cd) (3). The use of Ge is, however, not without its problems. High conductivity in the p-cladding layer is often desired for efficient confinement of carriers in the lasing active region and for reduced temperature dependence of the current threshold (4, 5). Increasing the Ge doping level to achieve high conductivities in the ternary decreases the aluminum segregation coefficient and radiative efficiency (6). Another approach to increase the conductivity would be to add a second acceptor dopant in the layer with Ge. Silicon might be thought to be a good candidate for this purpose since it has been reported to be a p-type dopant for growth under LPE conditions at temperatures below 800°C (7); it gives rise to a shallower acceptor level than Ge (8) and its segregation coefficient in (GaAl)As is at least an order of magnitude higher than Ge (6, 7). In this paper we report the results of adding varying amounts of Si in the range 10^{-4} to 1.5 atomic percent (a/o) to the LPE growth solution containing 5.5×10^{-1} a/o of Ge and 2×10^{-1} a/o of Al (for $x \sim 0.4$ in the solid). We find that addition of Si does not result in increased conductivity indicating that Si, which is amphoteric, is closely self-compensated in the solid under our growth conditions. This compensation also manifests itself in reduced low temperature photoluminescent intensities of pair transitions involving Si acceptors, relative to those involving Ge. An increase in the conductivity by a factor of 2-3 is observed when small amounts of O_2 are added to the generally used He growth ambient, for Si doping less than 5×10^{-3} a/o. However, the use of O_2 during LPE growth of (GaAl)As DH structures is

* Electrochemical Society Active Member.

Key words: photoluminescence, Hall measurements, compensation.

not always practical since it has been found to affect the uniformity of the layers (9, 10).

Experimental

The $Ga_{1-x}Al_xAs$ ($x \sim 0.39$-0.42) layers, typically 3-4 μm thick, were grown on Si-doped GaAs substrates at 780°C in a liquid phase epitaxial reactor. The growth was carried out in a nonreducing high purity He ambient and the GaAs saturation material had been synthesized in boron nitride crucibles.[1] The He was purified by passing it through three sets of stainless steel coils that were held at 77 K and contained 13× and 5A molecular sieve and activated charcoal. The stainless steel gas supply lines were maintained leak-free by using either welded or vacuum connections. The purified gas was found to contain less than 1 ppb H_2O[2] and less than 1 ppb O_2 (11). The layers were doped with Ge and Si. The atom fraction of Ge in the melt, X_{Ge}, was kept constant at $\sim 5.6 \times 10^{-3}$ while X_{Si} was varied between 3.5×10^{-6} and 1.5×10^{-2}. Samples grown in three different reactors were studied. For some runs either 0.3 or 0.9 ppm O_2 was added to the He ambient. This was achieved by mixing the He gas with a calibration sample[3] containing 10 ppm O_2 in He.

The aluminum composition of the as-grown layers was measured from the bound exciton lines (12) at low doping levels ($X_{Si} \sim 1.5 \times 10^{-5}$) and by double crystal x-ray diffractometry (13) and x-ray energy dispersive spectroscopy (14) at high doping levels. The carrier concentrations of the layers were measured at room temperature on cloverleaf van der Pauw samples by Hall effect after removal of the substrate at the center of the cloverleaf by etching in a solution of H_2O_2 buffered with NH_4OH (15). Zinc (2%)-gold wires were used for ohmic contacts and measurements were made with an applied magnetic field of 1 kG. The low temperature photoluminescence measurements were made at 5.5 K using the 5145A line from an Ar^+ ion laser, with power densities between 1.6 and 720 W/cm^2.

Results and Discussion

The aluminum composition of the layers varied between 0.39 and 0.42 in the doping range studied and all the layers were p-type. The room temperature hole concentration and the Hall mobility of the layers are shown in Fig. 1 and 2. The data from samples not doped with Si are arbitrarily marked at $X_{Si} \sim 10^{-6}$. From Fig. 1 it is seen that addition of Si in the range $X_{Si} \sim 1.5 \times 10^{-5}$ to 1.5×10^{-2} does not have any effect on the carrier concentration for the He and He + 0.3 ppm O_2 growth ambients described above.[4] An increase in the carrier concentration by a factor of 2-3 occurs for samples grown in He + 0.9 ppm O_2 ambient, as long as the Si level is below 5×10^{-3} a/o: at higher Si doping addition of O_2 does, in fact, reduce the hole concentration. While the hole concentration is virtually unaffected by Si doping, the room temperature Hall mobility, above $X_{Si} \sim 10^{-4}$, monotonically decreases with X_{Si} for all samples grown in either He ambient or He + O_2 ambient. The decreasing Hall mobility indicates an increasing number of ionized impurity centers with addition of Si. This and the relatively constant hole concentration suggest that Si is incorporated in Ge-doped $Ga_{1-x}Al_xAs$ as a closely compensated species just as it is in the absence of Ge (8). The increase in the carrier concentration at low Si levels in samples grown in He + 0.9 ppm O_2 ambient is most likely a result of removal of the background donors. Sulfur has been previously identified as

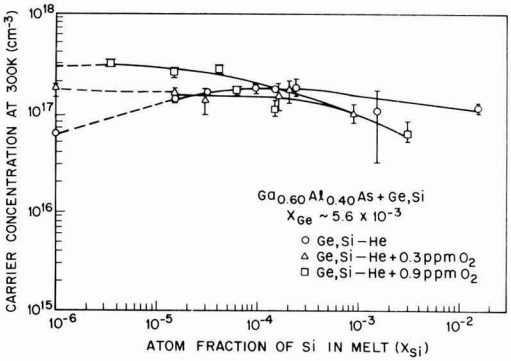

Fig. 1. Room temperature hole concentration (cm^{-3}) as a function of atom fraction of Si in melt (X_{Si}) for Ge-doped $Ga_{0.6}Al_{0.4}As$ ($X_{Ge} \sim 5.6 \times 10^{-3}$) for LPE growth under He, He + 0.3 ppm O_2, and He + 0.9 ppm O_2 ambients. The samples doped only with Ge are marked arbitrarily at $X_{Si} \sim 10^{-6}$ (see text).

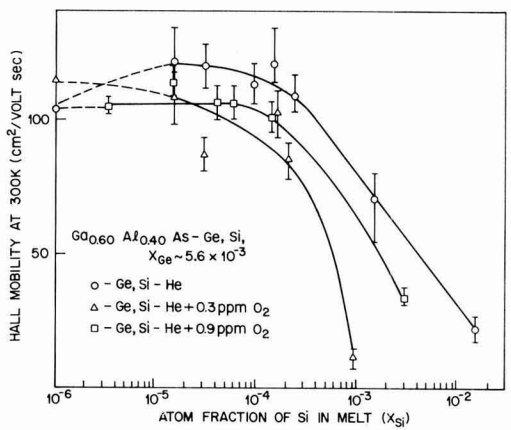

Fig. 2. Room temperature Hall mobility (cm^2/Vsec) as a function of atom fraction of Si in melt (X_{Si}) for Ge-doped $Ga_{0.6}Al_{0.4}As$ ($X_{Ge} \sim 5.6 \times 10^{-3}$) for LPE growth under He, He + 0.3 ppm O_2, and He + 0.9 ppm O_2 ambients. The samples doped only with Ge are marked arbitrarily at $X_{Si} \sim 10^{-6}$ (see text).

the major donor impurity in samples grown similarly to those used in the present study (16). Further, addition of $O_2 \leq 1$ ppm has been shown to remove (16, 17) $\sim 10^{17}$ cm^{-3} S,[5] which is the background donor level in our samples grown under He ambient. However, with further addition of Si the increase in the carrier concentration becomes less, suggesting that the addition of O_2 does not remove the Si donors contrary to what has been reported in GaAs (18-21).

The compensation of Si also manifests itself in the low temperature low excitation level photoluminescent spectra from these samples. Figure 3 shows spectra for three different Si concentrations for growth under He, He + 0.3 ppm O_2, and He + 0.9 ppm O_2. At low Si levels the spectra are generally characterized by two prominent donor-to-acceptor (D-A) pair transitions [Fig. 3(a)]. The higher energy band (1.95-1.96 eV) is observed in crystals doped only with Si (8) and is attributed to D-A transitions involving shallower Si_{As}

[1] This is done to minimize the unintentional Si contamination that could occur from the commonly used GaAs saturation material that has been synthesized in quartz containers.

[2] The water vapor content was measured using a Model 2100 hygrometer manufactured by Panametrics, Waltham, Massachusetts.

[3] Supplied by Airco.

[4] The hole concentrations of the samples grown in He ambient and doped with only Ge varied by a factor of 2-3 due to variations in the background donor level. For this reason, in these samples it was not possible to estimate the effect of adding Si below $X_{Si} < 10^{-5}$, on the hole concentration.

[5] The mechanism of removal of S by O_2 is not clear at present. While S can be removed as SO_2, thermodynamic considerations indicate that Al_2O_3 and Ga_2O_3 are much more stable than SO_2 at the growth temperature. However, there is clear indication that O_2 addition reduces S (see Ref. 16). Further, it should be noted that at the O_2 levels we have used we did not observe any systematic change in the Al composition in the layers.

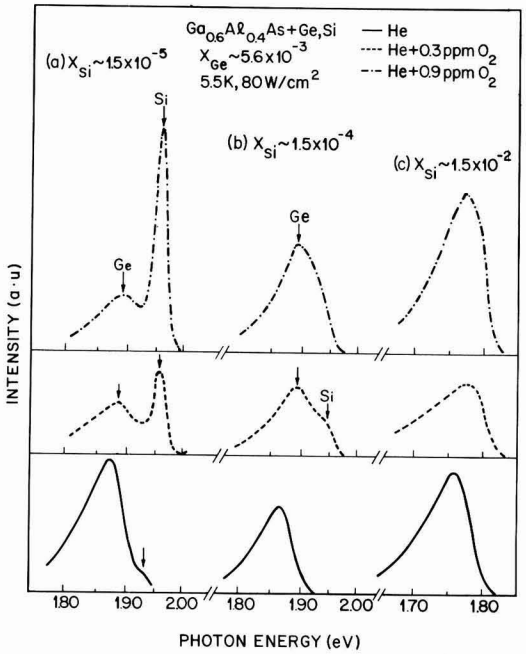

Fig. 3. Photoluminescent spectra at 5.5 K from Ge and Si-doped $Ga_{0.6}Al_{0.4}As$ ($X_{Ge} \sim 5.6 \times 10^{-3}$) for $X_{Si} \sim 1.5 \times 10^{-5}$ (a), 1.5×10^{-4} (b), and 1.5×10^{-2} (c) for LPE growth under He (solid), He + 0.3 ppm O_2 (dashed), and He + 0.9 ppm O_2 (dash dot) ambients at an excitation intensity of 80 W/cm^2.

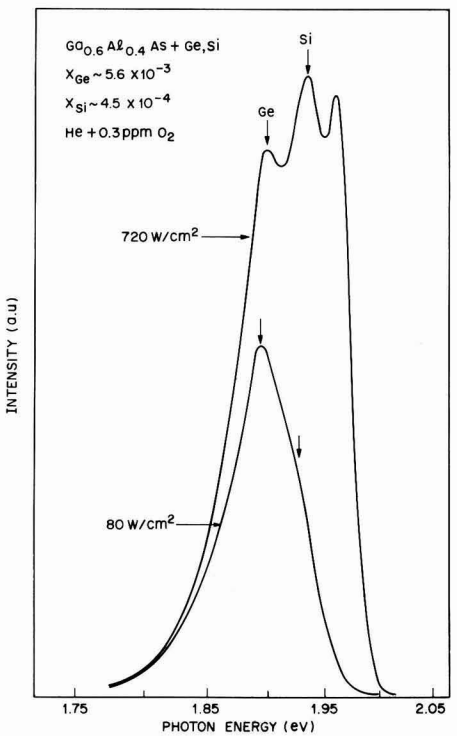

Fig. 4. Photoluminescent spectra at 5.5 K from Ge($X_{Ge} \sim 5.6 \times 10^{-3}$) and Si($X_{Si} \sim 4.5 \times 10^{-4}$)-doped $Ga_{0.6}Al_{0.4}As$ grown under He + 0.3 ppm O_2 at excitation densities of 80 and 720 W/cm^2. Note that the narrow band at 1.96 eV observed at 720 W/cm^2 is probably a free-to-bound transition associated with Si.

acceptors ($E_A \sim 60$ meV) (8) while the lower energy band (1.88-1.89 eV) is due to D-A transitions involving deeper Ge_{As} acceptors ($E_A \sim 100$ meV) (6). These transitions will be referred to as Si and Ge bands, respectively. As Si is added, the Si band completely disappears in Fig. 3(b) and (c) for samples grown in He ambient. This counterintuitive result is a consequence of compensation by an increasing concentration of Si donors. The shallow Si acceptors are all ionized in a compensated sample, and will not contribute to the D-A luminescence at an excitation level sufficiently low that the quasi-Fermi level remains above the shallow acceptor level [see Fig. 2 of Ref. (17)]. The addition of oxygen reduces the amount of compensation by removing S donors and thus the higher energy Si pair transition tends to dominate the spectra since more neutral shallow acceptors now become available. This effect of oxygen is most clearly seen as low Si doping [$X_{Si} \sim 1.5 \times 10^{-5}$, Fig. 3(a)] but it does persist weakly at higher doping levels [$X_{Si} \sim 1.5 \times 10^{-4}$, Fig. 3(b), where, in the absence of oxygen, the Si band is not seen at all.

This interpretation is confirmed by the fact that the Si band in samples grown with $X_{Si} > 1.5 \times 10^{-5}$, for which it is absent at low excitation intensities, can be observed at higher levels of excitation. This is shown in Fig. 4 for a sample grown with $X_{Si} \sim 4.5 \times 10^{-4}$ in He + 0.3 ppm O_2 ambient. The Si band, which is seen only as a weak shoulder at low excitation conditions, is dominant at high excitation levels. As the excitation power density increases, the quasi-Fermi level drops below the Si acceptor levels and makes them available for pair transitions (17). Consequently when compensation exists the intensity of radiative transitions through compensated acceptors increases superlinearly with excitation power density (17).

While the presence of oxygen drastically affects the intensity of the Si band, it hardly influences that of the Ge band, indicating that the density of Ge_{As} centers is not greatly affected. The integrated intensity of the Ge band is plotted as a function of X_{Si} in Fig. 5. For all the three growth ambients the Ge band initially increases with X_{Si} up to $X_{Si} \sim 10^{-4}$ and above this value it remains essentially constant. The increase in the Ge band

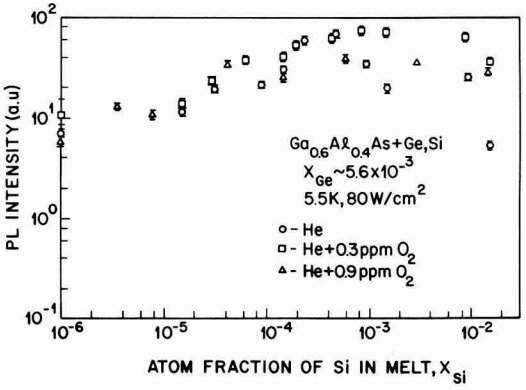

Fig. 5. Integrated photoluminescent intensity at 5.5 K of the Ge donor-to-acceptor pair band at an excitation intensity of 80 W/cm^2 as a function of atom fraction of Si(X_{Si}) in the melt for Ge-doped $Ga_{0.6}Al_{0.4}As$ ($X_{Ge} \sim 5.6 \times 10^{-3}$) for LPE growth under He, He + 0.3 ppm O_2, and He + 0.9 ppm O_2 ambients. The samples doped only with Ge are marked arbitrarily at $X_{Si} \sim 10^{-6}$.

with increasing X_{Si}, at low X_{Si}, is a natural consequence of increasing concentration of Si donors.

The Ge band shifts to longer wavelengths at high Si doping levels, as shown in Fig. 6. For all the three growth ambients the shift is more than 100 meV above $X_{Si} \sim 10^{-3}$. Such large shifts as a function of doping have been observed in heavily compensated samples (22, 23). Furthermore, at high doping levels the Ge band shifts to shorter wavelengths with increasing excitation intensity, the shifts being typically 20-30 meV for an order of magnitude change in excitation intensity. Once again such large shifts in D-A transitions with excitation intensity are characteristic of compensated samples (17, 22).

Implications of O_2 Addition during LPE Growth

Our results show that the conductivity of p-type Ge-doped $Ga_{1-x}Al_xAs$ ($x \sim 0.39$-0.42) is not affected by the addition of Si for LPE growth at 780°C under He ambient. This is a result of the incorporation of Si in $Ga_{1-x}Al_xAs$ as closely compensated species. However, for Si doping less than 5×10^{-3} a/o, addition of 0.9 ppm O_2 to the He growth ambient increases the hole concentration by a factor of 2-3, giving a room temperature carrier density of $\sim 3 \times 10^{17}$ cm^{-3} for a Ge doping level of $X_{Ge} \sim 5 \times 10^{-4}$ in the p-$Ga_{0.6}Al_{0.4}As$ cladding layer of the (GaAl)As DH laser structure. Though this level of carrier density in the p-cladding layer is adequate for carrier confinement (4) in the lasing active region, using O_2 to achieve this is not always practical. Oxygen contamination during LPE growth of (GaAl)As DH laser structures has been found to affect the uniformity of the layers (9) and cause absence or near absence of the active layer (rake lines) (24) in the stripe region of the laser (10).

The increase in the carrier density achieved by the use of O_2 is due to the removal of compensating donors (16) as evidenced by the relative changes in the intensities of the Si and Ge pair bands. The reduction in the compensation in p-$Ga_{1-x}Al_xAs$ has also been found to occur when H_2 is added to the growth ambient (16, 17). Therefore the use of H_2 during LPE growth has the same effect as O_2 in increasing the carrier density in p-$Ga_{1-x}Al_xAs$ and at the same time avoids the deleterious effects of O_2 on the uniformity of the layers. It should, however, be mentioned that for achieving carrier densities higher than 3×10^{17} cm^{-3} in the p-$Ga_{1-x}Al_xAs$ cladding layer dopants other than Ge and Si should be tried and in this regard the use of group II acceptors should be reexamined.

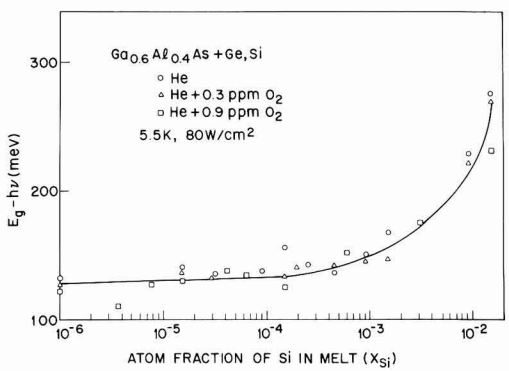

Fig. 6. The bandgap (E_g) minus the peak position of the Ge donor-to-acceptor pair band ($h\nu$) in meV as a function of atom fraction of Si(X_{Si}) in the melt for Ge-doped $Ga_{0.6}Al_{0.4}As$ ($X_{Ge} \sim 5.6 \times 10^{-3}$) for LPE growth under He, He + 0.3 ppm O_2, and He + 0.9 ppm O_2 ambients. The excitation intensity is 80 W/cm^2.

Acknowledgments

The authors are thankful to C. A. Parsons, J. W. Lee, D. Van Haren, and S. M. Woelfer for their technical assistance.

Manuscript submitted Aug. 19, 1981; revised manuscript received Nov. 23, 1981.

Any discussion of this paper will appear in a Discussion Section to be published in the June 1983 JOURNAL. All discussions for the June 1983 Discussion Section should be submitted by Feb. 1, 1983.

Publication costs of this article were assisted by Bell Laboratories.

REFERENCES

1. H. C. Casey and M. B. Panish, "Heterostructure Lasers," Part B, p. 103, Academic Press, New York (1978).
2. A. Flat, A. G. Milnes, and D. L. Feucht, *Solid State Electron.*, **20**, 1024 (1977).
3. J. L. Zilko, Unpublished.
4. P. J. Anthony and N. E. Schumaker, *IEEE Electron Device Lett.*, **edl-1**, 58 (1980).
5. P. J. Anthony and N. E. Schumaker, *J. Appl. Phys.*, **51**, 5038 (1980).
6. V. Swaminathan, N. E. Schumaker, J. L. Zilko, W. R. Wagner, and C. A. Parsons, *J. Appl. Phys.*, **52**, 412 (1981).
7. A. N. Imenkov, V. V. Negreskul, B. V. Tsarenkov, and Yu. P. Yakovlev, *Sov. Phys. Semicond.*, **8**, 947 (1975).
8. V. Swaminathan, M. D. Sturge, and J. L. Zilko, *J. Appl. Phys.*, **52**, 6306 (1981).
9. B. I. Miller, E. Pinkas, I. Hayashi, and R. J. Capik, *J. Appl. Phys.*, **43**, 2817 (1972).
10. P. J. Anthony, J. L. Zilko, D. L. VanHaren, and N. E. Schumaker, Unpublished.
11. N. E. Schumaker, Unpublished. Measured using a Model 2732 gas chromatograph with a flame ionization detector, manufactured by Varian, Walnut Creek, California.
12. R. Dingle, R. A. Logan, and J. R. Arthur, Jr., in Gallium Arsenide and Related Compounds," Edinburgh, C. Hilsum, Editor, p. 210, Inst. Phys. Conf. Ser. 33a (1976).
13. W. J. Bartels and W. Nijiman, *J. Cryst. Growth*, **44**, 518 (1978).
14. "Quantitative Scanning Electron Microscopy," D. B. Holt, M. D. Muir, P. R. Grant, and I. M. Boswarva, Editors, Academic Press, New York (1974).
15. R. A. Logan and F. K. Reinhart, *J. Appl. Phys.*, **44**, 4172 (1973).
16. P. J. Anthony, J. L. Zilko, V. Swaminathan, N. E. Schumaker, W. R. Wagner, and J. C. Norberg, *Appl. Phys. Lett.*, **38**, 434 (1981).
17. V. Swaminathan, P. J. Anthony, J. L. Zilko, M. D. Sturge, and N. E. Schumaker, *J. Appl. Phys.*, **52**, 5603 (1981).
18. J. F. Woods and N. G. Ainslie, *ibid.*, **34**, 1469 (1963).
19. M. E. Weiner and A. S. Jordan, *ibid.*, **43**, 1767 (1972).
20. L. Palm, H. Bruch, K. H. Bochem, and P. Balk, *J. Electron. Mater.*, **8**, 555 (1979).
21. S. J. Bass, *J. Cryst. Growth*, **47**, 613 (1979).
22. J. Mazzaschi, J. Barron, J. C. Brabaut, M. Brousseau, H. Maaref, F. Boillot, and M. C. Boissy, *Rev. Phys. Appl.*, **15**, 861 (1980).
23. Zh. I. Alferov, V. M. Andreev, D. Z. Garbuzov, and M. K. Trukan, *Sov. Phys. Semicond.*, **6**, 1718 (1973).
24. R. A. Logan, N. E. Schumaker, C. H. Henry, and F. R. Merritt, *J. Appl. Phys.*, **50**, 5972 (1979).

An Open-Tube Method for Diffusion of Zinc into GaAs

R. Jett Field* and Sorab K. Ghandhi**

Electrical, Computer, and Systems Engineering Department, Rensselaer Polytechnic Institute, Troy, New York 12181

ABSTRACT

Highly reproducible zinc diffusions from 0.03 to 1.5 μm have been made into GaAs using a CVD zinc-doped silica source capped with phosphosilicate glass. This structure permitted the use of an open-tube, flowing inert gas diffusion system. Diffusions were made from 400° to 700°C, with surface hole concentrations from 0.1 to 1.0 $\times$ 10^{20} cm^{-3}, and junction depths from 300Å to 1.5 μm. The diffusion coefficient and the hole concentration obtained by this technique are very close to those obtained by sealed ampul techniques using a Zn_3A_2 source. However, this open-tube system is more convenient to use, and gives highly reproducible results.

Highly doped p^+ layers in gallium arsenide are useful for ohmic contacts, as well as for forming p^+-n junctions. Zinc is often used in this application because of its high solid solubility. One approach for forming this layer is by diffusion, although epitaxy and ion implantation have also been used.

The diffusion of zinc in GaAs has been the subject of many investigations, most of which have involved the sealed ampul technique. Precise control of both the arsenic and the zinc vapor pressure in the ampul is required to give reproducible results (1). Moreover, the use of sealed ampul is generally considered to be a serious practical problem in commercial device fabrication.

This paper reports the formation of shallow, highly doped p^+-regions in GaAs by the open tube diffusion of zinc in a flowing inert gas ambient. The diffusion source is a layer of zinc-doped silica, grown by chemical vapor deposition (CVD), which can be easily removed after diffusion by buffered HF. A cap layer of phosphosilicate glass (PSG) is used to prevent loss of zinc and decomposition of the GaAs during the diffusion. No damage to the GaAs surface is caused by either the depositions or the diffusion process.

Preliminary results with this method have been reported previously (2). This paper presents further details, and covers a range of junction depths that are useful in modern devices. It shows that this technique provides precise control of junction depth, and is as simple to implement as diffusion processes for elemental semiconductors such as silicon. Hole concentrations obtained by this technique are higher than have been reported for ion-implanted layers in GaAs. Moreover, high temperature anneal steps, which are commonly used with ion implantation, are avoided by this approach.

Experimental

The technique used for these diffusions is briefly described as follows. A film of ZnO-SiO_2 is used as the dopant source, and is deposited on the gallium arsenide surface by chemical vapor deposition. This is followed by a cap layer of phosphosilicate glass (PSG). When necessary, a PSG layer is also deposited on the back-surface of the slice to prevent deterioration of the GaAs during the diffusion step. After deposition of these layers, diffusions are carried out in an open-tube furnace, in a flowing nitrogen gas ambient. Subsequently, the PSG and ZnO-SiO_2 layers are stripped in buffered HF.

Junction evaluation was carried out by four-point probing of the surface after successive anodization and stripping. Total junction depth was also measured on a step using a multiple beam interferometer, and served as a check against the anodization technique. Finally, Hall measurements were made to separate the contributions of mobility and carrier concentration to the resistivity of the diffused layer.

Layer growth.—The apparatus used for the ZnO-SiO_2 and PSG depositions was a resistance-heated, cold-wall chemical vapor deposition system. The depositions of PSG (3) and of ZnO (4) by this type of system have been described previously. Gases provided to this system were argon,[1] oxygen,[1] phosphine,[2] and silane[3]. Diethylzinc[4] (DEZ) was contained in a stainless steel bubbler maintained at 25°C. Its vapor pressure is 2.9 kPa (22 Torr) at this temperature, so that it can be readily transported in vapor form by this means.

ZnO-SiO_2 films were deposited at 350°C by the simultaneous oxidation if DEZ and silane using argon as a carrier gas. Flow conditions for these depositions were as follows: 40 ml/min argon flow through the DEZ bubbler; 0.5 ml/min silane flow (referenced to pure silane gas); 25 ml/min oxygen flow; and 7.0 l/min argon gas flow. The ZnO-SiO_2 film thickness was nominally 1000Å $\pm$ 10%, as determined by its interference color and by measurements with a multiple-beam interferometer. The typical growth time was 6 min for these layers.

The PSG cap was deposited at 350°C by the simultaneous oxidation of phosphine and silane with argon as a dilutant. Here, flow conditions were 2 ml/min pure silane, 0.3 ml/min pure phosphine, 15 ml/min oxygen, and 2 l/min argon. A cap thickness of 2000Å $\pm$ 10% was used, with a typical growth time of 6 min. Both the ZnO-SiO_2 and PSG layers were deposited in the same system. Layers on the top face of the GaAs were deposited in a single operation.

Diffusions.—Diffusions were carried out in an open-tube furnace at temperatures from 400° to 700°C, with nitrogen[5] flowing at 20 cm/min. Diffusion times between 5 min and 21 hr were used for these experiments. Some samples were diffused in a 1:1 nitrogen: hydrogen gas mixture. This gave the same results as diffusion in pure nitrogen, so that use of this gas mixture was discontinued. After diffusion, the glassy layers were removed by means of buffered HF.

Measurement techniques.—Junction depths and doping profiles were determined by making four-point sheet resistance measurements after successively removing thin layers from the surface until the diffused region was totally removed. This was done by anodization in an electrolyte (5) consisting of one part of a 3% aqueous solution of tartaric acid to two parts pro-

* Electrochemical Society Student Member.
** Electrochemical Society Active Member.
Key words: gallium arsenide, diffusion, zinc, open-tube, p^+.

[1] UHP Grade, Matheson Gas Products, East Rutherford, New Jersey.
[2] 500 ppm in UHP Argon, Matheson Gas Products, East Rutherford, New Jersey.
[3] 30,000 ppm in UHP Argon, Matheson Gas Products, East Rutherford, New Jersey.
[4] 5*N* Electronic Grade, Ventron Corporation, Danvers, Massachusetts.
[5] Commercial Grade, Air Products and Chemicals, Incorporated, Latham, New York.

pylene glycol, and removal of the anodic oxide with dilute HCl. The thickness of the removed layer was taken as 14Å of GaAs per volt of anodization potential. This was checked by masking part of the GaAs during these experiments and determining the total step height with a multiple beam interferometer and a scanning electron microscope. A second method of removal, which gave similar results, consisted of etching in a 150:3:1 $H_2O:NH_4OH:H_2O_2$ volume solution (6). The typical etch rate was 0.16 μm/min for the diffused region when this etch was used.

The average mobilities of samples diffused from 400° to 700°C were determined by a-c Hall effect measurements because of the low values of hole mobility associated with heavy doping. A Hall effect and four-point resistivity pattern was defined photolithographically and mesa-etched in Caro's etch.[6] Ohmic contacts were made without annealing, using conductive silver paint,[7] and were checked for linearity by means of a curve tracer. This pattern also verified the accuracy of the four-point probe measurements.

The hole concentration was determined assuming $N = 1(eR_H)$, with the Hall and drift mobilities assumed to be equal (7). Carrier concentration and mobility are given in Fig. 1 and 2.

[6] $H_2SO_4:H_2O_2:H_2$ ratio of 10:1:1 by volume.
[7] G.C. Electronics, Cat. No. 22-246, Hydrometals, Incorporated, Rockford, Illinois.

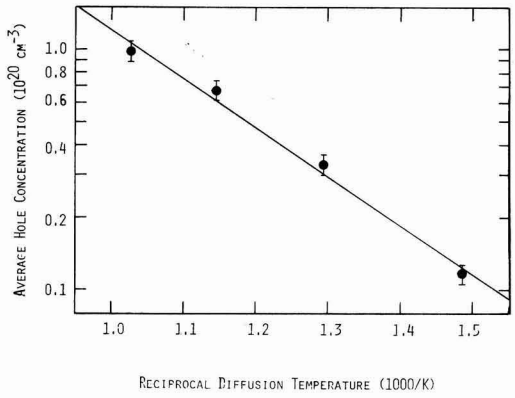

Fig. 1. Average hole concentration as a function of reciprocal temperature for diffusions from 400° to 700°C.

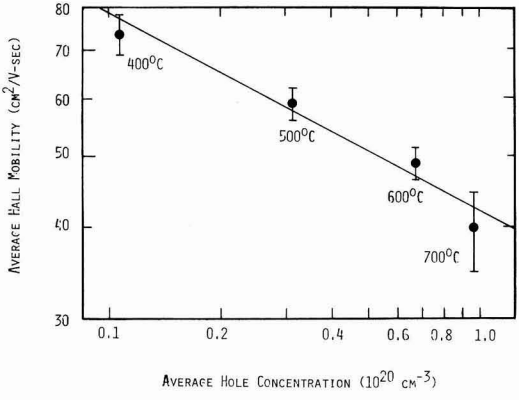

Fig. 2. Average Hall mobility as a function of average hole concentration for diffusions from 400° to 700°C.

Results and Discussion

All samples had clean, shiny surfaces after the removal of the PSG/ZnO-SiO_2 and ZnO-SiO_2 layers. Junction depths were determined by plotting sheet conductance *vs.* depth for each sample. The junction was assumed to occur where this plot intersected zero conductance (8). The sheet conductance data was differentiated to yield the bulk conductivity as a function of depth (8). Hole concentration was determined (7) to give the carrier profile as a function of depth. Typical profiles, for 3 samples diffused at 600°C for various times, are given[8] in Fig. 3, and are extremely abrupt in character. The nature of this doping profile can be explained with reference to the commonly accepted model for zinc diffusion in GaAs.

Zinc is known to follow the interstitial-substitutional diffusion model in GaAs (9). The charge state of the substitutional zinc is -1 (single acceptor), whereas that of the interstitial zinc has been determined (1) to be $+1$ (single donor). The solid solubility of substitutional zinc is higher than that of interstitial. During diffusion, the substitutional zinc dissociates, forming interstitial zinc and a neutral gallium vacancy. Interstitital zinc moves many orders of magnitude faster than the substitutional during the diffusion process.

Let Zn_i^+ and Zn_s^- denote the interstitial and substitutional zinc species, and P_{As4} the arsenic pressure over the sample. Then, it can be shown (10) that the effective diffusion coefficient is given by

$$D = D_s + D_i \frac{K_1}{n_i^2} \frac{[Zn_s^-]^2}{P_{As4}^{1/4}} \quad [1]$$

where D_s and D_i are the diffusion coefficients associated with substitutional and interstitial zinc, respectively. The substitutional term can be neglected, and the effective diffusion coefficient written in the normalized form

$$D = D_{surf} \left(\frac{N}{N_{surf}}\right)^2 \quad [2]$$

where

$$D_{surf} = K_3 N_{surf}^2 / P_{As4}^{1/4} \quad [3]$$

Solutions of Eq. [2] have been obtained (9) by Weisberg and Blanc, and result in extremely abrupt doping profiles of the type shown in Fig. 3. For these profiles the junction depth is relatively independent of the background concentration, and is given by

$$x_j = 1.092(D_{surf}t)^{1/2} \quad [4]$$

[8] Each curve represents 12-16 measured data points (2).

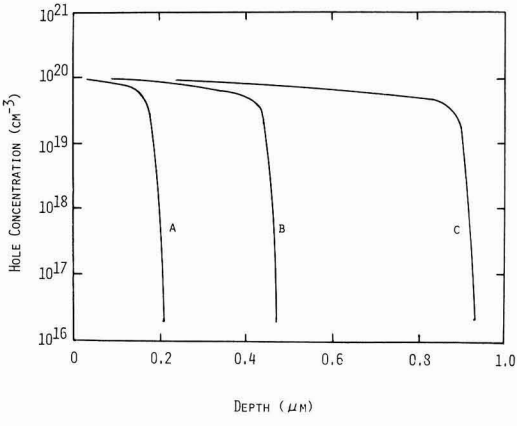

Fig. 3. Carrier concentration profiles for three diffusions at 600°C: (a) 5 min, (b) 20 min, and (c) 80 min.

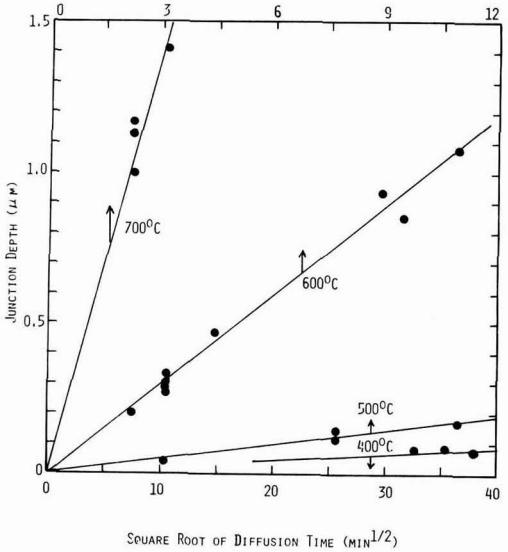

Fig. 4. Junction depth as a function of the square root of diffusion time for diffusion temperatures from 400° to 700°C.

Figure 4 shows curves of junction depth *vs.* $t^{1/2}$ for a series of diffusion over the 400°-700°C temperature range. These are seen to be closely represented by Eq. [4]. This linear dependence indicates that the ZnO-SiO_2 serves as an infinite diffusant source, and no anomalous depletion effects occur within the scope of this experiment, such as those reported previously for tin-doped oxides used for n-type diffusions (11). Consequently, the surface concentration for these diffusions is not a function of the diffusion time. Figure 1 shows a plot of this surface concentration, as obtained from Hall measurements of diffused layers, on the assumption that the layer is uniformly doped. This is approximately true in view of its extremely abrupt doping profile.

Equation [4] can be used to obtain the value of D_{surf} as a function of reciprocal temperature, which is plotted in Fig. 5. This curve is expected to be linear from the temperature-dependence of the junction depth (12)

$$x_j = K_5 \sqrt{t}\, e^{-E/kT} \quad [5]$$

The departure from linearity at 400°C can be attributed to a fall in the hole activity coefficient in the 4×10^{19} cm^{-3} concentration range (1).

The surface concentration is given by (12)

$$N_{surf} = K_6 P_{Zn}^{1/2} P_{As_4}^{1/6} \quad [6]$$

Combining Eq. [3], [4], and [6]

$$D_{surf} = K_3 K_6^2 P_{Zn} \quad [7]$$

so that

$$x_j = 1.092 K_6 (K_3 P_{Zn} t)^{1/2} \quad [8]$$

Thus the diffusion coefficient and the junction depth are independent of the arsenic pressure. In many diffusion situations (13), however, P_{Zn} and P_{As4} are related by the law of mass action.

Both the diffusion coefficient and hole concentration found in this study are very close to those obtained with a Zn_3As_2 source using the sealed ampul technique (13). This indicates, from [6] and [7], that the same effective P_{Zn} and P_{As4} occur with the PSG/ZnO-SiO_2 and the Zn_3As_2 sealed ampul systems.

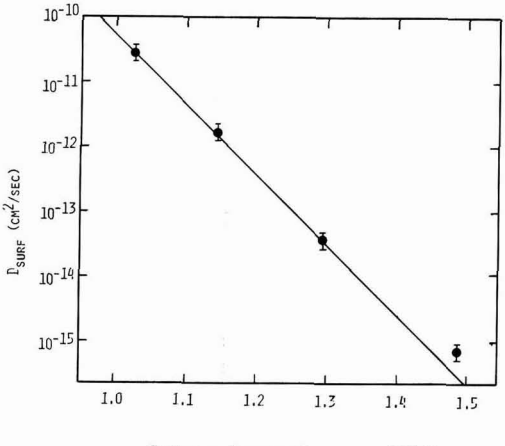

Fig. 5. D_{surf} *vs.* reciprocal diffusion temperature. The departure from linearity at 400°C is probably caused by the fall in hole activity coefficient in this concentration range. Equation [4] may be used to determine the junction depth for any diffusion time and temperature above 500°C.

Conclusions

Shallow open-tube diffusion of zinc into GaAs has been shown to be reproducible using a PSG/ZnO-SiO_2 structure, with no damage to the GaAs surface. Analysis of the diffusion data has shown diffusion constants and doping levels similar to the most reproducible sealed ampul diffusion methods, without using any toxic arsenic source, without the inconvenience of sealed ampuls. and using an inert gas ambient.

The p^+ regions formed by this method have been shown to be heavily doped, and are thus suitable for ohmic contacts to lightly doped p-regions, and for the fabrication of p^+-n junction structures. Any masking system used for IC fabrication in the sealed ampul technique should be directly applicable to the PSG/ZnO-SiO_2/GaAs diffusion structure. Furthermore, it should be possible to restrict the ZnO-SiO_2 source to specific areas of the GaAs.

In summary, the open-tube zinc diffusion technique described in this paper is very practical and reproducible, thus showing clear advantages over conventional sealed ampul techniques.

Acknowledgments

The authors wish to thank R. Reep and A. Hayner for manuscript preparation. This work was supported by the Solar Energy Research Institute, Golden, Colorado, under Contract No. XS-0-9002-4.

Manuscript submitted June 25, 1981; revised manuscript received Oct. 16, 1981.

Any discussion of this paper will appear in a Discussion Section to be published in the June 1983 JOURNAL. All discussions for the June 1983 Discussion Section should be submitted by Feb. 1, 1983.

Publication costs of this article were assisted by Rensselaer Polytechnic Institute.

REFERENCES

1. H. C. Casey, Jr., in "Atomic Diffusion in Semiconductors," D. Shaw, Editor, pp. 369-374, Plenum Publishing Company, New York (1973).
2. S. K. Ghandhi and R. J. Field, *Appl. Phys. Lett.*, **38**, 267 (1981).
3. B. J. Baliga and S. K. Ghandhi, *J. Appl. Phys.*, **44**, 990 (1973).

4. J. R. Shealy, B. J. Baliga, R. J. Field, and S. K. Ghandhi, *This Journal*, **128**, 559 (1981).
5. H. Hasegawa and H. L. Hartnagel, *ibid.*, **123**, 713 (1976).
6. J. J. Gannon and C. J. Nuese, *ibid.*, **121**, 1215 (1974).
7. S. M. Sze and J. C. Irvin, *Solid State Electron.*, **11**, 599 (1968).
8. M. H. Pilkuhn and H. Rupprecht, *Trans. Met. Soc. AIME*, **230**, 296 (1964).
9. L. R. Weisberg and J. Blanc, *Phys. Rev.*, **131**, 1548 (1963).
10. A. Luque, J. Martin, and G. L. Araujo, *This Journal*, **123**, 249 (1976).
11. B. J. Baliga and S. K. Ghandhi, *ibid.*, **126**, 135 (1979).
12. H. C. Casey, Jr. and M. B. Panish, *Trans. Met. Soc. AIME*, **242**, 406 (1968).
13. K. K. Shih, *This Journal*, **123**, 1737 (1976).

The Phase Relations in the Cu,In,S System and the Growth of $CuInS_2$ Crystals from the Melt

F. A. Thiel

Bell Laboratories, Murray Hill, New Jersey 07974

ABSTRACT

The liquidus in the Cu,In,S system along the $Cu_{0.5}In_{0.5}$-S pseudobinary has been measured. The melting point of $CuInS_2$ T_m = 1115°C is substantially above the earlier literature values. The growth of $CuInS_2$ crystals by zone melting is described and their defect structure is revealed by etching on the (11$\bar{2}$) face.

Recently we have explored the properties of photodiodes made from the ternary compound semiconductor $CuInS_2$ (1) that is, also, of interest for photovoltaic applications since its energy gap 1.545 eV at room temperature (2) is close to the optimum for solar power conversion by a single junction cell (3). Several homojunction (4), heterojunction (5, 6), and liquid junction (7) $CuInS_2$ based solar cells have been reported that, at the present state of the art, have power conversion efficiences that are well below the theoretical limit (8). The reason for this behavior is the dominance of native defects that control the electrical transport properties of $CuInS_2$ (9), interfacial reactions and possibly second phase formation that degrade the properties of the cells. A clarification of the relative importance of these phenomena and improvements in the device performance can be obtained only on the basis of experiments with well-characterized single crystal $CuInS_2$ substrates, and there exists a need for fundamental studies in the area of bulk crystal growth and characterization of $CuInS_2$. Of the possible choices of crystal growth methods for the fabrication of $CuInS_2$ single crystals, both melt and vapor transport techniques have been used (2, 10). Since incorporation of the transport agent during vapor growth quenches the luminescence of $CuInS_2$, we prefer in this study crystal growth from the melt selecting zone leveling as the most appropriate technique for controlling compositional variations. In order to pursue the crystal growth in an organized manner the phase relations in the Cu,In,S system must be established. There exist a number of investigations concerning the solidus at the Cu_2S-In_2S_3 pseudobinary where, in addition to the compound $CuInS_2$, several thiospinels have been identified (11, 12). Also, the homogeneity range on the $Cu_{1-x}In_{1+x/3}S_2$ pseudobinary has been studied resulting in a region of existence $0 \leq x \leq 0.05$ (13). Surprisingly the liquidus in the Cu,In,S system is not well documented. Therefore, we conducted a series of experiments determining the liquidus temperatures for a set of preset compositions by an experimental procedure similar as described in Ref. (14).

Figure 1 shows the liquidus temperature as a function of composition at the pseudobinary $Cu_{0.5}In_{0.5}$-S. We note that the melting point of $CuInS_2$, $T_m = 1115$°C, is well above the value quoted in the literature (15) and that the regions of immiscible liquids extend from the In-S and Cu-S binaries into the ternary phase field. An attempt was made at determining the equilibrium decomposition pressure of $CuInS_2$ P_m at T_m by a method described in Ref. (16). However, in view of the relatively large background correction required we are only able to specify an upper limit $P_m \lesssim 1$ atm.

Since for the purpose of photovoltaic applications p-type $CuInS_2$ is preferred, we grew most of our crystals under a sulfur pressure of 1 atm. The zone-melting apparatus consisted of two furnace sections adjacent to a narrow zone heated by SiC glow bars similar to those described in Ref. (17). The zone width to boat length ratio was usually 1:10 and was established by

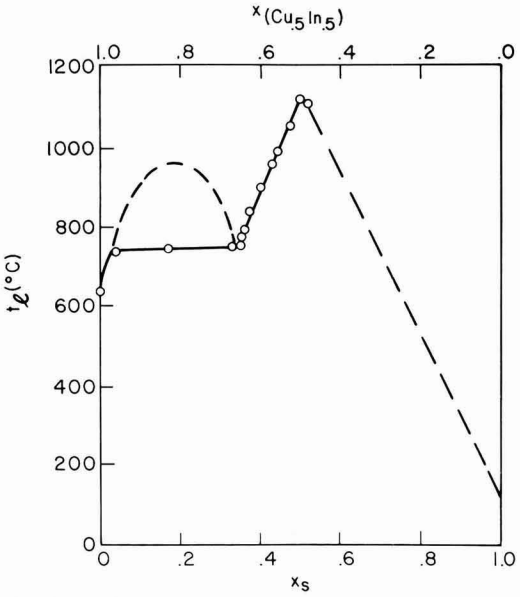

Fig. 1. Liquidus temperature t_l vs. composition at the $(Cu_{0.5}In_{0.5})$-S pseudobinary.

Key words: crystals, melting, defect structure.

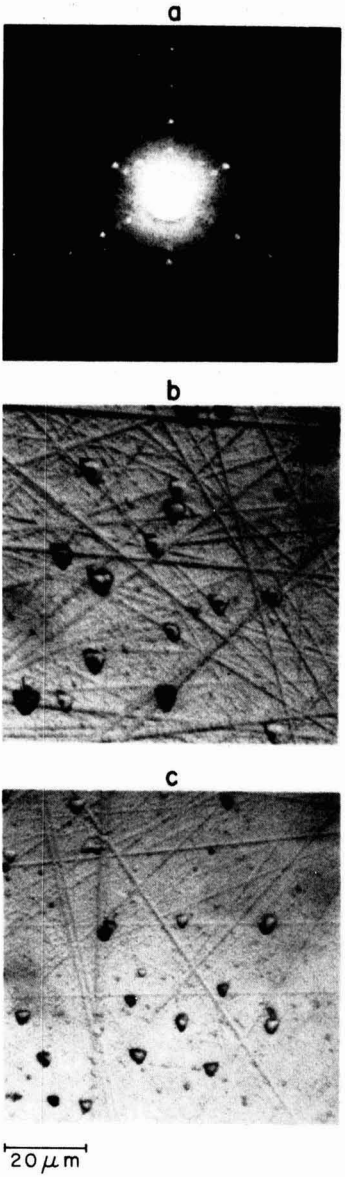

Fig. 2. (a) Laue x-ray photograph of a (112) wafer of $CuInS_2$; (b) etch pits on this (11$\bar{2}$) face, bromine-methanol etch; (c) etch pits on the same face generated by the 3:1:1 etch.

visual inspection. Twinning and gas bubbles are a problem but can be removed by repetitive zone scans in both directions. Single crystals of $CuInS_2$ of ~1 cm^2 cross section and several cm lengths have been obtained with carrier concentrations $N_A - N_D \approx 10^{16}$ cm^{-3} and hole mobilities $\mu_n = 10$ cm^2 V^{-1} sec^{-1}.

In order to evaluate the defect density in the material we etched wafers of our crystals oriented on the (11$\bar{2}$) plane. The polar nature of this plane is best revealed by etching in concentration HNO_3 for 3-4 min, which leaves the (11$\bar{2}$) face clear but develops on the opposite face a sulfur film. We tentatively identify this face as the B face. For a definite identification, x-ray measurements as described in Ref. (18) are required. Etch pits are developed on the 11$\bar{2}$-A face by etching in H_2SO_4:H_2O_2:H_2O = 3:1:1 for 45 min at 60°C or by exposure to 2% bromine methanol solution for 10-15 sec. Figure 2 shows microphotographs of etched 11$\bar{2}$ faces that reveal ~3.5 × 10^5 defects/cm^2.

Manuscript received Aug. 6, 1981.

Any discussion of this paper will appear in a Discussion Section to be published in the June 1983 JOURNAL. All discussions for the June 1983 Discussion Section should be submitted by Feb. 1, 1983.

Publication costs of this article were assisted by Bell Laboratories.

REFERENCES

1. B. Tell and F. A. Thiel, *J. Appl. Phys.*, **50,** 5045 (1979).
2. A. W. Verheijen, L. J. Giling, and J. Bloem, *Inst. Phys. Conf. Ser.*, **35,** 169 (1977).
3. J. J. Loferski, *J. Appl. Phys.*, **27,** 777 (1956).
4. L. L. Kazmerski, *ibid.*, **48,** 3178 (1977).
5. L. L. Kazmerski, F. R. White, M. S. Ayyagori, Y. J. Juang, and R. P. Patterson, *J. Vac. Sci. Technol.*, **14,** 65 (1977).
6. L. L. Kazmerski, F. R. White, and G. K. Morgan, *Appl. Phys. Lett.*, **29,** 268 (1976).
7. M. Robbins, K. J. Bachmann, V. G. Lambrecht, F. A. Thiel, J. Thomson, Jr., R. G. Vadimsky, S. Menezes, A. Heller, and B. Miller, *This Journal*, **125,** 831 (1978).
8. J. M. Meese, J. C. Manthuruthil, and D. R. Locker, *Bull. Am. Phys. Soc.*, **20,** 696 (1975).
9. D. C. Look and J. C. Manthuruthil, *J. Phys. Chem. Solids*, **37,** 173 (1976).
10. H. M. Kasper, in "Solid State Chemistry," R. S. Roth and S. J. Schneider, Editors, NBS Special Publication 364 (1972).
11. L. Gastaldi and L. Scaramuzza, *Acta Crystallogr. Sect. B*, **35,** 2283 (1979).
12. C. Paorici, L. Zanotti, and L. Gastaldi, *Mater. Res. Bull.*, **14,** 469 (1979).
13. A. W. Verheijen, L. J. Giling, and J. Bloem, *ibid.*, **14,** 237 (1979).
14. E. Buehler and K. J. Bachmann, *J. Cryst. Growth*, **35,** 60 (1976).
15. J. L. Shay and J. H. Wernick, "Ternary Chalcopyrite Semiconductors: Growth, Electronic Properties and Applications," Pergamon Press, Oxford (1975).
16. K. J. Bachmann and E. Buehler, *This Journal*, **121,** 835 (1974).
17. K. J. Bachmann, L. C. Clarke, Jr., E. Buehler, D. L. Malm, and J. L. Shay, *J. Electron. Mater.*, **4,** 741 (1975).
18. F. A. Thiel and R. Barns, *This Journal*, **126,** 1272 (1979).

A-C Anodizing Processes of Aluminum Alloys

Joseph Zahavi,*,[1] H. Kerbel, and O. Korotkina

Israel Institute of Metals, Technion, Haifa, Israel

ABSTRACT

Studies have been made of thick a-c anodic films on commercial purity aluminum and aluminum-copper alloys in sulfuric and oxalic acid solutions, with particular examination of the constituents in these alloys. Film structure, topography, and composition were characterized through electron microscopy and electron probe microanalysis. It was found that iron-rich second-phase particles and copper-rich, iron, and manganese dispersed intermetallics presented in the 1100-H14 aluminum alloy and in the 2024-T3 aluminum alloy, respectively, have been incorporated and retained in the a-c films during their growth. The embedment of these 0.5-10 μm intermetallic constituents did not substantially affect a-c thick porous film growth, film/electrolyte and film/metal interfaces, film pore and barrier layer structures, or uniformity of film thickness. The mechanisms of incorporation of nonreactive iron-rich second-phase particles and reactive copper-rich intermetallics into the growing film are discussed.

The second-phase constituents in commercial aluminum alloys can have an appreciable effect on anodic film properties, depending on their type and on conditions used in anodizing. The behavior of the various intermetallic constituents in aluminum alloys during d-c anodizing and their effects on d-c film formation have been investigated previously by several researchers (1-6). The intermetallic compounds were grouped in three classifications (4-6): those which were more reactive than the matrix, those which were equally reactive with the matrix, and those which were less reactive than the matrix.

D-C anodizing of aluminum alloys containing nonreactive or equally reactive particles, such as iron-rich intermetallics in sulfuric acid (1-2) and oxalic acid (4-6), respectively, results in embedment of these particles in the films during their formation. D-C anodizing of aluminum alloys containing very reactive particles such as copper-rich intermetallics results in nonuniform films with an irregular structure due to fast dissolution of these intermetallics (2, 5).

No substantial work has been reported on film formation and behavior of second-phase particles under a-c anodizing conditions. The present work is a study of a-c thick anodic films on a commercial pure aluminum alloy containing iron-rich intermetallic constituents and on an aluminum-copper alloy containing copper-rich, iron, and manganese dispersed particles. Particular attention is given to the incorporation of these particles into the growing film and to their effects on anodizing processes, film structure, composition, and properties.

Experimental Procedure

Specimens and surface preparation.—The materials used were commercial wrought pure aluminum and aluminum-copper alloys designated with AA numbers as Al 1100-H14 and Al 2024-T3, respectively. The chemical composition limits (all in weight percent) of the Al 1100-H14 were Si + Fe 1.0, Cu 0.20, Mn 0.05, Zn 0.1; and of the Al 2024-T3, Cu 3.8-4.9, Si 0.50, Fe 0.50, Mn 0.3-0.9, Mg 1.2-1.8, Cr 0.10, Zn 0.25. The Al 1100-H14 alloy is strain hardened, reaching tensile strength half-way between soft and full hard, half-hard, designated by H14.

The Al 2024-T3 alloy is solution heat-treated and cold-worked, naturally aged to substantially stable conditions.

Specimens were cut with a working area 20 × 15 × 1 mm with a narrow tab. All specimens were degreased in trichloroethylene, etched in 10% HF for 4 min, washed in distilled water, then electropolished in 20 volume percent 70% $HClO_4$ in ethanol at 8-12 A/dm^2 for 5-10 min at −10° to −15°C, and rinsed with a jet of ethanol.

Anodizing.—The specimens were anodized potentiostatically for 15-150 min in (a) 150-250 g/l sulfuric acid at 15°-25°C at constant a-c voltages of 20-30V rms, and in (b) 30-90 g/l oxalic acid at 15°-45°C at constant a-c voltages of 50-90V rms. Anodizing was done in a 2 liter glass beaker. A-C films were formed simultaneously on four specimens (total area of 28 cm^2), each electrode consisting of two specimens. The solution was agitated with a glass rod stirrer, and the temperature was kept within ±0.5°C of the required value. A stabilized a-c power supply of 10A, 200V, at frequency of 50 Hz was used for a-c anodizing.

Microscopy and electron probe microanalysis.—Information generated and achieved by a variety of techniques, such as scanning electron microscopy (SEM), direct and replica transmission electron microscopy (TEM), and electron probe microanalysis (EPMA) was found essential for investigating a-c film growth, film structure, morphology, and composition, particularly for the effect of intermetallics in the commercial pure aluminum and aluminum-copper alloys used in this work.

Film surfaces were examined by SEM after applying a thin carbon layer to prevent charging in the beam. For TEM observation, carbon replicas preshadowed at 45° with gold palladium were taken of outer film surfaces, the film being removed in 10% HF without attacking the gold palladium.

Ultramicrotomy (7) was used to produce ultrathin sections (up to 0.1 μm) of anodized specimens to be examined by direct transmission electron microscopy. Thin strips of an anodized specimen were cut, mounted in a polyethylene capsule, impregnated with a resin, and cured at 333 K for subsequent sectioning. Sectioning was carried out in a direction parallel to the metal/film interface, so the sections are compressed in that direction. Dimensions perpendicular to this direction are relatively reliable. Composition profiles of cross sections were obtained by EPMA.

Film thickness and impedance measurements.—Total film thickness was measured by an eddy current technique. Porous film barrier layer thickness was calculated from film impedance measurements made with an impedance bridge.

Results and Discussion

Kinetics and film growth.—Potentiostatic a-c anodizing in sulfuric and oxalic acid gave the current-time curves shown in Fig. 1 and 2, respectively. These are very similar to curves obtained for d-c formation of porous anodic films (8). The measured current reached a minimum value and then increased, after which it remained fairly constant or diminished gradually with anodizing time.

* Electrochemical Society Active Member.
[1] Visiting Senior Scientist, IBM Corporation, Poughkeepsie, New York 12602.
Key words: a-c anodizing, intermetallics, aluminum alloys, porous anodic films.

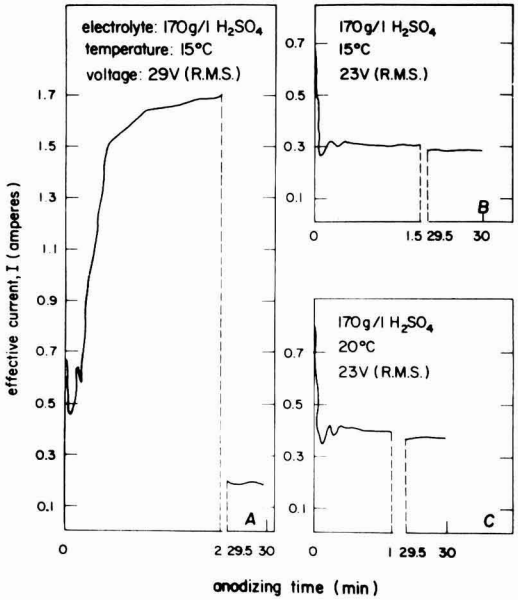

Fig. 1. Variation of effective current with a-c anodizing time of 2024-T3 aluminum alloy in H_2SO_4 at constant temperature and voltage. Anodized area was 28 cm^2.

The behavior of the current-time curves, both in oxalic and sulfuric acids, indicated the formation of porous type a-c films, while the current fluctuations probably indicated local processes of breakdown dissolution and repair. These were not further investigated in this study, and nonfluctuated current-time curves were chosen as yielding suitable conditions for this work.

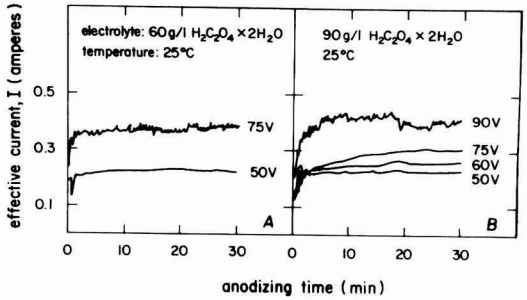

Fig. 2. Variation of effective current with a-c anodizing time of 2024-T3 aluminum alloy in oxalic acid solutions at 25°C and at various constant voltages. Anodized area was 28 cm^2.

SEM and EPMA observations.—Examination of a-c anodized surfaces by scanning electron microscopy revealed local, mostly elongated, dark sites up to 10 μm across, with a light rim. These dark sites are cavities in the film surface at the location of second-phase particles removed during the course of anodizing, both in sulfuric acid (Fig. 3) and in oxalic acid (Fig. 4). Furthermore, the cavities indicate that particles were embedded and retained in the films through their growth. However, those particles which were less deeply embedded in the film surface were removed, as found earlier in d-c anodizing (1). It was noted that these cavities maintained the same shape and size under the various anodizing conditions, implying that

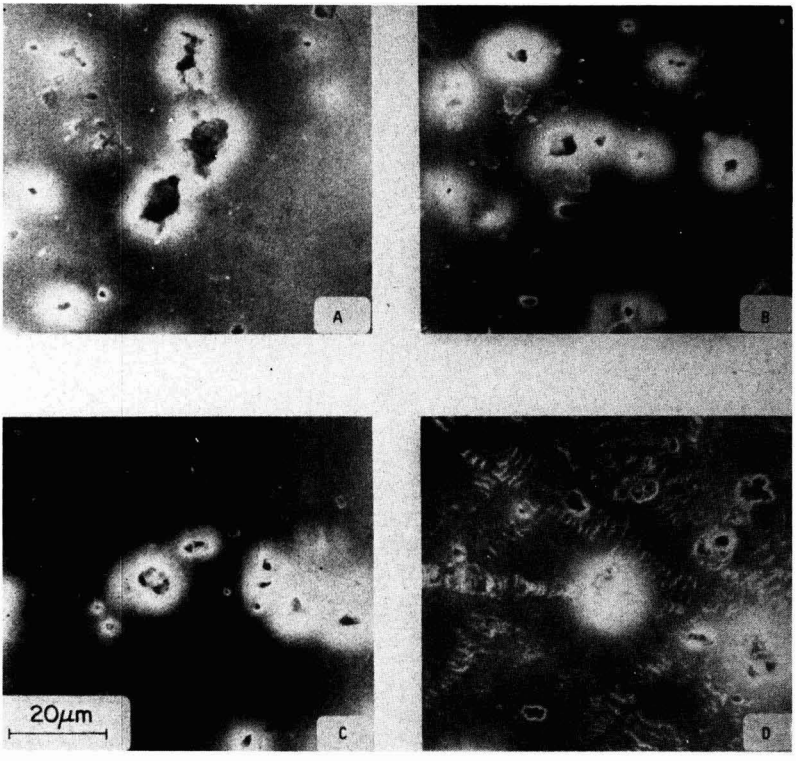

Fig. 3. SEM micrographs of anodized 2024-T3 aluminum alloy in 170 g/l H_2SO_4 at 15°C and at various voltages for 30 min. A, 21.5V; film thickness 6 μm. B, 23.0V; film thickness 8 μm. C, 24.5V; film thickness 11 μm. D, 29.0V; film thickness 39 μm.

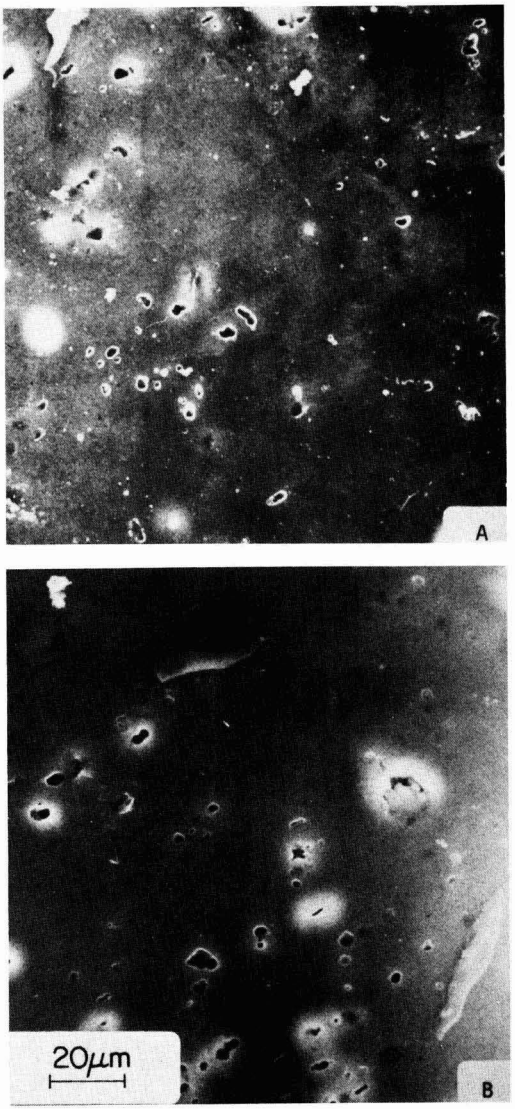

Fig. 4. SEM micrographs of anodized 2024-T3 aluminum alloy in oxalic acid solutions at 25°C and at constant alternating voltage of 75V for 30 min. A, 90 g/l oxalic acid; film thickness 8.5 μm. B, 30 g/l oxalic acid; film thickness 5.0 μm.

second-phase particles did not shrink or dissolve substantially during film growth.

A-C films formed in sulfuric acid at a relatively high potential of 29V showed the same shape and size of cavities in their surfaces, together with local bright distinct strips indicative probably of breakdown of the film, as can be seen in Fig. 3D. In this study we will not further discuss these extreme conditions (shown also in Fig. 1A).

EPMA observation of cross sections of a-c anodized specimens shows the distribution of intermetallics and alloying elements in the aluminum alloys along with the film thickness.

Aluminum-copper alloy.—Observations of aluminum-copper 2024-T3 alloy anodized in sulfuric acid and oxalic acid are shown in Fig. 5 and 6, respectively.

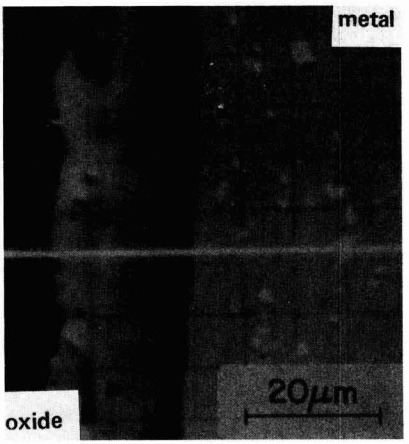

Fig. 5. Cross sectional image of 2024-T3 aluminum alloy specimen anodized in 170 g/l H_2SO_4 at 15°C and at alternating constant voltage of 26V for 30 min. EPMA observation.

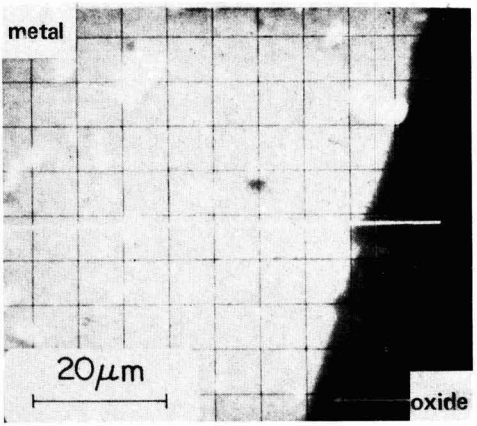

Fig. 6. Cross sectional image of 2024-T3 aluminum alloy specimen anodized in 90 g/l oxalic acid at 25°C and at constant alternating voltage of 75V for 30 min. EPMA observation.

Scanning electron micrographs of aluminum-copper specimen cross sections showed the presence and distribution of second-phase intermetallics in the alloy appearing as bright local sites in Fig. 5 and 6. Figure 5 also shows dark areas distributed throughout the film thickness, with a few also in the alloy. These dark sites, which are the same shape and size as the intermetallics in the alloy matrix, are probably cavities produced by the removal of intermetallics during preparation of the cross sections. They indicate the embedment of intermetallics in the films during their growth. The composition of the intermetallics in the aluminum-copper alloy was evaluated through x-ray distribution mapping for various elements (not shown). It was found that most of the intermetallics in the aluminum-copper were copper-rich, probably $CuAl_2$, while some of the second-phase particles contained high concentrations of iron and manganese besides copper; these were probably $Al_7Cu_2Fe(Mn)$, as found recently (9) in 2024 aluminum alloy.

Besides the second-phase particles, a uniform distribution of magnesium was detected in the alloy as well as through the film thickness. Furthermore, a uniform distribution of copper was detected in the aluminum matrix and, to a lesser extent, in the film itself.

A-C films formed in sulfuric acid contained a uniform distribution of sulfur, similar to d-c films (2, 3).

Moreover, electron scanning micrographs of a-c anodized aluminum-copper alloy in sulfuric and oxalic acids showed uniform film thickness and film-solution and film-substrate interfaces, indicating that the microconstituents did not substantially affect the a-c film growth processes when compared with d-c film growth, especially on aluminum-copper alloys (2, 5).

Aluminum 1100 alloy.—After a-c anodizing of Al 1100-H14 alloy in sulfuric and oxalic acids, specimens were sectioned and examined with an electron probe microanalyzer for the presence of alloying elements and second-phase particles in the matrix and in the oxide film. Electron scanning images of specimen cross sections are shown in Fig. 7 and 8. The appearance of the film cross section and of iron-rich intermetallics was qualitatively the same as for Al-Cu alloy (Fig. 5 and 6). The embedment of iron-rich particles, probably Al_3Fe constituents (1, 2), during a-c anodizing in sulfuric or oxalic acids did not affect the uniformity of film thickness and film-electrolyte and film-metal interfaces. The entrapment of Al_3Fe second-phase particles in d-c films formed in sulfuric acid was reported earlier (1, 2), while other researchers (4, 6) reported that iron-rich intermetallics (Al_3Fe) were anodized at the same rate as the aluminum matrix in sulfuric acid (4) and in oxalic acid (6).

TEM observations.—Direct transmission studies were limited to specimen cross sections produced by ultramicrotomy techniques (7). These TEM studies usually showed structures of film and metal substrate (Fig. 9). film/substrate interface, and film pore structure and morphology (Fig. 10).

The electron micrograph (Fig. 9A) of a-c film formed on aluminum-copper substrate (metal substrate is shown as dark zone at the bottom left corner) showed the presence of holes in the middle of the film originally occupied by intermetallic particles. In addition to intermetallic particle sites now filled with resin, tears which were introduced during sectioning are present, as shown at the right-hand edge of the picture. Usually no material other than resin was observed at the intermetallic sites. However, there appeared to be material present within the large intermetallic site shown in the middle of Fig. 9A. This material is probably a porous oxide film formed adjacent to the intermetallic particle surface where it probably stopped growing. thin enough to be examined and shown in transmission. The pores found in this piece of oxide film at the intermetallic site were around 10 nm in diameter, indicating anodizing voltage of ~10V at the site (deduced from the known experimental value of 1 nm/V for pore diameter in aluminum films formed in sulfuric acid) (10).

An electron micrograph (Fig. 9B) of an ultramicrotomed section through the aluminum-copper substrate

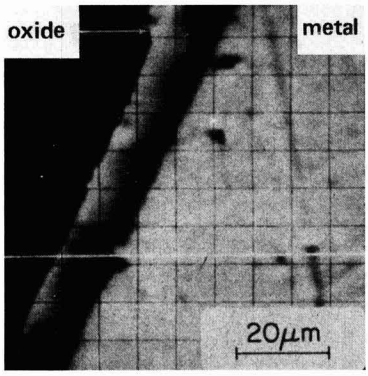

Fig. 7. Cross sectional image of 1100-H14 aluminum alloy specimen anodized in 170 g/l H_2SO_4 at 15°C and at constant alternating voltage of 23V for 30 min. EPMA observation.

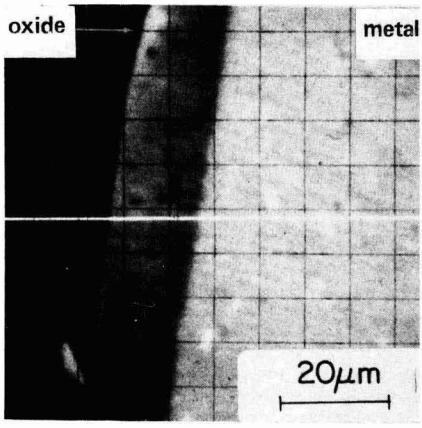

Fig. 8. Cross sectional image of 1100-H14 aluminum alloy specimen anodized in 90 g/l oxalic acid at 25°C and at alternating constant voltage of 75V for 30 min. EPMA observation.

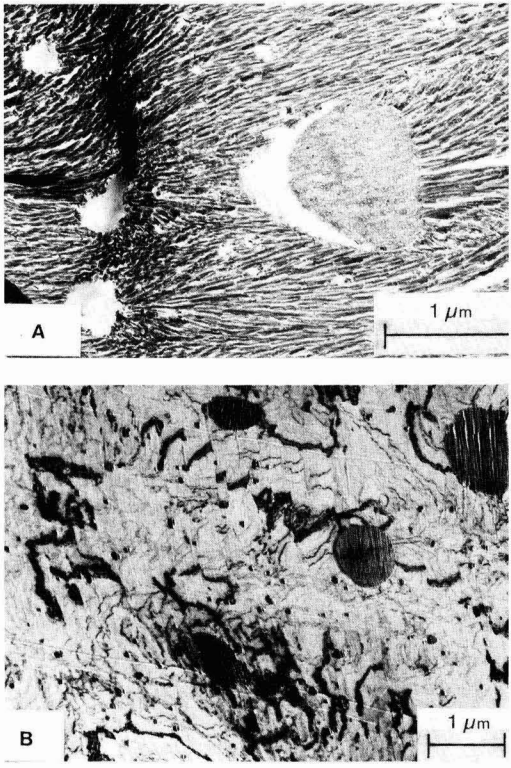

Fig. 9. Typical direct TEM of ultramicrotomed sections of a-c anodized aluminum-copper 2024 alloy. A, a-c oxide film produced in 170 g/l sulfuric acid at 25°C at constant voltage of 23V for 60 min, reaching film thickness of 19 μm. B, a section of the metal substrate showing intermetallic particles in the aluminum-copper 2024 alloy.

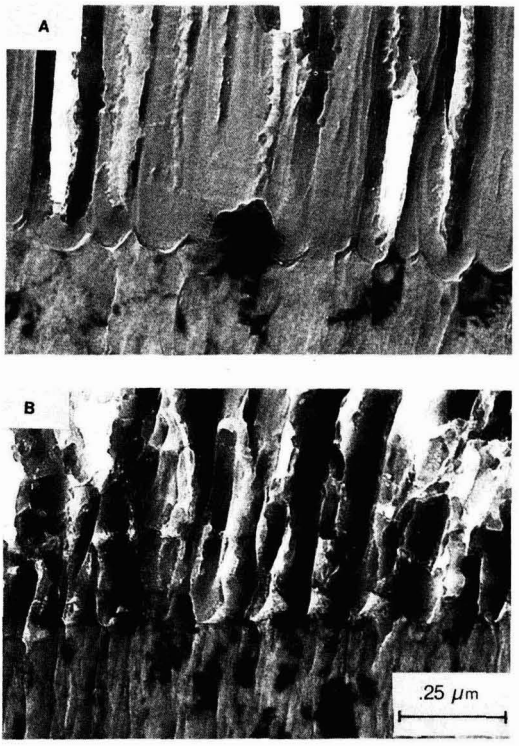

Fig. 10. Typical TEM's of ultramicrotomed sections of a-c anodized specimens.

showed intermetallic particles which were differentiated from the matrix because of their greater electron scattering cross section and different deformation behavior during slicing. The intermetallics characterized and identified by direct TEM observations in the metal substrate and in the film were up to 1 μm in size, some rounded and some elongated, as shown in Fig. 9.

The structure and morphology of metal/film interfaces were obtained through direct transmission electron microscopy observations of ultramicrotomed sections. Typical electron micrographs of anodized commercial pure aluminum and aluminum-copper in oxalic acid are shown in Fig. 10, where the lower portion of the micrographs shows a section through the metal substrate while the upper portion shows a section through the thick porous film.

A transmission electron micrograph of anodized Al 1100-H14 (Fig. 10A) shows the pores and the interface structure of the metal/film. The section examined shows that the plane of slicing did not coincide completely with the plane of the pores; therefore, the complete length and pattern of the pores could not be observed. Nevertheless, pores and a uniform scalloped barrier layer were evident both in Al 1100 alloy and in Al 2024 alloy. Furthermore, Fig. 10A shows that the barrier layer thickness was around 75 nm, giving ~1 nm V^{-1} for films formed on aluminum in oxalic acid, similar to the values obtained for d-c films in oxalic acid (7).

Impedance measurements of porous films formed at constant d-c and a-c voltages gave the film barrier layer thicknesses as shown in Fig. 11. D-C films formed on Al 2024 and Al 1100 alloys had barrier layer thicknesses of 0.88 and 1.08 nm V^{-1}, respectively, compared with a-c films with values of 0.76 and 0.87 nm V^{-1} for Al 2024 and Al 1100, respectively, within a range of anodizing voltage up to 25V.

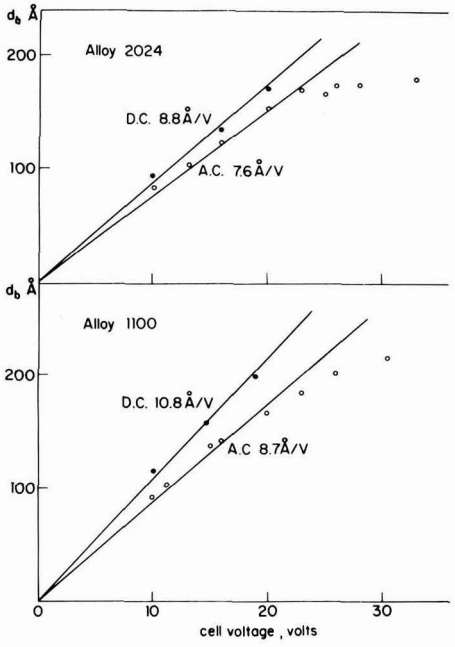

Fig. 11. Variation of barrier thickness d_b with cell voltage of d-c and a-c thick anodic films formed in 170 g/l sulfuric acid on Al 1100 and Al 2024 alloys.

These barrier thickness measurements indicate that the barrier layer thicknesses of a-c and d-c films formed under similar anodizing conditions are within 10% (11). It can be deduced, therefore, that the presence and the embedment of intermetallic particles during this growth did not grossly change the film barrier layer and its growth rate.

The embedment of an intermetallic particle into the film during its growth can be observed in Fig. 10A. The particle, probably Al_3Fe, appeared as a dark zone at the metal/film interface. It can be seen that film growth through the pore base ceased at the particle interface, resulting in film growth around the particle. This will lead to electrical isolation of the particle from the substrate.

In Fig. 10B, no particles were observed at the metal/film interface. The basic film pore structure of a-c films was not affected by the presence of intermetallic particles in these alloys. These particles were entrapped into the oxide films in the course of their growth, but did not cause substantial changes in film structure, as deduced from the TEM observations.

Replica observations.—Replicas of film external surfaces were made without further treatment of the specimens. Particles present at the surface after anodizing were replicated. Cavities in the film surface originally occupied by intermetallic particles which were removed toward the end of the anodizing processes were replicated as well.

Typical surface replica micrographs of a-c films are given in Fig. 12 and 13. Figure 12A shows, for Al 2024-T3 alloy anodized in sulfuric acid, a particle at the film surface (left side of the picture) which appeared substantially complete; that is, it did not dissolve in the course of anodizing. In addition to the embedded particle, two small cavities can be seen in the lower right side of the pictures. These are probably due to removal of second-phase particles from the film surface in the course of anodizing and film growth.

Through the course of prolonged a-c anodizing, the film structure might be affected and modified at the

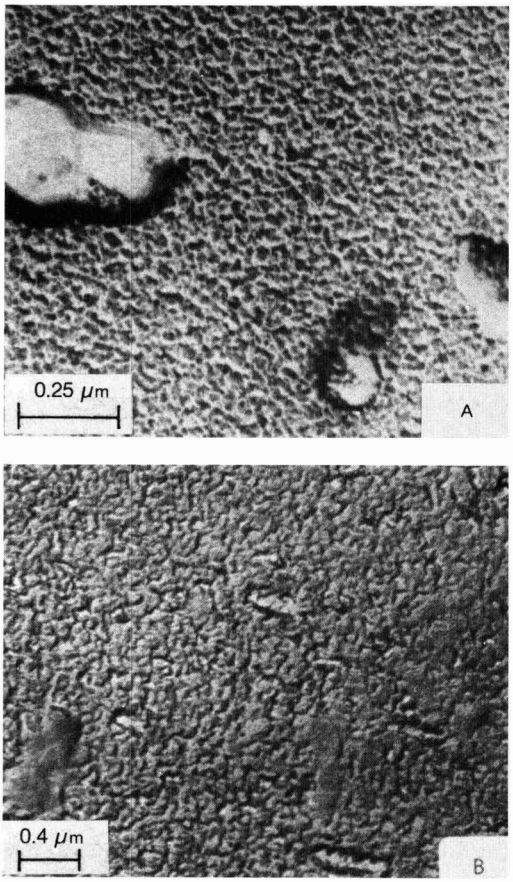

Fig. 12. Surface replicas of a-c anodized Al 2024-T3 alloy showing film surface structure, intermetallics, and intermetallic sites in film surface. A, a-c film formed in 170 g/l sulfuric acid at 15°C at constant potential of 23V for 30 min, reaching thickness of 8.0 μm. B, a-c film formed in 90 g/l oxalic acid at temperature of 25°C at constant potential of 75V for 30 min, reaching thickness of 8.5 μm.

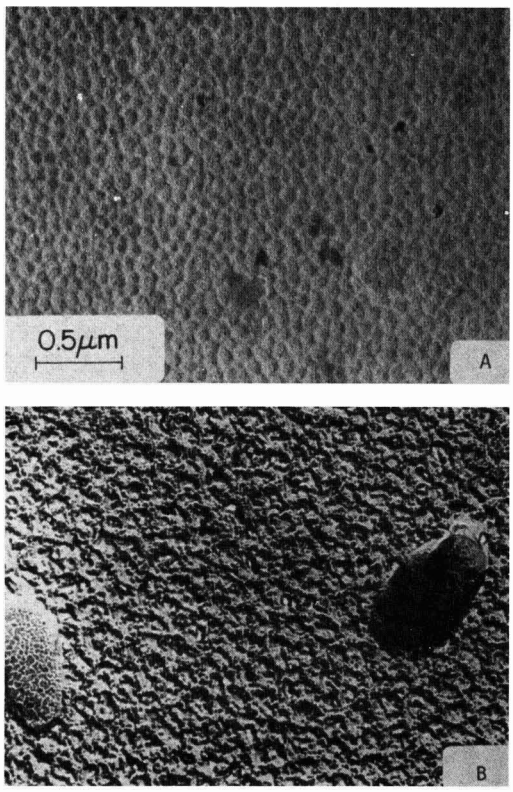

Fig. 13. Surface replicas of a-c anodic films formed on Al 1100-H-14 alloy showing film surface structure and sites of intermetallic particles in film surface. A, a-c film formed in 170 g/l sulfuric acid at temperature of 15°C at constant potential of 23V for 30 min, reaching thickness of 9.5 μm. B, a-c film formed in 90 g/l oxalic acid at temperature of 25°C, at constant voltage of 75V, for 60 min, reaching thickness of 20.5 μm.

film/electrolyte interface, primarily by various chemical dissolution processes. The film surface structure appearing in Fig. 12A was composed of cells up to 30 nm in size; it was not affected by the presence of intermetallic particles in the film surface.

Figure 12B shows for an a-c film formed in oxalic acid the embedment of elongated second-phase particles 0.5 μm in size in the film surface. These particles appeared as gray sites surrounded by dark rims. The surface of the film produced in oxalic acid appeared to be much rougher compared with the sulfuric acid film (Fig. 12A).

Surface replicas of a-c anodic films formed on Al 1100-H14 are shown in Fig. 13. Figure 13A shows a film surface structure in sulfuric acid which was composed of cells up to 60 nm in size, similar to a-c film formed on 2024-T3 in sulfuric acid (Fig. 12A). Figure 13B illustrates the anodic film surface structure obtained in oxalic acid. A rougher film surface was obtained in oxalic acid, probably due to excessive dissolution during film growth. In the area shown in Fig. 13B, two elongated intermetallic particles are observed protruding from the film surface. These surface replica observations of a-c film provide direct evidence of intermetallic particles being embedded in the film surface.

The overall view given by film observations is that intermetallic constituents in the size range of 0.5-10 μm which react either faster (copper-rich particles) or slower (iron-rich particles) than the aluminum alloy matrix were entrapped in the a-c thick porous films during their formation. Unlike d-c films, where particles, especially fast reacting ones, substantially affected film structure and morphology (2, 5, 6), no major modifications or changes were observed in a-c films.

Embedment of intermetallics and a-c film growth.—The mode of film formation and the entrapment of second-phase intermetallic constituents in the growing film under alternating voltage is illustrated schematically in Fig. 14. The interpretation in the present work of the processes taking place in the course of anodizing is based on previous studies of d-c porous film growth on aluminum alloys containing intermetallic particles (1-6).

Intermetallic constituents equally or less reactive than the matrix.—Under a-c anodizing conditions, film growth takes place during the positive half-cycle (Fig. 14A). The anodic film is assumed to grow uniformly on the surface free of particles, while the iron-

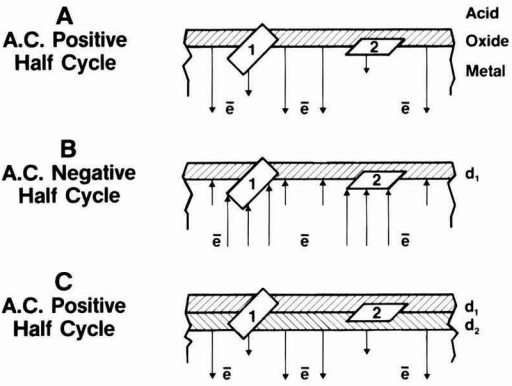

Fig. 14. Schematic of a-c film growth and the embedment of second-phase microconstituents during film growth.

rich particles remain almost inert (1, 2). The corresponding current densities are illustrated by arrows designating the electronic current in the metal. It might be noted that initially particle 1 was partly exposed to the solution and particle 2 resided underneath the metal surface. The metal surface above particle 2 was anodized, and film grew continuously in a normal growth of porous films, that is, through the barrier layer at the pore bases (see Fig. 10). At the end of the positive half-cycle, both particles were surrounded by oxide film.

During the negative half-cycle of the alternating voltage, the normal growth of porous anodic film came to a stop and cathodic reactions took place, such as hydrogen evolution and/or cathodic deposition (12, 13). The presence of inert or equally reactive intermetallic particles led to high cathodic current densities around them, compared with the already filmed particle-free surfaces, as shown in Fig. 14B.

Type 1 particles were highly conductive and therefore drew higher cathodic current, either because they remained inert, passive, and nonfilmed (Al_3Fe in H_2SO_4) or because thin highly conductive oxide film was formed on their surface (Al_3Fe in $H_2C_2O_4$). An anodic film formed on an iron-rich particle contained a high concentration of iron (4, 6), which made the film highly conductive electronically. The evolution of hydrogen at the particle/acid interface led to destruction or removal of the oxide on the particle surface (13), exposing the bare surface to the solution, which again drew a high cathodic current (Fig. 14B).

Type 2 particles served as local sites for high current density during the negative half-cycle. These particles were originally below the alloy surface, so that the oxide above them was the normal porous film. Most probably the main cathodic reaction that occurred above the particle site was the reduction of hydrogen ions, leading to formation of hydrogen gas (12, 13). The evolution of hydrogen gas, probably formed at pore base, could introduce cracks or peeling of fragments of the film, leading to a decrease in film local resistance and a subsequent increase in local cathodic current density. Furthermore, during the negative half-cycle, the intermetallics serving as local sites for conducting most of the current resulted in cathodic reactions. The already formed anodic porous film at particle-free alloy surfaces remained unchanged.

The system was then subjected to positive half-cycle of the alternating voltage (Fig. 14C). At this stage, anodic film grew to a thickness of d_2 in addition to film thickness d_1 which had been formed previously. The ionic current density in the anodic film and the corresponding electronic current density in the alloy were very small at particle sites compared with uniform high current density at the particle-free zones. Type 2 particle showed relatively small current density; however, it became surrounded with anodic film, leading to disconnecting electrically from the matrix alloy (4) and consequently to its embedment in the growing film. Complete entrapment of iron-rich particles in the course of a-c anodizing was illustrated in Fig. 7 and 8. Type 1 particle showed very low current density compared with the adjacent areas. This current was probably consumed in repairing the damaged film on the particle surface caused by cathodic reactions during the previous negative half-cycle alternating voltage. At this stage, type 1 particle became almost embedded in the film. Evidence can be seen in Fig. 13B, where two particles of type 1 are protruding from the surface.

Intermetallic constituents more reactive than the matrix.—The mode of a-c film formation on aluminum alloy containing constituents such as copper or magnesium-rich particles which reacted faster than the matrix (2, 5, 6) is illustrated schematically in Fig. 14.

At the start, processes occurring during the positive half-cycle (Fig. 14A) were composed of normal porous film growth together with oxidation and subsequent dissolution of the copper-rich particle (5, 6). Type 1 particle probably underwent oxidation-dissolution processes at the surface exposed to the electrolyte, while particle type 2, which initially was underneath the substrate surface, was not affected. The local current density at the particle 2 site was lower, as suggested previously (2). Film growth during the positive half-cycle was considered very similar to normal d-c film growth on aluminum-copper alloys resulting in dissolution of copper ions (2), yet still retaining low concentrations of copper in the anodic film (2, 5) above the matrix but not above second-phase particle (6) of type 2.

During the negative half-cycle of the alternating voltage, anodizing film growth was essentially stopped and cathodic reactions took place. It was assumed that the local cathodic high current densities were at particle sites. These reactions were probably the formation and evolution of hydrogen gas leading to an increase in the *p*H film/electrolyte (12, 14); and cathodic deposition of dissolved copper ions from the electrolyte, particularly at the particle/electrolyte interface (15).

As a result of these reactions, the particle surface (type 1 in Fig. 14A) probably became coated with copper. Upon applying the next positive half-cycle voltage (Fig. 14C), the coatings that had been electrodeposited on particle surface sites would have to dissolve directly or be oxidized and then dissolved. At the same time, film growth took place at particle free zones, reaching a total thickness of $d_2 + d_1$. At the end of this stage of film growth, particle 2 would be electrically disconnected from the matrix and particle 1 would be almost embedded before suffering further dissolution, which might change its dimensions substantially. The embedment of copper-rich particles in the growing film without major change in their original dimensions was found in this study, as shown in Fig. 5 and 6 (for particles of several micrometers in size) and in Fig. 9 and 12 (for particles up to 1 μm in size).

Conclusions

The contribution of this study was to show the formation of a-c anodic thick films on commercial aluminum and aluminum-copper alloys with special attention to the microconstituent effects. The formation of these films involved the flowing of anodic currents, mainly through the porous anodic film on the matrix, and of cathodic currents through the particles. Nonreactive particles were not damaged by the cathodic current, while reactive particles that had suffered some dissolution during the anodic cycle were covered with an electrodeposit of copper during the cath-

odic cycle and suffered little or no corrosion of the remaining part of the particle during the following anodic cycle. Thus, in a-c anodizing, as opposed to d-c anodizing, even reactive particles were "protected" for the few cycles necessary for them to be electrically isolated from the matrix around them and embedded in the anodic film.

Acknowledgments

The authors are grateful to Dr. G. C. Wood and Dr. R. C. Furneaux for performing the ultramicrotome anodic film sections and for their observations of the sections in the TEM at the University of Manchester, Institute of Science and Technology (UMIST), Manchester M60 12D, England.

Manuscript submitted May 13, 1981; revised manuscript received Nov. 30, 1981. This was Paper 31 presented at the Minneapolis, Minnesota, Meeting of the Society, May 10-15, 1981.

Any discussion of this paper will appear in a Discussion Section to be published in the June 1983 JOURNAL. All discussions for the June 1983 Discussion Section should be submitted by Feb. 1, 1983.

Publication costs of this article were assisted by IBM Corporation.

REFERENCES

1. J. Zahavi, A. Zangvil, and M. Metzger, *This Journal*, **125**, 438 (1978).
2. G. C. Wood and A. J. Brock, *Trans. Inst. Met. Finish.*, **44**, 189 (1966).
3. R. C. Spooner, *Plating*, **53**, 451 (1966).
4. J. Cote, E. E. Howlett, M. J. Wheeler, and H. J. Lamb, *ibid.*, **56**, 386 (1969).
5. J. Cote, E. E. Howlett, and H. J. Lamb, *ibid.*, **57**, 484 (1970).
6. R. D. Guminski, P. G. Sheasby, and H. J. Lamb, *Trans. Inst. Met. Finish.*, **46**, 44 (1968).
7. R. C. Furneaux, G. E. Thompson, and G. C. Wood, *Corros. Sci.*, **18**, 853 (1978).
8. T. P. Hoar and J. Yahalom, *This Journal*, **110**, 614 (1963).
9. A. Munitz, A. Zangvil, and M. Metzger, *Metall. Trans. A.*, **11**, 1863 (1980).
10. G. C. Wood and J. P. O'Sullivan, *Electrochim. Acta*, **15**, 1865 (1970).
11. F. Sacchi and Paolini, *Trans. Inst. Met. Finish.*, **40**, 229 (1963).
12. G. E. Thompson and G. C. Wood, *Corros. Sci.*, **18**, 721 (1978).
13. K. Nişancioğlu, K. Y. Davanger, O. Strandmyr, and H. Holtan, *This Journal*, **128**, 7, 1523 (1981).
14. C. K. Dyer and R. S. Alwitt, *ibid.*, **128**, 300 (1981).
15. D. A. L. Sicklen and D. R. Gabe, *Surf. Technol.*, **7**, 353 (1978).

Diffusion of Gold in Silicon

M. Hill,[1] M. Lietz, and R. Sittig

Brown Boveri Research Center, Baden, Switzerland

ABSTRACT

The spreading resistance technique has been used to measure the degree of resistivity compensation in NTD-Si samples following Au diffusion under many different conditions. From the theoretical curves of Thurber and Bullis (1) these can be converted to substitutional Au concentration distributions, C_s. Several new effects have been found, all of which can be interpreted using the "kick-out" mechanism, whereby Au atoms enter substitutional sites by removing an Si atom that becomes a self-interstitial, I. The Au diffusion process is then controlled entirely by the local concentration, C_I, and out-diffusion of these self-interstitials. Detailed analyses and numerical solutions of the diffusion equations are given, and the experimental results can all be fitted, for instance, at 845°C using an Si self-interstitial diffusion constant $D_I \geq 3 \times 10^{-7}$ cm^2 sec^{-1}. The time dependence of C_s is also explained. For the first time, direct evidence for the very rapid diffusion of interstitial gold, Au_i, is presented. It is shown that $D_i \geq 10^{-5}$ cm^2 sec^{-1} and that the equilibrium concentration of Au_i is probably greater than or equal to the equilibrium concentration of substitutional atoms, Au_s. The effect of swirl defects on Au diffusion is also demonstrated and explained.

A well-defined control of the charge carrier lifetime represents a major problem during the production of high voltage silicon power devices. Due to its well-suited combination of characteristics, gold is the preferred recombination center, particularly for thyristors. Therefore the properties of the gold centers and the diffusion of gold in silicon have been investigated many times over the last twenty years (2-4).

In spite of all these results, it is still not possible during production to obtain reproducible gold concentrations from batch to batch even when using identical gold diffusion conditions.

Thus on investigating gold diffusion one has to be aware of some influence of the pretreatment of the silicon wafers, of the surface preparation technique, or the interaction of gold with other impurities. The gettering of gold by a highly doped phosphorus profile is well known (5-7) and the interaction with carbon atoms has been reported (8).

In this paper we report on extensive experiments on gold diffusion. Dislocation-free silicon with controlled low carbon content was carefully annealed before it was used during these investigations. The influence of a high temperature process before gold diffusion is demonstrated.

Most important for these experiments is the evaluation of gold content from measuring its compensating effect on the resistivity of the starting material. This technique has proven especially powerful when applied to neutron transmutation doped silicon, which exhibits an absolutely homogeneous doping concentration (9). By these means, we can determine the gold concentration with high spatial resolution and accuracy. Several details of gold profiles are shown, which could not be observed in earlier experiments. These features provide important information for detailed analysis of the diffusion process.

Up to now it has generally been assumed that gold diffusion is controlled by the Frank-Turnbull mechanism (10). In recent papers (11, 12), however, it has been demonstrated that some characteristics are more easily explained using the so-called "kick-out" mechanism. Our results seem to clearly support this model.

Experimental

All work was carried out on float zone silicon slices from crystals having carbon concentrations of less than 3×10^{16} cm^{-3}. All n-type samples with starting

[1] Present address: Mullard, Hazel Grove, Stockport, England.

Key words: gold, diffusion, silicon.

resistivity greater than 30 Ωcm were produced by neutron transmutation doping so that no striations were visible using spreading resistance.

The initial silicon slices were 1200 μm thick. These were cleaned in organic solvents, then at least 50 μm were chemically polished from each side, to leave damage-free surfaces. The slices were then subjected to a high temperature process (anneal or B-diffusion) at a temperature of at least 1150°C for at least 2 hr and subsequently cooled at 1°C per min. The reasons for this will be discussed later. The slices were then given another short chemical polish to clean the surfaces followed immediately by evaporation of 500Å thick gold layers on both sides unless stated otherwise. The gold diffusion was carried out in air, usually for 5 hr with a cooling rate of 3°C per min.

After diffusion the resistivity of the samples was determined using spreading resistance. Conventional polished bevels through the slices were used to obtain the variation of resistivity with depth. In slices that had been evaporated with a masked pattern of gold, the lateral resistivity variations were plotted by lapping and polishing away half of the sample thickness and making spreading resistance measurements parallel to the surfaces.

In this way the change in resistivity compared to control samples, which had only been subjected to the same high temperature process, was obtained. The resistivity changes were then converted into gold concentrations using the calculated results of Ref. (1). The absolute precision of gold concentrations determined in this way is influenced by (*i*) changes in resistivity in very high resistivity samples (> 500 Ωcm), which are sometimes found after annealing only; (*ii*) uncertainties in spreading resistance values above about 5×10^7 Ω; and (*iii*) the very small resistivity compensation when the gold concentration is less than 0.2 times the background doping. The considerable advantage of this method over determination of gold concentration by activation analysis lies in the repeatability of the measurements and particularly the spatial resolution. Resistivity compensation is assumed to measure only the substitutional gold concentration.

Many samples were examined by x-ray topography before and after gold diffusion. In no case were more than 50 dislocations found and the majority of samples were completely free of dislocations.

Results

Extreme examples of depth profiles.—Some examples showing types of spreading resistance profiles that can be obtained are given in Fig. 1. All three samples were gold diffused at 1010°C for 5 hr.

Sample (a) is FZ silicon containing resistivity striations in the range 6.4-9.0 Ωcm. The phosphorus concentration has been considerably compensated by the diffused-in gold, but the sample has remained n-type throughout. We find here that the gold concentration decreases continuously from surface to center of the slice, which is not in agreement with other authors (3, 13-15). The gold concentrations are estimated to be $N_{Au}(0) = 14 \times 10^{14}$ cm^{-3} at the surface and N_{Au} (500 μm) $= 7.3 \times 10^{14}$ cm^{-3} at the center of the slice.

Sample (b) was initially 80 Ωcm NTD silicon. At the surfaces, the initial resistivity has been overcompensated and converted to p-type. At a depth of 140 μm the resistance reaches a maximum and at greater depths the silicon is still n-type. From Ref. (1) the gold concentration at the resistivity maximum is N_{Au} (140 μm) $= 22 \times 10^{14}$ cm^{-3} and the resistivity is 3×10^5 Ωcm. However, the measurements show a resistivity of 3×10^4 Ωcm. This rather large discrepancy is probably due to the poor reproducibility and nonlinearity of the spreading resistance equipment at these very high resistances.

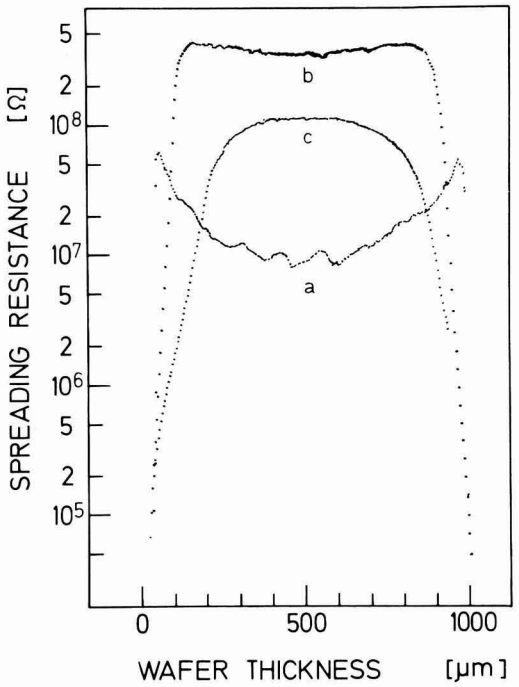

Fig. 1. Spreading resistance measurements perpendicular through three silicon slices, which were all gold diffused for 5 hr at a temperature of 1010°C. The starting resistivity was (a) 6.4-9.0 Ωcm FZ-Si, (b) 80 Ωcm NTD-Si, (c) 330 Ωcm NTD-Si.

Curve (c) was obtained after diffusion into 330 Ωcm starting silicon. The whole sample has been converted into p-type and the curvature is reversed compared to curve (a). It is thus clear that, regardless of the measured values of spreading resistance, the gold concentration throughout the whole sample must be greater than 6×10^{14} cm^{-3}.

Temperature dependence.—In all samples of approximately 1 mm thickness, the gold concentration at the surface is 2-3 times higher than in the center. The gold concentration in the centers of the slices after 5 hr of gold diffusion at temperatures between 810° and 1010°C are shown in Fig. 2. Each point represents an average value calculated from the results on slices from at least 10 different starting crystals. Maximum variations of ± 50% from the average value were found.

Single-sided gold diffusion.—A 330 Ωm n-type silicon slice was cut in half and one piece was gold evaporated on both sides, the other piece on one side only. Both pieces were simultaneously diffused for 5 hr at 825°C. Figure 3 shows spreading resistance measurements (a) on the piece with gold on both surfaces and (b) on the piece with gold on the surface at 0 μm but no gold on the surface at 1100 μm.

Whereas the gold concentrations for (a) and (b) are identical at 0 μm, the gold concentration near the back nonevaporated surface of sample (b) is considerably greater than that of the piece having both surfaces gold evaporated. At a depth of 800-900 μm the difference in gold concentration for samples (a) and (b) is ~ 30% while at 500 μm the difference is ~ 10%.

Double-sided, masked gold evaporation.—Figure 4 shows the lateral spreading resistance variation at a

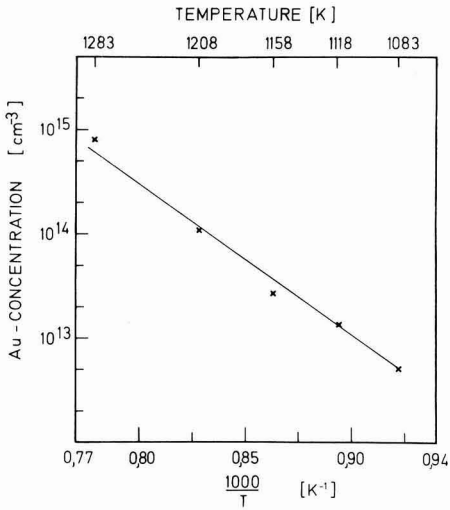

Fig. 2. Temperature-dependence of the gold concentration in the center of a 1 mm thick slice after a diffusion time of 5 hr.

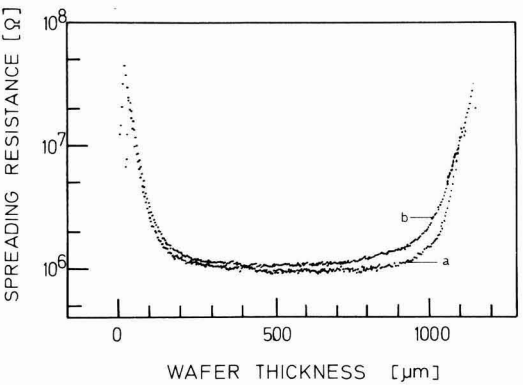

Fig. 3. Spreading resistance measurements after 5 hr of gold diffusion at 825°C, (a) with gold evaporated on both surfaces, (b) with gold on the left-hand surface, 0 μm.

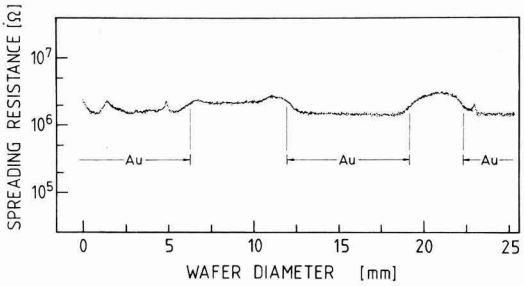

Fig. 4. Spreading resistance measurements parallel to the surfaces but at the center of the slice. Gold had been evaporated on both surfaces at the "Au" marked areas only. The gold concentration is lower in regions with gold-covered surfaces.

depth of 500 μm in a 1 mm thick gold diffused slice on which carefully matched stripes of gold had been evaporated onto both surfaces. As in Fig. 3, a markedly higher gold content is found below areas that had not been gold evaporated. The sharp spikes are due to the effect of carbon striations in the silicon (8).

A clearer picture of what is occurring here is obtained by studying a single boundary between double-sided gold evaporation and double sided bare silicon. Figure 5 shows the spreading resistance variation for this case again measured parallel to the surfaces in the center of the slice and perpendicular to the boundary between gold evaporated and not evaporated regions. The expected constant gold concentration is found under the gold-covered surfaces. Approaching the boundary, the gold concentration increases, goes through a maximum just outside the gold-covered region, and then decreases with a decay length of about 9 mm until the gold concentration is below the detection limit for the starting resistivity.

Influence of boron, aluminum, and phosphorus diffusion profiles.—In samples, into which boron or aluminum profiles had been diffused before the gold diffusion, no difference could be found compared with gold diffusion into samples which had only been annealed. On the other hand, it is known that phosphorus-diffused layers retard gold diffusion (5). In order to study this effect, phosphorus was diffused for 14 hr at 1000°C into 75 Ωcm n-type silicon. The slice was then halved into parts (a) and (b) and from part (a) 10 μm was chemically polished off both surfaces to remove completely the phosphorus-diffused region. Part (b) was cleaned only in perchloric acid. Both parts were then gold evaporated and diffused at 845°C. Figure 6 shows the spreading resistance measurements on both parts. In part (b) there is a maximum in the gold concentration at a depth of 42 μm, which is more than 30 μm

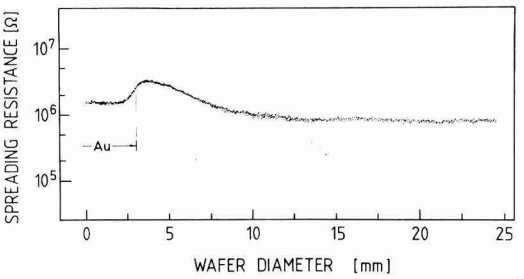

Fig. 5. Lateral spreading resistance variation measured at the center of a slice in a direction perpendicular to the edge of the gold cover, which was on both surfaces at the marked area only.

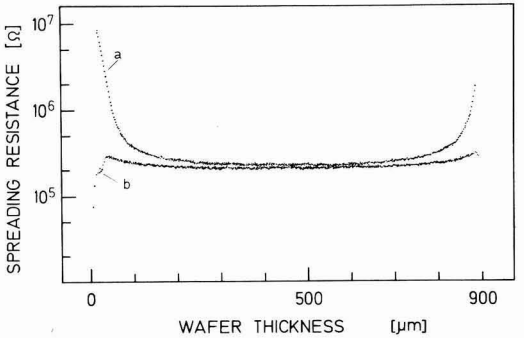

Fig. 6. Spreading resistance measurements vs. wafer depth of a previously phosphorus-diffused slice. (a) 10 μm of silicon containing the phosphorus profile polished off from both sides before gold evaporation, (b) containing the phosphorus profile at the surface during Au diffusion.

deeper than the phosphorus profile. The gold concentration at the center of the slice is only 30% of that in part (a).

Gold diffusion in nonannealed silicon.—Figure 7 shows spreading resistance measurements on a slice that had no previous high temperature treatment before the gold diffusion. The silicon had been neutron transmutation doped followed by a few minutes annealing at about 750°C. The resistivity was then 103 Ωcm. The slice was as usual gold evaporated on both surfaces, then divided into three parts, and diffused at 845°C. Curve (a) shows the spreading resistance variations after a diffusion time of 2 hr, (curve b) after 11 hr, and curve (c) after 26 hr. The incorporation of gold in the silicon lattice shows the following surprising properties: (*i*) the gold distribution follows a "striated" pattern; (*ii*) the amplitude decreases with increasing diffusion time; and (*iii*) decrease of the mean gold concentration in the center of the slice while simultaneously the in-diffusion profile becomes more pronounced near the surfaces with increasing diffusion time.

Analysis of the experimental results.—The experimental results exhibit some striking features, which directly give some information regardless of any theoretical model:

1. In our experiments all "normally" (a) diffused samples exhibit a slight but continuous variation of gold content throughout the slice thickness, showing that it is governed by a diffusion process. Even at the center we find a clear curvature (b) rather than a constant plateau as reported in Ref. (3), (13), and (15). The surface concentration, however, is only about a factor of 2-3 higher than the minimum in the middle of the slice.

2. Even near the surfaces the gold concentration curve does not resemble a complementary error function. This is in contrast to the evaluation of Wilcox and La Chapelle (2).

3. The surface concentration at a gold-covered surface must not be assumed to be the equilibrium concentration during the whole diffusion process. This becomes obvious from Fig. 3 where the gold content is higher at the bare surface. Therefore the generally assumed boundary condition, that the concentration reaches its equilibrium value at the surface covered with the corresponding impurity atoms, is not valid in this case (c).

4. From Fig. 3 it follows further that it is not the diffusion of gold atoms that determines the gold distribution during the "normal" (a) diffusion experiments. If this were the case, then the concentration could not be highest at the bare surfaces.

5. If it is not the gold source that causes the asymmetry of the distribution in Fig. 3, then the asymmetry

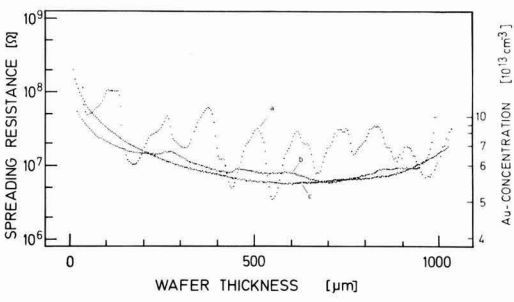

Fig. 7. Spreading resistance and Au concentration *vs.* wafer depth at a specimen without high temperature treatment before gold diffusion at 845°C for (a) 2 hr, (b) 11 hr, and (c) 26 hr diffusion time.

can only be due to another surface property, which differs for gold-covered and bare surfaces. One has to assume that some reaction takes place at or near the surface and influences the incorporation of gold atoms. This is in agreement with Fig. 5, where a maximum of the gold concentration is reached near the boundary between a gold-covered and a bare surface.

6. In the experiment used to obtain Fig. 5, however, the geometry is considerably changed. Both the gold-covered and the bare part of the slice represent areas with differing, but in each region constant, boundary conditions. The decrease of the gold content in the direction away from the gold source, therefore, has to be attributed to the fast diffusion of gold atoms.

7. The measurements shown in Fig. 7 demonstrate that an irregular behavior may occur for unannealed silicon. After 2 hr of diffusion the gold concentration reaches locally higher values than anywhere in an annealed slice after 5 hr of diffusion. This seems to support both observations 3 and 4.

a. Gold evaporated onto both surfaces; diffusion time 5 hr at temperatures in the range 800°-1000°C.

b. This can be seen directly in the spreading resistance curve of Fig. 7c, but in Fig. 6, for example, it is distorted by the nonlinearity of the relation between resistivity and gold concentration.

c. Due to experimental limitations we could not analyze the gold content within the first 3 μm from the surfaces. Thus we have to exclude this layer from the above statement. Possibly a diffusion of gold substitutional atoms could be occurring, starting from its equilibrium concentration at the very surface.

Theory and Interpretation

Since the paper of Dash (16) it is generally assumed that the diffusion of gold in silicon takes place via the Frank-Turnbull mechanism (10). Gold atoms diffuse very fast via interstitial lattice sites, Au_i, and then can occupy the place of a vacancy, V, according to the reaction

$$Au_i + V \rightleftarrows Au_s \qquad [1]$$

Only the gold atoms on substitutional lattice sites, Au_s, are electrically active and can be detected by spreading resistance measurements.

The interpretation of experimental results by this mechanism lead to the following statements: (*i*) Au_i—diffusion is very fast; (*ii*) Au_s—diffusion is very slow and may be neglected; (*iii*) vacancy sources have to be assumed inside the bulk material (14). These vacancy sources, however, could not be explained satisfactorily. In a recent paper (12) Gösele *et al.* have shown that the vacancy mechanism cannot explain the experimental results. Instead they have proposed a mechanism via silicon self-interstitials, I, and have shown that this can explain the correct time dependence of the gold concentration. In this mechanism gold atoms reach a substitutional site according to the "kick-out" reaction

$$Au_i \rightleftarrows Au_s + I \qquad [2]$$

This model assumes reactions that are nearly reciprocal to the vacancy mechanism: instead of vacancy indiffusion and vacancy sources in the bulk, now the gold concentration is controlled by self-interstitial out-diffusion or self-interstitial sinks in the bulk material. There is a difference, however. The I concentration can be several orders of magnitude larger than its equilibrium value, whereas the vacancy concentration can only be reduced to zero. Therefore differences of the diffusion process can be expected, which enable the two models to be distinguished.

Basic equations.—Our analysis is based on the self-interstitial mechanism. To use as few parameters as possible, no internal I-sinks are assumed for all the

pre-annealed samples. We then arrive at the following set of nonlinear partial differential equations

$$\frac{\partial C_s}{\partial t} = \frac{1}{\tau}(C_i - kC_sC_I) \quad [3]$$

$$\frac{\partial C_I}{\partial t} = \frac{1}{\tau}(C_i - kC_sC_I) + D_I\nabla^2 C_I \quad [4]$$

$$\frac{\partial C_i}{\partial t} = -\frac{1}{\tau}(C_i - kC_sC_I) + D_i\nabla^2 C_i \quad [5]$$

C_n denotes the concentrations of substitutional gold atoms, Au_s, for n = s; of self-interstitials, I, for n = I; and of interstitial gold atoms, Au_i, for n = i.

D_n denotes the corresponding diffusion coefficients. D_s is neglected in Eq. [3] since it is several orders of magnitude smaller than D_I or D_i. τ is the kick-out reaction time constant, and k is the constant of the law of mass action of reaction [2], which may be written as

$$k = \frac{C_i^{eq}}{C_s^{eq}C_I^{eq}} \quad [6]$$

The C_n^{eq} denote the corresponding equilibrium concentrations.

From experimental observation (feature 5) it follows that a fourth equation has to be introduced to describe the kinetic process of the self-interstitials leaving the crystal at the surface. From the continuity of the I-flux it follows at the surface

$$D_I\frac{\partial C_I}{\partial x} = \pm v_n(C_I - C_I^{eq}) \quad [7]$$

x denotes the coordinate perpendicular through the slice. The constant, v_n, has the dimension of a velocity and from (feature 5) it follows that it is different for gold-covered, ($v_n = v_g$), and for bare surfaces ($v_n = v_b$).

"Normal" diffusion perpendicular to Au-covered surfaces.—According to (features 1, 4, and 5) the I-diffusion and the surface reaction are the limiting processes in this case. The Au_i-diffusion and the kick-out mechanism may be treated as fast in comparison. Thus in a first phase these processes take place until the equilibrium concentration

$$C_i \cong C_i^{eq} \quad [8]$$

is approximately reached throughout the whole slice. The equilibrium of the kick-out reaction

$$\frac{C_s}{C_s^{eq}} \cdot \frac{C_I}{C_I^{eq}} \cong \frac{C_i}{C_i^{eq}} \quad [9]$$

is always nearly fulfilled and it follows that

$$C_sC_I \cong C_s^{eq}C_I^{eq} \quad [10]$$

holds in this case.

We define t_1 as the time when this first phase is finished. Since the I-diffusion has been neglected so far, it follows that

$$C_I(t_1) = C_s(t_1) = \sqrt{C_s^{eq} \cdot C_I^{eq}} =: C_1 \quad [11]$$

holds independently of x. Here we have assumed the starting condition $C_s(0) = 0$ and neglected $C_I(0)$, since from $C_s^{eq} >> C_I^{eq}$ it follows that

$$C_I(0) \leqq C_I^{eq} << C_1 \quad [12]$$

Even after a diffusion time of only 5 min at 850°C the gold concentration on the back of a gold-implanted slice of 250 μm thickness is higher than at the center (17). Thus one may estimate t_1 to amount to less than 20 min in our case.

During the second phase the I-out-diffusion has to be considered. Starting at the surfaces, C_I begins to decrease while simultaneously (due to the kick-out reaction) new Au_s and I are being produced. At the center, $x = d/2$, Eq. [11] still holds until at a time t_2 the out-diffusion profile is established throughout the whole slice. An estimate of t_2 will be given below.

The third phase is characterized by a monotonic decrease of C_I and increase of C_s. Equations [3]-[7] now reduce to

$$\frac{\partial C_s}{\partial t} = \frac{C_i^{eq}}{\tau}\frac{1}{C_1^2}(C_1^2 - C_sC_I) \quad [3']$$

$$\frac{\partial C_I}{\partial t} = \frac{\partial C_s}{\partial t} + D_I\frac{\partial^2 C_I}{\partial x^2} \quad [4']$$

$$D_I\frac{\partial C_I}{\partial x} = \pm v_gC_I \quad \text{at} \quad x = 0 \quad \text{and} \quad x = d \quad [7']$$

where we have used [12].

This implies the following

$$C_I(x,t) = A(x) \cdot B(t) \quad [13]$$

with

$$A(x) = a_o\left[1 - a_2\left(x - \frac{d}{2}\right)^2 - a_4\left(x - \frac{d}{2}\right)^4 - \dots\right] \quad [14]$$

and

$$B(t) = (t + t_o)^\alpha + b_1(t + t_o)^{\alpha-1} + \dots \quad [15]$$

Due to the symmetry only even terms of the spatial dependence are taken into account. t_o will be used to fulfill the starting condition $C_I(d/2, t_2) = C_1$.

With [13] one obtains from [4']

$$\frac{\partial C_s}{\partial t} = A \cdot \frac{\partial B}{\partial t} - D_I\frac{\partial^2 A}{\partial x^2} \cdot B \quad [16]$$

which may be time integrated to deliver

$$C_s(x,t) = A \cdot B - D_I\frac{\partial^2 A}{\partial x^2}\int B dt \quad [17]$$

The leading term of C_s is of the same order of time dependence as $\int B dt$ or of a dependence one order higher than C_I. It thus follows that $-1 < \alpha < 0$.

Insertion of [13] and [17] in [3'] yields

$$\frac{\partial C_s}{\partial t} = \frac{C_i^{eq}}{\tau}\frac{1}{C_1^2}C_1^2 - \left[A \cdot B - D_I\frac{\partial^2 A}{\partial x^2}\int B dt\right]AB \quad [18]$$

The term with highest order of time dependence has to cancel the constant inside the waved brackets. Since C_s increases and C_I decreases monotonically it follows that the leading term of $B\int B dt$ is independent of time, which delivers

$$\alpha = -\frac{1}{2} \quad [19]$$

Furthermore the coefficient of this term has to be independent of x and to fulfill the condition

$$C_1^2 = -2D_IA\frac{\partial^2 A}{\partial x^2} \quad [20]$$

For $x = d/2$ one finds

$$a_o = \frac{C_1}{2\sqrt{D_Ia_2}} \quad [21]$$

and for the higher order coefficients

$$a_4 = \frac{1}{6}a_2^2 \quad [22]$$

$$a_6 = \frac{7}{90} a_2^3 \qquad [23]$$

a_2 can be calculated from Eq. [7'], which results in

$$\frac{D_I}{v_g} = \frac{1 - a_2\left(\frac{d}{2}\right)^2 - a_4\left(\frac{d}{2}\right)^4 - \dots}{2a_2\left(\frac{d}{2}\right) + 4a_4\left(\frac{d}{2}\right)^3 + \dots} \qquad [24]$$

Neglecting a_4 and higher order coefficients one obtains

$$a_2 = \left(\frac{d^2}{4} + \frac{D_I}{v_g} d\right)^{-1} \qquad [25]$$

which may be rewritten to define a time t_{Ig} as

$$t_{Ig} = \frac{1}{2D_I a_2} = \frac{d}{2D_I}\left(\frac{d}{4} + \frac{D_I}{v_g}\right) \qquad [26]$$

Thus for the leading term of $C_I(x,t)$ during this third phase we arrive at

$$C_I(x,t) = C_1\left[1 - \frac{\left(x - \frac{d}{2}\right)^2}{2D_I t_{Ig}}\right]\sqrt{\frac{t_{Ig}}{t + (t_{Ig} - t_2)}} \qquad [27]$$

and for the leading term of $C_s(x,t)$ at

$$C_s(x,t) = C_1 \frac{1}{\left[1 - \frac{\left(x - \frac{d}{2}\right)^2}{2D_I t_{Ig}}\right]}\sqrt{\frac{t + (t_{Ig} - t_2)}{t_{Ig}}} \qquad [28]$$

C_s exhibits a $\sqrt{t}$-dependence only when $(t_{Ig} - t_2)$ may be neglected in comparison to t and only as long as the condition $C_I >> C_I^{eq}$ or $C_s << C_s^{eq}$, respectively, is valid.

When these latter inequalities become no longer valid a fourth phase follows, during which all concentrations approach their equilibrium values. A summary of the first three phases of this diffusion process is sketched in Fig. 8.

Although this is only an approximate description, it allows the influence of the different parameters to be determined. Conversion of Fig. 3, curve (a) to gold concentration results exactly in a shape of $C_s(x)$ according to [28], (see also Fig. 11). From the difference of $C_s(o)$ and $C_s(d/2)$ the value of $2D_I t_{Ig}$ can be determined with the relatively high accuracy of about ±30%. Since thickness d is known exactly, we obtain

$$\frac{D_I}{v_g} = (1.2 \pm 0.4) \cdot 10^{-2}\ \text{cm} \qquad [29]$$

Now we can estimate the time t_2. Since Au_s and I are produced simultaneously, the total amount of I which is diffused out of the slice up to time t_2 is given by

$$\int_0^d C_s(x,t_2)\,dx - \int_0^d C_I(x,t_2)\,dx$$

The surface concentration C_I is varying during this period from C_I^{eq} up to about C_1 and down again to about 1/3 C_1. Therefore an average I-current density of about $2 \cdot 2/3\ C_1\ v_g$ is flowing out of both surfaces. As a result we can estimate t_2 from the equation

$$\frac{4}{3} v_g t_2 C_1 = \int_0^d [C_s(x,t_2) - C_I(x,t_2)]\,dx \qquad [30]$$

The evaluation yields

$$t_2 = \frac{3d}{4v_g} \cdot \frac{1}{f}\left\{\frac{1}{2}\ln\left(\frac{1+f}{1-f}\right) - f + \frac{1}{3}f^3\right\} \qquad [31]$$

$$t_2 \cong \frac{4.5 \cdot 10^{-2}\ \text{cm}}{v_g}$$

with

$$f = \left(1 + \frac{4D_I}{dv_g}\right)^{-1/2} \cong 0.82$$

and thus using [26]

$$t_{Ig} - t_2 \cong \frac{0.1\ \text{cm}}{v_g} \qquad [32]$$

To determine a narrower range for D_I and v_g separately, we can now construct Table I for diffusion temperature of 845°C.

The values of D_I are chosen arbitrarily, v_g, $t_I - t_2$, and C_s are then evaluated using [29], [32], and [28], respectively. Taking the experimental value of C_s (d/2, 5 hr) = $1.15 \cdot 10^{13}\ \text{cm}^{-3}$ then C_1 can be determined. From these data it follows, that with $D_I = 10^{-7}\ \text{cm}^2\ \text{sec}^{-1}$ and a diffusion time of 5 hr, C_s would increase only by a factor of 1.3 and no $\sqrt{t}$-dependence of C_s can be observed. $D_I = 3 \cdot 10^{-7}\ \text{cm}^2\ \text{sec}^{-1}$ would result in a C_s-increase by a factor of 2 and a $\sqrt{t}$-dependence is approached after about 2 hr of diffusion, when $t > 2(t_{Ig} - t_2)$ holds. For still larger D_I values, the $\sqrt{t}$-dependence would be more pronounced.

Using the experimentally observed $\sqrt{t}$-dependence (3) of C_s, it thus follows that D_I has to be at least as large as $D_I \geqq 3 \cdot 10^{-7}\ \text{cm}^2\ \text{sec}^{-1}$, $C_1 \leqq 6 \cdot 10^{12}\ \text{cm}^{-3}$ and $C_s^{eq} C_I^{eq} \leqq 3.6 \times 10^{25}\ \text{cm}^{-6}$, all values at a temperature of 845°C.

When Eq. [3]-[7] are solved by a numerical computer program, it turns out that the experimental shape of $C_s(x, 5\ \text{hr})$ can be completely fitted equally well with $D_I = 3 \cdot 10^{-7}\ \text{cm}^2\ \text{sec}^{-1}$ as with $D_I = 10^{-6}\ \text{cm}^2\ \text{sec}^{-1}$ if only the ratio D_I/v_g is kept constant. Fig-

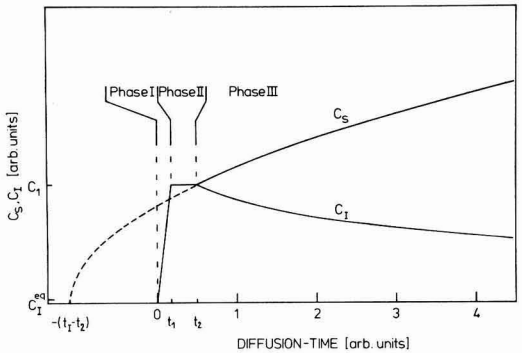

Fig. 8. Schematic sketch of the time dependence of the concentrations of substitutional gold atoms, C_s, and silicon self-interstitials, C_I, at the center of a slice during the first three phases. Both scales are linear.

Table I.

$D_I\left[\frac{\text{cm}^2}{\text{sec}}\right]$	$v_g\left[\frac{\text{cm}}{\text{sec}}\right]$	$(t_{Ig} - t_2)$ [sec]	$C_s\left(\frac{d}{2}, 5\ \text{hr}\right)$	$C_1[\text{cm}^{-3}]$
10^{-7}	$8.3 \cdot 10^{-6}$	$1.2 \cdot 10^{4}$	$1.3 \cdot C_1$	$8.8 \cdot 10^{12}$
$3 \cdot 10^{-7}$	$2.5 \cdot 10^{-5}$	$4.0 \cdot 10^{3}$	$2.0 \cdot C_1$	$5.8 \cdot 10^{12}$
10^{-6}	$8.3 \cdot 10^{-5}$	$1.2 \cdot 10^{3}$	$3.3 \cdot C_1$	$3.5 \cdot 10^{12}$

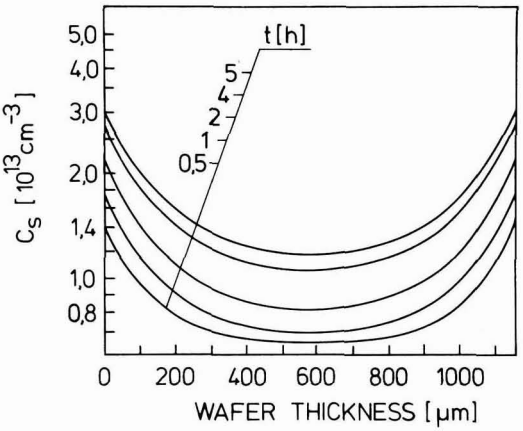

Fig. 9. Calculated Au_s concentrations vs. wafer depth for different diffusion times. The highest curve (5 hr) fits curve (a) of Fig. 3 using $D_I = 3 \cdot 10^{-7}$ cm^2 sec^{-1} in this case.

ure 9 shows $C_s(x)$-curves at different times. The time dependence $C_s(d/2, t)$ and $C_s(0, t)$ for the two cases $D_I = 3 \cdot 10^{-7}$ cm^2 sec^{-1} and $D_I = 10^{-6}$ cm^2 sec^{-1} are shown in Fig. 10.

The experiment with only one gold-covered surface (Fig. 3) can be simulated by taking into account a velocity v_b at the bare surface, which is larger than v_g. From [26] and [29] it follows that even $v_b = \infty$ will decrease t_{Ib} only by about 50%. In the numerical calculation $v_b = 15\ v_g$ has been used. The result is shown in Fig. 11, and agrees well with the experimentally observed curves.

Lateral diffusion.—As was already mentioned in feature 6, the lateral diffusion must be attributed to the fast diffusion of gold atoms. This means that the approximation [8] does not hold. Instead we have to assume a decreasing $C_I(z)$ starting from C_I^{eq} at $z = 0$, at the edge of the gold-covered region, where z denotes the coordinate parallel to the surface.

In the description of the perpendicular diffusion we have shown that during the third and fourth phases of diffusion

$$\frac{\partial C_I}{\partial t} < 0 < \frac{\partial C_s}{\partial t}$$

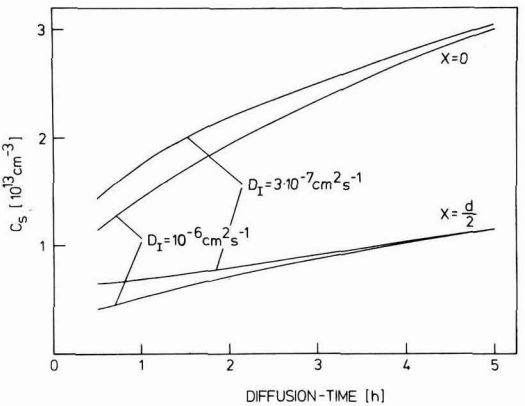

Fig. 10. Calculated Au_s concentrations vs. diffusion time at the surfaces ($x = 0$) and at the center ($x = d/2$) for $D_I = 3 \cdot 10^{-7}$ and $1 \cdot 10^{-6}$ cm^2 sec^{-1}. Both calculations are fitted to the measurements after a diffusion time of 5 hr.

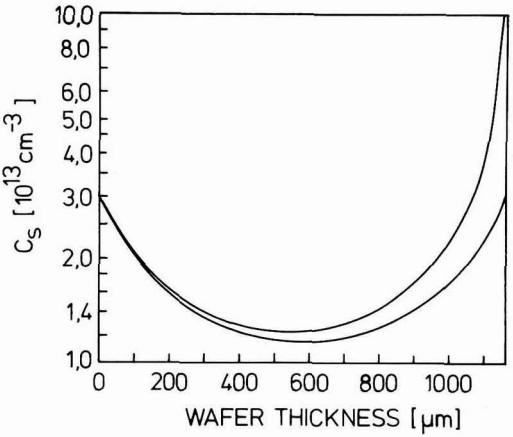

Fig. 11. Calculated Au_s concentrations vs. wafer depth after 5 hr diffusion fitting approximately the measurements of Fig. 3, using $D_I = 3 \cdot 10^{-7}$ cm^2 sec^{-1}. Lower curve: gold on both surfaces, $v_g = 2.2 \cdot 10^{-5}$ cm^2 sec^{-1}; upper curve: gold on left surface only, same v_g but $v_b = 15\ v_g$ on the right surface.

In the present case this inequality will be valid for small z-values by the same reasoning. For larger z-values, on the other hand, the I atoms always have only a constant short distance to the surface while the Au_i-atoms have to diffuse an increasingly long distance to the corresponding z-value. Therefore we may assume

$$\frac{\partial C_I}{\partial t} << \frac{\partial C_s}{\partial t} \text{ independent of } z \qquad [33]$$

Using this inequality the time derivative of [9] yields

$$\frac{C_I}{C_I^{eq}} \frac{1}{C_s^{eq}} \cdot \frac{\partial C_s}{\partial t} = \frac{1}{C_i^{eq}} \frac{\partial C_i}{\partial t} \qquad [34]$$

and transforms Eq. [5] to

$$\frac{\partial C_i}{\partial t} = -\frac{C_s^{eq}}{C_i^{eq}} \frac{C_I^{eq}}{C_I} \frac{\partial C_i}{\partial t} + D_i \frac{\partial^2 C_i}{\partial z^2} \qquad [35]$$

or to

$$\frac{\partial C_i}{\partial t} = D_{eff} \frac{\partial^2 C_i}{\partial z^2}$$

with the effective diffusion coefficient

$$D_{eff} = \frac{D_i}{1 + \dfrac{C_s^{eq} C_I^{eq}}{C_i^{eq} C_I}} \qquad [36]$$

The solution of [35] is

$$C_i(z, t) = C_i^{eq} \operatorname{erfc}\left(\frac{z}{2\sqrt{D_{eff} t}}\right) \qquad [37]$$

The equilibrium [9] of the "kick-out" reaction is nearly fulfilled in the z-direction, too. Therefore the resulting C_s distribution will approximate to

$$C_s = C_I \sqrt{\frac{t + (t_{Ib} - t_2)}{t_{Ib}}} \sqrt{\operatorname{erfc}\left(\frac{z}{2\sqrt{D_{eff} t}}\right)} \qquad [38]$$

for small z-values, where C_I is near to its equilibrium value C_i^{eq}, but

$$C_s = C_s^{eq} \operatorname{erfc}\left(\frac{z}{2\sqrt{D_{eff} t}}\right) \qquad [39]$$

for large z-values, where C_I is only slightly above C_I^{eq}.

We can compare these approximations with the experimental curve (Fig. 5). First one finds from [28] and [38] that the maximum of C_s compared to the value between the Au covered surfaces amounts to

$$\frac{C_s(z=0)}{C_s\left(\frac{d}{2}\right)} \cong \sqrt{\frac{t_{Ig}}{t_{Ib}}} \qquad \cong 1.22 \text{ at maximum} \quad [40]$$

when the leaving velocity v_b is larger than at least 10 times v_g. Experimentally we have observed values between 1.1 and 1.4.

From the slope of the experimental C_s-curve, which decreases from its maximum only by a factor of 3 over a distance of 1 cm, a value of

$$D_{eff} = 1.1 \cdot 10^{-5} \text{ cm}^2 \text{ sec}^{-1}$$

is determined using [38]. An evaluation according to [39] seems less appropriate, since the inaccuracy of the experimental values increases for large z (for small z [39] would lead to $D_{eff}^* = 3 \cdot 10^{-5}$ cm^2 sec^{-1}).

We can again use approximate formulas to gain some insight into the dependence between the unknown values of C_i^{eq} and D_i. The total amount of Au_I that is diffused through the plane at $z = 0$ is either contained in the region $z > 0$ or has become converted to Au_s. Thus

$$D_i \int_0^{t_t} C_i^{eq} \frac{\partial}{\partial z} \operatorname{erfc}\left(\frac{z}{2\sqrt{D_{eff} t}}\right)\Bigg|_{z=0} dt = \int_0^\infty C_i^{eq} \operatorname{erfc}\left(\frac{z}{2\sqrt{D_{eff} t}}\right) dz + \int_0^\infty C_s(z)\, dz \quad [41]$$

Approximating the C_s-curve by an erfc curve with D_{eff}^* (to simplify the integration) and evaluating these integrals leads to

$$1.7 \frac{C_{s\,max}}{C_i^{eq}} \cong \left(\frac{D_i}{D_{eff}} - 1\right) \quad [42]$$

If $C_i^{eq} \geqq C_s^{eq} >> C_{s\,max}$ were true, then it follows that $D_i \cong D_{eff}$. If on the other hand $C_i^{eq} << 1.7\ C_{s\,max}$, then $D_i >> D_{eff}$ must hold. Since D_{eff} is already of the order of 10^{-5} cm^2 sec^{-1} this second condition seems rather unlikely.

Numerical calculations of the lateral case were carried through only in one dimension. Instead of the complete x-dependence, the average values of the concentration were used and at the edge of the gold-covered surfaces a transition region of 1 mm length was introduced. The results that fitted the experimental curve best are shown in Fig. 12. Figure 13 is the corresponding distribution of I. Variation of C_i^{eq} and D_i over a broad range of values confirmed that a C_s-maximum will occur only for $C_i^{eq} > C_s^{eq}$ and $D_i > 10^{-5}$ cm^2 sec^{-1}.

Influence of phosphorus profile.—It is well known that a phosphorus profile acts as a getter layer during Au-diffusion (5-7). Moreover, the "emitter push effect" during a phosphorus diffusion has been widely investigated (18, 19). While previously this has been explained by the generation of vacancies, Strunk *et al.* (20) have shown that it is due to the generation of silicon self-interstitials instead.

This result is supported by our experiments. Let us assume that the diffusing phosphorus atoms act as sources of I near the surface with a constant generation rate. Then, with no gold present, the I atoms will diffuse into the bulk and to the surface. After some time a stationary state will be reached with constant $C_{I_{st}}$ throughout the bulk and a concentration gradient from the source to the surface, which just balances generation and outdiffusion. Now taking gold diffusion

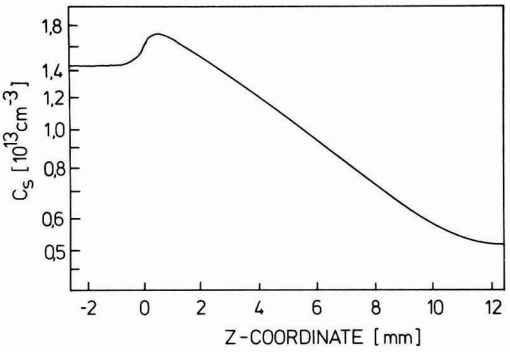

Fig. 12. Calculated lateral Au_s concentration after 5 hr diffusion, fitting the measurements of Fig. 5. During the calculation the average gold content was used and not the concentration at the center of the slice. The fit is obtained using $D_i = 1.6 \cdot 10^{-5}$ cm^2 sec^{-1} and $C_i^{eq} = 2\ C_s^{eq}$.

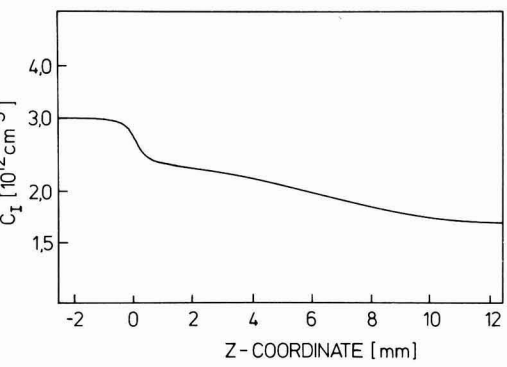

Fig. 13. Calculated lateral interstitial silicon concentration, C_I, corresponding to the C_s distribution of Fig. 12.

into account the same processes take place as described before with the exception that C_I will decrease from C_1 only to $C_{I_{st}}$ and not to C_I^{eq}. C_s will increase only to

$$C_{s_{st}} = \frac{C_1^2}{C_{I_{st}}}$$

correspondingly, even for very long diffusion time, as long as the I-source generation rate stays constant.

The $\sqrt{t}$-dependence of C_s will hold only as long as $C_I >> C_{I_{st}}$ is valid, afterward $C_s(x)$ flattens out and approximates $C_{s_{st}}$, as can be seen in the experimental curve, Fig. 6. In all experimental curves a clear dip in $C_s(x)$ is observed between the phosphorus profile and the C_s maximum. The reason for this is not clear.

Gold distribution in unannealed silicon.—The surprising features of the gold diffusion experiment in previously unannealed silicon (Fig. 7) were mentioned before. These phenomena can be explained consistently on the basis of the previous interpretation. It has been shown that the generation of Au_s is limited when $C_s \cdot C_I = C_1^2$ is reached. From Table I it follows that $C_1 \leqq 6 \cdot 10^{12}$ cm^{-3} whereas in the present case a concentration up to $C_s \cong 10^{14}$ cm^{-3} is reached within less than 2 hr. Therefore, we may conclude, that there are I sinks in the bulk material, which prohibit an increase of C_I and keep it near to C_I^{eq}, so that the gold concentration can approach C_s^{eq}. From the shape of the C_s-curve it becomes obvious that the distribution of I sinks is coupled to the swirl pattern.

The subsequent decrease of the C_s-maxima with increasing diffusion time can be explained on the assumption that the I sinks become saturated. The condition $C_I C_s = C_I^2$ is nearly fulfilled throughout the bulk all the time, but at saturation of the sinks C_I and C_s exhibit strong concentration gradients. Therefore I diffusion takes place toward the C_s maxima, the $C_I C_s$-product exceeds C_I^2 locally causing gold atoms to be kicked out of their substitutional sites and to diffuse as interstitials out of the bulk. One expects that the C_s-maxima are reduced nearly to the C_s-minima level, the shape flattens and then the usual diffusion process continues.

Summary and Discussion

The diffusion properties of gold in silicon have been investigated by a large number of carefully controlled diffusion experiments. The gold content is evaluated from spreading resistance measurements taking into account the compensation of the original resistivity by substitutional gold atoms. This method allows the substitutional gold concentration to be determined with high spatial resolution and good accuracy. This has allowed several new features to be observed. The experimental data are analyzed by a numerical simulation of the diffusion processes at 845°C.

For the first time the fast diffusion of interstitial gold atoms could be directly demonstrated by a lateral diffusion experiment. C_i^{eq} and D_i cannot be determined separately from this experiment, but is was shown that D_i is at least as large as 10^{-5} cm^2 sec^{-1} and that this value is valid only for $C_i^{eq} \geqq C_s^{eq}$. An even larger value for D_i results, if $C_i^{eq} << C_s^{eq}$ is assumed. This last condition was justified in the literature (2) by the fact that the substitutional gold concentration and the total gold concentration determined by activation analysis do agree. There are still uncertainties in this regard. Bullis and Strieter (21) observed a factor of two differences between tracer and resistivity measurements, but later on these results were not clearly reproduced (22). In a recent paper (23), however, it was shown that for the similar case of Co in silicon the concentration of interstitials evaluated at room temperature does not agree with its value at diffusion temperature. As an estimate of the diffusion time for an interstitial gold atom to walk from the center of a slice to the surface when the surface concentration amounts to one-half the center concentration one finds

$$t_d = \frac{d^2}{2D_i}$$

In our case this amounts to about 500 sec when $D_i = 10^{-5}$ cm^2 sec^{-1} is used. This value agrees with the value of t_1 estimated from the results of (17).

The present results support strongly the "kick-out" mechanism as the dominating process for the generation of substitutional gold atoms in the bulk. No further reactions have to be taken into account for previously well annealed silicon. The $C_s(x)$-curve through a slice perpendicular to the surfaces reflects the concentration of silicon self-interstitials diffusing out of the crystal. Again the experimental results do not allow us to determine the diffusion coefficient separately, but a lower limit of $D_I \geqq 3 \cdot 10^{-7}$ cm^2 sec^{-1} at 845°C is evaluated.

It was demonstrated, that there is some reaction which obviously hinders the I outdiffusion at a gold-covered surface. In the present paper this reaction is described by a "leaving velocity" v_g. The ratio D_I/v_g may be evaluated from the experimental curves, but this gives no hint as to the nature of this surface reaction. A slightly different explanation of the surface effect on Au diffusion may be possible.

The influence of phosphorus is discussed in terms of its action as an I source during phosphorus diffusion. The result is a reduced generation of substitutional gold. If one assumes that the diffusion of substitutional gold atoms at the very surface also acts as an I source, then the effect of an Au covered surface might be explained in a similar way as the lower gold concentration in a wafer containing phosphorus profiles.

Acknowledgment

It is a pleasure to thank U. Gösele, W. Frank, and A. Seeger for several discussions about the "kick out" mechanism.

Manuscript submitted April 1, 1981; revised manuscript received Dec. 2, 1981.

Any discussion of this paper will appear in a Discussion Section to be published in the June 1983 JOURNAL. All discussions for the June 1983 Discussion Section should be submitted by Feb. 1, 1983.

Publication costs of this article were assisted by BBC Brown, Boveri and Company, Limited.

REFERENCES

1. W. R. Thurber and W. M. Bullis, *Nat. Bur. Stand. Q. Rep.*, NBS Techn. Note, **743**, 14 (1972).
2. W. R. Wilcox and T. J. La Chapelle, *J. Appl. Phys.*, **35**, 240 (1964).
3. G. J. Sprokel and J. M. Fairfield, *This Journal*, **112**, 200 (1965).
4. W. M. Bullis, *Solid-State Electron.*, **9**, 143 (1966).
5. R. L. Meek, T. E. Seidel, and A. G. Cullis, *This Journal*, **122**, 787 (1975).
6. W. Mielke, *ibid.*, **122**, 965 (1975).
7. W. F. Tseng, T. Koji, J. W. Mayer, and T. E. Seidel, *Appl. Phys. Lett.*, **33**, 442 (1978).
8. M. J. Hill and P. M. Van Iseghem, in "Semiconductor Silicon 1977," H. R. Huff and E. Sirtl, Editors, p. 715, The Electrochemical Society Softbound Proceedings Series, Princeton, NJ (1977).
9. M. J. Hill, P. M. Van Iseghem, and W. Zimmermann, *IEEE Trans. Electron Devices*, **ed-23**, 809 (1976).
10. F. C. Frank and D. Turnbull, *Phys. Rev.*, **104**, 617 (1956).
11. M. J. Hill, M. Lietz, R. Sittig, W. Frank, U. Gösele, and A. Seeger, in "Proc. Int. Conf. on Radiation Physics of Semiconductors and Related Materials," Tbilisi (1979).
12. U. Gösele, W. Frank, and A. Seeger, *Appl. Phys.*, **23**, 361 (1980).
13. J. L. Lambert, *Wiss. Ber. AEG-Telefunken*, **45**, 153 (1972).
14. F. A. Huntley and A. F. W. Willoughby, *This Journal*, **120**, 414 (1973).
15. S. Kästner and J. Hesse, *Phys. Status Solidi A*, **25**, 261 (1979).
16. W. C. Dash, *J. Appl. Phys.*, **31**, 2275 (1960).
17. M. Schulz, A. Goetzberger, I. Fränz, and W. Langheinrich, *Appl. Phys.*, **3**, 275 (1974).
18. C. L. Jones and A. F. W. Willoughby, *This Journal*, **122**, 1531 (1975).
19. A. F. W. Willoughby, *J. Phys. D*, **10**, 455 (1977).
20. H. Strunk, U. Gösele, and B. O. Kolbesen, *Appl. Phys. Lett.*, **34**, 530 (1979).
21. W. M. Bullis and F. J. Strieter, *J. Appl. Phys.*, **39**, 314 (1968).
22. W. R. Thurber and W. M. Bullis, Air Force Cambridge Research Laboratories Report AFCRL-72-0076, Bedford, MA (1972).
23. W. Bergholz and W. Schröter, *Verhandlg. DPG*, (VI) **15**, 175 (1980).

Low Pressure Deposition of Phosphosilicate Glass Films

R. M. Levin and A. C. Adams*

Bell Laboratories, Murray Hill, New Jersey 07974

ABSTRACT

Phosphosilicate glass films have been deposited on silicon substrates by the reaction of tetraethyl orthosilicate (TEOS), phosphine, and oxygen. The depositions are carried out at 630°-700°C in a low pressure CVD reactor. The dependence of the deposition rate, the phosphorus oxide concentration, the thickness uniformity across a wafer, and the depletion in the deposition rate across the deposition zone upon the deposition conditions have been investigated. The step coverage obtained in the reaction is conformal. The refractive index, the etch rate, and the film stress are reported.

Phosphosilicate glass (PSG) films have been widely used in silicon integrated circuits as insulating films between metals and as passivating layers over devices. The PSG films are usually deposited at low temperatures in the range of 350°-450°C (1-4). The step coverage of films deposited at these low temperatures is nonconformal (5). Heat-treatment at ~1100°C is usually used to flow the glass in order to get uniform step coverage (6, 7). This high temperature treatment is not acceptable for very short channel devices where shallow junctions are required. Recently, there have been some reports of the deposition of PSG films in the mid-temperature range (600°-800°C) at reduced pressure, using the decomposition of organosilicon and organophosphorus compounds (5, 8, 9). The results indicate an improved step coverage (5).

In the present work we studied the deposition of phosphosilicate glass using the reaction of tetraethyl orthosilicate (TEOS), phosphine, and oxygen. The investigation is carried out at low pressures (0.1-0.5 Torr) in the temperature range of 630°-700°C. The dependence of the PSG deposition rate, the film composition, and the thickness uniformity on the deposition conditions is reported. The refractive index, the etch rate, and the film stress are also reported.

Experimental

The deposition equipment and the deposition procedure are similar to those recently described (9). Depositions are carried out using a flat temperature profile, ±1°C, over the deposition zone. The wafers are loaded so that axial position No. 1 is placed in the center of the first heating zone of the furnace (50 cm from the inlet end). A dummy wafer is placed in front of this position. The spacing between wafers is ½ in. The results are given for the first wafer (position 1) unless otherwise noted. The chemicals used in the depositions have been obtained from Eastman Kodak Company (TEOS) and Matheson Gas Products Incorporated (PH_3, N_2, and O_2). The phosphine was 99.999% pure. Flow rates of the gases are calibrated using a Brooks mercury sealed piston displacement calibrator. The liquid TEOS is contained in a quartz bubbler, which is maintained at constant temperature (±0.1°C). The amount of material introduced from the bubbler is controlled by the bubbler temperature (5°-50°C). The flow of TEOS vapor are estimated by measuring the flow of nitrogen required to give an identical reactor pressure. This procedure assumes a constant pumping speed for nitrogen and TEOS. The substrates are polished and chemically cleaned, (100) oriented, single crystal silicon wafers of 75 mm diam, boron-doped, with a resistivity of 5-20 Ω-cm.

The thickness and the refractive index of the films are measured by ellipsometry at $\lambda = 0.5461$ μm (10) or by prism coupling using an He-Ne laser at $\lambda = 0.6328$ μm (11). Thickness variations across a wafer are determined by measuring the film thickness at the center and ~8 mm from the edges of the wafer, and are given by the percentage difference between the thickest and thinnest points. The deposition rate is defined as the average of these measurements. Film stress is determined from substrate bending using an optically levered laser beam to measure the difference in the radii of curvature before and after depositiion (and after etching of SiO_2 from the back-side).

The phosphorus oxide concentration in the PSG films is determined from the infrared absorption spectra using the calibration curve given in Fig. 1. Infrared spectra are measured using a double beam infrared recording spectrophotometer (Perkin-Elmer, Model 580). Measurements have been carried out on as-deposited films within 24 hr from the deposition. A typical spectrum is shown in Fig. 2. Four absorption peaks are clearly observed at about 455, 810, 1100, and 1330 cm^{-1}.

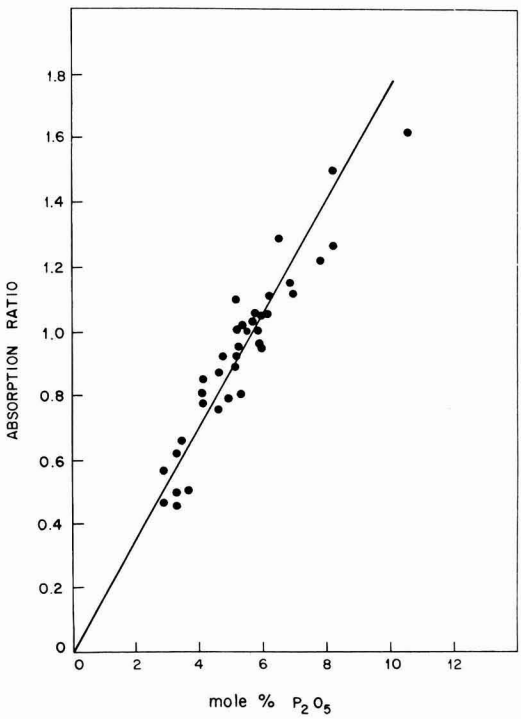

Fig. 1. The dependence of the absorption ratio (defined in Eq. [1]) on the film composition obtained from sheet resistance measurements.

* Electrochemical Society Active Member.

Key words: CVD, dielectrics, integrated circuits, P-glass.

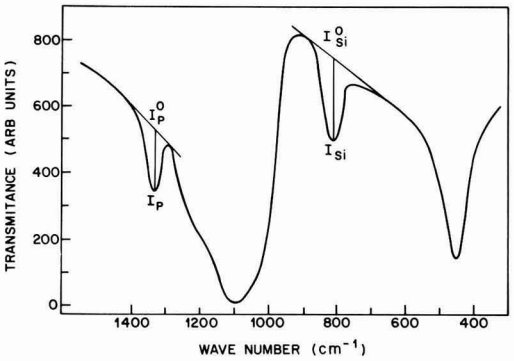

Fig. 2. Infrared absorption spectrum of phosphosilicate glass

The first three peaks result from the Si—O bonds, the last one from the P = 0 bonds. The absorption ratio

$$R = \log(I_P/I_P^\circ)/\log(I_{Si}/I_{Si}^\circ) \qquad [1]$$

is calculated using the absorptions at 810 and 1330 cm^{-1}. The wafers are then annealed at 1100°C for 20 min in N_2. The PSG films are removed by etching in hydrofluoric acid, and the phosphorus concentration is determined from the sheet resistance of the n-type diffused layers using a published calibration curve (12). The results are summarized in Fig. 1, where the absorption ratio R is given as a function of the phosphorus concentration obtained from the resistivity measurements. The composition of a few films was checked using the electron microprobe technique. A reasonable agreement is found between the phosphorus concentration obtained by the two methods.

Experimental Results and Discussions

Deposition of PSG.—The uniformity of the PSG films deposited using a simple oxidation boat is very poor. The variations in the film thickness and in the film composition across a wafer are higher than 30% and ±1.5 mol percent (m/o), respectively, in films containing ~6 m/o P_2O_5. This nonuniformity prevents a systematic study of the deposition parameters. The nonuniformity is attributed to the better reactant gas supply and product removal at the outer part of the wafers where the flow is turbulent (13). This assumption has been verified by depositing PSG films on 75 mm wafers, which are placed between 100 mm wafers. In this arrangement the film uniformity is expected to be improved because the distribution of the reactant molecules (and the removal of products) into each wafer to wafer space is dominated by diffusion. Experimentally, thickness variations of better than ±3% are achieved on the 75 mm wafers in PSG films containing ~6 m/o P_2O_5.

In order to slow the gas flow in the vicinity of the wafers and thus improve the film uniformity, we have used the boat shown in Fig. 3. This quartz boat is composed of two parts. After loading the lower part, the upper part is placed on the wafers. There is a small reduction in the deposition rate in comparison with the previous boat, but the uniformity of the film is improved.

The dependence of the deposition parameters on the deposition conditions, using the boat shown in Fig. 3, is presented in Fig. 4-6. The deposition rate increases sharply with increasing oxygen flow, tends to saturate at an oxygen to phosphine ratio of ~5, reaches a maximum, and then decreases at high oxygen flow rates (Fig. 4a, 5a). The maximum becomes broader when

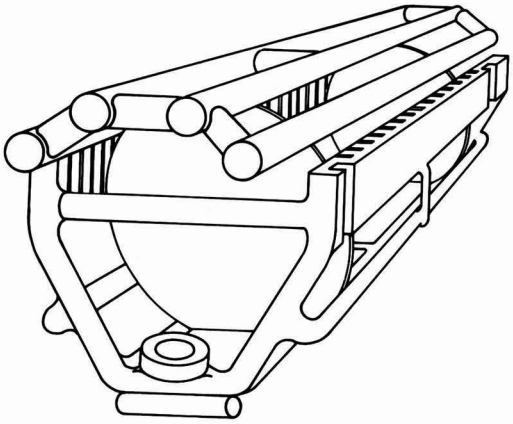

Fig. 3. The sample boat used to obtain the results presented in Fig. 4-7.

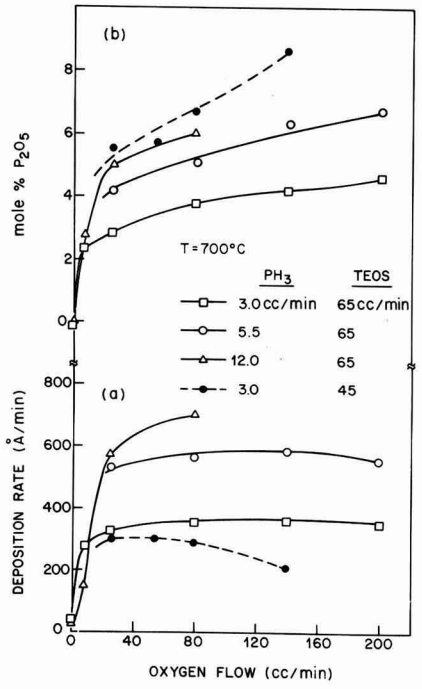

Fig. 4. PSG deposition rate and film composition vs. oxygen flow rate for different PH_3 and TEOS flow rates.

the TEOS flow rate or the temperature are increased. A maximum in the deposition rate also exists for increasing phosphine flow rate (Fig. 6a). In this case the maximum disappears when the TEOS flow rate is increased, although the deposition rate tends to saturate. We are not able to deposit films at higher phosphine flow rates due to the rapid gas phase reactions that exist at high phosphine concentration. In the absence of oxygen the deposition rate decreases with increasing phosphine flow rate (Fig. 6a).

Our results show that the silicon dioxide deposition rate is strongly enhanced in the presence of oxygen and phosphine. Enhancement in the SiO_2 deposition

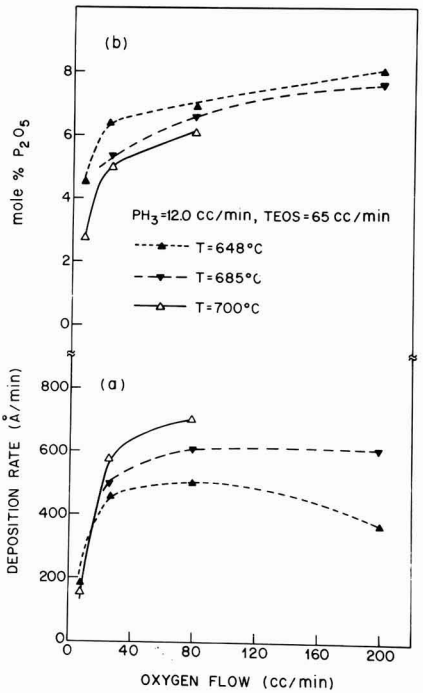

Fig. 5. PSG deposition rate and film composition vs. oxygen flow rate for three reaction temperatures.

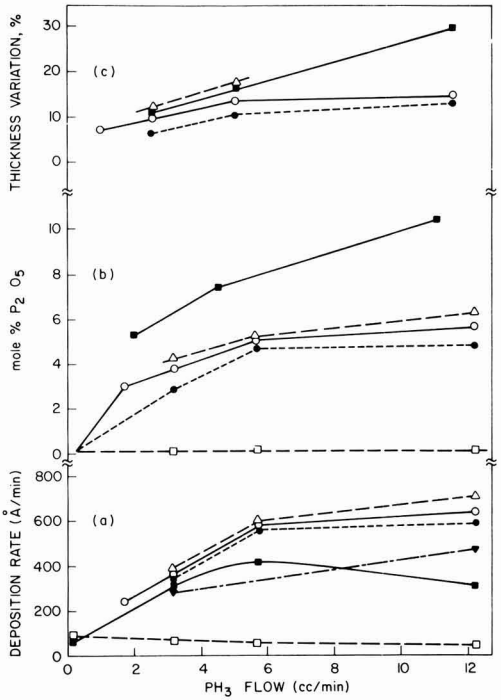

Fig. 6. PSG deposition rate, film composition, and thickness variations across a wafer vs. PH_3 flow rate. The depositions are carried out at T = 700°C (solid triangle, 685°C), using TEOS flow rate of 65 cm³/min (solid square, 45 cm³/min). The oxygen flow rate is: □, 0 cm³/min; ●, 26 cm³/min; ○, 80 cm³/min; △, 140 cm³/min; ■, 55 cm³/min; ▽, 26 cm³/min.

rate in the presence of a phosphorus oxide source has been observed previously in other low pressure depositions where inorganic as well as organic sources for SiO_2 and P_2O_5 were used (5, 8). The increase-maximum-decrease behavior of the deposition rate obtained with increasing oxygen or phosphine flow rates (Fig. 4-6) can be explained by the retardation theory (14). Atmospheric pressure CVD experiments indicate that oxygen behaves as a retardant in the oxygen-hydride reaction (14). As a result a maximum appears in the SiO_2 deposition rate with increasing oxygen flow rate (2, 14-17). The maximum tends to shift toward higher oxygen flow rates and to broaden with increasing hydride flow rate (17) or increasing temperature (2, 15, 16, 18). This dependence of the maximum upon the deposition conditions is very similar to that shown in Fig. 4a, 5a. The retardation behavior of phosphine has also been observed previously (2, 4, 18, 19). This behavior is also shown in Fig. 6a by the decrease in the deposition rate caused by increasing the phosphine flow rate, in the absence of oxygen.

The phosphorus oxide concentration increases with increasing oxygen and phosphine flow rates, and tends to saturate at high flow rates (Fig. 4b, 5b, 6b). It decreases when the TEOS flow rate or the temperature are increased. No P_2O_5 molecules are found in films deposited in the absence of oxygen in the reactant gas (as measured by infrared). However, sheet resistance measurements indicate the existence of ~1 weight percent phosphorus in the films.

The dependence of the thickness variations across a wafer on the deposition conditions is presented in Fig. 6c. The variation in the film thickness increases with increasing oxygen and phosphine flow rates and with decreasing TEOS flow rate. Decreasing the temperature causes a slight improvement in the thickness uniformity across a wafer.

Depletion in the deposition rate usually exists in the deposition of PSG (3, 9). In order to study the influence of the hot reactor walls on the deposition of PSG films on silicon wafers, we have also measured the PSG deposition rate on a wafer placed in position number 10 (a dummy wafer is placed at position number 9, other positions are unloaded). Due to the consumption of reactant gas on the walls, the partial pressure of the gases in the deposition zone is reduced and the deposition at the rear may be slower than that at the front. We define the depletion in the deposition rate as

$$\frac{\text{Dep. Rate (position 1)} - \text{Dep. Rate (position 10)}}{\text{Dep. Rate (position 1)}} \times 100$$

The results are summarized in Fig. 7 where the depletion is given as a function of the phosphine flow rate. The depletion increases with increasing phosphine and oxygen flow rates and with decreasing TEOS flow rate. Increasing the pump speed causes a decrease in the depletion in the deposition rate.

Step coverage.—Figure 8 shows an SEM cross section of a PSG film over a polycrystalline silicon step. The PSG film has been deposited at 630°C, using TEOS, O_2, and PH_3. It is clearly seen that the coverage over the step is uniform and conformal.

Refractive index.—The refractive indexes of PSG films deposited at 630°C and at 700°C are shown *vs.* the P_2O_5 concentration in Fig. 9. The refractive index increases with increasing P_2O_5 concentration. The results obtained at both reaction temperatures are similar. The refractive index for a given film composition is higher than that obtained on films deposited at 450°C but lower than the refractive index measured on films deposited at ~800°C (20). The increase in the refrac-

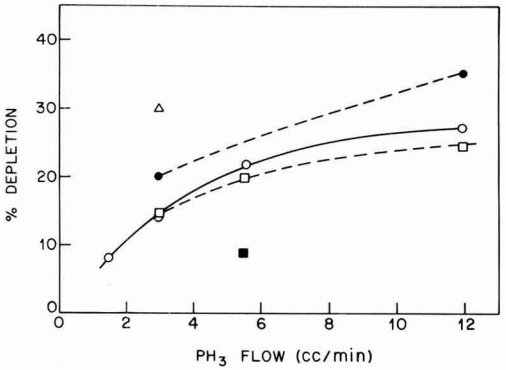

Fig. 7. The dependence of the depletion in the deposition rate on PH_3 flow rate. The depletion is measured between positions 1 and 10. (a) ○, $T = 700°C$, TEOS = 65 cm^3/min, O_2 = 80 cm^3/min, pressure = 0.352 Torr. (b) △, as (a) with TEOS = 45 cm^3/min, (c) ■, as (a) with higher pump speed, pressure = 0.300 Torr, (d) □, as (a) with $T = 685°C$, (e) ●, as (d) with O_2 = 200 cm^3/min.

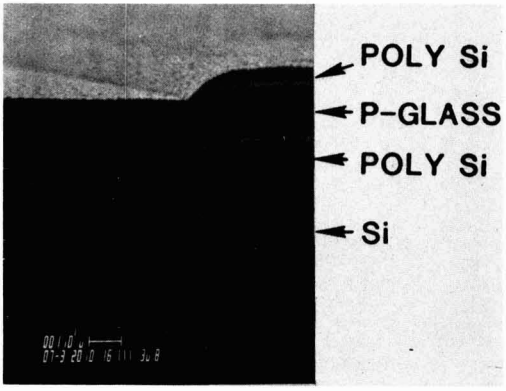

Fig. 8. Cross-sectional view of step coverage of PSG film over step in 3800Å of polycrystalline silicon on a silicon substrate. The deposition temperature is 630°C.

tive index with increasing deposition temperature may be attributed to an increase in the film density.

Etch rate.—Etch rates have been measured for films containing ~6 m/o P_2O_5 at 25°C using P-etch: 2 parts HNO_3, 3 parts HF, and 60 parts H_2O. The etch rate is ~90 Å/sec for as-deposited films. After densification (950°C, 10 min in argon or steam) the etch rate decreases to ~50 Å/sec.

Film stress.—The stresses measured in as-deposited films are very low ($< 0.2 \times 10^9$ dynes/cm^2). After densification (950°C, 10 min in steam or argon) the film stress increases to $\sim 1 \times 10^9$ dynes/cm^2. The stress of the as-deposited films increases to $\sim 1 \times 10^9$ dynes/cm^2 after exposing the film to water vapor. In all cases the films are under compressive stress. The tendency of the stress to become more compressive after annealing or after exposing the PSG film to water vapor is in agreement with previous results (2).

Summary

Low pressure deposition of phosphosilicate glass films on silicon wafers at 630°-700°C, using TEOS, PH_3, and O_2 has been investigated. The presence of oxygen and phosphine in the reaction catalyze the reaction. The deposition rate shows a tendency of increase-

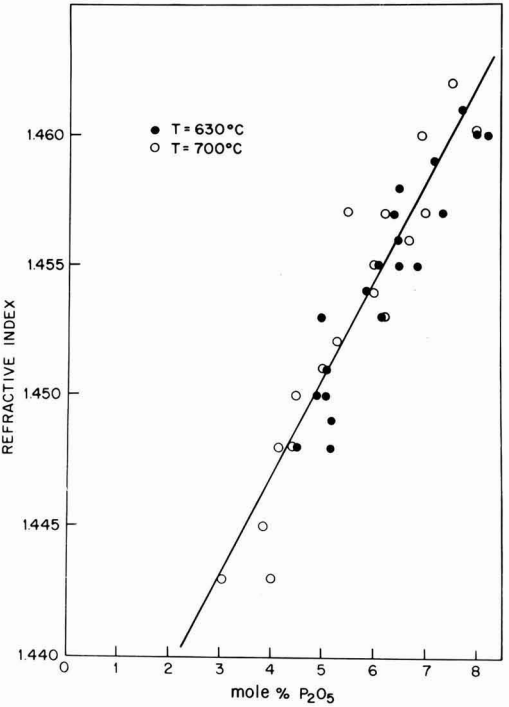

Fig. 9. Refractive index vs. film composition for PSG films deposited at 630°C (●) and at 700°C (○).

maximum-decrease with increasing oxygen or phosphine flow rates. The phosphorus oxide concentration increases with increasing oxygen or phosphine flow rates and with decreasing TEOS flow rate or decreasing temperature. The step coverage obtained in this process is conformal, thus making glass flow unnecessary. The stress in the PSG films is low and compressive.

Acknowledgment

The authors wish to thank H. J. Levinstein, W. T. Lynch, J. Drobek, and P. V. Lenzo for valuable discussions.

Manuscript submitted Sept. 9, 1981; revised manuscript received Nov. 9, 1981.

Any discussion of this paper will appear in a Discussion Section to be published in the June 1983 JOURNAL. All discussions for the June 1983 Discussion Section should be submitted by Feb. 1, 1983.

Publication costs of this article were assisted by Bell Laboratories.

REFERENCES

1. W. Kern, *Solid State Technol.*, **18**(2), 25 (1976).
2. W. Kern, G. L. Schnable, and A. W. Fisher, *RCA Rev.*, **37**, 3 (1976).
3. R. S. Rosler, *Solid State Technol.*, **20**(4), 63 (1977).
4. R. E. Logar, M. T. Wauk, and R. S. Rosler, in "Chemical Vapor Deposition," P. Rai-Choudhury and R. N. Tauber, Editors, p. 195, The Electrochemical Society Softbound Proceedings Series, Princeton, NJ (1978).
5. K. Sugawara, Y. Yoshimi, and H. Sakai, in "Chemical Vapor Deposition," J. M. Blocher, Jr., H. R. Hinterman, and L. H. Hall, Editors, p. 407, The Electrochemical Society Softbound Proceedings Series, Princeton, NJ (1975).
6. W. Kern, *RCA Rev.*, **34**, 655 (1973).

7. W. E. Armstrong and B. L. Tolliver, *This Journal*, **121**, 307 (1974).
8. E. Tanikawa, O. Takayama, and K. Maeda, in "Chemical Vapor Deposition," G. F. Wakefield and J. M. Blocher, Jr., Editors, p. 261, The Electrochemical Society Softbound Proceedings Series, Princeton, NJ (1973).
9. A. C. Adams and C. D. Capio, *This Journal*, **126**, 1042 (1979).
10. R. C. Archer, *J. Opt. Soc. Am.*, **52**, 970 (1962).
11. A. C. Adams, D. P. Schinke, and C. D. Capio, *This Journal*, **126**, 1539 (1979).
12. A. C. Adams and S. P. Murarka, *ibid.*, **126**, 334 (1979).
13. J. Monkoski and J. Stach, *Solid State Technol.*, **19**(11), 38 (1976).
14. B. J. Baliga and S. K. Ghandhi, *J. Appl. Phys.*, **44**, 990 (1973).
15. E. A. Taft, *This Journal*, **126**, 1728 (1979).
16. M. Shibata and K. Sugawara, *ibid.*, **122**, 155 (1975).
17. J. Middelhoeck and A. J. Klinkhamer, in "Chemical Vapor Deposition," J. M. Blocher, Jr., H. R. Hinterman, and L. H. Hall, Editors, p. 19, The Electrochemical Society Softbound Proceedings Series, Princeton, NJ (1975).
18. G. Wahl, in "Chemical Vapor Deposition," J. M. Blocher, Jr., H. R. Hinterman, and L. H. Hall, Editors, p. 391, The Electrochemical Society Softbound Proceedings Series, Princeton, NJ (1975).
19. M. Shibata, T. Yoshimi, and K. Sugawara, *This Journal*, **122**, 157 (1975).
20. A. C. Adams, C. D. Capio, S. H. Haszko, G. I. Parisi, E. I. Povilonis, and McD. Robinson, *ibid.*, **126**, 313 (1979).

A Model for Boron Deposition in Silicon Using a BBr_3 Source

S. F. Guo* and W. S. Chen

Institute of Electronics, National Chiao Tung University, Hsinchu, Taiwan, China

ABSTRACT

The sheet resistance and junction depth as a function of time at various temperatures have been obtained for the deposition of boron in silicon by using a BBr_3 liquid source. A simulation program incorporating a more realistic moving boundary condition is developed to analyze the deposition process under oxidizing atmosphere. By fitting numerical solutions to experimental data, the moving interface velocity and diffusion coefficient are determined. The profile of deposited layers as a function of doping gas composition can be modeled by the change of silicon self-interstitial concentration. The solid solubility of boron in silicon as a function of temperature has been determined. Different surface concentrations corresponding to different thicknesses of the boron-rich layer can be explained by the translation of the BRL-Si interface.

Boron tribromide (BBr_3) is the p-type dopant source most commonly used in silicon planar technology (1). Since the deposition of boron in silicon using BBr_3 is generally carried out in an oxidizing atmosphere, the physical process is more complicated than that using BN under inert ambient. A purely vacancy model gives a good prediction of the sheet resistance as a function of time for various temperatures when a boron nitride solid source is used (2). However, as shown in Fig. 1, the quantity of boron atoms deposited into silicon using BBr_3 is much larger than that using BN and is not increased linearly with the square root of time as predicted from a simple diffusion model (2).

It is well-known (3) that the diffusivity of boron in silicon depends not only on doping concentration but also on the oxidation rate of silicon at the surface. The concentration-dependent diffusion is generally modeled by a vacancy mechanism, while the oxidation-enhanced diffusion is related to the interstitialcy mechanism. In general, the vacancy contribution is determined from the multiple charge state vacancy statistics (2, 4) and the interstitialcy contribution is given as a function of oxidation rate (5, 6).

Naturally, the oxidation of silicon will consume silicon as well as some impurity atoms already deposited in it. The purpose of this paper is to show that the sheet resistance and junction depth as a function of time for various temperatures can be simulated by taking a moving boundary condition into account.

As shown by Negrini *et al.* (1), the deposition of boron in silicon using BBr_3 depends strongly on doping gas composition for a given temperature and time. However, for a suitably chosen doping gas composition, some reproducible results of sheet resistance and junction depth can be obtained. On the other hand, the increase of deposition quantity with oxygen flow rate can be modeled by the oxidation rate dependence of silicon self-interstitials (6), while the anomalous decrease of deposition quantity with BBr_3 flow rate can be explained by the reduction of the population of interstitial excess silicon in the $Si-SiO_2$ interface. The reaction of oxygen with silicon will generate some interstitial silicons (3) whose concentration will be reduced by interacting with boric oxide and bromine produced by the preliminary reaction of BBr_3 and O_2.

Experimental

The silicon materials used in this investigation were 2 in. diam n-type wafers with a resistivity of 3-7 Ω-cm. Wafers were about 300 μm thick and one side was mechanically and chemically polished.

Deposition processes were carried out at temperatures of 900°-1050°C while the liquid BBr_3 source was kept at 16°C which corresponds to a partial pressure of 42 Torr. High purity nitrogen was bubbled

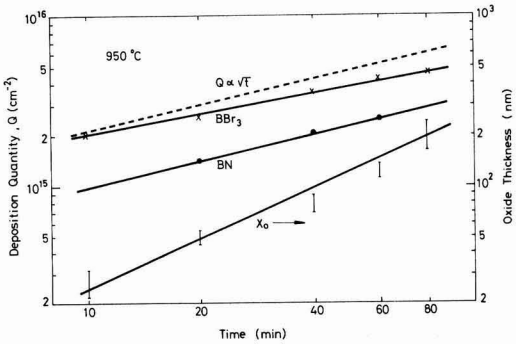

Fig. 1. Boron deposition quantity and oxide thickness as a function of time at 950°C.

* Electrochemical Society Active Member.
Key words: diffusion, boron deposition, BBr_3 source.

through the liquid and mixed with the main carrier gas consisting of nitrogen and oxygen.

The deposition cycle consisted of a 5 min preheating (N_2 and O_2), a given time of deposition (BBr_3 plus N_2 and O_2), and followed by a 1 min flush (N_2 and O_2). The gas flow rate was kept at N_2 1000 cm³/min, O_2 30 cm³/min, and N_2 + BBr_3 10 cm³/min. The gas composition was estimated as O_2 3% and BBr_3 0.05%.

The deposition of boron in silicon was actually a very complicated oxidation-diffusion process. It consisted of a preliminary reaction of BBr_3 with O_2 which results in the chemical deposition of boric oxide on the silicon wafers

$$4BBr_3 + 3\,O_2 \rightleftharpoons 2B_2O_3 + 6Br_2 \quad [1]$$

an interface reaction of oxygen with silicon to form silicon dioxide as well as some interstitial silicons (3)

$$Si + O_2 \rightarrow SiO_2 \quad [2]$$

a reaction of boric oxide with silicon to produce silicon dioxide and boron atoms

$$2B_2O_3 + 3Si \rightleftharpoons 3SiO_2 + 4B \quad [3]$$

and a possible etch of silicon by bromine

$$Si + 2Br_2 \rightarrow SiBr_4 \quad [4]$$

Boric oxide was a liquid at normal deposition temperatures. It mixed readily with the silicon dioxide on the silicon surface to form a boro-silicate glass. Boron atoms deposited would diffuse into silicon or form a boron-rich surface layer.

After the deposition operation, the boro-silicate glass on the surface was etched with dilute HF, while the boron-rich layer as generally detectable by its hydrophilic behavior was removed boiling the wafer in the nitric acid (1). The thickness of some boro-silicate glasses was measured by a Rudolph Auto EL-II ellipsometer. The glass thickness as a function of time at 950°C is also shown in Fig. 1. The sheet resistance of the boron-deposited layer was measured using a Veeco Model FPP-100 four-point probe with a light weight. Each sample was measured on several points for many times to obtain an average value. The sheet resistance of the deposited layers as a function of time for various temperatures is shown in Fig. 2. Generally the junction depth of the deposited layers is very shallow. The junction depth was measured from a Solid State Measurements ASR-100B spreading resistance probe. To avoid a rounding effect, the silicon surface was coated with a layer of oxide by low temperature chemical vapor deposition. The junction depth of the deposited layers as a function of time for various temperatures is shown in Fig. 3.

The impurity profile was determined from the anodic sectioning technique. Anodic oxidation was carried out with a constant current source by using as electrolyte a solution of

$$HOCH_2CH_2OH : KNO_3 : H_2O / 1 \text{ liter} : 404 \text{ mg} : 20 \text{ ml}$$

The thickness of each oxide layer was measured by an ellipsometer. The sheet resistance after oxide stripping was measured by a four-point probe.

The measured data of the oxide thickness and the sheet resistance were converted to an impurity concentration profile through a computer program (7). The volumetric ratio for silicon converted to silicon dioxide was taken as 0.4 for anodic oxidation. The hole mobility-boron concentration relation established by Antoniadis *et al.* (8) was used in this work. To avoid the error magnification commonly found in discrete data differentiation, the measured data of the sheet resistance *vs.* distance were smoothed through fitting the logarithmic values of each five data points to a parabola by a standard least squares technique. The profiles of boron concentration in silicon at different temperatures for the same deposition time (20 min) and those at the same temperature (950°C) for various times are shown in Fig. 4 and 5, respectively.

Diffusion Model

The deposition of boron in silicon by using a BBr_3 source under an oxidizing ambient is an oxidation-diffusion process depicted in Fig. 6. Actually, this is a moving boundary problem and, in general, there is no analytic solution. Therefore, a numerical method should be used to generate a computer solution (9). Furthermore, a moving coordinate system is chosen to solve the moving boundary problem encountered in this work. As usual, the space and time are discretized into intervals of Δy and Δt. The impurity concentration C_j is evaluated at a node lying in the middle of each discrete cell j. The impurity flux $F_{j+1/2}$ is evaluated at the boundary between cells j and j + 1. As time changes from t_o to $t = t_o + \Delta t$, the oxide thickness increases from X_o^0 to X_o and the oxide-silicon interface as well as all cell boundaries will translate a distance $\Delta X = V\Delta t$, where V is the velocity of silicon consumed to form the oxide. An implicit scheme of the finite difference method is more suitable for solving this moving boundary problem. In a discretized form, the impurity flux may be written as (9)

$$F_{j+1/2} = (D_jC_j - D_{j+1}C_{j+1})/\Delta y \quad [5]$$

where D_j and C_j are diffusivity and concentration of a

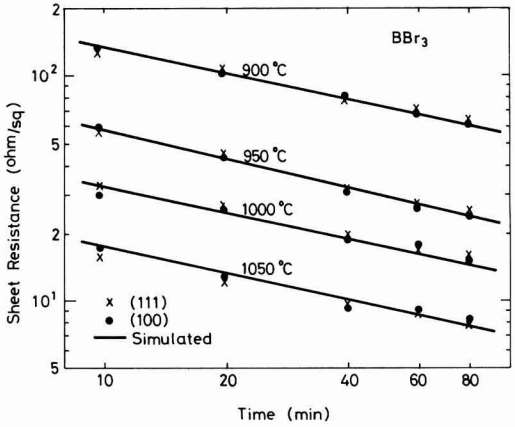

Fig. 2. Measured and simulated sheet resistances as a function of time for various temperatures.

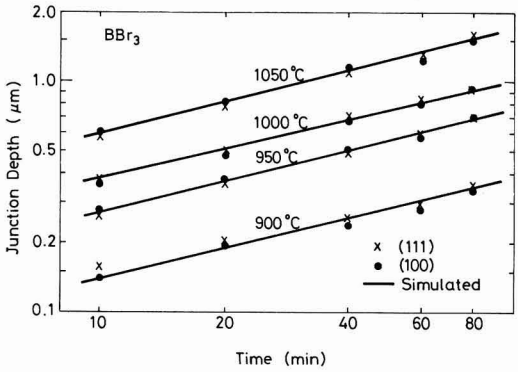

Fig. 3. Measured and simulated junction depths as a function of time for various temperatures.

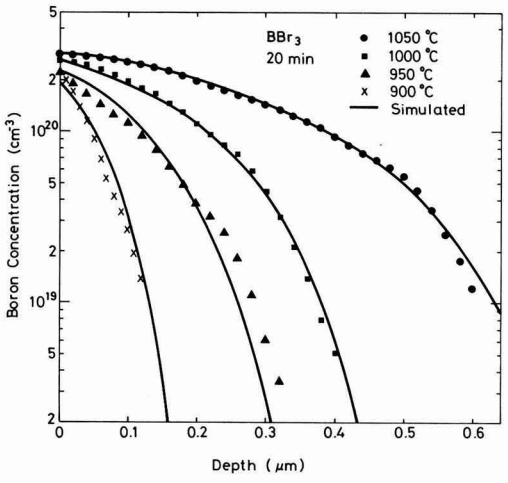

Fig. 4. Measured and simulated boron concentration profiles in silicon deposited for 20 min at various temperatures.

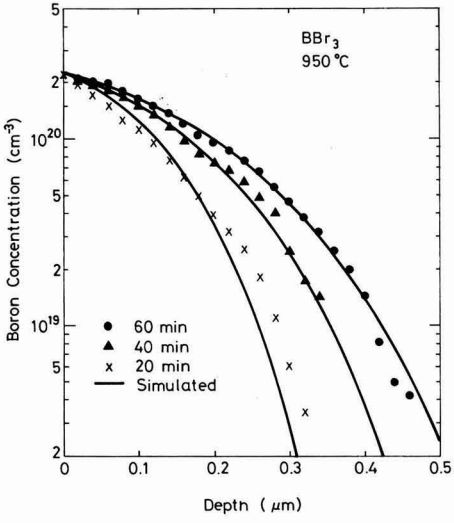

Fig. 5. Measured and simulated boron concentration profiles in silicon deposited at 950°C for various times.

j cell evaluated at time t. The continuity equation is given as

$$\frac{C_j - C_j'}{\Delta t} = \frac{F_{j-1/2} - F_{j+1/2}}{\Delta y} \qquad [6]$$

where C_j' is the average concentration of the j cell evaluated at time t_o with boundaries moved to the new positions at time t. From Fig. 6 it is easy to show that

$$C_j' = C_j^0 - (C_j^0 - C_{j+1}^0)\Delta x/\Delta y \qquad [7]$$

where C_j^0 is the concentration of the j cell at time t_o.

The cells at the two extreme boundaries deserve special attention. As shown in Fig. 6, the first discrete cell is actually a half-cell with its node at the oxide-silicon interface. The surface concentration C_S is assumed to be maintained at a constant value that corresponds to the solubility of boron in silicon in equilibrium with the concentration of boric oxide in the borosilicate glass.

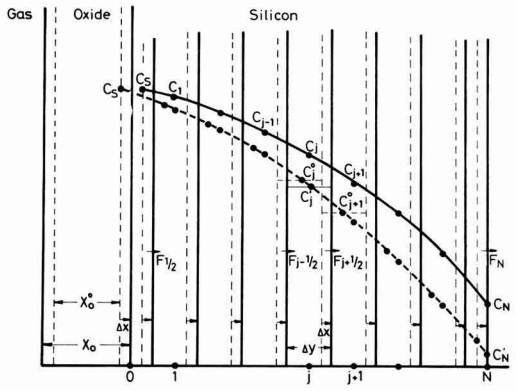

Fig. 6. A schematic diagram for boron deposition with a discretized moving coordinate.

The deep boundary usually lies inside the silicon substrate at the point where the simulated space terminates. The last cell in this end is also a half-cell similar to the first one. The impurity flux at the deep boundary F_N is taken as zero in the simulation program.

Results and Discussion

Measured values of the sheet resistance and junction depth of deposited layers as a function of time for various temperatures as well as measured profiles of boron in silicon at different temperatures and times can be simulated by properly choosing the boundary condition and modeling the diffusion coefficient. Simulated results are also illustrated in Fig. 2-5. The simulated values of surface concentration, moving boundary velocity, and diffusion coefficients as a function of temperature are given in Table I.

Surface concentration.—As shown in Fig. 4 and 5, simulated values of the surface concentration are in good agreement with the measured data. The results obtained in this work as well as those reported by Armigliato *et al.* (10) are shown in Fig. 7.

Moving boundary velocity.—The oxide-silicon interface is moved with a velocity V by the reactions of oxygen, boric oxide, and bromine to consume silicon as well as boron atoms. The reactions of oxygen and boric oxide with silicon, Eq. [2] and [3], result in the growth of silicon dioxide. The growth rate of silicon dioxide due to oxygen is generally given as (11)

$$v_1 = \frac{B_1}{2X_o + A_1} \qquad [8]$$

where B_1 and A_1 are the parameters defined by Deal and Grove (11). For thin oxide, $2X_o << A_1$, the oxidation rate is linearized as

$$v_1 \simeq B_1/A_1 \qquad [9]$$

The oxidation rate may be enhanced by a catalytic action (12) in the presence of bromine. It may also be enhanced by the high vacancy concentration generated in a heavily doped silicon (4, 13).

Table I. Some parameters used in profile simulations

T (°C)	900	950	1000	1050
C_S (cm^{-3})	1.9×10^{20}	2.3×10^{20}	2.6×10^{20}	2.9×10^{20}
V (cm/sec)	1.52×10^{-9}	2.24×10^{-9}	4.8×10^{-9}	8.0×10^{-9}
D_V^* (cm^2/sec)	1.21×10^{-15}	5.15×10^{-15}	1.96×10^{-14}	6.76×10^{-14}
γ	5.1	4	1.3	0.8

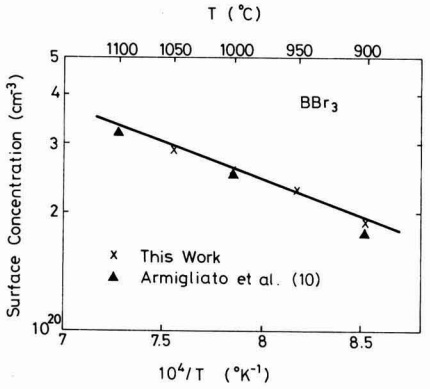

Fig. 7. Surface concentration of boron in silicon as a function of deposited temperature.

Due to oxidation enhancements as well as chemical deposition of boric oxide, Eq. [1], the oxide formation rate v_o estimated from the oxide thickness given in Fig. 1 is much larger than v_1 calculated from Eq. [9] using the parameters given by Deal and Grove (11). It is interesting to note that the ratio of silicon consuming rate V given in Table I to oxide formation rate v_o is around 0.55 which is slightly higher than the volumetric ratio of 0.45 for silicon converted to silicon dioxide during thermal oxidation. The difference may be attributed to the etching of silicon by bromine in the deposition process.

Diffusion coefficient.—From the study of oxidation-enhanced diffusion of boron and phosphorus in silicon, it is generally believed (14, 15) that a substitional impurity diffuses via a dual mechanism of vacancy and interstitialcy. An increase in the concentration of either vacancies C_V or interstitials C_I would cause the enhancement of impurity diffusion. Thus it is reasonable to assume that the effective diffusivity of an impurity may be expressed as

$$D = f_e(D_V + D_I) \qquad [10]$$

where f_e is the high concentration field enhancement factor given by (16)

$$f_e = 1 + [1 + (2n_i/C)^2]^{-1/2} \qquad [11]$$

D_V and D_I are the vacancy and interstitialcy motivated diffusivities given by (14)

$$D_V = D_V^* C_V/C_V^* \qquad [12]$$

$$D_I = D_I^* C_I/C_I^* \qquad [13]$$

with the asterisk denoting the corresponding intrinsic value.

The normalized vacancy concentration has been shown to follow the multiple charge state vacancy statistics (2, 4) and can be expressed as a function of hole concentration p as

$$\frac{C_V}{C_V^*} = \frac{1 + \beta^+(p/n_i) + \beta^-(n_i/p) + \beta^=(n_i/p)^2}{1 + \beta^+ + \beta^- + \beta^=} \qquad [14]$$

where β^+, β^-, and $\beta^=$ are the vacancy statistics parameters defined in Ref. (2).

The normalized concentration of self-interstitials has been related to the oxidation rate by a number of investigators (5, 6, 15) and can be expressed as

$$\frac{C_I}{C_I^*} = Kv_1^\nu \qquad [15]$$

where K is a proportional factor and ν is an exponent around 0.5 (3). Although v_1 is time dependent in general, Eq. [8], we will consider it as a constant, Eq. [9]. Substituting Eq. [12], [13], and [15] into Eq. [10], we obtain

$$D = f_e D_V^*(C_V/C_V^* + \gamma) \qquad [16]$$

where

$$\gamma = D_I^* K v_1^\nu / D_V^* \qquad [17]$$

is the interstitialcy contribution parameter with simulated values given in Table I. The intrinsic diffusivity reported by Fair (17) has been taken as D_V^* in this work. The intrinsic carrier concentration n_i which appears in Eq. [11] and [14] is calculated from Morin and Maita's empirical relation (18).

Doping composition effect.—The dependence of boron concentration profiles on doping gas composition can be modeled by the change of interstitialcy contribution parameter γ. Higher oxygen flow rate results in higher oxidation rate v_1 and hence higher interstitial concentration C_I. While higher BBr_3 concentration produces higher boric oxide concentration in the oxide layer which reacts with the excess silicon at the interface. Therefore the interstitial concentratiion C_I is reduced and a boron-rich layer (BRL) is formed at silicon surface.

Figure 8 reproduces the measured profiles of Negrini *et al.* (1) at 1000°C for 23 min with different gas compositions. The observed differences in the surface concentration can be modeled by the displacement δ of the BRL-Si interface from the original oxide-silicon interface. The simulated results for boron concentration profiles with different values of γ and δ are also shown in the figure. A constant surface concentration of 2.6×10^{20} cm^{-3} is taken at the oxide-silicon interface and the origins of all profiles are taken at the BRL-Si interface. Good agreement in profile shapes as well as deposition quantities has been obtained.

Deposition quantity.—The quantity Q of boron deposited in silicon can be determined in some cases by numerical integration of the measured doping profiles. However, as revealed from profile and sheet resistance simulations, the average mobilities of deposited layers are very close together (54.3 ± 1.1 cm^2/V-sec) and a sufficiently accurate value of Q can be obtained from the measured sheet resistance. Figure 1 shows the deposition quantity Q as a function of time at 950°C for BBr_3 and BN sources. Also shown in the figure is a

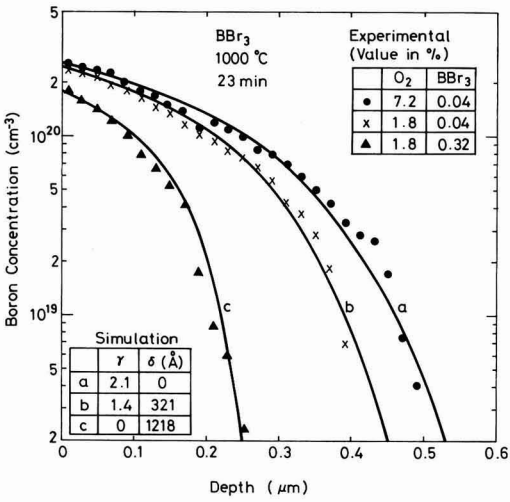

Fig. 8. Measured and simulated boron concentration profiles in silicon deposited at 1000°C for 23 min with different doping gas compositions.

relation of $Q \propto t^{1/2}$ which is obtained by taking the moving boundary velocity V as zero.

Conclusion

The sheet resistance and junction depth of boron-deposited layers as a function of time for various temperatures using a BBr_3 source can be simulated by properly choosing the boundary conditions and modeling the diffusion coefficient. The diminishing of the deposition quantity is modeled by a moving velocity of the oxide-silicon interface. The increase of the deposition quantity by using BBr_3 as compared to BN is attributed to the formation of silicon self-interstitials. The gas composition dependence of boron deposition is explained by the change of the interstitialcy contribution as well as the formation of a boron-rich layer.

Acknowledgments

The helpful discussions with Dr. W. P. Wang are highly appreciated. The authors are also grateful for the assistance by the staff of Semiconductor Research Laboratory of Tatung Institute of Technology in the impurity concentration profile measurements. This research work was sponsored through National Science Council Contract No. NSC70-0404-E009-03.

Manuscript submitted Aug. 31, 1981; revised manuscript received Dec. 18, 1981.

Any discussion of this paper will appear in a Discussion Section to be published in the June 1983 JOURNAL. All discussions for the June 1983 Discussion Section should be submitted by Feb. 1, 1983.

Publicatiion costs of this article were assisted by the National Chiao Tung University.

REFERENCES

1. P. Negrini, A. Ravaglia, and S. Solmi, *This Journal*, **125**, 609 (1978) and references therein.
2. S. F. Guo, *ibid.*, **127**, 2506 (1980).
3. R. B. Fair, *ibid.*, **128**, 1360 (1981) and references therein.
4. C. P. Ho and J. D. Plummer, *ibid.*, **126**, 1516 (1979).
5. S. M. Hu, *J. Appl. Phys.*, **45**, 1567 (1974).
6. A. M. Lin, D. A. Antoniadis, and R. W. Dutton, *This Journal*, **128**, 1131 (1981).
7. J. C. Plunkett, J. L. Stone, and A. Leu, *Solid State Electron.*, **20**, 447 (1977).
8. D. A. Antoniadis, A. G. Gonzaley, and K. W. Dutton, *This Journal*, **125**, 813 (1978).
9. D. A. Antoniadis, M. Rodoni, and R. W. Dutton, *ibid.*, **126**, 1939 (1979).
10. A. Armigliato, D. Nobili, P. Ostoja, M. Servidori, and S. Solmi, in "Semiconductor Silicon 1977," H. R. Huff and E. Sirtl, Editors, p. 638, The Electrochemical Society Softbound Proceedings Series, Princeton, NJ (1977).
11. B. E. Deal and A. S. Grove, *J. Appl. Phys.*, **36**, 3770 (1965).
12. K. Hirabayashi and J. Iwamura, *This Journal*, **120**, 1595 (1973).
13. J. D. Plummer, in "Semiconductor Silicon 1981," H. R. Huff, R. J. Kriegler, and Y. Takeishi, Editors, p. 445, The Electrochemical Society Softbound Proceedings Series, Pennington, NJ (1981).
14. D. A. Antoniadis, in "Semiconductor Silicon 1981," H. R. Huff, R. J. Kriegler, and Y. Takeishi, Editors, p. 947, The Electrochemical Society Softbound Proceedings Series, Pennington, NJ (1981).
15. K. Taniguchi, K. Kurosawa, and M. Kashiwagi, *This Journal*, **127**, 2243 (1980).
16. K. Lehovec and A. Slobodskoy, *Solid State Electron.*, **3**, 45 (1961).
17. R. B. Fair, *This Journal*, **122**, 800 (1975).
18. F. J. Morin and J. P. Maita, *Phys. Rev.*, **96**, 28 (1954).

Studies of Methacrylonitrile and Trichloroethyl Methacrylate Copolymers as Electron Sensitive Positive Resists

J. H. Lai

Honeywell Corporate Technology Center, Bloomington, Minnesota 55420

and J. H. Kwiatkowski and C. F. Cook, Jr.

U.S. Army Electronics Technology and Devices Laboratory, Fort Monmouth, New Jersey 07703

ABSTRACT

Positive electron resists derived from copolymers of methacrylonitrile (MCN) and trichloroethyl methacrylate (TCEM) have been synthesized, characterized, and evaluated. The sensitivity of 2:1 MCN/TCEM copolymer is 5 μC cm^{-2} with 40% unexposed area thickness loss. The plasma etch resistance of the copolymer is significantly higher than that of the TCEM homopolymer. The inclusion of the comonomer MCN, however, has not significantly broadened the exposure range for the copolymer as a positive-acting resist. The copolymer resists exhibited significant concurrent cross-linking at a dose $\geq$ 20 μC cm^{-2}.

Poly(methacrylonitrile) (PMCN) is one of the vinyl polymers that is highly sensitive to high energy radiation. On exposure to high energy electron beams, chain scission occurs predominantly in the polymer with negligible concurrent cross-linking. The G_s value, defined as the number of chain scission events per 100 eV of energy absorbed, of PMCN has been reported to be 3.3 (1). The value is significantly higher than 1.6 of PMMA [poly(methyl methacrylate)], the current standard E-beam resist. The thermal stability of the polymer is also better than PMMA. The glass transition temperature (T_g) of PMCN is 120°C (2), which is higher than the T_g of PMMA, which is 100°C. Further, it has been shown that PMCN is one of the few aliphatic vinyl polymers that has high plasma etch resistance (3).

Although PMCN has the attractive properties discussed above, the polymer has one major drawback. The polymer is highly solvent resistant (4). The poor solubility of the polymer has resulted in the use of less common solvents, *e.g.*, nitromethane and benzonitrile, for spin coating and development of the polymer resist (5). The poor solubility of the polymer also hinders the possibility of further enhancing the resist sensitivity through optimization of the development process.

Key words: positive electron resist, methacrylonitrile, trichloroethyl methacrylate, copolymer.

Modification of polymer properties through copolymerization is a well-known approach that has been used in the plastics industry for a number of years. The poor solubility of PMCN can be overcome by copolymerization with other suitable comonomers.

In previous work, we have reported the positive electron resist behavior of MCN and methyl α-chloroacrylate copolymers (6). The electron resist behavior of copolymer of MCN and methyl methacrylate (MMA) have been reported by Stillwagon *et al.* (7). The electron beam resist sensitivity of the homopolymer poly(trichloroethyl methacrylate) (PTCEM) (8) and copolymers of TCEM and MMA (9) have also been reported. In this paper, we wish to report the electron resist behaviors of copolymers of MCN and TCEM. The sensitivity, development behavior, and plasma etch rate for MCN/TCEM copolymer resists are reported. The comonomer TCEM was selected for the purpose of enhancing the solubility and sensitivity without sacrificing the plasma etch resistance of PMCN.

Experimental

Resist synthesis and characterization.—The MCN/TCEM copolymer resists were synthesized by free-radical emulsion polymerization. The emulsion polymerization conditions for MCN/TCEM copolymers are listed in Table I. The characteristics of the copolymers are listed in Table II. The initiator used for the polymerization was potassium persulfate. The emulsifier was sodium lauryl sulfate. The monomers MCN andTCEM were obtained from Eastman Kodak Chemicals and Polysciences, respectively. The monomers were vacuum distilled before use. The polymerization was carried out at 65° without using a chain-transfer agent. After polymerization, the mixture was poured into methanol, and aluminum sulfate was added to the mixture to coagulate the polymer. The polymer was washed twice with water and dried at 45° in a vacuum oven for 16 hr. An EDAX (energy dispersive analysis of x-ray) analysis of dried copolymers indicate no detectable amount of aluminum or sodium. The polymerization conditions for the copolymer-2 and the copolymer-5 are basically the same, and the characteristics of both polymers are found to be virtually identical. The copolymer-7 was synthesized according to the method for copolymer-2, except the quantity of the monomers, solvent, and initiator was increased by a factor of 2.

The composition of the copolymers was determined by the elemental analysis carried out by Galbraith Laboratory. The molecular weight distribution ($\overline{M}_w/\overline{M}_n$), glass transition temperature (T_g), and intrinsic viscosity [η] of the resists were determined using the following standard techniques: GPC, differential scanning calorimetry, and solution viscometry, respectively. The molecular weight distribution of ($\overline{M}_w/\overline{M}_n$) of most MCN/TCEM copolymers is lower than 2.0 except for the copolymer-4 when a nonionic emulsifier Triton X-405 was used in synthesizing the polymer. The composition of copolymer-1 and copolymer-2 (as well as copolymer-5 and copolymer-7) is, respectively, close to 1:1 and 2:1 MCN/TCEM copolymers. It is interesting to note that use of Triton X-405 as an emulsifier produces a 1:2 MCN/TCEM copolymer (copolymer-4) while use of sodium lauryl sulfate under the same polymerization conditions yields a 2:1 copolymer (copolymer-3).

Table III. Resist film thickness vs. spin speed for MCN/TCEM copolymers

Copolymer	Spinning solution	Film thickness (μm) 0.7K	1K	2K	3K rpm
Copolymer-1	5 wt./v. % chlorobenzene	0.73	0.57	0.41	
	7 wt./v. % chlorobenzene		1.11		0.65
Copolymer-2	5 wt./v. % nitromethane	0.69	0.66	0.42	
	7 wt./v. % nitromethane		1.23		0.70
	7 wt./v. % MIBK	1.61	1.30	0.95	
Copolymer-5	6 wt./v. % MIBK	1.35	1.07	0.76	

Electron beam exposure.—For E-beam exposure, the resist films were spin-coated on SiO_2 (2000Å), prebaked, and exposed. The resist film thickness (prebaked at 160°) *vs.* spin speed for MCN/TCEM copolymers are tabulated in Table III. To determine the sensitivity and the resolution of resists, the resists were exposed in a Honeywell micropattern generator with two test patterns that cover a wide range of exposure. The sensitivity test pattern contains fifty 1 μm wide, 1.5 mm long lines. The spacing between each line is 6 μm and the exposure ranges from 0.5 to 450 μC/cm². The resolution test pattern contains 20 sets of 100 μm long lines. Each set contains 6 lines of equal exposure. The spacing between each line is 1 μm for positive resists and 1.5 μm for negative resists, and the line charge density varies from 1×10^{-12} to 1×10^{-9} C cm^{-1}. The electron energy was 15 keV.

The film thicknesses before development were mostly 1 μm. The development of resist film patterns were carried out by spray development. The developed patterns were examined under optical or scanning electron mi-

Table I. Synthesis of MCN/TCEM copolymer by emulsion polymerization

MCN/TCEM copolymer	Monomer (ml) MCN	TCEM	Initiator (mg)	Emulsifier (mg)	Water (ml)	Polymerization time (°C)	Polymerization time (hr)	Yield (g)
Copolymer-1	17	18	150	200	120	65	2	16
Copolymer-2	22	13	200	200	200	65	2	
Copolymer-3	23	12	200	200	200	65	2	8.1
Copolymer-4*	23	12	200	300*	200	65	16	11.3
Copolymer-5	22	13	200	300	200	65	2	11.1
Copolymer-7	44	26	400	400	400	65	2	16.8

* Triton X-405 was used, see text of the paper.

Table II. Characteristics of MCN/TCEM copolymer resists

Copolymer	Composition (m/o) MCN	TCEM	GPC analysis $\overline{M}_w$	$\overline{M}_n$	$\overline{M}_w/\overline{M}_n$	$[\eta]_{MEK}$ at 25°C	T_g (°C)
Copolymer-1	54.2	45.8	461,800	263,300	1.75	1.52	125
Copolymer-2	64.6	35.4	441,800	237,600	1.86	1.31	123
Copolymer-3	68.2	31.8	237,500	129,600	1.83	1.27	124
Copolymer-4*	33.8	66.2	464,300	160,800	2.89	1.26	131
Copolymer-5	64.9	35.1	493,000	280,000	1.76	1.46	120
Copolymer-7	68.8	31.2	304,000	197,000	1.54	1.20	121

* The nonionic emulsifier Triton X-405 was used in synthesizing the copolymer-4.

croscopes. In some cases, SnO_2 wafers were further fractured to examine the line edge profile of the resist patterns.

Results and Discussions

Sensitivity.—Many organic solvents and solvent mixtures were tested as the developers for the resists. They included methyl ethyl ketone (MEK), methyl isobutyl ketone (MIBK), methyl cellosolve, cellosolve acetate, ethyl acetate, n-propyl acetate, i-propyl acetate, i-butyl acetate, and amyl acetate. Among the many developers that have been tested, MIBK was found to be the best developer for both 2:1 and 1:1 MCN/TCEM copolymer resists. SEM micrographs of developed resist line profiles are shown in Fig. 1 and 2. The sensitivity of both 1:1 MCN/TCEM copolymer (*i.e.*, MCN/TCEM copolymer-1) and 2:1 MCN/TCEM copolymer (MCN/TCEM copolymer-2 or copolymer-5 or copolymer-7) are very close, being 5 $\mu C\ cm^{-2}$ with approximately 40% thickness loss in the unexposed area. The cross-link sensitivity of both 1:1 and 2:1 copolymers is also similar. It has been found that cross-linking occurs predominantly in both copolymers when the exposure dose exceeds 20 $\mu C\ cm^{-2}$. The exposure range for both copolymers as positive-acting resists is relatively narrow, from 4 to 20 $\mu C\ cm^{-2}$. The 1:2 MCN/TCEM copolymer (copolymer-4) was not fully evaluated because of its relatively broad molecular weight distribution.

Electron resist behavior for the homopolymer PTCEM has been reported by Tada (8). The exposure range for PTCEM as a positive-acting resist was found to be in the range from 1.25 to 25 $\mu C\ cm^{-2}$. The developer used for the PTCEM was a mixture of methyl cellosolve and ethyl cellosolve. However, direct comparison of present results with Tada's results is not possible since the unexposed area film thickness loss after development was not reported by Tada for PTCEM. Nevertheless, it appears that the sensitivity and the exposure range for both MCN/TCEM copolymers and PTCEM homopolymers are similar.

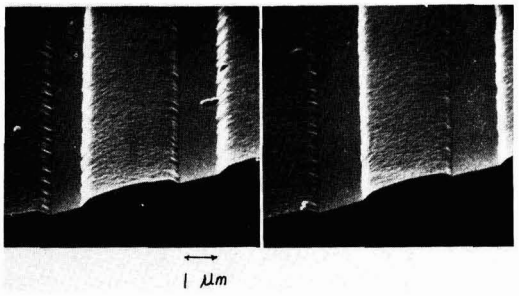

Fig. 1. Scanning electron micrograph of developed MCN/TCEM copolymer-2 lines. The SEM magnification is 10,000×. The images were developed with MIBK 60 sec spray. The exposure doses are, from left to right, 8, 10, 12, and 14 $\mu C\ cm^{-2}$.

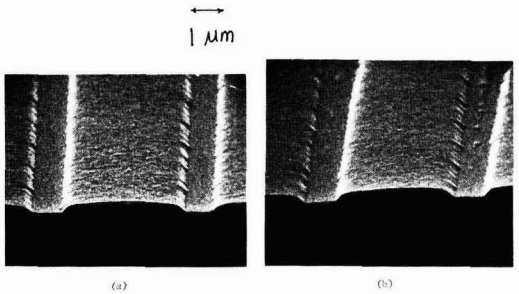

Fig. 2. Scanning electron micrographs of developed MCN/TCEM copolymer-7 lines. The SEM magnification is 10,000×. (a) The images were developed with MIBK; the exposures are, from right to left, 6 and 7 $\mu C\ cm^{-2}$. (b) The images were developed with ethyl acetate/i-propyl acetate (1:1); the exposures are, from right to left, 12 and 14 $\mu C\ cm^{-2}$.

It is not fully understood why the exposure range for the 2:1 MCN/TCEM copolymer as a positive-acting resist is not significantly broader than that of the homopolymer PTCEM. Although PTCEM is susceptible to cross-linking due to the presence of C—Cl bonds in the side chains as pointed out by Tada (8), the homopolymer PMCN has been known to degrade without significant concurrent cross-linking under high energy radiation (1, 5). Significant amounts of MCN comonomer in a copolymer, *e.g.*, 2:1 MCN/TCEM copolymer, is expected to decrease the rate of cross-linking in the copolymer (10) and therefore broaden the exposure range. The present observation, however, is contrary to the expectation and more studies are needed to understand this phenomenon.

The effect of development temperature on the development behavior of MCN/TCEM copolymer-2 using amyl acetate as a developer has also been studied. If the unexposed resist film thickness after development is maintained constant, the development temperature was found to have no significant effect on the sensitivity of the copolymer resist. The required development time, of course, decreases with an increase in development temperature.

Effect of prebake temperature.—The sensitivity and the resolution of both 1:1 MCN/TCEM copolymer (MCN/TCEM copolymer-1) and 2:1 MCN/TCEM copolymer (MCN/TCEM copolymer-2) have been studied as a function of prebake at three different temperatures: 160°, 180°, and 200°C. The prebake temperature appears to have no significant effect on the resist behavior of the copolymers. The observation is consistent with the TGA (thermogravimetric analysis) of the polymers. The thermograms for the MCN/TCEM copolymer-1 and copolymer-2 are shown in Fig. 3. Less than 1% weight loss was noted for both copolymers at 200°C. Although the homopolymer PTCEM [Poly(trichloroethylmethacrylate)] was reported to be thermally cross-linkable at 200°C (8), we have found no evidence of thermal cross-linking at 200° in any of the copolymer-1, -2, -3, or -5.

Plasma etch rate of resists.—The plasma etch rate of 2:1 MCN/TCEM (copolymer-2) in a planar etcher using Honeywell's SSED process (CHF_3 + 7% O_2) (11) has been determined. The etch rate of the copolymer-2 is 150 Å/min which is significantly lower than that of SiO_2, 300 Å/min. The high plasma resistance of the copolymer-2 suggests that it should be useful as an etch mask for submicron structure fabrication.

The plasma etch rate of both homopolymers PMCN and PTCEM in CF_4 + 4% O_2 and in a barrel etcher has been determined along with many other vinyl

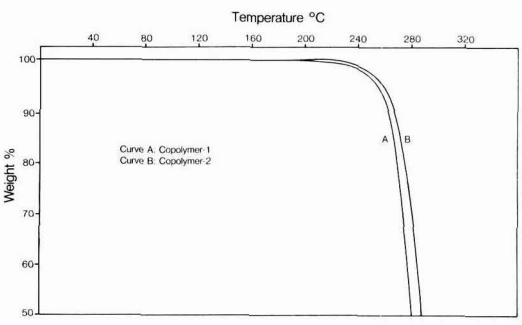

Fig. 3. TGA thermograms for MCN/TCEM copolymer-1 and copolymer-2.

polymers (3). The plasma etch rate of PMCN has been found to be one of the lowest. The high plasma resistance of 2:1 MCN/TCEM copolymer is consistent with the previous observation.

Acknowledgment

This work was supported at Honeywell by Contract No. DAAK20-80-C-0309 from the U.S. Army Electronics Technology and Devices Laboratory. The authors would like to thank the technical assistance from R. B. Douglas and B. Fure of Honeywell Corporate Technology Center and L. T. Shepherd and William Larson of Honeywell Solid State Electronics Division for their technical assistance.

Manuscript submitted Sept. 8, 1981; revised manuscript received Dec. 17, 1981.

Any discussion of this paper will appear in a Discussion Section to be published in the June 1983 JOURNAL. All discussions for the June 1983 Discussion Section should be submitted by Feb. 1, 1983.

Publication costs of this article were assisted by Honeywell.

REFERENCES

1. J. N. Helbert, E. H. Pointdexter, G. A. Stahl, C. Y. Chen, and C. U. Pittman, Jr., *J. Polym. Sci. Polym. Chem.*, **17**, 49 (1979).
2. J. Brandrup and E. H. Immergut, Editors, "Polymer Handbook," pp. 111-150, John Wiley and Sons, New York (1975).
3. J. N. Helbert, M. A. Schmidt, and J. H. Lai, Organic Coating and Plastics Chemistry Preprint, pp. 258-261, American Chemical Society Meeting, Las Vegas, August 24-29, 1980.
4. H. F. Mark, *et al.*, Editors, "Encyclopedia of Polymer Science and Technology," Vol. 15, p. 339, John Wiley and Sons, New York (1971).
5. J. N. Helbert, C. F. Cook, Jr., C. Y. Chen, and C. U. Pittman, Jr., *This Journal*, **126**, 694 (1979).
6. J. H. Lai, J. N. Helbert, C. F. Cook, Jr., and C. U. Pittman, Jr., *J. Vac. Sci. Technol.*, **16**, (1979).
7. L. E. Stillwagon, E. M. Doerries, L. F. Thompson, and M. J. Bowden, Organic Coatings and Plastics Chemistry Preprints, pp. 38-43, American Chemical Society Meeting, Chicago, August 9-September 2, 1977.
8. T. Tada, *This Journal*, **126**, 1635 (1979).
9. J. N. Helbert, J. H. Kwiatkowski, C. F. Cook, Jr., J. H. Lai, and C. U. Pittman, Jr., Abstract 322, p. 833, The Electrochemical Society Extended Abstracts, Hollywood, Florida, October 5-10, 1980.
10. J. H. Lai, L. T. Shepherd, R. Ulmer, and C. H. Griep, *Polym. Eng. Sci.*, **17**, 402 (1977).
11. W. L. Larson, J. H. Lai, T. L. Brewer, and L. T. Shepherd, Abstract 328, p. 848, The Electrochemical Society Extended Abstracts, Hollywood, Florida, October 5-10, 1980.

CCl_4 and Cl_2 Plasma Etching of III-V Semiconductors and the Role of Added O_2

Randolph H. Burton* and Gerald Smolinsky

Bell Laboratories, Murray Hill, New Jersey 07974

ABSTRACT

The kinetics of the CCl_4 and Cl_2 plasma etching of InP, GaAs, and GaP at 300°C and the role of added O_2 were investigated using atomic emission as a diagnostic aid. With the exception of the CCl_4/O_2 etching of InP, the etching rates were observed to be linear functions of the emission intensity from electronically excited Cl, regardless of the feed-gas composition. InP was observed to etch significantly faster in a CCl_4 discharge than would have been expected from the Cl emission intensity alone, indicating the active involvement of CCl_x species. Addition of a small amount of O_2 to either CCl_4 or Cl_2 resulted in an increase in the intensity of Cl atomic emission. With feed compositions of ~40% O_2 in $Cl_2(CCl_4)$, extremely fast etching rates of 7.3(2.5), 2.4(0.9), and 1.6(2.1) μm/min were obtained for GaAs, GaP, and InP, respectively. A vertical to horizontal etching rate ratio of less than two was obtained in all cases with the exception of CCl_4/O_2 etching of InP. Here it was found that the anisotropy of the etching process could be controlled by varying the fraction of O_2 in the feed; with ~40% O_2, the ratio was 4.

The utility of plasma-assisted etching as a technique for the dry processing of silicon is well documented (1). There is, therefore, strong interest in the extension of plasma etching techniques to the group III-V semiconductor materials system for use in the processing of opto-electronic devices. Although there have been a few reports on the plasma etching of III-V compounds (2-6), little is known about the etching characteristics of these materials. In this paper we report on the kinetics of etching indium phosphide (InP), gallium arsenide (GaAs), and gallium phosphide (GaP) at 300°C with etching gas combinations of oxygen (O_2) and either chlorine (Cl_2) or carbon tetrachloride (CCl_4) using atomic emission as a diagnostic aid.

Before discussing the extension of plasma techniques to the etching of III-V semiconductors, it is desirable to look first at the kinetics of the overall process. In general, the etching of a solid by reaction with a gas can be conveniently described as proceeding through several stages, any one of which may be rate limiting in the overall process: (*i*) the transport or diffusion of gas phase reactants to the surface; (*ii*) adsorption on the surface; (*iii*) product formation; (*iv*) product desorption; and (*v*) the transport of gas phase products from the surface. The overall chemistry can be "plasma assisted" in two ways: collisional processes in the discharge can cause the production of reactive species by dissociation of some precursor gas (1, 7), and bombardment of the substrate by energetic ions (and electrons) can enhance processes on the surface as well as aid in the evolution of products (8). The bombardment process generally is deemed responsible for anisotropy in the plasma etching profile.

The etching of III-V semiconductors with halogenated compounds can be inhibited by the low volatility of group-III halides. For this reason, the formation of chlorides has been the reaction of choice. The fact that product desorption is enhanced by ion bombardment of the surface has been used to advantage in the reactive ion etching of vertical walls as mirror facets in InP/InGaAsP stripe-geometry lasers (3). Our primary goal, however, is the maximization of the etching rate, while the anisotropy of the process is only

* Electrochemical Society Active Member.

Key words: gas discharge, plasma processing, indium phosphide, gallium arsenide, gallium phosphide.

of secondary interest. As a first-order approach to this goal, the rate of product desorption was augmented by raising the reactor temperature. In addition, by operating at a higher pressure than that of reactive ion etching, faster etching rates can be attained because of increased reactant number densities. An increase in rate occurs despite the concurrent reduction in the energetic-ion bombardment of the surface accorded by the reduced mean-free path of the ions. Extremely fast dry etching rates of up to several μm/min have been obtained with this approach, thus allowing the formation of deep features (> 75 μm) in reasonable periods of time. This technique has been applied successfully to the separation into individual chips of wafers of InP/InGaAsP light-emitting diodes (4).

Experimental Techniques

The plasma etching experiments were carried out in an Applied Materials Plasma II parallel plate reactor, described in Ref. (9), operating at 55 kHz. Wafers were placed ~7 cm from the center on the 66 cm diam grounded electrode, which was maintained at a temperature of 300°C. Reagent gases entered the reactor through a central opening in the grounded electrode with flow proceeding radially outwards. Gas flow was controlled with commercial mass flow controllers, although rotometers were used for some initial studies. Pressure, measured remotely with a capacitance manometer, was maintained independent of the gas flow by varying the pumping speed.

Etching experiments were performed on InP, GaAs, and GaP using Cl_2 or CCl_4, or either of these gases mixed with O_2. Carbon tetrachloride was withdrawn directly from the vapor over the liquid at room temperature. Sample substrates of {100} orientation were mechanically-chemically polished prior to use with 1% bromine in methanol. Etching masks were formed by photolithographically defining patterns of resist on 0.1-0.5 μm thick layers of plasma deposited silicon dioxide (SiO_2) or silicon nitride (Si_3N_4). These patterns were then transferred to the dielectric layer by plasma etching with 8% O_2/CF_4 followed by an O_2 plasma to strip the resist. Alternatively, for just etching rate measurements, the SiO_2 or Si_3N_4 etch masks were patterned by partially covering the surface with glycol phthalate wax, etching the exposed dielectric film with HF, and then stripping the wax with acetone. The SiO_2 masks did not etch appreciably with any of the gas combinations employed in this study, although some visible etching was observed with the Si_3N_4 masks. Etching depth and profile measurements were performed using scanning electron and optical microscopy. Etching depth measurements were also performed using a mechanical stylus (Tencor Instruments Alpha Stepper).

Optical emission intensities were measured through a quartz window on the side of the plasma reactor with a McKee-Pedersen Instruments MP-1018 B monochromator having 0.2 nm resolution and a photomultiplier detector. Chlorine atomic emission was monitored at the 837.59 nm line, which corresponds to the $3p^44p$ ($^4D_{7/2^o}$) → $3p^44s(^4P_{5/2})$ transition (10). For atomic oxygen, lines at 777.19, 777.42, and 777.54 nm were monitored simultaneously by increasing the spectrometer slit width so as to decrease the resolution. These lines correspond to fine structure of the $2p^33p(^5P_{3,2,1})$ → $2p^33s$ ($^5S_{2^o}$) transition (10, 11). For both Cl and O, the transitions observed were to the lowest lying excited state. This followed the initial excitation of a p-valence electron to a p orbital in the next higher lying energy shell. Transitions to the ground state, occurring in the vacuum ultraviolet, could not be observed with this experimental configuration.

Atomic emission from Cl and O was monitored for both the Cl_2/O_2 and the CCl_4/O_2 chemical systems. It should be noted, however, that for most experiments etching rate and optical emission measurements were not performed simultaneously because of difficulties in maintaining optical alignment while inserting and removing samples. Any difference was considered to be insignificant because of the large chamber area (~3400 cm²) relative to wafer size (~0.5 cm²), the large emission sampling volume (no lenses were employed), and the fact that the observed etching characteristics did not change with surface area or number of wafers etched (*i.e.*, no "loading effect" was observed.) A corroboration of this supposition was obtained by performing several experiments in which etching and optical data were taken simultaneously.

The radiative lifetimes of electronically excited $Cl(^4D_{7/2^o})$ and $O(^5P_{3,2,1})$ are ~4.5 and 2.0 nsec, respectively (10). This is at least two orders of magnitude lower than the mean-free time between quenching collisions. Based on this alone, the emission intensity may be taken as a direct measure of the number density of the emitting state. However, if the population of the relatively long-lived lower state of the observed O atom transition [radiative lifetime ~120 μsec (10)] were to build such that significant re-absorption of emitted light occurred over the long optical pathlength, then radiation trapping would result and the emission intensity would no longer be a direct measure of the emitting-state number density. In comparison, the radiative lifetime of the lower state of the observed Cl atom transition is much shorter [~725 nsec (10)] making a population build-up and subsequent radiation trapping less likely to occur.

Results and Discussion

It was apparent in all experiments that some initiation process had to occur before etching proceeded. This is illustrated in Fig. 1 by a delay of about 2.8 min before the onset of uniform CCl_4 plasma etching of InP. It is postulated that this induction period is associated with the slow removal of a thin surface layer of native oxide. Indeed, it was observed that wet etching with HF (for InP) immediately prior to plasma etching helped to minimize the onset delay, while O_2 plasma exposure prior to etching exaggerated the induction time. These observations are consistent with reports (6) in which slow etching was observed following the growth of native oxide films on GaAs. Furthermore, it was found that the initiation proceeded unevenly across the wafer surface, indicating a nonuniform penetration of the barrier layer. This resulted in a rough surface contour. Simple heat-treatment or sample preheating at

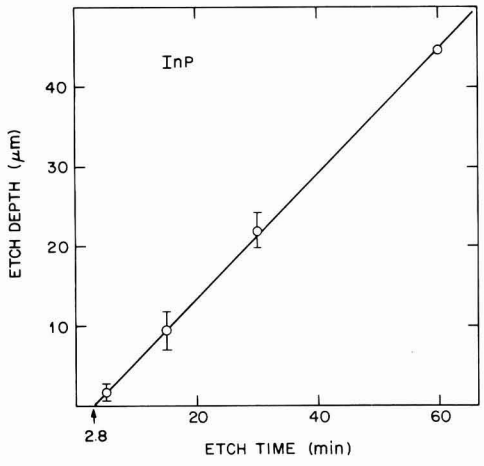

Fig. 1. Time evolution of the etching of InP in a 0.15 Torr, 500W (0.15 W/cm²), 55 kHz, CCl_4 discharge. Error bars represent one standard deviation.

the plate temperature of 300°C did not affect the observed behavior, although there apparently was no penetration of the native oxide for plate temperatures below about 270°C. The precise role of heating in the initiation process has yet to be determined, since exposure to the plasma of wafers which are not thermally bonded to the reactor plate can result in surface temperatures significantly above the plate temperature (14). Unfortunately, in the present work the maximum attainable reactor temperature of 300°C prevented *in situ* heat-treatment studies at higher temperatures.

The potential for surface heating by exposure to the plasma would portend that the near-surface loss of the group-V element by thermally induced out-diffusion (15, 16) plays an important role in the kinetics of the etching process. It is possible that thermally induced breakdown of the lattice structure will enhance the rate of reaction and could account for the extremely fast etch rates observed in this study. Obviously there is a need for further work to determine the precise nature of the temperature dependence of the etching process.

In order to gain information on the etching kinetics, different plasma conditions were examined. In particular, the importance of various chemical species was probed by looking at the effect on the discharge chemistry and etching behavior of the addition of O_2 to either Cl_2 or CCl_4. This is analogous to similar studies on the role of oxygen in the CF_4/O_2 plasma etching of silicon where atomic fluorine was identified as the principal etchant (11, 12, 17). Furthermore, in these studies oxygen was found to compete with fluorine for active surface sites and to increase the F atom number density by oxidizing fluorocarbon radicals.

Figure 2 shows the effects of added O_2 on the CCl_4 and Cl_2 plasma etching rates of InP, GaAs, and GaP. In all cases the addition of ~6 sccm of O_2 resulted in an increase in the plasma etching rates. Plotted in Fig. 3 are the intensities of the optical emission from both electronically excited Cl and O. Although these data are a direct measure only of the number density of the emitting state, they do provide insight into the discharge chemistry.

In order to interpret the data in Fig. 2 and 3 it is desirable first to look at oxygen emission from CCl_4/O_2 and Cl_2/O_2 discharges. Interestingly, for both these chemical systems the intensity of O atomic emission was found to rise linearly with the cube of the fraction of O_2 (f_{O_2}) in the feed. This power law dependence, plotted in Fig. 4, was used only for data smoothing and interpolation between points, and no attempt was made to interpret its meaning because of the limited amount of information available on the discharge chemistry. The saturation of the O atomic emission intensity above ~70% O_2 in Cl_2 is believed to be due to radiation trapping.

For the CCl_4/O_2 system, we propose that O atomic emission rises slowly with increasing O_2 addition to the feed (see Fig. 4) because oxygen is consumed by oxidation of carbon species in a manner analogous to the chemistry of the CF_4/O_2 discharge (11, 12, 17). These oxidation reactions thus act as sinks for both available oxygen and carbon species. Since reaction with the latter also provides a loss mechanism for Cl, their removal by oxidation would be expected to result in a concurrent increase in the relative amount of Cl. Indeed the Cl atomic emission intensity, normalized for dilution, was observed to linearly track the O atomic emission

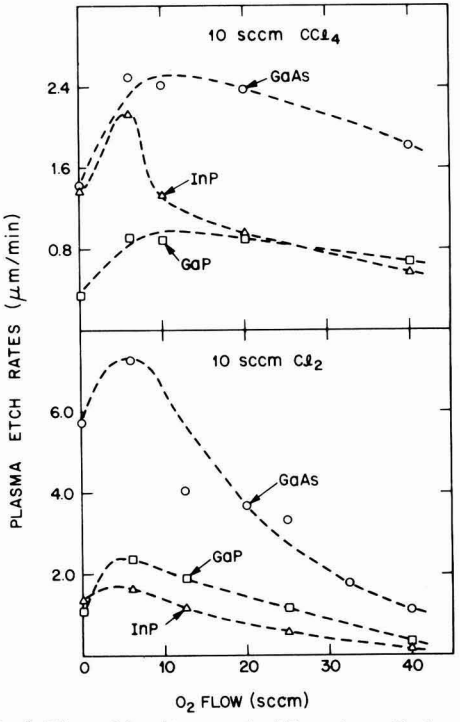

Fig. 2. Effects of O_2 addition on the CCl_4 (top) and Cl_2 (bottom) plasma etching of InP (triangles), GaAs (circles), and GaP (squares). Experimental conditions: 0.05 Torr, 750W (0.23 W/cm^2), 55 kHz. (Note the difference in vertical scales between the CCl_4 and Cl_2 curves.)

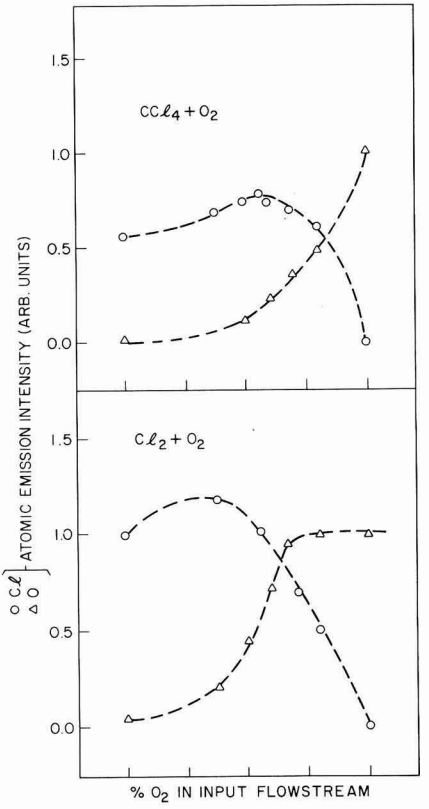

Fig. 3. Intensity of the optical emission from electronically excited Cl($^4D_{7/2} \rightarrow {}^4P_{5/2}$) and O($^5P_{3,2,1} \rightarrow {}^5S_2$) plotted as a function of O_2 concentration in a 0.05 Torr, 750W (0.23 W/cm^2), 55 kHz, CCl_4/O_2 (top) or Cl_2/O_2 (bottom) discharge. Circles and triangles represent Cl and O data, respectively.

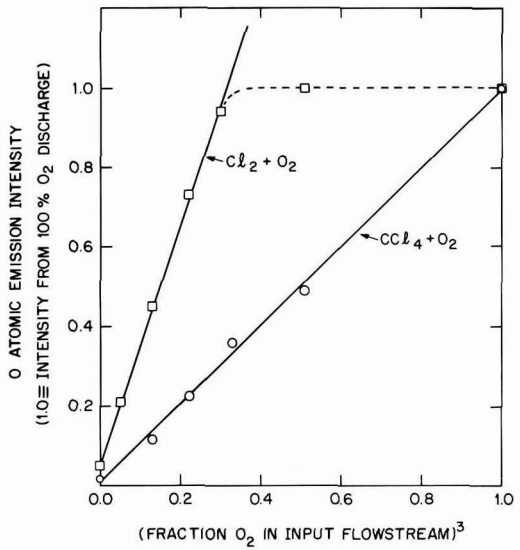

Fig. 4. Intensity of O atomic emission as a function of the cube of the O_2 fraction in the feed gas for 0.05 Torr, 750W (0.23 W/cm^2), 55 kHz, Cl_2/O_2 (squares) and CCl_4/O_2 (circles) discharges.

(see Fig. 5). Thus the addition of a small amount of O_2 to a CCl_4 discharge resulted in an increase in the number density of electronically excited Cl and a decrease in the amount of residual carbon. The importance of the latter process is to minimize the accumulation of carbon compounds on exposed surfaces, including those to be etched. This manifests itself as improved morphology of etched surfaces.

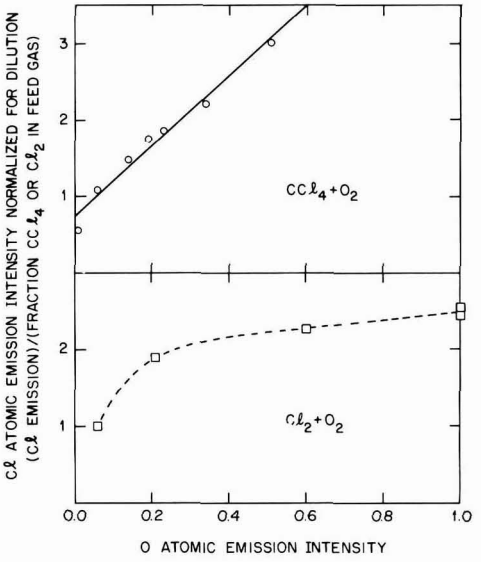

Fig. 5. Intensity of Cl atomic emission, normalized for dilution of the feed gas by added O_2, plotted as a function of the O atomic emission intensity. The O atomic emission data has been smoothed by fitting to the cube of the O_2 fraction in the feed (see Fig. 4). Experimental conditions: 0.05 Torr, 750W (0.23 W/cm^2), 55 kHz, CCl_4/O_2 (top) or Cl_2/O_2 (bottom) discharge.

A carbon-containing sink for available oxygen does not exist in the Cl_2/O_2 system. This resulted, as shown in Fig. 4, in a much faster rise in the O atomic emission intensity with added O_2, which approached the level of a pure O_2 discharge when f_{O_2} was only about 0.7 ($f_{O_2}{}^3 = 0.34$). Reference to the lower half of Fig. 5 shows, however, that the addition of oxygen to a Cl_2 discharge still produced an increase in the relative amount of excited Cl. In this case increased Cl production could occur because of the reaction of O with Cl_2 to give ClO. ClO can be subsequently dissociated in the discharge to Cl + O or react with another O to give Cl + O_2. The overall result would then be the production of two Cl atoms and the regeneration of oxygen.

The above results suggest that the addition of O_2 to either a Cl_2 or CCl_4 discharge enhances the production of atomic chlorine. In order to see how this affects the etching process, it is useful to look at Fig. 6. Here, it is seen that the etching rates of GaAs, GaP, and InP can be linearly correlated with the Cl emission intensities, and that for either GaAs or GaP this correspondence occurs regardless of the Cl source gas, Cl_2 or CCl_4, or the amount of O_2 in the feed. (Figure 6 does not show results obtained from the etching of InP with CCl_4/O_2 because this system was found to be anomalous and will be discussed later.) These findings suggest that atomic chlorine is the principal etchant and furthermore, that the Cl supply is the rate-limiting factor. The latter implication was substantiated by the observation that, in a CCl_4 discharge, the GaAs and GaP etching rates are a direct function of the total pressure. A similar study of etching rate dependence on total pressure in a Cl_2 discharge was not possible due to experimental difficulties in maintaining a constant pressure and rf power level at the required higher total pressures. It should also be noted that this argument is consistent with the observation of only limited anisotropy in the etching profile. This is to be expected since increased reactant adsorption is more important than enhanced product desorption and active site creation by ion bombardment. In this study, the vertical etching rate was less than twice the rate of undercutting.

It follows from the above discussion that the etching of GaAs or GaP with either a Cl_2/O_2 or a CCl_4/O_2 discharge can be modeled by a simple scheme in which the

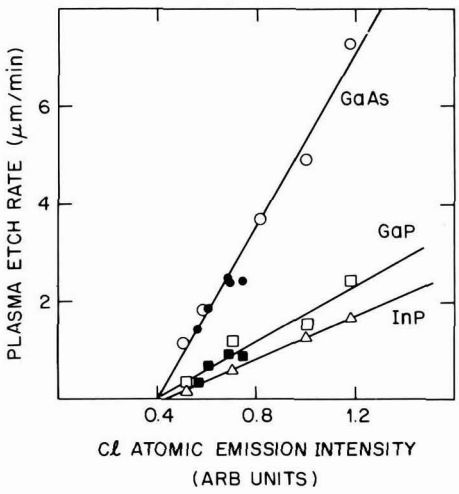

Fig. 6. Plasma etch rates of GaAs (circles), GaP (squares), and InP (triangles) plotted as a function of the Cl atomic emission intensity observed in 0.05 Torr, 750W (0.23 W/cm^2), 55 kHz, CCl_4/O_2 (closed symbols) and Cl_2/O_2 (open symbols) discharges. Note that for InP only data from the latter discharge are presented.

etching rate depends only on the number density of atomic chlorine and not its source. However, this model does not account for the etching of InP with CCl_4/O_2. While the InP etching rate in a Cl_2/O_2 plasma can be linearly correlated with the Cl atomic emission (see Fig. 6), the etching rate in a CCl_4/O_2 plasma cannot. With either a neat CCl_4 or Cl_2 discharge, at the same total pressure, InP is etched at the same rate (1.37 μm/min) even though the intensity of Cl emission is significantly lower with CCl_4 than with Cl_2 (0.56 *vs.* 1.00, respectively). In Fig. 6 it is seen that an emission intensity of 0.56 corresponds to an etching rate on the InP curve of about 0.28 μm/min, which is only 20% of the observed InP etching rate, leaving an 80% shortfall that requires the postulation of additional etchant species. We believe the most likely candidates for these new etchants are low valent carbon-chlorine moieties, analogous to the carbon-fluorine fragments derived from fluorocarbon discharges (18). However, it is unclear when InP differs from GaAs and GaP. Further study is clearly necessary in order to explain this difference.

Figure 7 shows that the degree of anisotropy in the InP etched profile is a strong function of the ratio of O_2 to CCl_4 in the feed gas. The anisotropy is actually enhanced at low O_2/CCl_4 flow ratios, a factor taken advantage of in Ref. (4) to limit undercutting in the plasma separation of InP device wafers. However, this behavior cannot be due to a protective coating of oxide as originally suggested in Ref. (4). Such a scheme would be inconsistent with the observation of this study that the etching is isotropic at large O_2/CCl_4 ratios. Instead, the data can be rationalized as follows: the bombardment of the sample surface by ions (accelerated vertically between the electrodes) enhances the reaction of adsorbed carbon-chlorine moieties, creates additional active sites, and speeds up product desorption. In the presence of oxygen the vertical etching rate is further enhanced since the oxidation of adsorbed CCl_4 creates additional Cl on the surface. As the proportion of O_2 to CCl_4 increases, gas phase oxidative reactions become more important, resulting in a decrease in the number density of carbon-chlorine species and an increase in the number density of chlorine atoms. At relatively high levels of O_2, the CCl_4/O_2 discharge would be expected to etch isotropically, as does a Cl_2/O_2 discharge. Indeed, this is seen to occur in Fig. 7 at about the 60% O_2 level. Finally, one would expect that at some intermediate O_2 level the degree of anisotropy should reach a maximum; this was found to occur at about 38% O_2 level.

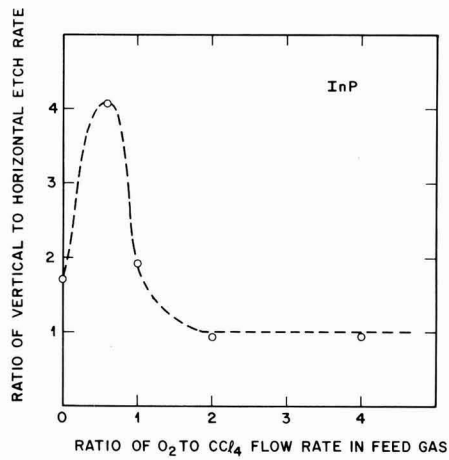

Fig. 7. The degree of anisotropy in the plasma etching of InP as a function of the fraction of O_2 in the feed of a 0.05 Torr, 750W (0.23 W/cm^2), 55 kHz, CCl_4/O_2 discharge.

Conclusion

Addition of oxygen to either a chlorine or carbon tetrachloride plasma increases the relative amount of atomic chlorine. With CCl_4, the reaction of oxygen with carbon-containing species generates additional Cl. With Cl_2, oxygen atoms dissociate molecular chlorine via the intermediate ClO. In the etching of GaAs or GaP with either CCl_4 or Cl_2 (and InP with Cl_2) discharges, oxygen addition acts primarily to enhance Cl production. In these cases the etching rates are strictly dependent on the Cl emission intensity, irrespective of the other constituents. In contrast, carbon-chlorine species actively participate in the CCl_4/O_2 etching of InP. Resulting from this is an ability to control the anisotropy of the InP etching profile by varying the ratio of O_2 to CCl_4 in the feed.

Extremely fast etching rates have been obtained for all three semiconductors. Thus the etching of large amounts of material, formerly possible only by wet-chemical processing, is now amenable to dry-chemical processing. The price for this enhanced rate of etching is reduced anisotropy. Despite this, there are immediate applications for this technique in III-V device processing (4).

Acknowledgments

The authors wish to thank V. G. Keramidas and S. Nygren for providing the substrates used in the study, D. D. Roccasecca for help with the processing, and T. M. Mayer for use of the monochromator. We also gratefully acknowledge many stimulating discussions with R. H. Saul, R. J. Roedel, R. A. Gottscho, H. Temkin, and M. J. Vasile. The experimental help of C. F. King and C. L. Hollien were invaluable to the completion of this work.

Manuscript submitted May 15, 1981; revised manuscript received Dec. 9, 1981. This was Paper 265 presented at the Denver, Colorado, Meeting of the Society, Oct. 11-16, 1981.

Any discussiion of this paper will appear in a Discussion Section to be published in the June 1983 JOURNAL. All discussions for the June 1983 Discussion Section should be submitted by Feb. 1, 1983.

Publication costs of this article were assisted by Bell Laboratories.

REFERENCES

1. See, for example, C. M. Melliar-Smith and C. J. Mogab, in "Thin Film Processes," J. A. Vossen and W. Kern, Editors, Academic Press, New York (1978).
2. C. B. Burstell, R. Y. Hung, and P. G. McMullin, *IBM Tech. Discl. Bull.*, **20**, 2451 (1977).
3. L. A. Coldren, K. Iga, B. I. Miller, and J. A. Rentschler, *Appl. Phys. Lett.*, **37**, 681 (1980).
4. R. H. Burton, H. Temkin, and V. G. Keramidas, *ibid.*, **37**, 411 (1980).
5. L. A. D'Asaro, A. D. Butherus, J. V. DiLorenzo, D. E. Iglesias, and S. H. Wemple, "Proc. Symp. GaAs and Related Compounds," p. 267, American Inst. Phys. Conf. Ser. No. 56 (1981).
6. G. Smolinsky, R. P. H. Chang, and T. M. Mayer, *J. Vac. Sci. Technol.*, **18**, 12 (1981).
7. J. W. Coburn and H. F. Winters, *J. Vac. Sci. Technol.*, **16**, 391 (1979).
8. J. W. Coburn and H. F. Winters, *J. Appl. Phys.*, **50**, 3189 (1979).
9. R. S. Rosler, W. C. Benzing, and J. Baldo, *Solid State Technol.*, 45 (June 1976).
10. See, for example, R. F. Bacher and S. Goudsmit, "Atomic Energy States," McGraw Hill, New York (1932); A. R. Striganov and N. S. Sventitskii, "Tables of Spectral Lines of Neutral and Ionized Atoms," IFI/Plenum, New York (1968); "American Institute of Physics Handbook," D. E. Gray, Editor, McGraw Hill, New York (1972).

11. W. R. Harshbarger, R. A. Porter, T. A. Miller, and P. Norton, *Appl. Spectrosc.*, **31**, 201 (1977).
12. G. Smolinsky and D. L. Flamm, *J. Appl. Phys.*, **50**, 4982 (1979).
13. M. J. Vasile and G. Smolinsky, *J. Phys. Chem.*, **81**, 2605 (1977).
14. G. C. Schwartz and P. M. Schaible, in "Plasma Processing," R. G. Frieser and C. J. Mogab, Editors, p. 133, The Electrochemical Society Softbound Proceedings Series, Pennington, NJ (1981).
15. C. R. Bayliss and D. L. Kirk, *Thin Solid Films*, **29**, 97 (1975).
16. C. R. Bayliss and D. L. Kirk, *J. Phys. D*, **9**, 233 (1976).
17. C. J. Mogab, A. C. Adams, and D. L. Flamm, *J. Appl. Phys.*, **49**, 3796 (1978).
18 E. A. Truesdale, G. Smolinsky, and T. M. Mayer, *ibid.*, **51**, 2909 (1980).

Heat-Treatment Effect on Boron Implantation in Polycrystalline Silicon

C. H. Lee*,[1]

IBM Corporation, General Technology Division, East Fishkill, Hopewell Junction, New York 12533

ABSTRACT

Polycrystalline silicon (LPCVD) has been studied for contact, gate metal, and resistor application in integrated circuits. In this study the effect of heat-treatment on boron-implanted low pressure chemical vapor deposited polycrystalline is investigated. In general, grain growth and morphology change take place in both preimplant and postimplant heat-treatment. Namely, the poly-Si films after heat-treatment consist of more equal axed grains than the mosaic dendrite structures in the untreated samples. However, the pre-implant heat-treatment appeared to be more effective for grain growth because of lack of impurity hindrance of grain boundary movement. The sheet resistivity of the pre-implant heat-treated samples is predominantly controlled by ion redistribution, and that of the postimplant annealed samples is controlled by both morphology change and ion redistribution. Both kinds of samples showed much lower resistivity due to heat-treatment reduction of grain boundary trapping centers and significant resistivity reversal anneal due to redistribution of the implanted ions.

Polycrystalline silicon has been studied for contact, gate metal, and resistor applications in integrated circuits for more than a decade (1-9). Because of the uncontrollable nature of morphology, it is rare to find reproducible data on the basic properties of the polycrystalline films in literature as compared with single crystalline silicon (10). The author does not attempt to resolve the discrepancies in literature. However, boron doping by ion implantation does provide an additional dimension of variables for investigating the properties of polycrystalline silicon. In this paper some experimental results on the aspect of heat-treatment effect on boron implantation are presented.

Most of the polycrystalline silicon films that are used for integrated circuits are prepared from pyrolysis of SiH_4. Due to different preparation temperature, pressure, and ambients, the polycrystalline silicon films have grain size varying from 100 to 2000Å (11-14). In order to obtain a better control of uniformity and reproducibility, the low pressure and temperature (LPCVD at 600°-700°C) process (15, 16) of SiH_4 pyrolysis has recently been investigated. This process generally provides polycrystalline Si of about 200-1000Å in grain size (16, 17) and resistivities greater than 10^6 Ωcm.

The electrical characteristics of polycrystalline silicon have been discussed by various groups of investigators (11, 13, 18-22). In general, a grain boundary trapping model has been successfully developed to explain the mobility and the doping characteristics. Briefly, the grain boundary contains a large number of trapping states that trap the conductive carriers and create a potential barrier. The barrier at the grain boundary reduces the mobility of the carriers moving from one grain to another. In case the trapping states are assumed to have the same energy level, the model can simply be expressed as

$$N_{cc} = N_{td} - N_{gb}$$

where N_{cc} is the free carrier concentration, N_{td} the total doping concentration, and N_{gb} numbered trapping centers. If the doping concentration is low as compared with the grain boundary trapping state density, very few carriers contribute to conduction, depending on the trapping state energy. In this case, the mobility decreases with the increase of doping concentration due to the increase of barrier height. On the other hand, for high doping concentrations carrier tunneling enhances with the increase of concentration in excess of the trapping state density. As a result, not only are more carriers available for conduction, but they can also move across the boundary faster. For boron-doped LPCVD polycrystalline Si samples, it was estimated that the trapping state density is near 6×10^{18} cm^{-3} with an energy level of about 0.37 eV (19).

Experimental

The samples of this work consist of films of different thicknesses, from 1000 to 4000Å, which are deposited on the oxidized Si wafers by means of SiH_4 (25%) pyrolysis in N_2 under a pressure of about 0.5 Torr at about 620°C. On the surface of the samples, a screen oxide of 500Å was also pyrolytically deposited at a temperature of 800°C by means of the SiH_4 and O_2 reaction. As illustrated in Fig. 1, the samples were categorized into two groups for convenience of selecting a proper energy for boron implant. The implant conditions are such that for the thinner samples (<2000Å), the peak concentration is placed at the center of the film so that the sample may receive an optimum boron doping from the implant. For the thicker samples (>2000Å), a constant energy of about 50 keV is used in order to place the peak concentration at a depth of about three stragglers into the poly-Si film. By doing so, the samples would receive better than 98% of the implanted boron dose. In addition, they can be probed for sheet resistance free from contact problems after a low temperature activation anneal without significant redistribution of boron.

A set of these samples received a pre-implant heat-treatment of 2 hr at 1000°C for comparison with the untreated samples. The postimplant activation anneal

* Electrochemical Society Active Member.
[1] Present address: Motorola, Mesa, Arizona 85202.
Key words: LPCVD, grain growth, morphology, crystallinity, reversal anneal.

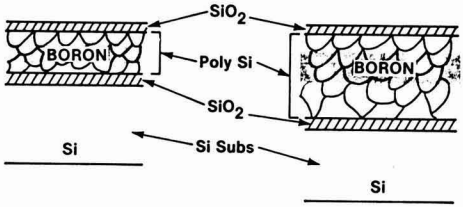

PROCESS CONDITION AND MEASUREMENT TECHNIQUE

(1) LPCVD Poly Si Samples

	THIN	THICK
	2000Å	3000Å
Gr. Size	400-800 Å	500-1200Å

Grown at 620°C on oxidized Si
Pressure: 0.5 Torr (100Å/min.)

(2) B^{11} Implant

Energy:	30 to 100 KeV (R_p – ½ sample thickness)
Dose:	10^{14} - 10^{15} cm^{-2}
Activation Anneal:	900°C/30 min. typical post implant anneal 500°C to 1000°C/30 min. for experiments

(3) Measurements: Optical Interferametry for thickness
4 point probe for Rs
TEM for morphology

Fig. 1. A sketch of samples with a list of process condition and measurement techniques.

was kept for 30 min at various temperatures. The sheet resistance was measured after the screen oxide was stripped by means of a set of four-point probes of tungsten carbide with a 25 μm spacing and a load of 50g in weight.

Results and Discussion

In order to facilitate reasoning the sheet resistance data, the grain sizes of a set of samples are determined by means of a transmission electron micrograph. As an example, the micrographs of two of these samples, one untreated and another annealed at 1000°C for 2 hr in N_2, which did not receive ion implant, are shown in Fig. 2(a) and (b), respectively. The untreated sample does not only have a smaller average grain size but also poorer morphology of more dendritic grains, while the annealed sample consists of more equal axed grains. This is a positive indication that grain growth and crystallinity improvement occur simultaneously during the high temperature and long time of heat-treatment. The rest of this set of samples received a boron implantation of 1.5×10^{14} ions with heat-treatment at various conditions. The results, as shown in Table I, clearly indicate that the pre-implant annealed samples showed the largest grain size and lowest sheet resistance. Apparently, without impurity hindrance, grain growth and crystallinity improvement are more effective. The postimplant heat-treated sample shows that many grains recrystallized into equal axed structures from the dendritic matrix, but not so much of growth as the pre-implant annealed samples. For example, the size of the postimplant annealed, 2000Å sample is slightly larger than that of its untreated counterpart. The 4000Å sample, however, showed a smaller average grain size than the untreated one. This can be attributed to the implant damage effect, which becomes significant in the thicker samples of larger grain size. Namely, the smaller equal axed grains are grown from the matrix of the damaged, dendritic material of larger grain size. Due to impurity hindrance, the grains did not grow to a large grain size, but crystallinity is improved. The sheet resistance of the postimplant treated samples are lower than that of the untreated and higher than the pre-implant annealed samples due to grain size and morphology improvement, respectively.

Table I. Grain size effect on R_S

Sample thickness	2000Å Grain (Å)	2000Å R_s (kΩ/□)	4000Å Grain (Å)	4000Å R_s (kΩ/□)
B^{11} dose (cm^{-2})		1.5×10^{14}		1.5×10^{14}
As-grown and (900°C/30 min, activation)	660	96.1	1100	102.4
1000°C/2 hr, and (900°C/30 min, activation)	950	10.5	1300	18.5
Post I/I, 1000°C/2 hr	890	12.1	950	29.7

As a function of the postimplant annealing temperature, the sheet resistances of a set of samples doped with 1.5×10^{14} ions/cm^2 are plotted in Fig. 3. As labeled along the curves, the data are from the samples of 2000 and 4000Å in thickness. They are grouped by the pre-implant anneal from the untreated samples with significant difference in sheet resistance. In general, in the untreated samples the sheet resistance of the 2000Å samples gradually decreases as the activation temperature increases because of the increase of activated boron concentration (Fig. 3, curve A). For the 4000Å samples (curve B), the general sheet resistance trend is similar for those annealed in the temperature range below 800°C. However, the resistance value is much lower due to a larger grain size in the thicker films. As soon as the activation anneal temperature increases further, a significant reversal anneal phenomenon occurs. This phenomenon is believed to be caused by redistribution of boron. Since the 4000Å sample is thicker, many boron atoms are redistributed to a wider range with a concentration below the trapping state density as if the dopant were lost from redistribution. The boron concentration in the 4000Å sample would be about one-half of that in the 2000Å sample after an ultimate redistribution anneal. The sheet resistance thus becomes higher, depending on the boron dose and the trap density. When

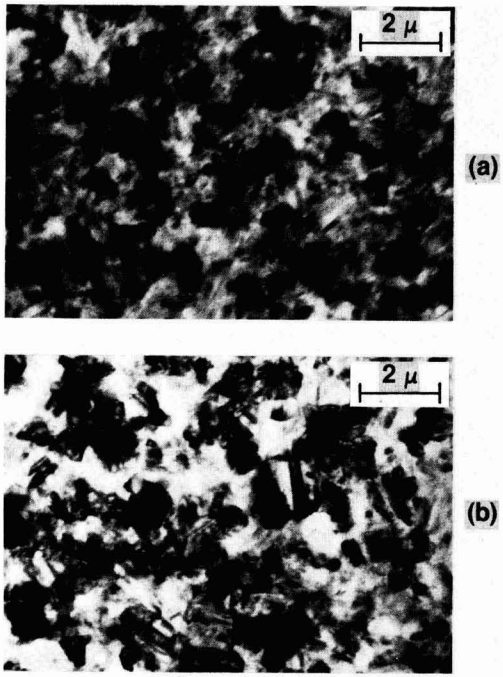

Fig. 2. Transmission electron micrographs from (a) as grown and (b) 1000°C/2 hr annealed samples of 4000Å in thickness.

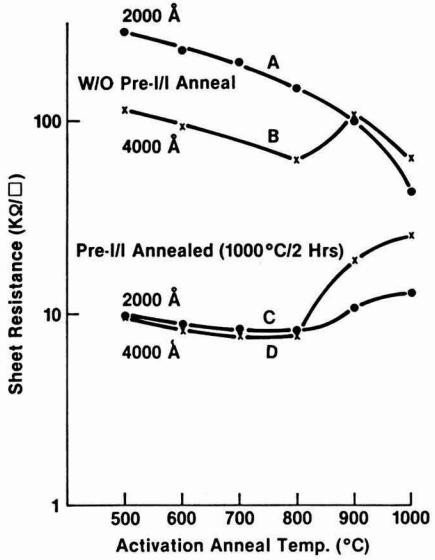

Fig. 3. Sheet resistance vs. boron activation temperature (1.5×10^{14} cm^{-2}).

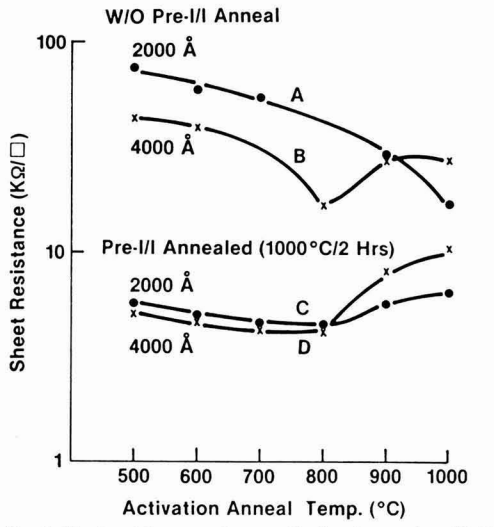

Fig. 4. Sheet resistance vs. boron activation temperature (2×10^{14} cm^{-2}).

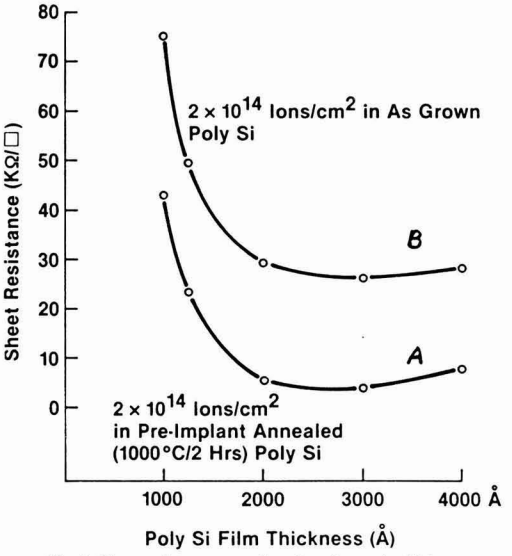

Fig. 5. Sheet resistance as a function of sample thickness

the annealing temperature is further increased, the sheet resistance resumes its decreasing trend, due to reduction of trapping states from crystallinity improvement.

For the second group of samples, a pre-implant heat-treatment was carried out at 1000°C for 2 hr. The implant and the activation anneal conditions are identical to those for the first set of experiments. As shown in curves C and D of Fig. 3, the sheet resistance of this group of wafers is much smaller than that of the untreated samples. This is caused by grain growth and morphology change from the pre-implant heat-treatment as discussed. Another characteristic of this group of samples is that the differences of sheet resistance between the 2000 and 4000Å samples are generally very small in the lower activation temperature range. This can be explained as follows. At low temperatures, boron ions are activated and similarly redistributed in both kinds of samples. In addition, the difference of crystallinity of the two kinds of samples after pre-implant anneal is smaller as compared with the untreated samples described earlier in the paper. However, when the activation is greater than 800°C, both the 2000 and 4000Å samples showed reversal anneal. The larger magnitude of resistance increase in the 4000Å samples is mainly due to a lower concentration of boron after redistribution. Since the conductivity of poly-Si is very sensitive to the doping level in the doping range of interest, minor difference (because of redistribution) can give significant difference in sheet resistance.

A similar set of samples that received a dose of 2×10^{14}/cm^2 of boron generally gave a much lower sheet resistance with the same trend of variation with the activation temperatures, as shown in Fig. 4. However, in the case where the dosage is lower than the 10^{14} range, the sheet resistance may change to a greater extent because the carrier concentration of the 4000Å sample after activation anneal is below the trapping state density.

As a function of sample thickness, the sheet resistances of the two sets of samples that received 2×10^{14} ions/cm^2 of boron implantation and activated at 900°C for 30 min are plotted in Fig. 5. As indicated in the figure, curve A represents the samples that also received a pre-implant anneal at 1000°C for 2 hr, and curve B is from the samples implanted in the untreated poly-Si. Because of the difference of the initial condition in the material, two distinct sets of data are obtained: namely, the sheet resistances of the pre-implant annealed samples are lower than that of the untreated samples because of the improvement of crystallinity from the heat-treatment.

In general, for the 2000Å and thicker samples the sheet resistance is less dependent on the sample thickness. It becomes more thickness dependent when the sample is thinner. In this case, the thinner samples have higher sheet resistances not only because of smaller grain size, but also receive a boron dose less than the implanted dose due to the loss into the dielectrics. However, for the thicker samples, very little variation of sheet resistance with sample thickness is observed, due to the fact that the activated boron is still concentrated in the three stragglers range of the poly-Si film. It happens that the amount of boron that spreads out in the 4000Å samples is below the trapping

state density, and it does not contribute carriers to conduction.

Another series of experiments were conducted to investigate the sheet resistance and implant dose relation. These experiments include two sets of samples 2000 and 4000Å in thickness, which receive a high temperature and long-time anneal (1000°C, 2 hr) under the pre-implant and postimplant conditions. The pre-implant annealed samples also see an additional boron activation heating cycle of 900°C for 30 min after the wafers were implanted. The results in terms of sheet resistance as a function of implant dose are plotted in Fig. 6. In general, the sheet resistance varies by two orders of magnitude with an implant dose change of a factor of less than seven, regardless of the process history of the samples. This observation is consistent with all of the literature data (23, 24) in trend but not in absolute values. Simply, the doping level is marginally above the trapping state density, which depends on the morphology of the poly-Si films. Regarding the relative magnitude of the sheet resistances of the samples in Fig. 6, the pre-implant annealed samples have lower values because they have larger grain sizes for the corresponding sample thickness. The 4000Å samples have higher sheet resistances, due to the sample thickness that led to a much lower concentration of conductive carriers.

Summary

The sheet resistance of the boron-implanted polycrystalline Si varies significantly with process history. Both the implant doping profile and the poly-Si morphology play a very important role in the sheet resistivity. Briefly, pre-implant heat-treatment effectively reduces grain boundary trapping centers because of grain growth and crystallinity improvement. The sheet resistance becomes less sample thickness-dependent at the relatively low activation temperatures.

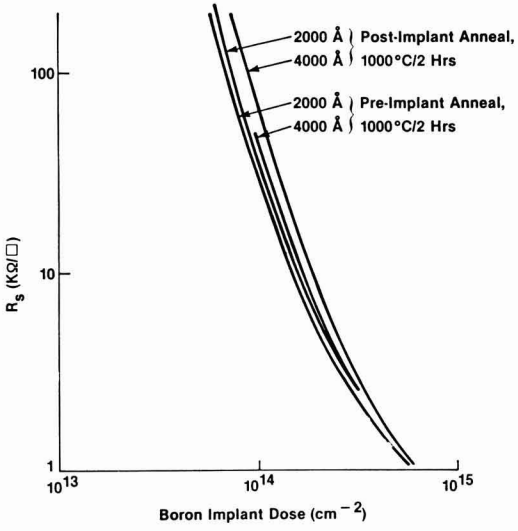

Fig. 6. Sheet resistance as a function of boron dose

Postimplant heat-treatment showed crystallinity change from more dendritic to more equally axed grain structures, but not much change of grain growth. The sheet resistance showed strong sample thickness dependence for those activated at lower temperatures. Reversal anneal of the sheet resistance was seen in both cases at an activation temperature of about 900°C for a half-hour anneal, mainly caused by redistribution of the implanted boron profiles.

Acknowledgment

The author wishes to acknowledge the help from S. Barbee, G. Devine, and S. Makarewicz for poly-Si and pyrolytic SiO_2 deposition, from J. Gardner and J. Seaboldt for ion implant, from R. Hallock and S. Woehlkins for annealing the samples, from E. Irene and R. Anderson for morphology assessment, and from R. Pistor for sheet resistance measurement for most of the work.

Manuscript submitted Dec. 12, 1980; revised manuscript received Oct. 9, 1981.

Any discussion of this paper will appear in a Discussion Section to be published in the June 1983 JOURNAL. All discussions for the June 1983 Discussion Section should be submitted by Feb. 1, 1983.

Publication costs of this article were assisted by IBM Corporation.

REFERENCES

1. F. Faggin and T. Kelin, *Solid State Electron.*, **13,** 1125 (1970).
2. C. H. Fa and T. T. Jew, *IEEE Trans. Electron Devices*, **ed-13,** 290 (1966).
3. T. I. Kamins, *Solid State Electron.*, **15,** 789 (1972).
4. V. S. Davidson and F. Lee, *Proc. IEEE*, **57,** 1532 (1969).
5. L. E. Clark and D. S. Zonoglu, *Solid State Electron.*, **15,** 653 (1972).
6. F. D. King *et al.*, *ibid.*, **16,** 701 (1973).
7. T. D. Sedgwick *et al.*, *J. Electron. Mater.*, **2,** 309 (1973).
8. C. H. Siquin *et al.*, *IEEE Trans. Electron Devices*, **ed-21,** 712 (1974).
9. Y. Arazawa *et al.*, ISSCC Digest of Technical Papers, p. 209, Feb. 1978.
10. J. C. Irvin, *Bell Syst. Tech. J.*, **41,** 387 (1962).
11. M. E. Cowher and T. O. Sedgwick, *This Journal*, **119,** 1565 (1972).
12. Y. Yasuda *et al.*, Proceedings of the 5th Conference on Solid State Devices, Tokyo, (1973); *J. Jpn. Soc. Appl. Phys. Suppl.*, **43** (1974).
13. P. Rai-Choudhury and P. L. Hower, *This Journal*, **120,** 1761 (1973).
14. J. Y. W. Seto, *ibid.*, **122,** 701 (1975).
15. R. S. Rosler, *Solid State Technol.*, **20,** 63 (1977).
16. T. I. Kamins, *This Journal*, **126,** 833 (1979).
17. E. Irene, Private communication.
18. A. L. Fripp, *J. Appl. Phys.*, **46,** 1240 (1975).
19. J. Y. W. Seto, *ibid.*, **46,** 5247 (1975).
20. T. I. Kamins, *ibid.*, **42,** 4357 (1971).
21. F. C. Eversteyn and B. H. Put, *This Journal*, **120,** 106 (1973).
22. J. M. Andrews, *J. Electron. Mater.*, **8,** 127 (1979).
23. J. Y. W. Seto, in "Semiconductor Silicon," H. R. Huff and E. Sirtl, Editors, p. 241, The Electrochemical Society Softbound Proceedings Series, Princeton, NJ (1977).
24. T. Tsuchimoto *et al.*, in "Ion Implant in Semicond. Sci. Technology," Proc. Int. Conf. 4th, S. Namba, Editor, p. 605 (1975).

Enthalpies of Formation of Niobium Aluminides as Determined by the Knudsen Effusion Method

I. Shilo, H. F. Franzen, and R. A. Schiffman

Ames Laboratory and Department of Chemistry, Iowa State University, Ames, Iowa 50011

ABSTRACT

The high temperature thermodynamics and phase diagram of the Nb-Al system have been studied in the temperature range $1844 \leq T \leq 2146$ K and the composition interval $0 \leq \mathrm{Al/Nb} \leq 0.36$. A weight-loss-mass-spectrometer apparatus was used to measure the rates of effusion and ion intensities of aluminum during incongruent vaporization from a Knudsen cell. Surface depletion problems were solved by using special intermediate annealing sequences. The composition ranges of the Nb_2Al and Nb_3Al compounds and the niobium-rich solid solution are reported. Enthalpies of the reactions: $NbAl_y(s) = Nb(g) + y\ Al(g)$ were determined by the second law and third law methods. Enthalpies of formation for the compounds are: $\Delta H_{f,298}^{\circ}[NbAl_3] = (-130.5 \pm 8.4)$ kJ mol^{-1}; $\Delta H_{f,298}^{\circ}[Nb_2Al] = (-74.9 \pm 0.8)$ kJ mol^{-1}, and $\Delta H_{f,298}^{\circ}[Nb_3Al] = (-77.0 \pm 0.6)$ kJ mol^{-1}.

In modern technology the importance of refractory materials has greatly increased, and thermodynamic data are needed to meet current materials problems. For instance, niobium aluminide coatings for refractory metals exhibit useful high temperature resistance to oxidation.

The superconducting behavior of Nb_3Al, and other physical properties of Nb-Al alloys have been well investigated by many laboratories (1) because of the high temperature of transition of Nb_3Al to the superconducting state, $T_c = 18.8$ K. Metallographic studies of samples quenched from high temperatures, as well as high temperature techniques (DTA, levitation thermal analysis, and simultaneous stepwise heating) (2-8), have been applied over several years by different groups to determine the correct phase diagram of the Nb-Al system. These studies yielded conflicting results, apparently as the result of difficulties in quenching the materials from high temperatures. The two most recently published phase diagrams (7, 8) are shown in Fig. 1. The 1966 phase diagram (7) shows lower melting point temperatures for all compounds and the phase boundaries are shifted toward higher aluminum contents. What is perhaps more important, the homogeneity range of the Nb_3Al compound is different in the two diagrams.

To date, no published reports of experiments carried out to determine the enthalpies of formation of Nb-Al compounds have appeared, although some estimated values of the heats of formation have been published (9, 10, 12, 13). In this paper we report the heats of formation of Nb-Al alloy compounds as determined by high temperature vaporization studies.

Experimental

Preparation and characterization.—Alloy compositions were prepared by arc melting 20g specimens under an argon atmosphere. The starting materials were niobium turnings (99.5%) from Alfa Products and aluminum rods (99.999%) from Spex Industries, Incorporated. Samples were remelted six times to assure homogeneity. Losses during the melting process were not critical since the initial compositions were determined before and after each effusion experiment. For wet chemical analysis, the samples were dissolved in HF, the niobium was retained on a Dowex I ion exchange resin, and aluminum was titrated with ethylenediaminetetraacetic acid at pH 5. The initial compositions were also determined by back calculation from the initial mass and total mass loss after volatilization of the total aluminum content. Each sample was annealed in a tungsten crucible at ~1570 K in a vacuum induction furnace for 12 hr prior to introduction into the weight-loss-mass-spectrometer apparatus. Once loaded in the apparatus the sample temperature was raised to approximately 100 K below the temperature at which any observable mass loss occurred and the sample was annealed for 16 hr before data were taken. Samples were examined microscopically and by x-ray diffraction using a Hägg-Guinier camera to verify the existence of two phase mixtures.

Key words: thermodynamics, enthalpy, phase diagram, mass spectrometry.

Weight-loss-mass-spectrometric study (W-L-M-S).—High temperature W-L-M-S experiments were performed in a high vacuum chamber equipped with CAHN-RH microbalance and quadrupole mass spectrometer, U.T.I. 100 C, 1-400 AMU. The chamber was pumped by means of a VHS-4 diffusion pump, the residual pressure being around 5×10^{-3} Pa.

Powdered samples were contained in semitoroidal TaC liners. The samples and liners were introduced into tungsten effusion cells with knife edge orifices at the bottom. The aluminum vapor flux was directed toward the mass spectrometer below the furnace. Samples were heated by a tungsten-mesh resistance element. The temperature was measured by a tantalum sheathed tungsten-rhenium thermocouple, the junction of which was located within the radiation field of the tungsten mesh furnace and about 0.5 cm from the Knudsen cell. The W-Re T/C was calibrated against an optical pyrometer which was in turn calibrated by the sector method relative to the melting point of gold. The prism and window correction was determined separately. Temperature fluctuations inside the furnace were ±1 K.

Ion intensities were taken as the difference between peak heights obtained by scanning the mass range of interest with the shutter open and the background in the same region with the shutter closed. An ionizer electron energy of 70 eV at 2 mA emission current was used.

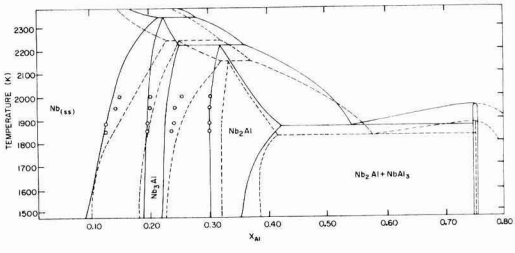

Fig. 1. The Nb-Al phase diagram. Solid line, *Jorda et al.* (8), dashed line, Lundin and Yamamoto (7), open circles, boundaries determined in this work.

For each individual experiment, rates of vaporization of aluminum at different temperatures were measured as composition changed from the starting two-phase region toward pure niobium, as aluminum was lost by sublimation. Simultaneously, during periods of constant vaporization rate, ion current (I_{Al}^+) measurements for calibration were taken by the mass spectrometer, thus providing a means of calibrating the ion current intensity against the pressure of aluminum as determined by the rate of mass loss. The aluminum pressures were calculated from the rate of vaporization using the Knudsen effusion equation with negligible Clausing correction

$$P_{Al}(\text{Pa}) = 3.81 \times 10^{-2} \cdot r[T/M_{Al}]^{1/2}/A \quad [1]$$

where r is the rate of mass loss in mg/min, T is the temperature in Kelvin, M_{Al} is the gram atomic mass of aluminum, and A is the orifice area in cm^2.

Although only 20-30 rates were measured per run, 200 I_{Al}^+ data points were collected and converted into P_{Al} utilizing the W-L-M-S calibration curve. A 250 mg sample of powdered Nb-Al alloy was used in the W-L-M-S studies.

Isotherms were obtained by collecting data points at different temperatures as a function of composition. This method gave rise to a potentially severe problem, namely surface depletion resulting from the relatively slow rate of diffusion of aluminum in the alloys. When the net rate of vaporization exceeds the rate of diffusion to the surface (especially at a composition where a phase transition occurs) the measured pressures are lower than the equilibrium pressures, leading to misinterpretation of phase widths and phase boundaries. Therefore the control of these two competitive processes was crucial. To provide this control a combination of low vaporization rate and special annealing sequences has been used. Low rates of vaporization were achieved by using small orifices (*e.g.*, 6.73×10^{-3} and 6.76×10^{-4} cm^2), and the measurement of pressures at temperatures at which the mass-loss rate was below 2×10^{-2} mg/min. It was found that the vaporization was not diffusion controlled when the rate of mass loss was below 3×10^{-3} mg/min. For the higher vaporization rates acceptable results were obtained when samples were annealed for 2-12 hr at temperatures ~200 K below the temperatures of measurement before each series of rate measurements. In order to maintain an adequate balance between vaporization and diffusion, the annealing temperatures were changed along with the composition changes. After each rate measurement (1 mg of aluminum vaporized) a set of ion intensities at five temperatures (1844, 1880, 1945, 1994, and 2146 K) was measured, once while the temperature was increased between measurements, and once while decreasing the temperature. At least 5 min were allowed to achieve thermal equilibrium at each experimental temperature. In the range $0.25 < X_{Al} < 0.35$ samples were annealed at least 10 times for 2 hr at 1670 K and two times for 12 hr at 1570 K. In the range $0.15 < X_{Al} < 0.25$ samples were annealed 10 times at 1720 K for 2-3 hr and two times for 12 hr at 1620 K. In the range $0.02 < X_{Al} < 0.15$ samples were annealed five times at 1820 K for 3 hr and two times at 1720 K for 12 hr.

Thermodynamic Calculations

The calculation of thermodynamic properties over all regions of the Nb-Al phase diagram was based on the general hypothetical vaporization reaction

$$NbAl_y(s) = Nb(g) + yAl(g) \quad [2]$$

where $y = X_{Al}/X_{Nb}$. Third law enthalpy changes for reaction [2] were calculated using the equation

$$\Delta H_{v,298}^\circ = T(\text{K})\,[-R \ln P_{Nb} \cdot P_{Al}^y + \Delta fef] \quad [3]$$

The numerical values of the Gibbs free energy function, $fef = (G_T^\circ - H_{298}^\circ)/T$, for Al(s), Al(g), Nb(s), and Nb(g) required for the evaluation of the measurements were taken from Hultgren (11).

Applying Neuman Kopp's rule to estimate the heat capacities of compounds formed from elements in the solid state as shown by

$$(C_p)NbAl_y(s) = (C_p)Nb(s) + y(C_p)Al(s) \quad [4]$$

the Δfef for the reaction

$$Nb(s) + yAl(s) = NbAl_y(s) \quad [5]$$

was assumed to be zero.

The second law enthalpies of vaporization at 298 K were obtained from the slopes when $-R \ln P_{Nb} \cdot P_{Al}^y + \Delta fef$ from [3] were plotted *vs.* $1/T$(K). Enthalpies of formation of $NbAl_y$ for compositions in the various phase diagram regions were then calculated using the equation

$$\Delta H_{f,298}^\circ[NbAl_y] = -\Delta H_{v,298}^\circ[NbAl_y] + \Delta H_{at,298}^\circ[Nb] + y\Delta H_{at,298}^\circ[Al] \quad [6]$$

Enthalpies of atomization, $\Delta H_{at,298}^\circ$, were taken from Hultgren (11).

In the niobium solid solution region, pressures of niobium were calculated from Raoult's law, $P_{Nb} = P_{Nb}^\circ \cdot X_{Nb}$, since the measured pressures of aluminum were repeatedly found to obey Henry's law, $P_{Al} = k \cdot X_{Al}$, to a high degree of precision. At the boundary between the Nb (ss) single phase and the Nb_3Al + Nb (ss) two phase region, $X_{Al}(T)$ values were obtained from the intersection of the Henry's law line and the horizontal (two condensed phases) line and thus niobium pressures could be calculated using Raoult's law. Pressures of niobium across the $Nb_3Al_{1\pm x}$ single phase region were calculated by Gibbs-Duhem integrations. The enthalpy of formation of the stoichiometric compound Nb_3Al was extrapolated from the enthalpy values in the single-phase region, since Nb_3Al does not exist in the single-phase region at low temperatures. The enthalpy of formation of Nb_2Al was calculated by the second law and third law methods using the same procedures. The aluminum pressures in the Nb_2Al + $NbAl_3$ two phase region were used to calculate the thermodynamic properties of $NbAl_3$. The $NbAl_3$ single-phase region is very narrow. Niobium pressures were not calculated by Gibbs-Duhem integration because of the mismatch in the range of temperature at which the pressures were measured in the Nb_2Al and $NbAl_3$ regions. It was therefore assumed that the equilibrium constant for reaction [2] for Nb_2Al at the stoichiometric composition equals the equilibrium constant at the phase boundary, *i.e.*, the variation in the activity of Nb_2Al with composition was neglected. Comparison with the other phases suggests that this approximation does not introduce a substantial error in the derived results.

Results

Sets of measurements of the variation of the ion intensities with temperature and simultaneously the rates of effusion of aluminum were performed. Aluminum equilibrium pressures were calculated from the rates using Eq. [1], and the mass spectrometer ion intensities were calibrated. The data from a selected calibration run are plotted in Fig. 2. The ion intensities were used to generate the Al partial pressure isotherms, which are shown in Fig. 3.

Solid solution region.—The experimental pressures of aluminum that were used to obtain the enthalpy changes in this region (as described in thermodynamic calculations) are given in Table I. The calculated pressures of niobium at each X_{Al} were obtained from the

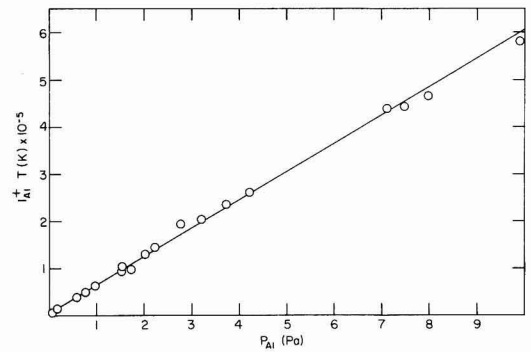

Fig. 2. Calibration curve for the mass spectrometer. Aluminum pressures as calculated by Knudsen Eq. [1] from the rate of effusion vs. the aluminum ion intensities times the temperature.

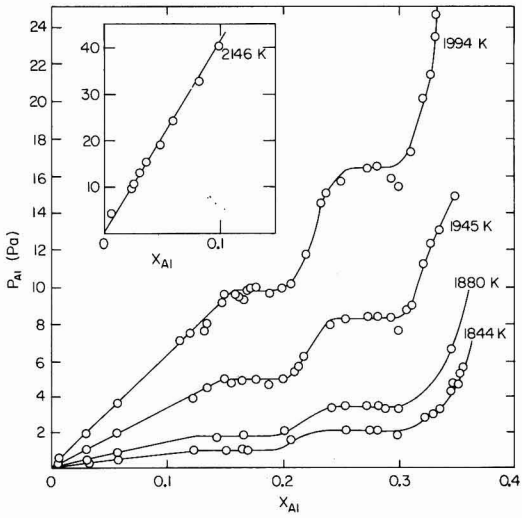

Fig. 3. Isotherms: Aluminum pressures vs. mole fraction aluminum

pressures of pure niobium (11) using Raoult's law. The linear least-squares fit for the pure niobium pressures is given by

$$\ln P_{Nb}^{\circ}(\text{Pa}) = (29.446 \pm 0.015) - (86{,}290 \pm 20/T \quad [7]$$

Enthalpy changes for reaction [2] were obtained for different X_{Al} and are given in Table II. The enthalpies of formation of the solid solution are shown in Table III.

$Nb_3Al_{1\pm x}$ phase.—Aluminum pressures and niobium pressures (obtained from the Gibbs-Duhem integration) were used to calculate the equilibrium constant

Table I. Pressures of Al(g) (in Pa ± 0.02 Pa) at selected mol fractions aluminum of Nb-Al solid solutions

T (K) \ X_{Al}	0.02	0.04	0.08	0.12
1772	0.091	0.14	0.32	0.48
1802	0.12	0.23	0.46	0.68
1827	0.17	0.37	0.71	0.97
1844	0.20	0.38	0.73	1.06
1856	0.25	0.51	1.01	1.52
1880	0.35	0.66	1.29	1.85
1945	0.73	1.46	2.82	4.16
1994	1.33	2.64	5.23	7.78
2146	8.27	16.3	32.53	48.94

Table II. Third law enthalpies of vaporization (±0.1 kJ mol^{-1}) for the niobium solid solution region

T (K) \ Y	$\Delta H_{v,298}^{\circ}$ kJ mol^{-1}		$NbAl_y(s) = Nb(g) + YAl(g)$	
	0.0204	0.04167	0.0867	0.1364
1722	730.65	739.81	758.56	778.68
1802	730.73	739.81	758.68	778.89
1827	730.73	739.77	758.52	778.10
1844	730.78	739.89	758.81	779.14
1856	730.78	739.77	758.60	778.77
1880	730.65	739.89	758.68	778.89
1945	730.86	739.94	758.77	778.98
1994	730.78	739.89	758.60	778.81
2146	730.82	739.81	758.43	778.26

for the reaction of vaporization of $Nb_3Al_{1\pm x}$ from which third law and second law enthalpies of vaporization as a function of y, ($y = X_{Al}/X_{Nb}$), were calculated. Third law values are shown in Table IV. Accurate pressures of aluminum were taken from the isotherms for which the diffusion problem was solved, and used in order to calculate the niobium pressures in the intermediate composition region, $0.244 < y < 0.312$. In the cases where those pressures were not available because of obvious diffusion problems, there is a blank space in Table IV. Second law enthalpies of vaporization and the average third law values are given in Table V. The extrapolated values to $y = 0.333$, namely stoichiometric Nb_3Al, are given as well. Sample second law plots for $X_{Al} = 0.196$ and $X_{Al} = 0.238$ are shown in Fig. 4. Since third law enthalpies of vaporization are preferred for the calculation of the enthalpy of formation, the preferred extrapolated value for Nb_3Al is $\Delta H_{f,298}^{\circ}[Nb_3Al] = (-77.0 \pm 0.6)$ kJ mol^{-1}.

Nb_2Al.—The experimental pressures of aluminum at $y = 0.5$ and the calculated third law enthalpies of vaporization of Nb_2Al are given in Table VI in the temperature range 1665-1994 K. Linear least-squares treatment of the pressures of niobium, which were derived by Gibbs-Duhem integration from $X_{Al} = 0.296$ to $X_{Al} = 0.333$, gave

$$\ln P_{Nb}(\text{Pa}) = (28.061 \pm 0.114) - (84{,}555 \pm 207)/T \quad [8]$$

The enthalpy of formation of Nb_2Al from the third law was calculated as $\Delta H_{f,298}^{\circ}[Nb_2Al] = (-74.9 \pm 0.8)$ kJ mol^{-1}. The second law treatment, which is shown in Fig. 5, gave $\Delta H_{v,298}^{\circ}[Nb_2Al] = (930.5 \pm 3.3)$ kJ mol^{-1}.

Table III. Second law and average third law enthalpies of vaporization for the solid solution region, and third law enthalpies of formation of the solid solutions

y	0.0204	0.04167	0.0867	0.1364
3rd law average $\Delta H_{v,298}^{\circ}$ kJ/mol	730.73 ± 0.09	739.86 ± 0.08	758.64 ± 0.15	778.73 ± 0.4
2nd law $\Delta H_{v,298}^{\circ}$ kJ/mol	730.5 ± 0.4	739.7 ± 0.5	759.4 ± 0.7	781.9 ± 2.9
$\Delta H_{f,298}^{\circ} \frac{1}{1+y}$ $NbAl_y$	2.665 ± 0.09	4.619 ± 0.08	8.008 ± 0.15	11.008 ± 0.4

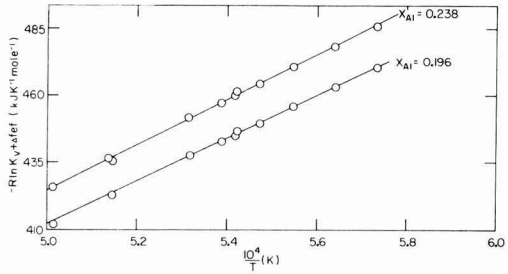

Fig. 4. Sample second law plots for $X_{Al} = 0.196$ and $X_{Al} = 0.238$.

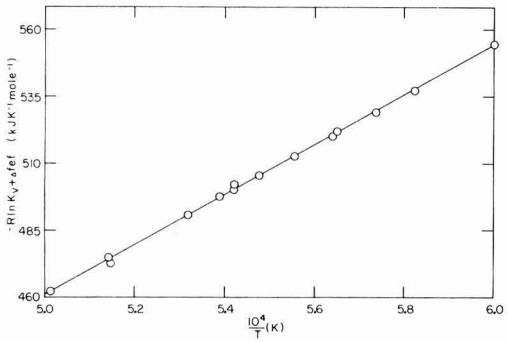

Fig. 5. Second law plot for the Nb_2Al phase using pressures of aluminum and niobium at $X_{Al} = 0.333$.

Nb_2Al + $NbAl_3$ two phase region.—Data were taken in the two phase region between $0.4 < X_{Al} < 0.6$. Pressures of aluminum for the reaction

$$2NbAl_3(s) = Nb_2Al(s) + 5Al(g) \qquad [9]$$

are plotted *vs.* the temperature in Fig. 6. The linear least-squares treatment of the 83 experimental data in the temperature range (1379-1785 K) gave

$$\ln P_{Al}(Pa) = (25.005 \pm 0.314) - (41{,}178 \pm 527)/T \quad [10]$$

Table IV. Third law enthalpies of vaporization of the $Nb_3Al_{1\pm x}$ phase

T (K) \ y	$\Delta H_{v,298}^\circ$ (±0.63) kJ mol^{-1}		$NbAl_y(s) = Nb(g) + yAl(g)$			
	0.244	0.264	0.274	0.282	0.299	0.312
1744	821.3					847.7
1772	821.3					848.1
1802	821.7					848.5
1827	821.7					848.5
1844	821.3	830.9	835.1	838.0	844.7	850.2
1844	821.7	829.7	833.4	836.8	843.5	848.5
1856	822.1					848.8
1880	823.0	830.9	834.7	838.0	844.7	849.8
1944	821.3	829.3	833.0	836.4	843.1	848.1
1945	822.6	830.5	834.3	837.6	844.3	849.4
1994	822.1	830.1	833.9	837.2	843.9	848.9

Table VI. Pressures of Al (g) and third law enthalpies of vaporization for $NbAl_{0.5}(s) = Nb(g) + 0.5\ Al(g)$

T (K)	P_{Al} (Pa) ± 0.02	$\Delta H_{v,298}^\circ$ kJ/mol
1665	0.185	923.8
1717	0.501	923.0
1743	0.735	923.4
1769	1.003	924.2
1770	1.034	923.8
1799	1.692	923.0
1826	2.401	923.8
1844	2.999	923.4
1844	3.182	924.2
1854	3.425	924.2
1880	5.097	923.8
1944	14.19	922.2
1945	13.48	923.4
1994	25.23	922.2
	Average	923.4 ± 0.8

Pressures of niobium, which were calculated as described earlier, gave

$$\ln P_{Nb}(Pa) = (29.53 \pm 0.52) - (88{,}654 \pm 896)/T \quad [11]$$

Using aluminum and niobium pressures in the two phase region, the enthalpy of vaporization of $NbAl_3$ was calculated by the third law; $\Delta H_{v,298}^\circ[NbAl_3] = (1839.7 \pm 8.4)$ kJ mol^{-1}. Second law results are shown in Fig. 7. The enthalpy of vaporization as calculated from the slope was $\Delta H_{v,298}^\circ[NbAl_3] = (1845.6 \pm 17.6)$ kJ mol^{-1}. The enthalpy of formation was calculated using the third law value, $\Delta H_{f,298}^\circ[NbAl_3] = (-130.5 \pm 8.4)$ kJ mol^{-1}.

Discussion

The recent phase diagram of Jorda *et al.* (8) differs from that of Lundin and Yamamoto (7) by a shift to higher temperatures and lower aluminum contents, a difference that can, in part, be explained by more rapid quenching in the more recent work. Our results are in very good agreement with the niobium-rich sides of the Nb_2Al and Nb_3Al regions as given by Jorda *et al.* The small discrepancies on the aluminum-rich boundaries, especially since they increase with increasing temperature as does the ratio of the rate of vaporization to rate of diffusion, can be attributed to a residual diffusion problem in our experiments since the regions of the discrepancies are exactly where the diffusion paths are expected to be the greatest. Accordingly our results can be taken as a confirmation of the recent phase diagram work by Jorda *et al.* Perhaps there remains a question concerning the stable existence of stoichiometric Nb_3Al at temperatures below the Nb_2Al peritectic temperature and, considering the importance of this compound, further work in this area is suggested.

Our enthalpies of formation of the Nb-Al compounds are summarized in Table VII together with the values predicted by Miedema *et al.* (12, 13) and the values calculated by Gelashvilli and Dzneladze (9, 10). The model of Miedema *et al.* is a two parameter bonding model where the metallic atom is characterized by its electronegativity parameter and the electron density at the boundary of the Wigner-Seitz atomic cell. The values calculated by this model as well as our values are plotted in Fig. 8. Comparing the model with experiment, all compositions except

Table V. Second law and average third law enthalpies of vaporization of the $Nb_3Al_{1\pm x}$ phase and the extrapolated values at $y = 0.333$

$\Delta H_{v,298}^\circ$ \ y	0.244	0.264	0.274	0.282	0.299	0.312	0.333
3rd law average $\Delta H_{v,298}^\circ$ kJ/mol	821.86 ± 0.63	830.23 ± 0.63	834.08 ± 0.63	837.34 ± 0.63	844.04 ± 0.63	848.72 ± 0.63	856.63 ± 0.21
2nd law $\Delta H_{v,298}^\circ$ kJ/mol	817.6 ± 4.2	837.2 ± 10.0	841.4 ± 10.5	843.5 ± 9.2	852.3 ± 10.0	840.6 ± 5.8	858.6 ± 8.4

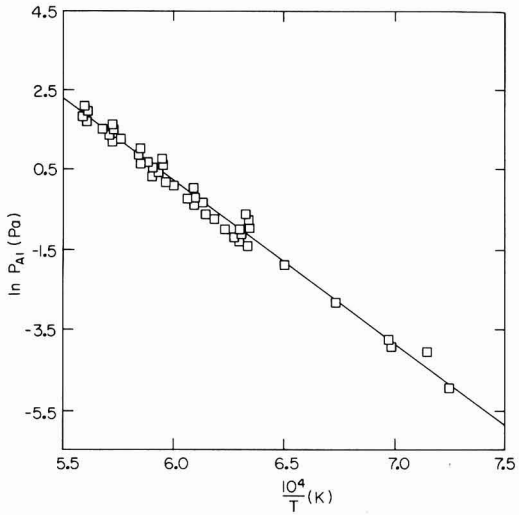

Fig. 6. Plot of the natural logarithms of the pressures of Al(g) in the Nb_2Al + $NbAl_3$ two phase region vs. the reciprocal temperature.

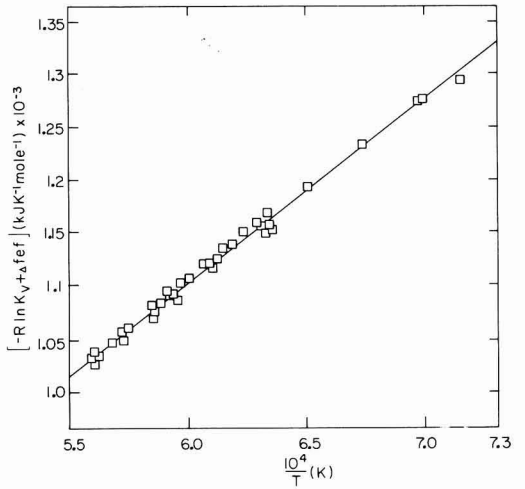

Fig. 7. Second law plot of the Nb_2Al + $NbAl_3$ two phase region as calculated from the measured Al(g) pressures and calculated Nb(g) pressures.

$NbAl_3$ were found to be less stable with respect to the solid elements than predicted by the model. The model values yield aluminum partial pressures which are lower by one order of magnitude compared with the experimental results. It seems that the model over-

Table VII. Enthalpies of formation of the Nb-Al compounds

	$\Delta H_{f,298}°$ (kJ mol^{-1})		
	1	2	3
$NbAl_3$	−130.5 ± 8.4	−122.4	−145.6
Nb_2Al	−74.9 ± 0.8	−177.0	−100.4
Nb_3Al	−77.0 ± 0.6	−128.0	−87.9

1. This work.
2. Miedema (12).
3. Gelashvilli (9, 10).

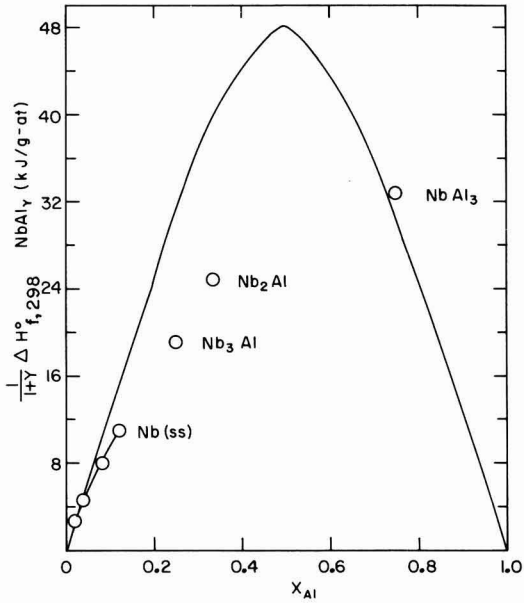

Fig. 8. Enthalpies of formation per gram atom of the Nb-Al compounds and solid solution. The solid line shows Miedema's predictions, open circles, values from this work.

estimates the bonding capability of niobium with aluminum. In addition we note that according to the model, Nb_2Al and $NbAl_3$ could not coexist in equilibrium since they would interact to form NbAl

$$2Nb_2Al(s) + NbAl_3(c) = 5NbAl(s)$$

where the calculated enthalpy of reaction is −122 kJ mol^{-1}. This result is in contradiction with the known phase diagram. For comparison, the enthalpy of formation, which yields a zero enthalpy change for the above reaction, and therefore provides an estimate to the upper limit for the stability of NbAl, provided that the entropies of formation of all compounds are about zero, is −28 kJ/g-at., a value which is 20 kJ/g-at. less negative than predicted by the Miedema model.

The results of Gelashvilli and Dzneladze (9, 10) are reported for comparison, however sufficient information about their method of obtaining these numbers is not available and therefore we present them without comment.

Acknowledgment

This research was supported by the Assistant Secretary for Energy Sciences.

Manuscript submitted Aug. 13, 1981; revised manuscript received Jan. 13, 1982. This was Paper 338 presented at the Minneapolis, Minnesota, Meeting of the Society, May 10-15, 1981.

Any discussion of this paper will appear in a Discussion Section to be published in the June 1983 JOURNAL. All discussions for the June 1983 Discussion Section should be submitted by Feb. 1, 1983.

Publication costs of this article were assisted by Ames Laboratory.

REFERENCES

1. R. H. Willens, T. H. Geballe, A. C. Gorrard, J. P. Maita, A. Meita, G. W. Hull, Jr., and R. R. Soden, *Solid State Commun.*, **7**, 837 (1969).
2. E. M. Savitskiy, "Rare Metals and Melting," p. 46, Technical House, Moscow (1959).
3. V. V. Baron and E. M. Savitskiy, *Zh. Neorg. Khim.*, **6**, 182 (1961).

4. A. Nedumov and B. I. Rabiezova, *Izv. Akad. Nauk SSSR Otd. Nauk Metall. Topl.*, **4**, 68 (1961).
5. M.-J. Richards, *Memoirs Scientifiques Rev. Metallurg.*, **4**, 265 (1964).
6. V. N. Svechnikov, B. M. Pan, and B. I. Latiesheva, *Metallofizika*, **2**, 54 (1968).
7. C. F. Lundin and A. S. Yamamoto, *Trans. Metall. Soc. AIME*, **236**, 863 (1966).
8. J. L. Jorda, R. Flukiger, and J. Muller, *J. Less-Common Met.*, **75**, 227 (1980).
9. G. A. Gelashvili and Zh. I. Dzneladze, *Sov. Powder Metall. Met. Ceram.*, **14**, 732 (1975).
10. G. A. Gelashvili and Zh. I. Dzneladze, *Sov. Powder Metall. Met. Ceram.*, **8**, 523 (1979).
11. R. Hultgren, P. D. Desai, D. T. Hawkins, M. Gleiser, and K. K. Kelley, "Selected Values of the Thermodynamic Properties of the Elements," American Society for Metals, Metals Park, OH (1973).
12. A. R. Miedema, P. F. Châtel, and F. R. DeBoer, *Physica*, **100B**, 1 (1980).
13. R. Boom, F. R. DeBoer, and A. R. Miedema, *J. Less-Common Met.*, **46**, 271 (1976).

Reactions of $SO_2(SO_3)$ with NiO-Na_2SO_4 in Nickel-Sodium Mixed Sulfate Formation and Low Temperature Hot Corrosion

R. L. Jones* and S. T. Gadomski

Naval Research Laboratory, Chemistry Division, Washington, D.C. 20375

ABSTRACT

Quantitative studies were made of the formation of low melting Ni, Na mixed sulfates by reaction of 50 m/o NiO-Na_2SO_4 with 400, 1000, 3000, and 5000 ppm equilibrated SO_2-SO_3 in air ($SO_2 + 1/2\ O_2 \leftrightarrows SO_3$) at 750°C. Equilibrium mixed sulfate compositions of 8, 12, 26, and 33 m/o $NiSO_4$, respectively, were formed, with the first two solid (solid solution) and the last two molten, in agreement with the $NiSO_4$-Na_2SO_4 phase diagram. Corrosion tests at 750°C with Nickel 200, Rene 80, and CoCrAlY coating alloy showed little corrosion when solid-solution mixed sulfates formed on the metal surface, but severe corrosion when molten sulfates formed. Nickel 200 corrosion proceeded by liquid Ni_3S_2-Ni formation below the surface oxide. No discernible sulfide was produced with Rene 80 and CoCrAlY which gave the characteristic low temperature hot corrosion morphology. Ternary Ni, Co, Na sulfates were detected in the CoCrAlY corrosion.

Marine gas turbines are subject to a "low temperature" mode of hot corrosion (LTHC) which gives maximum attack at 650°-750°C. This corrosion results from formation of molten mixed $CoSO_4$-Na_2SO_4 (eutectic mp 575°C) on the blade surface by reaction of SO_3 in the turbine gas with cobalt oxide and Na_2SO_4 blade surface deposits (1-4). Partial pressures of SO_3 of 5×10^{-5} to 1×10^{-4} atm are sufficient to produce a molten phase in the Co_3O_4-$CoSO_4$-Na_2SO_4 system at LTHC temperatures (1, 4). The reaction proceeds via SO_3 exclusively, but even when the SO_3/SO_2 ratio in the gas stream is very low, catalytic activity by Co_3O_4 may increase the SO_3 concentration at the oxide-Na_2SO_4 deposit surface sufficiently to allow molten phase formation (4).

Other mixed sulfates, especially $NiSO_4$-Na_2SO_4 (eutectic mp 671°C), may also produce LTHC. Approximately 5×10^{-4} atm SO_3 is predicted to yield molten $NiSO_4$-Na_2SO_4 at 750°C (1), and in fact water-soluble nickel is commonly found, along with cobalt, in sulfate deposits on LTHC-attacked blades. In addition, Luthra and Shores (1) have identified $NiSO_4$-Na_2SO_4 formation for Na_2SO_4 coated Ni-30Cr exposed under O_2-1% ($SO_2 + SO_3$) and associated the formation with corrosive attack that reached maximum severity at *ca.* 750°C.

The situation is complicated, however, because corrosion maxima at 700°-800°C have been found also when Ni and Ni-Cr alloys were corroded under SO_2-O_2 (5, 6), *i.e.*, without Na_2SO_4 and with no possibility, therefore, of forming the $NiSO_4$-Na_2SO_4 mixed sulfate. In these cases, the corrosion maxima were interpreted as related to the formation of Ni_3S_2 or eutectic Ni_3S_2-Ni. No $NiSO_4$ was detected, although thermodynamics predicted $NiSO_4$ to be stable under many of the experimental conditions employed. It is interesting, and potentially important in diagnosis of gas turbine corrosion, to note that the corrosion morphologies were sometimes very similar [*e.g.*, see Fig. 5 of Ref. (6)] to those found in LTHC, except for the absence of surface sulfate phases.

The present investigation was undertaken to explore the reactions of SO_3 with NiO-Na_2SO_4 in forming $NiSO_4$-Na_2SO_4 and to elucidate the corrosive effects produced by formation of molten $NiSO_4$-Na_2SO_4 on turbine metals.

Experimental

The experimental apparatus has been described previously (4). Electronic gas flow controllers are used to pass air containing low concentrations of SO_2 or SO_2-SO_3 over test specimens held in porcelain boats in a constant temperature zone furnace. The furnace is fitted with a quartz liner tube that has a trapping system at its outlet to allow quantitative analysis of the SO_3 and SO_2 in the exhaust air. Total air volume is determined by then passing the exhaust air through a wet test gas meter. The furnace air may be made to contain equilibrated SO_3-SO_2 or "pure" SO_2 (analyzed SO_3/SO_2 ratio below 0.05), depending on whether or not a platinum catalyst is placed upstream in the furnace. Overall, the system permits one to control and/or measure the SO_2 furnace input, the $SO_2 + \frac{1}{2}\ O_2 \leftrightarrows SO_3$ equilibrium, the SO_x ($SO_x = SO_2 + SO_3$) used in sulfation or corrosion reaction, and the concentrations of SO_2 and SO_3 in the exhaust air.

All experiments were run at 750° ± 5°C, with gas concentrations controlled to ±10% (verified by analysis) and with flow rates of 200 ml/min. Two types of experiments were conducted: (*i*) "$NiSO_4$-Na_2SO_4 formation" experiments where 250 mg mixtures of 50 mol percent (m/o) NiO-Na_2SO_4 spread evenly in porcelain boats (Coors 6A, 97 × 16 × 10 mm OD) were exposed to different concentrations of SO_3-SO_2 or SO_2, with periodic weighing to determine the sulfation kinetics and $NiSO_4$-Na_2SO_4 compositions obtained, and (*ii*) "$NiSO_4$-Na_2SO_4 corrosion" experiments where deposits of 50 m/o NiO-Na_2SO_4 on

* Electrochemical Society Active Member.
Key words: coatings, fused salts, metals, corrosion, sulfidation.

Nickel 200, Rene 80, or CoCrAlY blade coating specimens were sulfated under the same conditions as (i), and the corrosion effects produced by the generation of molten mixed $NiSO_4$-Na_2SO_4 on the metal surface analyzed.

Reagent grade chemicals and anhydrous SO_2 (Matheson 99.98%) were used in all experiments. The analyzed composition of the CoCrAlY coating alloy was 20.9Cr, 12.9Al, 0.32Y, and balance Co [weight percent (w/o)]. D-C argon plasma atomic emission analysis indicated the Nickel 200 to be 98.85Ni, 0.33Zn, 0.31Mn, 0.25Fe, 0.08Co, 0.05Cr, and 0.01Cu (w/o). No analysis was made of the Rene 80, but it should fall near alloy specifications, *i.e.*, 14Cr, 9.5Co, 5.0Ti, 4.0Mo, 4.0W, 3.0Al, 0.17C, 0.03Zr, 0.015B, balance Ni (w/o). The metal specimens were washed with hot water and detergent and rinsed with methanol before use.

Results and Discussion

Mixed $NiSO_4$-Na_2SO_4 formation.—The formation proceeds by the reaction

$$NiO + SO_3 \leftrightarrows NiSO_4 \quad [1]$$

with the nickel sulfate being taken into solid or molten solution and forming mixed sulfates with sodium sulfate

$$NiSO_4 + Na_2SO_4 \leftrightarrows NiSO_4\text{-}Na_2SO_4 \quad [2]$$

Since the NiO-SO_3-$NiSO_4$-Na_2SO_4 system is bivariant, some concentration of $NiSO_4$ in Na_2SO_4 will be formed even for sub-ppm SO_3 gas levels, in contrast to the univariant SO_3-NiO-$NiSO_4$ system where, for a given temperature, no $NiSO_4$ is formed until the "decomposition" SO_3 partial pressure is exceeded, and then there is complete conversion to $NiSO_4$. A 250 mg sample of 50 m/o NiO-Na_2SO_4 contains 86 mg NiO, and complete sulfation of NiO would produce a 92 mg weight gain.

The weight gains obtained under different sulfur oxide concentrations are shown in Fig. 1. These runs were made using the platinum catalyst, and thus with essentially equilibrated SO_2-SO_3. This is verified by the measured SO_3 and SO_x concentrations listed in Fig. 1 which correspond to SO_3/SO_2 ratios of ~0.6, or very near the 0.62 theoretical ratio calculated for SO_2-SO_3 in air (0.21 atm O_2) at 750°C (7). Abundant SO_2 is therefore present, but SO_3 nonetheless still appears to be the critical factor in mixed sulfate formation [cf. Ref. (4) and below].

For each SO_3 concentration in Fig. 1, there is a certain limiting weight gain that, as indicated, corresponds to formation of the m/o $NiSO_4$ which is in equilibrium with the given SO_3 concentration for the NiO-$NiSO_4$-Na_2SO_4-SO_3 system at 750°C. Note that sulfation is not complete and that excess NiO exists even under 1900 ppm SO_3. Visual examination as the boats were withdrawn from the furnace showed that the 8 and 12 m/o $NiSO_4$-Na_2SO_4 compositions remained solid (solid solution), while the 26 and 33 m/o compositions had clearly discernible liquid phases. This is in essential agreement with the $NiSO_4$-Na_2SO_4 phase diagram (Fig. 2). Also, interpolation of the Fig. 1 results suggests that liquid phases could begin to form at about 500 ppm, or converting units, 5×10^{-4} atm SO_3, which is the partial pressure predicted by Luthra and Shores (1) for liquid $NiSO_4$-Na_2SO_4 formation at 750°C.

X-ray diffraction confirmed the presence of α-$Na_2Ni(SO_4)_2$ and excess NiO in the 33 m/o $NiSO_4$-Na_2SO_4 specimen. Extra x-ray lines were found, but these could not be identified as $Na_3Ni(SO_4)_4$ (as would be expected from the phase diagram), possibly because of the rapid cooling of the specimen. The lines from the 8 and 12 m/o $NiSO_4$-Na_2SO_4 x-ray patterns could not be identified (aside from NiO) and presumably derived from the quenched β solid-solution phase. Nickel sulfate per se was never detected.

Catalytic activity of NiO.—When 50 m/o NiO-Na_2SO_4 was exposed under 5000 ppm pure (SO_3/SO_2 below 0.01) SO_2 at 750°C, a unique weight change behavior was observed, as shown in Fig. 3 where the different symbols on the weight curve (solid line) represent independent runs. The initial weight gain was essentially as rapid as with equilibrated 5000 ppm SO_2-SO_3 (cf. Fig. 1), but then after approximately 5 hr exposure and ~20 m/o $NiSO_4$ formation, the weight fell

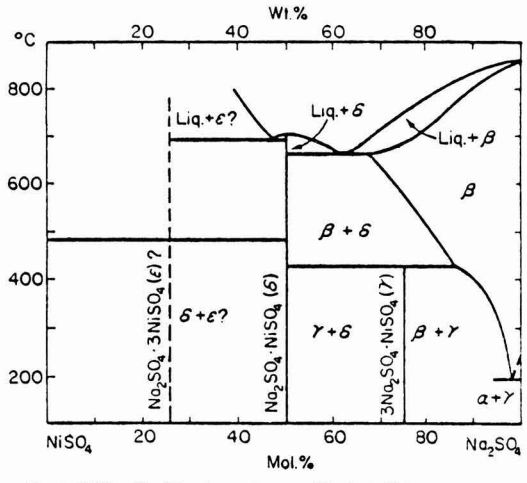

Fig. 2. $NiSO_4$-Na_2SO_4 phase diagram [K. A. Bol'shakov and P. I. Fedorov, *Zh. Obshch. Khim.*, **26**, 349 (1956)].

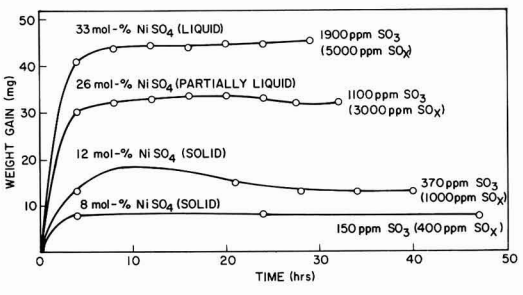

Fig. 1. Weight gain for 50 m/o NiO-Na_2SO_4 (250 mg) exposed to equilibrated SO_2-SO_3 in air at 750°C.

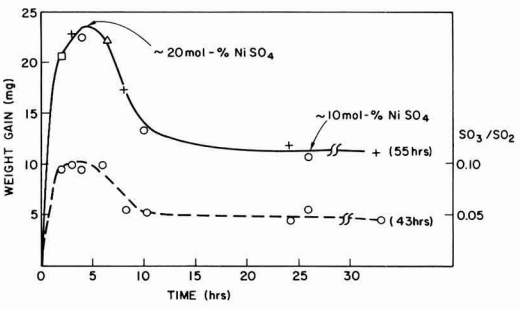

Fig. 3. Weight gain (solid line) and exhaust air SO_3/SO_2 ratio (dashed line) for 50 m/o NiO-Na_2SO_4 (250 mg) exposed to 5000 ppm SO_2 in air at 750°C. Different symbols are independent runs.

and, after 10-15 hr exposure, leveled off at a final weight gain corresponding to ~10 m/o $NiSO_4$ formation. The ~20 m/o $NiSO_4$ composition did not result in a liquid sulfate phase, but previous experience (4) indicates that a molten phase could be produced at higher SO_2 concentrations.

A similar (but less pronounced) behavior was observed for 50 m/o Co_3O_4-Na_2SO_4 exposed under SO_2 at 625°C (4). Our hypothesis is that the metal oxide (Co_3O_4 or NiO) has sufficient catalytic activity initially to produce appreciable SO_3 at the metal oxide-Na_2SO_4 mix surface, which gives mixed sulfate formation nearly as rapid as when equilibrium SO_3 partial pressure is provided via an external Pt catalyst. As the oxide is consumed by sulfate formation and/or incorporated in the mixed sulfate mass, however, its catalytic ability decreases, and the SO_3 pressure drops. This causes the mixed sulfate to decompose until a composition is reached which can be sustained by the lower SO_3 pressure produced by the now less effective metal oxide catalyst.

Results from the present NiO-Na_2SO_4 experiments support this hypothesis by showing that the SO_3/SO_2 ratio in the bulk air stream (dashed line in Fig. 3) is in fact higher in the times when maximum mixed sulfate formation occurs than it is later when the oxide catalytic effect is presumably less.

A comparison of the relative catalytic efficiency of Co_3O_4 *vs.* NiO was made by exposing samples of Co_3O_4 (115 mg) and NiO (140 mg) under 500 ppm SO_2 in air at 725°C and measuring the resultant SO_3/SO_2 ratios in the exhaust air. The sample weights were chosen to give equal volumes (if not areas) of the oxides, and the samples were spread, as nearly as possible, the same over the boat bottoms. Under these conditions Co_3O_4 gave an average SO_3/SO_2 ratio of 0.44 and NiO an average ratio of 0.39, indicating that they are essentially equal in catalytic efficiency for the $SO_2 \rightarrow SO_3$ reaction. There was no weight gain of the oxide or other evidence of reaction with SO_2-SO_3.

Mixed (Co,Ni)SO_4-Na_2SO_4 formation.—The possible formation of ternary (M_1, M_2, Na) mixed sulfates is important in LTHC because it may allow (*i*) molten sulfates to be formed at temperatures lower than with either binary system, or (*ii*) larger amounts of the molten sulfate phase to be produced at a given SO_3 partial pressure. Since water-soluble Ni and Co are found in sulfate deposits on LTHC-attacked blades, the Co,Ni,Na ternary sulfate system is especially relevant. The phase diagram for this system has been developed (8) and appears to contain no ternary eutectic points.

However, limited experiments here indicate that the SO_3 overpressure, which was neglected in the previous phase diagram development, may have a crucial role. In these experiments, 250 mg samples of 50 m/o Co_3O_4-Na_2SO_4 were equilibrated at 750°C under 150 and 1100 ppm SO_3, respectively, with molten $CoSO_4$-Na_2SO_4 phases being formed in each case. Then an additional 86 mg of NiO was added which produced the characteristic weight changes depicted in Fig. 4. With 150 ppm SO_3, there was no additional weight gain and indeed apparently a slight loss. With 1100 ppm SO_3, however, there was a clear additional weight gain of ~20 mg. Presumably concentrations between 1100 and 150 ppm SO_3 would give intermediate behavior.

These results are not sufficient to prove whether or not a ternary eutectic exists in the Co,Ni,Na sulfate system under SO_3; but they do clearly predict that when excess Co_3O_4 and NiO exist with Na_2SO_4 under not extraordinarily high levels of SO_3 (a possible engine blade situation), a larger amount of molten mixed sulfate will be produced than when either oxide occurs alone.

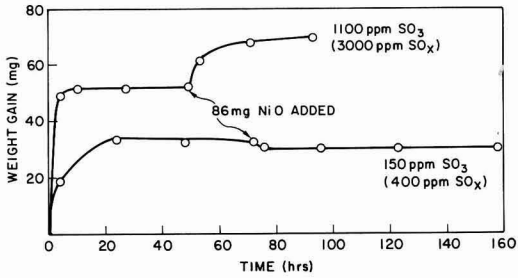

Fig. 4. Weight gain for 50 m/o Co_3O_4-Na_2SO_4 (250 mg) exposed to equilibrated SO_2-SO_3 in air at 750°C, with NiO additions.

Molten $NiSO_4$-Na_2SO_4 corrosion of Nickel 200.—For these experiments, small deposits (2-3 mm diam, 0.5-1 mm depth) of 50 m/o NiO-Na_2SO_4 were placed on specimens cut from Nickel 200 plate and exposed at 750°C to 370 ppm SO_3 (1000 ppm SO_x) and 1100 ppm SO_3 (3000 ppm SO_x) in air. The deposits exposed under 370 ppm SO_3 remained solid for times up to 60 hr, with little corrosion found under the deposits when the specimens were cross sectioned. Conversely, the deposits exposed under 1100 ppm SO_3 became molten and caused extensive corrosion of the nickel substrate after only 4 hr at temperature. It is important, and in some ways surprising, to note that the kinetics and ultimate degree of sulfation are essentially the same, regardless of whether the NiO-Na_2SO_4 occurs as small surface deposits or bulk (250 mg) samples, a behavior also observed for Co_3O_4-Na_2SO_4 (4).

The corrosion resulting from the molten $NiSO_4$-Na_2SO_4 appears to occur principally through the formation of a liquid sulfide, presumably Ni_3S_2-Ni eutectic, below the surface oxide. Figure 5 shows a typical area of heavy corrosion where the sulfide phase has extruded through cracks in the surface oxide. Somewhat more can be seen of the course of corrosion in cross-sectioned specimens as in Fig. 6. The extruded sulfide oxidizes rapidly once exposed to air, with oxidation proceeding inward so that a core of Ni_3S_2-Ni under an outer NiO layer is found at intermediate stages of the process (Fig. 6B-D). Air also enters the

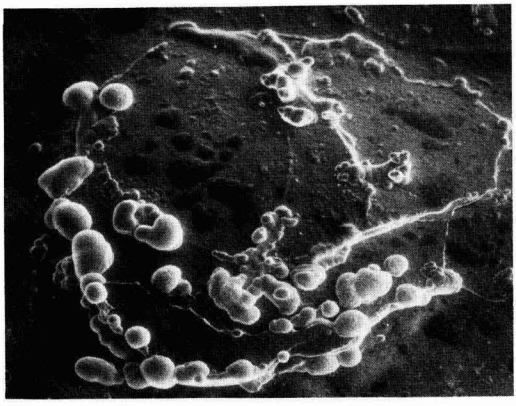

Fig. 5. Ni_3S_2-Ni nodules extruding through surface oxide on molten $NiSO_4$-Na_2SO_4 corroded Nickel 200. Dark patches are residual sulfate.

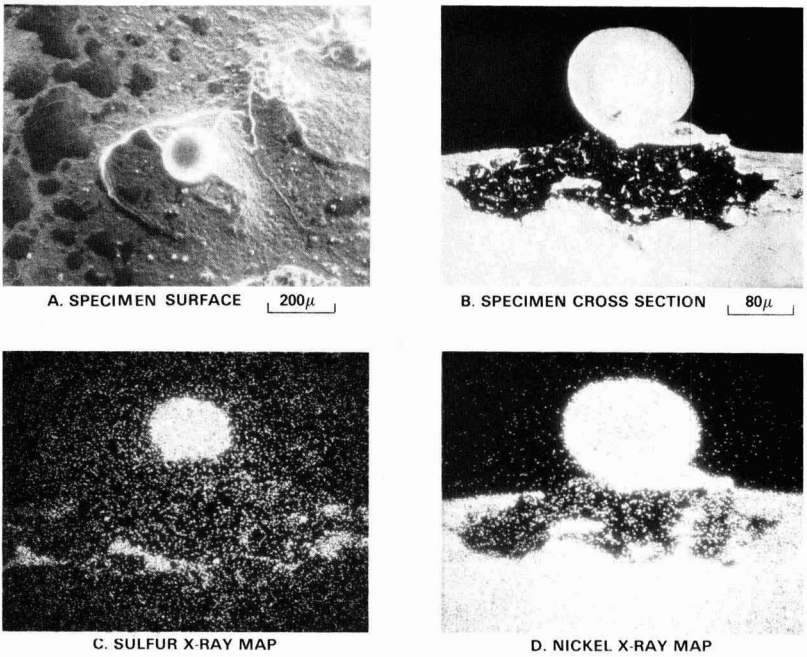

Fig. 6. Surface and cross-sectional views and x-ray maps of Ni_3S_2-Ni nodule corrosion site on Nickel 200.

voids left by the extruding sulfide and tends to oxidize the sulfide phases remaining in the metal at the void perimeter (Fig. 6B-C). Whether sulfidation-oxidation attack continues then will depend on different factors, including (presumably most important) whether the sulfur released by oxidation of the sulfide goes off as SO_2-SO_3, or penetrates further into the metal to form new oxidation-susceptible sulfide phases.

How the molten $NiSO_4$-Na_2SO_4 causes sulfidation and corrosion is not certain. The mixed sulfate clearly decomposes once it becomes molten and wets the nickel surface (decomposition does not occur when the liquid sulfate contacts an inert surface, *e.g.*, the porcelain boat). It is possible that the liquid sulfate penetrates the surface oxide and the $NiSO_4$ reacts directly with the underlying metal by

$$9Ni + 2NiSO_4 \leftrightarrows 8NiO + Ni_3S_2 \ (\Delta G^\circ = -77 \text{ kcal}) \quad [3]$$

However, substantial SO_3-SO_2 is released in the wetting-decomposition process and another possibility is that SO_3 (or SO_2) diffuses to the NiO-Ni interface and reacts there by

$$2SO_3 + 9Ni \leftrightarrows 6NiO + Ni_3S_2 \ (\Delta G^\circ = -110 \text{ kcal}) \quad [4]$$

Indication that the SO_3 gas mechanism could be viable was obtained in experiments where nickel sulfide nodules (Fig. 7), similar to those occurring with $NiSO_4$-Na_2SO_4, were found to develop on sulfate-free Nickel 200 after 65 hr exposure to 1100 ppm SO_3 (3000 ppm SO_x) at 750°C.

Conditions and temperatures for molten $NiSO_4$-Na_2SO_4 or eutectic Ni_3S_2-Ni formation are thus apparently very close and for both may peak near 750°C, so as to conceivably explain the corrosion maxima at 700°-800°C in the different earlier experiments (1, 5, 6). A test of this idea might be possible by the study of mixed sulfate *vs.* $SO_2(SO_3)$ gas attack on cobalt, where the sulfide eutectic, Co_3S_1-Co (mp 877°C), occurs at temperatures above the LTHC region. In any event, it is clear from the present results that sulfidation-oxidation corrosion having many common features can be produced either by SO_2-SO_3 gas attack on bare nickel, or molten $NiSO_4$-Na_2SO_4 formation on sulfate-coated nickel, with the latter, in our judgment, more relevant to gas turbine hot corrosion.

Molten $NiSO_4$-Na_2SO_4 corrosion of Rene 80.—Rapid corrosion resulted when molten $NiSO_4$-Na_2SO_4 was formed by SO_3-NiO-Na_2SO_4 reaction on the Rene 80 surface. No Ni_3S_2-Ni liquid sulfide was detected, however, and the characteristic morphology was as shown in Fig. 8. The Ni-rich outer oxide layer, marked by A in Fig. 8A, represents the residue of the decomposed $NiSO_4$-Na_2SO_4, plus NiO produced by Ni migration outward from the metal corrosion zone (marked B). The corroded metal is depleted in Ni (Fig. 8B), but retains Cr (Fig. 8D), and has sulfur concentrated near

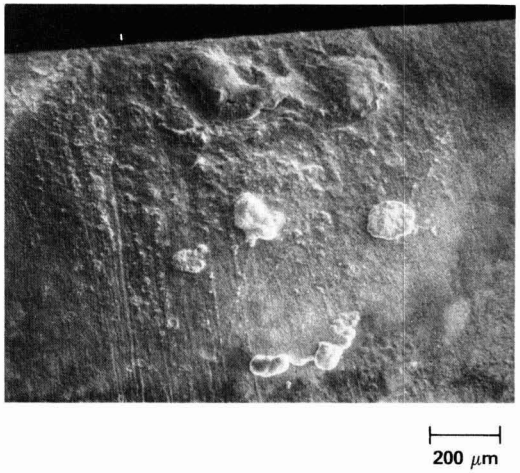

Fig. 7. Extruding Ni_3S_2-Ni nodules (lower center of micrograph) on Nickel 200 after 65 hr under 3000 ppm equilibrated SO_2-SO_3 in air at 750°C.

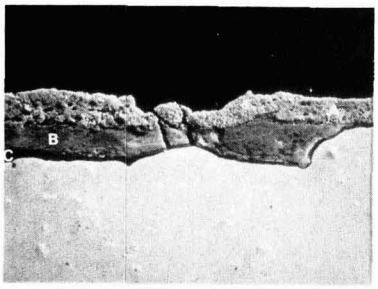

A. SPECIMEN CROSS SECTION 40μ

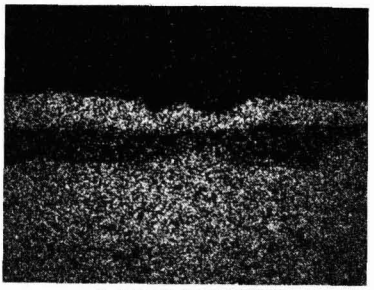

B. NICKEL X-RAY MAP

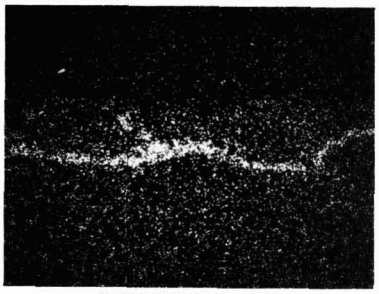

C. SULFUR X-RAY MAP

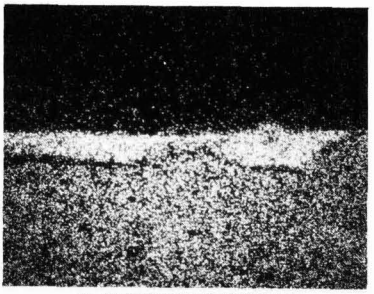

D. CHROMIUM X-RAY MAP

Fig. 8. Cross-sectional and x-ray maps of molten $NiSO_4$-Na_2SO_4 corroded Rene 80.

the inner edge of the corrosion phase (Fig. 8C). This is the typical LTHC morphology, as shown by many workers. It remains uncertain, however, what form (sulfate, sulfide, sulfite ?) the sulfur exists in at the corrosion pit front (1-4). Note that little sulfur is detected in the outer decomposed $NiSO_4$-Na_2SO_4 layer (the specimens are dry polished to avoid sulfate dissolution). Area C shows the separation of corrosion phase from metal that occurred characteristically in Rene 80 corrosion.

The differences between Rene 80 corrosion (clean corrosion front, lack of Ni_3S_2 formation, propensity for corrosion phase detachment) and Nickel 200 corrosion may reasonably be assumed to result from the influence of chromium or other elements in Rene 80. No information could be obtained in the present experiments, however, to indicate how this influence, be it by the formation of protective oxides or other means, might operate.

Molten $NiSO_4$-Na_2SO_4 corrosion of CoCrAlY.—Figure 9 shows a representative area of corrosion resulting from molten $NiSO_4$-Na_2SO_4 formation by NiO-Na_2SO_4 deposits on CoCrAlY after 16 hr under 1100 ppm SO_3 at 750°C. At this SO_3 level, LTHC by molten $CoSO_4$-Na_2SO_4 formation would ultimately be expected even if the surface deposit contained only Na_2SO_4. But, since little Co_3O_4 is initially available, and the deposit contains 50 m/o NiO, molten $NiSO_4$-Na_2SO_4 forms first, and approximately within the times indicated in Fig. 1. Corrosion then results with the features shown in Fig. 9 being produced.

Area A of Fig. 9A appears to be an area of at least partially decomposed sulfate. There is a Ni-rich outer layer (presumably NiO), but little Ni apparently remains in area A itself (Fig. 9C). Substantial sulfur and cobalt area still retained in area A however (Fig. 9B and D). Area C, on the other hand, contains all three, *i.e.*, Ni, Co, and S. Area B appears to be typically low temperature hot corroded CoCrAlY, but with more Co retained, and the sulfur more broadly spread across the corrosion zone (cf. Fig. 8C) than normally seen for LTHC attack, although not necessarily so if the corrosion pit (zone) is just formed (4).

The behavior in Fig. 9 seems to be best explained by postulating that (*i*) during initial decomposition of the molten $NiSO_4$-Na_2SO_4, a liquid sulfate and high SO_3 pressure exist at the CoCrAlY surface, (*ii*) this produces aggressive attack on the CoCrAlY, with cobalt transported outward where, still under high SO_3 pressure, it reacts with the surface melt, forming a ternary Co,Ni,Na sulfate, and (*iii*) as the effective SO_3 pressure within the melt later decreases, the ternary sulfate begins to decompose (area A), with NiO being rejected first from the ternary melt. Ultimately, depending on temperature, gas stream SO_3 partial pressure, and perhaps thickness of deposit, one would expect the majority of sulfate to be decomposed to the extent of area A or further. Since water-soluble nickel sulfate is found on turbine blades, however, complete decomposition of the $NiSO_4$ component of the sulfate melt must not occur at all blade sites.

Conclusion

Mixed $NiSO_4$-Na_2SO_4 results from reaction of SO_3 with NiO-Na_2SO_4, with equilibrium concentrations of $NiSO_4$ produced for each SO_3 concentration. The reaction is independent (within limits) of the amount of NiO-Na_2SO_4, since essentially the same kinetics and final $NiSO_4$ concentrations are obtained whether the NiO-Na_2SO_4 is exposed as small surface deposits or bulk (250 mg) samples. The resultant sulfates are solid or liquid, depending on their composition, and show good agreement with the $NiSO_4$-Na_2SO_4 phase diagram. Approximately 500 ppm (5×10^{-4} atm) SO_3 is sufficient to produce molten $NiSO_4$-Na_2SO_4 at 750°C, as predicted by Luthra and Shores (1).

Nickel oxide catalyzes the $SO_2 + \frac{1}{2}\ O_2 \leftrightarrows SO_3$ reaction, and an appreciable SO_3 concentration exists at the NiO-Na_2SO_4 mix surface even when the air stream contains only SO_2. This fact is manifested in the initial rapid weight gain (fresh NiO, high catalysis and SO_3 levels, $NiSO_4$-Na_2SO_4 formation) and then decline

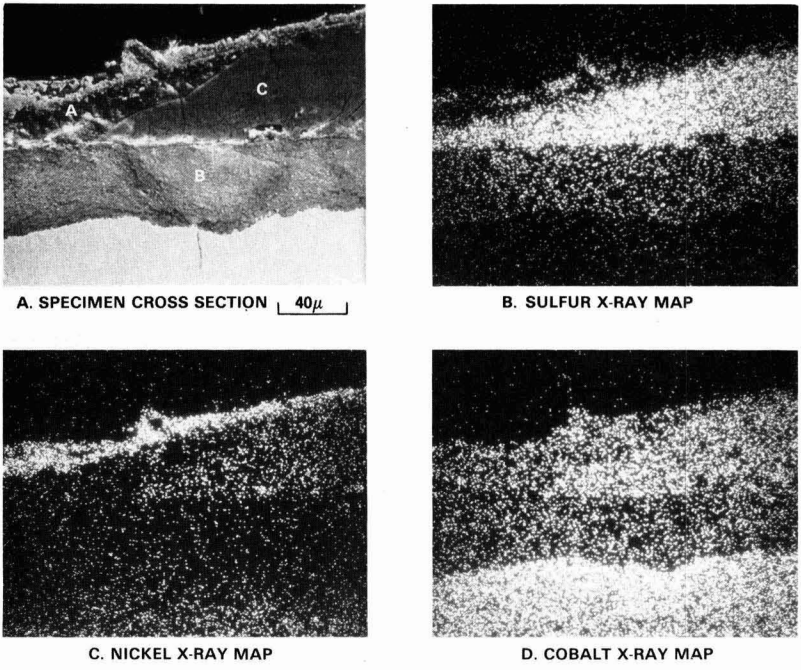

Fig. 9. Cross-sectional and x-ray maps of molten $NiSO_4$-Na_2SO_4 corroded CoCrAlY coating alloy.

(consumed or contaminated NiO, lower catalysis and SO_3 levels, sulfate decomposition) seen for NiO-Na_2SO_4 samples exposed under SO_2 in air. Conceivably, under high SO_2, initial $NiSO_4$-Na_2SO_4 formation could reach molten sulfate compositions (and bring corrosion) even though the requisite SO_3 does not appear available in the gas stream.

Reaction of Co_3O_4-NiO-Na_2SO_4 with 1100 ppm (and possibly somewhat lower) SO_3 produces the ternary Co,Ni,Na mixed sulfate. There is no evidence for formation of a ternary eutectic, but larger amounts of molten sulfate are produced than with either Co_3O_4 or NiO alone.

Rapid corrosion occurs when molten (but not solid) $NiSO_4$-Na_2SO_4 mixed sulfates are formed on the surface of Nickel 200, Rene 80, and CoCrAlY blade coating. Nickel 200 corrosion proceeds principally by formation of liquid eutectic Ni_3S_2-Ni under the surface oxide layer, giving an attack that is ultimately very similar, but of larger magnitude, to that produced by reaction of SO_3 (SO_2) gas alone with nickel at the same temperature. Rene 80 and CoCrAlY coating alloy corrode in a more characteristic LTHC manner, with no sulfide formation discernible. With Rene 80, the corrosion layer tends to become detached, which may reflect formation of Cr_2O_3 or other protective phases (although not detected) during the corrosion process. In CoCrAlY corrosion initiated by molten $NiSO_4$-Na_2SO_4 formation, one can detect ternary Co,Ni,Na sulfate formation, as well as an indication of NiO displacement from the ternary melt as sulfate decomposition occurs.

It is hoped that these results will aid in the understanding of low temperature hot corrosion and in the development and application of improved materials for marine gas turbines.

Acknowledgments

This research was funded under the Naval Sea Systems Command Program for Advanced Marine Gas Turbine Materials, and the support is gratefully acknowledged. We also wish to thank Dr. J. A. Goebel, of Pratt & Whitney Aircraft Group, who furnished the CoCrAlY and Rene 80 specimens, and Dr. Rm. Panayappan, of NRL, for analysis of the Nickel 200 stock.

Manuscript submitted Oct. 22, 1981; revised manuscript received Dec. 14, 1981. This was Paper 451 presented at the Denver, Colorado, Meeting of the Society, Oct. 11-16, 1981.

Any discussion of this paper will appear in a Discussion Section to be published in the June 1983 JOURNAL. All discussions for the June 1983 Discussion Section should be submitted by Feb. 1, 1983.

Publication costs of this article were assisted by the Naval Research Laboratory.

REFERENCES

1. K. L. Luthra and D. A. Shores, *This Journal*, **127**, 2202 (1980).
2. G. H. Meier, F. S. Pettit, and K. T. Chang, in International Conference on High Temperature Corrosion, San Diego, March 1981, NACE, To be published.
3. R. H. Barkalow and G. W. Goward, in International Conference on High Temperature Corrosion, San Diego, March 1981, NACE, To be published.
4. R. L. Jones, in International Conference on High Temperature Corrosion, San Diego, March 1981, NACE, To be published.
5. V. Vasantasree and M. G. Hocking, *Corros. Sci.*, **16**, 261 (1976).
6. K. N. Strafford and P. J. Hunt, *ibid.*, **19**, 1089 (1979).
7. K. H. Stern and E. L. Weise, Natl. Stand. Ref. Data Ser., Natl. Bur. Stand., No. 7 (Sulfates) (1966).
8. K. A. Bol'shakov and P. I. Fedorov, *J. Inorgan. Chem. USSR*, **III**, No. 8, 1896 (1958).

Photochemical Production, Infrared Absorptivity, and Chemical Reactions of Trichlorosilanol in Silicon Tetrachloride

Robert Gooden and J. W. Mitchell

Bell Laboratories, Murray Hill, New Jersey 07974

ABSTRACT

Selective photochemical oxidation of trichlorosilane, Cl_3SiH, and infrared spectroscopy are used to generate and then identify trichlorosilanol, Cl_3SiOH, in silicon tetrachloride, $SiCl_4$. The Cl_3SiOH, an impurity unavailable in pure form and existing normally in $SiCl_4$ as an intermediate specie in equilibrium with others, is produced quantitatively at trace levels. The chemistry of formation and subsequent reactions of the silanol in $SiCl_4$ are discussed and the infrared absorptivity of the photogenerated product is experimentally determined.

The analytical chemistry of silicon tetrachloride (pertaining to the determination and removal of molecular impurity species) has been investigated increasingly as greater emphasis has been placed on perfecting waveguide fibers for transmission at wavelengths beyond 0.85 microns. Previous reports by Kometani and colleagues (1) show that trichlorosilane (Cl_3SiH), an —OH containing impurity presumed to be trichlorosilanol (Cl_3SiOH), hydrogen chloride (HCl), occasional hydrocarbons (—CH) species, and iron are the most common contaminants. These impurities are capable of affecting the magnitude of absorbance loss at long wavelengths either directly or through contributions to the incorporation of —OH in the fiber core.

Suitable procedures have been devised for generating standard solutions of Cl_3Si—H, —CH species, and HCl in silicon tetrachloride. Thus it has been possible to perfect reliable quantitative infrared spectroscopic methods for determining these species (1). Direct experimental determinations of absorption coefficients of the silanol have been precluded by the nonavailability of this specie in pure form and by complications resulting from its reaction chemistry in $SiCl_4$. Consequently, quantitative assessments of the silanol have depended upon a conditional —Si—OH absorption coefficient measured experimentally for triphenylsilanol in carbon tetrachloride (1). Preparation of standard solutions of the silanol normally existing in silicon tetrachloride are required for investigations now underway to develop new ultrasensitive laser infrared absorption-photoacoustic spectroscopic methods for its determination.

Silicon tetrachloride has been ultrapurified with respect to all previously mentioned impurities by a partial hydrolysis technique (2, 3). A photochlorination method has also proven effective for removal of trichlorosilane in a continuous process (4, 5). By applying the former methods (2, 3) to produce $SiCl_4$ in controlled states of purity with respect to various impurities, it has been possible to vary the Cl_3SiH level over a wide concentration range in order to determine the influence of this reagent impurity on the —OH content and corresponding absorbance loss of fibers (6). Similar investigations of the —SiOH impurity have not been possible due to the apparent coexistence of several species (7), chemical reactivity, and an equilibrium level of ~80 ppm in partially hydrolyzed $SiCl_4$ (3).

In the present study a clarification of the identity of the silanol was sought by selective photochemical reactions combined with infrared spectroscopy. Additionally, this manuscript reports an analytically useful method for preparing standard solutions of Cl_3SiOH via quantitative photochemical oxidation of trichlorosilane. The infrared absorptivity of the resulting silanol is reported and chemical reactions explored.

Key words: inorganic, infrared, CVD, contamination.

Experimental

Chemicals.—Semiconductor grade $SiCl_4$ was obtained from various commercial sources and used without further purification if low levels of impurities were found. For those samples containing high impurity levels, see $SiCl_4$ purification below. A commercial sample of Cl_3SiH (Alfa 99.8%) was distilled under N_2 and a center fraction taken for use. High purity oxygen (Airco) was supplied in aluminum cylinders and contained less than 0.2 ppm hydrocarbons. It was further dried by slow passage through a dry ice cooled copper coil. Other gases were passed through an Ascarite filter.

Acetyl chloride (Aldrich) and trifluoroacetic anhydride (Aldrich) were distilled under nitrogen, center fractions taken, and stored in Teflon bottles. Other chemicals BCl_3 (Matheson), $B(OCH_3)_3$ (Aldrich), PCl_3 (Alfa), $AlCl_3$ (Aldrich), $POCl_3$ (Alfa), and P_2O_5 (J. T. Baker) were of the highest purity available commercially and used fresh without further purification.

Sample preparation and handling.—To minimize atmospheric hydrolysis, samples of $SiCl_4$ were stored inside polyethylene glove bags filled with dry nitrogen. All sample manipulations were performed in glove bags as well. Standard solutions of Cl_3SiH were prepared by transferring known amounts of 99.9% reagent via glass syringes with Teflon needles into silicon tetrachloride either containing small quantities of the silane or completely freed of this impurity.

Apparatus and procedures.—All glassware and plasticware were cleaned by rinsing in HF solution and distilled water, and then dried in a vacuum oven at 120° for at least 4 hr prior to use. Transfers were made in a glove bag under dried nitrogen with glass Luer-Lok syringes and Teflon needles. Solutions were mixed and stored in 60 ml Teflon bottles. Infrared and photochemical cells were filled inside glove bags and appropriately sealed prior to measurement or initiation of photochemical studies.

Infrared analysis.—The infrared spectra were obtained on a Perkin Elmer 421 spectrometer purged with N_2 to protect the instrument. Liquid cells of the Wood design (8) were constructed from 0.4 cm stainless steel barrels equipped with Luer-Lok syringe tips for filling. Silver chloride windows were cemented with epoxy onto the barrel. After use the cells were cleaned by rinsing with $CHCl_3$ and dried with nitrogen. Periodically the cells were rinsed with HF solution and distilled water and dried to remove silica deposits on the windows. A 10 cm cell (International Crystal Laboratories) with KBr windows and stopcocks for evacuation was used for gas phase spectra.

Photolysis.—The photolyses were carried out in a 10 × 2.5 cm cylindrical quartz cell equipped with a tube for bubbling oxygen through the contained liquid. Connections were made using Teflon tubing and stopcocks. The light source consisted of two 60W mercury reso-

nance lamps placed to face each other. The cell was mounted between the lamps approximately 10 cm from each lamp to maintain a cell temperature of 24°-26°. During photolysis, the cell was vented to the atmosphere of a hood through a charcoal-NaOH trap.

A 50 ml solution of $SiCl_4$ containing added Cl_3SiH was transferred to the photolysis cell under nitrogen. A sample was taken for infrared analysis after mixing in the cell. The cell was mounted between the lamps and connected to the oxygen line. Oxygen was bubbled through the solution at a rate of 3-4 ml/min for 15 min before turning the lamps on. After 2-3 hr, photolysis was stopped and the volume of $SiCl_4$ lost (usually 0.4-1 ml) was measured. Photolysis in closed vessels pressurized with oxygen and stirred continuously would have prevented small volatilization losses. However, such systems were not convenient for interim sampling and were not used. A sample of the photolyzed solution was removed for infrared analysis. It was found that at high concentrations of Cl_3SiH (>1% by wt in $SiCl_4$), a precipitate was formed appearing as shiny particles. In the range of 200-2500 ppm, no precipitation was observed. Blank runs of $SiCl_4$, with no added Cl_3SiH were also made. Corrections were made for volatilization losses and blanks.

Purification of $SiCl_4$.—Samples of silicon tetrachloride, pre-purified by partial hydrolysis or by chlorination, were obtained from available in-house suppliers. Partially hydrolyzed and some chlorinated materials were still too heavily contaminated with silanol and hexachlorodisiloxane for use in these experiments. In attempts to reduce the silanol concentration in silicon tetrachloride, 250 ml quantities were refluxed for up to 6 hr in a 500 ml round bottom flask fitted with a reflux column. At the top of the reflux unit a nitrogen purge tube provided a continuous supply of house nitrogen passed through a Dryite dying tube. Executions of this procedure in a standard hood led to increases in the —OH content of $SiCl_4$ even after extremely careful refluxing. Also, occasional contamination by CO_2 was observed. By flowing nitrogen successively through Dryrite, Ascarite, and liquid nitrogen cooled copper coils, it was possible to purge silicon tetrachloride to displace dissolved chlorine without significant increases in the —OH content. However, refluxing of silicon tetrachloride under conditions where vapors of the reagent are in direct contact with a purge gas was found to be very susceptible to moisture contamination.

Results and Discussions

Identification of —SiOH specie.—Hydrogen containing species in $SiCl_4$ can be easily observed and qualitatively identified by infrared spectroscopy. The two species of interest in this paper, trichlorosilane and the analogous silanol, have distinctive sharp absorbances at 2258 cm^{-1} (Si—H) and 3680 cm^{-1} (—OH), respectively. In addition, HCl absorbs at 2845 cm^{-1} and hydrocarbons absorb between 2900 and 3100 cm^{-1} (C—H). The sharpness of the band for the —OH moiety suggests a nonhydrogen bonded and nonassociated —OH group, and its proximity to that of —OH in fused silica (3663 cm^{-1}), where the band is presumed to arise from —OH attached to Si (9), has formed the basis for proposing that the specie in $SiCl_4$ is Cl_3SiOH (1). However, unequivocal assessments of the identity of this specie in $SiCl_4$ have not been made previously. The existence of Cl_3SiOH as an intermediate specie during gas phase reactions of $SiCl_4$ and water vapor has also been proposed, but not observed experimentally (10). Further speculations about the existence of Cl_3SiOH are also provided by the proposed stepwise hydrolysis of silicon tetrachloride via the reactions (11)

$$SiCl_4 + H_2O \rightarrow Cl_3SiOH + HCl \quad [1]$$

$$Cl_3SiOH + H_2O \rightarrow Cl_2Si(OH)_2 + HCl \quad [2]$$

$$Cl_2Si(OH)_2 + H_2O \rightarrow ClSi(OH)_3 + HCl \quad [3]$$

$$ClSi(OH)_3 + H_2O \rightarrow Si(OH)_4 + HCl \quad [4]$$

The first hydrolysis product can react further as indicated by

$$2Cl_3SiOH \rightarrow Si_2OCl_6 + H_2O \quad [5a]$$

or

$$Cl_3SiOH + SiCl_4 \rightarrow Si_2OCl_6 + HCl \quad [5b]$$

Additional reaction of products can proceed according to

$$Si_nO_{n-1}Cl_{2n+2} + H_2O \rightarrow Si_nO_{n-1}Cl_{2n+1}OH + HCl \quad [6]$$

and subsequent stepwise hydration and coupling will eventually produce the endpoint polymer, hydrated silica.

In the present investigation infrared spectroscopy has been applied to monitor the selective photochemical conversion of Cl_3SiH in silicon tetrachloride into Cl_3SiOH. Conditions were sought under which a single silanol specie could be produced and its subsequent chemical conversion into other products minimized.

Photogeneration of Cl_3SiOH in $SiCl_4$.—As seen in Fig. 1, the Si—H band resulting from Cl_3SiH in $SiCl_4$ can be removed completely by photolysis while the Si—OH band strongly increases. This selective and direct conversion of trichlorosilane to the silanol is further supported by the following observations:

1. Infrared spectra of photo-oxidized silicon tetrachloride without added Cl_3SiH show no detectable change in the intensity of the —OH band.
2. The infrared spectra and vibrational frequency of the —SiOH specie normally found in trace quantities in $SiCl_4$ are superimposable with that of the specie produced by photooxidation.
3. No evidence for the presence of peroxy-type silyl species was detected via infrared spectra.

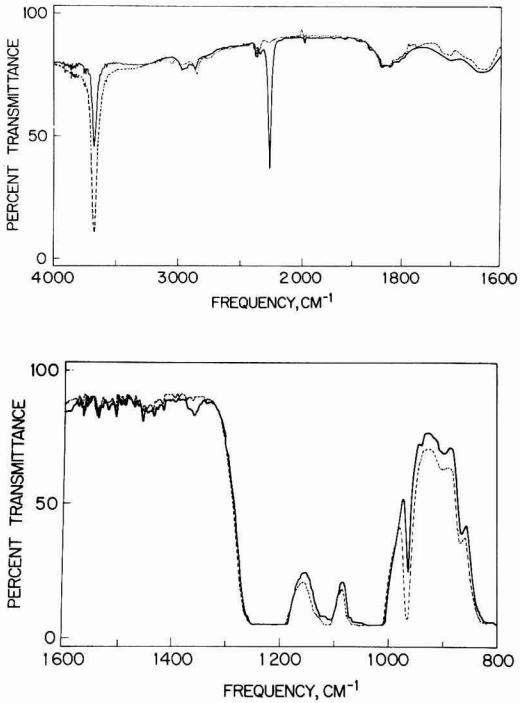

Fig. 1. Liquid phase infrared spectrum of the photoconversion of Cl_3SiH to Cl_3SiOH (——) before photolysis, and (---) after 3 hr photolysis in the presence of O_2.

4. Under the appropriate experimental conditions no precipitates [*e.g.*, $Si(OH)_4$] are observed.

The solutions obtained from photolysis are quite stable for hours on standing. Initially there is little or no change in the absorption bands of hexachlorodisiloxane at 1878, 1735, and 1575 cm^{-1}. Thus reaction [5] is minimal. However, after two days a build-up of HCl is apparent and after several weeks the Si—OH absorption noticeably decreases and the hexachlorodisiloxane bands become prominent. Kometani and Wood (1) have successfully removed the silanol during reflux of $SiCl_4$ with a concomitant increase in the Si_2OCl_6 content. This observation further confirms that reaction [5] occurs.

The formation of trichlorosilanol has been reported by Emeleus and Welch (12), also, by the photolyses of gaseous mixtures of trichlorosilane and oxygen. They trapped a liquid product that decomposed slowly at room temperature and on attempted distillation to HCL and $(SiOCl_2)_4$. Based on hydrogen chloride analyses they deduced the empirical formula, Cl_3SiOH, for the reactive liquid.

The mechanism of this mercury light initiated photooxidation is not yet fully understood. Because of the low absorption of low molecular weight chlorosilanes, most reactions studied were initiated by vacuum u.v. photolysis (13), mercury sensitization (14), or other radical sources (15). The absorption of light by Cl_3SiH or oxygen at 253.7 nm is expected to be very weak (16). In spite of this, many reactions were observed to proceed to completion in fairly short periods, strongly suggesting a radical chain pathway (17). Further work in elucidating the mechanism of trichlorosilane photooxidation is being done.

Properties and reaction of Cl_3SiOH.—Trichlorosilanol does not appear to be volatile. After repeated attempts it has not been observed in the gas phase. When 0.1 ml of the photolyzed solution containing >1500 ppm of Cl_3SiOH was placed in a 10 cm gas cell, only $SiCl_4$ and HCl were observed. After partial evacuation of the cell under vacuum, no —OH vibrations were observed. It is possible that the silanol when concentrated reacts rapidly to form nonvolatile linear products depicted by the reaction

$$n\,Cl_3SiOH \rightarrow Si_nO_{n-1}Cl_{2n+1}OH + (n-1)\,HCl \qquad [7]$$

or the cyclic analogues resulting from

$$n\,Cl_3SiOH \rightarrow Si_nO_nCl_{2n} + n\,HCl \qquad [8]$$

The avid chemical reactivity of the silanol is further evidenced by the inability to detect its presence in $SiCl_4$ by GC—MS (18). Either reaction in the injection port or on the column support is suspected.

The presence of monosilanol can be established by conversion to a more stable and analyzable derivative. One approach is to convert the silanol to a carboxylic ester via reaction [9]

$$Cl_3SiOH + RCOX \rightleftharpoons Cl_3SiOCOR + HX \qquad [9]$$

When acetyl chloride is added to solutions of the silanol at room temperature, a fast reaction occurs, as observed by infrared, giving rise to a spectrum too complex to analyze. When trifluoroacetic anhydride was added, the SiOH band gradually decreased in the liquid phase infrared spectrum. In a gas phase spectrum, new bands at 1875, 1810, 1200, and 1130 cm^{-1} were observed, which did not correspond to any of the bands of trifluoroacetic anhydride, $SiCl_4$, or Si_2OCl_6 (Fig. 2). The band at 1810 cm^{-1} is reported to be a characteristic absorption of the ester, $Cl_3SiOCOCF_3$ (20). Addition of the anhydride to $SiCl_4$ under the same conditions does not appear to give rise to any new bands. The direct GC—MS determination of this derivative is a potentially useful analytical method for the determination of Cl_3SiOH.

Trichlorosilanol in silicon tetrachloride undergoes several other chemical reactions. Conversion to hexachlorodisiloxane, Si_2OCl_6, ([5a] or [5b]) is assured as previously stated. In the presence of P_2O_5, reaction [5a] was not found to be accelerated at room temperature. However, on prolonged standing the formation of phosphoric acid may occur and catalyze the reaction (21). A rapid reaction of Cl_3SiOH with phosphorus oxychloride occurs, leading to a disappearance of the SiOH band from the infrared spectrum, Fig. 3

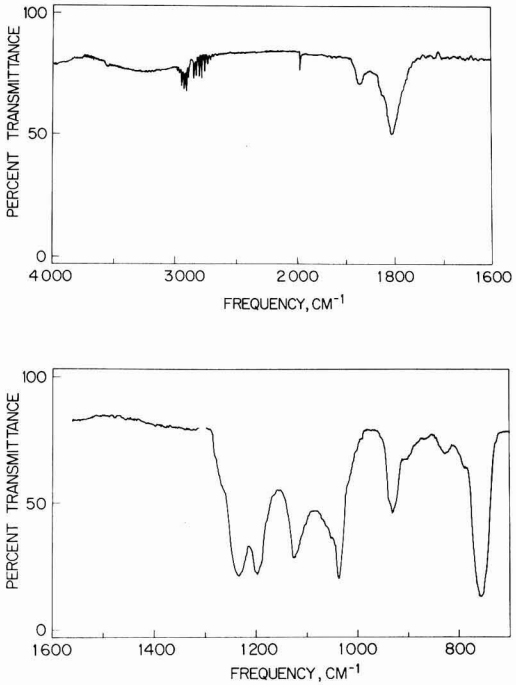

Fig. 2. Gas phase infrared spectrum of the reaction of Cl_3SiOH with $F_3COCOCOCF_3$ in $SiCl_4$.

$$Cl_3SiOH + OPCl_3 \rightarrow Cl_3SiOPOHCl_3 \qquad [10]$$

$$Cl_3SiOH + OPCl_3 \rightarrow Cl_3SiOPOCl_2 + HCl \qquad [11]$$

The reactions [10] and [11] are plausible, as well as

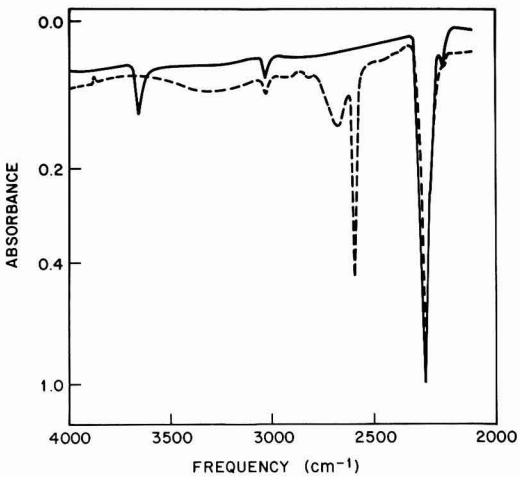

Fig. 3. Liquid phase spectrum of the reaction of Cl_3SiOH with $POCl_3$ in $SiCl_4$, (——) before and (---) after.

Table I. Infrared absorptivity and extinction coefficient of Cl_3SiOH

Experiment	Cl_3SiH		Cl_3SiOH		α	ϵ
	ΔA	ppm	ΔA	ppm	$\times 10^4$ ppm^{-1} cm^{-1}	liters mol^{-1} cm^{-1}
Photo 1	0.316	1263	0.532	1413	9.41	97
Photo 2	0.218	872	0.373	975	9.56	99
Photo 3	0.096	384	0.185	429	10.78	111
Average	—	—	—	—	9.92 ± 0.58	102 ± 6

strong hydrogen bonding to the phosphoryl oxygen, $Cl_3SiO - - - H - - - OPCl_3$. Trichlorosilanol has been found to react readily with a number of Lewis acids, BCl_3, $B(OCH_3)_3$, and $AlCl_3$ in $SiCl_4$, reaction [12], Fig. 4

$$Cl_3SiOH + RX_3 \rightarrow Cl_3SiORX_2 + HX \qquad [12]$$

This is not surprising since BCl_3 reacts with cyclic silaxones (22), and silyl ethers (23) at room temperature and $B(OCH_3)_3$ reacts with SiOH groups on silica gel (24). Mass spectral analyses of the reaction products will be sought in subsequent work. At room temperature in the presence of excess PCl_3, there is no reaction of Cl_3SiOH, as shown in Fig. 5.

Determination of infrared absorption coefficient.—If trichlorosilane is photo-oxidized to the monosilanol quantitatively under the appropriate experimental conditions, then it is possible to obtain a direct extinction coefficient or absorptivity for this compound. Table I shows the results obtained by photolyzing solutions of varying concentration of silane. The concentration of trichlorosilane has been determined quantitatively from the absorptivity measured by Kometani *et al.* (1). After our direct conversion of standard amounts of the silane to monosilanol under conditions minimizing further reaction of monosilanol, the absorptivity in units of ppm^{-1} cm^{-1} and extinction coefficient in units of liter mol^{-1} cm^{-1} were calculated. Corrections were made for volume and mass losses during photolysis and for —OH blank values resulting from photolyzing $SiCl_4$ alone. An average value of absorptivity of $9.92 \pm 0.58 \times 10^{-4}$ ppm^{-1} cm^{-1} or ϵ of 102 ± 6 liters mol^{-1} cm^{-1} was obtained. This is compared with the values obtained from measurements of Kometani *et al.* (1) for triphenyl silanol and diphenyl disilanol in CCl_4 of 1.56×10^{-3} ppm^{-1} cm^{-1} (159.3 liters mol^{-1} cm^{-1}), of Rouviere and Salvinen (21) for trimethyl silanol in CCl_4 of 1.24×10^{-3} ppm^{-1} cm^{-1} (127 liters mol^{-1} cm^{-1}), and various other literature values for SiOH ranging from 25 to 135 liters mol^{-1} cm^{-1} (21). The precision of measurements reported in this paper is quite acceptable in view of the reactivity of the Cl_3SiOH specie and reflect that generating ordinarily unavailable species by photochemical reactions is a viable approach to producing known quantities of trace species for comparison standards for trace analysis.

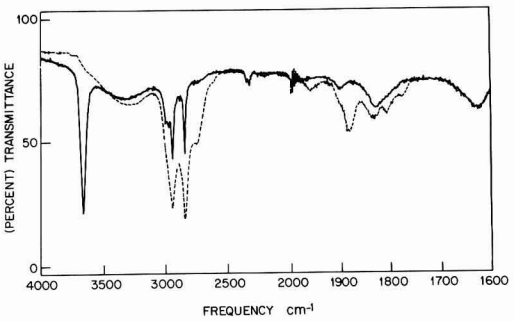

Fig. 4. Liquid phase spectrum of the reaction of BCl_3 with Cl_3SiOH in $SiCl_4$, (——) before and (---) after.

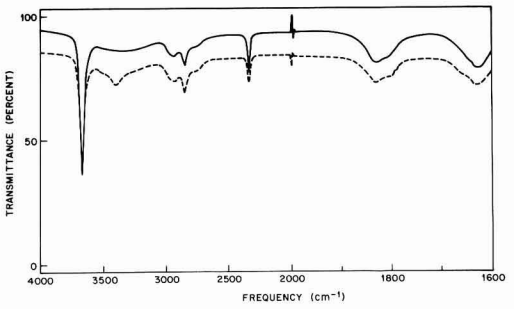

Fig. 5. Liquid phase spectrum of the addition of PCl_3 to Cl_3SiOH in $SiCl_4$, (——) before and (---) after.

Acknowledgments

The authors thank M. Grasso, J. E. Kessler, T. Y. Kometani, and M. Melliar-Smith for invaluable supplies of purified chemicals. J. P. Luongo, S. R. Nagel, and D. L. Wood also provided valuable assistance and helpful suggestions.

Manuscript submitted Oct. 2, 1981; revised manuscript received Dec. 18, 1981.

Any discussion of this paper will appear in a Discussion Section to be published in the June 1983 JOURNAL. All discussions for the June 1983 Discussion Section should be submitted by Feb. 1, 1983.

Publication costs of this article were assisted by Bell Laboratories.

REFERENCES

1. T. Y. Kometani, D. L. Wood, and J. P. Luongo, *Anal. Chem.*, In press.
2. T. Y. Kometani and F. Gholsten, Bell Labs Internal Publication, July 23, 1979.
3. T. Y. Kometani and D. L. Wood, Bell Labs Internal Publication, November 8, 1979.
4. R. L. Barnes, E. A. Chandross, and C. M. Melliar-Smith, Bell Labs Internal Publication, February 14, 1980.
5. (a) L. T. Manzione, Bell Labs Internal Publication, January 4, 1980; (b) J. S. Osinski and L. T. Manzione, Bell Labs Internal Publication, July 28, 1981.
6. D. L. Wood, T. Y. Kometani, J. P. Luongo, and M. Saifi, *J. Am. Ceram. Soc.*, **62,** 638 (1979).
7. J. E. Kessler, Unpublished results.
8. D. L. Wood, J. P. Luongo, and S. S. Debala, *Anal. Chem.*, **53,** 1967 (1981).
9. R. V. Adams, *Phys. Chem. Glasses*, **2,** 39 (1961).
10. I. R. Beattie and G. McQuillion, *J. Chem. Soc.*, 2072 (1962).
11. V. J. Goubeau and R. Warnecke, *Anorg. Chem.*, **259,** 109 (1949).
12. H. J. Emeleus and A. J. E. Welch, *J. Chem. Soc.*, London, 1928 (1939).
13. M. E. Jacox and D. E. Milligan, *J. Chem. Phys.*, **49,** 3130 (1968).
14. K. G. Sharp, P. A. Sutor, T. C. Farrar, and K. Ishibitsu, *J. Am. Chem. Soc.*, **97,** 5612 (1975).
15. (a) R. N. Haszeldine, C. R. Pool, and A. E. Tipping, *J. Chem. Soc. Dalton*, 2305 (1974), 2292 (1975); *J. Chem. Soc. Perkin I*, 2293 (1974); (b) J. A. Kerr, B. J. A. Smith, A. F. Trotman-Dickenson, and J. C. Young, *J. Chem. Soc. A*, 510 (1968).

16. The onset of light absorption in Cl_3SiH is at 170 nm, R. Roberge, C. Sandorfy, and O. P. Strausz, *Theort. Chim. Acta Berl.*, **52,** 171 (1979) and in $SiCl_4$ at 155 nm, G. C. Caisley and B. R. Russell, *J. Electron Spectrosc. Relat. Phenom.*, **8,** 71 (1976), **11,** 383 (1977). The onset of absorption by O_2 in the gas phase is 245 nm, see J. G. Calvert and J. N. Pitts, "Photochemistry," pp. 205-208, Wiley, New York (1966).
17. M. A. Nay, G. N. C. Woodall, O. P. Strausz, and H. E. Gunning, *J. Am. Chem. Soc.*, **87,** 179 (1965).
18. D. LaPerriere. ERC, Personal communications, September, 1980.
19. See V. Bazant, V. Chrlovsky, and J. Rathovsky, "Organosilicon Compounds," pp. 61-67, Academic Press, New York (1965).
20. P. Sartori and M. Weidenbruch, *Chem. Ber.*, **100,** 2049 (1967).
21. J. Rouviere and J. Salvinien, *J. Chim. Phys.*, **66,** 149 (1969).
22. P. A. McCusker and T. Ostdick, *J. Am. Chem. Soc.*, **80,** 1103 (1958).
23. W. Airey and G. M. Sheldrick, *J. Inorg. Nucl. Chem.*, **32,** 1827 (1970).
24. C. Morterra and M. J. D. Low, *Ann. NY Acad. Sci.*, **220,** 133 (1953).

The Role of Be in (GaAl)As/GaAs Solar Cells

Kazuya Masu[1], Shin-ichi Nakatsuka, Makoto Konagai, and Kiyoshi Takahashi

Department of Physical Electronics, Tokyo Institute of Technology, 2-12-1, Ohokayama, Meguro-ku, Tokyo 152, Japan

ABSTRACT

Some fundamental properties of beryllium in (GaAl)As/GaAs solar cells were investigated. The diffusion of Be into GaAs during LPE growth of Be-doped p-$Ga_{0.2}Al_{0.8}As$ was first investigated in order to control the junction depth. The temperature dependence of the diffusion coefficient was found to take the form $D = D_0 \exp(-E_0/kT)$, where $D_0 = 11.2$ $cm^2\ sec^{-1}$ and $E_0 = 2.43$ eV. The diffusion coefficient was also found to be approximately proportional to the beryllium concentration in the growth melt. The acceptor energy level for Be in $Ga_{0.2}Al_{0.8}As$ found from the temperature dependence of free carrier concentration was 47 meV, being smaller than that for Zn, 65-80 meV. (GaAl)As/GaAs p-p-n solar cells using Be as p-type dopant have high conversion efficiency in excess of 20% (AMl), and the highest output power 5 Wcm^{-2} was obtained at 400 suns.

(GaAl)As/GaAs p-p-n solar cells have demonstrated high conversion efficiency in excess of 20% under AMl illumination (1) and are particularly interesting for use in sunlight concentrating systems (2, 4-8). Of the various p-type dopants, such as Ge (3), Zn (1, 4), and Be (5-7, 9) used in the preparation of (GaAl)As/GaAs solar cells, beryllium seems to be one of the most attractive. However, there has been no reported fundamental study of Be in (GaAl)As/GaAs solar cells to determine Be diffusion and electrical properties of Be-doped layers.

In this paper, we describe diffusion and doping behavior of Be in (GaAl)As/GaAs solar cells. The diffusion of Be into GaAs during LPE growth of Be doped p-$Ga_{0.2}Al_{0.8}As$ was investigated, and the diffusion coefficient was found to vary with temperature and Be concentration in the growth melt of Ga-Al-As. The electrical properties of Be-doped p-$Ga_{0.2}Al_{0.8}As$ were measured by the modified van der Pauw method. The acceptor energy level for Be in $Ga_{0.2}Al_{0.8}As$ was found to be smaller than that for Zn. Photovoltaic characteristics of these Be-doped (GaAl)As/GaAs solar cells were also evaluated.

Diffusion of Be into GaAs during LPE Growth of Be-Doped p-(GaAl)As

(GaAl)As/GaAs p-p-n solar cell structures are often formed on n-GaAs substrate by LPE. This is most simply done by allowing the p-type dopant to diffuse into the n-GaAs substrate during growth of the GaAlAs window layer to produce the needed p-n junction. It is important to control the junction depth, *i.e.*, the thickness of p-GaAs diffused region, because the collection efficiency of the junction and the short-circuit current density of the cell depend strongly on junction depth.

Epitaxial $Ga_{0.2}Al_{0.8}As$ layers were grown on (111)B n-GaAs ($n \simeq 1 \times 10^{17}$ cm^{-3}) or (100) undoped n-GaAs ($n \simeq 1 \times 10^{16}$ cm^{-3}) substrate using the conventional sliding boat LPE systems. Beryllium was diffused into the n-GaAs substrate during the growth of Be-doped p-(GaAl)As to form the p-GaAs region in n-GaAs substrates. The growth conditions were as follows: (*i*) initial growth temperature T_1: 700°-900°C; (*ii*) cooling rate α: 0-0.5°C min^{-1}; (*iii*) growth duration t: 10-120 min; (*iv*) Be concentration in the growth melt of Ga-Al-As C_{Be}: 0.01-0.3 atomic percent (a/o).

The thickness of Be-doped p-$Ga_{0.2}Al_{0.8}As$ epitaxial layers varies with growth temperature from 1.3 μm at 700°C to 6.9 μm at 900°C for cooling rate 0.5°C min^{-1} and growth duration 30 min. For constant cooling rate, growth duration, and Be concentration in the melt, the thickness of the Be-diffused p-GaAs region was found to increase with increasing growth temperature. Figure 1 shows the temperature dependence of the diffusion coefficient of Be into GaAs for a cooling rate of 0.5°C min^{-1}, growth duration of 30 min, and Be concentration of 0.043 a/o. The diffusion coefficient D is defined as $W = (Dt)^{1/2}$, where W is the thickness of the p-GaAs region and t is the growth duration. The temperature dependence of the diffusion coefficient takes the form

$$D = D_0 \exp(-E_0/kT)$$

where $D_0 = 11.2$ $cm^2\ sec^{-1}$ and $E_0 = 2.43$ eV. These values are very similar to those for Zn reported by Goldstein (10). The other straight line in this figure is the Be diffusion coefficient into GaAs reported by Poltoratskii and Stuchebnikov (11): these data were obtained by using a closed-ampul annealing technique.

With other growth parameters held constant, the thickness of the p-GaAs region increases with increasing growth duration, *i.e.*, diffusion time. Figure 2 shows the thickness of p-GaAs region as a function of growth duration at a temperature of 750°C. For a given Be concentration in the growth melt, the thickness of the p-GaAs region was found to be proportional to the square root of the diffusion time and satisfies the empirical relation

$$W(\mu m) = 0.33t^{1/2} - 0.45$$

Figure 3 shows the Be concentration dependence of the thickness of p-GaAs region for growth tempera-

[1] Present address: Research Institute of Electrical Communication, Tohoku University, Kitahira, Sendai 980, Japan.
Key words: solar cells, GaAs, GaAlAs, beryllium doping.

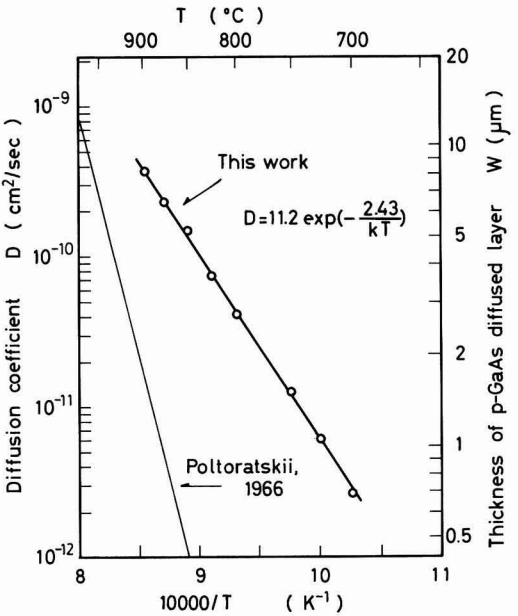

Fig. 1. Temperature dependence of Be diffusion coefficient and p-GaAs region thickness. The growth conditions are (1) cooling rate, 0.5°C min^{-1}; (2) growth duration, 30 min; (3) Be concentration in a growth melt, 0.043 a/o. The other straight line is the Be diffusion coefficient obtained by the closed-ampul annealing technique [see Ref. (11)].

ture 750°C and cooling rate 0.5°C min^{-1}. The thickness of p-GaAs increases with increasing Be concentration in the growth melt, and the free carrier concentration also tends to increase. Under the assumption of $W = (Dt)^{1/2}$, D is approximately directly proportional to the Be concentration, although there is some scattering of data points, as illustrated in Fig. 3.

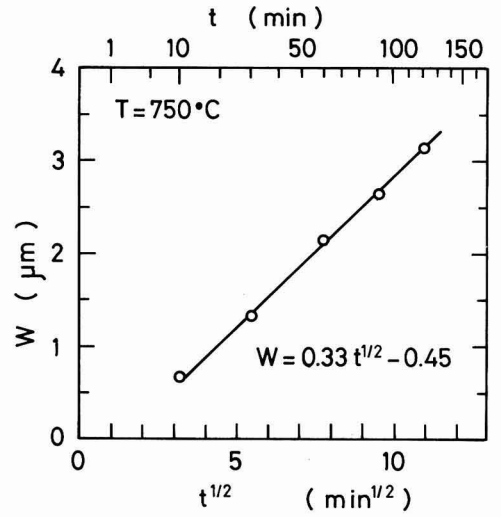

Fig. 2. Time dependence of the thickness of p-GaAs region. The growth conditions are (1) growth temperature, 750°C; (2) cooling rate, 0°C min^{-1}, (3) Be concentration, 0.043 a/o.

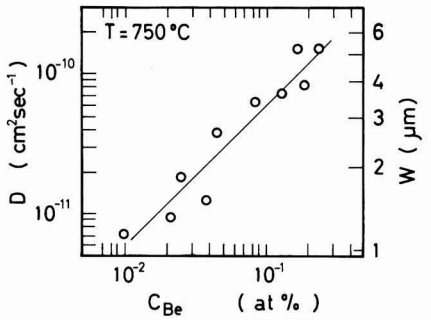

Fig. 3. Diffusion coefficient and p-GaAs region thickness as a function of Be concentration. The growth conditions are (1) temperature, 750°C; (2) cooling rate, 0-0.5°C min^{-1}; (3) growth duration, 30 min.

The identification and description of the detailed mechanism that dominates the diffusion process during LPE growth require more detailed work.

Electrical Properties of Be-Doped p-(GaAl)As and p-GaAs

Electrical properties such as resistivity of the surface p-(GaAl)As and p-GaAs are important because the photovoltaic efficiency under sunlight concentration conditions is increasingly degraded as the magnitude of the sheet resistance of the surface layers increases. The electron diffusion length in the p-GaAs region is also of importance in establishing the carrier collection efficiency and hence the short-circuit current density of the solar cells. Some electrical properties of beryllium-doped materials are reported in this section.

The modified van der Pauw method proposed by Petritz was used to measure the electrical properties of p-(GaAl)As and p-GaAs layers (12). The fundamental aspects are as follows. First, the average resistivity, hole mobility, and free-carrier concentration of p-(GaAl)As/p-GaAs structure were measured using the van der Pauw method. Then, the surface p-(GaAl)As layer was removed by selectively etching with HF, and the measurements for p-GaAs were repeated. After these measurements, resistivity, hole mobility, and free-carrier concentration of the etched off p-(GaAl)As layer were calculated as previously reported (13). These measurements were carried out over the temperature range of 90-420 K. While calculating the carrier concentration, the Hall coefficient factor was assumed to be unity for simplicity.

Figure 4 shows the temperature dependence of resistivity, hole mobility ,and free-carrier concentration for Be-doped p-$Ga_{0.2}Al_{0.8}As$ and Be-diffused p-GaAs. As illustrated in Fig. 4(a), the resistivity of p-$Ga_{0.2}Al_{0.8}As$ is about ten times higher than that of p-GaAs, being the same behavior as Zn-doped layers reported previously (13). The variation of free-carrier concentration with temperature [Fig. 4(c)] has been used to calculate the acceptor energy level E_a and the acceptor concentration N_a for Be. The acceptor energy level for Be in $Ga_{0.2}Al_{0.8}As$ was found to be 47 meV as compared to that for Zn, 65-80 meV. This small acceptor energy level for Be indicates the resistivity of the p-(GaAl)As layer could be reduced by use of Be. Thus, Be is considered to be a more suitable dopant for reduction of sheet resistance of (GaAl)As/GaAs solar cells.

The variation of room temperature free-carrier concentration and resistivity of p-$Ga_{0.2}Al_{0.8}As$ with the Be concentration C_{Be} in the growth melt are illustrated in Fig. 5. The free-carrier concentration is approximately proportional to the Be concentration C_{Be} in the

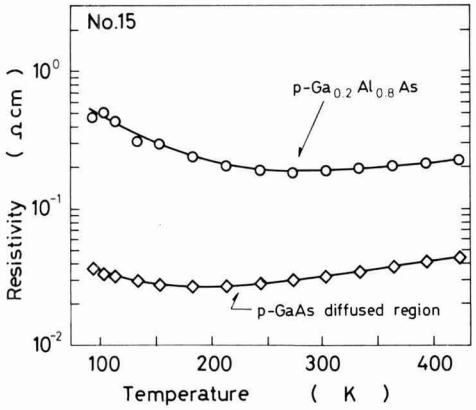

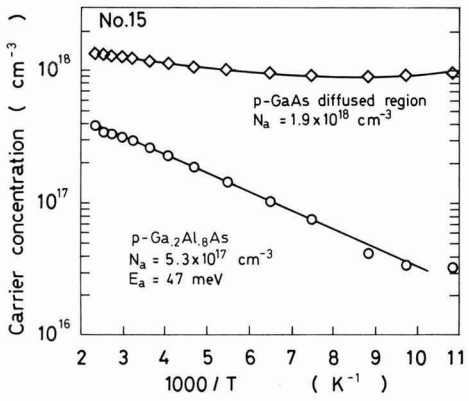

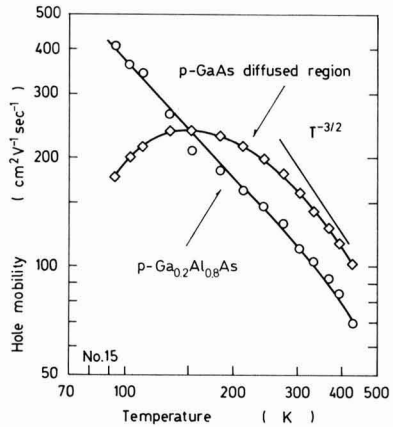

Fig. 4. Variation of (a, top left) resistivity, (b, top right) hole mobility, and (c, bottom left) carrier concentration with temperature for Be-doped p-$Ga_{0.2}Al_{0.8}As$ and p-GaAs. Beryllium concentration in a growth melt is 0.03 a/o. The acceptor energy levels E_a and the acceptor concentrations N_a in Fig. 4(c) are (1) $E_a < 15$ meV, $N_a = 1.9 \times 10^{18}$ cm^{-3} in p-GaAs, and (2) $E_a = 47$ meV, $N_a = 5.3 \times 10^{17}$ cm^{-3} in p-$Ga_{0.2}Al_{0.8}As$.

range of 0.02-0.2 a/o. The distribution coefficient k for Be in $Ga_{0.2}Al_{0.8}As$ is about 0.03. The resistivity decreases with increasing Be concentration in the growth melt, not being inversely proportional to C_{Be} because of the decrease of the mobility with increasing free-carrier concentration.

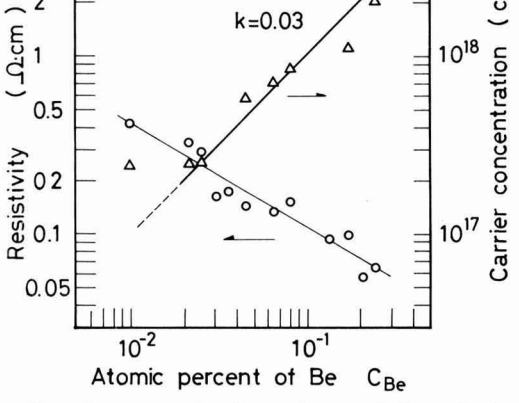

Fig. 5. Room temperature free-carrier concentration and resistivity of Be-doped p-$Ga_{0.2}Al_{0.8}As$ vs. C_{Be}. P-$Ga_{0.2}Al_{0.8}As$ layers were grown at 750°C.

The electron diffusion length L_n in the p-GaAs region was evaluated by the SEM beam-induced current technique (14). The beam energy was 20 keV and the induced current was measured point by point as the electron beam was scanned perpendicular across the junction (Fig. 6). The measured p-GaAs region was Be-diffused p-GaAs region in the undoped n-GaAs epitaxial layer. The thickness of p-GaAs region is 7 μm. The room temperature free-carrier concentration is about 1×10^{18} cm^{-3} on the average. The value of L_n was determined from the relation $I \propto \exp(-X/L_n)$, where X is the distance from the p-n junction. A more rapid decrease of induced current near the junction in Fig. 6 may be due to the surface recombination effect (14). L_n determined from the slope far from the junction was 4.3 μm.

It is noted that the doping level and free-carrier concentration are not uniform throughout the whole layer of p-GaAs, because the p-GaAs region was formed by the Be diffusion during LPE growth of p-(GaAl)As. The true carrier concentration at the heterointerface between p-(GaAl)As and p-GaAs, *i.e.*, $X \simeq 7$ μm in Fig. 6, is about 2×10^{18} cm^{-3} and that at the junction is about 10^{16} cm^{-3}. Thus the free-carrier concentration increases from about 5×10^{17} cm^{-3} at $X \simeq 4$ μm to about 2×10^{18} cm^{-3} at $X \simeq 7$ μm. There is no reported value for the diffusion length in Be-doped p-GaAs, however this value is comparable or slightly smaller than that for Zn (15).

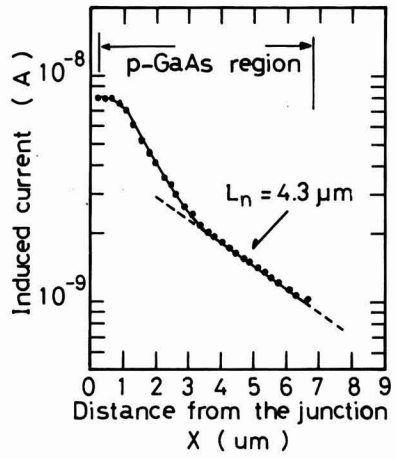

Fig. 6. Induced current vs. distance from the junction (V_{ac} = 20 kV). The free carrier concentration in p-GaAs is 1 × 10^{18} cm^{-3}.

A detailed paper about the distribution of free-carrier concentration in p-GaAs, which is formed by Be diffusion during LPE growth, will soon be submitted.

Photovoltaic Characteristics of (GaAl)As/GaAs p-p-n Solar Cells

(GaAl)As/GaAs solar cells were formed on (100) n^+-GaAs substrate by growing Sn-doped n-GaAs (2-5 × 10^{17} cm^{-3}) and Be-doped p-$Ga_{0.2}Al_{0.8}As$ at 750°C. Beryllium was diffused into the n-GaAs epitaxial region during the growing process of p-(GaAl)As to produce a GaAs p-n structure. The junction depth and the thickness of p-(GaAl)As surface layer were both 2 μm.

After the epitaxial growth, an Ag + Zn (10:1) front contact was formed on the p-GaAs layer, not on the p-(GaAl)As layer (4). The front pattern was formed by using the usual photoresist technique. Then the back-side was coated with Au + Ge (10:1), and the ohmic metals were sintered. The front grid pattern was again coated with thick layer of gold (1-3 μm) by an electroplating technique to reduce the grid strip resistance. The AR coating was applied by vacuum evaporation of Sb_2O_3. The refractive index of Sb_2O_3 is 1.94-1.97 and the reflection at 630 nm (Sb_2O_3 800Å) is less than 1%, so Sb_2O_3 could be considered one of the most suitable materials for single layer coating.

The cell characteristics under simulated AM1 and terrestrial insulation are shown in Table I. The n value, which is calculated from the slope of dark I-V characteristics, is 1.2-1.4. These cells have a conversion efficiency in excess of 20% calculated on the basis of active area only; contact coverage is about 10%. This efficiency is comparable to that reported previously for this type of cell.

Table I. Photovoltaic characteristics of (GaAl)As/GaAs p-p-n solar cells

No.	V_{oc} (V)	I_{sc}[a] (mA cm^{-2})	F.F.	η[a] (%)	P_{in} (mW cm^{-2})	AM	n[b]
36	0.984	25.4	0.83	20.7	100	1[c]	1.3
	0.987	22.9	0.83	24.7	76	1.3	
42	0.994	24.4	0.87	21.1	100	1[c]	1.25
49	1.00	23.0	0.84	19.4	100	1[c]	1.4

[a] Calculated for active area (coverage about 10%).
[b] Diode factor measured in dark I-V curve.
[c] Solar simulator.

Table II. Concentration dependence of cell performances (Cell No. 134)

C*	P_{in} (Wcm^{-2})	V_{oc} (V)	I_{sc} (Acm^{-2})	F.F.	η (%)	P_{out} (Wcm^{-2})
1	0.085	0.987	0.021	0.80	18.9	0.016
40	3.5	1.11	0.83	0.82	21.8	0.754
78	6.6	1.11	1.60	0.80	21.2	1.41
395	33.7	1.11	8.12	0.55	14.6	4.92

* Concentration ratio C and input power density P_{in} are assumed as $C = I_{sc}^{conc}/I_{sc}^{o}$, and $P_{in} = C \times P_{in}^{o}$, where I_{sc}^{conc} is the short-circuit current under concentration condition, I_{sc}^{o} is the short-circuit current without concentration, and P_{in}^{o} is the input power density of direct sunlight.

A different cell was placed in the concentrator assembly with flowing water and tested under solar concentration conditions. The photovoltaic characteristics of this cell are listed in Table II. The concentration ratio C is assumed to be the ratio of the short-circuit current under solar concentration condition to that without concentration. This cell has the peak efficiency at a concentration ratio of about 100 and the efficiency decreases at higher concentration due to a decrease in FF. The highest output power of about 5 Wcm^{-2} is obtained under 400 suns.

Summary

Some fundamental properties of beryllium in (GaAl)As/GaAs solar cells, the diffusion of Be into GaAs, electrical properties of Be-doped layers, and photovoltaic characteristics, were investigated. The diffusion of Be into GaAs during the growing process of Be-doped p-$Ga_{0.2}Al_{0.8}As$ was first investigated to control the junction depth. The temperature dependence of the diffusion coefficient has been found to take the form $D = D_o \exp(-E_o/kT)$, where D_o = 11.2 cm^2 sec^{-1} and E_o = 2.43 eV. The diffusion coefficient has also been found to be approximately proportional to the Be concentration in a growth melt of Ga-Al-As. The acceptor energy level for Be in $Ga_{0.2}Al_{0.8}As$ was 47 meV, being smaller than that for Zn, 65-80 meV. The electron diffusion length in Be-doped p-GaAs region was evaluated and L_n was found to be 4.3 μm for an average free-carrier concentration of 1 × 10^{18} cm^{-3}. Beryllium-doped (GaAl)As/GaAs solar cells have a conversion efficiency in excess of 20% (AM1), and the highest output power 5 Wcm^{-2} at a concentration ratio about 400 suns.

Manuscript submitted Aug. 14, 1981; revised manuscript received Nov. 17, 1981.

Any discussion of this paper will appear in a Discussion Section to be published in the June 1983 JOURNAL. All discussions for the June 1983 Discussion Section should be submitted by Feb. 1, 1983.

Publication costs of this article were assisted by Tokyo Institute of Technology.

REFERENCES

1. J. M. Woodall and H. J. Hovel, *Appl. Phys. Lett.*, **30,** 492 (1977).
2. L. W. James and R. L. Moon, *ibid.*, **26,** 467 (1975).
3. S. Charan, M. Konagai, and K. Takahashi, *ibid.*, **50,** 963 (1979).
4. J. Ewan, G. S. Kamath, and R. C. Knechtli, in "Proc. 11th IEEE Photovoltaic Specialists Conference," p. 409, IEEE, New York (1975).
5. J. Ewan, R. C. Knechtli, R. Loo, and G. S. Kamath, in "Proc. 13th IEEE Photovoltaic Specialists Conference," p. 941, IEEE, New York (1978).
6. R. Sahai, D. D. Edwall, and J. S. Harris, Jr., *Appl. Phys. Lett.*, **34,** 147 (1979).
7. R. Sahai, D. D. Edwall, and J. S. Harris, Jr., in "Proc. 13th IEEE Photovoltaic Specialists Conference," p. 946, IEEE, New York (1978).

8. H. A. VanderPlas, L. W. James, R. L. Moon, and N. J. Nelson, in "Proc. 13th IEEE Photovoltaic Specialists Conference," p. 934, IEEE, New York (1978).
9. K. Masu, M. Konagai, and K. Takahashi, in "Proc. 1st Photovoltaic Science and Engineering Conference in Japan," p. 191, (1979).
10. B. Goldstein, *Phys. Rev.*, **118**, 1024 (1960).
11. E. A. Poltoratskii and V. M. Stuchebnikov, *Sov. Phys. Solid State*, **8**, 770 (1960).
12. R. L. Petritz, *Phys. Rev.*, **110**, 1254 (1958).
13. K. Masu, M. Konagai, and K. Takahashi, *J. Appl. Phys.*, **51**, 1060 (1980).
14. W. H. Hackett, Jr., R. H. Saul, R. W. Dixon, and G. W. Kamlott, *ibid.*, **43**, 2857 (1972).
15. M. Ettenberg and C. J. Neuse, *ibid.*, **46**, 3500 (1975).

Phenomenological Model of the CVD Epitaxial Reactor

Jiří Jůza

Tesla Rožnov, Rožnov, Czechoslovakia

and Jan Cermák

Institute of Chemical Process Fundamentals, Czechoslovak Academy of Science, Prague, Czechoslovakia

ABSTRACT

A model of the epitaxial chemical vapor deposition reactor has been developed based on fundamental physicochemical principles. The kinetics of the heterogeneous deposition reaction is taken into account along with transport phenomena occurring in the gas phase above the deposition surface. The obtained set of partial differential equations is solved numerically, the results being compared with a representative set of experimental data and with previously published models. The comparison demonstrates the suitability of the model conception as well as its applicability for process design purposes.

The progress in semiconductor technology during the last 20 years has initiated development of industrial reactors for the chemical vapor deposition (CVD) of epitaxial silicon layers. Empirical methods have been used mostly for optimal design of these reactors and for the choice of their working regime. At the same time, however, the mechanism of the processes occurring in the deposition zone of an epitaxial reactor has been studied and numerous theoretical models have been developed that describe the distribution of silicon along the reactor deposition zone (1-14). The accuracy of these models and consequently their applicability for optimization of reactor construction and process regime has been limited, due to simplifying assumptions. In this work, a model is proposed based on the description of the physicochemical processes taking place in the deposition zone of an epitaxial reactor. This model was proved to be valid for those types of epitaxial reactors in which the direction of reaction mixture flow in the deposition zone is parallel to the deposition surface. The region of model applicability therefore includes the most common large-capacity epitaxial reactors: the so-called barrel reactors and horizontal reactors. Schematic presentation of both of these reactor types is given in Fig. 1.

Process Considerations

The character of the reaction mixture flow in the reactor deposition zone has not been clarified up to now, posing a major obstacle for process modeling. The reason for this is the existence of large temperature differences (up to 1000 K) between the deposition surface and reactor walls. Values of the Reynolds number, commonly used for the forced flow characterization, range between 10 and 300 in epitaxial reactors. Colburn (15) proved that the transition between laminar and turbulent flow takes place at Reynolds number values close to 2100 even when significant transverse temperature gradients exist in the system. Consequently, the epitaxial reactor should operate within the laminar flow region. However, for low reaction mixture flow rates, gravitational forces begin to play an important role in addition to the pressure forces that are responsible for the forced convection. As a result, free (natural) convection appears to be caused by density differences due to different temperatures in various parts of the deposition zone. This phenomenon has been commonly characterized by a criterion Gr/Re^2 (Gr = Grashof number), which can be understood as a ratio of buoyancy forces to the inertial ones. According to Sparrow (16) the transition between forced laminar flow and combined flow (forced and natural convection) occurs at $Gr/Re^2 = 0.3$ (combined flow exists at $Gr/Re^2 > 0.3$). Authors who studied the character of flow directly in the deposition zones of CVD reactors reported critical

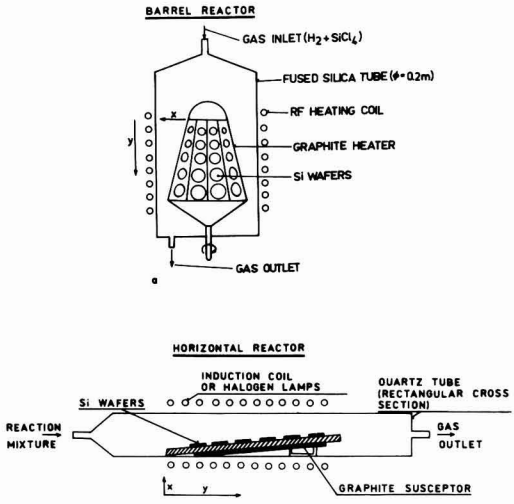

Fig. 1. Schematic picture of barrel and horizontal-type epitaxial reactors.

Key words: CVD, semiconductors, silicon epitaxy.

Gr/Re^2 values of the same order: Takahashi *et al.* (17), 0.4-4.1; Ban (18), 0.5; Hanzawa (19), 0.8-8. Values of $Gr/Re^2 = 0.004$-1.0 and 0.00004-0.01 correspond to typical conditions in the deposition zones of large-capacity epitaxial reactors at pressures of 100 and 10 kPa, respectively. Hence, epitaxial reactors work commonly in the region of forced convection or at the boundary of the transition region to combined convection.

In the last few years, several experimental studies have measured the transverse temperature and concentration profiles in the deposition zones of epitaxial reactors. Based on the result of such studies, gas phase transport phenomena can be evaluated in detail. Sedgwick *et al.* (20) used a noncontact measurement method to determine temperature profiles in a reactor deposition zone using pure hydrogen as a gas medium. Comparison of their experimental data with theoretical temperature profiles in corresponding regions of the deposition zone is shown in Fig. 2a; laminar flow was assumed in the theoretical profiles calculation. Even though the Gr/Re^2 criterion equaled 1.0 under conditions of the experiments, free convection due to gravitational forces was apparently insignificant, as can be judged from the agreement of the experimental data with theoretical profiles calculated for the laminar flow assumption. Ban (10, 18) measured temperature and concentration profiles in the deposition zone of a horizontal reactor. The reaction mixture was substituted by helium during the temperature profile measurements. (Values of the criterial product $Re \cdot Pr$ characterizing heat transfer are close to those for hydrogen.) Comparison of temperature profiles obtained in He with theoretical profiles calculated for H_2 assuming laminar flow conditions is presented in Fig. 2b. The agreement is good at lower gas flow rates (0.11 and 0.25 $msec^{-1}$) while significant differences were found at higher rates (0.5 $msec^{-1}$). Ban (18) proved in his work that temperature and concentration fluctuations existed in the gas phase at higher gas flow rates. Characteristic frequencies of these fluctuations were 3-5 Hz. Similarly Curtis (21), who measured temperatures at the surface of the heating susceptor of a barrel reactor, observed fluctuations at higher flow rates of hydrogen. Most likely, these fluctuations were not caused by the natural macroconvection since they were reported at higher values of Re and at low values of Gr/Re^2. The onset of turbulent instability should be considered in this respect in spite of low values of Re ($Re << 2100$). The flow instability mentioned above can generally bring about convective mixing of the gas phase and thus consequently a diminution of velocity, temperature, and concentration gradients. However, the typical period of the observed fluctuations (0.3-0.2 sec) was comparable with the residence time of the reaction mixture in the deposition zone. It is therefore impossible to assume in this case an intensive convective mixing of the reaction mixture. This conclusion is further supported by the fact that the rate of momentum, energy, and mass transport on the molecular scale was obviously higher than that of convective transport resulting from the flow instability. These considerations explain the existence of significant temperature gradients (up to 600 K cm^{-1}) proved experimentally (18), even in the presence of the fluctuations mentioned above. On the other hand, the existence of flow instabilities can explain the deterioration of the agreement between theoretical and experimental profiles with increasing gas flow rates (see Fig. 2b).

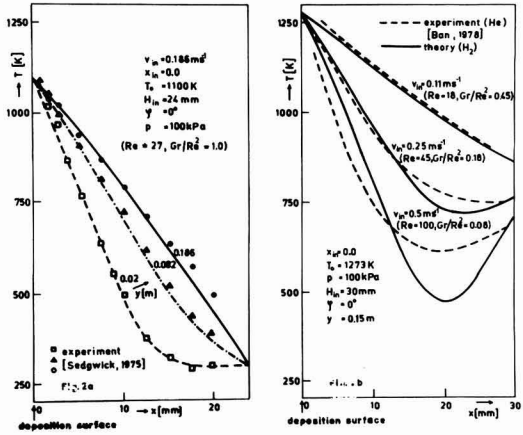

Fig. 2. Comparison of theoretical temperature profiles with experiment.

The "stagnant layer" model has to be mentioned in order to complete the discussion of flow patterns in deposition zones of epitaxial reactors. This model has been widely used (11-14) for its simplicity. It was developed on the basis of experimental data obtained by Eversteyn *et al.* (11), who fed a suspension of fine particles of TiO_2 in hydrogen into the deposition zone of a horizontal reactor. Formation of a gas layer with a lower content of TiO_2 particles closely attached to the deposition surface was observed at the deposition zone outlet in the range of values $Re = 30$-120 and $Gr/Re^2 = 0.02$-0.3. Based upon this observation, the authors assumed that a layer of relatively stagnant gas existed at the deposition surface while turbulent flow of the gas bulk could be expected above the "stagnant layer." However, an alternative explanation can be derived from the preceding experimental findings. At values $Gr/Re^2 < 0.3$, laminar gas flow takes place, exhibiting certain symptoms of turbulent instability at higher Re values. The "stagnant layer" can be then viewed as a diffusion boundary layer resulting from the thermodiffusion of TiO_2 particles in the direction perpendicular to the deposition surface.

Several authors (1-4) considered the deposition zone as a channel with laminar flow of the reaction mixture. A simplifying assumption of the existence of defined transverse velocity and temperature profiles, constant in the direction of gas flow, was further introduced. An alternative approach, used by other authors (7-10), was based on the application of a boundary layer theory for a description of momentum, energy, and mass transfer near the solid surfaces under conditions of laminar flow (22). Calculations of transverse profiles as well as the results presented by Manke and Donaghey (6) proved that for laminar flow conditions the assumption of constant transverse profiles was acceptable at the end of the reactor deposition zone, while the results yielded by the boundary layer theory corresponded to reality only at the deposition zone inlet. Apparently an adequate model has to take into consideration continuous development of transverse profiles along the whole deposition zone length (5).

In the process of the deposition of silicon epitaxial layers, the silicon-producing reaction has to proceed heterogeneously on the deposition surface. Reaction components are supplied by diffusion from the bulk of flowing gas phase. The rate of diffusion equals the rate of the heterogeneous reaction at a certain limit temperature, T_m. At significantly lower temperatures ($T << T_m$) the activated heterogeneous reaction is slow in comparison with diffusion and therefore becomes the rate-controlling step of deposition. On the other hand, at $T >> T_m$, deposition is controlled by the rate of diffusion in the gas phase. The temperature limit ranges between 1200 and 1400 K for the chemical vapor deposition of silicon layers, and depends on the reaction agent used ($SiCl_4$, $SiHCl_3$, SiH_2Cl_2, SiH_4). Epi-

taxial reactors work typically at temperatures 1200-1550 K, *i.e.*, in the transition region between kinetically and diffusionally controlled deposition. However, the heterogeneous reaction kinetics was not taken into consideration by the authors of previously suggested models (1-11). As a result these models are valid only in the region of diffusion-controlled deposition ($T >> T_m$).

The mechanism of heterogeneous reactions taking place during deposition of silicon epitaxial layers has not been satisfactorily explained up to now (14, 23). On the basis of theoretical considerations and experimental data from low pressure deposition, Duchemin (23) derived a relation for the rate of heterogeneous reaction for the case of silicon deposition from a mixture H_2 + reagent ($SiCl_4$, $SiHCl_3$, SiH_2Cl_2, SiH_4). For low reagent concentrations (which are typical for epitaxial deposition), this relation can be transformed into the form

$$r = k \cdot x_1 \sqrt{p} \qquad [1]$$

where r is the reaction rate ($\text{mol} \cdot \text{m}^{-2} \cdot \text{sec}^{-1}$), p the overall pressure in the deposition zone, and x_1 the mol fraction of a reagent at the deposition surface. The temperature dependence of the reaction rate constant k can be expressed by the Arrhenius equation

$$k = A \exp(-E/RT) \qquad [2]$$

The values of activation energy E (Eq. [2]) for chlorosilane reduction or for silane pyrolysis have been discussed frequently in the literature. No generally accepted value has been given. In most cases, the E values have been determined from experimental temperature dependencies of the deposition rate in the kinetics-controlled region of deposition ($T << T_m$). Differences in the published activation energy data [*e.g.*, data of E for $SiCl_4$ reduction are uniformly spread between 19 kcal/mol (24) and 60 kcal/mol (25)] cannot be ascribed solely to experimental errors. One of the possible reasons for the data discrepancies can be the neglect of the thermodiffusion effect in the evaluation of the rate constant, k, from experimental data. Significant concentration gradients can be observed in the deposition zone due to large temperature gradients that may arise, depending on the reactor construction and its working regime. As a result, the reagent concentration at the deposition surface x_1 can differ significantly from its concentration in the reaction mixture at the reactor inlet, x_{in}. Apparently, the temperature dependence of the x_1/x_{in} ratio can be responsible for the error in activation energy evaluation.

During chlorosilane reduction, $SiCl_2$ forms as a by-product. This compound, which is fairly stable at deposition temperatures, diffuses from the reaction surface to the bulk of the flowing reaction mixture, thus reducing the conversion of chlorosilane to silicon (26). Sedgwick (26), who measured transverse concentration profiles of $SiCl_2$ in the deposition zone of an epitaxial reactor, proved that $SiCl_2$ formation at the reaction surface increased with increasing content of hydrogen chloride in the reaction mixture. The content of hydrogen chloride (which is the main gaseous product of chlorosilane reduction) in the reaction mixture increases during the flow of the mixture through the deposition zone. The mechanism of $SiCl_2$ formation during chlorosilane reduction has not yet been satisfactorily explained. To derive a quantitative expression, a fast heterogeneous reaction was assumed

$$Si + 2HCl \leftrightharpoons SiCl_2 + H_2 \qquad [3]$$

Further assuming ideal behavior, a relation for the equilibrium constant of this reaction can be written in the form

$$K(T) = x_{SiCl_2}/x_{HCl}^2 \quad (x_{H_2} \doteq 1) \qquad [4]$$

where x denotes mol fraction. Thermodynamic equilibrium is not established at the reaction surface during silicon deposition (supersaturation by chlorosilane exists, especially at lower temperatures). Therefore, the constant $K(T)$ cannot be regarded as an equilibrium constant of reaction [3] but rather as an empirically adustable parameter of the model.

It is a well-established fact that the Si/Cl/H system encompasses, apart from $SiCl_4$, $SiCl_2$, and HCl, a whole spectrum of additional compounds. Formation of these compounds may be anticipated, particularly toward the end of the deposition zone. There, the mixture, being enriched by HCl and $SiCl_2$ (thermally unstable at 1200 K), may undergo a number of gas-phase reactions, especially the heterogeneous reactions on the reactor's wall (formation of polymers $(SiCl_2)_n$ etc.). Rigorous solution of the reaction kinetics and the transport of the reaction products poses a formidable task. From the modeling standpoint, however, these phenomena are only second to third order in magnitude, playing an important role mainly toward the end of the deposition zone.

The following conclusions can be drawn, based on the model considerations presented above:

1. Hydrodynamic regimes in the deposition zones of large-capacity epitaxial reactors with parallel flow range from natural convection to incipient turbulent instability. Laminar flow of the reaction mixture can be assumed between these two regions.
2. Transverse profiles of temperature, concentration, and longitudinal velocity develop along the whole length of the deposition zone.
3. Temperature and concentration dependencies of transport properties and of the reaction mixture density have to be considered, due to significant differences of temperature and concentration in a reactor deposition zone.
4. The effect of thermodiffusion has to be accounted for in the mass transfer description because of significant temperature gradients and large differences between molecular weight of the reagents and the gas carrier (H_2).
5. Epitaxial reactors work in the transition region between diffusion- and kinetics-controlled deposition.
6. In cases of chlorosilane reduction, the content of hydrogen chloride in the reaction mixture increases during its flow through the deposition zone. The yield of the deposition reaction consequently decreases [as the presence of HCl in the reaction mixture favors a competitive reaction (3)].

Model Formulation

Let us assume that the reaction mixture flows in the direction of coordinate y, where $y = 0$ at the deposition zone inlet. The coordinate x is directed transversely across the deposition zone channel: $x = 0$ at the deposition surface, $x = H(y)$ at the reactor wall.

The following assumptions were further used in model formulation:

1. The flow of the reaction mixture is laminar.
2. The reaction mixture can be considered as a two-component system (1, reagent; 2, gas carrier) for the description of gas phase transport phenomena.
3. No chemical reaction takes place in the bulk phase.
4. External forces (including the gravitation forces) are negligible.
5. The channel width is infinite in the direction of coordinate z.

Balance equations were then written in the form (22)

mass conservation equation for the component (1)

$$(\vec{\nabla} \cdot \vec{\mathbf{n}}_1) = 0 \qquad [5]$$

equation of mass conservation for the mixture

$$(\vec{\nabla} \cdot \rho \vec{\mathbf{v}}) = 0 \qquad [6]$$

equation of momentum conservation

$$|\vec{\nabla} \cdot \vec{\phi}| = 0 \qquad [7]$$

equation of energy conservation

$$(\vec{\nabla} \cdot \vec{e}) = 0 \qquad [8]$$

In Eq. [5]-[8] an arrow denotes a vector and two arrows a tensor of the second order. Symbol $\vec{\nabla}$ denotes the differential vector operator "nabla" defined as

$$\vec{\nabla} = i\,\partial/\partial_x + j\,\partial/\partial_y + k\,\partial/\partial_z \qquad [9]$$

Flow densities of individual balanced quantities are defined as

$$n_1 = \rho w_1 \vec{v} - \rho D \vec{\nabla} w_1 - D^T \vec{\nabla} \ln T \qquad [10]$$

$$\vec{\phi} = \rho \vec{v}\vec{v} + \vec{\tau} + p\vec{\delta} \qquad [11]$$

$$\vec{e} = -k\vec{\nabla}T + h\rho\vec{v} \qquad [12]$$

where ρ is density, w_1 mass fraction of a reagent, $\vec{v}$ velocity, D diffusion coefficient, T temperature, $\vec{\tau}$ stress tensor, p pressure, $\vec{\delta}$ a unit tensor, k heat conductivity coefficient, and h specific enthalpy of gas, which can be expressed (neglecting the heat of mixing) as

$$h = w_1 h_1 + (1 - w_1) h_2 \qquad [13]$$

The enthalpy of individual components can be expressed in the form

$$h_i = h_i^\circ + \bar{c}_{pi}(T - T^\circ) \qquad [14]$$

where h_i° denotes the enthalpy at a standard temperature T° and $\bar{c}_{pi}$ the average specific heat in the temperature interval (T°, T).

The flow density equations [10]-[12] were substituted into the mass, momentum, and energy balance equations [5]-[8], a tensor $\vec{\tau}$ was expressed for a Newtonian fluid, and the vector equation of motion (7) was rewritten as three scalar equations. A system of five partial differential equations was obtained after these arrangements, taking into consideration the independence of variables on the coordinate z.

Additional assumptions were then introduced stemming from the character of system modeled, as discussed above:

6. Axial diffusion and thermodiffusion are negligible.
7. Contribution of heat conduction in axial direction can be neglected.
8. Normal stress in axial direction can be neglected.
9. Both inertial and viscous effects of the transverse velocity are negligible.

The system of partial differential equations can be transformed under these assumptions into the final form

$$\rho\left(v_x\frac{\partial w_1}{\partial x} + v_y\frac{\partial w_1}{\partial y}\right) - \frac{\partial}{\partial x}\left(\frac{D^T}{T}\frac{\partial T}{\partial x}\right) = \frac{\partial}{\partial x}\left(\rho D\frac{\partial w_1}{\partial x}\right) \qquad [15]$$

$$\frac{\partial(\rho v_x)}{\partial x} + \frac{\partial(\rho v_y)}{\partial y} = 0 \qquad [16]$$

$$\rho\left(v_x\frac{\partial v_y}{\partial x} + v_y\frac{\partial v_y}{\partial y}\right) + \frac{\partial p}{\partial y} = \frac{\partial}{\partial x}\left(\mu\frac{\partial v_y}{\partial x}\right) \qquad [17]$$

$$\frac{\partial p}{\partial x} = 0 \qquad [18]$$

$$\rho C_P\left(v_x\frac{\partial T}{\partial x} + v_y\frac{\partial T}{\partial y}\right) + \rho\left[h_1^\circ - h_2^\circ + (\bar{c}_{p1} - \bar{c}_{p2})(T - T_o)\right] \cdot \left(v_x\frac{\partial w_1}{\partial x} + v_y\frac{\partial w_1}{\partial y}\right) = \frac{\partial}{\partial x}\left(k\frac{\partial T}{\partial x}\right) \qquad [19]$$

Equations [15]-[19] represent a system of five differential equations that can be solved for w_1, v_x, v_y, p, and T as functions of the independent variables x and y for the following boundary conditions

$$y = 0 \quad w_1 = w_{in}$$
$$v_x = 0 \quad v_y = v_{in}(x)$$
$$P = P_{in} \quad T = T_{in}(x) \qquad [20]$$

$$y > 0; \quad x = 0$$
$$\rho D\frac{\partial w_1}{\partial x} + \frac{D^T}{T}\frac{\partial T}{\partial x} = r M_1$$
$$v_x = 0 \quad v_y = 0$$
$$p = p_{in} + \int_o^y \frac{\partial p}{\partial y}dy \quad T = T_o(y) \qquad [21]$$

$$y > 0; \quad x = H(y)$$
$$\rho D\frac{\partial w_1}{\partial x} + \frac{D^T}{T}\frac{\partial T}{\partial x} = 0$$
$$v_x = 0 \quad v_y = 0$$
$$p = p_{in} + \int_o^y \frac{\partial p}{\partial y}dy \quad T = T_H(y) \qquad [22]$$

The first boundary condition in Eq. [21] represents a strongly nonlinear condition determining reagent concentration in the gas phase at the deposition surface. In this equation, r denotes the rate of heterogeneous reaction (kmol · m^{-2} · sec^{-1}) on the deposition surface determined by Eq. [1] or [1a]. This boundary condition corresponds to the demand of equality of reaction rate and diffusion flow from the gas phase at the deposition surface. After solving the system of partial differential equations [15]-[19] for the appropriate boundary conditions [20]-[22], the distribution of the silicon deposition rate along the reactor deposition zone can be determined from the relation

$$g(y) = \theta(y)\, M_{Si}/M_1\rho_{Si}\left(\rho D\frac{\partial w_1}{\partial x} + \frac{D^T}{T}\frac{\partial T}{\partial x}\right)\Bigg|_{y,x=0} \qquad [23]$$

Parameter θ represents the yield of the deposition reaction

$$\theta = 1 - (n_{SiCl_2}/n_{SiCl_4})(M_{SiCl_4}/M_{SiCl_2}) \qquad [24]$$

An estimation of the mass flux n_{SiCl_2} can be obtained from an approximate analytical solution of the steady diffusion of $SiCl_2$ in a laminar stream of hydrogen with a transverse temperature gradient. The concentration of $SiCl_2$ on the deposition surface can be calculated from Eq. [4] and the concentration of hydrogen chloride x_{HCl}, needed for evaluation of Eq. [4] can be obtained from the mass balance assuming constant concentration x_{HCl} across the channel. If SiH_4 is used as a reagent, $n_{SiCl_2} = 0$.

Discussion of Results

The numerical solution of the deposition zone model (Eq. [15]-[24]) is briefly characterized in Appendix A.

Methods used for description of the physical properties of the reaction mixture and values of physical parameters used for calculation are summarized in Appendix B.

The computer program (rem. 1)[1] used for numerical calculation yielded an estimation of the distribution of the silicon deposition rate along the reactor deposition zone for a specified reactor geometry and technological conditions in the reactor deposition zone. The program further gave transverse temperature, velocity, and concentration profiles in the deposition zone at various values of the length coordinate y. Examples of transverse profiles, calculated for typical deposition zone conditions in large-capacity epitaxial reactors, are presented in Fig. 3a, b, and c. Temperature profiles are shown in Fig. 3a, profiles of axial velocity in Fig. 3b, and profiles of $SiCl_4$ mass fraction, w_1, in Fig. 3c. The axial coordinate of the deposition zone, y, is a parameter in all three figures. As can be seen from Fig. 3, transverse temperature, velocity, and concentration profiles develop along the whole deposition zone length. In Fig. 3c (concentration profiles) a strong thermodiffusion effect is clearly apparent, especially near the reactor walls. A strong temperature gradient evokes a significant gradient of concentration, despite the fact that the diffusional mass flow through the reactor walls equals zero (Eq. [22]).

The effect of some model simplifications, discussed in the section "Process Considerations," is shown in Fig. 4. Experimental data on the distribution of deposition rate along the deposition zone, obtained by the authors from an industrial barrel-type reactor (with $SiCl_4$ as a reagent), are plotted in this figure. Details on the reactor design and experiments can be found in the next paragraphs. Curve A represents the estimation of the deposition rate obtained from the theoretical model

[1] rem. 1: The computer program is available on request at the Tesla Rožniv.

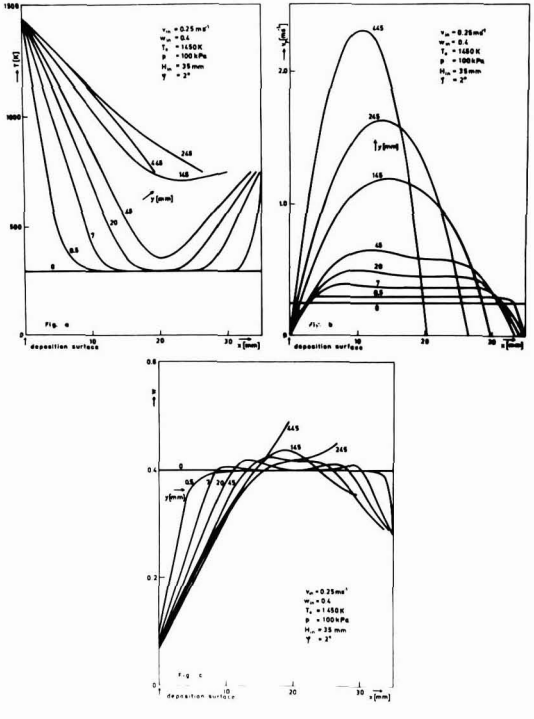

Fig. 3. Temperature, velocity, and concentration profiles in the deposition zone of the epitaxial reactor.

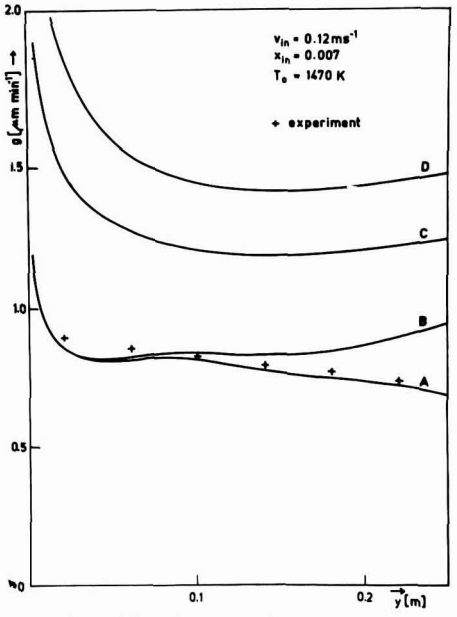

Fig. 4. Effect of some simplifying assumptions

(described above) for the experimental conditions. Curves B, C, and D were obtained using modified versions of the computation program corresponding to the neglect of various effects. Curve B corresponds to neglecting the effect of the reaction product HCl on the yield of the deposition reaction. The thermodiffusion effect was further neglected to obtain curve C. In the case of curve D, the additional simplifying assumption of a diffusion-controlled deposition (an assumption of zero reactant concentration at the deposition surface) was introduced. It is apparent from Fig. 4 that the effects of thermodiffusion and deposition reaction kinetics are significant and their neglect diminishes severely the model's applicability.

Low-pressure deposition (typically at 10 kPa) (27) appears to be a promising method for some types of epitaxial layers. Duchemin (23) published experimental data on the pressure dependency of the silicon deposition rate in the region 2-60 kPa; $SiCl_4$ was used as a reagent. Comparison of the experimental data with the pressure dependency estimated from the theoretical model (described above) for corresponding experimental conditions is presented in Fig. 5. Figure 5 shows rather poor agreement between calculated and experimental data at the lower pressure values. Due to the low deposition temperature (1263 K), the deposition was controlled mostly by heterogeneous reaction kinetics. Therefore, a contradiction of the theoretical model with experimental data proves the unsuitability of the pressure dependency of deposition reaction kinetics (Eq. [1]) used in the calculations. Apparently this reflects the fact that the reaction mechanism for the heterogeneous reduction of $SiCl_4$ is not properly understood. A purely empirical equation was suggested (for $SiCl_4$ as a reagent) by the authors

$$r = kx_1\, p^{3/4}/(1 + Bp) \qquad [1a]$$

as an alternative kinetic expression instead of Eq. [1]. The estimation of the pressure dependency of the deposition rate obtained from the model using Eq. [1a] for the description of deposition reaction kinetics is shown in Fig. 5 ($B = 1 \cdot 10^{-4}$ Pa^{-1}). The application of the empirical equation [1a], however, impairs the homogeneity of the model in which all other functional

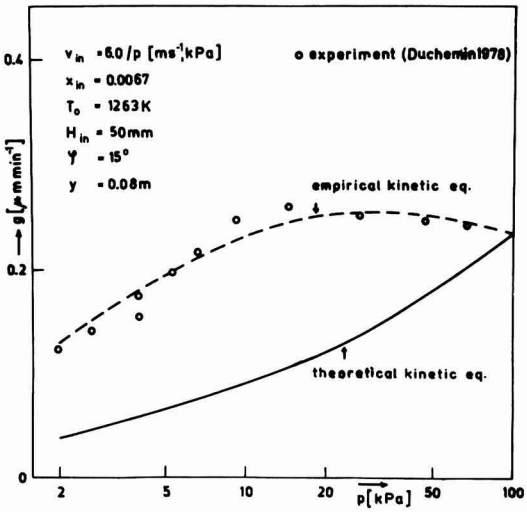

Fig. 5. Deposition rate pressure dependence

relations originate from physico-chemical considerations.

To compare the model with physical reality, a representative set of experimental data was at our disposal, characterizing the distribution of deposition rate along the length of deposition zone as a function of three factors, *i.e.*, velocity of the reaction mixture at the reactor inlet, reagent concentration in the reaction mixture, and deposition surface temperature. Ranges of these three factors were chosen to cover the region of technologically important regimes of the epitaxial reactor studied: v_{in} = 0.07-0.17 msec^{-1}; x_{in} = 0.002-0.012; and T_o = 1350-1590 K.

A set of experiments, designed according to principles of optimal search of the response surface, contained 30 experiments at 15 various reactor regimes. Experiments were carried out at atmospheric pressure using $SiCl_4$ as the reagent. The deposition rate was evaluated for each experiment at six points distributed equidistantly along the whole deposition zone in the direction of gas flow. Estimations of the deposition rate distribution along the deposition zone were calculated for each of the 15 reactor regimes using the model described above. Agreement of theoretical dependencies with experimental data was characterized separately for each of the regimes studied by the relative standard deviation. The average value of these deviations was: $\bar{s}_r$ = 8.2%. This value can be considered as an estimation of the model accuracy in the region of technologically important regimes of epitaxial reactors.

The computation program written for the numerical solution of the theoretical model was used for a rigorous comparison of the model suggested in this work with some previously published models; in particular, several models of diffusion in a channel with laminar flow of the reaction mixture, derived by Rundle (2), Fujii *et al.* (3), and by Manke and Donaghey (5, 6) were compared. Appropriate arrangements were made in the program for solution of individual models, corresponding to simplifying assumptions made by individual authors during model derivation. Results of the comparison are presented in Fig. 6, where curves E, F, and G represent dependencies obtained from the models of Rundle, Fujii, and Manke, respectively [GI = analytical solution (5), GII = numerical solution (6)]. Curve A corresponds to the theoretical model suggested in this work. Points in the graphs represent corresponding experimental data from a large-capacity barrel reactor. The distribution of deposition rates

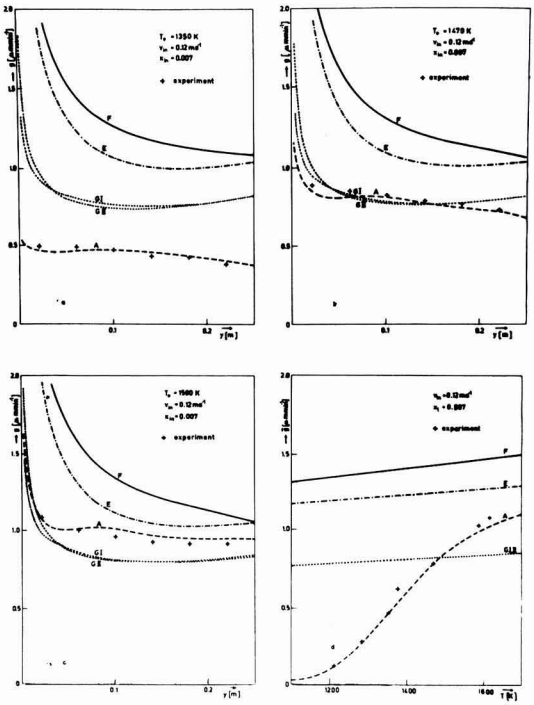

Fig. 6. Comparison of developed model with previously published ones and with experiment.

along the deposition zone is presented in Fig. 6a, b, and c for three different temperatures of the deposition surface. Figure 6d shows the dependency of the average deposition rate on the deposition surface temperature over a fairly broad range of temperatures. Figures 6a, b, c, and d prove that the agreement with experimental data obtained by Manke and Donaghey (5) at T_o = 1473 K (see Fig. 6b) was just coincidental.

It is apparent from Fig. 6 that models of deposition zones of epitaxial reactors based on strong simplifying assumptions cannot describe adequately the modeled systems. Comparison of curves GI and GII [see Ref. (5) and (6)] proves further that application of a more accurate numerical solution for the description of gas phase transport phenomena has brought no improvement of the model. Considering the models from the view point of computation demands, the simplest model is apparently that of Rundle (curves E), which can be conveniently solved on a pocket calculator. Manke's analytical model (curves GI) calls for the use of a programmable calculator, while application of a minicomputer seems appropriate for solution of Fujii's model (curves F). A mainframe computer should be used for the numerical solution of Manke's model (curves GII). Similarly, the model suggested in this work also demands the use of a mainframe computer. However, it is at present the only model adequately describing physical reality. Even for other previously published models (7-11), based on the concept of boundary (stagnant) layer at the deposition surface, better results cannot be expected without introducing some effective empirically adjustable parameters. Here again, the simplifying assumptions used in model development are apparently responsible for the models' inadequacy.

Conclusion

Comparison of the model designed in this work with a representative set of experimental data and with

approximate models described in literature proved the necessity of using sufficiently accurate model concepts as a base for the formulation of a theoretical model of a CVD reactor. On the other hand, this results in a relative complexity for a satisfactory model and consequently raises the computation demands. Comparison with experimental data proved the correctness of model concepts discussed in the section "Process Considerations." The main advantage of the theoretical model of the deposition zone is its generality. Unlike the empirical models, the theoretical model does not require the physical existence of the reactor to be described. It is possible to work with a hypothetical reactor, *e.g.*, in the case of design optimization of a new reactor. The analysis of sensitivity to effects of various factors (*e.g.*, geometrical ones) represents another interesting application of the theoretical model. Optimal design of reactor construction has to be understood also as the minimization of its sensitivity to various undesirable effects which can be encountered under real operational conditions. The theoretical model of an epitaxial reactor can be used also to solve numerous technological problems, the empirical solution of which would be costly and time consuming (rem. 2).

As of 1980 the model presented above has been used by Tesla Rožnov enterprise for the following purposes:

1. Analysis of the sensitivity of a large-capacity barrel-type reactor to the geometry of the deposition zone and solution of a number of associated technological problems.
2. Tune-up of the prototype of a large-capacity horizontal reactor and solution of a number of technological problems associated with the reactor's start-up.
3. Designing a new large-capacity reactor of the horizontal type.

Manuscript submitted Aug. 13, 1980; revised manuscript received Dec. 7, 1981.

Any discussion of this paper will appear in a Discussion Section to be published in the June 1983 JOURNAL. All discussions for the June 1983 Discussion Section should be submitted by Feb. 1, 1983.

APPENDIX A

Numerical Solution

A computation program has been written for a computer corresponding approximately to an IBM-370 to solve the system of partial differential equations (Eq. [15]-[22]) by the method of nets. The partial differential equations to be solved are second-order parabolic equations (28). The equations system does not contain second derivatives with respect to the longitudinal coordinate y, making it possible to start the numerical solution at the deposition zone inlet and to proceed in the direction of gas flow. Every calculation step is based on transverse profiles of temperature, velocity, and concentration calculated in a previous step for axial coordinate y. New velocity, temperature, and concentration profiles are then calculated for $y + dy$. Calculation is performed iteratively; in every iteration step Eq. [15], [17], and [19] were solved as partial differential equations with constant coefficients using the Crank-Nicolson implicit method (28). To evaluate the coefficients, the last known approximations of velocity, temperature, and concentration profiles are used in every iteration step. The temperature profiles can be calculated from Eq. [19] and the concentration profiles from Eq. [15]. Profiles of axial velocity v_y and pressure profiles can be obtained in each iteration step from simultaneous solution of Eq. [17] with an equation obtained by integration of Eq. [16] in the range of x from 0 to H. Profiles of transverse velocity v_x can be determined by integration of Eq. [16] in the range of x from H to 0. Using the iteration method (described above), transverse profiles of T, w_1, v_y, v_x and p can be calculated for the axial coordinate $y + dy$ assuming that a reagent concentration is known at the deposition surface. Temperature and concentration dependency of physical properties ρ, D, D^T, μ, K and c_P has to be taken into account. In our case, however, the reagent concentration at the deposition surface was determined implicitly by the boundary condition [21], which ensured the equality of the rate of heterogeneous reaction and diffusional flow of reagent from the gas phase. The algorithm of calculation of new profiles T, w_1, v_y, v_x, and p was therefore complemented by an external iteration cycle residing for fulfillment of this condition by searching for an appropriate concentration of reagent at the deposition surface, w_1.

Numerical solution of the system of Eq. [15]-[22] proceeds in the direction of reaction mixture flow and stops after reaching $y = L$ (deposition zone length). The effectiveness and accuracy of the calculation is ensured by an automatic adjustment of the length of the axial step dy. Calculation along the whole deposition zone of a reactor is performed with a constant number of nodal points on transverse profiles. Due to stepwise narrowing of the deposition zone in the gas flow direction, a new value of transverse difference dx should be calculated prior to each axial step and the values of axial velocity have to be corrected to keep the overall mass flow through the channel constant.

Program input data are: deposition zone geometry, temperature of the deposition surface and reactor wall, flow velocity of the reaction mixture and properties of state of the reaction mixture at the deposition zone inlet. Program output is (besides temperature, concentration, and velocity profiles if these are needed) the distribution of the deposition rate along the reaction zone in the direction of gas flow (y). Time of calculation is typically 3 min on a computer analogous to the IBM-370 (as mentioned above).

APPENDIX B

Physical Properties

Theoretical and semi-empirical methods were used for calculation of physical properties of the reactant mixture. Reactant mixture density, ρ, was calculated from the equation of state for an ideal gas. Determination of the thermal conductivity coefficient of the reactant mixtures was based on the kinetic molecular theory of gases (29-31). Similarly, to determine diffusion coefficient D, a relation based on the kinetic molecular theory of gases was applied in Wilke's empirical modification (32). Kihara's second-order approximation (29), based again on the kinetic molecular theory of gases, was used for calculation of the thermodiffusion coefficient, D^T. Specific heat capacities at constant pressure, c_{Pi}, and specific enthalpies, h_i^o, calculated for an ideal gas on the basis of statistical mechanics were taken from the JANAF tables (33). Collision integrals $\Omega^{(1,s)}$ were calculated from Neufeld's regression equation (34).

The following physical properties correspond to the system studied, $H_2 + SiCl_4$. Parameters of Lennard-Jones potential for hydrogen were taken from Hirschfelder's monograph (29) ($\sigma_2 = 2.915$Å, $\epsilon_2/k = 38$ K), analogous data for $SiCl_4$ from Sladkov's work (35) ($\sigma_1 = 6.17$Å, $\epsilon_1/k = 350$ K). Empirical combination relations were then used to obtain Lennard-Jones mutual interaction parameters

$$\sigma_{12} = \frac{1}{2}(\sigma_1 + \sigma_2) \qquad \epsilon_{12} = \sqrt{\epsilon_1 \epsilon_2} \qquad \text{[B-1]}$$

Physical properties calculated with these Lennard-Jones parameters were compared with experimental data for viscosity [$SiCl_4$, see Ref. (36); H_2, see Ref. (38)], thermal conductivity [$SiCl_4$, see Ref. (37); H_2, see Ref. (39-41)], specific heat at constant pressure for hydrogen (39), and diffusion coefficient of $SiCl_4$ in H_2 (42). Observed agreement was comparable with the accuracy of experimental data as published by individual authors.

Parameters of the Arrhenius equation (Eq. [2]) for the rate constant for the heterogeneous reduction of $SiCl_4$ by H_2, were determined from the temperature dependence of the deposition rate in the kinetics-controlled region of deposition ($T << T_m$). A decrease of reagent concentration at the deposition surface due to thermodiffusion (see "Process Considerations") was accounted for in the parameter evaluation. The following values of parameters were obtained

$$E = 1.94 \cdot 10^8 \text{ J} \cdot \text{kmol}^{-1}$$

$$A = 35.6 \text{ kmol} \cdot \text{m}^{-1.5} \cdot \text{kg}^{-0.5} \quad \text{(for Eq.[1])}$$

or

$$A = 22.1\ \text{kmol} \cdot \text{m}^{-1.25} \cdot \text{kg}^{-0.75} \cdot \text{sec}^{0.5}$$

(for Eq. [1a])

The temperature dependence of the constant $K(T)$ in Eq. [4] was determined using the theoretical model described in this work. The relation

$$K(T) = 8.7 \cdot 10^{-3} \exp\,(1.08 \cdot 10^{4}/T) \qquad \text{[B-2]}$$

was obtained from the comparison of theoretical and experimental deposition rates at the end of the deposition zone at three different temperatures.

LIST OF SYMBOLS

A	Arrhenius pre-exponential factor
c_P	mass specific heat
D	diffusion coefficient
D^T	thermal diffusion coefficient
e	heat flux
E	activation energy
g	growth rate
Gr	Grashof number
h	mass specific enthalpy
H	deposition zone width
k	thermal conductivity
M	molecular mass
m	mass flux
p	pressure
r	reaction rate
Re	Reynolds number
T	temperature
v	linear velocity
w	mass fraction
x	mol fraction
ϵ	characteristic energy
θ	yield
μ	dynamic viscosity
ρ	density
σ	collision diameter
τ	stress
ψ	tilt angle
ϕ	momentum flux

REFERENCES

1. W. H. Shepherd, *This Journal*, **112**, 988 (1965).
2. P. C. Rundle, *Int. J. Electron.*, **24**, 405 (1968).
3. E. Fujii, H. Nakamura, K. Haruna, and Y. Koga, *This Journal*, **119**, 1106 (1972).
4. E. P. Prokopjev, Ju. M. Kuznecov, Ju. A. Byčkov, V. I. Prilipko, and V. I. Mešков, *Elektron. Tech. Mater.*, No. 4, p. 43 (1973).
5. C. W. Manke and L. F. Donaghey, *This Journal*, **124**, 561 (1977).
6. C. W. Manke and L. F. Donaghey, in "Chemical Vapor Deposition," L. F. Donaghey, P. Rai-Choudhury, and R. N. Tauber, Editors, p. 151, The Electrochemical Society Softbound Proceedings Series, Princeton, NJ (1977).
7. S. E. Bradshaw, *Int. J. Electron.*, **21**, 205 (1966).
8. R. W. Andrews, D. H. Rynne, and E. G. Wright, *Solid State Technol.*, **12**, 61 (1969).
9. F. A. Kuznetzov and V. I. Belyi, *This Journal*, **117**, 785 (1970).
10. V. S. Ban, *J. Cryst. Growth*, **45**, 97 (1978).
11. F. C. Eversteyn, P. J. W. Severin, C. H. J. Brekel, and L. H. Peek, *This Journal*, **117**, 925 (1970).
12. C. H. J. Brekel, *Philips Res. Rep.*, **32**, 118 (1977).
13. J. Korec and J. Borkovicz, *Electron. Technol.*, **10**, 3 (1977).
14. J. Bloem and L. J. Giling, in "Current Topics in Material Science," Vol. 1, E. Kaldio, Editor, Elsevier, North Holland, Amsterdam (1977).
15. A. P. Colburn, *Trans. AIChE*, **29**, 174 (1933).
16. E. M. Sparrow, R. Eichhorn, and J. L. Gregg, *Phys. Fluids*, **2**, 319 (1959).
17. R. Takahashi, Y. Koga, and K. Sugawara, *This Journal*, **119**, 1406 (1972).
18. V. S. Ban, *ibid.*, **125**, 317 (1978).
19. T. Hanzawa, K. Sakauchi, K. Sato, and T. Tadaki, *J. Chem. Eng. Jpn.*, **10**, 313 (1977).
20. T. O. Sedgwick, J. E. Smith, R. Ghez, and M. E. Cowher, *J. Cryst. Growth*, **31**, 264 (1975).
21. B. J. Curtis, *This Journal*, **123**, 437 (1976).
22. R. B. Bird, W. E. Stewart, and E. N. Lightfoot, "Transport Phenomena," Wiley, New York (1960).
23. J. P. Duchemin, M. M. Bonnet, and M. F. Koelzch, *This Journal*, **125**, 637 (1978).
24. J. P. Duchemin, *Rev. Tech. Thomson CSF*, **9**, 33 (1977).
25. B. A. Lombos and T. R. Somogyi, *This Journal*, **111**, 1097 (1964).
26. T. O. Sedgwick, G. V. Arbach, and R. Ghez, in "Chemical Vapor Deposition," L. F. Donaghey, P. Rai-Choudhury, and R. N. Tauber, Editors, p. 79, The Electrochemical Society Softbound Proceedings Seris, Princeton, NJ (1977).
27. M. L. Hammond, *Solid State Technol.*, **21**, 68 (1978).
28. B. Carnahan, H. A. Luther, and J. O. Wilkes, "Applied Numerical Methods," Wiley, New York (1969).
29. J. O. Hirschfelder, C. F. Curtics, and R. B. Bird, "Molecular Theory of Gases and Liquids," Wiley, New York (1954).
30. J. O. Hirschfelder, "6th Symposium on Combustion," p. 351, Yale Univ., Reinhold, New York (1957).
31. J. O. Hirschfelder, *J. Chem. Phys.*, **26**, 282 (1957).
32. C. R. Wilke and C. Y. Lee, *Ind. Eng. Chem.*, **47**, 1253 (1955).
33. JANAF Thermochemical Tables, NSR DS-NBS, 2nd ed., Washington (1971).
34. P. D. Neufeld, A. R. Jansen, and R. A. Azis, *J. Chem. Phys.*, **57**, 1100 (1972).
35. I. B. Sladkov and V. V. Snegova, *Žur. Fiz. Chim.*, **48**, 1867 (1974).
36. H. Diaz Pena and F. Esteban, *An. Real Soc. Espan. Fis. Quim., Ser. A*, **62**, 347 (1966).
37. D. L. Timrot, V. N. Prostov, and V. E. Ljusternik, *Teplofiz. Vys. Temp.*, **5**, 926 (1967).
38. G. C. Maitland and B. E. Smith, *J. Chem. Eng. Data*, **17**, 150 (1977).
39. Y. S. Touloukian, "Thermophysical Properties of Matter," SFI/Plenum, New York (1970).
40. N. B. Vargaftik, "Spravočnik po Teplofizičeskim Svojstvam Gazov i Ridkostěj," 2nd ed., Nauka, Moskva (1972).
41. H. Landolt and R. Börnstein, "Zahlenwerte und Funktionen aus Physic, Chemie, Astronomie, Geophysik und Technik," G. Auflage, Springer, Berlin (1950).
42. I. B. Sladkov, *Žur. Fiz. Chim.*, **48**, 1052 (1974).

Technical Notes

A Novel Method to Measure Lateral Diffusion Length in Polycrystalline Silicon

Yoshiyuki Sato, Katsumi Murase, and Hiroyuki Harada

Nippon Telegraph and Telephone Public Corporation, Musashino Electrical Communication Laboratory, Tokyo, 180, Japan

The lateral diffusion length of impurities in polycrystalline silicon (poly-Si) is a very important factor in designing various LSI's and electrical components, such as load resistors made of highly resistive poly-Si for static RAM's (1), fused-type PROM's with PN junctions in poly-Si (2), and thin film transistors made of poly-Si (3).

A conventional method of observing lateral diffusion lengths in poly-Si films is the electrical resistivity measurement of poly-Si resistors with electrodes made of heavily doped poly-Si. However, it is rather difficult to separate the diffusion characteristics of impurities from the electrical resistivities using this method, because the electrical resistivities of poly-Si depend on properties such as the grain size and the structure. Another conventional method is delineation by means of concentration dependent wet etching. Good results with this method were reported for boron (B) diffusion (4). However, this method is unsuitable for arsenic (As) and phosphorus (P) because of the difficulty in controlling the etching rate. The purpose of this paper is to introduce a novel delineation method based on impurity enhanced oxidation effects (5) to measure the lateral diffusion length of As and P in poly-Si films.

A demonstrative experimental procedure to measure lateral diffusion lengths by this method is shown in Fig. 1. Poly-Si (thickness: 0.31 μm) was first deposited on silicon dioxide by thermal decomposition of silane gas in a low pressure CVD furnace. The deposition conditions are shown in Table I. The poly-Si grain size is less than 0.1 μm as revealed by transmission electron microscope (TEM) observation, and is confirmed to be stable after annealing at less than 1000°C. Next, the poly-Si surface was oxidized at 900°C for 45 min in a dry O_2 atmosphere to make an oxide film (thickness: 0.02 μm). Next, molybdenum (Mo) (thickness: 0.3 μm) was evaporated and then patterned using a photoetching process. Mo films are proper for ion implantation masks, because Mo is not tapered by photoetching (6) and has large stopping power. Next, impurity ions (As^+ or P^+) were selectively implanted in the poly-Si with the Mo masks [Fig. 1(A)]. The implanted dose was 2×10^{16} cm^{-2}. The implanted energy was 100 keV for As^+ and 50 keV for P^+. After the Mo masks were removed, the samples were heated at 900°-1100°C for 15-800 min in an N_2 atmosphere to investigate the diffusion characteristics [Fig. 1(B)]. After removing the surface oxide, the As^+ implanted samples were subsequently oxidized at 700°C for 300 min in a wet O_2 atmosphere and the P^+ implanted samples at 650°C for 300 min [Fig. 1(C)]. This process of oxidizing at a low temperature is the key to this method. The oxidation rate of poly-Si increases with impurities in poly-Si, thus the lateral distribution of impurity concentration can be estimated from the oxide thickness. Since the boundary between the oxidation enhanced region and the nonenhanced region can be clearly seen as the changes in interference color in these films (the poly-Si and the oxide), the lateral diffusion lengths of impurities in the poly-Si films were measured with an optical microscope. It was confirmed that the impurity diffusion in the oxidation process at a low temperature could be neglected in the measurement of the lateral diffusion lengths.

Key words: polycrystalline, silicon, diffusion, ion implantation.

Table I. Poly-Si deposition conditions

Temperature	650°C
Gas components	SiH_4:He = 1:3
Gas pressure	0.4 Torr
Growth rate	4 Å/sec

An example of measurement of the lateral diffusion length is shown in Fig. 2, where the width of the Mo mask pattern ("B") after Mo photoetching, l_1, and the width of undiffused region ("D") after the oxidation, l_2, were measured. The lateral diffusion length [the width of diffused region ("C" in Fig. 2)], l, was obtained by the relation $l = (l_1 - l_2)/2$. The measurement was taken using the patterns with the larger dimensions of the ion-implanted region (the diffusion sources) than the lateral diffusion lengths. The lateral diffusion lengths measured by this method (shown in

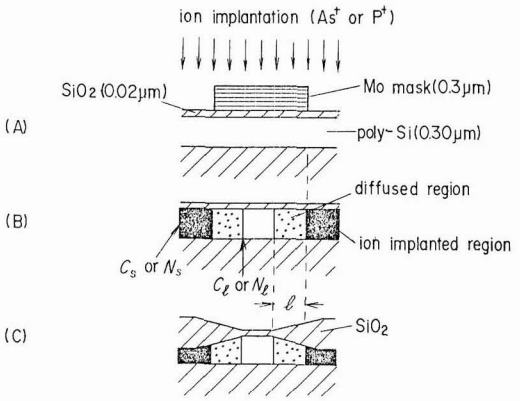

Fig. 1. Experimental procedure. l, lateral diffusion length; C_s, impurity concentration in the ion implanted region (cm^{-3}); N_s, number of impurities in the ion-implanted region (cm^{-2}); C_l, impurity concentration at a position distance l from the edge of the ion-implanted region (cm^{-3}); N_l, number of impurities at a position distance l from the edge of the ion-implanted region (cm^{-2}).

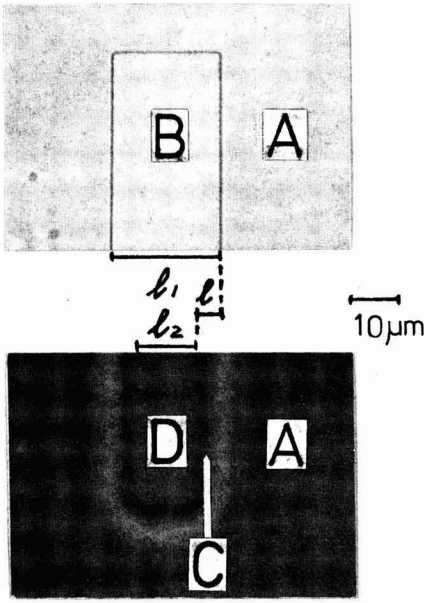

Fig. 2. Example of measurement of a lateral diffusion length. Impurity, As; annealing condition, 1100°C 15 min in an N_2 atmosphere; A, ion-implanted region; B, Mo mask pattern; C, diffused region; D, undiffused region; lateral diffusion length $l = (l_1 - l_2)/2 = (22.5\text{-}12.5)/2 = 5.0$ (μm).

Fig. 3) are proportional to the square root of diffusion time.

The impurity concentration at a position distance l from the edge of the ion-implanted region is the critical concentration C_l above which the oxidation is enhanced (see Fig. 1). In order to clarify the applicability of this method, C_l was studied by the same method mentioned above used to evaluate the oxide thickness. C_l can be obtained using the critical dose N_l, which is related to C_l by the following equation

$$N_l = C_l d/r \quad [1]$$

where d is the poly-Si thickness (3010Å), and r is the ratio of the number of impurities implanted in the poly-Si through the surface oxide (0.02 μm) to the total dose.

In order to determine N_l, the samples selectively implanted with doses of 1.5×10^{14}, 3×10^{14}, 6×10^{14}, 9×10^{14}, 1.2×10^{15}, 1.8×10^{15}, and 2.4×10^{15} cm^{-2} were prepared in the same way as those whose lateral diffusion lengths were measured. These samples were heated at 1000°C for 30 min in an N_2 atmosphere to obtain a constant impurity concentration throughout the thickness and were subsequently oxidized under the same conditions as the samples for lateral diffusion length measurement. As shown in Table II, the highest dose among the samples in which the oxide thicknesses of the implanted regions were the same as those of unimplanted regions is determined to be N_l. It is determined that N_l is 9×10^{14} cm^{-2} for the As$^+$ implanted samples and 1.2×10^{15} cm^{-2} for the P$^+$ implanted ones.

As l's and C_l's have been obtained, the effective diffusion coefficients D_l's can be calculated assuming that the following simple one-dimensional equation (7) holds:

$$C_l = C_s\,[1 - \mathrm{erf}(l/2\sqrt{D_l t})]/2 \quad [2]$$

where C_s is the impurity concentration of the diffusion source (ion-implanted region) and is expressed as

$$C_s = N_s r/d \quad [3]$$

where N_s is the ion-implanted dose (2×10^{16} cm^{-2}). From Eq. [1], [2], and [3] D_l can be given by

$$D_l(\mathrm{As}) = l^2/5.76t \quad [4]$$

$$D_l(\mathrm{P}) = l^2/4.84t \quad [5]$$

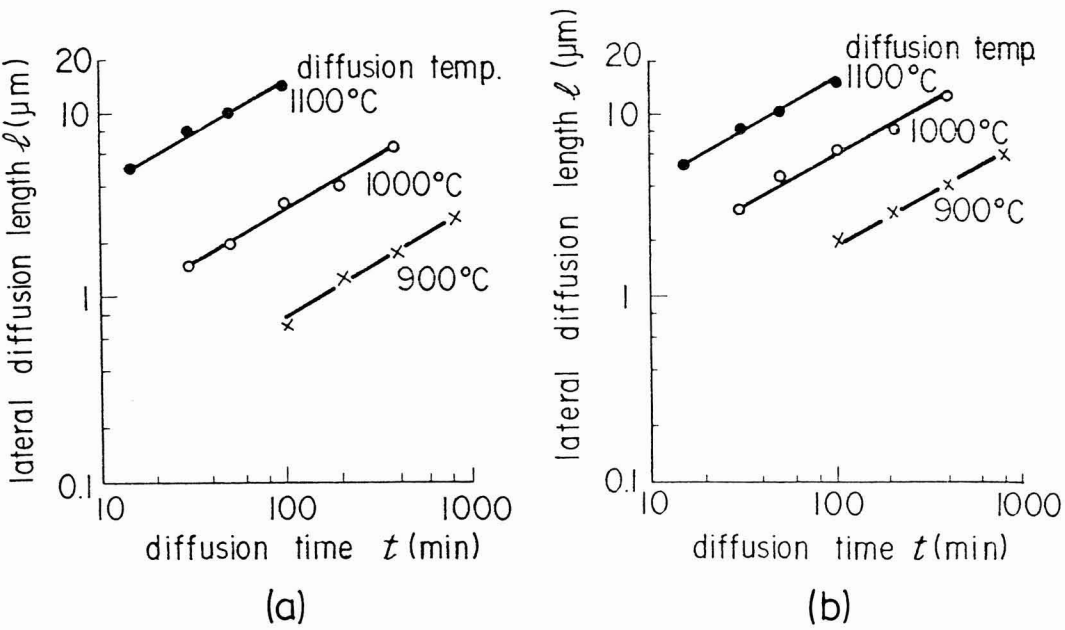

Fig. 3. Lateral diffusion lengths in poly-Si films. (a) implanted As; (b) implanted P

Table II. Determination of N_1. O, oxidation was enhanced by impurities (interference color of unimplanted region was different from that of the implanted region); X, oxidation was not enhanced by impurities (interference color of unimplanted region was the same as that of the implanted region)

Dose [cm^{-2}]		1.5×10^{14}	3×10^{14}	6×10^{14}	N_1(As) 9×10^{14}	N_1(P) 1.2×10^{15}	1.8×10^{15}	2.4×10^{15}
Impurity	As	X	X	X	X	O	O	O
	P	X	X	X	X	X	O	O

Impurities implanted selectively into poly-Si diffuse in the lateral direction and the perpendicular direction, simultaneously. However, in these cases, since the measured lateral diffusion lengths (about 1-15 μm) are much larger than the poly-Si thickness (0.3 μm) and the poly-Si lies between the upper and underlying SiO_2, the impurity concentration of the implanted region must become constant throughout the thickness in the short heat-treatment time. Therefore, it is thought that the ion-implanted region can be regarded as a diffusion source with a constant concentration throughout its thickness, and that the effective diffusion coefficients can be approximated by Eq. [4] and [5]. On the other hand the diffusion characteristics of impurities in poly-Si depend generally on the properties of poly-Si such as the grain size and the structure, and the difference in diffusion sources (4, 8, 9). Moreover, especially in cases where the impurity concentration is high, the diffusion processes are accompanied by poly-Si grain growth. It has been observed by TEM in this demonstrative experiment that the poly-Si grain size increases to some several thousand angstroms where the concentration of the impurities is more than about 10^{20} cm^{-3} with the impurity diffusion at high temperature (more than 1000°C for As, 900°C for P). Therefore, these diffusion phenomena are complex, and the D_l's calculated from Eq. [4] and [5] are at most only the effective values.

From the experimentally obtained relationship between l and $\sqrt{t}$ in Fig. 3, D_l(As) and D_l(P) in Fig. 4 were determined using Eq. [4] and [5]. The effective diffusion coefficients determined from perpendicular profiles of As or P in the poly-Si films at a temperature of 700°-800°C (D_p's) are also shown in Fig. 4 for comparison. The deposition conditions of the poly-Si in this case are the same as those shown in Table I. An example of D_p determination is given in Fig. 5. Curve "A" in Fig. 5 gives the as-implanted As distribution, and "B" shows the redistribution after annealing at 800°C for 30 min in an N_2 atmosphere. They were measured by secondary ion mass spectroscopy (SIMS). Although curve "B" does not follow a Gaussian distribution, D_p is determined so as to fit the calculated Gaussian redistribution (curve "C" in Fig. 5) (10) to curve "B" in the concentration range near C_l (C_l is 3×10^{19} cm^{-3} for As, and 4×10^{19} cm^{-3} for P). A comparison of D_l's with D_p's shown in Fig. 4 reveals that they are almost on the same lines. Thus it is considered that there is little difference between the effective diffusion coefficient of the perpendicular direction and that of the lateral direction in this poly-Si. Diffusion coefficients in poly-Si in other reports (8, 11) are also shown in Fig. 4 for comparison. It should be noted that these coefficients are a little smaller than those in our experiments. However, because of the extreme complexity of the diffusion phenomena in poly-Si, it is not possible to present a full and precise

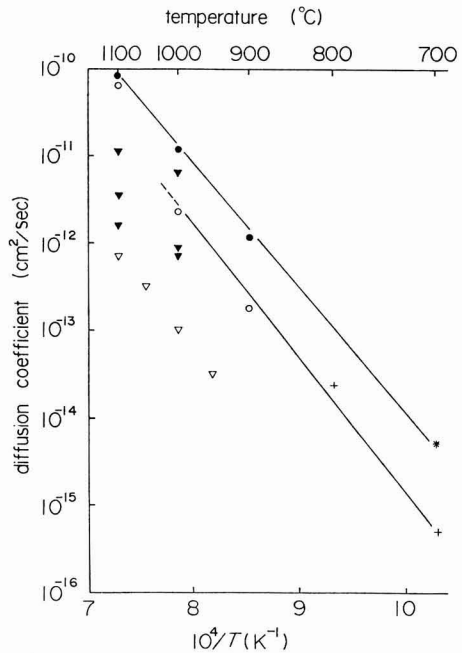

Fig. 4. Diffusion coefficients in poly-Si films. ○, D_l(As); ●, D_l(P) by this method; +, D_p(As); ✲, D_p(P) by SIMS; ▽, for As from Ref. (11); ▼, for P from Ref. (8).

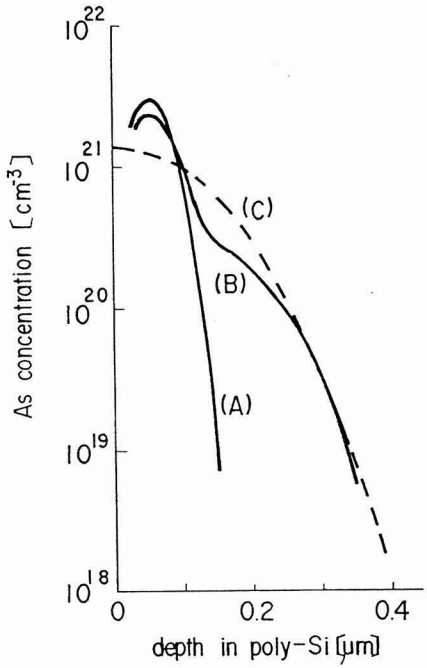

Fig. 5. Example of D_p determination. Poly-Si thickness, 0.45 μm; As dose, 2×10^{16} cm^{-2}; implanted energy, 80 keV; annealing condition, 800°C 30 min in an N_2 atmosphere; (A), as-implanted distribution; (B) redistribution after annealing; (C) calculated redistribution.

discussion of these differences based on these experimental data above.

It can be consequently concluded from the experimental results that this delineation method is effective and useful for investigating the lateral diffusion length of As and P in poly-Si.

Acknowledgments

The authors wish to thank Mamoru Kondo and Eisuke Arai for their encouragement and helpful discussions.

Manuscript submitted July 10, 1981; revised manuscript received Dec. 4, 1981.

Any discussion of this paper will appear in a Discussion Section to be published in the June 1983 JOURNAL. All discussions for the June 1983 Discussion Section should be submitted by Feb. 1, 1983.

Publication costs of this article were assisted by Nippon Telegraph and Telephone Public Corporation.

REFERENCES

1. O. Minato, T. Masuhara, T. Sasaki, H. Nakamura, Y. Sakai, T. Yasui, and K. Uchibori, *IEEE Trans. Electron Devices*, **ed-27,** 1591 (1980).
2. T. Mano, K. Takeya, T. Watanabe, N. Ieda, K. Kiuchi, E. Arai, T. Ogawa, and K. Hirata, *IEEE J. Solid-State Circuits*, **sc-15,** 865 (1980).
3. M. Matsumura, Y. Nara, and Y. Uchida, *IEEE IEDM Tech. Dig.*, 800 (1980).
4. D. J. Coe, *Solid-State Electron.*, **20,** 985 (1977).
5. H. Sunami, *This Journal*, **125,** 892 (1978).
6. F. Yanagawa, T. Amazawa, and H. Oikawa, *J. Appl. Phys.*, **18,** 237 (1979).
7. B. I. Boltaks, "Diffusion in Semiconductors," p. 99, Infoserch Limited, London (1963).
8. K. I. Kamins, J. Manoliu, and R. N. Tucker, *J. Appl. Phys.*, **43,** 83 (1972).
9. S. Horiuchi and R. Blanchard, *Solid-State Electron.*, **18,** 529 (1975).
10. E. C. Douglous and A. G. F. Dingwall, *IEEE Trans. Electron Devices*, **ed-21,** 324 (1974).
11. K. Tsukamoto, Y. Akasaka, and K. Horie, *J. Appl. Phys.*, **48,** 1815 (1977).

Method to Measure the Precipitated and Total Oxygen Concentration in Silicon

L. Jastrzebski,* P. Zanzucchi, D. Thebault, and J. Lagowski[1]

RCA Laboratories, Princeton, New Jersey 08540

The presence of oxygen as a major impurity in Czochralski (CZ) grown silicon is well known. The oxygen in CZ silicon is normally present in an amount exceeding the solubility limit at room temperature. Thus oxygen is incorporated into the CZ silicon lattice in various aggregated forms, *i.e.*, precipitates or complexes. The effect of the various forms of noninterstitial oxygen on the properties of silicon is complex (1). Some of the noninterstitial oxygen, thought to be incorporated as complexes, is known to improve the mechanical strength of silicon wafers, which increases wafer resistance to warpage (2). Other noninterstitial oxygen, thought to be incorporated in CZ silicon as precipitates, can introduce dislocations and reduce the mechanical strength of the silicon (3, 4). Furthermore, precipitates of this type, which are associated with stacking faults in the region of the semiconductor device (the substrate surface region), are detrimental to electrical performance (5, 6). However, these same defects can improve electrical performance if, as gettering sites, the oxygen related defects are outside the device region, *e.g.*, in the interior of the silicon wafer (7, 8).

Gettering by oxygen precipitates is a widely used procedure for which, in each device fabrication procedure, an optimum size, concentration, and spatial distribution of oxygen precipitates exist. The generation of the gettering precipitates, *i.e.*, the precipitation kinetics of oxygen in silicon, depends on the concentration of the interstitial oxygen (9), carbon (10), and, as has been shown indirectly (11), on the amount of initially precipitated oxygen in as-grown wafers.

Thus to achieve reproducible oxygen precipitation during device fabrication, the amount of oxygen in the form of precipitates and complexes in the as-received wafers should be measured in addition to monitoring the carbon and interstitial oxygen concentration. At present, a direct, easy to use method to measure precipitate content is not available. The infrared method widely used to measure the interstitial oxygen content of crystal silicon (12-14) cannot be used directly to measure the precipitated oxygen content. As recently noted by Hu (15) infrared absorption by some of the precipitated oxygen species in silicon is not unique and may overlap with the absorption of the interstitial oxygen species. In other forms of precipitates, a unique absorption band may be relatively weak or absent due to symmetry properties. Only by annealing for long periods of time has strong, unique infrared absorption related to oxygen precipitates been detected (16, 17). This procedure is not practical for evaluating silicon wafers prior to use in device manufacture.

The concentration of oxygen precipitates can, however, be determined indirectly by measuring the difference between the total and interstitial oxygen concentration of as-received wafers. An infrared absorption method for indirectly determining the precipitate, *i.e.*, noninterstitial oxygen, content in CZ grown silicon is reported here, and an example of the application of this method to evaluate the precipitate content in wafers used for device fabrication is given.

Commercially available (100) oriented, 3 and 4 in. diam, Czochralski grown silicon wafers were used in this study. The selection was random, *i.e.*, a given boule or position in a boule was not specified. The interstitial oxygen concentration in the samples was determined from the magnitude of the 0.9 μm absorption band (12) measured at room temperature with a Digilab FTS-15C Fourier Transform Spectrometer. Sets of silicon samples were heat-treated at temperatures of 1200°, 1240°, 1300°, or 1350°C for times ranging from a few minutes to about 2 hr in argon, oxygen, or air ambients. After heating, samples were rapidly cooled to room temperature with an average cooling rate of 300°C/min. Experimental data showed that a cooling rate exceeding 15°C/min was sufficient enough to prevent reprecipitation of oxygen. The surface oxide was stripped off in HF solution. The wafers were lapped to remove from the surface about a 40 μm layer thought to be depleted

* Electrochemical Society Active Member.
[1] Department of Materials Science, Massachusetts Institute of Technology, Cambridge, Massachusetts 02139.
Key words: gettering, infrared, impurities, integrated circuits, dissolution.

of oxygen by outdiffusion. This was determined by secondary ion mass spectrometry (SIMS). These were then repolished using colloidal silica and the concentration of the interstitial oxygen was remeasured.

The concentration of the interstitial oxygen in CZ grown silicon as a function of time for heat-treatment at 1300° and 1250°C is shown in Fig. 1. Initially the interstitial oxygen concentration increases, then reaches a maximum, constant concentration within the first hour of heat-treatment. With further heat-treatment the oxygen content tends to decrease due to outdiffusion of oxygen. The time required to reach a maximum, constant interstitial oxygen concentration, is reduced when the temperature is increased. The reduction of the oxygen concentration after heat-treatment for long periods of time is more significant at higher temperatures and it has been found to depend on the annealing atmosphere.

Figure 2 shows the interstitial oxygen concentration in samples from the same wafer as a function of heat-treatment temperature for a constant time of 1 hr. A significant increase in the interstitial oxygen concentration takes place after heat-treatment above 1250°C. For the samples studied, anneal at the highest temperature, *e.g.*, 1350°C, does not increase the interstitial oxygen concentration above the value obtained after a 1300°C heat-treatment.

Comparison of the data of Fig. 2 to the solubility curve for oxygen in silicon given by Hrostowski and Kaiser (18) and the interstitial oxygen content of CZ silicon determined by Tempelhoff *et al.* (17), Fig. 3, is significant. Clearly the data of the latter and this work are following the solubility curve for oxygen in silicon. The fact that the data of this work appear slightly above the solubility curve is not significant since there are errors in measuring the oxygen content of thin wafers by the infrared absorption method.

From these data, it is evident that the increase in the interstitial oxygen concentration after heat-treatment is caused by decomposition of oxygen precipitates. At high temperature, when the concentration of dissolved interstitial oxygen is below the solid solubility limit, the dissolution of oxygen precipitates will take place as, for example, reported by Yue and Ruiz in their study of oxygen precipitation kinetics (19). Oxygen from precipitates will be incorporated into silicon lattice at interstitial positions. During rapid cooling of the silicon to room temperature, the interstitial oxygen remains frozen in the silicon lattice. The oxygen does not have enough time to precipitate even when the oxygen concentration exceeds the solubility limit at the lower temperatures (16-18). The critical rate of cooling required to maintain oxygen frozen in the interstitial positions was established from measurements of the intensity of interstitial oxygen band (after 1300°C, 1 hr annealing) as a function of cooling rate. For cooling rates above 15°C/min, this intensity remains constant while for the cooling rates below 15°C/min it was decreasing with rate. The decrease has been interpretated as due to precipitation of oxygen and, therefore, it has been assumed that for cooling rates exceeding 15°C/min oxygen remains frozen in the interstitial positions. Because the solubility and diffusivity of oxygen in silicon increases with temperature, the increase in temperature from 1250° to 1300°C accelerates the precipitated dissolution process, which accounts for data

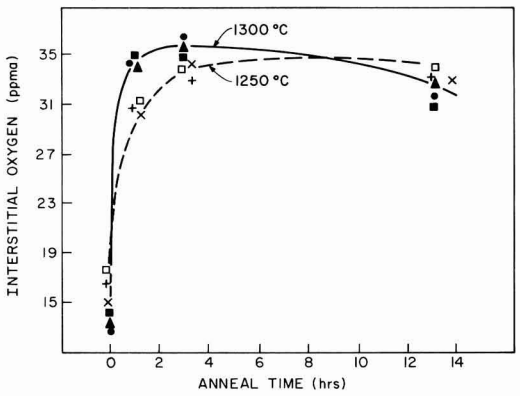

Fig. 1. Dependence of interstitial oxygen concentration on time for annealing at 1300° and 1350°C.

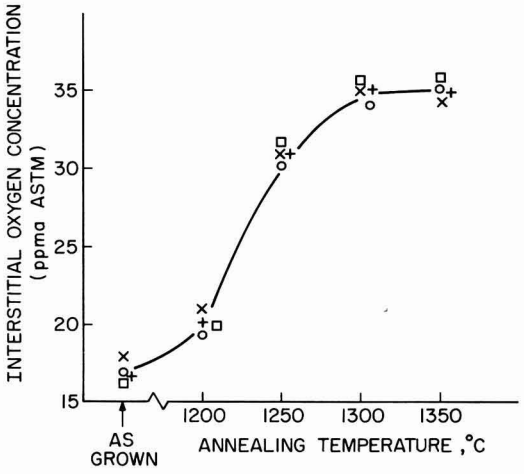

Fig. 2. Dependence of interstitial oxygen concentration on temperature for 1 hr annealing.

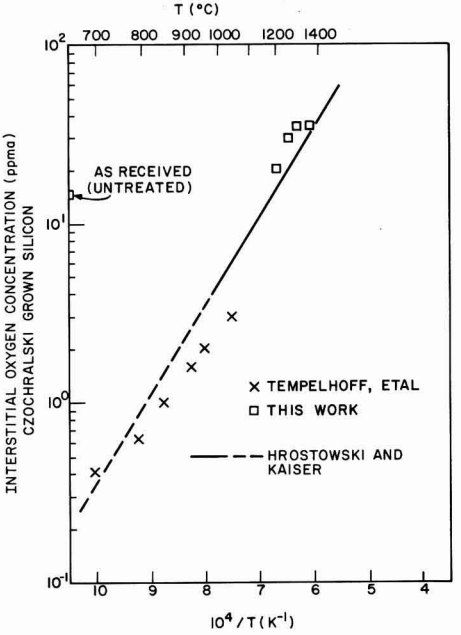

Fig. 3. Interstitial oxygen concentration in silicon as a function of temperature. Comparison of data by Hrostowski and Kaiser with those of Tempelhoff *et al.* and this work.

presented in Fig. 1. The observed decrease of the interstitial oxygen concentration during prolonged heat-treatment is caused by outdiffusion of oxygen from the silicon. Although the solubility of oxygen in silicon is significantly higher at 1350°C than it is at 1300°C (18), heating at 1350°C did not increase the oxygen concentration above that obtained after 1300°C heat-treatment (Fig. 2). Therefore, we conclude that all measurable oxygen in the silicon of this study has been introduced into interstitial sites by a 1 hr, 1300°C heat-treatment. The critical temperature, time, and cooling rate required to dissolve and maintain oxygen in interstitial positions is expected to vary depending on concentration and form of oxygen precipitates. The procedure presented here allows this to be established unambiguously in each case.

After heat-treatment for 1 hr at 1300°C, measurement of the infrared absorption at 9.0 μm gives the total oxygen concentration present in silicon. The difference between the interstitial oxygen concentration of the silicon after heating to 1300°C and prior to heating determines the amount of the oxygen bound in precipitates or complexes in as-grown crystals.

This procedure was used to determine the amount of precipitated oxygen present in as-received, CZ wafers normally used in device production. The concentration of the interstitial oxygen measured across 4 in. diam wafers at the center, center to edge midsection, and edges with a 0.5 cm diam aperture prior to and after the 1300°C heat-treatment for 1 hr in argon, is presented in Table I. In as-received wafers the radial distribution of oxygen is typical of CZ wafers as reported previously (20, 21), *i.e.*, the total oxygen concentration shows a slight decrease in the center, increases to a maximum in the center to edge midsection of the wafer, and decreases at the wafer edge. After a 1300°C heat-treatment, the oxygen concentration in the wafer center is practically the same as at the edge. Thus for this case, a reduction in the interstitial oxygen concentration measured at the edge of as-received wafers should not be attributed to the segregation of the oxygen during crystal growth process but to a difference in the amount of precipitated oxygen at the wafer center and edge.

Table I. Interstitial oxygen concentration (ppma) measured across silicon wafers

	Center	Middle	Edge
As grown	28	30	21
Annealed 1300°C	34	36	36
Oxygen in complexes in virgin wafers	7	6	15

Defect formation and oxygen precipitation kinetics in silicon during heat-treatments involved in IC fabrication can vary critically among wafers with similar interstitial oxygen and carbon concentrations for as-grown wafers but with different amounts of precipitated oxygen (22). Figure 4 presents the distribution of the precipitated oxygen measured in silicon wafers bought from two different suppliers but containing a similar concentration of interstitial oxygen and carbon ($\sim 4 \times 10^{16}$ cm^{-3}). For the concentration of the interstitial and precipitated oxygen measured at the center of each wafer, it is evident that the amount of precipitated oxygen in the two groups of wafers is quite different. The first group of wafers has a lower concentration of precipitated oxygen compared to the second group although the wafers from the second group have a narrower distribution of interstitial oxygen content than the wafers from the first group. The difference in the concentration of precipitated oxygen is probably caused by the difference in the silicon crystal growth conditions, especially the rate of cooling down the silicon crystals after growth (11).

The indirect analysis procedure of measuring the amount of oxygen precipitation is, therefore, useful in evaluating silicon wafers prior to use in device manufacturing. It is significant that in the wafers analyzed we did not detect infrared absorption related to some of the oxygen precipitates previously reported in literature (15-17). Even with improved sensitivity, *i.e.*, measurements made at liquid helium temperature, 4.2

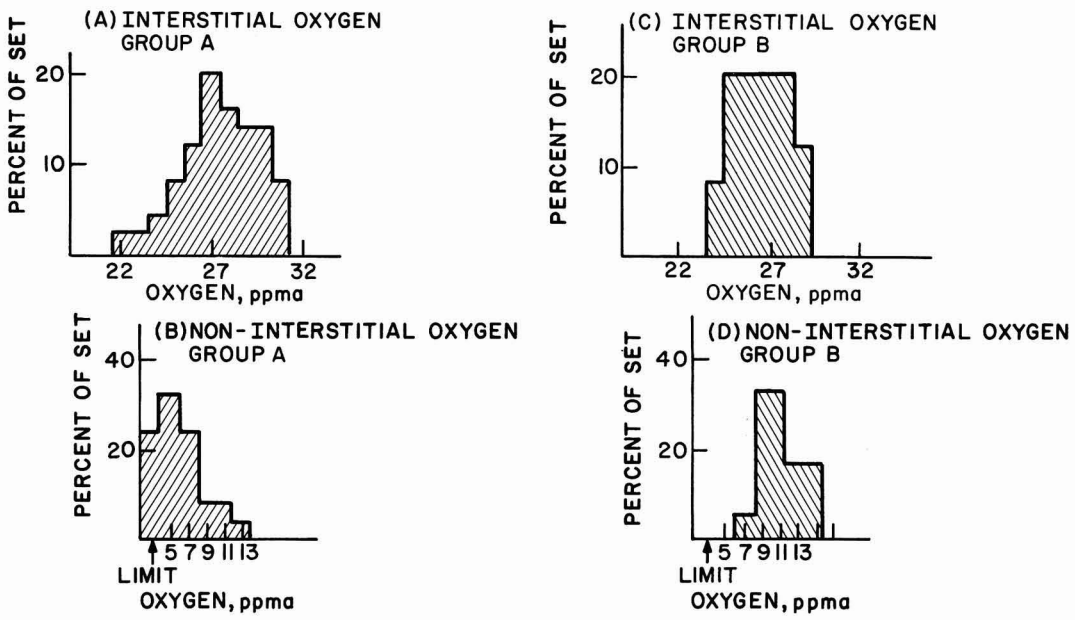

Fig. 4. Distribution of interstitial oxygen (Fig. 4A, C) and noninterstitial oxygen (Fig. 4B, D) in wafers from two different suppliers. The measurement was made at the center of the wafers.

K, and in a long path prism configuration (14, 23), direct measurement of oxygen precipitate content was not possible. In the second case the wafer thickness is effectively increased by the multiple reflection of light, and therefore, the sensitivity of the absorption method is increased by about one order of magnitude compared to normal transmittance. In general, infrared absorption modes related to the precipitates have not been observed in the wafers studied, even though large amounts of precipitated or complexed oxygen are thought to be present.

We conclude that the method described allows for determination of the total and, indirectly, the precipitated, *i.e.*, noninterstitial, oxygen content in silicon wafers. The oxygen precipitate content is an important parameter in the evaluation of the internal gettering process for IC manufacture.

Acknowledgments

The processing of the silicon wafers by R. Soydan and J. Shaw and the measurement of the oxygen content by W. R. Frenchu are greatly appreciated.

Manuscript submitted Oct. 21, 1981; revised manuscript received Dec. 28, 1981.

Any discussion of this paper will appear in a Discussion Section to be published in the June 1983 JOURNAL. All discussions for the June 1983 Discussion Section should be submitted by Feb. 1, 1983.

Publication costs of this article were assisted by RCA.

REFERENCES

1. For example, see in "Procedings of Microelectronics Measurements Technology Seminar," San Jose, March 1981, To be published, Benwill Publishing Corporation (1981).
2. S. M. Hu, *Appl. Phys. Lett.*, **31,** 53 (1977).
3. K. Sumino, in "Semiconductor Silicon 1981," H. R. Huff, R. J. Kriegler, and Y. Takeishi, Editors, p. 308, The Electrochemical Society Softbound Proceedings Series, Pennington, NJ (1981).
4. For a review see D. Thebault and L. Jastrzebski, *RCA Rev.*, **41,** 592 (1980).
5. J. M. Dishman, S. E. Hassko, R. B. Marcus, D. P. Murarka, and T. T. Sheng, *J. Appl. Phys.*, **50,** 2689 (1979).
6. S. P. Murarka, T. Seidel, J. Dalton, J. Dishman, and M. Read, *This Journal*, **127,** 716 (1980).
7. S. Kishino, Y. Matsushita, and M. Kanamon, *Appl. Phys. Lett.*, **35,** 213 (1979).
8. S. Kishino, K. Nagasawa, and T. Lizuka, *Jpn. J. Appl. Phys.*, **19,** L466 (1980).
9. C. Pearce, in "Proceedings of Microelectronics Measurements Technology Seminar," San Jose, March 1981, To be published, Benwill Publishing Corporation (1981).
10. K. Yasutake, M. Vmemo, and H. Kawabe, *Appl. Phys. Lett.*, **37,** 789 (1980).
11. H. Nakamishi, H. Kohda, H. Hirata, and K. Hoshikawa, *Jpn. J. Appl. Phys.*, **19,** 561 (1980).
12. J. A. Baker, *Solid State Electron.*, **13,** 1431 (1970).
13. K. Graff, E. Gallath, S. Ades, G. Goldbach, and G. Tolg, *ibid.*, **16,** 887 (1973).
14. B. Pajot, *Analusis*, **5,** 293 (1977).
15. S. M. Hu, *J. Appl. Phys.*, **51,** 5945 (1980).
16. E. M. Ryzhkova, I. I. Trapeznikova, V. E. Chelnokov, and A. A. Yakovenko, *Sov. Phys. Semicond.*, **11,** 628 (1977).
17. K. Tempelhoff, F. Spiegelberg, R. Gleichmann, and D. Wruck, *Phys. Status Solidi A*, **56,** 213 (1979).
18. H. J. Hrostowski and R. H. Kaiser, *J. Phys. Chem Solids*, **9,** 217 (1959).
19. J. T. Yue and H. J. Ruiz, in "Semiconductor Silicon 1977," H. R. Huff and E. Sirtl, Editors, p. 596, The Electrochemical Society Softbound Proceedings Series, Princeton, NJ (1977).
20. T. Abe, K. Kikuchi, S. Shirai, and S. Muraoka, in "Semiconductor Silicon 1981," H. R. Huff, R. J. Kriegler, and Y. Takeishi, Editors, p. 54, The Electrochemical Society Softbound Proceedings Series, Pennington, NJ (1981).
21. H. Foll, V. Gosele, and R. O. Kolbesen, in "Semiconductor Silicon 1977," H. R. Huff and E. Sirtl, Editors, p. 565, The Electrochemical Society Softbound Proceedings Series, Princeton, NJ (1977).
22. L. Jastrzebski, IEEE Trans. Electron. Dev., **ed-29,** 475 (1982).
23. N. J. Harrick, "Internal Reflection Spectroscopy," J. Wiley and Sons, Inc., New York (1967).

Erratum

In the paper "Preparation and Electrical Properties of V_2O_3 Single Crystals of Controlled Stoichiometry," by S. A. Shivashankar, R. Aragón, H. R. Harrison, C. J. Sandberg, and J. M. Honig, which appeared in the November 1981 issue of *This Journal*, pp. 2472-2475, the following corrections should be noted: In figures 2 and 4, y should be replaced by y/2.

JOURNAL OF THE ELECTROCHEMICAL SOCIETY

ACCELERATED

—BRIEF COMMUNICATIONS—

JULY 1982

Chemical Methods for the Deposition of Thin Films of Sb_2Se_3 and Sb_2O_3

R. N. Bhattacharya and P. Pramanik

Department of Chemistry, Indian Institute of Technology, Kharagpur- 721302, India

Thin film deposition of bismuth chalcogenides, lead selenide, lead oxide, thallium oxide by chemical method has been reported (1,2,3,4,5,6). This brief communication describes the authors' successful attempt in deposition of Sb_2Se_3 and Sb_2O_3 thin films by chemical means.

A sodium selenosulfate solution is prepared by refluxing 5 gm selenium powder with 12 gm of sodium sulfite (anhydrous) in 200 ml of water for about 10 hours and subsequently cooled for 10-12 hours. On cooling, a little selenium separates out from the solution. It is then filtered to obtain a clear solution.

22 gm potassium-antimonyl tartrate is dissolved in 250 ml water to obtain a saturated solution of potassium-antimonyl tartrate.

25 ml Sb^{3+} solution is taken in a glass beaker. 2.5 ml triethanolamine and 30 ml 17(N) NH_4OH are added to it and stirred. To this solution 12.5 ml sodium-selenosulfate solution is added.

Two cleaned glass slides are clamped vertically into the glass beaker containing the solution. When it is kept at room temperature (30°C) for about 10 hours, uniform films of Sb_2Se_3 are obtained on the glass substrates. They are then taken out, washed with water and dried in open air. The Sb_2Se_3 films are found to be 0.1-0.3 microns thick. Thickness of the film increases with the increasing amount of the ammonia solution and also with time.

In another experiment, 40 ml Sb^{3+} is taken in a beaker and 20 ml sodium selenosulfate is added to it. Two cleaned glass slides are clamped vertically into the glass beaker containing the solution. When it is kept at room temperature (30°C) for about 6 hours, uniform films of Sb_2O_3 are obtained on the glass substrates. As in the previous experiment, they are taken out, washed with water and dried in open air. The Sb_2O_3 films are found to be 0.2-0.3 microns thick.

X-ray diffraction data for Sb_2O_3 show distinct d-lines. The composition for both the films is confirmed by atomic absorption spectrophotometer method and gravimetric analysis. Scanning electron microscopy reveals random distribution of small crystallites for both the films. Fig. (1) and Fig. (2) show the distribution of Sb_2Se_3 and Sb_2O_3 crystallites respectively. Specific resistance of the films measured by four-probe method and also by electrometer is of the order of 10^7 ohm-cm for Sb_2Se_3 and 10^9 ohm-cm for Sb_2O_3. Electronic spectra of Sb_2Se_3 are shown in Fig. (3). Optical band gap is found to be 1.88 eV for Sb_2Se_3 at room temperature (30°C). The band gap and resistivity of Sb_2Se_3 single crystal reported by J. Black et al. (7) are 1.2 eV and 10^6 ohm-cm respectively. J.G.N. Braithwite (8) reported band gap of evaporated film of Sb_2Se_3 to be 1.35 eV.

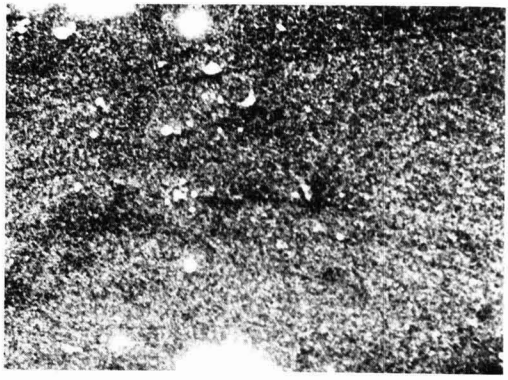

Fig. 1. Scanning Electron Micrograph of Sb_2Se_3 thin film (B.S.E.; 1210X)

Key words - Antimony Selenide, Antimony Oxide, Thin films, Chemical deposition

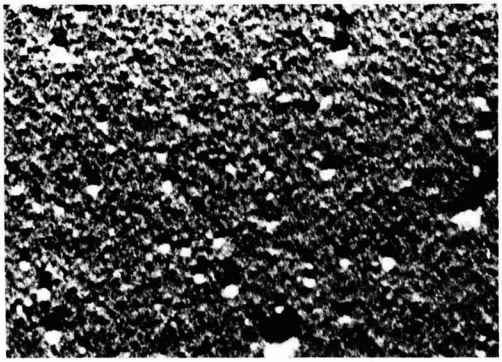

Fig. 2. Scanning Electron Micrograph of Sb_2O_3 thin film (B.S.E.; 1600X)

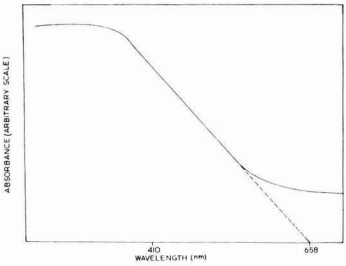

Fig. 3. Electronic Spectra of Sb_2Se_3

ACKNOWLEDGEMENT

We are grateful to Mr. A. Mondal for his assistance in our investigation.

REFERENCES

1. P. Pramanik and R.N. Bhattacharya, This Journal, 127 (9),2087 (1980).

2. P. Pramanik, R.N. Bhattacharya and A. Mondal, This Journal, 127 (8), 1857 (1980).

3. D.H. Roberts and J.E. Bains, J. Phys.Chem. Solids., 6, 184 (1958).

4. R.N. Bhattacharya and P. Pramanik, Bull. Mater. Sci., Vol. 2, Number 4, November 1980, pp. 287-291.

5. W. Mindt, This Journal, 117, 615(1970).

6. W. Mindt, This Journal, 118, 93 (1971).

7. J. Black et al., J. Phys. Chem. Solids., 2, 240-251 (1957).

8. J.G.N. Braithwite, Proc. Phys. Soc., B 64, 274 (1951).

Manuscript received April 29, 1981.

p-Type Amorphous Silicon/Liquid Junction Solar Cell

William M. Ayers*[1]

Exxon Research and Engineering Company, Linden, New Jersey 07036

The application of semiconductor photoelectrodes to liquid junction solar cells and chemical synthesis reactions requires the development of low cost, thin film, stable materials. Stability, in this context, means the lack of formation of an insulating oxide or surface phase that will block the passage of current. We report on the characteristics of such a material, p-type amorphous silicon (p-a-Si:H), and the first liquid junction solar cell based on this material. The second purpose of the note is to demonstrate that the Fermi level of p-a-Si:H is not pinned by aqueous electrolytes.

The p-a-Si:H samples were made by DC plasma decomposition of silane. The doping sequence was p+ (2% B_2H_6 in SiH_4) followed by a p- layer (10ppm B_2H_6) on either stainless steel or Corning EC7059 glass substrates. The band gap is approximately 1.7eV (1). The samples were 2μ in thickness with 0.18 cm^2 exposed to the electrolyte. Samples were etched in 4:1 ammonium fluoride/hydrofluoric acid prior to each experiment.

Heller et al have shown that the Fermi level of p-type crystalline silicon is not pinned in aqueous electrolytes (2). Their demonstration countered previous claims that the Fermi level of the crystalline material was pinned (3). The maximum photovoltage at an ideal electrolyte junction is the difference between the electrolyte potential and the flat-band potential. At light intensities insufficient to flatten the bands, the photovoltage is decreased by the extent of the band bending. Hence, the maximum photovoltage dependence on electrolyte potential is:

$$\left(\frac{dVph}{dE^o}\right) = 1 - \left(\frac{dVs}{dE^o}\right) \qquad [1]$$

Where Vph is the photovoltage, Vs is the potential at the electrode surface and E^o is the electrolyte potential. In the absence of surface states, the surface potential is constant and the photovoltage linearly follows changes in the electrolyte potential. As the surface state density increases, (dV_s/dE^o) approaches unity and the photovoltages become pinned or insensitive to changes in the electrolyte potential.

The redox potential of the vanadium used in these experiments drifts from -0.5V to +0.2V vs. SCE as oxygen diffuses into the solution. It is a convenient system for determining the photovoltage dependence on the electrolyte potential.

Fig. 1 illustrates the decrease in p-a-Si:H photovoltage as the vanadium electrolyte drifts to more oxidizing potentials. The total vanadium concentration of the p-a-Si:H/$V^n/^{n+1}$, HCl/Pt cell is 0.2M and the HCl concentration is 4M. At potentials more negative than -0.05V vs. SCE, the bands bend downward at the interface as would be expected from a p-type material. As the electrolyte drifts to more oxidizing (positive) potentials, the p-a-Si:H Fermi level drops flattening the bands and reducing the photovoltage. At electrolyte potentials more positive than +0.05V

*Electrochemical Society Active Member. Keywords: amorphous silicon, photoelectrode, Fermi level pinning.

[1] Present address: Energy Conversion Devices, Incorporated, North Branch, New Jersey 08876.

vs. SCE, the sign of the photovoltage changes indicating inversion of the band bending.

Since the photovoltage is near saturation, the initial slope of Fig.1 and Eq. (1), yield the dependence of the surface voltage on the electrolyte potential. With the assumption that the surface states behave like a capacitor of 5A thickness, δ, and dielectric constant of unity, an approximate calculation of the density of states yields:

$$\frac{dVs}{dE^o} = \frac{e_o \delta N_s}{\varepsilon_o} \quad [2]$$

and $N_s = 2 \times 10^{12}$ states/eV-cm^2

Although there are surface states present, the Fermi level of the p-type amorphous silicon is not pinned by them.

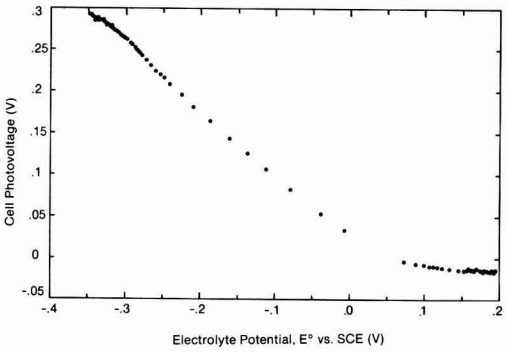

Figure 1. Decrease in cell photovoltage as electrolyte drifts to more positive (oxidizing) potentials vs. SCE.

As a check to insure that the decrease in photovoltage is due to the p-a-Si:H Fermi level shift and not to the growth of an insulating oxide layer, the rate of electrolyte potential and photovoltage change were measured. Their symmetrical time response (Fig.2) illustrates that the s-Si:H does follow the change in electrolyte potential even at rates as fast as 25mV/min.

The current voltage behavior of the cell in the dark and under illumination is illustrated in Fig. 3. Also shown on the figure is the current-voltage behavior of the electrolyte between two platinum electrodes. The rectifying behavior of the cell and sign of the photocurrent are those expected for a p-type material.

In these preliminary experiments, the largest but not optimized cell power output was obtained by driving the electrolyte potential to -0.51V vs. SCE through the addition of excess zinc powder to the solution. The open circuit voltage is 0.41V, the short circuit current is 0.18 mA/cm^2 and the fill factor is 0.3 (Fig. 4). At 40mW/cm^2 illumination from a tungsten lamp (uncorrected for reflection and solution absorbance), the cell has an efficiency of 0.06%. The low short circuit current suggests poor charge carrier transport in the material. The photovoltage saturates at low light intensity ($\sim$40mW/cm^2) in this electrolyte indicating that recombination and/or trapping are limiting the transport. It is not yet known whether larger photovoltages could be obtained with electrolyte contacts <-0.5V vs. SCE.

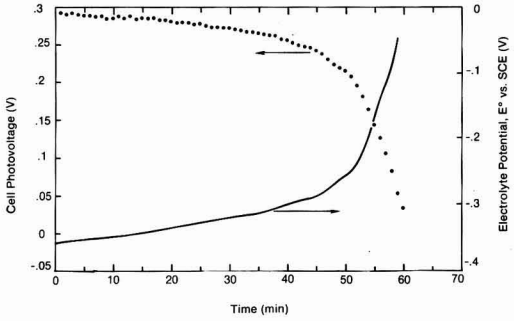

Figure 2. Rate of photovoltage and electrolyte potential change. Symmetrical response indicates photovoltage decrease is not due to insulating oxide growth.

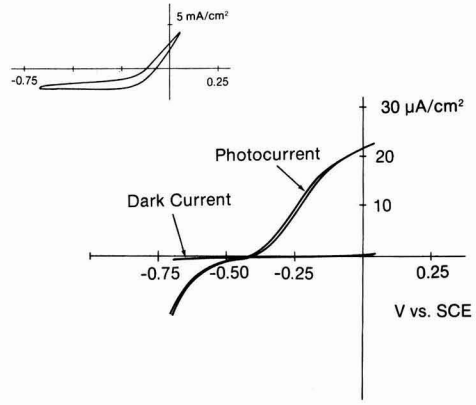

Figure 3. Current voltage behavior for p-a-Si:H/$V^n/^{n+1}$,HCl/Pt cell in dark and illuminated at 40mW/cm^2 (-0.39V vs. SCE). Insert shows current voltage response for same electrolyte between two platinum electrodes.

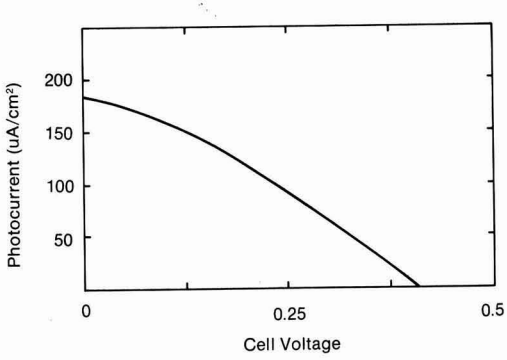

Figure 4. Cell power with electrolyte at -0.51V vs. SCE. Open circuit photovoltage, 0.42V, short circuit, 0.18 mA/cm^2 at 40 mW/cm^2. Fill factor 0.3.

As pointed out by Heller et al, p-type silicon photoelectrodes are stabilized by the depletion field driving electrons to the electrolyte interface. These carriers 'cathodically protect' the surface by inhibiting the silicon oxide reaction. The p-a-Si:H electrode is remarkably stable in this aqueous electrolyte. With the electrolyte potential at -0.4V vs. SCE, the cell sustained a 1.3μA/cm^2 current density (10mW HeNe) for over an hour without an indication of failure. Previous studies with undoped hydrogenated amorphous silicon (which forms n-type depletion region liquid junctions) showed that the material formed a blocking oxide within 30 minutes under similar conditions (4).

In summary, the visible absorption, variable junction potential, and stability make p-type amorphous silicon a promising thin film photocathode material. Its chief limitation at the moment is the low short circuit current. Better understanding of the silane decomposition process and silicon incorporation into the growing film will perhaps allow control of the structural disorder and transport properties of the material.

ACKNOWLEDGEMENTS

I wish to thank D. Morel for providing the amorphous silicon samples and G. D. Cody for helpful discussions.

REFERENCES

(1) D.E. Carlson, Solar Energy Materials 3, 503 (1980).

(2) A. Heller, H.J. Lewerenz and B. Miller, J. Am. Chem. Soc. 103, 200 (1981).

(3) A.B. Bocarsly, D.C. Bookbinder, R. N. Dominey, N.S. Lewis and M.S. Wrighton, J. Am. Chem. Soc. 102, 3683 (1980).

(4) W.M. Ayers, J. Appl. Phys. accepted for publication.

Manuscript submitted Dec. 22, 1981; revised manuscript received March 29, 1982.

Publication costs of this article were assisted by Exxon Research and Engineering Company.

Semiconductor Electrodes

XLVI. Stabilization of n-Silicon Electrodes in Aqueous Solution Photoelectrochemical Cells by Formation of Platinum Silicide Layers

F.-R. F. Fan, G. A. Hope, and Allen J. Bard*

Department of Chemistry, The University of Texas, Austin, Texas 78712

The stabilization of small bandgap semiconductors against photocorrosion in photoelectrochemical (PEC) cells is necessary in the design of practical cells for the conversion of solar energy to electricity, and is of critical importance in photoelectrosynthetic systems where the photogenerated holes produce highly oxidizing species (e.g., Br_2, O_2, Cl_2, etc.) at the semiconductor surface. One approach involves the utilization of thin films of metals (1) or semiconductors (2) to protect the surface. The deposition of conductive polymer layers (3) or protective polymer films (4) on the semiconductor surface can also decrease the rate of photocorrosion. Highly stable n-Si photoelectrodes can be achieved by coating the photoanode with a thin gold or platinum layer overcoated with a thick polypyrrole (PP) film (5). The increased stability can mainly be attributed to the rapid interfacial charge transfer kinetics between Si and the (metal/PP) overlayer and those between the (metal/PP) layer and solution species (6).

There is a wealth of information concerning thin film-semiconductor reactions, especially metal thin films on silicon (7,8). Metals deposited upon Si can react to form various compounds, which exhibit metallic conductivity, good mechanical adhesion, and reasonable chemical stability. We report here a study of the electrochemical (EC) and PEC behavior of silicide-coated silicon electrodes in aqueous solution, and amplify our preliminary report (9) of the stable PEC performance of such electrodes in aqueous solutions containing several redox couples. We demonstrate that Pt silicide coated n-Si electrodes can be employed to fabricate stable PEC cells with aqueous solutions containing various redox couples, e.g., $Fe^{2+/3+}$, I^-/I_3^-, $Fe(CN)_6^{3-/4-}$. Power conversion efficiences of 5 to 8% at 65 mW/cm^2 irradiation from a tungsten-halogen lamp can be achieved by choosing a suitable redox solution and by optimizing the conditions used to prepare the silicides.

Platinum silicides were prepared by procedures reported previously (8). N-Si single crystals (0.4 to 0.6 Ωcm) donated by Texas Instruments were ultrasonically cleaned in trichloroethylene, acetone, and methanol. Immediately prior to vacuum deposition of platinum, the n-Si crystals were etched twice with 48% HF solution for 10 min. The etched crystals were then rinsed thoroughly with distilled water and methanol and dried in vacuum. The platinum films were deposited by flash evaporation of a known amount of Pt on the n-Si crystals at a pressure of 10^{-6} torr. The thickness of the Pt film deposited was calibrated spectrophotometrically. Immediately after metal deposition, the Pt-coated n-Si crystals were annealed in situ at about 400°C for 5-15 min. at a pressure of 10^{-6} torr. The crystals obtained showed a mirror-like surface with no obvious pits when examined at a magnification of 500X.

The detailed procedures for preparing the ohmic contacts, mounting and sealing the electrodes are similar to those previously reported (5a). The voltammetric experiments and the solar cell measurements were performed with the same apparatus and procedures as reported previously (10). The light source used in the study of the PEC effect was a tungsten-halogen lamp fitted with a 13 cm thick water filter. The Auger electron spectroscopic (AES) measurements were performed with a Physical Electronics 590 system. Reagent grade chemicals were used without further purification. All solutions were prepared from triply distilled water. All experiments were carried out with the solution under a nitrogen atmosphere.

The Auger depth profile (Fig. 1) of the annealed specimen of Pt on n-Si showed that at the surface, a significant amount of Si, oxygen and Pt existed. At increasing sputter times the oxygen signal quickly disappeared and the Pt signal increased with increasing depth for the first 20 Å. Near 20 Å, the

---

* Electrochemical Society Active Member

Keywords: photoelectrochemistry, solar, semiconductor, stabilization

signal due to the oxygen vanished; on the other hand, a significant Pt signal remained to a depth of about 80 Å. The Si signal increased steadily up to a depth of about 80 Å. Thus Pt diffuses into the Si for a considerable distance and does not merely form an adlayer on the surface. Oxygen (perhaps from the thin native oxide layer) remains right on the surface and does not diffuse deeply into the Si substrate.

The current-voltage curve for an n-Si electrode, which was coated with about 40 Å of Pt and annealed at 400° C at 10^{-6} torr for 10 min., in a solution containing 1 M $FeCl_2$, 0.1 M $FeCl_3$, and 1 M HCl under illumination of 65 mW/cm^2 (tungsten halogen lamp) is shown in Fig. 2. The initial short-circuit current density is 16 mA/cm^2, the open-circuit voltage is 0.38 V and the fill factor 0.62. The maximum power conversion efficiency is thus 5.8%. Stability tests (Fig. 3) under illumination of 65 mW/cm^2 showed no deterioration in short-circuit current, a slight increase in open-circuit voltage, and about a 10% decrease in the fill factor (ff) after 20 days of discontinuous illumination with the passage of about 10,000 C/cm^2. No apparent change in the electrode surface was observed after this extended irradiation under a magnification of 500X.

A better fill factor was observed for I^-/I_3^- (ff = 0.72) and $Fe(CN)_6^{3-/4-}$ (ff = 0.70) couples. Under similar illumination conditions, these three couples show essentially the same open-circuit voltage. However, $Fe(CN)_6^{3-/4-}$ gives the highest short-circuit current density (ca. 20 mA/cm^2) and I^-/I_3^- the lowest (ca. 13 mA/cm^2) (perhaps because of solution absorption of incident light by I_3^-).

In conclusion, Pt silicide-coated n-Si electrodes have been shown to give highly stable PEC performance in aqueous solutions. The exceptional stability and performance of these PEC cells might be due to the following: (1) fast interfacial charge transfer kinetics between the n-Si substrate and the platinum silicide and between platinum silicide and solution redox species; (2) separation of region of photocharge carrier generation from solution contamination; (3) good mechanical stability of the silicide on the silicon substrate; (4) reasonable chemical and electrochemical stability of the silicide. Detailed EC and PEC studies on different silicide-coated electrodes and suitably modified forms of these electrodes for the stable photooxidation of Br^-, Cl^- and H_2O will be published elsewhere.

REFERENCES

1. (a) Y. Nakato, T. Ohnishi, and H. Tsubomura, Chem. Letts., 19, 883 (1975).
(b) Y. Nakato, K. Abe, and H. Tsubomura, Ber. Bunges. Phys. Chem., 80, 1002 (1976).
(c) K. W. Frese, Jr. and S. R. Morrison, presented in Third Electrochemical Photovoltaic Cells SERI Contractors' Review Meeting, Nov. 10-12, 1980, Denver, Colorado.
2. (a) P. A. Kohl, S. N. Frank and A. J. Bard, This Journal, 124, 225 (1977).
(b) M. Tomkiewicz and J. Modal, Ibid., 1436 (1977).
3. (a) R. Noufi, D. Tench and L. F. Warren, Ibid., 127, 2709 (1980) and references therein
(b) R. Noufi, A. J. Frank and A. J. Nozik J. Am. Chem. Soc., 103, 1849 (1981).
4. (a) A. B. Bocarsly, E. G. Walton, and M. S. Wrighton, Ibid., 102, 3390 (1980).
(b) J. M. Bolts, A. B. Bocarsly, M. C. Palazzotto, E. G. Walton, M. S. Lewis and M. S. Wrighton, Ibid., 101, 1378 (1979).
(c) J. M. Bolts and M. S. Wrighton, Ibid. 100, 5257, (1978).
5. (a) F.-R. F. Fan, B. L. Wheeler and A. J. Bard, This Journal, 128, 2042 (1981).
(b) T. Skotheim, I. Lundstrom and J. Prejza, Ibid., 1625.
6. R. Bull, F.-R. F. Fan and A. J. Bard, Ibid., in press.
7. M. P. Lepselter and J. M. Andrews in "Ohmic Contacts to Semiconductors," B. Schwartz, Editor, p. 159, The Electrochemical Society, New York (1969).
8. K. N. Tu and J. W. Mayer, in "Thin Films--Interdiffusion and Reactions," J. M. Poate, K. N. Tu and J. W. Mayer, Editors, p. 359, J. Wiley and Sons, New York (1978).
9. F.-R. Fan, G. Nagasubramanian, H. S. White, G. A. Hope, H. D. Abruña, B. L. Wheeler and A. J. Bard, presented in Fourth Electrochemical Photovoltaic Cells SERI Contractors' Review Meeting, October 16-17, 1981, Denver, Colorado.
10. F.-R. Fan, H. S. White, B. L. Wheeler and A. J. Bard, J. Am. Chem. Soc., 102, 5142 (1980).
11. The support of this research by grants from the National Science Foundation (CHE 8000682) and the Solar Energy Research Institute is gratefully acknowledged.

Manuscript received March 15, 1982.

Publication costs of this article were assisted by the University of Texas.

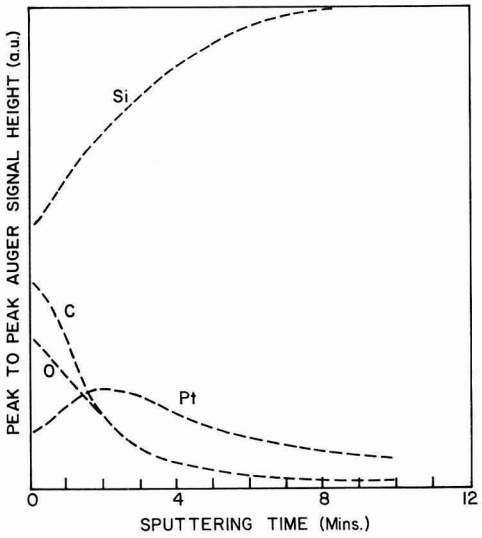

Fig. 1: Auger depth profile of annealed specimen of Pt on n-Si. Pt thickness deposited ∿40 Å. Annealing temperature 400° C at ∿ 10^{-6} torr for 15 min. Sputtering rate ∿ 10 Å/min.

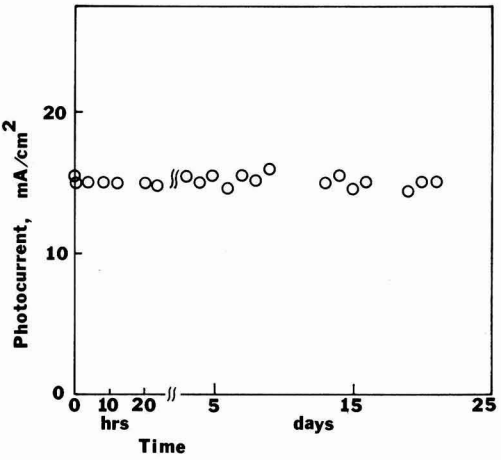

Fig. 3: Photocurrent-time behavior of platinum silicide coated n-Si electrodes illuminated with tungsten-halogen lamp at 65 mW/cm^2 at biasing potential at 0.4 V vs SCE. Solution and electrode are similar to those used in Figure 2. Illumination time per day ranged from 4 to 24 hours.

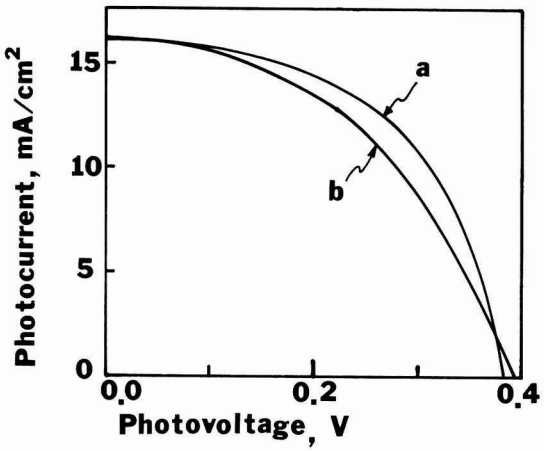

Fig. 2: Photocurrent-photovoltage characteristics of the cell n-Si (Pt silicide coated)/ 1.0 M $FeCl_2$, 0.1 M $FeCl_3$, 1 M HCl/Pt at 65 mW/cm^2 illumination. Pt thickness deposited ∿ 40 Å. Annealing temperature 400°C at ∿ 10^{-6} torr for 10 min. (a) Before long-term stability test. (b) After long-term stability test.

OUT-OF-PRINT SOCIETY VOLUMES

The following volumes sponsored or published by The Electrochemical Society, Inc. are now out-of-print. Xerographic copies* or reprints† of these volumes are available.

* **Vapor Plating.** C. F. Powell, I. E. Campbell, and B. W. Gonser, Editors. A 1955 symposium. 158 pages.

* **The Structure of Electrolytic Solutions.** W. J. Hamer, Editor. A 1957 symposium. 441 pages.

* **Technology of Columbium (Niobium).** B. W. Gonser and E. M. Sherwood, Editors. A 1958 symposium. 120 pages.

* **Surface Chemistry of Metals and Semiconductors.** H. C. Gatos, J. W. Faust, Jr., and W. J. La Fleur, Editors. A 1959 symposium. 526 pages.

* **Electrode Processes,** First Conference. E. Yeager, Editor. A 1959 symposium. 374 pages.

* **Mechanical Properties of Intermetallic Compounds.** J. H. Westbrook, Editor. A 1959 symposium. 435 pages.

* **Zirconium and Its Alloys.** J. P. Pemsler, E. C. W. Perryman, and W. W. Smeltzer, Editors. A 1965 symposium. 205 pages.

† **Measurement Techniques for Thin Films.** B. Schwartz and N. Schwartz, Editors. 1965 and 1966 symposia. 347 pages.

† **Electrode Processes,** Second Conference. E. Yeager, H. Hoffman, and E. Eisenmann, Editors. A 1966 symposium. 190 pages.

* **Electrolytic Rectification and Conduction Mechanisms in Anodic Oxide Films.** P. F. Schmidt and D. M. Smyth, Editors. A 1967 symposium. 230 pages.

* **Electrets and Related Electrostatic Charge Storage Phenomena.** L. M. Baxt and M. M. Perlman, Editors. A 1967 symposium. 150 pages.

* **Dielectrophoretic and Electrophoretic Deposition.** E. F. Pickard and H. A. Pohl, Editors. A 1967 symposium. 138 pages.

* **Electron and Ion Beam Science and Technology,** Third International Conference. R. Bakish, Editor. A 1968 symposium. 725 pages.

* **Optical Properties of Dielectric Films.** N. Axelrod, Editor. A 1968 symposium. 325 pages.

* **Thin Film Dielectrics.** F. Vratny, Editor. A 1968 symposium. 680 pages.

* **Ohmic Contacts to Semiconductors.** B. Schwartz, Editor. A 1968 symposium. 356 pages.

* **Semiconductor Silicon.** R. R. Haberecht and E. L. Kern, Editors. A 1969 symposium. 750 pages.

* **Chemical Vapor Deposition,** Second International Conference. J. M. Blocher, Jr. and J. C. Withers, Editors. A 1970 symposium. 872 pages.

* **Marine Electrochemistry.** J. B. Berkowitz, M. Banus, M. J. Pryor, R. Horne, P. L. Howard, G. C. Whitnack, and H. V. Weiss, Editors. A 1972 symposium. 416 pages.

* **Semiconductor Silicon 1973.** H. R. Huff and R. R. Burgess, Editors. A 1973 symposium. 936 pages.

* **High Temperature Oxidation of Metals.** By P. Kofstad. The Corrosion Monograph Series. 340 pages.

* **Chemical Vapor Deposition,** Fourth International Conference. G. F. Wakefield and J. M. Blocher, Jr., Editors. A 1973 symposium. 595 pages.

* **Electrets, Charge Storage and Transport in Dielectrics.** M. M. Perlman, Editor. A 1973 symposium. 675 pages.

* **Fine Particles.** W. E. Kuhn and J. Ehretsmann, Editors. A 1974 symposium. 352 pages.

* **Corrosion Problems in Energy Conversion and Generation.** C. S. Tedmon, Editor. A 1974 symposium. 484 pages.

* **Electrocatalysis.** M. W. Breiter, Editor. A 1974 symposium. 378 pages.

* **Electron and Ion Beam Science and Technology,** Sixth International Conference. R. Bakish, Editor. A 1974 symposium. 594 pages.

* **Energy Storage.** H. P. Silverman and J. B. Berkowitz, Editors. A 1975 symposium. 258 pages.

* **Chemical Vapor Deposition,** Fifth International Conference. J. M. Blocher, Jr., H. E. Hintermann, and L. H. Hall, Editors. A 1975 symposium. 848 pages.

* **Etching.** H. G. Hughes and M. J. Rand, Editors. A 1976 symposium. 203 pages.

* **Electrode Materials and Processes for Energy Conversion and Storage.** J. D. E. McIntyre, S. Srinivasan, and F. G. Will, Editors. A 1977 symposium. 340 pages.

* **Electron and Ion Beam Science and Technology,** Eighth International Conference. R. Bakish, Editor. A 1978 symposium. 297 pages.

* **International Symposium on Solar Energy.** J. B. Berkowitz and I. A. Lesk, Editors. A 1976 symposium. 372 pages.

* **High-Temperature Metallic Corrosion of Sulfur and Its Compounds.** Z. A. Foroulis, Editor. A 1969 symposium. 276 pages.

* **Properties of Electrodeposits—Their Measurement and Significance.** R. Sard, H. Leidheiser, Jr., and F. Ogburn, Editors. A 1974 symposium. 430 pages.

* **Chemical Vapor Deposition,** Sixth International Conference. L. F. Donaghey, P. Rai-Choudhury, and R. N. Tauber, Editors. A 1977 symposium. 596 pages.

* **Battery Design and Optimization.** S. Gross, Editor. A 1978 symposium. 486 pages.

* **The Electrocatalysis of Fuel Cell Reactions.** W. E. O'Grady, S. Srinivasan, and R. F. Dudley, Editors. A 1978 workshop. 228 pages.

* **Electron and Ion Beam Science and Technology,** Fourth International Conference. R. Bakish, Editor. A 1970 symposium. 680 pages.

* **Plasma Processing.** R. G. Frieser and C. J. Mogab, Editors. A 1980 symposium. 360 pages.

* Order from University Microfilms, Inc., 300 North Zeeb Street, Ann Arbor, Mich. 48106. Specify an Electrochemical Society volume.

† Order from Johnson Reprint Co., 355 Chestnut St., Norwood, N.J. 07648. Specify an Electrochemical Society volume.

7/82

JOURNAL OF THE ELECTROCHEMICAL SOCIETY

REVIEWS AND NEWS

JULY 1982

SECTION NEWS

Chicago Section

The seventh meeting of the Chicago Section was Graduate Student Mini-Symposium on "Research in Electrochemistry and Surfaces." It was held on April 15, 1982 at Allen Center, Northwestern University. Prof. Donald Smith, Northwestern University, was the technical chairman and organizer. The program covered six papers of recent electrochemical research interest such as the development of a new electroanalytical technique for organic drug assay, characterization of porous electrode and gas-metal interface, electron transport process in polymer film coated electrode, quantitative evaluation of electrode reaction kinetics, and thin electrode film characterization by surface enhanced Raman spectroscopy. Graduate students and faculty members of five universities, three from Illinois and two from Wisconsin, took part in this event. Forty-five members, students, and guests attended the meeting. The symposium was followed by a tour of the electrochemical research laboratory.

Basanta Mahato
Secretary

Southern California-Nevada Section

On April 6, 1982, the Southern California-Nevada Section met for its regularly scheduled dinner meeting. Dr. Ralph Brodd, immediate Past-President of The Electrochemical Society, spoke on "Batteries and Electric Vehicles," comparing electric vehicle battery candidates and speculating as to which technology might dominate in the future. Dr. Brodd also discussed current ECS affairs, detailing the fiscal and membership growth of the Society. He noted that Joseph C. Schumacher of the local section is the recipient of the Vittorio de Nora-Diamond Shamrock Award for his work in electrochemical technology.

NEW MEMBERS

It is a pleasure to announce the following new members of The Electrochemical Society as recommended by the Admissions Committee and approved by the Board of Directors in May 1982.

Active Members

Abu-Zeid, M. M., Nuenen, The Netherlands
Ahmad, A., Ottawa, Ont., Canada
Alderman, J. C., Northants, England
Anderson, C. R., Silver Spring, MD
Battista, M. A., Ridgefield, CT
Blanco, M. E., Wayne, NJ
Bomchil, G., Meylan, France
Bradley, M. C., Philadelphia, PA
Bukin, C. I., Richardson, TX
Castor, W. S., Jr., Bethlehem, PA
Chan, W. K., Murray Hill, NJ
Chang, P., San Jose, CA
Chen, J.-R., Taiwan, China
Clapper, T. W., Oklahoma City, OK
Cookingham, R., Rochester, NY
Darken, L., Oak Ridge, TN
De Battisti, A., Borsari, Italy
Donepudi, V. S., Ottawa, Ont., Canada
Elliott, J. K., Albuquerque, NM
Esquivel, A. L., Dallas, TX
Gillespie, L. J., Brooklyn Center, MN
Gross, M., Murray Hill, NJ
Harrington, D. A., Ottawa, Ont., Canada
Huq, R., Philadelphia, PA
Hyde, P. J., Los Alamos, NM
Itoh, H., Arlington, MA
Jack, R., Poughkeepsie, NY
Jacy, D., Campbell, CA
James, R. W., Nepean, Ont., Canada
Jenkins, G. M., Kanata, Ont., Canada
Karoly, R. F., Whitehall, PA
Khosla, R. P., Rochester, NY
Khoyetsan, R., Toronto, Ont., Canada
Koike, A., Tokyo, Japan
Kuwana, T., Columbus, OH
Lasky, J. B., Essex Junction, VT
Leef, A., Burlington, MA
Levy, I. I., Valdosta, GA
Lie-Wei, Y., Taiwan, China
Liu, J.-C., Taiwan, China
Liu, P.-H., Redondo Beach, CA
Malinski, T., Houston, TX
Merritt, D. R., Brooklyn Center, MN
Miller, B. E., Wheaton, IL
Morioka, Y., Hyogo, Japan
Morrison, A. D., Pasadena, CA
Motamedi, M. E., Thousand Oaks, CA
Nadezhdin, D. S., Ottawa, Ont., Canada
Nguyen, V. S., Essex Junction, VT
Nirdosh, I., Thunder Bay, Ont., Canada
Novotny, D. B., Bethesda, MD
Ong, E., Murray Hill, NJ
O'Toole, M. M., Palo Alto, CA
Pace, L. J., Rochester, NY
Patton, J. C., Columbia, MD
Powell, J. L., Hopewell Junction, NY
Rekhtman, R., El Segundo, CA
Roth, W. L., Schenectady, NY
Rusling, J. F., Storrs, CT
Salmon, M., Coyoacan, Mexico
Sarkar, N., New Orleans, LA
Sato, K., Danbury, CT
Schaeffer, C. A., Colchester, VT
Schmidt, T., Edmonton, Alta., Canada
Sereda, M. W., Wellesley, MA
Sharma, L. R., Chandigarh, India
Sirkin, E. R., Palo Alto, CA
Smith, G. C., Dallas, TX
Takagi, M., Kawasaki, Japan
Tan, Z. C. H., Rochester, NY
Ting, C. H., Santa Clara, CA
Tong, H.-S., Edison, NJ
Van Roode, J. H. G., Oakville, Ont., Canada
Vaynshteyn, M., Edison, NJ
Von Gutfeld, R. J., Yorktown Heights, NY
Wang, D. C., Anahelm, CA
Warren, L. F., Thousand Oaks, CA
Westendorf, G., Santa Clara, CA
Wettstrom, R., Skoghall, Sweden
Williams, D. S., Murray Hill, NJ
Yamamoto, T., Yokohama, Japan
Yang, K.-H., Poughkeepsie, NY
Yasar, T., West Hurley, NY
Zhiming, C., London, Ont., Canada

Student Members

Akano, U. G., Hamilton, Ont., Canada
Dogan, N.S., Ann Arbor, MI
Dubetz, T. A., Edmonton, Alta., Canada
Graham, J. A., Los Angeles, CA
Harkness, T. L., State College, PA
Herrera, P., Santiago, Chile
Lee, B. I., Gainesville, FL
Pardo, J. E., Rio Piedras, PR
Perino, S., Stanford, CA
Quinones, A. G., Bayamon, PR
Stratton, T. G., Cambridge, MA
Wessel, S., Coquitlam, B.C., Canada

Reinstatements

Fan, J. C. C., Lexington, MA
Hansen, W. N., Logan, UT
Raistrick, I. D., Stanford, CA

NEWS ITEMS

Symposium on Electro-Organic Synthesis

The Royal Society of Chemistry is sponsoring a symposium on Electro-Organic Synthesis at the North E. Wales Institute, Cartrefle College, Wrexham, on Sept. 22-24, 1982.

For further information, contact Dr. D. R. Palmer, Palmer Research Ltd., Mostyn Road, Holywell, Clwyd CH8 9DN, U.K.

Symposium on Electrochemical Engineering Aspects of Electroplating

A Symposium on Electrochemical Engineering Aspects of Electroplating will be held Aug. 29-Sept. 1, 1982, in Cleveland, Ohio. These sessions are being organized under the auspices of the American Institute of Chemical Engineers. For further information, contact Mr. G. Chiffriller, American Institute of Chemical Engineers, 345 East 47th St., New York, NY 10017.

Senior Technical/ Scientific Coordinator

Lawrence Berkeley Laboratory invites all persons with electrochemical expertise to apply for this position. As Sr. Coordinator responsibilities will include: handling technical contract management, reviewing and evaluating research proposals, and planning and coordinating long range technical programs.

A BS in science or engineering with emphasis in electrochemistry strongly recommended. A background in electrochemical energy conversion research is preferred as well as familiarity with contract management with emphasis on technical areas. Demonstrated organizational and writing skills are a must. Salary range is $2150-$3130 per month.

Please send two copies of your resume, including salary history to: **Cathy Boyd, Job #C/0230, Lawrence Berkeley Laboratory, Building 65, 1 Cyclotron Road, Berkeley, CA 94720.** An equal opportunity employer m/f/h.

LAWRENCE BERKELEY LABORATORY

POSITIONS WANTED

Please address replies to the box number shown, c/o The Electrochemical Society, Inc., 10 South Main Street, Pennington, N.J. 08534-2896.

Technical Librarian—With a background in chemistry and experience in the battery field is seeking work which will utilize these special abilities. Please contact Mr. Philip E. Krouse, 216 Big Oak Road, Morrisville, Pennsylvania 19067.

Metallurgist/Electrochemist—Ph.D., industrial/academic experience. Process/product development; process design; metal plating, corrosion, extraction, and reduction; materials/surface characterization; electrolyte/solution formulation; transient and steady-state electrochemical techniques; statistical optimization. Accomplishments. Publications and reports. Sintering and casting. Available immediately. Willing to relocate. Reply Box C-238.

ECS Membership Statistics

The following three tables give a breakdown of membership as of May 1, 1982.

Table I. ECS Membership by Sections

Section	1979	1980	1981	1982
Boston	295	345	377	391
Chicago	243	245	235	235
Cleveland	134	131	141	142
Columbus	75	78	74	68
Detroit	124	117	128	129
European (not officially formed—no bylaws)	—	—	20	59
Indianapolis	27	24	31	31
Metropolitan/New York	601	636	652	657
Midland	28	32	27	24
National Capital Area	151	168	164	164
Niagara Falls (Inactive)	73	141	139	113
North Texas	142	189	201	205
Ontario/Quebec	137	145	151	163
Oregon	—	—	11	70
Pacific Northwest	91	84	82	26
Philadelphia	204	216	228	217
Pittsburgh	129	129	120	114
Rocky Mountain	88	103	126	148
San Francisco	404	479	559	626
South Texas (Inactive)	47	39	27	24
Southern California/Nevada	271	305	308	308
Twin Cities	—	—	46	97
Non-Section	1128	1019	1063	1098
Subtotal—In Good Standing	4392	4625	4910	5109
Delinquents (Active and Student)	554	758	739	840
TOTAL	4946	5383	5649	5949

Table II. ECS Membership by Divisions or Group*

Division/Group	1979	1980	1981	1982
Battery	1355	1409	1457	1509
Corrosion	1291	1213	1245	1284
Dielectrics and Insulation	941	957	1032	1091
Electrodeposition	1149	1032	1053	1088
Electronics	2111	2345	2579	2724
New Electronic Technologies	1433	1194	1307	1374
Semiconductors	1714	1919	2136	2263
Electrothermics and Metallurgy	819	674	707	714
Industrial Electrolytic	657	600	623	625
Luminescence and Display Materials Group	474	426	438	443
Organic and Biological Electrochemistry	595	552	595	654
Physical Electrochemistry	1595	1519	1617	1716
Energy Technology Group	320	1132	1215	1304

* A member may be included in the count of several divisions or groups.

Table III. ECS Membership by Grade

Category	May 1 1978	1979	1980	1981	1982	1982/1981 % Increase
Active	3569	3763	3916	4188	4319	3.13
Member Reps. of Contributing Companies	139	142	142	132	139	5.30
Emeritus	112	117	128	130	142	9.23
Life	48	51	52	52	54	3.85
Honorary	12	13	13	15	17	13.33
Subtotal Active in Good Standing	3880	4086	4251	4517	4671	3.41
Delinquent	417	484	684	621	716	15.30
Total Active on Record	4297	4570	4935	5138	5387	4.85
Student Members in Good Standing	269	306	374	393	438	11.45
Delinquent	68	70	74	118	124	5.08
Total Students on Record	337	376	448	511	562	9.98
Total Individual Members	4634	4946	5383	5649	5949	5.31

CALL FOR RECENT NEWS PAPERS AND EXTENDED RECENT NEWS PAPERS

Detroit, Michigan Meeting October 17-22, 1982

TRIPLICATE copies of a 75-word abstract of a Recent News Paper, for a 10-minute presentation, must be received by the Symposium Chairman not later than August 23, 1982.
TRIPLICATE copies of a 75-word abstract and, ALSO a 200-300 word abstract of an Extended Recent News Paper, for a 20-minute presentation, must be RECEIVED by the Symposium Chairman not later than August 16, 1982.

ELECTRONICS DIVISION AND DIELECTRICS AND INSULATION DIVISION

Recent News Papers and Extended Recent News Papers are invited for the sessions sponsored by the Electronics and Dielectrics and Insulation Divisions for the 1982 Fall Meeting in Detroit, Michigan. The time allotted for the 75-word Recent News Paper will be 10 minutes, including 2 minutes for discussion. The time allotted for the Extended Recent News Paper will be 20 minutes, including the question/answer period.

The Extended Recent News Paper requires, in addition to the 75-word abstract, a 200-300 word abstract in triplicate and should be received significantly earlier than the normal deadline date because these papers will be reviewed for technical content, appropriateness of the paper, time limitations, duplication of material, etc. Topics for Recent News Papers and Extended Recent News Papers include:

1. Automotive Microelectronics and Reliability
2. Very Large Scale Integration Science and Technology as well as topics of general interest.

Copies of all abstracts, as outlined above, should be sent to the Recent News Papers Symposium Chairman: G. C. Schwartz, IBM Corporation, Department 206, Zip 48A, Route 52, Hopewell Junction, New York 12533. PLEASE NOTE THE DEADLINES ARE FOR RECEIVING THE PAPERS AND NOT FOR MAILING THEM.

The Energy and Environment Division has a Staff Scientist position to conduct research relevant to electrochemical energy storage. Will participate in LBL's Electrochemical Research Program by monitoring external research projects, reviewing research proposals and making site visits. Requires substantial demonstrated research expertise in membrane transport, materials science, polymer science fuel cells and/or photoelectrochemistry. Prefer a PhD. in chemical engineering, materials science or applicable scientific field.

Please send two resumes including salary history to: Employment Office, Lawrence Berkeley Laboratory, University of California, One Cyclotron Road, Berkeley, CA 94720. An Equal Opportunity Employer M/F/H. Please specify Job #A0228.

Gould Inc., an international developer and manufacturer of electronic and electrical products, is expanding its materials research capabilities at its modern research center in Rolling Meadows, a city 30 miles northwest of Chicago.

Materials Science Opportunities

GOULD

Materials Science
This is a senior position with responsibility for initiating and managing projects covering a variety of materials needs. Candidates should have an advanced degree and a wide experience and interest in materials R&D in relation to high technology products. Good planning and interpersonal skills necessary as there will be considerable interaction with operating divisions.

III-V Materials
This is a key position in a new electronic materials group. Candidates will be responsible for growth of III-V compounds and should have an advanced degree. Experience in MBE preferred and familiarity with other growth techniques desirable.

For immediate and confidential consideration, send a resume to: The Employee Relations Department, Dept. #115-82, Gould Inc., Gould Laboratories, 40 Gould Center, Rolling Meadows, IL 60008. An Equal Opportunity Employer M/F/H.

Electronics & Electrical Products

The Electrochemical Society, Inc.*
Financial Statements as of December 31, 1981

COMBINED BALANCE SHEET

ASSETS

UNRESTRICTED FUNDS	
CURRENT ASSETS:	
Cash and time deposits	$ 51,970
Certificates of deposit	365,357
Accounts receivable, less allowance for doubtful accounts of $1,500	76,260
Inventories	72,077
Prepaid expenses and deposits	18,186
TOTAL CURRENT ASSETS	583,850
PROPERTY, PLANT, AND EQUIPMENT, at cost—Note 3:	
Land	30,000
Building	167,681
Furniture and equipment	34,162
	231,843
Less accumulated depreciation	29,285
NET PROPERTY, PLANT, AND EQUIPMENT	202,558
SHARED INVESTMENT FUND—Note 2	681,485
OTHER ASSETS, NET OF ACCUMULATED AMORTIZATION	3,196
	$1,471,089
ENDOWMENT FUNDS	
SHARED INVESTMENT FUND—Note 2	$ 274,613

LIABILITIES AND FUND BALANCES

UNRESTRICTED FUNDS	
CURRENT LIABILITIES:	
Current installments of mortgage note payable—Note 3	$ 9,549
Accounts payable	27,752
Deferred revenue	444,148
TOTAL CURRENT LIABILITIES	481,449
MORTGAGE NOTE PAYABLE, less current installments—Note 3	124,984
FUND BALANCES:	
General operating	49,668
Net investment in property, plant, and equipment	68,025
Custodial	681,485
Divisions, Group, and Local sections	65,478
TOTAL FUND BALANCES	864,656
	$1,471,089
ENDOWMENT FUNDS	
FUND BALANCES	$ 274,613

See accompanying notes to combined financial statements.

COMBINED STATEMENT OF REVENUES, EXPENSES AND CHANGES IN FUND BALANCES

	Unrestricted Funds	Endowment Funds
REVENUES:		
Publications	$ 644,399	—
Membership	225,461	—
Society meetings	259,300	—
Monograph royalties	6,524	—
Investment income—Note 2	90,031	23,776
Gifts	21,541	36,500
Other income	16,493	—
	1,263,749	60,276
EXPENSES:		
Publications	668,489	—
Membership	17,885	—
Society meetings	90,025	—
Society activities	57,507	—
General and administrative	286,357	—
Society office building	21,068	—
Prizes, awards, and fellowships	23,970	12,860
Interest—Note 3	16,705	—
	1,182,006	12,860
EXCESS OF REVENUES OVER EXPENSES	81,743	47,416
Fund balances at beginning of year	782,913	227,197
FUND BALANCES AT END OF YEAR	$ 864,656	274,613

See accompanying notes to combined financial statements.

*** Includes the Society, its Divisions, Group, and Local Sections. See notes to financial statements.**

NOTES TO COMBINED FINANCIAL STATEMENTS

THE ELECTROCHEMICAL SOCIETY, INC.
December 31, 1981

NOTE 1—SUMMARY OF SIGNIFICANT ACCOUNTING POLICIES

Financial statement presentation: The combined financial statements include the accounts of the Society and its Divisions, Group, and Local Sections.

Fund accounting: To ensure observance of limitations and restrictions placed on the use of resources available to The Electrochemical Society, Inc., the accounts of the Society are maintained in accordance with the principles of fund accounting. This is the procedure by which resources for various purposes are classified for accounting and reporting purposes into funds established according to their nature and purposes. Separate accounts are maintained for each fund; however, in the accompanying combined financial statements, funds that have similar characteristics have been combined into fund groups. Accordingly, all financial transactions have been recorded and reported by fund group.

The assets, liabilities, and fund balances of the Society are reported in two self-balancing fund groups as follows:

Unrestricted funds:
- General operating funds—funds available for general operations of the Society.
- Net investment in property, plant, and equipment—represents the Society's net investment in property, plant, and equipment.
- Custodial funds—funds held by the Society for the Divisions, Group, and Local Sections to be invested and expended as specified by the Divisions, Group, and Local Sections and certain funds held by the Society for designed purposes.

Endowment funds:
- Endowment funds are subject to the restrictions of gift instruments requiring in perpetuity that the principal be invested and the income only be utilized. Fund balances at December 31, 1981 include $43,913 of unexpended income.

Revenue recognition: Income received in advance for extended abstracts and proceedings volumes, which have not yet been printed, and membership dues paid in advance are recorded as deferred revenue.

Investments: Investments are carried at cost and are generally held until maturity.

Inventories: Inventories of publications are stated at the lower of cost, first-in, first-out (FIFO) method, or market.

Depreciation and amortization: The Society provides for depreciation and amortization of plant, equipment, and software costs over their estimated useful lives on the straight-line method. The estimated useful lives in computing depreciation and amortization are as follows:

Building	40 years
Furniture and equipment	10 years
Software costs	3 years

Income taxes: The Society qualifies as a tax-exempt organization under Section 501(c)(3) of the Internal Revenue Code and all of its income, except income generated through the advertising included in its technical journal, is exempt from Federal and State income taxes.

The Electrochemical Society, Inc.
Financial Statements as of December 31, 1981

NOTE 2—SHARED INVESTMENT FUND

Unrestricted and endowment funds are included in the shared investment fund managed by the Society. Investment income earned by the assets is allocated to the funds twice a year as of June 30 and December 31. Assets of the fund at December 31, 1981 are as follows:

Certificates of deposit	$172,666
Investments, at cost (market value $511,151)	764,826
Accrued interest receivable	18,606
	$956,098

The assets of the fund are reflected in the combined balance sheet as follows:

Unrestricted funds	$681,485
Endowment funds	274,613
	$956,098

NOTE 3—MORTGAGE NOTE PAYABLE

The Society has a mortgage note payable, at 12% per annum, collateralized by land and building, payable in monthly installments of $2,098 including interest through July 1985. At that time, the remaining principal balance of $94,000 is payable in total $134,533

Less current installments	9,549
Mortgage note payable, excluding current installments	$124,984

NOTE 4—PENSION PLAN

The Society has a pension plan under which annuity contracts are purchased for all eligible employees. The Society's policy is to fund pension costs accrued. Total pension expense was approximately $8,400, net of $2,100 premium adjustment due to voluntary employee resignation.

The Board of Directors
The Electrochemical Society, Inc.:

We have examined the combined balance sheet of The Electrochemical Society, Inc. as of December 31, 1981 and the related combined statement of revenues, expenses and changes in fund balances and changes in financial position of unrestricted funds for the year then ended. Our examination was made in accordance with generally accepted auditing standards and, accordingly, included such tests of the accounting records and such other auditing procedures as we considered necessary in the circumstances.

In our opinion, the aforementioned combined financial statements present fairly the financial position of The Electrochemical Society, Inc. at December 31, 1981 and the results of its operations, changes in fund balances and changes in financial position of unrestricted funds for the year then ended, in conformity with generally accepted accounting principles applied on a basis consistent with that of the preceding year.

The examination referred to above was directed primarily toward formulating an opinion on the combined financial statements of The Electrochemical Society, Inc., taken as a whole. The supplementary data included in Schedule 1 is presented for supplementary analysis purposes and is not necessary for a fair presentation of the financial position, results of operations, changes in fund balances and changes in financial position of unrestricted funds of The Electrochemical Society, Inc. The supplementary data has been subjected to the auditing procedures applied in the examination of the basic combined financial statements and, in our opinion, is stated fairly in all material respects only when considered in conjunction with the combined financial statements taken as a whole.

Peat, Marwick, Mitchell & Co.

April 21, 1982

COMBINED STATEMENT OF CHANGES IN FINANCIAL POSITION OF UNRESTRICTED FUNDS
Year ended December 31, 1981

SOURCES OF WORKING CAPITAL:	
Funds provided from operations:	
Excess of revenues over expenses	$ 81,743
Items which do not require working capital:	
Depreciation and amortization	9,001
WORKING CAPITAL PROVIDED BY OPERATIONS	90,744
Decrease in working capital	4,473
	$ 95,217
USES OF WORKING CAPITAL:	
Purchase of property, plant, and equipment	364
Retirement of mortgage note payable	9,549
Purchases of long-term investments	85,304
	$ 95,217
CHANGES IN COMPONENTS OF WORKING CAPITAL:	
Increase (decrease) in current assets:	
Cash and time deposits	(6,406)
Certificates of deposit	128,258
Accounts receivable, net	(2,747)
Inventories	9,313
Prepaid expenses and deposits	(921)
	127,497
Increase (decrease) in current liabilities:	
Current installments of mortgage note payable	1,075
Accounts payable	10,658
Deferred revenue	120,237
	131,970
NET DECREASE IN WORKING CAPITAL	$ 4,473

DETAILS OF CHANGES IN FUND BALANCES
Year Ended December 31, 1981

Schedule 1

Unrestricted Funds:	Balance at January 1, 1981	Excess (Deficiency) of Revenues over Expenses	Balance at December 31, 1981
General operating fund	$ 50,013	(345)	49,668
Net investment in property, plant, and equipment	64,994	3,031	68,025
	115,007	2,686	117,693
Divisions, Group, and Local Sections	71,726	(6,248)	65,478
Society Reserve Fund	308,340	28,401	336,741
Building Fund	11,211	35,645	46,856
Battery Division Fund	3,572	6	3,578
Battery Division Monograph Fund	9,577	662	10,239
Colin Garfield Fink Fellowship Fund	16,144	(60)	16,084
Consolidated Fellowship Fund	104,014	8,465	112,479
Corrosion Division Fund	—	1,644	1,644
Corrosion Division Monograph Fund	51,985	2,098	54,083
Detroit Local Section	2,618	258	2,876
Detroit Section Fund	1,777	270	2,047
Dielectrics and Insulation Division Fund	5,134	209	5,343
Electrodeposition Division—Monograph Fund	19,419	689	20,108
Electronics Division Fund	13,041	(1,848)	11,193
Electrothermics and Metallurgy Division Fund	19,953	(464)	19,489
Electrothermics and Metallurgy Division—Monograph Fund	11,753	22	11,775
Industrial Electrolytic Division Fund	1,684	3,345	5,029
Niagara Falls Section Fund	1,011	153	1,164
Organic and Biological Division Fund	1,793	631	2,424
Pacific-Northwest Section Fund	629	62	691
Philadelphia Section Fund	—	4,742	4,742
Physical Electrochemistry Division Fund	2,956	(44)	2,912
Physical Electrochemistry Division—Monograph Fund	1,936	93	2,029
PSC—Publication Fund	3,000	—	3,000
South Texas Section Fund	324	49	373
Southern California-Nevada Section Fund	2,809	277	3,086
Young Authors' Fund	1,500	—	1,500
	$782,913	81,743	864,656
Endowment Funds:			
Carl Wagner Fund	20,005	(718)	19,287
Edward Goodrich Acheson Fund	67,541	30,792	98,333
F. M. Becket Memorial Fund	18,281	(63)	18,218
Grahame Award Fund	—	4,861	4,861
Henry Linford Fund	10,551	1,038	11,589
Olin Fund	24,532	768	25,300
Solid State Fund	16,926	5,073	21,999
Vittorio De Nora-Diamond Shamrock Fund	69,361	5,665	75,026
	$227,197	47,416	274,613

Committees of The Electrochemical Society, Inc., 1982-1983

Executive Committee of the Board of Directors

Frederick J. Strieter, Chairman	Spring 1983
J. Bruce Wagner, Jr.	Spring 1983
Paul C. Milner	Spring 1983
Richard C. Alkire	Spring 1983
Forrest A. Trumbore	Spring 1983
Jerome Kruger	Spring 1983

Admissions Committee

Gunnar Stendahl, Chairman	Spring 1985
Martin F. Quaely	Spring 1984
John L. Everhart	Spring 1983

Contributing Membership Committee

Henry F. Ivey, Chairman	Spring 1983
Kathryn R. Bullock	Spring 1983
Richard Goodin	Spring 1983

Education Committee

James McBreen, Chairman	Spring 1983
W. Jean Horkans	Spring 1984
Sigurd Wagner	Spring 1984
B. E. Conway	Spring 1985
William H. Smyrl	Spring 1986
Walter O. Freitag	Term as Chairman, Council of Local Sections
Paul C. Milner	Term as Chairman, Technical Affairs Committee
William A. Pliskin	Term as Chairman, Individual Membership Committee

Finance Committee

Jerome Kruger, Chairman	Elected Term as Treasurer
Forrest A. Trumbore	Elected Term as Secretary
J. Bruce Wagner, Jr.	Elected Term as Sr. Vice-President
Elton J. Cairns	Spring 1983
Arthur Smith	Spring 1983
William McAllister	Spring 1984
Laura Rothman	Spring 1984

Financial Policy Advisory Committee

Robert E. Visco, Chairman	Spring 1985
Dennis R. Turner	Spring 1984
Patricia L. Castro	Spring 1983
Ken Pickar	Spring 1986
Jerome Kruger	Elected Term as Treasurer

Honors and Awards Committee

Fritz G. Will, Chairman	Spring 1984
Edward McCafferty	Spring 1984
Robert A. Rapp	Spring 1983
James A. Amick	Spring 1983
James D. E. McIntyre	Spring 1985
Philip N. Ross, Jr.	Spring 1985
Bruce E. Deal	Spring 1986
Michael J. Pryor	Spring 1986
Frederick J. Strieter	Ex Officio as President

Individual Membership Committee

William A. Pliskin, Chairman	Spring 1985
David L. Nelson	Spring 1983
Brooke Schumm, Jr.	Spring 1984

Nominating Committee

Ralph J. Brodd, Chairman	Spring 1983
Forrest A. Trumbore	Spring 1983
J. Bruce Wagner, Jr.	Spring 1983
Robert P. Frankenthal	Spring 1983
Ronald E. Enstrom	Spring 1983

Perkin Medal Award Committee

Frederick J. Strieter	Elected Term as President
J. Bruce Wagner, Jr.	Spring 1983

Publication Committee

Robert P. Frankenthal, Chairman	Spring 1986
Forrest A. Trumbore	Elected Term as Secretary
Norman Hackerman	Term as Editor of the JOURNAL
Newton Schwartz	Spring 1984
Rudolf G. Frieser	Spring 1984
Glenn W. Cullen	Spring 1983
Rudolf Keller	Spring 1983
Isaac Trachtenberg	Spring 1985
Gary McGuire	Spring 1985

Society Meeting Committee

Forrest A. Trumbore, Chairman	Elected Term as Secretary
Jerome Kruger	Elected Term as Treasurer
Kenneth A. Bowman	Spring 1985
James R. Huff	Spring 1984
Kenneth E. Bean	Spring 1983
V. H. Branneky	Term as Executive Secretary (ex-officio non-voting)

Technical Affairs Committee

Paul C. Milner, Chairman	Elected Term as 2nd Vice-President
Richard C. Alkire	Elected Term as 3rd Vice-President
Ernest Littauer	Term as Chairman, New Technology Subcommittee
Glenn W. Cullen	Spring 1985
Robert A. Huggins	Spring 1984
William H. Tiedemann	Spring 1983

Tellers of Election

Sigurd Wagner, Chairman	Spring 1983
P. N. Yocom	Spring 1983
Ronald K. Smeltzer	Spring 1983
Paul R. Mucenieks, Alternate	Spring 1983
Stephen G. Wechter, Alternate	Spring 1983
Gary N. Taylor, Alternate	Spring 1983

Ways and Means Committee

J. Bruce Wagner, Jr., Chairman	Elected Term as 1st Vice-President
Paul C. Milner	Elected Term as 2nd Vice-President
Richard C. Alkire	Elected Term as 3rd Vice-President
Eric Brooman	Spring 1983
Herbert P. Silverman	Spring 1983
Geraldine C. Schwartz	Spring 1984
W. Murray Bullis	Spring 1984

Board Representative for Administration of the Corrosion Monograph Fund

Jerome Kruger	Spring 1983

REPRESENTATIVES TO OTHER SOCIETIES

American Association for Advancement of Science

Richard C. Alkire	Spring 1983

American National Standards Institute

Bernard Bergum	Spring 1983

National Research Council—Assembly of Mathematical and Physical Sciences

Forrest A. Trumbore	Elected Term as Secretary

American Society for Testing and Materials

Robert T. Foley	Spring 1983

American Electroplaters Society—Representative of Electrodeposition Division

John L. Griffin	Spring 1983

Intersociety Energy Conversion Engineering

Ernest Littauer	Spring 1983

National Inventors Hall of Fame

Fritz G. Will (Selection Committee)	Spring 1983

Federation of Materials Societies

Edward McCafferty	Spring 1983
V. H. Branneky, Member, Advisory Board	Term as Executive Secretary

OPPORTUNITIES IN MOS/VLSI TECHNOLOGY DEVELOPMENT

Join our dynamic, growing team of experts engaged in the development of advanced MOS structures and processes for application to next-generation VLSI memory and microprocessor products. From conception through prototyping to product introduction, you will be involved in all aspects of MOS technology.

These highly visible positions require experimentalists with an advanced degree in Solid State Physics, Electrical Engineering or Materials Science and a high level of demonstrated technical ability. A background including semiconductor device physics is essential and MOS processing experience is desirable. Well-qualified recent graduates will be considered.

If you fit this description and are interested in tangible work with a challenging future at Texas Instruments, a recognized leader in electronics, send your resume in confidence to: Dr. Greg Armstrong/P.O. Box 1443, M.S. 631/Houston, Texas 77001.

TEXAS INSTRUMENTS

INCORPORATED

An equal opportunity employer M/F

Instrumentation for Electrochemistry and Chemistry Research

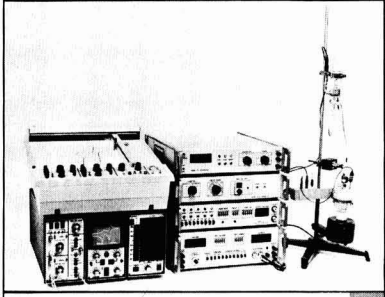

ELECTROCHEMOSCOPE I

A complete line of versatile instruments for the electrochemist includes the unique ELECTROCHEMOSCOPE I which makes available for the first time . . .

- All digital circuitry • Real time CRT display plus X-Y Recorder
- Floppy disc storage of 16 plots • Scale expansion and background subtraction of stored data • Computer interface
- Digital display of current, voltage and coulombs.

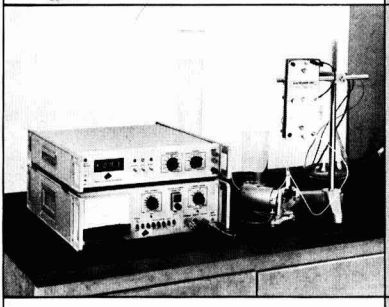

ELECTROPREP™ SYSTEM

A complete system for preparative electrosynthesis and coulometry is based on the unique ELECTROPREP cell which offers a wide choice of easily interchanged electrodes, optimized cell geometry and choice of interchangeable separators. Optimally matched components of the system provide . . .

- Production of up to 200 millimoles per hour
- Completely automated operation
- Controlled voltage and constant current operation.

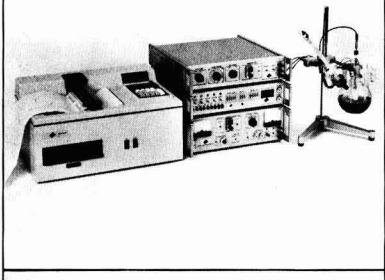

COMPUTER-AIDED CORROSION MEASUREMENTS

Included in the wide choice of instruments for corrosion research from ECO INSTRUMENTS, the CMS-10 Computer-Aided Electrochemical Corrosion Measurement System introduces the advantages of data processing including . . .

- Raw data stored on floppy discs for instant retreival
- Standard corrosion calculations done automatically, displayed digitally and/or printed out
- User programmable for new and non-standard calculations
- Sample testing time reduced to a few minutes.

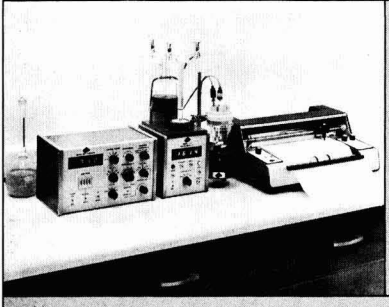

TITRISTAT™ II

The TITRISTAT II offers a unique combination of capabilities and conveniences, such as . . .

- First derivative plots plus $\frac{\Delta E}{\Delta V}$ providing true equivalence point
- Potentiometric, amperometric, Karl Fischer and both direct and incremental thermometric titrations
- Automatic end-point search, pH Stat, and preset end-point search
- Two digital displays — ml's added and actual parameter sensed
- Computer compatible outputs for both displays.

ECO INSTRUMENTS
Division of Sea Data Corporation

153 California Street – Newton, Mass. 02158, U.S.A.
Tel. (617) 661-8080 – Telex: 951107 – Cable: Seadata New

EG&G PRINCETON APPLIED RESEARCH PROUDLY INTRODUCES...

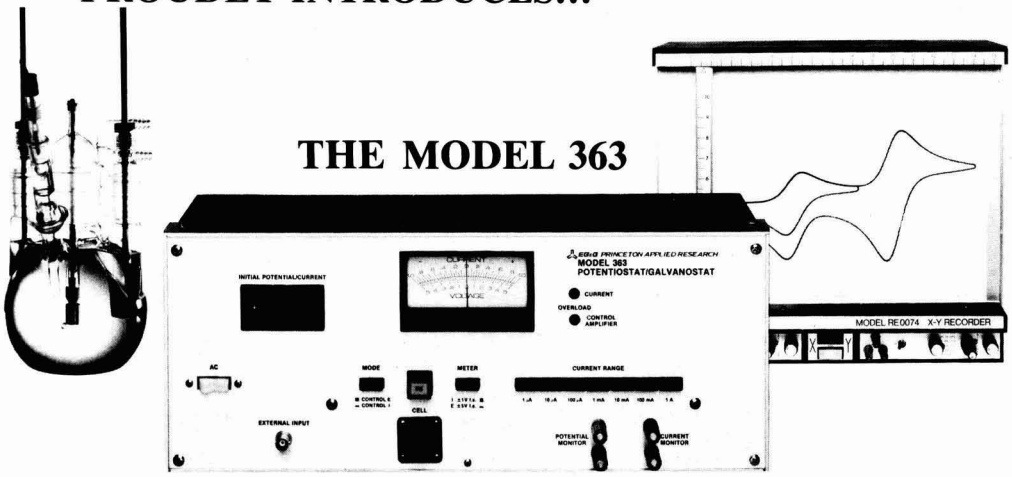

Potentiostat/ Galvanostat

for use in electrochemical applications requiring either potential or current control. This powerful yet cost-effective unit will find broad application in such diverse fields as corrosion measurements, battery and fuel cell testing, electrochemical thickness determinations, and electro-organic synthesis.

HIGH PERFORMANCE MADE COST EFFECTIVE

The bipolar potentiostat features ±1 A current capability with a compliance voltage of ±30 V. A four-digit thumbwheel switch controls the applied voltage or current. The range of potential control is ±9.999 V, while current ranges from 1 μA to 1 A are available. The convenient front panel meter allows the user to visually monitor either the current or potential while front panel outputs are available so that current and potential can be recorded. A connector is available on the front panel to accept externally-supplied waveforms such as ramps, triangles, sinusoids, and trapezoids for various types of voltammetry. The built-in electrometer prevents reference electrode loading and provides a low-impedance, unity-gain monitoring point for the working electrode potential.

The Model 363 complements our Model 173 Potentiostat for research work and our Model 371 Potentiostat for high-current applications. The Model 363 Potentiostat/Galvanostat has been designed for easy interface with other EG&G PARC instruments such as the Model 379 Digital Coulometer and the Model 175 Universal Programmer. Call or write for more information.

P. O. BOX 2565 • PRINCETON, NJ 08540, USA • 609/452-2111 • TELEX: 843409

EG&G PRINCETON APPLIED RESEARCH

565

1 "Progress in Batteries & Solar Cells" Vol. 4 (1982), 400 Pages

Edited by A. Kozawa, K. V. Kordesch, H. Tamura, E. Voss, H. Joseph, H. Shimotake, etc. About 400 pages. Published by JEC Press Inc. $55. (Shipping $18 for air, $4 for surface) Contents: about 100 articles under "View From The Top," "Miniature Cells, Li-cells, Silver Cells, etc.", "MnO_2 and MnO_2 Cells," "Lead-acid Batteries," "Electric Vehicles, Fuel Cells, Military or Energy-Related Batteries," "Ni-Cd, Ni-H_2, and Other Rechargeable Batteries," "Solar Cells, Photoelectrochemical Cells," "Patents and News."

2 Battery Active MnO_2 Samples and New Carbon Samples for Batteries

I.C. No. 1 Electrolytic MnO_2 made by Ti anode
I.C. No. 2 Electrolytic MnO_2 made by Pb anode
I.C. No. 3 Electrolytic MnO_2 made by C anode
I.C. No. 4 Electrolytic MnO_2
I.C. No. 5 Chemically prepared MnO_2
I.C. No. 6 Beta MnO_2
I.C. No. 7 Natural MnO_2 ore
I.C. No. 8 Chemically prepared MnO_2
I.C. No. 9 Electrolytic MnO_2 (coarse grade)
I.C. No. 10 Electrolytic MnO_2
I.C. No. 12 Chemical MnO_2
I.C. No. 13 Natural MnO_2 ore (Comilog)
I.C. Carbon No. 1 (graphite)
I.C. Carbon No. 2 (acetylene black)

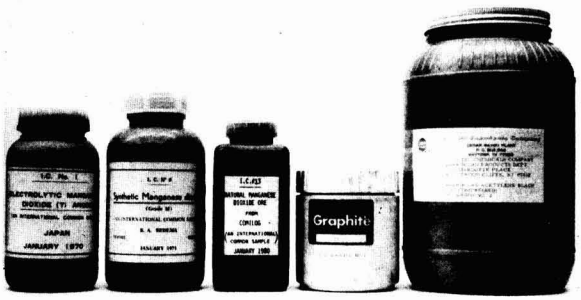

Left to right: I.C. No. 1 MnO_2, I.C. No. 2 MnO_2, I.C. No. 13 MnO_2, I.C. Carbon No. 1 (graphite), I.C. Carbon No. 2 (acetylene black)

Price: MnO_2 $18 per bottle (1 Kg, except No. 6, 500g). **Carbon** $18 per bottle, **graphite** (No. 1) 400g per bottle, acetylene black (No. 2), 450g. **Shipping charge:** about $4 for surface and about $18 for air.

3 Manganese Dioxide Symposium, Vol. 2 (Tokyo) 1980, 700 pages

Compiled and Edited by B. Schumm, Jr., H. M. Joseph and A. Kozawa (The I.C. Sample Office). $48 (Shipping: $4.00 surface and $18 for air). This book is a collection of full papers presented at the 2nd MnO_2 Symposium in Tokyo with the discussions in the meeting and other related papers which have not been presented in the symposium.

Contents: Basic structure of MnO_2, Electrochemical properties of EMD, CMD, and natural MnO_2. Use of MnO_2 for batteries, catalysts, etc. Some examples of papers are: A New Activated MnO_2 Evaluated by the Practical $ZnCl_2$ Cell by Y. Uetani, et al, On the Synthesis of CMD from Mn-Ammonium Carbamate and Its Properties by I. Tanabe, et al, Mixed Oxide of Manganese as Catalysts for Hydrogen Peroxide Decomposition in Oxygen Cathodes in Alkaline Solution by K. Matsuki, H. Takahashi and E. Yeager, Review of Structural Studies of MnO_2 in Relation to Battery Activity by R. G. Burns and V. M. Burns, The Relation Between the Electrochemical Potential of Electrodeposited Manganese Dioxide and its Content of Combined Water by E. Preisler (Hoechst AG, W. Germany), An Interpretation of the Specific Reactivity of MnO_2 Having a Gamma or a Gamma-Rho Crystal Structure by M. J. Brenet, P. C. Picquet and J. Y. Welsh (Sedema S.A., Belgium), Pykometric Density of Manganese Dioxides by D. M. Holton and F. L. Tye (Berec Group Ltd., England), Electrical and Physical Properties of MnO_2 Layer for the High Performance Tantalum Solid Electrolytic Capacitor by A. Nishino, A. Yoshida and H. Hayakawa (Matsushita Electric Ind. Co., Ltd., Japan).

Vol. 1 (Cleveland) 1975 is also available

4 NEW SERIES: New Materials and New Processes, Vol. 1 & Vol. 2 Vol. 2 will be a Special Issue on Batteries & Surface Finishing

Edited by M. Nagayama, E. B. Yeager, Y. Okinaka, A. Kozawa, etc. $55, about 350 pages. This book will be available in Nov. 1982. Order now so you can receive the book directly from the printer as soon as it is completed in Oct. 1982. No need to send money now.

Contents: About 25 articles on metal finishing; about 25 articles on batteries; other papers in electrochemical, energy and medical fields.

More than 50% of the articles are on Japanese Electrochemical Technology

5 Other Books on Carbon, Battery and Electrochemistry in English

1. **Surface Electrochemistry by T. Takamura and A. Kozawa,** $50, 250 pages (Hard cover book)
2. **Rechargeable Batteries in Japan by Y. Miake and A. Kozawa,** $45, 528 pages (Hard cover book)
3. **Manganese Dioxide Symposium Vol. 1 by A. Kozawa and R. J. Brodd,** $48, 535 pages
4. **Progress in Batteries & Solar Cells, Vol. 2, 3,** $48, 300-400 pages
5. **Electrochemistry of MnO_2 and MnO_2 Batteries,** $35, 400 pages
6. **An Electric Car and Lead-Acid Batteries,** $25, 154 pages
7. **Lithium Batteries by Hirai,** $55 (will be completed Nov. 1982. Order now)
8. **Recent Carbon Technology by Ishikawa and Nagaoki,** $55, about 400 pages (will be completed Nov. 1982. Order now)
9. **Applications of Solid Electrolyte by T. Takahashi and A. Kozawa,** 210 pages, $48.

How To Order

Please send your order for (1), (4) and (5) above to JEC Press, P.O. Box 35241, Cleveland, Ohio 44135 USA. Please send orders for (2) and (3) above to the I.C. Sample Office, Box 6116, Cleveland, Ohio 44101 USA (Tel: 216-676-2268)

PHOENIX SERIES 1100 CHEMICAL VAPOR DEPOSITION SYSTEMS

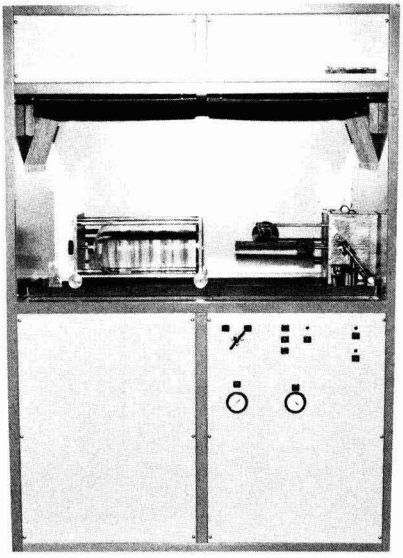

(Control Console required with unit not shown)

The Phoenix 1100 Series CVD Systems are designed for laboratory deposition of epitaxial silicon, nitride, oxide, and polysilicon. The resistance heater/susceptor is capable of operating at temperature up to 1400°C (fourteen hundred degrees). Our unique design assures that there is no thermal stress in the heater providing a long lifetime for this part.

The four inch by six inch work surface has a capacity of six two-inch, two three-inch or one four-inch wafer. The 1100 systems are ideal for research with their fast cycle time and small capacity. The susceptor can be heated to and stabilized at 1000°C in five minutes.

The heater/susceptor is contained within a horizontally mounted, quartz bell jar. The quartz bell jar, in turn, is captured in a movable carriage so the seal at the open end of the bell jar is stationary. The carriage assembly moves with a captured o-ring. All wetted metal parts are fabricated from Inconel and water cooled to assure long life and corrosion resistance. Deposition can be carried out at or below atmospheric pressure. The entire reactor assembly is contained within a lighted laminar flow hood. HEPA filters above the work area provide a dust-free environment for loading and unloading specimens.

Ten flow circuits are supplied with the PMC 1100 systems. Three of these circuits, Nitrogen,* Oxygen and Spare are directed into the deposition chamber through an inlet in the baseplate to provide a background ambient. The second group of circuits, consisting of Nitrogen,* Hydrogen,* Silane, Carbon Dioxide, Ammonia, Etchant and Dopant flow into the reactor through a spray nozzle. The nozzle sprays any combination of these gasses from above the susceptor. The Nitrogen,* and Hydrogen,* circuits are dual flow level circuits which can be used both for purging the reactor at high flow, and as carriers at low flow. A flow circuit which regulates the flow of a carrier gas to an external vaporizer can be supplied.

Two versions of the PMC 1100 are available. The PMC 1111 is a microprocessor controlled system with a programmable sequencer for all gas circuits and heater power. Multiple temperature setpoints are optional and can be selected by the sequencer. The PMC 1101 system is manually controlled with the exception that the deposition cycle is timed with an electro-mechanical timer.

Call or write for additional details on the 1100 CVD Systems. We are interested in your applications.

PHOENIX MATERIALS CORPORATION
833 BUTLER RD. KITTANNING, PA. 16201
(412) 548-1531

The Electrochemical Society, Inc.
10 South Main Street, Pennington, New Jersey 08534-2896 • Telephone: 609-737-1902

Instructions to Authors

The **JOURNAL OF THE ELECTROCHEMICAL SOCIETY** is the official monthly journal of the Society. It contains three sections: Electrochemical Science and Technology, Solid-State Science and Technology, and Reviews and News. Technical Papers, Technical Notes, and Accelerated Brief Communications are published in the first two sections and Review Papers in the third. All manuscripts submitted are considered for publication, with the understanding that they have not been submitted, accepted for publication, or published elsewhere. A wide range of subject matter is acceptable. Manuscripts can be handled promptly and efficiently if these instructions are followed.

TYPES OF PAPERS

Technical Papers describe fundamental or applied studies in depth. They contain new data and/or new interpretations of existing data. Abstracts summarizing the results are required.

Technical Notes report briefly on limited research or development that is not being pursued further. No abstracts are required.

Accelerated Brief Communications present, in camera-ready format of limited length, scientific or technological information warranting rapid dissemination. No abstracts are required.

Review Papers furnish critical analyses of topical subjects. Abstracts are required.

SUBMISSION

Submit three complete, clear copies of each manuscript and the originals of all figures and illustrations to:

Editorial Office
The Electrochemical Society, Inc.
10 South Main Street
Pennington, New Jersey 08534-2896

A letter accompanying the manuscript should give (a) the name and mailing address of the author to whom correspondence should be sent, (b) reference to any presentation of the work at a meeting of The Electrochemical Society, (c) the Division or Group of the Society or the Divisional or Group Editor (both are listed in the front of each issue of the Journal) whose interests are most closely related to the work being discussed, (d) the section of the Journal in which the work should appear, and (e) the names and addresses of people able to act as reviewers.

EDITORIAL PRACTICES

Following receipt by the Editorial Office, each manuscript is sent to a Divisional or Group Editor with knowledge of the subject matter. This editor arranges for review of the manuscript and communicates with the author(s) regarding revisions. Final acceptance or rejection of a manuscript is determined by the Editor.

Accelerated Brief Communications are handled as rapidly as possible, ordinarily with a response to the author(s) from the Divisional Editor, the Group Editor, or the Editor within three weeks of their arrival at Pennington. Response to the authors of other manuscripts usually takes place within six weeks. Following acceptance, authors are notified of the Journal issue in which publication is scheduled; about one month before publication, page proofs and an order blank for reprints are provided. Proofs must be promptly corrected and returned. Extensive alterations by the author may delay publication; their cost will be billed to the author(s).

PUBLICATION CHARGE

To help meet publication costs, a payment of $65.00 per printed page is requested for the publication of technical material. If at least one author is a Society member or an employee of a Patron or Sustaining member, a 10% reduction is allowed. Acceptance of manuscripts for publication is, however, based on merit and is in no way dependent on such payment, which may be waived in individual cases upon request.

PRESENTATION

Organization and clarity are essential elements of successful written communication. Identify the subject matter in the title, using words useful in indexing. State the purpose of the work early in the text. Avoid introductory and explanatory material that is overly familiar to those in the field. Present the work and the arguments in an order that leads naturally to clearly specified conclusions. Provide enough information for the work to be reproduced and the logic behind it to be understood. Identify and justify any assumptions that are made; avoid tacit assumptions. Omit details that are generally known or that can be covered by reference to other publications. Give the magnitude and define the significance of experimental errors. Use headings and subheadings as appropriate. Avoid proprietary and trade names, but capitalize them where their use is necessary. Define unusual technical terms and abbreviations. Where symbols are used extensively, list them with their definitions at the end of the paper. Avoid repetition in the text and duplication of material in figures and tables. Be brief but clear.

Edit and proofread the manuscript carefully; these are not the responsibilities of the editors or reviewers.

KEY-DESCRIPTORS

To aid in indexing, authors must supply standard key-descriptors, preferably four of them, from a list with instructions published annually in the December issue of the Journal and available from the Editorial Office. These key-descriptors must appear at the bottom of the first page of the manuscript.

MANUSCRIPT PREPARATION

Accelerated Brief Communications must be typewritten or printed on standard forms obtained, with detailed instructions for their use, from the Pennington Editorial Office.

All other manuscripts must be typewritten or printed, double-spaced throughout, on one side only of white 21.6 x 27.0 cm paper, with 2.5-3.8 cm margins. Do not use single spacing anywhere, in title, abstract, text, references, tables, or figure captions.

For general matters of style and format, see papers in recent issues of the **Journal** and consult a style manual such as that of the American Chemical Society or that of the American Institute of Physics. These also provide lists of common abbreviations and units. The following specific items should be noted:

(a) Système Internationale (SI) units are to be used; a description may be found in NBS Special Publication 330 or ASTM Metric Practice Guide E-380-72.

(b) The signs of cell and electrode potentials are to follow the IUPAC conventions of 1953.

(c) **Mathematical equations** should be written on a single line, if possible, using parentheses, brackets, the solidus, negative exponents, etc.

(d) **References** are to be listed separately at the end of the paper in the order they are cited in the text, being sure that each listed reference is cited. Authors' initials must be given, and Chemical Abstracts abbreviations must be used. Citations of other than the generally available literature should be avoided if possible.

(e) **Tables** are to be presented on individual sheets, with both captions and body double-spaced.

(f) **Figure captions** and numbers are to be included on a separate sheet and must not appear in the body of any figure or illustration.

(g) **Drawings** and **graphs** will ordinarily be reduced to column width (8.3 cm) and after such reduction should have lettering at least 0.15 cm high. Lettering must be of letter-guide quality. Originals in India ink on tracing cloth or paper are preferred, but India ink on coordinate paper with blue ruling is acceptable. When several curves are shown, each may be lettered and identified in the caption. The Editorial Office will not make corrections or additions to figures.

(h) **Photographs** should be used sparingly. The originals supplied must be glossy prints and should be protected against bending. Micrographs must have a labeled unit length within the body of the picture; reduction for printing makes magnifications meaningless.

Revised December 1, 1980

Printed in the United States of America

Call for Papers
163rd Meeting, San Francisco, California, May 8-13, 1983

Divisions which have scheduled sessions are listed on the overleaf, along with the symposium topics.

1. Symposium Papers.

Authors desiring to contribute papers to a symposium listed on the overleaf should check first with the symposium chairman to ascertain appropriateness of the topic.

2. General Session Papers.

Each of the Society Divisions or Group which will meet in San Francisco, California, can plan a general session. If your paper does not fit readily into a planned symposium, you should specify "General Session."

3. To Submit a Meeting Paper.

Each author who submits a paper for presentation at a Society Meeting must do three things:

A—Submit one original 75-word abstract of the paper on the attached form or a facsimile thereof. **Deadline for receipt of 75-word abstract is December 1, 1982.**

B—Submit original and one copy of an Extended Abstract of the paper. **Deadline for receipt of Extended Abstract is January 1, 1983.** See (6) below for details.

C—Determine whether the meeting paper is to be submitted to the Society Journal for publication. See (7) below for details.

Send all material to The Electrochemical Society, Inc., 10 South Main Street, Pennington, NJ 08534-2896.

Unless the 75-word and required Extended Abstracts are received at Society Headquarters by stated deadlines, the papers will not be considered for inclusion in the program.

4. To Submit a Recent News Paper.

Recent News Papers and Extended Recent News Papers are invited for this meeting. Each author must submit one of the following items to the Session Chairman:

A—Triplicate copies of a 75-word abstract of a Recent News Paper, for a 10-minute presentation. Deadline for receipt is March 24, 1983.

B—Triplicate copies of a 75-word abstract and, also, a 200-300 word abstract of an Extended Recent News Paper, for a 20-minute presentation. Deadline for receipt is March 14, 1983.

Send all material to the appropriate Session Chairman listed, for Recent News Papers only.

5. Meeting Paper Acceptance.

Notification of acceptance for meeting presentation, along with scheduled time, will be mailed to authors with general instructions no earlier than two months before the meeting. Those authors who require more prompt notification are requested to submit with their abstracts a self-addressed postal card with full author-title listing on the reverse.

6. Extended Abstract Volume Publication.

All scheduled papers will be published in the EXTENDED ABSTRACTS volume of the meeting. The volume is published by photo-offset directly from typewritten copy submitted by the author. Please note that the EXTENDED ABSTRACTS will be in a new double column format. Please follow the NEW instructions listed below.

A—Abstracts are to be from 500 to 1000 words in length. The abstract should contain to whatever extent practical all significant data to be presented during oral delivery.

B—Abstracts are to be typed single spaced on the special double column typing forms which are sent to each author after the submission of a short abstract. The Extended Abstract, including title, author's name and affiliation, and references, cannot exceed one page (two columns). An additional two columns is permitted, if necessary, for figures only. Abstracts not meeting these criteria will be rejected and returned to the authors.

C—Title of paper is to be in capital letters centered. Author(s) name, affiliation, and address is typed immediately below in capital and lower case letters centered.

D—All tables and figures must be securely mounted on the special typing guides within the margins; rubber cement is recommended for this purpose. What is submitted will be reproduced photographically exactly as it is sent. However, it will be reduced so that graphs and tables will be half their original size. Keep the lettering large enough to be legible when later reduced to half size. Place references and figures after the text.

E—Mail original and one copy of the abstract to: The Electrochemical Society, Inc., 10 South Main St., Pennington, NJ 08534-2896.

7. Manuscript Publication in Society Journal.

All meeting papers upon presentation become the property of The Electrochemical Society, Inc. However, presentation incurs no obligation to publish. If publication in **Journal** is desired, papers should be submitted as promptly as possible in full manuscript form in order to be considered. If publication elsewhere after presentation is desired, written permission from Society Headquarters is required.

San Francisco, California, Meeting Symposia Plans—Spring 1983
May 8-13, 1983

a.) For receipt no later than December 1, 1982, submit a 75-word abstract of the paper to be delivered on the attached overleaf.
b.) For receipt no later than January 1, 1983, submit two copies of an extended abstract, 500-1000 words.
c.) Send all abstracts to The Electrochemical Society, Inc., 10 South Main Street, Pennington, NJ 08534-2896 with the exception of Recent News Papers. For Recent News Papers see preceding page.

BATTERY

Cell Design and Optimization

This symposium covering cell design and optimization will focus particularly on batteries having already reached the stage of hardware where design is already established and improvements are still being made in view of optimization. Design is understood to cover either the whole cell or a specific component. Systems considered can be aqueous or nonaqueous.

The publication of a proceedings volume is planned and, consequently, full papers are expected to be submitted to the Symposium Chairman within 30 days after acceptance of the 75-word abstract and the extended abstract.

Suggestions and inquiries should be sent to the Symposium Chairman: A. Himy, Navy Department, Naval Sea Systems Command, Code 5433, Washington, DC 20362.

Cell Testing and Reliability

The objective of this symposium is to provide a forum for the discussion of methods for testing batteries and the correlation of test results with reliability. Reliability requirements vary with the types of applications. Discussion of the relative needs for different levels of reliability in battery applications areas such as aircraft, communications, ordinance, automotive, consumer products, and medical devices is appropriate.

Previous symposia have considered the topic of battery design and performance optimization. In the present symposium the intent is to focus on methods for the evaluation and testing of batteries and the techniques by which such results are used to establish reliability. The symposium encompasses both primary and secondary batteries and batteries for all types of commercial applications as well as space, defense, and medical batteries.

Suggestions and inquiries should be sent to the Symposium Co-Chairmen: S. C. Levy, Sandia National Laboratories, Div. 2523, P.O. Box 5800, Albuquerque, NM 87185; or B. B. Owens, Medtronic Energy Technology, 6700 Shingle Creek Parkway, Brooklyn Center, MN 55430.

CORROSION

General Session

Papers on all aspects of low and high temperature corrosion and associated phenomena will be considered. Experimental techniques for the study of corrosion processes and corrosion products are also of interest.

Suggestions and inquiries should be sent to the Session Chairman: F. Mansfeld, Rockwell International Science Center, 1049 Camino Dos Rios, Thousand Oaks, CA 91360.

DIELECTRICS AND INSULATION/ ELECTRONICS

Dielectric Isolation

Papers are solicited from all areas relative to the preparation, properties, and application of dielectric materials for the isolation of device structures. A forum will be provided for the presentation and discussion of various isolation techniques and papers concerning all aspects of partial, vertical, or total dielectric isolation are invited. Papers dealing with the isolation of various device and circuit elements will also be considered.

Topics of interest include: 1. performance and density improvements obtained by various isolation techniques; 2. process sensitivity to yield detractors; 3. critical processing parameters, problems, and solutions; 4. new processes related to dielectric isolation; 5. new materials for isolation (either organic or inorganic); and 6. planarization techniques for VLSI technology. Emphasis will be placed on both experimental and theoretical analysis of the isolation processes and the resultant structures.

Suggestions and inquiries should be sent to the Symposium Co-Chairmen: B. Kemlage, IBM Corp., Dept. 453, Zip 48A, Hopewell Junction, NY 12533; or J. Berthold, Bell Laboratories, Rm. 7E-317, Murray Hill, NJ 07974.

Silicon Nitride Thin Insulating Films

The purpose of this symposium is to provide a forum for the presentation and discussion of topics concerning the fundamental characteristics of silicon nitride films. The objective is to link material studies and technological applications to allow for a clearer design and processing considerations for the fabrication of devices and integrated circuits (LSI/VLSI) which incorporate silicon nitride films. The symposium will include both invited and contributed papers to cover a wide range of topics related to silicon nitride, including film preparation, characterization, modeling, processing, device physics, present applications, and future requirements of the insulator in VLSI and VHSIC.

Both experimental and theoretical contributed papers are solicited from the following general areas: 1. film preparation (CVD, plasma, ion implantation, sputtering, thermal nitridation, etc.); 2. film and film/substrate interface analysis by RBS, AES, XPS, SIMS, and other new and novel analysis techniques; 3. charge trapping, characteristics and origin of traps, role of interface states, defects and impurities; 4. optical and electrical properties, electronic structure, tunneling phenomena, charge transport, and dielectric breakdown; 5. silicon nitride/silicon dioxide dual dielectrics and interfaces; 6. write/erase characteristics, retention, endurance, temperature effects, aging, modeling, reliability and radiation hardness of memory devices with active silicon nitride films; 7. silicon nitride for multilayer-metal IC's and for potential use in VLSI; 8. silicon nitride on compound semiconductors (passivation studies, interfaces, electrical and optical properties of devices); 9. plasma science and plasma processing technology for silicon nitride films; and 10. quality verification, environmental effects, new applications, and new devices.

Publication of a proceedings volume is being considered. Papers for this volume must be provided, in camera-ready form, at the time of presentation.

Suggestions and inquiries should be sent to the Symposium Co-Chairmen: V. J. Kapoor, Case Western Reserve University, Dept. of Electrical Engineering and Applied Physics, Solid State Integrated Circuit Laboratory, Cleveland, OH 44106; or H. J. Stein, Sandia National Labs, Div. 5112, Albuquerque, NM 87185.

Fourth Symposium on Plasma Processing

Papers are solicited on all aspects of the science and technology of plasma processes. Of particular interest, though not exclusively, is the application of plasma techniques to semiconductors materials including semiconductors, metals, organic and inorganic dielectrics, as well as photosensitive materials. Some suggested topics are: 1. plasma science—identification and concentration of chemically active species in the plasma, energy distribution of ions, electrons, and neutrals in and near the plasma, mass and optical spectroscopy of plasma, other plasma diagnostics techniques; 2. plasma technology—plasma etch processes, plasma initiated deposition or reaction processes, plasma enhanced CVD deposition processes, topology and its control in plasma etching and deposition; 3. plasma reactor design—design considerations, process endpoint detection, novel reactor designs; and 4. device results—dimensional control of plasma processed components, influence of plasma operating parameters on device performance including radiation damage, and novel use of plasma etching and deposition in device structures.

A proceedings volume of the symposium will be published and distributed shortly after the meeting. In order to have a paper considered for inclusion in the symposium, a written commitment is required stating that a typed, camera-ready copy of the talk, including a list of key words for the subject index, will be submitted to G. Smolinsky by June 10, 1983. The inclusion of a paper in the proceedings volume does not preclude its publication in the JOURNAL.

Suggestions and inquiries should be sent to the Symposium Co-Chairmen: (America) G. Smolinsky, Bell Laboratories, Rm. 1D-205, Murray Hill, NJ 07974 or G. C. Schwartz, IBM Corp., Zip 48A, Route 52, Hopewell Junction, NY 12533, (Europe) J. Dieleman, Philips Research Laboratories, 5600 MD, Eindhoven, The Netherlands, (Japan) J. Nishizawa, Institute of Electrical Communications, Tohoku University, 2-1-1 Katahira, Sendai 980, Japan.

DIELECTRICS AND INSULATION/ ELECTRONICS/CORROSION/ ELECTROTHERMICS AND METALLURGY/ ENERGY TECHNOLOGY

Materials and New Processing Technologies for Photovoltaics

This symposium will deal with novel aspects of materials, processing, and characterization of photovoltaic devices. Papers are especially solicited on low cost silicon technologies, novel thin film cell materials and processes including amorphous silicon and other emerging materials, and new packaging/encapsulation materials and processes. Papers on concentrator and on flat panel systems, and on low cost automated assembly techniques will be welcome, as will presentations on integrated photovoltaic systems.

Publication of a proceedings volume is being considered. Papers for this volume must be provided, in camera-ready form, at the time of presentation.

Suggestions and inquiries should be sent to the Symposium Co-Chairmen: J. A. Amick, Exxon Research and Engineering Co., P.O. Box 8, Linden, NJ 07036; V. K. Kapur, ARCO Solar Inc., 20554 Plummer St., Chatsworth, CA 91311; or J. Dietl, Heliotronic GmbH, Postfach 1129, D-8263 Burghausen, West Germany.

DIELECTRICS AND INSULATION/ ELECTROTHERMICS AND METALLURGY

High Temperature Adhesives

High temperature adhesives have been developed for a wide variety of applications. These materials, although developed for one purpose, quite often exhibit utility in many other areas. The objective of this symposium is to transcend these specialty areas, cross-fertilize, and focus on high temperature adhesives in general. Participants should become familiar with novel high temperature adhesives and techniques that will prove useful in their particular fields.

Papers are solicited on the preparation, evaluation, and/or characterization of adhesives or polymer systems which may function as adhesives. Materials in the following categories are examples: 1. thermoplastics; 2. thermosets; 3. solvent-based; and 4. hot-melts. Adhesive applications may include, but are not necessarily limited to, areas such as laminating, structural fabrication, and coatings. For the purpose of this meeting the term "high temperature" will refer to 125°C and above.

The publication of a proceedings volume is being considered.

Suggestions and inquiries should be sent to the Symposium Chairman: T. L. St. Clair, NASA Langley Research Center, MS 226, Hampton, VA 23665.

ELECTRONICS

Computer Controlled IC Processing and Monitoring

Recent advances in computer-aided IC manufacturing technology are basic to profitable production of VLSI circuits. For this symposium, papers are invited on: 1. process control of unit processes, closed loop endpoint control, techniques to establish verification of process control parameters; 2. in-process monitoring and parametric test data measurement techniques, methods of analysis of engineering data, data base formats and reduction techniques; 3. fabrication management systems for optimization of work-in-process, cycle time, fabrication yield; and 4. system approaches to computer-controlled IC facility design.

Papers on both methodology and experimental results are solicited. Invited papers will keynote the sessions. A proceedings volume, which will be available at the time of the symposium, is planned. Manuscripts must be submitted, in triplicate, by November 1, 1982, for review. Detailed instructions on manuscript preparation for the proceedings volume are available from the Symposium Co-Chairmen.

Suggestions and inquiries should be sent to the Symposium Co-Chairmen: E. H. Nicollian, Bell Laboratories, Murray Hill, NJ 07974; or P. L. Castro, Hewlett Packard Laboratories, 3500 Deer Creek Rd., Palo Alto, CA 94304.

Defects in Semiconductors

This symposium will focus on both the science and the technological implications of chemical and crystallographic defects in silicon. Among the defects of concern are oxygen, carbon, nitrogen, and other electrically "inactive" species; heavy metals, vacancies; self-interstitials; dislocations; and stacking faults. Topics appropriate for inclusion in the symposium include the origins of these defects; mechanical, chemical, and electrical effects of defects with particular emphasis on the influence of defects in semiconductor device fabrication and operation; interactions between two or more defect species; and techniques for characterizing and controlling defects. Both theoretical and experimental papers are solicited. It is expected that the papers will be grouped into cohesive sessions, each introduced by an invited state-of-the-art overview.

Publication of a proceedings volume is being considered. If a volume is published, full camera-ready manuscripts of the papers presented at the symposium would be required at the time of the meeting.

Suggestions and inquiries should be sent to the Symposium Co-Chairmen: W. M. Bullis, Fairchild Advanced Research and Development Laboratory, MS 30-402, 4001 Miranda Ave., Palo Alto, CA 94304; or L. C. Kimerling, Bell Laboratories, Rm. 1E-310, Murray Hill, NJ 07974.

III-V Opto-Electronics Epitaxy and Device Related Processes

III-V compound semiconductors are becoming increasingly more important in electronics and photonics. It is the aim of this symposium to provide a forum for the discussion of the growth and properties of bulk and epitaxial materials and device-related processes. Papers are solicited that enhance the science, technology, and understanding of III-V materials, metal-semiconductor interactions, and processing. Sessions are planned for the following topics: 1. bulk growth of III-V crystals by LEC and Bridgman; 2. liquid phase epitaxy (LPE), theoretical and experimental considerations; 3. molecular beam epitaxy (MBE), recent advances and unique capabilities; 4. chemical vapor deposition (CVD); 5. organometallic chemical vapor deposition (OMCVD); 6. metal-semiconductor interactions; Schottky barriers ohmic contacts basic studies and their effects on device performance; and 7. semiconductor processing; basic studies and the effects of device-related processing on binary, ternary, and quaternary heterojunction structures.

Each of the above sessions will open with an invited presentation which will put the topic in perspective and then will be followed by contributed papers.

A proceedings volume is planned. In order for the volume to be available at the time of the symposium, manuscripts should be submitted to the Symposium Co-Chairmen by December 1, 1982.

Suggestions and inquiries should be sent to the Symposium Co-Chairmen: V. G. Keramidas or S. Mahajan, Bell Laboratories, Murray Hill, NJ 07974.

Joint General Session

Papers that deal with all aspects of materials of interest for electronic devices including their preparation, characterization, interactions, and device applications, and whose subject matter is not covered by the special symposia are invited to be submitted to this session. Also invited are papers on the basic chemistry and physics of materials processing, and computer modeling of the formation and of the characterization of materials and devices. Of particular interest are new materials and processes.

Suggestions and inquiries should be sent to the Session Co-Chairmen: E. H. Nicollian, Bell Laboratories, Murray Hill, NJ 07974; F. N. Schwettmann, Hewlett Packard Laboratories, 3500 Deer Creek Rd., Palo Alto, CA 94304; or G. C. Schwartz, IBM Corp., Dept. 206, Bldg. 300-48A, Hopewell Junction, NY 12533.

Joint Recent News Papers Session

Recent News Papers and Extended Recent News Papers consisting of topics covered by the symposia and sessions being sponsored or co-sponsored by the Electronics and Dielectrics and Insulation Divisions are invited for presentation.

Suggestions and inquiries should be sent to the Session Chairman: W. A. Pliskin, IBM Corp., Dept. 025, Internal Zip 48A, Hopewell Junction, NY 12533. A special Call for Recent News Papers will appear in the January, February, and March 1983 issues of the JOURNAL.

ELECTROTHERMICS AND METALLURGY

High Temperature Materials Chemistry

This symposium addresses the chemical behavior of materials at high temperatures. Pertinent topics include thermodynamics and kinetics of high temperature reactions and chemical problems of materials in high temperature applications. Sessions on the following topics are planned: 1. high temperature ceramic and metal synthesis; 2. electronic materials; 3. nucleation and condensation from high temperature vapors; 4. high temperature mass spectrometry; 5. high temperature problems in coal combustion and utilization; 6. evaporation and decomposition phenomena; and 7. chemical aspects of high temperature metal-gas reactions.

Publication of a proceedings volume is being considered. Manuscripts, in camera-ready form, will be required at the time of the meeting.

Suggestions and inquiries should be sent to the Symposium Co-Chairmen: Z. A. Munir, Div. of Materials Science and Engineering, University of California, Davis, CA 95616; or D. Cubicciotti, Electric Power Research Institute, P.O. Box 10412, Palo Alto, CA 94303.

ELECTROTHERMICS AND METALLURGY/ PHYSICAL ELECTROCHEMISTRY/ BATTERY/ENERGY TECHNOLOGY

New Solid Electrolytes for Energy Conversion

Papers are solicited discussing new solid electrolytes for possible application in energy conversion technology. Three categories will be covered: 1. ceramic electrolytes; 2. glassy electrolytes; and 3. polymeric electrolytes. Of particular interest are the identification, structural and electrochemical characterization, transport mechanisms, and chemical and electrochemical stability.

The publication of a processing volume is planned.

Suggestions and inquiries should be sent to the Symposium Co-Chairmen: L. C. De Jonghe, Lawrence Berkeley Laboratory, Materials and Molecular Research Div., University of California, Berkeley, CA 94720; R. A. Huggins, Dept. of Materials Science and Engineering, Stanford University, Stanford, CA 94305; or G. C. Farrington, University of Pennsylvania, LRSM Bldg., Philadelphia, PA 19104.

ENERGY TECHNOLOGY

Novel Photoelectrochemical Synthetic Routes

This symposium will focus on new synthetic (organic and inorganic) approaches involving semiconductor electrodes in photoelectrolytic, photocatalytic, and related processes. Single crystal, polycrystalline, and particulate semiconductor systems will be emphasized. It is planned to issue a proceedings volume; final manuscripts will be required at the time of the symposium.

Suggestions and inquiries should be sent to the Symposium Co-Chairmen: H. L. Chum or A. J. Nozik, Solar Energy Research Institute, 1617 Cole Blvd., Golden, CO 80401.

General Session

Papers are solicited in areas of the energy technology not covered by current symposia. Of particular interest are photoelectrochemical energy conversion devices and novel methods for energy storage and transmission. Suggestions and inquiries should be sent to the Session Co-Chairmen: J. McBreen, Brookhaven National Laboratory, Dept. of Energy and Environment, Bldg. 801, Upton, NY 11973 or A. J. Nozik, Solar Energy Research Institute, 1617 Cole Blvd., Boulder, CO 80401.

ENERGY TECHNOLOGY/BATTERY/ DIELECTRICS AND INSULATION

Conducting Organic Polymers in Energy Conversion and Storage

The purpose of this symposium is to: 1. present, for the nonspecialist, by means of invited papers of a tutorial type, the qualitative theoretical basis of metallic and semiconducting organic and inorganic covalent polymers and related novel materials; 2. disseminate by means of invited and contributed papers the results of chemical and physical investigations and pertinent theoretical studies concerning the above materials; and 3. present by means of invited review papers the synthesis, structure, bonding, chemical and physical properties, and theory of the principal examples of the above types of materials and their application to the fabrication of photovoltaic and photoelectrochemical devices and batteries of potential technological importance. Information describing technological applications will be encouraged. It is intended that this symposium be as interdisciplinary as possible in order to promote interactions between appropriate areas of physics, chemistry, electronics, engineering, and related fields.

The subject matter for the symposium includes polymers such as $(SN)_x$, $(CH)_x$, $(C_6H_4)_x$, covalently linked metal chain compounds, conducting charge transfer complexes, and other novel related metallic and semiconducting materials.

Suggestions and inquiries should be sent to the Symposium Co-Chairmen: A. G. MacDiarmid, Dept. of Chemistry, University of Pennsylvania, Philadelphia, PA 19104; or W. M. Ayers, Energy Conversion Devices, P.O. Box 5357, North Branch, NJ 08876.

INDUSTRIAL ELECTROLYTIC

Science and Engineering of Membranes and Separators

Recent advances in the design of porous separators and high performance membranes are of important significance to several electrolytic technologies. Papers that deal with fundamental properties of these materials, as well as engineering aspects of their applications, are solicited for this symposium. The transport, equilibrium, and morphological properties of membranes/separators are of interest here, as are such diverse topics as surface treatments, concentrated solution properties, novel characterization methods, and engineering aspects of electrolytic membrane cells. Relevant technological areas include chlor-alkali production, water electrolysis (acid and alkaline systems), electrodialysis, fuel cells, and batteries.

Suggestions and inquiries should be sent to the Symposium Chairman: H. L. Yeager, Dept. of Chemistry, University of Calgary, 2500 University Dr., NW, Calgary, Alta., Canada T2N 1N4 or R. Dotson, Olin Chemicals Group, P.O. Box 248, Charleston, TN 17310.

INDUSTRIAL ELECTROLYTIC/ CORROSION/ELECTRODEPOSITION

Anode and Cathode Materials

This symposium will be concerned with anode and cathode materials used in electrochemical processes. Theoretical and experimental aspects of the subject will be included dealing with mechanisms, laboratory studies, engineering work, and applications in industrial production. Papers are solicited

on the following general topics: 1. soluble anode dissolution in electroplating and other applications; 2. insoluble anodes for the generation of gases and the electrosynthesis of organic and inorganic compounds; and 3. cathode materials for the generation of hydrogen, electroforming, electrowinning, fluidized bed electrodes, and the electrosynthesis of organic and inorganic compounds.

The symposium will consist of both invited and contributed papers.

Suggestions and inquiries should be sent to the Symposium Co-Chairmen: M. R. Tighe, Diamond Shamrock Corp., 470 Center St., Chardon, OH 44024; or D. R. Turner, Bell Laboratories, Rm. 7F-506, Murray Hill, NJ 07974.

LUMINESCENCE AND DISPLAY MATERIALS

Display Technology

The object of the symposium is to stimulate the interchange of information among workers in various aspects of display technology. Papers are solicited in the areas of liquid crystals, plasmas, vacuum fluorescence, cathodoluminescence, electroluminescence, electrochromics, electrophoretics, other electrochemical display approaches, and the addressing schemes required for the practical utilization of any of these display processes.

Papers containing new and unpublished information dealing with the above topics or any other novel display techniques will be considered.

Suggestions and inquiries should be sent to the Symposium Chairman: P. N. Yocom, RCA Laboratories, David Sarnoff Research Center, Princeton, NJ 08540.

Phosphor Synthesis and Characterization

Papers are solicited for a symposium on phosphor synthesis and characterization. The symposium is defined very broadly. New methods and processes for synthesis, comparison of luminescence behavior with preparation method or with bulk or surface structure, and methods for the characterization of phosphors are suitable subjects for papers. Some suggested topics are: alternate preparation routes to phosphor powders, properties of single crystal phosphors in comparison with powders, thin film luminescence in relation to crystal perfection and microstructure, and luminescence efficiency in relation to structural order.

Suggestions and inquiries should be sent to the Symposium Chairman: W. B. White, Materials Research Laboratory, The Pennsylvania State University, University Park, PA 16802.

General Session

Papers concerning any aspect of luminescence are invited. Groups of papers will be organized, wherever possible, into such topics as: luminescent properties of lamp cathode-ray tube and x-ray phosphors; organic and organometallic phosphors; lasers; electroluminescence, thermoluminescence, or chemiluminescence; ultraviolet phosphors and lamps; special properties or uses of luminescent materials; and luminescence theory.

Synthesis papers and display materials papers should be submitted to the appropriate special subject symposium.

Twenty-five minutes will be allotted for each paper, including discussion. Review or survey papers requiring a longer time will also be considered.

Suggestions and inquiries should be sent to the Symposium Chairman: G. R. Gillooly, General Electric Co., 1099 Ivanhoe Rd., Cleveland, OH 44110.

ORGANIC AND BIOLOGICAL ELECTROCHEMISTRY

Mechanisms and Modeling of Electrochemical Membrane Processes

This symposium will be concerned with recent progress on the mechanisms of molecular and charge transport in derivatized, biological, and polymeric membrane electrodes. Papers are solicited on the following topics, although related submissions are welcome: 1. charge and molecular transport models in membrane electrodes; 2. preparation and characterization of membrane electrodes; and 3. spectroscopic and other in situ methods for direct observance or transport phenomena in membranes.

Suggestions and inquiries should be sent to the Symposium Co-Chairmen: S. Pons, Dept. of Chemistry, University of Alberta, Edmonton, Alta., Canada T6G 2G2; J. Evans, Dept. of Chemistry, University of Minnesota, Minneapolis, MN 55455; H. Blount, Dept. of Chemistry, University of Delaware, Newark, DE 19711; or F. Hawkridge, Dept. of Chemistry, Virginia Commonwealth University, Richmond, VA 23284.

Structure and Reactivity in Organic Chemistry and Electrochemistry

This symposium will present papers dealing with the similarities and differences between homogeneous chemical reactions and electrochemical reactions of organic compounds. It is the aim of the symposium to enable a dialogue between organic chemists and electrochemists, particularly in the areas of structure-reactivity correlations. Reactions of radicals and radical ions, comparison of photochemical and electrochemical processes, of ring closure reactions and of reactions of biochemically important molecules are some of the examples, but papers are solicited covering other aspects as well.

Presentations of both invited and contributed papers are planned. A symposium volume is being considered.

Suggestions and inquiries should be sent to the Symposium Chairman: P. Zuman, Dept. of Chemistry, Clarkson College of Technology, Potsdam, NY 13676.

Ions and the Electrochemical Control of Cell Functions

The role of ions in cell regulation has been the subject of increasing study by the biological and bioelectrochemical communities. This symposium brings both disciplines together to discuss the mechanisms of these interactions. In vitro and in vivo studies will be reviewed with emphasis upon the biological transduction of ion and relevant hormone interactions at cell surfaces and junctions for functional activity. Both normal and neoplastic cell development will be among the topics to be covered. Electrochemical studies of the kinetics and mechanisms of ionic interactions at cell membranes and their extension to therapeutic applications will be discussed.

Suggestions and inquiries should be sent to the Symposium Co-Chairmen: A. L. Boynton, National Research Council of Canada, Animal and Cell Physiology Section, Div. of Biological Sciences, Ottawa, Ont., Canada K1A 0R6; or A. A. Pilla, Bioelectrochemistry Laboratory, Dept. of Orthopedic Surgery, Mount Sinai School of Medicine, 100th St. and Madison Ave., New York, NY 10028.

General Session

Suggestions and inquiries should be sent to the Session Chairman: J. H. Wagenknecht, Monsanto Co., 800 North Lindbergh Blvd., St. Louis, MO 63166.

PHYSICAL ELECTROCHEMISTRY

The Chemistry and Physics of Electrocatalysis

This symposium will focus on the fundamental chemical and physical factors responsible for the catalysis of electrochemical reactions at the electrode-electrolyte interface. Of particular interest are the interactive roles of the following in determining adsorption and rates of electron transfer at the interface: 1. the chemical composition of the electrode and the electronic and crystallographic or molecular structure of its surface; and 2. the chemical composition and structure of the Helmholtz layer of the electrolyte.

Both experimental and theoretical aspects will be considered. Invited papers will emphasize recent fundamental advances in interfacial electrochemistry, surface chemistry, and surface physics (including characterization techniques) and their mutual significance for electrocatalysis and heterogeneous chemical catalysis. Selected contributed papers will also be included. Publication of a proceedings volume is being considered. Manuscripts will be required by May 1, 1983.

Suggestions and inquiries should be sent to the Symposium Co-Chairmen: J. D. E. McIntyre and E. B. Yeager, Dept. of Chemistry, Case Western Reserve University, Cleveland, OH 44106; or M. J. Weaver, Dept. of Chemistry, Michigan State University, East Lansing, MI 48824.

Fourth International Symposium on Molten Salts

This symposium will cover all aspects of molten salt studies. Special emphasis will be given to three subjects: 1. molten salts containing aluminum ions; 2. organic reactions and catalysis in molten salts; and 3. fundamental aspects of molten salt chemistry.

Some topics suitable for this symposium include: 1. studies and uses of cryolite and chloroaluminate melts; 2. studies of organic reactions and catalysis in molten salt media; 3. measurements, concepts, and theories of electrochemical, thermodynamic, structural, spectroscopic, and transport properties of melts; 4. advances in the scientific and technological applications of molten salt media; and 5. the chemistry and physics of corrosion in molten salts.

A proceedings volume is being planned.

Suggestions and inquiries should be sent to the Symposium Co-Chairmen: M. Blander or M. L. Saboungi, Argonne National Laboratory, Argonne, IL 60439; G. P. Smith, Oak Ridge National Laboratory, P.O. Box X, Oak Ridge, TN 37830; G. Mamantov, Dept. of Chemistry, University of Tennessee, Knoxville, TN 37916; or K. E. Johnson, Dept. of Chemistry, University of Regina, Regina, Sask., Canada S4S 0A2.

General Session

Papers concerning any aspect of physical electrochemistry not included in the topic areas of the symposia are welcome.

Suggestions and inquiries should be sent to the Session Chairman: R. A. Osteryoung, Dept. of Chemistry, State University of New York, Buffalo, NY 14214.

---

a.) For receipt no later than December 1, 1982, submit a 75-word abstract of the paper to be delivered on the attached overleaf.
b.) For receipt no later than January 1, 1983, submit two copies of an extended abstract, 500-1000 words.
c.) Send all abstracts to The Electrochemical Society, Inc., 10 South Main Street, Pennington, NJ 08534-2896 with the exception of Recent News Papers. For Recent News Papers see preceding pages.

Use overleaf in submitting your abstract for
The 1983 Spring Meeting
of
The Electrochemical Society, Inc.
to be held at the
St. Francis Hotel
San Francisco, California
May 8-13, 1983

75-Word Abstract Form

(Deadline for receipt—December 1, 1982)

SAN FRANCISCO, CALIFORNIA, MEETING—MAY 8-13, 1983

Submit to: The Electrochemical Society, Inc.
10 South Main Street, Pennington, NJ 08534-2896

Schedule for ..... of .....
Symposium **ECS Division**

Abstract No. .....
(do not write in this space)

(Title of paper) .....

.....

(Authors) *(Underline name of author presenting paper)* .....

.....

(Business Affiliation and Address) .....

.....

.....
(ZIP Code) (Tel. No.)

(Type abstract in this area—double spaced.)

Do you require any audiovisual equipment?
☐ **35 mm (2 x 2 in.) slide projector**
☐ **Vu-Graph**
☐ **other (specify)**
Is a full length paper on this work to be submitted for Society Journal publication?
☐ **Yes** ☐ **No**

Papers presented before a Society technical meeting become the property of the Society and may not be published elsewhere without written permission of the Society. Papers presented at Society technical meetings must be authored by a member or sponsored by an active member.

.....
Insert name of Society member author or sponsor

THE ELECTROCHEMICAL SOCIETY PATRON MEMBERS

Bell Laboratories
Murray Hill, NJ

Dow Chemical Co.
Inorganic Chemicals Dept.
Midland, MI

Exxon Research and Engineering Co.
Corporate Research
Advanced Energy Systems Laboratory,
Materials and Catalysis Sciences Laboratory
Linden, NJ
Technology Department
Chemical Engineering Technology Div.
Materials Technology Div.
Florham Park, NJ

General Electric Co.
Battery Business Dept., Gainesville, FL
Chemical Laboratory, Knolls Atomic Power Laboratory,
Schenectady, NY
Lamp Div., Cleveland, OH
Materials & Process Laboratory, Large Steam
Turbine-Generator Dept., Schenectady, NY
Research and Development Center,
Chemical Systems & Technology
Laboratory & Physical Chemistry Laboratory,

General Electric Co. (continued)
Signal Processing & Communication Laboratory,
Schenectady, NY
Semiconductor Products Dept.,
Syracuse, NY

International Business Machines Corp.
New York, NY

INCO Research and Development Center
Suffern, NY

Olin Corp.
Chemicals Div.
Charleston Technology Center
Charleston, TN

Philips Research Laboratories
Eindhoven, The Netherlands

Tadiran, Israel Electronics Industries, Ltd.
Tel Aviv, Israel

Westinghouse Electric Corp.
Electronic Tube Div., Elmira, NY
Lamp Div., Bloomfield, NJ
Semiconductor Div., Youngwood, PA
Research Laboratories, Pittsburgh, PA

THE ELECTROCHEMICAL SOCIETY SUSTAINING MEMBERS

The Aerospace Corp.
Los Angeles, CA

Airco Industrial Gases
Murray Hill, NJ

Airco Speer Carbon Graphite
St. Marys, PA

Allied Corporation
Syracuse Research Laboratories
Solvay, NY

Aluminum Co. of America
New Kensington, PA

Aluminum Co. of Canada, Ltd.
Montreal, Que., Canada

AMAX Inc.
Greenwich, CT

AMP Inc.
Harrisburg, PA

Analog Devices, Inc.
Norwood, MA

Applied Materials, Inc.
Santa Clara, CA

Asahi Chemical Industry Canada, Ltd.
Toronto, Ont., Canada

ASARCO, Inc.
South Plainfield, NJ

Battelle Memorial Institute
Columbus, OH

Battery Technology Co.
A Division of Duracell International
Tarrytown, NY (2 memberships)

Bell-Northern Research
Ottawa, Ont., Canada

Boeing Co.
Seattle, WA

The Borg-Warner Corp.
Roy C. Ingersoll Research Center
Des Plaines, IL

BP Research Centre
Middlesex, England

Brown, Boveri & Co., Ltd.
Research Center
Baden, Switzerland

C-I-L Inc.
Industrial Chemicals Div.
Montreal, Que., Canada

Chloride Automotive Batteries
Tampa, FL

Cominco Ltd.
Trail, B.C., Canada

Corning Glass Works
Corning, NY

Crawford & Russell Inc.
Stamford, CT

Diamond Shamrock Corp.
Painesville, OH (2 memberships)

Duro-Test Corp.
North Bergen, NJ

Eagle-Picher Industries, Inc.
Electronics Div.
Joplin, MO

Eastman Kodak Co.
Rochester, NY

EG&G Princeton Applied Research Corp.
Princeton, NJ

Electric Power Research Institute
Palo Alto, CA

Electrochemical Technology Corp.
Seattle, WA

Eltra Corp.
Prestolite Div., Toledo, OH
C&D Batteries, Conshohocken, PA

Energy Development Associates
A Gulf and Western Co.
Madison Heights, MI

Ever Ready Co. (Holdings) Ltd.
Whetstone, London, England

Exmet Corp.
Bridgeport, CT

SUSTAINING MEMBERS (CONTINUED)

Fairchild Camera & Instrument Corp.
Research & Development Laboratory
Palo Alto, CA

FMC Corp.
Inorganic Chemicals Div.
Buffalo, NY

Ford Motor Co.
Dearborn, MI

The Gates Corporation
Denver, CO

General Motors Corp.
Delco-Remy Div., Anderson, IN
Research Laboratories Div.
Warren, MI

Gould Inc.
Gould Laboratories—
Energy Research
Rolling Meadows, IL

Great Lakes Carbon Corp.
New York, NY

GTE Laboratories
Waltham, MA

GTE Sylvania Inc.
Chemical & Metallurgical Div.
Towanda, PA

The Harshaw Chemical Co.
Cleveland, OH

Heliotronic GmbH
Burghausen, Germany

Hewlett Packard Co.
Loveland, CO

Hewlett Packard Laboratories
Palo Alto, CA

Hill Cross Co., Inc.
West New York, NJ

Hoechst-Uhde Corp.
Englewood Cliffs, NJ

Honeywell, Inc.
Power Sources Center
Horsham, PA

Hooker Chemical Corp.
Niagara Falls, NY (2 memberships)

Hughes Research Laboratories
Div. of Hughes Aircraft Co.
Malibu, CA

IMI Marston Limited
Wolverhampton, England

Imperial Clevite, Inc.
Technology Center
Cleveland, OH

INCO ElectroEnergy Corp.
Engineering & Development Center
Ray-O-Vac Corp.
Madison, WI
Engineering & Development Center
Exide Corp.
Yardley, PA

International Lead Zinc Research Organization, Inc.
New York, NY

International Minerals and Chemical Corp.
Electrochemical Div.
Orrington, ME

Johnson Controls, Inc.
Milwaukee, WI

Kaiser Aluminum & Chemical Corp.
Pleasanton, CA

KBI
a division of Cabot Corp.
Boyertown, PA

KW Battery Co.
Skokie, IL

Arthur D. Little, Inc.
Cambridge, MA

Lockheed Missiles & Space Co., Inc.
Research Laboratory
Palo Alto, CA

Marathon Battery Co.
Waco, TX

Matsushita Electric Industrial Co., Ltd.
Osaka, Japan

Mead Advanced Systems Research and Development Laboratories
Dayton, OH

Medtronic Energy Technology
Minneapolis, MN

Mepco/Electra, Inc.
Columbia, SC

Microwave Associates, Inc.
Burlington, MA

Molycorp, Inc.
New York, NY

Monsanto Co.
St. Louis, MO

Motorola Inc.
Phoenix, AZ

M&T Chemicals Inc.
Detroit, MI

NIFE Jungner AB
Oskarshamn, Sweden

Noranda Research Centre
Pointe Claire, Que., Canada

Occidental Research Corp.
La Verne, CA

Olin Corp.
Metals Research Laboratories
New Haven, CT

Owens-Illinois Inc.
Toledo, OH

Oxy Metal Industries Corp.
Warren, MI

Perkin-Elmer Corp.
Norwalk, CT

Phelps Dodge Refining Corp.
Maspeth, NY

Philips Laboratories, Inc.
Briarcliff Manor, NY

PPG Industries, Inc.
Chemical Div.
Pittsburgh, PA

Prototech Co.
Newton Highlands, MA

Public Service Electric and Gas Co.
PSE&G Research Corp.
Newark, NJ

RCA Corp.
Color Picture Tube Div.
Lancaster, PA

Reynolds Metals Co.
Reduction Research Div.
Sheffield, AL

Rockwell International
El Segundo, CA

SAFT America, Inc.
Valdosta, GA

Sandia National Laboratories
Albuquerque, NM

Sanyo Electric Co., Ltd.
Shioya Research Center
Kobe, Japan

J. C. Schumacher Co.
Oceanside, CA

SCORE, Inc.
Cockeysville, MD

Shipley Company, Inc.
Newton, MA

Siemens Aktiengesellschaft
Munich, Germany

Signetics Corp.
Sunnyvale, CA

Siltec Corp.
Menlo Park, CA

Sperry Research Center
Sudbury, MA

Sprague Electric Co.
North Adams, MA

Standard Telecommunication Laboratories Ltd.
Essex, England

Stauffer Chemical Co.
Dobbs Ferry, NY

St. Joe Minerals Corp.
Monaca, PA

Tektronix, Inc.
Beaverton, OR

Teletype Corp.
Skokie, IL

Texas Instruments Inc.
Attleboro, MA
Dallas, TX

Tokyo Shibaura Electric Co., Ltd.
Toshiba Research and
Development Center
Kawasaki, Japan

Toyota Central Research and Development Labs, Inc.
Nagoya, Japan

Union Carbide Corp.
Battery Products Div.,
Corporate Research Dept.
New York, NY

United States Steel Corp.
Research Laboratory
Monroeville, PA

Varian Associates
Palo Alto, CA

Wacker Chemitronic
Burghausen, Germany

Western Electric
Princeton, NJ

Xerox Corp.
Webster Research Center
Rochester, NY

Yardney Electric Corp.
Pawcatuck, CT

Yuasa Battery Co., Ltd.
Osaka, Japan

14.8.85